# HB2014

## 54th ICFA
## Advanced Beam Dynamics
### Workshop on High-Intensity, High Brightness and High Power Hadron Beams

## 10-14 November 2014

*hosted by the*
### Facility for Rare Isotope Beams

**Kellogg Hotel & Conference Center**
**East Lansing, MI**

## Plenary Speakers

Richard Baartman (TRIUMF)

Riccardo de Maria (CERN)

Nobuhisa Fukunishi (RIKEN)

Stuart Henderson (FNAL)

Hideaki Hotchi (J-PARC)

Mats Lindroos (ESS)

Thomas Roser (BNL)

Peter Spiller (GSI)

Jie Wei (MSU)

Hongwei Zhao (IMP)

*photo courtesy of MSU Communications and Brand Strategy*

## MICHIGAN STATE
### UNIVERSITY

Abstract Deadline: 11 August 2014
Early Registration Deadline: 12 September 2014

FRIB

ICFA

## frib.msu.edu/hb2014

# Foreword

The 54th ICFA Advanced Beam Dynamics Workshop on High Intensity, High-Brightness and High-Power Hadron Beams took place on 10-14 November 2014 in East Lansing, Michigan. The workshop was hosted by the Facility for Rare Isotope Beams (FRIB), and is a continuation of the successful biennial HB workshop series started in 2002.

HB2014 keeps the traditions in the workshop series to provide a platform for presenting and discussing new progresses, status and future developments of high-intensity, high-brightness and high-power hadron beams, including beam physics in circular and linear hadron machines, technical systems and accelerator projects (under construction or in design) around the world. The workshop venue was the Kellogg Center Hotel and Conference Center located on the campus of Michigan State University with a tour of FRIB, the cutting-edge research facility currently under construction on the final day of the workshop. There were 139 registered participants.

The five day workshop began with a plenary session comprising 9 invited talks followed by poster session. The following three days were dedicated to two parallel sessions organized by six working groups, which included 98 talks and working group discussions. A majority of the oral presentations were invited by the working group conveners, and the contributed orals were selected from the submitted abstracts. On the final day, summary talks were presented by the working group conveners.

Following its precedent HB workshops, HB2014 proved to be a successful and fruitful workshop that highlighted the rapid and comprehensive progress made in high-intensity hadron accelerators from around the world. With new projects evolving, the growing interest in the field is further made evident by the high participation at the HB series.

The proceedings, which include copies of presentations are available on the JACoW website.

During the IOC Meeting at HB2014, the next HB workshop (HB2016) was determined to be held in Malmö, Sweden. It follows the tradition of the HB workshops biennial cycle rotating among the three regions (Asia, Europe and North America).

We look forward to seeing you in Malmö.

Yoshishige Yamazaki
HB2014 IOC Chair

Yan Zhang
HB2014 LOC Chair

# Contents

Contents

Contents

## International Organizing Committee (IOC)

| | | | |
|---|---|---|---|
| Caterina Biscari | INFN, Italy | Jean-Michel Lagniel | CEA-Saclay, France |
| Alex Chao | SLAC, USA | Yoshi Mori | Kyoto University, Japan |
| Jia-er Chen | Peking University, China | Christopher Prior | RAL, UK |
| Yong Ho Chin | KEK, Japan | Ji Qiang | LBNL, USA |
| Weiren Chou | FNAL, USA | Thomas Roser | BNL, USA |
| Ronald Davidson | PPPL, USA | Amit Roy | IUAC, India |
| John Galambos | ORNL, USA | Lawrence Rybarcyk | LANL, USA |
| Roland Garoby | CERN, Switzerland | Mike Seidel | PSI, Switzerland |
| Ingo Hofmann | GSI, Germany | Jingyu Tang (Co-Chair) | IHEP, China |
| Stephen Holmes | FNAL, USA | Maury Tigner | Cornell University, USA |
| Andrew Hutton | JLAB, USA | Jiuqing Wang (Co-Chair) | IHEP, China |
| Sergey Ivanov | IHEP, Russia | Jie Wei | FRIB, USA |
| Ji-Ho Jang | KAERI, Korea | Bill Weng | BNL, USA |
| In Soo Ko | PAL, Korea | Yoshishige Yamazaki | FRIB, USA |

## Local Organizing Committee (LOC)

| | |
|---|---|
| Yoshishige Yamazaki (IOC Conference Chair) | MSU, USA |
| Yan Zhang (LOC Conference Chair) | MSU, USA |
| Chris Compton | MSU, USA |
| Larry Hoff | MSU, USA |
| Masanori Ikegami | MSU, USA |
| Steve Lund | MSU, USA |
| Amy McCausey (Scientific Secretariat, Conference Coordinator & JACow Editor) | MSU, USA |

Preface
Group Picture

# THE HIGH LUMINOSITY CHALLENGE:
# POTENTIAL AND LIMITATIONS OF HIGH INTESITY HIGH
# BRIGHTNESS BEAMS IN THE LHC AND ITS INJECTORS*

R. De Maria, G. Arduini, D. Banfi, J. Barranco, H. Bartosik, E. Benedetto, R. Bruce, O. Brüning,
R.Calaga, F. Cerutti, H. Damerau, L. Esposito, S. Fartoukh, M. Fitterer, R. Garoby, S. Gilardoni,
M. Giovannozzi, B. Goddard, B. Gorini, K. Hanke, G. Iadarola, M. Lamont, M. Meddahi, E. Métral,
B. Mikulec, N. Mounet, Y. Papaphilippou, T. Pieloni, S. Redaelli, L. Rossi, G. Rumolo,
E. Shaposhnikova, G. Sterbini, E. Todesco, R. Tomás, F. Zimmermann (CERN, Geneva),
A. Valishev (Fermilab, Batavia, Illinois)

*Abstract*

High-intensity and high-brightness beams are key ingredients to maximize the LHC integrated luminosity and to exploit its full potential. This contribution describes the optimization of beam and machine parameters to maximize the integrated luminosity as seen by the LHC experiments, by taking into account the expected intensity and brightness reach of LHC itself and its injector chain as well as the capabilities of the detectors for next run and foreseen upgrade scenarios.

## INTRODUCTION

The LHC proton-proton programme aims at steadily increasing the luminosity production rate in the next two decades, in order to reach the target of 3000 fb$^{-1}$ with the High-Luminosity LHC project (HL-LHC) [1, 2]. High intensity, high brightness beams are key ingredients to reach these goals. Several interventions associated to long shutdowns (LS), will address and overcome several limitations. Notably the LHC injector upgrade project (LIU) [3, 4], scheduled for implementation during LS2, aims at providing the most intense and bright beams that LHC can store, accelerate, and collide with high efficiency and reliability. In the following we discuss the intensity and brightness limitations in LHC and injectors, together with their potential in terms of expected integrated luminosity for ATLAS and CMS experiments.

## LHC LIMITATIONS

The LHC has being designed to store and collide 2808 25 ns spaced bunches populated by 1.1 10$^{11}$ protons in two counter-rotating beams. Magnet apertures have been specified to allow a normalized emittance of 3.75 μrad to be used operationally [5]. Together with β*=55 cm, the beam parameters allow reaching the so-called nominal luminosity of 1 10$^{34}$ cm$^{-2}$s$^{-1}$. During Run I the LHC operated at 50 ns and with up to 1.7 10$^{11}$ protons per bunch (ppb) in 1380 bunches, which represented the best parameters to maximize the integrated luminosity in the presence of strong e-cloud effects observed and anticipated for 25 ns beams [6]. However, 50 ns beams saturate quickly the reconstruction capabilities of the detectors due to the large pile up of events per crossing. Therefore, Run II will be devoted to establish 25 ns bunch spacing beams to aim at doubling the integrated luminosity for about the same pile up, thanks to the higher-than-nominal bunch intensities that may be obtained from the injectors' chain after mitigation measures addressed during LS1, and an aggressive plan of scrubbing with special beams [7].

On a longer time scales, it is expected to be possible to bring in collision 2.2·10$^{11}$ ppb for a total of about 1 A of circulating beam current, provided that: a) e-cloud issues are solved by increasing the cooling capacity of the standalone quadrupoles (possibly including also coating of the upgraded ones), and by efficient scrubbing of the arcs; b) coupled-bunch instabilities are stabilized by the transverse damper; c) single-bunch instabilities can be stabilized by means of Landau octupoles or by the head-on beam-beam tune spread in a collide-and-squeeze operation mode (see Ref. [8] and references therein). It is expected that 5% of the total intensity is lost during the whole cycle, but keeping and average lifetime below 22 h and in any case never lower than 0.2 h.

Large bunch intensities associated with small emittance result also in large emittance blow-up due to intra-beam scattering (IBS), which has to be added to that generated by unknown noise sources (about 10 % from injection to stable beam and more in the vertical plane). Figure 1 shows the expected horizontal emittance blow-up as predicted by an IBS model through an injection, ramp and squeeze cycle [9], to which a 10 % should be added to account for observed and unknown sources of emittance growth. High brightness beams, in particular those that can be obtained with small emittance, may surpass the damage limit of the injection protection devices in case of failure scenarios, because of the energy density. A programme to replace these devices with more robust material is foreseen for after LS2 [10]. Nonetheless, it is worth noting that small emittances, even if not completely exploitable due to, e.g., IBS effects, provide a natural safety margin against growth effects. For large emittance, the very good alignment of the LHC magnets resulted in ample margins to fit comfortably nominal emittance beams with the typical injection oscillations.
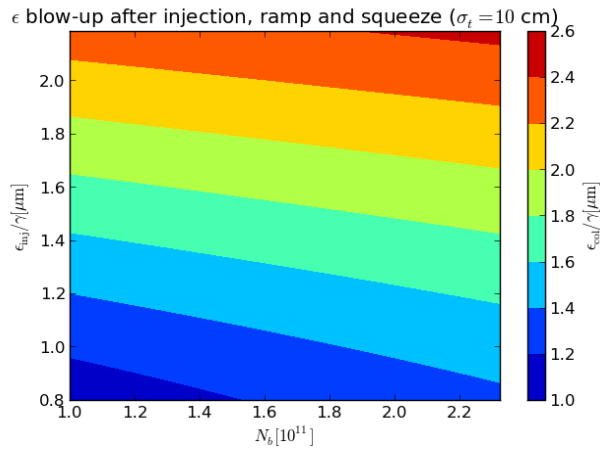
Figure 1: IBS emittance growth through injection, ramp and squeeze as a function of the injected emittance and bunch population for longer-than-nominal bunches. The emittance growth can be fairly fitted in almost all the parameter space by $\Delta\epsilon \approx 0.2\ \mu m \cdot N_b/\epsilon_{inj}$, where $N_b$ is the bunch population in units of $10^{11}$ and $\epsilon_{inj}$ is the emittance in units of $\mu m$.

## INJECTORS' LIMITATIONS

LHC injectors existed long before the LHC ring and served former experiments, while now provide beams also to fixed target experiments at different extraction energies. The injector chains for proton LHC beams [11] starts with Linac2 that provides 50 MeV bunches to the four rings the PSB, which accelerates them to 1.4 GeV for the injection of 4+2 bunches in two PS injections. During the PS cycles, the injected bunches are further split multiple times to obtain a train of 72 bunches with a 25 ns structure that is injected from 2 or 4 times in the SPS at 26 GeV. The SPS accelerates the bunch trains that are injected 12 times to fill the LHC. The injector chain proved already to be able to provide beams that exceed the nominal LHC beams [12]. Further progress are expected during the Run II thanks to an alternative beam production scheme called BCMS that allows to inject less bright beams in the PSB for the same final intensity in the SPS thanks to 4+4 bunches injected in the PS and a reduced number of longitudinal bunch splitting [13]. The cost is however producing fewer bunches per train, resulting in less bunches available in the LHC. Some of the known injector limitations will be further mitigated by the LIU project that with the new Linac 4 [14], the PS injection energy increase to 2 GeV [15] and the upgrade of the SPS RF system [16] will lower the brightness limitations of the Booster and PS and increase the maximum intensity in the SPS (see Ref. [17] and reference therein). It is possible to summarize the beam parameter for different scenarios configurations by a brightness limitation coming from either the Booster or

the PS and a total intensity limitation given by the accelerating system of the SPS [18]. Figure 2 shows a synthesis of the above-mentioned limitations as a function of injected emittance and bunch population for scenarios post-LS1 and post-LS2 on top of the integrated luminosity expectations of the LHC that will be discussed in the next section.

## LUMINOSITY POTENTIAL REACH

The LHC hosts four detectors: ATLAS and CMS for high luminosity collision, LHCb for precise measurements at lower luminosity and Alice devoted to the Heavy Ion program. The experiments require the maximum usable integrated luminosity not exceeding the event pile-up or peak luminosity limits [19]. The present limits need to be increased after LS3 (with about 300 fb[-1] accumulated) in order to keep increasing the statistical significance of the acquired data, that will otherwise saturate at constant luminosity. The HL-LHC upgrade foresees both an upgrade of the experiments [20] and of the LHC ring to fulfil the goal of reaching 3000 fb[-1] in the following decade of LHC operations thanks not only to the increased intensity but also to the reduction of $\beta^*$ and the installation of crab cavities (see Ref. [21] and reference there in). Table 1 shows the present and upgraded pile-up and luminosity limits.

Table 1: Assumed detector limits for the LHC after LS1 and after LS3 in terms of maximum average event pile-up or maximum luminosity

| Exp. | LHC | HL-LHC |
|------|-----|--------|
| ATLAS | 50 events/crossing | 140 events/crossing |
| CMS | 50 events/crossing | 140 events/crossing |
| LHCb | 4 to 6 $10^{32}$ cm$^{-2}$s$^{-1}$ | 4.5 events/crossing |
| Alice | 5 $10^{29}$ to 2 $10^{30}$ cm$^{-2}$s$^{-1}$ | 2 $10^{31}$ cm$^{-2}$s$^{-1}$ |

The LHC annual operation planning consists in about 160 days of scheduled physics time and the rest is needed for shutdown, maintenance, intensity ramp-up and machine development. The registered performance efficiency is around 50 % due to faults of several origins [22]. The minimum turnaround time is estimated to be about 3 hours [23]. The maximum number of bunches depends on the production scheme. The standard one is favoured with 2748 bunches over the 2608 of the BCMS, due to the larger number of PS injections needed to fill the SPS and correspondingly more gaps in the LHC filling scheme [24].
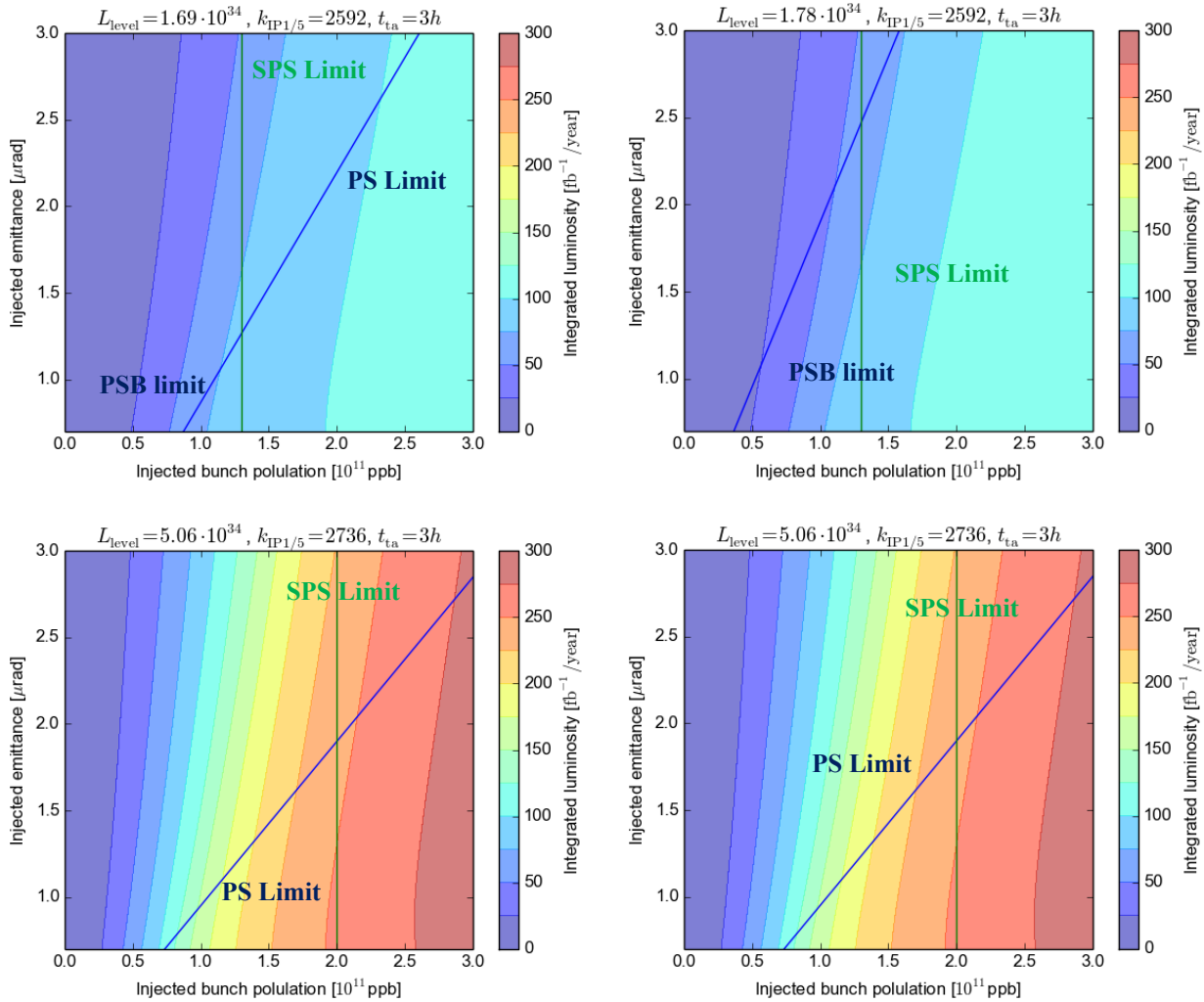
Figure 2: Yearly luminosity expectation as a function of the injected emittance and bunch population from the injectors for different post-LS1 (top, β*=60 cm) and post-LS3 (bottom, β*=15 cm, crab cavities) scenarios with the BCMS (left) and standard (right) beam production scheme for the same pile up limit. The luminosity model only includes burn-off and injection to stable beam expected losses and emittance blow-up (IBS plus noise sources). 80 days of continuous successful fills are assumed resulting from 160 days of scheduled physics and 50% of performance efficiency. The green lines represent the bunch population limitation of the SPS and the blue lines the brightness limit in the PSB and PS.

For a given scenario it is possible to compare the brightness curves obtainable by the experiments and the expected yearly-integrated luminosity in order to identify the optimal working point. Figure 2 shows the expected yearly luminosities using a simple luminosity evolution model that includes only the burn-off [25] as a function of the injected emittance and intensity assuming the 10 % of emittance blow-up plus IBS and 5 % losses. This simplified model is realistic in the parameter range of interest, although is optimistic for low emittance beams for which the IBS growths during collision contribute to decrease the luminosity lifetime, which is partially restored by radiation damping at 7 TeV. Table 2 shows the expected daily luminosities with a more refined differential model that includes burn-off, IBS and synchrotron radiations. From the plots one can conclude that for any scenario the optimal point is when the brightness is larger with the maximum intensity. The BCMS scenario, although offering higher brightness, pays a large price due to the smaller number of bunches, which still makes it attractive for after LS2, but it is definitely less performing for the HL-LHC case for which the luminosity lifetime is the only lever arm to reduce the number of fills per year. It has to be noted that for the HL-LHC it is essential to be able to obtain long fills as shown in Table 2. Due to the key role of bunch intensity on the integrated luminosity, an alternative scenario, in which a 200 MHz main RF system is installed in the LHC ([26], and references therein) in the LHC, is under study and can potentially allow an increase in the injected intensity from the SPS, although studies needs to confirm it. The system,

Table 2: Daily luminosity expectation for different LHC scenarios Post LS1 and Post LS2 by using differential luminosity model that includes burn-off, IBS and radiation damping

| Scenario | Bunch Spacing (ns) | Bunch Population $(10^{11})$ | Production scheme | $\varepsilon_{coll}$ ($\mu$m) | Pile-up Max/Lev. | Daily Luminosity (fb$^{-1}$) | Fill duration (h) | Levelled time (h) |
|---|---|---|---|---|---|---|---|---|
| LHC 6.5 TeV $\beta^*$=60 cm | 25 | 1.2 | Standard | 2.8 | 30/50 | 0.58 | 10.1 | no level |
| | | | BCMS | 1.7 | 50/50 | 0.78 | 7.5 | no level |
| | 50 | 1.6 | Standard | 2.0 | 76/50 | 0.53 | 8.1 | 5.6 |
| | | | BCMS | 1.6 | 95/50 | 0.52 | 7.8 | 4.4 |
| HL-LHC 7 TeV $\beta^*$=15 cm | 25 | 1.9 | Standard | 2.3 | 419/140 | 2.99 | 7.2 | 5.7 |
| | | | BCMS | 1.9 | 510/140 | 2.93 | 7.8 | 6.7 |
| | 25 | 2.2 | Standard | 2.5 | 517/140 | 3.17 | 8.6 | 7.3 |
| | 50 | 3.5 | Standard | 3.0 | 517/140 | 1.7 | 15 | 14.1 |

together with the existing 400 MHz RF system, could allow increasing the bunch length to reduce electron cloud effects, reduce IBS growth rates, and provide flat longitudinal bunch charge density. Yet another bunch production scheme called 8b+4e [27], which replaces few bunches with empty buckets in 72 bunch trains, can substantially decrease the electron cloud thank to the increase gaps at the cost of 30% less bunches and therefore being half-way in between 25 ns and 50 ns integrated luminosity expectations.

## CONCLUSION

The LHC and HL-LHC rely on high brightness high intensity beams to fulfill the target performance, thanks to the upgrade plans involving not only the LHC ring, but also the whole injectors' chain, together with the progress in understanding and overcoming the potential performance limitations. At constant brightness, larger intensity offers the best performance reach when coupled with long fills, thanks to the larger luminosity lifetime that compensates the physics efficiency loss due to the turnaround time. Conversely, if unexpected beam dumps are very frequent, brightness through low emittance is competitive if it also contributes to increase the reliability. If lower emittance is associated with smaller number of bunches, the brightness gains is outweighed by the resulting smaller leveled luminosity leading to overall smaller integrated luminosity in HL-LHC scenarios. Gains from very low emittance are also mitigated by early blow-up due to IBS.

## REFERENCES

[1]  L. Rossi, "LHC Upgrade Options and Plans", in Proceedings of IPAC2011, San Sebastian, Spain.
[2]  HL-LHC web site http://cern.ch/HiLumiLHC
[3]  R. Garoby, "Plans for the upgrade of the LHC injectors", in Proceedings of IPAC2011, San Sebastian, Spain.
[4]  LIU web site http://cern.ch/liu-project
[5]  O. Brüning, et al. (eds.), "LHC Design Report, Vol. 1: the LHC main ring", CERN-2004-003-V-1 (2004).
[6]  G. Iadarola et al. "Analysis of the electron cloud observations with 25 ns bunch spacing at LHC", in proceedings of IPAC2014, Dresden, United States, 2014.
[7]  G. Iadarola and G. Rumolo, "Scrubbing: Expectations and Strategy, Long Range Perspective", presented at the LHC Performance Workshop, Chamonix, 2014.
[8]  G. Arduini et al., "HL-LHC Preliminary Design Report, Chapter 2", to be published.
[9]  R. Tomás, "IBS blow-up estimates and alternative scenarios for HL-LHC", 17th HiLumi WP2 Task Leader Meeting.
[10] V. Kain, "Concerns on low emittance beams", presented at the LHC Performance Workshop, Chamonix, 2014.
[11] M. Benedikt et al. (eds.), "LHC Design Report, Vol. 3: the LHC injector chain", CERN-2004-003-V-3 (2004).
[12] Y. Papaphilippou, "Operational Beams for the LHC", presented at the LHC Performance Workshop, Chamonix, 2014.
[13] H. Damerau et al., "RF manipulations for higher beam brightness LHC-type beams", CERN-ACC-2013-0210.
[14] F. Gerigk and M. Vretenar (eds.), "Linac4 Technical Design Report", CERN-AB-2006-084 ABP/RF.
[15] M. Giovannozzi et al. "Possible improvements to the existing pre-injector complex in the framework of continued consolidation", presented at the LHC Performance Workshop, Chamonix, 2010.

[16] E. Shaposhikova et al., "Upgrade of the 200 MHz RF system in the CERN SPS for future high intensity beams", in proceedings for IPAC2011, San Sebastian, Spain, 2011.

[17] M. Meddahi et al., "LIU Technical design report", to be published.

[18] G. Rumolo, "Protons: Baseline and Alternatives, Studies Plan", presented at the LHC Performance Workshop, Chamonix, 2014.

[19] E. Meschi, "Experiments' Expectations for 2015", presented at the LHC Performance Workshop, Chamonix, 2014.

[20] R. Jacobsson, "Plans and physics outlook for non-high luminosity experiments until and after LS3", in the proceedings of "RLIUP: Review of LHC and Injector Upgrade Plans", CERN-2014-006.

[21] S. Fartoukh and F. Zimmermann, "The HL-LHC accelerator physics challenges", CERN-ACC-2014-0209.

[22] G. Arduini et al., "PICS: what do we gain in beam performance", in the proceedings of "RLIUP: Review of LHC and Injector Upgrade Plans", CERN-2014-006.

[23] M. Lamont, "How to reach the required availability in the LHC era", in the proceedings of "RLIUP: Review of LHC and Injector Upgrade Plans", CERN-2014-006.

[24] B. Gorini, private communications.

[25] O. Brüning, F. Zimmermann, "Parameter Space for the LHC High-Luminosity Upgrade", in proceedings of IPAC2012, New Orleans, United States, 2012.

[26] R. Tomas et al., "HL-LHC: Exploring alternative ideas", in the proceedings of "RLIUP: Review of LHC and Injector Upgrade Plans", CERN-2014-006.

[27] H. Damerau, "LIU: Exploring Alternative Ideas", in the proceedings of "RLIUP: Review of LHC and Injector Upgrade Plans", CERN-2014-006.

# LESSONS FROM 1-MW PROTON RCS BEAM TUNING

Hideaki Hotchi[#] for the J-PARC RCS beam commissioning group

J-PARC center, Japan Atomic Energy Agency, Tokai, Naka, Ibaraki, 319-1195 Japan

## Abstract

Via a series of the injector linac upgrades in 2013 and 2014, the J-PARC 3-GeV RCS got all the hardware parameters required for the 1-MW design beam operation. This paper presents the recent high intensity beam experimental results in the RCS including the first 1-MW trial, mainly focusing on our approaches to beam loss issues that appeared on the process of the beam power ramp-up.

## INTRODUCTION

The J-PARC 3-GeV Rapid Cycling Synchrotron (RCS) is the world's highest class of high-power pulsed proton driver aiming at the output beam power of 1 MW [1]. The injector linac delivers a 400-MeV H$^-$ beam to the RCS injection point, where it is multi-turn charge-exchange injected through a 300-μg/cm$^2$-thick carbon stripping foil over a period of 0.5 ms. RCS accelerates the injected protons up to 3 GeV with a repetition rate of 25 Hz, alternately providing the 3-GeV proton beam to the Material and Life Science Experimental Facility (MLF) and to the following 50-GeV Main Ring Synchrotron (MR) by switching the beam destination pulse by pulse.

In the last summer shutdown in 2013, the ACS linac section was installed [2], by which the injection beam energy from the linac was upgraded from 181 MeV to the design value of 400 MeV. In addition, in this summer shutdown in 2014, the front-end system (IS and RFQ) of the linac was replaced [3], by which the maximum peak current of the injection beam was increased from 30 mA to the design value of 50 mA. Via these series of the injector linac upgrades, the RCS has got all the design parameters. Thus the RCS is now in the final beam commissioning phase aiming for the 1-MW design output beam power.

Fig. 1 shows the history of the RCS beam operation. Since the start-up of the user program in December, 2008, the output beam power from the RCS has been steadily increasing as per progressions in beam tuning and hardware improvements [4,5]. The output beam power for the routine user program has been increased to 300 kW as planned to date. In addition to such a routine user operation, the RCS have intermittently been continuing the high intensity beam tests toward the design output beam power of 1 MW. As shown in Fig. 1, the RCS successfully achieved high intensity beam accelerations of up to 539-573 kW for both injection energies of 181 MeV and 400 MeV before and after the installation of the ACS. Besides, the RCS has very recently conducted the first 1-MW trial right after the replacement of the front-end system. The most important issues in increasing the
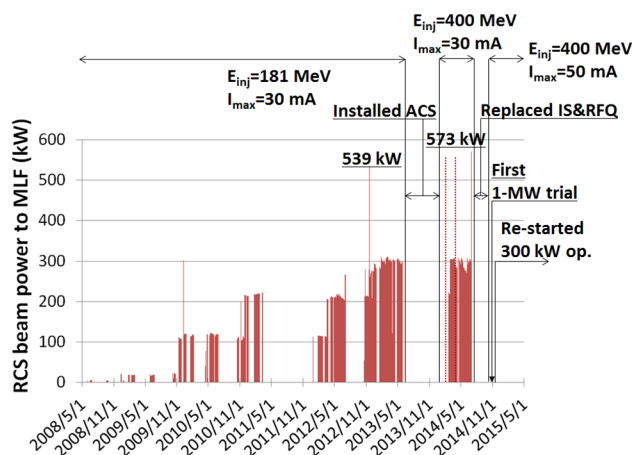


Figure 1: History of the RCS output beam power.

output beam power are control and minimization of beam loss to keep the machine activation within the permissible level. This paper presents the experimental results of these series of recent high intensity beam tests in the RCS mainly focusing on our approaches to beam loss issues that appeared on the process of the beam power ramp-up.

## HIGH INTENSITY BEAM TESTS OF UP TO 553-573 kW

In April (Run#54) and June (Run#56), 2014 after installing the ACS, the RCS conducted high intensity beam tests of up to 553 (Run#54)-573 (Run#56) kW with the upgraded injection energy of 400 MeV, using a 0.5 ms-long injection pulse with a peak current of 24.6 (Run#54)-25.5 (Run#56) mA and a chopper beam-on duty factor of 60%. In these beam tests, the operating point was set at (6.45, 6.42), where the systematic beam loss measurements were performed with various injection painting parameters and beam intensities.

### Painting parameter dependence of beam loss (Run#54)

In order to minimize space-charge induced beam loss at the low energy, the RCS employs injection painting both for the transverse and longitudinal phase spaces [6]. On the transverse plane, correlated painting with a painting emittance of $100\pi$ mm mrad ($\varepsilon_{tp}$) was applied. On the other hand, for longitudinal painting [7,8], the momentum offset injection of 0.0, −0.1 and −0.2% ($\Delta p/p$) was tested in combination with superposing a 2nd harmonic rf with an amplitude of 80% ($V_2/V_1$) of the fundamental rf. As an additional control in longitudinal painting, the phase sweep of the 2nd harmonic rf was also employed during injection from −100 to 0 degrees ($\phi_2$) relatively to that of the fundamental rf.

_____

#hotchi.hideaki@jaea.go.jp

**Painting parameter ID**

| Parameter ID | $\epsilon_{tp}$ ($\pi$ mm mrad) | $V_2/V_1$ (%) | $\phi_2$ (degrees) | $\Delta p/p$ (%) |
|---|---|---|---|---|
| 1 | – | – | – | – |
| 2 | 100 | – | – | – |
| 3 | – | 80 | −100 | – |
| 4 | – | 80 | −100 | −0.1 |
| 5 | – | 80 | −100 | −0.2 |
| 6 | 100 | 80 | −100 | – |
| 7 | 100 | 80 | −100 | −0.1 |
| 8 | 100 | 80 | −100 | −0.2 |
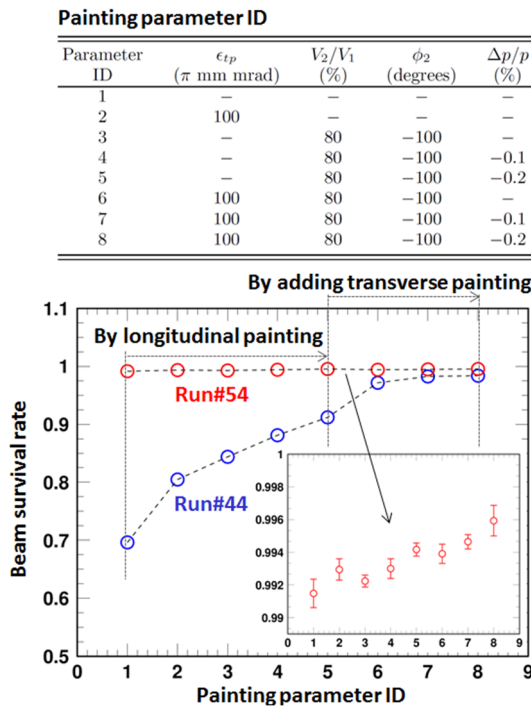


Figure 2: Beam survival rates measured with the systematic combinations of transverse and longitudinal painting (IDs 1 to 8), where the red circles correspond to the data taken for the injection energy of 400 MeV with a beam intensity of 553 kW, while the blue ones are the old data taken for the lower injection energy of 181 MeV with a similar beam intensity of 539 kW before installing the ACS linac.

Fig. 2 shows the beam survival rates measured with the systematic combinations of transverse and longitudinal painting (IDs 1 to 8), where the red circles correspond to the data taken for the injection energy of 400 MeV with a beam intensity of 553 kW ($4.60 \times 10^{13}$ ppp), while the blue ones are the old data (Run#44 in November, 2012) taken for the lower injection energy of 181 MeV with a similar beam intensity of 539 kW ($4.49 \times 10^{13}$ ppp) before installing the ACS linac.

As shown by the blue circles in Fig. 2, the larger painting parameter dependence was observed for the lower injection energy of 181 MeV, since the space-charge effect is more critical. In this case, 30%-big beam loss appeared with no painting. But this beam loss was drastically decreased from ID 1 to ID 5 by longitudinal painting, and from ID 5 to ID 8 by adding transverse painting. The plots (a) and (b) in Fig. 3 show tune footprints without and with injection painting calculated at the injection energy of 181 MeV with a beam intensity of 539 kW. As shown in the plot (a), a core part of the beam particles crosses various low-order systematic resonances for the case with no painting. Such particles on the resonances suffer from emittance dilutions. This is the main cause of the 30%-big beam loss observed with no painting. But the space-charge tune depression of (a) is well mitigated to (b) by injection painting, which results in the significant beam loss mitigation from IDs 1 to 8.
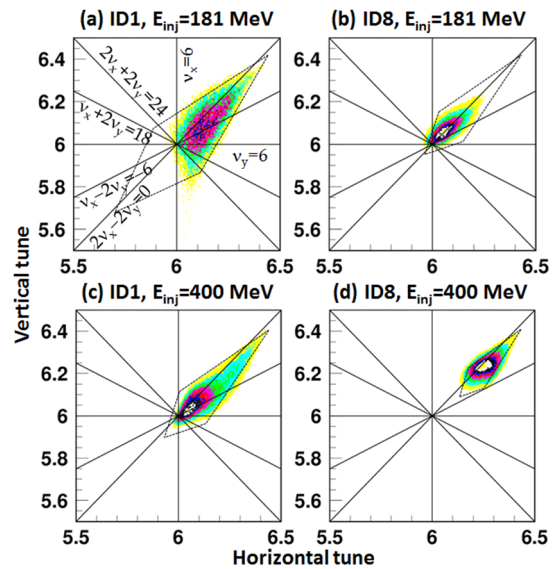


Figure 3: Tune footprints without (ID 1) and with (ID 8) injection painting calculated at the injection energy of 181 MeV with a beam intensity of 539 kW (top) and at the injection energy of 400 MeV with a beam intensity of 553 kW (bottom).

Fig. 2.

As shown by the red circles in Fig. 2, the beam survival was still improved for the higher injection energy of 400 MeV. This results from the further space-charge mitigation through the injection energy upgrade from 181 MeV to 400 MeV, as shown in the lower plots (c) and (d) of Fig. 3. The painting parameter dependence for the red circles is nearly flat, but this case also has a similar dependence to that for the blue circles, as shown in the inset of Fig. 2; the beam loss was reduced from ID1 to ID5 by longitudinal painting, and from ID5 to ID8 by adding transverse painting.

The above experimental data clearly shows the enormous gain from the injection energy upgrade this time as well as the excellent ability of injection painting.

*Intensity dependence of beam loss (Run#56)*

Next, the intensity dependence of beam loss was measured with the injection energy of 400 MeV, where the painting injection parameter was fixed to ID8. In this measurement, the beam intensity was varied from 107 kW ($0.889 \times 10^{13}$ ppp) to 573 kW ($4.775 \times 10^{13}$ ppp) by thinning the number of the intermediate pulses while maintaining the injection pulse length at 0.5 ms. This type of intensity variation does not change both the injection painting condition and the foil hitting rate during injection.

The top-left plot in Fig. 4 shows the beam loss monitor signals at the collimator section measured over the first 3 ms in the low energy region with various beam intensities from 107 kW to 573 kW. In this figure, one can clearly see the time structure of beam loss and its intensity dependence. The top-right plot in Fig. 4 shows the intensity dependence of beam loss amount evaluated from the integration of the beam loss monitor signal. The beam
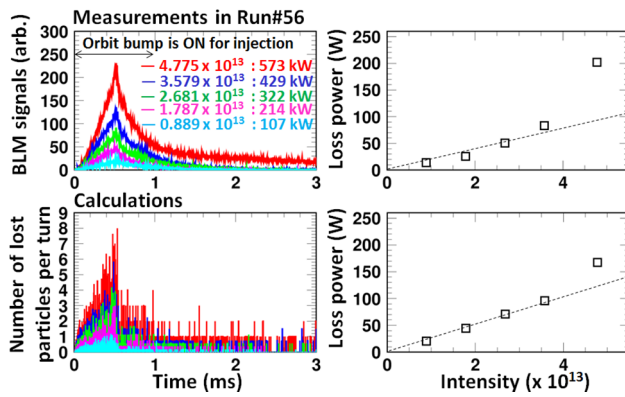
Figure 4: (Top-left) Intensity dependence of beam loss monitor signals at the collimator section measured over the first 3 ms in the low energy region with various beam intensities from 107 kW to 573 kW. (Top-right) Intensity dependence of beam loss amount estimated from the integration of the beam loss monitor signal. (Bottom) Corresponding numerical simulation results.
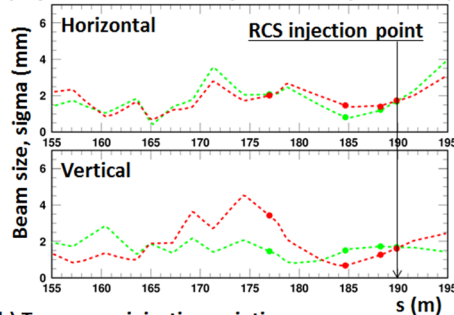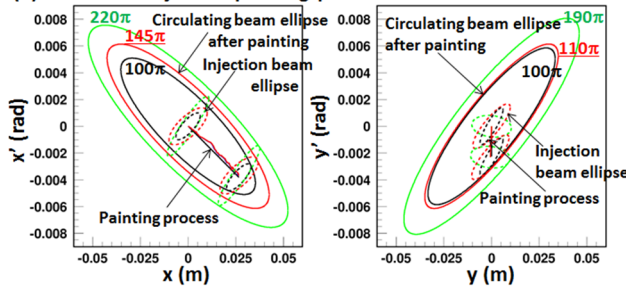


Figure 5: (a) Injection beam envelop reconstructed by the model fitting to the measured injection beam profiles (circles) before (dashed-green) and after (dashed-red) the Twiss parameter correction. (b) Transverse painting process, where the black ellipses correspond to the design one, while the other ellipses show the painting process estimated from the actual injection beam quality before (green) and after (red) its Twiss parameter correction.

loss amount shows a linear response up to the 429-kW intensity beam, but the extra beam loss increase occurs for the 573-kW intensity beam. This empirical intensity dependence of beam loss was well reproduced by the corresponding numerical simulations, as shown in the bottom plots in Fig. 4. This numerical simulation implied

that the extra beam loss arises from large amplitude particles formed through the transverse injection painting
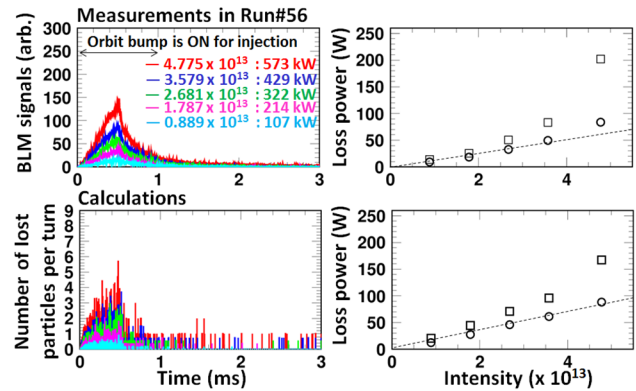


Figure 6: (Top) Similar results to the top plots in Fig. 4, observed after the Twiss parameter correction of the injection beam. (Bottom) Corresponding numerical simulation results.

process. Fig. 5-(b) shows the transverse injection painting process. The black solid ellipse in the figure shows the design painting area of $100\pi$ mm mrad, which is formed from the design beam emittance ($0.25\pi$ mm mrad, rms, un-normalized) and Twiss parameter of the injection beam. But, in fact, the linac beam had a larger beam emittance than the design; $0.60\pi$ (horizontal) and $0.54\pi$ (vertical) mm mrad. In addition, its Twiss parameter at the RCS injection point had not been adjusted well at that time. Due to such a large injection beam emittance and its un-adjusted Twiss parameter, terribly large amplitude particles, which deviate from the design painting range of $100\pi$ mm mrad, are formed through the injection painting process, as shown by the green solid ellipse in Fig. 5-(b). The numerical simulation confirmed that such large amplitude particles cause the extra beam loss for the higher intensity beam in combination with the space-charge effect. Based on this analysis, we tried to mitigate the extra beam loss first by adjusting the injection beam Twiss parameter.

*Further beam loss reduction by adjusting the Twiss parameter of the injection beam (Run#56)*

Fig. 5-(a) shows the injection beam envelop along the injection beam transport line reconstructed by the model fitting to the measured injection beam profiles. The injection beam Twiss parameter at the RCS injection point was evaluated from this beam envelop analysis, and corrected so that the injection beam ellipse matches the circulating beam ellipse with the design painting emittance. The red solid ellipse in Fig. 5-(b) shows the painting area estimated after the correction. It is still larger than the design, since the large emittance of the injection beam remains un-touched, but it well came to fit within the permissible range. By this effort, the beam loss was well mitigated from Fig. 4 to Fig. 6 as expected. The peak value of the beam loss at the end of injection was decreased, and the following long tail beam loss was also well mitigated, with the result that the intensity dependence of beam loss

amount got to have a linear response up to the 573-kW intensity beam as shown in the top-right plot in Fig. 6. These observations were well reproduced by the corresponding numerical simulations, as shown in the bottom plots in Fig. 6. The beam loss after the injection beam adjustment appears only for the first 1 ms of the beam injection, and also its amount shows a linear response for the beam intensity. These empirical results conclude the beam loss of up to the 573-kW intensity beam is well minimized and its remaining beam loss is mainly from foil scattering during injection.

## THE FIRST 1-MW TRIAL

Right after the high intensity beam tests mentioned in the last section, J-PARC had a long beam shutdown from July to September, 2014 to install the new front-end system. After completing the installation, beam tuning and tests were resumed from the linac at the end of September, 2014. Via the initial beam tuning of the linac, the RCS conducted the first 1-MW trial in October, 2014 (Run#57) at the same operating point of (6.45, 6.42) and with the same injection painting parameter of ID8. The maximum input beam intensity in this high intensity beam test reached $8.61 \times 10^{13}$ ppp, using a 0.5 ms-long injection pulse with the higher peak current of 45.9 mA and a chopper beam-on duty factor of 60%, which corresponds to 1.033-MW output beam power from RCS.

### Quality of the injection beam with the higher peak current of 45.9 mA (Run#57)

From the beam envelop analysis in Fig. 7-(a), the beam emittance (rms, un-normalized) for the 45.9-mA injection beam was evaluated to be $0.957\pi$ (horizontal) and $0.564\pi$ (vertical) mm mrad. Thus the 45.9-mA injection beam had a larger beam emittance than that in the previous high intensity beam test (Run#56) conducted with the peak current of 25.5 mA before replacing the front-end system. Therefore, the deviation of the painting area from the design still got worse especially on the horizontal plane as compared to that in Run#56, as shown in Fig. 7-(b), though the injection beam ellipse was similarly corrected at the injection point. Consequently, there occurs a larger imbalance between the horizontal and vertical painting areas. The present beam emittance for the 45.9-mA injection beam is 2-4 times larger than the design value of $0.25\pi$ mm mrad. As is mentioned later, this injection beam does not lead to serious issues in the RCS to date, but its quality has to be improved from now on in order to obtain the better quality for the 3-GeV beam that meets the requirements from the downstream facilities as well as to minimize beam loss in the RCS.

### Result of the first 1-MW trial (Run#57)

Fig. 8 shows the circulating beam intensity measured over 20 ms from injection to extraction. As shown in the figure, the input beam intensity was gradually increased from 252 kW toward 1 MW by changing the beam thinning

parameter. The beam intensity was smoothly increased up to 773 kW with no significant beam loss.
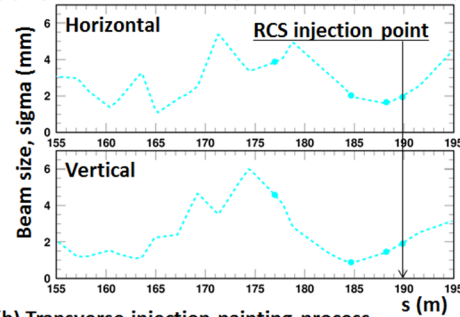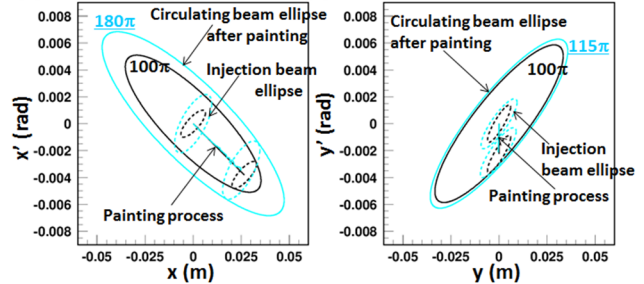


Figure 7: (a) Injection beam envelop reconstructed by the model fitting to the measured injection beam profiles (circles) after the Twiss parameter correction. (b) Transverse painting process, where the black ellipses correspond to the design one, while the light-blue ones are the painting process estimated from the actual injection beam quality after its Twiss parameter correction.

But, when the beam intensity got to over 800 kW, the anode power supply of the RF cavity system suddenly stumbled due to the over current. The circles in Fig. 9 show the anode current measured as a function of the beam intensity [9]. In the RCS, the multi-harmonic feed-forward method (h=2, 4 and 6) is employed for beam loading compensation [10]. Therefore the required anode current increases following the ramp-up of the beam intensity. The blue line in the figure corresponds to the present interlock level for the anode current. Thus, in the present condition, the required anode current surpasses the interlock level when the beam intensity gets to over 800 kW. This is the main cause of the RF trip this time.

We are now considering several possible measures against this issue. The first one is to use a remaining margin of the anode power supply. The interlock level is now set to 110 A, but it can be safely increased up to 115 A in design. The second one is to shift the resonant frequency of the RF cavity by removing a capacitor. The resonant frequency shift of the RF cavity acts to tilt the beam intensity dependence of the anode current from the circles to the squares in Fig. 9, by which the required anode current for the 1-MW beam acceleration decreases from 124 A to 109 A [9]. By taking these possible measures, the anode current required for the 1-MW beam acceleration comes to stay within the limit. After taking these quick measures, we will re-try the 1-MW beam acceleration in

December, 2014. We are also planning to increase the anode power supply itself to secure sufficient
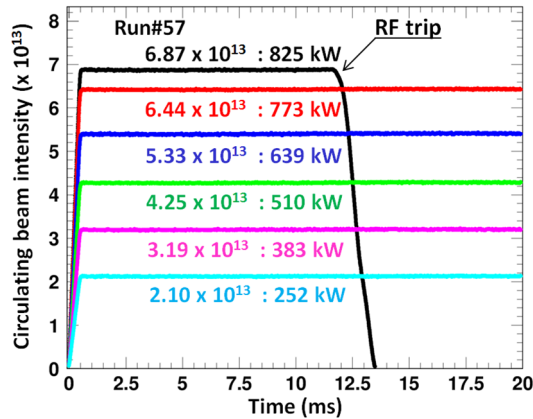


Figure 8: Circulating beam intensity measured over 20 ms from injection to extraction.
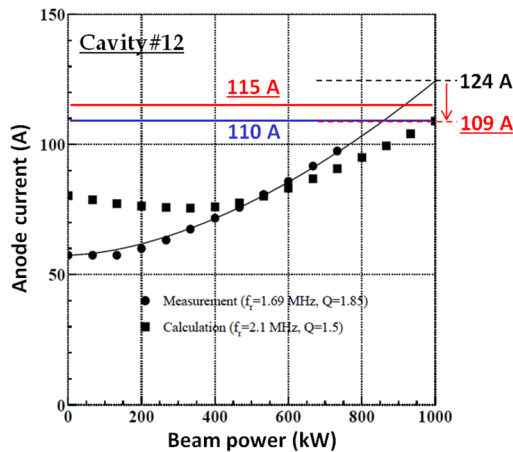


Figure 9: Anode current for the RF cavity#12 measured as a function of the beam intensity (circles). The intensity dependence of the anode current can be tilted to the squares by the resonant frequency shift of the RF cavity.

margin for the 1-MW beam acceleration using the next summer shutdown period in 2015, aiming to start up the 1-MW routine user operation in October, 2015 as originally planned.

Though the 1-MW beam acceleration was not reached this time, the RCS successfully demonstrated high intensity beam accelerations of up to 773 kW. The upper plot in Fig. 10 shows the beam loss monitor signals at the collimator section measured over the first 3 ms in the low energy region with various beam intensities from 252 kW to 773 kW. As shown in the plot, the beam losses mainly appear for the first 1 ms of the beam injection. In addition, their time structures are very similar to each other, and also to the beam loss data taken in the previous high intensity beam test (Run#56) given in Fig. 6. Inevitably, the beam loss amount nearly shows a linear response for the beam intensity, as shown in the lower plot in Fig. 10. These empirical results similarly conclude the beam loss of up to the 773-kW intensity beam is nearly minimized and its

remaining beam loss is mainly from foil scattering during injection. The beam loss for the 773-kW intensity beam was estimated to be less than 0.2%, most of which
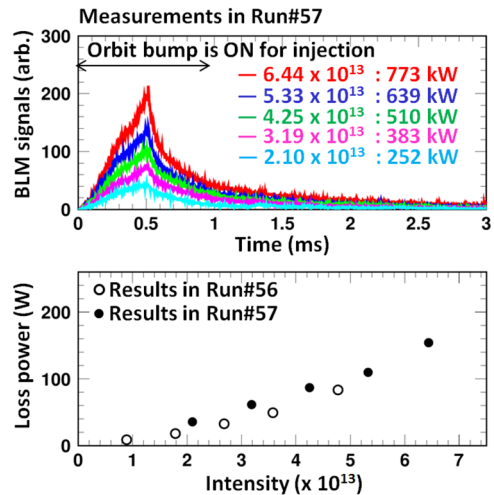


Figure 10: (Top) Intensity dependence of beam loss monitor signals at the collimator section measured over the first 3 ms in the low energy region with various beam intensities from 252 kW to 773 kW. (Bottom) Intensity dependence of beam loss amount estimated from the integration of the beam loss monitor signal in the top plot (closed circles), where the open circles correspond to the previous data shown in the top-right plot of Fig. 6.

was well localized at the collimator section. The beam loss power of 160 W is still much less than the 4-kW collimator capability.

## SUMMARY

Via a series of the injector linac upgrades in 2013 and 2014, the RCS conducted the first 1-MW trial in October, 2014. Although the 1-MW beam acceleration was not reached this time due to the RF trip, the RCS successfully demonstrated a high intense beam acceleration of 773 kW at a low-level intensity loss of less than 0.2%. Most of the 0.2%-beam loss, which is mainly from foil scattering during injection, was well localized at the collimator section. The beam loss power of 160 W is still much less than the 4-kW collimator capability.

We plan to re-try the 1-MW beam acceleration in December, 2014 after taking several quick measures against the RF trip. The RCS beam commissioning is steadily progressing, and now we are nearly approaching the final goal.

## REFERENCES

[1]  JAERI-Tech 2003-044 and KEK Report No. 2002-13.
[2]  H. Ao et al., PRST-AB **15**, 011001 (2012).
[3]  H. Oguri, Proc. of IPAC2013, WEYB101.
[4]  H. Hotchi et al., PRST-AB **12**, 040402 (2009).
[5]  H. Hotchi et al., PTEP **2012**, 02B003 (2012).
[6]  H. Hotchi et al., PRST-AB **15**, 040402 (2012).

[7]   F. Tamura et al., PRST-AB **12**, 041001 (2009).

[8]   M. Yamamoto et al., NIM, A **621**, 15 (2010).

[9]   M. Yamamoto, Private communication.

[10] F. Tamura et al., PRST-AB **14**, 051004 (2011).

# ACCELERATOR CHALLENGES OF HIGH INTENSITY LINACS AND THE FACILITY FOR RARE ISOTOPE BEAMS*

J. Wei[#1], N. Bultman[1], F. Casagrande[1], C. Compton[1], K. Davidson[1], B. Drewyor[1], K. Dixon[2], A. Facco[1,4], F. Feyzi[1], V. Ganni[2], P. Gibson[1], T. Glasmacher[1], L. Hoff[1], K. Holland[1], M. Ikegami[1], M. Johnson[1], S. Jones[1], M. Kelly[3], R.E. Laxdal[5], S. Lidia[1], G. Machicoane[1], F. Marti[1], S. Miller[1], D. Morris[1], P. Ostroumov[3], J. Nolen[1,3], S. Peng[1], J. Popielarski[1], L. Popielarski[1], E. Pozdeyev[1], T. Russo[1], K. Saito[1], T. Xu[1], Y. Yamazaki[1]

[1] Facility for Rare Isotope Beams, Michigan State University, East Lansing, MI 48824 USA
[2] Thomas Jefferson National Accelerator Facility, Newport News, VA 23606, USA
[3]Argonne National Laboratory, Argonne, IL 60439, USA
[4] INFN - Laboratori Nazionali di Legnaro, Legnaro (Padova), Italy
[5] TRIUMF, Vancouver, Canada

*Abstract*

This paper surveys the key technologies and design challenges that form a basis for the next generation of high intensity hadron accelerators, including projects operating, under construction, and under design for science and applications at MW beam power level. Emphasis is made on high intensity linacs like the Facility for Rare Isotope Beams (FRIB).

## INTRODUCTION

During the past decades, accelerator-based neutron-generating facilities like SNS [1], J-PARC [2], PSI [3] and LANSCE [4] advanced the frontier of proton beam power to 1 MW level, as shown in Fig. 1 with the beam-on-target power as the product of the average beam current and the beam kinetic energy [5]. For heavy ion, the power frontier will be advanced by more than two-order-of-magnitudes to 400 kW with the construction of the Facility for Rare Isotope Beams currently underway at Michigan State University [6].

Cutting edge technologies continuously developed for accelerator systems have sustained continuous growth in beam intensity and power. High-power operations have been made possible by various types of accelerators: linac, cyclotron, synchrotron and accumulator. During the past decade, superconducting RF related technology has becoming indispensable for next generation machines.

High power hadron accelerators [5] can be categorized by their goals for high-energy physics (AGS [7], SPS [8], MI [9], J-PARC/MR [2], PIP-II [10] for neutrino, Kaon and Muon physics), nuclear physics (RIKEN [11], SPIRAL2 [12], FAIR [13], FRIB for rare isotope physics; FAIR for antiproton physics; LANSCE), basic energy science and applications (LANSCE, PSI, SNS, J-PARC/RCS [2], ISIS [14], SARAF [15], SPIRAL2, CSNS [16], ESS [17] for neutron sources; KOMAC [18] for proton applications), radioisotope production (SARAF), material neutron irradiation (IFMIF and its validation prototype LIPAc [19]), and accelerator driven subcritical systems (CADS [20] and MYRRHA [21] for

nuclear waste transmutation and power generation). Other operating or proposed projects include LEDA [22], PSR [23], HIAF [24], RAON [25], CPHS [26] and those proposed at CERN (SPL, LAGUNA-LBNO, SHIP) [27] and RAL [28].
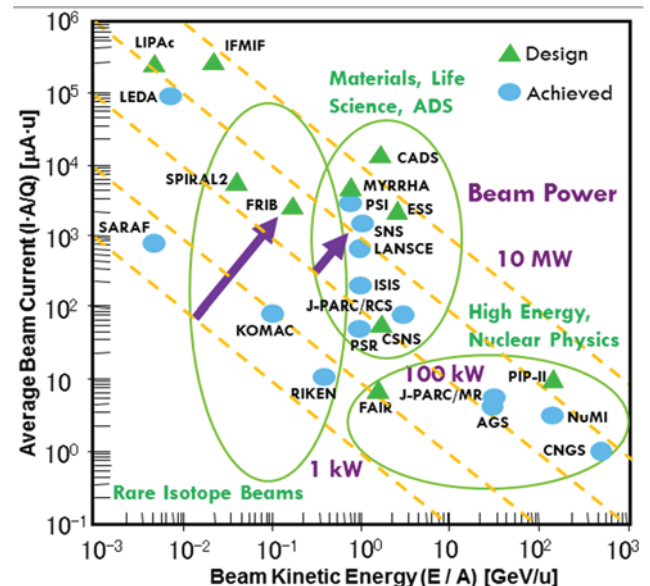


Figure 1: Hadron accelerator power frontier at design, construction, and operation stages.

The figure of merit of these accelerator facilities is the amount of useful secondary beams produced from the target. It is proportional to the target yield and the primary beam intensity. As the optimum energy range is often determined by the target yield, high beam intensity corresponds to a high beam-on-target power.

The beam structure on target largely determines the accelerator type. Synchrotrons (AGS, SPS, MI, J-PARC, ISIS, FAIR, CSNS, PIP-II) and accumulators (PSR, SNS) are used downstream of the injector accelerators to

produce pulsed beams on target. When pulsed operation is not required, cyclotrons (RIKEN and PSI) and linacs (LANSCE, KOMAC, SARAF, FRIB, SPIRAL2, IFMIF, ESS, CADS, and MYRRHA) are used to reach high beam power at high beam duty factors.

The type of primary beams is largely determined by the facility purpose. Rare isotope production using the projectile fragmentation method requires heavy ion beams (RIKEN, FRIB, SPIRAL2). Neutron production at high energy using the spallation process prefers high intensity proton beams (SNS, J-PARC, LANSCE, PSI, ISIS, CSNS, ESS, CADS, MYRRHA). Neutron production at lower energy favours deuteron beams (SARAF, IFMIF, and SPIRAL2). In synchrotron and accumulators for proton beams (ISIS, PSR, SNS, J-PARC, CSNS), the injector linac often accelerates H$^-$ beams for multi-turn injection to reach high peak intensity on target.

This paper focuses on the physical and technological challenges pertaining to high intensity hadron linacs including the Facility for Rare Isotope Beams.

## KEY TECHNOLOGIES

### Superconducting RF (SRF)

For hadrons, SRF technology is first extensively used in the SNS linacs for the high energy-efficiency, high accelerating gradient, and operational robustness (Fig. 2) [29]. For pulsed operations, resonance control by means of fast tuners and feedforward techniques is often required to counteract Lorentz force detuning [30], and the need of higher order mode damping is to be expected [31]. FRIB as a heavy ion continuous-wave (CW) linac extends SRF to low energy of 500 keV/u. 330 low-β (from 0.041 to 0.53) cavities are housed in 49 cryomodules. The resonators (at 2 K temperature) and magnets (at 4.5 K) supported from the bottom to facilitate alignment and the cryogenic headers suspended from the top for vibration isolation. High performance subsystems including resonator, coupler, tuner, mechanical damper, solenoid and magnetic shielding are necessary [32].
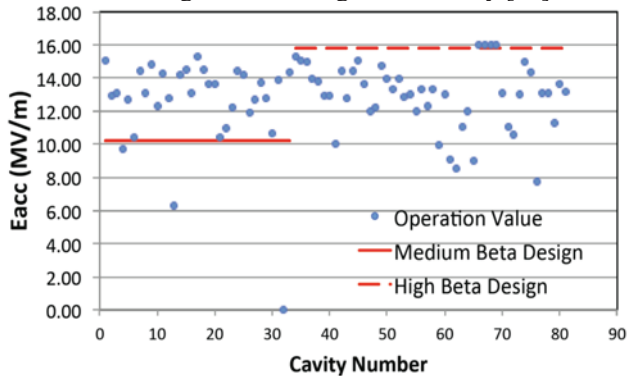


Figure 2: Accelerating gradients of the 81 SNS β=0.61 (medium) and β=0.81 (high) cavities in 23 cryomodules.

### Large-scale Cryogenics

An integrated design of the cryogenic refrigeration, distribution, and cryomodule systems is key to efficient SRF operations. The FRIB refrigeration system adopts the floating pressure process – Ganni Cycle [33] for efficient adaptation to the actual loads. Distribution lines are segmented and cryomodules are connected with the U-tubes to facilitate stage-wise commissioning and maintenance (Fig. 3). The 4-2 K heat exchangers are housed inside the cryomodules for enhanced efficiency.



Figure 3: FRIB cryomodule with U-tube connections.

### Loss Detection and Machine Protection

Machine protection is crucial to the availability of the high power accelerators. FRIB adopts multi-time scale, multi-layer approaches: the fast protection system (FPS) is designed to prevent damage from acute beam loss by quickly activating the beam inhibit device; the run permit system (RPS) continuously queries the machine state and provides permission to operate with beam; the even slower but highly sensitive RPS prevent slow degradation of SRF system under small beam loss (Table 1).

Table 1: Machine Protection for the FRIB Driver Linac

| Mode | Time | Detection | Mitigation |
|---|---|---|---|
| FPS | ~ 35 µs | LLRF controller; Dipole current monitor; Differential BCM; Ion chamber monitor; Halo monitor ring; Fast neutron detector; Differential BPM | LEBT bend electro-static deflector |
| RPS (1) | ~ 100 ms | Vacuum status; Cryomodule status; Non-dipole PS; Quench signal | As above; ECR source HV |
| RPS (2) | > 1 s | Thermo-sensor; Cryo. heater power | As above |

Challenges remain for intense low-energy heavy ion beams due to the low detection sensitivity and high power concentration/short range. Innovative techniques include the halo monitor ring [34] for high-sensitivity loss detection and current monitoring modules for critical magnet power supply inhibition. ADS machines like MYRRHA demand mean-time-between-failure of trips exceeding 3 s to be longer than 250 h [19].

*Front End (Ion Source, RFQ, LEBT Transport)*

Among a wide range of ion sources meeting different primary-beam requirements, Electron Cyclotron Resonance (ECR) ion sources are essentially the only choice for high intensity (CW), high charge state beams. To reach higher plasma densities, ECRs continue to be developed for higher resonance frequency and magnetic field. High power ECR sources operate at frequencies up to 28 GHz and RF power of ~10 kW [35]. The required superconducting (SC) sextupole and solenoids push the state-of-the-art in SC clamping technology. Cesium-seeded, volume production sources are most promising for the demand on high current, long pulse, low emittance H⁻ beams [36].

Four-vane, room temperature RFQs are commonly used for high intensity operations. LEDA RFQ with a variable voltage profile accelerated 100 mA CW proton beam to 6.7 MeV [37]. Alternatively, RFQ with trapezoidal vane modulation is tested for shunt impedance and acceleration efficiency enhancement (Fig. 4) [38]. The LEBT transport between the source and RFQ is often used for chopping, collimation, beam inhibition, and prebunching.
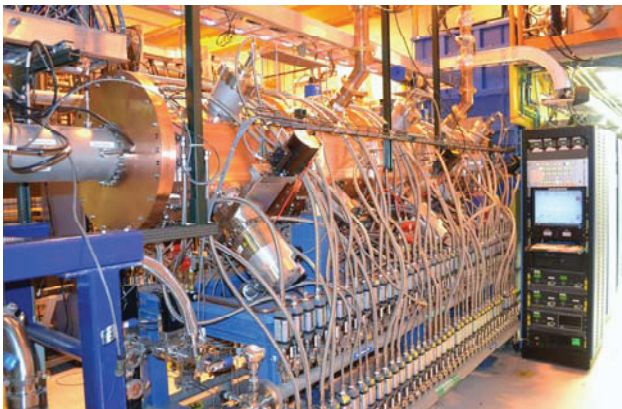


Figure 4: ATLAS heavy-ion CW RFQ in operation since December 2012 [38].

*High-power Charge Stripping*

Intense heavy ions at low energies may cause severe damage on stripping material. Innovative stripping mechanisms are under development worldwide. RIKEN uses helium gas with differential pumping (Fig. 5) [39]. Plasma windows are being tested to establish a high gas density [40]. FRIB uses a liquid lithium film moving at ~50 m/s speed. Tests with a proton beam produced by the LEDA source demonstrated that power depositions similar to the FRIB uranium beams could be achieved without destroying the film (Fig. 6) [41].

Injection of intense H⁻ beams into rings require sophisticated charge stripping designs [5]. Innovative schemes like laser stripping are tested [42]. Stripping can also be used to split H⁻ beam to multiple beam lines [43].

*Collimator*

Collimators are indispensable to reduce uncontrolled beam loss for hands-on maintainability [5]. Collimation

can be performed in both the transverse and longitudinal phase space (momentum cleaning and beam gap cleaning). Charge stripping is often used for H⁻ and partially stripped heavy ions for efficient collimation. Multi-stage collimations are used on fully stripped beams like protons [44] (Fig. 7).

For heavy ions, beams of unwanted charge states need to be removed downstream of the stripper. Such "charge selector" must sustain high power, low energy beams of short range. The FRIB charge selector, designed to absorb ~42 kW of heavy ions at 12 – 20 MeV/u, consists of two rotating graphite discs similar to the FRIB target [45].



Figure 5: Test of He gas charge stripper using Uranium beams at RIKEN [39].
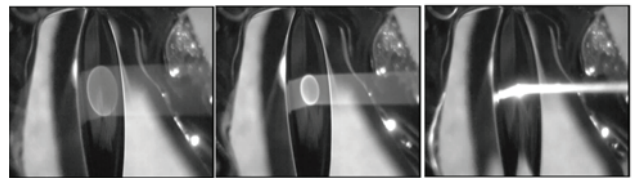


Figure 6: Liquid lithium film intercepting a proton beam of ~ 60 kV for beam power survival test [41].



Figure 7: SNS multi-layered collimators, each designed to withstand 10 kW protons at 1 GeV.

*Target, Radiation-resistant Magnets, Handling*

Target scenario is chosen based on secondary-beam requirements [46]. High-power primary beams often demand non-stationary targets like circulating liquid or rotating solid targets. For pulsed neutron production at MW level, both SNS and J-PARC/RCS use liquid mercury. Target pitting issues are largely mitigated by vessel surface treatment, mercury flow and bubble controls [47]. For lower-energy neutron production both SARAF [48] and IFMIF use liquid lithium (Fig. 8) while SPIRAL2 prefers a rotating carbon wheel. MYRRHA's

ADS target uses liquid Pb-Bi eutectic [49]. For in-flight RIB production FRIB needs to focus 400 kW of heavy ion beam onto an area of 1 mm diameter (~60 MW/cm$^3$). A radiation-cooled multi-slice graphite target of 30 cm diameter rotates at 5000 rpm [45]. While neutron targets are designed to absorb most beam power, FRIB's RIB target is designed to absorb ~25% power; targets for high-energy physics (ν, μ, K) typically absorb <5% power.
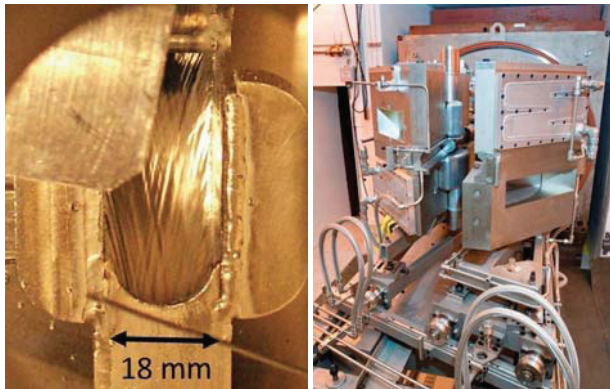


Figure 8: (left) SARAF's liquid lithium target under test [48] and ISIS spallation target station 2 [46].

Radiation resistance is important for magnets in the target region. Quadrupoles wound with mineral-insulated cables are built as an integral part of the shielding in front of the SNS target [50]. Quick-disconnect vacuum flanges and remote water fittings allow easy access. FRIB uses high-temperature SC magnets (YBCO) in the high radiation area of the target and primary beam dump [51].

## ACCELERATOR PHYSICS CHALLENGES

### Beam Loss Control

Key to the design and operations of a high-power accelerator is to control the beam loss. Measures of loss control include beam collimation, beam dump and shielding for charge stripping and charge selection (Table 2). Uncontrolled losses must be kept below a level (about 1 W/m for protons around 1 GeV and less stringent for heavy ions [52]) to facilitate hands-on maintenance. Personnel protection system is designed against radiation exposure under both normal and fault machine conditions.

Table 2: Estimated FRIB Beam Losses

| Type and location | Energy [MeV/u] | Peak power | Duty factor |
|---|---|---|---|
| Uncontrolled loss | 0 – 200 | ~1 W/m | 100% |
| Controlled loss: | | | |
| Charge selector | 12 – 20 | 42 kW | 100% |
| Charge stripper | 12 – 20 | ~1 kW | 100% |
| Collimators | 0 – 200 | ~1 kW | 100% |
| Dump FS1-a | 12 – 20 | 42 kW | 0.03% |
| Dump FS1-b | 12 – 20 | 12 kW | 5% |
| Dump FS2 | 15 – 160 | 300 kW | 0.03% |
| Dump BDS | 150 – 300 | 400 kW | 0.03% |

### Space Charge, Coupling Impedance, Instability

Space charge and other coupling impedances can have performance-limiting effects for machines of low energy, high peak intensity beams. In linacs beam halo can be generated through core-halo parametric resonances and resonances between the transverse and longitudinal motion [53 – 56] (Fig. 9).
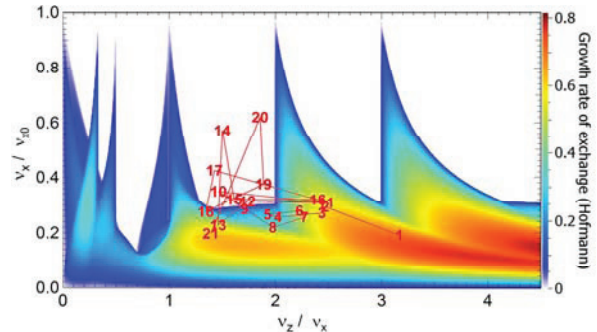


Figure 9: Tune footprint along the four IFMIF cryomodules superimposed to the Hofmann chart [60].

### Multiple Charge State Acceleration

To reach high design beam intensity, simultaneous acceleration of heavy ion beams of multiple charge state is often needed due to the broad charge spectrum upon stripping. The FRIB driver linac accelerates up to five charge states simultaneously, transversely overlapping at charge stripper location and at the target (Fig. 10). Machine optics, diagnostics, and fault mitigation are designed in detail to meet the performance goals.
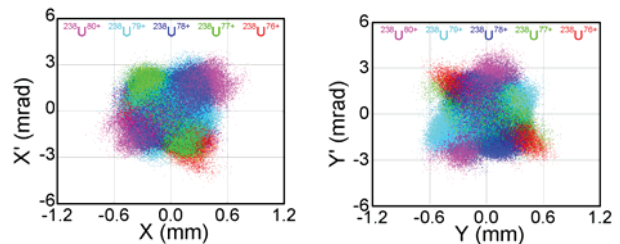


Figure 10: Five charge states of the uranium beam designed to overlap at the FRIB target.

Other topics include magnet interference [57] and fringe field [58] pertaining to large aperture and tight spacing, and H$^-$ stripping issues [59 - 61].

## FRIB PROJECT STATUS

In August 2013, the Department of Energy's Office of Science approved Critical Decision-2, Approve Performance Baseline, and Critical Decision-3a, Approve Start of Civil Construction and Long Lead Procurements, for the FRIB Project. The ground was broken in March 2014. In October 2014, the Critical Decision-3b was approved allowing the start of technical construction. The Total Project Cost for FRIB is $730M, of which $635.5M will be provided by DOE and $94.5M will be provided by Michigan State University. The project will be completed by June 2022 [62]. "When completed, FRIB will provide access to completely uncharted territory at the limits of

nuclear stability, revolutionizing our understanding of the structure of nuclei as well as the origin of the elements and related astrophysical processes."
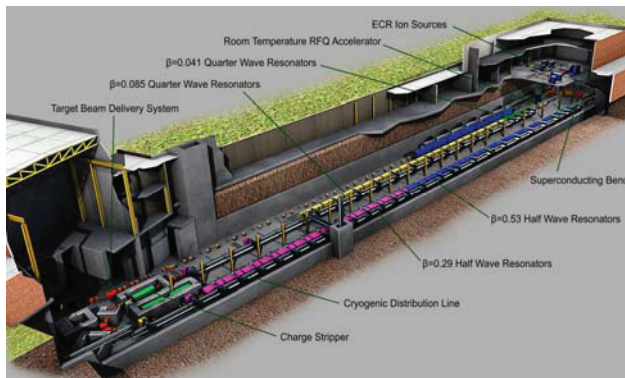


Figure 11: Layout of the FRIB driver accelerator.

## Specific Challenges and Design Philosophy

FRIB shares the physical and technological challenges described in the previous Sections. In addition, FRIB is sited in the middle of university campus with tight real estate constraints. The driver linac is "folded" twice demanding special design considerations (Fig. 11). The folding segments must be designed as 2nd order achromats allowing a wide momentum acceptance. Beam loss at high energy interferes with loss detection of low-energy beams. Hazard analysis upon beam faults is complicated, and installation and commissioning are interlaced. Finally, as the linac service/utility area and cryogenics area are near the accelerator tunnel housing cryomodules, the vibration issue must be carefully addressed.

Full-energy linac technology is chosen to deliver primary beam that can meet the FRIB requirements of rare-isotope productivity and separation accuracy. Up to 400 kW of beams are focused to a diameter of 1 mm (90%), energy spread of 1% (95% peak-to-peak), and bunch length of < 3 ns (95%) on the target.

Superconducting (SC) technology is the energy-efficient choice for the CW linac. SC acceleration of heavy-ion beams is feasible from low energy (500 keV/u) with practically sized cavity bores by housing both the cavities and solenoids in a cryomodule. A two-gap scheme is chosen throughout the entire linac providing both efficient acceleration and focusing. Developments of digital low-level RF control and solid-state RF amplifier technologies have made individual cavity powering and control reliable and cost efficient.

High availability, maintainability, reliability, tunability, and upgradability are especially required for FRIIB to operate as a national scientific user facility [62].

## Collaboration and Partnership

FRIB accelerator systems design has been assisted under work-for-others agreements by many national laboratories including ANL, BNL, FNAL, JLab, LANL, LBNL, ORNL, and SLAC, and in collaboration with many institutes including BINP, KEK, IMP, INFN, INR, RIKEN, TRIUMF, and Tsinghua University.

The cryogenics system is designed in collaboration with the JLab cryogenics team. The refrigeration process incorporates the cumulative experience from both JLab and SNS cryogenic systems. The recent experience gained from the JLab 12 GeV cryogenic system design is utilized for both the refrigerator cold box and the compression system designs. The cryogenic distribution adopting a modular design is prototyped at JLab and tested at MSU along with the cryomodule prototype.

The charge stripping system is under development in collaboration with ANL. Upon successful prototyping and integrated test (Fig. 5), the present focus is on the development of the electromagnetic pump for lithium circulation and on the production design including safety considerations. BNL collaborated on the development of the alternative helium gas stripper.

The SRF development benefited greatly from the expertise of the low-β SRF community. FRIB adopted the ANL design of the QWR coupler and HWR tuner and is further assisted in the design and validation of critical SRF subsystems. We are assisted by JLAB on cavity processing and cryomodule developments, and by FNAL on cavity heat treatment and material analysis.

The high-power ECR ion source coldmass and magnets are under development in collaboration with LBNL.

## PERSPECTIVES

At a time when accelerator projects at the high-energy frontier are experiencing difficulties in gaining financial support, projects at the high-intensity frontier are flourishing worldwide. Demands for such accelerators extend from science to applications, and for primary beams from proton to heavy ions. Efforts worldwide are readying the technologies and designs meeting the requirements of user facilities with high reliability, availability, maintainability, tunability, and upgradability. With the present technology, we speculate to reach multi MW beam power using cyclotrons, synchrotrons or accumulators, and up to 100 MW with SRF linacs [5].

## ACKNOWLEDGMENT

Hartman, S. Henderson, G. Hoffstaetter, J. Hogan, S. Holmes, M. Howell, R. Kersevan, N. Holtkamp, H. Horiike, C. Hovater, D. Hseuh, H. Imao, R. Janssens, R. Keller, J. Kelley, P. Kelley, J. Kerby, A. Klebaner, J. Knobloch, R. Lambiase, M. Lamm, C. LoCocq, C. Luongo, K. Mahoney, J. Mammosser, T. Mann, W. Meng, N. Mokhov, Y. Momozaki, G. Murdoch, H. Okuno, R. Pardo, S. Peggs, T. Peterson, C. Piller, J. Power, T. Powers, J. Preble, D. Raparia, T. Roser, M. Ross, R. Ruland, J. Sandberg, R. Schmidt, W.J. Schneider, D. Schrage, I. Silverman, J. Sondericker, W. Soyars, C. Spencer, R. Stanek, M. Stettler, J. Stovall, Y. Than, J. Theilacker, J. Tuozzolo, V. Verzilov, R. Vondrasek, P. Wanderer, M. Wiseman, P. Wright, L. Young, and A. Zaltsman, and colleagues who advised and collaborated with the FRIB team including A. Burrill, A.C. Crawford, K. Davis, X. Guan, W. Hartung, K. Hosoyama, A. Hutton, S.H. Kim, P. Kneisel, K. Macha, G. Maler, E.A. McEwen, S. Prestemon, J. Qiang, T. Reilly, R. Talman, J. Vincent, X.W. Wang, Q.Z. Xing. The FRIB accelerator design is executed by a dedicated team of the FRIB Accelerator Systems Division with close collaboration with the Experimental Systems Division headed by G. Bollen, the Conventional Facility Division headed by B. Bull, the Chief Engineer's team headed by D. Stout, and supported by the project controls, procurements, ES&H of the FRIB Project, by the NSCL, and by the MSU.

# REFERENCES

[1]     N. Holtkamp, EPAC'02, 164 (2002); S. Henderson, LINAC'10, 11 (2010); J. Galambos, PAC'13, 1443 (2013)

[2]     Y. Yamazaki, PAC'09, 18 (2009); K. Hasegawa et al, IPAC'13, 3830 (2013)

[3]     M. Seidel et al, IPAC'10, 1309 (2010); P.A. Schmelzbach et al, HB'06, 274 (2006)

[4]     D.E. Nagle, LINAC'72, 4 (1972); R.W. Garnett et al, PAC'11, 2107 (2011)

[5]     J. Wei, Rev. Mod. Phys. 75, 1383 (2003); J. Wei, IPAC'14, 17 (2014)

[6]     J. Wei et al, NA-PAC'13, 1453 (2013)

[7]     T. Roser, PAC'01, 714 (2001)

[8]     The CNGS Conceptual Technical Design, ed. K. Elsener, CERN Report CERN 98-02 (1998)

[9]     M. Martens et al, PAC'07, 1712 (2007)

[10]    PIP-II Whitepaper, FNAL Report: http://projectx-docdb.fnal.gov/cgi-bin/ShowDocument?docid=1232

[11]    O. Kamigaito et al, IPAC'13, 333 (2013)

[12]    R. Ferdinand et al, IPAC'13, 3755 (2013)

[13]    O. Kester, IPAC'13, 1085 (2013)

[14]    D. Findlay, PAC 695 (2007); J. Thomason et al, IPAC'13, 2678 (2013)

[15]    D. Berkovits et al, LINAC'12, 100 (2012)

[16]    S. Fu et al, IPAC'13, 3995 (2013)

[17]    M. Lindroos et al, LINAC'12, 768 (2012)

[18]    B. Choi et al, APAC'04, 231 (2004); Y. Cho et al, IPAC'13, 2052 (2013)

[19]    J. Knaster et al, Nucl. Fusion 53, 116001 (2013)

[20]    W. Zhan, IPAC'13, MOXAB101 (2013)

[21]    D. Vandeplassche et al, IPAC'11, 2718 (2011)

[22]    H.V. Smith Jr., et al, PAC'01, 3296 (2001)

[23]    G.P. Lawrence et al, PAC'85, 2662 (1985)

[24]    J. Yang et al, Nucl. Instrum. Meth. B 317, 263 (2013)

[25]    D. Jeon, IPAC'13, 3898 (2013)

[26]    X. Guan et al, HIAT'13, 112 (2012)

[27]    R. Garoby et al, J. Phys. 408, 012016 (2013); W. Bonivento et al, CERN Report CERN-SPSC-2013-024 / SPSC-EOI-010 (2013)

[28]    C. Plostinar et al, LINAC'12, 924 (2012)

[29]    T.P. Wangler et al, SRF'99, (336 (1999); Y. Cho, SRF'01, 95 (2001); S. Kim et al, APAC'04, 30 (2004)

[30]    S. Simrock, SRF'03, 254 (2003); W. Schappert et al, SRF'11, 940 (2011); A. Neumann et al, Phys. Rev. ST-AB 13, 082001 (2010)

[31]    J. Sekutowicz, LINAC'06, 506 (2006)

[32]    A. Facco et al, IPAC'12, 61 (2012)

[33]    V. Ganni et al, CEC-ICMC 59, 323 (2013)

[34]    Z. Liu et al, Nucl. Instrum. Meth. A767, 262 (2014)

[35]    D. Leitner et al, Rev. Sci. Instrum 79 02C710 (2008); C. Lyneis et al, Rev. Sci. Instrum. 79, 02A321 (2013)

[36]    M.P. Stockli et al, Rev. Sci. Instrum. 85, 265 (2013)

[37]    L. Young et al, LINAC'00, 336 (2000)

[38]    P. Ostroumov et al, Phys. Rev. ST-AB 15, 110101 (2012)

[39]    H. Imao et al, IPAC'13, 3851 (2013)

[40]    A. Hershcovitch, J. Appl. Phys. 79, 5283 (1995)

[41]    J. Nolen et al, FRIB Report FRIB-T30705-TD-000450 (2013)

[42]    I. Yamane, Phys. Rev. ST-AB 1, 053501 (1998); V. Danilov et al, Phys. Rev. ST-AB 10, 053501 (2007)

[43]    A. Facco et al, Phys. Rev. ST-AB 10, 091001 (2007)

[44]    H. Ludewig et al, PAC'99, 548 (1999); N. Catalan-Lasheras et al, Phys. Rev. ST-AB 4, 010101 (2001)

[45]    F. Pellemoine, Nucl. Instrum. Meth. B317, 369 (2013)

[46]    D.M. Jenkins, ICANS XIX (2010)

[47]    B. Riemer et al, AccApp'13, THZTA02 (2013)

[48]    S. Halfon et al, Rev. Sci. Instrum. 85, 056105 (2014)

[49]    H. Aït Abderrahim, AccApp'11, 1 (2011)

[50]    J. Wei, EPAC'04, 156 (2004); G.R. Murdoch et al, EPAC'06, 1831 (2006)

[51]    R. Gupta et al., IEEE Trans. Appl. Superconduct. 21, 1888 (2011)

[52]    R. Ronningen et al, FRIB Report FRIB-Z00000-TR-000025 (2010)

[53]    I. Hofmann, et al, PAC'01, 2902 (2001)

[54]    A. Fedotov et al, Phys. Rev. ST-AB 5, 024202 (2002)

[55]    P.A.P. Nghiem et al, Laser Part. Beams 32, 109 (2014)

[56]    F. Scantamburlo et al, these proceedings

[57]    Y. Papaphilippou et al, PAC'01, 1667 (2001)

[58]    J. Wei et al, Part. Accel. 55, 339 (1996); Y. Papaphilippou et al, Phys. Rev. E 67, 046502 (2003)

[59]    G.M. Stinson et al, Nucl. Instrum. Meth. 74, 333 (1969); A. J. Jason et al, LANL Report LA-UR-81-1257 (1981)

[60]    H.C. Bryant et al, J. Mod. Optics 53, 45 (2006)

[61]    V. Lebedev et al, LINAC'10, 929 (2010)

[62]    J. Wei et al, NA-PAC'13, 1453 (2013)

# HEAVY-ION CYCLOTRON GYMNASTICS AND ASSOCIATED BEAM DYNAMICS ISSUES

N. Fukunishi, Nishina Center for Accelerator-Based Science, RIKEN, Wako, Japan

## Abstract

After a brief introduction to heavy-ion cyclotrons, their beam dynamics are outlined, with an emphasis on the space-charge effect, and important achievements in both proton and heavy-ion cyclotrons are described.

## INTRODUCTION

The first heavy-ion acceleration using a cyclotron was a 50-MeV $^{12}$C beam accelerated by the 37-inch Berkeley cyclotron in 1940 [1]. The beam intensity was only 8 particles/s. To illustrate the subsequent development of heavy-ion cyclotrons, data compiled by Livingston [1] (up to 1969) and data taken from the "List of Cyclotrons" published in 2004 [2] are combined in Fig. 1. Each cyclotron is classified according to its type and first-beam date (or the date of acceleration of the heavy-ion beam as listed in Livingston's tables). Although Fig. 1 is an incomplete historical review, we can observe a remarkable increase in energy. Beam intensity seems to stay relatively constant, but that is because the beam intensity of very light ions was high even in the very early stages of cyclotron history. However, beam intensities for heavier ions, such as $^{48}$Ca and $^{238}$U, have greatly increased thanks to advances in ion sources. Because recent low-energy nuclear physics experiments pursue very rare events, beam intensity has become a crucial issue.
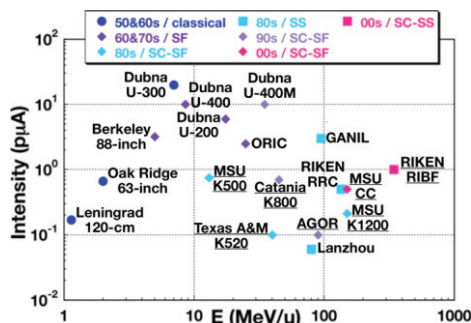


Figure 1: Historical development of heavy-ion cyclotrons.

Nuclear physics is one of the most important applications of heavy-ion cyclotrons: unstable nuclei far from the β-stability line are being extensively studied and many new superheavy elements have been synthesized at JINR FLNR [3]. Heavy-ion beams are also widely used for material modification and analysis (PIXE, RBS, etc.) [4]. The high biological effectiveness of energetic heavy ions has also enabled applications in medical science, biology, agriculture and so on. A compact superconducting cyclotron capable of delivering a 400 MeV/amu carbon beam for cancer therapy has been designed by an IBA-JINR collaboration [5]. Also, wide variety of plant mutations have been induced by energetic

light ions [6] accelerated in the RIKEN Ring Cyclotron (RRC) [7]. The reviews of Onishchenko [8] and Goto [9] provide more detail.

## BASIC FEATURES OF CYCLOTRONS

### Types of Cyclotron

The classical cyclotron invented by Lawrence [10] employed an azimuthally uniform and radially decreasing magnetic field to produce approximate isochronism and vertical stability of particle motion. However, as Bethe pointed out [11], the relativistic mass increase of ions requires a radially increasing field, which impairs vertical stability. The inventions of synchrocyclotrons [12-14] and Thomas cyclotrons solved this conflict. Thomas proposed the use of an azimuthally varying field [15] (AVF) for an isochronous magnetic field. In this case, an ion's orbit is non-circular and ions can experience edge focusing in the vertical direction. The Thomas cyclotron, also called the isochronous or sector focusing cyclotron, was first demonstrated by Richardson but this fact was classified until 1956 [16]. A further modification of the isochronous magnetic field by using spirally ridged magnet poles was proposed by Kerst et al. [17], which is effective to increase vertical focusing. Cyclotrons with spirally ridged poles are widely used, especially for high-energy cyclotrons.

To realize meson factories, a separate sector or ring cyclotron was proposed [18,19]. A single magnet producing an isochronous magnetic field is divided into sector magnets which are arranged in a ring with spaces between them. This configuration loses one virtue of cyclotrons, compactness, but gains stronger vertical focusing and higher acceleration voltages because azimuthal modulation of the isochronous magnetic field is much stronger than in AVF cyclotrons and high-voltage resonators can be installed in the spaces between the sector magnets. Thus, separate sector cyclotrons are used to produce high-intensity beams. A separated orbit cyclotron (SOC), proposed by Russell [20] and Martin [21], and demonstrated by Trinks [22], is another important variation, but there are no SOCs routinely serving heavy-ion beams to users. For more details of cyclotron development, many review articles are available: for example, the review by Craddock [16].

Among the currently working heavy-ion cyclotrons, GANIL, IMP-Lanzhou, RCNP and RIBF use separate sector cyclotrons, U-400 and U-400m of JINR FLNR are normal conducting AVF cyclotrons, and K500 and K1200 (MSU/NSCL), K500 (TAM), K800 (Catania) and AGOR (K600) are very compact superconducting AVF-type cyclotrons. A coupled cyclotron system at MSU/NSCL accelerates heavy ions up to 160 MeV/amu, though their

cyclotrons use magnets weighing 90 ~ 240 tons, which are one order of magnitude smaller than those used in normal-conducting separate sector cyclotrons.

### Beam Optics in Cyclotrons

In a cyclotron, beam optics is determined by a given isochronous magnetic field and depends on ion energy. If we neglect acceleration, a periodic solution, representing an equilibrium orbit of an ion moving under the isochronous magnetic field is obtained. Betatron tunes and beta functions can also be determined. Figure 2 shows tune diagrams for the four ring cyclotrons of RIBF for accelerating uranium ions up to 345 MeV/amu. Numerical methods are usually used to evaluate tunes, but the analytic expressions [23,24]

$$\nu_r^2 = 1 + n + O(N^{-2}) \quad \nu_z^2 = -n + \frac{1}{2}f^2(1 + 2\tan^2\theta) + O(N^{-2})$$

are widely used as a starting point in cyclotron design. Here, $n$, $\theta$, $f^2$ and $N$ are the field index, spiral angle, flutter and harmonic number of each Fourier component of the magnetic field. The flutter indicates strength of azimuthal modulation of the isochronous magnetic field. For an azimuthally uniform or azimuthally averaged isochronous magnetic field, the relation $B = B_0\gamma$ with constant $B_0$ holds and we obtain $n = \beta^2\gamma^2$ and $\nu_r = \gamma$. The vertical tune $\nu_z$ decreases as beam energy increases and vertical focusing is given by the $f^2(1 + 2\tan^2\theta)$ term.
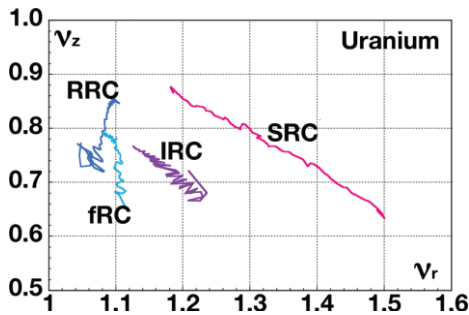


Figure 2: Tune diagrams of a 345 MeV/amu uranium beam in RIBF. A cascade of these four ring cyclotrons is used in practice.
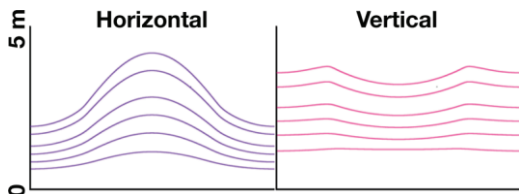


Figure 3: Beta functions of uranium ions accelerated by RRC from 0.7 to 10.8 MeV/amu. Beta functions of one unit cell starting from the valley center are shown for six different energies (from the bottom to top, 0.7, 1.3, 2.3, 3.4, 5.7 and 7.5 MeV/amu).

Beta functions ($\hat{\beta}$) increase in proportion to the ion's orbital radius and are modulated, to a certain extent,

reflecting changes of focusing strength (see Fig. 3). The matched beam radius $\sigma$ ($\sigma^2 = \hat{\beta}\varepsilon$) scales as $\sigma \propto \sigma_0/\gamma$ ($\sigma_0$ constant) if we use the smooth approximation $\hat{\beta} = R/\nu$. In any case, beam radiuses change gradually in both horizontal and vertical directions during acceleration, if a beam is matched to its eigen-ellipses at injection. Whether all the relevant matching conditions, such as emittance and dispersion matching, are fulfilled is examined by measuring the charge density distribution (turn pattern) of a beam.

## INTENSITY LIMITING FACTORS OF HEAVY-ION CYCLOTRONS

Compared with the success of PSI that routinely accelerates a 1.3 MW proton beam [25,26], beam powers obtained by heavy-ion cyclotrons are limited to less than 10 kW [27-29]. Stetson et al. [29] classified the intensity-limiting factors of the MSU/NSCL coupled cyclotron system into three categories: source, stripper and power limited. The last of these can be generalized to include all the limits imposed by unacceptable beam loss in cyclotrons. At MSU/NSCL, medium-heavy metal elements such as Ni, Zr and Sn are source limited. At RIBF, 345A-MeV $^{48}$Ca (415 pnA) and $^{70}$Zn (123 pnA) beams are also source limited. Because the ion sources used there are not state-of-the-art, the present situation will be improved in the near future.

On the other hand, the remaining two factors will remain serious problems. Beam intensity for very heavy ions like uranium is frequently limited by stripper lifetime. The lifetime of carbon foils reported by Stetson [29] is less than a few minutes for a 7.7-MeV/amu $^{238}$U beam with an intensity of 20 pnA. Our experience is typically less than 12 h for a 15-pnA $^{238}$U beam at 10.8 MeV/amu. (The reason for this large discrepancy between the lifetimes of the two facilities is not understood.) To solve this lifetime problem, a helium gas stripper was successfully introduced [30] at RIBF. However, RIBF adopts a two-step charge-stripping scheme to accelerate uranium ions up to 345 MeV/amu. Rotating beryllium disks (~18 mg/cm$^2$) now serve as the second-stage charge-state stripper [31] at 50 MeV/amu and the beam-intensity limit is less than 150 pnA for a 50-MeV/amu uranium beam based on our operating experience. Beyond this, beryllium disks are not only seriously deformed but also crack due to heat deposited from the beam.

Although beam loss at injection and during acceleration sometimes causes serious problems [32], beam loss at extraction has been the major concern in cyclotron development. With the exceptions of charge-stripping extraction used at JINR FLNR [33], TRIUMF [34] and so on, an electrostatic deflector is widely used as the first stage of beam extraction. Because heavy-ion cyclotrons pursue versatility of ion species and beam energy, the use of deflectors is a reasonable choice at present. A septum electrode of the deflector is placed between the final turn to be extracted and the other turns. If separations between these turns are insufficient at extraction, sizable beam loss

occurs. The maximally allowed heat deposit on a septum electrode is typically about 0.3-0.5 kW, which eventually limits available beam intensity in high-power cyclotrons.

The beam-intensity limit imposed by a requirement for hands-on maintenance is usually higher than the present power limit for heavy-ion cyclotrons because energetic heavy ions produce much less radioactivity than energetic protons do [35].

## MEASURES USED FOR CLEAN BEAM EXTRACTION

As mentioned above, insufficient turn separation at beam extraction causes sizable beam losses. The azimuthally averaged turn separation ($\Delta R$) in cyclotrons is given by

$$\Delta R = \frac{qeV_{acc}}{mc^2}\frac{\gamma}{(\gamma^2-1)\nu_r^2}R$$

Here, $m$ and $qe$ are the mass and charge of the ion, respectively, $V_{acc}$ is the acceleration voltage per turn, $R$ is the average orbital radius and $\nu_r$ is the horizontal tune. So, a combination of a high acceleration voltage and a smaller average magnetic field is essential to obtain a sufficient turn separation—an approach that is adopted in PSI injector 2 [36]. However, heavy-ion cyclotrons have pursued high magnetic fields to realize higher-energy beams and their turn separations are not large enough for high-intensity beams. This is one of the difficulties in heavy-ion cyclotron design.

To overcome this difficulty, several measures are used [37,38], one of which is inducing coherent radial motions. Techniques that can be applied are precessional (off-centring) acceleration, regenerative acceleration, beam orbit expansion [39] and so on. RIBF routinely uses precessional acceleration, in which a coherent radial betatron motion is induced at injection. The turn pattern has alternating sparse- and dense-turn regions and the beam is extracted from a sparse-turn region by adjusting acceleration voltage.

The situation becomes more serious for small cyclotrons used as first-stage accelerators. In this case, the beam injected into the cyclotron is not well bunched. If we use an acceleration voltage in the form of a single sinusoidal wave, a long bunch experiences a banana-shaped deformation in the radial-longitudinal plane due to an energy spread caused by a time-varying acceleration voltage and dispersion of the applied isochronous magnetic field. This banana-shaped deformation reduces turn separation. Flat-topping resonators improve the uniformity of the acceleration voltage by producing decelerating RF fields working at a frequency which is an integer multiple of the acceleration voltage. Using a radially increasing accelerating field is also effective for long bunches. The radial increase of the electric field produces a time-dependent magnetic field in a polar direction. Leading (trailing) particles are deflected outward (inward) and are moved backward (forward) by the RF magnetic field. As a result, beam bunches are compressed in the longitudinal direction [40] and the energy spread is reduced.

However, the effectiveness of these measures is established for only low-intensity beams. Space-charge effects, in many cases, destroy the gain expected by these measures.

## BEAM DYNAMICS IN CYCLOTRONS

Space-charge effects have been studied extensively for both proton and heavy-ion cyclotrons. A brief summary is given here.

### Vortex Motion

Gordon [41] emphasized the importance of vortex motion induced by a strong radial-longitudinal coupling in cyclotrons. Assuming a uniform magnetic field and $\gamma \sim 1$, particle motion relative to the bunch center is expressed in the rotating frame as

$$\frac{d\vec{v}}{dt} + \vec{\omega} \times \vec{v} = \frac{q}{m}\vec{E}.$$

Here, $\vec{E}$ and $\omega$ are the space-charge electric field and cyclotron angular frequency, respectively. Gordon discussed a steady state of the equation by neglecting the first term of the left side. (This corresponds to averaging out fast particle motions such as betatron oscillations.) In this case, we can easily understand a characteristic feature of the steady state under the space-charge force; in other words, particles move along an equipotential surface of the space-charge field. Gordon described two kinds of vortex motions: an overall vortex motion and a local vortex motion. The former occurs when neighboring turns overlap each other and equipotential surfaces extend in the radial direction over many adjacent bunches. The latter occurs when turns are separated. In this case, the orbital radius of a particle accelerated (decelerated) by the space-charge force increases (decreases) due to the isochronous magnetic field. An outer (inner) particle experiences an outward (inward) kick from the space-charge force and moves backward (forward). Hence, particles rotate around the bunch center. The local vortex motion washes out the energy gain obtained from the space-charge force.

The local vortex motion described by Gordon was later discovered as a "round beam". Its existence was confirmed by a series of studies [42-44] for PSI injector 2. The reason why this discovery attracts much attention is that a round beam seems to keep its shape all the way to beam extraction and indicates the possibility of accelerating a beam bunch that is near its space-charge limit [45].

Kleeven's theoretical work [46] is based on a smooth approximation to the isochronous magnetic field and Sacherer's linearization technique [47] applied to space-charge forces. Kleeven derived a set of equations describing the time evolution of all the second moments relevant to particle motion and demonstrated the existence of a stationary solution with rotational symmetry, that is, a round beam.

Bertrand and Ricaud [48] also employed a linear analysis as their starting point. For a non-relativistic particle (mass $m$ and charge $q$) moving under a uniform magnetic field ($B_z$), with the assumption that a beam bunch is a uniformly charged sphere, the equation of motion in a radial-longitudinal plane is given by

$$\ddot{z} = i\omega\dot{z} + \lambda(z - z_0).$$

Here a complex variable $z = x + iy$ has been introduced, where $x$ and $y$ denote radial and longitudinal coordinates in the laboratory frame, respectively. The subscript 0 indicates the bunch center, $\omega$ is the cyclotron angular frequency, $\lambda$ is defined as $\lambda = qk/m$, and $k$ is the gradient of the space-charge electric field. The gradient is given by $k = Q/4\pi\epsilon_0 r_0^3$, where $Q$ and $r_0$ are the charge and radius of the assumed charged sphere. The solution is easily obtained as

$$z - z_0 = Ae^{i\omega\nu_+ t} + Be^{i\omega\nu_- t}.$$

Here, tunes $\nu_{\pm}$ are determined by solving the characteristic equation $\omega^2\nu_{\pm}^2 - \omega^2\nu_{\pm} + \lambda = 0$ to obtain

$$\nu_{\pm} = \frac{1 \pm \sqrt{1 - 4\lambda\omega^{-2}}}{2}.$$

In this model, particle motion is described by a superposition of sinusoidal waves. Examples of particle motion are shown in Fig. 4. Using these solutions, Bertrand and Ricaud constructed a transfer matrix and obtained a stationary solution of the beam matrix. Hence the K-V distribution [49] was determined in this simplified model. The stationary solution should fulfil several matching conditions on the parameters describing a four-dimensional phase-space ellipse. One of them is that the distribution should be rotationally symmetric in the radial-longitudinal plane; hence, the assumption of a uniformly charged sphere is consistent with the stationary condition. Starting with these matching conditions, Bertrand and Ricaud investigated the stability of a round beam that has a finite six-dimensional emittance (inside a ellipse) in their fully three-dimensional space-charge simulations. They reported that a stable round beam, not exhibiting pulsation and halo formation, was obtained after an adjustment.
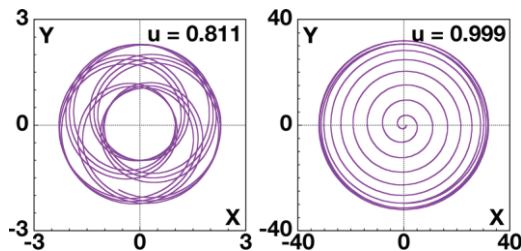


Figure 4: Solutions of the linearized equation of Bertrand and Ricaud. The parameter $u$ is an index of the space-charge effect, defined by $u = 4\lambda\omega^{-2}$.

In the linear analysis, particle motion is bound for only $4\lambda/\omega^2 < 1$ and a particle's orbital radius increases exponentially beyond the space-charge limit. This is, of course, unrealistic. For particles outside the beam core, an analysis of Chasman and Baltz [50] can be applied. In

their model, the electric field experienced by a test particle moving outside the beam core is $E(\rho) = Q\vec{\rho}/4\pi\epsilon_0\rho^3$, where $Q$ is the charge of the beam core and $\rho$ is the radial distance of the test particle from the center of the beam core. Chasman and Baltz obtained an exact analytic solution using elliptic integrals and also presented an intuitively understandable approximate solution. In this case, a test particle placed at the surface of the beam core with no kinetic energy undergoes a cloverleaf-shaped motion and all particles are bound by a strong magnetic field.

## SPACE-CHARGE SIMULATION

To analyze particle motion in realistic cyclotrons, numerical simulations are necessary; only then can effects from acceleration, the strongly modulated magnetic fields of separate sector cyclotrons, neighboring turns and so on be precisely taken into account. Many simulation codes have been developed [43,48,51-54] and one of the most advanced is OPAL [55]. We have also developed a classical particle-in-cell code in order to reproduce important results made by previous authors. Characteristic features of our code include Runge-Kutta integration for the time evolution of particle motion, evaluation of the space-charge force in the particle-rest frame (only the electrostatic potential is included), use of an area-weighted charge density distribution for Poisson's equation, a DFT-based direct Poisson solver. The Poisson computation box is chosen to be a rectangular parallelepiped and the potential is set to zero at two vertical boundaries simulating a beam chamber. The longitudinal boundary condition is virtually open and the radial boundary condition is chosen carefully. The number of test particles used is $10^5$ to $10^6$.

We made space-charge simulations for uranium ions accelerated by RRC with an assumption of separated turns. While a long bunch exhibits a spiral galaxy-shaped distribution even for beam intensities much less than the space-charge limit (Fig. 5(a)), a short bunch remains round (Fig. 5(b)). This result reproduces preceding work [43] and demonstrates the effectiveness of the round-beam acceleration scheme [45].
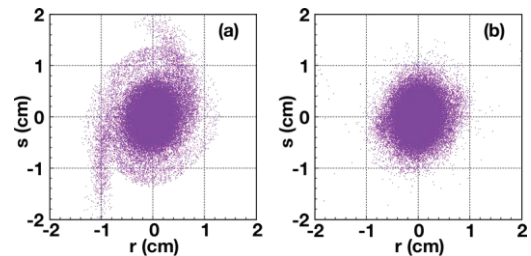


Figure 5: Particle distributions in horizontal (r) and longitudinal (s) planes for $^{238}U^{35+}$ 10.8 MeV/amu beams with intensities and initial phase widths of (a) 1 pμA and 6° and (b) 5 pμA and 3°.

The effectiveness of accelerating much longer bunches ($\Delta\phi = \sim 20°$) using flat-topping resonators should be

investigated because the charge density of bunches substantially decreases and the linear part of the space-charge force can be compensated by shifting the phases of the flat-topping resonators. Our simulations for RRC show that a long-bunch acceleration scheme gives a lower intensity limit, as in the case of PSI injector 2. However, this does not mean the round-beam scheme is always superior to the long-bunch scheme. A formula recently proposed for separated turns by Baartman [56] predicts an intensity limit of 2.6 pμA for a 345-MeV/amu uranium beam accelerated in SRC [57], our final stage accelerator. On the other hand, a space-charge simulation predicts an intensity limit of 6 pμA [58] for a uranium beam consisting of long bunches using a flat-topping resonator. Of course these two estimations do not strictly employ the same criteria for allowable beam loss and also include some uncertainties, but the reason why the latter simulation yields a similar intensity limit is that the bunch is very long (~16 cm at extraction).
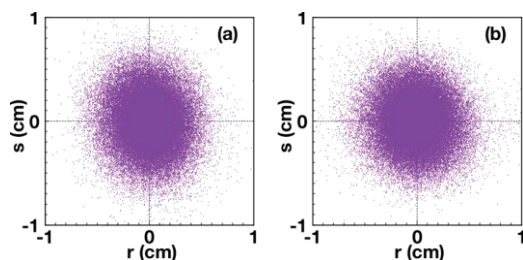


Figure 6: Particle distributions at extraction for a 10.8-MeV/amu $^{238}U^{35+}$ beam in case of the 24.33 MHz acceleration scheme. Results of (a) a 5-bunch simulation and (b) a 7-bunch simulation are shown.

A round beam is stable for separated turns. However, separated turns are not easily available in many heavy-ion cyclotrons because their acceleration voltages are insufficient compared with the large mass-to-charge ratio of the accelerated ions, or because of the high magnetic field employed in order to produce high-energy beams. The straightforward solution is to increase the acceleration voltage. At present, we operate the RF resonators of RRC at 18.25 MHz and the maximum available acceleration voltage is 0.28 MV/turn, which is insufficient to obtain separated turns. Hence usage of 24.33 MHz is proposed. In this case, an acceleration voltage increases up to 0.48 MV/turn, although we need some modifications for the present accelerator complex.

However, even in this case, effects from neighboring turns should be taken into account because they are not negligibly small. There are two methods to include the neighboring turn effects. The first is to impose a periodic boundary condition in the radial direction. This is justified for only a case of centering acceleration under a perfect isochronous magnetic field because coherent radial betatron motion or an imperfection of the isochronous magnetic field induces longitudinal misalignment of bunches. The other is to treat explicitly relevant neighboring bunches in the space-charge simulation. Yang et al. [59] pioneered space-charge simulation of this type

using OPAL-CYCL, a "flavor" of the OPAL framework. Their result that neighboring turns reduce the transverse profile and the energy spread of the beam bunch is encouraging. So, we conducted multi-bunch simulations where a single Lorentz frame is used. It may be justified for $\gamma \approx 1$. Results for nearly centering acceleration are shown in Fig. 6. Compared with a result obtained by a single-bunch simulation under a periodic boundary condition, we find no drastic change in multi-bunch simulations. However, we found that simulation results fluctuate depending on the number of bunches included, that is, convergence is not yet obtained. It means that we need more bunches but it is difficult to increase the number of turns due to limitation of our computing resources at present. We need further studies on the effects of neighboring turns in order to understand quantitatively beam loss at extraction in heavy-ion cyclotrons.

## SUMMARY

The "golden rule" for accelerating high-intensity beams in cyclotrons is to increase the acceleration voltage to obtain a sufficient turn separation at extraction so as to make maximal use of the local vortex motion. This was established by the success of PSI. To optimize the design of heavy-ion cyclotrons, a deeper understanding of neighboring-turn effects, both numerically and experimentally, is necessary.

## REFERENCES

[1] R.S. Livingston, Proc. 5th Int. Cyclotron Conf., Oxford (1969) 423.

[2] A. Goto and Y. Yano (editors). Proceedings of the 17th Int. Conf. on Cyclotrons and their Applications, Tokyo (2004).

[3] G. Gulbekyan et al., Proc. 19th Int. Conf. Cyclotrons and their Applications, Lanzhou, China (2010) 33.

[4] for example, A. Denker et al., NIM B **240** (2005) 61.

[5] Y. Jongen et al., NIM A **624** (2010) 47.

[6] T. Abe et al., Plant Mutation Breeding and Biotechnology (Shu. Q.Y., ed.), The Joint FAO/IAEA programme (2010) pp. 95-102.

[7] Y. Yano, Proc. 12th Int. Conf. on Cyclotrons and their Applications, Berlin, Germany (1989) 13.

[8] L.M. Onishchenko, Phys. Part. Nuclei **39** (2008) 950.

[9] A. Goto, Proc. 19th Int. Conf. on Cyclotrons and their Applications, Lanzhou, China (2010) 9.

[10] E.O. Lawrence and N.E. Edlefsen, Science **72** (1930) 376.

[11] H.A. Bethe and M.E. Rose, Phys. Rev. **52** (1937) 1254.

[12] E.M. McMillan, Phys. Rev. **68** (1945) 143.

[13] V.I. Veksler, Phys. USSR **9** (1945) 153.

[14] J.R. Richardson et al., Phys. Rev. **69** (1946) 669.

[15] L.H. Thomas, Phys. Rev. **54** (1938) 580.

[16] M.K. Craddock, Proc. 19th Int. Conf. Cyclotrons and their Applications, Lanzhou, China (2010) 1.

[17] D.W. Kerst et al., Phys. Rev. **98** (1955) 1153.

[18] H.A. Willax, Proc. Int. Conf. on Sector-Focused Cyclotrons and Meson Factories, Geneva (1963) 386.

[19] V.P. Domitrievskii, "Relativistic Cyclotron with Space Variation of Magnetic Field", Report Presenting the Doctoral Dissertation Manuscript in Mathematical Physics, Dubna (1961).

[20] F.M. Russell, Nucl. Instr. and Meth. **23** (1963) 229.

[21] J. A. Martin, IEEE-NS-**13** (1966) 288.

[22] U. Trinks, Nucl. Instr. and Meth. **220** (1984) 186.

[23] L. Smith and A.A. Garren, "Orbit Dynamics in the Spiral-ridged Cyclotrons", UCRL-8598 (1959).

[24] K.R. Symon et al., Phys. Rev. **103** (1956) 1837.

[25] M. Seidel, "Cyclotrons for high-intensity beams", arXiv:1302.10011v1 [phyics.acc-ph] 5 Feb 2013.

[26] J. Grillenberger et al., Proc. 20th Int. Conf. Cyclotrons and their Applications, Vancouver, Canada (2013) 37.

[27] N. Fukunishi et al., Proc. 20th Int. Conf. on Cyclotrons and their Applications, Vancouver, Canada (2013) 1.

[28] F. Chautard et al., Proc. 19th Int. Conf. on Cyclotrons and their Applications, Lanzhou, China (2010) 16.

[29] J. Stetson et al., Proc. 19th Int. Conf. on Cyclotrons and their Applications, Lanzhou, China (2010) 27.

[30] H. Imao et al., Phys. Rev. ST Accel. Beams **15** (2012) 123501.

[31] H. Hasebe et al., INTDS-2014, Tokyo, Japan (2014).

[32] for example, A. Sen et al., Proc. 20th Int. Conf. on Cyclotrons and their Applications, Vancouver, Canada (2013) 420.

[33] G.G. Gulbekyan et al., Proc. 18th Int. Conf. on Cyclotrons and their Applications, (2007) 308.

[34] J.R. Richardson, Proc. 7th Int. Conf. Cyclotrons and their Applications, Basel, Switzerland (1975) 41.

[35] I. Strašík et al., Phys. Rev. ST Accel. Beams **13** (2010) 071004.

[36] W. Joho, Proc. 11th Int. Conf. Cyclotrons and their Applications, Tokyo, Japan (1986) 31.

[37] J.M. van Nieuwland, "Extraction of Particles from a Compact Isochronous Cyclotron", Doctoral thesis, Techinical Universiteit Eindhoven (1972).

[38] W. Joho, "Extraction of a 590 MeV Proton Beam from the SIN Ring Cyclotron", SIN-Report TM-11-8, Thesis (1970).

[39] V.P. Dmitrievsky et al., Proc. 9th Int. Conf. on Cyclotrons and their Applications, Caen, France (1981) 505.

[40] W. Joho, Part. Accel. **6** (1974) 41.

[41] M.M. Gordon, Proc. 5th Int. Cyclotron Conf., Oxford (1969) 305.

[42] Th. Stammbach, 13th Int. Conf. on Cyclotrons and their Applications, Vancouver, Canada (1992) 28.

[43] S. Adam, 14th Int. Conf. on Cyclotrons and their Applications, Cape Town, South Africa (1995) 446.

[44] R. Dölling, Proc. DIPAC2001, Grenoble (2001) 111.

[45] Th. Stammbach, 15th Int. Conf. on Cyclotrons and their Applications, Caen, France (1998) 369.

[46] W.J.G.M. Kleeven, "Theory of Accelerated Orbits and Space Charge Effects in an AVF Cyclotron", Doctoral thesis, Technische Universiteit Eindhoven (1988).

[47] F.J. Sacherer, Proc. PAC (1971) 1105.

[48] P. Bertrand and Ch. Ricaud, 16th Int. Conf. on Cyclotrons and their Applications, East Lansing, USA (2001) 379.

[49] I.M. Kapchinsky and V.V. Vladimirsky, Proc. Int, Conf. on High Energy Accelerators, CERN, Geneva (1959) 274.

[50] C. Chasman and A.J. Baltz, Nucl. Instrum. and Meth. Phys. Res. **219** (1984) 279.

[51] S.R. Koscielniak and S. Adam, Proc. 1993 Part. Accel. Conf., Washington, USA (1993).

[52] L.M. Onishchenko et al., NUKLEONIKA **48** (Supplement 2) (2003) S45-S48.

[53] E. Pozdeyev et al, Proc. Hadron Beam 2008, Nashville, Tennessee, USA (2008) 157.

[54] E.E. Perepelkin and S.B. Vorozhtsov, Proc. Of RuPAC 2997, Zvenigorod, Russia (2008) 40.

[55] A. Adelmann et al., Proc. ICAP09, San Francisco, CA, USA (2009) 107.

[56] R. Baartman, Proc. 20th Int. Conf. on Cyclotrons and their Applications, Vancouver, Canada (2013) 305.

[57] H. Okuno et al., IEEE Trans. Appl. Supercond., **17**, (2007) 1063.

[58] S.B. Vorojtsov et al., Proc. 16th Int. Conf. Cyclotrons and their Applications, East Lansing, USA (2001) 402.

[59] J.J. Yang et al., Phys. Rev. ST Accel. Beams **13** (2010) 064201.

# PROGRESS IN THE UPGRADE OF THE CERN PS BOOSTER RECOMBINATION

J. L. Abelleira, W. Bartmann, J. Borburgh, E. Bravin, U. Raich, , CERN, Geneva, Switzerland

## Abstract

The CERN PS Booster recombination lines (BT) will be upgraded following the extraction energy increase foreseen for the long shutdown 2 (LS2) and meant to reduce the direct space-charge tune shift in the PS injection for the future HL-LHC beams. Henceforth the main line elements, recombination septa, quadrupoles and dipoles must be scaled up to this energy. An increase in the beam rigidity by a factor 1.3 requires the same factor in the field integral of the septa, $\int Bdl$, in order to bend the same angle and preserve the present recombination geometry, which is one of the main upgrade constraints. This paper describes the new optics, in particular in the new and longer septa. In addition we consider the upgrade of the so called BTM line that brings the beam to the external dump and where emittance measurements are taken thanks to three pairs of grids. The new proposed optics has also the advantage to simplify the design of the new dipoles. Here we study this new optics and the issues related to the emittance measurement at the new higher energy.

## INTRODUCTION TO THE RECOMBINATION LINES

The four transfer lines that extract protons from each ring of the PSB to the PS (BT1, BT2, BT3, BT4) are recombined in the BT line (Fig. 1).
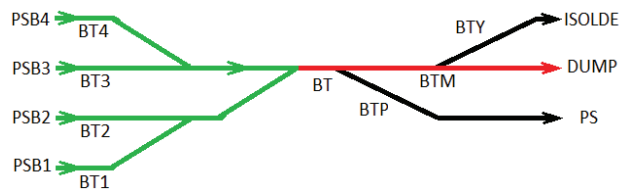


Figure 1: Scheme of the PSB ejection lines, not to scale

From the BT line, the beam can go to three different locations: to the PS (BTP line), to the ISOLDE facility (BTY) or to a dump (BTM). BT.BHZ10 is the switch magnet to the BTP line and BTY.BVT101 is the switch magnet to BTY (off when sending to the dump). Figure 2 represents the scheme of the BT-BTM magnets. A set of three couples of SEM grids lo-cated in the BTM line is used for the emittance measurement in the two planes. In this paper we describe the works on the recombination part (in green in Fig. 1) and the BT-BTM line (in red).
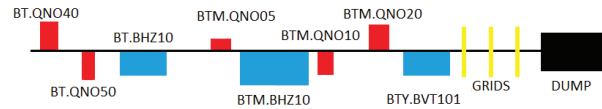


Figure 2: Scheme of the BT-BTM line. Quadrupoles are shown in red and dipoles in blue. It corresponds to the red line in Fig. 1.

## UPGRADING

The LHC Injectors Upgrade (LIU) project [1] aims to an injection energy in the PS of 2 GeV, so that the present lines must work at that energy. In addition, the upgrade of the recombination lines must not hinder a possible upgrade of the ISOLDE faclity from 1.4 to 2.0 GeV. In particular, the energy upgrade translates into a 30% increase in beam rigidity, so that the same increase have to followed by the field integral $\int Bdl$ in all the bending elements: dipoles, septa and kickers. At the same time, a working energy of 1.4 GeV must be allowed in terms of element acceptances. The present 1.0-GeV working energy will be discarded after long shutdown 2 (LS2).

## OPTICS

In order to deal with the different users of the extracted beams from the PSB, four different optics configurations for the BT-BTM line exist [2]:

1. Dump optics

2. $\epsilon_x$ (Horizontal emittance) measurement: large $D_x$

3. $\epsilon_x$ measurement: small $D_x$

4. $\epsilon_y$ (Vertical emittance) measurement

The first one is a common configuration to dump the beam and to send it to the ISOLDE facility, while the optics 2, 3 and 4 are used to measure the beam emittances. The reason for having two configurations for the $\epsilon_x$-measurement is the large variety of beams that the PSB is supposed to deal with, which are summarized in Table 1.

Table 1: Expected Normalized rms Emittances and Momentum Spreads of the Different Beam Types in the PS Complex, after LS2

| Beam | $\epsilon_{N,x}[\mu m]$ | $\epsilon_{N,y}[\mu m]$ | $\sigma_\delta$ |
|---|---|---|---|
| LHC (BCMS) | 1.2 | 1.2 | $1.1 \times 10^{-3}$ |
| LHC | 1.6 | 1.6 | $1.5 \times 10^{-3}$ |
| Fixed target | 10 | 5 | $1.35 \times 10^{-3}$ |
| ISOLDE | 15 | 9 | $1.35 \times 10^{-3}$ |

In the following, the half beam sizes are calculated as a function of the number of sigma ($n_\sigma$) as:

$$A_{x,y} = n_\sigma \sqrt{k_\beta \beta_{x,y} \frac{\epsilon_{N;x,y}}{\gamma_r \beta_r} + \left|k_\beta D_{x,y}\sigma_\delta\right| + c.o.} \sqrt{\frac{\beta_{x,y}}{\beta_{M;x,y}}};$$

(1)

where $k_\beta$ represents the uncertainty factor on the betatron ($\beta$) and dispersion ($D$) functions; while $\gamma_r$ and $\beta_r$ are the relativistic parameters. $\beta_M$ represents the maximum value of the $\beta$-functions and $c.o.$ is the trajectory variation, 1.5 mm.

For the LHC beams, the first term in Eq. 1 is very small and in order to reduce the contribution of the second one, the small-$D_x$ optics is used, On the other hand, this optics presents reduced horizontal acceptance due to larger values of $\beta_x$ so that the large-$D_x$ optics has to be kept for beams where the emittance contribution is significant, that is, for non-LHC beams.

### Limitation of present optics

Studies have been performed to check possible bottlenecks of the present optics. Figures 3 and 4 show the two worst cases in aperture limitation. Beam sizes are represented (using the definition in Eq. 1 with $n_\sigma$=3, $k_\beta$ = 1.2 and 1.4 GeV) and compared with the physical aperture of the line.
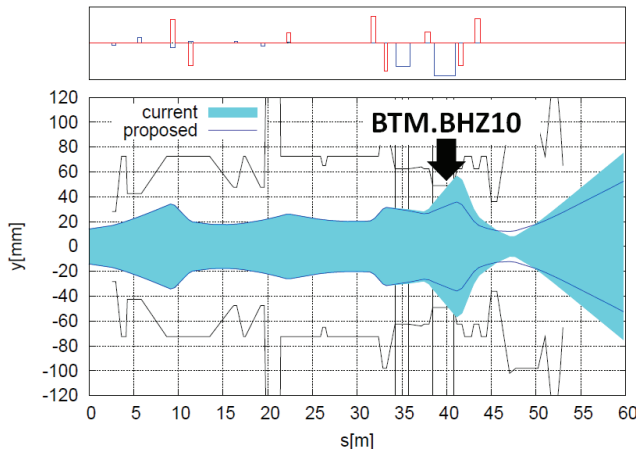


Figure 3: Aperture and beam envelope in the horizontal plane, for the dump optics and ISOLDE beam.

We can observe that the aperture is narrower than the 3-$\sigma$ beam size at BTM.BHZ10 (horizontal plane) and BTM.QNO20 (vertical plane). The aperture bottleneck into the BTM.BHZ10 aperture may be the cause of an excess observed during a radiation survey performed in 2013 (Figure 5). A reduction of the beam size at these locations would reduce the beam losses and would ease the design of the new bending magnet for the 2-GeV upgrade at the position BTM.BHZ10 [3]. In fact its vertical gap can be reduced from the present value.
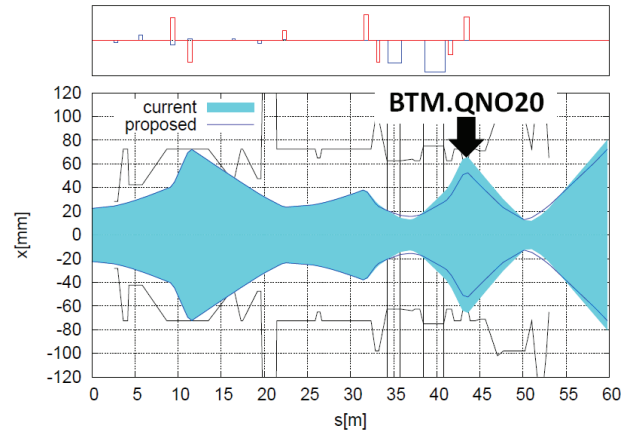


Figure 4: Aperture and beam envelope in the vertical plane, for the large-$D_x$ emittance measurement optics and ISOLDE beam.
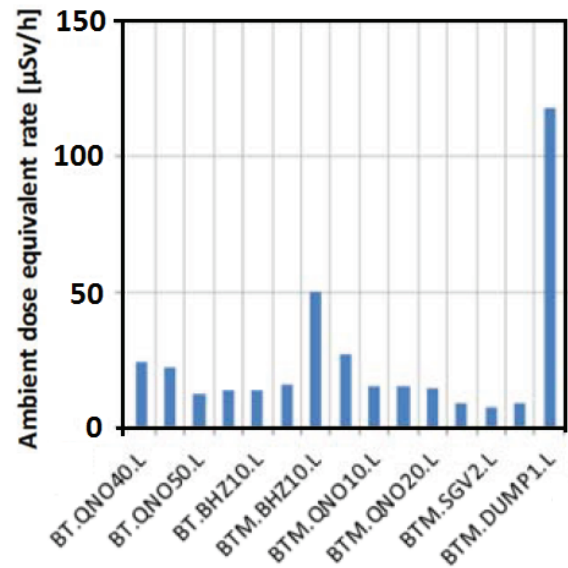


Figure 5: Radiation survey [4] for the BT-BTM line after recombination.

## THE NEW OPTICS FOR THE BTM LINE

In order to reduce the beam size at locations BTM.QNO20 and specially BTM.BHZ10, a new full set of optics has been prepared, by rematching the quadrupoles BT.QNO40, BT.QNO50, BTM.QNO05, BTM.QNO10 and BTM.QNO20, while respecting the specification for the maximum energy desposition on the beam dump [5]. In addition, the following conditions of the optics in the grids must be fulfilled for either plane:

$$\alpha_2 = 0 \tag{2}$$

$$\Delta\mu_{1-2} = \Delta\mu_{2-3} = \pi/3 \tag{3}$$

$$min\left[\frac{D^2}{\beta} + \left(\alpha\frac{D}{\sqrt{\beta}} + \sqrt{\beta}D'\right)^2\right] \tag{4}$$

Here the subindex refers to the corresponding grid and the Twiss functions to those whose emittance is to be measured.

The comparison between the two optics is done in Fig. 6 for the dump configuration. We can appreciate how the $\beta$-function has been strongly reduced at BTM.BHZ10. Figure 7 compares the two optics for the large-$D_x$ $\epsilon_x$-measurement. Here the horizontal $\beta$-function is reduced at BTM.QNO20.
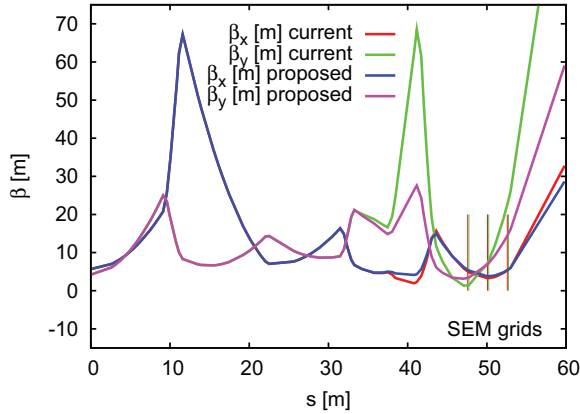


Figure 6: Comparison between the current and the proposed optics for the dump configuration.
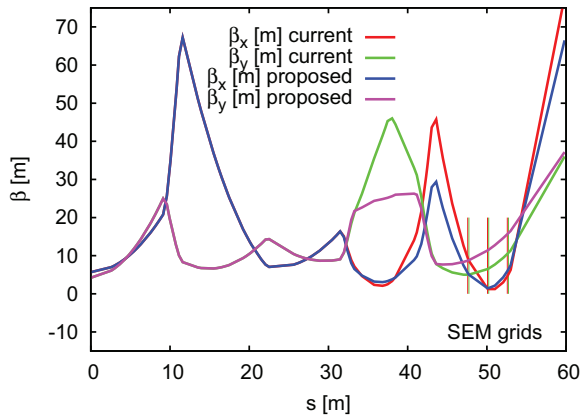


Figure 7: Comparison between the current and the proposed optics for the large-$D_x$ $\epsilon_x$-measurement configuration.

Figures 3 and 4 also compare the beam sizes with the present and with the new optics. It is evident the reduction on the beam at the two problematic locations.

Table 2 summarizes the maximum beam sizes for the present and for the proposed values of the ensemble of the four optics configurations. The maximum $A_y$ in BTM.BHZ10 has been reduced by 19 mm and by the maximum $A_x$ in BTM.QNO20 by 14 mm.

In order to ensure compatibility with possible upgrade of the ISOLDE facility to 2.0 GeV, the optics changes at the location of BTY.BVT101 have been kept to the minimum. This assures the optics matching to a future upgrade of this line and a reasonable beam acceptance at this location if this magnet is upgraded to a longer one.

Table 2: Maximum Beam Sizes for each of the Elements of the BT-BTM Line [mm].

|  | present | | proposed | |
| --- | --- | --- | --- | --- |
|  | $A_x$ | $A_y$ | $A_x$ | $A_y$ |
| BT.QNO40 | 57 | 25 | 57 | 25 |
| BT.QNO50 | 40 | 34 | 40 | 34 |
| BT.BHZ10 | 35 | 42 | 34 | 36 |
| BTM.QNO05 | 29 | 48 | 27 | 38 |
| BTM.BHZ10 | 36 | **56** | 33 | **37** |
| BTM.QNO10 | 45 | 59 | 35 | 37 |
| BTM.QNO20 | **67** | 41 | **53** | 40 |
| BTY.BVT101 | 49 | 29 | 38 | 29 |

With respect to the beam dump, the minimum value of beam size in the dump core is not reduced with respect to the specified value [6].

## EMITTANCE MEASUREMENT WITH THE NEW OPTICS

The new optics would improve the emittance measurement, as the conditions in Eqs. 2, 3, 4 are met with more precision. However, at the upgraded energy of 2.0 GeV, the beam sizes become smaller due to the adiabatic damping. We need to evaluate if the present hardware will be capable to measure the emittance of the future beams. First of all, we have to consider the wire separation on the present grids. For the inner couple of SEM grids it has a value of 0.5 mm, while the outer ones feature 1 mm. In principle we consider that the beam profile can be well measured if the rms beam size is above the wire seperation [7].

The minimum rms beam size that the we can measure is given by:

$$\sigma_{x,y} = \sqrt{\beta_{x,y} \frac{\epsilon_{N;x,y}}{\gamma_r \beta_r} + \left(D_{x,y}\sigma_\delta\right)^2}; \qquad (5)$$

For the smallest future beam to be measured (LHC BCMS), the beam size in the central grid is $\sigma_y \sim 0.7$ mm and for the outer ones, $\sim 1.6$ mm. These values are above the wire separation, so in principle it will be possible to measure the emittance with the present systems. These studies will continue in order to account for the precise value of the error in the emittance measurement for all kind of beams.

## APERTURE STUDY OF THE RECOMBINATION SEPTA

The recombination of the four beam lines is done by three septa and three kickers, as shown schematically in Fig. 8.

Septa and kickers are required to increase their field integral $\int Bdl$ by a 30% in order to deal with the higher energy, while bending the same angle and preserving the present recombination geometry. The new septa are longer, with their dimensions compared with the present ones shown in (Fig. 9). In addition, the deflection center is assumed to be moved downstream by 82 mm. The new septa have
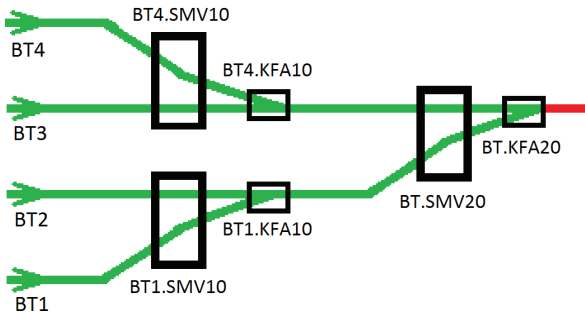
Figure 8: Scheme of the PSB recombination, showing the 3 septa (SMV) and the 3 kickers (KFA), not to scale.

been introduced in the model and the trajectories had been rematched. A study has been performed to evaluate the acceptance of the septa ($A_{x,y}$, Eq. 1) in terms of $n_\sigma$, comparing the case of the present with the upgraded septa and evaluating how to improve this acceptance.
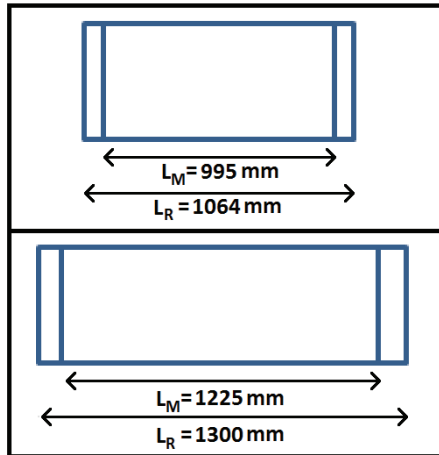


Figure 9: Comparison between the present (top) and new (bottom) septa, indicating the corresponding magnetic ($L_M$) and physical lengths ($L_R$) [8].

Figure 10 shows the septum that recombines the beams coming from ring 3 (undeflected) and ring 4 (deflected). The beam envelope corresponds to $n_\sigma = 2.6$ for the ISOLDE beam.

The first thing we observe is that this beam touches the septum blade at the exit while there is still some aperture margin at the entry face of the magnet. This situation is the same for the lengthened septa, as we can see in Fig. 11.

In the last case, we can observe a loss in the beam acceptance, $\sim 0.1\ n_\sigma$. The case is simular for the other two recombinations (BT1.SMV10 and BT.SMV20), and also for the horizontal plane (see Figs. 12 and 13), with losses in acceptance while moving to larger septa in all cases below this quantity. In SMV20 the vertical acceptance is more reduced: $n_\sigma = 2.0$ for the present septum and 1.9 for the upgraded one.
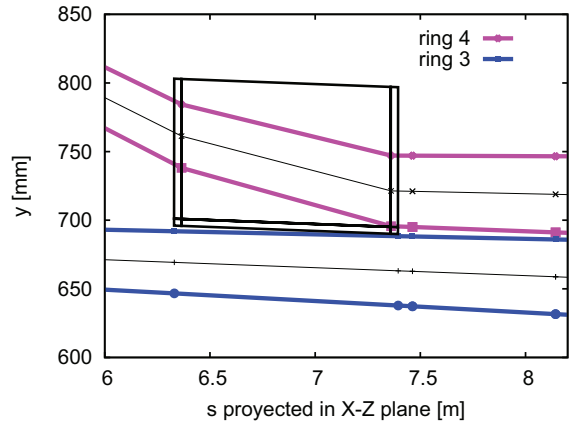


Figure 10: BT4.SMV10 vertical recombination with present septum ($n_\sigma = 2.6$).
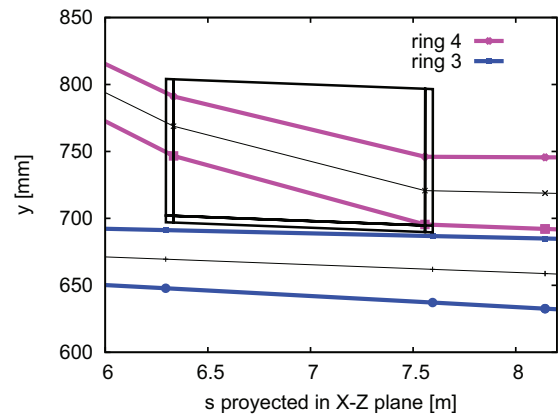


Figure 11: BT4.SMV10 vertical recombination with lengthened septum ($n_\sigma = 2.5$).
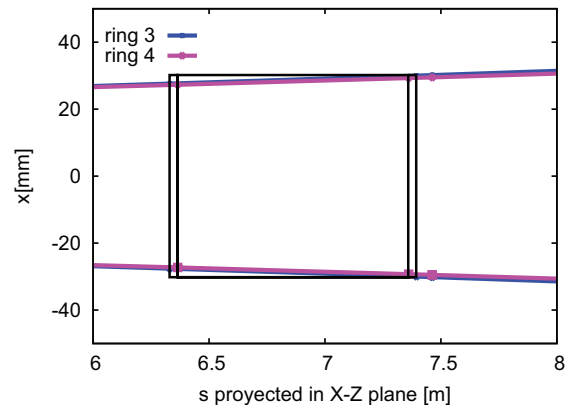


Figure 12: BT4.SMV10 horizontal recombination with present septum ($n_\sigma = 2.5$).

The fact that the limitation in acceptance is given by the vertical beam separation at the exit of the septum makes unnecessary to increase the transverse dimensions of the septa. This is not the case for magnets where the trajectories of the beam at the entry and the exit are symmetric, where a
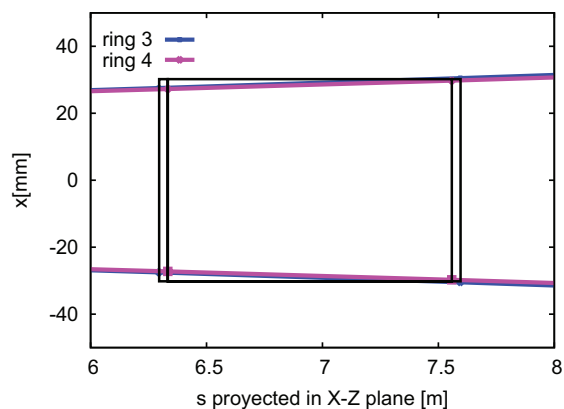
Figure 13: BT4.SMV10 horizontal recombination with lengthened septum ($n_\sigma = 2.5$).

longer magnet means a longer sagitta and the need to increse the gap.

In order to increase the acceptance of the septum, one could increase the separation of the orbit centers at the exit of the septum. However, one would need a increase in the angle of the recombination kickers (~8.5 mrad for KFA10 and ~5.4 mrad for KFA20). The KFAs will be upgraded to 2.0GeV; a further increase would be a major upgrade, that is the reason why the option of increasing the angle is discarded. There would be a solution to increase the beam separation at the septum exit without increasing the kicker angle, consisting on moving the quadrupoles between septa and kickers bringing them closer to the septa. But this option cannot be realized due to the lack of space in the line.

## CONCLUSIONS

- For the present machine (1.4 GeV), the new optics is able to improve the transmission efficiency of the BT-BTM line, reducing potentially the beam losses and the radiation associated with these losses. It also offers improved conditions for the emittance measurements. It will be benchmarked with a machine development study (MD).

- For the upgrade of the PSB at 2 GeV, this new optics will ease the design of the bending magnet BTM.BHZ10, by reducing its gap height. It does not hinder, in principle, a future upgrade of the BTY line at 2GeV.

- The future beams will have a beam size in the SEM grids above the wire separation, so it seems possible to continue measuring the emittance at the same precision.

- The limitation on the septum acceptance is given by the orbit separation at the exit.

- The new longer septa can be built with the same vertical and horizontal gap with a negligible loss in acceptance.

- The work described here concerns the BT and BTM lines. For an update of the works on the BTP line and PS injection see [9].

.

## REFERENCES

[1] LIU website: https://espace.cern.ch/liu-project/default.aspx

[2] Ch. Carli, "New Optics of the BT/BTM Transfer Line for Horizontal Emittance Measurements", CERN AB-Note-2003-056 (ABP).

[3] K. Hanke, G.B. Smith *et al.*, "Upgrades for the CERN PSB-to-PS transfer at 2 GeV", IPAC'13, Shanghai, China. p. 404

[4] G. Dumont, "Radiation Survey Results 2013", EDMS 1279669. https://edms.cern.ch/document/1279669/1

[5] A. Perillo-Marcone *et al*, "Design of Air Cooled Beam Dump for Extraction Line of PS Booster," IPAC'13, Shanghai, China. p. 3436

[6] W. Bartmann, B. Mikulec, "PS Booster dump upgrade," CERN EDMS 1229493

[7] E. Bravin, "Statistical effects in beam profile monitors," AB-Note-2004-016 BDI

[8] V. Pricop, B. Balhan, "Summary of OPERA simulations for lenghtened SMV10 to be used for extreaction from PSB at 2GeV". CERN EDMS 1350789

[9] W. Bartmann, J.L. Abelleira, K. Hanke, M. Kowalska, "Upgrades of the CERN PS Booster Ejection Lines".

**ISBN 978-3-95450-173-1**

# AN OVERVIEW OF THE PREPARATION AND CHARACTERISTICS OF THE ISIS STRIPPING FOIL

H.V. Smith, B. Jones, ISIS, STFC, Rutherford Appleton Laboratory, UK

*Abstract*

The ISIS facility at the Rutherford Appleton Laboratory is a pulsed neutron and muon source, for materials and life science research. H⁻ ions are injected into an 800 MeV, 50 Hz rapid cycling synchrotron from a 70 MeV linear accelerator, over ~130 turns by charge exchange injection. Up to $3\times10^{13}$ protons per pulse can be accelerated, with the beam current of 240 µA split between the two spallation neutron targets.

The 40 × 120 mm aluminium oxide stripping foils used for injection are manufactured on-site. This paper gives an overview of the preparation and characteristics of the ISIS foils, including measurements of foil thickness and elemental composition. Consideration is also given to the beam footprint on the foil and how this could be optimised.

## THE ISIS INJECTION SYSTEM

Injection into the synchrotron occurs via 70 MeV H⁻ charge exchange injection over 200 µs (~130 turns) beginning 400 µs before field minimum of the 50 Hz sinusoidal main dipole field. The foil is mounted in the middle of four dipole magnets which create a 65 mm symmetrical horizontal orbit bump and remove any un-stripped beam, Fig. 1. The bump collapses immediately after injection, in 100 µs, limiting re-circulations to ~30.
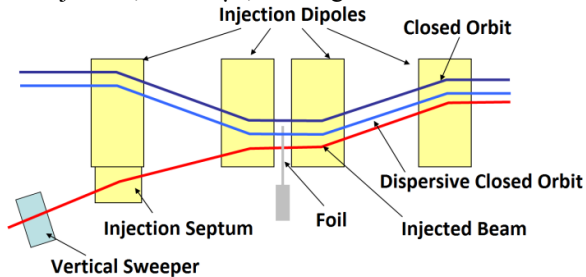


Figure 1: Schematic of the bump and injection magnets overlaid with the trajectories of the incoming H⁻ beam, and circulating protons.

Throughout the injection process the beam is painted transversely to reduce the effect of space charge forces, Fig. 2. The injected beam spot is fixed horizontally but painting is realised in this plane by the 20 mm movement of the dispersive closed orbit generated by the energy mismatch between the constant injection energy and changing synchronous energy of the ring. Vertical painting is achieved with a programmable dipole located upstream of the foil. The dipole current is swept such that the beam is moved 12 mm on the foil. The flexible positioning and painting system allows beam to be injected even when some areas of the foil are damaged, this can extend the useful foil life and avoid a foil change.

Operational experience shows that foil lifetimes are often in excess of 200,000 µA hrs, with an average of ~80,000 µA hrs, limited primarily by mechanical factors. A new foil is posted in preparation for each ISIS user cycle in order to avoid a foil change during the cycle which would require access to the synchrotron hall and result in ~4 hrs without beam.
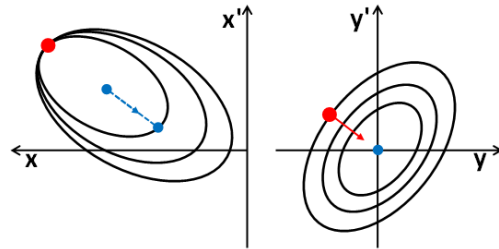


Figure 2: Phase space painting (schematic) on the foil in the horizontal and vertical planes. The injection spot is marked in red, with the closed orbit marked in blue.

## MOTIVATIONS

It is important to understand the properties of the stripping foil to optimise machine operations and design future upgrades.

Previous papers and reports [1, 2] give conflicting statements about the thickness and composition of the stripping foil. Most state that the foil is aluminium oxide (alumina) and that the thickness is 0.25 µm or 50 µg cm⁻². Using the accepted density of aluminium oxide, 3.95 g cm⁻³, the quoted areal density and thickness of the foil are inconsistent. These discrepancies prompted a fresh study of the foil production mechanism and measurements of the resulting foil properties.

## FOIL PREPARATION

The stripping foils used in ISIS operations are manufactured on site. Production requires numerous complex, non-automated stages and the skill, experience and judgement of staff is heavily relied upon to create usable foils. In total it takes around 20 hours to produce a single foil via the following eight stages, Fig. 3:

1. A 0.15 mm thick sheet of 99% pure aluminium is cut to 70 × 130 mm, two mounting holes are punched through and two wedges clipped out of the edges of the sheet in preparation for final installation.
2. One long edge of the aluminium sheet is then bent in a custom jig to strengthen it. The top short edge of the sheet is slid into a slot in a pre-prepared custom made mounting pin that is used to hold the foil in the mounting mechanism in the synchrotron.

3. At this stage the aluminium sheet is annealed in a vacuum furnace at a temperature of 360 °C for eight hours. The sheet is then anodised at 180 V, for 10-15 minutes, creating an alumina coating. The anodising solution is made from a mixture of 10 ml of analytical water and 6 g of ammonium hydrogen tetrahydrate. The annealing process is then completed by heating the sheet to 280 °C for another eight hours.

4. The edges of one side are masked in a custom jig and the alumina layer inside the masked region is removed by hand with wire wool.

5. The sheet is then suspended in a solution of methanol (1000 ml) and (30 ml) bromine to etch away the exposed aluminium, leaving just a thin transparent film surrounded by a frame. Once a visual inspection confirms that all of the required aluminium has been removed the thin foil is washed in an acetone bath.

6. The delicate foil is then placed in a vacuum chamber ($10^{-7}$ Torr) and a 0.18 μm layer of aluminium is electrostatically evaporated onto both sides of the foil. The deposited thickness is monitored by a quartz crystal.

7. The non-mounting edge of the frame is removed using a scalpel to expose the foil edge and then the foil is stored for up to six months over silica beads in (non-vacuum) containers. The silica beads act as a desiccant to prevent the foils from deteriorating due to hydration in air. After six months any unused foils are disposed of.

8. Immediately prior to installation in the synchrotron a scalpel is used to detach other parts of the foil from the frame. The extra cuts leave only the top edge, very bottom corner and top half of the secured edge supported, Fig. 4. These cuts reduce any residual mechanical stress, increasing the foil lifetime.
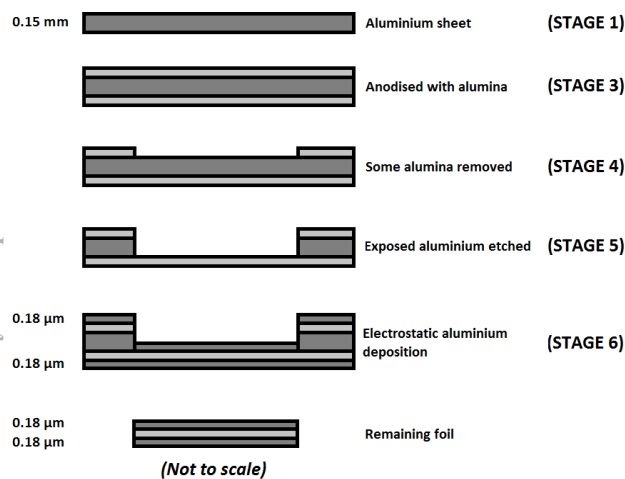


Figure 3: 'Cut-through' schematic of the production of the ISIS stripping foil. The stages identified correspond to those outlined in the foil preparation section.
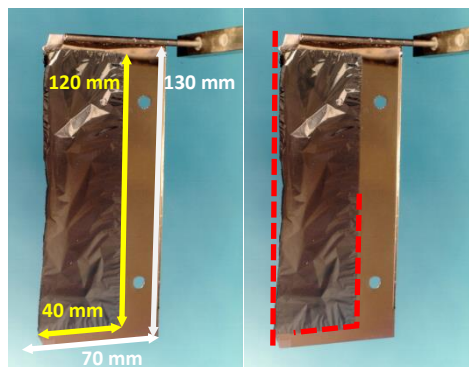


Figure 4: Two completed stripping foils. Left shows the dimensions of the final foil area compared to the original aluminium sheet. Right shows the cuts made to the foil.

## FOIL MEASUREMENTS

A series of studies were undertaken to measure and understand the thickness and composition of the ISIS stripping foil.

### Thickness

From the foil preparation stages, Fig. 3, it can be seen that the thickness due to electrostatically deposited aluminium is expected to be 0.36 μm. The amount of the alumina onto which the aluminium is deposited is controlled by the anodising conditions. Because the anodising is conducted at a constant voltage, rather than constant current, it is not possible to calculate the expected thickness of the anodised layer. However, early foil development documents [3] refer to the anodic layer being built up at a rate of 13 Å V$^{-1}$ when using 190 V and an assumed current density of <2 mA cm$^{-2}$. This would give an expected thickness of alumina of 0.247 μm.

Thickness measurements on foil samples were made using a surface profiler [4]. In this technique a probe was used to measure the step-height at the foil edge, Fig. 5. Measurements were made for cases where the probe moved onto the foil from the substrate and conversely from the foil onto the substrate. For the four samples the average thickness was measured as 0.5450 ±0.0005 μm with a standard deviation of 0.02 μm.
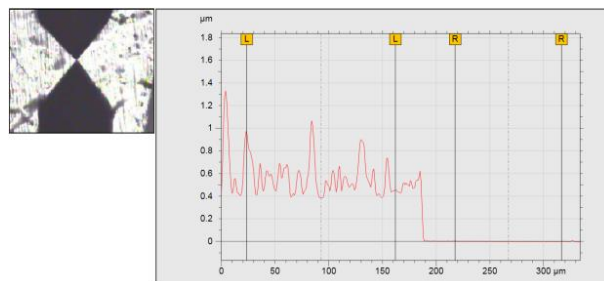


Figure 5: Top left shows the probe (and probe shadow) moving along the sample foil surface. Right shows the probe position which is used to obtain the step-height of the foil.

Some significant (~0.5-1 μm) changes in foil thickness were observed over ~10 μm probe movements. An Atomic Force Microscope (AFM) [5] was used to assess the surface roughness and measured it to be ~200 nm, Fig. 6. The changes in the profiler probe height could be attributed to the probe dragging and piling up foil material as it moves.
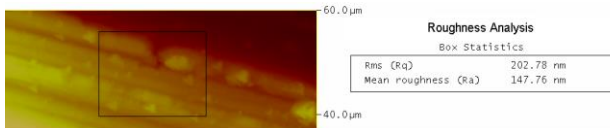


Figure 6: AFM image of surface roughness.

A total measured thickness of 0.545 μm and a known thickness of deposited aluminium of 0.36 μm indicates that the thickness of the remaining alumina in the foil samples is 0.185 μm, which is thinner than the 0.247 μm expected. The constant voltage anodising method results in many uncertainties in the thickness control of the anodic layer for each foil and the components and concentration of anodising solution may have changed since the initial development [3].

*Mass*

Using the accepted density of aluminium (2.7 g cm$^{-3}$) and aluminium oxide (3.95 g cm$^{-3}$), along with the measured thickness, the expected mass of a foil sample with dimensions $40 \pm 5 \times 120 \pm 5$ mm is $8.2 \pm 1.4$ mg. Samples of ISIS foils, removed from their frames, were weighed by carefully sandwiching a foil between sheets of weighing paper (of measured mass) [6]. The resulting average mass was $11.530 \pm 0.005$ mg with a standard deviation of 0.070 mg between three samples. This discrepancy suggests that there may be other impurities present in the foil.

*Composition*

The foil composition was analysed using energy dispersive x-ray spectroscopy (20 keV) [7, 8]. Twelve separate points on a small foil sample were analysed with the resulting spectra showing the proportion of each material detected. As expected, the main foil constituents were oxygen (60.45%) and aluminium (37.11%), with traces of other elements present, Table 1. The spectroscopy composition results match well to the expected distribution in aluminium oxide, $Al_2O_3$.

Table 1: Elemental Composition (%) of the Foil Sample

| Element | Composition (%) |
|---|---|
| Oxygen (O) | 60.45 |
| Aluminium (Al) | 37.11 |
| Sulphur (S) | 1.33 |
| Copper (Cu) | 0.48 |
| Silicon (Si) | 0.32 |
| Titanium (Ti) | 0.10 |
| Iron (Fe) | 0.08 |
| Potassium (K) | 0.08 |
| Magnesium (Mg) | 0.05 |

It is possible that small amounts of impurities could have been introduced during the foil manufacture, or may have arisen from the substrate adhesive used in the spectroscopy measurement. Assuming all of the aluminium detected is associated with the aluminium oxide compound then there is 4.79% more oxygen present than anticipated. This is likely to be due to the oxidation of the impurities. Similar to the AFM result an image from the Scanning Electron Microscope (SEM) used in the spectroscopy showed some non-uniformity in the foil structure.

A neutron diffraction pattern was also obtained from the foil samples using the medium resolution powder diffraction instrument at ISIS, Polaris [9]. This instrument specialises in the rapid characterisation of crystal structures in small samples. It was hoped that this technique would show the sample crystal structure, including any trace impurities. Three entire foils were required in order to see any crystalline diffraction above the noise, Fig. 7. The foils were compressed into a thin walled glass capillary tube for the measurement.
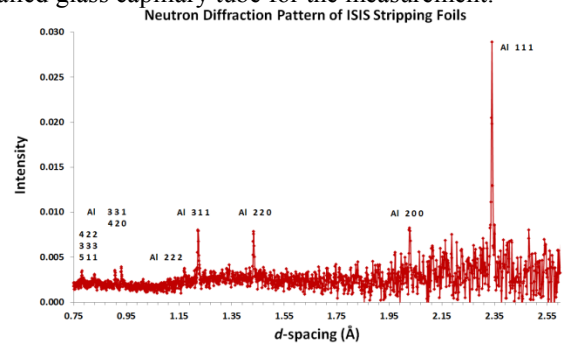


Figure 7: Neutron diffraction pattern observed from an experiment on Polaris showing the miller indices of the planes present in crystalline aluminium.

Simulated diffraction patterns for crystalline aluminium and alumina were compared to the obtained diffraction pattern, Fig. 7. This analysis showed that all the peaks present were associated with pure aluminium. There were no strong peaks present at d-spacings of 1.4, 1.6 or 2.1 Å which would be expected for crystalline alumina. This was anticipated because the anodising technique produces amorphous alumina. Because of the small sample size there is a high noise level in the data, if there were any crystalline alumina it would be <10% of the total content. The low intensity of crystalline aluminium detected is assumed to be the remnants of any un-etched aluminium sheet, or non-oxidised deposited aluminium.

*Results Summary*

Results from the composition analysis suggest that oxidation of the final layers of electrostatically deposited aluminium had occurred. An oxide layer naturally forms on an exposed aluminium surface and this is expected on the foil samples as they are not stored under vacuum conditions after preparation. If it is assumed that the entire foil material is aluminium oxide the expected mass would be $10.3 \pm 1.8$ mg, which is consistent with the

measured mass of 11.53 mg. As observed through the AFM and SEM measurements there is an inherent surface roughness and any non-uniformity in the anodising, etching or deposition processes could result in variation in foil mass.

The consistent results obtained in this series of measurements suggest that the ISIS stripping foil is best described as a 0.55 μm, 215 μg cm$^{-2}$, aluminium oxide foil. Previously quoted thicknesses of 0.25 μm or 50 μg cm$^{-2}$ may correspond to the expected thickness of the anodised alumina layer or the thickness of electrostatically deposited aluminium on a single side, respectively. It is also possible that the foil production method has drifted over time towards the production of thicker foils than originally specified to achieve the increased foil lifetimes. The effect of thicker foils on accelerator operations is discussed in a later section of this paper.

## BEAM MEASUREMENTS

### Beam Size

Injection efficiency may be improved by decreasing the transverse foil size. A smaller foil means less re-circulating beam hits the foil so the effects of beam scattering, energy straggling and heat stress on the foil are reduced. Measurements have been undertaken to understand the minimum foil size that could be acceptable for use in ISIS operations. Using a beam diluted to 10% with a pepper-pot absorber, to limit component activation, the circulating beam intensity was measured as a function of horizontal foil position, Fig. 8.
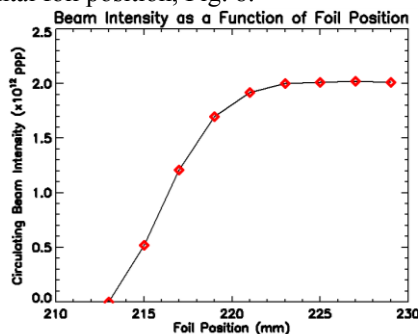


Figure 8: Graph of horizontal foil position against measured circulating beam intensity showing that the injected beam has a diameter of ~10 mm.

Results show that under typical operating conditions the beam has a horizontal diameter of 10 ±2 mm. Errors in the measurement arise from pulse-to-pulse variations in injection position and intensity as well as fluctuations in circulating beam current. The foil position is routinely set at ~230 mm to accommodate the unstable injection spot and any potential halo on in the injected beam.

There is no capability for moving the foil in the vertical plane, but the painting amplitude of the vertical beam is 12 mm. At the end of injection the beam footprint on the foil is ~10 × 50 mm [10], Fig. 9. Although the foil takes up the full vertical aperture only the top half is used for

stripping. Removing the bottom half of the foil would significantly reduce the number of foil re-circulations but may affect the structural integrity of the foil.

The Chinese Spallation Neutron Source (CSNS) plans to run with a smaller, 21 × 60 mm, 100 μg cm$^{-2}$ boron-doped carbon stripping foil [11]. Mounting and supporting a smaller foil poses extra challenges, with many solutions involving the use of thin silicon carbide support wires [12]. Aiding the research of both organisations, plans are being made to test CSNS foils on ISIS during dedicated machine study time.
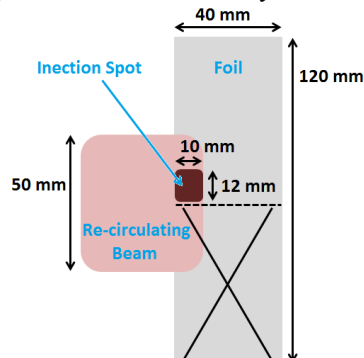


Figure 9: Schematic of the beam footprint on the foil at the end of injection. The dark red spot is the painted space and the light red area is accumulated beam.

### Energy Loss

Predictions of expected energy loss per traversal for alumina foils of 50-215 μg cm$^{-2}$ are 0.4 and 1.6 keV respectively.

One technique identified for measuring this energy loss on ISIS involves producing ~100 extra foil traversals by moving the start time of the injection bump. The additional energy losses would correspond to changes in beam revolution frequency of 0.35-1.5 ns. This measurement is very challenging at currently available data acquisition rates. Studies to further increase the number of foil traversals by moving the horizontal closed orbit onto the foil are planned in the future.

## EFFECT OF FOIL MATERIAL AND THICKNESS

With improved knowledge of the foil characteristics, simulations of the ISIS stripping foil were reviewed using an in-house single pass code [13]. Assessments were made of the stripping efficiency and scattering that would be expected from both the previously assumed 50 μg cm$^{-2}$ and newly measured 215 μg cm$^{-2}$ aluminium oxide foil. The code includes the effects of inelastic nuclear interactions, single large-angle Coulomb scattering and multiple small-angle Coulomb scattering.

Results show that the increase in thickness yields an increase in stripping efficiency from 97.2% to 99.9%. However, it also leads to increases in scattering which could result in loss. Further detailed simulations should be completed to understand the current extent of foil scattering at ISIS.

Operationally the ISIS injection efficiency, calculated from toroid current monitors, is ~97-99%. A high stripping efficiency is consistent with experience as this measure of injection efficiency includes contributions from all injection loss mechanisms.

## CONCLUSIONS AND FURTHER WORK

Measurements of the properties of the ISIS stripping foil have been made, resulting in a more consistent understanding of the foil preparation techniques, material composition and thickness. Combining all of the measurement results together the foil used for ISIS operations is best described as 0.55 μm, 215 μg cm$^{-2}$, aluminium oxide.

Details of the foil production mechanism have been provided. The foil manufacture is a complex multi-stage process that relies on individual skill. It is thought that certain stages of the foil production (masking, anodising, electrostatic deposition) may have drifted from the initial method over time as operations at increasing beam intensities and the ability to store foils without degradation necessitated longer-lasting foils. A new foil is posted, as a conservative approach, for each ISIS user cycle even though the lifetimes can be far in excess of this.

At $40 \times 120$ mm the ISIS foil occupies a large proportion of the machine aperture. For future upgrades to ISIS it is anticipated that a smaller foil could be used to reduce the number of re-circulating particles interacting with the foil, thereby reducing unwanted scattering and heating effects. As part of this study the minimum horizontal foil size currently required on ISIS was measured. Mounting a smaller foil could be a challenge; it is hoped that experience of operating with smaller foils will be gained by testing CSNS foils on ISIS.

## ACKNOWLEDGEMENTS

## REFERENCES

[1] B. Boardman, "Spallation Neutron Source: Description of Accelerator and Target", RAL Report RL-82-006 (1982).
[2] D.J.S. Findlay et al., "ISIS – Pulsed Neutron and Muon Source", PAC '07, p. 695.
[3] N.J. Archer, "A Study of Methods for the Production of Stripping Foils with High Temperature Capability", Fulmer Research Institute Report, 1979.
[4] KLA Tencor Alpha Step IQ Surface Profiler.
[5] Bruker Dimension 3100 Scanning Probe Microscope.
[6] Sartorius ME235S.
[7] JEOL 6610LV Scanning Electron Microscope.
[8] Oxford Instruments Xact 80 mm SDD.
[9] http://www.isis.stfc.ac.uk/instruments/polaris/
[10] B. Jones et al., "Injection Optimisation on the ISIS Synchrotron", EPAC '08, p. 3587.
[11] H.E. Zhe-Xi et al., "Wrinkle analysis and mounting optimization of the primary stripper foil for CSNS", Chinese Physics C, Vol 37, No. 10 (2013), p. 107003.
[12] Y. Yamazaki et al., "Analysis of Hybrid Type Boron-Doped Carbon Stripper Foils in J-PARC RCS", ICTF-15, Journal of Physics: Conference Series 417 (2013) 012071.
[13] H.V. Smith et al., "Stripping Foil Simulations for ISIS Injection Upgrades", IPAC '11, p. 3556.

# GLOBAL LINEAR OPTICS CORRECTION FOR LOW ENERGY RHIC RUN*

C. Liu†, K.A. Drees, A. Marusic, M. Minty, C. Montag, BNL, Upton, NY 11973, USA

## Abstract

There has been increasing interest in low energy runs in RHIC, in order to probe the phase diagram at the low energy end. The optics is one of the critical pieces for a successful low energy run since it affects the beam lifetime and thus the achievable luminosity. While acquiring optics measurement data remains difficult, progress has been made in recent years in the analysis of such data and in correcting global optics errors. The analysis technique and the results of optics correction for low energy runs are presented in this report.

## INTRODUCTION

Collisions in the low energy range are motivated by one of the key questions of quantum chromodynamics (QCD) about the existence and location of a critical point on the QCD phase diagram [1]. The beam energy range for low energy runs is between 2.5 and 20 GeV/nucleon. Within this range an energy scan will be conducted over 7 different energies. The luminosity of low energy collisions is expected to improve substantially with the help of low energy electron cooling of the colliding beams [2].

The dynamic aperture of the low energy beam has been improved over the years by fixing the machine nonlinearity [3]. On the other hand, it was not possible to systematically measure the optical functions due to the low beam intensity and its short lifetime. During the 2013 and 2014 runs, we managed to measure the linear optics using injection oscillations recorded by turn-by-turn beam position monitors (BPMs), which avoided exciting coherent betatron oscillation. Furthermore, optics corrections were implemented which reduced the global relative errors of beta functions (beta-beat) and corrected the beta functions at the collision points. The analysis technique applied to the turn-by-turn BPM data is presented in the following together with the measured and successfully corrected linear optics during the low energy runs.

## OPTICS MEASUREMENTS DURING LOW ENERGY TEST IN 2013

RHIC was operated for a dedicated test with proton beams at ∼ 6 GeV in 2013. One horizontal injection oscillation BPM data is shown in Fig. 1. Two irregularities can be seen in this data set. One is the beam positions reported around turn 200, which looks like pure noise and is present in data recorded by all BPMs. The other one is the sudden

increase of the coherent oscillation amplitude around turn 800. Both remain not understood due to time limitations during the test.
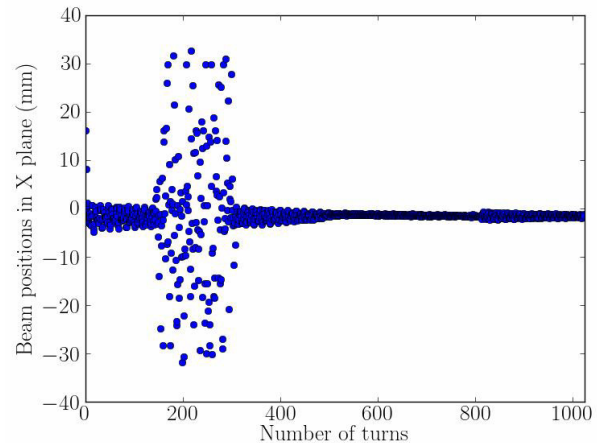


Figure 1: The horizontal injection oscillation BPM data in the Yellow ring during the low energy test in 2013.

The acquired injection oscillation data imposed difficulties on the analysis, which is based on a frequency domain Fourier transform. The Fast Fourier Transform (FFT) produced a spectrum shown in Fig. 2, which is dominated by noise. Therefore, one can neither extract useful tune information nor any other optical functions.
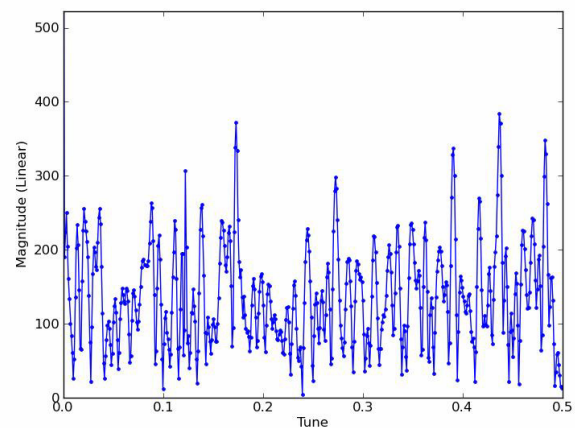


Figure 2: The raw spectrum of the injection oscillation obtained using the FFT technique.

The noise problem was solved later by applying a window (or filter in frequency domain) on the turn-by-turn

BPM data [4]. Two clearly visible peaks, corresponding to the horizontal and vertical tune, are dominating the spectrum. It is obvious that strong coupling was present in the machine during the test. We had to tweak the tune setting and check the response of the peaks to determine which one corresponded to the horizontal or vertical tune.
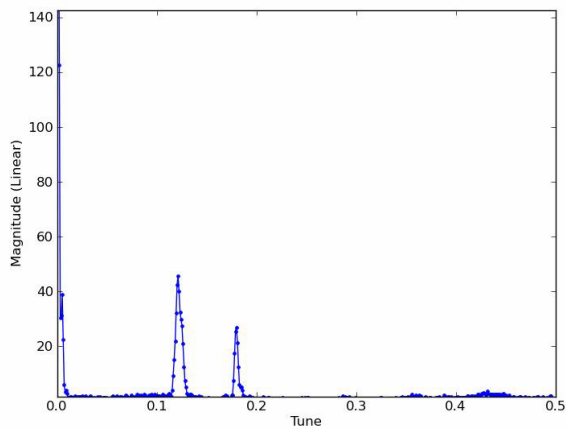


Figure 3: The spectrum of the injection oscillation obtained by applying window and then using FFT technique. The peaks correspond to the horizontal and vertical tune respectively.

By going through the spectrum of all available BPMs, one could obtain the measured tunes from all the functioning BPMs. The histogram of the horizontal tune retrieved from one data set (contains turn-by-turn data from $\sim$ 160 BPMs) is plotted in Fig. 4.
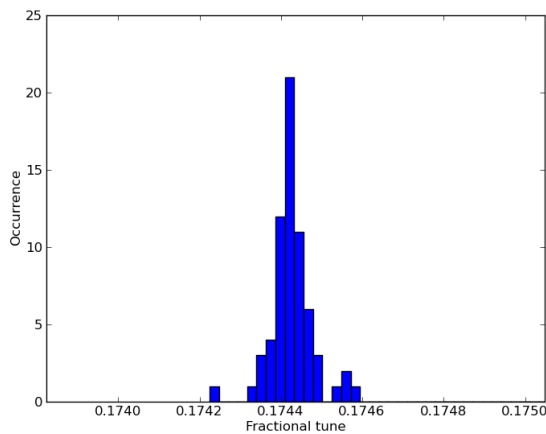


Figure 4: The histogram of the horizontal tunes, measured by all BPMs.

Based on the amplitude of the tune peaks, the relative error of the beta functions at all available BPMs was calculated and is shown in Fig. 5. We did not attempt optics corrections at that time since the analysis was offline and

took some time.
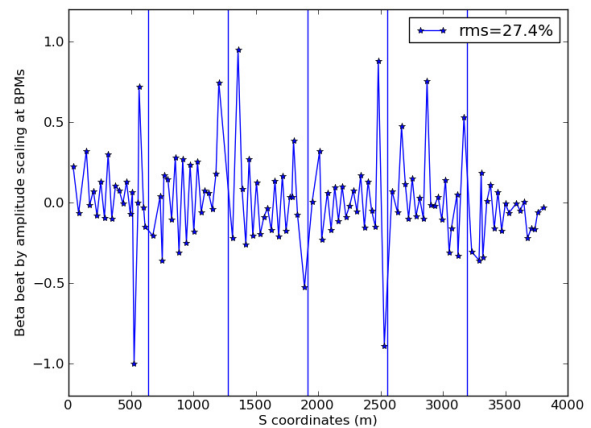


Figure 5: The global beta-beat in the horizontal plane measured during a low energy proton test in 2013.

## OPTICS MEASUREMENTS AND CORRECTIONS DURING LOW ENERGY RUN IN 2014

In 2014 Au-Au collisions at 7.3 GeV/nucleon beam energy was provided to the experiments for a period of $\sim$ 3 weeks. Noise was no longer dominating the injection oscillation BPM data (Fig. 6).
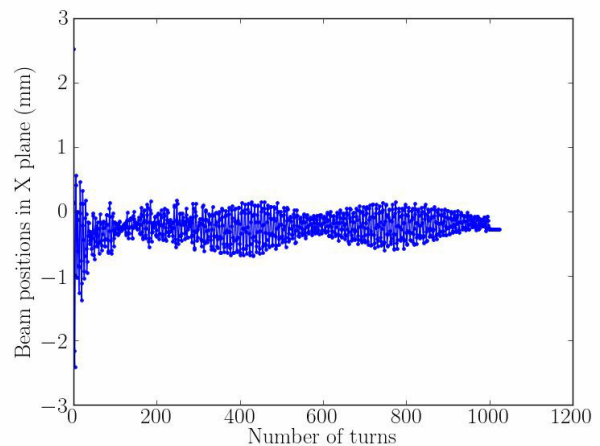


Figure 6: Horizontal injection oscillations recorded by a BPM in the Yellow ring during the low energy run in 2014.

To improve the measurement precision, a Gaussian window was applied to the turn-by-turn BPM data. The beta functions, and thus the beta-beat, were retrieved using the same technique as described in Ref. 4. The correction strengths for the 72 trim quadrupole power supplies were calculated using the SVD algorithm [5]. The corrections were implemented in the machine and the resulting optics

were remeasured. The global beta-beat before and after correction are plotted in Figs. 7-10 for both planes in both rings. Significant improvement of the global optics were observed in all cases.
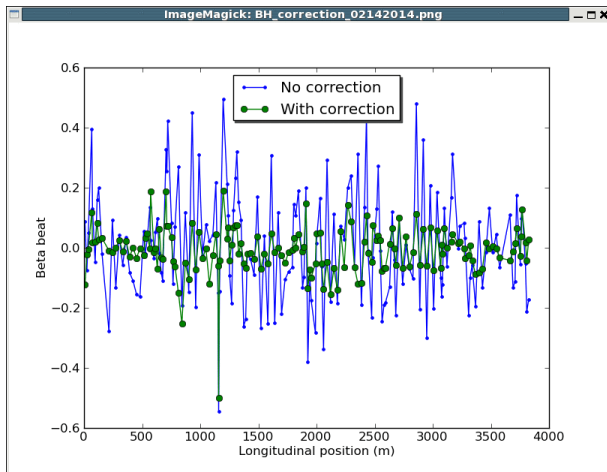


Figure 7: The global beta-beat before and after correction in the Blue horizontal plane. Only one iteration of correction was implemented in the 72 trim quadrupole power supplies.
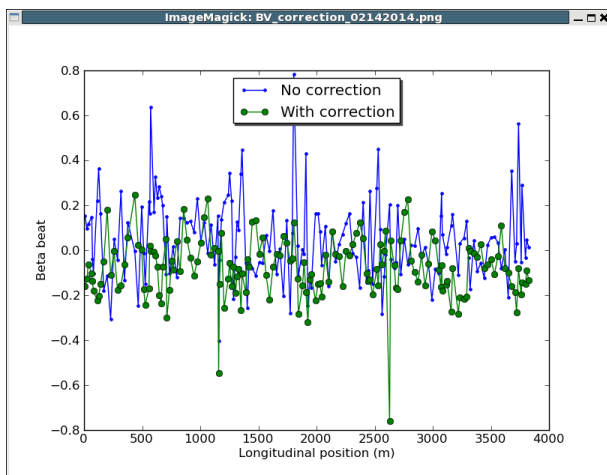


Figure 8: The global beta-beat before and after correction in the Blue vertical plane.

## SUMMARY

For low energy runs in RHIC, injection oscillation BPM data sets were used for the analysis of optical functions. In 2013, even though the BPM data was dominated by noise, we managed to extract reasonable optical functions by applying a window to the raw data before performing an FFT. In 2014, the global optical functions were analyzed without much difficulty. The optics corrections were calculated and implemented in operation for the first time in a low energy run. Substantial improvement of the global optics were observed by the subsequent measurements.
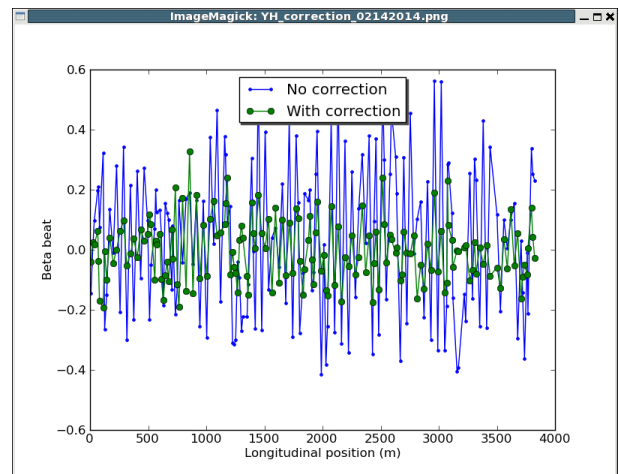
Figure 9: The global beta-beat before and after correction in the Yellow horizontal plane.
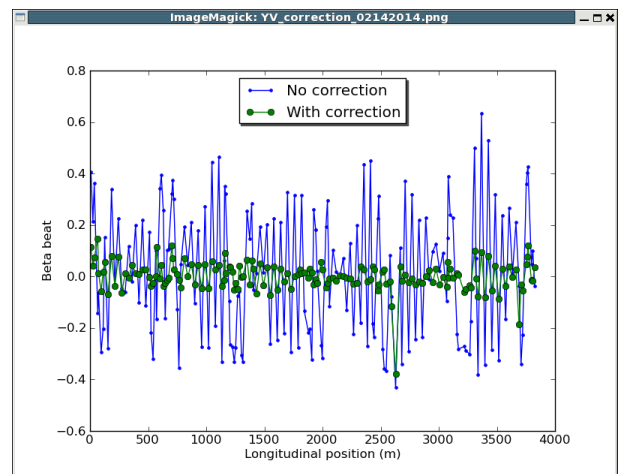


Figure 10: The global beta-beat before and after correction in the Yellow vertical plane.

## REFERENCES

[1] Proc. of Workshop Can we discover QCD critical point at RHIC? (BNL, March 2006) RIKEN BNL Research Center Report No. BNL-75692-2006; http://www..bnl.gov/riken/QCDRhic

[2] Fedotov, A. V., et al. "Electron cooling for low-energy RHIC program." Proc. of COOL09 Workshop (Lanzhou, China, 2009).

[3] Montag, C., et al. 'Experience with low-energy gold-gold operations in RHIC during FY 2010.' CA/AP/435, 2011.

[4] Liu, C., et al. "Precision tune, phase and beta function measurement by frequency analysis in RHIC." Proceedings of the IPAC 2013.

[5] Liu, C., et al. "Global Optics Correction in RHIC based on Turn-by-Turn Data from the ARTUS Tune Meter." Proceedings of the NA-PAC 2013.

# LONGITUDINAL DYNAMICS SIMULATION AT TRANSITION CROSSING IN RHIC WITH NEW LANDAU CAVITY*

C. Liu[†], M. Blaskiewicz, J.M. Brennan, K. Mernick, M. Minty, C. Montag, K. Smith
BNL, Upton, NY 11973, USA

## Abstract

At the Relativistic Heavy Ion Collider (RHIC), heavy ion beams cross transition energy during acceleration to energies required by the physics programs. In the past, to battle longitudinal instabilities, a Landau cavity was turned on just after acceleration through transition energy. The Landau cavity with modified frequency will be implemented before beam crosses transition in Run-14. Longitudinal dynamics with this new configuration have been simulated to optimize the phase and amplitude of the Landau cavity. We will present simulation results in the report.

## INTRODUCTION

At RHIC, heavy ion beams cross transition energy during acceleration to full energies. For example, Au beam is injected into RHIC with $\gamma = 10.5$. It crosses the transition energy ($\gamma = 23$) at ~85 s after the start of the acceleration. The heavy ion beams are accelerated by the 28 MHz cavities, whose harmonic number is 360. In the past, the Landau cavity (~197 MHz) was turned on after transition. For Run-14, it was proposed by J.M. Brennan to turn on the Landau cavity before transition crossing for better beam transmission efficiency. In addition, the frequency of the Landau cavity was slightly modified (harmonic number from 2640 to 2580) to better control coupled bunch instability [1]. There were several questions associated with the mentioned changes: what is the impact on the beam emittance if we turn on the Landau cavity before transition? what to do with the phase of the Landau cavity at transition? and what is the optimal configuration for the voltage of the Landau cavity? The simulations will be presented in this report were carried out to answer these questions.

The simulation was performed with a tracking program, ESME [2], which calculates the evolution of a distribution of particles in energy and azimuth as it is acted upon by the radio frequency system of a synchrotron or storage ring. The basis of the program is the pair of single particle difference equations

$$\vartheta_{i,n} = [\frac{\tau_{s,n-1}}{\tau_{s,n}}\vartheta_{i,n-1} + 2\pi(\frac{\tau_{i,n}}{\tau_{s,n}} - 1)]_{mod(\pi)}$$
$$E_{i,n} = E_{i,n-1} + eV(\phi_{s,n} + h\vartheta_{i,n}) - eV(\phi_{s,n}) \quad (1)$$

where $\vartheta$ is the particle azimuth, in the range of $(-\pi, \pi)$. $E_{i,n}$ is the beam energy of the $i$th particle at the $n$th turn, relative to that of the synchronous particle. $\tau_{i,n}$ is the revolution period of the $i$th particle at the $n$th turn. $\phi_{i,n}$ is the synchronous phase at the $n$th turn.

As one of the inputs to the program, the revolution period is correlated with the machine lattice design. According to Ref. [3], the revolution period is expanded as follows

$$\frac{\tau}{\tau_0} = 1 + (\alpha_0 - \frac{1}{\gamma_0^2})\delta + (\alpha_0\alpha_1 - \frac{\alpha_0}{\gamma_0^2} + \frac{3}{2\gamma_0^2} - \frac{1}{2\gamma_0^4})\delta^2 + O(\delta^3)$$
$$(2)$$

where the $\gamma_0$ is the Lorentz factor of the beam. $\delta$ is the beam energy spread. The first and second order compaction factors, $\alpha_0$ and $\alpha_1$, can be obtained from the optics model or measurement. It was showed in Ref. [3] that the agreement between measured and the model $\alpha_1$ was within 10%. The measurement ($\alpha_1 = -1.15$) was used in the simulation.

## HEAVY ION BEAM ACCELERATION AT RHIC

The $\gamma_t$ jump scheme [4], changing the $\gamma_t$ by quickly switching the polarity of a group of designated quadrupoles, has been implemented at transition crossing for the heavy ion beams. It takes 35 ms to change the $\gamma_t$ by 1 unit at RHIC.

The voltage of the 28 MHz cavity during acceleration is shown in Fig. 1. The initial RF voltage was set to the maximum value to reduce intra-beam scatterring contribution to longitudinal emittance by sacrificing momentum spread. The voltage is halved around transition to reduce the bucket height.
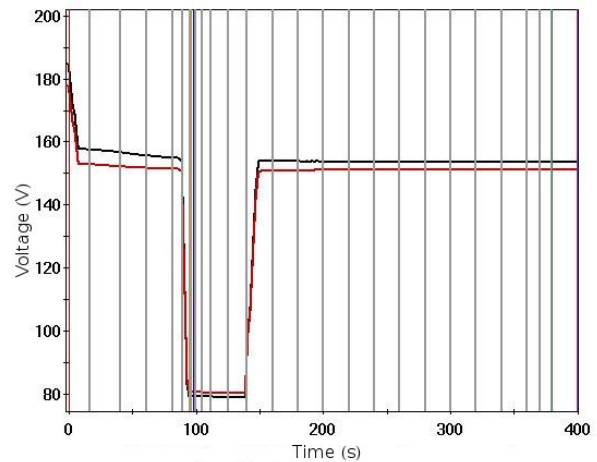


Figure 1: The voltage of the two 28 MHz cavities during acceleration in 2011 Au-Au physics program.

The synchronous phase is determined by the voltage evolution and the beam energy on the ramp. The beam rigidity and its derivatives are shown in Fig. 2.
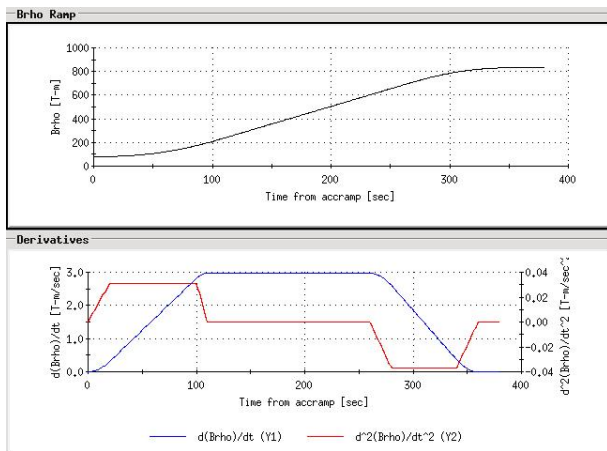
Figure 2: The beam rigidity during acceleration (the upper plot) and the first (the blue curve in the lower plot) and second derivatives (the red curve in the lower plot).



Figure 4: The slip factor ($\eta$) during the first half of the acceleration cycle. The transition crossing was zoomed in and shown in the lower right. The slip factor crossing zero fast was enabled by the $\gamma_t$ jump scheme.

## SIMULATION OF THE LONGITUDINAL DYNAMICS WHILE CROSSING TRANSITION

The simulation was performed for the first 150 s of the acceleration cycle. The initial longitudinal emittance was 0.1 eV·s. There were 10,000 particle in the tracking. The longitudinal phase space distribution of the bunch can be displayed at any turn. However, it is more practical to view other derived quantities for monitoring the dynamics.

The beam energy during the first half of the acceleration cycle is shown in Fig. 3. It agrees with the design value. The



Figure 5: The emittance evolution during the first half of the acceleration cycle without Landau cavity. The $\gamma_t$ jump scheme was implemented.

Then, we studied the case that beam crosses transition with Landau cavity, and the phase of the Landau cavity was kept constant. The emittance evolution during the first half of the acceleration cycle for this case is shown in Fig 6. Apparently, the emittance blowup at transition was unacceptable.

After that, we studied the case that beam crosses transition with Landau cavity, and the phase of the Landau cavity was switched from 0 *deg* to 180 *deg*. The emittance evolution during the first half of the acceleration cycle for this case is shown in Fig. 7. The emittance increased by $\sim 10\%$, which is slightly worse than that in Fig. 6., but still acceptable. This implies that it is feasible to turn on the Landau cavity before transition for better transmission.

There is one bunch every three 28 MHz RF buckets, every 21.5 Landau RF buckets with its modified frequency. Therefore, the second bunch sits on 180 deg phase of the Landau when the first bunch on 0 *deg* phase of the Landau cavity (see Fig. 8).



Figure 3: The beam rigidity during acceleration (the upper plot) and the first (the blue curve in the lower plot) and second derivatives (the red curve in the lower plot).

slip factor ($\eta$) during the first half of the acceleration cycle is shown in Fig. 4.

We studied the beam emittance behavior at transition without Landau cavity as a baseline. The emittance evolution during the first half of the acceleration cycle is shown in Fig. 5. The emittance increase due to transition crossing is $\sim 3\%$.

Figure 6: The emittance evolution during the first half of the acceleration cycle with Landau cavity kept on a constant phase. The $\gamma_t$ jump scheme was implemented.
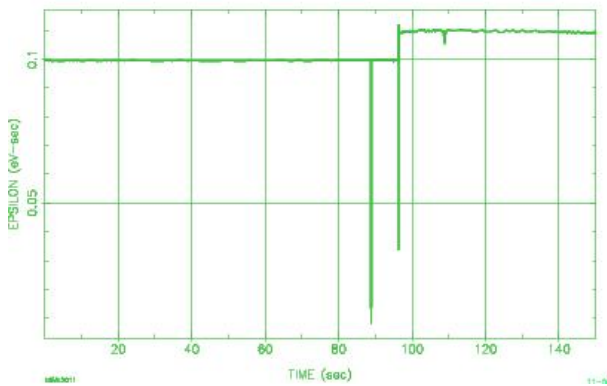


Figure 7: The emittance evolution during the first half of the acceleration cycle, with Landau cavity phase jumps from 0 *deg* to 180 *deg*. The $\gamma_t$ jump scheme was implemented.
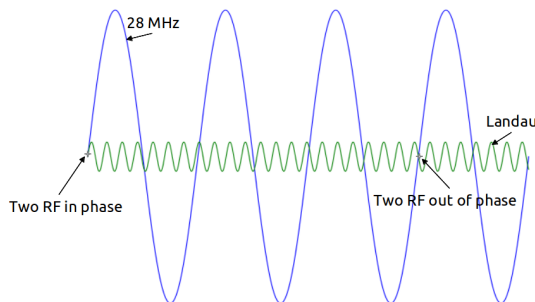


Figure 8: The phase of the 28 MHz and Landau cavity at two nearby bunches (stars) in RHIC. The phase of the Landau cavity is 0 deg at the first bunch, 180 deg at the second bunch.

This means the Landau cavity phase switches back and forth between 0 *deg* and 180 *deg* at the bunches in the bunch train. Also, when the phase of the Landau jumps from 0 *deg* to 180 *deg* for half of the bunches, the phase of the Landau cavity would jump from 180 *deg* to 0 *deg* for the other half. The emittance evolution of those bunches crossing transition is shown in Fig. 9. The emittance increase was ~ 5%.
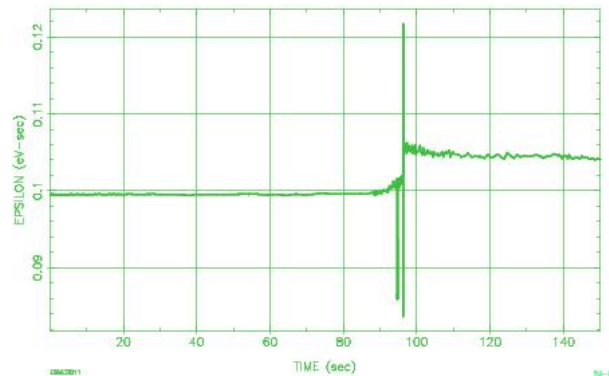


Figure 9: The emittance evolution during the first half of the acceleration cycle, with Landau cavity phase jumps from 180 *deg* to 0 *deg*. The $\gamma_t$ jump scheme was implemented.

## SUMMARY

The longitudinal dynamics simulation was performed with code ESME, to answer questions related to utilizing Landau cavity for transition crossing. The beam emittance evolution through transition, with turning on Landau before transition, was studied in the simulation. It was shown that the beam emittance would blow up if the Landau cavity phase was held constant. The beam emittance would be preserved if the phase of Landau cavity was changed from 0 to 180 *deg* for half of the bunches and 180 to 0 *deg* for the other bunches at transition in RHIC. The configuration of the Landau cavity in Run-14 was guided by the simulation results. The longitudinal beam emittance was well preserved during the transition crossing in the operation.

## REFERENCES

[1] J.M. Brennan, Private Communication

[2] James A. MacLachlan, "Multiparticle dynamics in the E-phi tracking code ESME," AIP Conference Proceedings. IOP INSTITUTE OF PHYSICS PUBLISHING LTD, 2002.

[3] M. Blaskiewicz, "Measuring $\alpha_1$ in RHIC," BNL tech-note, C-A/AP/19.

[4] C. Montag, J. Kewisch, "Commissioning of a first-order matched transition jump at the Brookhaven Relativistic Heavy Ion Collider," Physical Review Special Topics-Accelerators and Beams 7.1 (2004): 011001.

# BEAM-BASED PERFORMANCE OF THE CERN PS TRANSVERSE FEEDBACK

G. Sterbini, A. Blas, S. Gilardoni, CERN, Geneva, Switzerland

*Abstract*

The CERN PS transverse damper is a flexible wideband system to damp injection coherent oscillations, inter and intra-bunch transverse instabilities at different energies along the cycle, to perform controlled emittance blow-up and to serve as abort cleaning device. In this paper we summarise some beam-based observations of the CERN PS transverse feedback performance and compare them with the expected results.

## INTRODUCTION

The CERN PS has to cope with several beam dynamic challenges to produce the present and the future high brightness and high intensity beams [1]. The PS Transverse Feedback (TFB) will be used mainly to address three aspects of the PS beam dynamics to reach the required performance:

- *The injection missteering* due to an injection error. This is expected to be an important source of the emittance growth [2] which drove the specifications of the TFB system. The system has been designed to damp a 3 mm$_p$ oscillation with a time constant < 50 turns at injection energy ($E_k$=1.4 GeV) while its bandwidth should cover from the first betatron line at Q=6.1 (40 kHz) up to 23 MHz corresponding to the ripple observed on the injection kicker bending field. Given the TFB kicker design, this translates into the power specifications for the present driving amplifiers of 3 kW per kicker plate. Considering a $E_k$=2 GeV injection and maintaining the same requirements of the 1.4 GeV case, the amplifier power should be increased to 5 kW. The new amplifiers are presently under construction and will be commissioned during the 2015 in the framework of the LHC Injectors Upgrade project [3].

- *The head-tail instability*. This effect is due to the interplay between the machine transverse impedance, its chromaticity and the bunch longitudinal motion [4–6]. It can have a detrimental effect of the beam characteristics up to prevent the beam transmission or to degrade the beam emittance to unacceptable level. The TFB proved to be a valuable tool against this issue.

- *The transverse coupled instability at extraction*. In specific, not yet operational, conditions it has been observed a coupled bunch instabilities at the PS extraction flattop with the 25 ns bunch train. Investigations are ongoing to understand if a similar instabilities will be present with the production LIU beams. Measurements demonstrate that the PS TFB can delay by 10 ms the the instability rise [7]. This result may indicate that an increase of the loop gain should cure the instability.

In addition to that, the TFB can perform controlled emittance blow-up, serve as abort cleaning device, excite the beam for tune measurement and machine development studies.

## THE SYSTEM AND ITS PERFORMANCE

A description of the present system is provided in the following, highlighting its performance and limits. A more detailed description can be found in [8–10]. The envisaged upgrade for 2015 will also be discussed. A simplified block diagram of the present system from the pick-up to the kicker is shown in Fig. 1 (only the horizontal plane is depicted). The transverse pick-up [9, 11], PU, feeding the TFB is positioned in section 98. The PU signal is amplified to match the input dynamic of the digital card (DSPU). The output of the digital card is amplified, combined with the Q-meter signal and splitted on the input of the two power amplifiers that drives the two horizontal plates of the kicker. The matching between the output impedance of the power amplifier (50 Ω) and the kicker impedance (100 Ω) is performed with a transformer. The transverse kicker is positioned in section 97. The TFB is composed of the subsystems described in the following sections.

### The Pick-up Pre-amplifier

The PU preamplifier is a critical subsystem for the TFB since it is used to set the feedback loop gain and to adjust the ΔH and ΔV signals to the 1 V$_p$ input dynamics of the DSPU ADC. It is a low-noise pre-amplifier with a gain range of −60 to +40 dB (down to −60 dB provided by an attenuator in 3 steps of -20 dB and up to +40 dB provided by an amplifier in 255 steps of ≈ 0.155 dB) that allows to adjust it to the different PS beam flavours [9]. The pre-amplifier has a global attenuation block shared by all three channels (Σ, ΔH and ΔV) together with an analog gain separately adjustable on each single channel. Attenuation and gain can vary from cycle to cycle but not within a cycle. This implies that if the TFB has to address different problems within one cycle (e.g. damping injection oscillation, head-tail instability, coupled bunches instabilities at extraction) the loop gain cannot be adjusted and optimised for each physical process. The −10 dB bandwidth of the PU amplifier is 60 MHz with less than 10 degrees of non-linear phase error on the entire amplification and attenuation range. Presently the transverse signals are not normalised therefore the gain of the feedback loop varies along the bunch for not uniform longitudinal distributions.

### The Digital Signal Processing Unit

There is one digital signal processing unit (DSPU) for each plane, clocked with harmonic 200 of the beam revolution
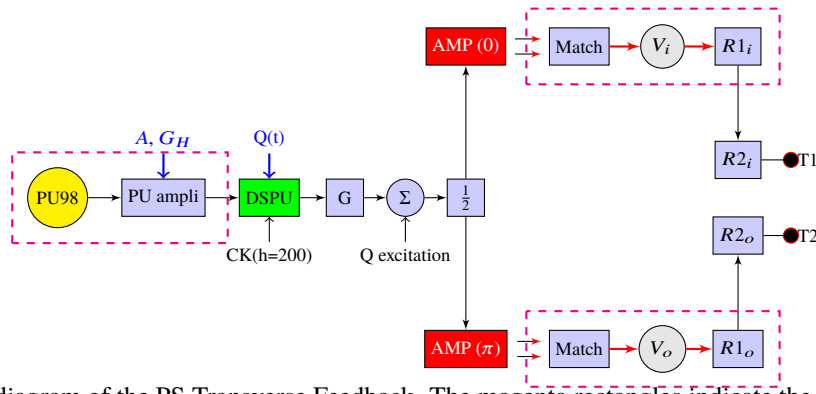
Figure 1: The block diagram of the PS Transverse Feedback. The magenta rectangles indicate the devices installed in the tunnel. Let us assume to have a bunch of 160e10 proton with a $4\sigma$ length of 180 ns with and injection error of 3 $\text{mm}_p$. The pre-amplifier can be set to a gain of 0.3 V/mm to match the 3 $\text{mm}_p$ to the 1 $\text{V}_p$ dynamic of the DSPU. We assume that the DSPU will not add any gain (1 V/V). From the exit of the DSPU to the entry of the power amplifier, AMP, the gain as to be fixed at 0.3 V/V (chain of post-amplifier, G, combiner and splitter). Each amplifier has two modules of 62 dB gain (1.5 kW RMS on 50 $\Omega$), the two modules will be summed in power (+3 dB) and then the matching network will increase by 3 dB the voltage (68 dB) to adapt the amplifier output impedance (50 $\Omega$) to the kicker plate input impedance (100 $\Omega$). The total voltage gain from the amplifier input to the kicker (2 plates, $V_i$ and $V_o$) is 74 dB. The kicker will deliver $7.9 \ 10^{-9}$ rad/V and the angle form the kicker will be transported in variation of position on the PU with 17 m/rad at injection energy. Summing all contributions and considering 1.5 dB losses for the cable attenuation the total gain the loop is G=0.05 mm/mm that is 40 turns of damping time in the centre of the system bandwidth and for the peak density of the bunch.

frequency. As discussed later this choice introduces the first limit to the bandwidth of the system .

The DSPU is responsible for

1. Adding the fixed (due to the cable length) and variable (due to the decreasing time-of-flight along the acceleration of the beam between the section 98 PU and the section 97 kicker) time delay to the PU signal.

2. Suppressing the revolution line harmonics, related to the closed orbit, using a notch filter.

3. De-phasing the error signal feeding the kicker by the correct betatron angle using the measured machine-tune information supplied by a function generator. Once the delay of the TFB are set correctly the only source of dephasing between PU and kicker is assumed to be the notch filter transfer function, N, and the Hilbert filter transverse function, H. The phase of the Hilbert filter has to be chosen to satisfy the equation

$$\angle H(\phi_H, Q) + \angle N(Q) = 2\pi Q + \Delta\mu(Q) + \frac{3\pi}{2} + \arctan \alpha(Q).$$
(1)

where $Q$ is the machine tune, $\mu$ is the phase advance between the pick-up and the kicker and $\alpha$ is the $\alpha$-Twiss function at the position of the kicker. A look-up table provides the Hilbert phase angle versus the machine tune.

Due to circuitry constraints, the maximum clock rate of the present DSPU is limited to $\approx 105$ MHz while the h=200 clock ranges from 87.4 MHz up to 96 MHz for protons. After the digital treatment the signal is converted by a DAC and sent to an additional programmable amplifier before being input to a combiner and a splitter feeding the pair of power amplifiers used for the H or V plane. The pro-

grammable amplifier is used to adjust further the output voltage of the DSPU (1 $\text{V}_p$) to the input saturation value of the final stage (300 $\text{mV}_p$), taking into account the attenuation of the combiner and the splitter. At the moment for an optimal exploitation of the DSPU dynamic, the closed orbit at the PU should be minimised all along the beam cycle.

### The Power Amplifiers

There is one 3 kW power amplifier driving each kicker plate. The two face-to-face kicker plates, for a given H or V plan, work in push-pull mode with their rf signal in opposite phase. These devices are designed for a -3 dB bandwidth of 23 MHz thus representing the bandwidth bottleneck of the entire system. During the damping of the injection oscillations the final stage can work at maximum power. These amplifiers provide 62 dB voltage gain on each of the $2 \times 1.5$ kW RMS outputs to be combined. This RMS power can be provided only for a limited duration (3 ms) and afterwards the amplifier provides 0.8 kW CW. In addition to this limit, the power amplifier output is not back-matched to 50 $\Omega$: this implies that the signal induced on the kicker by the beam will reach the amplifier and be reflected back to the kicker, potentially causing a cross talk between the different bunches. From preliminary investigations this cross talk appears to have a negligible effect. The new power amplifiers will have a 50 $\Omega$ output impedance.

### The Strip-line Kicker

The TFB kicker installed in section 97 is a strip-line kicker. It is a combined horizontal and vertical kicker (the optics in section 97 privileges the horizontal plane in term of kick effectiveness). The kicker as a characteristic impedance
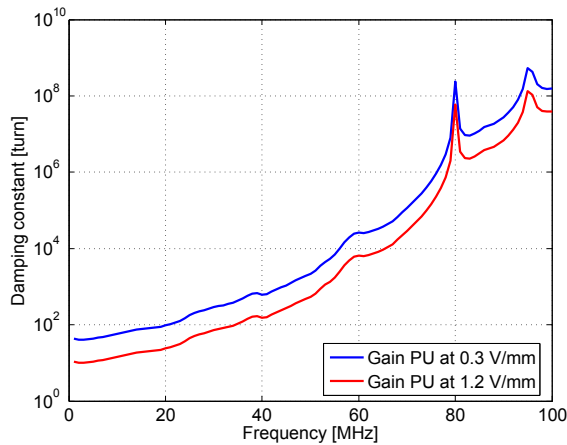
Figure 2: The TFB damping constant of the TFB as function of the frequency with the loop gain set for saturation with a 3 mm$_p$ beam position error at low frequency. Increasing further the gain is presently limited by the PS RMS closed orbit.

of 100 Ω in both planes. The 2 power amplifier signals conveyed on 50 Ω lines are matched to the 100 Ω kicker using a power transformer.

### Upgrade of the TFB Power Amplifiers

To cope with the 2 GeV injection energy while preserving the same performance, the power amplifiers of the system have to be upgraded to 5 kW CW (3 kW peak down to 800 W CW presently). The commissioning of the new power amplifiers is expected by 2015. With the new power amplifiers the problem of the matching of the output and the consequent reflection signals will be addressed. As explained the power amplifiers are presently bandwidth bottleneck of the system. For this reason the new devices will provide a 3 dB bandwidth at 100 MHz. The full power available in CW will allow more flexibility for transverse blow-up purposes

By combining the measured frequency responses of the main components of the TFB one can compute the damping constant of the system as function of the frequency (Fig.2). By increasing the pre-amplifier gain from 0.3 V/mm to 1.2 V/mm one would use the amplifier in "bang-bang" mode for the injection oscillations (that provides the maximum efficiency in extracting the beam transverse energy) and would gain in TFB damping time for the beam instabilities. Increasing the gain of the loop will increase also the noise excitation of the TFB but this problem is not relevant for relatively short PS cycle. It is worth noting that due to the Nyquist sampling criteria, only a total bandwidth of half the sampling frequency can be effective. Selecting the right frequency offset by steps of half the sampling frequency, is left to the choice of the user who should then apply the adequate band-pass analogue filtering. Presently there is no such an interest since all the transverse instabilities observed fall below 40 MHz with the exception of the the fast insta-

bility at transition that lies anyhow far beyond the limit of the system (≈700 MHz, [12]).

## BEAM-BASED PERFORMANCE

In this section the following examples of beam-based performance of the PS TFB are reported
- damping of intra-bunch oscillation at the injection,
- damping of head-tail instabilities,
- some preliminaries results on the use the damper as TFB as abort cleaning device.

### Damping of Intra-bunch Oscillation at Injection

As explained in [13], for high intensity bunches a mis-steering at injection can evolve in high frequency intra-bunch oscillations due to the transverse tune difference along the longitudinal position of the bunch. This phenomena is very rapid (much less than a synchrotron period) and it is an ideal check case for testing the PS TFB performance. The TFB was tested with 4 LHC-type bunches at the PS injection (160e10 ppb). In Fig. 3 we can compare observe the first 50 turns of the beam without (*top*) and with the TFB (*bottom*).



Figure 3: LHC-type bunches injection oscillation without (*top*) and with (*bottom*) the TFB. Σ (yellow), ΔH (green), ΔV (magenta) (200 ns/div, 200 mV/div). On the plots 50 consecutive turns of 4 LHC-type bunches in the PS are overlapped.

The oscillation evolved mostly on the vertical plane (magenta line) and could be successfully damped by the TFB. It is important to note that the closed orbit at the position of the PU was not minimised so the loop gain could not be maximised. Even in this non optimal condition, the TFB could damp this intra-bunch oscillation.

### Damping of Head-tail Instabilities

In the PS, head-tail instabilities (HT) were systematically observed during the early commissioning and studies of the LHC beam [14] on the 1.2 s injection plateau needed for the double batch injection. It was a horizontal instability with a growth time in the order of 100-200 ms for a bunch injected in h=8, 4 $\sigma$ bunch length of 200 ns, $N_b = 200 \cdot 10^{10}$ ppb at $E_k = 1$ GeV injection. Depending on the chromaticity the number of observed modes varied between m=3 and m=8. The beam loss was between 20-30%.The main responsible of the instability has been associated with the machine resistive wall impedance. In general there are three possible solutions to cure this instability:

- transverse coupling,
- Landau damping using non linear element (octuples),
- and transverse feedback.

Starting from 1996 this instability was addressed by using transverse coupling [15, 16] to avoid strong non linear elements in the optics and because, at that time, PS Transverse Feedback could not cope with it. Since then the HT was successfully suppressed in the PS using the machine natural coupling, introducing additional coupling using the skew quadrupoles, setting the working points close to the main diagonal the HT and exploiting the asymmetry between the two planes (in terms of impedances and chromaticities). The drawback of this approach is that it restricts the machine operability to a confined space of parameters, restricting thus its flexibility. For example, with the new space-charge regime expected for the LIU the choice of the working point needs as much freedom as possible in order to better accommodate the tune footprint. For these reasons, in the LIU perspective, the coupling solution becomes problematic. The TFB system appears as the natural candidate to cure the HT: one of its goal is to address the HT issue at the injection energy in the LIU parameter space, for a wide range of working points and without any residual coupling. In [17] a comparison of the PS case between Sacherer's theory and direct simulation is presented. The results show that varying the horizontal chromaticity between -1 and -0.1 with an uncouple machine the theory and the simulations results are in good agreement. The faster HT instability predicted has $\tau = 32$ ms with $N_b = 1.6e12$ and $E_k = 1.4$ GeV. Doubling the bunch population we expect to halve the rise time constant ($\tau = 16$ ms). This corresponds to $\approx 7000$ turns and can be qualitatively compares to the damping capability of Fig. 2. Assuming, parabolic bunches and a full length of the bunch of 180 ns from the bunch spectrum computation with m=10, most of the power spectrum is confined below 50 MHz. This lead us to the conclusion that the present system PS TFB can successfully stabilise the PS HT instability at $E_k = 1.4$ GeV.

At $E_k = 2$ GeV the maximum feedback loop gain will remain constant thanks to the new amplifiers. On the other hand being closer to the transition will increase significantly the frequency of the instability spectrum. The improvement of the TFB power is justified by the damping of the injection errors at the higher energy and to allow for a more efficient blow-up for applications like the Multi-Turn Extraction [18]. Its increase in bandwidth is needed for curing the HT and the instability at flattop. In the following we will present some results of beam based measurements in the PS. In the space of parameters explored (varying chromaticity with an uncoupled machine) the TFB proved to be always capable to cure the instability. In Figs. 4 we show an example of HT instability without (*top*) and with the TFB (*bottom*) .
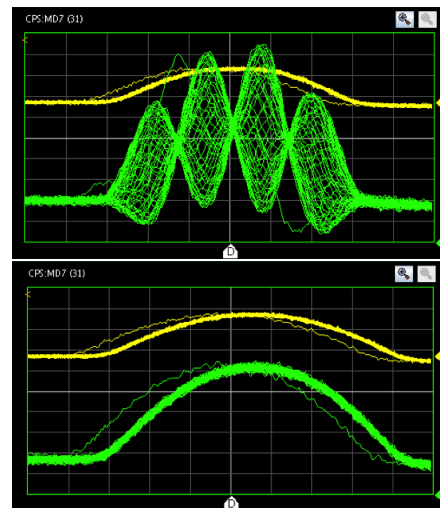


Figure 4: Head-tail instabilities (*above*) cure by the TFB (*below*). Σ (yellow) and ΔH (green) signals with 10 ns/div. On the plot 100 turns are overlapped. The frequency of the shown instability is about 20 MHz. Natural chromaticity and fully uncoupled machine.

### The TFB as Abort Cleaning Device

Recently it was proposed to use the TFB as abort cleaning device [19]. This would add flexibility in the filling scheme of the SPS and the LHC. As a proof of principle a test has been prepared to verify that an open loop excitation at the beam tune frequency could make the bunch unstable until its complete loss. In order to achieve this result it is important to correct the nominal chromaticity of the machine. Since the plane of excitation was the horizontal one, the $\xi_H$ was increase from -0.8 to -0.1 in absolute unit. The result can be observed in Fig. 5. With the reduced chromaticity the beam is almost unstable (slow losses on the beam current, cyan curve). When the excitation of the TFB is switched on, almost the 90% of the beam is lost in few milliseconds. The rationale behind this abort cleaning approach is to push the beam towards and instability (by reducing the chromaticity) and, by using convenient gating intervals, stabilise the bunches that have to be accelerated while exciting those that
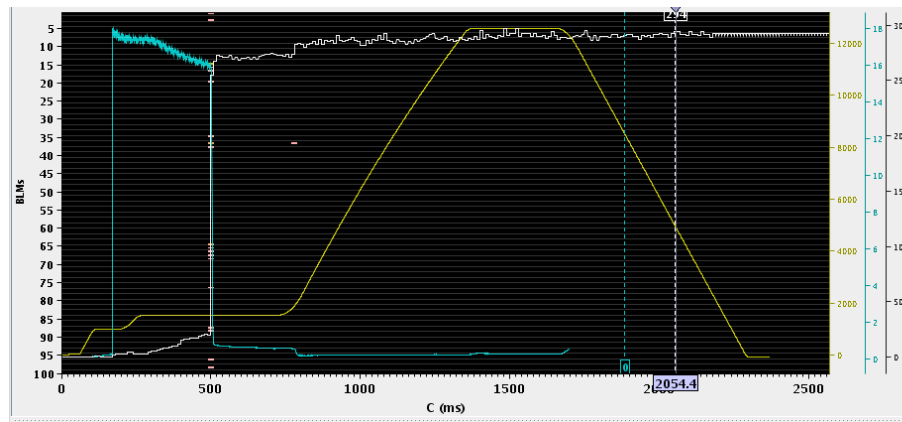
Figure 5: Proof of principle of using the TFB as abort gap cleaner. A single bunch is excited and lost in the machine at 2.5 GeV using the present TFB. The cyan curve represent the beam intensity in $10^{10}$ protons (scale on the right), the yellow curve is the magnetic cycle in Gauss and the white curve is proportional to the losses in the ring is in arbitrary units.

have to be lost. The losses can be localised to specific location of the machine by close orbit distortion. The firmware needed for the gating capability of the TFB is presently under preparation and will be commissioned during the end of the 2014 and the beginning of the 2015.

## CONCLUSIONS

The CERN PS transverse damper proved to be a flexible system to damp injection coherent oscillations, inter and intra-bunch transverse instabilities. After an introduction of the system and a prediction of its performance some significant examples of beam-based observations were discussed. The measurements are consistent with the expectations.

## ACKNOWLEDGMENT

## REFERENCES

[1] S Gilardoni et al. Long-term beam losses in the CERN Injector Chain. THO1LR01, HB2013, East Lansing, MI, USA (2014).

[2] A. Chao and M. Tigner. Handbook of accelerator physics and engineering, 3rd Printing, Chapter 4.5.6, 2006.

[3] LHC Injector Upgrade Project. https://espace.cern.ch/liu-project/default.aspx

[4] C. Pellegrini. On a new instability in electron-positron storage rings (The head-tail effect) Nuovo Cimento, LXIV, 1969.

[5] F. J. Sacherer. Transverse bunched beam instabilities: theory. 9th Inter. Conference on High-energy Accelerators, 1974.

[6] F. J. Sacherer. Theoretical aspects of the behaviour of beams in accelerators and storage rings. In First Course of the In-

[6] F. J. Sacherer. Theoretical aspects of the behaviour of beams in accelerators and storage rings. In First Course of the International School of Particle Accelerators of the "Ettore Majorana" Centre for Scientific Culture, Erice, 1977.

[7] A. Blas et al. Beam tests and plans for the CERN PS transverse damper system. IPAC13, Shanghai, 2013.

[8] J. Belleman et al. PS transverse damping system for the LHC beams. AB/RF-Note-2005-027,CERN,2005.

[9] J. Belleman. PS Transverse Feedback pick-up, http://jeroen.home.cern.ch/jeroen/tfpu/overview.shtml

[10] A. Blas et al. The new CERN PS transverse damper. PAC09, Vancouver, 2009.

[11] J. Belleman. A proposal for new head electronics for the PS orbit measurement system. AB-Note-2005-057, CERN, 2003.

[12] S. Aumon. HIgh Intensity Beam Issue in the CERN Proton Synchrotron, CERN-THESIS-2012-261.

[13] A. Huschauer et al. paper submitted to PRSTAB.

[14] R. Cappi. Observation of high-order head-tail instabilities at the CERN-PS, CERN/PS 95-02, CERN, 1994.

[15] E. Métral. Coupled Landau Damping of Transverse Coherent Instabilities in Particle Accelerators, PhD Thesis, CERN, 1999.

[16] R. Cappi et al. Control of Coherent Instabilities by Linear Coupling, 18th International Conference on High Energy Accelerators, 2001.

[17] E. Métral et al. Simulation Study of the Horizontal Head-Tail Instability Observed at Injection of the CERN Proton Synchrotron, PAC07, Albuquerque, 2007.

[18] Multi-Turn Extraction. http://ab-project-mte.web.cern.ch/AB-Project-MTE/

[19] H. Bartosik et al. Other Means to increase the SPS 25 ns Performance. LHC performance workshop, Chamonix, 2014.

# TRANSVERSE DECOHERENCE OF ION BUNCHES WITH SPACE CHARGE AND FEEDBACK SYSTEM

I. Karpov[1], V. Kornilov[2], O. Boine-Frankenheim[1,2]

[1]TEMF, TU Darmstadt, Schloßgartenstraße 8, 64289 Darmstadt, Germany

[2]GSI, Planckstr. 1, 64291 Darmstadt, Germany

## Abstract

The transverse decoherence of the bunch signal after an initial bunch displacement is an important process in synchrotrons and storage rings. It can be useful, for the diagnostic purposes, or undesirable. Collective bunch oscillations can appear after the bunch-to-bucket transfer between synchrotrons and can lead to the emittance blow-up. In order to preserve the beam quality and to control the emittance blow-up, transverse feedback system (TFS) are used. In heavy ion and proton beams, like in SIS18 and SIS100 synchrotrons of the FAIR project, transverse space charge strongly modify decoherence. The resulting bunch decoherence and beam blow-up is due to a combination of the lattice settings (like chromaticity), nonlinearities (residual or imposed by octupole magnets), strong space-charge, and the TFS. We study these effects using particle tracking simulations with the objective of correct combinations for a controlled beam blow-up.

## DECOHERENCE DUE TO TRANSVERSE NONLINEARITY AND CHROMATICITY

A beam after an initial transverse displacement performs betatron oscillations. In the absence of collective effects, the evolution of the beam centroid has been described in [1, 2]. Calculations are performed for the case of transverse nonlinearity in one plane, the initial Gaussian distribution (GS) in $(x, x')$, the linear synchrotron motion and the Gaussian energy distribution. Extension to 2-D, including $x - y$ coupling in the tune dependence from amplitudes, is addressed in [3]. Here we present the 1D results for the KV (Kapchinsky-Vladimirsky) distribution in the transverse plane in the case of uncoupled transverse oscillations and compare with the results for the GS distribution and with particle tracking simulations.

We use the constant focusing for derivations and for simulations. In this case it is convenient to use the normalized coordinates,

$$q = \frac{x}{\sigma_{x0}} \text{ and } p = \frac{Rx'}{Q_0 \sigma_{x0}}, \quad (1)$$

where $R$ is the ring radius, $Q_0$ is the bare tune, $\sigma_{x0} = \sqrt{R\epsilon_{rms0}/Q_0}$ is the initial rms beam size, $\epsilon_{rms0}$ is the initial rms emittance. We normalize the initial beam offset in x plane by defining $Z = \Delta x/\sigma_{x0}$. The amplitude $a$ and the phase $\phi$ of single particle oscillations are defined by relations $q = a \cos(\phi)$ and $p = -a \sin(\phi)$, where $a = \sqrt{q^2 + p^2}$.
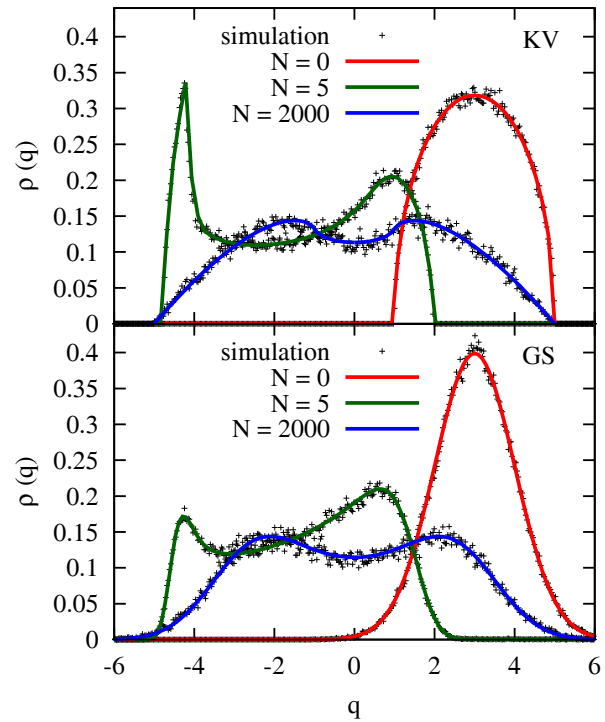


Figure 1: Beam profiles at different turn numbers for the KV (top plot) and for the GS (bottom plot) distributions. Crosses are simulation results. Solid lines are obtained by the numerical integration of Eq. (7). $Z = 3$, $Q_0 = 4.18$, $q_{nl} = 0.3$.

The initial beam distribution at turn $N = 0$ is

$$\rho_0(a, \phi_0) = \frac{a}{4\pi} H \left[ 1 - \frac{1}{4} \left( a^2 + Z^2 - 2aZ \cos(\phi_0) \right) \right], \quad (2)$$

where $H$ is the Heaviside function and $\phi_0$ is the initial betatron phase of the particle. External nonlinearities induce amplitude-dependent incoherent tune shifts. We assume that a transverse nonlinearity is produced by the cubic component of the octupole magnetic field,

$$B_x = -K_3 \frac{B\rho}{6} y^3, \quad B_y = K_3 \frac{B\rho}{6} x^3,$$

$$\text{with } K_3 = \frac{1}{B\rho} \frac{d^3 B_y}{dx^3}. \quad (3)$$

The resulting tune shift in $x$ plane is given by

$$\Delta Q_{nl}(a) = -\frac{K_3 R^3}{16 Q_0^2} \epsilon_{rms0} a^2 = -\mu a^2, \quad (4)$$

where $\mu$ is the lattice detuning. The parameter for the effect of transverse nonlinearity is defined as a ratio of the nonlinearity tune shift Eq. (4) of a particle with the amplitude $a = 2$ to to the synchrotron tune $Q_s$,

$$q_{nl} = \frac{4\mu}{Q_s}. \tag{5}$$

For single particle motion the amplitude $a$ stays constant and the phase changes as

$$\phi = \phi_0 + 2\pi N(Q_0 - \mu a^2) = \phi_0 + \Delta\phi_N. \tag{6}$$

This allows us to get the particle distribution at arbitrary turn number $N$ with substitution of $\phi_0$ by $(\phi - \Delta\phi_N)$ in Eq. (2). Using Eqs. (2) and (6) a beam profile can be calculated as

$$\rho(q) = \frac{1}{4\pi} \int dp H\left[1 - \frac{1}{4}(q - Z\cos(\Delta\phi_N))^2 \right. \tag{7}$$
$$\left. - \frac{1}{4}(p - Z\sin(\Delta\phi_N))^2\right].$$

and Figure 1 demonstrates a comparison of the beam profiles for the GS and the KV distributions at different turn numbers. $N = 2000$ corresponds to complete filamentation of the initial distribution due to transverse nonlinearities.

In the case of the linear synchrotron oscillation the tune shift due to chromaticity is defined as

$$\Delta Q_\xi = \xi Q_0 \delta \tag{8}$$

where $\xi$ is the normalized chromaticity and $\delta = \Delta p/p_0$ is the relative momentum offset of the particle.

Similar to [1,2] we calculate time evolution of the beam centroid. The amplitude is

$$A_{KV} = \sqrt{\langle q\rangle^2 + \langle p\rangle^2} = \frac{J_1(2Z\theta)}{\theta}F_\xi, \tag{9}$$

and the phase is

$$\psi = 2\pi N\left(Q_0 - \mu(4 + Z^2)\right), \tag{10}$$

where $J_n$ is the Bessel function of the first kind of the nth order, $\theta = 4\pi\mu N$ is the normalized time and the chromatic factor $F_\xi$,

$$F_\xi = \exp\left[-2\left(\frac{\xi Q_0 \sigma_\delta}{Q_s}\right)^2 \sin^2(\pi Q_s N)\right], \tag{11}$$

which provides an additional modulation due to the synchrotron motion with the tune $Q_s$ [1], where $\sigma_\delta$ is the normalized rms momentum spread.

For comparison, the amplitude evolution for the initial GS distribution is given by [2]

$$A_{GS} = \frac{ZF_\xi}{1 + \theta^2}\exp\left[-\frac{Z^2\theta^2}{2(1 + \theta^2)}\right]. \tag{12}$$

The second momenta are given by

$$\begin{bmatrix}\langle q^2\rangle \\ \langle qp\rangle \\ \langle p^2\rangle\end{bmatrix} = \left(1 + \frac{Z^2}{2}\right)\begin{bmatrix}1 \\ 0 \\ 1\end{bmatrix} + \frac{ZF_\xi^2 J_1(4Z\theta)}{4\theta}\begin{bmatrix}\cos(2\psi) \\ -\sin(2\psi) \\ -\cos(2\psi)\end{bmatrix}$$

**46**
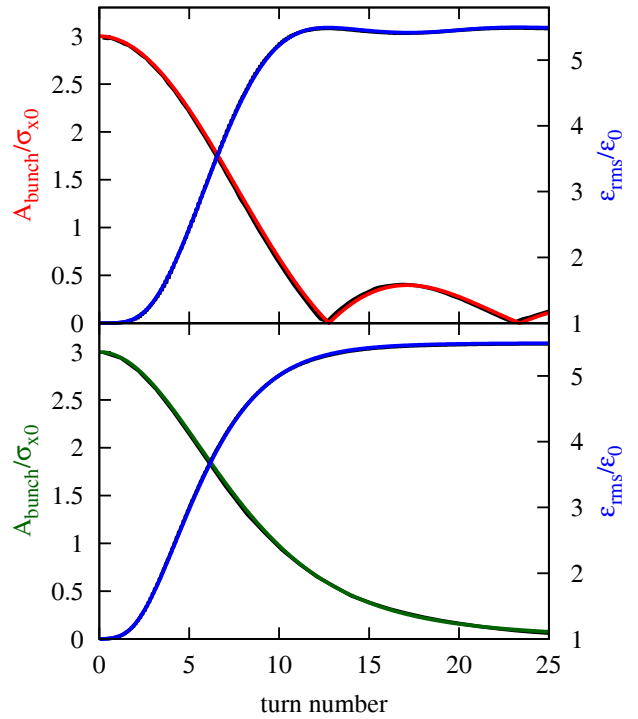


Figure 2: Time evolution of the beam offset amplitude and of the rms emittance for the KV (top plot) and for the GS (bottom plot) distributions. Black curves are simulation results, red curves are given by Eq. (9), green curves are given by Eq. (12) and blue curves are given by Eq. (14). $Z = 3$, $Q_0 = 4.18$, $q_{nl} = 0.3$.

$$+\frac{F_\xi^2 J_2(4Z\theta)}{2\theta}\begin{bmatrix}\sin(2\psi) \\ -\cos(2\psi) \\ -\sin(2\psi)\end{bmatrix} \tag{13}$$

Using Equations (9, 10, 13) we calculate the normalized rms beam size and the normalized rms emittance as $\sigma_q = \sqrt{\langle q^2\rangle - \langle q\rangle^2}$ and

$$\epsilon_{rms} = \epsilon_{rms0}\sqrt{\sigma_q^2 \sigma_p^2 - (\langle qp\rangle - \langle q\rangle\langle p\rangle)^2} \tag{14}$$

correspondingly. Figure 2 shows a comparison of the offset amplitude $A_{bunch}$ and the rms emittance from particle tracking simulations for both distributions of the same initial rms size with Eqs. (9, 12, 14). According to Eq. (14), the final emittance does not depend on the initial distribution and for $N \to \infty$ we have

$$\epsilon_{rms} = \epsilon_{rms0}(1 + Z^2/2) \tag{15}$$

## DECOHERENCE WITH SPACE CHARGE

The particle tracking code PATRIC [4] is used to study to damping of coherent oscillations and emittance blow-up due to decoherence with space charge [5]. As have been shown in Fig. 1 the beam profile significantly changes from the initial shape during the filamentation process. It requires to use a 2.5D self-consistent space charge solver in simulations.
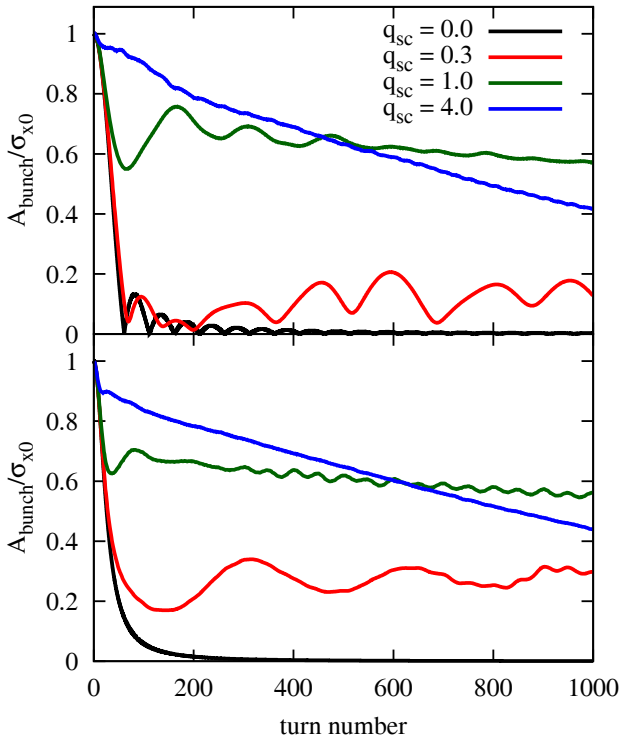
Figure 3: Time evolution of the bunch offset amplitude for the KV (top plot) and for the GS (bottom plot) distributions for $q_{nl} = 1$.
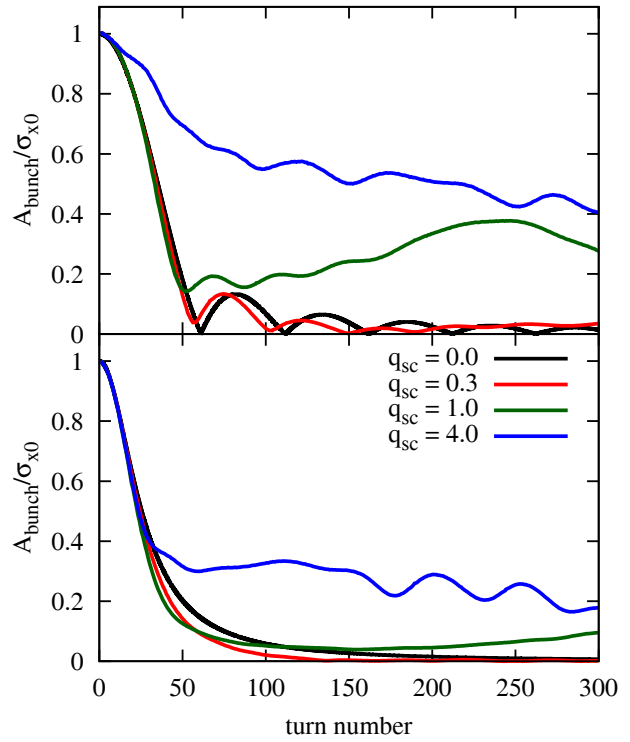


Figure 5: Time evolution of the bunch offset amplitude for the KV (top plot) and for the GS (bottom plot) distributions for $q_{nl} = -1$.
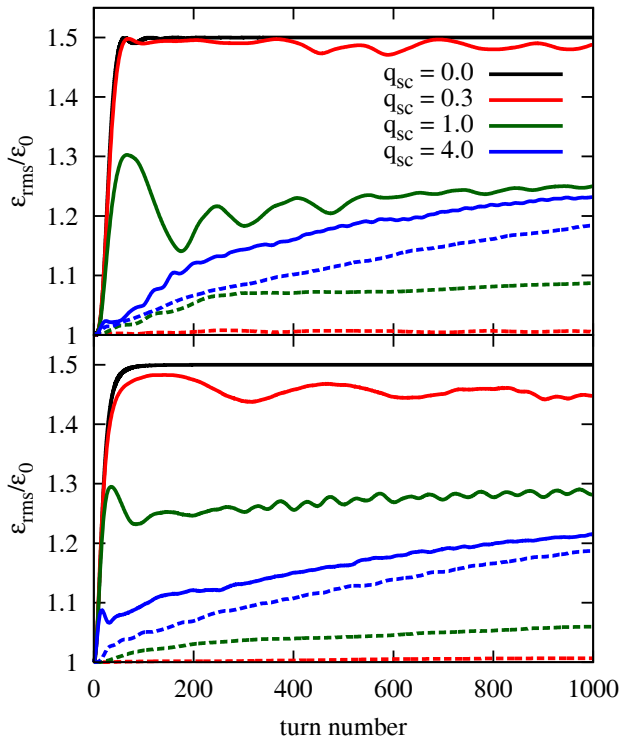


Figure 4: Time evolution of the rms emittance for the KV (top plot) and for the GS (bottom plot) distributions for $q_{nl} = 1$. Solid lines are $\epsilon_x$, dashed lines are $\epsilon_y$.
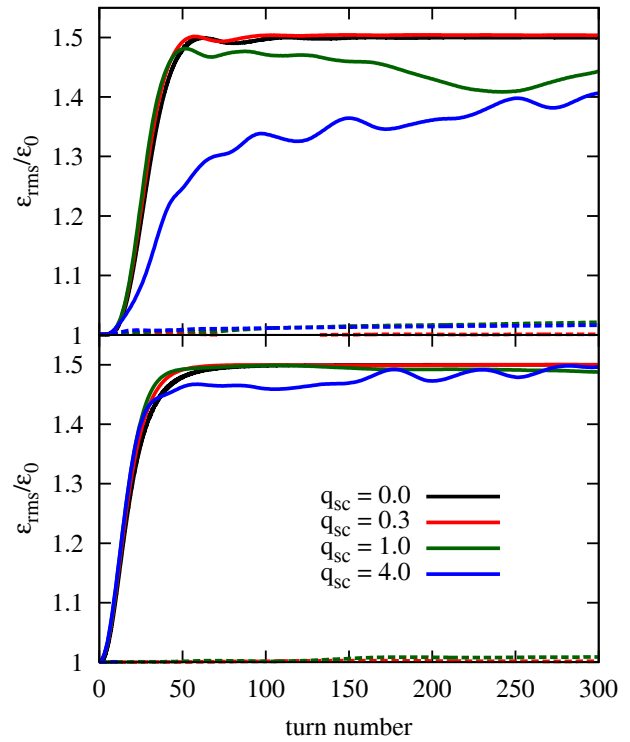


Figure 6: Time evolution of the rms emittance for the KV (top plot) and for the GS (bottom plot) distributions for $q_{nl} = -1$. Solid lines are $\epsilon_x$, dashed lines are $\epsilon_y$.

Transverse space charge effects are described using the characteristic tune shift,

$$\Delta Q_{\text{sc}} = \frac{\lambda_0 r_p R}{\gamma^3 \beta^2 \epsilon_\perp} \qquad (16)$$

where $\beta$ and $\gamma$ are the relativistic parameters, $r_p = q_{\text{ion}}^2/4\pi\varepsilon_0 mc^2$ is the classical particle radius, $\lambda_0$ is the peak line density (at the bunch center), and $\epsilon_\perp$ is the transverse total emittance. The tune shift corresponds to a round cross section with the KV distribution, and is defined as the modulus of the negative shift. In the rms-equivalent bunch with the GS transverse profile, i.e., the transverse rms emittance is $\epsilon_{\text{rms}} = \epsilon_\perp/4$, the maximum space charge tune shift is twice this value, $\Delta Q_{\text{sc}}^{\text{max}} = 2\Delta Q_{\text{sc}}$. The parameter for the effect of space charge in a bunch is defined as a ratio of the characteristic tune shift Eq. (16) to the synchrotron tune,

$$q_{\text{sc}} = \frac{\Delta Q_{\text{sc}}}{Q_{\text{s}}}. \qquad (17)$$

All simulations below are performed for $Q_{\text{s}} = 0.01$, $Q_0 = 4.18$, $Z = 1$ and $\xi = 0$. Figures 3 and 4 demonstrate particle tracking simulations for an initially offset bunch with a round cross section for the KV (top plots) and the GS (bottom plots) distributions, for $q_{\text{nl}} = 1$. For $q_{\text{sc}} = 0$ (black lines) in Fig. 3 we see fast decrease of the bunch offset amplitude, as expected from Eqs. (9, 12), but for $q_{\text{sc}} = 0.3$ the bunch offset oscillations are not finally damped. For stronger space charge initial behavior of the bunch offset corresponds to Eqs. (9, 12) and then it changes to a different damping regime. In Fig. 4 one can see that the rms emittance approaches the asymptotic value (Eq. 15) only for $q_{\text{sc}} = 0$ and for $q_{\text{sc}} = 0.3$ in a bunch with the initial KV distribution. Note a slow emittance increase in both transverse planes for $q_{\text{sc}} > 1$. According to simulations, the emittance blow-up for both initial distributions is comparable.

In Figures 5 and 6 we show particle tracking simulations for the same bunch parameters in case of opposite polarity of transverse nonlinearity $q_{\text{nl}} = -1$ for the KV (top plots) and the GS (bottom plots) distributions. Damping of coherent oscillations is faster for both distributions in comparison to the case of $q_{\text{nl}} = 1$ (Fig. 3) . The final emittance in $x$ plane for the GS distribution reaches the asymptotic value (Eq. 15) for all cases and is negligible in $y$ plane. In the case of moderate and strong space charge for the KV distribution we observe the smaller emittance increase in $x$ plane than for the GS distribution.

As we can see the damping process extremely depends on the sign of the transverse nonlinearity tune shift in the case of moderate and strong space charge. Figure 7 demonstrates comparison of the final particle distribution in a normalized phase space for $q_{\text{nl}} = 1$ and $q_{\text{nl}} = -1$ with the initial KV distribution. Strong space charge ($q_{\text{sc}} = 4$) in combination with nonlinearity polarity provides different redistribution of particles in the phase space and different emittance increase. To understand these effects an additional study is required.

## TRANSVERSE FEEDBACK SYSTEM VS DECOHERENCE

In our simulations we use a simplified transverse feedback system (TFS) module with two elements: a beam position monitor (BPM) which measures the bunch offset and combines values from two turns to provide the correctional signal $\Delta p_N$ with the required phase for the kicker. For the constant focusing lattice the correctional signal is given by

$$\Delta p_N = G q_N \frac{\cos(\Delta\phi + 2\pi Q_0)}{\sin(2\pi Q_0)}$$
$$-G q_{N-1} \frac{\cos(\Delta\phi + 4\pi Q_0)}{\sin(2\pi Q_0)}, \qquad (18)$$

where $\Delta\phi$ is the phase advance between the BPM and the kicker, $G$ is the TFS gain which defines the damping time,

$$N_{\text{TFS}} = \frac{2}{G}. \qquad (19)$$

In this model we assume that the TFS module has no bandwidth limitations, delay errors and noise amplification. In order to prevent emittance blow-up the damping time
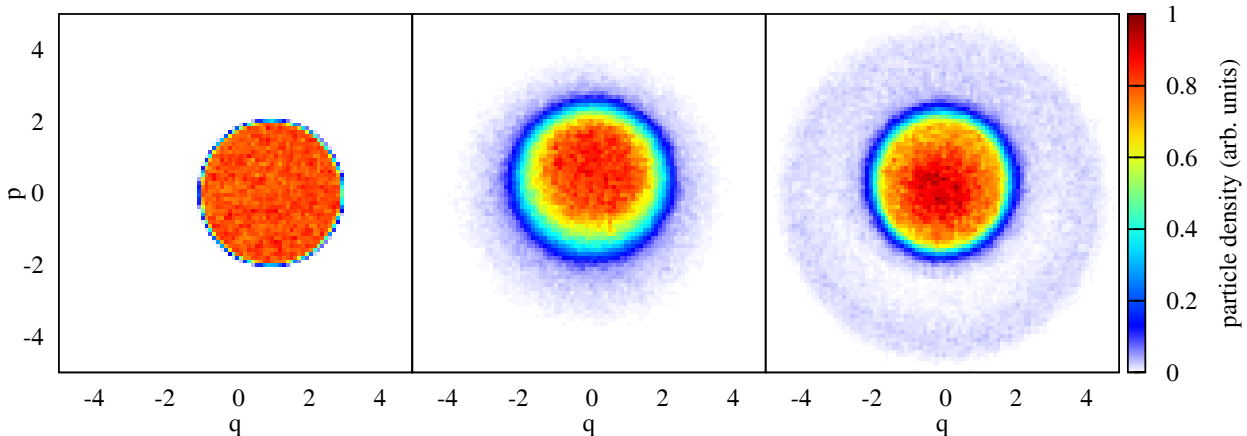
Figure 7: A particle density in the normalized phase space $(p, q)$ for the initial KV distribution at $N = 0$ (left plot), $N = 1000$ $q_{\text{nl}} = 1$ (center plot) and $N = 1000$ $q_{\text{nl}} = -1$ (right plot), $q_{\text{sc}} = 4$.

                                                            **Beam Dynamics in Rings**
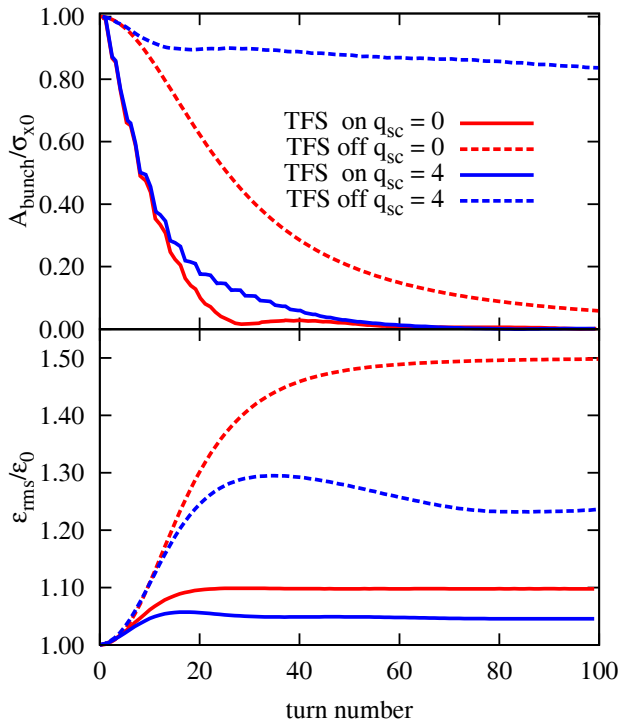
Figure 8: Time evolution of the bunch offset amplitude (top plot) and the rms emittance (bottom plot) for the initial GS distribution with TFS (solid lines) and without TFS (dashed lines). The parameters of simulations: $q_{nl} = 1$, $q_{sc} = 0; 4$, $N_{TFS} = 10$, $\Delta\phi = \pi/8$ .

$N_{TFS}$ should be smaller than characteristic decoherence time. Figure 8 shows an example of particle tracking simulations of an initially offset bunch with a round cross section for the GS distribution, for $Z = 1$, $q_{nl} = 1$ and the TFS damping time $N_{TFS} = 10$ turns. For comparison dashed lines correspond to simulations without TFS. We see that a simplified TFS module can considerably reduce the emittance blow-up due to transverse nonlinearity and space charge. The emittance increase with TFS in $y$ plane is smaller than 1% and is not shown. One can also see that space charge could be helpful for emittance preservation.

## CONCLUSIONS

The analytical prediction of emittance blow-up due to bunch decoherence with transverse nonlinearities for the initial transverse Kapchinsky-Vladimirsky distribution has been derived and compared, with the case of the initial Gaussian distribution. The bunch offset decoherence and transverse emittance blow-up have been studied using the particle tracking code PATRIC for different space charge strength. The different damping regimes of coherent oscillations for positive and negative polarity of octupole nonlinearity have been observed. The emittance blow-up reduction using an ideal Transverse Feedback System module has been shown.

## ACKNOWLEDGMENTS

## REFERENCES

[1] R.E. Miller, A.W. Chao, J.M. Peterson, S.G. Peggs, M. Furman, SSC Report SSC-N-360 (1987)

[2] M.G. Minty, A.W. Chao, W.L. Spence, Proceedings of PAC95, Dallas, Texas, USA, p. 3037 (1995)

[3] S.Y. Lee, SSC Report SSCL-N-749 (1991)

[4] O. Boine-Frankenheim, V. Kornilov, Proc. of ICAP2006, Oct 2-6, Chamonix Mont-Blanc, (2006)

[5] V. Kornilov, O. Boine-Frankenheim, Transverse decoherence and coherent spectra in long bunches with space charge Phys. Rev. ST Accel. Beams 15, 114201 (2012).

# SLIP-STACKING DYNAMICS AND THE 20 Hz BOOSTER

J. Eldred, Department of Physics, Indiana University, Bloomington, IN 47405, USA

R. Zwaska, FNAL, Batavia, IL 60510, USA

## Abstract

Slip-stacking is an accumulation technique used at Fermilab since 2004 which nearly doubles the proton intensity. The Proton Improvement Plan II intensity upgrades require a reduction in slip-stacking losses by approximately a factor of 2. We introduce universal area factors to calculate the available phase space area for any set of beam parameters without individual simulation. We show the particle loss as a function of time and slip-stacking resonances. We calculate the injection efficiency as a function of longitudinal emittance and aspect-ratio. We demonstrate that the losses from RF single particle dynamics can be reduced by a factor of 4-10 (depending on beam parameters) by upgrading the Fermilab Booster from a 15-Hz cycle-rate to a 20-Hz cycle-rate. We recommend a change in injection scheme to eliminate the need for a greater momentum aperture in the Fermilab Recycler.

## INTRODUCTION

Slip-stacking is integral to high-intensity operation at Fermilab and will play a central role in upgrades to the accelerator complex [1–3]. the Fermilab Proton Improvement Plan-II [1] calls for an improvement in beam power from 700 kW (with slip-stacking) to 1.2 MW with an eye towards multi-MW improvements. The increase in proton intensity requires a commensurate decrease in the slip-stacking loss-rate to limit activation in the tunnel. Single-particle dynamics associated with slip-stacking contribute directly to the particle losses. Our numerical results completely characterize the stable phase-space boundary and expresss this information as limits on the Booster beam quality. We show that including a 20-Hz Booster cycle-rate in the PIP-II upgrade relaxes the limits on the Booster beam quality and cuts particle losses due to slip-stacking.

## BACKGROUND

Slip-stacking is a particle accelerator configuration that permits two high-energy particle beams of different momenta to use the same transverse space in a cyclic accelerator. The two beams are longitudinally focused by two sets of rf cavities with a small frequency difference between them. Each frequency is tuned to the momentum of one of the beams.

The two azimuthal beam distributions are manipulated as a consequence of their difference in rf frequency. Figure 1 shows the slip-stacking accumulation process. The two beams injected on separated portions of azimuth with a small frequency difference and overlap gradually, allowing injection [4]. When the cyclic accelerator is filled and the azimuthal distribution of the two beams coincide then the two beams are accelerated together by RF cavities operating at the average frequency. The potential beam intensity of a synchrotron is doubled through the application of this technique.
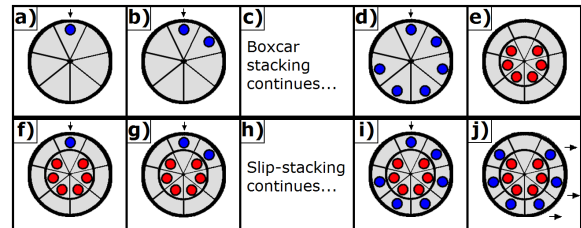


Figure 1: The Booster batch is represented by the circles and the Recycler (or Main Injector) is represented by the seven-sector wheel. **a)** The first batch is injected into the ring. **b)** One Booster cycle later the second batch is injected in the azimuthal space immediately behind the first batch. This is known as boxcar stacking. **c, d)** Boxcar stacking injections continue until six Booster batches are stored in the ring. **e)** The RF frequency is adiabatically lowered in between the sixth and seventh batch injection. **f)** The seventh batch is injected in the gap left by the previous six batches. Both cavities are operating at different frequency (slip-stacking). The first RF cavity matches the first six batches and the second RF cavity matches the next set of batches. **g)** One Booster cycler later the eighth batch is boxcar stacked with respect to the seventh batch but the frequency difference allows the injection to occur in the gap left by the first six batches. **h, i)** Slip-stacking injections continue until twelve Booster batches are stored in the ring. **j)** One Booster cycle later the kicker gaps of the first six and last six batches are aligned. At that time the batches are extracted to the Main Injector (if needed) and both beams are accelerated as one.

A preliminary study explored the beam dynamics in a 2-rf system [5]. The slipping of bunched beams was first demonstrated at the CERN SPS [6] but the emittance growth led to unacceptable particle losses. Fermilab has subsequently implemented slip-stacking operationally since 2004 [4, 7, 8]. Initially, the higher beam intensity was used to increase antiproton production for proton-antiproton collider experiments [9]. Subsequently, slip-stacking was applied to neutrino production for Neutrinos at Main Injector (NuMI) experiments [10–12].

Beam-loading effects can impact the effectveness of slip-stacking and were addressed in the Main Injector by the development of a beam-loading compensation system with -14dB feedback and -20dB feedforward [13–15]. The beam-loading effects on slip-stacking in the Recycler will be an order of magnitude weaker than in the Main Injector and

Table 1: Recycler and Booster Parameters Used in Analysis

| | |
|---|---|
| Recycler Kinetic Energy ($E$) | 8 GeV |
| Recycler Reference RF freq. ($f$) | 52.8 MHz |
| Recycler Harmonic number ($h$) | 588 |
| Recycler Phase-slip factor ($\eta$) | $-8.6*10^{-3}$ |
| Maximum Recycler RF Voltage ($V$) | $2 \times 150$ kV |
| Booster harmonic number ($h_B$) | 84 |
| Booster cycle rate ($f_B$) | 15/20 Hz |
| Difference in Recycler RF freq. ($\Delta f$) | 1260/1680 Hz |
| Nom. Booster emittance ($\epsilon_{97\%}$) | 0.12 eV·s |
| Nom. Booster Aspect Ratio | 3.00 MeV/ns |
| Nom. Recycler Aspect Ratio (100 kV) | 1.06 MeV/ns |
| Nom. Recycler Aspect Ratio (57 kV) | 0.80 MeV/ns |

can be compensated if necessary. The typical beam-loading voltage is ~2kV [14] compared to a typical rf cavity voltage of 90kV [15]. In the Main Injector the $R_{sh}/Q$ of the rf cavities is 100Ω [14], while in the Recycler the $R_{sh}/Q$ is 13Ω [16]. This paper focuses on the constraints on the stable phase-space area fro

As Fig. 1 shows, the slipping rate of the buckets must be properly synchronized to the injection rate of new batches. The difference between the two RF frequencies must be equal to the product of the harmonic number of the Booster RF and the cycle rate of the Fermilab Booster. So for a Booster with a 15-Hz cycle-rate we have

$$\Delta f = h_B f_B = 84 \times 15 \text{ Hz} = 1260 \text{ Hz}$$

and for the proposed 20-Hz cycle-rate

$$\Delta f = h_B f_B = 84 \times 20 \text{ Hz} = 1680 \text{ Hz}.$$

The difference in the frequency of the two RF cavities is related to the difference in momentum of the two beams by:

$$\Delta \delta = \frac{\Delta f}{f_{rev} h \eta} \tag{1}$$

where $h$ is the harmonic number of the Recycler and $\eta$ is the phase-slip factor of the Recycler (see Table 1). Consequently, the momentum difference between the two beams is 0.28% for the 15-Hz Booster and 0.37% for the 20-Hz Booster.

A 20-Hz Booster also reduces the time required to accumulate 12 batches in the Recycler, making more beam available for 8-GeV experiments [17–19]. For example, a 1.333 s MI cycle time would consume 9 Hz of the Booster's cycles, the additional available 8-GeV beam would increase from 6 Hz to 11 Hz. Furthermore, if the Main Injector ramp cycle is shortened to extract protons for LBNE at 60 GeV [20], then a 20-Hz Booster could deliver more beam to LBNE than a 15-Hz Booster.

## SLIP-STACKING PARAMETER AND STABILITY MAPS

The equations of motion for a single particle under the influence of two rf cavities with identical voltage and different frequencies are

$$\dot{\phi} = 2\pi f_{rev} h \eta \delta$$
$$\dot{\delta} = f_{rev} V_\delta [\sin(\phi) + \sin(\phi - \Delta f t)]. \tag{2}$$

where $V_\delta$ is the maximum change in $\delta$ during a single revolution[1] and $\Delta f$ is the frequency difference between the two RF cavities.

This is an explicitly time-dependent system which is the subject of ongoing research in dynamical mathematics [21, 22]. Broadly speaking, slip-stacking is complicated by the fact that the two RF systems will interfere and reduce the stable bucket area. The further the buckets are away from each other in phase-space, the less interference there is. To quantify this, the literature [5–7, 21] has identified the importance of the slip-stacking parameter

$$\alpha_s = \frac{\Delta f}{f_s} \tag{3}$$

as the criterion for effective slip-stacking. $\Delta f$ is the frequency difference between the two RF cavities and $f_s$ is the single-RF synchrotron frequency $f_s = f_{rev} \sqrt{\frac{V h |\eta|}{2\pi \beta^2 E}}$.

In fact, all nontrivial dynamics of slip-stacking depend only on $\alpha_s$. For example, if one slip-stacking configuration has RF frequency separation $\Delta f = 15$ Hz and another configuration with the same $\alpha_s$ has RF frequency separation $\Delta f' = 20$ Hz then the second phase space diagram is isomorphic to the first where the $\delta$ axis must be scaled by $\Delta f'/\Delta f = 4/3$.

The greater the slip-stacking parameter $\alpha_s$, the less the buckets interfere. Increasing the synchrotron frequency $f_s$ by increasing the voltage will increase the bucket height, but also increase the interference. So, for a fixed frequency difference $\Delta f$, there is a tradeoff encountered when tuning the voltage for maximum phase-space area. To optimize the bucket area more precisely, we must simulate the single particle dynamics. Fortunately we can use the slip-stacking parameter to simplify the parameter space.

We create a stability map for each value of the slip-stacking parameter $\alpha_s$. We map the stability of initial particle positions by integrating the equations of motion for each initial position. Each position is mapped independently and only the single particle dynamics are considered. The integration is iterated for 100 synchrotron periods. The stability of the particle is tested after every phase-slipping period. A particle is considered lost if its phase with respect to each of the first RF cavity, the second RF cavity, and the average of the two RF cavities, is larger than a certain cut-off (we used $3\pi/2$). Figure 2 shows an example of such a stability map; the large stable regions at the top-center and bottom-center are the buckets used for slip-stacking and the interference effect is clearly evident.

---

[1] $V_\delta = \frac{eV}{\beta^2 E}$, where $V$ is the effective voltage of the RF cavity, $e$ is the charge of the particle, $\beta = v/c$ is the velocity fraction of the speed of light, $E$ is the total energy of the particle.
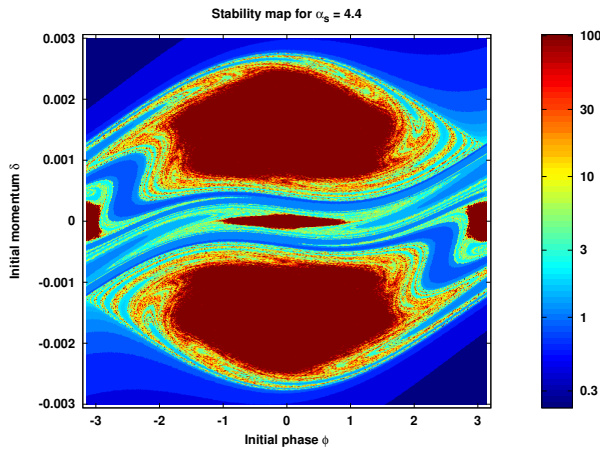
Figure 2: Stability of initial coordinates for $\alpha_s = 4.4$. The color corresponds to the number of synchrotron periods a particle with the corresponding initial coordinates survives before it is lost. The two large stable regions correspond to the higher and lower RF buckets where beam is injected and maintained.

We find some trajectories are "metastable" because they lead to particle loss only after thousands of revolutions. The stable phase-space area as a function of time is shown in Fig. 3 for several values of $\alpha_s$. The loss of metastable phase-space area occurs at a rater that is faster than exponential decay.
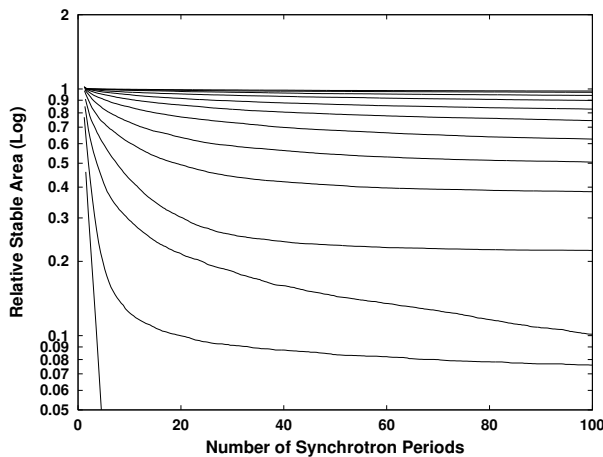


Figure 3: The stable area of the slip-stacking bucket relative to a single rf bucket, is plotted on a log scale and plotted over time. Each curve corresponds to a simulation with a different value of $\alpha_s$ with $\alpha_s$ = 2.0, 2.5, 3.0, 3.5, 4.0, 4.5, 5.0, 5.5, 6.0, 6.5, 7.0, 7.5, 8.0 (going from the bottom line to the top line).

The bucket area is computed as the product of the total number of ultimately surviving points and the cell area. We define the slip-stacking area factor $F(\alpha_s) = \mathcal{A}_s/\mathcal{A}_0$ as the ratio of the slip-stacking bucket area to that of a single-rf bucket with the same rf voltage and frequency. Then the phase space area ($\phi \cdot \delta$ units) can be expressed in terms of this factor $F(\alpha_s)$:

$$\mathcal{A}_s = \mathcal{A}_0 F(\alpha_s) = \frac{16}{h|\eta|} \frac{f_s}{f_{rev}} F(\alpha_s). \quad (4)$$

Figure 4(a) plots the numerically derived slip-stacking area factor $F(\alpha_s)$. Using Fig. 4(a) with Eq. 4 provides the first method for calculating the slip-stacking stable phase-space area without requiring each case to be simulated individually. $F(\alpha_s)$ increases rapidly above $\alpha_s \approx 3$ and asymptotically approaches 1. $F(\alpha_s)$ has several local minimum where resonances are crossed; this loss of area occurs when large amplitude trajectories have a parametric resonance and therefore does not occur at precise integer values of $\alpha_s$.
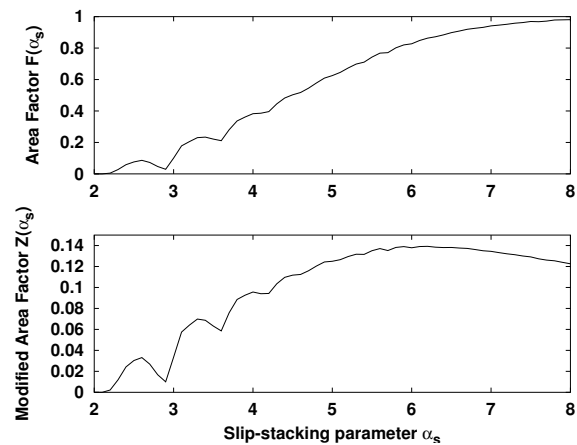


Figure 4: (a) The slip-stacking area factor as a function of $\alpha_s$. As $\alpha_s$ increases the distance between the rf buckets becomes greater, the buckets become more independent, and the slip-stacking bucket area approaches the single-rf bucket area. (b) The modified slip-stacking area factor as a function of $\alpha_s$. The modified slip-stacking area factor is maximized near $\alpha_s = 6.2$.

For a given Booster cycle-rate, the slip-stacking parameter $\alpha_s$ can be tuned by changing the RF voltage. The synchrotron frequency $f_s$ which is proportional to the square root of the applied RF voltage and changes the bucket area by both the slip-stacking area factor $F(\alpha_s)$ and the single-rf bucket area. To identify the optimal voltage, we rewrite Eq. 4 to separate the parameters that are held constant from those dependent on $\alpha_s$:

$$\mathcal{A}_s = \frac{16}{h|\eta|} \frac{\Delta f}{f_{rev}} \left( \frac{F(\alpha_s)}{\alpha_s} \right) = \frac{16}{h|\eta|} \frac{\Delta f}{f_{rev}} Z(\alpha_s). \quad (5)$$

This modified area factor $Z(\alpha_s)$ is graphed in Fig. 4(b). $Z(\alpha_s)$ is maximal near $\alpha_s = 6.2$ and when considering other optimization criteria 5.5 to 7 is is a practical tuning range for $\alpha_s$. In particular, the maximum bucket height is obtained when the rf voltage is tuned such that $\alpha_s = 5.5$ - the additional bucket height normally obtained at higher RF

voltages is eliminated by the focusing interference between the slip-stacking cavities.

For low $\alpha_s$ many of the losses are driven by a parametric resonance between $f_s$ and $\Delta f$. It can be shown [21] that the resonance condition is

$$m f_s (1 + \sigma) = n \Delta f$$

where the RF separation $\Delta f$ is a rational multiple of the synchroton frequency $f_s$ with a synchrotron frequency shift $\sigma$ corresponding to its synchrotron oscillation amplitude $\rho$. In that case, the growth rate of the instability becomes

$$\ddot{\phi} \propto \rho^m \alpha_s^{-2(n-1)}$$

. Figure 5 shows the stability map for $\alpha_s = 3.6$ and depicts strong parameter resonance at the synchrotron amplitude where $f_s (1 + \sigma) = 4\Delta f$.
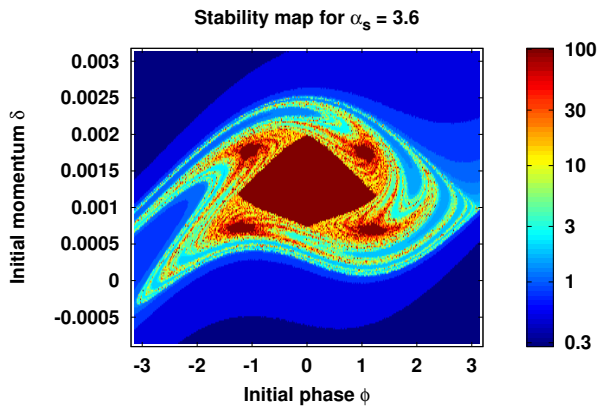


Figure 5: Stability of initial coordinates for $\alpha_s = 3.6$ (top bucket only). The color corresponds to the number of synchrotron periods a particle with the corresponding initial coordinates survives before it is lost. The four resonance islands are created by the $\omega_s (1 + \sigma) = 4\omega_\phi$ parametric resonance.

## INJECTION SCENARIOS AND COMPARISON OF CYCLE-RATES

These stability maps can be used to analyze injection scenarios, by weighting the (appropriately scaled) stability maps according to a distribution that represents the number of incoming particles injected into that region of phase-space. We used this technique to identify the greatest longitudinal emittance an incoming Gaussian-distributed beam could have and still achieve 97% injection efficiency at its optimal RF cavity voltage - the 97$ admittance. The longitudinal beam emittance is given in Eq. 6 below:

$$\epsilon = \pi \sigma_P \sigma_T, \; \epsilon_{97\%} = 2.17^2 \pi \sigma_P \sigma_T \tag{6}$$

The current accelerator upgrade proposal, Proton Improvement Plan II (PIP-II) [1], defines a minimum 97% slip-stacking efficiency required to maintain current loss

levels while increasing intensity. Figure 6 shows the 97% admittance as a function of aspect ratio and demonstrates the consequences of a mismatched injection into a slip-stacking bucket. The optimal RF cavity voltage as a function of aspect ratio is shown in Fig. 7. Figure 8 show the slip-stacking parameter at which the injection efficiency is optimized. These results were obtaining using parameter values shown in Table. 1.
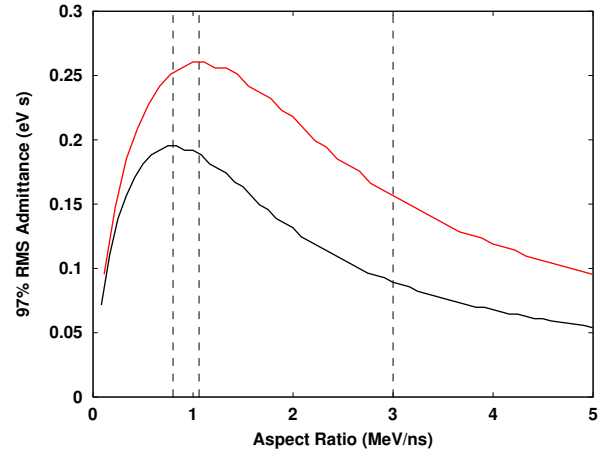


Figure 6: The 97% admittance at 97% efficiency (at an optimal value of $\alpha_s$) is shown as a function of aspect ratio. The bottom line (black) is for the 15-Hz Booster cycle-rate (status quo) and top line (red) is for 20-Hz Booster cycle-rate (proposed upgrade). The vertical dashed lines represent the nominal aspect ratios given in Table 1.
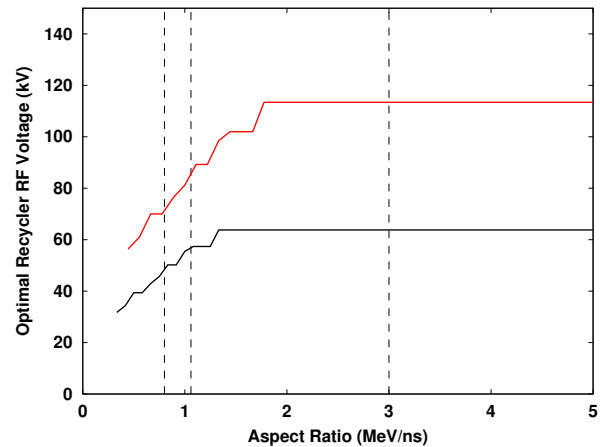


Figure 7: The optimal Recycler rf voltage for 97% admittance (at 97% efficiency) is shown as a function of aspect ratio. The bottom line (black) is for the 15-Hz Booster cycle-rate (status quo) and top line (red) is for 20-Hz Booster cycle-rate (proposed upgrade). The vertical dashed lines represent the nominal aspect ratios given in Table 1.

A nominal value for the Booster emittance is 0.12 eV·s [23]. The Fermilab Booster uses bunch rotation via quadrupole excitation [24, 25], with parameters that are
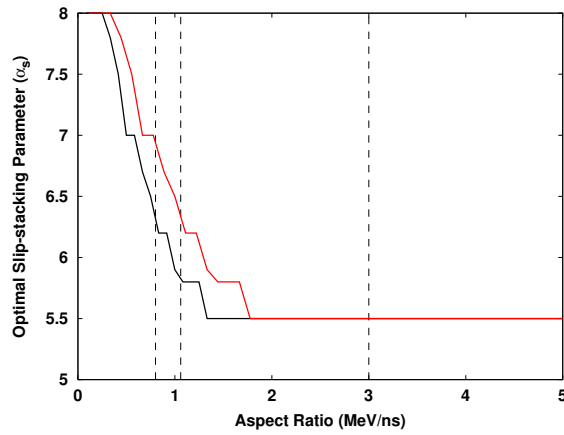
Figure 8: The optimal slip-stacking parameter $\alpha_s$ for 97% admittance (at 97% efficiency) is shown as a function of aspect ratio. Values of $\alpha_s$ greater than 8 are not evaluated. The bottom line (black) is for the 15-Hz Booster cycle-rate (status quo) and top line (red) is for 20-Hz Booster cycle-rate (proposed upgrade). The vertical dashed lines represent the nominal aspect ratios given in Table 1.

Table 2: Holding the aspect ratio and 97% efficiency constant, the 97% admittance is increased in a 20-Hz Booster.

| 97% Admittance | 15 Hz | 20 Hz |
|---|---|---|
| 3.00 MeV/ns | 0.089 eV·s | 0.157 eV·s |
| 2.00 MeV/ns | 0.132 eV·s | 0.218 eV·s |

actively tuned to minimize losses. With bunch rotation, the aspect ratio of at least 2.6 MeV/ns is achievable at extraction from the Booster [23]. At Recycler rf cavity voltage $V_0 = 100$kV, the slip-stacking parameter for the Recycler is $\alpha_s(V_0) \approx 4.39$ for a 15-Hz Booster cycle-rate and $\alpha_s(V_0) \approx 5.86$ for a 20-Hz Booster cycle-rate. For other voltages, the Recycler slip-stacking parameter is given by $\alpha_s(V) = \alpha_s(V_0) \sqrt{V/V_0}$.

We examine the 97% efficiency benchmark for both a 15-Hz Booster cycle-rate and a 20-Hz Booster cycle-rate. A 20-Hz Booster cycle-rate increases the RF frequency separation by a factor of 4/3 and therefore permits a 4/3 higher bucket height (for the same level of bucket independence $\alpha_s$). Consequently a 20-Hz Booster cycle-rate permits operation with either a significantly greater Booster admittance or injection efficiency. Figure 9 superimposes the Booster beam injection (natural aspect ratio without bunch rotation) for a 15-Hz Booster slip-stacking bucket and 20-Hz Booster slip-stacking bucket. Table 2 shows the improvement from a 20-Hz Booster cycle-rate expressed as a relaxation of Booster emittance limits. Table 3 shows the improvement from a 20-Hz Booster cycle-rate as greater efficiency. A 20-Hz Booster cycle-rate is clearly superior for high-intensity operation. Consequently, recent PIP-II documents have formally incorporated a 20-Hz Booster cycle rate into the specifications of the PIP-II upgrades [26].
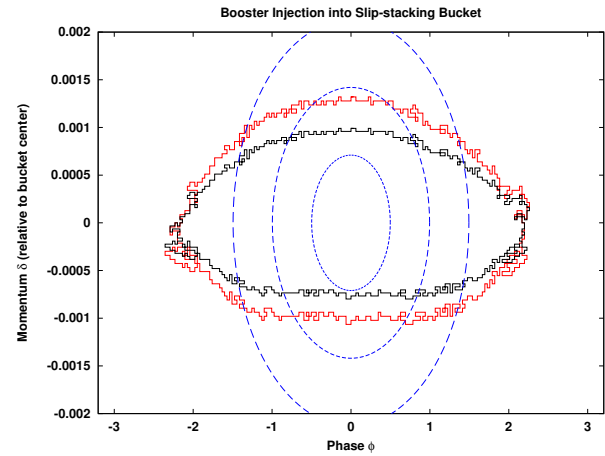
Figure 9: The shape of the slip-stacking Bucket is shown in black for the case of the 15-Hz Booster and in red for the case of the 20-Hz Booster. Both slip-stacking buckets are calculated for $\alpha_s = 5.5$ and optimized for bucket height. The three dashed blue lines represent $1\sigma$, $2\sigma$, and $3\sigma$ of a Gaussian distribution representing a typical Booster injection. In this case, the beam emittance is 0.1 eV·s and the aspect ratio is 3 MeV/ns.

Table 3: Holding aspect ratio and emittance constant, the slip-stacking losses are dramatically reduced in a 20-Hz Booster. Bolded values pass the 97% efficiency benchmark.

| Losses | 15 Hz | 20 Hz |
|---|---|---|
| with 3.00 MeV/ns & 0.08 eV·s | **2.22 %** | **0.30 %** |
| with 3.00 MeV/ns & 0.1 eV·s | 3.97 % | **0.73 %** |
| with 3.00 MeV/ns & 0.12 eV·s | 5.95 % | **1.38 %** |
| with 3.00 MeV/ns & 0.18 eV·s | 12.11 % | 4.29 % |
| with 2.00 MeV/ns & 0.08 eV·s | **0.61 %** | **0.04 %** |
| with 2.00 MeV/ns & 0.1 eV·s | **1.36 %** | **0.14 %** |
| with 2.00 MeV/ns & 0.12 eV·s | **2.39 %** | **0.33 %** |
| with 2.00 MeV/ns & 0.18 eV·s | 6.58 % | **1.67 %** |

A 20-Hz Booster would best be implemented in conjunction with a change in the slip-stacking injection scheme to avoid encountering limits in momentum aperture. Kourbanis measured the Recycler momentum aperture in May 2014 to be 0.74% for 95% transmission and 0.53% for 99% transmission [27]. It should be noted that this momentum aperture is limited by the dynamic aperture, which means that it is sensitive to chromaticity and betatron tuning; it is less than half of the physical aperture, the momentum aperture the could conceivably be achieved with improvements to the lattice (see [28]).

The total momentum range used during slip-stacking is shown in Table 4. The 20-Hz Booster requires greater RF frequency separation and therefore the total momentum used in any injection scheme would increase. However as Table 4 indicates, switching from the "On-Energy" injection with a 15-Hz Booster (status quo) to "Off-Energy" injection 20-Hz Booster (proposed) is actually a net decrease in the total

Table 4: The required momentum aperture for slip-stacking in the Recycler depending on the momentum range of the incoming beam, the injection scheme, and the Booster cycle-rate. Figures 10 and 11 depict the two injection schemes. Bolded values pass a 0.6% benchmark.

| Momentum Usage | 15 Hz | 20 Hz |
|---|---|---|
| with ± 12 MeV & "On-Energy" Inj. | 0.72 % | 0.86 % |
| with ± 12 MeV & "Off-Energy" Inj. | **0.58 %** | 0.67 % |
| with ± 8 MeV & "On-Energy" Inj. | 0.63 % | 0.76 % |
| with ± 8 MeV & "Off-Energy" Inj. | **0.48 %** | **0.57 %** |
| with ± 4 MeV & "On-Energy" Inj. | **0.52 %** | 0.66 % |
| with ± 4 MeV & "Off-Energy" Inj. | **0.38 %** | **0.47 %** |

momentum usage. These two injection schemes are depicted in Fig. 10 and Fig. 11.

In the "On-Energy" injection scheme (see Fig. 10), the extraction energy from the Booster is the injection energy into the Recycler. The frequencies of the Recycler RF cavities move to ensure the injection and extraction is simple, but at the cost of greater momentum usage. In the "Off-Energy" injection scheme (see Fig. 11), the Recycler must be tuned to extract at a momentum $\Delta\delta/2$ lower or higher than the momentum of the beam injected into the Main Injector ( [12], p. 8-109). The advantage offered by this alternate injection scheme is that only $\Delta\delta$ and the full bucket height must be accommodated, rather than the $(3/2)\Delta\delta$ and the full bucket height required by the On-Energy injection scheme. Eq. 1 relates the frequency difference with the momentum difference.
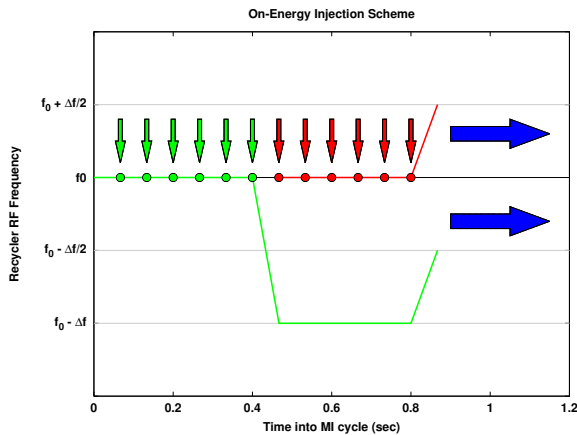


Figure 10: The On-Energy injection scheme spans the frequencies $f_0 - \Delta f$ to $f_0 + \Delta f/2$.

The gains in slip-stacking efficiency under the 20-Hz Booster scenario also require an increase in RF cavity voltage (see Fig. 7). The ideal RF cavity voltage increases from 64 kV to 114 kV, which is a factor of $(4/3)^2 \approx 1.78$. The duty factor may also decrease (by no more than 3/4) in the case of a 20-Hz Booster; the power dissipation would increase by at least $(4/3)^3 \approx 2.37$. The maximum Recycler RF voltage is 150 kV and the maximum Recycle RF power
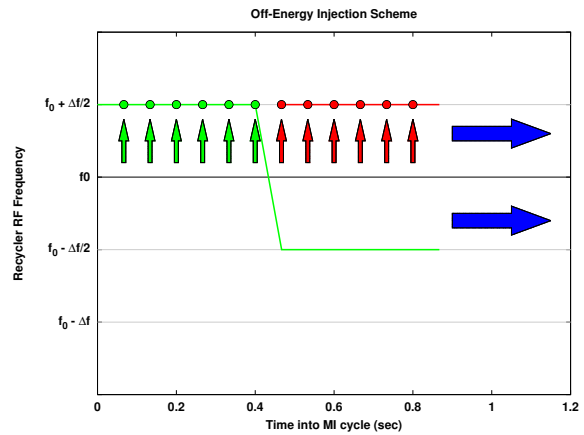


Figure 11: The Off-Energy injection scheme spans the frequencies $f_0 - \Delta f/2$ to $f_0 + \Delta f/2$.

is 150 kW, according to [16]. The possibility of the Recycler RF cavities overheating would have to be investigated.

The scaling symmetry used to analyze the 20-Hz Booster cycle-rate can generalized. An optimization at RF frequency separation $\Delta f$ and aspect ratio $r$ is equivalent to an optimization at RF frequency separation $\Delta f'$ and aspect ratio $(\Delta f'/\Delta f)r$. The same optimal slip-stacking parameter would be obtained at a higher synchrotron frequency $(\Delta f'/\Delta f)f_s$, increasing the rf voltage at $(\Delta f'/\Delta f)r$ to $(\Delta f'/\Delta f)^2 V$.

## CONCLUSION

In summary, we have provided a framework for addressing both stability of particles in a slip-stacking potential. We introduce the slip-stacking area factor $F(\alpha_s)$ and the modified area factor $Z(\alpha_s)$ as tools to calculate the stable slip-stacking bucket area for any combination of accelerator parameters. We provide a general method for analyzing slip-stacking injection scenarios. We demonstrate that the 20-Hz Booster cycle rate provides a consequential improvement to the slip-stacking efficiency and bucket area. We recommend an injection scheme which wholly compensates for the the increased momentum usage required by the larger RF frequency separation. We predict the optimal RV cavity voltage for the 20-Hz Booster and identify the potential overheating issue.

## REFERENCES

[1] P. Derwent et al., Proton Improvement Plan-II December 2013, 2013 [http://projectx-docdb.fnal.gov/cgi-bin/ShowDocument?docid=1232].

[2] C. Mariani (LBNE/DUSEL Collaborations), Proc. NOW 2010, [http://dx.doi.org/10.1016/j.nuclphysbps.2011.04.134].

[3] J. Galambos, M. Bai, and S. Nagaitsev, Snowmass Workshop on Frontier Capability Summary Report, 2013 [http://www.bnl.gov/swif2013/files/pdf/WorkshopSummary_Rev11.pdf].

[4] B. C. Brown, P. Adamson, D. Capista et al., Phys. Rev. ST Accel. Beams **16** , 071001 (2013) [`http://dx.doi.org/10.1103/PhysRevSTAB.16.071001`].

[5] F. E. Mills, Brookhaven National Laboratory Report No. 15936, 1971.

[6] D. Boussard, Y. Mizumachi, IEEE Trans. Nucl. Sci. **26**, 3623 (1979) [`http://ieeexplore.ieee.org/xpls/abs_all.jsp?arnumber=4330122`].

[7] J. A. MacLachlan, Fermilab Report No. FERMILAB-FN-0711, 2001 [`http://lss.fnal.gov/archive/test-fn/0000/fermilab-fn-0711.pdf`].

[8] K. Seiya, T. Berenc, B. Chase et al., Proc. HB2006, [`www.jacow.org/abdwhb06/PAPERS/THAY02.PDF`].

[9] T. Aaltonen *et al.* (CDF and D0 Collaborations), Phys. Rev. D **86**, 092003 (2012) [`http://journals.aps.org/prd/abstract/10.1103/PhysRevD.86.092003`].

[10] P. Adamson et al., (MINOS Collaboration), Phys. Rev. Lett. **110**, 251801 (2013) [`http://journals.aps.org/prl/abstract/10.1103/PhysRevLett.110.251801`].

[11] L. Fields et al., (MINERvA Collaboration), Phys. Rev. Lett. **111**, 022501 (2013) [`http://journals.aps.org/prl/abstract/10.1103/PhysRevLett.111.022501`].
G. A. Fiorentini et al., (MINERvA Collaboration), Phys. Rev. Lett. **111**, 022502 (2013) [`http://journals.aps.org/prl/abstract/10.1103/PhysRevLett.111.022502`].

[12] D. Ayres et al. (NOvA Collaboration), The NOvA Technical Design Report, FERMILAB-DESIGN-2007-01, 2007, [`http://inspirehep.net/record/774999`].

[13] K. Seiya *et al.*, Proc. PAC05, [`http://dx.doi.org/10.1109/PAC.2005.1590430`].

[14] J. Dey, K. Koba, I. Kourbanis et al., Proc. PAC01 [`www.jacow.org/p01/papers/mpph048.pdf`].

[15] J. Dey, I. Kourbanis, Proc. PAC05, [`http://dx.doi.org/10.1109/PAC.2005.1590972`].

[16] R. Madrak, D. Wildman, Proc. PAC13, [`www.jacow.org/PAC2013/papers/wepma13.pdf`].

[17] A. A. Aguilar-Arevalo et al. (MiniBooNE Collaboration), Phys. Rev. Lett. **98**, 231801 (2007)[`http://journals.aps.org/prl/abstract/10.1103/PhysRevLett.98.231801`].

[18] R. E. Ray (mu2e Collaboration), Mu2e Conceptual Design Report, 2012, [`http://mu2e-docdb.fnal.gov/cgi-bin/ShowDocument?docid=1169`].

[19] B. L. Roberts (New Muon (g-2) Collaboration), Chinese Physics C **34**, 741 (2010) [`http://iopscience.iop.org/1674-1137/34/6/021`].

[20] C. Adams et al., (LBNE Collaboration), Fermilab Report No. FERMILAB-PUB-13-438-A, 2013, [`http://inspirehep.net/record/1245018`].

[21] J. Eldred, R. Zwaska, Phys. Rev. ST Accel. Beams **17** , 094001 (2014) [`https://journals.aps.org/prstab/pdf/10.1103/PhysRevSTAB.17.094001`].

[22] H. W. Broer, I. Hoveijn, M. van Noort et al., J. Dyn. Diff. Eq. **16**, 897 (2004) [`http://link.springer.com/article/10.1007%2Fs10884-004-7829-5`].

[23] K. Seiya, B. Chase, J. Dey et al., Proc. BEAM07, [`http://cds.cern.ch/record/1133130/files/p66.pdf`]

[24] X. Yang, A. I. Drozhdin, W. Pellico, Proc. PAC07, [`http://inspirehep.net/record/758224`].

[25] L. A. Ahrens et al., Proc. PAC99, [`www.jacow.org/p99/PAPERS/THP140.PDF`].

[26] P. Derwent, S. Holmes, V. Lebedev, Fermilab Report No. BEAMS-DOC-4662-v1, 2014, [`https://beamdocs.fnal.gov/AD/DocDB/0046/004662/001/THIOA05_talk.pdf`].

[27] I. Kourbanis, Fermilab Report No. BEAMS-DOC-4606-v1, 2014 [`https://beamdocs.fnal.gov/AD/DocDB/0046/004606/001/Doubling_MI_Power_20140520_IK.pdf`].

[28] M. J. Yang, C. S. Mishra, Proc. PAC03, [`www.jacow.org/p03/PAPERS/FPAB074.PDF`].

# RMS EMITTANCE MEASURES FOR SOLENOID TRANSPORT AND FACILITY FOR RARE ISOTOPE BEAMS FRONT-END SIMULATIONS*

Steven M Lund†, Eduard Pozdeyev, Haitao Ren, and Qiang Zhao

Facility for Rare Isotope Beams, Michigan State University, East Lansing, MI , USA 48824

*Abstract*

Measurement of beam phase-space area via rms emittances in solenoid focusing channels with $x$-$y$ coupling is complicated relative to transport channels with decoupled plane focusing. This stems from correlated azimuthal flow of the beam induced by the coupled focusing influencing how the thermal component of the flow should be measured. This is exacerbated when the beam has net canonical angular momentum — as is the case for beams born in a magnetic field within ECR-type sources. In this study, a systematic analysis is carried out to derive an multi-species beam envelope equation and motivate measures of rms emittance and phase-space area for use in solenoid transport for beams with canonical angular momentum. These results are applied in Warp PIC simulations of the near-source region of the front-end of the Facility for Rare Isotope Beams (FRIB) linac. In these simulations, a multi-species heavy-ion DC beam emerging from an ECR source are simulated in transverse slice mode using a realistic lattice description. Emittance growth due to nonlinear applied fields and space-charge is analyzed including the influence of net canonical angular momentum. It is found that emittance growth in the near source region of FRIB front-end should in most cases be minimal and that the beam size can be readily controlled over a wide range of parameter uncertainties.

## INTRODUCTION

The Facility for Rare Isotope Beams (FRIB) is a high continuous-wave power (CW) linear accelerator now under construction at Michigan State University to enable state-of-the-art nuclear physics experiments [1]. It will simultaneously accelerate multiple charge states of heavy ions to kinetic energies above 200 MeV/u with 400 kW power on target delivered within a compact spot. Although the FRIB linac has high CW power, space-charge intensity is modest in most of the machine. However, near the electron cyclotron resonance (ECR) sources in the front end (see Fig. 1), space-charge can be an issue [2]. Here, kinetic energy is low ($\sim$ 35 kV ECR extraction bias followed by a grated dc gap typically biased to $\sim$ 50 kV to achieve 12 kV/u in target species) and the ECRs produce numerous charge states and ions resulting in relatively high DC current until extra species are removed downstream beginning with the first bending dipole. Uranium and Oxygen species, (unneutralized) particle currents, and particle rigidities (at

extractor bias) expected for Uranium ECR operation are given in Table 1. It is anticipated that space-charge of the DC beam will be $\sim$ 75% electron neutralized outside of the grated gap (strong sweep and guarded downstream by a negatively biased suppressor electrode). Typically only two target species will be transported downstream of the front-end. A compact beam phase-space (low emittance and halo suppressed) in the target species must be preserved in transport near the source in the presence of the parasitic species to insure reliable machine operation with minimal potential losses. In the transport immediately downstream of the ECR two solenoids are employed to transversely focus the multi-species beam. Solenoids are short with poor aspect ratio (39.5 cm length and 7.75 cm radius aperture) and the extended fringe fields overlap with the solenoid field from the ECR source and the grated gap. Ions are born relatively cold (expect $\sim$ 1–3 eV thermal temperature expected) with a compact radius ($R \simeq 4$ mm) but are strongly magnetized in the hight magnetic fields within the ECR sources resulting in significant canonical angular momentum contributions to the transverse beam size.

Table 1: (Color) Species from FRIB Venus-like ECR source for U operation. Color coding shown for species identification in simulations. $U^{+33}$ and $U^{+34}$ are target species.

| Ion | $I$ (pmA) | $Q/A$ | $[B\rho]$ (Telsa-m) |
|---|---|---|---|
| $U^{+25}$ | 0.035 | 0.105 | 0.0831 |
| $U^{+26}$ | 0.051 | 0.109 | 0.0815 |
| $U^{+27}$ | 0.068 | 0.113 | 0.0800 |
| $U^{+28}$ | 0.088 | 0.118 | 0.0785 |
| $U^{+29}$ | 0.115 | 0.122 | 0.0772 |
| $U^{+30}$ | 0.150 | 0.126 | 0.0759 |
| $U^{+31}$ | 0.175 | 0.130 | 0.0746 |
| $U^{+32}$ | 0.192 | 0.134 | 0.0735 |
| $U^{+33}$ | 0.210 | 0.139 | 0.0723 |
| $U^{+34}$ | 0.205 | 0.143 | 0.0713 |
| $U^{+35}$ | 0.178 | 0.147 | 0.0702 |
| $U^{+36}$ | 0.142 | 0.151 | 0.0693 |
| $U^{+37}$ | 0.11 | 0.155 | 0.0683 |
| $U^{+38}$ | 0.072 | 0.160 | 0.0674 |
| $U^{+39}$ | 0.043 | 0.163 | 0.0665 |
| $U^{+40}$ | 0.031 | 0.168 | 0.0657 |
| $O^{+1}$ | 0.3 | 0.063 | 0.1077 |
| $O^{+2}$ | 0.3 | 0.125 | 0.0762 |
| $O^{+3}$ | 0.3 | 0.188 | 0.0622 |
| $O^{+4}$ | 0.2 | 0.250 | 0.0539 |

In this study we employ theory to develop an envelope model (Sec. Envelope Model) and report preliminary particle-in-cell simulations with the Warp code [3] (Sec. Simulations). The envelope model is employed to better understand how to measure effective beam phase-space area for the multi-species beam with canonical angular momentum and solenoid focusing which both induce coherent azimuthal flow in the beam components. The simulations
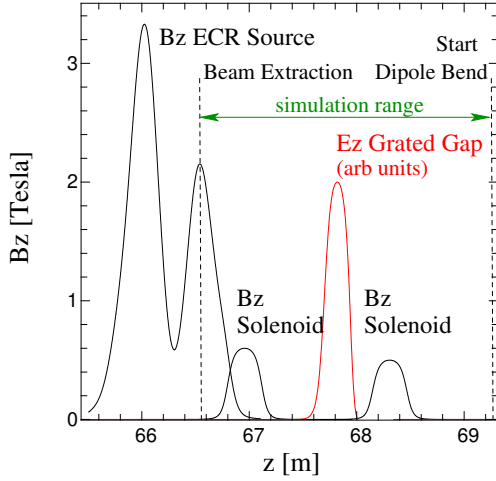
Figure 1: (Color) Applied fields (on-axis nonlinear components) of FRIB front-end near ECR source. FRIB lattice reference $z = 200$ m at the start of the RFQ.

allow inclusion of detailed geometry, multiple species with part electron neutralization, and coupled dynamics with solenoid focusing and overlapping element fringe fields. The simulations enable evaluation of system performance under increasingly realistic conditions.

## ENVELOPE MODEL

A systematic derivation of an rms envelope equation describing an unbunched, multi-species DC beam propagating in a solenoid focusing channel with electrostatic accelerating gaps is carried out to better understand how to measure the effective phase-space area (emittance) and the relative strength of various focusing/defocusing effects. Consider a species $j$ composed of particles of mass $m_j$ and charge $q_j$ propagating with axial velocity $\beta_{bj} c$ with $c$ the speed of light in *vacuuo*. The nonrelativistic transverse equations of motion describing the particles evolving in a applied solenoid magnetic field (linear approximation) $\mathbf{B}^{\mathrm{appl}} = -\frac{1}{2} \frac{\partial B_{z0}(z)}{\partial z} r \hat{\mathbf{e}}_r + B_{z0}(z) \hat{\mathbf{e}}_z$ with $B_{z0}(z) = B_z(r = 0, z)$ the on-axis magnetic field and an applied electric accelerating field from electrostatic gaps (linear approximation) $\mathbf{E}^{\mathrm{appl}} = -\frac{1}{2} \frac{\partial E_{z0}(z)}{\partial z} r \hat{\mathbf{e}}_r + E_{z0}(z) \hat{\mathbf{e}}_z$ with on-axis field $E_{z0}(z) \equiv E_z^{\mathrm{a}}(r = 0, z)$ can be cast in the form [4, 5]

$$
\begin{aligned}
x'' &- \frac{q_j V'}{2\mathcal{E}_{kj}} x' - \frac{q_j V''}{4\mathcal{E}_{kj}} x - \frac{q_j B'_{z0}}{2 m_j \beta_{bj} c} y - \frac{q_j B_{z0}}{m_j \beta_{bj} c} y' \\
&= \frac{q_j}{m_j \beta_{bj}^2 c^2} E_x^{self}, \\
y'' &- \frac{q_j V'}{2\mathcal{E}_{kj}} y' - \frac{q_j V''}{4\mathcal{E}_{kj}} y + \frac{q_j B'_{z0}}{2 m_j \beta_{bj} c} x + \frac{q_j B_{z0}}{m_j \beta_{bj} c} x' \\
&= \frac{q_j}{m_j \beta_{bj}^2 c^2} E_y^{self}.
\end{aligned}
\tag{1}
$$

Here, primes denote derivatives with respect to the axial coordinate $z$, $E_x^{\mathrm{self}}$ and $E_x^{\mathrm{self}}$ are the transverse components

of the electrostatic self-electric field of the beam, and $V(z)$ is the accelerating potential that relates to the on-axis applied electric field via $E_{z0}(z) = -\frac{\partial V(z)}{\partial z}$ and gives the gain in particle axial velocity $\beta_{bj} c$ and kinetic energy $\mathcal{E}_{kj} = \frac{1}{2} m_j \beta_{bj}^2 c^2$ from the initial value as

$$
\begin{aligned}
\mathcal{E}_{kj} &= \mathcal{E}_{kj}|_{\mathrm{initial}} + q_j [V|_{\mathrm{initial}} - V], \\
\beta_{bj} &= \sqrt{\frac{2\mathcal{E}_{kj}}{m_j c^2}}.
\end{aligned}
\tag{2}
$$

Note that the $x$- and $y$-plane particle equations of motion 1 are cross-coupled due to the solenoid focusing field. Both the applied magnetic (solenoid focusing) and electric (accelerating) fields include fringe effects from the axial variation in $z$ which produces consistent focusing/defocusing effects within the approximation of linear applied fields.

To derive an envelope equation, we neglect energy spreads within each species and carry out transverse averages $\langle \cdots \rangle_j$ over the $j$th species and analyze the rms radius $\sigma_{rj} \equiv \langle x^2 + y^2 \rangle_j^{1/2}$. As standard, $\sigma_{rj}$ is differentiated several times with respect to $z$ and the equations of motion (1) are applied to calculate $\langle xx'' \rangle_j$ and $\langle yy'' \rangle_j$ [4]. An extensive analysis with the additional assumption that the charge distributions of the species are axisymmetric ($\partial/\partial\theta = 0$) with Gaussian distributed radial density profiles (possibly part electron neutralized) shows that the rms envelope equation for the $j$th species can be expressed as

$$
\begin{aligned}
\sigma''_{rj} &- \frac{q_j V'}{2\mathcal{E}_{kj}} \sigma'_{rj} - \frac{q_j V''}{4\mathcal{E}_{kj}} \sigma_{rj} + \left( \frac{q_j B_{z0}}{2 m_j \beta_{bj} c} \right)^2 \sigma_{rj}, \\
&- \sum_{s, \mathrm{species}} Q_{js} f_s \frac{\sigma_{rj}}{\sigma_{rj}^2 + \sigma_{rs}^2} \\
&- \frac{\varepsilon_{rj}^{\mathrm{rms}\,2} + \langle P_\theta \rangle_j^2 / (m_j \beta_{bj} c)^2}{\sigma_{rj}^3} = 0.
\end{aligned}
\tag{3}
$$

Here,

$$
Q_{js} = \frac{q_j I_s}{2\pi \epsilon_0 m_j \beta_{bj}^2 \beta_{bs} c^3}
\tag{4}
$$

is the "matrix" preveance that measures the strength of species $s$ space-charge associated with current $I_s = \mathrm{const}$ (electron neutralized by specified fraction $f_s \in [0, 1]$ with $f_s = 1$ being unneutralized) of species $s$ on the $j$th species, $\epsilon_0$ is the permitivity of free-space,

$$
\begin{aligned}
\frac{\langle P_\theta \rangle_j}{m_j \beta_{bj} c} &= \langle xy' - yx' \rangle_j + \frac{q_j B_{z0}}{2 m_j \beta_{bj} c} \langle x^2 + y^2 \rangle_j \\
&= \langle r^2 \theta' \rangle_j + \frac{q B_{z0}}{2 m \beta_b c} \langle r^2 \rangle_j
\end{aligned}
\tag{5}
$$

specifies the average canonical angular momentum $\langle P_\theta \rangle_j$ of species $j$, and

$$
\begin{aligned}
\varepsilon_{rj}^{\mathrm{rms}\,2} &= \langle x^2 + y^2 \rangle_j \langle x'^2 + y'^2 \rangle_j - \langle xx' + yy' \rangle_j^2 \\
&\quad - \langle xy' - yx' \rangle_j^2 \\
&= \langle r^2 \rangle_j \langle r'^2 \rangle_j - \langle rr' \rangle_j^2 + \langle r^2 \theta'^2 \rangle_j - \langle r^2 \theta' \rangle_j^2
\end{aligned}
\tag{6}
$$

is a proper *thermal* (i.e., coherent flow contribution induced by solenoid removed) measure of the transverse phase-space area. Both $\langle P_\theta \rangle_j$ and $\varepsilon_{rj}^{\text{rms}}$ are given in both transverse $x,y$ Cartesian components and $r,\theta$ cylindrical coordinates. The canonical angular momentum $\langle P_\theta \rangle_j$ is conserved (even for nonlinear self-field forces), and for the case of linear or negligible self-field forces, it can be shown that the normalized thermal emittance

$$\varepsilon_{nrj}^{\text{rms}} \equiv \beta_{bj} \varepsilon_{rj}^{\text{rms}} = \text{const} \qquad (7)$$

is also conserved. Note that the applied focusing coefficient from the solenoid focusing in Eq. (3) can be expressed as $[q_j B_{z0}/(2m_j \beta_{bj} c)]^2 \sigma_{rj} = k_{Lj}^2 \sigma_{rj}$ where $k_{Lj} \equiv q_j B_{z0}/(2m_j \beta_{bj} c)$ is the Larmor wavenumber. Employing the conservations in Eqs. (5) and (7) allows integration of the envelope equation (3) from a specified initial condition.

It should be stressed that all terms occurring in Eq. (3) are *independent* of the details of the transverse distribution (and are therefore valid for nonaxisymmetric species with $\partial/\partial\theta \neq 0$) with exception of the space-charge (perveance) term $\propto Q_{js}$ which requires axisymmetry for the relatively simple form given. Inter-species coupling is provided only by the radial electrostatic force acting on the particles which the space-charge term describes. The perveance term is derived by taking the species radial charge density profile to have Gaussian form with

$$\rho_j(r) = \frac{I_j}{2\pi \beta_{bj} c \, \sigma_{rj}^2} e^{-r^2/\sigma_{rj}^2}, \qquad (8)$$

and solving the electrostatic Gauss' law Maxwell equation $\frac{1}{r}\frac{\partial}{\partial r}(r E_r^{\text{self}}) = \sum_{\text{species},s} \frac{f_s \rho_s}{\epsilon_0}$ (axial self-fields neglected) for the radial self-electric field as

$$E_r^{\text{self}} = \sum_{s,\text{species}} \frac{f_s}{2\pi \epsilon_0} \frac{\lambda_s(r)}{r}, \qquad (9)$$

where $\lambda_s(r) = 2\pi \int_0^r d\bar{r} \, \bar{r} \rho_s(\bar{r})$ is the line-charge of species $s$ within radius $r$ $[\lambda_s(\infty) = I/(\beta_b s)]$. Using this result, the average $\langle r E_r^{\text{self}} \rangle_j$ needed to derive the perveance term in Eq. (3) can be calculated using the result

$$\langle \lambda_s(r) \rangle_j = \left( \frac{I_s}{\beta_{bs} c} \right) \frac{\sigma_{rj}^2}{\sigma_{rj}^2 + \sigma_{sj}^2} \qquad (10)$$

to express contributing terms. Interestingly, it can be shown that the $s = j$ component of the perveance term in Eq. (3) is independent of the form of the radial charge distribution — suggesting somewhat broader validity of the envelope equation than just Gaussian distributed radial charge profiles [4,6]. If there is a single species, the perveance term reduces (independent of the form of the radial charge distribution) to the familiar form $Qf/(2\sigma_r)$ with $Q = \frac{qI}{2\pi\epsilon_0 m \beta_b^3 c^3}$. Here, we drop the species subscripts since there is one species. Comparing the perveance (space-charge defocusing strength) and the emittance + canonical angular momentum (phase-space area defocusing) terms in the envelope

equation (3), note that the space-charge term will eventually dominate as the beam radially expands (term $\sim 1/\sigma_{rj}$), and conversely, the emittance + canonical angular momentum term eventually dominates as the beam is radially focused down ($\sim 1/\sigma_{rj}^3$).

The envelope equation (3) shows that the total effective phase-space area acting to defocus beam species $j$ is

$$\varepsilon_{\text{tot}j}^{\text{rms}} \equiv \sqrt{\varepsilon_{rj}^{\text{rms}\,2} + \frac{\langle P_\theta \rangle_j^2}{(m_j \beta_{bj} c)^2}}. \qquad (11)$$

The total emittance $\varepsilon_{\text{tot}j}^{\text{rms}}$ contains a component $\varepsilon_{rj}^{\text{rms}}$ [Eq. (6)] from the thermal spread of particle angles (normalized form $\beta_{bj} \varepsilon_{rj}^{\text{rms}}$ conserved for linear forces) and component $\langle P_\theta \rangle_j^2$ [Eq. (5)] from the coherent flow associated with canonical angular momentum (conserved nonlinearly if a consistent nonlinear form for the associated magnetic vector potential is employed). Properties of the thermal emittance can be further clarified by the axisymmetric ($\partial/\partial\theta = 0$) limit formula,

$$\varepsilon_{rj}^{\text{rms}\,2} = 4\varepsilon_{xj}^{\text{rms}\,2} - \langle xy' - yx' \rangle_j^2 \qquad (12)$$

with $\varepsilon_{xj}^{\text{rms}} \equiv \left[ \langle x^2 \rangle_j \langle x'^2 \rangle_j - \langle xx' \rangle_j^2 \right]^{1/2}$ denoting the usual $x$-plane rms emittance. This clarifies within the simpler axisymmetric limit how the radial emittance $\varepsilon_{rj}^{\text{rms}}$ subtracts the coherent flow associated with mechanical angular momentum $\propto \langle xy' - yx' \rangle_j$ to provide a proper thermal measure of the contribution of the spread in particle angles to the emittance. Because the regular $x$-plane rms emittance $\varepsilon_x^{\text{rms}}$ contains (typically large) coherent flow associated with coherent rotation inducted by the solenoid, it provides a poor measure to employ to measure potential emittance growth due to nonlinear applied focusing and space-charge effects. This issue is exacerbated for the case with beams with net canonical angular momentum ($\langle P_\theta \rangle_j \neq 0$) as should be expected for beams produced by ECR type sources. This follows because beams with $\langle P_\theta \rangle_j \neq 0$ will have correlated flow terms in $\varepsilon_x^{\text{rms}}$ even outside the axial extent of the fringe field of the magnetic solenoids. Use of the canonical angular momentum $\langle P_\theta \rangle_j^2$ [Eq. (5)], radial thermal emittance $\varepsilon_{rj}^{\text{rms}}$ [Eq. (5)], and the total emittance $\varepsilon_{\text{tot}j}^{\text{rms}}$ [Eq. (11)] helps clarify issues in such systems.

For purposes of estimating the emittance of a beam emerging from a source where ions are not born in a state of macroscopic rotation in a finite axial magnetic field ($B_{z0} \neq 0$), Eqs. (5) and (6) suggest taking

$$\frac{\langle P_\theta \rangle_j}{m_j c} = \frac{q_j B_{z0}}{2 m_j c} \sigma_{rj}^2 \bigg|_{\text{Birth}}$$

$$\varepsilon_{nrj}^{\text{rms}} = \beta_{bj} \varepsilon_{rj}^{\text{rms}} = \sqrt{2} \sqrt{\left( \frac{T_j}{m_j c^2} \right)} \sigma_{rj} \bigg|_{\text{Birth}} \qquad (13)$$

Here, $T_j$ is the thermal temperature of the $j$th ion species (energy units) and the formulas are presented in appropriate form for direct comparison in "normalized" emittance

units. Both these results neglect the influence of the sextupole field and other physics in the ECR source, and therefore can only be regarded as an estimate of possible characteristic values for such sources.

Finally, we stress that the forms of the canonical angular momentum [Eq. (5)] and radial thermal emittance [Eq. (6)] apply to beams that are not axisymmetric ($\partial/\partial\theta \neq 0$) and can therefore be applied in this generalized context in detailed simulations even if the space-charge term cannot. If there is centroid offset, all terms other than the space-charge perveance one ($\propto Q_{js}$) in the envelope equation (3) also remain valid and can be defined with respect to coordinates relative to the centroid ($x \to x - \langle x \rangle_j$, $x' \to x' - \langle x' \rangle_j$, etc.). These features make the $x, y$, $x', y'$, versions of the formulas useful for interpreting simulations under increasingly realistic conditions. For an nonaxisymmetric and/or centroid offset beam, the space-charge term becomes considerably more complicated and simulations become more essential.

## SIMULATIONS

We employ the Warp particle-in-cell (PIC) code [3] to simulate the transport of the beam emerging from the ECR source to the start of the bending dipole (see Sec. Introduction). The code is run in a transverse ($xy$) slice mode using the 3D applied fields of elements (axisymmetric solenoids and grated acceleration gap input on a $r$–$z$ for the aligned system). High resolution models ($\sim$ 1 mm mesh increments in $r$, $z$) are employed for the ECR solenoid, focusing solenoids, and the grated gap. Solenoid fringe fields are resolved to $\sim 10^{-6}$ of the peak value and the nonlinear vector potential is input to verify nonlinear conservation of canonical angular momentum. Fringe resolutions of $\sim 10^{-2}$ were found to induce large errors in $\langle P_\theta \rangle_j$. Element fields are input both in linear (using nonlinear on-axis field and the model in Sec. Envelope Model) and nonlinear form to allow nonlinear applied fields to be turned off. Self-fields are calculated with a specified neutralization fraction using a multi-grid field solver ($\lesssim 0.5$ mm mesh increments in $x$, $y$) and any lost particles scraped at the local aperture radius. Macro-particles (typically using > 100 per grid cell within beam corresponding to $\sim$ 40k/species) are advanced in time with individual time increments iterated so that the code tracks from axial slice to axial slice with increment $\Delta z \lesssim 2$ mm. Species weights (physical particles per macro-particle) are adjusted consistent with acceleration from the applied gap DC current conservation in each species to model a slice of the unbunched DC beam. Note this model does not assume beam axisymmetry allowing distribution asymmetries emerging from the ECR and misaligned elements to be evaluated. The $xy$-slice model neglects any longitudinal self-field effects which should be weak and idealizes electron effects. However, Warp can be run in a 3D mode (inputs/setup essentially the same) to address these issues. The efficient slice model allows rapid ($\sim$minutes on PC) simulations to efficiently explore issues.

Simulations are carried out for a Uranium beam injecting the species in Table 1. It is verified that currents and canonical angular momentum are consistent, and that energy gains in the on-axis potential of the gap are correct (gap biased 50.26 kV so average of "target" U$^{+33}$ and U$^{+34}$ species achieves 12 Ks/u). Diagnostics are carried out by species results colorized consistent with entries in Table 1. Emittance measures developed in Sec. Envelope Model are employed to allow sensitive evaluation of emittance evolution in the transport. Series of runs were carried out to explore sensitivities of the target species rms beam envelopes and emittance growth to: unmagnetized (unrealistic: $\langle P_\theta \rangle_j = 0$) and magnetized (estimate appropriate for ECR with $B_{z0} = 2.15$ Tesla giving $\langle P_\theta \rangle_j/(m_j c) \sim$ 0.38 mm-mrad for ref species)initial ions emerging from the ECR source with low ($T_j = 3$ eV giving for all U species $\varepsilon_{nrj}^{\rm rms} = 0.015$ mm-mrad) and high ($T_j = 140$ eV giving for all U species $\varepsilon_{nrj}^{\rm rms} = 0.1$ mm-mrad) ion thermal temperatures, the phase-space form of the initial distribution (thermal and waterbag including self-field potential in the Hamiltonian, semi-Gaussian with uniform density and Gaussian angle spreads, and KV), linear and nonlinear applied fields (both solenoids and grated gap), and electron neutralization fraction (unneutralized, 25%, 50%, 75%, and fully neutralized). In all cases, the same initial axisymmetric beam sizes ($\sigma_{rj}/\sqrt{2} = \langle x^2 \rangle_j^{1/2} = \langle y^2 \rangle_j^{1/2} = 2.0$ mm and zero angle) were used emerging from the ECR source. Note that the high ion temperature case (i.e., $T_j = 140$ eV) is tuned such that the initial thermal emittance corresponds to measured values (including coherent flow) of the total on a similar ECR source emittance [2,7]. Relatively modest sensitivities were observed in most cases outside of extreme values and the two focusing solenoids are easily adjusted to produce a final (entering dipole) rms beam size $\langle x^2 \rangle_j^{1/2} \simeq 10$ mm with a slightly converging envelope (few mrad) for the target species. A partial exception to this is the case of low initial ion temperatures where some normalized thermal emittance ($\varepsilon_{nrj}^{\rm rms}$) growth occurs from very low initial values. But the growth is not sufficient to result in high final emittance or to significantly impact the envelope because the canonical angular momentum contribution to the defocusing [see Eq. (11)] is larger (and constant).

Characteristic results of simulations are shown in Figs. 2 (rms envelope and emittance evolution) and 3 (final phase-space projections of species) for an initial waterbag distribution beam for initially magnetized ions with low temperature, a 75% neutralization fraction, and nonlinear applied fields (solenoids and grated gap). First and second solenoid excitations (see Fig. 1) correspond to 0.6 and 0.5 Tesla peak field on-axis (ECR solenoids fixed for source performance). Cases with the higher initial ion temperature undergo no significant growth. The modest growth for cold initial, but magnetized ions does little to change the effective emittance ($\varepsilon_{\rm totj}^{\rm rms}$) or envelope for initially magnetized ions since the contribution of the canonical angular momentum ($\langle P_\theta \rangle_j$) dominates relative to the contribution from the thermal component of the emittance ($\varepsilon_{rj}^{\rm rms}$) [i.e, see Eq. (11),
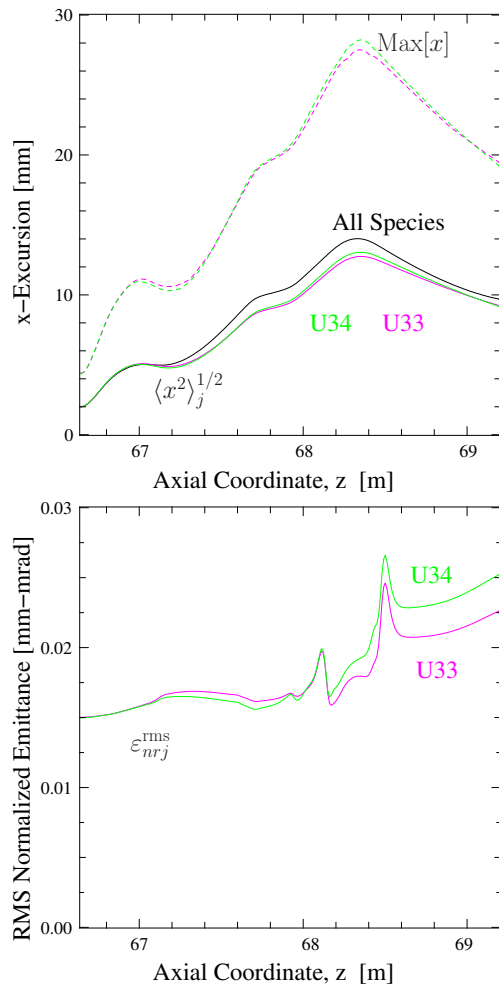
Figure 2: (Color) rms envelope and emittance evolution.



Figure 3: (Color) Phase-space projections at end of simulation (before dipole): particle $x$-$x'$ with tilt removed, and final target species densities.

$\beta_{bj} \varepsilon_{\mathrm{tot}j}^{\mathrm{rms}} \simeq \langle P_\theta \rangle_j / (m_j c) = 0.38$ mm-mrad]. Phase-space projections of target species (see Fig. 3)) typically have surprisingly low distortion.

## CONCLUSIONS

Preliminary theory and simulations of the near-source transport of the FRIB front-end suggests that potential deleterious effects from nonlinear space-charge in the many-species, part electron neutralized beam immediately downstream of the ECR sources (before species separation) is minimal. The system appears relatively insensitive to neutralization fraction and can be retuned for a wide range of potential beam parameters emerging from the sources. Proper separation of coherent flow induced by solenoid focusing and canonical angular momentum in emittance measures allows sensitive probing of contributions to any growth in beam phase-space area. Detailed Warp simulations should help us address any problems encountered during front-end commissioning by augmenting limited laboratory diagnostics. In future work, simulations will be extended downstream to evaluate species separation in the presence of beam space-charge and canonical angular mo-

mentum and evaluate the impact of more realistic distributions (including sextupole effects, asymmetries, and halo) to model the beam emerging from the ECR source.

## ACKNOWLEDGMENT

The authors benefited from unpublished work by J.J. Barnard (LLNL) on aspects of the envelope model and D.P. Grote (LLNL) provided support for the Warp code.

## REFERENCES

[1] J. Wei, et al., LINAC 2012, Tel Aviv, Israel, TU1A04.

[2] E. Pozdeyev, et al., NA-PAC 2013, Pasadena CA, WEOAB1.

[3] For info on the Warp code see: http://warp.lbl.gov

[4] S. Lund and J. Barnard, US Particle Accel. School, *Beam Physics with Intense Space Charge,* 2015, 2011: https://people.nscl.msu.edu/~lund/uspas/bpisc_2015/

[5] M. Reiser, *Theory and Design of Charged Particle Beams*, (New York: Wiley, 2nd Edition, 2008).

[6] F.J. Sacherer, IEEE Tans. Nuc. Sci. **18**, 1105 (1971).

[7] L. Su, et al., Rev. Sci. Instr. **83**, 02B705 (2012).

# AN ESS LINAC COLLIMATION STUDY

R. Miyamoto*, ESS, Lund, Sweden

## Abstract

The European Spallation Source is planned in Lund, Sweden, and will be a neutron source based on a proton linac with an unprecedented 5 MW beam power. Mitigation of beam losses is the most crucial challenge in beam physics for such a high power proton linac and collimation systems are planned in sections of the medium and high energy beam transport (MEBT and HEBT). A preliminary study of the collimation systems was presented in the previous time of this workshop but the linac design went through a significant revise since then. The system to expand the beam for the target, located in the HEBT, was changed from one based on nonlinear magnets to a raster system and this change particularly had a significant impact on the demand on the collimation systems. This paper presents an updated beam dynamics study of the collimation systems for the present layout of the ESS Linac.

## INTRODUCTION

The European Spallation Source (ESS) will be a neutron source in Lund, Sweden, based on a proton linac with an unprecedented 5 MW beam power [1]. Figure 1 shows a layout of the ESS Linac and Table 1 summarizes its high level parameters. The linac consists of normal conducting accelerating structures, sections of superconducting cavities, and low, medium, and high energy beam transports (LEBT, MEBT, and HEBT). The normal conducting accelerating structures include an ion source (IS), radio frequency quadrupole (RFQ), and drift tube linac (DTL). The ESS Linac uses three types of superconducting cavities: spoke, medium-$\beta$ elliptical, and high-$\beta$ elliptical cavities. The sections of the superconducting cavities are also referred to as the Superconducting (SC) Linac as a whole.

For a high power machine such as the ESS Linac, minimization of beam losses is crucial to allow hands-on maintenance as well as to protect machine components and imposes difficult challenges on the design and machine tuning. Based on the experience of SNS [2], a system of beam scrapers is planned for the MEBT to improve beam quality in an early stage of the linac and thus to lower the risk of the beam losses as possible. Beam dynamics simulations indicated its use for the ESS Linac too [3–5] but its effect throughout the entire linac, taking into account various errors, has not been thoroughly studied yet. Collimation systems have been also considered for the HEBT where the beam power is the highest 5 MW [3, 6]. However, since the design revision in 2013 [7], the system to expand the beam for the target has been switched from one based on nonlinear magnets [8] to the other using raster magnet [9] and the present system is much less sensitive to the transverse beam halo. This



Figure 1: Layout of the ESS Linac. Blue color indicates a section of superconducting cavities.

Table 1: High Level Parameters of the ESS Linac

| Parameter | Unit | Value |
|---|---|---|
| Average beam power | MW | 5 |
| Maximum beam energy | GeV | 2 |
| Peak beam current | mA | 62.5 |
| Beam pulse length | ms | 2.86 |
| Beam pulse repetition rate | Hz | 14 |
| Duty cycle | % | 4 |
| RF frequency | MHz | 352.21/704.42 |

led present reconsideration of the collimation systems in the HEBT. An input to make the decision is quality of the beam entering the HEBT. Thus, on this occasion, impact of the MEBT scrapers on the beam quality and losses throughout the entire linac, especially the later part of the linac, is studied in detail in this paper

## CONDITIONS FOR SIMULATIONS

This section discusses conditions of the simulations in the following sections. Throughout the paper, the lattice in [1] is used. All the simulations are done by tracking the pre-calculated RFQ output beam from the MEBT entrance with the TraceWin code [10]. Space-charge force is calculated with the 3D PICNIC routine [11] with a step size of 15 per [(relativistic-$\beta$) × (wavelength)] and a mesh of $10 \times 10 \times 10$.

### RFQ Output

The output beam from the RFQ is simulated with the Toutatis code [12] by assuming 2D Gaussian distribution with a normalized emittance of 0.25 $\pi$ mm mrad at its entrance. The number of macro-particles is either $1 \times 10^5$, $1 \times 10^6$, or $1 \times 10^7$, depending on a type of a study. Table 2 summarizes the parameters of the simulated output beam.

Table 2: RMS Normalized Emittances ($\epsilon$) and Courant-Snyder Parameters ($\beta$ and $\alpha$) of the RFQ Output Beam

| Plane | $\epsilon$ [$\pi$ mm mrad] | $\beta$ [m] | $\alpha$ |
|---|---|---|---|
| $x$ | 0.253 | 0.210 | $-0.052$ |
| $y$ | 0.252 | 0.371 | $-0.310$ |
| $z$ | 0.361 | 0.926 | $-0.481$ |
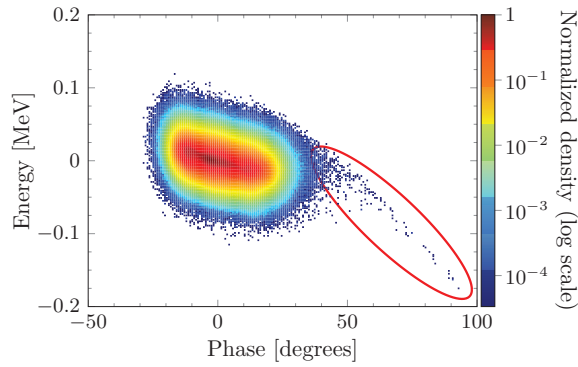
Figure 2: RFQ output distribution on the longitudinal phase space. The longitudinal tail is marked with a red ellipse.

Figure 2 shows the RFQ output distribution on the longitudinal phase space ($1 \times 10^7$ macro-particles case). An RFQ output beam often has a structure referred to as *longitudinal tail* (the part marked with an ellipse), and these off-momentum particles are of concern for beam losses.

*MEBT Scrapers*

Figure 3 shows the present MEBT layout together with beam envelopes and apertures, where three locations with tight apertures at 0.85, 2.19, and 3.39 m correspond to the scrapers. The scraper system at each location has two blades per plane and four in total for both plane. At present, the scraper is being designed so that each blade can absorb ~12 W or ~0.14% of the beam, corresponding a $3\sigma$ distance to the beam center for a Gaussian beam. This specification is based on the previous beam simulations [3, 4] and its engineering feasibility is supported by [3, 13]. The set of three scrapers provides an efficient cleaning in case the beam out of the RFQ has transverse halos and also improves quality of the nominal beam [4].

The IS and LEBT have transient times during turning on and off and bunches from these times, positioned at the head and tail of a macro-pulse, are likely to have wrong parameters. One of main functions of the MEBT is to house a fast chopper of an electric deflector to remove these bunches.
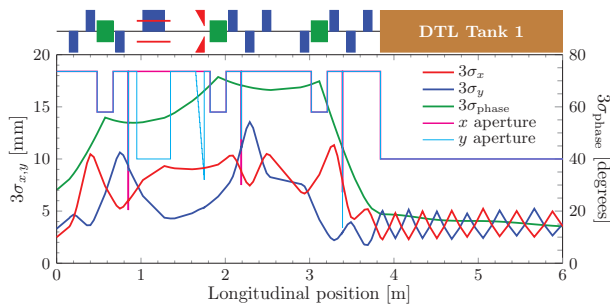


Figure 3: MEBT layout, $3\sigma$ beam envelopes, and apertures. On the top, blue boxes above (below) the line represent focusing (defocusing) quadrupoles, green boxes buncher cavities, and red lines and triangles a chopper and its dump. Three locations with tight apertures correspond to the scrapers.

Table 3: Lattice Error Tolerances (the distributions are uniform with the listed amplitudes. For DTL, the cavity error is random for each accelerating gap whereas the tank error is a systematic and common for all the gaps in one tank)

| Sect | Elem | Mode | $\delta x, \delta y$ mm | $\delta\theta_x, \delta\theta_y$ deg | $\delta\theta_z$ deg | $\delta E, \delta B$ % | $\delta\phi$ deg |
|---|---|---|---|---|---|---|---|
| MEBT | Quad | Stat | 0.2 | 0 | 0.06 | 0.5 | — |
|  | Cav | Stat | 0.5 | 0.115 | — | 1 | 1 |
|  | Cav | Dyn | 0 | 0 | — | 0.2 | 0.2 |
| DTL | Quad | Stat | 0.1 | 0.5 | 0.2 | 0.5 | — |
|  | Cav | Stat | 0 | 0 | — | 1 | 0.5 |
|  | Tank | Stat | 0 | 0 | — | 1 | 1 |
|  | Tank | Dyn | 0 | 0 | — | 0.2 | 0.2 |
| SC | Quad | Stat | 0.2 | 0 | 0.06 | 0.5 | — |
|  | Cav | Stat | 1.5 | 0.129 | — | 1 | 1 |
|  | Cav | Dyn | 0 | 0 | — | 0.1 | 0.1 |
| HEBT | Quad | Stat | 0.2 | 0 | 0.06 | 0.5 | — |
|  | Bend | Stat | 0.2 | 0 | 0.06 | 0.05 | — |

The rise time of the fast chopper is specified as ~10 ns at present and, given the bunch space is 2.84 ns, a few bunches receive a partial voltage. These *partially-chopped* bunches could have large trajectory excursions and raise a concern, but the scrapers also improve the situation of the beam losses due to these bunches [5].

*Input Beam and Lattice Errors*

To estimate the situation of the beam loss, the effects of all possible errors must be taken into account. A campaign of identifying the tolerances of lattice element errors was conducted this year based on a criteria to limit an emittance growth of each plane per section to ~10% [14, 15]. Table 3 lists the found tolerance values where the distribution of each error type is uniform with an amplitude of the given value. Table 4 lists the expected errors in the RFQ output when the tolerance values of the lattice element errors are applied to the RFQ. In statistical studies of the following sections, the error values listed in these two tables are used.

Table 4: Errors in the RFQ Output Beams (a uniform distribution with the listed amplitude is assumed for each error in a simulation. The symbol $M_{x,y,z}$ is the mismatch factor)

| Parameter | Unit | Value |
|---|---|---|
| $\delta x, \delta y$ | mm | 0.3 |
| $\delta x', \delta y'$ | mrad | 1 |
| $\delta\phi$ | degrees | 0 |
| $\delta W$ | keV | 10 |
| $\delta\epsilon_x, \delta\epsilon_y, \delta\epsilon_z$ | % | 5 |
| $M_x, M_y, M_z$ | % | 5 |
| $\delta I$ | mA | 0.625 |
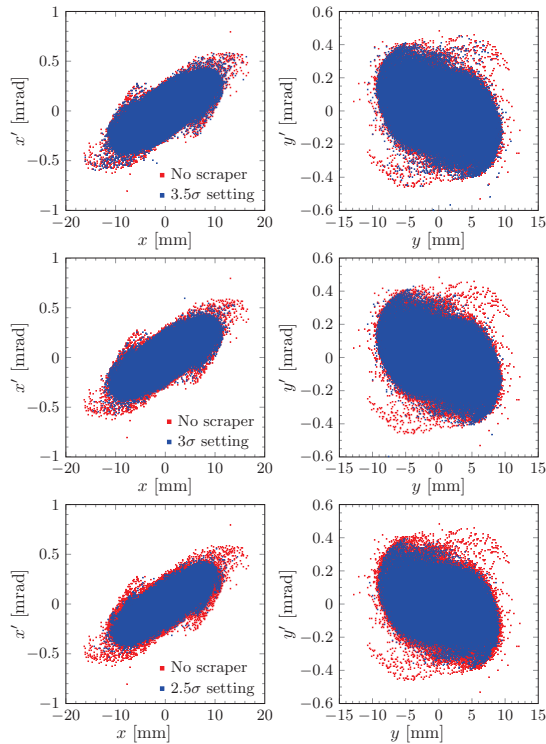
Figure 4: Transverse phase space distributions at the HEBT entrance for the scraper positions of $3.5\sigma$, $3\sigma$, and $2.5\sigma$.

## FORWARD TRACKING

The simplest way to study the effect of the MEBT scrapers is to track the beam with and without the scrapers and to observe the distribution at locations of interest. Figure 4 compares the distributions on the transverse phase spaces at the HEBT entrance ($1 \times 10^7$ macro-particles) for the cases when each scraper blade is positioned so as to absorb ~2.1 W (0.02%), ~12 W (0.14%), and ~56 W (0.621%). These correspond to the $3.5\sigma$, $3\sigma$, and $2.5\sigma$ distances to the beam center if the distribution is a Gaussian. The distribution in red represents the case of no scraper as a reference. The improvement for the $3.5\sigma$ case is hard to see but the $3\sigma$ and $2.5\sigma$ cases are showing a clear cleaning effect of the outermost particles, particularly for the vertical plane.

Figure 5 shows the histograms of the radial distributions on the normalized phase spaces for the distributions of Fig. 4. Though the cleaning effects of the $3\sigma$ and $2.5\sigma$ cases are clear, the outermost particles extend as far as $10\sigma$ toward the end of the linac and the scrapers can remove only particles beyond $8\sigma$. Figure 6 shows the histograms of the radial distributions on the normalized phase space along several locations in the linac, comparing the cases with and without the scrapers. The extent of the outermost particles gradually increases along the linac. The scrapers could reduce this extent but cannot maintain it to the level of the MEBT exit.

## BACKWARD TRACKING

To understand the situation of the halo better, this section tries another type of analysis. In Figure 7, the particles
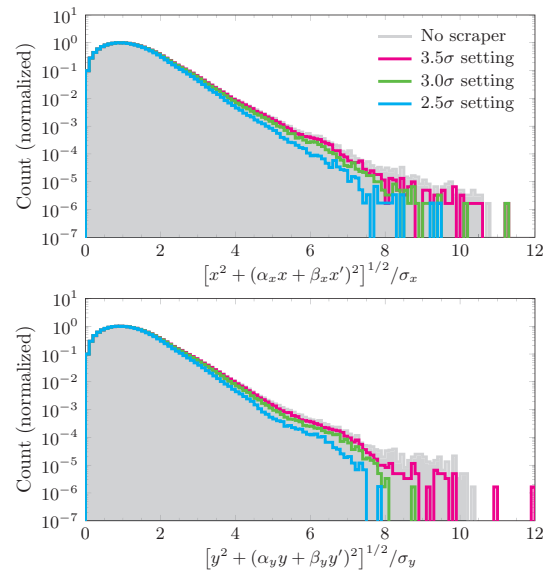
Figure 5: Radial distributions on the normalized phase spaces for the distributions of Fig. 4.
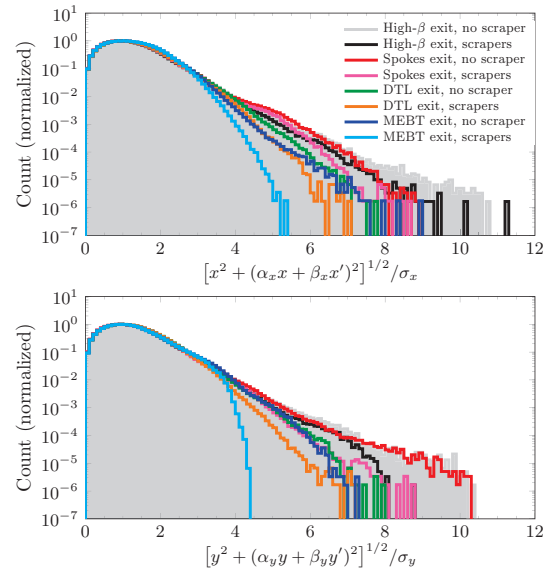


Figure 6: Evolution of the distribution along the linac with and without the scrapers ($3\sigma$ case).

beyond $4\sigma$ on the normalized phase spaces of the transverse planes are defined as halo (illustrated on the first row) and their phase space positions are observed at several upstream locations. The part in magenta represents the core which ends up within $4\sigma$ at the HEBT entrance. This analysis is memory consuming and only $1 \times 10^6$ macro-particle are used. As seen in the figure, a significant fraction of the halo particles is originally well within the core in an early part of the linac but gradually diffused out along the linac. Please note this is due to the strong space-charge force and do not occur for the case of a weak current. Figure 8 shows the histograms of the radial distribution on the normalized phase spaces for the distributions of Fig. 7. The figure again shows the trend of particles within the core in an early part of the
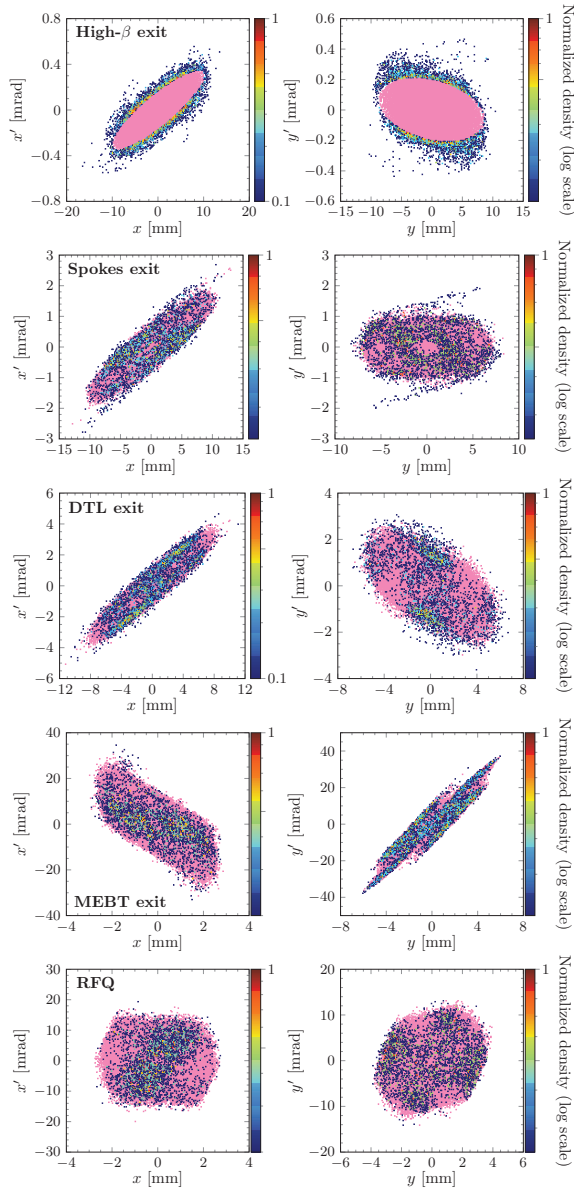
Figure 7: Distributions of the halo particles (particles beyond $4\sigma$ at the HEBT entrance) at upstream locations.

linac ending up being the halo toward the end. It also shows that a large fraction of this diffusive process occur after the section of spoke cavities. This result indicates there is also a fundamental limitation in the cleaning with the MEBT scrapers.

## BEAM LOSS

### Beam Loss with and without Errors

   This section discusses the beam losses in the ESS Linac and the impact of the MEBT scrapers on it. Before taking into account the errors, Figure 9 shows the beam losses in the case of no lattice error when $1 \times 10^7$ macro-particles shown in Fig. 2 are tracked. The location near the upstream vertical bend in the HEBT and the DTL are typical places of the beam losses in the ESS Linac. Please note that the most
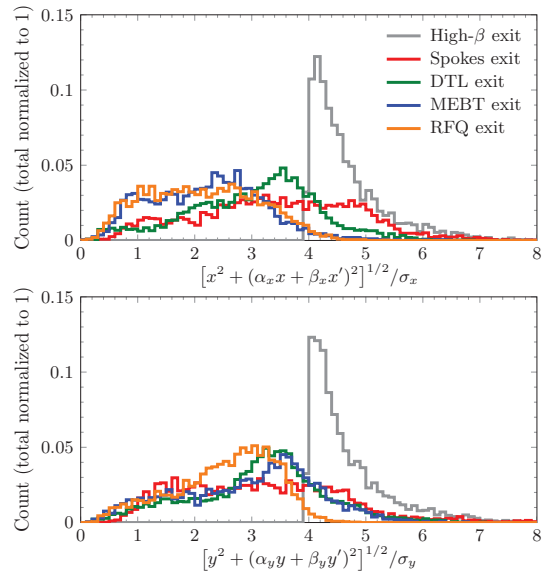


Figure 8: Radial distributions on the normalized phase spaces for the halo particles of Fig. 7.

of the lost particles are originally in the longitudinal tail and, because of that, the scrapers do not make a big difference.

   Figure 10 shows the losses when the errors in Tables 3 and 4 are included. In the calculation, $1 \times 10^5$ macro-particles are tracked in 1000 linacs of different random seeds. The *confidence level loss* of 90% and 99% are the maximum loss at each location after excluding the largest 10% and 1% cases. Please note that the trajectory error is corrected with steerer dipoles based on simulated beam position monitors with anticipated finite accuracy. When the lattice errors are introduced, the scrapers are placed so that the 99% confidence level loss per blade does not exceed 12 W, giving slightly less cleaning than the $3\sigma$ setting for the no error
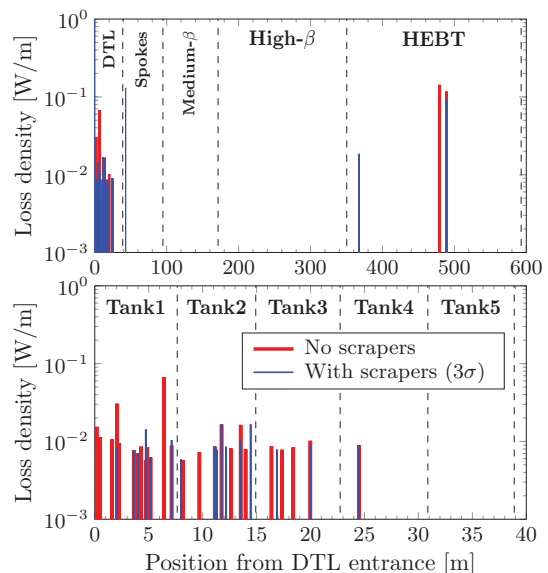


Figure 9: Beam losses due to $1 \times 10^7$ macro-particles in case of no lattice error. The bottom is a close-up of the DTL.
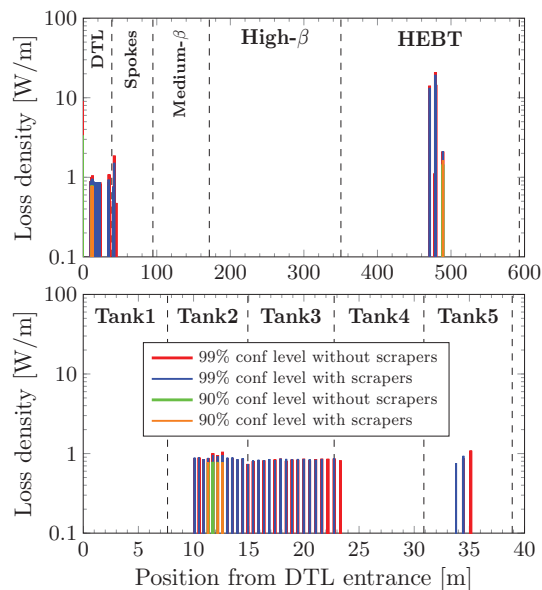
Figure 10: Confidence level losses when the errors in Tables 3 and 4 are taken into account.
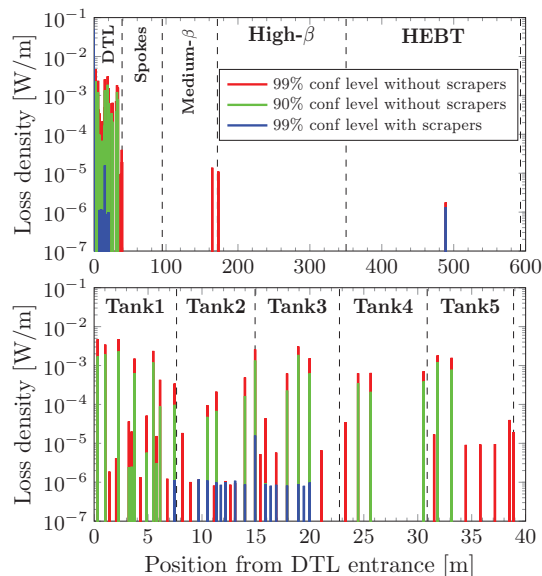


Figure 11: Confidence level losses due to a partially-chopped bunch for the case of 1.5 kV chopper voltage (nominal 4 kV).

case. As the case of no error in Fig. 9, the scrapers do not make a big difference, indicating that the beam loss is due to dynamics of longitudinal plane even with the lattice errors and the linac has a wide enough aperture for the given error.

*Beam Loss Due to Partially-chopped Bunches*

As discussed in Section *MEBT Scrapers*, the partially-chopped bunches cause some beam losses. Because the result in [5] did not include the HEBT, the simulation is repeated here. Both the chopper and lattice errors introduce trajectory excursions but the latter one should be compensated as mentioned above. However, due to the limitations in the setup of the simulation, this was not done properly and the

result in [5] included the excursions from both sources, thus providing unnecessary pessimistic result. In addition to include the HEBT, this limitation was also solved in the following result. Figure 11 shows the confidence level losses due to one partially-chopped bunch when $1 \times 10^5$ macro-particles are tracked in 500 linacs. The previous study showed that the beam loss situation is worst when the chopper voltage is around 1.5 kV (the nominal is 4 kV) [5] so the 1.5 kV is applied as a representative case. The lattice errors in Table 3 are again applied, but the input beam error of Table 4 and the lattice errors up to the chopper dump in the MEBT are not applied to keep the condition up to the dump the same. The loss in the HEBT is only $\sim 1 \times 10^{-5}$ W/m level with 99% confidence even without the scrapers and is not a concern. As the previous study indicated [5], the scrapers make a significant reduction of the losses, particularly in the DTL, since these losses are due to the dynamics on the transverse plane (trajectory excursion).

## CONCLUSIONS

The impact of the MEBT scrapers on the beam quality and losses throughout the ESS Linac is studied in detail. The cleaning effect of the scrapers are evident, but there are fundamental limitations and the scrapers can only prevent the outermost particles from exceeding $\sim 8\sigma$ toward the end of the linac. The beam loss in the ESS Linac is likely caused by dynamics on the longitudinal plane and thus the scrapers look to have no significant effect on the beam losses, except those caused by the partially-chopped bunches.

## ACKNOWLEDGMENTS

## REFERENCES

[1] M. Eshraqi et al., in Proc. of IPAC'14, THPME043.

[2] M. A. Plum, in Proc. of HB'12, TUO3C04.

[3] R. Miyamoto et al., in Proc. of HB'12, WEO3A02.

[4] R. Miyamoto et al., in Proc. of IPAC'14, THPME045.

[5] R. Miyamoto et al., in Proc. of LINAC'14, MOPP039.

[6] H. D. Thomsen and S. P. Møller, in Proc. of IPAC'12, MOPPD072.

[7] M. Eshraqi et al., in Proc. of IPAC'13, THPWO072.

[8] A. I. S. Holm et al., in Proc. of IPAC'12, MOPPD049.

[9] H. D. Thomsen and S. P. Møller, in Proc. of IPAC'14, WEPRO072.

[10] R. Duperrier et al., in Proc. of ICCS'02, p. 411.

[11] N. Pichoff et al., in Proc. of Linac'98, MO4042.

[12] R. Duperrier, PRST-AB **3**, 124201 (2000).

[13] I. Bustinduy et at., in Proc. of HB'14, TUO1AB04, to be published.

[14] M. Eshraqi et al., in Proc. of IPAC'14, THPME044.

[15] H. D. Thomsen and S. P. Møller, in Proc. of IPAC'14, WEPRO074.

# SPACE-CHARGE COMPENSATION OF INTENSE ION BEAMS BY NONNEUTRAL PLASMA COLUMNS*

K. Schulte[†], M. Droba, S. Klaproth, O. Meusel, D. Noll, U. Ratzinger, K. Zerbe
Institute for Applied Physics, Goethe University Frankfurt a.M., Germany
O. Kester, GSI, Darmstadt, Germany

## Abstract

Gabor lenses were conceived to focus a passing ion beam using the electrical field of a confined nonneutral plasma column. Beside its application as focusing device, in Gabor lenses space-charge effects can be studied in detail.

The influence of the electron distribution on emittance and space-charge dominated ion beams was investigated in beam transport experiments [1]. In this contribution we want to emphasize one result of these experiments. The measurements indicated a strong contribution of secondary electrons on beam dynamics. Secondary electrons are produced within the transport channel, particularly by interaction of the beam with the surface of the slit-grid emittance scanner. This effect might lead to an increase of the filling degree and to an improved focusing performance of the lens.

Assuming that the loss and production rates within the lens volume and the transport channel determine the equilibrium state of the nonneutral plasma column, the electron cloud was characterized as a function of the external fields and the residual gas pressure in small-scale table top experiments.

In this contribution experimental results will be presented in comparison with numerical simulations.

## BEAM TRANSPORT EXPERIMENTS

A number of diagnostic as well as beam transport experiments were performed in order to investigate how the nonneutral plasma properties are mapped onto the ion beam. At first, the electron density distribution and the plasma parameters were determined in diagnostic experiments without beam. Afterwards the lens was used as focusing device for the transport of an emittance dominated helium and a space charge dominated argon beam to study its performance with respect to image quality and space charge compensation.

### Electron Density Distribution

Figure 1 represents the results of the emittance dominated beam transport experiments.

One important result is that the electron density distribution determines the phase space distribution of the beam. In case of a hollow electron distribution, passing beam ions experience a strong force at the edge of the column and none in the center. For a homogeneous electron density distribution the focusing is linear and therefore the beam is transported without aberrations if the radius of the column is larger than the beam radius. Still, it was found that for given lens parameters the measured electron densities and the electron
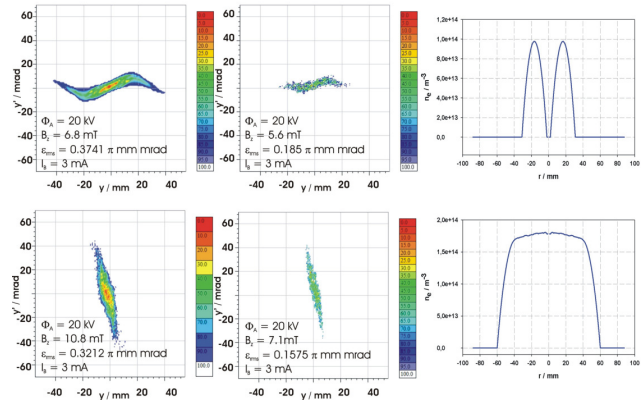


Figure 1: Comparison of measurement (left) and simulation of the transported He+ beam (center) as well as simulated electron density distribution (right) [2].

density distribution in the diagnostic experiments differed from the results of the beam transport experiments.

An example of the space-charge dominated beam experiments is depicted in Fig. 2.
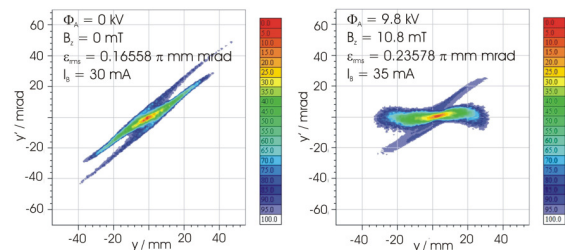


Figure 2: Phase space distribution of the drifted beam when the lens was switched off (left) and of the transported Ar+ beam when the lens was switched on (right) [2].

Indeed, the focusing performance of the Gabor lens looks very promising, but neither the diagnostic measurements nor the performed numerical simulations show comparable results.

### Influence of Beam Intensity on the Focusing Performance

Furthermore, for the same parameter set-up of the Gabor lens it was observed that the focusing strength increases with the beam current which indicates an increased density of the confined electron column. Figure 3 illustartes the phase space distribution of a 2.2 keV/u Ar+ beam measured behind the lens for different beam currents.

---
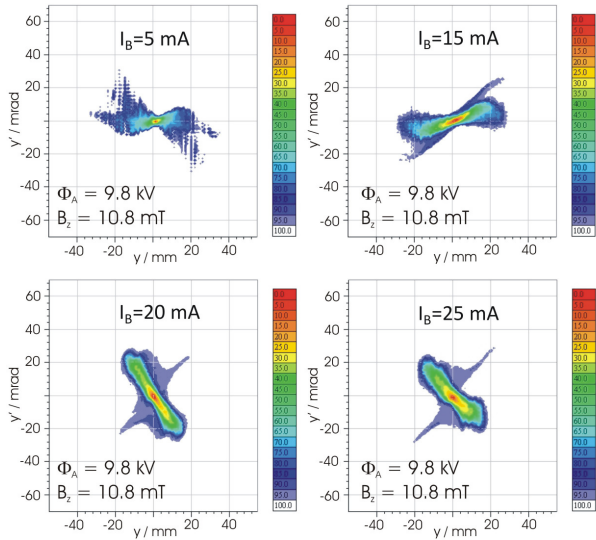
Figure 3: Influence of the ion current on the focusing performance of the lens.

One possible explanation for this observation is the enhanced ionization rate of the residual gas due to the higher beam intensity. Another source of electrons could be transmission losses of the beam on the chamber wall or secondary electrons produced during the measurement by the slit-grid emittance scanner. However, as a result of the external fields no additional electrons should be confined inside the lens volume.

In order to further investigate the confinement with respect to the external parameters, the production and loss processes within the Gabor lens have been investigated.

## ELECTRON PRODUCTION AND LOSSES

Several diagnostic experiments were performed in order to investigate the electron loss and production processes in more detail. These processes are assumed to have a major impact on the equilibrium state of the nonneutral plasma.
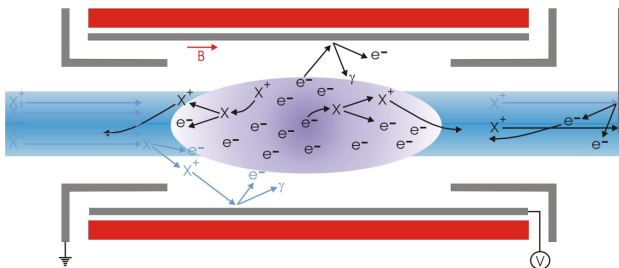


Figure 4: Scheme of the assumed production processes.

Interactions of electrons, atoms, ions from residual gas and the beam as depicted in Fig. 4 lead to an electron built-up within small time scales below 1 ms [3]. The build-up as a function of the external fields and the residual gas pressure was measured by a CCD camera with high quantuum efficiency. The first signal of plasma emission that results from

residual gas excited by electrons was defined as "ignition point" for a given parameter set-up.

The results of these measurements for different confinement lengths are presented in Fig. 5. Note that the anode potential $\Phi_A$ is normalized to the square of the lens' radius in order to compare different lens types.
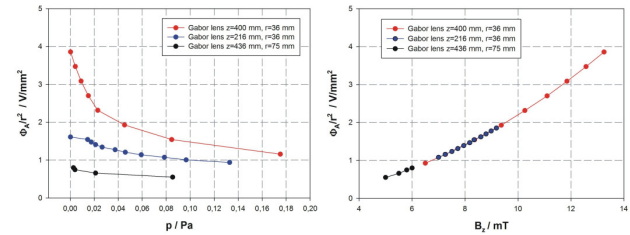


Figure 5: Measured ignition curves of the nonneutral plasma for helium as a function of the potential (left). The anode potential was configured according to the lens work function and normalized to the radius in order to compare all lens types (right).

The confinement of electrons within the Gabor lens is not perfect. Owing to particle collisions, field inhomogeneities and the finite electron temperature, electrons are lost in transverse and longitudinal direction. In longitudinal direction the electron is confined by the potential well created by the electrode system, while it has a degree of freedom along the magnetic field lines. Electrons are lost if the kinetic energy is high enough to leave the potential. Since residual gas ions are also extracted from the lens the experimental evidence of these losses is very difficult.

The transverse electron losses are a result of collisional transport across the magnetic field lines. Depending on their kinetic energy lost electrons can produce X-ray radiation and are detected by a $\gamma$-spectrometer. Figure 6 shows the measured gamma count rate as a function of the anode potential $\Phi_A$ (for $B_z$=11.9 mT, p=1.7·$10^{-5}$ Pa) and the magnetic field on axis $B_z$ (for $\Phi_A$=22 kV, p=5.1·$10^{-5}$ Pa). The detected intensity $I_x$ was divided by the ion current I and the residual gas pressure p to minimize the influence of a variation in the plasma state during the measurement.

The loss rate represented by the X-ray intensity increases exponentially as a function of the anode potential while it decreases for stronger magnetic confining fields.

### Influence on Secondary Electron Production on Plasma State

Another indirect evidence for the influence of produced secondary electrons on the plasma state is shown in Fig. 7. The residual gas ion current is measured by a Faraday cup (FDC) including a repeller electrode which is used to keep produced secondary electrons inside the detector.

It is assumed that these electrons are confined in the potential of the extracted residual gas ions and retroact on the electron column. By increasing the negative potential of the repeller electrodes the emission intensity decreases as a result of less electrons interacting with the residual gas.
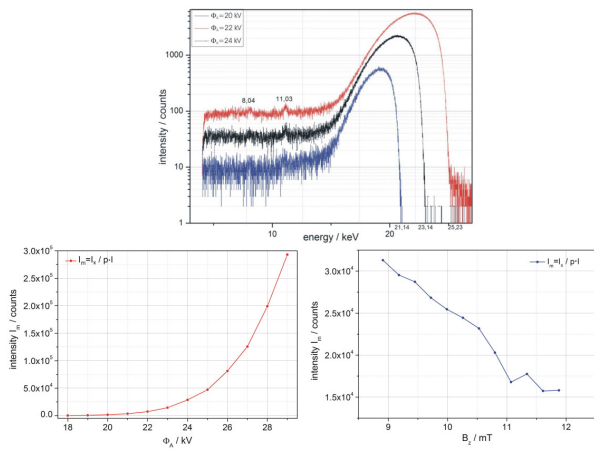
Figure 6: Example of measured X-ray emission spectrum (top), x-ray emission as a function of the anode potential $\Phi_A$ (bottom, left) and the magnetic field $B_z$ (bottom, right) [4].
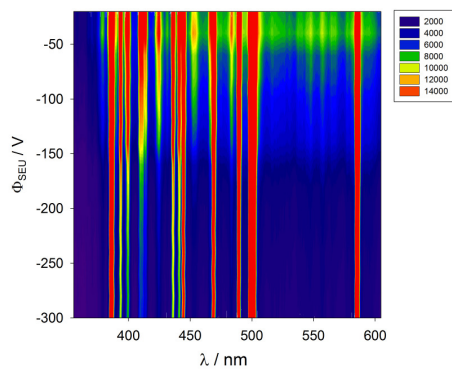


Figure 7: Measured intensity profile in the wavelength region from 360 to 600 nm as a function of the repeller potential for lens parameters of $\Phi_A$=5.4 kV and $B_z$=8.72 mT [5].

## DISCUSSION AND OUTLOOK

In this contribution assumed production and loss mechanisms are discussed and first measurements of electron production and losses within the volume of a Gabor lens are presented.

The results of beam transport as well as diagnostic experiments indicate a strong influence of the secondary electron production on the nonneutral plasma state. Yet, a measurement of the different contributions is difficult to realize and an experimental evidence is still needed.

Another possible explanation for the observed change in the focusing strength discussed in the first paragraph is the reduction of the electron loss channels due to the positive beam potential. As presented in Fig. 8 the superposition of the beam, the space charge and the anode potential creates a barrier for electrons that are able to escape in longitudinal direction.

Beside reliable non-invasive diagnostic techniques an extensive numerical model is needed to understand the influence of the previously discussed effects on the electron
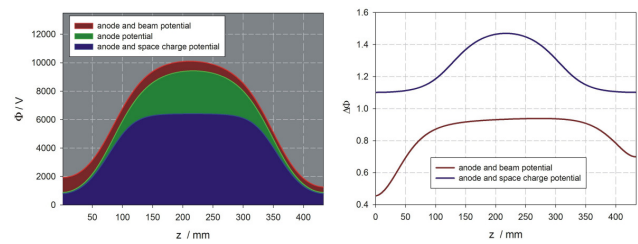


Figure 8: Superposition of the anode potential, the space charge potential of the electron cloud and the uncompensated beam potential for an 3.1 keV/u, 35 mA Ar$^+$-beam in longitudinal direction.

confinement and on the transport of high intensity ion beams using Gabor lenses.

The 3D Particle-in-Cell Code bender has been developed to improve the understanding of the dynamics of the compensation and the resultant steady state by implementing ionization of residual gas as well as secondary electron production on surfaces [6]. First simulations using bender were performed to study the electron cloud build-up inside the Gabor lens and are shown in Fig. 9.
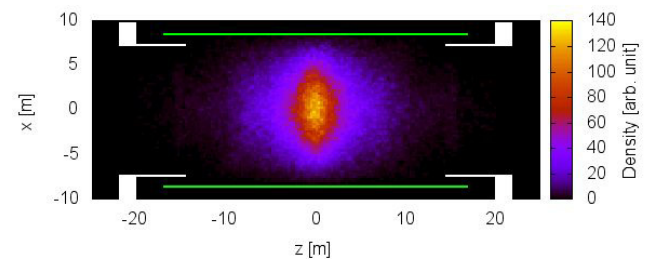


Figure 9: State of the nonneutral plasma after 140 $\mu$s for $\Phi_A$=9.8 kV, $B_z$=10.8 mT and p=1·10$^{-3}$ Pa (Ar) [3].

In future work the interaction of the ion beam with the confined electron cloud with respect to the production and loss processes will be studied numerically and experimentally in more detail.

## REFERENCES

[1] K. Schulte, "Studies on the Focusing Performance of a Gabor lens Depending on Nonneutral Plasma Properties", PhD thesis, Goethe University Frankfurt, 2013.

[2] K. Schulte et al., "Prototype Testing of the Frankfurt Gabor Lens at HOSTI", GSI Scientific Report, 2013.

[3] D. Noll, private communication.

[4] S. Klaproth, "Indirekte Messung von Teilchenverlusten in einer Gabor-Linse" BSc thesis, Goethe University Frankfurt, 2013. (New York: Knopf, 2007), 52.

[5] K. Schulte, "Untersuchung von Messmethoden zur Parameterbestimmung eines Nichtneutralen Plasmas", MSc thesis, 2008.

[6] D. Noll, "The Particle-In-Cell Code bender and its Application to Non-relativistic Beam Transport", These Proceedings, HB2014, East Lansing, USA, November (2014).

# A NOVEL CODE WITH HIGH-ORDER ADAPTIVE DYNAMICS TO SOLVE THE N-BODY PROBLEM

S. Abeyratneˆ, B. Erdelyi*ˆ, H. Schaumburgˆ
ˆDepartment of Physics, Northern Illinois University, DeKalb, IL 60115
*Physics Division, Argonne National Laboratory, Argonne, IL 60439

## Abstract

Although there are several publicly available algorithms to model the behavior of natural systems such as the N-body system, limited computing power hinders the attempt to simulate them efficiently. With the improvement of high performance computing, scientists will be able to run simulations at an unprecedented scale in the future. Therefore, it is necessary to develop new algorithms and data structures to harness the power of high performance computing. In this paper we show a newly developed code, particles' high order adaptive dynamics (PHAD), to serve future computing demands. We use Fast Multipole Method (FMM) to calculate the interactions among charged particles. We use the Strang splitting technique to reduce the number of FMM calls and enhance the efficiency. Picard iterations-based novel integrators are employed to achieve very high accuracies. Electron cooling in the proposed Electron Ion Collider (EIC) has been identified as a potential testing environment for PHAD.

## INTRODUCTION

Computer simulations are heavily used in designing particle accelerators and the efficiency and accuracy of them can be improved with ever changing computational power. Clearly, this demands dramatic improvements on existing code for beam dynamics. In this paper we present a new code developed using novel ideas to significantly divert the existing trend and electron cooling will be one of the potential candidates of its application.

The densely packed particles in a beam, which can be considered as our N-body system, experience two types of forces, long range and short range. The long-range forces are the Coulomb forces and the short-range forces are Coulomb collisions. Also, the motion of the particles in the beam should be taken into consideration for precise modeling and simulation of the beam. Therefore, our code enables to calculate Coulomb interactions and study the changes in the particle configuration with time.

## ALGORITHM

In an N-body system each object continuously interacts with every other object in the system. The direct computation or pairwise calculation of such interactions gives the exact results and needs a computational complexity in the order of $N^2$. For very large N, this method quickly becomes untenable. Using some approximate methods, such as the basis function methods, particle-mesh methods, and hierarchical subdivision methods, can circumvent this drawback. The challenge is to mitigate the approximation artifacts. The

hierarchical (or recursive) subdivision method has three distinct flavors: tree, cluster and fast multipole method and the algorithm used to develop our code belongs to the hierarchical fast multipole method (FMM). In FMM particles are confined to spatially bound cells and the interaction between cells are computed. Therefore, the force experienced by any particle inside a cell can be approximated to the addition of Taylor expansions calculated from the multipole expansion of the far away cells. Also, FMM can calculate interactions among N-bodies while retaining accuracy because its computational time typically grows linearly with the number of bodies.

Again, FMM has different versions and they vary with the dimensionality and the type of particle distribution. The code described in this paper uses the 3D adaptive FMM; it is well suited for any arbitrary distribution [1, 2]. Even though FMM is considered as an approximation to get the solution of the Poisson equation, its accuracy can be set a priori and can be tuned to get even more accurate results than the direct summation method.

In order to study the beam propagation as time progresses, we need to split the total time into smaller steps and examine the beam dynamics after each small time step. A fixed time step size is not a good choice to study the behavior of the beam. For example, to study the close encounters of particles the step size should be adjustable. Hence, we used a variable order Picard iteration-based integrator. It is an integrator with dense output and flexible for automatic adjustment of the optimal order and time step to achieve a prescribed accuracy with a minimum computational cost.

The implementation of the automatic step size and order selection is not yet completed. Therefore, our code is tested only for the variable order with the fixed time step size [3,4].

To further enhance the computational throughput, we use Strang splitting [5]. Strang splitting is a second order accurate operator splitting method. This method splits a complicated problem into a few simpler parts and solves them separately and composes all solutions to get the final solution of the problem. Two types of forces—strong forces that change rapidly and smooth forces that vary slowly, act upon each particle in a beam. When the particles get closer they experience a very strong force and undergo rapid changes. This type of behavior occurs in the nearby region or the neighborhood of an evaluation point. Therefore, small time steps are needed to model the strong forces and it is possible each particle in the close encounter to have its own time step size. The influence caused by the far away particles can be considered as the mean force exerted by them and

it varies slowly. In this simulation we work on three time scales. The first time scale is the total time, or the entire simulation time. The second scale is created by dividing the first to equal step sizes and used to study the motion of particles due to slowly varying forces. The third scale is the subdivision of the second and as explained above it can vary from particle to particle. Since the FMM is the most time consuming process we need to minimize number of FMM calls. This led us to call FMM only in the second time scale, i.e. in the case of slowly varying forces.

There are two types of frames involved in this problem: the lab frame and the beam frame. In fact, under the influence of self-fields the motion of the particles in the beam frame is nonrelativistic and therefore the forces are electrostatic. The external electric and magnetic fields are given in the lab frame. Since the Lorentz force due to the external fields and the self-fields determine the beam dynamics, we need to consider the collective effects of the fields. There are two choices: calculate the forces due to self-fields and convert them into the lab frame or calculate the forces due to the external fields and convert them to the beam frame. As the intention is to study the particles' behavior in the lab frame, the straightforward approach is to transform the fields from the beam frame to the lab frame, and solve the equations of the motion in the lab frame.

The immediate testing environment of this code is the electron cooling section in the proposed Electron Ion Collider (EIC). Therefore, our code should work for the design parameters suggested in the Electron Ion Collider accelerator design [6]. The cooling device will be installed in the pre-booster ring and the collider ring of the EIC and each part of the collider carries ions with distinct energy ranges. The kinetic energy of the ions injected into the pre-booster ring is about 280 MeV and they are accelerated to 3 GeV, while the kinetic energy of ions during the collision in the collider ring varies from 60 to 100 GeV. The lowest gamma value in the pre-booster is about 1.3. In the collider ring the corresponding gamma values vary from 60 to 107.

## PERFORMANCE ANALYSIS

In a previous paper [7], using the same particle distribution for both source points and target points, we have shown that the results produced from PHAD and N-body (SA) codes are in good agreement. We obtained those results for the case where points are normally distributed and they move with nonrelativistic speeds. Hence, the initial momenta, $p_x$, $p_y$, $p_z$, are all near-zero. In this paper we introduce relativistic corrections to both our codes, PHAD and SA. For details on these codes, please see [7]. The relativistic gamma value is reflected in the initial momentum in the z direction, $p_z$, by assigning the corresponding momentum value to $p_z$ while $p_x$ and $p_y$ are still near-zero.

As indicated in the introduction, we have identified that the lowest gamma value is 1.3 and the highest is 100. We tested our code for three specific gamma values, 1.3, 60 and 1000. Figure 1 shows the comparison of trajectories of

PHAD with those of the N-body code for gamma value 1.3 when each particle carries a unit positive charge and a unit mass. The total time is 0.05 with time step size of 0.001.
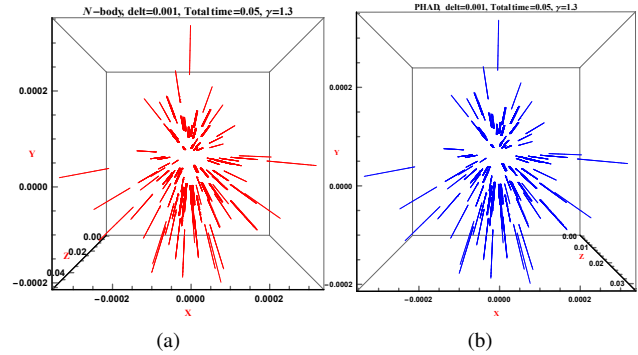


Figure 1: Trajectories of N-body and PHAD for the particles with unit mass and $\gamma$=1.3.

Figure 2 shows the comparison of trajectories of PHAD with those of N-body code for gamma value of 1.3 when each particle carries a unit positive charge and different masses ranging from 2 to 99. The total time is 0.05 with time step size of 0.001.
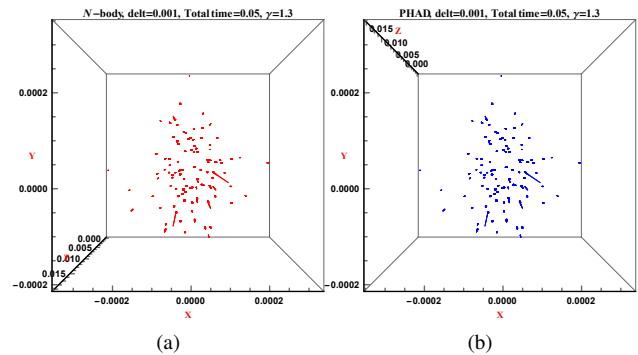


Figure 2: Trajectories of N-body and PHAD for the particles with different masses and $\gamma$=1.3.

Table 1: Spread in x, y, z after 50 Time Steps of Size 100

| $\gamma$ | Spread in x | Spread in y | Spread in z |
|---|---|---|---|
| 1.3 | $1.07 \times 10^{-2}$ | $1.07 \times 10^{-2}$ | 3194.85 |
| 1000 | $6.69 \times 10^{-4}$ | $5.67 \times 10^{-4}$ | 5000.00 |

After a single time step of 100 the coordinates of points (y vs x and z vs x) with relativistic gamma values 1.3 and 1000 are shown in Figures 3 and 4, respectively. Each point carries a unit charge and a unit mass. We choose $\gamma$=1000 due to the fact that in the ultra-relativistic limit the space charge effect vanishes, so it is a straightforward sanity check of our codes. After 50 time steps of step size 100, the spread in x, y, and z are shown in Table 1. The particles with the high gamma value of 1000 are displaced more along the z
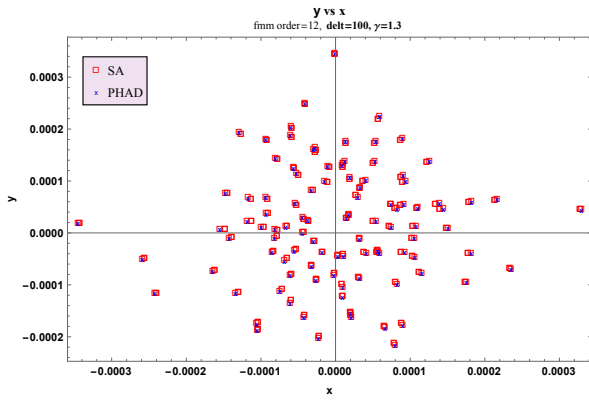
(a) y vs x
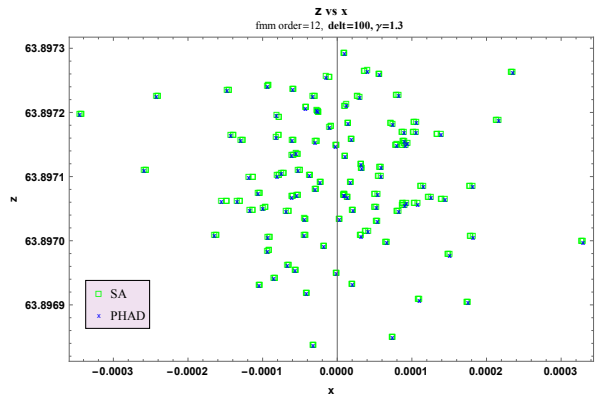


(b) z vs x

Figure 3: $\gamma=1.3$
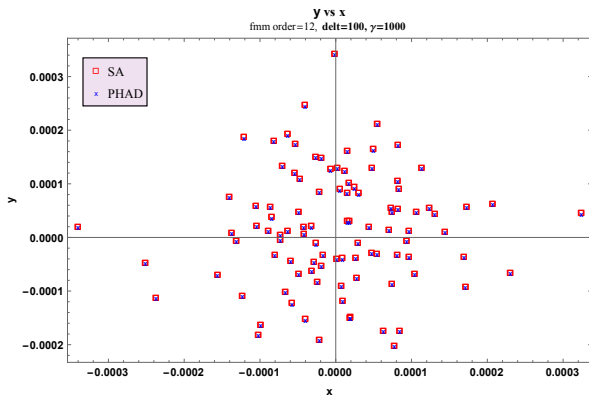


(a) y vs x
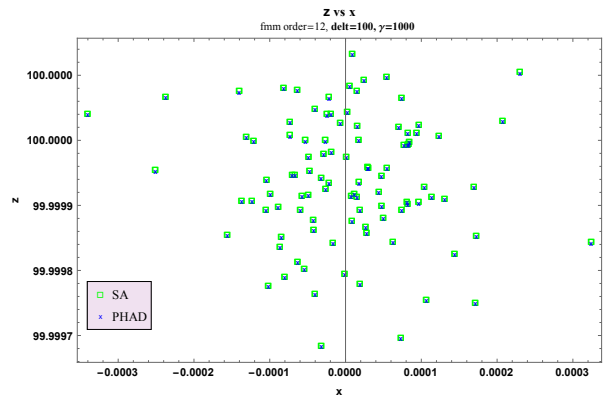


(b) z vs x

Figure 4: $\gamma=1000$

direction than those with low gamma value of 1.3. This is can be attributed to the fact that our initial configuration has a low/high momentum corresponding to a low/high gamma value. As expected, the space charge effect diminishes at higher energies (or higher gamma), and when $\gamma=1000$ points get closer to each other compared to those for $\gamma=1.3$. The values in Table 1 shows that both x and y spread become smaller for $\gamma=1000$.

We are still investigating if the discrepancies observed in the transverse momentum figure (Figure 5) are within the expected numerical errors or a still uncovered coding bug. The data structuring part of the code is implemented in C++. Picard iteration based integrator and calculations of Coulomb interactions are implemented in COSY INFINITY [8].

## SUMMARY

In order to achieve highly accurate results efficiently we have to exploit the high processing power of computers through new approaches of modelling and simulations of N-body systems. In this paper we presented a new code developed to model and simulate a particle beam efficiently while maintaining high accuracy. Three key measures are
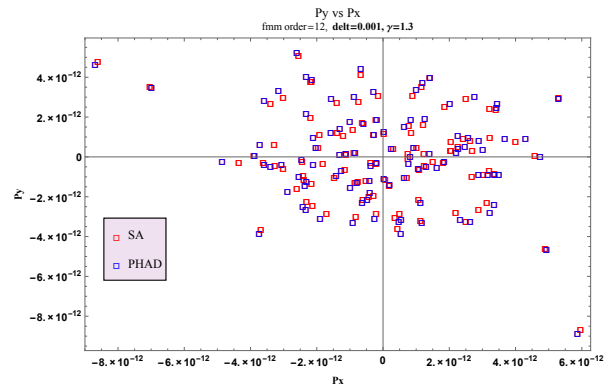


Figure 5: Transverse momenta ($p_x$ and $p_y$) for $\gamma=1.3$

taken to ameliorate the challenges: Fast multipole method to calculate Coulomb interactions, Picard Integrator with dense output to study close encounters with small time steps, Strang splitting to improve speed up reducing the number of FMM calls.

The approximation errors due to FMM and the estimation errors due to Strang splitting are unavoidable. We showed

that PHAD and SA give similar results and they indicate that influence of the errors incurred is negligible. The drawn conclusions can be extended for any arbitrary distributions, any charge and mass magnitudes and for relativistic or non-relativistic particle motions.

## ACKNOWLEDGEMENT

## REFERENCES

[1] S. Abeyratne, S. Manikonda, B. Erdelyi, "A Novel Differential Algebraic Adaptive Fast Multipole Method", in proceedings of IPAC'13, Shanghai (2013) 1055-1057.

[2] S. Abeyratne, B. Erdelyi, "Optimization of the Multipole to Local Translation Operator in the Adapative Fast Multipole Method", in proceedings of NA-PAC'13, Pasadena (2013) 201-203.

[3] A. al Marzouk, B. Erdelyi, "Numerical Integrator for Coulomb Collisions", in proceedings of NA-PAC'13, Pasadena (2013) 204-206.

[4] H.N. Schaumburg, B. Erdelyi, "A Picard-Iteration-Based Integrator", in proceedings of NA-PAC'13, Pasadena (2013) 210-212.

[5] E. Hairer, G. Wanner, C. Lubich, "Geometric Numerical Integration", (New York: Springer Berlin Heidelberg, 2006).

[6] S. Abeyratne et al., "Science Requirements and Conceptual Design for a Polarized Medium Electron-Ion Collider at Jefferson Lab".

[7] B. Erdelyi, S. Abeyratne, "A New High-Order Adaptive Dynamics Code with Applications to Electron-Ion Collider", in proceedings of EIC14, Virginia (2014).

[8] K. Makino and M. Berz, "COSY INFINITY Version 9", Nuclear Instruments and Methods in Research Physics Section A, 558:345-350 December (2005).

# RESONANCE STRUCTURES IN THE IMPEDANCE OF A CERAMIC BREAK AND THE MEASURED RESULTS

Y. Shobuda, T. Toyama, J-PARC Center, JAEA/KEK, Ibaraki, Japan
Y.H. Chin, K. Takata, KEK, Ibaraki, Japan

## Abstract

Recently, we have developed a new theory to evaluate longitudinal and transverse impedances of any size of ceramic break sandwiched between metal chambers. The theory successfully reproduces the resonance structures in the impedance due to trapped modes inside the ceramic break. The comparisons between the theoretical and the simulation results such as ABCI and CST Studio show excellent agreements, indicating that they can be used as a good benchmark test for accuracy of simulation codes. To demonstrate the existence of such resonances, the transverse impedance of the ceramic break is measured using the wire-method. The measurement results reproduce the simulations well. The theory is particularly useful for the evaluation of the impedance of the ceramic break with titanium nitride coating.

## INTRODUCTION

A short ceramic ring sandwiched by metal chambers is called a ceramic break. Such ceramic breaks are often inserted between the chambers near bending magnets in proton synchrotrons. Their purpose is to mitigate the eddy current effects over the chambers excited by the outside time-varying magnetic fields, and the induced magnetic turbulence is confined in the chamber between the ceramic breaks [1].

On the other hand, capacitors are typically attached on the outer surface of the ceramic breaks as RF shields to prevent the radiation fields to propagate out of the ceramic breaks. The radiated fields may cause malfunctioning of devices along the accelerators.

In the J-PARC main ring (MR), two ceramic breaks have been additionally installed since 2011. At first, they forgot to attach RF shields around them. When the beam with particles more than $3.75 \times 10^{13}$ was shot into MR, they discovered that the power source of the quadrupole magnets were suddenly tripped, and the noise level in the adjacent monitors were increased intolerably high. The problems were put under control by attaching RF shields around the ceramic breaks. This accident reminded them the importance of the RF shields to the ceramic breaks.

In the rapid cycling synchrotron (RCS) in J-PARC, titanium nitride (TiN) is coated on the inner surface of the ceramic chambers, to suppress the secondary emission of electrons, caused by the collisions between a part of a proton beam and the chamber surface. The TiN coating is supposed to prevent the build-up of the electron cloud from destabilizing the beams [2, 3].

These ceramic breaks become also sources of the beam impedance [4, 5]. The precise estimation of impedance is an important step toward realization of high intensity beams

in proton synchrotrons [6]. Recently, a new theory is developed to understand the characteristic of the ceramic break impedance [7], which enables us to get an insight about the resonance structure cased by the trapped mode inside the ceramic.

Next, let us show an example of the resonance in the ceramic break.

## IMPEDANCES OF CERAMIC BREAK AND THEIR RESONANCE STRUCTURES

Let us assume that the ceramic has the dielectric constant $\epsilon'$. The inner and the outer radii and the length of the ceramic are $a$, $a_2$ and $g$, respectively. Applying the formulae (7) and (18) in the reference [7], we obtain the theoretical impedance. The longitudinal and the transverse impedances are shown in Figs. 1 and 2, respectively. For the longitudinal impedance, the real and the imaginary parts of the impedance are shown in the left and the right figures, respectively. For the transverse impedance, the real and imaginary parts of impedances are shown in the same figure by the solid and the dot lines, respectively.

The large resonance at low frequency in the transverse impedance is approximately given by

$$f \sim \frac{c}{2\pi a} \sqrt{\frac{a^2 + 1.5(a_2^2 - a^2)}{a^2 + 1.5\epsilon'(a_2^2 - a^2)}}, \qquad (1)$$

which essentially shows the resonance around the circumference ($2\pi a$) of the ceramic break [8]. The frequency is lowered compared to that for the vacuum gap ($\epsilon' = 1$) case due to the wavelength contraction effects of the ceramic.
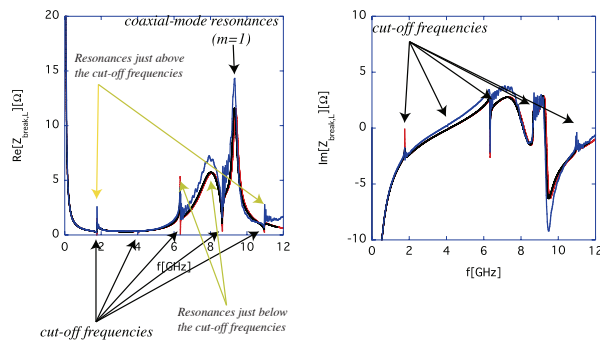


Figure 1: Longitudinal impedances of the ceramic break ($a = 65$ mm, $a_2 = 70$ mm, $g = 10$ mm and $\epsilon' = 11$) calculated by the theory (red), the simulation codes ABCI (black) and CST Studio (blue).

All the calculation results (the theory, ABCI [9] and CST [10]) reproduce the same resonance structures and show
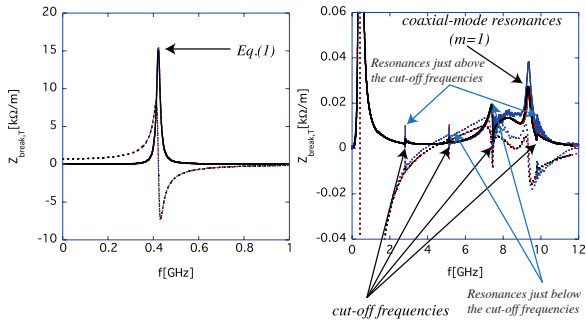
Figure 2: Transverse impedances of the ceramic break ($a = 65$ mm, $a_2 = 70$ mm, $g = 10$ mm and $\epsilon' = 11$) calculated by the theory (red), the simulation codes ABCI (black) and CST Studio (blue). The left and the right figures show the results up to 1 GHz frequency, and those up to 12 GHz, respectively.

good agreements between them, in particular, between the theory and ABCI. The comparison between theory and different simulation codes can indeed provide a good benchmark for accuracy test of the codes.

Next, let us discuss the resonance structure appeared in the impedance of the ceramic breaks.

*Cavity-mode Resonance*

One type of resonances is characterized by the cut-off frequencies. In other words, they behave like cavity-mode resonances. The cut-off frequencies are given by

$$f_{c,L} = \frac{j_{0,k} c}{2\pi a}, \qquad (2)$$

$$f_{c,T} = \frac{j_{1,k} c}{2\pi a}, \qquad (3)$$

for the longitudinal and the transverse impedances, respectively, where $j_{n,k}$ are the $k$-th zeros of the Bessel function $J_n(z)$ [11]. This type of resonances appear in the impedances of the vacuum gap, as well [8].

As shown in Figs. 1 and 2, two types exist in the resonances around the cut-off frequencies. In one case, the resonance appears just above the cut-off frequency. In the other case, the resonance appears just below the cut-off frequency [12].

The physical reason for the first case (resonances just above the cut-off frequencies) is as follows. The difference of the dielectric constants between the ceramic and the vacuum introduces the reflection of waves at the boundaries. This reflection of electromagnetic fields at the lower and the upper boundaries of the ceramic creates trapped mode inside. These trapped modes can leak out of the ceramic either to the outside or the inside of the chamber. Below the cut-off frequencies, they couple with unpropagating modes inside the chamber, and the interaction between the beam and these unpropagating modes takes place only in a limited space around the ceramic location. Above the cut-off frequencies, however, the trapped modes couple with propagating modes inside the chamber and the interaction between the beam and

the propagating modes is extended for much longer distance, and as a result, the impedance is enhanced.

The second case (resonances just below the cut-off frequencies) is excited by another mechanism. The impedance of the ceramic break is approximately obtained by adding the impedances (the impedance of the gap and that of the capacitor made by the ceramic) in parallel. For a thick gap, the admittance of the ceramic break is capacitive at low and high frequency. However, there is a frequency region between them where the admittance is switched to inductive. On the other hand, the gap itself works as a capacitor below the cut-off frequencies, since the electromagnetic fields can be stored inside without propagating away through the beam chamber. As a result, the coupling between the inductance of the ceramic and the capacitance of the gap creates resonances below the cut-off frequencies in the intermediate frequency region.

*Coaxial-mode Resonance*

There is another type of resonances in the ceramic break. This behaves like the coaxial-like mode whose fields are mainly localized inside the ceramic. The resonant frequencies are roughly estimated by the conditions given by

$$\frac{\partial(Y_0'(\tilde{\mu}_m a) J_0(\tilde{\mu}_m a_2) - J_0'(\tilde{\mu}_m a) Y_0(\tilde{\mu}_m a_2))}{\partial f} = 0, \quad (4)$$

$$\frac{\partial(Y_1'(\tilde{\mu}_m a) J_1(\tilde{\mu}_m a_2) - J_1'(\tilde{\mu}_m a) Y_1(\tilde{\mu}_m a_2))}{\partial f} = 0, \quad (5)$$

for the longitudinal and the transverse impedances, respectively, where

$$\tilde{\mu}_m = \sqrt{\frac{4\pi^2 \epsilon' f^2}{c^2} - \frac{m^2 \pi^2}{g^2}}, \qquad (6)$$

$Y_n(z)$ is the Neumann function [11], and the prime in the Neumann and the Bessel functions denotes the differential with their argument $z$. The positive integer $m$ is longitudinal (coaxial)-mode number, and describes the number of half-wavelengths in the ceramic. The $m = 1$ order coaxial mode resonance is identified in Figs.1 and 2 in the shown frequency scope. The resonant frequencies are estimated as about 9.28 GHz both for the longitudinal and the transverse impedances.

At the coaxial-mode resonant frequency, the electric fields are almost parallel to the longitudinal direction at $\rho = a$ and $\rho = a_2$. In other words, the fields behave like antenna both on the inner and outer surface of the ceramic, and the fields can propagate away both inside and outside of the chamber. Consequently, the impedance has sharp peaks at the frequencies.

**MEASUREMENT RESULTS**

Let us experimentally study the existence of such resonance structures, especially in the transverse impedance of the ceramic break. A straightforward way to measure the transverse impedance is to use stretching twin wires inside
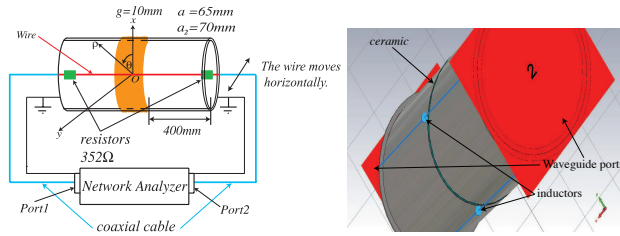
Figure 3: A schematic picture of the measurement setup. The orange in the left figure is the ceramic, which is replaced by the aluminum ring when $S_{21}^{ref}$ is measured.

the chambers and to observe the transmission coefficients for the differential mode. However, this method has an accuracy problem, since it is critical to enhance the ratio of the signal to the noise for precise measurements.

In this regard, we decided to take another method as a first step. We measure the longitudinal impedance by using a single wire, then, evaluate the transverse impedance by changing the wire position from $-30$ mm to $+30$ mm by 5 mm step in the horizontal direction. The transverse impedance is provided by detecting the second order coefficient for the wire position in the longitudinal impedance and by dividing it by the wavelength $k$ [13].

A schematic picture of the setup is shown in the left figure of Fig. 3. The longitudinal impedance is measured by stretching the wire with the radius 80 μm. The impedance is calculated by using the standard log-formula [5]:

$$ Z_L(x_w) = -2Z_{cc} \log \frac{S_{21}^{ceramic}}{S_{21}^{ref}}, \qquad (7) $$

where $Z_{cc}$ ($\simeq 402\,\Omega$ in our case) is the characteristic impedance for the coaxial-structure, $S_{21}^{ceramic}$ and $S_{21}^{ref}$ are the transmission coefficients for the case of the ceramic break sandwiched by the aluminum chambers and for the case that the ceramic break is replaced by the reference (aluminum) ring, respectively. The transmission coefficient $S_{21}$ is measured with 4-port Agilent technologies ENA Series Network Analyzer E5071C [14] by connecting the ports of the analyzer to the ends of the aluminum chamber through two coaxial cables. In order to assure the matching condition between the characteristic impedance $Z_{cc}$ and the impedance of the cable 50 Ω, 352 Ω resistors are connected at both the ends of the wire. The calibration is done by 2-port electric calibration module 85092,b.

A significant concern related to the measurement of the impedance of the ceramic break is intrinsic to that using Network Analyzer. The ceramic break has no electric path over the ceramic for DC current. The image current may find a different path from the one inside the ceramic gap for lower frequency, if the path provides a smaller impedance. It may be the internal of the Network Analyzer.

In order to cope with the effect, let us consider the model in the right figure of Fig. 3. To simulate the impedance concerning the image currents, four artificial inductors are

symmetrically connected between two waveguide ports, describing the signals from the Network Analyzer. In reality, when one terminal at the chamber is connected to one port at the Network Analyzer with 1 m long coaxial cable and the other terminal is done to the other port in the same way, the inductance due to the circuit composed of two cables and the Network Analyzer may be roughly estimated as a few μH.

Now, let us investigate the inductance dependence of the longitudinal impedance by the simulation with CST Studio [10]. The left figure of Fig. 4 shows the result for $x_w = 0$ with 0.9 μH inductors (red) and that with 2 μH inductors (black). The right figure of Fig. 4 shows the simulation result of the transverse impedance evaluated by the position dependence of the longitudinal impedance with the inductances (For reference, the result without the inductors is shown by the blue lines). Those results indicate that the longitudinal impedance can be reliably measured for the frequency higher than 0.3 GHz, which means that the resonance peak can be clearly identified in the transverse impedance. In other words, the amount of the peak value does not depend on the inductances under consideration.
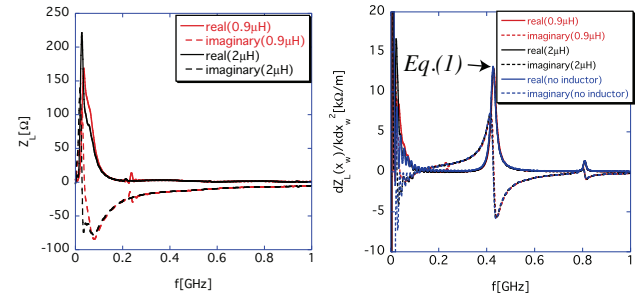


Figure 4: The inductance dependence of the simulated longitudinal impedance (left) and the corresponding result for the transverse impedance (right) evaluated by the longitudinal impedances with the several wire positions.
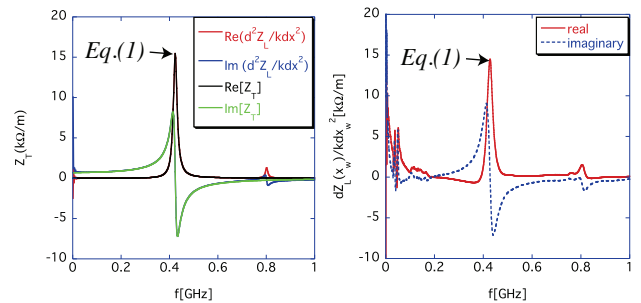


Figure 5: The simulation results by using a charged particle (left) and the wire-measurement results of the transverse impedance (right).

The right figure of Fig. 5 shows the measurement result. As expected, the measurement results at lower frequency are not reliable. Nevertheless, the resonance peak predicted by Eq.(1) can be identified. Moreover, the resonance peak around 0.8 GHz can be seen in the result. Such small peak

is visible also in the simulation result shown in the right figure of Fig. 4. But, notice that the peak does not appear in the original transverse impedance shown in the left figure of Fig. 2. In the simulation results, the transverse impedance is calculated according to its definition. Namely, it was done by integrating the transverse wake field excited by the horizontally shifted source particle (not the wire) along the center of the chamber, and by dividing it by the amount of the value of the horizontal position of the particle.

However, the longitudinal impedance measured by the shifted wire is equivalent to the impedance evaluated by integrating the longitudinal electric field along the same path as that on the shifted source particle, because the position of the witness particle and that of the source particle cannot be distinguished in this measurement setup. In order to demonstrate the speculation, let us calculate the longitudinal impedances by using a charged particle with and without the horizontal shift, where the integration path of the longitudinal electric field is identical to the path of the source particles. After that, let us evaluate the transverse impedance by detecting the position dependence of the longitudinal impedances. The red and blue lines in the left figure of Fig. 5 show the real and the imaginary parts of the results, respectively. For reference, the real and the imaginary parts of the transverse impedance based on the definition are shown by the black and green lines, respectively. While the resonance given by Eq. (1) is identical for both the cases, the small resonance peak around 0.8 GHz is missing in the black and green lines. From this excise, we can conclude that the peak around 0.8 GHz in the right figure of Fig. 5 is artificially created by intrinsic errors associated with the evaluation scheme of the transverse impedance by using the longitudinal impedance.

The measured result (the right figure of Fig. 5) is reliable, because it well-reproduces both the simulation results in the right figure of Fig4 and in the left figure of Fig. 5, including the artificial resonance peak around 0.8 GHz. It demonstrates the large resonance peak (shown by Eq. (1)) in the transverse impedance.

On the other hand, a disadvantage of the scheme using the shifted single wire is to produce the artificial resonances in the results. Consequently, a special care should be taken to compare the measurement result with the theoretical transverse impedance.

As shown in the left figure of Fig. 6, the ceramic break of MR is routinely covered by 12 capacitors. The impedance of one capacitor is measured, and it behaves like an inductor ($\sim 34.5$ nH) at high frequency. The transverse impedance is simulation by CST, by assuming that 12 inductors cover the ceramic break. The result is shown in the right figure of Fig. 6. The 16 k$\Omega$/m peak at 0.4 GHz in Fig. 2 is reduced to the 4.5 k$\Omega$/m peak at 0.7 GHz in Fig. 6 at MR.
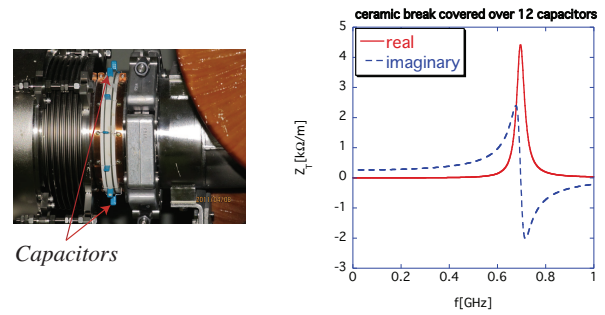


Figure 6: The ceramic break covered over 12 capacitors (left) and the simulation results of the transverse impedance by CST Studio (right).

## IMPEDANCES OF A CERAMIC BREAK COATED WITH TiN

Finally, we theoretically analyze the impedances of a ceramic break, where the inner surface of the ceramic is coated with resistive material (TiN) with the conductivity $\sigma_{TiN}(= 5.88 \times 10^6 S/m)$ and the thickness $t$. Numerical simulations are not suitable for the calculation of this kind of impedance, because extremely small mesh sizes are necessary (smaller than the thin TiN coating). In reality, typical coating size of TiN is a few ten nm in the ceramic break.
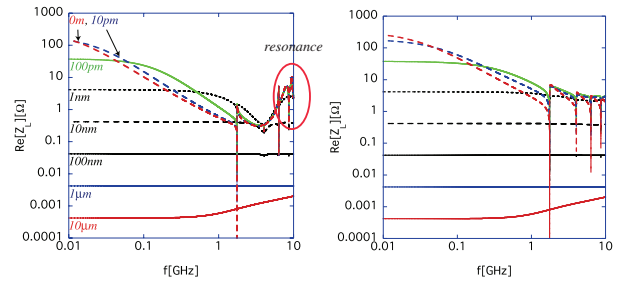


Figure 7: The thickness dependence of the longitudinal impedances of the ceramic break ($\epsilon' = 11$) with the TiN coating (left) and that of the resistive insert without the ceramic ($\epsilon' = 1$, right) for the size of $a = 65$ mm, $a_2 = 70$ mm and $g = 10$ mm.
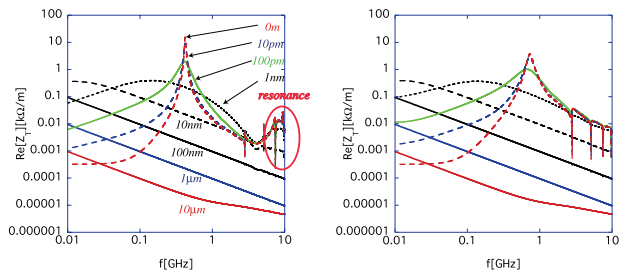


Figure 8: The thickness dependence of the transverse impedances of the ceramic break ($\epsilon' = 11$) with the TiN coating (left) and that of the resistive insert without the ceramic ($\epsilon' = 1$, right) for the size of $a = 65$ mm, $a_2 = 70$ mm and $g = 10$ mm.

Here, let us investigate the characteristic of the impedance with the thin TiN coating. Figures 7 and 8 show the longitudinal and the transverse impedances, respectively. The thickness dependence of the impedances is shown both for the ceramic break ($\epsilon' = 11$) with the TiN coating and the corresponding thin resistive insert without the ceramic ($\epsilon' = 1$) for the same size of gap. With the help of the discussion of the previous study [15], let us categorize the impedances of the ceramic break with the TiN coating for various TiN thickness. The frequency parameter $f_\delta$ (the frequency at which the skin depth is equal to the TiN thickness) is introduced as

$$f_\delta \equiv \frac{c}{\pi Z_0 \sigma_c t^2}, \qquad (8)$$

and the thickness parameter $t_{min}$ is as

$$t_{min} \equiv (\frac{4g}{\pi^2 Z_0^3 \sigma_c^3})^{\frac{1}{4}}, \qquad (9)$$

which is typically of the order of a few ten nm in the short ceramic break.

In all the cases, the TiN coating is sufficiently thin so that its thickness is less than the skin depth within the frequency frame of the figures ($f < 10\,\mathrm{GHz}$) except the $t = 10\,\mu\mathrm{m}$ case where the skin depth starts to fall short of the TiN thickness above $f_\delta$ ($\sim 1\,\mathrm{GHz}$). When the TiN coating is thick enough ($t > t_{min}$), but less than the skin depth, the entire image current runs on the TiN coating, and the impedance becomes proportional to $1/t$. Since the TiN coating almost perfectly shields the electromagnetic fields inside the beam chamber from leaking out to the ceramic, the appearance of resonances inside the ceramic is greatly suppressed. When the TiN coating is much thinner than $t_{min}$ (e.g. $t < 1\,\mathrm{nm}$), the electromagnetic fields starts to leak out through the TiN coating, and the existence of the ceramic and their resonance structures start to form the impedance (the left figures in Figs. 7 and 8).

## SUMMARY

The theoretical and numerical simulation results calculated by ABCI and CST Studio are compared. They are all in good agreement for the ceramic break without the TiN coating. Particularly, the agreements between the theoretical and ABCI's results are excellent, while CST Studio tends to provide higher impedances, notably at resonance frequencies, than the others.

The impedance of the ceramic break has resonance structures, because the difference of the dielectric constants between ceramic and the vacuum introduces the reflection of waves at their boundaries, and this reflection of electromagnetic fields at the lower and the upper boundaries of the ceramic creates trapped modes inside. The resonances can be categorized into the cavity-mode resonances and the coaxial-mode resonances.

Bench measurements have been done for the evaluation of the transverse impedance of the ceramic break. The measurement results demonstrate the existence of the large resonance peak at low frequency (0.4 GHz).

The theory can be applied to the calculation of the impedance of a ceramic break whose inner surface is coated with thin TiN. When the TiN coating is thick (larger than $t_{min}$), the entire image current runs in the TiN coating, which shields wake fields inside the chamber from reaching out to the ceramic. In this case, the existence of ceramic has no effect on the impedance. Consequently, the impedance becomes higher as the TiN becomes thinner.

## REFERENCES

[1] Y. Shobuda *et al.*, Physical Review ST Accelerators and Beams, **12**, 032401, (2009).

[2] K. Ohmi *et al.*, Physical Review ST Accelerators and Beams, **5**, 114402, (2002); PRST, **6**, 029901(E), (2003).

[3] Y.H. Chin *et al.*, in *proceedings of HB2006*, 125, Tsukuba, Japan, (2006).

[4] A.W. Chao, *Physics of collective beam instabilities in high energy accelerators*, Wiley, New York, (1993).

[5] *Handbook of Accelerator Physics and Engineering* edited by A.W. Chao and M. Tigner, World Scientific, Singapore, (1999).

[6] http://j-parc.jp/index-e.html

[7] Y. Shobuda *et al.*, Physical Review ST Accelerators and Beams, **17**, 091001, (2014).

[8] Y. Shobuda *et al.*, Physical Review ST Accelerators and Beams, **10**, 044403, (2007).

[9] Y. H. Chin, KEK Report 2005-06, (2005).

[10] CST STUDIO SUITE, https://www.cst.com/

[11] M. Abramowitz and I. Stegun, *Handbook of mathematical functions–with formulas, graphs, and mathematical tables*, (Dover Pub., New York, 1974).

[12] N. Biancacci *et al.*, Physical Review ST Accelerators and Beams, **17**, 021001, (2014).

[13] G. Nassibian and F. Sacherer, NIMA **159**, 21, (1971).

[14] http://www.agilent.com/home

[15] Y. Shobuda *et al.*, Physical Review ST Accelerators and Beams, **12**, 094401, (2009).

# IDENTIFICATION OF INTRA-BUNCH TRANSVERSE DYNAMICS FOR FEEDBACK CONTROL PURPOSES AT CERN SUPER PROTON SYNCHROTRON*

O. Turgut[†], C. Rivetta, and J.D. Fox, SLAC, Menlo Park, CA 94305, USA
W, Hofle, CERN, Geneva, Switzerland
S.M. Rock[‡], Stanford University, Stanford, CA, USA

## Abstract

A promising new approach for designing controllers to stabilize intra-bunch transverse instabilities is to use multi-input multi-output (MIMO) feedback design techniques. However, these techniques require a reduced model and estimation of model parameters based on measurements. We present a method to identify a linear reduced order MIMO model for the vertical intra-bunch dynamics. The effort is motivated by the plans to increase currents in the Super Proton Synchrotron as part of the HL-LHC upgrade where feedback control techniques could be applied to stabilize the bunch dynamics, allowing greater freedom in the machine lattice parameters. Identification algorithms use subspace methods to compute a discrete linear MIMO representation of the nonlinear bunch dynamics. Data from macro particle simulation codes (CMAD and HEADTAIL) and SPS machine measurements are used to identify the reduced model for the bunch dynamics. These models capture the essential dynamics of the bunch motion or instability at a particular operating point, and can then be used analytically to design model-based feedback controllers. The robustness of the model parameters against noise and external excitation signals is studied, as is the effect of the MIMO model order on the accuracy of the identification algorithms.

## INTRODUCTION

Electron clouds and machine impedance can cause intra-bunch instabilities at the CERN Super Proton Synchrotron (SPS). The high current operation of the SPS for LHC injection requires mitigation of these problems. Modern control techniques can be used to stabilize the bunch. These techniques are powerful tools allowing us to evaluate and understand the performance and the limits of the system beforehand. Yet, they require reduced order models of intra-bunch dynamics to design optimal or robust controllers for wideband feedback systems. System identification techniques can be used to get these required reduced order models.

Nanosecond-scale bunch stabilization is more challenging compared to the case of rigid body dipole coupled bunch oscillations. It requires sufficient bandwidth to sense transverse motion at multiple locations along the bunch and apply correction signals to the corresponding parts of the bunch.

Apart from these technological constraints, modeling the intra-bunch dynamics is also more challenging compared to the case of modeling the beam dynamics including bunch to bunch interactions.

The feedback system senses the vertical positions at multiple locations within the nanosecond-scale bunch. Control filters use these measurements to calculate correction signals and apply them back onto the bunch using the kicker as actuator. A 4 Gs/Sec. digital feedback system has been developed to process the motion signals and generate the correction actions [1]. Due to very the fast intrinsic time characteristics of the system, a parallel computation control filter architecture has been developed. A very similar method had been used for bunch by bunch feedback control systems [2].

In this paper, we show the use of system identification techniques to estimate parameters of linear models representing single bunch dynamics. We define the form of the reduced order model. We pose the identification problem in a least squares form [3] for given input-output data set. After a brief discussion of identification constraints, we show results of identification applied to data from SPS measurements and nonlinear macro particle simulation codes.

## MODEL AND IDENTIFICATION

### Reduced Order Model and Identification

Any linear dynamical system can be represented in state space matrix form. A discrete time system sampled at every revolution period $k$ with $p$ inputs and $q$ outputs is represented by

$$X_{k+1} = AX_k + BU_k$$
$$Y_k = CX_k \tag{1}$$

where $U \in R^p$ is the control variable (external excitation), $Y \in R^q$ is the vertical displacement measurement, $A \in R^{n \times n}$ is the system matrix, $B \in R^{n \times p}$ is the input matrix, and $C \in R^{q \times n}$ is the output matrix. For a MIMO system, the model order determines the complexity. In this study, we assumed time invariant dynamics which means having constant A, B and C matrices in the state space model. When it comes to the interactions between the bunch with electron clouds or during energy ramping operations, time variant dynamics has to be accounted for tune shifts, changing beam parameters, etc.

System identification techniques require exciting the system with appropriate signals and observing the response.

A dynamical model is estimated based on the measured input-output data. In particular for the bunch dynamics identification, the bunch is driven by a wide-band kicker using a persistent excitation and measuring the vertical displacements along the 3.2ns bunch length. The signals used in the identification process are input $U(k)$, where the vector represents the multiple momentum kicks applied to the different locations along the bunch and the output $Y(k)$ are the vertical displacements measured at those locations.

$$Y(z) = \left[ D^{-1}(z)N(z) \right] U(z) \qquad (2)$$

where [] represents the transfer function matrix ($\in R^{q \times p}$) for a system with $p$ inputs and $q$ outputs. $D(z)$ and $N(z)$ represent denominator and numerator of each discrete time transfer function between input-output couples.

$$N(z)U(z) - D(z)Y(z) = 0 \qquad (3)$$

$$U(z) = \sum_{i=0}^{T} U_i z^i, \quad Y(z) = \sum_{i=0}^{T} Y_i z^i \qquad (4)$$

$$D(z) = \sum_{i=0}^{m} D_i z^i, \quad N(z) = \sum_{i=0}^{n} N_i z^i \qquad (5)$$

$$\left[ N_r \mid -D_r \right] \begin{bmatrix} U(k) \\ Y(k) \end{bmatrix} = 0 \qquad (6)$$

Given the input and output signals, the estimation of the parameter matrices $N_r$ and $D_r$ is obtained by solving the last linear equation. There are many different subspace based methods to solve this linear MIMO problem. These methods use projections or singular value decomposition (SVD) to cast the problem into linear least squares [4]. We follow [3] where the construction of the data matrix from input and output signals, the solution algorithm for Equation 6 and the relationship between the transfer function coefficients and the observable canonical state space form are shown. Assuming full observability of the system, we can represent our state space in discrete time observable canonical form. This will enable us to estimate the minimum number of parameters [3]. However, even for linear systems there are two well known limitations for identification. These are the effect of noise and lack of persistent excitation.

*Persistent Input and Noise Sensitivity*

Input signal design and persistent excitation are critical aspects of system identification. Given a quasi-stationary input of $u$ with a dimension $nu$ and with a spectrum $\phi_u(\omega)$, $\phi_u(\omega) > 0$ should hold for at least $n$ distinct frequencies for $u$ to be a persistent excitation [5]. Random noise would be ideal to excite all the modes in the system but requires high excitation power and bandwidth. The hardware used in these measurements puts constraints on both power and bandwidth. The design of an input signal for identification under given constraints becomes an important question for the future studies.

Noise affects the performance of the identification, and in certain cases can make identification impossible. We
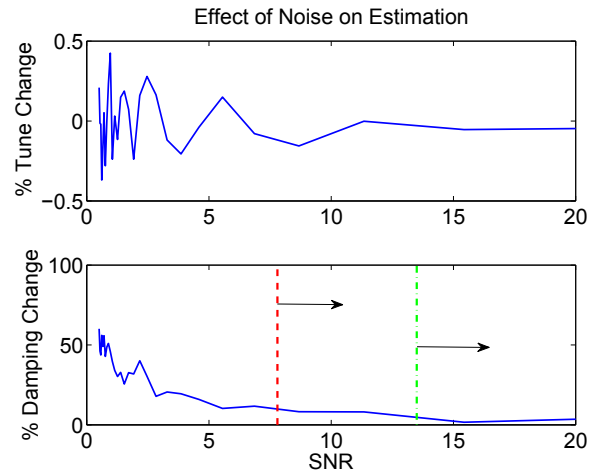
Figure 1: Deviation of estimated natural tune and damping of the $1^{st}$ mode from the true value for different SNR values. Red line shows min SNR to get errors less than 10%, green line is for errors less than 5%.

can quantify its effect by adding noise at different power levels into a known system until the identification can no longer clearly estimate the known dynamics. We drive a synthetic $2 \times 2$ coupled MIMO system using a band limited frequency chirp signal. Random noise at different power levels was added to the output signals. The effect of noise is tested by running the identification algorithm on input - output data as we increase the noise level. Parameters of the model and the corresponding modes of the identified model are estimated for different noise level cases. We quantify the effect of the signal to noise ratio (SNR) by comparing the estimated parameters of the system with the original $2 \times 2$ MIMO system. Figure 1 shows the impact of noise on the estimation of system parameters. For identification algorithm to perform well, we need a SNR $> \sim 8$.

## APPLICATIONS

Multiples MDs have been conducted at the CERN SPS ring to drive the bunch with different excitations (open loop) and also test feedback controllers to stabilize the bunch (closed loop). Those measurements were conducted using a single bunch in the machine with intensities of about $1 - 1.5 \times 10^{11}$ protons at the injection energy, 26 GeV and Q26 lattice configuration [6, 7]. The driven tests with different excitation signals have been designed such that the kicking signal is a persistent input for the system, and the collected data can be use to study the identification algorithms and quantify a reduced parametric model of the beam dynamics. Similarly, data obtained from macro-particle simulation codes (CMAD-HEADTAIL) has been used to test the identification algorithms and compare the dynamic model results with those obtained from machine measurements.

*SPS Measurements*

The hardware installed in the CERN SPS allows us to drive the bunch with limited bandwidth. The kicker used for

these tests has a maximum bandwidth of 160 MHz, limiting the spectrum of the momentum applied to the bunch. This limit conditions the number of modes that can be identified in the dynamic model because the final momentum is not a persistent input to detect high order transverse modes in the bunch. New kicker designs, fabrication and installation in the CERN SPS ring are in progress to be able to drive the bunch at higher frequencies [8].

The existing limited bandwidth kicker forces us to set our reduced model to detect low order modes corresponding to frequencies up to the second sideband ($2f_s$) around the betatron frequency ($f_\beta$). We use both mode 0 (barycentric shape along longitudinal axis) and mode 1 (a 200 MHz single cycle sine wave shape) excitation signals for which the amplitude is modulated with a frequency chirp [1]. The chirp covers $f_\beta \pm 2f_s$ in $\sim$ 15000 turns. Time alignment between excitation signals and bunch gives us the flexibility to excite a specific mode more dominantly. To improve the SNR used in the identification, the vertical motion signal is processed using a time-varying band-pass filter whose central frequency follows the frequency variation of the excitation signal applied.

Tailoring the reduced model to the low-order modes, it is possible to use 4 coupled $2^{nd}$ order differential equations to capture the low-order dynamics of the bunch (mode 0 - barycentric motion and mode ±1 - head-tail motion). The input-output relationship (momentum kick to vertical displacement) of the bunch is defined by a 4 ×4 MIMO system with $p = 4$, $q = 4$ and $n = 8$. This MIMO model sets the input and output vectors dimension (equation 1) to 4 for each sampling instance $k$. The measurement set-up acquires either 16 or 32 samples across the bunch at each sampling time $k$ for the momentum kick and the vertical displacement signals. To do identification with the corresponding MIMO model, each sample in vectors $U_k$ and $Y_k$ ($\in R^{4 \times 1}$) is calculated averaging either 4 or 8 consecutive non overlapping samples of the 16 or 32 samples long original data (e.g $U(1,k), Y(1,k)$ is the average of samples 1-4, $U(2,k), Y(2,k)$, the average of samples 5-8 …etc).

Using these input-output signals, the identification algorithm is evaluated and some results are analyzed. Figure 2 shows the time evolution of the 4 components of the vertical displacement vector $Y_k$ for about 10000 turns. Measured data is represented by the blue trace and the response of the identified model is the red trace. It is important to notice that the reduced order model is linear time invariant and cannot capture external perturbations or parameter variations in the bunch. Still, the envelope of the amplitude of the intra-bunch vertical motion is captured in the time domain. The plots on the right show measurements and the response of the model in frequency domain for the same samples.

Figure 3 shows another data with strong excitation of both mode 0 and $1^{st}$ sideband (mode 1). We also see some motion around $2^{nd}$ and $3^{rd}$ sideband. On the left, we see the RMS spectrogram of the driven measurement with clear mode 0, mode 1, mode 2 and mode 3 excitation around turns $\sim$ 7000, $\sim$ 11500, $\sim$ 15500 and and $\sim$ 15500. On

the right side, we show the RMS spectrogram of bunch's vertical motion predicted by reduced model. It is important to notice from the measured data (Fig. 3 - left) the effect of nonlinearities either in the driving system or in the bunch. The spectrogram analysis of the measured signal shows that the $2^{nd}$ ($f_\beta + 2f_s = 0.189$) and $3^{rd}$ sidebands are excited before the chirp excitation drives the bunch motion at that particular frequency. As expected, our linear model is able to capture dominant characteristics and linear dynamics such as motions at mode 0, mode 1 and mode 2 tunes, but not the effect attributed to the non-linearity in the system.

*Nonlinear Simulations*

Similar techniques were applied to data obtained by nonlinear macro particle simulation codes such as HEADTAIL and CMAD. These tools are especially very useful and helpful because they are accessible to study beam dynamics without beam time in the machine. As soon as simulations are benchmarked with machine measurements, the intra-bunch dynamics can also be identified using data from these simulations. As opposed to machine conditions and experiments, simulations have control over noise, disturbances, etc. This gives more flexibility and control to check the performance of the identification algorithm.

In the simulation, the bunch is represented by 64 slices. The bunch is excited by a chirp signal similar to the one used in the experimental tests at CERN SPS. The shape (along longitudinal axis) of the excitation signal is a 200 MHz sine wave (single cycle in a 5ns RF bucket) for a given turn and the amplitude of this head-tail shaped signal is modulated by a frequency sweep. The sweep covers from the $2^{nd}$ lower sideband to $2^{nd}$ upper sideband where betatron tune is 0.18 and synchrotron separation is 0.017 as given in Q-20 optics.

Figure 4 shows on the left side the vertical displacement data across the bunch for 1000 turns. Due to the shape of excitation signal across the bunch in this specific case, most of the excitation energy is coupled to ±1 lateral bands and we see very small amount of barycentric oscillations due to residual kick. With appropriate excitation signals we can study many multi-modal dynamics with the help of these simulations.

Figure 4 shows on the right side the response of the reduced order model to the same excitation in time domain. The relative error, which is calculated based on the maximum deviation of the model's response from the original simulation data, is less than $\sim$ 10%. The reduced order model can capture the dominant dynamics of the bunch successfully. Similarly, results can also be seen in frequency domain as show in Fig. 5 where on the left we see the spectrogram of the vertical displacement data from the simulation and on the right we have the spectrogram of the vertical displacement obtained by the reduced order model.

One of the important identification parameters that we can study is the estimation of the MIMO model order. Two different approaches could be used. In the first approach, as briefly explained in the "SPS Measurement" section we proposed the order of the system based on the persistent
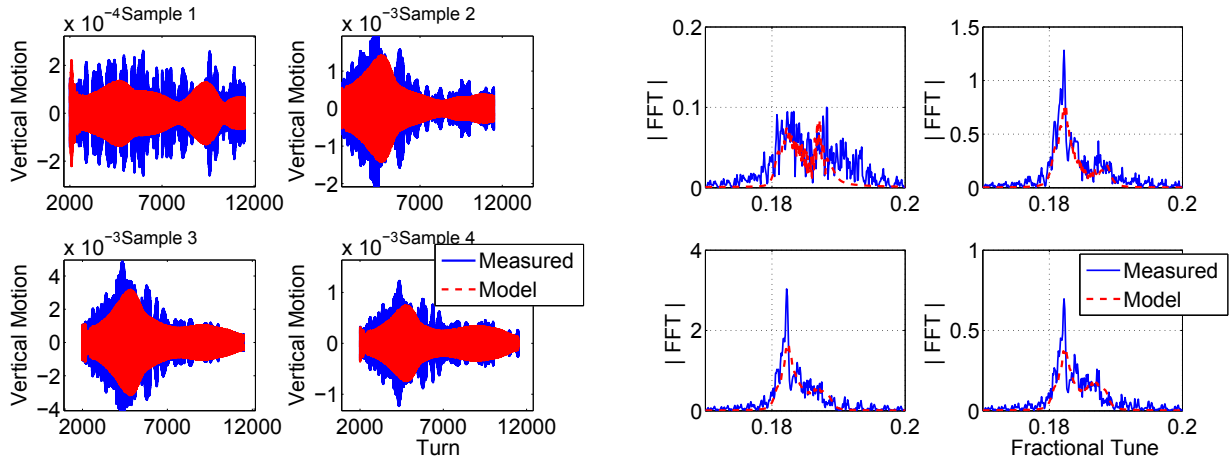
Figure 2: Comparison of the reduced order model responses with machine measurements in time (amplitude of vertical motion vs turns) and frequency domain. Dominant modes are mode 0 and mode 1 ($1^{st}$ upper sideband ).
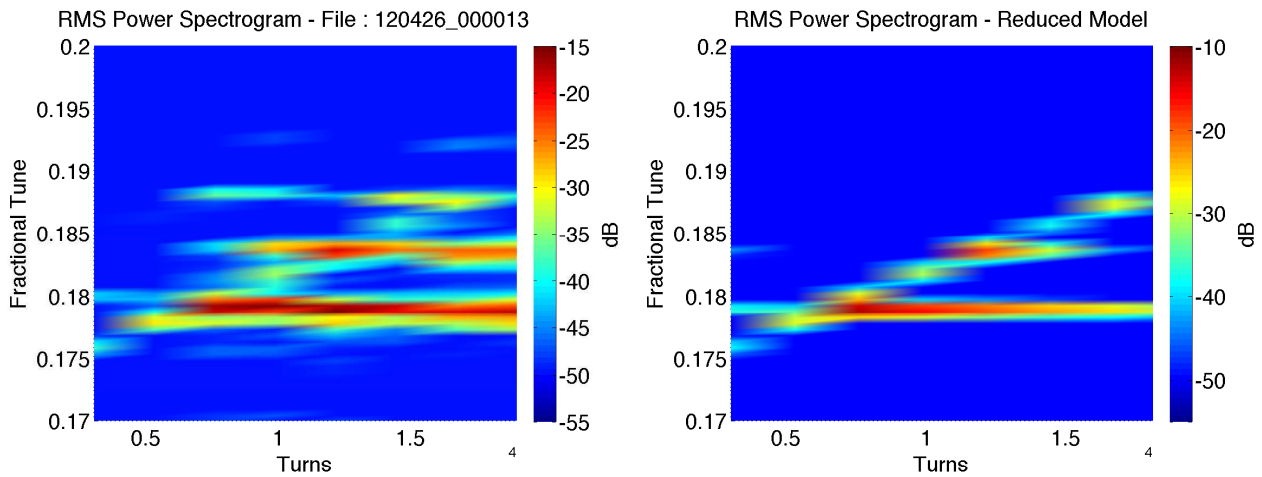


Figure 3: On the left we see the spectrogram of physical measurement showing chirp excitation where we excite mode 0, mode 1, mode 2, and mode 3 excitation around turns $\sim 7000$, $\sim 11500$, $\sim 15500$, and $\sim 17500$ respectively. On the right, we see the same excitation and analysis applied to the reduced order model capturing linear dynamics.
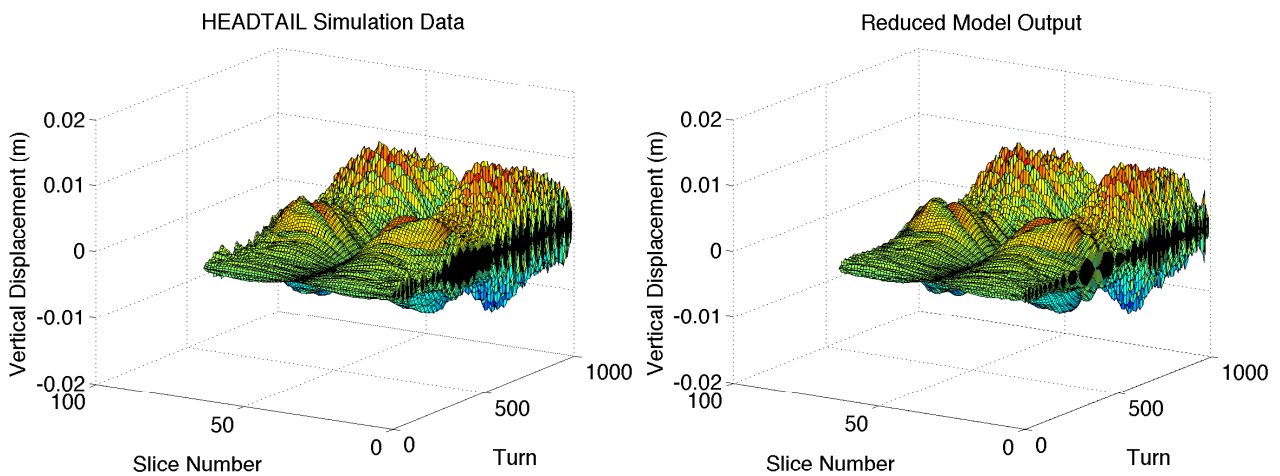


Figure 4: Comparison of the reduced order model response with HEADTAIL simulation data in time domain. Relative error between these two results are less than $\sim 10\%$. The reduced model and HEADTAIL simulation are driven by same excitation signal.
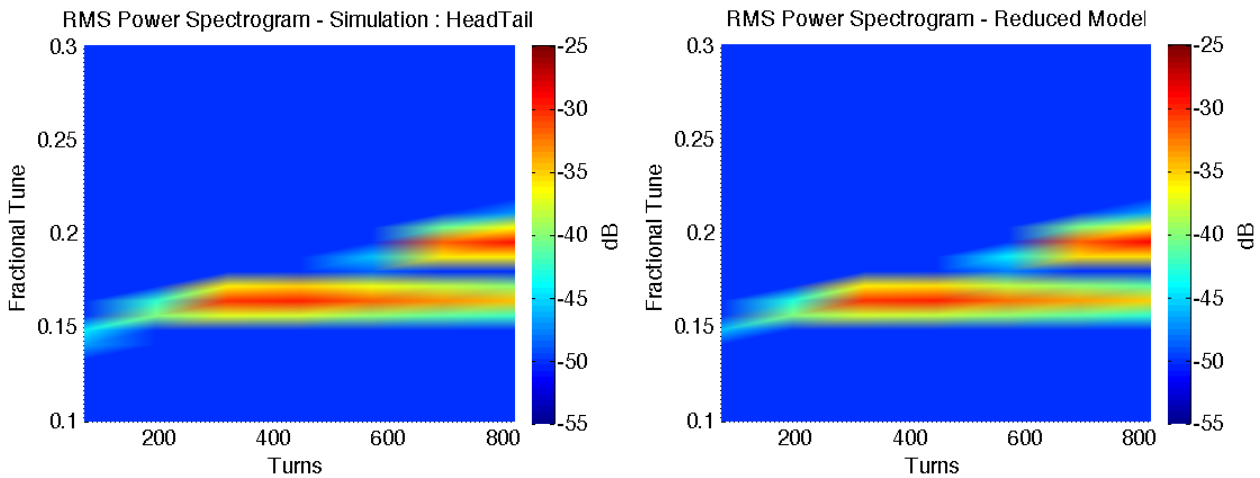
Figure 5: Comparison of the reduced order model response with HEADTAIL simulation data in frequency domain.

input signal. The model order was estimated based on the modes that the excitation signal is able to drive in the bunch and we constrained the input-output signals to identify that reduced model (e.g. we averaged the measured samples in order to reduce the number of inputs and outputs to identify a $4 \times 4$ MIMO system with $p = 4$, $q = 4$ and $n = 8$.). With the simulation data, we used the second approach in the analysis. All the individual samples across the bunch were taken into account to set $N \times N$ MIMO system with N inputs, N outputs and 2N states. Identification is performed based on an $N \times N$ MIMO model and then a model reduction technique is applied to the result based on Henkel Singular Value (HSVD) analysis to get a minimum order balanced realization of the model [4]. HSVD analysis indicates that relative contributions of the first 6 states of 128 states ($N = 64$ case) are noticeable higher than the contributions of the remaining states. Therefore, we can conclude that there are 6 states - 3 modes as dominant dynamics in the system and a reduced order model with 6 states (order of 6) is enough to capture dominant dynamics driven by this excitation signal.

## CONCLUSION AND FUTURE WORK

Model-based control design techniques for intra-bunch instabilities require a reduced model of the intra-bunch dynamics. We propose reduced order models and show initial results of the identification of those models. We identify parameters of a reduced order model that captures mode 0, mode 1 and mode 2 dynamics from the CERN SPS machine measurements. The natural tunes, damping values and the separation of modes associated with the motion seen in measurements are estimated correctly using a linear model. We also show similar results using macro particle simulation codes data. Dominant dynamics are captured with a reduced order model and simulation data is regenerated successfully in time domain. Future work is aimed at estimating more internal modes as the wideband kicker will be available early 2015. Availability of the new wideband kicker also requires careful analysis of persistency and optimality of the new excitation signals for the estimation of higher order internal

modes. Optimal and robust controllers will be designed using identified reduced order models. These new model based control architectures will be compared with the existing parallelized control filter architecture in terms of performance, processing power and complexity requirements. We plan to evaluate new controllers using macro particle simulations and test in the SPS with single bunch mid 2015.

## ACKNOWLEDGEMENTS

## REFERENCES

[1] J. D. Fox et al., "A 4 GS/s Feedback Processing System for Control Of Intra-Bunch Instabilities", IBIC2013, Oxford, UK 2013.

[2] D. Teytelman, "Architectures and algorithms for control and diagnostics of coupled bunch instabilities in circular accelerators, 2003, PhD Thesis, Stanford University.

[3] NF. Al-Muthairi et al., "Identification of discrete-time MIMO system using observable canonical-form" , IEE Proceedings - Control Theory and Applications, 2002.

[4] T. Katayama, "Subspace methods for system identification" , Springer-Verlag, 2007.

[5] M. A. Dahleh, "Lecture Notes - 6.435 System Identification", EECS, MIT, Spring-2005.

[6] J.M. Cesaratto et al., "First Results and Analysis of the Performances of a 4GS/s Intra-Bunch Vertical Feedback System at the SPS", IPAC2013, Shanghai, China 2013.

[7] C. Rivetta et al.,"Control of Intrabunch Dynamics at CERN SPS Ring using 3.2 GS/s Digital Feedback Channel", NA-PAC2013, Pasadena, CA, USA, 2013.

[8] J.M. Cesaratto et al., "A Wideband Slotted Kicker Design for SPS Transverse Intra-Bunch Feedback", IPAC2014, Dresden, Germany 2014.

# STUDY OF BEAM DYNAMICS IN LINEAR PAUL TRAPS

D.J. Kelliher, S. Machida, C.R. Prior, S.L Sheehy
STFC Rutherford Laboratory, ASTeC, UK.

## Abstract

The Hamiltonian governing the dynamics in a Linear Paul Trap (LPT) is identical in form to that of a beam in a focusing channel. This similarity, together with the LPT's flexibility, compactness and low cost, make it a useful tool for the study of a wide range of accelerator physics topics. Existing work has focused on high intensity collective effects as well as, more recently, the study of integer resonance crossing in the low intensity regime. A natural extension of this work is to investigate space-charge effects of intense beams in more realistic lattices to directly inform accelerator design and development. For this purpose we propose to construct a modified Paul Trap specifically for these studies. Among other features, it is envisaged that this new LPT should be able to model non-linear elements and a wider range of lattice configurations. This work will be undertaken in collaboration with Hiroshimi University.

## INTRODUCTION

In a linear Paul Trap ions are trapped transervsely by an oscillating RF field and axially by a static DC field. The use of such a device to study the transverse dynamics in a quadrupole channel was first proposed in ref. [1]. The equivalence between the two cases includes not only the Hamiltonian but also the Vlasov-Poisson equation [2]. It follows that the collective processes and transverse dynamics are identical in the two systems.

A LPT allows the study of beam dynamics in a relatively cheap and compact device. It also allows more flexibility in the choice of parameters (e.g. radio-activation by beam loss does not apply). The time allocated to study accelerator physics on production machines is normally limited - this is not an issue in an ion trap.

A wide range of beam dynamics experiments have already been conducted in LPTs including the study of collective modes [3, 4], the crossing of parametric resonances [5], the role of noise in emittance growth and halo production [6, 7], the adiabatic compression of a bunch [7] and resonance instability bands in doublet lattices [8].

Experiments to date have been done either on the Paul Trap Simulator Experiment (PTSX) device at Princeton, USA or on the Simulator of Particle Orbit Dynamics (S-POD) series of traps at Hiroshima, Japan. It is proposed to construct a new trap (or series of traps) at Rutherford Appleton Laboratory, UK. This will be done in close collaboration with the Hiroshima group.

While there is certainly much more that could be done using existing traps, it is worth investigating the broader range of experiments that might be made possible with modified designs. Here we consider a multipole trap to allow non-linear lattices to be studied. In the next section the essential formulae that inform the choice of the principal trap parameters are given. In later sections, collective effects, halo production, detuning and the flexibility in lattice choice are covered.

## LPT DESIGN

In the original "3D" Paul trap, the RF field is zero at just a single point at the centre of the device thus limiting the number of ions that can be cooled. By contrast a "linear" quadrupole field allows a string of ions to be cooled along the axis, hence the development of the linear Paul trap (also called a "linear quadrupole trap"). This device can be generalised to the "linear multipole trap" (henceforth referred to as a multipole trap) in which additional electrodes add non-linear field components [9].

For the case of a linear quadrupole trap, we follow the analysis in ref. [10], which starts with the envelope equation for each transverse plane. Throughout this paper we use $x$ and $y$ to refer to the two transverse coordinates and $z$ for the axial coordinate. In the horizontal case, assuming an rms radius $a$ and applying the smooth approximation, the equation is

$$\frac{d^2a}{d\tau^2} + \kappa^2 a - \frac{\epsilon_x^2}{a^3} = \frac{Nr_P}{2a} \tag{1}$$

where $r_p = q^2/4\pi\varepsilon mc^2$ is the classical particle radius, $N$ is the line density, $\kappa$ is a focusing constant and $\tau = ct$ and $\epsilon_x$ is the horizontal emittance given by

$$\epsilon_x = \frac{1}{mc}\sqrt{\langle x^2 \rangle \langle p_x^2 \rangle - \langle xp_x \rangle^2} \tag{2}$$

A similar equation applies in the vertical plane. The vacuum phase advance per RF oscillation $\sigma_0$ (equivalent to the phase advance per cell in an accelerator lattice) is defined as

$$\sigma_0 \equiv \kappa c/f = \frac{2\sqrt{2}qgV_0}{\pi^2 m}\left(\frac{1}{fR}\right)^2 \tag{3}$$

where f is the RF frequency, $R$ is the radius of the trap, $V_0$ is the amplitude of the RF waveform applied to the electrodes and $g$ is a shape function defined in [10]. Note - the transverse oscillation frequency $\omega_0$, which will be useful later, is given by $f\sigma_0$ and the transverse tune $\nu_0$ is $2\pi\sigma_0$. Assuming a stationary plasma ($\frac{d^2a}{d\tau^2} = 0$) and defining the transverse temperature $T_\perp$ to be

$$k_B T_\perp = \frac{\langle p_x^2 \rangle}{m} \tag{4}$$

where $k_B$ is the Boltzmann constant. One obtains

$$N = \frac{2}{r_P}\left[\sigma_0^2\left(\frac{af}{c}\right)^2 - \frac{k_B T_\perp}{mc^2}\right] \tag{5}$$

Equation (3) can be rearranged in terms of RF frequency

$$f = \frac{1}{\pi R} \sqrt{\frac{2\sqrt{2}q}{m} \frac{V_0 g}{\sigma_0}} \qquad (6)$$

and by substituting a $\sigma_0$ term in Eqn. (5) with Eqn. (3) yields the following

$$N = \frac{8\pi\epsilon}{q^2} \left[ \frac{2\sqrt{2}g\alpha^2}{\pi^2} qV_0\sigma_0 - k_B T_\perp \right] \qquad (7)$$

where $\alpha = a/R$ ($0 < \alpha < 1$). By arranging the equation for the line density in this way, it is made clear that it is proportional to $V_0$ for any fixed phase advance.

Table 1: PTSX and S-POD Trap Parameters

| Parameter | PTSX | S-POD |
|---|---|---|
| Length (m) | 2.0 | 0.1 |
| Radius (m) | 0.1 | 0.005 |
| Max voltage (V) | 235 | 100 |
| RF frequency (MHz) | 0.075 | 1.0 |
| Plasma radius (m) | $\sim 0.01$ | $\sim 0.001$ |
| Ion species | Cs-133, Ba-137 | Ar-40, Ca-40 |

From Eqn. 1 it can be shown that the depressed transverse oscillation frequency $\omega$ is given by

$$\omega^2 = \omega_0^2 - \frac{\omega_p^2}{2} \qquad (8)$$

where $\omega_0$ is the frequency in the zero intensity limit and $\omega_p = \sqrt{Nr_p c^2/a^2}$ is the plasma frequency (here we assumed the plasma density is uniform). The normalised tune depression $\eta$ is then given by

$$\eta \equiv \frac{\nu}{\nu_0} = \frac{\omega}{\omega_0} \qquad (9)$$

In the space-charge limit $\omega_p \to \sqrt{2}\omega_0$ and $\eta \to 0$. Recalling that the phase advance is given by $\omega/f$ then Eqn. (8) becomes

$$\sigma^2 = \sigma_0^2 - \frac{Nr_p}{2} \left( \frac{c}{fa} \right)^2 \qquad (10)$$

Using Eqn. (5), the above can be rewritten in terms of $\eta$

$$\eta = \sqrt{1 - \frac{1}{1 + (2/Nr_p)(k_B T_\perp/mc^2)}} \qquad (11)$$

Note, $\eta$ is independent of the mass of the ion species since $r_p \propto 1/m$. By cooling the plasma (using laser cooling techniques) towards absolute zero one can achieve $\eta \sim 0$ at which point the plasma enters a crysalline state (Coulomb crystal).

The main parameters to choose when designing a LPT are the frequency and voltage to apply to the electrodes, the trap radius and length and the choice of ion species. The
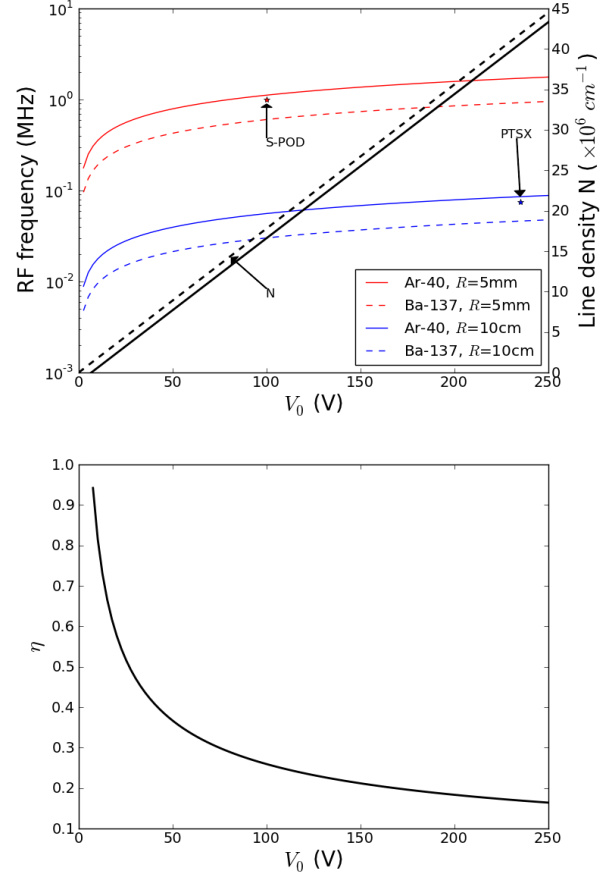




Figure 1: Top: Estimated line density and required RF frequency as a function of peak voltage $V_0$ for a stationary plasma with the phase advance set at $\pi/2$ in Eqns. (6, 7). The line density is shown with the temperature set to 1000 K (solid black line) and 0 K (dash black line). The RF frequency is shown for the case of Ar-40 and Ba-137 ions when the radius $R$ is 5 mm (red) and 10 cm (blue). The actual RF frequency and peak voltage employed by S-POD and PTSX are also indicated. The shape function $g \approx 0.712$ and $\alpha = 0.2$ have been assumed as in ref. [10]. Bottom: Normalised tune depression $\eta$ obtained from Eqn. (11), making use of the line density in upper figure, and assuming the temperature is 1000 K. At 0 K it is trivially equal to zero.

line density (and hence $\eta$) for a particular phase advance is given by the voltage and temperature (Eqn. (5, 11)). Once the voltage is chosen, the product of the RF frequency and the trap radius is a constant (Eqn. (6)).

This is illustrated in Fig 1 which shows the RF frequency versus voltage when the trap radius is 5 mm and 10 cm, corresponding to the radii of S-POD and PTSX, respectively. The principal parameters of these traps given in Table. 1. As can be seen in the table a substantially lower RF frequency is needed at the higher radius but at the expense of a much longer trap (the required length roughly scales with the radius to ensure end effects can be neglected). It is also apparent that very low values of $\eta$ (in accelerator terms)

can, in principle, be obtained in both traps at typical plasma temperatures of 1000 K.

## COLLECTIVE MODES

Sacherer found that coherent resonance condition is satisfied when the tune of a collective mode $\Omega_m$ is integer [11]. In terms of incoherent tune shift the resonance condition becomes

$$\nu_0 - C_m \Delta \nu \approx \frac{n}{m} \tag{12}$$

where $\nu_0$ is the bare tune, $\Delta \nu$ is the incoherent tune shift induced by space-charge and $C_m$ is a coherent mode coefficient which is less than unity for every mode [12]. It was later found [13] that resonances may also be driven at $\Omega_m \approx n/2$ which leads to

$$\nu_0 - C_m \Delta \nu \approx \frac{n}{2m} \tag{13}$$

The above implies the existence of a space-charge driven resonance at a quarter integer for the $m = 2$ mode. This resonance (among others) has been identified in LPT experiments in which both the stopband was measured [3] and the resonance crossed [5].

Direct detection of a collective mode can be made by measuring the signal it produces. It may not be feasible to detect the typically small perturbation voltage induced on the main electrodes. A separate capacitive pickup electrode was installed in one LPT in order to measure the collective mode signal [14]. This consisted of azimuthally segmented ring electrodes placed inside the main confining electrodes. The segmentation allows the discrimination of different azimuthal mode numbers. The radius of the electrode was carefully selected to allow the signal to be detected while not intercepting the plasma. Using this diagnostic the axisymmetric body-wave mode and quadrupolar surface mode were detected [14].

It is of interest to study how space-charge induced resonances can be enhanced or mitigated by applying nonlinear fields. In fact emittance growth and beam loss is often caused by chaotic motion near non-linear resonances which can be driven either by space-charge effects and/or non-linear elements [15]. An octupole introduces an amplitude dependent tune spread which can damp the effect of resonances [16]. For this study a multipole trap would be required.

Instabilites arising from various self-forces of a bunch are mainly of particular interest in cases where the space-charge is high (e.g. in high intensity linacs). Emittance exchange driven by the self-field of the perturbed bunch can lead to harmful instabilities. Assuming the unperturbed bunch has uniform density within the elliptic cross section defined by

$$\left(\frac{x}{a}\right)^2 + \left(\frac{y}{b}\right)^2 \leq 1 \tag{14}$$

we may write, assuming the smooth approximation, the transverse emittance ratio $\epsilon_x/\epsilon_y$ as follows

$$\frac{\epsilon_x}{\epsilon_y} = \frac{a^2 \nu_x}{b^2 \nu_y} \tag{15}$$

and the energy (temperature) anistropy $\tau$ as

$$\tau = \frac{\epsilon_x \nu_x}{\epsilon_y \nu_y} \tag{16}$$

for tunes $\nu_x, \nu_y$.

Dispersion relations for modes of various order are given in terms of these dimensionless parameters in ref. [17]. It is found that, in some cases and in certain parameter regimes, stable modes for round isotropic beams ($a/b = 1$, $\tau = 1$) become unstable in the anisotropic case. For example, the second order odd (tilting) mode is unstable for a sufficiently large anisotropy.

Although ref. [17] deals with anisotropy between the horizontal and vertical planes, the same results apply for the transverse and longitudinal planes. For a particular choice of emittance ratio, regions of instability can be found in terms of the normalised radial depressed tune $\nu_r/\nu_{r0}$ versus tune ratio $\nu_z/\nu_r$. These so-called "Hofmann Stability Charts" (Fig. 2 is an example) are widely used in the design of high intensity linacs. Experiments performed in linacs provide evidence of expected instabilities for certain values of temperature anisotropy [18].
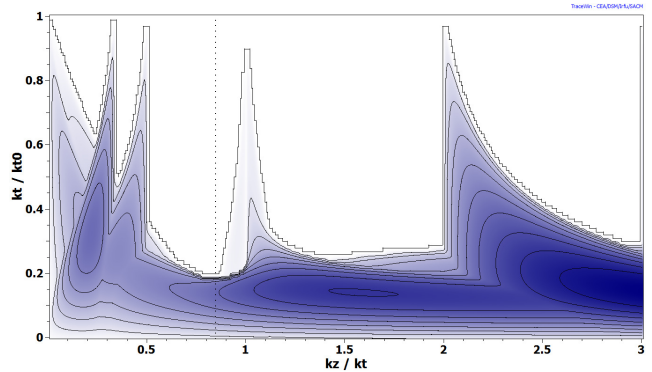


Figure 2: Example of a Hofmann Stability Chart for the emittance ratio $\epsilon_z/\epsilon_t = 1.2$ where $z$ and $t$ refer to the longitudinal and transverse planes, respectively. The vertical axis covers the full range of depressed tunes $k_t/k_{t0}$ while the horizontal axis is the tune ratio $k_z/k_t$. The contours show low to high emittance exchange between the two planes in increasingly dark shades of blue. The vertical dotted line corresponds to equal temperatures in the two planes, $\tau = 1$. This figure is from ref. [18] provided courtesy of the authors.

The idea of studying emittance exchange in a LPT is under consideration. For a stationary plasma in a linear Paul trap, the temperature among the three degrees of freedom is approximately uniform $T_x = T_y = T_z$. In order to investigate equipartition, it is desired that a controlled level of temperature anisotropy is introduced. This can be done by cooling along one or more degrees of freedom. Using laser cooling directed along the $z$ axis, the axial temperature $T_z$ can be substantially reduced while the transverse temperature $T_\perp$ remains relatively unaffected.

## HALO FORMATION

Halo formation was among the first beam dynamics topics to be suggested for study in ion traps [1]. In one study, by adding noise to the quadrupole electrodes for many oscillations of the confining RF the growth of a non-thermal tail of trapped ions was observed [6]. Halo formation has also been observed in a Penning trap [19]. Evidence for halo formation can be found by extracting the ion plasma and measuring the charge as a function of radius using a multi-channel or transversely moveable Faraday Cup [1, 6] (or phosphor plate imaged by CCD camera). In modern high intensity accelerators, beam loss may be even lower than the 1% level [20]. It follows that diagnostics used on the LPT should have sufficient resolution to detect very small halo populations.

In recent years, studies of halo formation have concentrated on the interplay of space-charge forces, non-linear lattice elements (e.g. octupole) and synchrotron motion. Frozen core models have been developed which allow the particles outside the core to be treated separately from those within. The synchrotron motion modulates the tune via the uncorrected chromaticity, but also modulates the space-charge force in the transverse plane and hence the depressed betatron tune [21]. Since the synchrotron tune is much less than the betatron tune, the effect is an adiabatic modulation of transverse phase space [22]. Although longitudinal effects cannot be studied in a conventional LPT, the transverse phase space could be adiabatically modulated, for example by slowly varying the RF voltage of the quadrupole electrodes (and so the tune), to emulate this process.

In order to study halo formation in detail, and see evidence for effects such as scattering from or trapping in resonant islands and diffusion from chaotic regions, a real-time, high-resolution, non-destructive measurement of phase space would be invaluable. Such a measurement is in principle possible using the technique of laser-induced fluorescence (LIF) [23].

## RESONANCE CROSSING AND DETUNING

One or more resonances can be crossed in a LPT and the effect on the number of trapped ions can be measured. As well as the space-charge induced resonances mentioned earlier, the crossing of integer tune resonances excited by dipole errors has also been studied [24]. The tune can be varied in a single experiment by varying either the voltage or frequency of the waveform applied to the confining electrodes (Eqn. (3)). A dipole error is introduced by applying an additional RF signal to one or two of the electrodes. This perturbation waveform should be a harmonic of the confining RF in order to create a stopband around a single integer only. Multiple integer resonances can be excited by perturbing with a superposition of harmonics.

Some of the results from the integer tune crossing study suggests the influence of high order multipoles [25]. Imperfections in the electrode construction and alignment results in non-zero multipole components [10]. It would be interesting to carry out a resonance crossing study in a multipole trap to measure the effect of a controllable level of non-linearity.

If the tune is set to be exactly on an integer resonance, a dipole kick should cause the magnitude of coherent oscillations to grow without bound. Non-linearities may cause the tune to move away from the resonance via amplitude detuning. If the non-linearity is strong enough, or the dipole kick low enough, the growth of the centroid amplitude of the plasma will reach a plateau. It is predicted that in the case of linear amplitude detuning ($\nu = \nu_0 + \mu I$), the plateau should scale with $(F/\mu)^{1/3}$ where $F$ is the magntitude of the dipole perturbation, $I$ is the amplitude in $\mu$ the detuning coeficient [26]. Detuning with amplitude could be a topic for study in a multipole trap.

## LATTICE FLEXIBILITY

Most beam dynamics studies to date have simulated FODO lattices since it can be implemented by simply applying a sinusoidal waveform to each electrode. Doublet, triplet and FFDD lattices have recently been created by adding waveforms with the appropriate structure [19]. Lattices with unequal tunes in the two transverse planes can also be realised by applying different pulse widths to each pair of electrodes. The dependence of space-charge resonances on the lattice configuration was investigated for the doublet case [8], a study that could be extended to other lattice configurations.

It would be of interest to implement the lattices of existing or planned accelerators for study in a LPT. A multipole trap would greater extend the reach of ion trap experiments by allowing non-linear elements to be included. The relative timing of the voltage pulses applied to the electrodes for each multipole order would allow the ordering of the "magnets" to be chosen.

For example, the field in a scaling FFAG varies with radius $r$ according to $B = B_0(r/r_0)^k$ where $k$ is the field index and $B_0$, $r_0$ are defined at some reference radius. Though this field profile contains multipoles of every order, it can be approximated by truncating around $r_0$ the multipole expansion of the field profile $B = \sum_n k!/(n!(k-n)!) * ((r-r0)/r0)^n$ (as was done for the PAMELA FFAG design [27]). The practicalities of trap design would need to be considered for a significant number of multipoles.

## DISCUSSION

The potential for beam physics studies in LPTs would be greatly extended in traps with higher order multipoles and by the use of a non-destructive, in-situ diagnostic such as LIF. Pure multipole traps have already been constructed for the purpose of reducing rf heating (and so create a greater volume in which ions are cooled). However, as far as the authors know, no LPT in which more than one multipole may be individually set has yet been constructed.

A design for such a trap, with adjustable quadrupole and octupole electrodes is presented in [10]. Inside the main

confining quadrupole electrodes, sit four octupole electrodes with much smaller radii. Simulations confirm that the octupole component can be specified by sending a separate waveform to this set of electrodes. Further progress has recently been made on multipole trap designs [28].

Several practical difficulties are envisaged - including the screening of the potential from one set of electrodes by another, the effect of unwanted multipoles induced by imperfections in the electrode smoothness or alignment and the extra electronics and feedthrough cables required to feed ~MHz signals to many electrodes without reflections, and with the correct phase and amplitude.

## ACKNOWLEDGMENT

## REFERENCES

[1] H. Okamoto, H. Tanaka, Nucl. Instr. Meth. A 437, 178 (1999).

[2] R.C. Davidson, H. Qin and G. Shvets, Phys. Plasmas 7,1020 (2000).

[3] S. Ohtsubo et al., Phys. Rev. ST Accel. Beams 13, 044201 (2010).

[4] E. Gilson et al., Phys. Plasmas 20, 055706 (2013).

[5] H. Takeuchi et al., Phys. Rev. ST Accel. Beams 15, 074201 (2012).

[6] M. Chung et al., Phys. Rev. Lett. 102, 145003 (2009).

[7] E. Gilson et al., Phys. Plasmas 17, 056707 (2010).

[8] K. Fukushima et al., Nucl. Instr. Meth A 733, 18-24 (2014).

[9] F.G Major, V.N. Gheorghe, G. Werth, *Charged Particle Traps*, (Berlin: Springer, 2005), 109.

[10] H. Okamoto et al., Nucl. Instr. Meth A 485, 244-254 (2002).

[11] F.J. Sacherer, Ph.D thesis, Lawrence Radiation Laboratory [Report No. UCRL-18454].

[12] R. Baartman, Proc. of the Workshop on Space Charge Physics in High Intensity Hadron Rings (AIP, Shelter Island, 1998), p. 56.

[13] H. Okamoto, K. Yokoya, Nucl. Instr. Meth. A 482, 51 (2002).

[14] E. Gilson et al., Nucl. Instr. Meth A 606, 48-52 (2009).

[15] K. Ohmi, Proc. of IPAC13, Shanghai, China, 1589 (2013).

[16] A.V. Fedotov, J. Wie, V. Danilov, Proc. of IPAC13, Shanghai, China, 1589 (2013).

[17] I. Hofmann, Phys. Rev. E 57(4), 4713 (1998).

[18] C. Plostinar, M. Ikegami, Y. Liu, T. Maruta, Proc. of IPAC13, Shanghai, China, 3966 (2013).

[19] H. Okamoto et al., Proc of IPAC14, Dresden, Germany, 4056 (2014).

[20] H. Hotchi, Prog. Theor. Exp. Phys. 02B003 (2012).

[21] G. Franchetti et al., Phys. Rev. ST Accel. Beams 13, 114203 (2010).

[22] A. Bazzani et al., AIP Conf. Proc. 773, 158 (2005).

[23] M. Chung et al., Nucl. Instr. and Meth. A 544, 514-519 (2005).

[24] D.J. Kelliher et al., Proc of IPAC14, Dresden, Germany (2014).

[25] K. Moriya et al., Submitted for publication (2014).

[26] S.R. Mane and W.T. Weng, Nucl. Instr. Meth. A 306, 9-20 (1991).

[27] S.L. Sheehy et al, Phys. Rev. ST Accel. Beams 13, 040101 (2010).

[28] H. Okamoto, K. Fukushima, K. Ito, T. Okano, TUO2LR03, HB2014, these proceedings (2014).

# CHARACTERISATION OF THE KURRI 150 MeV FFAG AND PLANS FOR HIGH INTENSITY EXPERIMENTS

S. L. Sheehy*, D. Kelliher, S. Machida, C. Rogers, C. R. Prior, ASTeC/STFC/RAL, United Kingdom
On behalf of the KURRI-FFAG collaboration

## Abstract

Fixed field alternating gradient (FFAG) accelerators hold a lot of promise for high power operation due to their high repetition rate and strong focusing optics. However, to date these machines have not been operated with high intensity beams. Since November 2013 an experimental collaboration has been underway to characterise the 150 MeV proton FFAG at KURRI, Japan. Here we report on the results of characterisation experiments and discuss plans for further experiments in the high intensity regime.

## INTRODUCTION

Fixed field Alternating Gradient (FFAG) accelerators combine strong focusing optics like a synchrotron with a fixed magnetic field like a cyclotron. Unlike a synchrotron, the magnetic field experienced by the particles is designed to vary with radius, rather than time. This naturally leads to the potential to operate at high repetition rates limited only by the available rf system, while strong focusing provides a possibility of maintaining higher intensity beams than in cyclotrons.

A revival in interest since the 1990s has seen a number of FFAGs constructed, including scaling and linear non-scaling variants. However, high bunch charge operation remains to be demonstrated. A collaboration has been formed to use an existing proton FFAG accelerator at Kyoto University Research Reactor Institute (KURRI) in Japan to explore the high intensity regime in FFAG accelerators. Work has so far been aimed at characterising this machine in detail. Later experiments will be aimed at demonstrating high bunch charge operation in an FFAG accelerator and exploring the fundamental intensity limitations of these machines.

### The KURRI 150 MeV ADSR-FFAG

The 11–150 MeV ADSR-FFAG at KURRI [1] (shown in Fig. 1) is a scaling FFAG where the main magnetic field follows a power law with radius,

$$B_z(r) = B_0(r/r_0)^k. \quad (1)$$

The field index, k, is designed to be 7.6 and other parameters are given in Table 1.

The primary operational goal of the 150 MeV FFAG is to undertake basic studies toward the realisation of Accelerator Driven Systems (ADS) [2]. It is also used for irradiation experiments for industrial use, medical applications such as BNCT as well as radiobiology experiments.

Figure 1: The KURRI 150 MeV FFAG is the larger ring shown here with the pre-2011 injector ring. Injection from the new linac occurs in the top left of the image.

The ring consists of twelve DFD magnet triplets which are an innovative 'yoke-free' design [3] which allows the beam to be injected and extracted through the side of the magnets.

Originally injected by a low energy proton booster ring, in 2011 the injector was upgraded to an 11 MeV H$^-$ linac to increase the beam intensity from roughly $6 \times 10^8$ ppp to up to $3.12 \times 10^{12}$ ppp [4]. The beam is now injected using H$^-$ charge exchange injection on a 20 μg.cm$^{-2}$ carbon foil. No bump system is used as the beam moves radially away from the foil as it is accelerated.

At present the linac provides 10 nA average current ($3.12 \times 10^9$ ppp) with a bunch length of 100 μs at injection and 0.1 μs at extraction, operating at a 20 Hz repetition rate. In principle the linac can provide up to 5 μA average current.

Table 1: Parameters of the 150 MeV FFAG

| Parameter | Value | |
|---|---|---|
| $r_0$ | 4.54 | m |
| Cell structure | DFD | |
| $N_{cells}$ | 12 | |
| k, field index | 7.6 | |
| Injection Energy | 11 | MeV |
| Extraction Energy | 100 or 150 | MeV |
| $f_{rf}$ | 1.6-5.2 | MHz |
| $B_{max}$ | 1.6 | T |

## CHARACTERISATION EXPERIMENTS

Two experimental periods in early to mid-2014 were allocated to characterisation of the FFAG. Here we describe a few selected results.

### Injection Matching

The H⁻ beam follows a complex trajectory from the outside of the main ring magnets, through the open magnet side and in to the stripping foil. A simulation of this trajectory based on 3D design field maps, benchmarked in ZGOUBI [5] and an in-house code at KURRI, is shown in Fig. 2. Matching of position and angle at the stripping foil is achieved by adjusting horizontal and vertical steerers upstream. The vertical orbit is considered matched when the amplitude of coherent oscillations observed on the bunch monitors is minimised. For the purposes of characterisation experiments, horizontal orbit matching is adjusted empirically to maximise the number of circulating turns of a coasting beam at injection energy. In user operation this is optimised to give the best extracted beam current.
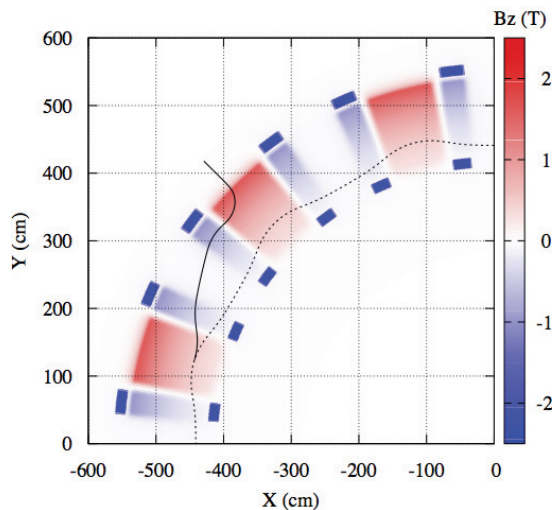


Figure 2: Injection trajectory of H⁻ beam shown as a solid line overlaid on the design $B_z$ field. The dashed line corresponds to the circulating closed orbit and the stripping foil is located where the two paths intersect.

### Closed Orbit Distortion

One of the most challenging aspects of this FFAG is the existence of a large closed orbit distortion (COD), consistent with a single large perturbation at the location of the rf cavity. The rf cavity shown in Fig. 3 is a broadband cavity employing magnetic alloy material [6] which was thought to be absorbing stray magnetic field from the main magnets and thus affecting the closed orbit.

The drawback of the yoke-free magnet design is that the magnets have been found to produce significant stray field.
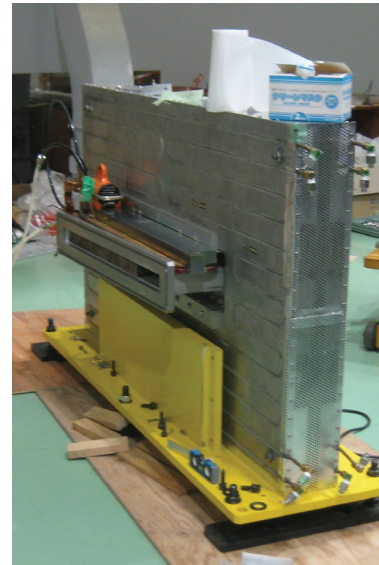


Figure 3: The broadband magnetic alloy rf cavity.

The rf cavity is located in one of the straight sections and is thought to be absorbing this stray field, breaking the symmetry of the ring and affecting the orbits and overall dynamics of the FFAG.

In late 2013 the rf cavity was temporarily removed to install new corrector magnets. With the cavity physically removed the opportunity was taken to test the assertion that the cavity is the main source of COD. A beam was injected into the ring and the closed orbit measured using three radial probes at different azimuthal locations around the ring. Despite being located at different azimuths, the probes are all in the centre of F magnets. As such the radial position of the orbit should be the same at all three locations. This was confirmed and no discernible COD was measured.

After re-installing the cavity the COD was re-measured, confirming that the major source of COD is the cavity itself. The new corrector poles were then tested to check how well they corrected the COD. Radial probes at three azimuthal locations were inserted into the ring and the time to loss of the beam was measured as a function of radius during acceleration. If there was no COD present, the three probes would measure the same time to loss at a given radius, as they are all located in the centre of F magnets. Thus for each corrector setting and for a given time, the deviation from the mean of the beam radius between the three probes gives us an estimate of the COD. The mean of the three probes is used as the zero point as there is no easily definable 'closed orbit' in an FFAG accelerator as there would be in a synchrotron.

The COD is fairly constant throughout the acceleration cycle, so can be represented simply as the average over time with a standard deviation error bar to indicating the variation of COD during the acceleration cycle. This is plotted for each probe in Fig. 4.

These results indicate that the corrector is reducing the COD, but further correction is still needed. Unfortunately the corrector excitation current was limited during this ex-

perimental run to a maximum of 700 A. Correction of the COD is a priority and work is continuing on this, including changing the corrector power supply to increase the field provided.
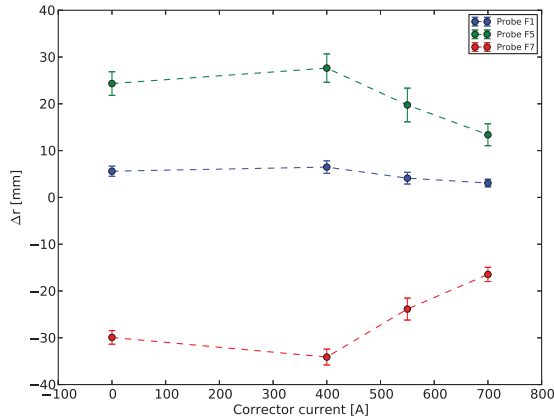


Figure 4: Closed orbit distortion quantified in terms of the variation in radial beam position from the mean at three different azimuthal locations, averaged over the acceleration cycle.

## *Dispersion in the Main Ring*

The dispersion was measured in the injection line, at the position of the stripping foil and in the main ring. Figure 6 shows the dispersion in the main ring measured using the same three radial probes as in the closed orbit distortion measurement. The dispersion can be calculated using the radius vs time radial probe data where momentum values are inferred from the applied rf programme shown in Fig. 5.

$$D = \frac{\Delta r}{dp/p} \quad (2)$$
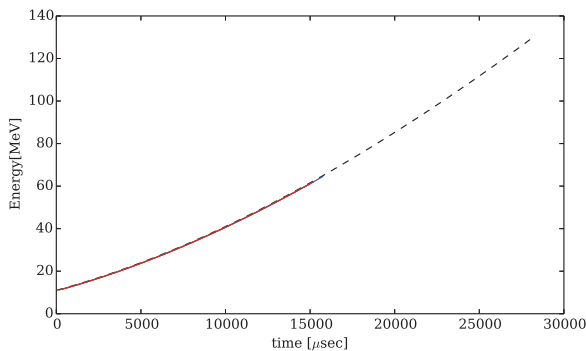


Figure 5: Energy gain vs time of the applied rf pattern. The red line corresponds to the part used for analysis of the dispersion data.

Ideally all three results would be identical, but the discrepancy between them arises due to the presence of closed orbit
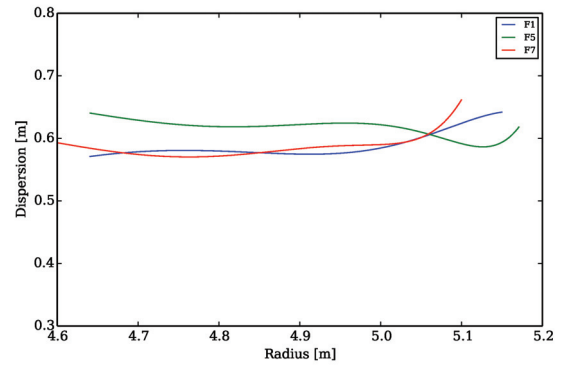


Figure 6: Dispersion in the ring as a function of radius measured using three different radial probes.

distortion. This is currently being studied in detailed simulations. However, the measurement shows that the dispersion is close to the design value of D=0.55 m at the centre of the F magnet.

## *Field Index*

The field index, k, is defined in the design procedure to be 7.6, but in reality the field produced by the magnets does not follow the scaling law of Eq. 1 perfectly. We can define an effective field index which can then be measured throughout the acceleration cycle based on the revolution frequency and radial beam position variation.

$$k = \gamma^2 \frac{df/f}{dr/r} - (1 - \gamma^2) \quad (3)$$

The frequency is obtained from the rf programme and the radial beam position is measured throughout the acceleration cycle. The relativistic $\gamma$ factor is inferred from the rf programme. The measured effective field index is shown in Fig. 7, where again there is a discrepancy between the three measurements of the different radial probes.
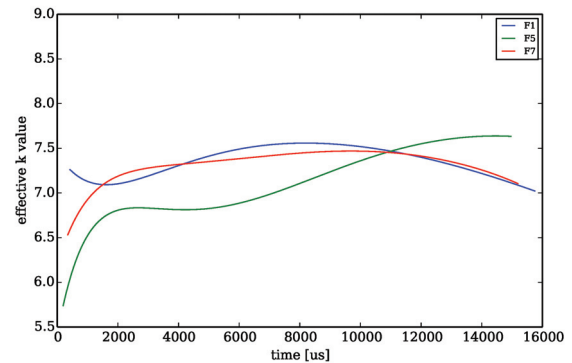


Figure 7: Effective field index, k, as a function of time during the acceleration cycle measured using three different radial probes.

*Betatron Tunes*

A number of methods can be used to measure the betatron tunes in this machine. The results shown in Fig. 8 were obtained using horizontal and vertical rf 'perturbator' devices and analysing the bunch turn-by-turn data using a real time spectrum analyser to find sidebands in the frequency spectrum. This required the design and implementation of a range of devices including a radially movable horizontal rf perturbator device and radially movable horizontal triangle BPM.
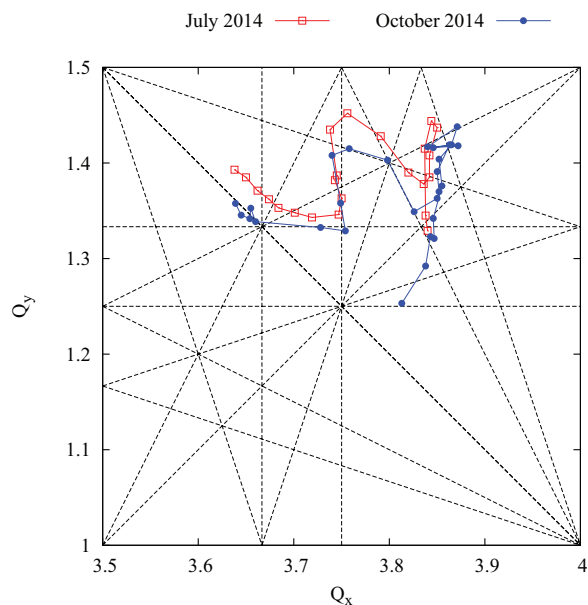


Figure 8: Measured horizontal and vertical ring tunes ($Q_x$, $Q_y$) throughout acceleration measured in July 2014 and an additional recent measurement in October 2014 with adjusted F/D ratio and after removal of unnecessary magnetic material.

*Effects of the Stripping Foil*

A key issue in this FFAG for high intensity operation is the effect of the stripping foil on the beam. In order to perform detailed studies at high intensity it is desirable to be able to measure the increase in beam emittance caused by space charge effects. This will compete with the emittance growth from foil scattering as the beam passes many times through the stripping foil at injection.

It is also necessary to understand the energy loss of the beam as it passes through the foil. Simulation work has been performed to study the energy loss and energy distribution after passing through the foil multiple times. An experimental measurement of the energy loss per turn in the foil has been carried out to measure the synchronous phase as a function of rf voltage. Analysis of the experimental data is in progress.

## DISCUSSION AND FUTURE PLANS

Although the present beam intensity is sufficient for ADS experiments, there remains substantial beam loss throughout the acceleration cycle, as shown in Fig. 9. The major loss point is right after injection, with other loss points corresponding to resonance lines in the tune diagram.
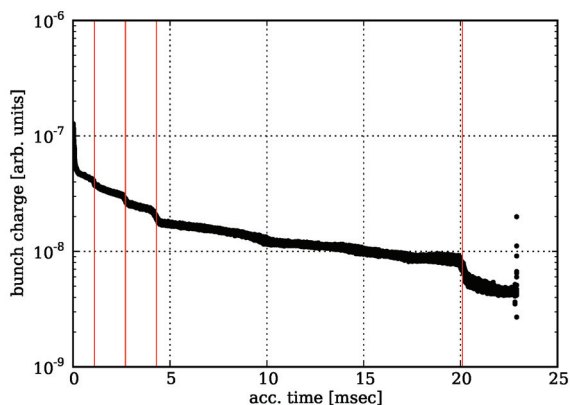


Figure 9: Present beam loss throughout the acceleration cycle. Major loss points marked with red lines occur at 1.1 ms, 2.7 ms, 4.3 ms and 20.1 ms.

A multi-faceted approach will enable the machine to operate with a higher average beam power.

It is clear that the dominant loss point is at the point of injection, where only roughly 10 to 40% of the beam survives depending on choice of phase and quality of injection matching. Optimisation of the rf pattern should improve this in future, but only to a limited extent.

One suspected additional source of imperfection in the ring was the presence of additional iron-based magnets from the previous injector. This additional iron was recently removed and the working point adjusted slightly, however no improvement was discernible in terms of beam loss. This is because the adjusted working point lies close to a betatron resonance, as can be clearly seen in the tune diagram. Further adjustment of the working point should improve this.

The installation of a second rf cavity is planned in early 2015 in order to increase the repetition rate from 20 Hz to 100 Hz. Faster acceleration should pull the beam off the foil more quickly and also reduce the impact of losses due to resonance crossing effects.

To reduce beam loss further the matching at injection needs to be optimised to reduce multiple scattering on the foil and reduce emittance growth. This is a key item to be measured and the use of a wire scanner is being investigated. Multiple scattering will also be reduced by an increase in the acceleration rate so the beam moves off the foil more quickly at injection.

The other key to enabling high power operation is an accurate model of the machine. A lot of work has been carried out at KURRI toward modelling this machine previously. To enhance these studies a detailed simulation campaign

is underway including code benchmarking, comparison to experiment and a parallel strand of code development and wider investigation into high intensity effects in FFAG accelerators.

# REFERENCES

[1] M. Tanigaki, K. Mishima, and S. Shiroya, "Construction of FFAG accelerators in KURRI for ADS study", EPAC'04, Lucerne, July 2004, pp. 2676, `http://www.JACoW.org`.

[2] C. H. Pyeon et al., J. Nucl. Sci. Technol., vol. 46, no. 12 (2009) pp. 1091.

[3] T. Adachi et al., "A 150 MeV FFAG synchrotron with 'Return-Yoke Free' magnet", PAC 2001, Chicago, pp. 3254,

[3] T. Adachi et al., "A 150 MeV FFAG synchrotron with 'Return-Yoke Free' magnet", PAC 2001, Chicago, pp. 3254, `http://www.JACoW.org`.

[4] K. Okabe et al., "Development of H- injection of proton-FFAG at KURRI", IPAC 2010, Kyoto, THPEB009, pp. 3897, `http://www.JACoW.org`.

[5] F. Méot, "The ray-tracing code Zgoubi - status," Nucl. Instruments Methods Phys. Res. Sect. A, 767 (2014) pp. 112.

[6] Y. Yonemura, et al. "Development of RF acceleration system for 150MeV FFAG accelerator". Nucl. Instruments Methods Phys. Res. Sect. A, 576.2 (2007), pp. 294.

[7] Y. Ishi et al., "Present status and future of FFAGs at KURRI and the first ADSR experiment", IPAC 2010, Kyoto, TUOCRA03, pp. 1327, `http://www.JACoW.org`.

# EFFICIENT 3D POISSON SOLVERS FOR
# SPACE-CHARGE SIMULATION*

J. Qiang[†], LBNL, Berkeley, CA 94720, USA

## Abstract

Three-dimensional Poisson solver plays an important role in the self-consistent space-charge simulation. In this paper, we present several efficient 3D Poisson solvers inside an open rectangular conducting pipe for space-charge simulation. We describe numerical algorithm of each solver, show comparative results for these solvers and discuss the pros and cons associated with each solver.

## INTRODUCTION

Nonlinear space-charge effect in charged particle beam has significant impact to particle beam dynamics in high intensity accelerators. A natural way to include the space-charge effect in the simulation is through self-consistent particle-in-cell (PIC) method [1–4]. In the PIC method, macroparticles are advanced step by step in phase space subject to both the external forces and the space-charge forces. Normally, at each step, the external forces can be quickly computed using the given external fields. The space-charge forces are calculated self-consistently using the charge density distribution at that step by solving the Poisson equation. This involves a large number of numerical operations and is much more computational expensive compared with the external force calculation. An efficient Poisson solver will be of importance in the PIC simulation in order to quickly calculate the space-charge forces and to reduce the total simulation time.

In previous studies, a number of Poisson solvers have been studied subject to different boundary conditions [5–12]. In this paper, we proposed three new Poisson solvers in an open rectangular conducting pipe. Figure 1 shows a schematic plot of charged particle beam inside an open rectangular conducting pipe. Even with the longitudinal open boundary condition, these three Poisson solvers will use a computational domain that longitudinally contains the beam itself. No extra computational domain is needed in the longitudinal direction in order to meet the open boundary conditions on both sides of the beam.
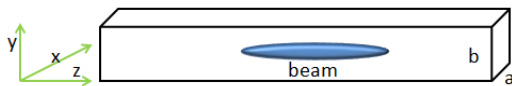


Figure 1: A schematic plot of a charged particle beam inside an open rectangular conducting pipe.

## NUMERICAL METHODS

For a perfect conducting pipe with rectangular cross section, we write the three-dimensional (3D) Poisson equation as:

$$\frac{\partial^2 \phi}{\partial x^2} + \frac{\partial^2 \phi}{\partial y^2} + \frac{\partial^2 \phi}{\partial z^2} = -\frac{\rho}{\epsilon_0} \qquad (1)$$

Here, $\phi$ denotes the electrostatic potential, $\rho$ the dimensionless charge density function, $x, y$ and $z$ denote the horizontal, vertical, and longitudinal coordinates respectively. The boundary conditions for the potential in the open perfect rectangular conducting pipe are:

$$\phi(x = 0, y, z) = 0 \qquad (2)$$
$$\phi(x = a, y, z) = 0 \qquad (3)$$
$$\phi(x, y = 0, z) = 0 \qquad (4)$$
$$\phi(x, y = b, z) = 0 \qquad (5)$$
$$\phi(x, y, z = \pm\infty) = 0 \qquad (6)$$

where $a$ is the horizontal width of the pipe and $b$ is the vertical width of the pipe. In the following, we propose three efficient numerical methods to solve the Poisson equation subject to above boundary conditions.

### Spectral-Integrated Green Function Method

Given the boundary conditions in Eq. 2-6, the potential $\phi$ and the source term $\rho$ can be approximated using two sine functions as:

$$\rho(x, y, z) = \sum_{l=1}^{N_l} \sum_{m=1}^{N_m} \rho^{lm}(z) \sin(\alpha_l x) \sin(\beta_m y) \qquad (7)$$

$$\phi(x, y, z) = \sum_{l=1}^{N_l} \sum_{m=1}^{N_m} \phi^{lm}(z) \sin(\alpha_l x) \sin(\beta_m y) \qquad (8)$$

where

$$\rho^{lm}(x, y, z) = \frac{4}{ab} \int_0^a \int_0^b \rho(x, y, z) \sin(\alpha_l x) \sin(\beta_m y) \, dxdy \qquad (9)$$

$$\phi^{lm}(x, y, z) = \frac{4}{ab} \int_0^a \int_0^b \phi(x, y, z) \sin(\alpha_l x) \sin(\beta_m y) \, dxdy \qquad (10)$$

where $\alpha_l = l\pi/a$ and $\beta_m = m\pi/b$. Substituting above expansions into the Poisson equation and making use of the orthnormal conditions of the sine functions, we obtain

$$\frac{\partial^2 \phi^{lm}(z)}{\partial z^2} - \gamma_{lm}^2 \phi^{lm}(z) = -\frac{\rho^{lm}}{\epsilon_0} \qquad (11)$$

where $\gamma_{lm}^2 = \alpha_l^2 + \beta_m^2$. The above ordinary differential equation for each mode $lm$ can be solved using a Green function method. This solution can be written as:

$$\phi^{lm}(z) = \frac{1}{2\gamma_{lm}\epsilon_0} \int G_{lm}(z - z')\rho^{lm}(z') \, dz' \qquad (12)$$

where the Green function $G$ is given by:

$$G_{lm}(z - z') = \exp\left(-\gamma_{lm}|z - z'|\right) \qquad (13)$$

The above convolution integral can be discretized on a mesh that longitudinally contains only the beam. The discrete potential on a grid point $z_i, i = 1, \cdots, N_z$ is given as:

$$\phi^{lm}(z_i) = \frac{h_z}{2\gamma_{lm}\epsilon_0} \sum_{j=1}^{N_z} G_{lm}(z_i - z_j)\rho^{lm}(z_j) \qquad (14)$$

where $h_z = (z_{max} - z_{min})/(N_z - 1)$, $z_{min}$ is the minimum and maximum locations of the beam along the $z$ direction, and $N_z$ is the number of grid points. The direct brute-force calculation of above summation for all $N_z$ grid data points takes $O(N_z^2)$ operations. Fortunately, by using the zero padding method [12–15], the computational cost of the summation for all $N_z$ data points can be reduced to $O(N_z log(N_z))$.

The Green function given in Eq. 13 is exponentially damped with the increase of the separation between two grid points. In the numerical calculation of Eq. 12, resolving such fast damping may not be necessary if the variation of beam density along $z$ is slow. The convolution integral Eq. 12 can be rewritten as

$$\phi^{lm}(z) = \frac{1}{2\gamma_{lm}\epsilon_0} \sum_j \int_{z_j - h_z/2}^{z_j + h_z/2} G_{lm}(z - z')\rho^{lm}(z') \, dz' \quad (15)$$

If we assume that the charge density $\rho^{lm}$ stays constant within the interval $[z_j - h_z/2, z_j + h_z/2]$, the above equation can be reduced into:

$$\phi^{lm}(z) = \frac{1}{2\gamma_{lm}\epsilon_0} \sum_j G_{lm}^{int}(z - z_j)\rho^{lm}(z_j) \quad (16)$$

where

$$G_{lm}^{int}(z - z_j) = \int_{z_j - h_z/2}^{z_j + h_z/2} G_{lm}(z - t) \, dt \qquad (17)$$

Substituting Eq. 13 into above equation, we obtain the integrated Green's function as:

$$G_{lm}^{int}(z_i - z_j) = \begin{cases} \frac{\exp(\gamma_{lm}|z_i - z_j|)}{\gamma_{lm}}(\exp(\gamma_{lm}h_z/2) - \\ \exp(-\gamma_{lm}h_z/2)), \text{ if } i \neq j \\ \frac{2}{\gamma_{lm}}(1 - \exp(-\gamma_{lm}h_z/2)) \text{ otherwise} \end{cases} \quad (18)$$

Using the integrated Green's function $G^{int}$, the convolution summation Eq. 16 can be calculated using the same zero padding method as the standard Green function method. The advantage of this method is that the fast decrease of the Green function does not need to be resolved in the numerical

approximation to the convolution integral 12, which can significantly save computational resources.

The numerical calculation of the sine function transform in both $x$ and $y$ directions can be done efficiently using an FFT method. The computational cost in transverse $x$ and $y$ dimensions scales as $O(N_x N_y N_z (\log(N_x N_y)))$. Using the zero padding and the FFT for the cyclic summation, the cost to compute the convolution also scales as $O(N_x N_y N_z log(N_z))$. This results in a total computational cost to solve the 3D Poisson equation in an open conducting pipe scaling as $O(N_x N_y N_z \log(N_x N_y N_z))$.

### 3D Spectral Method

In many accelerator physics application, the longitudinal density distribution of the charged particle beam has a Gaussian distribution. This suggests that the ordinary differential equation 11 can also be solved efficiently using a Hermite-Gaussian expansion, which naturally satisfies the open boundary conditions (Eq. 6) in the $z$ direction.

The charge density $\rho$ and electrostatic potential $\phi$ can be approximated as:

$$\rho^{lm}(z) = \sum_{n=0}^{n=N_n} \rho_n^{lm}\mathcal{H}_n(z) \qquad (19)$$

$$\phi^{lm}(z) = \sum_{n=0}^{n=N_n} \phi_n^{lm}\mathcal{H}_n(z) \qquad (20)$$

where the scaled Hermite-Gaussian function $\mathcal{H}_n$ is defined as:

$$\mathcal{H}_n(z) = H_n\left(\frac{z}{A}\right) \exp\left(-\frac{1}{2}\frac{z^2}{A^2}\right) \qquad (21)$$

where $A$ is a longitudinal scaling constant, which can be $A = \sigma_z$ with $\sigma_z$ the beam longitudinal RMS size, $H_n$ is the $n^{th}$ order Hermite polynomial with properties: $H_0(z) = 1$, $H_1(z) = 2z, \cdots, H_n(z) = 2zH_{n-1} - 2(n-1)H_{n-2}$. The scaled Hermite-Gaussian function $\mathcal{H}$ has the properties:

$$\int_{-\infty}^{\infty} \mathcal{H}_n(z)\mathcal{H}_m(z)dz = 2^n n! \sqrt{\pi} A \delta_{nm} \qquad (22)$$

and

$$\frac{\partial^2 \mathcal{H}_n}{\partial z^2} = \frac{1}{4A^2}\mathcal{H}_{n+2} + \frac{n(n-1)}{A^2}\mathcal{H}_{n-2} - \frac{2n+1}{2A^2}\mathcal{H}_n \quad (23)$$

where $\delta_{mn} = 1$ for $m = n$ and $\delta_{mn} = 0$ for $m \neq n$. The expansion coefficients $\rho_n$ and $\phi_n$ can be obtained from

$$\rho_n^{lm} = \frac{1}{2^n n! \sqrt{\pi} A} \int_{-\infty}^{\infty} \rho^{lm}(z)\mathcal{H}_n(z)dz \qquad (24)$$

$$\phi_n^{lm} = \frac{1}{2^n n! \sqrt{\pi} A} \int_{-\infty}^{\infty} \phi^{lm}(z)\mathcal{H}_n(z)dz \qquad (25)$$

Substituting the functions $\rho$ and $\phi$ into the Eq. 11, and using the orthogonality of the scaled Hermite-Gaussian functions

**Computational Challenges, New Concepts and New Projects**

and Eq. 22, the Poisson equation is reduced into a group of linear algebraic equations:

$$\frac{1}{4}\phi^{lm}_{n-2} - (\frac{1}{2}(2n+1) + \gamma^2_{lm}A^2)\phi^{lm}_n + (n+2)(n+1)\phi^{lm}_{n+2}$$
$$= -A^2\rho^{lm}_n/\epsilon_0 \quad (26)$$

where $n = 1, 2, \cdots, N_n$ and $N_n$ is the number of Hermite-Gaussian modes. This group of algebraic equations is a band-limited matrix equation, which can be solved effectively using direct Gaussian elimination with a computational cost of $O(N_n)$ for each transverse mode $l$ and $m$, which results in a total cost as $O(N_l N_m N_n)$. The computational cost of the sine transform scales as $O(N_x N_y N_z \log(N_x N_y))$. The calculation of the Hermite-Gaussian expansion coefficients are more expensive and scales as $O(N_l N_m N_n N_z)$. If the number of Hermite-Gaussian modes can be controlled within a reasonable limit taking advantage of the high order accuracy of the spectral method, this method can still be very efficient. Another advantage of this method is that it provides a natural smoothing of electrostatic function in the self-consistent particle-in-cell simulation by neglecting the high frequency modes in the expansion.

### 3D Integrated Green Function Method

Another method to solve the 3D Poisson equation inside the open rectangular pipe is to use an integrated Green function method directly. This method has the advantage of using a computational domain that contains only the beam itself instead of the whole transverse pipe cross-section. The solution of the 3D Poisson equation can be written as:

$$\phi(x, y, z) = \frac{2}{ab\epsilon_0} \sum_{l=1}^{\infty} \sum_{m=1}^{\infty} \frac{1}{\gamma_{lm}} \sin(\alpha_l x) \sin(\beta_m y) \times$$
$$\int_{x_{min}}^{x_{max}} \int_{y_{min}}^{y_{max}} \int_{z_{min}}^{z_{max}} \sin(\alpha_l x') \sin(\beta_m y') \times$$
$$\exp(-\gamma_{lm}|z - z'|)\rho(x', y', z') \, dx'dy'dz' \quad (27)$$

The above equation can be rewritten as:

$$\phi(x, y, z) = \frac{1}{2ab\epsilon_0} \int_{x_{min}}^{x_{max}} \int_{y_{min}}^{y_{max}} \int_{z_{min}}^{z_{max}} \sum_{l=1}^{\infty} \sum_{m=1}^{\infty}$$
$$\frac{1}{\gamma_{lm}}[\cos(\alpha_l(x - x')) - \cos(\alpha_l(x + x'))] \times$$
$$(\cos(\beta_m(y - y')) - \cos(\beta_m(y + y'))) \times$$
$$\exp(-\gamma_{lm}|z - z'|)\rho(x', y', z') \, dx'dy'dz' \quad (28)$$

Following the same idea of preceding section, we can define a three-dimensional integrated Green's function as:

$$G^{int}_{3D}(x, x', y, y', z, z') = \frac{1}{2ab\epsilon_0}(R(x - x', y - y', z - z') -$$
$$R(x - x', y + y', z - z') - R(x + x', y - y', z - z') +$$
$$R(x + x', y + y', z - z')) \quad (29)$$

where

$$R(u, v, w) = \sum_{l=1}^{\infty} \sum_{m=1}^{\infty} \frac{1}{\alpha_l \beta_m}[\sin(\alpha_l(u - h_x/2)) -$$
$$\sin(\alpha_l(u + h_x/2))] \times$$
$$(\sin(\beta_m(v - h_y/2)) - \sin(\beta_m(v + h_y/2)))G^{int}_{lm}(w) \quad (30)$$

The discrete potential on a grid $(i, j, k)$ can be written as:

$$\phi(x_i, y_j, z_k) = \sum_{i=1}^{N_x} \sum_{j=1}^{N_y} \sum_{k=1}^{N_z} G^{int}_{3D}(x_i, y_j, z_k, x'_i, y'_j, z'_k) \times$$
$$\rho(x'_i, y'_j, z'_k) \quad (31)$$

The above summation can also be calculated on a doubled computational domain using an FFT-based zero padding method. In order to compute this summation using the FFT-based method, besides the direct convolution term $R(x - x', y - y', z - z')\rho(x', y', z')$, there are also terms that contain auto-correlation in $R(x - x', y + y', z - z')$, $R(x + x', y - y', z - z')$, and $R(x + x', y + y', z - z')$. It turns out that those auto-correlations can be handled in a similar way to the convolution term except that a backward/forward FFT is used in the dimension with auto-correlation while a forward/backward FFT is used in the dimension of convolution [12]. The computational cost for such cyclic summation scale as $O(N_x N_y N_z \log(N_x N_y N_z))$.

## NUMERICAL TESTS

In the following, we show a numerical test example for above proposed algorithms. Here, we assume that the beam has a 3D normalized Gaussian density distribution as:

$$\rho(x, y, z) = \exp(-\frac{(x - x_0)^2}{2\sigma_x^2} - \frac{(y - y_0)^2}{2\sigma_y^2} - \frac{(z - z_0)^2}{2\sigma_z^2}) \quad (32)$$

where $\sigma_x$, $\sigma_y$, and $\sigma_z$ denote RMS (root mean square) sizes of the beam, and $x_0$, $y_0$, and $z_0$ denote the centroid of the beam. We assume that the transverse aperture sizes of the pipe $a = b = 2$, transverse RMS beam sizes $\sigma_x = \sigma_y = 1/6$, and $\sigma_z = 100/6$. This results in an aspect ratio $A = 100$ for the beam. The computational grid used in this example is $65 \times 65 \times 64$.

Figure 2 shows the electrostatic potential solution and the relative errors along the central horizontal axis from the above three numerical methods (the spectral-integrated Green's function, the 3D spectral method, the 3D integrated Green's function method) and the analytical solution. All three methods have relative errors below 0.1%. The 3D spectral method has the least relative errors as expected. The 3D integrated Green's function method has the largest relative errors but is still below 0.1%.

Figure 3 shows the electrostatic potential solutions and relative errors along center longitudinal axis in this test example using the three numerical methods together with the analytical solution. All three methods give a good approximation to the analytical solution with the maximum relative error below 0.1%. Again, the 3D spectral method shows the least relative error among the three methods.
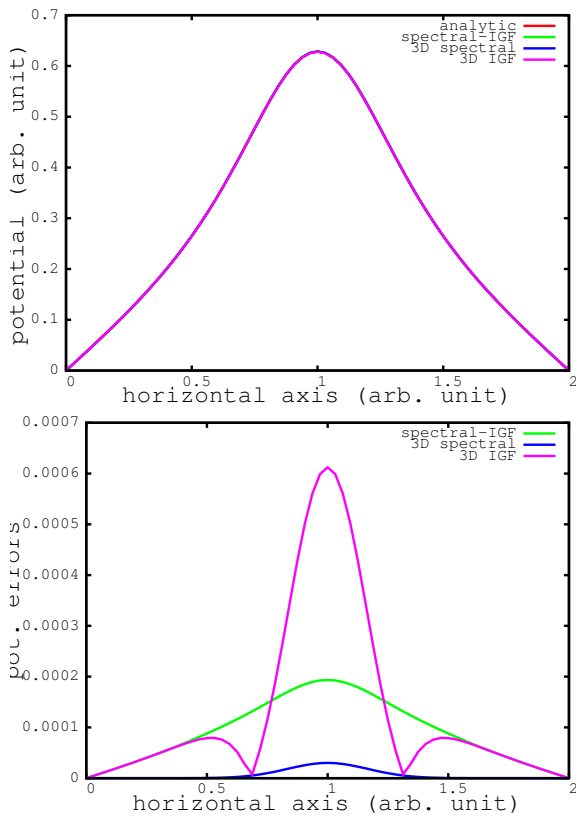
Figure 2: The electrostatic potential solutions (top) and relative errors (bottom) along the horizontal axis from the three proposed numerical algorithms and from the analytical solution.
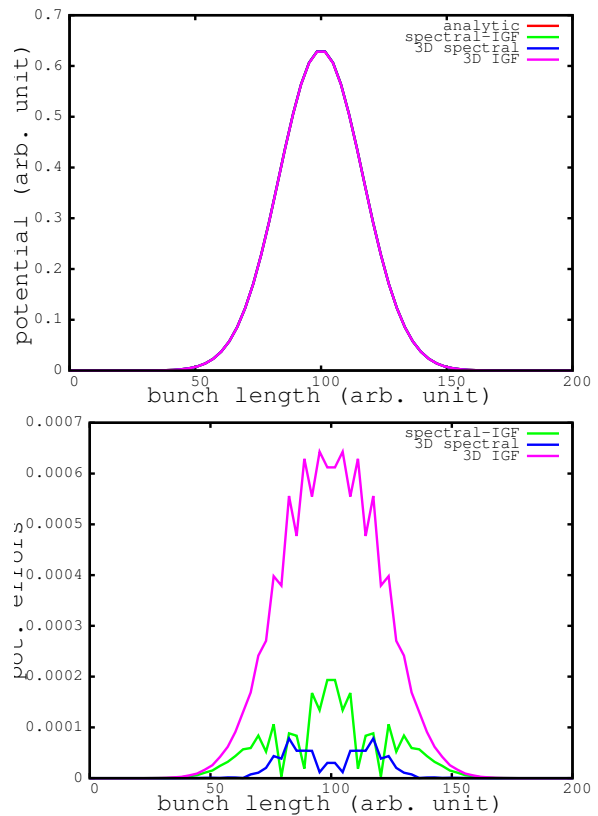


Figure 3: The electrostatic potential solutions (top) and relative errors (bottom) along the longitudinal axis from the three proposed numerical algorithms and from the analytical solution.

## CONCLUSIONS

In this paper, we presented three 3D Poisson solvers to calculate the electrostatic potential of a charged particle beam in an open conducting rectangular pipe. Those three Poisson solvers effectively save the computational resource by using a computational domain that longitudinally contains the beam itself. The spectral-integrated Green function solver and the 3D integrated Green function solver have a computational complexity of $O(N \log(N))$, where $N$ is the total number of grid points. The computational cost of the 3D spectral solver scales as $O(N_n N)$, where $N_n$ is the number of Hermite-Gaussian modes used in the solution. Given the fast convergence rate of the spectral solver, the mode number might be kept as small. In the scaling estimation, all these three Poisson solvers are efficient in the numerical operations. In practical application, the 3D integrated Green function method is most time consuming due to the double summation in the calculation of the Green function. However, it has the advantage that the computational domain only needs to contain the beam itself in both transverse and longitudinal directions. This saves computational cost when the transverse size of the beam is much smaller than the transverse pipe aperture. The 3D spectral solver has an extra cost factor depending on the Hermite-Gaussian mode number. However, this solver normally leads to less numer-

ical error and can also provide smooth potential solution when the charge density function contains numerical noise from the discrete macroparticle deposition in the PIC simulation. The spectral-integrated Green function solver has a numerical accuracy between the 3D spectral solver and the 3D integrated Green function solver, but a very favorable computational cost scaling.

## ACKNOWLEDGMENTS

## REFERENCES

[1] A. Friedman, D.P. Grote and I. Haber, Phys. Fluids **B 4**, 2203 (1992).

[2] T. Takeda, J.H. Billen, "Recent developments of the accelerator design code PARMILA," Proceedings of the XIX International Linac Conference, Chicago, IL, August 1998, pp. 156-158.

[3] J. Qiang, R.D. Ryne, S. Habib, V. Decyk, J. Comput. Phys. **163**, 434 (2000).

[4] J. Qiang, S. Lidia, R.D. Ryne, and C. Limborg-Deprey, Phys. Rev. ST Accel. Beams **9**, 044204 (2006).

[5] D.B. Haidvogel and T. Zang, J. Comput. Phys. **30**, 167 (1979).

[6] S. Ohring, J. Comput. Phys. **50**, 307 (1983).

[7] H. Dang-Vu and C. Delcarte, J. Comput. Phys. **104**, 211 (1993).

[8] E. Braverman, M. Israeli, A. Averbuch, and L. Vozovoi, J. Comput. Phys. **144**, (1998).

[9] L. Plagne and J. Berthou, J. Comput. Phys. **157**, 419 (2000).

[10] J. Qiang and R.D. Ryne, Comp. Phys. Comm. **138**, 18 (2001).

[11] J. Qiang and R. Gluckstern, Comp. Phys. Comm. **160**, 120, (2004).

[12] R.D. Ryne, "On FFT based convolutions and correlations, with application to solving Poisson's equation in an open rectangular pipe," arXiv:111.4971v1, 2011.

[13] J.W. Eastwood, D.R.K. Brownrigg, J. Comput. Phys. 32 (1979) 24.

[14] W.H. Press, B.P. Flannery, S.A. Teukolsky, W.T. Vetterling, Numerical Recipes in FORTRAN: The Art of Scientific Computing, 2nd ed., Cambridge University Press, Cambridge, England, 1992.

[15] J. Qiang, Comp. Phys. Comm. **181**, 313, (2010).

**Computational Challenges, New Concepts and New Projects**

# A MULTI-PARTICLE ONLINE BEAM DYNAMICS SIMULATOR FOR HIGH POWER ION LINAC OPERATIONS*

X. Pang†, L.J. Rybarcyk, S.A. Baily

Los Alamos National Laboratory, Los Alamos, NM, 87544, USA

## Abstract

A fast multi-particle online beam dynamics simulator has been developed at LANL. It is a marriage of multi-particle beam physics algorithms and graphics processing unit (GPU) technology. It combines the execution efficiency of the C/C++ programming language and a powerful yet flexible user interface via Python scripts. Therefore, it is not only accurate and fast, but also very easy to use. We have used this simulator at LANSCE to guide linac tuning, explore optimal operational settings, and test new ideas.

## INTRODUCTION

### Why Another Simulator?

Accelerator control rooms are usually equipped with on-line beam modeling tools to help guide machine tuning. These tools, which typically have access to machine set points through the control system, can not only help physicists and operators set up the machine faster, but also provide information on the beam properties in areas where no measurements can be made. However, almost all of the existing online modeling tools today are either based on single-particle tracking or on envelope models. While they might perform sufficiently well for nicely formed beams, they cannot predict the nonlinear motions of a real beam or estimate losses, especially in high-power operations when beams can be highly nonlinear and chaotic.

The logical next step to improve the status quo is to use a multi-particle beam dynamics code to provide more realistic predictions. However, most of the existing multi-particle simulation tools need either significant computational time or supercomputer resources. This makes them impractical to use during real world machine operations where fast turn-around is required and where they may be in use for long periods of time. In addition, they are typically not configured to have ready access to online machine specific set points.

One can clearly see the gap that exists between the over-simplified but fast models used in control rooms and the highly sophisticated yet slow multi-particle simulation tools which are usually used during the design process. The goal of our development is to fill this gap by providing a multi-particle simulation tool that is both accurate and fast enough to be used in real world accelerator tuning and operation.

### Why Use a GPU?

The graphics processing unit (GPU) is at the frontier of high performance computing [1]. It powers several of the world's most powerful supercomputers and it has also democratized super-computing by enabling cluster performance on people's personal desktops. For us, the GPU offers outstanding parallel performance and it is also the most cost effective way to provide 24/7 availability for our online simulator. With around a $600 USD investment in the GPU hardware, one can get up to 100 times speedup compared to a single threaded CPU. And this GPU workstation can be dedicated to accelerator operations 24/7.

### How to Use It?

This is where the users can freely apply their creativity. We have applied this tool to guide turn-on of the LANSCE linac, to test what-if scenarios, to optimize operational machine settings by combining it with the multi-objective optimization algorithms, and to test a new automatic tuning/control scheme. More details will be covered in later sections.

## THE SIMULATOR

### Code Design

The goal of our code design is to ensure fast execution and ease of use. This led us to adopt a combination of a low-level compiled language, i.e. C++/CUDA and a high-level scripting language, i.e. Python. The number-crunching is efficiently carried out by CUDA and C++, however, the users don't have to deal with the complex syntax and the lengthy compilation processes associated with them, but instead can configure and execute a simulation with a high-level script. Figure 1 shows the code hierarchy. The shallow learning
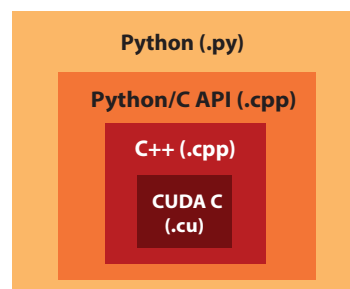


Figure 1: Lower-level CUDA and C++ are wrapped up by Python/C API and compiled into a shared library that can be imported in Python.

curve of Python and the richness of its application libraries allow users with the minimal programming experiences to quickly prototype their ideas.

The major components of the code structure design are shown in Figure 2. The components that are shaded in blue

---
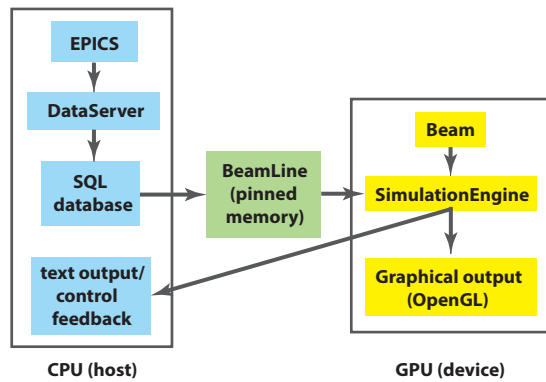
Figure 2: High level code structure and data flow indicated by the arrows.

are generated and stored by the CPUs (host), while the ones in yellow are generated and stored in the GPU (device) during the simulation. The C APIs of the Experimental Physics and Industrial Control System (EPICS) [2] have been used to get real-time machine data from the accelerator control system. The data are then stored in a SQLite database and processed into model physics units that are required for the simulations. The pinned memory (shaded in green) physically sits on the CPU side however, can be accessed by both the CPU and the GPU. It is used in our case to store the beam line information which has to be accessed by the GPU to simulate a beam, and also needs to be updated by the CPU using the information queried in real-time. More detailed description about the code structure can be found in [3].

### GPU Performance

One can refer to [3] for more details about the GPU algorithms and optimization we have applied. We compared the code performance using an Intel Xeon E5520 2.27GHz CPU and a NVIDIA GTX 580 GPU (Fermi architecture). For a section of beam line at LANSCE, up to 112 times speedup has been achieved for beam transported without space charge. A speedup factor up to 45 has been achieved for the space charge routine.

Our initial test with the LANSCE CCL (4960 RF gaps + 206 quads + 460 drift spaces) on a NVIDIA Tesla K20 GPU showed that it took the simulator about a second to push 32K particles through it without space charge, and about 10 seconds with space charge (> 6000 space charge kicks). It is likely that this performance will improve as we do not need to apply space charge kicks this often in the CCL due to the lattice design and the diminishing effects of the space charge for the higher energy beam. With a more intelligent space charge routine and further GPU optimization, we can expect the front-to-end simulation for the half mile 800-MeV LANSCE linac to finish within just several seconds.

## APPLICATIONS

### Tuning Guide

At LANSCE, the half-mile long 800-MeV linac provides both $H^+$ and $H^-$ beams for user programs. The tune-up pro-

cedures usually begin with direct low-power beam measurements and set up of the beam lines based on the predictions from an envelope model. However, in the transition to high-power operations, due to the lack of direct measurement of the beam and a good modeling tool for the high power beam, machine settings are empirically adjusted by operators to achieve minimal beam loss along the linac. These adjustments are usually done in a high dimensional parameter space, which can make the tuning process lengthy, and the machine settings subjective and inconsistent. This is where the simulator can help. Once correctly calibrated, one can use the simulator to predict beam properties at any location along the linac for any beam condition. Therefore, the operators and physicists would no longer be tuning with limited information, but instead are provided with new insight into the beam propagation along the linac. Moreover, they can simulate real beam distributions that are generated directly from emittance scans.
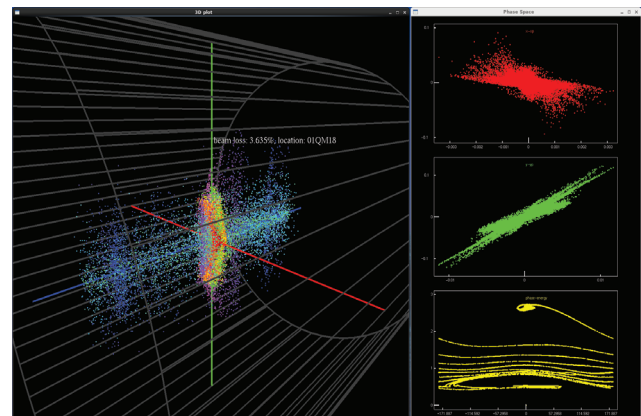


Figure 3: Screen shot of the online simulator graphical output. Left: 3D beam display in x, y, phase coordinates. Right: transverse and longitudinal phase space plots.

Figure 3 shows part of the graphics interface of the simulator. Figure 4 shows a simulated beam distribution at the end of the 100-MeV DTL. One can clearly see the low-energy particles in the longitudinal phase space that make it to the end of the DTL. However, they become beam losses in the chicane following the DTL. The bottom right plot shows the appearance of the nonlinear beam core. The tail of the core can also produce loss in the subsequent elements. These are the features that only multi-particle simulations can provide. They will be very useful in machine tuning especially in high power operations. Figure 5 shows that the simulations can reproduce the actual phase scan experiments for the DTL and CCL to very high accuracy.

### Multi-objective Optimization

We have used the simulator in combination with the multi-objective optimization techniques to find optimal operational settings in a high-dimensional parameter space [4]. Figure 6 shows the 2D projection of the estimated Pareto front in the 3D objective space obtained both by the multi-objective genetic algorithm (MOGA) (the left column) and the multi-
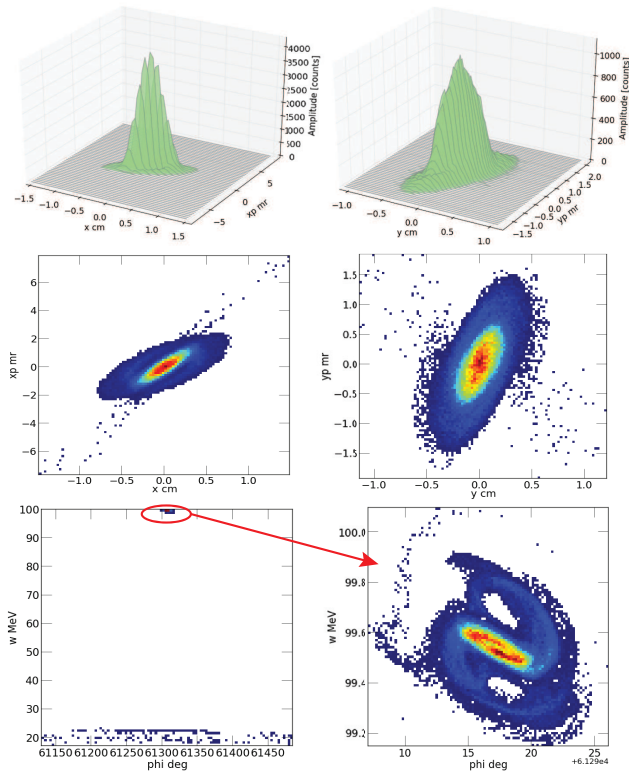
Figure 4: Beam distribution at the end of the LANSCE DTL (100 MeV). Top: beam distribution in x,x' and y,y'. Middle: phase space in x and y. Bottom: longitudinal phase space, $\phi$, w showing low-energy particles well below design energy, and a closer look at the beam core around 100 MeV.

objective particle swarm optimization (MOPSO) (the right column). For this graph, the three objectives the MO algorithms are trying to minimize are the longitudinal phase space and phase width at the end of the LANSCE DTL, and power of the lost beam throughout the DTL. There are 11 free parameters for the algorithms to adjust including quadrupole gradients and RF phases and amplitudes of the four DTL tanks. The simulator acts as a virtual experimental environment and provides a cost functions for the MO algorithms to minimize in the process. From this study, we were able to find optimal operating conditions and the fact that the MOPSO converges much faster than the MOGA.

## Accelerator Automatic Tuning

An automatic accelerator tuning method has been developed using the simulator as its test bed [5]. This real-time method can simultaneously tune several coupled components of an accelerator to achieve good beam quality. Using the simulator, it has proven to be very efficient and robust to noise. It can even quickly adjust the beam to its best condition with failing elements in the accelerator.

## CONCLUSION

The GPU-based online simulator has been proven to be a very useful tool for accelerator operations. By combining
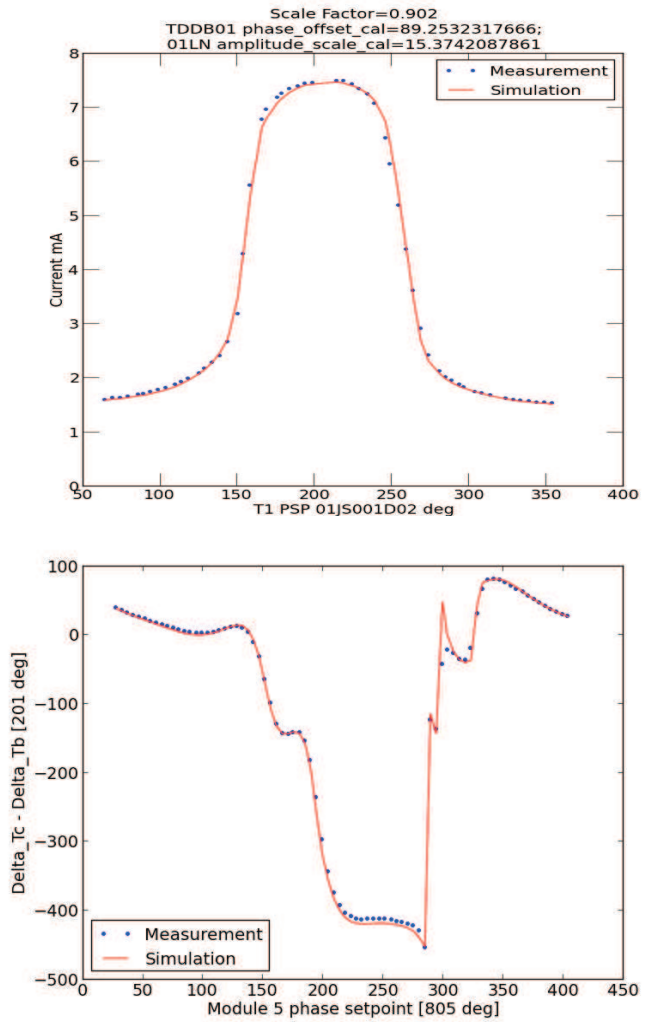


Figure 5: Top: DTL tank 1 phase scan which utilizes an absorber/collector diagnostic. Bottom CCL module 5 phase scan, which utilizes beam phase measurement diagnostics.
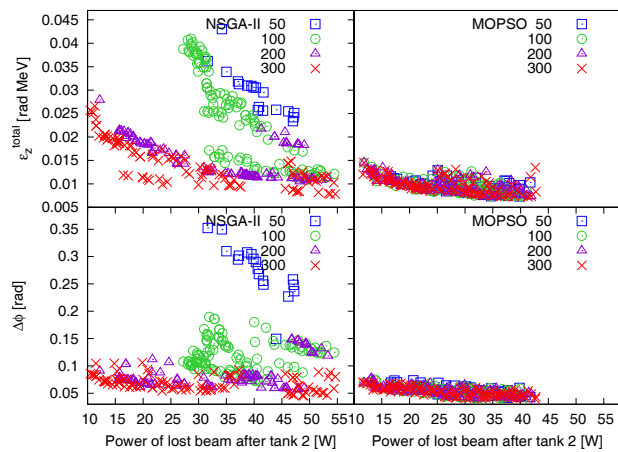


Figure 6: The 2D projections of the estimated 3D Pareto front in the objective space obtained by the NSGA-II and MOPSO at different iterations.

multiparticle beam physics algorithms with GPU technology we are able to bring high-fidelity beam dynamics modeling

capabilities to the control room environment in a cost effective way. Furthermore, by enabling real-time acquisition of machine parameter setpoints, the simulator is able to track the operation of the accelerator and provide operators and physicists with new insight into beam performance in an operational setting. The list of possible applications is by no means limited to the examples given above. Instead, the high-level Python interface enables the user to easily create and explore new application. Further development of the simulator and its applications are ongoing.

## REFERENCES

[1] NVIDIA Corporation, CUDA C Programming Guide, 2014.

[2] EPICS, http://www.aps.anl.gov/epics

[3] X. Pang, L. Rybarcyk, GPU Accelerated Online Beam Dynamics Simulator for Linear Particle Accelerators, Computer Physics Communications, 185, pp. 744-753, 2014.

[4] X. Pang, L. Rybarcyk, Multi-objective Particle Swarm and Genetic Algorithm for the Optimization of the LANSCE Linac Operation, Nuclear Instruments and Methods in Physics Research Section A, 741, pp. 124-129, 2014.

[5] A. Scheinker, X. Pang, and L. Rybarcyk, Model Independent Particle Accelerator Tuning, Physics Review Special Topics - Accelerators and Beams, 16, 102803, 2013.

# SPACE CHARGE MAP EXTRACTION AND ANALYSIS IN A DIFFERENTIAL ALGEBRAIC FRAMEWORK

A. Gee[*], B. Erdelyi[†]

Physics Dept., Northern Illinois University, DeKalb, IL 60115, USA

## Abstract

Space charge is a leading concern in high-intensity beams, causing effects such as emittance growth, beam halos, etc. As the need for high-intensity beams spreads, the demand for efficient space charge analysis grows. We developed a self consistent space charge simulation method for this purpose [1]. In order to facilitate space charge analysis, we implemented a method that allows space charge map extraction and analysis from any tracking method [1, 2]. We demonstrate the method by calculating the transverse space charge. We compare the method of moments and the fast multipole method as the tracking methods employed in the transfer map extraction process. We show results from analysis of the raw map elements as well as quantities obtained from normal forms.

## INTRODUCTION

Transfer maps are powerful tools in the analysis of beam dynamics. The information even at low order is invaluable in the design and optimization of charged particle beam guidance systems. Now, we may study multi-particle beam dynamics using transfer maps. For the first time, we can extract a self-consistent space charge transfer map from simulation, opening new possibilities in the field of beam physics. Details of the theory and development can be found in [1].

The map extraction method can be employed in conjunction with any tracking method available. The map itself is smooth as it captures the mean-field limit. The tracking methods themselves are based on splitting and composition methods, more precisely Strang splitting. We implemented two tracking methods: the moment method (MoM) and the fast multipole method (FMM). The tracking methods necessarily produce slightly different results due to innate approximations, thus it is prudent to check that the map extraction procedure itself smooths out the differences, resulting in the same transfer maps for all practical purposes. That is the main goal of this paper.

A few points should be mentioned. To efficiently extract the polynomial representation of beamline elements, we employed differential algebra methods. Differential algebra methods (DA) efficiently calculate Taylor expansions to high order with machine precision and no truncation error, providing polynomial representations for any beamline element of interest. We model the space charge kick as one such element with infinitesimal length. We limit ourselves to a single space charge kick at the center of a beamline element with open boundary conditions. Furthermore, to emphasize

---
[*] agee1@niu.edu
[†] erdelyi@anl.gov

Table 1: Beam Parameters

| Species | Proton |
|---|---|
| No. of Particles | 5000 |
| Energy [MeV] | 5 |
| Shape | Ellipse |
| Initial spatial distribution | Uniform |
| Initial maximum radius [m] | 0.001 |
| Initial angle distribution | Uniform |
| Initial maximum angle [rad] | 0.03 |
| Initial emittance (X,Y) [μm] | (7.63 , 7.50) |

the effects of space charge, we limited the beamline element maps to first order and calculated the space charge kick up to eighth order with the MoM and the FMM. Previous studies suggested results at the same order would be comparable.

## BEAMLINE SIMULATION

We set up a space-charge dominant beam for our simulations. The parameters are shown in Table 1. We used the same beam conditions for all runs. We chose the number of particles, $N = 5000$, for speed with acceptable accuracy.

To analyze some simple maps, we simulated two basic examples. We set up a magnetic triplet and adjusted the quadrupole gradients to achieve imaging as our first example. Our second example is a periodic FODO cell, where we adjusted the quadrupole gradients to match an arbitrarily chosen horizontal and vertical tune.

### Imaging Triplet

The triplet we set up consists of an outer drift, quad (Q1), inner drift, quad (Q2), inner drift, quad (Q3), and outer drift. The system parameters are in Table 2 and the first order system map is shown in (1).

$$\begin{pmatrix} -1 & 3.20 \times 10^{-14} & 0 & 0 \\ 5.69 & -1 & 0 & 0 \\ 0 & 0 & -1 & -1.91 \times 10^{-14} \\ 0 & 0 & -4.39 & -1 \end{pmatrix} \quad (1)$$

A ray trace of the system without space charge is also shown in Figure 1. We drew 3 independent rays in both the $X$-$Z$ and $Y$-$Z$ planes and generated the trajectory by applying the calculated map. The ray diagram includes an extra end drift of 6.25 cm to show the focal point at $z = 1.4$ m. This drift was left out of the system map since it would not affect our analysis.

Table 2: Imaging Triplet System Parameters

| | |
|---|---|
| Aperture radius [m] | 0.08 |
| Outer drift lengths [m] | 0.25 |
| Inner drift lengths [m] | 0.15 |
| Q1 length [m] | 0.2 |
| Q2 length [m] | 0.2 |
| Q3 length [m] | 0.2 |
| Initial Q1 $\left[\dfrac{T}{m}\right]$ | 0.65525 |
| Initial Q2 $\left[\dfrac{T}{m}\right]$ | -0.66566 |
| Initial Q3 $\left[\dfrac{T}{m}\right]$ | 0.65525 |

Table 3: FODO Cell System Parameters

| | |
|---|---|
| Aperture radius [m] | 0.08 |
| Inner drift lengths [m] | 0.15 |
| Q1 length [m] | 0.1 |
| Q2 length [m] | 0.2 |
| Initial Q1 $\left[\dfrac{T}{m}\right]$ | -0.39045 |
| Initial Q2 $\left[\dfrac{T}{m}\right]$ | 0.39045 |
| Horizontal tune | 0.1362 |
| Vertical tune | 0.1362 |

$$\begin{pmatrix} 0.656 & 0.425 & 0 & 0 \\ -1.34 & 0.656 & 0 & 0 \\ 0 & 0 & 0.656 & .951 \\ 0 & 0 & -.599 & 0.656 \end{pmatrix} \quad (2)$$

## EFFECTS DUE TO SPACE CHARGE

To study the effects of space charge, we fixed the settings shown in Table 2 and Table 3. We then increased the current, or equivalently the intensity, of the beam with fixed particle number. Using the same initial beam distribution and particle quantity, the only changes must be caused by space charge for the same tracking method.

### Imaging Triplet

The triplet shows some interesting behavior with higher intensity beams. From Equation 1, $(x|a)$ and $(y|b)$ are almost zero with the settings in Table 2. As the current increases, these elements grow as shown in Figure 2.

We can also see the behavior of the third order geometric aberrations $(x|x^3)$ and $(y|y^3)$ as a function of current, shown in Figure 3. Since the system map was limited to first order, the third order aberrations obtained are due to space charge. Comparing the FMM and MoM, we see the FMM predicts a slightly stronger self-field, which was seen in previous testing [3]. This is likely due inclusion of collisional forces which are negligible in the MoM. $(x|x^3)$ stands out in the beginning; space charge appears to inflate $(x|x^3)$ until around 0.25 A before reversing direction and becoming negative.

At 1.5 A, the focal point shifts as shown in Figure 4. Although subtle, the focal point is now around $z = 1.43$ m in $X$-$Z$, Figure 4a, and $z = 1.44$ m in $Y$-$Z$, Figure 4b, suggesting a slight astigmatism. The shift of the focal point is also observed due to third order terms in the system elements if included, suggesting the cause is spherical aberrations. The maximum width of the rays are increased slightly and the rays split at the point of maximum width. The split appears in both projections. This suggests a ray in $Y$-$Z$ shifted in $X$ and vice versa, leading to the extra trajectory in each projection. This split seems to come from nonlinear coupling



(a) X Projection



(b) Y Projection

Figure 1: Imaging triplet rays w/o space charge. Focal point is at $z = 1.4$ m.

### FODO Cell

The FODO cell consists of one half quad (Q1), inner drift, full quad (Q2), inner drift, and one half quad (Q1). The system parameters are shown in Table 3. The first order system map is shown in (2). To understand its behavior, we decided to study quantities from the normal form of the map. We chose to match the system to a horizontal and vertical tune away from resonance and study its behavior.

(a) $(x|a)$ vs. Current



(b) $(y|b)$ vs. Current

Figure 2: Behavior of $(x|a)$ and $(y|b)$ vs. current in the imaging triplet, as calculated by the moment method and the fast multipole method.



(a) $(x|x^3)$ vs. Current
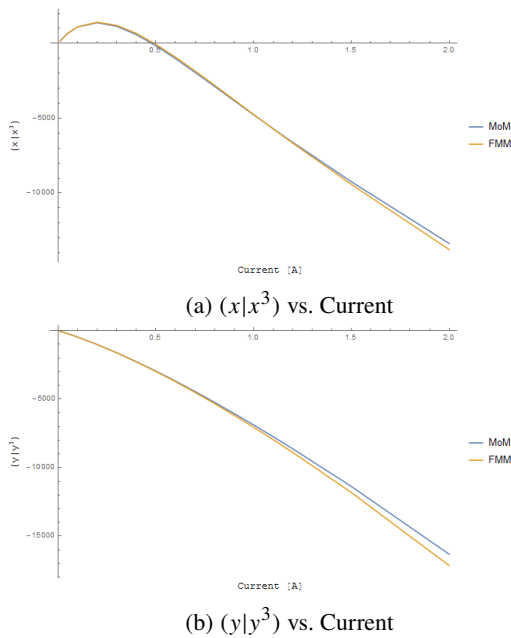


(b) $(y|y^3)$ vs. Current

Figure 3: Behavior of $(x|x^3)$ and $(y|y^3)$ vs. current in the imaging triplet, as calculated by the moment method and the fast multipole method.

introduced by fourth order space charge terms but requires more careful investigation.

## FODO Cell

Settings for the quads in the FODO cell were easily found such that the calculated tunes almost perfectly matched our chosen parameters. However, its behavior changed signifi-



(a) X Projection



(b) Y Projection
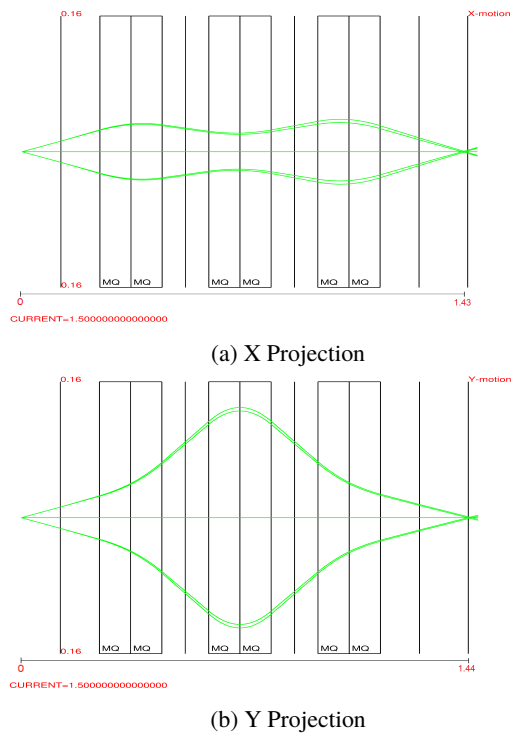
Figure 4: Imaging Triplet rays w/ current = 1.5 A. The focal point has shifted to $z = 1.43$ m in $X$-$Z$ and to $z = 1.44$ m in $Y$-$Z$.

cantly with higher intensity. From Figure 5, the deviation in the horizontal and vertical tune rapidly increases with current, displaying greater rate in the vertical. For $\beta_x$, the system stays periodic until 0.5 A, where the tune becomes imaginary. $\beta_y$'s periodicity is lost around 0.3 A.

For the FODO cell, both the MoM and FMM predict the same tune. The differences displayed in the triplet map elements suggest a very small deviation between the two methods in the map elements, which would be negligible in calculating the tune.

## MINIMIZING EFFECTS DUE TO SPACE CHARGE

To reduce or eliminate the effect of space charge, we simply fit the quad gradients for each current to match our desired parameters. In some cases, the ideal solution could not be achieved, but a desired property of the system is preserved.

### Imaging Triplet

In the triplet, we fit the quad gradients with the condition of only minimizing $(x|a)$ and $(y|b)$. The quad gradients steadily grew with current as shown in Figure 6. Figure 7 plots the absolute value of $(x|a)$ and $(y|b)$. These elements calculated from the FMM oddly oscillated between positive and negative values, but we are more interested in their deviation from 0. The deviation increases by about two or three orders of magnitude in $(x|a)$ and four or five orders of
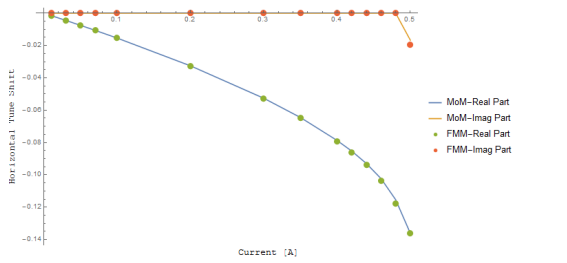
(a) Space charge induced horizontal tune shift vs. Current
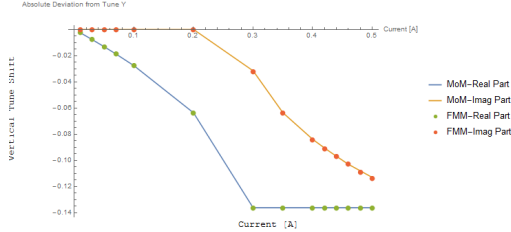


(b) Space charge induced vertical tune shift vs. Current

Figure 5: Tune shift due to space charge from tune = 0.1362 vs. current in the FODO lattice, as calculated by the moment method and the fast multipole method.
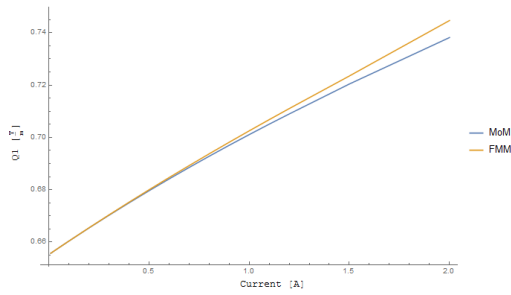


(a) Fitted Q1 vs. Current
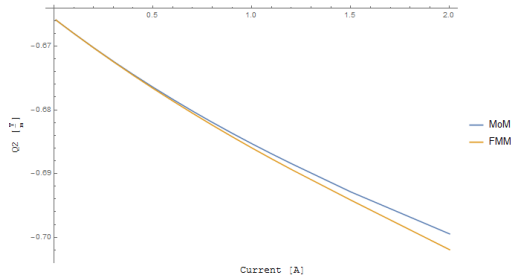


(b) Fitted Q2 vs. Current

Figure 6: Behavior of quad gradients vs. current in the imaging triplet after fitting for imaging, as calculated by the moment method and the fast multipole method.



(a) $(x|a)$ vs. Current



(b) $(y|b)$ vs. Current

Figure 7: Behavior of $(x|a)$ and $(y|b)$ vs. current in the imaging triplet after fitting, as calculated by the moment method and the fast multipole method.

around 0.3 A. We found this is due to the different fitted quad settings for the MoM and FMM. When using the settings found with the MoM, the FMM predicted similar $(x|x^3)$ and $(y|y^3)$ but $(x|a)$ and $(y|b)$ increased by seven orders of magnitude. This will be subject to further investigation. For $(y|y^3)$, both methods predict the aberration behaves similar to Figure 3b.

The ray diagram for 1.5 A after fitting is shown in Figure 9. Figure 9 shows the fitted quad gradients may be overcompensating as the focal points are now around $z = 1.37$ m in $X$-$Z$ and $z = 1.35$ m in $Y$-$Z$. The maximum width is slightly less than in Figure 4, but the split in the ray is still present.

*FODO Cell*

We fit the quad gradients of the FODO Cell by matching the calculated tune to our desired tune; see Figure 10. As current increased, we found it more difficult to match the tune precisely. Vertical stability is lost around 0.3 A. To preserve stability, we allowed for higher tune fitting tolerance. Again, here the MoM and FMM give essentially identical results.

## CONCLUSIONS

We presented some tests related to the performance of our self-consistent transfer map extraction method involving space charge dominated beams. The emphasis of this paper was the comparison of two different tracking methods that underlie the process, namely the Method of Moments and the Fast Multipole Method. In general, the two methods give substantially similar results. Small differences are visible at high currents due to the collisionality of the FMM versus the mean-field nature of the MoM. Still, in one case of a third

magnitude in $(y|b)$. Again, the self-field appears stronger in $Y$ than $X$, leading to the larger increase in $(y|b)$. The peak at 0.6 A in $(x|a)$ appears due to difficulty in minimizing $(x|a)$. We can also see fitting to the MoM is generally smoother than for the FMM. Most likely, this is due to the inclusion of collisional forces.

The behavior of $(x|x^3)$ and $(y|y^3)$ after fitting is shown in Figure 8. The third order aberration $(x|x^3)$ shows different behavior than before, as the two results start to diverge

(a) $(x|x^3)$ vs. Current



(b) $(y|y^3)$ vs. Current

Figure 8: Behavior of the geometric aberrations $(x|x^3)$ and $(y|y^3)$ vs. current in the imaging triplet after fitting, as calculated by the moment method and the fast multipole method.



(a) X Projection



(b) Y Projection

Figure 9: Imaging Triplet rays w/ current = 1.5 A after fitting the quads for imaging. The focal points are at $z = 1.37$ m in $X$ and $z = 1.35$ m in $Y$.

order spherical aberration, large discrepancy was observed due to the different settings, and this will be the subject of further studies involving larger number of particles and Plummer softening in the FMM.



(a) Q1 vs. Current



(b) Q2 vs. Current

Figure 10: Behavior of the quad gradients vs. current in the FODO lattice after fitting to the desired tune, as calculated by the moment method and the fast multipole method.

More specifically, the triplet case showed imaging properties were lost rapidly due to space charge. Spherical aberrations like $(x|x^3)$ and $(y|y^3)$ also displayed significant magnitudes. The FODO cell loses its stability quite rapidly with current, particularly in the vertical plane. When the cell is refitted, the bare tunes cannot be recovered exactly. Relaxing the constraint of equal tunes leaves more options open.

Space charge has a complex role in even these two basic examples. To control higher intensity beams, it is crucial we understand it at a fundamental level. Extracting the space charge map for analysis is a big step for beam dynamics at the intensity frontier and advancing accelerator technology.

## ACKNOWLEDGMENTS

## REFERENCES

[1] B. Erdelyi, E. Nissen, and S. Manikonda, "A Differential Algebraic Method for the Solution of the Poisson Equation for Charged Particle Beams", Commun. Comput. Phys. **17**, 1, 47-78, June 2014.

[2] M. Berz, *Modern Map Methods in Particle Beam Physics*, (San Diego: Academic Press, 1999).

[3] A. Gee and B. Erdelyi, "Study and Comparison of the Method of Moments and the Single Level Fast Multipole Method for 2D Space Charge Tracking", Conf. Proc., NAPAC 2013, Pasadena, CA, USA.

# BEAM DYNAMICS INFLUENCE FROM QUADRUPOLE COMPONENTS IN FRIB QUARTER WAVE RESONATORS*

Z. He, Y. Zhang, Z. Zheng, Z. Liu, J. Wei, FRIB, Michigan State University, USA

## Abstract

Non-axisymmetric RF cavities, such as quarter-wave resonators (QWRs), can produce axially asymmetric multipole field components that can influence beam dynamics. For example, dipole components can cause beam steering, an effect that has been well known to the community since 2001. However, higher order multipole field components, such as quadrupole components, which have potential influence on beam dynamics, have never received enough attention yet. In this paper, we choose FRIB QWRs as an example and quadrupole components are extracted by multipole expansion. Then, influence of quadrupole components on a single cavity is studied using thin lens model. After that, the influence of quadrupole components on a whole FRIB linac segment one is studied, and effects such as transverse profile ovalization and blow up of beam size are witnessed. Lastly, a possible way of quadrupole components compensation for FRIB driving linac is discussed.

# INTRODUCTION

Non-axisymmetric RF cavities such as quarter-wave resonators (QWRs), half-wave resonators (HWR), spoke cavities and crab cavities, are now widely used in accelerators. Because of their geometry, dipole terms, quadrupole terms and other higher order multipole terms appear and can influence beam dynamics [1–4]. Dating back to 2001, A. Facco first pointed out possible beam steering effect coming from QWR and described the issue thoroughly in a later paper [1]. In the paper, a physics model is built to estimate the beam steering effect, and an easy way to compensate the steering effect using defocusing effect by shifting the beam axis is proposed.

Besides dipole term which causes beam steering, quadrupole term can cause beam shape deformation [2], and higher order terms can introduce non-linear effect and decrease dynamic aperture. By now, these effects haven't received enough attention yet. In this paper, we choose the QWR at FRIB [5] as an example. A scheme is developed to draw out multipole components through Fourier-Taylor multipole expansion. Then, a thin lens model based on transit time factor (TTF) [6, 7] is used to include multipole components into traditional cavity model. After that, the quadrupole effect is closely examined in both single cavity and whole linac segment one (LS1). At last, the possibility of self-cancelation of quadrupole components by fine tuning of solenoid polarity is discussed. The first two section has been discussed more thoroughly in our previous paper [8],
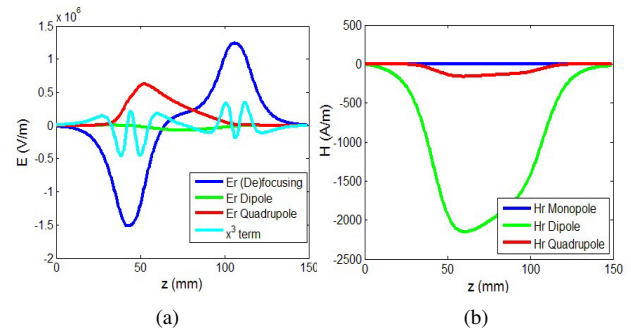
Figure 1: Result of multipole strength curve for radial electric and magnetic field. (a) Radial electric field multipole strength. Blue curve is focusing term, green curve is dipole term, red curve is quadrupole term, and cyan curve is cubic term. (b) Radial magnetic field multipole strength. Blue curve is monopole term, green curve is dipole term, and red curve is quadrupole term.

here, we just list some important results in order to complete the whole story.

# FIELD MULTIPOLE EXPANSION

FRIB QWR 3D field simulated by CST [9] is chosen as the starting point and the numerical approach of Fourier-Taylor multipole expansion is used to draw out the field multipole terms. By expanding radial direction to Taylor series and azimuthal direction to Fourier series in a polar coordinate system, we are able to draw out multipole terms from a certain transverse E&M field to any arbitrary order. The process can be expressed as Eq. 1:

$$
\begin{cases}
F_{\rho,nm}(\rho,\theta) = F_{max} \sum_{n,m=0}^{\infty} P_n A_{nm} \Theta_m \\
P_n = \rho^n \\
\Theta_m = e^{im\theta}
\end{cases}
\tag{1}
$$

By sampling all transverse plane along the longitudinal direction, we can get a plot indicating multipole strength along longitudinal direction, which is shown in Fig. 1.

# MULTIPOLE THIN LENS MODEL

Assuming small thin lens kick, we can split the kick into electric part and magnetic part of contribution:

$$
\begin{aligned}
\Delta y' &= \frac{qe\mu_0}{\gamma m_0} \int_{t_1}^{t_2} H_x(x,y,z,t)dt + \frac{qe}{\gamma m_0 \beta c} \int_{t_1}^{t_2} E_y(x,y,z,t)dt \\
&= \Delta y'_{H,y} + \Delta y'_{E,y}
\end{aligned}
\tag{2}
$$
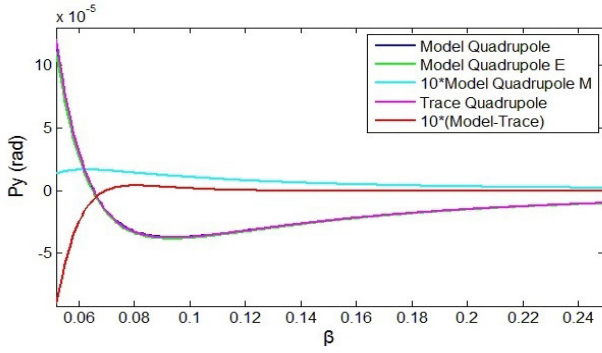
Figure 2: Prediction of quadrupole strength by model and tracking vs. $\beta$, synchronous phase $\phi_s = -\pi/6$ for $\beta$=0.085 QWR. Blue curve shows the total quadrupole strength calculated by model, green and cyan curve each stands for electric quadrupole and 10 times magnetic quadrupole by model, magenta curve shows result calculate from tracking, and red curve shows 10 times the error between model and tracking.

where $q$ is the number of charge, $e$ is the elementary charge amount, $m_0$ is the particle static mass, $\mu_0$ is the permeability, $c$ is the speed of light. Then, we absorb the time changing effect into the TTF factors and then we can easily derive the formulation for calculating the multipole thin lens kick:

$$\Delta y'_{E,y} = \frac{qe}{\gamma\beta^2 m_0 c^2} \sum_{i,j=0}^{n} t_{ij} V_{ij} (T_{ij}\cos\phi - S_{ij}\sin\phi)$$

$$\Delta y'_{H,y} = \frac{qe\mu_0}{\gamma\beta m_0 c^2} \sum_{i,j=0}^{n} t_{ij} U_{ij} (T_{ij}\cos\phi - S_{ij}\sin\phi)$$

(3)

$V_{ij}(U_{ij})$ is the strength of the multipole term $i, j$ with a unit of Volt (Ampere). It is defined by integration of multipole term strength along longitudinal direction. $T_{ij}$ and $S_{ij}$ is the transit time factors of multipole term $i, j$. $\phi$ is the multipole phase. $t_{ij}$ is the coordinate transferring factor, which is a constant for dipole term and is proportional to coordinate for focusing and quadrupole term.

From now, we put our focus mainly on quadrupole component. The term with $i = 1, j = 2$ stands for quadrupole term. For vertical electric field, $E_{max}(z) = E_{max,\rho}(z) = E_{max,\theta}(z)$, coordinate transferring factor $t_{ij} = y/\rho_{max}$; for magnetic field, $H_{max}(z) = H_{max,\rho}(z) = H_{max,\theta}(z), t_{ij} = y/\rho_{max}$. Calculation of FRIB $\beta = 0.085$ QWR quadrupole strength versus $\beta$ can be seen in Fig. 2. Synchronous phase is fixed at $-\pi/6$. Good agreement between model and particle tracking result has been confirmed. According to the model, we can draw the conclusion that, quadrupole kick mainly comes from electric field and there is nearly no contribution from magnetic field. Quadrupole effect would be damping with $\beta$ growing and would be more significant when at low $\beta$. The quadrupole polarity switched once at a certain $\beta$.

By putting the multipole thin lens kick at their electric center, it is easy to add multipole influence into traditional



(a)                              (b)
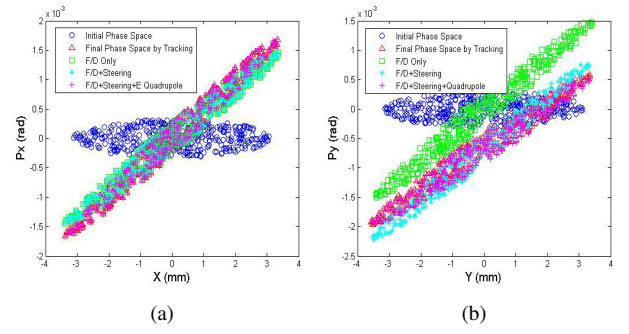
Figure 3: X-Px phase space and Y-Py phase space of a KV distribution beam using tracking and model including different multipole terms of $\beta$=0.085 QWR, particle $\beta$ is 0.055; (a), X-Px phase space; (b), Y-Py phase space.



(a)                              (b)
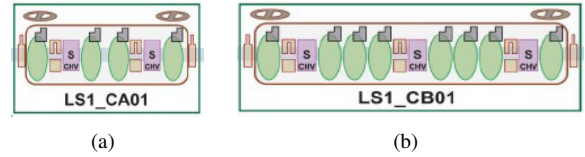
Figure 4: Schematic plot of a single $\beta$=0.041 QWR cryomodule (a) and $\beta$=0.085 QWR cryomodule (b). Green oval represents RF cavity and magenta rectangle represents solenoid.

cavity model. Then, we track a whole cavity and compare the result with 3D field tracking. The result can be seen in Fig. 3. The $\beta = 0.085$ QWR is chosen, and a particular particle $\beta = 0.055$, where quadrupole component is quite large as indicated in Fig. 2, is used.

In Fig. 3, left figure is the X-Px phase space and right figure is the Y-Py phase space, particle $\beta$ equals 0.055, synchronous phase is $-\pi/6$. Blue circle is the initial phase space. Red triangle is the result from 3D field tracking. Green square indicates phase space after adding defocusing term. After adding steering term, phase space become cyan star. After adding quadrupole term, phase space become magenta cross, which is close to 3D field tracking, with error down to 1% for momentum. As a result, we can see that, quadrupole term of QWR would influence beam dynamics significantly, and there is no way of modelling the beam to a high precision if the the quadrupole term is neglected.

## QUADRUPOLE INFLUENCE ON LS1

FRIB LS1 is using two kinds of QWRs, mainly $\beta = 0.041$ QWR and $\beta = 0.085$ QWR. The lattice is following a cryomodule-based periodic structure, and each kind of QWR corresponds to a certain kind of cryomodule. The lattice for a single $\beta = 0.041$ or $\beta = 0.085$ cryomodule is shown in Fig. 4. There are 3 $\beta = 0.041$ cryomodules and 11 $\beta = 0.085$ cryomodules in LS1. An all-solenoid transverse focusing scheme is applied. The main advantage of all-solenoid focusing lattice is that it preserves round shape of a beam and provide convenience for beam matching.
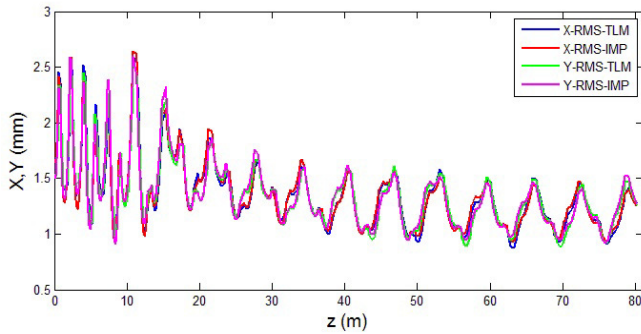
Figure 5: Benchmark thin lens model against IMPACT without the quadrupole term and for a round injection beam. Blue, X rms radius by thin lens model; Red, X rms radius by IMPACT; Green, Y rms radius by thin lens model; Magenta, Y rms radius by IMPACT.
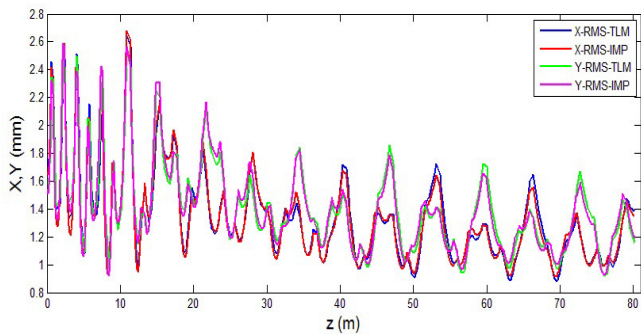


Figure 6: Benchmark thin lens model against IMPACT with the quadrupole term, and for a round injection beam, constant solenoid polarity. Blue, X rms radius by thin lens model; Red, X rms radius by IMPACT; Green, Y rms radius by thin lens model; Magenta, Y rms radius by IMPACT.

Then, we extend our simulation to the whole LS1. For the time being, we are using axisymmetric RF field. The model for solenoid is the traditional hard-edge model. The result is shown in Fig. 5. We can see that the model benchmarked very well with IMPACT [10], and round input beam persists to be round when no quadrupole term is considered.

Then, we can do the similar simulation by switching on the quadrupole component. For IMPACT case, the 3D field particle tracking scheme is used, and for the model, quadrupole thin lens kick is added. The result is shown in Fig. 6. As we can see, both IMPACT and model show discrepancy between x and y direction rms radius because of quadrupole effect, the initial round input beam become oval in shape. And the model is still good enough to benchmark with IMPACT with 3% of average error.

Transverse RMS plot alone isn't good enough to measure the ovalization effect quantitatively. Therefore, we define the $L/S$ parameter, which equals the ratio between long axis and short axis for the oval shape transverse real space. We can calculate the $L/S$ parameter from any theta matrix element by Eq. 4:
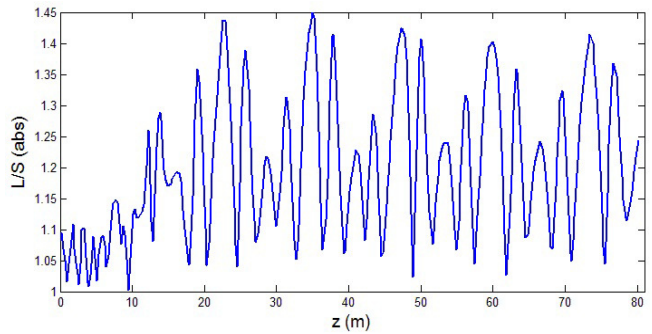
Figure 7: $L/S$ line of constant solenoid polarity case.

$$L/S = \sqrt{\frac{\langle x^2 \rangle + \langle y^2 \rangle + \sqrt{((\langle x^2 \rangle - \langle y^2 \rangle)^2 + 4\langle xy \rangle^2}}{\langle x^2 \rangle + \langle y^2 \rangle - \sqrt{((\langle x^2 \rangle - \langle y^2 \rangle)^2 + 4\langle xy \rangle^2}}} \quad (4)$$

By using Eq. 4, we can calculate the $L/S$ plot of Fig. 6, which can be seen in Fig. 7. The maximum value of $L/S$ is around 1.45.

## POSSIBILITIES OF SELF-CANCELATION OF QUADRUPOLE COMPONENTS

A straight forward way of taking care of the quadrupole component is to add correction quadrupoles at certain location. However, in this chapter, we are going to talk about a different way of self-cancelation of quadrupole components by fine tuning of solenoid polarity.

The original idea comes from comparison between original FRIB lattice design and updated FRIB lattice design. To avoid too strong coupling between horizontal and vertical direction, the original FRIB lattice is utilizing an alternative solenoid polarity scheme. However, after the insight of quadrupole components in QWR cavities, we find out that alternative solenoid polarity setting, which causes Larmor frameto rotate back-and-forth, thus having a clear anisotropic orientation, tends to add up quadrupole influence because quadrupole components mostly have the same polarity according to Fig. 2. The transverse rms size plot and $L/S$ parameter plot for alternative solenoid polarity case can be seen in Fig. 8(a).

From Fig. 8(b), we can see that alternative solenoid polarity increases ovalization of the beam. $L/S$ parameter climbs up to 1.9. That is why we decided to switch to constant solenoid polarity lattice. With Larmor frame constantly rotating towards the same direction, quadrupole components can possibly be smeared out due to self-cancellation. From Fig. 6 and Fig. 7, we can see that the scheme really works well.

However, constant polarity and alternative polarity are just two specific case of $2^{39}$ possible settings of all 39 solenoids in LS1. Constant polarity setting can provide perfect self-cancellation only when Larmor frame is rotating fast enough and when all quadrupole components have the same polarity

(a)



(b)
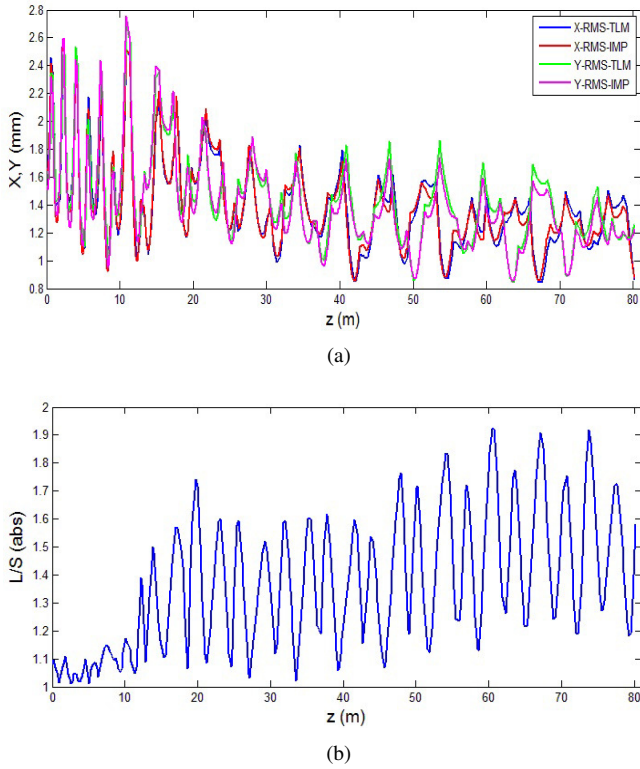
Figure 8: Transverse rms size plot and $L/S$ parameter plot for a round injection beam, alternative solenoid polarity. (a) Benchmark of thin lens model against IMPACT, Blue, X rms radius by thin lens model; red, X rms radius by IMPACT; Green, Y rms radius by thin lens model; Magenta, Y rms radius by IMPACT. (b) L/S line of alternative solenoid polarity case.



Figure 9: Schematic plot of possibility of self-cancelation of quadrupole component.



(a)



(b)
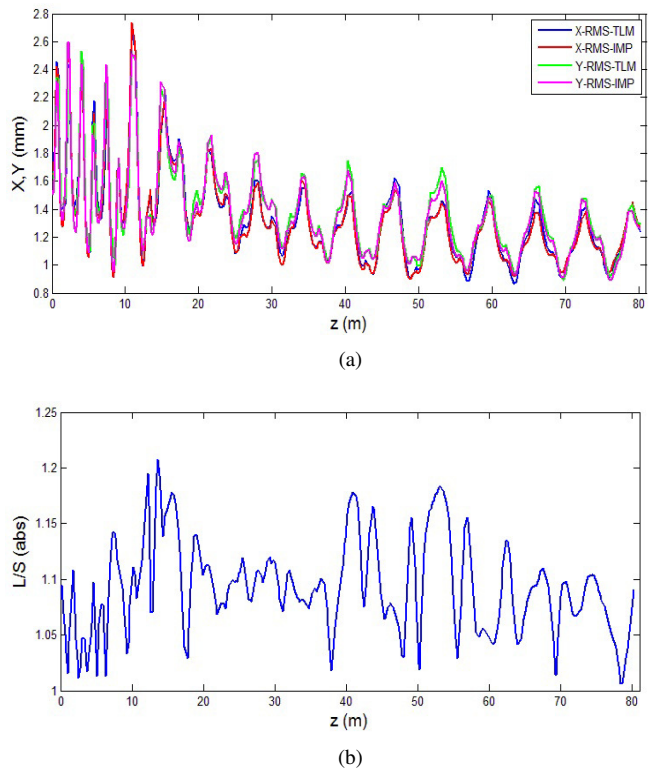
Figure 10: Transverse rms size plot and $L/S$ parameter plot for a round injection beam, optimized solenoid polarity. (a) Benchmark of thin lens model against IMPACT, Blue, X rms radius by thin lens model; red, X rms radius by IMPACT; Green, Y rms radius by thin lens model; Magenta, Y rms radius by IMPACT. (b) $L/S$ line of alternative solenoid polarity case.

and strength, which is quite far away from the real situation. So in theory, there could exist a better case where the solenoid polarity are fine tuned to better cancel out the quadrupole component. The schematic plot of the idea is shown in Fig. 9. If we come to a situation described by Fig. 9, we get two choice to rotate the beam according to the solenoid polarity, and rotating the beam counter clockwise would be better than clockwise. The real situation is not that simple and straight forward and a global optimization would be preferred.

Because we've got 39 solenoids and two possible polarity for each solenoid, we are solving a global optimization problem with 39 dimension and two possible value for each dimension. Thus, the Genetic Algorithm [11] is chosen as the global optimization algorithm. The characteristic volume (defined by mean value times standard deviation times maximum value) of $L/S$ plot is chosen as the minimizing target. Thin lens model, which takes 50 ms per run is used instead of IMPACT, which uses particle tracking and is much slower, in the searching process. Fig. 10 shows one of the optimized cases.

From Fig. 10, we can see that, the quadrupole term largely got suppressed and transverse beam profile becomes closer to

circle, the maximum $L/S$ parameter drops to around 1.2. The result confirms that it is possible to achieve self-cancelation of quadrupole components by fine tuning of solenoid polarity, and no extra component for correction is really needed.

However, we found out that, the global optimization method doesn't always give a fixed pattern, which implies that the optimum solenoid setting may not be stable and universal enough to be realistic and useful. Further study of the physics behind the scheme of self-cancelation of quadrupole components is needed before we can get something really useful.

## CONCLUSION

Quadrupole components in non-axisymmetric RF cavities have been modelled by thin lens model which is based on multipole expansion of numerical 3D field. FRIB $\beta = 0.085$ QWR has been chosen as an example and we show the importance in taking quadrupole term into consideration when building the right linear model for the QWR. Study of the whole LS1 of FRIB indicates quadrupole term would significantly ovalize the originally round beam, and the amount of ovalization would highly depend on solenoid polarity. A comparison between constant solenoid polarity and alternative solenoid polarity shows that the constant solenoid polarity setting has less ovalization. A genetic algorithm is developed to further exploit the possibility of better self-cancelation of quadrupole component by fine tuning the solenoid polarity. An optimized solenoid polarity pattern shows better self-cancelation and the beam profile becomes closer to circle. More physics study is needed in order to come up with a universal and stable solenoid polarity pattern which can be useful.

## ACKNOWLEDGMENT

## REFERENCES

[1] Alberto Facco and Vladimir Zvyagintsev. Beam steering in superconducting quarter-wave resonators: An analytical approach. *Physical Review Special Topics-Accelerators and Beams*, 14(7):070101, 2011.

[2] Marco Cavenago. Determining the radiofrequency dipole and quadrupole effects in quarter wave resonators. *Nuclear Instruments and Methods in Physics Research Section A: Accelerators, Spectrometers, Detectors and Associated Equipment*, 311(1):19–29, 1992.

[3] RG Olave, JR Delayen, and CS Hopper. Multipole expansion of the fields in superconducting high-velocity spoke cavities. *Proc. LINAC2012, Tel-Aviv Israel, MOPB072*, 2012.

[4] SU De Silva and Jean R Delayen. Design evolution and properties of superconducting parallel-bar rf-dipole deflecting and crabbing cavities. *Physical Review Special Topics-Accelerators and Beams*, 16(1):012004, 2013.

[5] J Wei, D Arenius, E Bernard, N Bultman, F Casagrande, S Chouhan, C Compton, K Davidson, A Facco, V Ganni, et al. The frib project–accelerator challenges and progress. *HIATC2012, Chicago, USA*, 51, 2012.

[6] Thomas P Wangler. *RF Linear accelerators*. John Wiley & Sons, 2008.

[7] Kenneth R Crandall. Trace 3-d documentation. Technical report, Los Alamos National Lab., NM (USA), 1987.

[8] Zhengqi He, Zhihong Zheng, Zhengzheng Liu, Yan Zhang, and Jie Wei. An analytical cavity model for fast linac-beam tuning. In *Proc. of LINAC*, volume 12, 2012.

[9] CST Microwave Studio. Computer simulation technology. *GmbH, Darmstadt, Germany*, 2009.

[10] Ji Qiang, Robert D Ryne, Salman Habib, and Viktor Decyk. An object-oriented parallel particle-in-cell code for beam dynamics simulation in linear accelerators. In *Proceedings of the 1999 ACM/IEEE conference on Supercomputing*, page 55. ACM, 1999.

[11] David E Goldberg. *Genetic algorithms*. Pearson Education India, 2006.

# SIMULATIONS OF THE HEAD-TAIL INSTABILITY ON THE ISIS SYNCHROTRON

R.E. Williamson, D.J. Adams, B. Jones, C.M. Warsop, ISIS, STFC, RAL, UK
V. Kornilov, GSI, Darmstadt, Germany

## Abstract

ISIS is the pulsed spallation neutron and muon source at the Rutherford Appleton Laboratory in the UK. Operation is centred on a loss limited 50 Hz proton synchrotron which accelerates $3 \times 10^{13}$ protons per pulse (ppp) from 70 MeV to 800 MeV, delivering a mean beam power of 0.2 MW.

Present studies are focussed on key aspects of high intensity beam dynamics with a view to increasing operational intensity, understanding loss mechanisms and identifying possible upgrade routes. Of particular interest is the head-tail instability observed on ISIS, which is currently a main limitation on beam intensity.

This paper presents initial simulations using HEADTAIL to compare with experimental data taken on the ISIS synchrotron. The details and assumptions of the impedance model and simulations are discussed. Plans for future head-tail measurements, simulations and analysis are outlined.

## INTRODUCTION

The transverse head-tail instability represents a possible intensity limit for bunched beams in many synchrotrons including ISIS and its proposed upgrades. The standard theory of Sacherer [1] does not include space charge and associated incoherent tune spreads. However, recent works [2, 3, 4] have proposed theoretical models to treat head-tail motion in the presence of space charge. In parallel with this, numerical simulations are required to analyse beam behaviour with various collective effects included, as noted in [5].

## ISIS Synchrotron

ISIS operations centre on a rapid cycling synchrotron (RCS) which accelerates $3 \times 10^{13}$ protons per pulse (ppp) from 70 MeV to 800 MeV on the 10 ms rising edge of a sinusoidal main magnet field. Injection is via charge exchange of a 70 MeV, 25 mA H⁻ beam over ~130 turns of the falling main magnet field just prior to field minimum. The unchopped, injected beam is non-adiabatically bunched by the ring dual harmonic RF system (DHRF, $h = 2$ and 4). Nominal betatron tunes are $(Q_x, Q_y) = (4.31, 3.83)$, with peak incoherent tune shifts exceeding ~0.5. The intensity is loss limited with longitudinal trapping, transverse space charge and the head-tail instability being the main driving mechanisms.

Observations on ISIS have shown that the two proton bunches develop coherent vertical growth approximately 2 ms into the acceleration cycle [6]. The growth is suppressed by ramping the vertical tune away from the integer ($Q_y = 4$) during that time. However the growth

rate scales strongly with intensity and lowering the tune further tends to increase loss associated with the half integer resonance [7]. Work is ongoing to develop a beam feedback system [8] to damp the instability. Recent studies have shown that the instability is present both with just the fundamental ($h = 2$) RF system [6] as well as with the DHRF system.

This study presents initial simulations of low intensity head-tail dynamics using HEADTAIL [9] to compare with experimental data using single harmonic RF on the ISIS synchrotron. Calculations of chromatic phase shifts and growth rates from Sacherer theory [1] are compared to HEADTAIL results. Plans for future experimental studies alongside simulation and theory work are outlined.

## SACHERER THEORY

A non-zero value for the chromaticity, $\xi$, results in a momentum dependent betatron tune and an accumulated phase shift along the bunch $\chi = \xi Q \omega_0 \tau / \eta$, where $Q$ is the tune, $\omega_0$ is the angular revolution frequency, $\tau$ is the bunch length in time and $\eta = 1/\gamma_t^2 - 1/\gamma^2$. This chromatic phase shift determines the head-tail mode structure observed through the form factor shown below.

An impedance acting on a beam can introduce a real frequency shift, through its reactive component, as well as instability from its resistive part. The instability growth rate may be calculated for a coasting beam from the equation of motion for a single particle acted on by an impedance. For a bunched beam, the coasting beam growth rate is modified by a sum over the bunch mode spectra. The instability frequency shift [1] is given by

$$\Delta \omega_m = \frac{1}{1+m} \frac{i}{2Q\omega_0} \frac{e\beta}{\gamma m_0} \frac{I_b}{L_b} \frac{\sum Z_\perp(\omega) h_m(\omega - \omega_\xi)}{\sum h_m(\omega - \omega_\xi)}, \quad (1)$$

where $m$ is the oscillation mode number, $m_0$ is the rest mass, $I_b$ is the bunch current, $L_b$ is the bunch length in metres, $Z_\perp(\omega)$ is the transverse impedance as a function of frequency, $h_m(\omega - \omega_\xi)$ is the envelope of the bunch line spectrum

$$h_m(\omega) = (m+1)^2 \frac{\tau^2}{2\pi^4} \frac{1 \pm \cos \omega\tau}{[(\omega\tau/\pi)^2 - (m+1)^2]^2} \quad (2)$$

where $\tau$ is the bunch length in seconds. The associated growth rate from equation 1 is $\tau_m^{-1} = -\text{Im}(\Delta \omega_m)$.

The resistive wall impedance is thought to be the main driving impedance of the head-tail instability on ISIS. The impedance becomes large for small $\omega$ predicting large growth rates for the lowest betatron sideband when $Q$ is just below an integer. It can therefore be approximated by

a narrowband impedance where only one frequency contributes to the summation in the numerator of equation 1. The summation can then be replaced by the impedance at the lowest sideband frequency ($Z_{RW}$) multiplied by a form factor $F_m$,

$$\Delta\omega_m = \frac{1}{1+m}\frac{i}{2Q\omega_0}\frac{e\beta}{\gamma m_0}\frac{I_b}{L_b}Z_{RW}F_m(\omega)\,, \qquad (3)$$

where $F_m$ is shown in  igure 1 for the first few modes and is given by

$$F_m(\omega) = \frac{h_m(\omega)}{\sum h_m(\omega)}\,. \qquad (4)$$
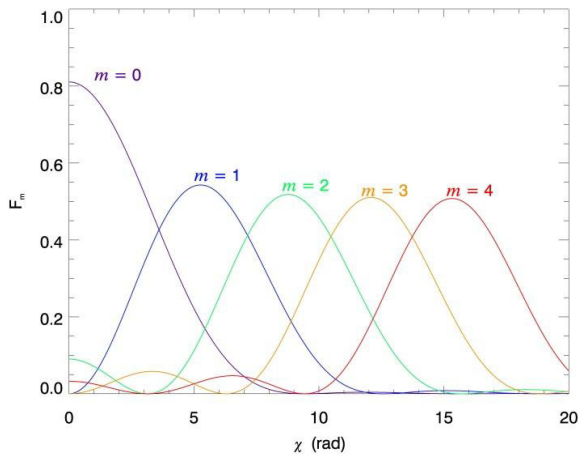


Figure 1: Form factor $F_m$ (defined in equation 4) as a function of the chromatic phase shift $\chi$ for modes 0 to 4.

## EXPERIMENTAL OBSERVATIONS

ISIS currently operates at the natural value of the machine chromaticity ($\xi_x = \xi_y = -1.4$, [10]). The impedance acting on the beam leads to a coherent vertical instability early in the 10 ms acceleration cycle. Measurements were taken at a vertical position monitor over 0 - 5 ms during acceleration. A low intensity beam ($5 \times 10^{12}$ ppp) was injected as a simple case, minimising complications due to space charge, to compare with the theoretical model described above. As there is currently no theory to describe head-tail motion for the case of dual harmonic RF, measurements were made in the more straightforward single harmonic ($h = 2$) case. The vertical tune was increased at 2 and 2.5 ms to 3.87 and 3.75 respectively (from 3.84 and 3.73 for normal single harmonic RF operation) to induce stronger head-tail behaviour.

Figure 2 shows a typical position monitor sum and difference signal over several turns showing clear head-tail motion with mode $m = 1$, one displacement node along the bunch. Using the tune and natural chromaticity we obtain $\chi = 9.11$ rad. However, putting this into the form factor, equation 3, this corresponds to a larger growth rate for $m = 2$ mode with a smaller contribution

from $m = 1$ mode, see Figure 1. A modified theory that could explain this observation may be found in [6].
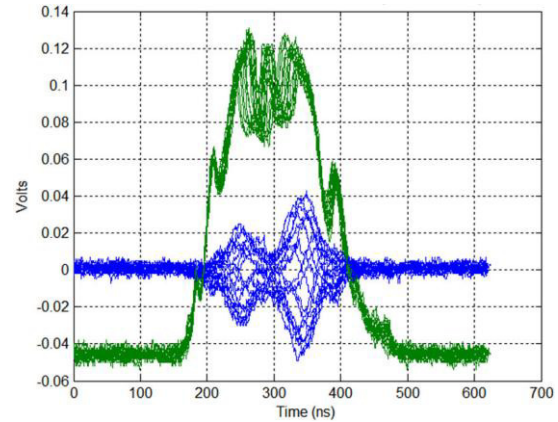


Figure 2: Sum (green) and difference (blue) vertical position monitor signals over several turns at ~1 ms through the ISIS acceleration cycle.
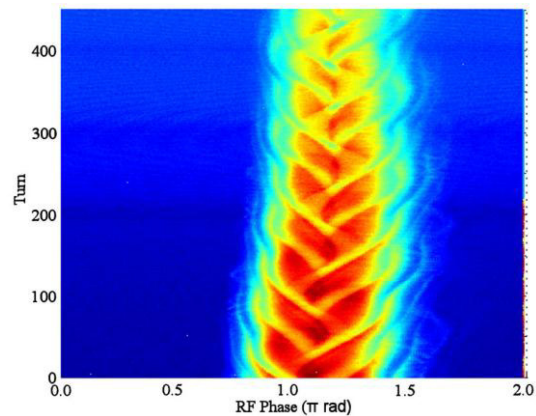


Figure 3: Vertical position monitor sum signal, longitudinal pulse shape as a function of turn from ~1 ms. Red denotes high beam density and blue, no beam.
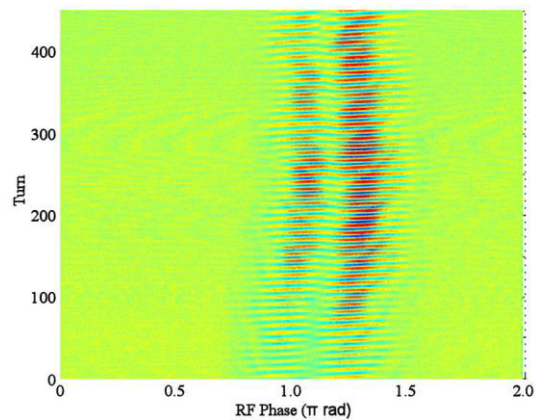


Figure 4: Vertical position monitor difference signal as a function of turn from ~1 ms. Red denotes large positive beam offset, blue negative offset and green zero offset.

Figures 3 and 4 show waterfall plots of the vertical position monitor sum and difference signals respectively for both bunches from ~1–1.5 ms through the ISIS acceleration cycle. During this time the RF frequency

sweeps between 1.43 – 1.53 MHz. The frequency sweep has been removed from Figures 3 and 4.

Figure 3 clearly shows that there is sustained non-uniform longitudinal structure. This indicates non-optimal longitudinal capture and bunching and could influence the head-tail mechanism. However, the instability growth rate is much faster than the longitudinal motion and, as shown in Figure 4, the $m = 1$ mode is persistent over many hundreds of turns despite the non-uniform longitudinal behaviour and ramping RF frequency. Therefore it is reasonable to assume that these do not play a significant role in the head-tail motion. Figure 4 also shows that there is strong coupling between the two bunches.

## SIMULATIONS

The macro-particle simulation code HEADTAIL [9] was used to perform comparative simulations of the low-intensity head-tail behaviour seen on ISIS with single harmonic RF. The code utilises a simple smooth focussing model for transverse motion and applies wakefield kicks to simulate the interaction of the beam with its environment.

It is noted that the HEADTAIL code, and most theoretical models, assume $\beta \sim 1$. However, head-tail behaviour on ISIS is observed at much lower $\beta$ values ($\beta \sim 0.4$). The importance of this is currently being investigated.

For initial simulations, parameters at 1 ms were assumed with intensities and tunes as per the experiment. Longitudinal motion was simulated with single harmonic RF and acceleration. The thick resistive wall wakefield was assumed with the wake function [5],

$$W_{RW}(z) = -\frac{cL_{RW}}{b^3}\left(\frac{\beta}{\pi}\right)^{3/2}\sqrt{\frac{Z_0}{z\sigma_{RW}}}, \qquad (5)$$

where $L_{RW}$ is the length of the resistive wall, $b$ is the beampipe radius, $Z_0$ is the impedance of free space and $\sigma_{RW}$ is the pipe conductivity.

Measurements at ISIS have shown the impedance to be $\sim 200\,\text{k}\Omega/\text{m}$ at 110 kHz [11]. The thick-wall approximation underestimates this impedance as, at low frequencies, the skin depth becomes comparable to or larger than the pipe thickness and the thick-wall approximation is no longer valid. However, a wakefield interpretation of thin resistive wall has not yet been implemented in HEADTAIL. Instead, for these initial, exploratory simulations, the conductivity has been modified to artificially match the impedance at the dominant frequency harmonic.

Figures 5 and 6 show the simulated vertical difference signal over several turns and maximum vertical amplitude over 800 turns. The pattern in Figure 5 shows a $m = 2$ mode oscillation which is consistent with theory given the chromatic phase shift along the bunch. However, it is noted that the growth rate in Figure 6 is much faster than predicted using equation 1 (e-folding time constant of

160 µs as compared to 2.24 ms respectively). In comparison, the experimental growth rate is much closer to the simulated value of order 100 µs.
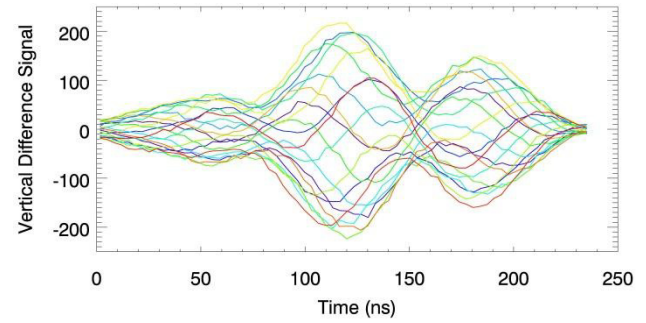


Figure 5: Simulated vertical difference signal over the last 20 turns of the simulation with nominal tune at 1 ms.
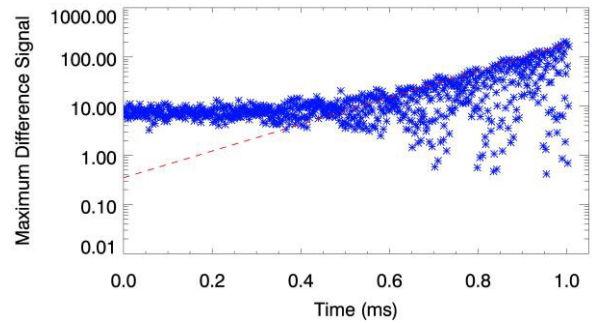


Figure 6: Simulated maximum vertical offset over 800 turns (blue) with exponential fit (red).

### Chromaticity Scan

In order to compare better the simulation results to theory, the chromaticity in HEADTAIL was scanned from zero to the operating, natural chromaticity whilst holding all other parameters constant. ISIS does not currently have the capability to control chromaticity so no experimental comparisons were possible. Results are summarised in Figures 7 – 12.

Figures 7 and 8 show head-tail behaviour with zero chromaticity. This leads to strong $m = 0$ mode vertical motion as is predicted from Figure 1 with $\chi = 0$. The growth rate fit in Figure 7 produces an e-folding time of 26 µs. Using the narrowband assumption, theory predicts a much slower e-folding time of 473 µs.
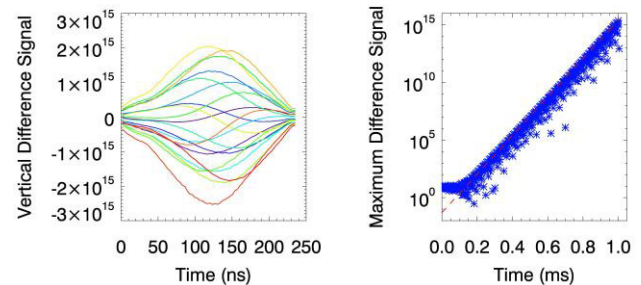


Figure 7: Left - Simulated vertical difference signal over the last 20 turns. Right - Maximum vertical offset over 800 turns (blue) with exponential fit (red) for $\xi = 0$.

The vertical offset from bunch centre for the zero chromaticity case is shown as a function of longitudinal phase space in Figure 8 for 2000 sample particles. A banded structure is clearly visible across the phase space. Further analysis may allow the ideas of Rees [6] to be explored in more detail.
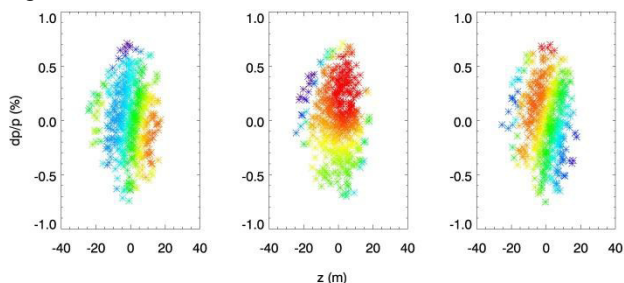


Figure 8: Longitudinal phase space on turn 780 (left), 790 (centre) and 800 (right) for ξ = 0. Colour denotes vertical offset for 2000 sample particles from negative (blue) to positive (red) with respect to centre.

Figures 9 and 10 show results of HEADTAIL simulations for an ISIS chromaticity of -0.82. According to theory this results in a maxima for *m* = 1 head-tail motion. This is borne out in Figure 9 with one node, although *m* = 0 and 2 are also present with similar yet smaller growth rates to the dominant *m* = 1 mode. As previously, the simulated growth rate is much faster than in theory (an e-folding time of 62 μs as compared to 1.41 ms).
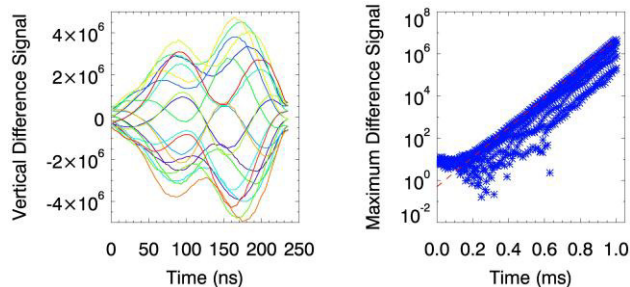


Figure 9: Left - Simulated vertical difference signal over the last 20 turns. Right - Maximum vertical offset over 800 turns (blue) with exponential fit (red) for ξ = -0.82 (χ = 5.31 rad).
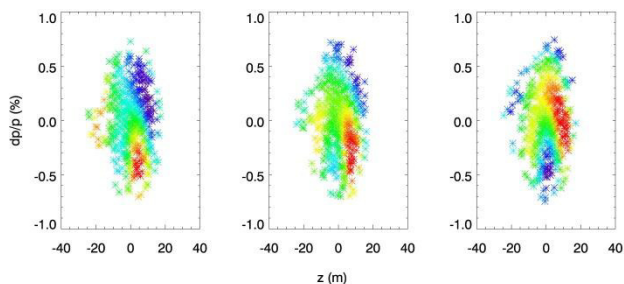


Figure 10: Longitudinal phase space on turn 780 (left), 790 (centre) and 800 (right) for ξ = -0.82. Colour denotes vertical offset for 2000 sample particles from negative (blue) to positive (red) with respect to centre.

Figure 10 shows the vertical offset as a function of longitudinal phase space. The displacement structure across the phase space suggests more complicated motion of the higher mode.

Figures 11 and 12 show results from HEADTAIL simulations for ISIS with a chromaticity of -1.2. Sacherer theory suggests a strong m = 2 mode which is shown clearly in Figure 11. From Figure 11 the fitted e-folding time is 140 μs, much faster than that calculated from theory, 2.37 ms.
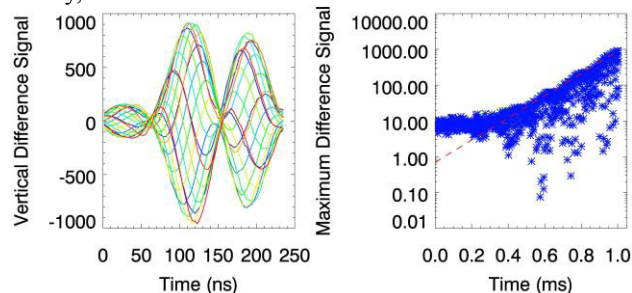


Figure 11: Left - Simulated vertical difference signal over the last 20 turns. Right - Maximum vertical offset over 800 turns (blue) with exponential fit (red) for ξ = -1.2 (χ = 7.83 rad).
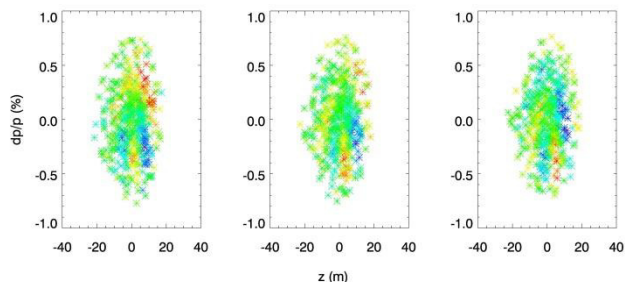


Figure 12: Longitudinal phase space on turn 780 (left), 790 (centre) and 800 (right) for ξ = -1.2. Colour denotes vertical offset for 2000 sample particles from negative (blue) to positive (red) with respect to centre.

Figure 12 shows the vertical offset as a function of position in longitudinal phase space for ξ = -0.82. There is clear non-uniform structure present with different displacement patterns from lower values of chromaticity.

The difference in the predicted growth rate from theory and that calculated from simulation may be due to the large changes in the thick resistive wall impedance at low frequencies. A small shift in frequency can cause a much larger change in impedance. This will be the subject of further study.

## SUMMARY

Head-tail instability has been identified on the ISIS synchrotron and is a key intensity limit for operations. A sample of a recent experimental study into the simplified case of low intensity, single harmonic RF driven head-tail at ISIS has been presented together with current theory based on work by Sacherer [1]. As previously noted [6], the head-tail mode observed on ISIS does not match predictions from theory.

Complementary to these studies work has begun on developing a beam feedback system to damp instabilities [8]. The proposal sees the installation of two identical strip-line monitors, one to be used as a pick-up and the other as a kicker.

Initial HEADTAIL [9] simulations have been compared to the experimental results and theoretical calculations. The mode structure observed in simulation results has been shown to conform to the theory of Sacherer as chromaticity is varied. However, the growth rates calculated from simulated data are much faster than predicted from theory but are of the same order of magnitude as that observed experimentally. It is thought this may be due to the limitations of the impedance model used and approximations to a narrowband impedance as other, higher harmonics may be important.

## FUTURE WORK

A key first step is to make measurements of the resistive wall impedance on ISIS. These are planned using coasting beams in storage ring mode, with the main magnet field set at a DC level appropriate for the 70 MeV injected beam and RF systems switched off. As outlined above, the precise impedance model can cause large changes in beam dynamics and instability. These valuable additions to our existing models will inform further experiments, simulations and influence the design of the planned damping system.

Simulation work is planned to understand better both the HEADTAIL implementation and its relation to the theory of Sacherer. An existing in-house longitudinal code [12] may be modified to implement smooth focussing transverse motion and include a model of the resistive wall impedance. Results will then be compared to theory, experimental results and those of HEADTAIL. It is also planned to analyse the experimental and simulation data with reference to the theory of Rees [6].

Once the case of low intensity, single harmonic RF driven head-tail is understood, studies will move toward high intensity single harmonic behaviour. This will require the addition of a model of transverse space charge in simulations. Finally, it is planned to investigate dual harmonic RF head-tail where there is currently no theory to describe the observations.

## REFERENCES

[1] F. Sacherer, "Transverse Bunched Beam Instabilities", Proc. First Course of the International School of Particle Accelerators of the 'Ettore Majorana' Centre for Scientific Culture, CERN 77-13, pp. 198 – 218 (1977).

[2] M. Blaskiewicz, "Fast Head-Tail Instability with Space Charge", Phys. Rev. ST Accel. Beams **1**, 044201 (1998)

[3] A. Burov, "Head-tail Modes for Strong Space Charge", Phys. Rev. ST Accel. Beams **12**, 044202 (2009).

[4] V. Balbekov, "Transverse Modes of a Bunched Beam with Space Charge Dominated Impedance", Phys. Rev. ST Accel. Beams **12**, 124402 (2009).

[5] V. Kornilov, O. Boine-Frankenheim, "Head-tail Instability and Landau Damping in Bunches with Space Charge", Phys. Rev. ST Accel. Beams **13**, 114201 (2010).

[6] G.H. Rees, "Interpretation of the Higher Mode, Head Tail Motion Observed on ISIS", Particle Accelerators, Vol.39, pp.159 – 167 (1992).

[7] C.M. Warsop *et al*., "Studies of Loss Mechanisms Associated with the Half Integer Limit on the ISIS Ring", Proc. HB2014, East Lansing, MI, USA, to be published (2014).

[8] S.J. Payne, "Strip Line Monitor Design for the ISIS Proton Synchrotron Using the FEA Program HFSS", Proc. IBIC2013, Oxford, UK, pp. 435 – 437 (2013).

[9] G. Rumolo, F. Zimmermann, "Electron Cloud Simulations: Beam Instabilities and Wakefields", Phys. Rev. ST Accel. Beams **5**, 121002 (2002).

[10] C.M. Warsop, *Special Diagnostic Methods and Beam Loss Control on High Intensity Proton Synchrotrons and Storage Rings*, PhD Thesis, Sheffield University, UK, pp. 86 – 90 (2002).

[11] C.M. Warsop *et al*., "High Intensity Studies on the ISIS Synchrotron, Including Key Factors for Upgrades and the Effects of Half Integer Resonance", Proc. HB2010, Morschach, Switzerland, pp. 619 – 623 (2010).

[12] R.E. Williamson *et al*., "High Intensity Longitudinal Dynamics Studies for an ISIS Injection Upgrade", Proc. HB2012, Beijing, China, pp. 492 – 496 (2012).

# IMAGE FIELDS IN THE RECTANGULAR VACUUM VESSELS OF THE ISIS SYNCHROTRON

B.G. Pine, ISIS, RAL, STFC, UK and JAI, Oxford, UK
C.M. Warsop, ISIS, RAL, STFC, UK

## Abstract

ISIS is the pulsed spallation neutron source based at Rutherford Appleton Laboratory in the UK. Operation is based on a 50 Hz, 800 MeV proton synchrotron, accelerating up to $3 \times 10^{13}$ protons per pulse, which provides beam to two target stations. Space charge effects contribute significantly to beam loss. Fields from the intense beam interact strongly with their environment. At ISIS the vacuum vessel is rectangular and profiled to follow the shape of the design beam envelope.

Past studies have suggested that closed orbit induced image fields may contribute to beam loss under certain conditions. Image fields for parallel plate and rectangular geometries are reviewed, in particular their expansion as power series is determined. A simulation tool has been developed for particle tracking with space charge. The code contains both Fast Fourier Transform and Finite Element Analysis based field solvers, which have been used here to test the range of validity for the power series expansions for centred and off-centred beams.

These expansions are then used to determine driving terms for the transverse beam motion. Of particular interest for ISIS is the resonant behaviour of beams with a harmonic closed orbit, which can be compared with the output of beam tracking simulations.

# INTRODUCTION

At the highest intensities it is believed that image forces from off-centred beams can contribute to losses on ISIS [1,2]. These beam losses are difficult to isolate during normal operation of the facility. Therefore a program of analysis and simulation has been established in order to describe the effect of image forces and try to estimate the level of beam loss they could potentially cause. In the future it is hoped that a better understanding of the image forces may allow them to be identified experimentally. Analyses for parallel plate and rectangular geometry including centred and off-centred beams are reviewed. The results are then compared with the output of particle-in-cell (PIC) simulations.

The ISIS rapid cycling synchrotron (RCS) accelerates a high intensity beam at a fast repetition rate of 50 Hz. The synchrotron has a circumference of 163 m. It is composed of 10 super periods, with specialised sections for injection, extraction and collimation. The peak incoherent tune shifts are 0.5 or larger in both planes. Many different loss mechanisms may contribute to beam loss at any particular point in the machine cycle, especially during the time between injection and bunching of the beam, when space charge forces peak. In order to gain insight into the individual loss processes it is
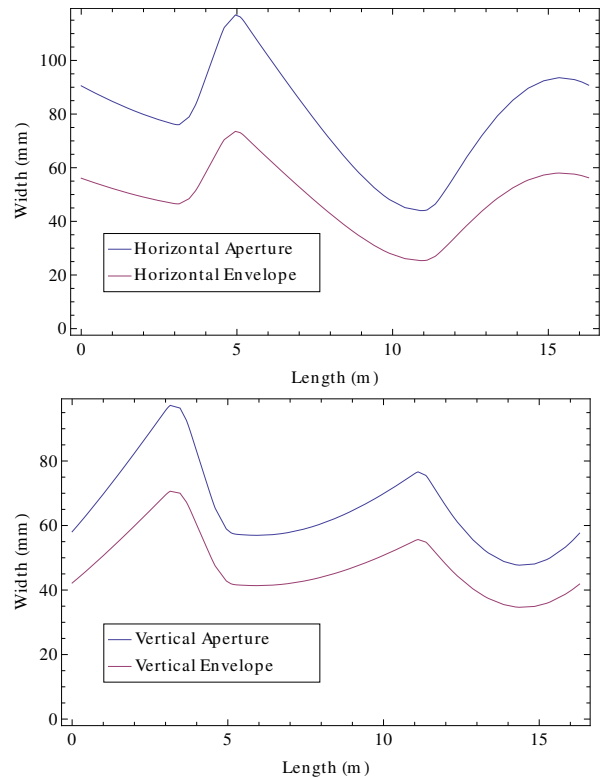


Figure 1: Apertures and envelopes for one super period of the ISIS RCS: (top) horizontal, (bottom) vertical.

helpful to separate out different effects to study. For the purpose of the present paper attention is focused purely on the transverse plane, and in particular a geometrical approach to the image forces.

ISIS has rectangular vacuum vessels and RF shields whose cross section runs parallel to the design beam envelope in both planes (Figure 1). Of particular interest for ISIS are the higher order image terms due to off-centered beams. It has been suggested that these may affect beam loss at the highest intensities [1].

# IMAGE FIELDS IN PARALLEL PLATE AND RECTANGULAR GEOMETRY

## Image Terms due to Laslett

Following Laslett [3], parallel plate geometry is used as an approximation to rectangular. For a beam centred at $y_1$ between two infinite parallel plates at $\pm h$ and a field point at $y$ as shown in Figure 2, there are an infinite series of images above and below the beam. Conformal mapping may be used to transform to a new system where the images are
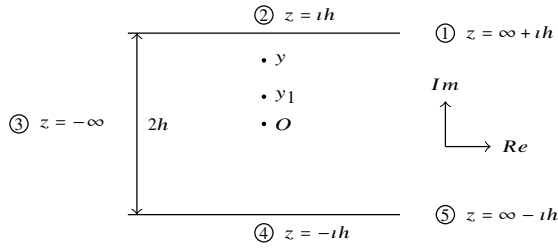
Figure 2: Parallel plate geometry before conformal mapping.
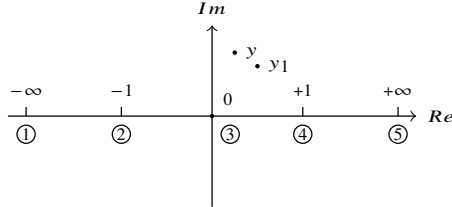


Figure 3: Parallel plate geometry after a conformal mapping into the real axis.

easier to obtain. The transformation $z' = e^{\pi(z+\iota h)/2h}$ carries points 1 - 5 from Figure 2 into the real number line in $z'$ as shown in Figure 3.

The potential due to a line charge is $W = -2\lambda \ln|z|$

$$W = -2\lambda(\ln\left|e^{\iota\pi(y+h)/2h} - e^{\iota\pi(y_1+h)/2h}\right|$$
$$- \ln\left|e^{\iota\pi(y+h)/2h} - e^{-\iota\pi(y_1+h)/2h}\right|).$$

The real potential is obtained from this

$$U = -2\lambda \ln\left|\frac{\sin(\pi y/2h) - \sin(\pi y_1/2h)}{1 + \cos(\pi(y + y_1)/2h))}\right|. \quad (1)$$

Equation 1 is exact. The answer is then approximated using power series expansions. Expanding to second order

$$U \simeq -2\lambda\left(\ln\left|\frac{\pi(y - y_1)}{4h}\right| + \frac{\pi^2(y^2 + 4yy_1 + y_1^2)}{48h^2}\right).$$

The first term is the potential of a bare line charge, the second is Laslett's expansion for images between parallel plates. While real, high intensity beams are not point like, the image terms are still a reasonable approximation if the beam is far enough away from the chamber wall.

If Laslett's image term is differentiated with respect to $y$ we obtain the image component of the electric field

$$E_y \simeq -2\lambda\frac{\pi^2}{48h^2}(2y + 4y_1).$$

Changing variables to $\bar{y} = y_1$ and $\hat{y} = y - y_1$ then gives

$$E_y \simeq -2\lambda\frac{\pi^2}{48h^2}(2\hat{y} + 6\bar{y}).$$

Laslett's image co-efficients are divided by 4 to obtain $\epsilon_1 = \frac{\pi^2}{48}$ for images due to the offset of the field point from the

centre of the beam (known as the incoherent term), and $\xi_1 = \frac{\pi^2}{16}$ for images due to the offset of the beam from the centre of the beam pipe (known as the coherent term), finally giving for the electric field due to images

$$E_y \simeq -4\frac{\lambda}{h^2}(\epsilon_1\hat{y} + \xi_1\bar{y}). \quad (2)$$

### Expansion due to Baartman

Baartman [2] starts with Equation 1, but expands the power series to the 5th power to obtain

$$U \simeq -2\lambda(\ln\left|\frac{\pi(y - y_1)}{4h}\right| + \frac{\pi^2(y^2 + 4yy_1 + y_1^2)}{48h^2}$$
$$+ \frac{\pi^4(7y^4 + 32y^3y_1 + 42y^2y_1^2 + 32yy_1^3 + 7y_1^4)}{23040h^4}).$$

Leaving out the term due to the free line charge and differentiating with respect to $y$ to get $E_y$

$$E_y = \frac{\lambda\pi^2}{24h^2}(2y + 4y_1)+$$
$$\frac{\lambda\pi^4}{11520h^4}(28y^3 + 96y^2y_1 + 84yy_1^2 + 32y_1^3).$$

Baartman then rearranged this in terms of $\bar{y} = y_1$ and $\hat{y} = y - y_1$ to give

$$E_y = \frac{\lambda\pi^2}{24h^2}(2\hat{y} + 6\bar{y})+$$
$$\frac{\lambda\pi^4}{11520h^4}(28\hat{y}^3 + 180\hat{y}^2\bar{y} + 360\hat{y}\bar{y}^2 + 240\bar{y}^3)$$

$$= \frac{\lambda\pi^2\hat{y}}{12h^2} + \frac{\lambda\pi^2\bar{y}}{4h^2} + \frac{28\lambda\pi^4\hat{y}^3}{11520h^4} + \frac{\lambda\pi^4\hat{y}^2\bar{y}}{64h^4} + \frac{\lambda\pi^4\hat{y}\bar{y}^2}{32h^4} + \frac{\lambda\pi^4\bar{y}^3}{48h^4}.$$

The first two terms are Laslett's linear image terms. The others represent non-linear terms which are functions of both the distance of the field point from the beam centre, and the beam centre offset from the origin. It is these higher order terms that Rees, Prior [1] and Baartman suggested as a source of closed orbit image driven losses at ISIS.

### Elliptical Function Solution due to Ng

Ng also uses conformal mapping to derive the potential but then uses elliptical functions, $K(k)$, to solve for the exact solution with a rectangular boundary [4, 5]. For a centred beam the elliptical functions simplify to (see Equation 3.109 from [5]):

$$sn\left(\frac{K(k')}{2}, k'\right) = \frac{1}{\sqrt{1 + k}},$$
$$cn\left(\frac{K(k')}{2}, k'\right) = \frac{\sqrt{k}}{\sqrt{1 + k}},$$
$$dn\left(\frac{K(k')}{2}, k'\right) = \sqrt{k}.$$
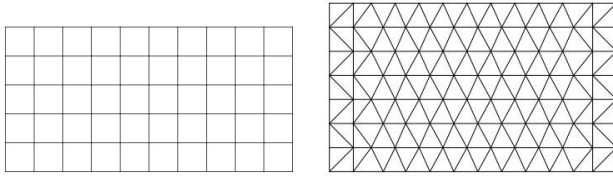
Figure 4: Mesh for Poisson solvers: (left) FFT solver using finite difference approach, (right) FEA solver using iterative relaxation.



Figure 5: (Left) KV distribution in a square aperture showing $10^4$ particles, (right) density plot of the KV distribution.

The nome for rectangular geometry is $q = e^{-2\pi\omega/h}$. The argument of the doubly periodic functions can be approximated if the ratio of the vacuum vessels satisfies certain conditions:

$$k^2 = 16q(1-8q+44q^2-192q^3+718q^4-2400q^5+7352q^6$$
$$-\ 20992q^7 + 56549q^8).$$

$$K(k) = \frac{\pi}{2}\left[1 + \frac{1}{4}k^2 + \frac{9}{64}k^4 + O(k^6)\right].$$

Following these steps a simple estimate may be made for the image co-efficient for a centred beam cf. Equation 2

$$\epsilon_1 = \frac{K^2(k)}{12}(1 - 6k + k^2).$$

## SIMULATION MODEL

In this section the Poisson solvers are presented and some initial results demonstrated, then in the next sections they are used to investigate the different models that have been introduced. The simulation model allows the generation of a beam distribution in a rectangular boundary, and calculation of the resulting potential and electric fields. Two Poisson solvers were compared for this task, one using a rectangular mesh with a Fast Fourier Transform (FFT) solver and the other using a triangular mesh and a Finite Element Analysis (FEA) solver, see Figure 4. The solvers are from the beam tracking code, Set [6].

The FFT solver was originally created to solve for the potential of beam fields in the ISIS conformal vacuum vessel. The FEA solver was added to allow the calculation of beam fields in other geometries. Their main requirements are speed and accuracy, as normally they have to solve for beam potentials hundreds of times per simulated turn in the beam tracking code, Set. The FFT solver uses matrix methods to directly solve for the potential, while the FEA solver uses an iterative relaxation approach. For these simulations a KV beam distribution was used as it has a linear space charge force which can easily be compared with theory. $5 \times 10^5$ macro particles were used for each of the simulations as this number gave acceptably low statistical noise. Figure 5 (left) shows a scatter plot of the particles in a square aperture, while Figure 5 (right) shows a density plot of the same. Figures 6 and 7 show the potential and electric fields calculated from a KV beam in a square aperture. Figure 8 shows the horizontal and vertical fields on lines through
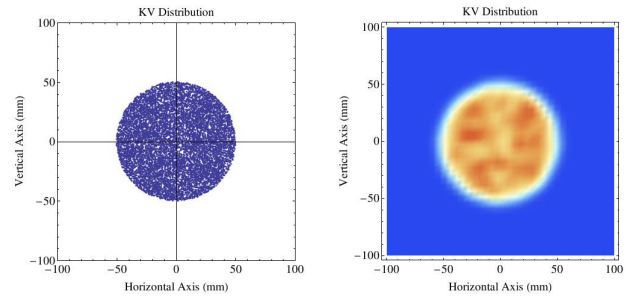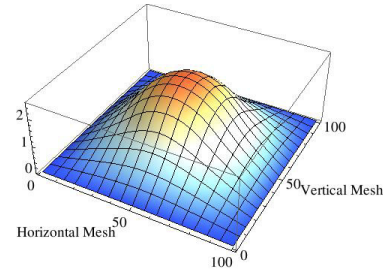


Figure 6: 3D plot of potential due to KV beam in square aperture, units $\epsilon_0$ V.

the centre of the beam, compared with the calculated fields for a KV beam. There was an excellent level of agreement between the FFT and FEA solvers for both the obtained potential and fields, presented more fully elsewhere [7].

### Results for Centred Beam

The range of validity for the parallel plate approximation was compared with the full rectangular geometry solution. In this case a centred beam was investigated, so only the image terms due to a centred beam were considered. An image co-efficient equivalent to Laslett's (Equation 2) could be obtained by taking the gradient of the electric field across the beam. A linear fit provided the best match to the image co-efficient. Baartman's expansion only adds very small terms to the solution for a centred beam. A set of simulations was run in which the beam pipe width was varied from 75 to 300 mm while the height was held constant at 100 mm. The beam radius was 50 mm. Image coefficients were calculated from each simulation and the results plotted in Figure 9, along with Laslett's prediction for a centred beam between parallel plates. Laslett's image term is the solution that the simulation tends to as the ratio of horizontal to vertical beam pipe size becomes larger. As Laslett's solution is for infinite parallel plates this is to be expected. It is also clear that Laslett's solution is the "worst case scenario" and so represents a pessimistic estimate, useful for machine designs where one wants to err on the side of caution. It is also interesting that the incoherent image term approaches zero when the beam pipe ratio is 1.

Ng's solution was also compared with these results, also in Figure 9. As can be seen this value for the image coefficient had an excellent agreement with the simulation results.
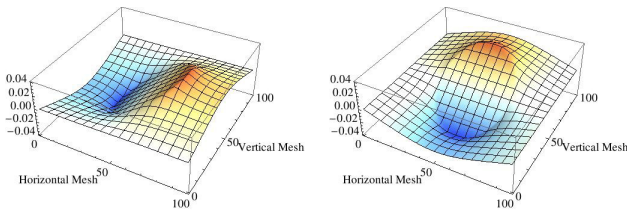
Figure 7: Fields produced by FFT solver: (left) horizontal and (right) vertical, units $\epsilon_0$ V / mm.
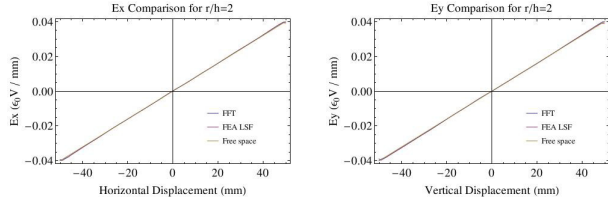


Figure 8: Fields produced by FFT and FEA solvers, compared with those for a KV beam in free space: (left) horizontal axis and (right) vertical axis.

### Results for Off-Centred Beam

For these results, in addition to scanning the beam pipe aspect ratio between 0.75 and 3, the beam offset from centre was varied between 0 and 30 mm in steps of 5 mm. In each case the electric fields along the horizontal and vertical axes of the beam were recorded. For an off-centred beam the higher order image terms become significant. Baartman introduces the higher order image coefficients $\kappa$ in [2] as follows

$$\frac{E_{yimage}}{4\lambda} = \epsilon_1 \frac{\hat{y}}{h^2} + \xi_1 \frac{\bar{y}}{h^2} + \kappa_{30}\frac{\bar{y}^3}{h^4} + \kappa_{21}\frac{\hat{y}\bar{y}^2}{h^4}$$
$$+ \kappa_{12}\frac{\hat{y}^2\bar{y}}{h^4} + \kappa_{03}\frac{\hat{y}^3}{h^4} + ... \quad (3)$$

A third order polynomial function with respect to $\hat{y}$ was fitted to the electric field obtained from the simulations. Further
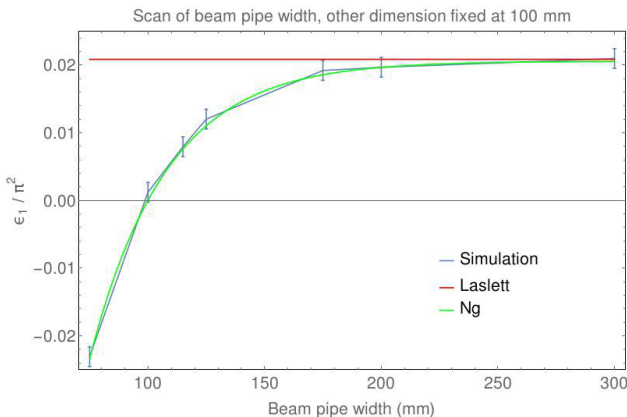


Figure 9: Results for a scan of beam pipe width from 75 - 300 mm, while height is held fixed at 100 mm. Laslett and Ng's image co-efficients for a centred beam compared with simulations.
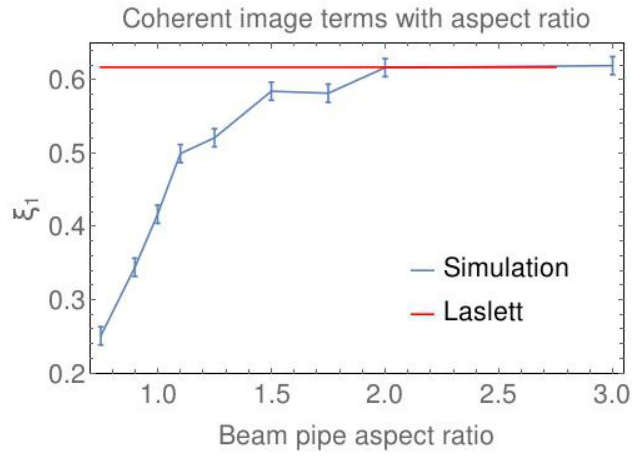


Figure 10: Laslett's image co-efficient for an off-centred beam, as a function of beam pipe aspect ratio from 0.75 - 3, compared with simulations.
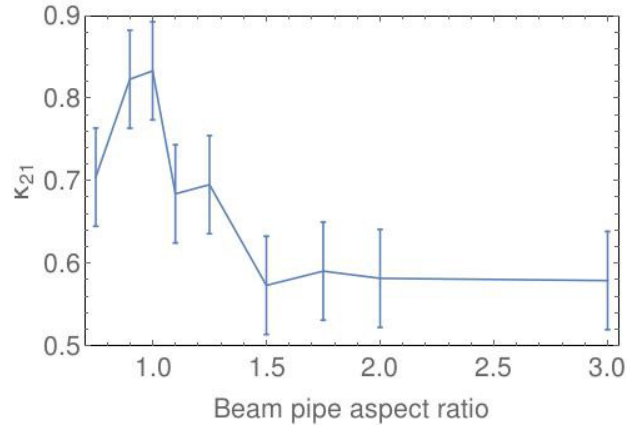


Figure 11: The higher order image term $\kappa_{21}$ as a function of beam pipe aspect ratio from 0.75 - 3.

fitting was carried out to obtain functions with respect to $\bar{y}$ in order to obtain the values of the $\kappa$ terms from Equation 3. Errors were calculated by generating 10 sets of additional values at beam pipe aspect ratios of 1 and 3, and the averages taken. These errors are representative of noise in the KV beam. The same method was used for the errors in the previous section.

Figure 10 shows the value of the coherent image term $\xi_1$ as the beam pipe aspect ratio was scanned from 0.75 to 3. Laslett's value for the coherent term of $\frac{\pi^2}{16}$ is also included. As can be seen the simulation results approach Laslett's solution as the beam pipe aspect ratio becomes close to 2. However, where the ratio is around 1 the coherent term is nearer to half of this value.

Figure 11 shows the simulation results for the $\kappa_{21}$ term from Equation 3. This is a quadrupole term whose strength is proportional to the square of the closed orbit offset. Rees, Prior and Baartman [1, 2] believed it could be responsible for some intensity dependent loss at ISIS. As can be seen from the plot, This term peaks where the beam pipe aspect
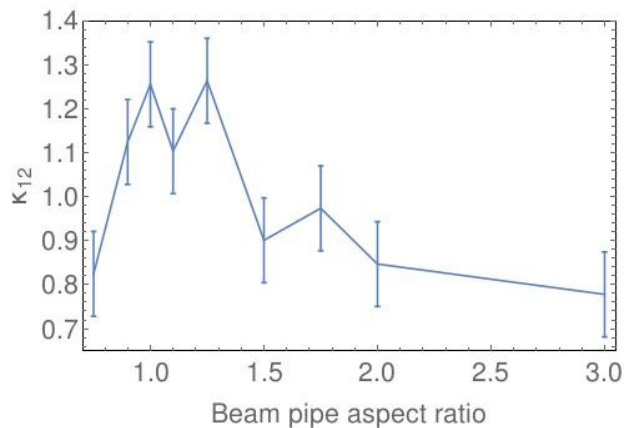
Figure 12: The higher order image term $\kappa_{12}$ as a function of beam pipe aspect ratio from 0.75 - 3.

ratio is near to 1, and therefore where $\epsilon_1$ and $\xi_1$ are smallest. While it is a small contribution to the overall image forces further work is required to explore its role in beam dynamics and loss.

There is also a sextupole term whose strength is proportional to the closed orbit offset, $\kappa_{12}$. The results for this term are shown in Figure 12. This term also peaks where the beam pipe aspect ratio is near to 1. Again as this is where $\epsilon_1$ and $\xi_1$ are smallest there may be an observable effect on the beam dynamics.

In each of these cases the higher order image terms from the simulations did not tend to the parallel plates result which was obtained by Baartman. The reason for this is under investigation.

Image terms were also explored in the vertical plane (if the beam offset is in the horizontal plane). In the vertical plane $\epsilon_1$ was equal to minus the value horizontally, as expected. $\xi_1$ and $\kappa_{21}$ had values indistinguishable from zero, while $\kappa_{30}$, $\kappa_{12}$ and $\kappa_{03}$ all had finite values. This will be explored further in future work.

## CONCLUSION

Theory for centred and off-centred beams in parallel plates, and for centred beams in rectangular geometry has been reviewed. Image term co-efficients, including the coherent and incoherent terms due to Laslett and Ng, as well as higher order terms due to Baartman have been identified.

A systematic simulation study including both FFT and FEA PIC solvers has been carried out to obtain these image terms numerically. There is a high level of agreement between the two functionally different solvers. The results of these simulations have been compared with theoretically obtained values.

For the case of a centred beam, a linear fit to the image terms is sufficient and this tends to Laslett's incoherent term as the beam pipe aspect ratio diverges. For a beam pipe

aspect ratio greater than 2 Laslett's term is a close approximation to the image term. Ng's elliptical function solution for centred beams is an extremely good fit for the incoherent term generally, and describes it well when the beam pipe aspect ratio is near to 1.

When the beam is off-centre additional higher order image terms become evident. Laslett's coherent term is a good fit if the beam pipe aspect ratio is greater than 2. However when the beam pipe aspect ratio is near to 1, as it is on ISIS, this term is about half of Laslett's value.

Baartman describes the high order terms as $\kappa$ terms. Of these, $\kappa_{21}$ and $\kappa_{12}$ have their greatest value when the aspect ratio is near to one, which is comparable to the situation on ISIS. While these terms are small it is possible that they have an effect on beam dynamics and this will be explored further.

Additionally there are equivalent image terms in the orthogonal (vertical) plane. Their contribution to beam dynamics likewise requires further study.

## FURTHER WORK

High order image driving terms have been identified. The next step is to use these driving terms to predict the strength and stop-band width of associated resonances. The results of this analysis can then be compared with PIC simulations including the relevant dynamics. Ultimately it is hoped that any image related dynamic effects may be observed experimentally on ISIS.

Additionally further work is planned exploring Ng's elliptical function solution for off-centre beams, and seeing if this approach may provide another way to gain access to the high order image terms.

## REFERENCES

[1] GH Rees and CR Prior, Image Effects on Crossing an Integer Resonance, Particle Accelerators Vol 48, p251, 1995.

[2] R Baartman, Betatron Resonances with Space Charge, Proceedings of Workshop in High Intensity Hadron Rings, Shelter Island, New York, 1998.

[3] LJ Laslett, On the Intensity Limitations Imposed by Transverse Space Charge Effects in Circular Accelerators, Proc. 1963 Summer Study on Storage Rings, Accelerators and Experimentation at Super-High Energies.

[4] KY Ng, Exact Solutions for the Longitudinal and Transverse Impedances of an Off-Centred Beam in a Rectangular Beampipe, Particle Accelerators Vol 16, p63, 1984.

[5] KY Ng, Physics of Intensity Dependent Beam Instabilities, p117, World Scientific, 2006.

[6] BG Pine et al, Set Code Developments and Space Charge Studies on ISIS, ICAP09, San Francisco, USA.

[7] BG Pine, Image Field Terms for 2D KV Beams in Rectangular Geometry at the ISIS Synchrotron, ISIS Technical Report, 2014.

# STUDIES OF LOSS MECHANISMS ASSOCIATED WITH THE HALF INTEGER LIMIT ON THE ISIS RING

C.M. Warsop, D.J. Adams, B. Jones, B.G. Pine, H.V. Smith, C. Wilcox, R.E. Williamson
RAL, Oxfordshire, UK

## Abstract

ISIS is the spallation neutron source at the Rutherford Appleton Laboratory in the UK. The facility centres on an 800 MeV rapid cycling proton synchrotron, which provides 0.2 MW of beam power operating at high levels of transverse space charge (peak incoherent tune shift ~ 0.5), but with low loss. Half integer resonance is considered to be a main driver for loss that limits the intensity in high power, medium energy proton rings like ISIS. However, the detailed mechanisms causing loss as the half integer limit is approached are not well understood, particularly in the context of a real machine. In this paper we report progress on experiments on the ISIS synchrotron inducing half integer loss, comparing with detailed simulations, and attempts to relate these to simplified theoretical and simulation models. Studies here concentrate on 2D coasting beams, with a view to extending later to the more complicated 3D, bunched beam case of an operational machine.

## INTRODUCTION

### Motivation and Aims

Half integer resonance is considered to be a main intensity limitation in medium energy, high intensity proton machines. The existing incoherent and coherent resonance theories give valuable indications of intensity limits, but limited information on the beam behaviour as the half integer limit is approached and particles lost. The aim of this work is to understand more about the detailed mechanisms driving this loss and thus limiting intensity.

The starting point for the study is experimental observations, with the machine configuration optimised as far as possible to allow study of the essential processes. Detailed experimental studies of beam approaching half integer resonance are followed by comparison with (and benchmarking of) simulation codes. It is hoped these results can then be used to guide interpretation in terms of simplified and predictive beam models. This experimental emphasis forces the inclusion of important processes (e.g. approach of resonance) that are simplified in theoretical models, but are important in understanding real loss.

The underlying aim is to understand losses on an operational high intensity machine like ISIS, and requires a treatment of the full 3D dynamics including effects due to longitudinal motion. Presently, the simpler 2D transverse problem is studied with unbunched, coasting beams. In the longer term, experiments and studies will be extended to non-accelerated and accelerated bunched beams.

### The ISIS Synchrotron

The ISIS synchrotron accelerates $3\times10^{13}$ protons per pulse (ppp) from 70-800 MeV on the 10 ms ramp of the sinusoidal main magnet field. At the repetition rate of 50 Hz this provides an average beam power of 0.2 MW. Charge exchange injection takes place over 130 turns, with painting in both transverse planes as the high intensity beam is accumulated and contained in the collimated acceptances of ~300 $\pi$ mm mr. The ring has a circumference of 163 m and a revolution time of 1.48 µs at injection. Nominal betatron tunes are $(Q_x, Q_y)$=(4.31, 3.83), but these are varied using two families of ten trim quadrupoles. The dual harmonic RF system captures and accelerates the initially unbunched beam, and allows enhanced bunching factors. Peak incoherent tune shifts of $\Delta Q$~0.5 are reached at about 80 MeV, during bunching. Single turn extraction uses a fast vertical kicker at 800 MeV. Main loss mechanisms are associated with non-adiabatic trapping, transverse space charge and transverse instability. Understanding the action of half integer loss is central to minimising losses on the present machine, as well as guiding optimal designs for future upgrades.

## EXPERIMENTAL OUTLINE

### Machine and Beam Configuration

In order to study the essentials of transverse half integer resonance, these experiments make use of unbunched, coasting beams, with the ISIS ring in storage ring mode. The main magnet field is set at a DC level appropriate for the 70 MeV injected beam and RF systems are off. Betatron tunes are controlled with the trim quadrupoles. In these experiments lattice tunes are constant. A small emittance beam of $\varepsilon_{rms}$ ~ 20 $\pi$ mm mr in both planes is injected: painting amplitudes are constant through the pulse and of small amplitude. These beams ($\varepsilon_{100\%}$ ~ 100 $\pi$ mm mr) fill a small fraction of the machine acceptance and thus allow the evolution of the beam profile to be observed. As beam accumulates, the increasing intensity depresses the coherent tune and pushes the beam over resonance [1]. Tunes are selected such that only one resonance is approached in the vertical plane: a harmonic driving term is applied to the $2Q_y$=7 line with the trim quadrupoles. Beam loss and transverse profiles are recorded as a function of key parameters such as tune, driving term strength and intensity. Transverse and longitudinal beam spectra are monitored to ensure coherent instabilities are avoided.
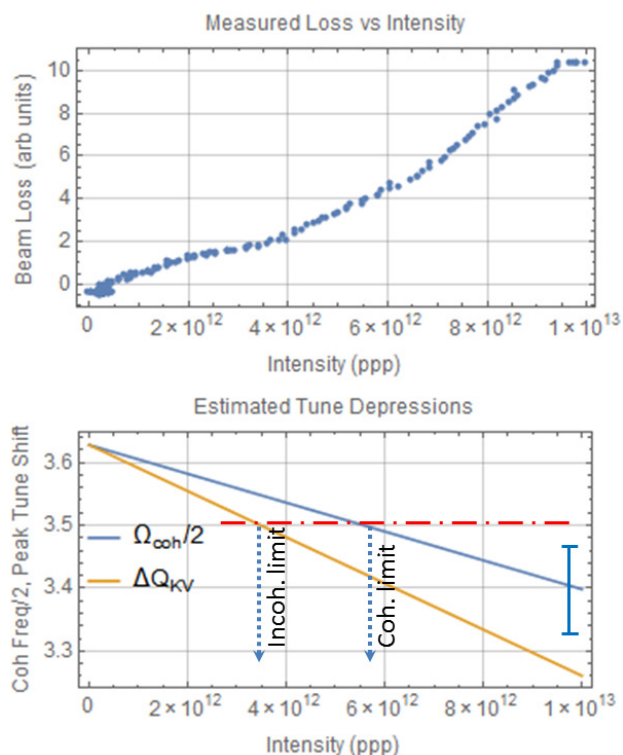
Figure 1: Observed beam loss vs intensity and corresponding estimated resonance conditions.

## Review of Previous Experimental Results

These experiments continue work reported in [1]. Based on the same method, previous results indicated the appearance of large loss *near* intensities predicted by the coherent resonance theory, and which clearly correlated with quadrupole driving term strength. Measurement of transverse beam profiles showed development of half integer halo, "hips" or lobes that agreed well with detailed 3D ORBIT [2] simulations. Importantly, these lobes were shown to be controllable in the expected way by changing the phase of the applied driving term, effectively rotating the lobed structure in ($y$, $y'$) space at the lattice location of the profile monitor. In this paper we build on this work, look in more detail at the time evolution of profiles and halo, and explore its dependence on driving term strength, tune and intensity. This work is still in progress, with continuing efforts to reduce measurement errors and develop models.

## Experimental Developments

Measurements of transverse beam distributions make use of residual gas ionisation profile monitors. Previous studies [3] have demonstrated the corrections required for effects of drift field non-uniformities and beam space charge. More complete simulation models of the monitors are now being used to understand detailed behaviour with the complicated beam profiles generated in these experiments [4], and have confirmed the validity of measurements. Work is also under way verifying profile measurements by comparison with output from "harp" type profile monitors in the extraction line and comparing

with profiles constructed from steering vs loss measurements. Developments in instrumentation and beam control are providing more accurate measurements of lattice parameters and errors [5]. A programme of diagnostics upgrades will also provide new capabilities, e.g. quadrupole kickers and detectors.

## EXPERIMENTAL STUDIES OF HALO

### Resonance and Evolution of Profiles

Recent experiments have used measurements of low intensity beams to establish with more certainty the initial painted emittance of the beam in the machine, before the action of space charge. This allows the calculation of intensity for coherent and incoherent resonance crossing, assuming no emittance growth. Results are shown in Figure 1 from an experiment where the initial $\varepsilon_{rmsx}=\varepsilon_{rmsy}$=10±5 $\pi$ mm mr, $(Q_x, Q_y)$=(4.38, 3.63), the $2Q_y$=7 driving term strength (stop band integral) $J_7$=0.08, and the beam ramps from 0-1×10$^{13}$ ppp over 130 turns of injection. The upper plot shows accumulated intensity vs beam loss (arbitrary units, peak is ~10% total loss). The lower plot shows the coherent envelope frequency halved (with estimated error) and the calculated peak incoherent tune shifts for a KV distribution. It is noted that loss builds up continually with intensity, with no obvious peaks that might be identified with particular resonance conditions. These are typical experimental results.

As reported previously [1], detailed ORBIT models of the experiment have been developed, which reproduce most experimental features. The model includes a detailed AG lattice, 3D beam dynamics, space charge, injection painting, the foil, apertures and collimation. It should be noted that not all machine parameters are known precisely during the experiment, so some judgement is required in specifying the beam. Results from the simulation of this experiment are summarised in Figure 2. This shows vertical phase space and profile evolution (at the location of the profile monitor) on turns ~30-130. It can be seen that the beam starts to blow up early during injection, presumably as the beam encounters the effects of the driving term with space charge, and continues to grow throughout the injected pulse. This is consistent with the observed continuous loss as the beam grows and repeatedly approaches resonance. It is noted that in previous studies [1] we observed a "brick wall" effect where very large losses occurred. The better estimates of emittance found here now suggest this effect occurs when beam grows enough to hit the collimator aperture, rather than indicating an initial resonance condition.

An example of the time evolution of corresponding measured profiles in the experiment is shown in Figure 3, and is a typical result (here $Q_y$=3.67). Note that corrections have been applied to the profiles, and whilst small distortions will be present, errors in the location of lobes are estimated to be within ~± 6 mm. These show the same essential features as the simulation, with the development of distinctive lobes and a peaked core,

which is then gradually lost, leaving a smooth, single peaked distribution. This is discussed further below.
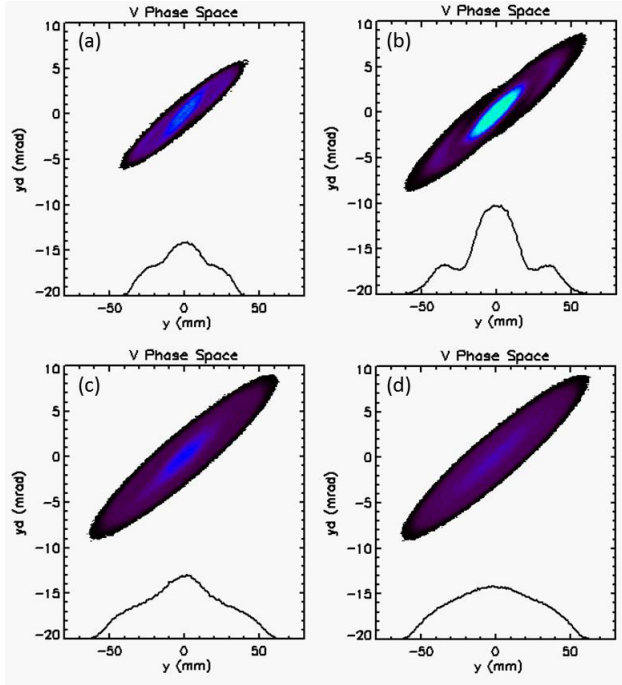


Figure 2: ORBIT results showing typical evolution of the beam in $(y, y')$ space, over turns 30-130 (order a, b, c, d).
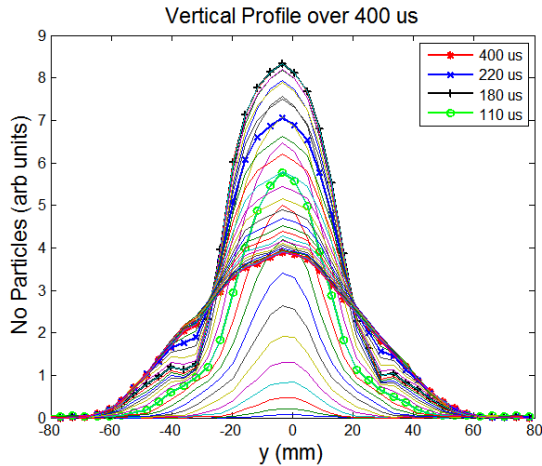


Figure 3: Measured vertical profiles at 10 μs intervals over 400 μs, including injection. Highlighted profiles show distinctive shapes developing through the pulse.

### Effect of Quadrupole Driving Term Strength

The measurement above was repeated, but as a function of the strength of the $2Q_y$=7 driving term. Parameters were as above, with $Q_y$=3.63. The results are shown in the left column of Figure 4, driving term strengths (DT1, DT2, DT3) correspond to $J_7$= (0.06, 0.03, 0.02). The plots show the evolution over 400 μs (including injection) at 10 μs intervals, with the characteristic lobes highlighted. Representative vertical phase space and profiles from a corresponding set of ORBIT simulations are shown in the right column of Figure 4. It can be seen that the lobes move outward with increasing driving term strength in

both experiment and simulation. Not all profile features agree, in spatial and time dependence, this being attributable to limited knowledge of beam parameters and imperfections in profile corrections (all under study). However, the essential features of increasing lobes and beam extent agree.
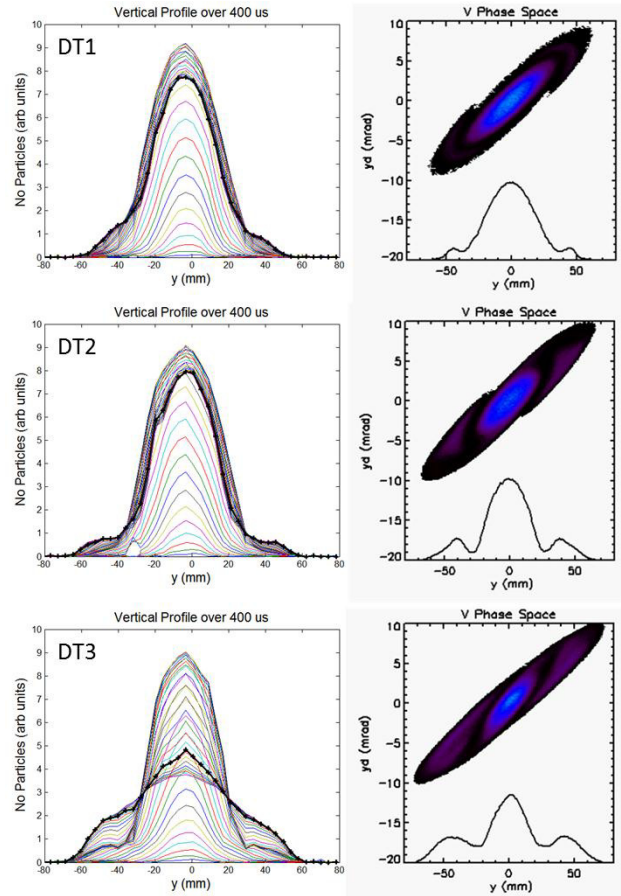


Figure 4: Variation of beam profiles with increasing driving term strength, top to bottom; left - measured profiles, right - ORBIT results (see text).

### Effect of Lattice Tune

In these experiments the lattice tune is held constant throughout the beam pulse. A set of measurements was taken setting the lattice $Q_y$ at different constant values, thereby changing the distance to the resonance condition. Driving term strength was constant at $J_7$=0.08, with other parameters as above. The left column in Figure 5 shows measurements for $Q_y$ with (Q1, Q2, Q3)=(3.71, 3.67, 3.63), again over 400 μs, with characteristic features highlighted. The corresponding ORBIT simulation results are shown in the right column. Measurement and simulation again show the same behaviour, with lobes moving out as the lattice tune is nearer to the resonant value. As before there are differences in details between simulation and measurement, but essential features agree.

### Measurements with Stabilised Halo

As described above, the beam distribution evolves in a complicated way with time, depending on the

instantaneous injected intensity and the redistribution of previous injected turns. New experiments reducing the injector current (from ~22 to 11 mA), thus slowing down the intensity ramp and accumulation, have produced some interesting results. Careful selection of injection pulse lengths has produced lobes that have lasted for ~10 times longer than previous experiments. Figure 6, I1 shows the profile of a shorter pulse, totalling $1.15\times10^{13}$ ppp. The lobe structure lasts for ~100 μs. Figure 6, I2 shows how a longer pulse with $1.4\times10^{13}$ ppp produces a halo and core structure lasting for ~1 ms. This is not presently understood, but simulation studies are underway. It is thought that during the complex redistribution process, which frequently involves significant beam loss, stable or invariant distributions are formed. Understanding these observations could be most informative. The stable lobes also allow for experiments varying parameters during a single pulse, and initial trials are very promising.
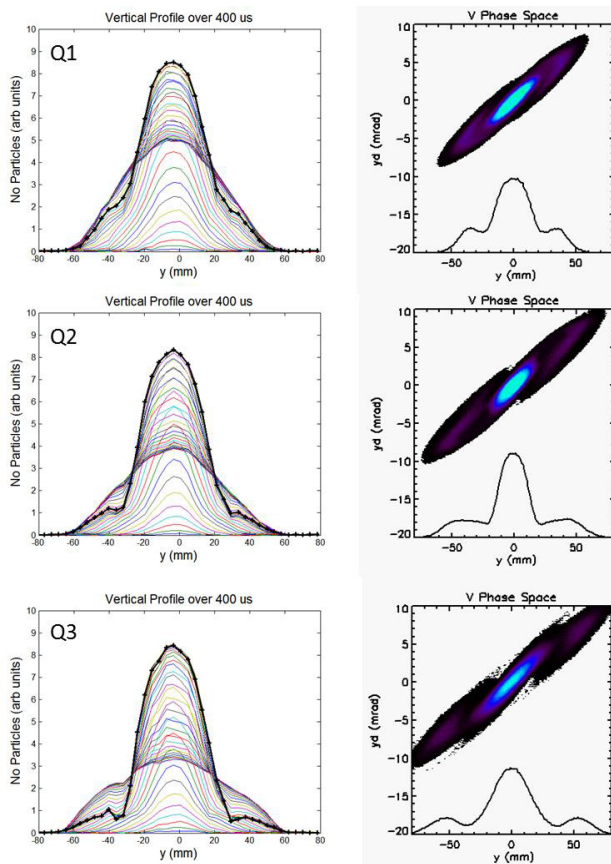


Figure 5: Variation of beam profiles with lattice tune: top to bottom $Q_y$=(3.71, 3.67, 3.63). Left measured profiles through injection, right ORBIT results.

## BEAM MODELS AND BEHAVIOUR

### Review of Beam Models and Behaviour

Comparison with expectations from key theory [6], and standard resonance theory below, suggests the behaviour observed (with lobes moving outward with increasing driving term strength, decreasing tune and increasing

intensity) is reasonable. However, the motion here is more complicated than these simplified models.

Incoherent theory suggests loss nearer the lower intensity resonance condition in Figure 1 and incorrectly ignores any coherent response of the beam. Standard coherent theory, the higher limit in Figure 1, is not applicable once the beam redistributes and $\varepsilon_{rms}$ changes.
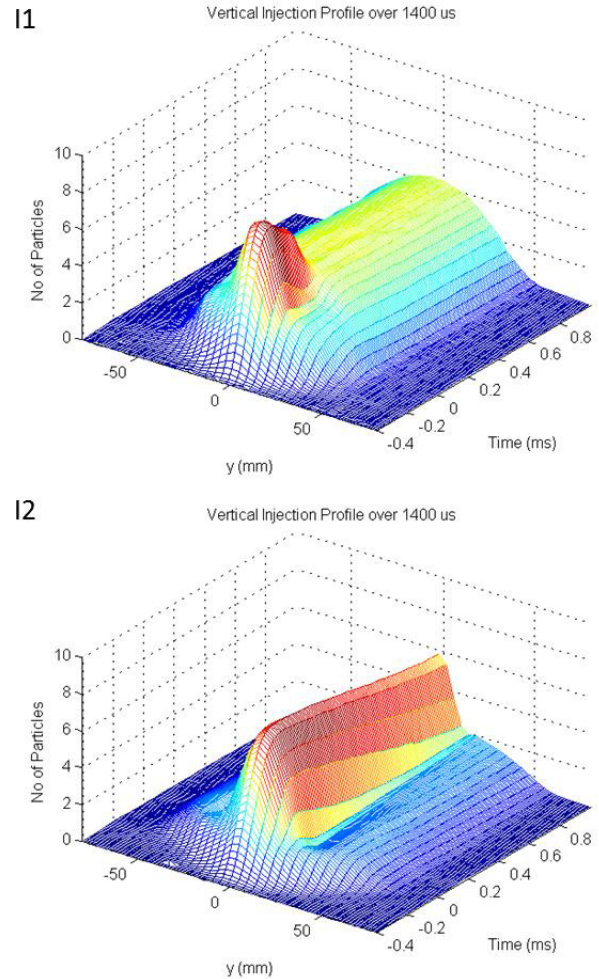


Figure 6: Time structure of beam profiles over 1 ms using slower intensity ramp rates, with total injected intensities of I1=$1.15\times10^{13}$ and I2=$1.40\times10^{13}$ ppp.

One of the more complete models is [6], which solves the driven resonance problem with space charge self consistently for a KV beam. However, for a realistic beam the stationary KV distribution must be replaced with a non-uniform real space density where motion will be non-linear in the beam core. Therefore this model cannot predict likely loss mechanisms. Effects of non-uniform charge densities in periodic quadrupole channels are studied in [7], which suggests near-regular, non-chaotic motion can only be expected at low space charge levels (and therefore perhaps at the *onset* of resonance).

In general the actual processes at work are dependent on the details of the particular machine. Mechanisms are potentially complicated, with multiple 1D or 2D resonances. However, in these experiments, it appears

that just one resonance is excited in the vertical plane. Examination of beam motion in vertical $(y,y')$ phase space from the ORBIT simulations (Figures 2, 4, 5), and corresponding experiments, suggests that over short time intervals trajectories trace out a two lobed half integer structure – very similar to that expected for a single particle quadrupole resonance with non-linear terms present. Below, we use this simplified model in a first attempt to *qualitatively* explain observations.

### Simple Initial Model

The most basic 1D model of a half integer resonance with non-linearity comes from *single particle theory*, and is described by the Hamiltonian of the form:

$$H(J, \varphi) = \delta J + G_2 J \cos(2\varphi) + G_4 J^2 \qquad (1)$$

where $(J, \varphi)$ are action angle variables, $\delta$ the distance from resonance and $G_2$ and $G_4$ represent quadrupole error driving strength and an octupole term respectively. It is understood that this simple model is in many ways incorrect for the system being considered, not least because the potential outside the beam core is different $(\alpha \log(r))$. Also, unlike the single particle case, non-linear fields from space charge are a function of the time dependent beam distributions. However, it is possible that time averaged motion, over intervals in which beam distributions change little, may behave in key respects as expected from this Hamiltonian.
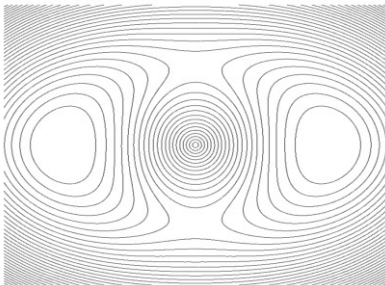


Figure 7: Example of resonant phase space structure from Equation (1) in normalised $(Y, Y')$ space.

For these experiments, during early turns intensity is low and external non-linear terms small, and so $G_4$ can be neglected (1). The parameter $\delta$ is finite, beam is off resonance, and motion linear and stable. As intensity increases the tune depression will push particles toward resonance, reducing $\delta$, and increasing non-linearity $G_4$, perhaps forming a characteristic two-lobed structure: e.g. Figure 7. Observed motion follows contours suggestive of Figure 7, until significant numbers of particles redistribute. We suggest that recent experimental results, Figure 6, I2, may correspond to a longer term invariant. Models based on (1), but with more realistic beam potentials are being studied.

### Comparison with Simple 2D Simulations

In order to confirm that observations can be explained by the basic elements described, a simplified simulation was run with a 2D version of the ISIS code Set. This included a smooth focusing approximation to ISIS, PIC solvers for space charge, the vertical driving term ($J_7$=0.05), and tracking of a 4D waterbag distribution of $10^5$ macro particles for 100 turns. Parameters paralleled experiments above: energy 70 MeV, intensity $4\times10^{12}$ ppp, $(Q_x, Q_y)$=(4.31, 3.63), $\varepsilon_{rmsx,y}$=10 $\pi$ mm mr. A waterbag beam was injected in a single turn, a simplification on actual multi-turn accumulation. The results are shown in Figure 8. The characteristic lobes are clear, as is the similarity to Figure 7 in phase space.
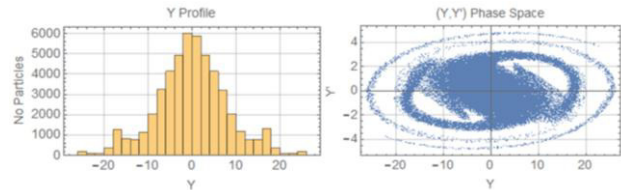


Figure 8: Set 2D simulations of the experiments.

## SUMMARY AND FUTURE PLANS

Detailed experimental studies of beam as it approaches half integer resonance are providing more detailed observations of behaviour under the action of this key loss mechanism. General agreement with simulations is good, and work is under way to develop models that explain what is observed. Recent observations of "stable halo" are expected to provide more valuable information. Ongoing developments of machine measurements and diagnostics will improve knowledge of the beam and thus models. Work to develop simulations will continue, guided by experimental results. Studies looking at half integer effects in 3D bunched beam simulations will start soon.

## ACKNOWLEDGEMENTS

## REFERENCES

[1] C.M. Warsop et al, Simulation and Measurement of Half Integer Resonance in Coasting Beams in the ISIS Ring, Proc. HB12, Beijing, China, p434.

[2] J. Galambos, ORBIT–A Ring Injection Code with Space Charge, Proc. PAC99, p3143.

[3] R. E. Williamson et al., Analysis of Measurement Errors in Residual Gas Ionisation Profile Monitors in a High Intensity Proton Beam, Proc. EPAC08, p1317

[4] C. Wilcox, private communication.

[5] B. Jones et al, Progress on Beam Measurement and Control Systems for the ISIS Synchrotron, Proc. IPAC14, p3700.

[6] M. Venturini, R.L. Gluckstern, Resonance Analysis for a Space Charge Dominated Beam in a Circular Lattice, PRST-AB, V3, 034203 (2000).

[7] Q. Qian et al, Chaotic particle dynamics in a periodic focusing quadrupole magnetic field, Phys. Plasmas 1 (5), p1328 (1994).

# FEASIBILITY STUDY OF A NOVEL, FAST READ-OUT SYSTEM FOR AN IONIZATION PROFILE MONITOR BASED ON A HYBRID PIXEL DETECTOR

O. Keller, B. Dehning, S. Levasseur, M. Sapinski, CERN, Geneva, Switzerland

## Abstract

The ability to continuously monitor the transverse beam size is one of the priorities for the upgrade and consolidation of the CERN Proton Synchrotron for the High Luminosity LHC era. As well as providing an average beam size measurement throughout the acceleration cycle, the requirements also cover bunch-by-bunch measurements of up to 72 bunches with a spacing of 25 ns within 1 ms. An ionization profile monitor with a hybrid pixel detector read-out is therefore being investigated as a possible candidate to provide such measurements. In this contribution the concept, based on a Timepix chip, is presented along with first laboratory measurements showing the imaging of low-energy electrons in vacuum.

## INTRODUCTION

Ionization Profile Monitors (IPM) are devices measuring the transverse size of a particle beam. Electrons or ions resulting from ionization of the residual gas in the beam vacuum are extracted and used to reconstruct the beam profile. Electrons are used if fast measurements are required. They are accelerated towards a detector by an electric field. In addition a parallel magnetic field provides confinement of their orbits along the electric field lines.

Two main types of electron readout systems are commonly used in the current IPMs:

- Multi-strip metal anodes, e.g. at Fermilab [1], BNL [2] and J-PARC [3].

- Optical readout, based on the conversion of electrons into light which is captured by a camera, e.g. in the LHC [4, 5] or at GSI [6].

Both of these methods require amplification of the electron signal in front of the detector which is achieved by Multi-Channel Plates (MCP). Here a novel system based on the emerging technology of hybrid pixel detector is investigated. The detector consist of two pixelated elements, a sensor slab and a readout chip. The sensor reassembles an array of diodes operating in reverse-bias mode. A charged particle traversing the sensor generates free charge carriers in the material which are converted into a voltage pulse and further analyzed by the readout chip.

The Timepix3 is currently the most versatile and one of the fastest hybrid pixel detector readout chips available. It was developed within the Medipix Collaboration hosted by CERN and the first chips have been tested in 2013 [7]. It is designed for a sensor size of $14 \times 14$ mm$^2$ and a resolution of 255 by 255 pixels. The size of one pixel is $55 \times 55 \ \mu$m$^2$.

When bump-bonded to a thin silicon sensor, the hybrid detector becomes sensitive to single low-energy electrons of a few keV. With the ability to set a threshold per pixel, high and homogeneous signal-to-noise ratios can be maintained. The pixels can operate in one of three measurements modes: deposited charge (TOT mode), time of arrival (TOA) and counting the number of events together with the total charge in one shutter period (PC/iTOT). The digital link transceivers of Timepix3 can send the recorded data continuously at a maximum hit rate of 85 Mhits/s/chip or 42.5 Mhits/s/cm$^2$.

The main advantages of the proposed technology are:

- The thickness is reduced with respect to the optical readout method, since no bulky light guides are needed; a magnet with a smaller aperture can be used.

- The fast readout speed enables to measure the beam size bunch-by-bunch with a spacing of 25 ns.

- No need for MCP amplification; MCPs exhibit complex behaviour in cases of prolonged usage with strong and highly repetitive input signals [8].

- Coupling to beam RF fields is expected to be small.

- Currently available charge integrators for strip detectors, with a comparable fast readout like the QIE10 [9], are orders of magnitude less radiation hard than the readout chips of the Medipix/Timepix family [10].

In addition to the readout system, we investigate here the geometry of the electrodes providing the extraction field.

## OPERATIONAL SPECIFICATION

The circumference of the CERN Proton Synchrotron [11] is 628.3 meters and the revolution time varies from $\tau_{\text{rev}} = 5.63 \mu s$ for Pb$^{54+}$ beams at injection to $2.1 \mu s$ for proton beams. It was first put in operation in 1959. Today it is used to generate a broad variety of beams: for test beam areas, fixed target experiments and for the LHC [12]. The proton beams in PS undergo transition crossing and bunch splitting - two phenomena which severely affect the beam emittance.

Operators of any accelerator would like to measure the beam parameters in the best possible way, however the technology does not always allow to fulfill their requests. In case of transverse profile measurements the operational specification for the foreseen PS upgrade is as follows:

1. Continuous, bunch-by-bunch monitoring of the beam emittance over the machine acceleration cycle (2.1 s) with an acquisition rate of 0.1-1 kHz.

Instrumentations and Beam Material Interactions

2. Turn-by-turn measurement of a single bunch emittance.

3. Main use: qualification of LHC beams. These beams are small, therefore 5 cm of detector width will be enough to perform the measurements (vacuum chamber horizontal dimension is 15 cm).

Currently installed emittance monitors - wire scanners - cannot fulfill these specification. They can perform measurements only every several seconds and the two planes are multiplexed. In addition with the increase of the beam brightness planned by the LHC Injection Upgrade (LIU) project [13], scanners may suffer from extensive carbon fibre sublimation [14], which may restrict their use for certain beams.

The beam amplitude function varies between $\beta_{x,y}$ = 12-22 m and dispersion $D_x$ = 2.4-3.2 m. In the following calculations $\beta_x$ = 12 m and $D_x$ = 2.4 m are assumed as these are the values in the probable future location of the IPM.

## ELECTRON RATES

The static pressure in the PS machines reaches p = $10^{-9}$ mbar during operation since no bake-out is performed in advance. The composition of the rest gas is initially dominated by water and $CO_2$. The ionization cross sections for various gases calculated according to Bethe model (cf. [15]) are shown in Table 1. A conservative assumption that the residual gas is mainly composed of hydrogen ($H_2$) is used in the following calculations, but one should keep in mind that about 5-10 times higher rates can be expected.

Table 1: Ionization Cross Section for Different Gases and Beams

|  | $\sigma_{\mathrm{ion,p}}$ 2 GeV [Mbarn] | $\sigma_{\mathrm{ion,p}}$ 25 GeV [Mbarn] | $\sigma_{\mathrm{ion,Pb54+}}$ 15 GeV [Gbarn] | $\sigma_{\mathrm{ion,Pb54+}}$ 1.2 TeV [Gbarn] |
|---|---|---|---|---|
| $H_2$ | 0.19 | 0.23 | 2.6 | 0.6 |
| $H_2O$ | 0.76 | 0.95 | 11 | 2.3 |
| $CO_2$ | 1.32 | 1.66 | 19 | 4.0 |
| Ne | 0.43 | 0.55 | 6.0 | 1.3 |
| Ar | 0.9 | 1.16 | 12 | 3.0 |
| Xe | 1.7 | 2.2 | 24 | 5.3 |

The number of electrons produced per bunch and per machine turn is estimated from:

$$n_e = d \cdot \sigma_{\mathrm{ion}} \cdot N_b \cdot p \cdot \frac{N_A}{R \cdot T} \qquad (1)$$

where $N_b$ is number of particles per bunch, $N_A$ the Avogadro constant, R the ideal gas constant and T =~ 293K.

Table 2 shows the typical number of electrons ($n_e$) expected to be produced by a single bunch, assuming that they are collected along an active detector length of d = 15 mm. The low number of electrons emitted per bunch show that turn-by-turn measurements will be difficult to achieve since

the relative error on the gaussian width is roughly equal to $1/\sqrt{n_e}$ (cf. figure 3.32 in [16]). Consequently a minimum acquisition of $10^4$ electrons is needed to limit the error to 1% for the beam profile reconstruction. In order to increase the number of electrons per bunch, an injection of a heavy noble gas may be foreseen. An increase of the pressure together with the cross section could lead to a 1000-fold increase of the signal. However, the pressure bump would have to be confined around the IPM because of its influence on the emittance of ion beams. Another method would be to increase the pixel detector length. The good field region is designed to be 50 mm long, thus an installation of four Timepix detectors along the beam would allow to increase the signal.

Table 2 shows also the expected hit rates which approach the limits of state-of-the-art pixel detector readout chip capabilities:

- $R_{\mathrm{chip}}^{\mathrm{av}}$ is the averaged hit rate per chip over a machine revolution period.

- $R_{\mathrm{chip}}^{\mathrm{max}}$ is the hit rate per chip within a bunch.

- $R_{\mathrm{pixel}}^{\mathrm{av}}$ is the average rate at which pixels below the beam center are triggered per machine revolution period.

## READOUT MODES

The Timepix3 readout chip consist of an analog front-end and digital back-end to distribute the recorded hit data. Both parts impose their own constraints on the readout possibilities in the proposed IPM. The predecessor chip, Medipix3, showed a continuous front-end readout capability of about 2 MHz/pixel [17]. Since the Timepix3 front-end is designed for faster pulse processing, an even better performance is expected. If the maximum pixel hit rate would be surpassed, the pulse processing signal of these pixels in the front-end would be constantly over threshold rendering the data output unusable. In order to limit this rate on the detector front-end, the usage of a gating grid controlled by a fast HV switch in front of the sensor is considered. An accurate trigger signal is critical in this case.

The second constraint stems from the digital back-end. The Timepix3 uses eight low voltage differential data lines (SLVS type) plus one clock line to distribute the recorded hit data. In the nominal maximum speed configuration these lines can transmit at a rate of 640 Mbit/s resulting in 5.12 Gbit/s (including 8b/10b line encoding) of data per Timepix3 chip. Divided by 65k pixels and a gross data packet size of 60 bits per pixel, this results in the mentioned maximum hit rate of 85 Mhits/s/chip. Multiplied by a bunch spacing of 25 ns we can recover about two electron hits per bunch, if every pixel is operated in the TOT+TOA or *TOA only* mode. While the evaluation of the TOT value may be interesting to compensate for the charge sharing effect in silicon pixel sensors, the *TOA only* mode bears the advantage of an additional pile-up counter. This counter enables the conservation of otherwise missed hits occurring between consecutive data transmissions.

Table 2: Electron Production Rate for Various Beams

| name | achieved 25 ns | | LIU 50 ns | | HL-LHC 25 ns | | LHC ion | |
|---|---|---|---|---|---|---|---|---|
| particles | p | p | p | p | p | p | $Pb^{54+}$ | $Pb^{54+}$ |
| $E_k$ [GeV] | 1.4 | 25 | 2 | 25 | 2 | 25 | 15.02 | 1227 |
| emittance [$\mu m$] | 2.25 | 2.36 | 1.7 | 1.8 | 1.8 | 1.9 | 0.7 | 1.0 |
| $N_b$ [$\cdot 10^{10}$] | 168 | 13 | 189 | 30 | 325 | 25.7 | 0.03 | 0.025 |
| bunch length ($4\sigma_1$) [ns] | 180 | 3 | 205 | 3 | 205 | 3 | 200 | 4 |
| $\Delta p/p$ [$10^{-3}$] | 0.9 | 1.5 | 1.0 | 1.5 | 1.5 | 1.5 | 1.2 | 1.1 |
| $\sigma_{beam}$ [mm] | 3.9 | 3.7 | 3.5 | 3.7 | 4.4 | 3.7 | 4.0 | 2.9 |
| number of bunches ($n_b$) | 6 | 72 | 6 | 36 | 6 | 72 | 2 | 2 |
| $n_e$ ($H_2$) | 13 | 1 | 14 | 2 | 24 | 2 | 30 | 5 |
| $R_{chip}^{av}$[MHz] $= \frac{n_e \cdot n_b}{\tau_{rev}[s]}$ | 37 | 34 | 40 | 34 | 69 | 69 | 11 | 4.8 |
| $R_{chip}^{max}$[GHz] $= \frac{0.68 \cdot n_e}{2 \cdot \sigma_1[s]}$ | 0.1 | 0.5 | 0.1 | 0.9 | 0.2 | 0.9 | 0.2 | 1.7 |
| $R_{pixel}^{av}$[kHz] $= \frac{n_e \cdot n_b \cdot 55[\mu m]}{255 \cdot \sigma_{beam}[\mu m] \cdot \tau_{rev}[s]}$ | 2.0 | 2.0 | 2.5 | 2.0 | 3.4 | 4.0 | 0.2 | 1.7 |

Besides different measurement modes per pixel, Timepix3 can be operated in two acquisition modes: event-based or frame-based. In frame-based mode an external shutter signal sets the exposure time for the whole frame. This acquisition mode is mandatory for the accumulative iTOT pixel mode. However, using the external shutter signal can be also useful in combination with the TOT and TOA pixel modes. It provides means to throttle the data output for certain bunch schemes where $n_e$ is higher than required to recover the beam size. The iTOT mode is the only possibility for recording the whole profile of a single bunch at once. Consecutive measurements will be delayed based on the number of recorded hits. For continuous bunch-by-bunch measurements over multiple machine cycles the event-based mode is better suited. It has the advantage that no bunch-synchronous external trigger signal is required to control the shutter. Because of changes in the cycle period, complex bunch splitting and merging processes (often referred as RF gymnastics) it is necessary to use special techniques to detect bunch presence and position. A possible mechanism is presented in [18].

## RADIATION LEVELS

During every machine cycle a small part of the beam is lost due to various mechanisms, originating from beam-gas interaction, beam instabilities and particles hitting the aperture limits. These losses have been simulated for a standard PS cell. Results are visualized in Fig. 1. In the center of the cell, close to the beam, the yearly dose reaches 10 kGy. The sensor and the Timepix3 detector shall withstand at least this dose in order to be not exchanged more often than once per year. Additional radiation monitors have been installed in the planned device location in order to compare the measurements with simulations.

When operated at maximum speed, the digital SLVS links of Timepix3 need to be handled by an FPGA. Currently, there is no fast enough and radiation hard transceiver like the GBTx available that could convert the signals into long-distance optical fiber links. In first chip tests, 3 m of SCSI ca-

bles with VHDCI connectors have been successfully used to connect the Timepix3 data lines to the FPGA-based SPIDR readout board developed by NIKHEF.

With few meters of cable, the FPGA could be installed under a shielding visible under the beam line in Fig. 1 or away from the beam pipe in the PS utility funnel, which reduces the dose by about a factor 10. The radiation hardness of Timepix3 is expected to be larger than the one of the sensor. In order to extend the lifetime of the sensor by limiting the radiation damage effects, it is planned to cool it down to about $0°C$.
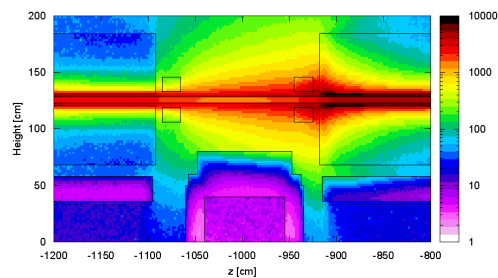


Figure 1: Radiation field in the typical PS straight section. The radiation is produced by beam-gas interaction. A shielding is proposed under the beam pipe in order to protect radiation-sensitive tunnel electronics. The radiation level is expressed in Gy/year. Courtesy of J.P. Saraiva.

## ELECTRIC CAGE

The electric cage is a set of electrodes designed to provide a uniform electric field along the electrons path. The magnitude of the electric field has negligible impact on the profile deformation [19], but it must extract and accelerate electrons to energy levels which allow an efficient detection. With thin silicon sensors the efficiency reaches 100% for electrons of about 10 keV energy, therefore it is proposed to operate at an extraction voltage of at least 20 kV. The electric cage is also the main support structure of the device. Studying existing IPMs revealed a large variety of approaches to the

cage design. Several of these designs were investigated as possible candidate for the new IPM.

In order to be compared, all cages were modeled and simulated using the software suite CST Studio. Each design was adapted to our dimension requirements and only the field shaping elements were taken into account (top, bottom and side electrodes). Some designs were also modified in order to extend our comparison panel. Such designs include the cage from BNL and the cage from the LHC-BGI [4]. Figure 2 shows one of the modeled cages.
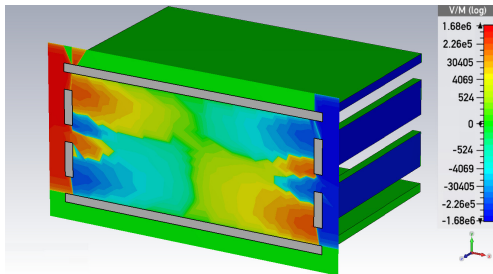


Figure 2: Plot of the electric field in the cross-section of the modified LHC-BGI design.

The electrostatic simulations give a complete picture of the electric field in each cage, while the particle tracking simulations are used to map the behavior of electrons along the transverse and vertical paths. The initial energy of the electrons is 5 eV [20]. Moreover, the effects of a 0.2 T magnetic field are also taken into account.

After post-processing an estimation of the electron signal distortion caused by the non-uniformity of the electric field was obtained. This estimation was used to compare the different cages and choose the best suited for our requirements. In total eight cages were studied and six proved to be relevant. As can be seen in Fig. 3, the comparison of the relative broadening of the beam size shows a clear leading of the modified LHC-BGI design.

In addition, it was found that the magnetic field of 0.2 T improves the signal distortion due to electric field nonhomogenity by up to three orders of magnitude. Such a field is also needed to overcome the space-charge driven profile distortion as described in [20]. A special magnet is being designed for the future PS IPM. Because of the impact on the beam trajectory, the magnet will contain a region with inverted magnetic field compensating for the effect within the IPM itself. Detailed results of the electric cage study will be published later.

## TESTS WITH LOW-ENERGY ELECTRONS

In order to prove the concept of measuring low-energy electrons with the proposed detector a test setup has been constructed. The electric cage used in these tests is an old cage from a IPM of the SPS machine. It is equipped with
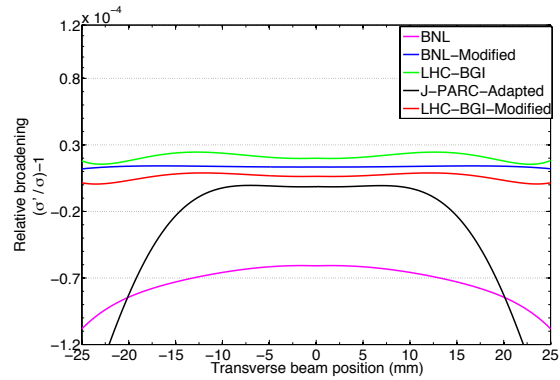


Figure 3: Relative broadening of the reconstructed beam size as a function of the transverse beam position.

an Electron Generation Plate (EGP) which is a cold and uniform electron source.

A Fitpix USB adapter housing a Timepix1 chip bonded to a 100 $\mu$m silicon sensor is placed at a distance of 10 cm from the EGP. The sensor is of p-on-n type. Instead of the common surface metallization, a thin n+ doped layer is used to provide the sensor bias voltage of 20 V. This leaves the detector sensitive to light, requiring a shaded operation, but also enables the penetration of low-energy electrons into the depletion region.

The detector is powered and connected to a computer via USB by a vacuum feedthrough. The electron hits are recorded with the Pixelman software and analyzed in the ROOT-based MAFalda framework [21].

The signals have been observed for extraction voltages of 3 to 5 kV. The system was running for several days and no degradation of the signal has been observed. As a byproduct of the experiments a clustered emission from the EGP was observed. This effect was unknown before because a much longer integration time is used in the previous optical readout method. Thanks to the short shutter times of the Timepix1, it can be seen that cascades of electrons are emitted from small areas of the EGP. However, after adding up many of these cascades, the distribution of the electrons is uniform as the EGP specification states. The background and signal images are shown in Fig. 4 for an extraction potential of 4.5 kV, Timepix shutter period of 10 ms and a pressure of about $6 \cdot 10^{-6}$ mbar. Because of the clustered emission it is not possible to obtain the energy spectrum of single electrons in this setup.

## CONCLUSIONS

This preliminary study shows that a continuous beam emittance monitoring can be achieved in the CERN Proton Synchrotron by an Ionization Profile Monitor equipped with hybrid silicon pixel detectors based on Timepix3. This modern technology allows to perform fast, bunch-by-bunch measurements of the beam emittance during the PS acceler-
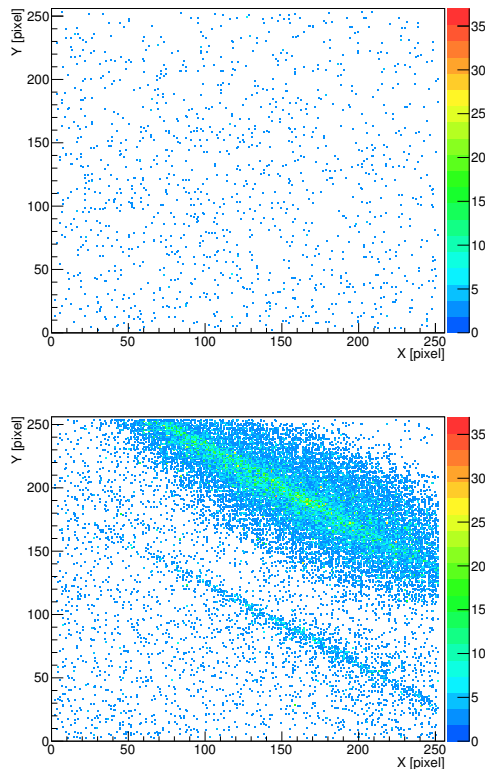
Figure 4: The image above shows the background. Below are electron clusters emitted from the EGP. An extraction potential of 4.5 kV was applied in both cases. The strong non-uniformity of the electric field close to the detector in the test cage is supposedly producing the stripe shape.

ation cycle. It is expected that the chip-sensor assembly will withstand radiation damage for at least a period of 2-3 years.

## ACKNOWLEDGMENT

## REFERENCES

[1] J. Zagel et al., "Operational use of Ionization Profile Monitors at Fermilab", BIW'10, Santa Fe, 2010, TUPSM009.

[2] R. Connolly et al., "Residual-Gas-Ionization Beam Profile Monitors in RHIC", BIW'10, Santa Fe, 2010, TUPSM010.

[3] H. Harada et al., "Upgrade of Ionization Profile Monitor in the J-PARC 3-GeV RCS", IPAC'12, New Orleans, 2012, MOPPR029.

[4] CERN IPM website: `http://cern.ch/bgi`

[5] M. Sapinski et al., *The First Experience with LHC Beam Gas Ionization Monitor*, IBIC'12, Tsukuba, 2012, TUPB61.

[6] T. Giacomini, P. Forck, D. Liakin, J. Dietrich, G. v. Villiers, "Ionization Profile Monitors at GSI", DIPAC'11, Hamburg, 2011, TUPD51.

[7] T. Poikela et al., *Timepix3: a 65K channel hybrid pixel readout chip with simultaneous ToA/ToT and sparse readout*, Journal of Instrumentation, Volume 9, May 2014.

[8] L. Giudicotti *Time dependent model of gain saturation in microchannel plates and channel electron multipliers*, Nucl. Instrum. Meth. A 659, 336 (2011).

[9] A. Baumbaugh et al., *QIE10: a new front-end custom integrated circuit for high-rate experiments*, Journal of Instrumentation, Volume 9, January 2014.

[10] R. Plackett et al., *Measurement of Radiation Damage to 130nm Hybrid Pixel Detector Readout Chips*, Topical Workshop on Electronics for Particle Physics, Paris, Sep 2009, pp.157-160.

[11] S. Gilardoni, D. Manglunki et al., *Fifty years of the CERN Proton Synchrotron*, CERN-2011-004.

[12] *LIU Proton Beam Parameters*, CERN-EDMS-1296306, September 2013.

[13] *LIU PS Technical Design Report*, in preparation.

[14] M. Sapinski, B. Dehning, A. Guerrero, M. Meyer, T. Kroyer, *Carbon Fiber Damage in Particle Beam*, HB'10, Morschach, 2010, MOPD61.

[15] F.F. Rieke, W. Prepejchal, *Ionization cross sections of gaseous atoms and molecules for high-energy electrons and positrons*, Phys. Rev. A. 1972;6(4):1507.

[16] F. Roncarolo, *Accuracy of the Transverse Emittance Measurements of the CERN Large Hadron Collider*, CERN-THESIS-2005-082.

[17] E. Frojdh et al., *Count rate linearity and spectral response of the Medipix3RX chip coupled to a 300 μm silicon sensor under high flux conditions*, 15th international workshop on radiation imaging detectors, Paris, June 2013.

[18] J.M. Belleman, *A New Trajectory Measurement System for the CERN Proton Synchrotron*, proceedings of DIPAC2005.

[19] M. Patecki, *Analysis of LHC Beam Gas Ionization monitor data and simulation of the electron transport in the detector*, CERN-THESIS-2013-15.

[20] D. Vilsmeier, B. Dehning, M. Sapinski, "Investigation of the Effect of Beam Space Charge on Electron Trajectories in Ionization Profile Monitors", MOPAB42, *These proceedings*, HB2014, East Lansing, USA (2014).

[21] MAFalda website, developed by John Idarraga: `http://twiki.cern.ch/twiki/bin/view/Main/MAFalda`

# INVESTIGATION OF THE EFFECT OF BEAM SPACE-CHARGE ON ELECTRON TRAJECTORIES IN IONIZATION PROFILE MONITORS

D. Vilsmeier, B. Dehning, M. Sapinski, CERN, Geneva, Switzerland

## Abstract

The correct measurement of beam size using an ionization profile monitor relies on the confinement of electron trajectories from their source to the electron-sensitive detector. This confinement is provided by a magnetic field aligned with electric extraction field. As the initial electron velocities are boosted by the presence of a high-charge density beam, the value of the magnetic field depends on both the beam size and on the charge density. If the magnetic field is not strong enough a deformation of the observed beam profile occurs. In this paper the results of a study of electron trajectories in the presence of high charge density beams is presented along with an estimation of the required magnetic field for various scenarios. A correction procedure for compensating any residual distortions in the measured profile is also discussed.

## INTRODUCTION

During the calibration procedure of the LHC Ionization Profile Monitor (IPM) [1] it has been found that the obtained profiles at high beam energy are broader than expected [2,3]. Several reasons for this effect have been investigated:

- wrong correction for camera tilt with respect to the beam direction,

- optical point-spread-function (PSF),

- PSF due to multi-channel plate granularity,

- underestimation of electron gyroradius.

Finally the problem was tracked down to the beam space charge which kicks electrons before they leave the beam, significantly increasing their gyroradius. An increase of the magnetic field was suggested, however it is a costly solution. In this paper the details of the interaction of electrons with the beam field are investigated and numerical methods to correct the profiles are suggested.

In order to simulate the beam space charge impact on electron trajectories a modified version of PyECLOUD [4] code is used. PyECLOUD is a 2D tracking code which does not take into account the longitudinal electric field nor the magnetic field of the bunches. Both limitations are a good approximation for high-relativistic beams interacting with slowly-moving electrons. The external fields in the simulation are perfectly aligned and uniform. The beam optics functions in the monitor are assumed to be: $\beta_x$ = 213 m, $\beta_y$ = 217 m (corresponding to vertical device on beam 2) and dispersion is zero. The emittance has the same value in horizontal and vertical plane. Table 1 shows beam parameters of cases analyzed in detail.

Table 1: Simulated Cases Studied in Detail

| parameter | 450 GeV | 4 TeV | 6.5 TeV |
|---|---|---|---|
| emittance [$\mu$m] | 1.7 | 2.4 | 1.7 |
| bunch | | | |
| -intensity [$\cdot 10^{11}$] | 1.5 | 1.7 | 1.3 |
| -length [ns] | 1.2 | 1.2 | 1.25 |
| $\sigma_{\text{beam}}$ [$\mu$m] | 869 | 346 | 229 |

In addition three cases of beam energy ramps are considered, for beams with normalized emittance $\epsilon_n$ = 1.5 $\mu$m, bunch length of 1.1 ns and bunch charge of $N_b = 1.1 \cdot 10^{11}$, $1.3 \cdot 10^{11}$ and $1.5 \cdot 10^{11}$ protons. Fifteen beam energies between 450 GeV and 7 TeV are simulated in each case. The simulated bunches are gaussian in transverse and longitudinal directions.

In the following we describe the initial velocity distribution of electrons and effects of space charge on profile shape and the gyroradius. In the end we discuss the corrections for the observed distortions of the beam profiles.

## INITIAL VELOCITIES

In the previous work it has been estimated that the distribution of initial velocities of electrons plays an important role in the shape of the beam profile observed in IPM (see Fig. 4.5 in [5]). This distribution was obtained using Geant4 program and turned out to be significantly overestimated. Here the generation of initial velocities is based on an analytic model [6].
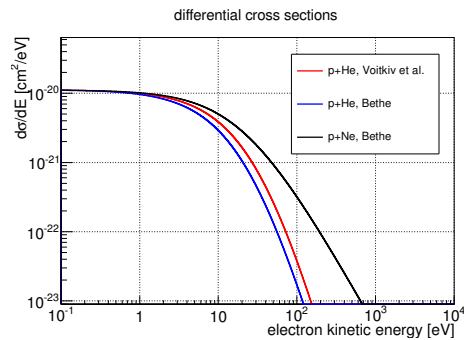


Figure 1: Example of cross-sections calculated with Bethe [7] approximation and a more accurate [6] model for 4 TeV protons.

The main contribution to the ionization process is due to electric dipole interaction between the projectile and the target electron. Most of the interactions are associated with small momentum transfer and the produced electrons are soft.
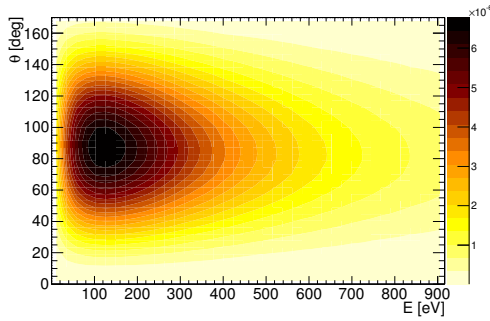
Figure 2: Double differential cross section [6]. Electrons are emitted transversely to the beam direction.

Figure 1 presents the comparison of distributions of the kinetic energy of electrons produced in proton interactions with helium and neon gases. The used approximation neglects forward processes (for instance binary peak) which have negligible contribution for relativistic projectiles.

The gyrofrequency of the circular component of electron motion is about 35.1 GHz. The time in which electrons reach the detector is about 3.2 ns and the number of revolutions is around 100.

## BUNCH FIELD

The magnitude of the electric fields inside the atom is about $5 \cdot 10^{11}$ V/m. The IPM extraction field is about $5 \cdot 10^4$ V/m. The field inside the bunch is shown in Fig. 3. For the case of 6.5 TeV beam it reaches $E_{bunch}^{max} = 8 \cdot 10^5$ V/m. The scalar polarizability of neon atoms is about $4.41 \cdot 10^{-41} C^2 m^2 J^{-1}$, therefore the Stark effect due to bunch field leads to a negligible shift of atomic levels and does not affect the ionization potential.
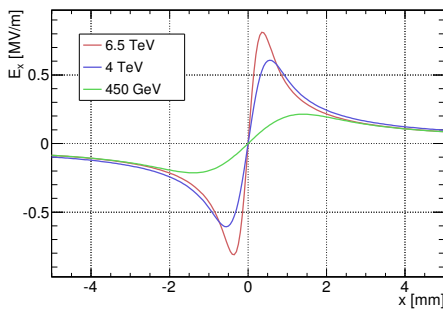


Figure 3: The radial component of the electric field as a function of distance from the bunch center for the three cases from Table 1.

## EFFECT OF SPACE CHARGE ON PROFILES

The observed deformation of the beam profile is non-gaussian and depends on the local charge density inside the bunch. In Fig. 4 the initial (original) and deformed (final) profiles are shown. The profiles become more peaked then

gaussian and with larger tails. One way to measure non-gaussianity of the obtained distribution is squared kurtosis. Kurtosis is zero for gaussian and becomes positive if the peak of the distribution is spikier then gaussian[1].
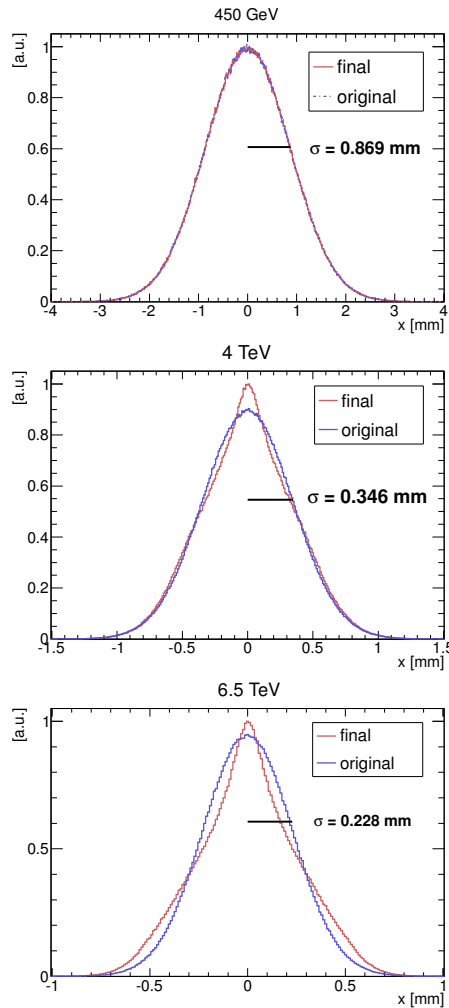


Figure 4: Deformation of the profile for the three cases from Table 1. The blue lines are original beam profiles while red ones are profiles registered by the IPM, deformed due to beam space charge.

Figure 5 shows the squared kurtosis for profiles obtained from various beams (ramp cases). For beam sizes below 0.3 mm an increase of the kurtosis is observed. Similar behaviour is observed when trying to fit gaussian (using ROOT [8] fit procedure) to the distorted profile. The non-gaussianity of the profiles becomes strong for the beam sizes corresponding to energies of about 3-4 TeV.

A lot of functions have been tested trying to find the best description of the distorted profiles. One of the best candidates is a combination of Gauss and Laplace functions:

---

[1] Kurtosis is sensitive to outliers but this is not important for the simulation study, however for real data analysis another way to quantify non-gaussianity, for instance differential entropy, should be used.
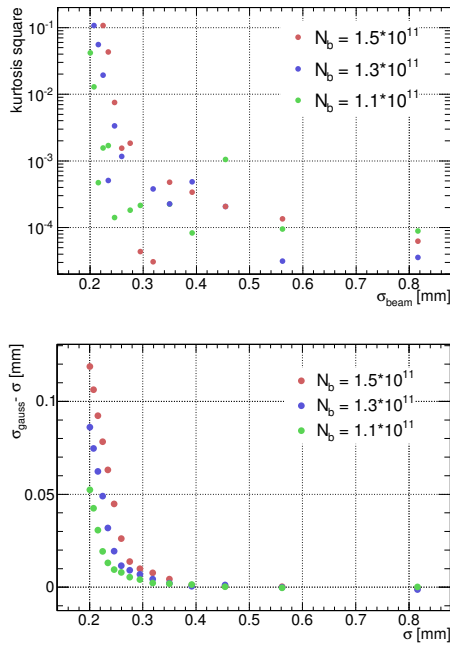
Figure 5: Non-gaussianity for various beams. Upper plot: kurtosis as a function of the original beam size, bottom one: difference between fitted and original gaussian.

$$f(x) = p_0 \cdot \exp\left(-\frac{x^2}{2\sigma_g^2}\right) + p_1 \cdot \exp\left(-\frac{|x|}{\sigma_l}\right) + p_2 \qquad (1)$$

Using this 5-parameter function nearly every profile could be fitted - see for example Fig. 6. Unfortunately no simple correlation has been found between the original profile width ($\sigma_{\text{beam}}$) and fit parameters ($p_0, p_1, \sigma_g, \sigma_l$).
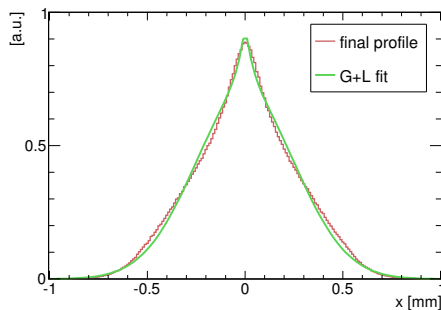


Figure 6: Results of fitting the distorted profile at 6.5 TeV with function 1.

## EFFECT OF SPACE CHARGE ON GYRORADIUS

The simulations show that the effect driving the profile distortion is a dramatic increase of gyroradii. The gyration center is also shifted with respect to the production point,
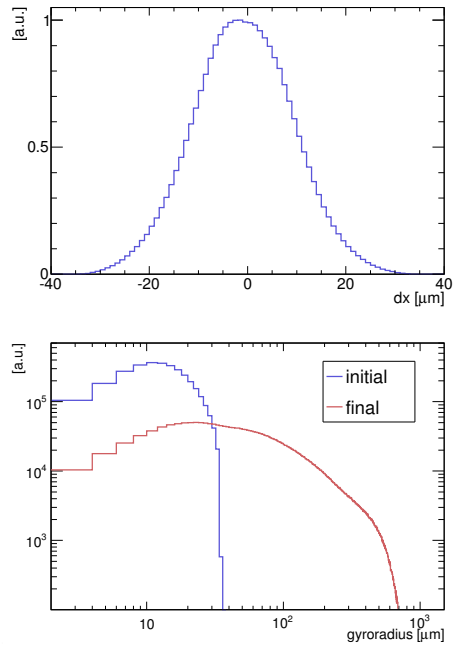


Figure 7: The position of the gyration center with respect to the position where electrons are produced (upper plot) and increase of electron gyroradii due to the beam space charge effect. The blue curve shows the gyroradius distribution for initial velocities while the red one is made after the interaction with beam space charge (6.5 TeV case).

but this effect is not affected by the bunch charge and is small ($\approx 10~\mu$m), as shown in Fig. 7.

Further investigations show (cf. Fig. 8) a strong dependence of the boosted gyroradius on the initial positions of the electrons inside the bunch. Interestingly the maximum gyroradius boost is observed for electrons produced a little closer to the bunch center than the maximum of the bunch field as shown in Fig. 9.
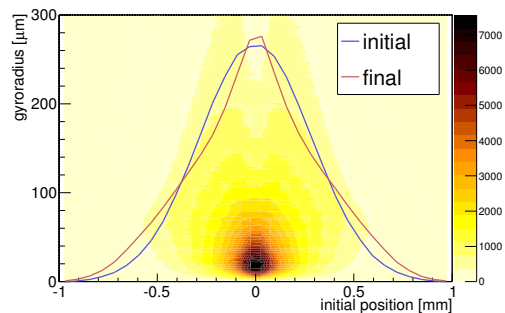


Figure 8: Increase of electron gyroradii as a function of the transverse position along the beam for 6.5 TeV case. The original and distorted beam profiles are shown, a correlation between gyroradius and transverse position is visible.
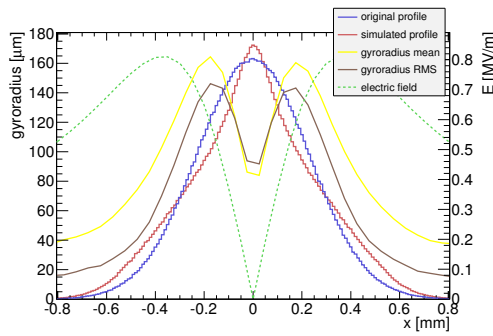
Figure 9: Correlation between gyroradius distribution properties, the bunch electric field and the beam profiles (6.5 TeV case).

## PROPOSAL OF CORRECTIONS

The previous studies of corrections for the beam space charge effect were based on an iterative procedure using a set of matrices obtained with tracking simulations [9]. Here we analyze three proposals: increase of the magnetic field, use of generic properties of the distorted distributions and correction with point-spread-function depending on gyroradius.

### Increase of Magnetic Field

It has been shown that an increase of the magnetic field strength to B = 1.0 T is sufficient to suppress space charge effects also for very high beam energies (see Fig. 4.11 in [5]). Here the calculations are repeated for a more realistic distribution of initial electron velocities. Figure 10 shows a comparison between the results obtained with a magnetic field strength of B = 0.2 T and B = 1.0 T. The original profile is clearly restored.
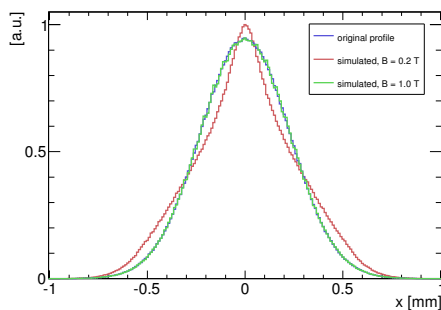


Figure 10: Comparison of distorted beam profile for B = 0.2 T and B = 1.0 T. In the latter case there is no distortion.

### Interquartile Method

Because no function describing the distorted beam distribution has been found, a correlation between generic properties of a distribution and the initial beam size have been investigated. The Root Mean Square (RMS), Full Width At Half Maximum (FWHM) and Interquartile Range (Q3-Q1)

have been investigated showing usually reasonable correlations and therefore giving a hope to resolve the beam size. In Fig. 11 this correlation is shown for between Q3-Q1 and the original beam size. The correlation is almost identical for all three investigated bunch intensity cases down to beam size of 0.3 mm, however for smaller beams and high bunch charges the curve becomes flat indicating the limit of this method. Similar results could be obtained using other properties of a distribution as RMS or FWHM.

The bottom plot presents that the relative blow of the emittance should still be visible, despite problems with absolute value measurement, especially if the procedure follows the accurate measurement of the beam size at injection.
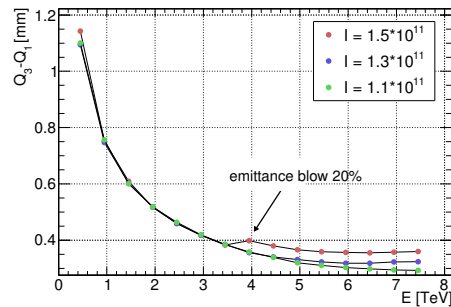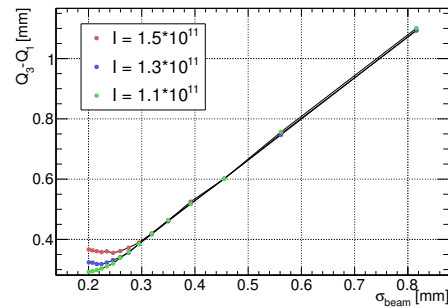


Figure 11: Upper plot: correlation between registered electron distribution interquartile range and $\sigma_{beam}$ for ramps of various beam. Bottom plot: interquartile range as a function of the beam energy. For the case $N_b = 1.5 \cdot 10^{11}$ an emittance blow of 20% at 4 TeV is simulated.

### Electron Sieve

The original distribution of the beam can be reconstructed if the gyroradius is known and is the same for all electrons. Fig. 12 shows the point spread function for an electron produced at x = 0 with a gyroradius of 120 $\mu$m.

The determination of the contributions to the observed profile from electrons with various gyroradii could be realized using an "electron sieve" with holes of various diameters. One should note that the sieve shall be relatively thick as the pitch of the electron helical trajectory reaches a few millimeters close to the detector.

In order to perform a deconvolution of the partial profile using the PSF from Fig. 12 a TSpectrum class from ROOT package [8] has been used. In Fig.13 a profile obtained after
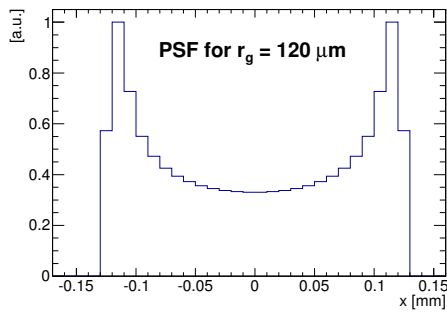
Figure 12: The distribution of the electron position at the detector for electron generated in the center and moving on helical trajectory with gyroradius 120 $\mu$m.

selecting the electrons with gyroradiuses between 100 $\mu$m and 150 is shown for 4 TeV case. The applied PSF corresponds to gyroradius of 120 $\mu$m. The deconvolution procedure recovers original shape of the two-peaked distorted profile, mainly recovers the height of the peaks as well as the depth of the central minimum. It is interesting to note that the electrons with small gyroradius (up to 75 $\mu$m) come mainly from the bunch center, while electrons with large gyroradius form characteristic double-peak distributions.
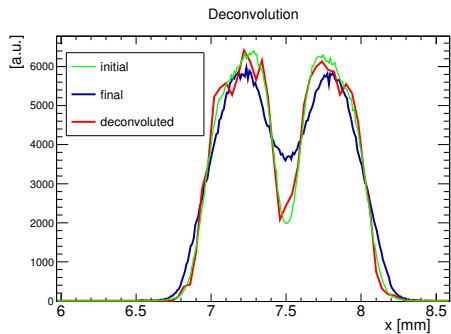


Figure 13: Deconvolution of the partial profile obtained with electrons with gyroradius between 100 and 150 $\mu$m. The PSF applied was obtained for gyroradius of 120 $\mu$m.

Fig.14 presents result of the procedure, using sieve with holes of the following diameters: 75, 100, 150 and 200 $\mu$m. For each partial profile a deconvolution procedure has been applied, using PSF obtained for gyroradii: 50, 85, 120, 170 and 200 $\mu$m respectively. The corrected profiles have been summed up and reproduce quite well the original profile.

## CONCLUSIONS

In case of very high brightness LHC beams the Ionization Profile Monitors suffers from a distortion of the measured profiles due to lack of strength of the external magnetic field. The tracking simulations show a significant increase of de-

formation for the beam size below 0.3 mm. Observed profile shapes becomes more peaked then the initial gaussian with excess in the tails starting at about $1 - 1.5$ $\sigma_{\text{beam}}$ from the profile center. The average gyroradii increase from about
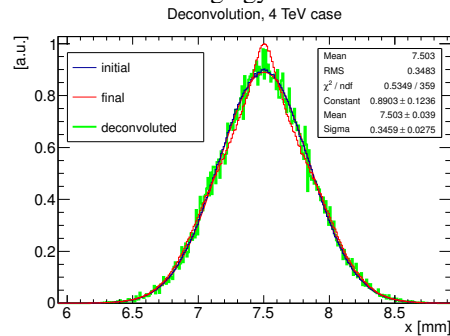


Figure 14: The result of electron sieve method.

20 $\mu$m to about 140 $\mu$m with maximum reaching 0.8 mm for 6.5 TeV beam. Attempts to fit distorted profiles with function related to the original beam width were not successful, however basic properties of the distribution, for instance interquartile range, have been found to correlate with $\sigma_{\text{beam}}$. A method based on point spread function deconvolution is being developed and the first results are promising.

## REFERENCES

[1] http://cern.ch/bgi

[2] M. Sapinski et al., "The First Experience with LHC Beam Gas Ionization Monitor", IBIC'12, Tsukuba, 2012, TUPB61.

[3] R. Versteegen et al., "First Proton-Nucleus Collisions in the LHC: the p-Pb pilot physics fill", CERN-ATS-2012-094 MD.

[4] G. Iadarola et al., "Electron Cloud Simulations with PyEcloud", ICAP2012, Paris, 2012, WESAI4.

[5] M. Patecki, "Analysis of LHC Beam Gas Ionization monitor data and simulation of the electron transport in the detector", CERN-THESIS-2013-15.

[6] A.B. Voitkiv, N. Grun and W. Scheid, "Hydrogen and helium ionization by relativistic projectiles in collisions with small momentum transfer", J. Phys. B: At. Mol. Opt. Phys. **32** (1999) 3923-3937.

[7] M.E. Rudd, Y.-K. Kim, D.H. Madison and T.J. Gray, "Electron production in proton collisions with atoms and molecules: energy distributions", Rev. Mod. Phys. 64, 441 (1992).

[8] http://cern.ch/root

[9] J. Egberts, "IFMIF-LIPAc Beam Diagnostics: Profiling and Loss Monitoring Systems", PhD thesis CEA Saclay, 2012.

# STUDIES ON HEAVY ION LOSSES FROM COLLIMATION CLEANING AT THE LHC

P. D. Hermes*, CERN, Geneva, Switzerland and University of Münster, Germany

R. Bruce, J. M. Jowett, S. Redaelli, B. M. Salvachua, G. Valentino,

D. Wollmann, CERN, Geneva, Switzerland

## Abstract

The LHC collimation system protects superconducting magnets from beam losses. By design, it was optimized for the high-intensity proton challenges but so far provided adequate protection also during the LHC heavy-ion runs with $^{208}$Pb$^{82+}$ ions up to a beam energy of 4 $Z$ TeV. Ion beam cleaning brings specific challenges due to different physical interactions with the collimator materials and might require further improvements for operation at 7 $Z$ TeV. In this article, we study heavy-ion beam losses leaking out of the LHC collimation system, both in measurement and simulations. The simulations are carried out using both ICOSIM, with a simplified ion physics model implemented, and SixTrack, including more detailed starting conditions from FLUKA but without including online scattering in subsequent collimator hits. The results agree well with measurements overall, although some discrepancies are present. The reasons for the discrepancies are investigated and, on this basis, the requirements for an improved simulation tool are outlined.

## INTRODUCTION

The CERN Large Hadron Collider (LHC) [1] is equipped with a multi-stage collimation system [2] designed to intercept halo-particles at large amplitudes which could hit otherwise the superconducting magnets and potentially cause them to quench. The efficiency of the collimation system depends on the collimator and optics settings. Simulation tools have been developed to enable a thorough analysis of the cleaning efficiency before operating with specific machine configurations. At the passage through the collimator material, proton and heavy-ion beams are subject to different physics processes. Unlike protons, heavy ions can break up into lighter isotopes having a different magnetic rigidity from the reference beam. Both the tracking and scattering/fragmentation routine of a simulation code for heavy-ion collimation must be able to handle the different isotopes. LHC collimation simulations for protons are usually realized with the SixTrack code, while heavy ion loss maps have previously been simulated with the ICOSIM software [3]. The aim of this study is the comparison of the measured losses during the first LHC run with simulated loss maps using either ICOSIM or SixTrack, where for the latter we track protons of equivalent magnetic rigidity.

---

* phermes@cern.ch

## SIMULATION SETUP

### ICOSIM

ICOSIM (Ion COllimation SIMulation) is the present state of the art simulation code for heavy-ion loss maps [3]. Ions are tracked by means of a linear transfer matrix formalism, until all particles have hit a collimator. Chromatic effects are taken into account in linear approximation. Nuclear fragmentation and electromagnetic dissociation due to the ion-matter interaction in collimators are simulated using a built-in routine based on tabulated cross section tables generated by FLUKA [4–6]. From the particles generated by these processes, only the heaviest fragment in each interaction is kept track of and kicks in energy or angle are not taken into account. Besides, the software contains an integrated routine to calculate multiple scattering in Gaussian approximation and ionization using the Bethe-Bloch equation [7]. Information about the beam and optics properties as well as the collimator settings is given by the user via input files. Optics input is generated using MAD-X [8] which facilitates the simulation with new machine configurations. ICOSIM generates the beam halo based on different models which can be chosen by the user. For the presented simulation $2 \cdot 10^6$ initial ions are generated as an annular halo at IP1, sufficiently large to hit the primary collimators (TCP) without including diffusion, following the methods outlined in Ref. [9, 10]. Based on the the hierarchy of the LHC collimation system the TCPs in the betatron collimation region IR7 are the only collimators which should be exposed to the initial beam halo.

### SixTrack with Protons of Ion-Equivalent Rigidity

SixTrack with protons of ion-equivalent rigidity is introduced as an alternative tool for the simulation of heavy-ion loss maps. In this framework, protons of effective energies are tracked to simulate the rigidities of the different isotopes. In the presented approach, the tracking of effective protons starts from a distribution of fragments exiting the TCP in IR7. No subsequent scattering at the collimators is applied.

**Tracking tool**    SixTrack [11, 12] provides an integrated environment for the magnetic tracking of protons together with a Monte-Carlo module to simulate interactions of protons with the collimator material. The software provides predictions of the performance of the LHC collimation system which have proved to be very consistent with the measured proton losses in the LHC [9]. A thin lens model of the accelerator lattice is used to calculate the particle transport. Chromatic effects are taken into account up to 20$^{\text{th}}$ order.
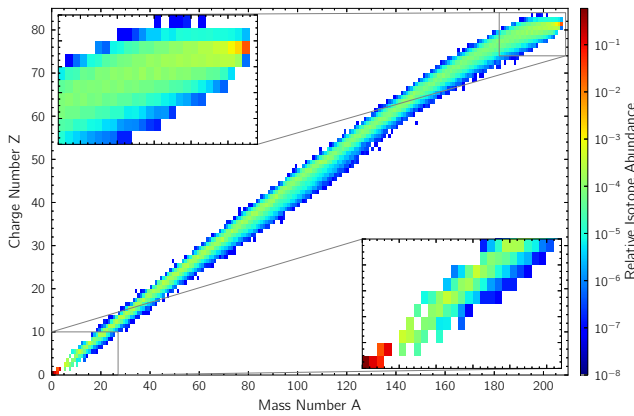
Figure 1: Abundances of the individual fragments from the lead ion beam impacting the carbon collimator material.

The software is designed for simulating proton beams, so no information about the ion charge or mass is stored or processed to provide the tracking. The implementation of the scattering routine is also specific to protons.

**Simulation of fragmentation at the TCP**   We simulate the ion fragmentation at the TCP using the Monte-Carlo package FLUKA, with exactly the same simulation setup that was previously used for the SPS [7]. A beam of $10^6$ ions was simulated to impact the TCP, modeled as a simple block of carbon with an impact parameter (the transverse distance of an impacting ion from the collimator edge) of $b = 1$ $\mu$m. This choice is somewhat arbitrary since the actual impact parameters in the machine are not precisely known, but are believed to follow approximately an exponential distribution of $b$. The angle of incidence is calculated from phase-space information extracted from MAD-X and assuming that the collimator is hit at the phase of the maximum excursion. Fig. 1 shows the simulated abundances of the various ions coming out of the collimator as a function of the nuclear charge number $Z$ and the nuclear mass number $A$.

In the fragmentation process, the isotopes are subject to kicks in the kinetic energy and in the angle of movement. Both can differ significantly from the central angle or the reference kinetic energy. In the next step, we use the FLUKA output for the generation of the SixTrack initial conditions.

**Setup of the ion tracking with SixTrack**   SixTrack is designed for the exclusive handling of protons. Heavy ions of the reference ion species can however be tracked as protons if the synchrotron motion is neglected (which is acceptable for the simulation case as the particles are only tracked for 100 turns) and if the total ion energy is substituted by the energy per charge. Rigidities of isotopes different from the main beam can be accounted for by introducing a momentum offset of the tracked protons. One can show that the magnetic rigidity of an isotope (described by the nuclear mass number, charge number and the ion mass $A, Z, m$), different from the ion type ($A_0, Z_0, m_0$) of the reference beam, can be taken into account by an effective momentum offset $\delta_{\text{eff}}$. It is related

to the ion mass and charge as described by the formula [7]:

$$(1 + \delta_{\text{eff}}) = \frac{Z_0}{Z} \frac{m}{m_0} (1 + \delta_{\text{kin}}), \qquad (1)$$

where $\delta_{\text{kin}}$ is the kinetic momentum offset of the ion. Every particle obtained from the fragmentation simulation is tracked twice, with $(x, x')$ being mirrored, to simulate the particle generation at both collimator jaws. The equivalent energy $E_{\text{eq}}$ of the protons we use to represent the heavy ions is calculated based on the total ion energy $E_{\text{ion}}$ extracted from the fragmentation simulation. For ultra-relativistic particles the equivalent proton energy can be described as

$$E_{\text{eq}} = \frac{E_{\text{ion}}}{Z} = \frac{E_{\text{Pb},0}}{Z_0} (1 + \delta_{\text{eff}}), \qquad (2)$$

where $E_{\text{Pb},0}$ is the energy of an on-momentum $^{208}$Pb nucleus. For this simulation, all particles are assumed to have no initial offset or angle in the vertical direction, thus $y = 0$ and $y' = 0$. Note that all generated secondary particles other than ion fragments are ignored in the generation of the SixTrack input. For the particle tracking in SixTrack, all collimator materials are set to black absorbers to avoid calling the proton-specific scattering routine. The tracking is done for 100 turns, which is sufficient for the vast majority of fragments to be lost on collimators or machine aperture.

## SIMULATION RESULTS

All simulations are carried out considering a beam of $^{208}$Pb$^{82+}$ ions at an energy of 1.38 $A$ TeV, corresponding to an equivalent proton energy of 3.5 TeV. The considered optics and collimator settings are the same as in the 2011 heavy ion run, with $\beta^* = 1$ m in IP1, IP2, IP5 and 3 m in IP8. The collimator settings are summarized in [13]. All simulations are carried out for LHC Beam 1. The results are compared to loss maps measured using the LHC beam loss monitors (BLM) in the 2011 heavy ion run. The BLMs are ionization chambers which are installed on the outside of the LHC magnets and beam pipes recording particle showers generated by particles hitting the aperture or a collimator [14]. For a loss map measurement, the beam emittance is artificially blown up using either tune resonance methods or beam excitations with the transverse damper [9]. The losses are then large enough for a satisfactory signal to noise ratio. Note that, contrary to the simulations where the losses of the incident ions are recorded, the BLMs measure the secondary shower particles with a limited azimuthal coverage. Therefore, the simulated loss distribution of primary ion fragments cannot be directly compared to measurements with a high quantitative accuracy.

### ICOSIM Simulation

Figure 2 a) and Fig. 3 a) show the loss map from the simulation using ICOSIM with the optics and collimator settings of the 2011 LHC run compared to the losses measured with the BLMs, shown in subplot d). The energetic weight of each impacting ion scales roughly with the nuclear mass number $A$
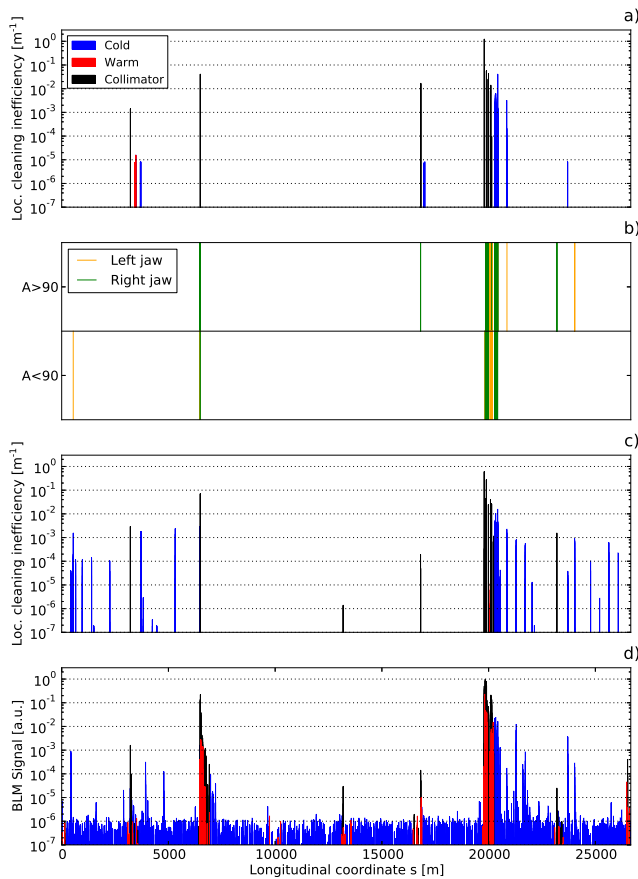
Figure 2: a) LHC loss map simulation of the 2011 heavy ion run using ICOSIM for the full LHC ring. b) SixTrack simulation with starting conditions at the TCP, without considering kicks in angle and energy. The upper half of the plot on top shows losses from particles with a nuclear mass number $A > 90$, the lower half for $A < 90$. c) SixTrack simulation for ion fragments including kicks in energy and angle. d) BLM signals measured in the 2011 heavy ion run. The simulations a) and c) include a weighting of the losses with the nuclear mass number $A$.

which is accounted for in the normalization of the losses in each bin. The lightest ion generated from the fragmentation algorithm has a nuclear mass number of $A = 90$. The average impact parameter on all collimators is $b = 1.7\,\mu$m. The two clusters in the IR7 dispersion suppressor (DS) are clearly visible and at the same order of magnitude as the measurements (see Fig. 4 for a more detailed comparison). Some of the major loss peaks in the cold magnets of the arc region are not predicted by the ICOSIM simulation. Furthermore, none of the measured losses in warm regions are visible.

### SixTrack with Protons of Ion-Equivalent Rigidity

**Tracking of light fragments** The impact of the lack of light fragments in ICOSIM (e.g. particles with $A < 90$ as mentioned above), is first simulated using SixTrack with the isotopes obtained by the fragmentation simulation. For this



Figure 3: Comparison of the different simulation tools with the measured heavy-ion loss map for the betatron collimation region IR7. The subplots are labeled identically to Fig. 2.

part of the study, kicks in angle and energy are neglected as done in ICOSIM. The angle of incidence is determined by the phase-space and the effective energy is calculated using Eq. (1) with $\delta_{\text{kin}} = 0$. Thus, every isotope starting at one collimator jaw is lost in a specific location. The unweighted result of the simulation is shown in Fig. 2 b) and Fig. 3 b). The loss distribution for the heavy isotopes essentially reproduces the ICOSIM result. The color coding shows that in distinct regions only particles starting from one collimator jaw are being lost. This effect can be traced back to the interplay between the betatron oscillations and the locally generated dispersion function. Betatron motion can either partly compensate or enhance dispersive offsets. With these approximations, the inclusion of the light fragments does not improve the simulation result in the arc region after IR7.

**Tracking of all fragments including energetic and angular kicks** The full simulation result, including the energetic/angular kicks as well as all light fragments from the fragmentation simulation is shown in Fig. 2 c) and Fig. 3 c). Also here, the ion impacts are weighted with $A$. In this simulation losses in the warm regions become visible. A traceback of the losses confirms that particles lost in the

Figure 4: Comparison of the losses in the IR7 dispersion suppressor. a) Losses simulated with ICOSIM. b) Losses simulated with SixTrack with protons of ion-equivalent rigidity. c) BLM signals measured in the 2011 heavy-ion run.

warm regions are mainly very light fragments, from protons to helium nuclei. Ions scattered out from all other collimators are not visible, since they are set to black absorbers. The main contribution to the final losses at the TCP is from $^{208}Pb^{82+}$ ions which survive at least one full turn of the machine. With the inclusion of the angles and energies, more of the measured losses in the arcs become visible in the simulation. The individual peaks in the arcs are composed of a number of different isotopes, also of very light fragments (e.g. $^3H^+$). Complementary simulations showed that with increasing impact parameter, the fraction of light fragments composing these peaks is increasing. In this new setup, the losses of one isotope starting at a given collimator jaw are not confined to one specific location but distributed all over the LHC ring. This is a consequence of a smearing of the trajectories of the fragmented ions for a given type of isotope. As shown in Fig. 4, the smearing of the loss positions leads also to a longitudinal enlargement of the IR7 DS clusters. In the regions far downstream of IR7, new loss peaks appear that are not seen in the measurements. Additional simulations are planned in order to investigate the origin of these losses. The discrepancies could for example be caused by small magnet misalignments in the machine, which shift the local bottlenecks to other locations.

**ICOSIM/SixTrack comparison for ions with large $\delta_{eff}$**
In the case of isotopes with with large $\delta_{eff}$, significant differences between the chromatic tracking of SixTrack and

ICOSIM can be expected. To evaluate the importance of the chromatic modeling, a simulation of specific isotopes with initial conditions using both ICOSIM and SixTrack was realized. As an example we present the light isotope $^8Li^{3+}$ with an effective momentum offset of $\delta_{eff} = 0.054$. The comparison of the particle tracks is presented in Fig. 5.

After a longitudinal distance of 200 m, the horizontal difference between the two tracks is in the order of 1 mm. This is particularly remarkable, as the locally generated dispersion function in this region is still small compared to the values it reaches in the bending dipoles of the arc regions. Such deviations can have considerable impacts on the simulation of the cleaning efficiency. Thus, higher orders in the chromatic modeling should be considered to provide appropriate tracking precision for such particles with large $\delta_{eff}$. This is particularly important if all light fragments are included in the simulation.

## HEAVY-ION SIXTRACK

As shown in the previous chapters, the accuracy of the ICOSIM code is limited by the approximations it makes, in particular the simplifications of the fragmentation routine and the linear chromatic modeling. The SixTrack simulation with protons of ion-equivalent energy provides better accuracy compared to the measurements, but still suffers from the absence of multiply fragmented ions.

The remaining discrepancies between simulations and measurements show the need for an improved simulation tool. Such a tool should include the better chromatic tracking of SixTrack *and* keep track of all light fragments. It should also include heavy-ion scattering in all collimators, accounting for the offsets in energy and angle. This could possibly be achieved by using an online coupling of SixTrack with FLUKA, similar to what is under development for protons [15–17].
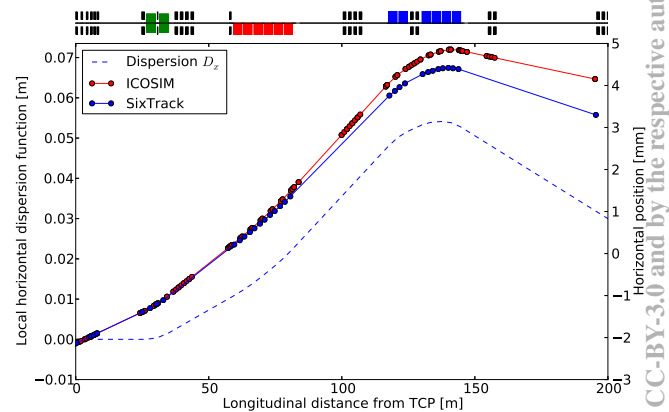


Figure 5: Tracks of $^8Li^{3+}$ starting from the left collimator jaw calculated using ICOSIM (red) and SixTrack (blue). The local dispersion function $D_x$ is calculated using MAD-X.

# SUMMARY AND OUTLOOK

In this paper simulations of the performance of the LHC collimation system for heavy ions using different tracking and particle-matter interaction models were compared. Using the ICOSIM code, which provides a simplified modeling of the particle-matter interaction but a multi-pass model of the generated fragments, the main loss locations in the IR7 DS, but not the losses in the arc after IR7, could be reproduced.

Another method was to use SixTrack and track protons of ion-equivalent rigidities. A sample of ion fragments coming out of the primary collimator, generated with FLUKA, was used as starting conditions. All subsequent collimators were acting as perfect absorbers without scattering. When the changes in angles and energies from the fragmentation process were ignored, the ICOSIM result was reproduced. Further, it was shown that the loss map prediction at locations far from IR7 could not be improved by adding light fragments if the kicks in angle and energy were neglected.

By adding the kicks in angle and energy to the initial distribution of fragments, the agreement with measurements could be significantly improved. The highest measured loss locations in the arc were reproduced. Warm losses became apparent by adding also the light fragments into the simulation. However, this simulation approach could still not reproduce all small loss peaks in the arc region. These losses might be induced by fragments starting from secondary collimators which are neglected in the present single-pass setup.

The chromatic modeling used in the two simulation codes was compared. For particles with magnetic rigidities very different from the main beam, the discrepancies are significant. Therefore, a higher order treatment of these effects must be considered.

Both codes provide good results within the limits of the approximations made. However, the results presented indicate that the general level of agreement with the measurements could be improved if the advantages of both simulation codes were combined. To close this gap, a new simulation code for heavy-ion collimation is envisaged.

# ACKNOWLEDGEMENTS

# REFERENCES

[1] O. S. Brüning et al., "LHC design report v.1 : The LHC main ring", CERN-2004-003-V1 (2004).

[2] R. W. Assmann et al., "The Final Collimation System for the LHC", Proc. EPAC 2006, Edinburgh, Scotland, page 986 (2006).

[3] H.H. Braun et al., "Collimation of heavy ion beams in the LHC", Proc. EPAC 2004, Lucerne, Switzerland, p 551 (2004).

[4] T.T. Böhlen et al., "The FLUKA Code: Developments and Challenges for High Energy and Medical Applications", Nuclear Data Sheets 120, 211-214 (2014).

[5] A. Ferrari, P.R. Sala, A. Fasso', and J. Ranft, "FLUKA: a multi-particle transport code", CERN-2005-10 (2005), INFN/TC_05/11, SLAC-R-773.

[6] G. I. Smirnov et al., "Hadronic and electromagnetic fragmentation of ultrarelativistic heavy ions at LHC", PRSTAB 17, 021006 (2014).

[7] R. Bruce et al., "Measurements of heavy ion beam losses from collimation", PRSTAB 12 011001 (2009).

[8] MAD-X webpage, http://www.cern.ch/madx

[9] R. Bruce et al., "Simulations and measurements of beam loss patterns at the CERN Large Hadron Collider", Phys. Rev. ST Accel. Beams 17, 081004 (2014).

[10] G. Bellodi et al., "First ion collimation commissioning results at the LHC", Proc. IPAC 2011, San Sebastian, Spain, 1813-1815 (2011).

[11] F. Schmidt, "SixTrack Version 4.2.16 Single Particle Tracking Code Treating Transverse Motion with Synchrotron Oscillations in a Symplectic Manner", CERN/SL/94–56 (AP).

[12] SixTrack webpage, http://sixtrack.web.cern.ch/SixTrack/

[13] R. Bruce et al., "Collimator settings and performance in 2011 and 2012", Proc. Chamonix 2012 LHC Performance workshop (2012).

[14] E. B. Holzer et al., "Development, production and testing of 4500 Beam loss monitors", Proc. EPAC 2008, Genoa, Italy , p 1134 (2008).

[15] A. Mereghetti et al. "Sixtrack-FLUKA active coupling for the upgrade of the SPS scrapers", Proc. of IPAC 2013, Shanghai, China, page 2657, (2013).

[16] R. Bruce et al., "Integrated Simulation Tools for Collimation Cleaning in HL-LHC", Proc. of IPAC 2014, Dresden, Germany, page 160, (2014).

[17] P. Garcia Ortega, "Status of SixTrack-FLUKA coupling", presentation in the LHC Collimation Working Group, 06.10.2014, (2014).

# BEAM HALO MEASUREMENT USING A COMBINATION OF A WIRE SCANNER TYPE BEAM SCRAPER AND SOME BEAM LOSS MONITORS IN J-PARC 3-GEV RCS.

M. Yoshimoto#, H. Harada, K. Okabe, M. Kinsho,
J-PARC, JAEA, Tokai, Ibaraki, 319-1195, Japan

## Abstract

Transverse beam halo is one of the most important beam parameters because it should limit the performance of the high intensity beam accelerator. Therefore the transverse beam halo measurement is one of the important issues to achieve the design beam power of 1MW in the J-PARC 3-GeV RCS. Thus the new beam halo monitor, which is combined a wire scanner and some beam loss monitors, was developed and installed in the extraction beam transport line. By using several beam loss monitors with different sensitivities, an ultra-wide dynamic range can be achieved and beam profile including both of the beam core and halo can be obtained.

## INTRODUCTION

The 3-GeV Rapid Cycling Synchrotron (RCS) has been beam commissioned for initial beam tuning tests since October 2007 [1] and afterwards we started user operation for the Material and Life science experimental Facility (MLF) and the 50-GeV Main Ring synchrotron (MR). Since December 2009, we have started a beam tuning for high-intensity beams and 420kW beam operation could be demonstrated successfully [2]. In order to achieve the design performance of the 1MW of the RCS, the LINAC is required both of the beam energy upgrade from 181MeV to 400MeV and the beam current upgrade from 25mA to 50mA. For the beam energy upgrade, a new accelerating structure "Annular-ring Coupled Structure (ACS)" had been installed in 2013. And then, during the summer shutdown in 2014, new front-end consisted both of the ion source and the Radio Frequency Quadrupole (RFQ) are replaced for the beam current upgrade in the LINAC [3]. Then the beam energy upgrade and the beam current upgrade in the LINAC were completed. After completing these LINAC upgrades, the RCS is to start the final beam tuning toward the design output beam power of 1 MW.

To provide such a high power proton beam for the MR with small injection beam loss or for the MLF with broad range and uniformity irradiation to the target using the octupole magnet [4], it is required to improve the extraction beam quality, namely to achieve the Low-Halo and High-Intensity beam by finer beam tuning in the RCS. Therefore the measurement of the transverse beam profile including both of the beam core and the beam halo is one of the key issues for the high power beam operation in the RCS. Thus a new beam halo monitor was developed and installed at the 3GeV-RCS to Neutron source Beam Transport (3NBT) line as shown in Fig. 1. And examination of the new halo monitor with the extraction

beam was started. In this paper, we report the first trial test of the new beam halo monitor after the LINAC energy upgrade.
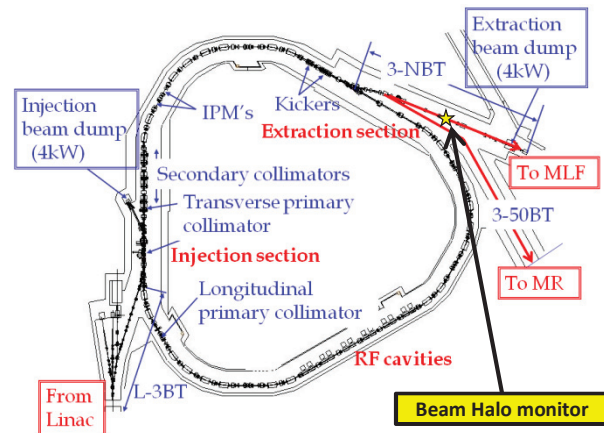


Figure 1: Top view of the RCS and location of the beam halo monitor installation.

## NEW BEAM HALO MONITOR

### Concept Design

For the halo measurement of the extraction beam from the RCS, the original beam halo monitor, which was a scraper plate type detecting the emissive secondary electron and the plate temperature during the beam irradiation into the scraper plate, had been installed at the 3NBT line [5]. The scraper plate was limited to scanning within the beam halo area, thus the beam core cannot be observed. Moreover, it is difficult to obtain the pure signal due to the secondary electron emission because there are much floating electrons in the vacuum chamber and they disturb the raw signal of the halo monitor. On the other hand, the temperature did not increase during the beam irradiation because the sensitivity is too low to detect the beam halo component.

To resolve these problems, the new halo monitor installed at the 3NBT adjoining the original halo monitor. The conception of this new halo monitor is that the beam signal disturbance by the floating electrons should be suppressed and the quick signal response should be achieved. Thus the new halo monitor is combined a wire scanner and the several kinds of beam loss monitors (BLM), and it detects the radiation due to the beam scraping by the wire scanner. Figure 2 shows the schematic diagram of the

new halo monitor. It has two wire scanners for horizontal and vertical scanning respectively, and a head of the wire scanner is composed a stainless steel wire put on the aluminium frame. The diameter of the wire was change from 1mm to 0.1mm after the LINAC energy upgrade. The wire scanner can be scanning during the full range of the extraction beam distribution. By using the several kinds of BLM with the different sensitivities, an ultra-wide dynamic range can be achieved and the transverse beam profile including the beam core and beam halo elements can be reconstructed.
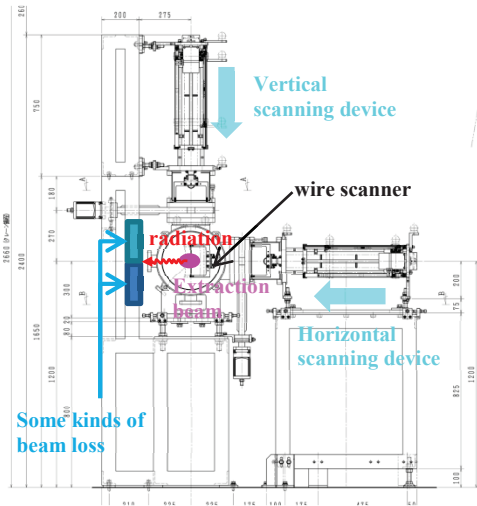


Figure 2: Schematic diagram of the new beam halo monitor.
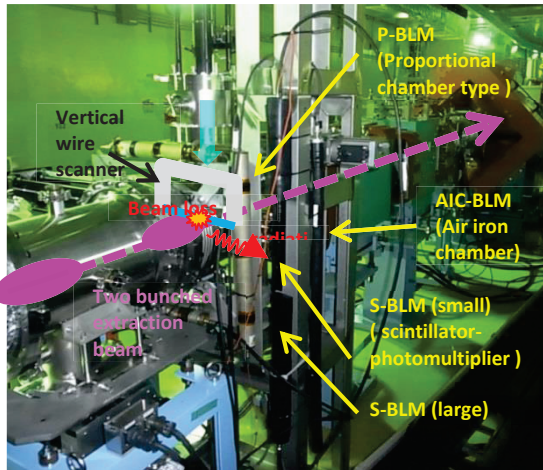


Figure 3: Photograph of the new beam halo monitor. Several kinds of beam loss monitor were attached.

## Newly-devised Radiation Detect Systems

In the RCS, several kinds of BLM were installed as following; proportional counter type (P-BLM), plastic scintillator and photomultiplier pair type (S-BLM), and air ionization chamber type (AIC-BLM) [6]. At first all type

of the BLMs were used for the beam halo measurement as shown in Fig. 3. However the AIC-BLM cannot detect the radiation signal due to the downsizing of the wire diameter. Moreover not only the sensitivities but also the time responsibilities are different among these BLMs; especially it is difficult to obtain the time structure of the bunched beam by using the P-BLM. From these results of the demonstrational beam test, S-BLMs are adopted for the beam halo monitor because they have good time responsiveness. We chose a common photomultiplier tube (PMT). And we controlled the sensitivities of the S-BLM by changing the size of the plastic scintillator or the distance from the wire scanner to S-BLM. For the first trial test, two kinds of S-BLM were assembled. One is the small plastic scintillator type as shown in Fig. 4, and the other is the large plastic scintillator type in Fig. 5. The small type S-BLM has a light guide for a support of the thin plastic scintillator. Two large type S-BLMs were assembled. One wsa installed close to the wire scanner together with the small type S-BLM as shown in Fig. 3. The other was installed upstream of about 5m away from the wire scanner. The aim of the near large type S-BLM is a high sensitivity detector to measure beam halo elements. And the aim of both the near small type and the far large type S-BLMs are a low sensitivity detectors to measure beam core elements.
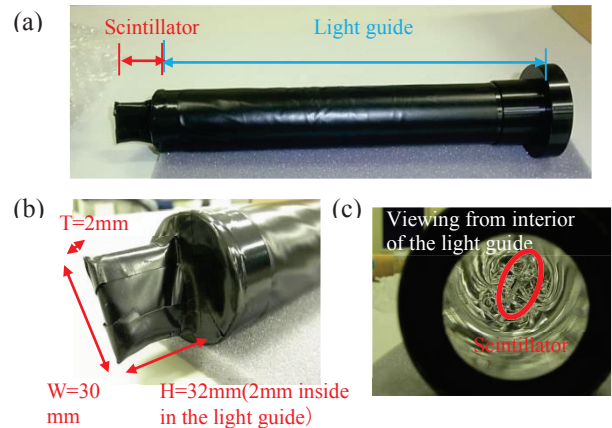


Figure 4: Photographs of the Small Scintillator type BLM. It has a light guide for a support of the thin plastic scintillator.

Figure 5: Photograph of the Large Scintillator type BLMs

## BEAM HALO MEASUREMENT

### Background Suppression

Beam loss monitor detects the whole radiations which are generated at the all over the place around the new halo monitor. In order to reconstruct the beam profile from the S-BLM signals, we need to search for the pure signal of the radiation generated at the wire scanner among the whole radiation signal detected by the S-BLMs. Background signal, which is defined as a signal of the radiation generated at everywhere without the wire scanner, can be measured from the S-BLM during the wire scanner retracting. And then, pure S-BLM signals from the wire scanner can be obtained by subtracting the background signal from the whole signal as shown in Fig. 6.
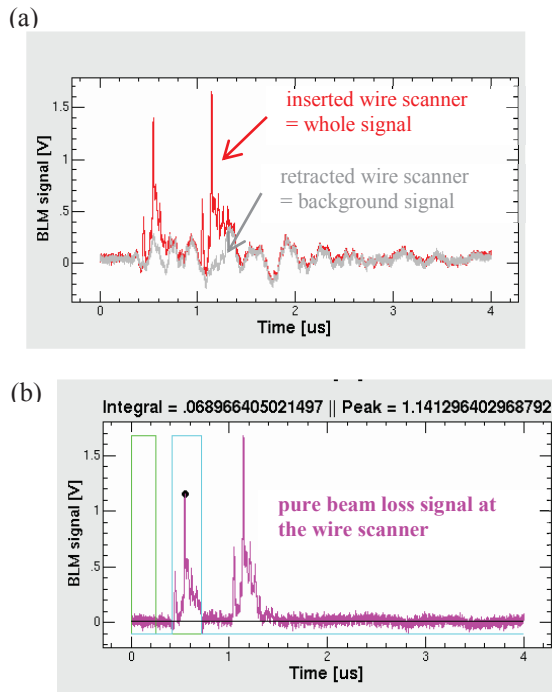


Figure 6: Typical result of the noise reduction of the S-BLM signal. (a): Comparison of the raw S-BLM signals between inserted and retracted the wire scanner. (b): pure beam loss signal at the wire scanner after the background noise reduction.

### Calibration Curve Acquiring

In order to reconstruct the beam profile from the S-BLM signals, every calibration curve formula between the number of particles and each S-BLM signals must be determined. To control the number of particles in the RCS, we can adjust some parameters of the injected LINAC

beam as follows; a macro pulse width, a chopped intermediate pulse width, and number of the intermediate pulses.

For the high sensitivity detector; the near large type S-BLM, we can control the ultra-low beam intensity by adjusting the number of the chopped intermediate pulses in which the pulse width of 56ns was fixed. The measurement result of the ultra-low particle numbers was summarized in Fig. 7. At the same time, we obtained the scanning data of the near large type S-BLM signal. Assuming that all signals of the S-BLM were not saturated, total radiation signal due to each ultra-low intensity beam can be estimated by integrating the distribution of the scanning data. Figure 8 shows the result of the estimated total radiation signal. By combining these two results, we can acquire the calibration curve formula as shown in Fig. 9.
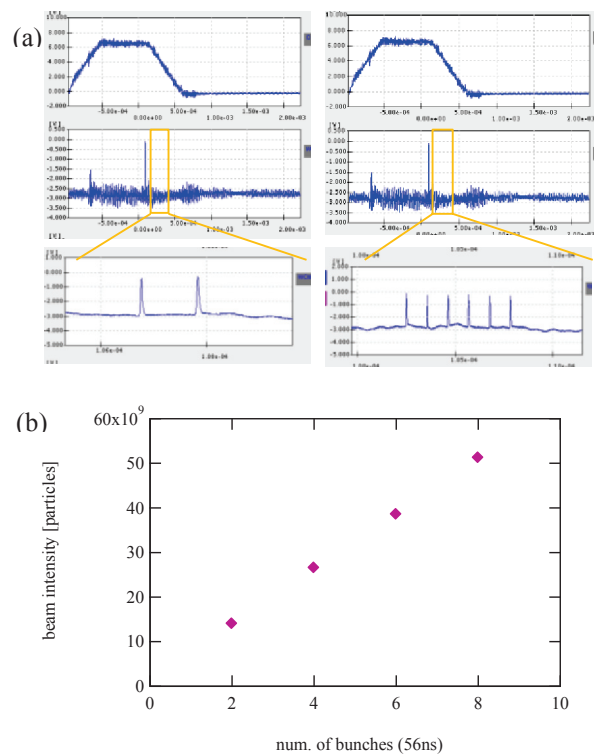


Figure 7: Particle numbers measurement in the ultra-low intensity beam. (a): Typical wave forms of the shift bump magnet and the injected intermediate pulses. (b): Beam intensity plot dependent on the number of bunches.

(a)



(b)
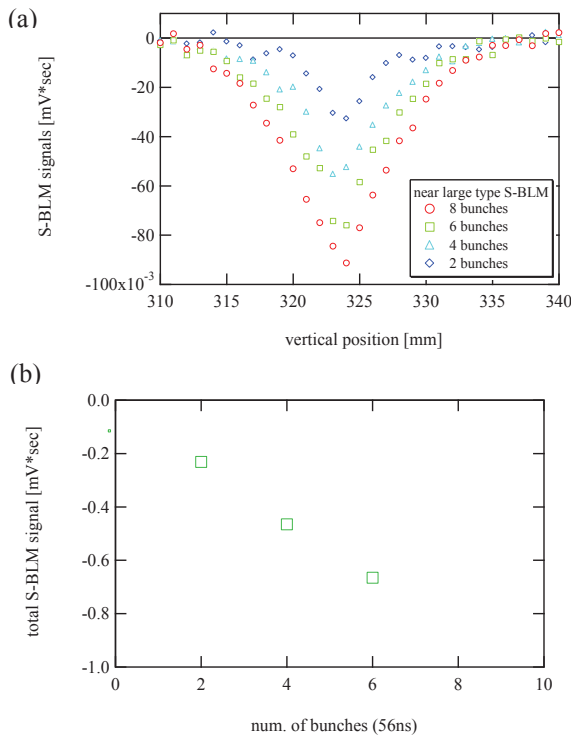


Figure 8: S-BLM signal measurement in case of low sensitivity detector. (a) :Beam profiles obtained from the scanning signals of the near large type S-BLM. (b): Total S-BLM signal plot dependent on the number of bunches.
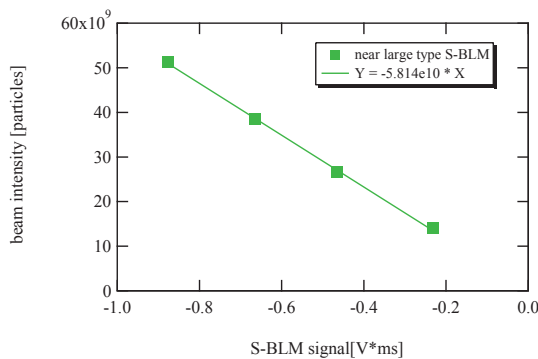


Figure 9: High sensitivity calibration curve for the near large type S-BLM.

For two low sensitivity detectors; the near small type S-BLM and the far large type S-BLM, we acquired the calibration curve with the same method. In this high beam intensity case, we controlled the beam intensity by adjusting the macro pulse width in which the chopped intermediate pulse width was 432ns and full intermediate pulses were used. Figure 10 shows the calibration curve formulas for each S-BLM.
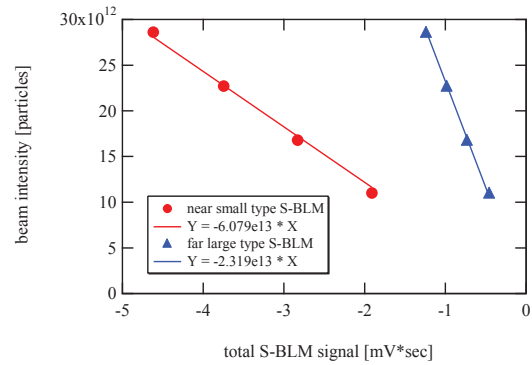


Figure 10: low intensity calibration curves for the near small type S-BLM and far large type S-BLM.

## Reconstruction of the Transverse Profile

After completing each calibration curve acquiring, we demonstrated the transverse beam profile reconstruction with the new halo monitor. In this first trial beam test, the output beam power was 340kW equivalent. All PMTs were excited by a common power supply and the high voltage was fixed on -1kV.

Three plots in the Fig. 11(a) show the all scanning S-BLM data. The red circle and blue triangle plots were obtained by the near small type S-BLM and the far large type S-BLM respectively. The green square plots were obtained by the near large type S-BLM. By using the low sensitivity detectors, the beam core profile can be measured. However beam halo elements cannot be measured and then beam edge is underestimated. On the other hand, by using the high sensitivity detector, the beam core cannot be measured because the S-BLM signals are saturated. But the beam halo element can be measured. These results indicate that the beam core and halo elements can be measured separately by using the different sensitivity detectors.

Next step was reconstruction of the transverse beam profile from these scanning data. Only by using each sensitivity calibration curve formula, transverse beam profile with wide dynamic range can be reconstructed directly as shown in Fig. 11(b). These plotted the conversion data and any other correction was not necessary to join together all measured plots. Two beam core profiles overlapped thoroughly, and beam core and halo profiles adjoined smoothly. Thus we approve that the new halo monitor can measure the transverse beam profile with wide dynamic rage and the absolute value of the beam halo components can be evaluated.

In this first trial beam test, we verified to achieve the wide dynamic range of $10^8$ - $10^{13}$ particles. Now, in order to expand the dynamic range more widely, additional S-BLMs with different sensitivity were installed and the HV power supplies to excite all PMT independently were set up. Then we will examine the new halo monitor in more detail in the next beam test.

(a)



(b)
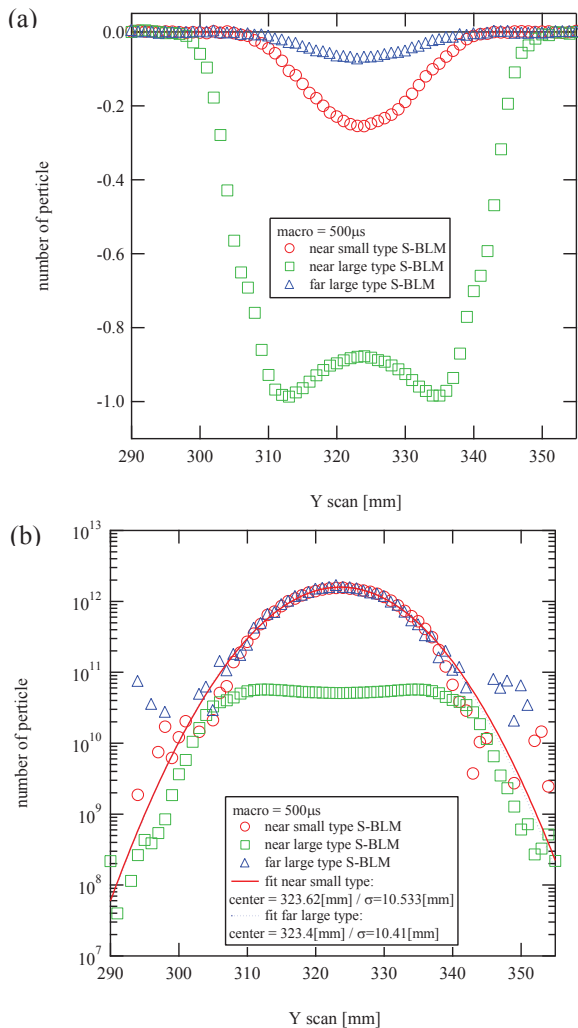


Figure 11: Demonstration of the transverse beam profile reconstruction with the output beam power of 320kW equivalent. (a) : Each S-BLM signal plots. (b) : Conversion data plots by using each sensitivity calibration curve formula.

## SUMMARY

In the J-PARC RCS, new beam halo monitor, which is combined a wire scanner and some beam loss monitors, was developed to measure the transverse profile of the extraction beam. This new halo monitor aims to achieve the ultra-wide dynamic range. By using several beam loss monitors of plastic scintillator type with different

sensitivities, the transverse beam profile including the beam core and halo elements can be reconstructed.

In the first trial beam test, we set up one high sensitivity S-BLM and two low sensitivity S-BLMs. The sensitivity of the S-BLM is controlled by changing the size of the plastic scintillator or by changing the distance from the wire scanner. At first, each calibration curve formulas for three S-BLMs were acquired. And next, we demonstrated the reconstruction of the transverse beam profile. Only by using sensitivity calibration curve formulas for the each S-BLM, transverse beam profile with wide dynamic range can be reconstructed directly. Any other correction was not necessary to join together all measured plots. It is great advantage of the new halo monitor, and we can approve that the absolute value of the beam core and halo components can be evaluated.

In this first trial beam test, we verified to achieve the wide dynamic range of $10^8$ - $10^{13}$ particles. Now, in order to expand the dynamic range more widely, additional S-BLMs with different sensitivity was installed and the HV power supplies to excite all PMT independently were set up. Then we will examine the new halo monitor in more detail in the next beam test.

## REFERENCES

[1] H. Hotchi, et. al., "Beam commissioning of the 3-GeV rapid cycling synchrotron of the Japan Proton Accelerator Research Complex", Phys. Rev. ST Accel. Beams 12, 040402 (2009).

[2] H. Hotchi, et. al., "Beam loss reduction by injection painting in the 3-GeV rapid cycling synchrotron of the Japan Proton Accelerator Research Complex", Phys. Rev. ST Accel. Beams 15, 040402 (2012).

[3] K. Hasegawa. JPS Conf. Proc. "Proceedings of the J-PARC Symposium 2014", to be published.

[4] S. Meigo, et. al., "BEAM FLATTENING SYSTEM BASED ON NON-LINEAR OPTICS FOR HIGH POWER SPALLATION NEUTRON TARGET AT J-PARC", Proc. IPAC2014, Dresden, Germany (2014), MOPRI116.

[5] M. Yoshimoto, et. al., "DEVELOPMENT OF THE BEAM HALO MONITOR IN THE J-PARC 3-GEV RCS", Proc. IPAC2012, NewOrlins, USA (2012), WEOAA03.

[6] N. Hayashi, et. al., "BEAM INSTRUMENTATIONS FOR THE J-PARC RCS COMMISSIONING", Proc. EPAC08, Genoa, Italy (2004), TUPC034.

# PROPOSED VARYING AMPLITUDE RASTER PATTERN TO UNIFORMLY COVER TARGET FOR THE ISOTOPE PRODUCTION FACILITY (IPF) AT LANSCE*

J. Kolski[†], LANL, Los Alamos, NM, 87545, USA

## Abstract

The Isotope Production Facility (IPF) at LANSCE[1] produces medical isotopes strontium-82 and germanium-68 by bombarding rubidium chloride and gallium metal targets respectively with a 100 MeV proton beam, 230 uA average current. Rastering the proton beam is necessary to distribute heat load on the target and target window, allowing higher average beam current for isotope production. Currently, we use a simple circular raster pattern with constant amplitude and frequency. The constant amplitude raster pattern does not expose the target center to beam and few isotopes are produced there. We propose a raster pattern with varying amplitude to increase isotope production at the target center, achieve uniform beam flux over the target, and expose more of the target surface to beam heating. Using multiparticle simulations, we discuss the uniformity of target coverage using the proposed varying amplitude raster pattern, compare with the constant amplitude raster pattern currently used, and consider dependencies on transverse beam size, beam centroid offset, and macropulse length and repetition rate.

## INTRODUCTION

Beam rastering for IPF is controlled by a horizontal and a vertical steering magnet[2]. The steering magnets are modulated by the same frequency generator with maximum bandwidth 5 kHz. Steering magnet amplitude can be con-



Figure 1: Measured beam at the IPF target by foil irradiation: 300 s exposure time at 2 Hz, 7 $\mu$A average current.
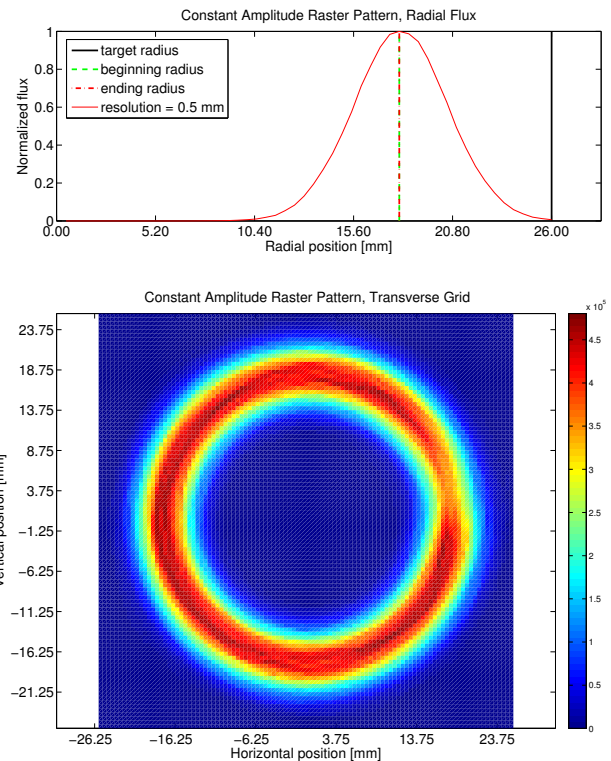
Figure 2: Simulated beam at the IPF target with constant radius 18 mm: 1 macropulse, beam $\sigma = 2.5$ mm, gird resolutions 0.5 mm. Top: beam flux binned radially. Bottom: beam binned transversely.

trolled separately via digital controllers. During production, IPF receives 625 $\mu$s long marcopulses at an uneven 40 Hz rep rate, consisting of micorpulses separated by 5 ns due to the RF acceleration at 201.25 MHz. Due to the raster frequency and pulse length, there are ~3 raster revolutions during a macropulse.

The current raster pattern is a simple circle with 18 mm radius. The beam measured at the IPF target by foil irradiation is shown in Fig. 1, and a one macropulse simulation (described later) using the constant amplitude raster pattern is shown in Fig. 2. The beam appears wider in measurement, but the foil coloration results from heating effects which saturate. It is clear from both measurement and simulation that little beam hits the target center and few isotopes are produced there. This is an inefficient use of expensive solid targets.

The goal of this investigation is to obtain a raster pattern

that yields uniform target coverage with the constraints of the present equipment. Uniform beam flux on the target utilizes more of the target, lowering heat load by spreading the beam over a larger surface. This allows for an increase in average current. Steering the beam center increases the overall flux because less beam hits the collimator.

## AMPLITUDE VARIATION

We tried to achieve uniform beam coverage in a single marcopulse using a spiral-type raster pattern (constant frequency, varied amplitude), but given the constraints of the present equipment (~3 rastering revolutions in a macropulse), we determined it is not possible. Our studies show uniform coverage is possible if the last revolution of the spiral is within a radius of ~2 rms beam widths. For our beam with typical rms beam width 2.5 mm, the raster frequency necessary for uniform beam coverage in one marcopulse is ~25 kHz.

However, uniform coverage in one macropulse is not required because isotope production and heating effects have longer time scales. We will concentrate on obtaining uniform radial flux and rely on the pulse-to-pulse phase shift between the raster frequency and the beam rep rate to fill in the transverse grid after several macropulses.

We take advantage of the circular symmetry and separate the rastering into radial and azimuthal components

$$\begin{pmatrix} x_0 \\ y_0 \end{pmatrix} = R(t) \times \Phi(t) = R(t) \times \begin{cases} \cos(2\pi f t + \phi) \\ \sin(2\pi f t + \phi) \end{cases} . \quad (1)$$

For simplicity, we choose to keep a constant frequency azimuthal component and vary the amplitude of the raster pattern to achieve a uniform radial flux.

We define a radial grid. The area of the bins, or rings, increase with position. The area of the $i^{\text{th}}$ ring with outer radius $r$ and width $\Delta r$ is $A_i(r) = 2\pi(\Delta r)r - \pi \Delta r^2 = A_{i-1}(r - \Delta r) + 2A_0(\Delta r)$, where $A_0(\Delta r) = \pi \Delta r^2$ is the area of the inner most radial bin. We desire the amount of beam in each radial bin to be proportional to the area of the ring. We equate the amount of beam in a radial bin with the time the raster pattern spends in the bin and define a time unit $\tau$, which amounts to the beam equivalent for area $A_0(\Delta r)$. Thus, the raster pattern must be present in the four inner radial bins for 1, 3, 5, and $7\tau$ time units respectively. This is a square root dependence, $R(t) \sim \sqrt{\tau}$, which duplicates the result in Ref. [3]. The proposed amplitude variation raster scheme with the square root dependence is illustrated in Fig. 3.

## SIMULATION

The simulation results shown in this paper are generated with a simple multiparticle simulation. For each micropulse (5 ns time steps) in a macropulse (625 $\mu$s long), a 2D gaussian distribution of 10,000 particles and rms widths $\sigma_x = \sigma_y = 2.5$ mm (as determined by beam measurements with a harp) is generated with beam centroid determined by the rastering pattern shown in Fig. 3. The particles are binned to a 0.5 mm radial grid and to a grid of
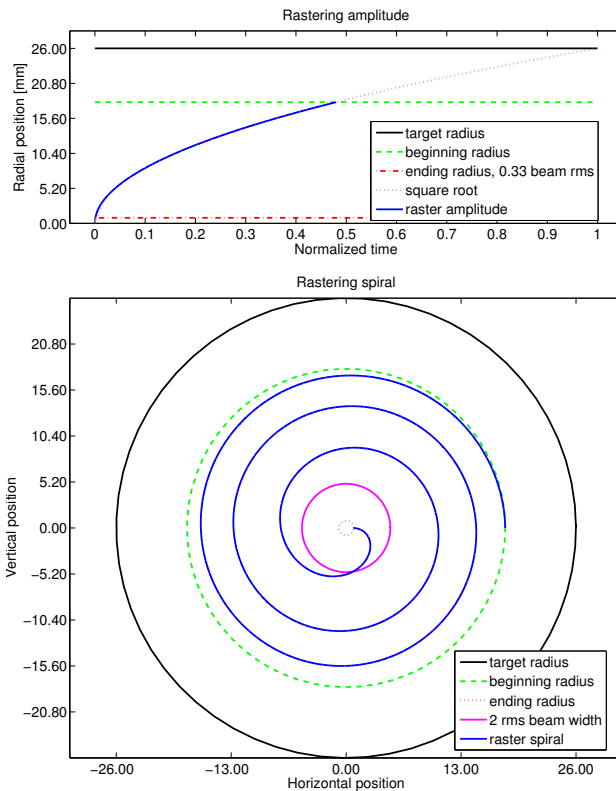


Figure 3: Amplitude variation raster pattern for 1 macropulse: radial position of the raster pattern (top) and horizontal and vertical position of the raster pattern (bottom) on the IPF target.

0.5 mm square bins. The simulation can run for multiple macropulses, in which case, it calculates the phase shift between the raster frequency and the beam rep rate. After all micropulses from all macropulses are binned, the number of particles in each radial bin is divided by the area of the ring to obtain the beam flux, which is graphed in the top plots of Figs. 2 and 4.

## UNIFORM TARGET COVERAGE

The result of a single macropulse simulation with the square root amplitude variation is shown in Fig. 4. This raster pattern produces an even radial flux out to ~13 mm with only 5% variation.

The amplitude variation covers more of the target than in the constant amplitude case. However, there is still a bit of the target that is not hit by beam and a corresponding "hot spot" that receives about twice as much beam. Note, the "hot spot" is only ~20% more than the hottest location in the constant amplitude raster pattern. Even though the amplitude variation raster pattern yields a uniform radial flux, the transverse grid is not uniformly covered with a single macropulse. However, we observe very uniform transverse coverage when we run 1 s worth of macropulses at an uneven 40 Hz rep rate as in typically IPF production, Fig. 5.
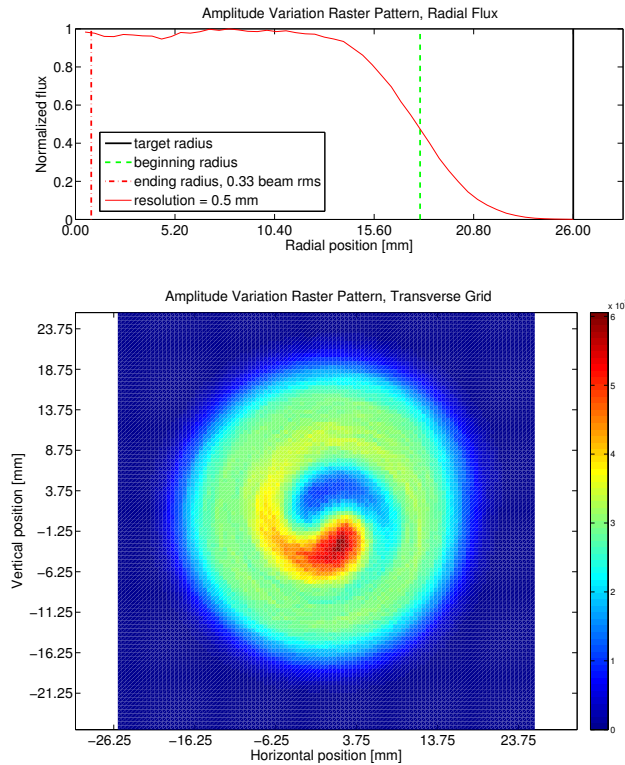
Figure 4: Beam simulated at the IPF target using the amplitude variation raster pattern with beginning radius 18 mm and ending radius 0.83 mm ($0.33\sigma$): 1 macropulse, beam $\sigma = 2.5$ mm, gird resolution 0.5 mm. Top: beam flux binned radially. Bottom: beam binned transversely.

Figure 5: Beam simulated at the IPF target using the amplitude variation raster pattern with beginning radius 18 mm and ending radius 0.66 mm ($0.33\sigma$): 40 macropulses at uneven 40 Hz, beam $\sigma = 2$ mm, gird resolution 0.5 mm.

Note the small dip in beam flux at the center of the target in Fig. 5, which is determined by the transverse beam size and the minimum raster amplitude. In optimization studies, we found that a minimum raster radius of $\sim0.2\sigma$ smoothed the beam flux at the center of the target the best.

## BEAM DEPENDENCIES

The transverse beam size changes the smoothness of the beam flux when filling the center of the target with a single macropulse and the edge fall-off effects. Smaller beam size will expose less of the target center to beam, sharpen the fall off of the beam flux on the target, and require higher raster frequency to uniformly cover the target in a single macropulse.

The raster spot on the target is only shifted with upstream steering. This is consistent with current operations, though beam signal on guard rings and collimator will be less because the amplitude variation raster pattern moves most of the macropulse way away from the outer radius.

The macropulse length has little direct effect. Longer pulse lengths lead to more raster revolutions which is better for faster uniform coverage. There is a lower limit on the macropulse length in which the amplitude variation scheme does not readily lead to uniform coverage, even after 1 s.

At least one raster revolution per macropulse is required for the amplitude variation raster pattern to yield uniform target coverage. Thus, typical tune up beam of 150 $\mu$s long macropulses ($\sim0.7$ raster revolutions) will not uniformly fill the transverse grid. Likewise, the beam rep rate does not have much effect on the accumulative effects of the amplitude variation raster scheme unless the raster frequency is a multiple of the 60 Hz machine rep rate. Our studies showed uniform target coverage for a series of macropulses at 1 Hz, even 4 Hz, and uneven 40 Hz.

## CONCLUSIONS

We have shown through multiparticle simulation that uniform coverage of the IPF target at LANSCE is possible with existing equipment. We determined that the amplitude variation of the rastering should be proportional to the square root of time. Although the amplitude variation raster scheme does not uniformly cover the target transversely in once macropulse, it achieves less than 5% variation in uniformity after 1 second at production beam parameters. We also considered effects of the raster spot on the target with respect to beam size, steering, and macropulse length.

## REFERENCES

[1] M.S. Gulley, "Isotope Production Facility Beam Line Commissioning Plan", LANL memo, LANSCE-6-03-072, Oct.14, 2003.

[2] R. Meyer, "Specifications for Rastering Magnet Coils", IPF Specification Number IPF-SPC-0599-0017-00-R00, (1999).

[3] Y.K. Batygin, et al. , "Uniform target irradiation by circular beam sweeping", Nucl. Instrum. Methods Phys. Res. A **363**, 128 - 130 (1995).

# SIMULATION OF A NEW BEAM CURRENT MONITOR UNDER HEAVY HEAT LOAD*

J. Sun, P.A. Duperrex[#], Paul Scherrer Institut, Villigen PSI, Switzerland

## Abstract

At the Paul Scherrer Institute (PSI), the High Intensity Proton Accelerator (HIPA) feeds a pion and muon source target with protons. A beam current monitor, called MHC5, installed 8 meters downstream from the target is heated by the scattered particles from the target. This thermal load on the monitor causes the resonance frequency to drift much more than expected.

A novel new beam current monitor using graphite has been developed. In order to have a good understanding of its performance, the simulation software ANSYS has been used to carry out thermal and high frequency simulations. With this software, it was possible to perform a detailed design of the thermal self-compensation scheme and to check the structural stability of the whole system. In this paper, simulation results show that frequency drift can be reduced to only 8 kHz from previous 730 kHz when expected operating conditions are assumed.

## INTRODUCTION

The proton beam current monitor, MHC5, has been operated for several years in the PSI 590 MeV proton cyclotron. The scattered particles and their secondaries from the target 8 meters upstream cause the resonance frequency of the current monitor to drift due to radiation heating. The originally designed MHC5 made of aluminium showed its operational limits with the increased beam intensity of the last few years. A newer version presently in operation still has large system gain variations caused by the frequency drift even with an active cooling system [1, 2].

To have a good understanding of the MHC5 performance and its limitations, simulations for an old prototype and for the MHC5 version in operation have been carried out using ANSYS.

## FUNDAMENTAL BEHAVIOUR OF THE MONITOR

The MHC5 is a coaxial resonator tuned at 101.26 MHz, the $2^{nd}$ harmonic of the proton beam pulse frequency. The size of the capacity gap, as shown the red ellipse in Figure 1, is a critical parameter influence the resonance frequency. Figure 2 shows the relationship between the size of capacity gap and the resonance frequency of MHC5. As the capacity gap increases, the resonance frequency of the monitor is increasing non-linearly.
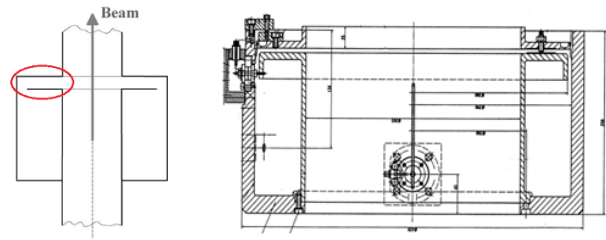


Figure 1: Schematic (left) and section view (right) of the MHC5.
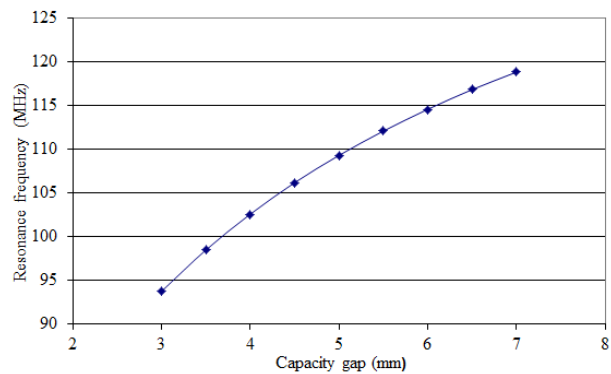


Figure 2: Resonance frequency changing with capacity gap.

Scattered particles from the target deposited on the MHC5 heat up the monitor and provoke frequency drift. Figure 3 shows the resonance frequency drift with increasing temperature on the monitor.
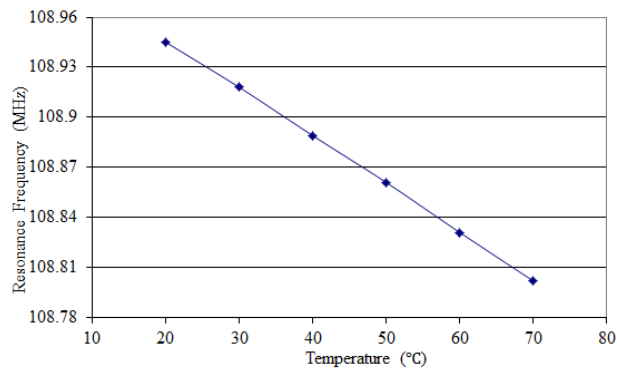


Figure 3: Resonance frequency drifting trend.

The monitor needed to be divided to 7 segments in simulation, since the distribution of the scattered particles is Gaussian in transverse plane, which means each segment has different power deposition.

## VALIDATION WITH PROTOTYPE

In order to validate the simulation results, a cross check between simulation and experiment is necessary. An old

prototype made of aluminium was used to carry out some laboratory tests.

An old prototype was put into a climate chamber and heated from 20 ℃ to 60 ℃. Figure 4 shows the frequency drift of the prototype was 24 kHz/10 ℃. A 2D model was set up in simulation. The frequency drift is 24.5 kHz/10 ℃ in simulation. With the thermal expansion as shown in Figure 5, the diameter increased 0.394 mm and the height increased 0.197 mm, which show good agreement with the experiment results in Table 1.
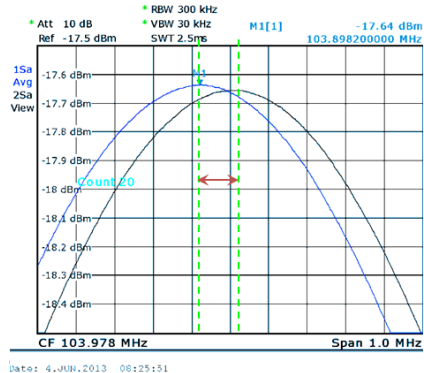


Figure 4: Sensitivity curves from 20 ℃ (black) to 60 ℃ (blue).
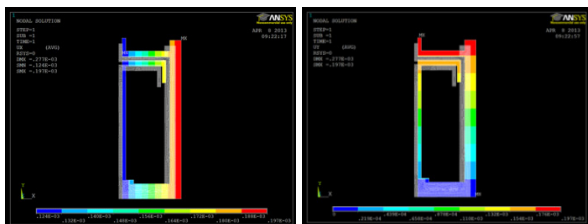


Figure 5: Simulations of the thermal expansion of the diameter (left) and the height (right).

Table 1 Measured and simulated thermal expansion for a temperature increase from 20 ℃ to 60 ℃

|  | Measured | Simulated |
|---|---|---|
| Height (mm) | 0.2 | 0.197 |
| Diameter (mm) | 0.4 | 0.394 |

## SIMULATION AND VALIDATION WITH THE EXISTING OPERATIONAL MONITOR

### Simulation

The MHC5 presently in operation is made of aluminium as well. Compared to the old prototype the present monitor has a water pipe mounted on the beam entry side to provide an active cooling. A 3D model was set up, as shown in Figure 6.
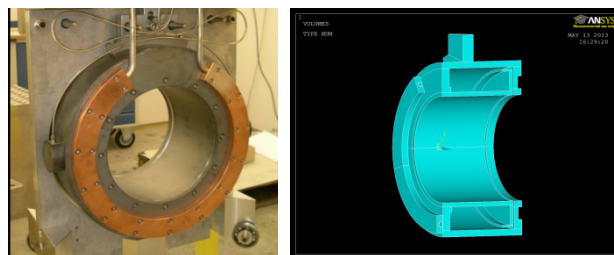


Figure 6: The MHC5 in operation, the water cooling pipe at the beam entry side (left), 3D model setup (right).

Normally the cooling efficiency will be increasing with the water velocity increasing. But once the turbulence is fully developed, the improvement of the cooling efficiency with increasing water inlet speed is marginal. Different water velocity was applied and the simulation results show in Figure 7. When the velocity of the water ups to 2 m/s, there is no significant improvement of the cooling efficiency to be expected, just as earlier simulation shows [3].
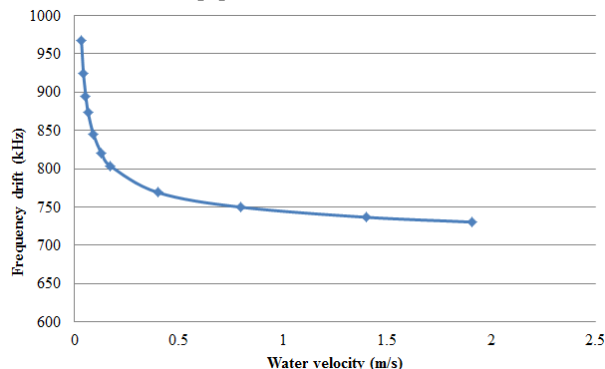


Figure 7: Frequency drifts dependent water velocity.

### Validation

The temperature of the monitor presently in operation can be controlled by modulating the cooling water speed using a valve. In the routine operation the velocity of the cooling water is 1.91 m/s, the temperature of the water is around 48 ℃. Through simulation the frequency drift of the MHC5 in operation is 730 kHz when 3 mA proton beams is applied.

The resonance frequency was measured with two different cooling water speeds, as shown in Figure 8, the blue line is the sensitive curve under 51.8 ℃ and the green line is under 74.1 ℃. From this figure the frequency drifts between 51.8 ℃ and 74.1 ℃ can be estimated around 100 kHz. Table 2 compares the results from experiment and simulation.

Table 2 Frequency drifts comparison

|  | Temperature | Frequency drift |
|---|---|---|
| Experiment | 51.8 ~ 74.1 ℃ | ~ 100 kHz |
| Simulation | 52 ~ 74.1 ℃ | ~ 110 kHz |
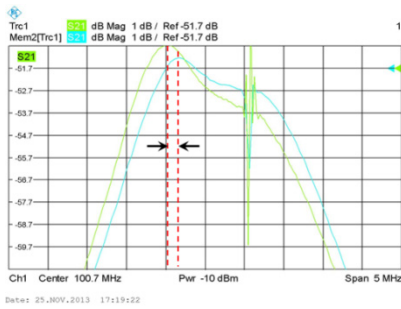
Figure 8: Sensitivity curves from measurement. The blue curve is for 51.8 °C, the green curve is for 74.1 °C.

## DESIGN OPTIMIZATION

Through the simulations described before, the origin of frequency drift is caused by the thermal expansion and the thermal gradient between inner parts and outer parts. Graphite is proposed instead of aluminium to make the new monitor, since it has a lower thermal expansion coefficient and a very high emissivity. As a result, the active cooling is no more required and the thermal gradient can also be strongly reduced.

### Improvement in Geometry

A simplified model of graphite without the water cooling pipe is shown in Figure 9. The power deposition in this structure is 400 W [4].
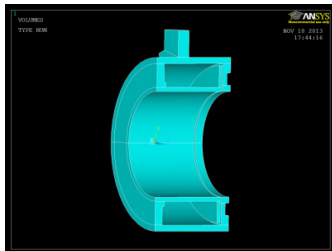


Figure 9: Simplified model without water pipe.

In order to decrease the power deposition, the inner diameter of the MHC5 is increased from 255 mm to 280 mm, the corresponding power deposition is decreased from 400 W down to 169 W. But the capacity gap has to be reduced from 4.5mm to 2.5mm to keep the same resonance frequency. This makes the manufacture more difficult, since the resonance frequency is very sensitive to the size of the capacity gap.

### Improvement and Compensation of the Capacity Gap

To relax the mechanical tolerance, ceramic is used to fill partially the capacity gap. Since the capacity between two plates is directly proportional to the permittivity $\varepsilon$ of the material filling the gap, a larger permittivity (typically 10) allows a larger the capacity gap.

A 6.1 mm thick ceramic ring can be inserted between the capacitor plates and to give the same resonance frequency.

In addition, a 2 mm thick aluminium shim is used to compensate the capacitance increase due to the thermal

expansion. The shim is placed so that its thermal expansion leads to an increase of the capacitor gap. The thermal expansion coefficient of aluminium is about 8 times higher than graphite so by calculating the thickness of the shim proportionally, the capacitance can be kept approximately constant.

Figure 10 shows the final design of the new MHC5. The frequency drift of this model under 3 mA proton beams is only 8 kHz in simulation, much lower than the unit in operation.
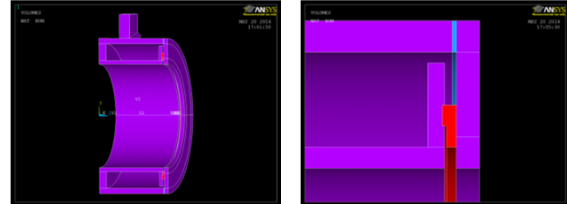


Figure 10: Final design of the new MHC5 with aluminium shim and ceramic ring.

### Tuning Method

Eight M20 size screws are distributed on the beam exit side for the fine tuning, as shown in Figure 11. The tuning capability of these screws is [0, -2.2 MHz].
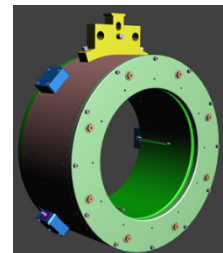


Figure 11: Eight screws for fine tuning on the beam exit side.

## CONCLUSION

Simulation study has been carried out for the design of a new current monitor. First the simulation has been validated by comparing experimental and simulated results using existing current monitor. The simulation has then been used to test the design and the improvements of the new current monitor. According to these simulations, the frequency drifts of the new design can be ideally reduced to 8 kHz from the previous value of 730 kHz.

## REFERENCES

[1] P. A. Duperrex et al., "Design and Operation of a Current Monitor under Heavy Heat Load", DIPAC'09, Basel, Switzerland, 2009, p. 336.

[2] P. A. Duperrex et al., "On-Line Calibration Schemes for RF-Based Beam Diagnostics", HB'2012, Beijing, China, 2012, p. 601.

[3] Y. Lee et al., "A Simulation Based Thermal Analysis of a New Current Monitor at PSI Proton Accelerator", PAC'09, Vancouver, Canada, 2009, p. 3979.

[4] National Institute of Standards and Technology web site: http://physics.nist.gov/PhysRefData/Star/Text/PSTAR.html

# DESIGN OF A NEW BEAM CURRENT MONITOR
# UNDER HEAVY HEAT LOAD*

J. Sun, P.A. Duperrex[#], G. Kotrle, Paul Scherrer Institut, Villigen PSI, Switzerland

## Abstract

At the Paul Scherrer Institute (PSI), a 590 MeV 50 MHz High Intensity Proton Accelerator (HIPA) has been operated for many years at 2.2 mA / 1.3 MW and it will be in future upgraded to 3 mA / 1.8 MW. Downstream from a target for pion and muon production is a beam current monitor, called MHC5. The thermal load in MHC5 induced by the scattered particles from the target causes its resonance to drift. Even with an active cooling system, the drift remains a problem.

A new beam current monitor has been designed to overcome this shortcoming. The mechanical design of the new monitor has been completed and manufactured. Different improvements have been implemented compared to the monitor in operation. For instance, graphite has been used as material for the resonator instead of aluminium to minimize the thermal expansion, a thermal self-compensation scheme has been implemented to counteract the frequency drift, its structural stability has been improved and the thermal load has been reduced. The design and the preliminary lab test results are presented in this paper.

## INTRODUCTION

A proton beam current monitor called "MHC5" has been installed in the PSI 590 MeV proton cyclotron for several years. The MHC5 is a coaxial resonator tuned at 101.26 MHz, the 2nd harmonic of the proton beam pulse frequency. The magnetic field in the resonator is directly proportional to the beam current. It is located approximately 8 m behind a 4 cm thick graphite target used for muon and pion production. As a consequence, the monitor is exposed to scattered particles and their secondaries from this target and the resulting thermal load causes the resonance frequency to drift. For the current system, the variations of the system gain caused by the frequency drift are too large (10-20%) even with an active cooling system [1]. These drifts should be minimized. A new beam current monitor should be designed and aimed to future high intensity beam operation (3 mA, 1.8 MW).

## PRELIMINARY SIMULATION

In order to have a good understanding of the performance of MHC5 in the beam tunnel, preliminary simulation about the monitor in operation was carried out by ANSYS.

The MHC5 in operation is made of aluminium (anticorodal 110), with a 10 μm coating layer of silver to improve the electrical conductivity. The monitor itself is in vacuum and the active water cooling keeps the resonator at an average temperature of about 50℃. Four thermocouples monitor the resonator temperature [2], as shown in Figure 1.



Figure 1: The MHC5 in operation, the pipe for water cooling at the beam entry side (left), the thermocouples installed on the beam exit side (right).

The energy deposition on MHC5 in operation under 3 mA proton beams is about 345 W, calculated by MARS [3]. The velocity and temperature of the cooling water is 1.91 m/s and 48℃, by which the convection coefficient can be calculated out, which is about 10500 W/(m²·K). The ambient temperature in the tunnel is 50℃. The thermal distribution and deformation of MHC5 in operation as shown in Figure 2. The frequency drift of this case is 730 kHz.
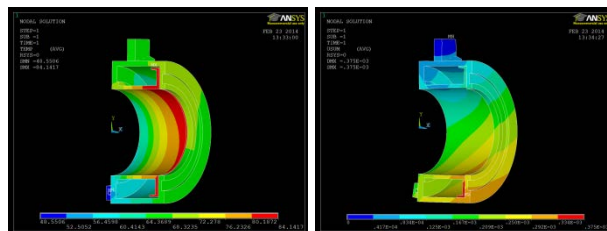


Figure 2: Thermal distribution (left) and thermal expansion (right) of MHC5 in operation with water cooling.

## Causes of the Frequency Drift

In addition to the frequency drift due to the thermal expansion of the resonator, the thermal gradient due to the active cooling is making the shift larger. From simulation calculations (Figure 2), the peak temperature and the maximum expansion part are located at the inner part of the monitor. Inner parts have larger deformations than the outer parts because of the thermal gradient, which decreases the capacity gap and lead to additional resonance frequency drifts.

To reduce the frequency drift, it is therefore essential to minimize the deformations of the monitor. Thus the

power deposition, the thermal expansion and the thermal gradient on the monitor have to be minimized.

## MATERIAL SELECTION

A reduction of the thermal expansion can be achieved by selecting a material for the resonator that has a lower thermal expansion coefficient than the one of the existing resonator (anticorodal 110).

Graphite has been selected for this reason. It has a lower thermal expansion coefficient (see Table 1). Furthermore, it has a very high emissivity. As a result, the active cooling is no more required and the thermal gradient can also be strongly reduced.

Consider all the requirements graphite is selected to make the new MHC5. Table 1 compares the main properties of graphite and anticorodal 110. Compare to anticorodal 110 graphite has much higher emissivity, lower resistivity and lower thermal expansion coefficient.

Table 1: Main Properties of Graphite and Anticorodal 110

|  | **Graphite** | **Anticorodal 110** |
|---|---|---|
| Thermal expansion coefficient ($K^{-1}$) | 2.9e-6 | 23.4e-6 |
| Emissivity | 0.95 | 0.05 |
| Electrical resistivity ($\Omega \cdot m$) | 9.8e-6 | 3.5e-8 |
| Thermal conductivity ($W/(m \cdot K)$) | 129 | 162 |

The lower electrical conductivity might have been an issue if a high Q factor was required. In fact, it is not needed or even not desired. Since a high Q factor requires a high temperature stability. A mismatch between the resonance frequency and the beam harmonic frequency has a stronger impact on the resonator gain at the beam frequency. For instance, to achieve a gain variation lower than 2%, the shift range must be lower than 200 kHz if the resonator Q value is 100 whereas for a Q of 1000, the maximal shift is 20 kHz (see Figure 3).

Our goal is to reach a gain variation lower than 1% for a Q of ~150, which requires a maximum frequency shift of 100kHz.
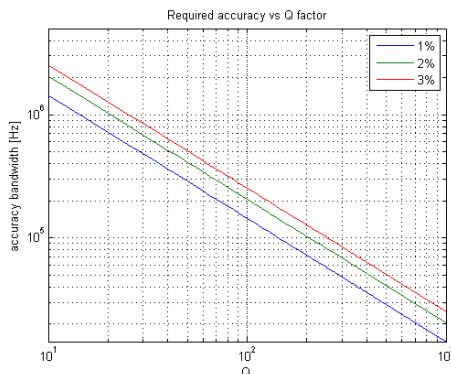


Figure 3: Required accuracy VS. Q factor.

## DESIGN OPTIMIZATION

By simply replacing the aluminium by graphite and keeping otherwise the same design, the expected total power deposition on the graphite monitor is around 400 W. The calculated frequency drift in this case for a 3 mA proton beam is ~400 kHz, which is too large compared to a 100 kHz maximum limit. The thermal distribution of this case shows in Figure 4.
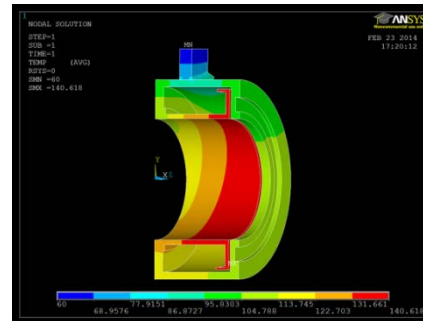


Figure 4: Thermal distribution of the graphite MHC5 with same dimension as the operation one (minimum Temperature: 60℃, maximum temperature: 140℃).

### Power Load Reduction

The power load deposition has been reduced by increasing the inner diameter of the resonator. Indeed, the distribution of the scattered particles is Gaussian in transverse plane; that is, the number of scattered particles decreases with the radius. Therefore, increasing the inner diameter leads to a reduction of the power load. When the inner diameter of the MHC5 is increased from 255 mm to 280 mm, the corresponding power deposition is decreased from 400 W down to 169 W.

One thing should be pointed out, that the capacity gap of this case needed to decrease from 4.5mm down to 2.5mm to keep the same resonance frequency. This will make the manufacture more difficult, since the resonance frequency is very sensitive to the size of the capacity gap.

### Self-compensation Scheme

The frequency shift is mainly caused by the thermal expansion of the resonator itself, a higher temperature leading to a low resonance frequency. One possible way to counteract this effect is to use a second material with much larger expansion coefficient in such a way to increase the capacitor gap (e.g. increases the resonance frequency) while keeping the other characteristics unchanged. This has been done by inserting a thin aluminium shim as shown in Figure 5.
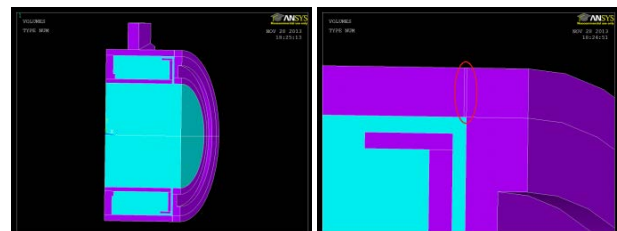


Figure 5: Position of the aluminium shim (red elliptical).

For a case where the power load is 169 W the simulations with a 5 mm thick shim shows a frequency shift of 10 kHz compared to 200 kHz in the case without aluminium shim.

### Capacity Gap Improvement

High permittivity material such as Ceramic (99.5% $Al_2O_3$) [4] can be used to fill in the capacity gap to increase the gap's size and while keeping the same resonance. This relaxes the mechanical tolerance as well as providing more rigidity to the capacitor plates.

Simulations with a ceramic ring and a resulting 6.1 mm capacitor gap indicate the frequency drift can be reduced to 8 kHz. The simulated thermal distribution is shown in Figure 6.

An advantage of using a ceramic plate between the capacitor plates is that the ceramic acts as a thermal bridge. It balances the thermal distribution between the inner and the outer parts, diminishing its gradient, thus proving a further stabilization effect as far the frequency shift is concerned.
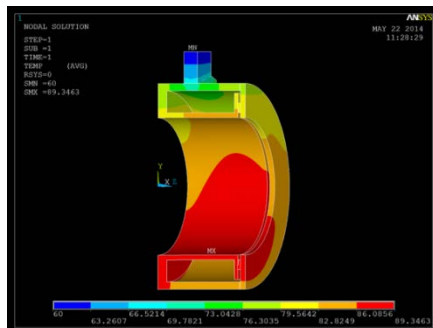


Figure 6: Thermal distribution of the final design.

## FINAL DESIGN

Figure 7 shows the final model for the simulations, the capacity gap is set to 6.1 mm filled with a ceramic cirque (the red part) and the thickness of aluminium shim (the blue part) is 2 mm and with inner diameter 280 mm.
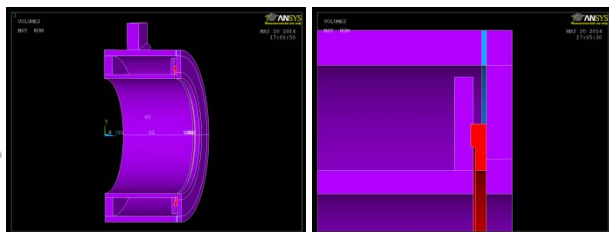


Figure 7: Half model over view (left) and details (right) of the new design of MHC5.

### Combination of BCM and BPM

Beside the beam current measurements, 4 pickups have been mounted on the inside wall to measure the beam position, as shown in Figure 8(left). On the both side of the MHC5, 6 thermocouples in total are mounted to monitor the temperature of the MHC5. 8 tuning screws are used to do the fine tuning work, as shown in Figure 8 (right).
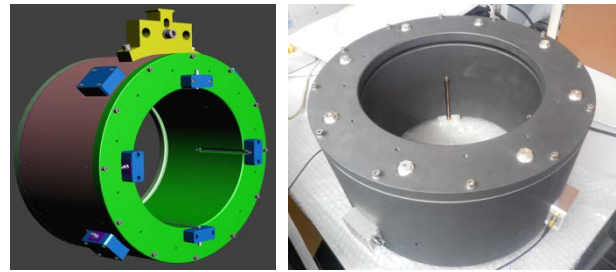
Figure 8: New MHC5 after mechanical drawing (left) and the new monitor lying in the lab (right).

## FIRST LAB TEST

After the new monitor delivered to PSI, first lab test is carried out immediately. For the resonance frequency, the new MHC5 can be easily tuned to 101.26 MHz with 8 tuning screws (Figure 9). The Q factor in room temperature is 130 when a pair of small pickup loop (1 $cm^2$) are used and 92 when a pair of big pickup loop (13.5 $cm^2$) are used.
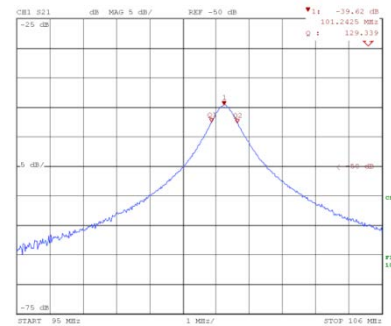


Figure 9: Result of the first lab test.

## CONCLUSION

From our first lab test, the new beam current monitor made of graphite does have less frequency drift than the aluminium one. Further test is still going on and the new monitor will be mounted on the beam line next February, its performance will be checked then.

## ACKNOWLEDGMENT

It is a pleasure to acknowledge valuable discussions with D. Kiselev for the energy deposition aspects.

## REFERENCES

[1] P. A. Duperrex et al., "New On-Line Gain Drift Compensation for Resonant Current Monitor under Heavy Heat Load", IPAC'10, Kyoto, Japan, 2010, p. 1122.

[2] P. A. Duperrex et al., "Design and Operation of a Current Monitor under Heavy Heat Load", DIPAC'09, Basel, Switzerland, 2009, p. 336.

[3] D. Kiselev et al., PSI internal memorandum, TM-85-09-01.

[4] Accuratus Corporation website:
http://accuratus.com/alumox.html

# BEAM DYNAMICS STUDY FOR J-PARC MAIN RING BY USING THE 'PENCIL' AND SPACE-CHARGE DOMINATED BEAM: MEASUREMENTS AND SIMULATIONS

A.Molodozhentsev, S.Igarashi, Y.Sato, J.Takano, KEK, Tsukuba, Oho 1-1, 305-0801, Japan

## Abstract

In frame of this report we discuss existing experimental results and compare it with simulations, performed extensively for different machine operation scenario, including the 'pencil' low intensity beam and the 'space-charge dominated' beam. The obtained results demonstrate agreement between simulations and measurements for emittance evolution and losses for different cases. The modelling of the beam dynamics has been performed by using the 'PTC-ORBIT' combined code, installed on the KEK supercomputer * [1,2]. The developed MR computational model will be used to optimize the machine performance for the 'Mega-Watt' MR operation scenario with limited losses.

## INTRODUCTION

J-PARC Main Ring (MR) study has been performed during 2012-2014 to optimize the machine performance. As the result of this activity the '200 kW' proton beam has been delivered successfully to the 'Neutrino' beamline for the 'Super-Kamiokande' experiment. Total particle losses, localized at the MR collimation section, have been estimated as 120 W. The 'low-losses' MR operation has been achieved after optimization the injection process, stabilizing the power supply ripple, after searching the optimized setting for the MR RF system, dynamic control of the chromaticity, optimization of the 'bare' working point and compensation the linear coupling resonance.

Effects of the machine resonances, caused by imperfections of different kind of the MR magnets, have been studied experimentally by using a low intensity 'pencil' beam. The 'space-charge dominated' beam has been used to observed the effects of the machine resonances in combination with the space-charge effects, like the space charge detuning and space-charge resonances.

The appropriate scheme to compensate the 'sum' linear coupling resonance $Q_x+Q_y=43$ has been proposed, tested and implemented successfully for J-PARC MR [3,4] for the 'basic' working point. The benchmark activity was initiated to improve the machine model, which should be used to study the Main Ring operation scenario in the case of the 'Mega-Watt' machine operation.

## 'PENCIL' BEAM

During the J-PARC Main Ring study (RUN44,

---

Nov.2012) the low intensity proton beam with small transverse emittance was used to study the [1,1,43] resonance and its compensation. The resonance correction approach now is based on dedicated four skew quadrupole magnets, installed in two straight sections of MR [4,5]. The single bunch injection into MR from RCS was performed to provide small beam intensity of 4e11 proton per bunch. The 2σ horizontal beam emittance of the 'pencil' beam, injected into MR, was just 3π mm.mrad. The beam profile measurements were performed by using the 'Flying Wire' monitor, installed in the dispersion-free straight section of MR

The PTC code was used to prepare the MR description taking into account measured imperfections of the machine magnets and realistic alignment of the elements. By using this machine description one can perform single or multi-particle tracking by the PTC-ORBIT code to study the beam dynamics for different scenario of the machine operation, including different time pattern for machine magnets and RF system. The ripple of the power supply can be also introduced into the machine mode. The KEK Super Computer system was used to simulate the injection and acceleration processes for J-PARC MR.

### Effect of Isolated Resonance

To model the effect of the 'isolated' [1,1,43] resonance for MR, the resonance was excited by using the negative strength of the skew quads, defined experimentally to compensate the resonance (RUN44).

The study, based on single particle tracking, shows that the periodical crossing the [1,1,43] resonance stop-band by the off-momentum particles in the case of the realistic parameters for the RF system leads to significant limitation of the maximum beam emittance, which can survive if the 'bare' working point is close to the corresponding resonance line [5].

The performed multi-particle tracking was based on the 6D particle distribution, which represented the 3GeV 'pencil' beam, injection into MR from RCS. To make the long-term multi-particle tracking during 60'000 turns (corresponds to 320 ms at the energy of 3GeV) and to compare it with the observations we used 20'000 macro-particles in order to represent the 6D particle distribution in the single bunch.

The benchmark between the simulations and measurements (RUN44) was performed without any resonance correction for the 'bare' working point near the resonance line ($Q_x$=22.2875, $Q_y$=20.6975). The particle losses during the injection and beginning of acceleration were simulated for the realistic time pattern of the MR RF

system and for the collimator acceptance of 70 $\pi$ mm.mr. The simulated losses are in agreement with the results of the measurements [5] for the 'bare' working point $Q_x$=22.2875 and $Q_y$=20.6975 (Fig.1).
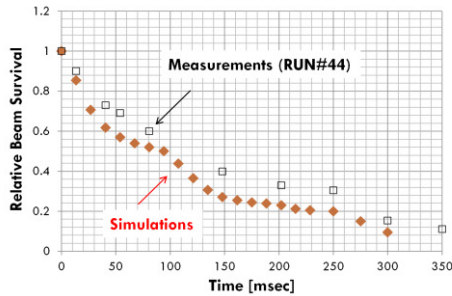


Figure 1: Reproduction the measured particle losses during the injection and acceleration processes for the case of the isolated linear coupling resonance.

*Effect of Combined Resonances*
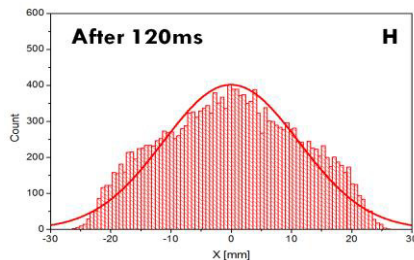


Figure 2: Simulated horizontal beam profile at the end of the tracking for the 'bare' working point $Q_x$=22.195 and $Q_y$=20.795.
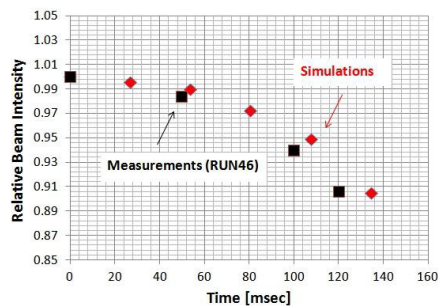


Figure 3: Reproduction the measured particle losses for the case of the combined resonances.

By using the developed computational model of MR it was demonstrated successfully [5] that the correction of the 'sum' linear coupling resonance [1,1,43] for the 'bare' working point ($Q_x$=22.195 and $Q_y$=20.795) prevents the trapping the large amplitude particles by the high-order horizontal resonance $5Q_x$=111.

To obtain a reasonable agreement with the experimental results, it is necessary to have appropriate number of macro-particles of in the 6D distribution and high-order field errors of the MR magnets have to be

added into the model of the machine. The simulated (120ms after the injection) beam profile is presented in Figure 2. The simulated horizontal $1\sigma$ beam size after 120ms from the injection becomes 13.8mm. The measured one was 15.4mm, which shows good agreement between the simulations and measurements for this case. The simulated losses are in agreement with the measurements too (Fig.3).

## SPACE CHARGE DOMINATED BEAM

Dedicated measurements (RUN54-RUN55/2014) and simulations were performed for the 'low-energy' 'space charge dominated' case to check the ability of the computational model to reproduce the experimental observations.

The RCS beam power at 3GeV was fixed to keep it on the level of 315kW (Ion Souce: 25mA / Chopping Time: 460ns / LINAC: 400MeV). Different painting areas were used to accumulate in RCS the required beam power at the injection energy of 400MeV: $100\pi$ and $50\pi$.

Different machine conditions with different beam parameters (for the fixed beam intensity) were studied experimentally and used for the extensive simulations to reproduce beam survival in MR for different parameters of the RF system; transverse beam emittance evolution for different initial beam parameters and for different levels of the chromaticity compensation and effect of the [1,1,43] resonance compensation for the space-charge dominated beam. All these studies are extremely useful for better understanding the MR peculiarities for the 'high-beam power' operation.

*Observation: 'RF' Effects*

The particle losses at the injection energy of 3GeV for different sets of the MR RF system were studied experimentally. The 'painting' area for the RCS injection was set as $100\pi$. The 'basic' lattice working point ($Q_{xo}$=22.40, $Q_{yo}$=20.75) with the partial 'linear' chromaticity correction (~85%) was used during RUN54. The fundamental RF system (h=9) of MR was used with different RF voltages: 160kV and 200kV.

The compensation of the linear coupling resonance [1,1,43] was not activated to check the effect of this resonance at the injection energy. Different RF voltage at the DC mode in the 'mismatched' case leads to changing the longitudinal particle distribution in the bunch (the bunching factor variation) so that the effect of the periodical crossing the [1,1,43] resonance can be observed.

The measured beam survival at the MR injection energy of 3GeV (DC mode) is presented in Figure 4 for the RF voltage of 160kV and 200kV. The beam intensity was 2.75e13 ppp (2 bunches per pulse). The collimator in the 3-50BT beam line between RCS and MR was opened during this study. The aperture of the MR collimator was not optimized, so that the horizontal acceptance was in the range (60÷80)$\pi$ and the vertical collimator was opened. The observed particle losses were localized in the

MR collimator section. The losses observed for the 160kV RF voltage are about twice smaller than for the case of 200kV for the 'basic' working point.
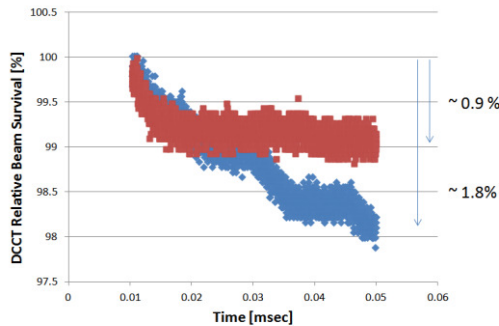


Figure 4: Measured beam survival at 3GeV (DC mode) in MR for different sets of the RF system (h=9): 160kV (brown) and 200 kV (blue).

## Observation: [1,1,43] Resonance Effects

The beam profile measurements were performed for different beam conditions, injected into MR from RCS to observe the effect of the 'sum' linear coupling resonance [1,1,43] in the case of the 'basic' MR operation ($V_{RF}$=160kV(h=9) and $Q_{xo}$=22.40, $Q_{yo}$=20.75). The beam profile in the horizontal plane has been measured by using the flying-wire profile monitor.

The beam with different 'painting' area during the multi-turn injection into RCS has been used for this study, in particular, the '50π' and '100π' cases.

During this study the dedicated skew-quadrupole magnets were activated to observe the effect of the [1,1,43] resonance compensation for the different beams from RCS. The set for the skew-quads was optimized for the case of the MR operation with the 'pencil' beam (4e11 ppb) with the lattice tunes close to the resonance line $Q_x+Q_y$=43. The optimization of the current pattern for the skew-quads was performed for both injection and acceleration regions to minimize the losses.
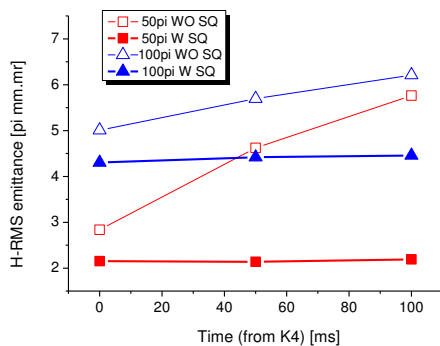


Figure 5: Measured horizontal RMS emittance at the 3GeV energy (MR 'DC' mode) for different beam parameters and machine setting.

The measured horizontal RMS emittance at the 3GeV ('DC' mode) in MR is presented in Figure 5 for the cases without ('WO') and with ('W') dedicated skew-quadrupoles for different beam conditions, injected into MR from RCS. After activation the skew-quads the RMS emittance growth in the horizontal plane has been eliminated for both cases: '50π' and '100π'.

The obtained experimental results have been used to compare it with the results of the modelling the beam dynamics in the case of the space-charge dominated regime.

## SPACE-CHARGE DOMINATED BEAM: SIMULATIONS

The 'low-energy' space charge dominated regime of the MR operation was simulated extensively by using different beam and machine conditions, as it was made experimentally during the MR study (RUN54 and RUN55 during the 2014 machine study).

The MR model is based on the lattice representation, which takes into consideration measured imperfections of the MR magnets including field and alignment errors [3]. The space charge effects in combination with the lattice resonances, caused by the machine imperfections, were studied by using the combined PTC-ORBIT code [1,2]. In this combination, the ORBIT part of the code can be used to simulate collective effects ('PIC' type of code) in 'space-charge' nodes. The PTC in this combination is the 'symplectic' integrator, which integrates the particle motion between the 'space-charge' nodes. The integration method, used by PTC for MR study, was optimized to minimize the multi-particle tracking time. The 'ORBIT' parameters, to simulate the space-charge kicks, were optimized for the MR simulations during the convergence study [3]. It was shown that for the MR case one can use the 2.5D space charge model, implemented into the 'ORBIT' code, in particular, the 'fixed grid' method (128x128 mesh) with the distance between the space charge nodes not more than 1.5m.

The performed modelling of the beam dynamic is based on the pre-simulated 6D distribution of the beam, accelerated by RCS from 400MeV up to 3GeV. The total number of macro-particles in this distribution is 498'622. Different conditions for the multi-turn 'painting' injection in RCS has been used to prepare the initial particle distribution for the MR study to be in agreement with the experimental study.

## Incoherent Space Charge Detuning

The incoherent space charge detuning in the case of the low-energy high-power beam for MR depends on the MR RF setting, the bunch length of the beam extracted from RCS (200ns for the present RCS extraction kicker) and the 'painting' area for the RCS injection. The beam intensity was 2.75e13/2 ppb (2 bunches per pulse). The performed simulations show that after 1200 turns (a few synchrotron periods for MR at 3GeV) the maximum space charge detuning is about (-0.15) for the '100π' RCS

painting area and about (-0.35) for the '50π' RCS painting area, respectively. The simulated incoherent space charge detuning at the injection energy of 3GeV after 1200 turns for different RCS painting area is shown in Figure 6. The 'basic' lattice tunes ($Q_x$=22.40, $Q_y$=20.75) and $V_{rf}$=160kV (h=9) have been used for these simulations.
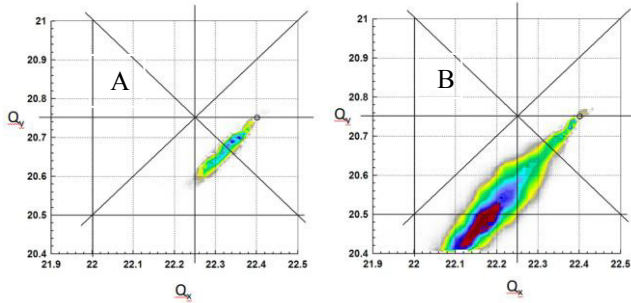


Figure 6: 2D histogram of the incoherent space charge detuning (3GeV with the intensity of 1.375e13 ppb) in MR for the RCS 'paint' emittance at 400MeV: (A) '100π' and (B) '50π'.

## Modelling the 'RF' Effect at Injection

Modelling the beam survival in MR at the injection energy of 3GeV was performed for different RF parameters to compare it with the results of measurements, performed during RUN54 (Fig.7). For the multi-particle tracking the following parameters have been used: MR collimator acceptance of 70π, partial 'linear' chromaticity correction (85%) and the RF voltage of 160kV and 200kV for the case of the fundamental RF system (h=9).

The obtained results of the beam survival (Fig.7) are in a qualitative agreement with the experimental observation (Fig.4). Some discrepancy between the observations and simulations can be explained by different definitions for the MR collimator aperture, which was not defined clearly during RUN54. The 'basic' lattice tunes ($Q_x$=22.40, $Q_y$=20.75) were used for this study.
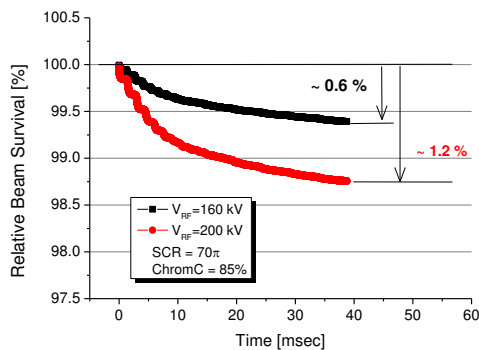


Figure 7: Simulated beam survival in the MR collimator for different RF voltages.

## Modelling the [1,1,43] Resonance Effect

The effect of the [1,1,43] resonance by using the computational MR model has been simulated by using a simplified MR model.

Comparison between the performed simulations and measurements for different beam emittance from RCS (with the intensity of 1.375e13ppb) is presented in Figure 8 for the '100π' case and the 'basic' lattice tunes ($Q_x$=22.40, $Q_y$=20.75). The 'black' dots with the 'error'-bar represent the results of the measurements. The 'blue' and 'green' lines show the simulated RMS emittance evolution before and after the [1,1,43] compensation, respectively.
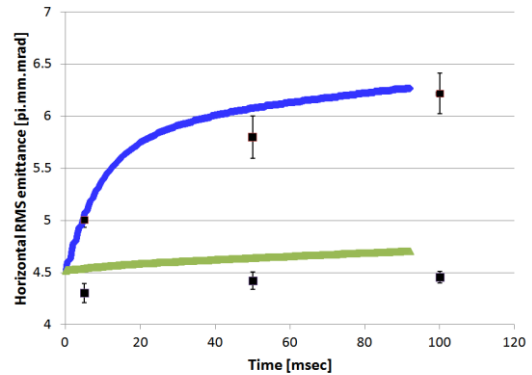


Figure 8: Horizontal RMS emittance evolution (measured and simulated) for the '100π' paint RCS beam.

The agreement between the measured RMS emittance and the simulated one for the case of the '100π' paint RCS emittance is quite reasonable (Fig.8). Similar agreement has been demonstrated and for the case of the '50π' paining RCS area. Some discrepancy can be explained by the effect of the initial beam mismatching, which becomes important for the case of 'strong' space-charge.

Losses at the MR collimator were analyzed during the multi-particle tracking for the case of the physical acceptance of the MR primary collimator of 65π for different levels of the 'linear' chromaticity compensation. The simulated particle losses at the MR collimator before and after the [1,1,43] resonance compensation are shown in Figure 9 and Figure 10, respectively. The effect of the partial chromaticity correction at the injection energy was observed experimentally and reproduced by using the MR computational model.

The particle losses for the case of the 93% chromaticity correction are smaller, which is in agreement with the experimental observation. Before the [1,1,43] resonance compensation the minimum simulated particle losses (during 55msec), observed for the case of the '50π' paint RCS emittance at 400MeV and for the 93% chromaticity correction (the 'red' line, Fig.9) can be estimated as 330W for the initial beam intensity of 1.375e13ppb (which corresponds to the MR beam power of 22kW at 3GeV).
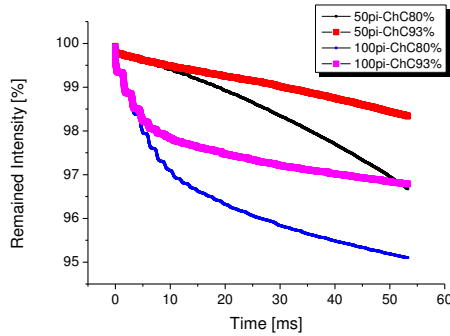
Figure 9: Particle losses at the MR collimator at 3GeV for different partial chromaticity correction and different initial RCS beam.

After the [1,1,43] resonance compensation the particle losses at the MR collimator were reduced significantly. The simulated losses for this case are presented in Figure 10 for the case of the 93% partial chromaticity correction and for the 'paint' RCS emittance of $50\pi$ and $100\pi$. The particle losses in MR for the '$100\pi$' case during 55msec becomes 110W. For the case of the '$50\pi$' paint RCS emittance at 400MeV and for the 93% chromaticity correction the particle losses at the MR collimator (with the acceptance of $65\pi$) the particle losses during 55msec after the injection can be estimated as 44W. The 'fast' losses, observed at the beginning of the injection process, are caused by the initial beam mismatching in the transverse and longitudinal planes.

The particle losses, observed experimentally for the same settings of the main parameters of the injected beam and MR, are in agreement with the simulated results. The total losses in MR for the case of the '$50\pi$' paint RCS emittance at 400MeV and for the 93% chromaticity correction, obtained experimentally after the compensation the [1,1,43] resonance, was about 120W totally including losses during the injection and acceleration processes.
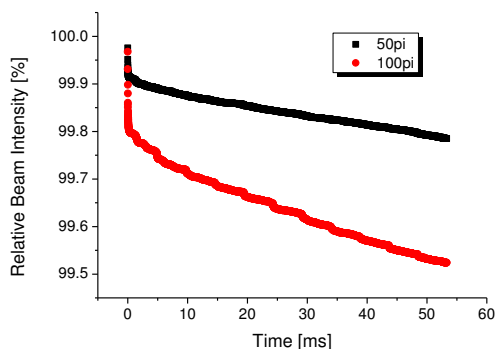


Figure 10: Simulated particle losses in MR at 3GeV after the compensation of the [1,1,43] resonance.

The 'fast' losses of the beam (Fig.10) just after the injection can be reduced by optimizing the initial beam conditions and the 'RF' matching by using the second harmonic RF system for the MR operation. The observed losses after the [1,1,43] compensation (Fig.10) can be explained by effects of other remained high order resonances, which caused by the combined effect of the machine imperfections and the space charge nonlinear effects. This subject requires further dedicated machine study and modelling using the computational MR model with the low-energy space charge effects.

## CONCLUSION

The benchmark has been performed for the 'pencil' beam J-PARC MR operation by using the developed computational model of the machine. Acceptable agreement between the results of measurements and simulations is demonstrated for both losses and emittance evolution for different 'bare' working points. The observed effects of the isolated and combined resonances are explained and reproduced by using the computational model of J-PARC Man Ring.

The effects, observed for the 'basic' working point in the case of the 'space-charge dominated' beam, are reproduced by using the developed computational model of the machine. As the result, the low-loss MR operation has been achieved for the beam power of 315kW from RCS.

Improvement of the machine model should be continued to be able to suppress effects of the high-order resonances and optimize the MR performance in the case of the 'Mega-Watt' operation.

## ACKNOWLEDGMENT

## REFERENCES

[1] E. Forest, A.Molodozhentsev, A.Shishlo, J.Holmes, "Synopsis of the PTC and ORBIT Integration", KEK Internal Report (A), 2007-4, November 2007.

[2] A.Molodozhenstev, E.Forest, Further improvement of the PTC-ORBIT code to model realistic operation of high-beam power synchrotrons, PAC13, Shanghai, China, May 12-17, 2013.

[3] A.Molodozhentsev, E.Forest, Beam dynamics and lowloss operation od the J-PARC Main Ring, KEK Preprint 2009-29, November 2009.

[4] A.Molodozhentsev, Operation J-PARC Main Ring with the moderate beam power: predictions and observations, ICFA HB10 workshop, Morshach, 2010.

[5] A.Molodozhentsev, S.Igarashi, Y.Sato, J.Takano, Study linear coupling resonance for J-PARC Main Ring: observations and simulations, IPAC14, Dresden, 15-20 June 2014.

# HIGH GRADIENT RF SYSTEM FOR UPGRADE OF J-PARC

C. Ohmori, K. Hara, K. Hasegawa, M. Toda, M. Yoshii, KEK/J-PARC, Ibaraki, Japan
M. Nomura, F. Tamura, M. Yamamoto, T. Shimada, JAEA/J-PARC, Ibaraki, Japan
A. Schnase, GSI, Darmstadt, Germany

## Abstract

Magnetic alloy cavities are successfully used for J-PARC synchrotrons. These cavities generate much higher RF voltage than ordinary ferrite-loaded cavities. The MR (Main Ring) upgrade project aims to deliver the beam power of 750 kW to the neutrino experiment. It includes replacements of all RF cavities for high repetition rate of about 1 Hz. By the replacements, the total acceleration voltage will be doubled, while power supplies and amplifiers remain the same. The key issue is the development of a high gradient RF system using high impedance magnetic alloy, FT3L. A dedicated production system for the Finemet® FT3L cores with 80 cm diameter was assembled in the J-PARC and demonstrated that we can produce material with two times higher $\mu Qf$ product compared to the cores used for present cavities. The first 5-cell FT3L cavity was assembled and the high power test was performed. The cavity was installed in the long shut down from summer to fall. The cavity is used for the beam acceleration with two times high RF voltage.

## UPGRADE SCENARIO OF THE J-PARC

The J-PARC aims to deliver 750 kW beam to the neutrino experiment, T2K. To avoid a significant beam loss by the space charge effects and instability, the original plan was modified and a double repetition rate scenario was chosen. The scenario includes about 1 Hz operation of the MR instead of the present 2.48 sec. cycle. It requires replacements of main magnet power supplies, upgrade of injection and extraction systems and increase of the total RF voltage for the acceleration. To store new magnet power supplies, new power supply buildings will be constructed. Because the acceleration time will be 0.5 sec. instead of the present 1.4 sec, required RF voltage is 560 kV which is two times higher than the present 280 kV. To avoid the renewal of RF power supplies which is very expensive, all 9 RF cavities will be replaced by new high gradient ones which can generate two times higher voltage than the present cavities as shown in Figs. 1. The cavity becomes longer than the present one. The spaces where the present 9 cavities are sitting in will be used to install new 7 cavities. An empty drift space between the extraction kickers is used to install two cavities. To fit to these spaces, two cavities with 4 cell structure and seven cavities with 5 cell structure are prepared. In 2015, 4 FT3L cavities will be installed. And, the replacements of all cavities will be finished in 2016. To guarantee the stable operation, we plan to manage the acceleration voltage of 560 kV with 8 RF systems to reserve one system as a spare.
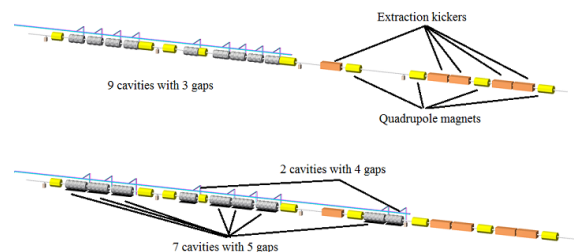
Figure 1: Upgrade scenario of the J-PARC MR cavities. The present cavities (upper) will be replaced by the FT3L cavities (lower) in 2014-2016. The total RF voltage will become more than 630 kV providing enough margin for 1 Hz operation.

## DEVELOPMENTS OF FT3L CAVITY

Magnetic alloy, FT3L, has higher shunt impedance than the FT3M, which is used in the J-PARC RCS and MR. However, there did not exist the production system which can anneal them in a magnetic field. To prove the performance of FT3L cores for the accelerator usage, we developed an annealing oven and proof-of-principle tests were carried out [1]. After the success of test production of large size FT3L, a mass production system was constructed and shipped to a company for the production of 280 FT3L cores for the MR upgrade [2].

In 2014, the first FT3L 5-cell cavity was assembled and tested at the RF test bench in summer and fall as shown in Fig. 2 [3]. After the high power test, the cavity was installed as shown in Fig. 3. The cavity was tested with 80 kV RF voltage and is used with 70 kV for beam acceleration (Fig. 4). By the replacement, the beam acceleration can be managed by 7 cavities and 2 present cavities will be used for the second harmonic RF to increase the beam power.

## DESIGN OF FT3L CAVITY

Figure 5 shows the characteristics of magnetic materials for the accelerator usage. Ferrites materials show the degradation according to increasing RF magnetic flux in the material. Magnetic alloys, FT3M and FT3L, show stable characteristics in the examined measurement ranges. The FT3L shows two times higher characteristic than the FT3M. Adopting the FT3L material, higher voltage becomes available and the length of cavity cells was reduced.

The present J-PARC MR cavity using the FT3M consists of 3 cavity cells and each cell generate 12.7 kV. To double the RF voltage of the cavity, the gap voltage increases to 15 kV and the number of cells becomes 5 instead of 3.

Figure 2: The FT3L cavity during high power test. The cavity consists of 5 cells. Each cell connected to two common bus bars driven by a tube amplifier behind the cavity. The total RF voltage of 80 kV was generated during the high power test in the summer and fall. In total, the cavity system was tested for more than 1000 hours.



Figure 3: The FT3L cavity installed in the MR tunnel. As the length of the cavity including the beam pipe becomes 2.6 m from 1.87 m, a special instrument was prepared to move the cavity into place. The cavity is installed between two kicker magnets as shown in Fig. 1.

The thickness of the FT3L cores becomes 25 mm instead of 35 mm of the present FT3M cores. The cell length reduces from 592 mm to 502 mm to install 3 FT3L cavities in a long straight section of about 8 m. Although the thickness of the core becomes thinner, the impedance is 1450 Ω and is still higher than the present cavity cell of 1000-1100Ω. Therefore number of cavity cells can be increased from 3 to 5.

As the anode power supply is the most expensive part in the cavity system, we plan to achieve to double the RF voltage without replacements and large modifications. Adopting the FT3L material, the cell impedance was increased by about 40 %. The cavity impedance from the final stage amplifier is 290 Ω and it is as high as the RCS RF cavity.
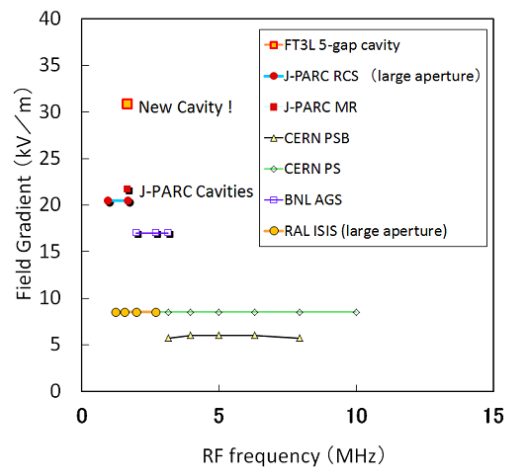


Figure 4: The field gradient of the RF cavities for proton beam acceleration. The field gradients of ferrite cavities (CERN PSB, CERN PS, BNL AGS, RAL ISIS cavities) were limited because of the saturation of the RF magnetic field. The field gradient of the MA cavity was improved by using the FT3L material.

## POWER SUPPLIES

The FT3L cavity is used for the 240 kW beam operation and the beam test with 260 kW equivalent. The system is designed to be managed by the present power supplies. Figures 6 show the anode current of the final stage amplifier during the operation with and without the beam. The current limit of the power supply is 110 A. The anode current will be reduced by optimizing the resonant frequency of the cavity to be more inductive. It is expected $2.0 \times 10^{14}$ protons which corresponds to 750 kW will be handled by the anode power supply.
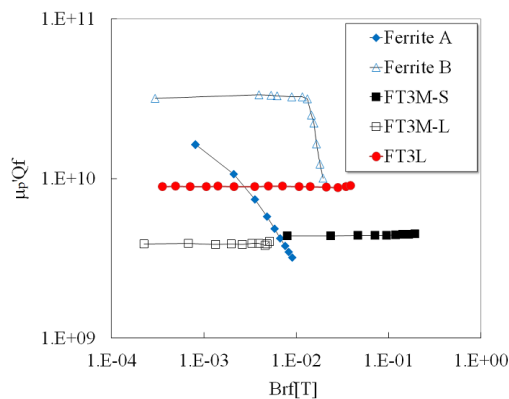
Figure 5: Characteristics of magnetic materials. Horizontal axis is the RF magnetic field in a ring core which is proportional to the RF voltage. Vertical axis is the product of parallel parmeability, Q-value and frequency which is proportional to the shunt impedance. Ferrite A shows typical behavior by the saturation. Ferrite B is high-Q material and shows the "High Loss" effect. A magnetic alloy, FT3L, shows high $\mu$Qf product and stable characteristics at the high field.

## DISCUSSIONS

To improve the field gradient of a loaded RF cavity, the improvements of the cavity shunt impedance is the key issue. Adopting the FT3L material instead of the FT3M, the cavity voltage can be doubled. For the further improvements, we should note that improvements of the materials and developments of thinner amorphous ribbon to reduce the eddy current loss by RF magnetic flux are important issues.

For other applications which need higher field gradient, it should be noted that the materials also fits the usages at higher frequency according to data sheet. Although the RF voltage is low, the material is used to chop the cyclotron beam [4]. And, it should be noted that hybrid cavity of ferrite and magnetic alloy might be a solution for higher frequency [5]. A hybrid cavity system with a magnetic alloy cavity and an external inductor has been adopted for the J-PARC RCS [6] to increase the effective Q-value of the system. The optimum band width of the RCS was obtained by the hybrid cavity system for the beam acceleration and dual harmonic RF. In this ten years, the cut core configuration was established and this cavity can be used for the hybrid systems for the high frequency usages.

## CONCLUSION

A 5-cell FT3L cavity has been tested and installed in the J-PARC MR tunnel. It is already used for the beam operation of 240 kW for neutrino experiment. In next summer shut down, 4 more FT3L cavities will be installed. In 2016, all cavities will be replaced with 4-cell and 5-cell FT3L cavities for the high repetition rate operation of the MR. The FT3L cavity will be used for the RCS for the multi-MW operation in future.
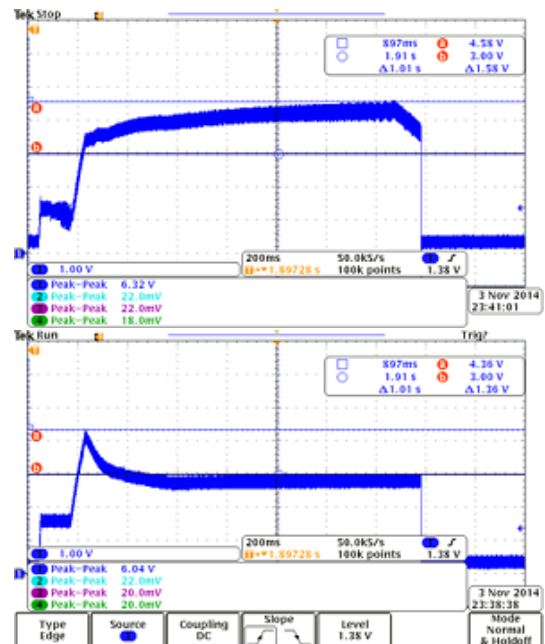
Figure 6: The anode current during operation with the 200 kW beam (top) and without beam (bottom). As the resonant frequency of the cavity does not change during the beam acceleration, the anode current becomes maximum at the beginning of the acceleration when detuning is large. In case of the high power beam acceleration, the maximum anode current is needed at the end of acceleration when the AC component of the beam is high.

## REFERENCES

[1] C. Ohmori et al., IPAC11, San Sebastian, September 2011, p. 2885. http://accelconf.web.cern.ch/AccelConf/IPAC2011/papers/thobb02.pdf

[2] C. Ohmori et al., Phys. Rev. ST Accel. Beams, vol.16, 112002, (2013). http://link.aps.org/doi/10.1103/PhysRevSTAB.16.112002

[3] K. Hasegawa et al., "DEVELOPMENT OF THE RF CAVITY WITH FT3L MA CORES", Proceedings of 11th PASJ, Aug., 2014, Aomori Japan, in Japanese, http://www.pasj.jp/web_publish/pasj2014/proceedings/PDF/SAP0/SAP053.pdf

[4] T. Koseki et al., "DEVELOPMENT OF A BUNCER CAVITY USING MA CORES", Proceedings of 2nd PASJ, July, 2005, Tosu Japan, in Japanese. http://www.pasj.jp/web_publish/pasj2_lam30/Proceedings/20P037.pdf

[5] J. Griffin, private comunication.

[6] A. Schnaseit et al., "MA CAVITIES FOR J-PARC WITH CONTROLLED Q-VALUE BY EXTERNAL INDUCTOR", Proceedings of PAC07, Albuquerque, New Mexico, USA,

# UPGRADES OF THE RF SYSTEMS IN THE LHC INJECTOR COMPLEX

H. Damerau*, M. E. Angoletta, T. Argyropoulos, P. Baudrenghien, A. Blas, T. Bohl,
A. Butterworth, A. Findlay, R. Garoby, S. Gilardoni, S. Hancock, W. Höfle, J. Molendijk,
E. Montesinos, M. Paoluzzi, D. Perrelet, C. Rossi, E. Shaposhnikova
CERN, Geneva, Switzerland

## Abstract

In the framework of the LHC Injector Upgrade (LIU) project the radio-frequency (RF) systems of the synchrotrons in the LHC injector chain will undergo significant improvements to reach the high beam intensity and quality required by the High-Luminosity (HL) LHC. Following the recent upgrade of the longitudinal beam control system in the PS Booster (PSB), tests with Finemet cavities are being performed in view of a complete replacement of the existing RF systems in the PSB by ones based on this technology. In the PS a similar wide-band Finemet cavity has been installed as a longitudinal damper. New 1-turn delay feedbacks on the main accelerating cavities to reduce their impedance have also been commissioned. Additional feedback and beam control improvements are foreseen. A major upgrade of the main RF system in the SPS by regrouping sections of its travelling wave cavities, increasing the number of cavities from four to six, will reduce beam-loading and allow higher intensities to be accelerated. This upgrade includes the installation of two new RF power plants and new feedback systems. All upgrades will be evaluated with respect to their expected benefits for the beams to the LHC.

## INTRODUCTION

After the upgrades within the LIU project [1] the intensity of the LHC-type beams is expected to double in the injector chain. However, the longitudinal parameters, bunch length and longitudinal emittance, remain similar. This implies an important increase in longitudinal density and the need to significantly upgrade the RF systems in all accelerators of the LHC injector chain [2] to cope with an intensity of more than $2 \cdot 10^{13}$ ppb instead of the present $1.3 \cdot 10^{13}$ ppb with 25 ns bunch spacing [3, 4].

Although an extensive number of alternatives for the production of LHC-type beam with various RF manipulations has been studied [5, 6], the original scheme for nominal LHC beam [7] remains the baseline. In total $4 + 2$ bunches, one per the PS Booster (PSB) ring, undergo triple splitting in the PS and batches of 72 bunches spaced by 25 ns are delivered to the SPS. Up to four of these batches are accelerated to an energy of $450\,\mathrm{GeV}$ in the SPS and extracted towards the LHC.

_____
* heiko.damerau@cern.ch

## PS BOOSTER

The PSB presently accelerates up to $1 \cdot 10^{13}$ ppb in a single bunch eventually doubling with its connection to Linac4. It is equipped with three ferrite-loaded cavities per ring. Two of these are operated at $0.59 - 1.75\,\mathrm{MHz}$ ($h = 1$) and twice that frequency for the second harmonic cavity. A further ferrite-loaded cavity at about $6 - 16\,\mathrm{MHz}$ serves for controlled longitudinal blow-up. Almost the entirety of the RF systems in the PSB is affected by the upgrades. The beam-control system has been exchanged by a fully digital low-level RF (LLRF) system [8, 9, 10] during the recent long shutdown (LS1). On the high-power side the replacement of the ferrite-loaded cavities at $h = 1$ and $h = 2$ by Finemet cavities covering both harmonics simultaneously is being prepared.

### Beam Controls

Each of the four PSB rings is equipped with a largely independent beam control system, implementing beam phase, radial and synchronization loops. It generates drive signals for the three ferrite-loaded cavities, as well as for present and future Finemet systems. With the start-up after LS1, fully digital beam control systems have been successfully commissioned for all beams on all rings. Figure 1 shows an overview of the new, modular digital beam control of the PSB. For each ring it consists of three digital signal processing (DSP) boards with slots for ADC, DAC or digital synthesizer mezzanine modules. The different beam
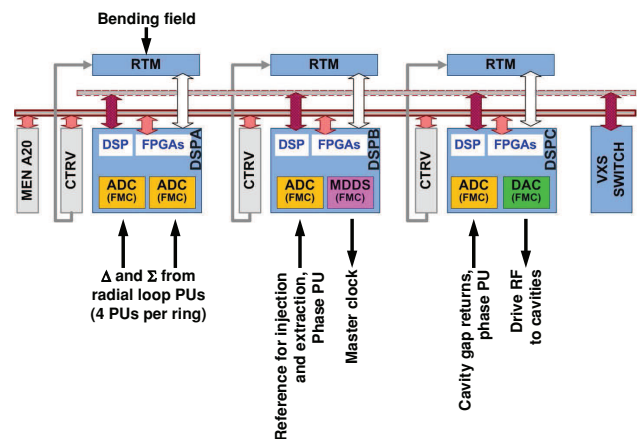


Figure 1: Digital beam control implementation in the PSB. RTM: Rear Transition Module, MDDS: Master Direct Digital Synthesizer, MEN A20: processor card, CTRV: timing card, VXS: VMEbus-switched serial standard.

and cavity controls loops are distributed over the DSP systems. The first signal processing board (Fig. 1, DSP A) takes care of the frequency program and the radial loop. The beam phase and synchronization loops for injection and extraction are integrated in DSP B, while DSP C generates the drive signals to the RF cavities and reads back the cavity gap returns. The modular approach of the beam control allows to add further DSP units to integrate more PU signals or to drive more cavities. An additional DSP board equipped with one ADC and one DAC module is added for processing Finemet signals and implementing four or more cavity loops.

Flexibility and stability are the key advantages of the upgraded beam control system. All control parameters, like sensitivities, loop gains and phases are settable in pulse-to-pulse (PPM) so that optimum parameters can be chosen for each beam type. The flexibility goes well beyond the choice of parameter settings. As the loops are implemented in DSP firmware, the system is reconfigurable so that extensions, like new algorithms for synchronization, can be added without hardware change.

### Finemet Cavities

The aging ferrite-loaded cavities and their power amplifiers would require significant upgrades to cope with the increased beam-loading after the second long shutdown (LS2). Replacing them by Finemet cavities driven by solid state amplifiers [11] is thus the preferred upgrade path for the high-power RF system, which will significantly simplify the hardware and its maintenance. Due to the large bandwidth of Finemet cavities, no tuning will be needed and the frequency of both main RF systems at $h = 1$ and $h = 2$ can be covered by one cavity. Only the cavity for longitudinal blow-up would remain with traditional ferrite technology. A first prototype Finemet cavity (5 cells, Fig. 2, left) has been installed in ring 4 of the PSB and tested with beam in 2012. Driven by the digital LLRF, it
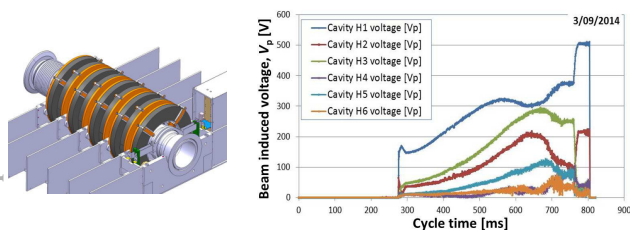


Figure 2: Sketch of the 5-cell Finemet cavity used for beam tests in 2012 (left). The last Finemet ring is not shown to leave the view to the gap. Beam induced voltage (right) at the first six harmonics during acceleration of a single bunch with $7.3 \cdot 10^{11}$ ppb as recorded by the digital LLRF. Injection is at 275 ms and ejection at 805 ms.

has been demonstrated that, together with the ferrite-loaded cavity at reduced voltage, a beam intensity of $4.6 \cdot 10^{12}$ ppb could be handled. The Finemet cavity delivered a voltage of about 2 kV. Since the amplitude control loop was only

closed around $h = 1$, a distortion of the gap voltage without noticeable effect on beam quality was observed.

These encouraging results [12] led to the installation of a 10-cell cavity with new amplifiers and an improved fast RF feedback during LS1. This second prototype delivers sufficient voltage for acceleration on $h = 1$ to replace the ferrite-loaded cavity or to serve for bunch flattening at $h = 2$. Due to the large bandwidth of the Finemet cavity, the digital LLRF will servo the gap voltage at different harmonics simultaneously. Two voltage control (AVC) loops at the first two harmonics, as well as further loops to reduce the beam induced voltage at higher harmonics are foreseen, easily possible with the digital LLRF. Figure 2, right shows a first measurement of the beam induced voltage during the cycle at the first six harmonics. A series of beam tests to verify reliability and limitations of the prototype Finemet cavity is planned for 2015. The decision whether to move to a Finemet-based acceleration system or to upgrade the existing ferrite-loaded cavities will be taken by the end of 2015.

### PS

The final bunch spacing for the LHC is prepared by RF manipulations in the PS. Acceleration and these manipulations are achieved with, in total, 25 RF cavities (11 × 2.8 − 10 MHz, 2 × 20 MHz, 2 × 40 MHz, 3 × 80 MHz, 6 × 200 MHz and a Finemet wide-band cavity). Two major limitations are observed with LHC-type beams [13]. Firstly, longitudinal coupled-bunch (CB) instabilities are excited during acceleration, after transition crossing and on the flat-top. Secondly, differing transient beam-loading behaviour of the cavities for bunch-splittings causes an unequal bunch population along the batch. To suppress CB instabilities a Finemet cavity has been installed as a wide-band longitudinal kicker. In addition to increase the direct feedback gain, improved 1-turn delay feedbacks for the 10 MHz cavities have been commissioned. Similar feedbacks are foreseen for the cavities at 20 MHz, 40 MHz and 80 MHz.

### Beam Control Improvements and Upgrade

Gradual improvements have been implemented in the longitudinal beam control to follow the demand for more complicated RF manipulations for the LHC-type beams [14, 15]. Figure 3 illustrates the measured evolution of the bunches during the batch compression, merging and triple splitting (BCMS) manipulations in closed loop. It involves RF systems at $h = 7, 9, 10, 11, 12, 13, 14, 21$ and requires beam phase and radial loops at harmonic 7, 9, 11, 13, 21. RF manipulations involving even more harmonics will be tested during the 2014/2015 runs. To keep full flexibility of the beam control and to assure reliable operation for HL-LHC, a complete replacement of the LLRF by a fully digital system is planned during LS2.
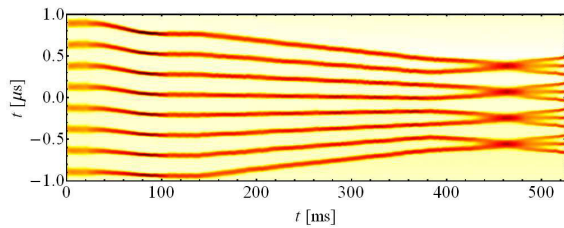
Figure 3: Measured bunch profile evolution during batch compression, merging and triple splitting (BCMS).

## Direct RF Feedback

To reduce the residual impedance of the RF cavities all $10\,\mathrm{MHz}$, $20\,\mathrm{MHz}$, $40\,\mathrm{MHz}$, and $80\,\mathrm{MHz}$ systems are equipped with direct RF feedback around the amplifier. The maximum gain, ranging from $24\,\mathrm{dB}$ to more than $40\,\mathrm{dB}$, depends on the bandwidth requirement and the delay of the amplifier chain. Extensive studies have been performed for the $10\,\mathrm{MHz}$ cavities and a possible increase of the feedback gain (at least $3\,\mathrm{dB}$) has been demonstrated. Further improvements are foreseen before any cavity in the PS ring will be equipped with the new feedback circuit. The direct feedbacks of the $40\,\mathrm{MHz}$ and $80\,\mathrm{MHz}$ RF systems are also being reviewed. The feedback amplifiers are located in separated alcoves, but could be moved closer to the cavity to reduce delay in the signal path.

## 1-Turn Delay Feedbacks

During LS1 a first generation 1-turn delay feedback [16] has been replaced by new flexible hardware based on programmable logic (FPGA) making it applicable to all beams, notably the LHC-type beams accelerated on $h = 7$ and $h = 21$ with various intermediate harmonics for RF manipulations.

It consists of a comb filter periodic with the revolution frequency to pass only the revolution frequency harmonics and synchrotron frequency side-bands, a notch filter to remove any gain on the RF harmonic and an automatic delay to make the total loop delay equal to the time-of-flight of one turn. The simulated and measured open-loop transfer function of the feedback system is shown in Fig. 4, left. Closing the feedback system around the cav-



Figure 4: Simulated/measured open-loop transfer function (left) and closed-loop transfer function of the 1-turn delay feedback for the $10\,\mathrm{MHz}$ cavities.

ity (Fig. 4, right) shows the cavity transfer function with the impedance reduction at the revolution frequency lines. The new 1-turn delay feedback has been commissioned on all eleven $10\,\mathrm{MHz}$ cavities during the 2014 start-up.

The new feedback hardware will also be installed on the high-frequency cavities. The impedance of the $40\,\mathrm{MHz}$ and $80\,\mathrm{MHz}$ cavities with their mechanical short-circuit, which cannot be moved in PPM, will be reduced by 1-turn delay feedback.

## Coupled-Bunch Feedback

To suppress the CB instabilities observed during acceleration and on the flat-top a new feedback system is under development [17]. To cover all possible CB oscillation modes, a Finemet cavity as a wide-band longitudinal feedback kicker has been installed in the PS during LS1. The six cavity cells are designed for an RF voltage of about $5\,\mathrm{kV}$ in the range from $0.4\,\mathrm{MHz}$ ($f_{\mathrm{rev}}$) to $5\,\mathrm{MHz}$ ($f_{\mathrm{RF}}/2$).

The digital LLRF for the Finemet cavity will detect synchrotron frequency side-bands indicating CB oscillations and feed them back to the beam via the Finemet cavity. Additionally, a multi-harmonic beam-loading compensation feedback based on a bank of narrow-band filters at the relevant revolution frequency harmonics is being tested to reduce the shunt impedance of the wide-band cavity. Due to the large bandwidth requirement and the signal delay between cavity in power amplifiers, direct feedback would only be possible with low gain. Figure 5 illustrates the spectrum of the cavity voltage induced by a short single bunch. At the four harmonics at which a prototype beam-
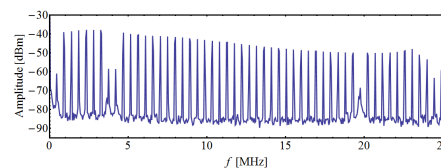


Figure 5: Beam induced voltage in the PS Finemet cavity of a single bunch close to transition. The prototype beam-loading compensation is set to harmonics $h = 1$, 8, 9 and 42, reducing the induced voltage by approximately $20\,\mathrm{dB}$.

loading compensation is programmed, significant reduction of the beam induced voltage is measured, compatible with the gain of the open-loop transfer function. First beam tests with the new CB feedbacks have started in 2014 and it will be made operational during the 2015 run.

# SPS

The main RF system of the SPS at $200\,\mathrm{MHz}$ consists of travelling wave cavities made up from sections of cross-bar structure cells [18] driven by tetrode amplifiers. The maximum RF voltage for a given input power depends on cavity length and beam current. In view of the increased intensity for LHC-type beams in the SPS, the sections will be rearranged to shorter cavities [19]. The RF system at

200 MHz is complemented by two travelling wave cavities at 800 MHz (200 kW per cavity) delivering about $10-15\,\%$ of the main RF voltage. The phase between both RF systems must be precisely controlled during acceleration for optimum beam stability and blow-up. The LLRF system of the 800 MHz RF system has therefore been redesigned.

## RF Power Considerations

Presently in total 18 cavity sections are arranged to two 4-section and two 5-section cavities with a continuous power of $0.7\,\mathrm{MW}$ per cavity. However, this configuration leaves no margin for intensity increase [20] as the maximum amplifier power is reached with a bunch population of $1.2 \cdot 10^{11}$ ppb (25 ns spacing). To keep longitudinal stability during acceleration, the longitudinal emittance is increased from 0.35 eVs to 0.5 eVs by controlled longitudinal blow-up. At higher intensity, due to beam-loading, the voltage per cavity becomes insufficient, especially for the long 5-section cavities [21].

During LS2, the travelling wave cavity sections will therefore be rearranged in four 3-section and two 4-section cavities, using two additional spare sections and reducing the beam coupling impedance by $18\,\%$. Moving from four to six cavities requires two additional RF power plants with an RF power of $1.6\,\mathrm{MW}$ delivered to the 4-section cavities. Civil engineering for a new building is progressing. The four 3-section cavities will be powered by the existing amplifiers. Their present continuous power limit of $0.7\,\mathrm{MW}$ increases to $1.05\,\mathrm{MW}$ when operated in pulsed mode (LHC-type beams only fill up to $4/11$ of the circumference).

The bucket area during acceleration with four 3-section and two 4-section cavities at maximum RF power is illustrated in Fig. 6 for various bunch populations. At a bunch



Figure 6: Bucket area (blue) for bunch populations from $1.8 \cdot 10^{11}$ ppb to $2.6 \cdot 10^{11}$ ppb at maximum RF power (1.05/1.6 MW) during the acceleration cycle (2014, $\gamma_{\mathrm{tr}} = 18$, 25 ns bunch spacing). From one trace to the next, the number of protons increases by $0.2 \cdot 10^{11}$ ppb.

population of about $2.5 \cdot 10^{11}$ ppb the bucket area does not increase during acceleration anymore, leaving no margin for controlled longitudinal emittance blow-up. It is therefore being considered to decrease the ramp rate (Fig. 7) to gain in longitudinal acceptance or to raise transition energy to $\gamma_{\mathrm{tr}} = 20$ [5].

Figure 7: RF power requirement for a bunch population of $2.5 \cdot 10^{11}$ ppb during the cycle (2014, left) and for twice longer acceleration (right).

The bunches must be shortened to 1.7 ns ($4\sigma$ Gaussian fit) prior to extraction to fit into the 2.5 ns long buckets in the LHC. Again the maximum achievable voltage is reduced by beam-loading with increasing beam current (Fig. 8). At the same time, taking the voltage reduction by potential-well distortion (PWD) and the single-bunch instability due to loss of Landau damping into account [20], the RF voltage required for constant bunch length rises linearly with intensity [22, 23]. The measured beam parameters



Figure 8: RF voltage versus beam current (in units of bunch population for 25 ns spacing) for present and upgraded cavity configuration together with the linearly increasing voltage requirement. The equivalent RF current for the bunch spacing $\tau_{\mathrm{bb}}$ is $I_{\mathrm{RF}} = 2N_b e_0/\tau_{\mathrm{bb}}$.

at $1.3 \cdot 10^{11}$ ppb and 7 MV for 1.7 ns long bunches (2012) are the reference point for instability line in Fig. 8. With the present longitudinal emittance and no increase in bunch length nor ramp time, the maximum achievable bunch population after the RF upgrade is estimated to $2.0 \cdot 10^{11}$ ppb.

Significant effort has been made to identify sources of longitudinal impedance [24, 25] driving instabilities. Figure 9 shows the measured amplitude projection of the bunch spectrum as observed when injecting long bunches into the SPS. While the impedance at 200 MHz due to the RF cavities are well understood, the vacuum flanges (about 550) have been identified (Fig. 9) as most probable source for the important peak at 1.4 GHz. The seven flange types all have a resonance frequencies from 1.2 GHz to 1.6 GHz with shunt impedances from $120\,\Omega$ to $2.8\,\mathrm{k}\Omega$. Possible shielding to reduce their $R/Q$ is being investigated. Assuming an impedance reduction of approximately

Figure 9: Bunch spectrum of 25 ns long bunches injected with RF off and different types of SPS vacuum flanges.



Figure 10: Simplified diagram of the RF loops around one 800 MHz cavity.

50 % could raise the bunch population to $2.4 \cdot 10^{11}$ ppb for LHC-type beams with 25 ns spacing.

Bunch rotation is studied as complementary approach to achieve short bunches at transfer to the LHC. In the context of the plasma wake field experiment AWAKE at the SPS, single bunches of $2.8 \cdot 10^{11}$ ppb have been successfully compressed from 2.2 ns to 1.2 ns [26]. Tracking simulation studies with multi-bunch beams indicate that bunches of $2.3 \cdot 10^{11}$ ppb could be compressed from 2.2 ns to 1.6 ns average bunch length applying a voltage step from 5 MV to 10 MV [5]. These simulations include effects of the SPS impedance as well as the feedback and feed-forward systems of the 200 MHz RF cavities.

*Feedbacks and Beam Controls*

In the framework of the upgrades, new LLRF systems will be installed for both, 200 MHz and 800 MHz systems. Priority has been given to feedback and feed-forward [27] of the 800 MHz cavities as precisely controlling their phase with respect to the 200 MHz RF system is essential for the stability and quality of LHC-type beams. The phase must be kept constant with respect to the 200 MHz RF voltage along the batch to achieve bunches with equal parameters. Uniform controlled longitudinal blow-up requires the same synchrotron frequency distribution for all bunches.

A new multi-function feedback controller has been developed which contains an I/Q-loop for the cavity field control, as well as a comb-filter based feedback including a cavity filter to compensate the frequency response of the travelling wave structure and a direct RF feed-forward demodulating the beam signal from a PU. Figure 10 sketches the main loops around one 800 MHz cavity. Additionally, the feedback controller contains a polar loop to correct amplitude and phase drifts of the high power amplifiers (four inductive output tubes). The new LLRF has been installed on one cavity and commissioning has started. Both cavities will be operational with the new hardware by mid 2015.

## CONCLUSIONS

The RF systems in the injector chain will be improved to reach a bunch population beyond $2.0 \cdot 10^{11}$ ppb with 25 ns bunch spacing for HL-LHC. First upgrades were put in place during LS1, but the major part will be implemented during LS2.
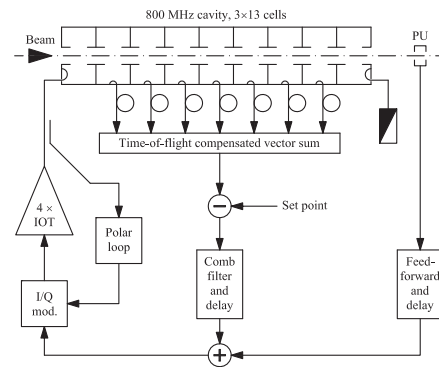
## REFERENCES

[1] R. Garoby et al., IPAC2012, p. 1010.

[2] E. Jensen, Chamonix 2012 LHC Performance Workshop, CERN-2012-006, p. 261.

[3] G. Rumolo et al., Review of LHC and Injector Upgrade Plans (RLIUP), p. 17.

[4] G. Rumolo et al., Chamonix 2014 LHC Performance Workshop, to be published.

[5] T. Argyropoulos et al., Chamonix 2014 LHC Performance Workshop, to be published.

[6] H. Damerau et al., Review of LHC and Injector Upgrade Plans (RLIUP), CERN-2014-006, p. 127.

[7] M. Benedikt et al., CERN-2004-003.

[8] M. E. Angoletta et al., IPAC2010, p. 1461.

[9] M. E. Angoletta et al., IPAC2010, p. 1464.

[10] M. E. Angoletta et al., IBIC2013, p. 575.

[11] M. M. Paoluzzi et al., IPAC12, p. 3749.

[12] M. M. Paoluzzi et al., IPAC2013, p. 2660.

[13] H. Damerau et al., HB2010, p. 193.

[14] H. Damerau, et al., IPAC10, p. 2716.

[15] H. Damerau et al., IPAC2013, p. 2600.

[16] F. Blas, R. Garoby, PAC91, p. 1398.

[17] H. Damerau et al., IPAC2013, p. 1808.

[18] G. Dôme, LINAC76, p. 138.

[19] E. Shaposhnikova, et al., IPAC2011, p. 2014.

[20] E. Shaposhnikova, http://paf-spsu.web.cern.ch/paf-spsu/meetings/2013/m11-07/SPSRF_US1_BD.pptx.

[21] T. Bohl, Chamonix 2000 SPS and LEP Performance Workshop, CERN-SL-2000-007-DI, p. 58.

[22] E. Shaposhnikova, LHC Project Note 242.

[23] E. Shaposhnikova, SL-Note-2001-031 HRF.

[24] T. Argyropoulos et al., IPAC2013, p. 1793.

[25] E. Shaposhnikova et al., IPAC14, p. 1416.

[26] H. Timko et al., IPAC2013, p. 1820.

[27] P. Baudrenghien, G. Lambert, Chamonix 2000 SPS and LEP Performance Workshop, CERN-SL-2000-007-DI, p. 94.

# CURRENT STATUS ON ESS MEDIUM ENERGY BEAM TRANSPORT

I. Bustinduy*, M. Magan, F. Sordo, ESS-Bilbao, Spain
R. Miyamoto†, ESS, Sweden

## Abstract

The European Spallation Source, ESS, uses a high power linear accelerator for producing intense beams of neutrons. During last year the ESS linac cost was reevaluated, as a consequence important modifications were introduced to the linac design that affected Medium Energy Beam Transport (MEBT) section. RFQ output beam energy increased from 3 MeV to 3.62 MeV, and beam current under nominal conditions was increased from 50 to 62.5 mA. The considered MEBT is being designed primarily to match the RFQ output beam characteristics to the DTL input both transversally and longitudinally. For this purpose a set of eleven quadrupoles is used to match the beam characteristics transversally, combined with three 352.2 MHz CCL type buncher cavities, which are used to adjust the beam in order to fulfill the required longitudinal parameters. Finally, thermo-mechanical calculations for adjustable halo scraping blades, with significant impact on the HEBT, will be discussed.

# INTRODUCTION

The European Spallation Source (ESS) is a neutron source currently under construction in Lund, Sweden. The design and operation of the proton linac of ESS, which will ultimately produce a 5 MW beam power, is imposing challenges in various aspects of accelerator science and engineering. The main focus of this paper is the medium energy beam transport (MEBT), located between the RFQ and DTL.

Including all required devices in a relatively short space imposes significant challenges not only on engineering design of components but also beam physics since good beam quality and good matching to the DTL must be achieved under engineering limitations and strong space charge force. Table 1 shows selected parameters of the ESS MEBT. This paper presents status on works of beam physics and engineering component designs for the MEBT. However, due to the limitation in space, only the recent works for the scraper system are presented in detail and status on the rest of works is summarized in the next section.

# SUMMARY OF ESS MEBT STATUS

## Lattice Design and Beam Physics

Figure 1 shows the present MEBT layout as well as the power beam density contours. A substantial effort has been made to construct a lattice with good matching to the DTL and good beam quality, while housing the chopper and other necessary devices [1]. The impacts from various lattice element errors have been studies as a part of the campaign to find tolerances of the lattice element errors throughout

Table 1: Selected ESS MEBT Parameters

| Parameter | Unit | Value |
|---|---|---|
| Beam energy | MeV | 3.62 |
| Peak beam current | mA | 62.5 |
| Average beam power | kW | 9.05 |
| Beam pulse length | ms | 2.86 |
| Beam pulse repetition rate | Hz | 14 |
| Duty cycle | % | 4 |
| RF frequency | MHz | 352.21 |

the entire ESS Linac [2]. A further detailed beam dynamics calculation including effects such as multipole components of a quadrupole and the field profiles of the buncher cavity and quadrupole will be conducted in near future.

To ensure a good chopping efficiency, the optics and beam dynamics during the chopper operation must be studied in addition to the nominal case [1]. Given the rise and fall time of the chopper is presently specified as ∼10 ns, which is longer than the bunch spacing of 2.84 ns (inverse of 352.2 MHz), there are a few *partially-chopped* bunches. These bunches have large trajectory excursions but not entirely intercepted by the chopper dump, and thus raise a concern of beam losses. The dynamics and beam losses of these bunches are studied in detail and it is ensured that the losses are acceptable [3,4].

In Fig. 1, three locations at 0.85, 2.19, and 3.39 m correspond to the scrapers. The use of the scrapers for the ESS Linac has been studied in detail [1,3–5]. The scrapers not only improve the beam quality in the nominal condition but also efficiently remove halos in the RFQ output, in case the sections upstream of the MEBT produce a bad quality beam [1] and improve the situation of the beam losses due to the partially-chopped bunches [3]. The locations of the scrapers are determined to optimize these three functions under the mechanical constraints. An analysis of the location optimization of the scrapers is presented in a following section. An ability of a scraper is estimated with a thermo-mechanical calculation and this gives an important input to the beam dynamics calculation. This is also presented in a following section.

## Component Design and Prototyping

In order to proceed with detailed engineering phase some constrains have to be taken into account: The elected beam pipe is the standard *DN35*. This beam pipe gives an upper limit of 18.4 mm radius for the beam aperture and also determines aperture for the rest of the foreseen devices (quadrupoles, bunchers, etc.). Constituting thus, the backbone of the MEBT engineering design.

* ibon.bustinduy@essbilbao.org
† ryoichi.miyamoto@esss.se
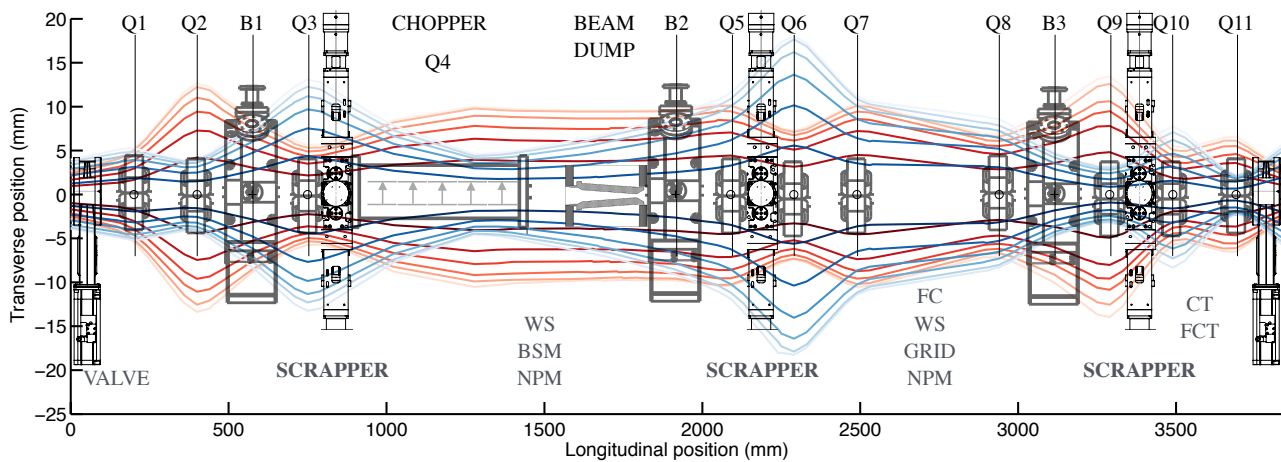
Figure 1: ESS MEBT 2014.v1 layout; comprised of 11 quadrupoles 3 bunchers and 3 scrapers. Power density contours for x (*red*) and y (*blue*) are represented from dark ($10^3$ W) to light ($10^{-2}$ W) beam power contour lines extracted from TRACEWIN. Both axis are expressed in mm.

One of the main purposes of the ESS MEBT is to house a fast chopper. The bunches produced during the transient times of the IS and LEBT, positioned in the head and tail of a pulse and anticipated with a time scale of a few µs, are likely to have wrong parameters and hence a higher risk of causing beam losses [6]. In a worst case scenario, machine protection system also expects a 1 ms train of bunches to be deflected against the beam dump. In order to prevent excessive heat deposition on the beam dump, Ion source magnetron should be used as an actuator [7]. Once required rise time has been relaxed significantly (10 ns), an approach based on fast high voltage switches seems to be the most reliable approach; due to its resistance to beam spills and much simpler fabrication [8].

For this MEBT layout, an optimization of the magnetic design of the quadrupoles is being taking place in order to fulfill with following specifications: Ø41 mm aperture, $\int B = 2.5$ T with 100 mm maximum physical size (length) and ~20 G.m deflection for the steerers. This magnetic design is closely linked to the optical layout and the imposed mechanical constraints. In particular, this design has to accommodate strip-line BPM as well as the required four fiducial points at the top of the yoke. The field quality must be cross examined by particle tracking simulations, and it is especially important for these devices because the steering dipoles are integrated inside the quadrupoles.

For the longitudinal plane, a new electromagnetic design is in progress to fulfill new specifications of the foreseen three CCL type buncher cavities. The increasing transported beam energy and current affect primarily to transit time factor and required effective voltage, which increases up-to 146 kV for the last buncher under nominal conditions. In order to reach required performance in the available space, optic design has been adapted to allow a lower aperture for the bunchers (Ø29 mm).

## SCRAPERS LOCATION

The use of scrapers before entering DTL tanks is strongly recommended to avoid emittance growth and halo development in high-intensity linacs [9]. In our current design, beam should be scraped in the both transverse plane at each location. For this, 4 stepping motors are needed per locations. The scrapers will be used during nominal operation, therefore integrated in the interlock system in order to avoid interaction with the beam core. The position of the beam will be provided by a beam position monitor (BPM) positioned as close as possible and the movement has to be limited. In addition, the temperature can be measure in the scraper and also the charge deposition.

### Procedure

Although a simple method was use to place these scrapers [5]. It seems necessary to identify a procedure to find the best possible locations to scrape halo particles while maximizing core particles transmission, in case scraper locations could be optimized for present or forthcoming MEBT layouts.
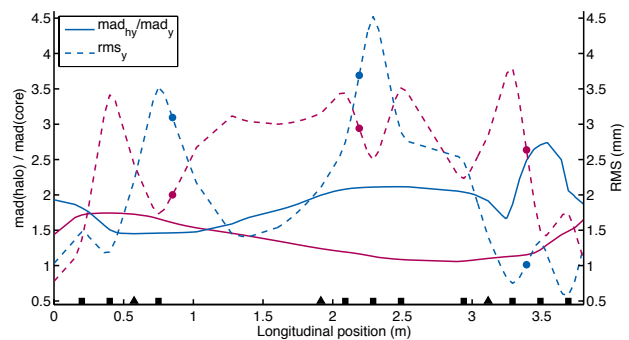


Figure 2: Beam $\sigma$ beam envelopes (*dashed line*), and quadratic mean ratios (*solid line*) for x and y projections along MEBT.
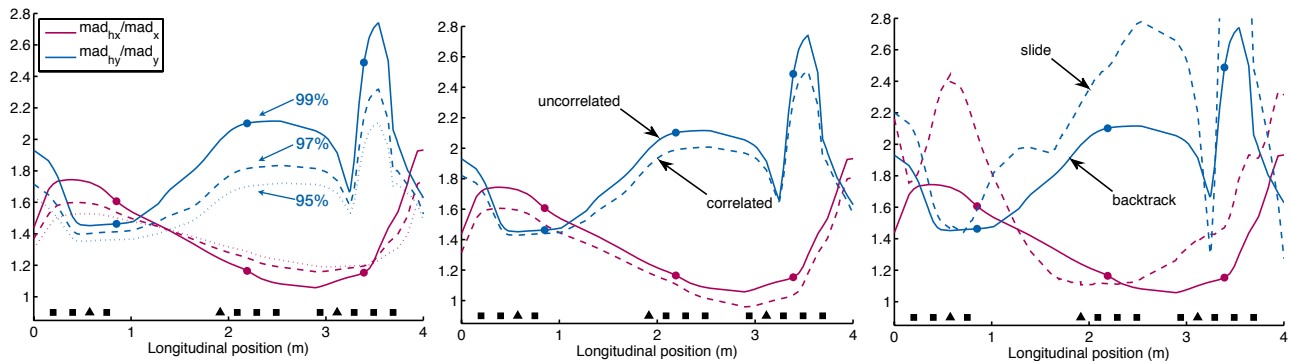
Figure 3: *Left frame:* Study of different threshold levels. *Middle frame:* Comparison between correlated or uncorrelated x/y approach. *Right frame:* Comparing tracking approach with slide by slide analysis.

Considering the mean deviation as a robust measure of population of a univariate distribution, representing the ratio of the population of particles that conform the halo respect to the particles from the core, one can identify the best possible locations to scrape halo particles maximizing *core* particles transmission. For a sample size $n$, the mean deviation (MAD) is defined by the following formula:

$$ \text{MAD} = \frac{1}{n} \sum_{i=1}^{n} |x_i - \bar{x}|, \qquad (1) $$

Particle distribution at the end of the ESS *warm linac* section [1] is scrutinized in each transverse plane. From there, particles that belong to halo are identified as those lying above a particular threshold (99% emittance). Those particles which we intend to remove, are backtracked along this medium energy beam section of the linac.

Figure 2 represents beam root mean square (RMS) in dashed lines along the MEBT. Simultaneously, the ratio of *halo/core* populations is represented when core bunch is considered within 99% emittance as solid lines. In this Figure $x$ dimension is represented in red, while blue is used for $y$ projection. Colored circles represent current location for scrapers ($x/y$). Black squares and triangles represent location of quadrupoles and bunchers respectively along the line, as presented in Fig. 1.

*Robustness Testing*

In order to test this method, different variations have been studied. In particular, a modification of the *threshold level*, that is used to determine the fraction of particles considered within *core*, or belonging to *halo* region could mislead the actual optimum location. For that, three different levels have been considered (see Fig. 3 left frame) 99, 97, and 95%. Here, little differences can be appreciated in the overall pattern. Another variation is to evaluate the net effect of considering $x$ and $y$ distributions completely independent each other, compared to the correlated case. As Fig. 3 middle frame shows, a smoothing effect arises again, but the same patterns can be identified.

---
[1] MEBT and DTL versions are *2014.v1* and *v86* respectively

Finally, an *slice by slice* approach is studied, in this alternative approach, beam through the MEBT is sliced and core and halo populations identified for each slide. Figure 3 right frame, represents the backtracking approach (solid lines) and slice by slice approach (dashed lines). Compared to the presented approach, where beam evolution along the warm linac accelerator is considered, slide by slide approach does not take into account core particles, that might become part of the halo downstream. It is remarkable that in both approaches same pattern arise. In particular, the best possible location for y-axis (highest values) is identified at *Q10* for both cases. Other possible good locations seem to be slightly shifted respect to *backtracking* approach. For instance, in vertical plane it can be identified a good location near *Q7*, while horizontal plane slits optimal position can be identified near *Q2*.

*Discussion*

Table 2 compares obtained optimal locations using the method explained above, with nominal locations, where mechanical constrains have been taken into account. From here, we can identify scraper #2 and scraper #3 as good locations to clean particles in the *y* dimension. while, *x* projection cleaning could be more effective with scraper #1. Considering mechanical constrains, performance of scraper #1 could be increased by placing it closer to the entrance. This could be achieved by exchanging positions with Wire-Scanner #1. But this, will have an impact on the beam instrumentation and the studied phase space cleaning performance, in case the beam out of the RFQ has a too populated halo.

Table 2: Beam Population Ratios per Scraper Potential Location

|         | Optimum | | Nominal | |
|---------|---------|------------|---------|------------|
| Scraper | z (m)   | RATIO (x/y) | z (m)  | RATIO (x/y) |
| #1      | 0.36    | 1.74/1.57  | 0.85    | 1.61/1.46  |
| #2      | 2.45    | 1.09/2.12  | 2.19    | 1.16/2.10  |
| #3      | 3.54    | 1.29/2.74  | 3.39    | 1.15/2.48  |
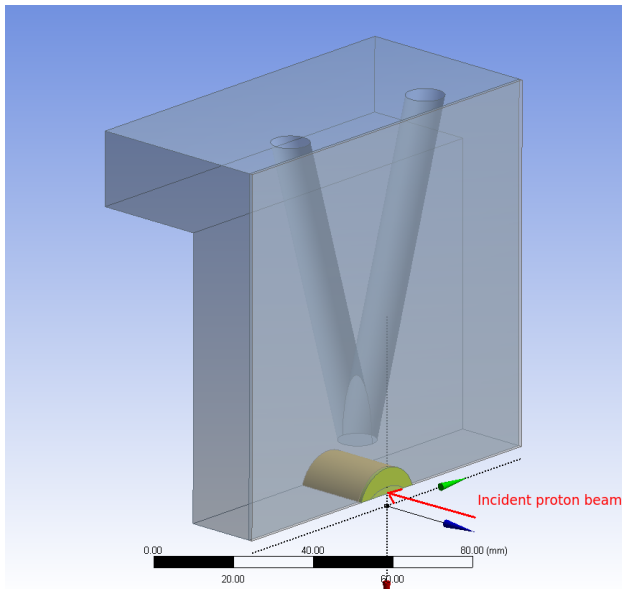
Figure 4: 3D representation of the geometry.

Table 3: Summary of the Results (Each Blade)

| Insertion ($\sigma$) | Max. heat flux (W/cm$^2$) | Max Temp (°C) | Max Stress (MPa) |
|---|---|---|---|
| 3.48 | 1700 | 50.0 | 25.5 |
| 3.29 | 3350 | 80.0 | 53.2 |
| 3.1 | 4810 | 105.3 | 75.9 |
| 3.02 | 5550 | 120.4 | 90.3 |
| 2.97 | 6740 | 138.8 | 107 |
| 2.81 | 9130 | 185.7 | 149 |
| 2.67 | 12900 | 249.1 | 208 |
| 2.54 | 17600 | 334.0 | 283 |



Figure 5: Peak temperature over time.

## THERMO-MECHANICAL PROBLEM

Under the new beam parameters, the beam has a peak intensity of 62.5 mA at 3.62 MeV, with a repetition rate of 14 Hz, and a pulse length of 2.857 ms. This is a significant increase over previous conditions (50 mA and 3 MeV). In fact, the new beam conveys 50% more energy per pulse. Thus, for any given fraction of the beam that a design aims to stop, the loads are far greater than in the previous case. As a reference, each of the pulses now carry 643 J.

Considering the nominal location for each scraper (see Fig. 1), which fulfill mechanical constrains. In order to study the thermo-mechanical limits of the proposed design, the *extreme case* of a $\sigma_y = 1.01$ mm will be considered. This last scraper deals with the more focused beam in the $y$ dimension. The area of the beam in this particular location is $\approx 15 \times 6 = 90$ mm$^2$, which highlights the concentration of the beam.

In order to scrape this highly concentrated beam, the geometry presented in Fig. 4 is proposed. This L-shaped piece embraces a small cylinder of a highly temperature resistant material where the protons hit. In this case, tungsten is studied as the base candidate, although other materials have shown superior performance on theory, their manufacturability is unclear. The piece is cooled by an V-shaped cavity. While this offers a much lower cooling efficiency than an U-shaped one, as there is much less area near the area to cool, it is also much easier to manufacture, and means that the scraper can be manufactured in one piece, as opposed to the two welded pieces design an U-shape requires. Thus, removing welded parts inside vacuum, leakage problem reduces significantly, which is a remarkable reliability advantage. For these calculations, an uniform heat transfer coefficient of 10 000 W/(m$^2$· K) is assumed.

### Methodology and Tools

An ANSYS™ Workbench simulation is set up with the geometry described previously. A transient thermal simulation is performed, where the heat load is given as a surface heat flux matching the beam profile during the beam pulses, and considered zero outside of them. The properties considered for the tungsten are temperature-dependent.

### Results

The temperature over time, max temperature and the stress at the time of maximum temperature (pulse ending) have been calculated in several scenarios, characterized by the proximity of the scraper edge to the center of the beam in terms of the times of its RMS ($\sigma$) value. Thus, as this value decreases, the scraper is nearer the beam, and stops a larger fraction of it. A summary of all data is given in Table 3. An example of the maximum temperature over time is given in Fig. 5, for $\sigma = 2.8$, with the qualitative behavior of the temperature being the same in all cases. As all the heat deposition takes place along the 2.86 ms pulse length, there is not enough time for any significant cooling. Thus, it can be concluded that no enhancement in the cooling conditions (increase of heat transfer coefficient, area cooled, or proximity) will be of any use. As an example of the temperature field distribution, Fig. 6 represents the temperature at the end of the pulse for $\sigma = 2.8$.

Stresses are heavily located in the corner, as it suffers sudden, localized temperature increase, and is subject to thermal stress. An example of the distribution is given in Fig. 7.

It is necessary to remark that the values presented in Table 3, consider a 100 MPa stress limit in the tungsten without entering a detailed fatigue stress analysis, it can be inferred that the usage of this design is valid for values up-to $\sigma = 2.8$, or 0.15% beam scraped per blade, which would imply a 54 W, shared among the 4 blades that conform the last scraper.
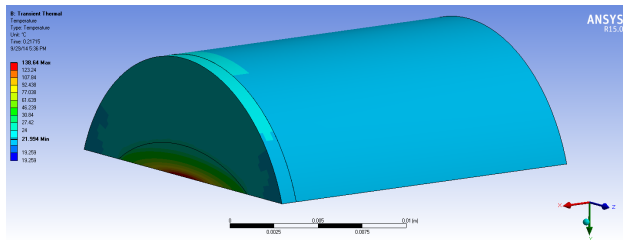
Figure 6: Temperature distribution at the end of the 2.86 ms, 14Hz repetition rate pulse.
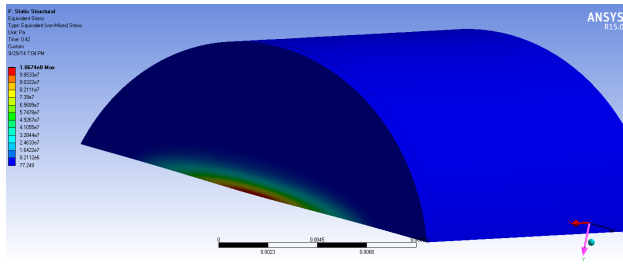


Figure 7: Stress distribution at the end of the 2.86 ms, 14Hz repetition rate pulse.

Finally, Fig. 8 presents the studied extreme case of $\sigma$ = 1.01 mm in red accompanied with wider beam footprint results. $\sigma$ = 3.5 mm (blue) and 7 mm (green). For a given beam cross-section, the parameter that fixes the performance requirement is the amount of beam to be scraped, which can be represented by either the percentage of the power to be scraped, or by the RMS ($\sigma$) value at which the beam is cut.
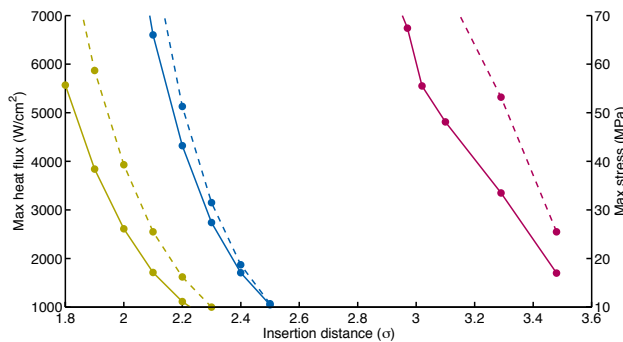


Figure 8: Max heat flux represented against insertion distance in solid lines, for three different beam footprints $\sigma$ = 1.01 (red), 3.5 (blue) and 7 mm (green). Max Stress is also presented as dashed lines.

## CONCLUSIONS

Overall presented method provides optimal locations for the scrapers that are in good agreement with the nominal positions (see Table 2), where, mechanical constrains, beam instrumentation needs and beam cleaning effects were also considered. This results are in good agreement with previously presented locations [5] and confirm that a typical scheme using a set of collimators separated by a fix value of phase advance, such as two scrapers separated by 90 degrees, may not be optimum for the MEBT due to the strong space charge force.

The mechanical design has been simulated under different conditions, namely, loads depending on the fraction of beam scraped, and the stress and temperature results have been analyzed. The induced stress in the beam scraper has been observed to be directly correlated to the maximum surface heat flux. Therefore, the design seems viable for values below 7000·W/cm$^2$. Thus, particles can be removed near $3\sigma$ as required [5], even in the highest concentration conditions. In case these collimation blades are used in the other expected locations, where beam concentration is relaxed, a higher fraction of beam can be removed safely.

## ACKNOWLEDGMENT

## REFERENCES

[1] R. Miyamoto et al., in Proc. of IPAC'14, THPME045.

[2] M. Eshraqi et al., in Proc. of IPAC'14, THPME043.

[3] R. Miyamoto et al., in Proc. of LINAC'14, MOPP039.

[4] R. Miyamoto, in Proc. of HB'14, MOPAB18.

[5] R. Miyamoto et al., in Proc. of HB'12, WEO3A02.

[6] M. Comunian et al., in Proc. of HB'12, TUO3B01.

[7] A. Nordt et al., in Proc. of IPAC'14, MOPME045.

[8] S. Varnasseri et al., DIAG-00-CH01-ESS-00-DOC.

[9] F. Gerigk, et al., in Proc. of LINAC'02, TH103.

# NEEDS AND CONSIDERATIONS FOR A CONSORTIUM OF ACCELERATOR MODELING*

J.-L. Vay[#], J. Qiang, LBNL, Berkeley, CA 94720, USA
C.-K. Ng, Z. Li, SLAC, Menlo Park, CA 94025, USA
J. Amundson, E. G. Stern, FNAL, Batavia, IL 60510, USA

*Abstract*

Thanks to sustained advances in hardware and software technologies, computer modeling is playing an increasingly important role in the design of particle accelerators. This rise in importance is further fuelled by the economic pressure for reducing uncertainties and costs of development, construction and commissioning, thus pushing the field toward an increase use of "virtual prototyping". Until now, the development of accelerator codes has been left to projects without mandate and programmatic funding for coordination, distribution and user support. While this is adequate for the development of relatively small-scale codes on targeted applications, a more coordinated approach is needed to enable general codes with user bases that extend beyond individual projects, as well as cross-cutting activities. In light of this, it is desirable to strengthen and coordinate programmatic activities of particle accelerator modeling within the accelerator community. This increased focus on computational activities is all the more timely as computer architectures are transitioning to new technologies that require the adaptation of existing - and emergence of new - algorithms and codes.

## INTRODUCTION

Particle accelerators are essential tools of science and technology, with over 30,000 accelerators in operation around the world, in support of discovery science, medicine, industry, energy, the environment and national security [1]. The size and cost of the accelerators are a limiting factor for many applications, and there is active research worldwide targeted at the development of smaller and cheaper accelerators. Computer modeling is playing a key role in the progress toward bringing the size and cost down. It is essential for the optimization of existing accelerators, cost effective design and the development of game changing technologies. Thanks to sustained advances in hardware and software technologies, computer modeling is playing an increasingly important role. This rise in importance is further fuelled by the economic pressure for reducing uncertainties and costs of development, construction and commissioning, thus pushing the field toward an increase use of "virtual prototyping".

Until now, the development of accelerator codes has been largely left to projects without mandate and programmatic funding for coordination, distribution and user support. While this is adequate for the development of relatively small-scale codes on targeted applications, a more coordinated approach is needed to enable general codes with user bases that extend beyond individual projects, as well as cross-cutting activities. In light of this, it is desirable to strengthen and coordinate programmatic activities of particle accelerator modeling within the accelerator community. This increased focus on computational activities is all the more timely as computer architectures are transitioning to new technologies that require the adaptation of existing - and emergence of new - algorithms and codes.

Many computer simulation codes have been developed (over 70 worldwide) for the modeling of particle accelerators and beam transport. There has been little coordination of the development of the accelerator physics codes whose aggregate involves a mix of complementarity and duplication, and they are not all actively developed and maintained. Many of the codes have been developed by a single developer (often a physicist) for a specialized purpose or accelerator. Several multi-physics frameworks were developed by small teams, some in large part with the support of SciDAC, and are capable of incorporating many physics models. A substantial fraction of the codes is serial, but a number of the codes have been ported to parallel computers and some are capable of handling massive parallelism. A small fraction of the codes were ported to GPUs. Many of the codes are written in FORTRAN, C or C++, with a growing number combining the compiled language modules (for number crunching) with a Python scripting interface.

## THE VIEW OF THE COMMUNITY

The key roles of computing, and the needs for a more cohesive approach to development, maintenance, support and training have been recognized by the community, in the 2013 DOE-HEP Snowmass report [2], the 2014 Report from the Topical Panel Meeting on Computing and Simulations in High Energy Physics [3], and the 2014 P5 report [4].

Reports [2] and [3] recommended an increased coordination of modeling effort, dedicated support of code modernization, maintenance & dissemination, increase emphasis on use & development of common tools, better user support, and more training in HEP computational physics. In addition, [3] calls for the establishment of an HEP distributed center for computational excellence (single point-of-contact, cross-cutting activities). As a result, a Forum for Computational Excellence was created [5] aiming at promoting excellence in computing,

simulation, and data management across all of HEP science and technology.

The P5 report [4] underlines the key role of both accelerator research and computing, stating that:

- "the future of particle physics depends critically on transformational accelerator R&D to enable new capabilities and to advance existing technologies at lower cost."
- "The use of high-performance computing, combined with new algorithms, is advancing full 3-D simulations at realistic beam intensities of nearly all types of accelerators."
- "This will enable "virtual prototyping" of accelerator components on a larger scale than is currently possible."

These led to the recommendation 29 about computing that proposes to "strengthen the global cooperation among laboratories and universities to address computing and scientific software needs, and provide efficient training in next-generation hardware and data-science software relevant to particle physics. Investigate models for the development and maintenance of major software within and across research areas, including long-term data and software preservation."

Those reports and recommendations are consistent with community inputs that were submitted beforehand [6-8].

## NEED FOR ADIABATIC TRANSITION

The existing pool of codes is a result of significant investments from the community, and it is essential to minimize disruptions to developers and users, while enabling interoperability and expandability. This can be accomplished by adopting an incremental (near adiabatic) approach for transitioning from the existing collection of codes into a modular ecosystem of interoperable components that facilitate cooperation and reuse. It is also important that innovation in algorithms, which is a strength of the accelerator modeling community, is not hindered by the transition.

Challenges to the coordination of efforts are technical (different programming languages, data formats, parallelism strategies, or code architectures, open vs proprietary sources) and human (resistance to changing habits, different visions, trust, corporatism, rivalry, fear of loss of recognition, distance). A coordination that builds incrementally upon the existing tools and is not binding offers a path toward a smooth transition that mitigates many of the difficulties listed above. Hence, an approach is proposed that is based on bridging the codes at the outer (input and output) and inner (core functions) levels, enabling an incremental and non-disruptive transition, in contrast to the alternatives of down-selecting toward a handful of community codes, or coalescing toward a new unique code or framework. Such a strategy will open the way to creating an ecosystem combining the following: a unified input/output interface, shared functionalities, collaborative development of common units, "natural" down selection of modules, developers and users assembling new functions through creative combinations

of individual units that can be viewed as "Lego bricks" or "code genes".

The realization of this strategy is facilitated by the emergence of the scripting language Python as a language of choice in the scientific community for simulations management such as, e.g., steering, chaining, parametric studies, parallel parameter optimization. Thanks to its flexible interface to compiled languages like C, C++ and FORTRAN, it is even used as the frontend of an increasing number of codes: Warp, Synergia, Py-ORBIT, Py-ECLOUD, PyHeadTail, BLonD.

## CONSORTIUM FOR ADVANCED MODELING OF PARTICLE ACCELERATORS (CAMPA)

A new collaboration was formed to initiate a Consortium for Advanced Modeling of Particle Accelerators (CAMPA), spanning at present three major U.S. national laboratories (Lawrence Berkeley National Laboratory, SLAC National Accelerator Laboratory and Fermi National Accelerator Laboratory). The consortium is currently funded by the High Energy Physics program of the U.S. Department of Energy Office of Science, and its mission encompasses the following:

- push the frontier of accelerator science through advanced simulation and modeling; push the computing frontier in accelerator science through algorithmic advances;
- provide the scientific community with a comprehensive and integrated toolset of state-of-the-art simulation codes for multi-scale, multi-physics accelerator modeling, in support of the mission of the Office of Science within the Department of Energy (DOE);
- develop and maintain the codes on DOE's supercomputing facilities; distribute and support codes for installation on smaller scale clusters, desktops or laptops;
- support users;
- use the codes as education tools to train students and young researchers on the science and the modeling of accelerators;
- promote collaboration and re-use of accelerator simulation codes and data through common interfaces, data standards, and integrated visualization and analysis capabilities;
- establish a framework aimed at its extension to a national (possibly international) consortium.

## BENEFITS

Ultimately, the consortium is expected to benefit science, the funding agencies, the users and the developers. It offers a path toward game changer modeling tools leading to virtual prototyping and experiments, as well as online modeling for real time feedback on experiments. This will speed up design and innovation that will likely result in better accelerator and technology. This, in turn,

increases the rate of discoveries, providing higher return on investment to the funding agencies. The consortium also provides a singular point of contact for modeling activities to both the funding agencies and the users. To the latter, it also offers an integrated, comprehensive and more capable (multiphysics/multiscale) simulation tool solution. To the developers, the consortium provides a much needed source of funding that is dedicated to user support, algorithmic improvement, code implementation and maintenance, as well as recognition for accelerator software development, and more evident carrier paths.

# REFERENCES

[1] http://www.acceleratorsamerica.org

[2] "Computing Frontier: Accelerator Science", P. Spentzouris *et al.*, DOE's Community Summer Study Snowmass 2013; http://arxiv.org/abs/1310.2203

[3] "Computing in High Energy Physics", Report from the Topical Panel Meeting on Computing and Simulations in High Energy Physics, 2014 http://science.energy.gov/~/media/hep/pdf/files/Banner%20PDFs/Computing_Meeting_Report_final.pdf

[4] Report of the Particle Physics Project Prioritization Panel http://www.usparticlephysics.org/p5

[5] http://press3.mcs.anl.gov/hepfce/

[6] "White Paper on DOE-HEP Accelerator Modeling Science Activities", J.-L. Vay *et al.*, Input to Snowmass 2013 http://arxiv.org/pdf/1309.3541

[7] "Input to the P5 panel on DOE-HEP Accelerator Modeling Science Activities", J.-L. Vay *et al.*, December 2013 http://www.usparticlephysics.org/sites/default/files/webform/p5/P5_modeling_consortium.pdf

[8] Input to the HEPAP Accelerator R&D subpanel on: DOE-HEP, J.-L. Vay et al, http://www.usparticlephysics.org/sites/default/files/webform/ards/HEPAP_ARDS_modeling_consortium.pdf

# RECENT RESULTS FROM THE S-POD TRAP SYSTEMS
# ON THE STABILITY OF INTENSE HADRON BEAMS*

H. Okamoto[#], K. Ito, K. Fukushima, T. Okano,
AdSM, Hiroshima University, Higashi-Hiroshima 739-8530, Japan

*Abstract*

S-POD (Simulator of Particle Orbit Dynamics) is a tabletop experimental apparatus developed at Hiroshima University for systematic studies of various beam dynamic effects in modern particle accelerators. This novel experiment is based on an isomorphism between the basic equations governing the collective motion of a non-neutral plasma in a trap and that of a charged-particle beam in an alternating-gradient (AG) focusing channel. The system is particularly useful in exploring space-charge-induced collective phenomena whose accurate study is often troublesome in practice or quite time-consuming to simulate even with high-performance computers. This paper addresses recent experimental results on the stability of intense hadron beams traveling through long periodic AG transport channels. Emphasis is placed upon coherent resonances that occur depending on the lattice design, beam intensity, error fields, etc.

## INTRODUCTION

It is often difficult to perform systematic investigation of intense beam behavior not only in an experimental way but also in a numerical way. Experimentally, the overall lattice structure of a large machine is not changeable once it is constructed. Other fundamental parameters such as tunes, beam density, etc. are also not very flexible in general as long as we rely on real accelerators or beam transport channels. Although these parameters can be chosen freely in numerical simulations, high-precision tracking of charged particles interacting each other via the Coulomb fields is quite time-consuming even with modern parallel computers whenever the beam intensity is high. To overcome or lighten these practical difficulties that we face in fundamental beam dynamics studies, we proposed the concept "Laboratory Accelerator Physics" where the tabletop system called "S-POD" is employed instead of a large-scale machine to *experimentally* simulate the collective motion of high-intensity beams [1,2]. This accelerator-free experiment allows us to explore a wide range of parameter space simply by controlling the AC and DC voltages applied to the electrodes. Since everything is stationary in the laboratory frame, high-resolution measurements can readily be done and we do not have to worry about radio-activation due to heavy particle losses. S-POD experiment, indeed, has practical limitations [3], but it gives us useful insight into intense beam dynamics easily and quickly.

Three independent S-POD systems based on linear Paul traps (LPT) [4] were designed and constructed at Hiroshima University, which have been applied to different beam-physics purposes [2,5-7]. In this paper, we summarize recent experimental results from S-POD II and III on collective resonance instability depending on AG lattices. As mentioned above, such an experimental study cannot be conducted systematically in any real machine whose lattice structure is fixed. We here control the radio-frequency (rf) waveform of quadrupole focusing to emulate the beam behavior in several standard AG lattices involving doublet and FDDF sequence.

## S-POD

S-POD is composed mainly of a compact LPT, DC and AC power sources, a vacuum system, and a personal computer that controls a series of measurements and data saving. Figure 1 shows a side view of a typical multi-sectioned LPT employed for S-POD. Four cylindrical rods are symmetrically placed to generate the rf quadrupole potential for strong transverse focusing of ions. The transverse motion of an ion confined in a LPT is governed by the Hamiltonian [1]

$$H = \frac{p_x^2 + p_y^2}{2} + \frac{1}{2}K_{\mathrm{rf}}(\tau)(x^2 - y^2) + I\phi, \qquad (1)$$

where the independent variable is $\tau = ct$ with $c$ being the speed of light, $I$ is a constant depending on the ion species, and the function $K_{\mathrm{rf}}(\tau)$ is proportional to the rf voltage applied to the quadrupole rods. Since the collective Coulomb potential $\phi$ and the time-evolution of the ion distribution in phase space obey the Vlasov-Poisson equations, this many-body system is physically equivalent to a charged-particle beam traveling through an AG
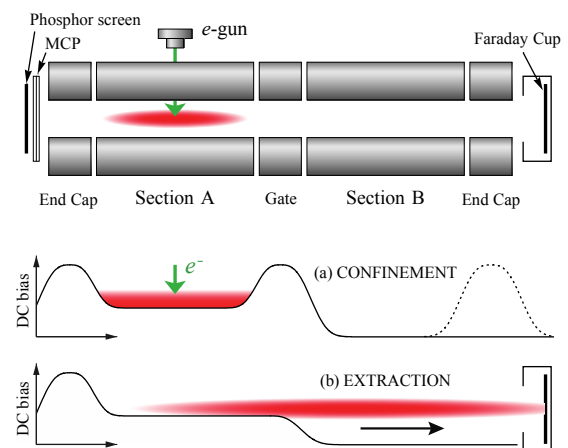


Figure 1: Typical measurement steps [8].

transport channel. We can thus study the fundamental features of intense beams by observing the collective behavior of an ion plasma in a LPT. Unlike the case of actual beam transport channels with many Q-magnets, the AG focusing function $K_{rf}(\tau)$ in S-POD is controllable over a wide range without any mechanical change to the trap geometry; all we need is to change the waveform of the rf voltage. It is possible to introduce imbalance between the horizontal and vertical focusing strengths if necessary, so that we can independently adjust the two bare tunes.

S-POD II and III are both operated at the frequency of 1 MHz (in the case of standard sinusoidal or doublet focusing). The ion species chosen for the present experiment is $^{40}Ar^+$. Then, the maximum rf amplitude required to survey the full tune space is less than around 100 V. As illustrated in Fig. 1, the quadrupole electrodes of the LPT are divided into five electrically isolated pieces in the axial direction. In addition to the transverse rf voltages, we add proper DC bias voltages to these five quadrupole sections to form a longitudinal potential well. After a necessary experimental procedure is completed, one of the longitudinal potential barriers is dropped to extract the plasma toward the Faraday cup or the MCP detector on the other side.

## DOUBLET FOCUSING

The rf power generator of S-POD has been designed to produce a wide range of stepwise waveforms. While the sinusoidal waveform is commonly used in regular LPTs, we have tried more complex waveforms including doublet, triplet, FDDF, etc [8]. Figure 2 shows a doublet waveform that has the quadrupole filling factor of 0.25. The distance from QF (focusing pulse) to QD (defocusing pulse) has been set equal to that from QD to QF in this example. The number of $^{40}Ar^+$ ions surviving after 10 ms ($10^4$ rf periods) in this AG potential is plotted in Fig. 3 as a function of the bare phase advance per single doublet cell. Since the horizontal and vertical focusing are symmetric, the phase advances $(\sigma_{0x}, \sigma_{0y})$ in both directions are identical; namely, $\sigma_{0x} = \sigma_{0y}(\equiv \sigma_0)$. We find three clear instability regions, all of which shift to the higher $\sigma_0$ side as the initial plasma density increases. Essentially the same stop-band distribution has been repeatedly observed in past S-POD experiments where the sinusoidal rf waveform was employed for transverse ion confinement [5-7]. According to a Vlasov theory [9] as well as past numerical work [10], the instability of the linear collective mode should be responsible for major ion losses near $\sigma_0 \approx 90$ [deg]. The other two stop bands near $\sigma_0 \approx 60$ and 120 [deg] are probably due to the third-order resonances. Since the instabilities near $\sigma_0 \approx 60$ and 90 [deg] are driven by the space-charge potential rather than external nonlinear error fields, these collective resonances are considerably weakened or even almost disappear at low density. We have carried out a number of stop-band measurements using various doublet waveforms with different geometric

factors. We then observe the same stop band distribution as indicated in Fig. 3 as long as the symmetric transverse focusing ($\sigma_{0x} = \sigma_{0y}$) is assumed.
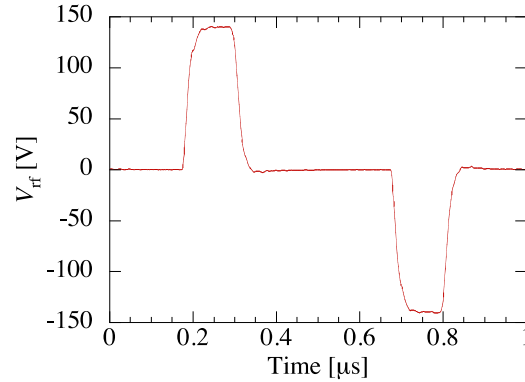


Figure 2: A doublet-type waveform produced by the rf power source of S-POD II.
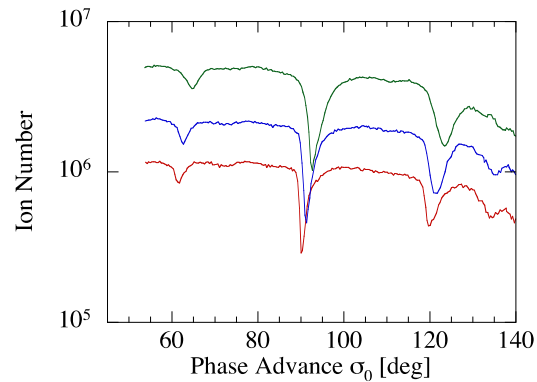


Figure 3: Resonance instability bands corresponding to the doublet focusing in Fig. 2.

## COUPLING RESONANCE

The ion losses near $\sigma_0 \approx 60$ and 90 [deg] in Fig. 3 should be caused by purely horizontal and vertical resonances overlapping each other. For instance, at $\sigma_0 \approx 90$ [deg], we have a possibility of relatively low order (2nd- and 4th-order) resonances independently in both transverse directions; namely, the conditions of primary resonances are given by $2\sigma_{0x} \approx 180$ [deg], $2\sigma_{0y} \approx 180$ [deg], $4\sigma_{0x} \approx 360$ [deg], and $4\sigma_{0y} \approx 360$ while the former two resonances become prominent only at high intensity [9]. Each of these stop bands splits into two parts when we introduce weak asymmetry in the transverse focusing strengths such that $\sigma_{0x} \neq \sigma_{0y}$ and then plot the stop band distribution as a function of either $\sigma_{0x}$ or $\sigma_{0y}$. On the other hand, coupling resonance lines that depend simultaneously on $\sigma_{0x}$ and $\sigma_{0y}$ may also be created if sufficiently strong error fields are present. The resonance condition at zero intensity is given by $m\sigma_{0x} \pm n\sigma_{0y} = (\text{integer}) \times 360°$ for the driving field of

the form $x^m y^n$ where $m$ and $n$ are positive integers. In the case of the lowest-order nonlinearity, i.e. sexupole, $(m, n) = (1, 2)$ or $(2, 1)$. To confirm the existence of such coupling resonance lines, we employed S-POD III driven by the sinusoidal rf waveform, instead of the doublet type, for the sake of simplicity. Figure 4 is the phase-advance diagrams experimentally obtained at different ion densities. The ion loss rate after a certain storage period is color-coded in the region of relatively high phase advances where we expect the occurrence of nonlinear coupling resonances [11]. The two third-order sum resonance lines can be identified while the forth-order difference resonance line $2\sigma_{0x} - 2\sigma_{0y} = 0$ is invisible in this data. We recognize the stop-band shifts depending on the plasma intensity. Recent S-POD experiments as well as 2D Vlasov analysis suggest that at high beam intensity, coupling resonance is expected to occur under the condition

$$m(\sigma_{0x} - \Delta\sigma_x) \pm n(\sigma_{0y} - \Delta\sigma_y) = (\text{integer}) \times 360°, \quad (2)$$

where $\Delta\sigma_x$ and $\Delta\sigma_y$ are the phase-advance shifts induced by the Coulomb potential. If this condition is correct, the vertical (or horizontal) shift of a coupling resonance line in the phase-advance diagram depends on the combination of the integers $m$ and $n$. For example, when $(m, n) = (2, 1)$ and $\Delta\sigma_x \approx \Delta\sigma_y$, the space-charge-induced shift of the sum resonance line is three times larger than that of the difference resonance. When $m = n$, the difference resonance line does not move depending on the plasma density (as long as $\Delta\sigma_x \approx \Delta\sigma_y$). In the case of a circular machine with the lattice superperiodicity of $N_{sp}$, the coupling resonance condition corresponding to Eq. (2) can be expressed as

$$m(\nu_{0x} - \Delta\nu_x) \pm n(\nu_{0y} - \Delta\nu_y) = kN_{sp}, \quad (3)$$

where $k$ is an integer, and $(\nu_{0x}, \nu_{0y})$ are the transverse bare tunes depressed by the amount of $(\Delta\nu_x, \Delta\nu_y)$ at high intensity.
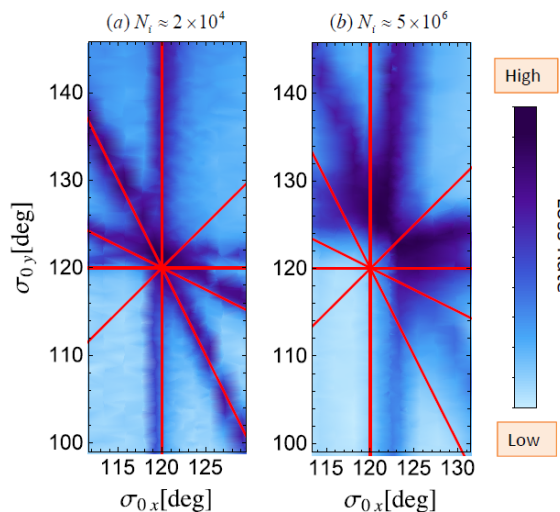


Figure 4: Resonance instability lines of sinusoidal focusing measured at different initial ion densities.

## FDDF SEQUENCE

The FDDF (or FFDD) waveform is another popular lattice often adopted in modern accelerators. One such example is the UNILAC at GSI [12]. Although the unit cell contains four quadrupoles (two are focusing and the other two defocusing in one transverse plane), we reasonably expect that the overall resonance behavior should be similar to that of the doublet focusing. Recent S-POD experiments actually revealed that the stop band distribution of the FFDD lattice is the same as what we observe in Fig. 3. Three instability bands are found near $\sigma_0 \approx 60$, 90, and 120 [deg]. The stop band at $\sigma_0 \approx 90$ [deg] usually gives rise to the most severe ion losses provided the initial plasma density is high. However, as already mentioned, this instability becomes quite weak at low density unless a non-negligible source of fourth-order external driving force exists.

### Highly Symmetric Ring

The three-stop-band feature as shown in Fig. 3 should be more or less universal among long linear transport channels whose structures are simple repetition of short focusing cells like FODO, symmetric doublet, and FFDD. In contrast, the resonance feature can be more complex in a circular machine because the focusing period is generally much longer. Each superperiod often contains several or more unit focusing blocks. The stored beam receives strictly periodic kicks every turn, even including imperfection fields. Such complex nature of a large closed system can make the stop-band distribution essentially different from that in Fig. 3.

Let us consider a circular machine consisting of $N$ FDDF cells [13]. According to our past experience with S-POD, the condition of the transverse collective resonance excited independently in either the horizontal or vertical direction by the $m$-th order space-charge force is likely to have the form [9]

$$m(\nu_{0x(0y)} - \Delta\nu_{x(y)}) \approx \frac{kN_{sp}}{2}, \quad (4)$$

where the coherent tune shifts $\Delta\nu_{x(y)}$ depend on the order number $m$. Sacherer first pointed out theoretically that $\Delta\nu_{x(y)}$ is somewhat smaller for a lower-order resonance at a specific beam density [14]. As for the coupling resonance driven by the potential $x^m y^n$, the resonance condition (3) should hold.

As an example, we assume $N = 50$. If all 50 FDDF cells are perfectly identical, $N_{sp}$ is also equal to 50. We then predict from Eq. (4) that the three stop bands as in Fig. 3 will appear at the tunes slightly above $50/6$, $50/4$, and $50/3$ in both transverse directions. The corresponding S-POD experiment was performed which resulted in the stop band distribution of Fig. 5(a) where $\nu_{0x} = \nu_{0y} (\equiv \nu_0)$ for simplicity. The number of ions initially stored in the trap is either $10^5$ or $10^6$. The ordinate represents the number of ions surviving after 100 turns around the 50-fold

Computational Challenges, New Concepts and New Projects

symmetric ring. We observe three instability regions as expected.

*Effect of Lattice Symmetry Breaking*

The proton synchrotron (PS) at CERN is composed of 50 FDDF cells [15], similarly to the example taken in the last section. Therefore, three stop bands in Fig. 5(a) must be found also at CERN-PS near the bare tunes $\nu_{0x(0y)} = 50/6$, $50/4$, and $50/3$ at high beam intensity even without imperfection fields. The actual focusing period around the ring is, however, not necessarily 50,
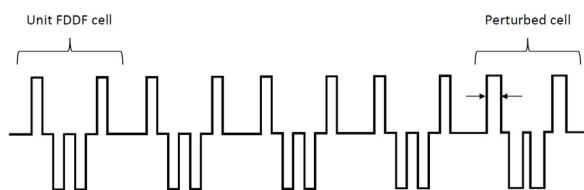
namely, $N_{sp} \neq N$, but the lattice functions may be less symmetric depending on the choice of the tunes and other parameters. For instance, we here look into the case where the external driving force has 10-fold symmetry around the ring; namely, $N = 50$ but $N_{sp} = 10$. A single lattice superperiod then contains five FDDF blocks. Such type of lattice symmetry breaking has been considered in a possible new optics of PS to ensure a larger distance from nearby nonlinear resonance lines [16]. Among a wide variety of ways to reduce the symmetry of the rf focusing force, in the present study we took the waveform as illustrated in Fig. 6. Each superperiodic cell consists of four identical FDDF blocks plus one more FDDF with a slightly different geometric factor. This long focusing wave repeats 10 times every turn around the ring. The corresponding stop-band distribution measured with S-POD II is shown in Fig. 5(b). In this experiment, we changed the quadrupole filling factor of the fifth FDDF block by 2% compared to the other four blocks (that have the filling factor of 0.5). The focusing and defocusing pulse shapes were chosen identical so that $\nu_{0x} = \nu_{0y}(\equiv \nu_0)$. In addition to the three stop bands, several more unstable regions appear due to the reduction of the lattice symmetry. Specifically, rather severe instabilities are newly excited near $\nu_0 \approx 5$, 10, 15, and 20. It is interesting to see that at least two independent ion-loss mechanisms are present within each of these new instability regions; there is always a relatively wide instability band accompanied by very sharp and heavy ion losses on the low tune side. We notice that the sharp stop bands do not move much depending on the ion density. Another series of S-POD experiments have demonstrated that these stop bands are widened as we enhance the perturbation to the fifth FDDF cell in each superperiod.



Figure 5: Resonance instability bands in a closed AG lattice consisting of 50 FDDF cells. (a) 50-fold symmetric case where all FDDF cells are identical. (b) 10-fold symmetric case where the pulse widths in every five FDDF cells are weakly perturbed as indicated in Fig. 6. The horizontal and vertical bare tunes are set equal in both cases.



Figure 6: FDDF waveform with a perturbed cell.



Figure 7: Resonance instability bands in the 10-fold symmetric lattice considered in Fig. 5(b). The two transverse tunes are not equal here but slightly different satisfying the relation $\nu_{0y} = \nu_{0x} + 0.02$.

It is also important to ask what happens when the transverse tunes are unequal (which corresponds to possible operating conditions of PS). To answer this question, we slightly modified all 50 FDDF pulses in an asymmetric way to develop imbalance between the horizontal and vertical focusing forces. Figure 7 shows the stop-band distribution obtained under the condition $\nu_{0y} = \nu_{0x} + 0.02$. Note that the measured data are plotted as a function of the vertical bare tune $\nu_{0x}$. We confirm that the major stop bands in Fig. 5(b) split into two instability bands. This implies that most stop bands observed under the symmetric focusing condition $\nu_{0x} = \nu_{0y}$ have been created by two independent (horizontal and vertical) resonances overlapping at the same tune. The two sharp ion losses at $\nu_{0x} \approx 14$ and 15 in Fig. 7 probably originate from the narrow stop band at $\nu_0 \approx 15$ in Fig. 5. Since the abscissa of Fig. 7 is $\nu_{0x}$, we assume that the ion losses staying at $\nu_{0x} \approx 15$ are due to horizontal instability while those shifted to $\nu_{0x} \approx 14$ occur vertically. On the other hand, it appears as if the narrow band at $\nu_{0x} \approx 10$ in Fig. 5(b) moved to $\nu_{0x} \approx 9$ without splitting, but we believe that there should still be the horizontal instability band at $\nu_{0x} \approx 10$ (which was too narrow to be detected in this experiment). In fact, we found very sharp instability at $\nu_{0x} \approx 10$ in another experiment performed under $\nu_{0y} = \nu_{0x} + 0.05$.

## SUMMARY

The S-POD systems at Hiroshima University have been employed to explore fundamental beam dynamics issues in particle accelerators. In the present experimental study, we focused on transverse resonance instability caused by the periodic nature of AG focusing lattices. Several standard AG waveforms, such as sinusoid, doublet, and FDDF, was taken to demonstrate how such instability arises depending on particle density, bare tunes, and lattice symmetry breaking. It has been verified that the stop-band distributions are similar in long transport channels simply repeating any of these short, symmetric AG waveforms. We always encounter the distribution as depicted in Fig. 3, no matter what waveform geometric factors are chosen for doublet and FDDF. Needless to say, the stop-band distribution becomes much more complex when a unit lattice period contains not one but many AG focusing blocks of non-identical geometries. In any case, the coherent resonance condition in Eq. (4) seems to roughly explain the locations of major horizontal and vertical stop bands observed at high beam density. (At low density, the factor $1/2$ on the right hand side should be omitted.) Provided relatively strong nonlinear coupling potentials are present, we also expect the sum and/or difference resonances excited under the condition of Eq. (3). The existence of such coupling resonance lines was confirmed in S-POD III using the sinusoidal focusing waveform.

An interesting stop-band behavior has been found when a highly symmetric closed lattice is perturbed to have lower symmetry (Fig. 5). The symmetry breaking excites additional instability regions, each of which often includes a very narrow stop band and a wider one on the right. The origin of such double stop bands that appear side by side is presently unclear. While preliminary particle-in-cell simulations suggest that nonlinear driving fields may be responsible for the excitation of the sharp stop bands, we still need further careful investigation to reach a definitive conclusion on this issue. We are now planning to develop a unique multipole LPT that enables us to control the time structure and strengths of low-order nonlinearity independently of the primary quadrupole focusing potential [17].

## REFERENCES

[1] H. Okamoto and H. Tanaka, Nucl. Instrum. Meth. A **437**, 178 (1999).

[2] H. Okamoto *et al*., Nucl. Instrum. Meth. A **733**, 119 (2014).

[3] The S-POD experiment described here is based on linear Paul traps that utilize only electric fields for particle confinement. It is thus impossible to exactly reproduce *dispersive* effects induced by dipole magnetic fields in circular machines.

[4] P. K. Ghosh, *Ion Traps* (Oxford Science, Oxford, 1995) and references therein.

[5] S. Ohtsubo *et al*., Phys. Rev. ST Accel. Beams **13**, 044201 (2010).

[6] H. Takeuchi *et al*., Phys. Rev. ST Accel. Beams **15**, 074201 (2012).

[7] K. Fukushima *et al*., Nucl. Instrum. Meth. A **733**, 18 (2014).

[8] H. Okamoto *et al*., FRXAA01, IPAC'14, Dresden, Germany, June 2014, p. 4052 (2014).

[9] H. Okamoto and K. Yokoya, Nucl. Instrum. Meth. A **482**, 51 (2002).

[10] See, e.g., M. Reiser, *Theory and Design of Charged Particle Beams*, John Wiley & Sons, New York (1994), and references therein.

[11] The ion storage period in the low-intensity experiment (left figure) was 100 $\mu$s while we extended the period to 1 ms at high intensity (right figure) to enhance the loss rate.

[12] L. Groening *et al*., Phys. Rev. Lett. **102**, 234801 (2009).

[13] We here ignore the effect from bending magnets.

[14] F. J. Sacherer, Ph.D thesis, Lawrence Radiation Laboratory [Report No. UCRL-18454, 1968].

[15] R. Wasef *et al*., WEPEA070, IPAC'13, Shanghai, China, May 2013, p. 2669 (2013).

[16] S. Machida, private communication.

[17] H. Okamoto, Y. Wada, R. Takai, Nucl. Instrum. Meth. A **485**, 244 (2002).

# BEAM DIAGNOSTICS FOR THE DETECTION AND UNDERSTANDING OF BEAM HALO

Kay Wittenburg, DESY, Hamburg, Germany

*Abstract*

A general view that has been recently reached by different methods of halo diagnostics of high brightness hadron beams will be given. The performance (dynamic range, accuracy …) of various monitor types will be combined with the demands from beam dynamics of different machines to discuss which methods can be envisaged for the future. The discussion will include low and high energy machines and their related halo detection schemes

## INTRODUCTION

Especially in the high power proton accelerator already a very small number of lost protons may cause serious radiation dose. In particle accelerator beam experiments, background due to beam halo can mask the rare physics processes in the experiment detectors. Both are unwanted effects of beam halo and therefore the high intensity beam quality is strongly connected to the existence of (transverse) beam halo. However, the definition of halo is still open:

In the summary of the HALO'03 workshop [1] is written: "…it became clear that even at this workshop (HALO'03) a general definition of "Beam Halo" could not be given, because of the very different requirements in different machines, and because of the differing perspectives of instrumentation specialists and accelerator physicists… ". At IPAC2014 [2] wrote: "It is very difficult to give a simple definition of the "halo". It could be a sole beam characteristic or a beam accelerator system characteristic linked to the potential losses it can produced. It could be defined by a number of particles (in the halo) or a size (of the halo). It could be described in the geometric space or in the phase-spaces… ".

This report has a look to "Halo" from the beam instrumentation point of view, that is focused more on the number of particles (in the halo) or on the size (of the halo); and on the dynamic range for halo measurements that should be of the order of $10^5$ or better (e.g. > 12 bit).

There are numerous sources of halo formation, in linear and circular accelerators, which are not discussed here. A good summary for that topic can be found in [3].

## WHAT IS BEAM HALO

It should be stressed that there is an important difference between beam tails and beam halo: Tails are deviants from the expected beam profile in the order of percent or per mille while halo goes much beyond. As a consequence one should note that the topic "emittance" is related to the beam tails only. The emittance of the beam

is defined by the core of the beam while including more or less of the tails. The emittance can be measured with special emittance measurement devices (e.g. pepperpot) and/or by profile monitors by knowing the β-function, momentum spread and dispersion at the location of the measurement (see e.g. [4]). A good profile monitor can reach a dynamic range of $\approx 10^3$ (e.g. > 8 bit), and a resolution of < 1% which is often sufficient for the emittance determination of the beam.

Unfortunately quite often the terms "tails" and "halo" are used in an undefined way. See Fig. 1 as an example of reported "halo" generation due to mismatch, while almost all effects happened in the tail regime. The reason of this uncertainty of definition might lie in the beam dynamics simulation tools which are very useful to understand the core beam behavior while computing with a limited number of particles. Therefore results in the real halo-regime have larger uncertainties or can't even be reached by these tools.

From the instrumentation point of view it is very useful to have a definition of halo in 1D spatial projection for which experimental measurements are easier to obtain by a beam profile/halo monitor. But note that the phase-space rotations of the beam might result in oscillations of the 1D projection along the accelerator. For example, at some locations the halo may project strongly along the spatial coordinate and only weakly along the momentum coordinate, while at other positions the reverse is true; with the consequence that the halo can be hidden from the 1D spatial projection [see e.g. 6]. For a complete understanding it is necessary to extend the 1D work to the whole phase space, in the measurement (resulting in many monitors at different location) as well as in the theoretical work and in the simulations [7, 8].

High power accelerators need very low losses during the beam transport to avoid serious activation and damage of components. Beam halo far beyond the beam core is one of the major reasons for these losses and therefore for activation of components. This can be illustrated by the following: Beam losses should be limited at least to a level which ensures hands-on-maintenance of accelerator components during shutdown. The hands-on limit has been found approximately between 0.1 W/m ≤ $H_L$ ≤ 1 W/m [9, 10]. Without any major beam disturbance losses are typically distributed along ½ of a β-period $L_β$ (typical near the focusing quadrupole). The fraction of losses which will generate the hands on limit activation is than:

$$H_W = H_L * \tfrac{1}{2} * L_β / P_B$$
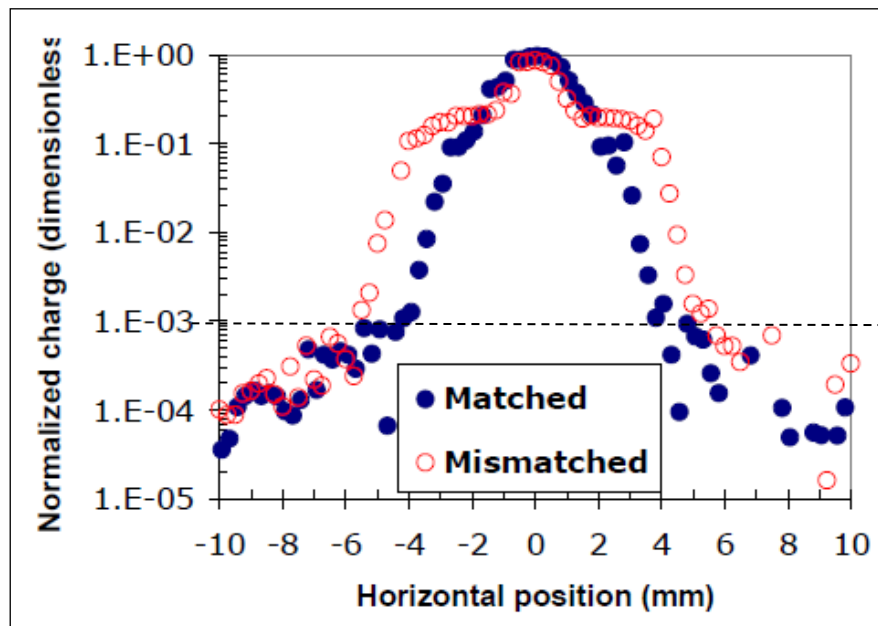
Figure 1: From [5]. Reported "Halo" generation due to mismatch. But note that almost no effect is observed below $10^{-3}$ (halo) while a large beam tail $> 10^{-3}$ is generated.

while $P_B$ is the total beam Power. Assuming a total beam power of $P_B = 1$ MW, $H_L = 1$ W/m and $L_\beta = 20$ m, it results in

$$H_W = 10^{-5}$$

## BEAM HALO QUANTIFICATION

A measurement of the halo should result in a quantification of the halo; at least in 1D spatial projection. Four different methods will be discussed shortly in the following which are used to characterize beam halo:

1) Kurtosis
2) Ratio of beam core to offset
3) Ratio of halo to core
4) Gaussian area ratio

An important feature of such quantifiers is that they are model independent and rely only on the characteristics of the beam distribution itself.

### 1) Kurtosis

This method is based on analyzing the fourth moment of the beam profile. The kurtosis k is a measure of whether a data set is peaked or flat relative to a normal (Gaussian) distribution:

$$k \equiv \frac{\left\langle (x - x_0)^4 \right\rangle}{\left\langle (x - x_0)^2 \right\rangle^2} - 2 \; ,$$

where $x_0$ is the beam center coordinate and x is the measured value of the profile distribution. The denominator is the standard deviation of the distribution and the numerator is the $4^{th}$ order moment. The sample kurtosis of n values with mean $x_0$ is defined by:

Therefore a constant loss of 10ppm of the beam is enough to reach the activation limit under these assumptions. These small losses can easily be generated by beam halo and halo monitoring might become useful to quantify the halo and finally to find measures to its generation.

$$k \equiv \frac{\frac{1}{n} \sum_{i=1}^{n} (x_i - x_0)^4}{\left( \frac{1}{n} \sum_{i=1}^{n} (x_i - x_0)^2 \right)^2} - 2$$

Distributions with high kurtosis have sharp peaks near the mean that come down rapidly to heavy tails. For more details see [7,11,12]. It is obvious, that this more theoretical method is much more sensitive to tails and almost not sensitive to halo.

### 2) Ratio of Halo to Core

[13] proposed recently a new method for determining the core-halo limit applicable to any particle distribution type: The core-halo limit is defined as the location where there is the largest slope variation in the density profile, i.e. where the density second derivative is maximum. A pure Gaussian profile with σ RMS has with such a definition already a halo starting from $\sqrt{3}*σ$, containing thus 8.3% particles of the beam while a triangular or K-V distribution does not have a halo. Since the largest slope variation is mainly created by the beam core, this method is quite sensitive to tails, too.

### 3) Ratio of Core to Offset

An experimentally robust technique to quantify the halo was used at Fermilab [14]. The raw data of the detector (profile monitor) are fitted to the function:

$$f(x) = g(x) \cdot l(x),$$

where g(x) is a Gaussian core

$$A \cdot e^{\frac{-(x-x_0)^2}{2\sigma^2}}$$

and l(x) is the non-Gaussian halo of the beam:

$$l(x) = c_0 + c_1 x.$$

Defining a region of interest (ROI) which includes the tails/halo of the interesting beam profile, one can define the properties L and G as

$$L = \int_{ROI} l(x)dx$$

and

$$G = \int_{ROI} g(x)dx.$$

The beam halo can be calculated by the ratio L/G. A perfectly Gaussian beam will have L/G = 0, whereas a beam with tails/halo will have L/G > 0. It is very important for this procedure to eliminate noisy and dead channels for the fit as well as knowing the pedestal for each channel. Each pedestal has to be subtracted from the data set. The standard deviation of many pedestal measurements can help to find noisy ($\sigma_{ped}$ is large) and dead channels ($\sigma_{ped}$=0). Studies have shown that the L/G method is a good indicator for beam tails by using a profile monitor. However, this method can easily extend into the halo regime e.g. by adding a second baseline below the beam tail and by using a halo monitor.

### 4) Gaussian Area Ratio

The method quantifies the "non-Gaussian" component of the beam profile by comparing a Gaussian fit of the core with the complete data set. Typically the Gaussian fit is applied to the top (90 percent) of the profile to represent the core (most beam core distributions can be represented by a Gaussian). The next step is to find the integral or area of the measured distribution (e.g. by summation of the midpoint [15]) and to normalize it to (divide it by) the area under the Gaussian fit. Since the core (±some σ) is the same in both cases one can use the area outside some σ only. The result (>1) gives a quantitative value of the halo content while a result =1 represents a beam without halo. If the measured distribution has also tails, one might use 2 gaussians to represent the core plus tails and compare it with the measured distribution.

### Comments

The methods 1) and 2) are quite sensitive to beam tails and not to beam halo but these are robust methods in simulations (with low numbers of particles) where the behavior of the beam in the tail region is studied. The methods 3) and 4) are more useful for beam halo measurements and large number of particles. With their help one can derive two halo parameters [13] which can be used to compare and optimize the accelerator settings:

PHS = 100 * Halo size/Total beam size

= Percentage of halo size

PHP = 100*Nb of particles in halo/total Nb of particles

= Percentage of halo particles

Note that a measurement always contains instrumental effects. To define the halo contents in such a theoretical way one has to exclude these effects in advance. Therefore a useful halo instrument and measurement should reach a resolution of (much) better than $10^{-2}$ of the beam size and a noise level $<< 10^{-5}$ of the beam peak. When comparing halo measurements with simulations it is obvious that even powerful simulations are useless if significant physical mechanisms are missing or if the beam input distribution is unrealistic.

## TRANSVERSAL HALO MEASUREMENTS

One can find two types of halo monitors; the first type measures the whole beam with very high dynamic range and very good resolution (e.g. wire scanner), the second type is a sensitive monitor at a more or less fixed transversal position which measures the rate of particles hitting this monitor (see e.g. [16, 17]).

Halo calibration of the second type is done by normalizing the measurement to the whole beam current resulting in PHP. Moveable scrapers equipped with beam loss monitors fall into this type although the distribution of the halo can be measured by moving the jaws and recording the loss rate [18]. Since a cross calibration with a beam current monitor is required, the resulting resolution in terms of an absolute number of halo particles might be limited but a relative observation of changes in the halo can be done with very high resolution.

A detailed discussion of the first halo monitor type can be found in [19] and references herein (some additional references are listed below). One of the most used halo monitors are wire scanners which are able to measure the profile of the whole beam (PHS) with very high dynamic ranges and very good resolution (< 10 microns). Various techniques are used to archive dynamic ranges up to $10^8$, including counting techniques at high and at low energies [20] and vibrating wire techniques [21]. Since scanning techniques are often very time consuming (up to minutes), optical methods can be much faster: [22] reported recently results of using different types of screens with higher sensitivity in the tails and halo regime. For a high dynamic readout of screens CID cameras with a dynamic range of $\approx 10^6$ are commercial available. Scintillation screens might be limited in their linearity but OTR screens did not show any saturation effects even at these high dynamic ranges. Adaptive masking techniques with micro mirror arrays [23] and by coronagraph [24] show reliable beam halos of smaller than $10^{-6}$.

## CONCLUSION

Some definitions of halo have discussed in this report showing the requirement to distinguish clearly between the halo and tail of the beam. Different methods of quantization of halo were discussed in view of their sensitivity to tails and to their utility to halo

measurements. The "state of the art" instrument for a full horizontal halo measurements is still the wire scanner; a dynamic range of better than $10^8$ has been achieved. Optical methods using readout by a CID camera or a coronagraph have the potential to reach even higher dynamic range.

# REFERENCES

[1]  P. Camron, K. Wittenburg, "Halo Diagnostics Summary", 29th ICFA Advanced Beam Dynamics Workshop on Beam Halo Dynamics, Diagnostics and Collimation, Halo'03, May 19-23, 2003, Long Island, New York.

[2]  N. Pichoff et al, "Calculations of Halo in TraceWin Code", 5th International Particle Accelerator Conference IPAC'14, Dresden, Germany, June 15 - 20, 2014.

[3]  A. V. Fedotov, "Mechanisms of Halo Formation", 29th ICFA Advanced Beam Dynamics Workshop on Beam Halo Dynamics, Diagnostics, and Collimation, Halo'03, May 19-23, 2003, Long Island, New York and References therein.

[4]  K. Wittenburg, "Specific Instrumentation and Diagnostics for High-Intensity Hadron Beams", CERN Accelerator School on High Power Hadrons Machines, Bilbao, Spain, 2011, CERN-2013-001.

[5]  T.P Wanger, "Physics Results from the Los Alamos Beam-Halo Experiment", 29th ICFA Advanced Beam Dynamics Workshop on Beam Halo Dynamics, Diagnostics and Collimation, Halo'03, May 19-23, 2003, Long Island, New York.

[6]  Hongping Jiang et al, "Beam Dynamics Analysis in the Beam Halo Experiments at IHEP", 5th International Particle Accelerator Conference IPAC'14, Dresden, Germany, June 15 - 20, 2014.

[7]  C. K. Allen, T. P. Wangler, "Beam Halo Definitions based upon Moments of the Particle Distribution", Physical Review Special Topics – Accelerator and Beams, Vol. 5, (2002).

[8]  J. Qiang, et al., Macroparticle simulation studies of a proton beam halo experiment, *Phys. Rev. ST Accel. Beams,* **5** (2002) 124201.

[9]  O. E. Krivosheev, N. V. Mokhov, "Tolerable Beam Loss at High-Intensity Proton Machines", FERMILAB-Conf-00/192 August 2000, Proc. ICFA Beam Halo and Scraping Workshop, Lake Como, WI, Sep 13-15, 1999.

[10] T. Wangler, RF Linear Accelerators, Wiley & Son, p 285.

[11] T. P. Wangler et al., "Beam Halo in Proton Linac Beams", Linac 2000, 10th International Linac Conference, August 21 - 25, 2000, Monterey, California.

[12] C.K. Allen, T.P. Wangler, "Parameters for Quantifying Beam Halo", Proc. of the 2001 Particle Accelerator Conference; PAC2001, Chicago, Illinois USA. June 18-22, 2001.

[13] P.A.P. Nghiem et al., "A Precise Determination of the Core-Halo Limit", 5th International Particle Accelerator Conference IPAC'14, Dresden, Germany, June 15 - 20, 2014.

[14] J. Amundson et al., "An experimentally robust technique for halo measurement using the IPM at the Fermilab Booster", Nuclear instruments & methods in physics research; Section A, 2007, Vol. 570, no1, pp. 1-9.

[15] D. A. Bartkoski et al., "The Development of Computational Tools for Halo Analysis and Study of Halo Growth in the Spallation Neutron Source Linear Accelerator", Proc. 10th European Particle Accelerator Conference, EPAC06; June 26 - 30, 2006, Edinburgh, Scotland.

[16] A. Ignatenko et al., "Beam Halo Monitor for FLASH and the European XFEL", 3rd International Particle Accelerator Conference IPAC'12, New Orleans, USA, May 20 - 25, 2012.

[17] Z. Liu et al., "Ion Chambers and Halo Rings for Loss Detection at FRIB", 3rd International Particle Accelerator Conference IPAC'12, New Orleans, USA, May 20 - 25, 2012.

[18] H. Burkhardt, I. Reichel, G. Roy, "Transverse Beam Tails due to Inelastic Scattering", CERN-SL-99-068

[19] K. Wittenburg, "Overview of recent halo diagnosis and non-destructive beam profile monitoring", Proc 39th ICFA Advanced Beam Dynamics Workshop on High Intensity High Brightness Hadron Beams, HB2006, 29 May – 2. June 2006 Tsukuba, Japan. and K. Wittenburg, "Beam Halo and Bunch Purity Monitoring", CERN Accelerator School on Beam Diagnostics, Le Normont Hotel, Dourdan, France 28 May - 6 June 2008, CERN-2009-005.

[20] R. Dölling, "Bunch-Shape Measurements at PSI's High-power Cyclotrons and Proton Beam Lines", 20th International Conference on Cyclotrons and their Applications (CYCLOTRONS'13), Vancouver, British Columbia, September 16th to 20th, 2013.

[21] K. Okabe et al., "A Preliminary Study of the Vibration Wire Monitor for Beam Halo Diagnostic in J-PARC L3BT", 4th International Particle Accelerator Conference, IPAC13, Shanghai, China, 12th to 17th May, 2013.

[22] T. Mitsuhashi et al., "Two-dimensional and wide-dynamic-range profile monitor using OTR/fluorescent screens for diagnosing beam halo of intense proton beam", Talk at the Workshop on Beam Halo Monitoring, 19 Sept., 2014, SLAC National Accelerator Laboratory.

[23] B.B.D. Lomberg, C.P. Welsch., "Beam Halo Monitor Based on an HD Digital Micro Mirror Array", 2nd International Beam Instrumentation Conference (IBIC13), Oxford, UK, 16-19 Sept. 2013.

[24] T. Mitsuhashi et al., "Coronagraph for diagnosing beam halo", Talk at the Workshop on Beam Halo Monitoring, 19 Sept., 2014, SLAC National Accelerator Laboratory.

# TWO-DIMENSIONAL AND WIDE DYNAMIC RANGE PROFILE MONITOR USING OTR /FLUORESCENCE SCREENS FOR DIAGNOSING BEAM HALO OF INTENSE PROTON BEAMS

Y. Hashimoto[#], T. Mitsuhashi, M. Tejima, T. Toyama, KEK/J-PARC, Tsukuba/Tokai, JAPAN
H. Akino, Y. Omori, S. Otsu, H. Sakai, Mitsubishi Electric System & Service Co., Ltd., JAPAN

*Abstract*

The use of Optical Transition Radiation (OTR) and fluorescence screens to obtain a high dynamic range approximately six orders of magnitude in light intensity for two-dimensional beam profile measurement was demonstrated with intense 3GeV proton beams in the J-PARC in 2013[1]. A new four-section alumina screen for beam-halo measurement was installed just in front of the pre-existing titanium screen this year in order to measure the beam halo and the beam core simultaneously. Two-dimensional beam profile measurements with a high dynamic range are described in this paper.

## INTRODUCTION

The objective was to measure the two-dimensional intensity distribution from the beam core to the beam halo of the injection beam to the Main Ring (MR) of the J-PARC. The beam halo brings serious contamination by radio-activation to the accelerator by beam losses in the case of beam intensities greater than $1.5 \times 10^{13}$ / bunch. In order to measure such a beam profile, a high dynamic range up to six orders of magnitude in light intensity was required. By using such a wide measurement range, we can
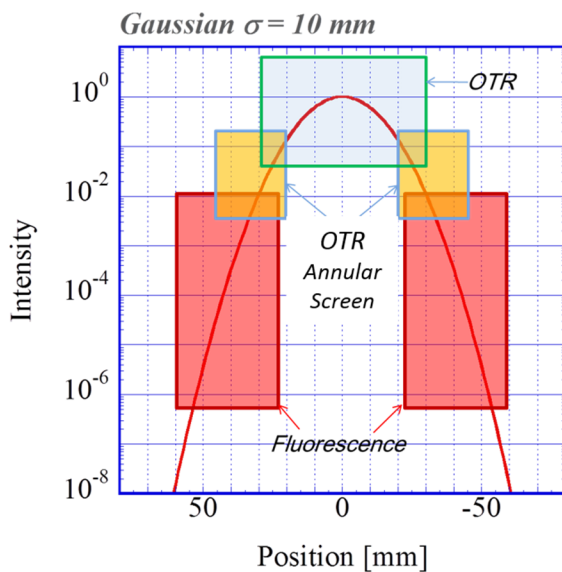


Figure 1: Six orders of magnitude measurement with three kinds of screens.

not only evaluate the beam-halo eliminations by the collimator, but also perform precise beam diagnosis for the

# yoshinori.hashimoto@kek.jp

Rapid Cycling Synchrotron (RCS) in beam extraction, which is a preceding accelerator of the MR.

## CONCEPTS

*Function of OTR and Fluorescence*

We used the OTR from the titanium screen and the fluorescence from the chromium-doped alumina screen. Optical intensities of the light depend on the beam intensity at the positions of these screens. In order to detect the light, a Charge-Injection-Device (CID) camera attached to a gated Image Intensifier (II) was employed. The gain of the II was optimized for these optical intensities.

Figure 1 shows the functional range for each kind of screen. The beam intensity distribution curve shown in the figure assumes that the beam intensity is over $10^{13}$ proton/bunch and the sigma of the Gaussian distribution is 10 mm. The measurement techniques and their ranges are as follows: the OTR from the beam core covers down to -1.5 orders of magnitude, the next OTR from the beam tail from the 50 mm diameter annular screen covers down to -2.5 orders, and finally the fluorescence from the beam halo covers down to almost -6 orders from the peak.

*Energy Losses in Screens*

The screen materials for intense proton beams should be chosen carefully. Preferred materials include a 10 micron thick titanium foil for the OTR production and alumina screens of 500 μm thickness for the fluorescence production. As for the energy loss with 3 GeV proton beam, alumina has 48 times larger loss than titanium as shown in Table 1. However, when it is only used in the halo region where the intensity is two orders of magnitude lower than the peak values, the total energy loss of alumina becomes about half of that of titanium: i.e. 4.7e-3 J/bunch equivalent. These energy losses are small enough to avoid damaging the screens.

Table 1: Energy losses in material [2] in the case of proton beam energy of 3 GeV, and bunch intensity of 1 x $10^{13}$ protons.

| Material | Thickness [μm] | Energy Loss [keV/proton] | Total Energy Loss [J/bunch] |
|---|---|---|---|
| Ti | 10 | 6.79 | 9.8e-3 |
| Cr + Al$_2$O$_3$ | 500 | 330 | 4.7e-1 |

(a)



(b)
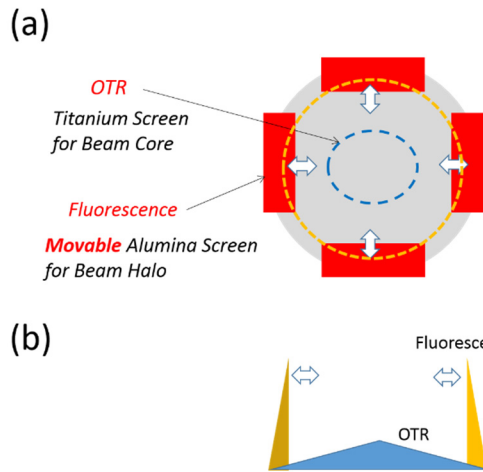


Figure 2: Configuration of screens. (a) Front view, (b) A layout of horizontal projected beam profiles.

## Configuration of Screens

Figure 2 shows the configuration of the screens. The grey circle is the titanium foil screen for OTR production by the beam core. Immediately in front of the circle, four red rectangles indicate the alumina screens located in the beam halo region. These alumina screens are movable in the horizontal and the vertical directions as shown.
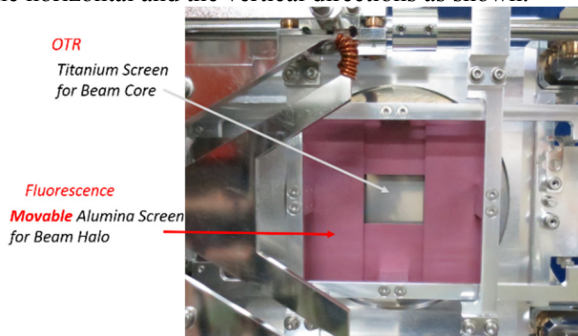


Figure 3: A photograph of the screens from the front side. The titanium screen positioned to the rear is of triple screen construction (Fig.4).

These screen targets consist of layered structures, as shown in Figs.3 and 4. The front side of the target is a new four-section alumina screen which was installed this year. The aperture between the edges of the opposed screen can be changed from 125 mm down to 30 mm, in both the horizontal and vertical directions.

The rear side of the target is the pre-existing triple screen [1] shown in Fig. 4, which is inserted just after the four-section alumina screen. Figure 5 shows a sectional layout of these screens. The alumina screen is located 13 mm in front of the titanium screen. Shadow masks made of 0.5-mm thick stainless steel were put on the back of the alumina screen to prevent the fluorescence from lighting up the titanium screen. The OTR with an angular distribution [1] is emitted from the titanium screen, in contrast, the fluorescence radiates isotropically.
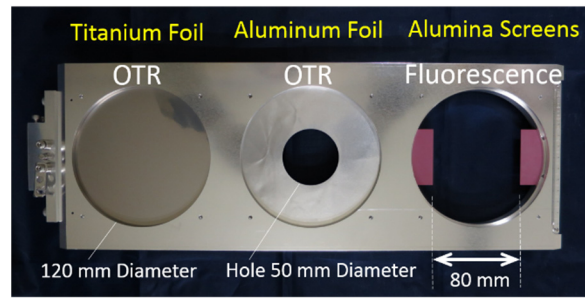


Figure 4: Triple screen geometry
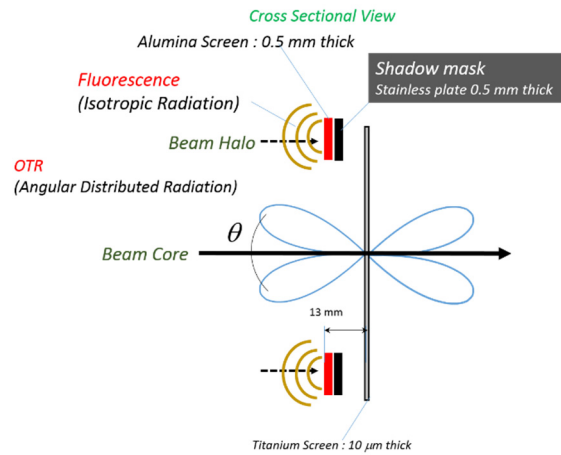


Figure 5: Cross-sectional view of the target screen

(a)



(b)
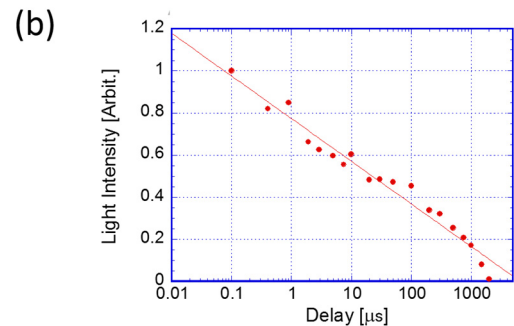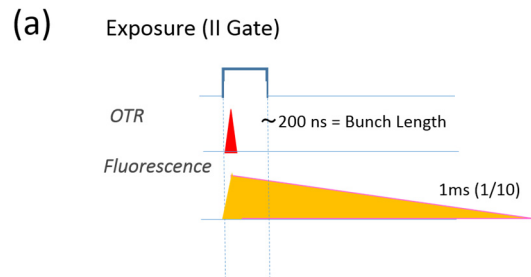


Figure 6: Fluorescence time of alumina with 3 GeV proton. (a) Schematic comparison with the emission time of OTR, (b) Measured data were taken by sweeping the gate timing of the II with a gate width of 10 µs.

## Persistence Times

The persistence time of the fluorescence from the alumina screen was over 1 ms as shown in Fig.6 (b). These data were measured with a 3 GeV proton beam. The fluorescence decays logarithmically.

On the other hand, the OTR emits for only about 200ns, corresponding to the length of the beam bunch (Fig.6 (a)).

It is an advantage that the yield ratio of the fluorescence to the OTR can be controlled by changing the exposure time of measurement with the gate of the II.

## DEVICE CONFIGURATION

Figure 7 shows the device configuration schematically. Devices drawn within the skeleton frame of the vacuum chamber [1] were pre-existing at the 3-50 Beam Transport line (3-50 BT) in the J-PARC, in addition, the new four-section alumina screen (Fig.3) was installed at the target point this year. The Offner optical system has a large acceptance angle of ±15 degrees for focusing the OTR [1] having larger peak-spread angle of ±13.5 degrees. We observe a beam image focused on the projection screen within the vacuum chamber from the back side with the II attached CID camera located outside across a viewport.
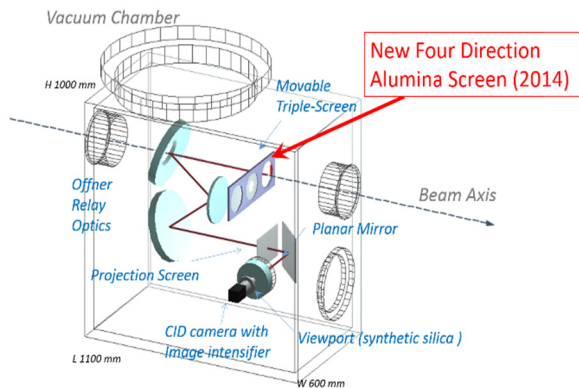


Figure 7:  Device configuration.

## SCALING FOR UNIFIED PROFILE

The features of our method to obtain higher dynamic ranges are as follows: i) the gain of the II is optimized depending on the region of the beam to be measured, ii) two kinds of light with different emission efficiencies are
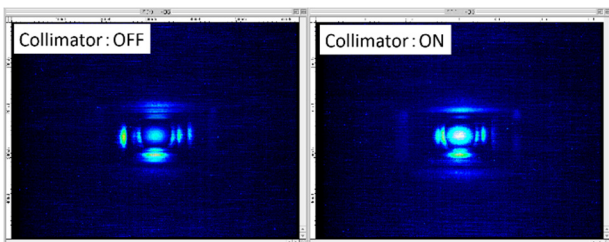


Figure 8: Superimposed beam images with 25 different various alumina screen positions each.

employed, namely the OTR and the fluorescence.  For this reason, the pixel intensities of the image data must to be scaled to obtain a unified beam profile. We use two coefficients in this scaling as follows: i) the gain value of the II in measurement as G, ii) the yield ratio of the fluorescence to the OTR as $Y_R$. Thus, we scaled the pixel data with a simple treatment as follows,

$$\text{OTR data scaled} \quad \rightarrow \quad \text{data}/G \qquad (1)$$

$$\text{Fluorescence data scaled} \quad \rightarrow \quad \text{data}/G/Y_R \qquad (2).$$
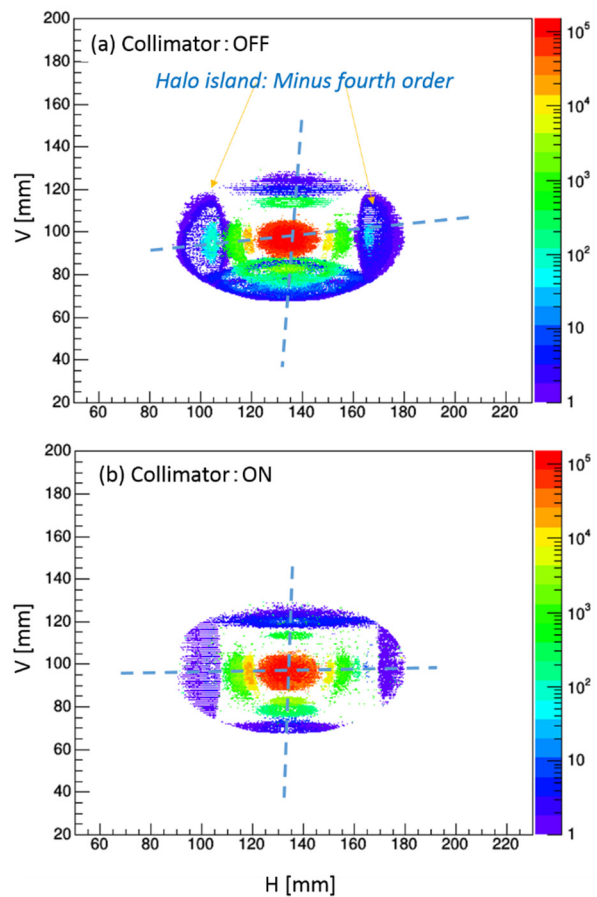


Figure 9:  Two-dimensional color contour map with log scale obtained by the scaling. (a) Collimator OFF, and (b) Collimator ON.

We have obtained $Y_R$ by comparison of actual light quantity between the fluorescence and the OTR with a measurement [1]. In our usual case, the gate time of the image intensifier was 10 μs, and then $Y_R$ was measured as 1314.6.

## COMBINATION MEASUREMENT WITH OTR AND FLUORESCENCE

### Effect of Beam-Halo Elimination

The effects of the beam-halo elimination by the 3-50 BT collimator [3] were examined from the point of view of the two-dimensional beam distribution. Figure 8 shows superimposed beam images which were taken by changing the position of the alumina screens 25 times in the horizontal and in the vertical directions with a certain distance step. The gain of the II was changed to the appropriate value in each step. So with these pictures alone we cannot properly understand the beam shapes and the distributions; these data must be modified with the scaling treatment shown in equations (1) and (2). After the scaling,
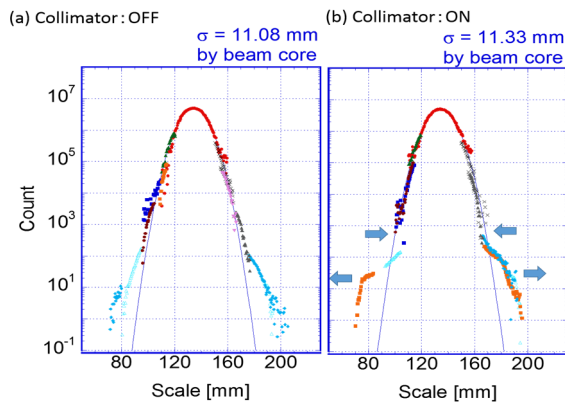
Figure 10:   Projection beam profiles in the horizontal direction. (a) Collimator OFF, and (b) Collimator ON.

two-dimensional colored contour maps with log scale are obtained as shown in Fig. 9. The color scale is five orders of magnitude from red to blue.

   It is a remarkable collimator effect that islands of the beam halo appeared on both the right and left sides of the minus fourth order in the case of collimator-OFF, but they disappeared in the case of collimator-ON. In addition, two dashed lines can be drawn in each map which link the center of the regions of the beam halo at the top and the bottom sides, or the regions of the left and the right sides. In case of collimator-OFF, these lines had significant angular difference from the horizontal and the vertical
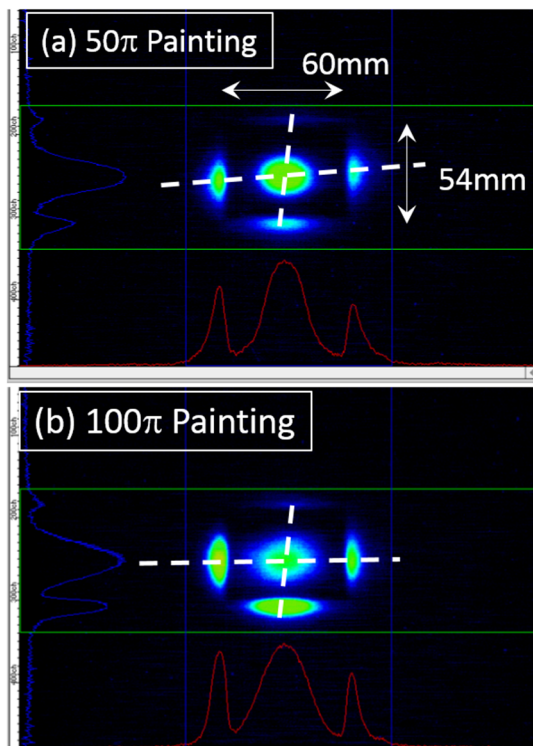


Figure 11: Simultaneous measurement of the beam core and the halo at minus fourth order. The difference between the two beam images is the size of the injection painting area of the RCS.

axes, respectively. But in case of collimator-ON, the angular displacement became smaller.

   The horizontal-projection profiles of these data of Fig. 9 are plotted with a vertical log scale in Fig. 10. The solid lines in the plots are the Gaussian curves fitted with only the beam core measured by the OTR from the solid titanium screen. In both cases of collimator-OFF and -ON, the sigma of the Gaussians has the almost same value of 11 mm. And down to around the minus fourth order from the peak, the measured data agree with the Gaussians. In the case of collimator-ON, a waist occurred at about the minus fourth order and the beam size at the minus sixth order or less was expanded. Plotted points can be seen down to the minus seventh order, in these regions the beam sizes spread up to 120 mm. This value of 120 mm is the limit of this instrument, because the apertures of the upper mirror hole of the Offner optical system, of the titanium solid screen, and of the projection screen are all 120 mm.

*Simultaneous Measurement of the Beam Core and the Halo*

   A simultaneous measurement of the beam core and the beam halo was carried out by using the titanium screen and the four-section alumina screen. The following measurement examples examined a correlation of injection beam-painting [4-6] conditions in the RCS and the beam halo of injection beams of the MR. In the measurement the edge distance of the horizontal alumina-screen pair was 60 mm, and that of the vertical pair was 54 mm. In this way the beam halo at the minus forth order could be measured at the same time as the beam core, as shown in Fig.11. Each measurement was averaged over five shots with beams consisting of two bunches having an intensity of $3.2 \times 10^{13}$ protons. Two-dimensional beam profiles were measured with different conditions in painting area of the RCS beam injection as $50\,\pi$ and $100\,\pi$ mm.mrad. Their projections are shown in Fig. 12.

   In Fig. 11, the dashed lines mean the same as before; they link the centers of facing pairs of the beam-halo regions. The horizontal dashed line links the left and the right sides of the beam-halo region in the beam image of 50   painting; in this case a remarkable counter-clockwise rotation appeared, although there was no rotation of the beam core. The beam of 100   painting, unlike with the beam of 50 pi painting, under the fourth-order, the height of the peak of the beam halo was around two times larger in the horizontal direction, and the beam halo at the bottom became remarkably large in the vertical direction. When these beams were injected into the MR, the beam loss was significantly smaller in the case of the 50   beam than in the case of the 100   beam. The rotation shown in the beam image was assumed to be caused by so-called xy-coupling. By taking advantage of the two-dimensional measurement technique, asymmetric beam halos could be measured.
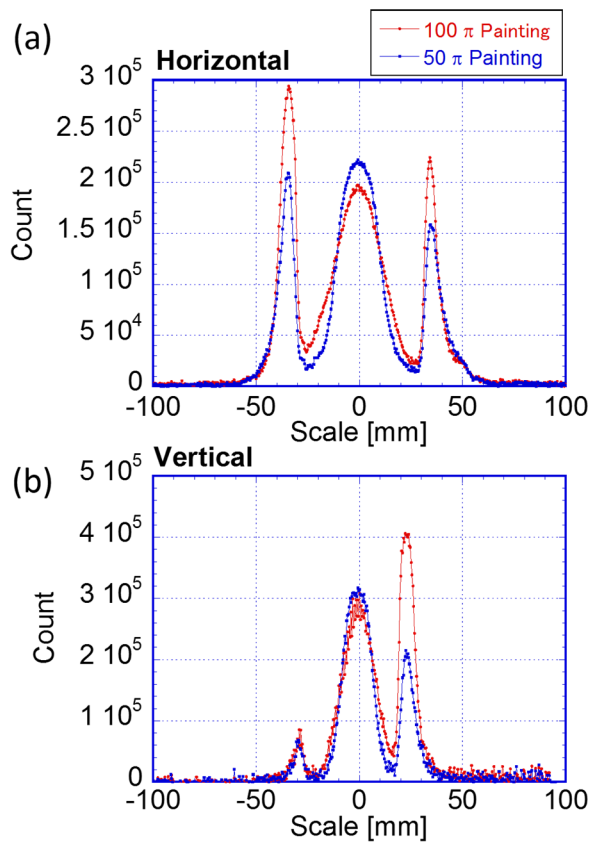
Figure 12: Projections of beam images shown in Fig. 11, (a) in the horizontal and (b) in the vertical directions

### Next Steps

The previous simultaneous measurements mentioned above had a gap between the beam core and the beam halo. We have already mentioned above a simple method for the simultaneous measurement so that the gap between the beam core and the halo is almost closed. For such a detection, a detector having around three orders of magnitude of dynamic range should be used, for example, a CMOS camera. And both the light intensity of the OTR from the beam core and the fluorescence from the beam halo should be put in the detector range.

Firstly, it is supposed that two orders of the beam core intensity is to be measured with OTR and three orders of the beam halo is to be measured with fluorescence as indicated in Fig. 13(a). Next, as shown in Fig. 13(b), the fluorescence should be amplified one thousand times more than the OTR. This amplification is achieved by adjusting exposure time with the gate time of the II as mentioned above in the sub-section on persistence time. Finally three orders from the peak of the fluorescence with the OTR should be measured by a camera with appropriate II gain. In order to use such a CMOS camera, note that the camera should be treated with sufficient radiation shielding to reduce the radiation dose down to about several hundred mGy/week.
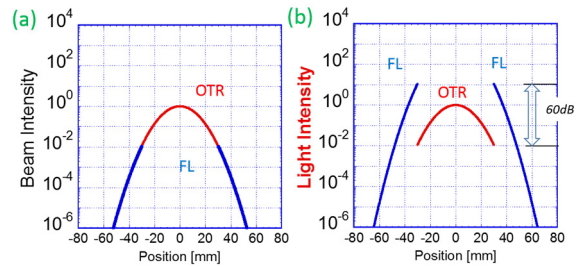


Figure 13: Adjustment of light yield ratio of the fluorescence to the OTR (FL/OTR) for simultaneous measurement of the beam core and the beam halo. (a) Beam intensity distribution curve with the kind of light to be measured denoted by line-color. (b) Light intensity distribution curve in the case where FL/OTR equals one thousand.

## CONCLUSIONS

A two-dimensional, high dynamic range profile monitor was developed for intense proton beams by using a combination measurement of the OTR from the beam core with the titanium foil screen and the fluorescence from the beam halo with the alumina screens. Projection beam profile with a dynamic range of around six orders of magnitude was measured for a proton beam whose intensity was about $1.5 \times 10^{13}$ protons / bunch. The asymmetric beam shape or the rotation in the transverse plane, including the halo, were measured by taking advantage of two-dimensional beam measurement. These results greatly benefit the investigation of beam dynamics.

## REFERENCES

[1] Y. Hashimoto, et al., Proc. IBIC2013, Oxford, 338-341.
[2] ICRU Report 49, Stopping Power and Ranges for Protons and Alpha Particles.
[3] M. J. Shirakata, et al., Proc. IPAC2010, Kyoto, Japan, 4246-4248.
[4] P.K. Saha et al., PRST-AB, Accel. and Beams 12, 040403 (2009).
[5] H. Hotchi et al., PRST-AB Accel. and Beams 15, 040402 (2012).
[6] P.K. Saha et al., PRST-AB Accel. and Beams 16, 120102 (2013)

# UNDERSTANDING BEAM LOSSES IN HIGH-INTENSITY PROTON ACCUMULATOR RINGS*

Robert J. Macek[#] and Jeffrey S. Kolski, LANL, Los Alamos, NM 87545, USA

## Abstract

Beam losses and the resulting radio-activation of accelerator components are major considerations governing the operations and performance of medium-energy, high-intensity proton accumulator rings using H-charge exchange injection such as the Los Alamos Proton Storage Ring (PSR). Several beam loss mechanisms contribute including beam scattering (nuclear and large angle Coulomb scattering) in the injection foil, production of excited states of H0 in the H- injection stripper foil that subsequently field strip in the magnetic fields down stream of the foil, halo growth from space charge effects, beam instabilities and losses from the fast extraction process. These are now well understood based on the progress in the diagnosis, measurement, and modeling of beam losses at PSR and related rings. The roles of the computer codes MAD8 [1], ORBIT [2], G4Beamline [3], and others used in modeling beam losses are discussed, and the modeling results are compared with relevant experimental data.

## INTRODUCTION

Minimizing uncontrolled beam losses is one of the most important objectives in the design, operations and development of high-intensity proton accumulator rings that use many hundreds to thousands of turns of H-charge exchange injection such as the Los Alamos Proton Storage Ring (PSR) or the accumulator ring for the Spallation Neutron Source (SSN) at the Oak Ridge National Laboratory.  Similar concerns hold for the rapid cycling synchrotrons at the heart of the spallation neutron sources at the Rutherford Appleton Laboratory in the UK and the Japan Proton Accelerator Complex (J-PARC). To limit radio-activation of accelerator components in order to permit hands-on maintenance, it has become a rule-of-thumb to limit uncontrolled beam losses to the 1 Watt/meter level.

The Los Alamos PSR was a pioneering effort in the use of charge exchange injection for a full power, high intensity accumulator ring to drive a short pulse spallation neutron source [4]. Much has been learned about beam losses in this ring since first beam in 1985.  Until 1998, PSR used a two-step injection process i.e., stripping of H- to H0 in a high field dipole then stripping to H+ in a stripper foil.  By 1993 the beam losses for the two-step injection were reasonably well understood and had been reduced significantly by a number of improvements [5]. It should also be noted that by 1993, it was shown that the 0.2-0.3% fractional losses on the first turn were explained

by the production and stripping of H0(n=3, and 4) excited states produced in the stripper foil that subsequently Lorentz strip in the first dipole down stream of the injection foil [6].

In 1998, the upgrade of PSR to direct (one step) H-injection was completed [7] and resulted in a factor of ~3 reduction in the fractional beam losses.  PSR has since then operated at 100-125 μA with total fractional uncontrolled losses of 0.2% - 0.3%.

## PSR LAYOUT

A layout of PSR after the 1998 upgrade is shown in Figure 1. It is a small ring of 90.2 m circumference with 10 sections and FODO lattice.  In normal operations, 800 MeV beam is accumulated for ~1750 turns to provide 100-120 μA (5-6 μC/pulse) at 20 Hz for the main user, the LANSCE spallation neutron source at the Lujan Center.  The "waste" beam i.e., H- that did not strip and H0 is transported via a large aperture beam line to a graphite beam dump capable of handling 10 μA or 8 kW of beam power.  Single turn extraction is accomplished with two strip line kickers and a septum magnet system. It is worth noting that in high peak intensity beam studies, as much as 10 μC was successfully accumulated in 3400 turns.
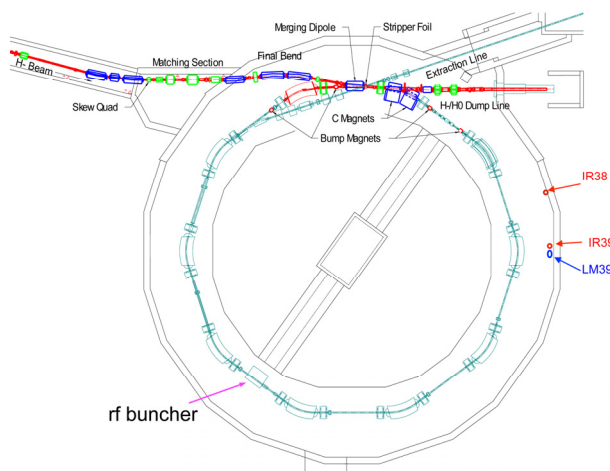


Figure 1: PSR layout since 1998.

The injection stripper foil is a ribbon 12 mm wide by 40 some mm long made up of two 200 microgram/cm$^2$ layers. Today, each layer is a hybrid composite of carbon and boron in a method developed by Professor Sugai at KEK for enhancing foil lifetime [8]. Numerous 4 micron carbon fibers are stretched across the frame to keep the foil from moving.

The stripper foil is offset from the final H+ closed orbit, and the H- beam strikes the foil on a corner. A

programmed closed orbit bump in the vertical is used for phase space painting as shown in the diagrams of Figure 2. The objective is to minimize the number of foil hits by the stored beam and minimize the space charge density of the beam.
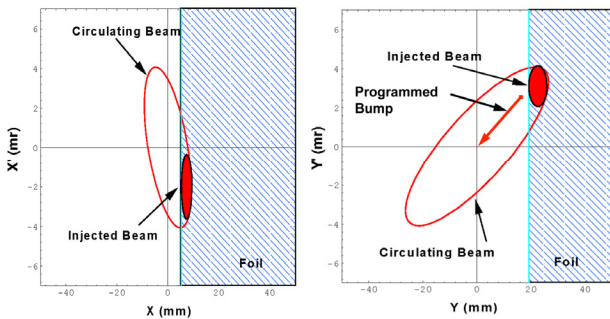


Figure 2: Injection phase space painting at the stripper foil location.

## PSR BEAM LOSS MONITORING

Total beams losses are measured by the sum of the average current from 19 ion chambers (**IR**) located on tunnel wall opposite each dipole and halfway in between. These locations for IR38 and IR39 are illustrated in Figure 1. This pattern is repeated for each section of ring. The IR sum is calibrated by injecting up to 0.4 µC and letting it all be lost with no extraction. We check the uniformity (15-30%) of the system response by spilling locally using various closed orbit bumps. A newer method to calibrate and check uniformity of response is described at the end of this section.

A fast response loss monitoring system (~10 ns) consists of 10 scintillation detectors (**LM**) located opposite each dipole and next to the IRn9's. The location for LM39 is also shown in Figure 1. Again, the pattern is repeated for each section of the ring.

Typical beam losses and activation data are shown on a control room loss monitor display in Figure 3. The activation measurements added in color to the display were taken from a 2008 survey ~1 day after the beam was turned off for a regular maintenance period. The beta-gamma activation readings are taken 30 cm from the beam pipe. The graphic shows a typical beam for operations of ~110 µA with a typical beam loss ~0.0025 (0.28 µA, 225W). Losses were measured from the sum of Ion Chamber (IR) readings and a calibration constant.

The high loss regions and high activation regions are located in the injection section plus the following section as well as the extraction region. The graphic in Figure 4 shows that activation has a reasonable correlation with the loss monitor data.

A new method of IR "calibration" and uniformity checks was carried out in 2012. The previous method used a known low-intensity coasting beam that was not extracted, hence was lost entirely. This assured that that the amount of lost beam was well determined. Our concern was that even with various local bumps the losses

appeared mostly in just a few spots. The new method used a standard bunched beam accumulation and a short store (100 µs) plus extraction but used large bumps (35-45 mm) in order to lose a large fraction (50% or more) of the beam. In this way the amount of beam lost could be well determined with current monitors in the ring. We used a low intensity beam of ≤ 0.4 µA average current in order to limit activation of ring during the large fractional loss measurements.
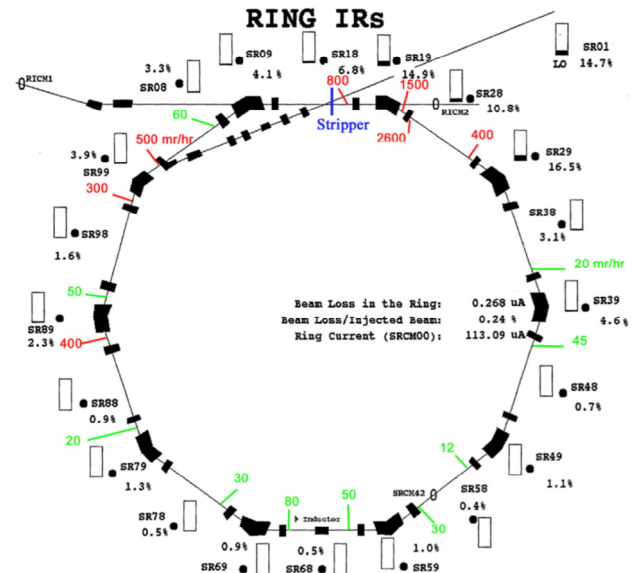


Figure 3: Control room display of beam losses with activation map added. Each IR is % of full scale.

An ORBIT simulation with large bumps showed most of the beam was lost in one quadrupole at the bump location. Thus, losses were more localized at calculated bump locations and avoided the uncertainty of loss locations and shielding effects during the long store of the coasting beam method. For each large bump, a calibration number (equal to the sum of all 19 IR values divided by the current lost) was obtained. Figure 4 is a plot of the "calibration" value for the bumps used in each section of the ring in the 2012 study.
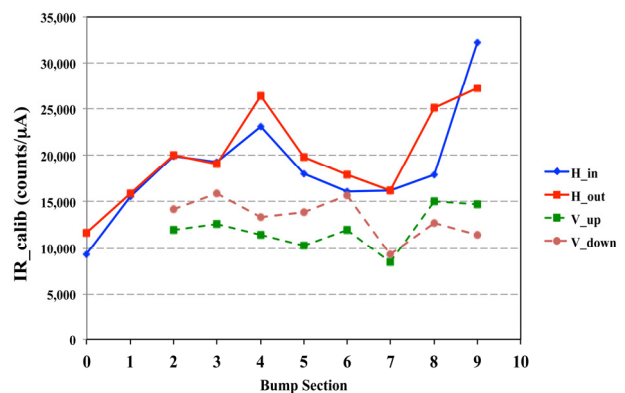


Figure 4: Plot of IR_calibration values for the various bumps in the 2012 study.

# BEAM LOSS MECHANISMS

Several significant loss mechanisms for PSR have been identified and studied extensively. These include:

1. Foil scattering, which includes:
   a. Nuclear elastic and inelastic scattering.
   b. Rutherford scattering, which we designate as "large angle Coulomb scattering"
2. Excited states of H0(n) (n>2) produced from H- in the stripper foil that subsequently Lorentz strip in the first dipole down stream of the foil.
3. Extraction losses during the single turn extraction process at the end of accumulation.
4. Betatron resonance crossing, which can be avoided by a suitable operating point.
5. Beam instabilities, in particular, the two-stream e-p instability [9,10] which is generally avoided for production beams by sufficient rf buncher voltage.
6. Space charge emittance growth, which is not very significant for routine production beam intensities less than 6 μC/macropulse.

Items 1., 2., and 3., above are important for routine production beams and are discussed more fully in the following sections. In general, each of these was studied both experimentally and by various modeling methods.

## Foil Scattering

The major component of losses (60-75% of total loss) is from foil scattering i.e., nuclear elastic and inelastic scattering plus large angle Coulomb scattering (larger than the angles given by the limiting apertures in the ring. Cross-sections for these are well known, but we need to know the number of foil hits by the accumulated beam, which are typically 100-150 for the average proton, and which we obtain from simulations and/or from calibrated foil current measurements.

We can measure the current from the foil, which is primarily from secondary emission from beam hitting the foil. The graph in Figure 5 shows signals from 1/17/03 production at 115 μA and demonstrates that the beam loss signal tracks the foil current. By knowing the secondary emission yield (SEY) we can get the number of foil hits per stored proton from the foil current signal. For an SEY of 1.06% for carbon foils (measured 6/13/02), the foil signal implies 70 foil hits per average proton in the beam. We measure SEY at low intensity by running the foil for nearly on axis injection so that all protons hit the foil every turn. This has not been done for about a decade so the simulation probably gives a more reliable foil hit number for contemporary foils.
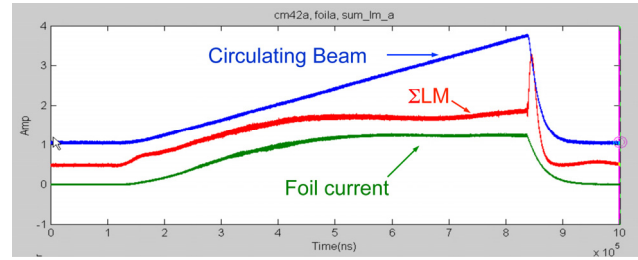


Figure 5: Signals from 1/17/03 production, foil current (green), LM sum (red), circulating beam current (blue).

For a simple estimate of losses from **nuclear interactions** including elastic and quasi-elastic scattering, we use published data (from PDG handbook) on nuclear collision lengths for carbon i.e., $\lambda_T = 59.2$ g cm$^{-2}$, thus the fractional loss from 150 foil traversals is 0.00102.

For **large angle Coulomb scattering** we use a simple model of an on-axis, pencil beam hitting the foil with limiting acceptance angles, $\theta_{xl}$ or $\theta_{yl}$ , obtained from limiting apertures, $X_A$ and $Y_A$ given by:

$$\theta_{xl}^2 = \frac{X_A^2}{\beta_{fx}\beta_{xA}} \quad \text{and} \quad \theta_{yl}^2 = \frac{Y_A^2}{\beta_{fy}\beta_{yA}}$$

For typical PSR production beam parameters, $\theta_{xl} = 7$ mr, $\theta_{yl} = 3.3$ mr. Next, we integrate the Rutherford scattering differential cross-section in the small angle approximation (form Jackson, "Electrodynamics, equation 13.92 [11]) over the region outside the ring acceptance from $|\theta x| = \theta xl$ to $\infty$ and $|\theta y| = \theta yl$ and obtain the cross-section $\sigma_{lost}$ for lost protons:

$$\sigma_{lost} = C_0 \left[ \frac{1}{\theta_{xl}\theta_{yl}} + \frac{1}{\theta_{xl}^2}\tan^{-1}\left(\frac{\theta_{yl}}{\theta_{xl}}\right) + \frac{1}{\theta_{yl}^2}\tan^{-1}\left(\frac{\theta_{xl}}{\theta_{yl}}\right) \right]$$

The probability (per foil traversal) of a single large angle scattering that leads to particle loss is $P=N\sigma_{lost}t$ where N is the number of atoms per unit volume and t the foil thickness. Using PSR parameters and a 400 μg/cm$^2$ carbon, $P = 6.1\times10^{-6}$ per foil traversal, or for a typical 150 foil hits/proton, the fractional loss from large angle Coulomb scattering is 0.00091.

Thus, the fractional loss from foil scattering = sum losses from large angle Coulomb loss + the loss from nuclear scattering = 0.0019 (for 150 foil traversals per proton) as estimated by the simple model models above. This compares favourably with typical measured total fractional loss of ~0.0025.

## Excited States of H0(n) (n>2)

A small faction (~5x10$^{-4}$) of the H- atoms hitting the stripper foil emerge as excited states of H0 [6,12], which can subsequently be field stripped part way into the first dipole downstream of the foil and fall outside of the acceptance of the ring and are lost. A horizontal phase space diagram to illustrate this is shown in Figure 6 for a particular n=4 Stark state (n1=3, n2=0, m=0 for the remaining parabolic quantum numbers).
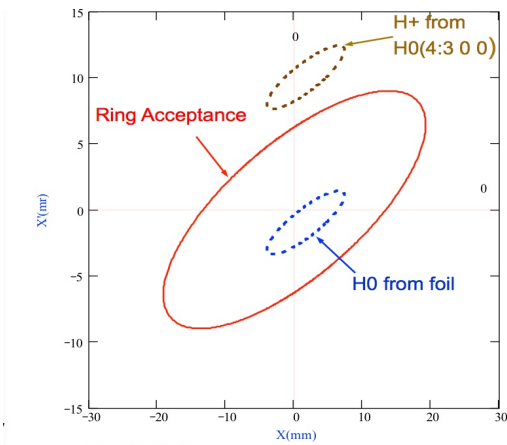
Figure 6: Horizontal phase space diagram depicting beam loss from an excited Stark state H0(4:3 0 0).

The various phase ellipses are projected to the entrance of first dipole (SRBM11) downstream of the stripper foil. The H+ from the H0(4: 3 0 0) state is bent by ~11 mr less than protons from the foil and thus falls outside of the acceptance of the ring and is lost.

To obtain the angle deficit, theta, for this stripped Stark state, we use formulas from Damburg and Kolosov [13] for the line width of Stark states and obtain the stripping probability as a function of magnetic field. From these and the magnetic field as a function of distance into the magnet we can obtain the probability distribution for theta (units of mr). From similar calculations for other Stark states, we find that n=1 and 2 states are not stripped in the first dipole while all of n=3, n=4 and n=5 Stark states are stripped and most are lost. Higher Stark states strip easily and contribute to beam halo in the ring acceptance.

Total losses during accumulation can also be monitored by a fast response system (~10 ns) of 10 scintillation detectors (LM) opposite each ring dipole. The fast response of the LMsum signal is useful for measuring losses from excited states, which would cease at the end of accumulation and show a step drop in the signal if the beam is stored for a 100 μs or so. When these were first observed in the early days of PSR, the step drop was designated "1st turn losses". An example of such signals from an experiment 6/11/2002 is shown in Figure 7, where a typical 4-layer carbon foils (~400 μg/cm²) of that era was used. Total fractional losses during accumulation were ~ 0.0047, and the data indicates "excited state losses" of 44% of the total losses. Data for an HBC 2-layer foil in 2010 showed 18% of the total loss was from excited states.
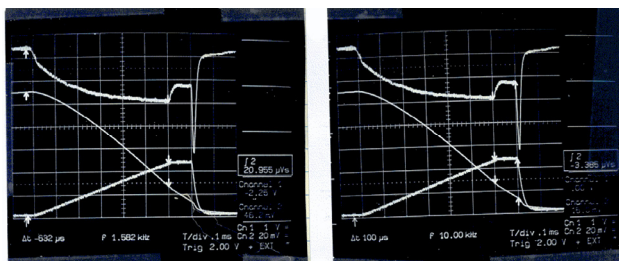


Figure 7: Measurement of 1st turn loss 6/11/2002. Top curves LMsum signal, center integral of LMsum, bottom CM42 current monitor.

## Extraction Losses

These are measured by special fast detectors located on wall opposite dipoles in sections 8, 9, 0, 1 and 2 designed to avoid saturation on fast loss. Two types of detectors are used designated as SRLV's and SRVE's. SRLV's are standard scintillation-based loss monitors with the last 4 photo multiplier dynodes shorted to reduce gain, while the SRVE's are plastic scintillator detectors using vacuum photodiodes which won't saturate on extraction losses. Figure 8 shows a sample ΣSRVE signal (integrated) from a logbook showing a jump at extraction, which is proportional to the extraction loss. This system was calibrated by spilling (extraction septum magnets off) single beam pulse with known charge in the 1-turn extraction. The calibration constant has a factor of 2 or so uncertainty. With this system we measure a typical extraction loss of ~1 nC (~5-10% of total loss), which is roughly consistent with activation at the extraction septum region.
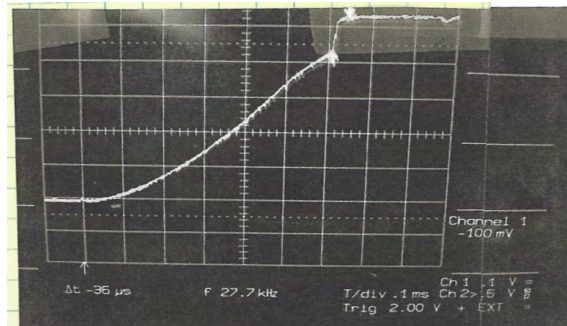


Figure 8: Example of extraction loss observed using an integrated ΣSRVE signal.

## Space Charge Effect on Losses

The effect of space on beam losses was systematically measured on two occasions in 2001. Beam was accumulated for 1225 μs using the standard production injection offset and then the intensity was varied with jaws at the front of linac. All other accelerator parameters were held constant. The bunch width (aka pattern width PW) at injection was 280 ns (out of 358 ns revolution period) on 9/18/01 while on 10/17/01 it was 260 ns. The total fractional losses are plotted in Figure 9 as a function of accumulated charge per macropulse, Q. From this data we see that space charge does not significantly influence losses below 6 μC/pulse.
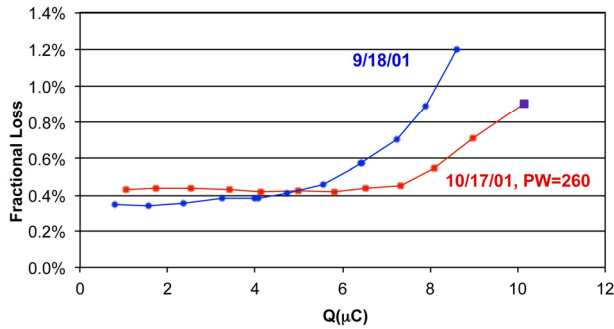
Figure 9: Fractional beam losses as a function of Q, the charge per macropulse.

## MODELING LOSSES AT PSR

The ORBIT beam tracking code [2] with MAD8 matrices for the lattice model is used extensively at PSR to model beam dynamics effects including losses. It includes nuclear and Coulomb scattering in the foil, space charge effects, painting with programed bump magnets but production and stripping of H0(n) excited states are not included. We use numerous planar "black" apertures in various ring elements to obtain losses of proton beam. An example is shown in Figure 10 of the loss distribution from ORBIT modeling of the accumulation of a 5μC/macropulse production beam using the measured injection offset (2/3/14) and a measured injected beam phase space distribution (from 2010 experiment).

We use G4beamline code [3] to simulate the energy deposited in IR loss monitors with the local phase space distribution of proton loss from ORBIT as input. For an informative example we discuss the modeling of the energy deposited in IR's for the large (43 mm) horizontal bump in PSR Section 4.
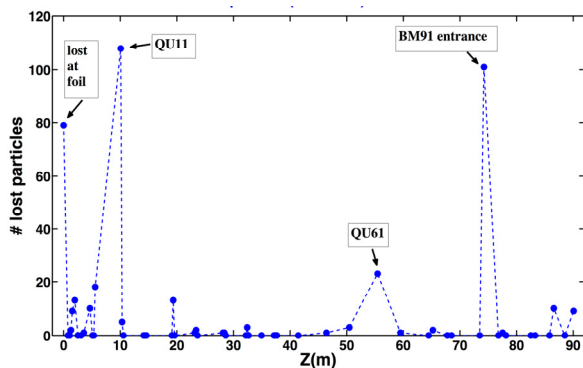


Figure 10: Lost particles as a function of distance Z from ORBIT modeling of production beam.

ORBIT modeling of the bump showed that 98 % of the loss was in one quad (SRQF41). The phase space distribution at the loss plane was extrapolated back to a point 0.5 m in front of the quad and used as input to G4beamline of this region. This is depicted in the

G4Beamline visualization of the area with secondary's from 10 lost protons in Figure 11.
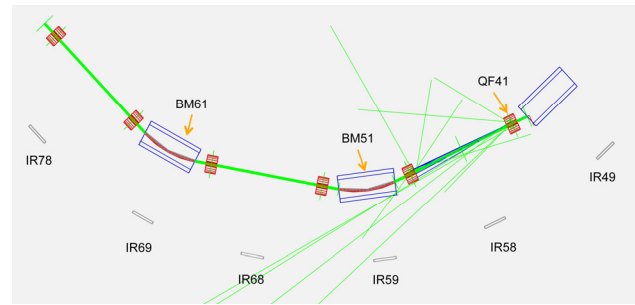


Figure 11: G4Beamline visualization plot of secondary particles from a spill in QF41 (positives: blue, neutrals: green, negatives: red).
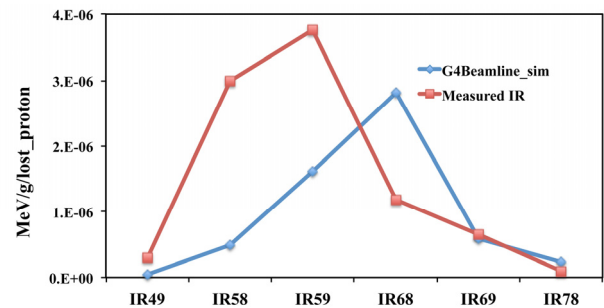


Figure 12: Energy deposited in IR's in region of SRQF41.

The energy deposited (MeV/g/lost_proton) in IR's from the G4Beamline simulation is plotted in Figure 12 and compared with the measured IR's signals converted to energy deposited (MeV/g/lost_proton) using the known calibration (5600 nC·Gy$^{-1}$) [14] of the ion chambers at PSR. For the summed energy of 6 IR's (IR49 through IR78), the simulation gave $5.78 \times 10^{-6}$ MeV/g/lost_proton, which compares favorably to $8.98 \times 10^{-6}$ MeV/g/lost_proton obtained from the measured IR signals, given the significant approximations in the material layout for the simulation.

## CONCLUSIONS

Beam losses at high intensity proton accumulator rings such as PSR and SNS, in particular, PSR have been studied extensively for years and are now well understood. The observed fractional beam loss at PSR is typically $0.0025 \pm 0.0005$ for production beams after empirical optimization by operators. The breakdown by main components for PSR is: a) large angle Coulomb scattering = 0.0009, b) nuclear interactions plus elastic and inelastic scattering = 0.0010, c) H0(n) excited states = 0.0004, d) extraction loss ≤ 0.0002. It is worth noting that SNS has an order of magnitude lower loss but for a factor of 12 higher beam power.

The combination of ORBIT and G4beamline codes are valuable tools for modeling both losses and the loss monitoring system (IRs) response. In addition to the

energy deposited in IR's, G4Beamline gives distribution of secondary particles striking down stream chamber walls, which is needed for modeling electron generation for the e-p instability. At PSR, beam loss from the e-p instability is just under control for production beams but is easily invoked especially during additional store time.

## ACKNOWLEDGMENT

## REFERENCES

[1]   F. Christoph Iselin, The MAD Program 8.13, CERN-BE/ABP, (1994).

[2]   Jeffrey A. Holmes et al., ICFA BD Newsletter, No. 30, p 100, (2003).

[3]   T. Roberts, "G4Beamline User's Guide", http://www.muonsinternal.com/muons3/G4beamline

[4]   George P. Lawrence, PAC 1987, p825 (1987).

[5]   R. J. Macek et al, PAC 1993, p3739 (1993).

[6]   R. Hutson and R. Macek, PAC 1993, p363 (1993).

[7]   D. Fitzgerald et al., PAC 1999, p518 (1999).

[8]   I. Sugai, HB2008, WGC08, p300, (2008).

[9]   R. J. Macek et al., Proceedings of ECLOUD'04, CERN-2005-011, p63 (2005).

[10]  R. Macek et al., Proceedings of ECLOUD10, OPR00, p1 (2010).

[11]  J. D. Jackson, "Classical Electrodynamics", Wiley and Sons, (New York 1965).

[12]  M. S. Gulley et al., Phys. Rev. A, **53**, 3201 (1996).

[13]  "Rydberg States of Atoms and Molecules", Edited by R. F. Stebbings (CambridgeUniversity Press, Cambridge 1986).

[14]  D. Brown et al., Nucl. Inst. and Meth. in Phys. Res. A **420** (1999) 494-506.

# BOOSTER UPGRADE FOR 700kW NOVA OPERATIONS *

K. Seiya#, FNAL, Batavia, IL 60510, USA

## Abstract

The Fermilab Proton Source is in the process of an upgrade referred to as the Proton Improvement Plan (PIP) [1]. One PIP goal is to have Booster capable of delivering ~2.3E17 protons/hour, 130% higher than the present typical flux of ~1E17 protons/hour. The increase will be achieved mainly by increasing the Booster beam cycle rate from 9 Hz to 15 Hz. Beam loss due to the increased flux will need to be controlled, so as not to create larger integrated doses. The status of present operations and progress of beam studies will be discussed in this paper.

## 700KW OPERATION WITH RECYCLER AND MAIN INJECTOR

Fermilab is going to provide 700kW proton beam to the NOvA experiment [2]. Prior to the 2012 shutdown, Main Injector (MI) had been delivering 360 kW routinely and up to 400 kW of beam power to the NuMI target. Booster had injected 11 batches of 4E13 protons per pulse [ppp] to the MI. After the injection, the MI accelerated the beam from 8 GeV to 120 GeV every 2.2 sec.

For NOvA operation, 12 batches are injected into the Recycler Ring (RR) which is located on top of the MI in the same tunnel. The RR is an 8GeV fixed energy synchrotron using permanent magnets. Two 53MHz cavities were installed in the RR during 2012 shutdown for slip stacking. The harmonic number of the RR is 588 which is the same as MI. The MI power supply was upgraded and shortened the ramp from 1.6 to 1.33 sec as shown in Figure 1.

In the RR, 6 Booster batches are injected and then another 6 batches are injected and slip stacked. After the slip stacking, the beam density is doubled. This process takes 12 Booster cycles which is 0.8 sec.

In order to achieve 700 kW of beam power, the MI cycle has been shortened from 2.2 sec to 1.33 sec. This was accomplished by using the RR to manage the injection and stacking of beam from the Booster while the MI is ramping.
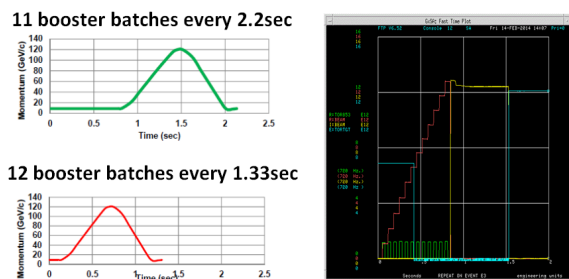
## REQUIREMENTS FOR THE BOOSTER AND BEAM LOSS LIMIT

Booster is a 15 Hz resonant circuit synchrotron and accelerates proton beams from 400 MeV to 8 GeV. The required intensity in the Booster for NOvA is 4.3E12 ppp, the same as it was for 400 kW operation. However, the cycle rate will be increased from 9 Hz to 15 Hz to accommodate both NOvA and other users. The RF system and utilities are being upgraded to 15 Hz operations and are nearing completion. The plan is to start 15 Hz operations in FY15.

The beam loss limit has been set to 525W to allow workers to maintain all elements in the Booster tunnel without excessive radiation exposure. Figure 2 shows the historical beam loss in the Booster versus protons per hour. The total loss depends on the beam intensity. Given the required intensity of 2.3E17 protons per hour, the loss has to be reduced to half by 2016.

The present operational beam intensity at injection is about 5E12 ppp and extraction is 4.5E12 ppp. The total energy loss is 0.075 kJ in one Booster cycle and hence 1150 W when the cycle rate is 15Hz. The loss has to be reduced to half by 2016. Figure 3 shows the intensity and loss during normal operations. The points where significant beam loss occurs are when the RF feedback is turned on, when the extraction kicker gap is created and when beam acceleration passes through transition. There are slow losses from injection to 5 ms into the ramp and after transition. Beam studies and upgrades that will be done to reduce the beam losses will be discussed in this paper.



Figure 1: Left pictures; The MI ramp for 400 kW (upper) and 700 kW (lower) operations. Right picture; Intensity in the RR (red), MI (yellow) and Booster (green).
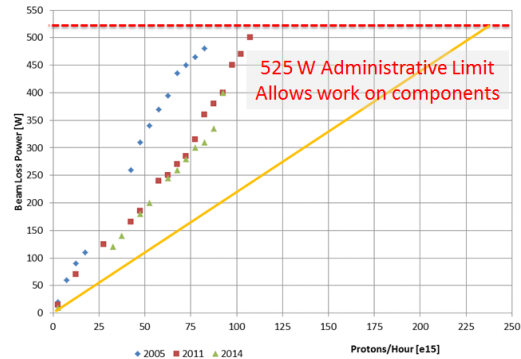
Figure 2: Beam power loss for 3 year operations (blue: 2005, red: 2011 and green: 2014)
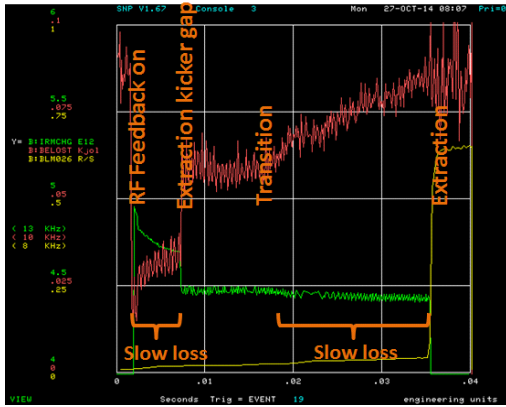
Figure 3: Beam intensity (green), energy loss (red) and extraction loss (yellow) signals.

## BEAM STUDIES AT THE BOOSTER

Booster has 24 periods. Each period consists of a 0.6 m straight section (short straight section), a focusing combined function main dipole magnet (F magnet), a defocusing main dipole magnet (D magnet), a 6 m straight section (long straight), and another D magnet and F magnet. 48 correctors were installed in the long and short straight sections in 2006. Each corrector (Figure 4) has horizontal and vertical dipoles, a quadrupole, a skew quadrupole, a sextupole, a skew sextupole and horizontal and vertical beam position monitors. Figure 5 shows the beta function and dispersion for one Booster period. The typical horizontal emittance is $14\pi$ mm-mrad and $16\pi$ mm-mrad vertical emittance. The RF parameters are listed in Table 1.

Table 1: RF Parameters

| Energy | 400 MeV – 8GeV |
|---|---|
| RF frequency | 37.9 – 52.8MHz |
| Harmonic number | 84 |
| Maximum voltage | 1MV with 19 cavities |
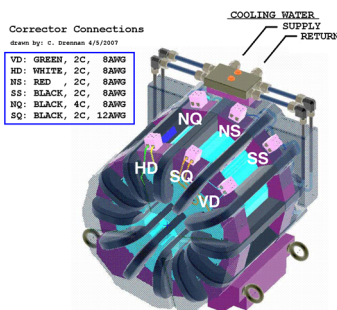


Figure 4: The corrector package is 0.6 m long.
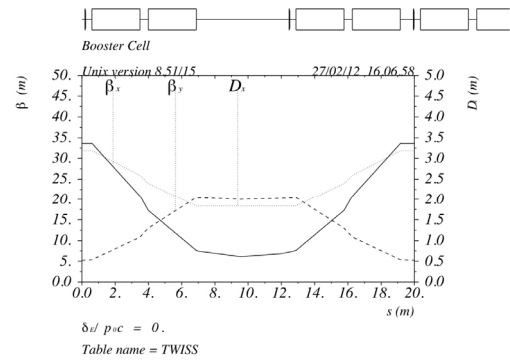


Figure 5: Booster lattice for one period.

### Aperture Scan and Magnet Moves

Horizontal and vertical beam sizes are largest at the short and long straight sections respectively. The short straight section has one corrector and all other components are in the long straight section. Booster has 19 RF cavities in the long straight sections from period 14 to 24. The diameter of the beam pipe in the RF cavities is the smallest of all the components in the long straight sections. Therefore, we find the smallest beam aperture located at periods 14 to 24 in the vertical plane.

Magnet moves were performed based on survey data and beam aperture scan results [3]. By moving more than two magnets at one time, the beam orbit was kept at the same position to within +/- 1 mm. Magnets were moved at 4 locations where RF cavities were installed. Figure 6 shows the aperture at period 16 before and after the magnets were moved. Aperture scans were done using combinations of 5 and 3 bumps. The colors represent the ratio between beam intensity sampled at injection and after the bumps were made.

Figure 7 shows the aperture before and after re-alignments around the ring. The apertures were larger after the realignments were done. The aperture is currently smallest at periods 6 and 7 where collimators are located. The next step is to optimize the collimator settings.
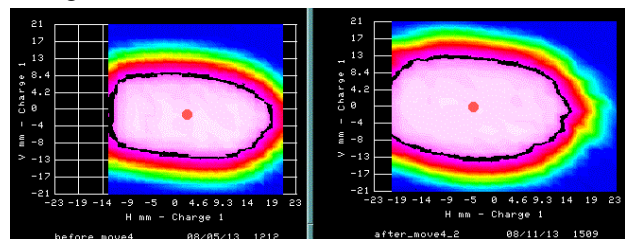


Figure 6: The aperture at injection and long 16 where RF cavities are installed.
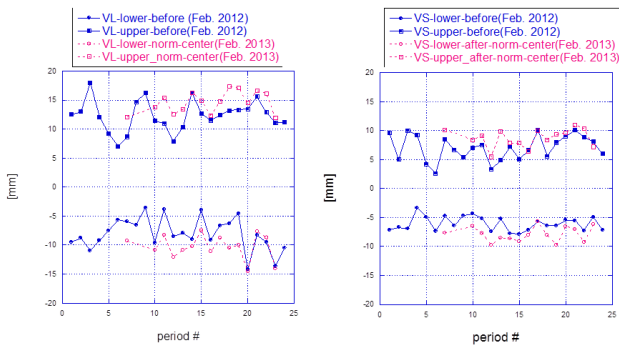
Figure 7: Vertical apertures at the long (left) and short (right) straight sections before (magenta) and after (blue) re-alignments around the ring.

### Beam Capture at Injection

Booster is a resonant circuit synchrotron and the B field at injection is not flat. 200 MHz bunches are injected from Linac with multi turn injection which takes 40 μsec. The current mode of Booster operation has injection occurring at the minimum of the B field. The 200MHz bunches are debunched without RF voltage for 60 μsec and then adiabatically captured with 37.9 MHz RF voltage. The magnetic field ramp and frequency change happens during adiabatic capture without RF feedback. There is a beam loss at injection especially with the RF feedback turned on.

A new injection scheme has been proposed to move the injection timing earlier and remove the debunching [4]. The injected beam stays near 400 MeV until capture is done. Figure 8 shows the injection timing difference between the present scheme and the proposed scheme. Both schemes were simulated and the longitudinal phase space was compared at 400 μsec after the B field was at its minimum. Simulation results in Figure 9 show that 4% of the particles were already outside of the bucket with the present scheme. There were no particles outside of the RF bucket with the new scheme and the bunch area at the end of the capture was found to be ~40% smaller than that observed with the present scheme. Consequently, the required RF power could be reduced by ~30%.
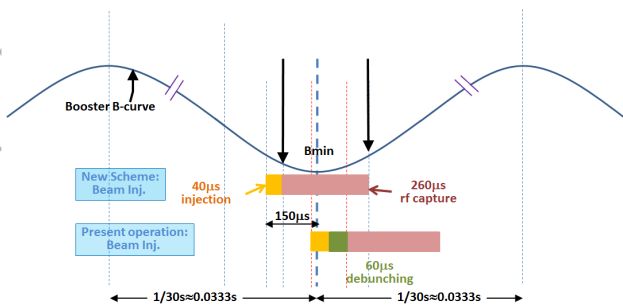


Figure 8: Injection timing for the new scheme and present operation.
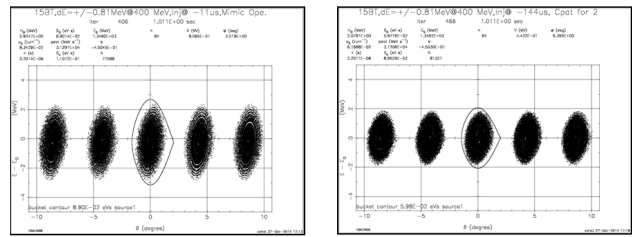




Figure 9: Simulation results for the RF capture at 400 μsec respected to the minimum B field. Present scheme (left) and proposed scheme (right).

### Cogging

An extraction kicker gap must be created during the cycle because the beam completely fills the Booster after the multi-turn injection and adiabatic capture at the injection energy. The gap has to be synchronized to the Booster extraction kicker and RR injection kicker. The variation in the Booster main dipole fields causes errors in the gap position at extraction. Cogging eliminates this error by controlling the bucket positions throughout the cycle [5].

The gap position is controlled by changing the revolution frequency. The present cogging system changes the revolution frequency by moving radial position of the beam. Since the transverse emittance is large at low energy and any radial position change can cause beam loss. In order to reduce losses, the gap is created at 700 MeV and this is where radial position changes occur.

The new Magnetic Cogging changes the revolution frequency by changing the bend field using 48 dipole correctors. The Booster radial position feedback is regulated to a fixed radial position of the beam. Figure 10 shows how the magnetic cogging feedback system works: the revolution frequency is measured by counting Booster RF cycles within a Recycler revolution period. The counts from each period are compared with the one from the initial reference cycle and the error is integrated through the cycle. The error is the correction signal for the dipole corrector. Figure 11 shows that magnetic cogging does work by comparing the integrated errors with and without magnetic cogging.

The extraction kicker gap creation can happen at any time after injection with the new magnetic cogging system instead of only at 700 MeV with the present cogging system, therefore it will reduce beam energy loss. Since the Linac laser notcher is going to be available in 2016, the gap will not be created in the Booster.
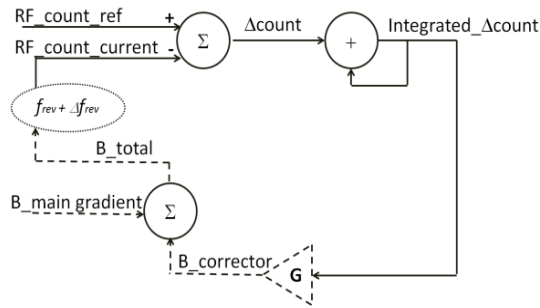
Figure 10: Block diagram of cogging feedback.
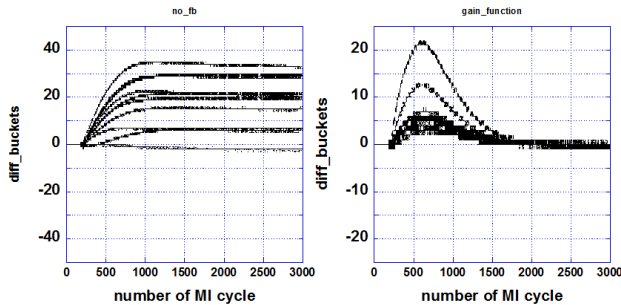


Figure 11: Integrated bucket error signal with (right) and without (left) cogging.

## Optics Control

The beta functions were modulated from Injection to extraction in the Booster and it could cause emittance mismatch and thus beam loss. Figure 12 shows the comparison of the beta functions between the lattice with the injection bump turned on and the lattice after correcting the beta errors arising from this bump. These beta function errors caused by the injection bump were corrected with a set of quadrupoles around this bump [6].

LOCO (Linear Optics from Closed Orbit) calculates the quad and skew quad currents that corrects the measured lattice to make it closer to the ideal lattice. This method uses a set of kicks made at each dipole corrector and the response of the beam at every BPM was measured. The kick angle was changed by changing the corrector current so that the ratio between the position changes: dx and kick angle change: dθ could be measured at each location. Then dx/dθ was compared with the one from the ideal lattice calculated with MADX. From the difference between the measurements and the ideal lattice, the correction for the quad and skew quad was calculated using LOCO.

The beam response at every BPM to every dipole kick was measured at 7 break points from injection to extraction. Figure 13 shows the Booster lattice at injection before and after the correction in horizontal and vertical planes. It is clear that the beta errors were reduced around the ring. Studies are continuing to incorporate these corrections into the operational lattice.
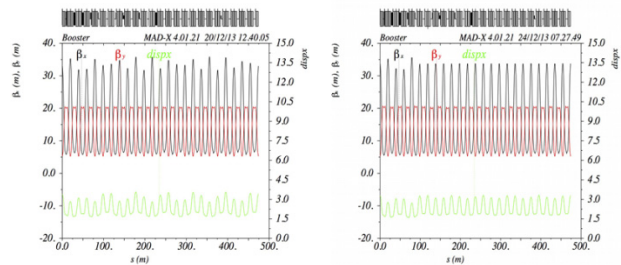


Figure 12: The calculated lattice with the injection bump turned on (left) and the corrected lattice (right).
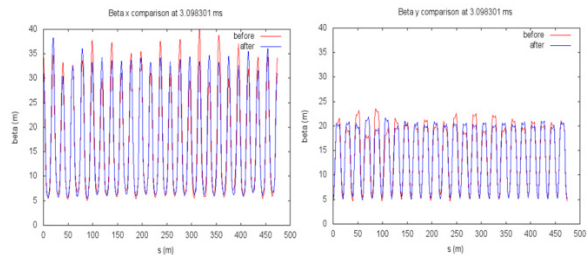


Figure 13: The measured Booster lattice at injection before (red) and after (blue) the correction in the horizontal (left) and vertical (right) planes.

## Tune Measurements and Control

Tunes can now be measured from injection through extraction by transversely exciting the beam every 500 turns with a pinger (Figure 14). The tunes in the entire ramp can be set to any point in the tune plane using the new corrector quadrupoles. By setting these tunes in a controlled fashion, the beam can be moved away from resonances and thus reduce beam loss.

The coupling was also measured and it has been corrected with the new skew quadrupoles [7].

For tune measurements, the present tune monitor excites large transverse oscillations that causes beam loss for high intensity beam. In order to fix this problem, a new damper/pinger is currently being commissioned. This new tune meter uses the horizontal bunch by the bunch damper to excite just one bunch out of 84 bunches by using random noise or by anti-damping (Figure 15) [8].
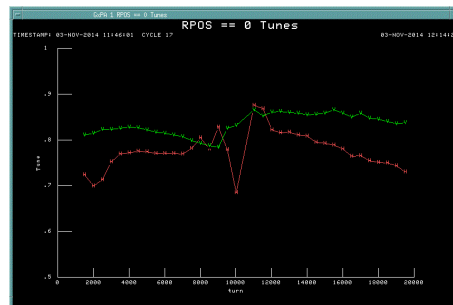


Figure 14: Horizontal and vertical tune measured by present tune monitor what uses BPMs and pinger. Horizontal tune is in red and vertical is green.
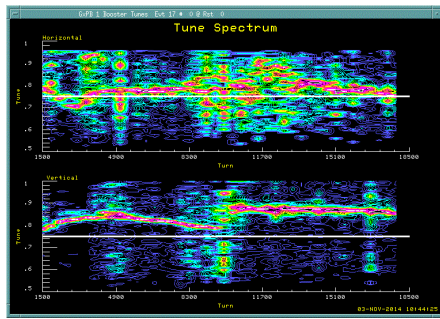
Figure 15: Horizontal (upper) and vertical (lower) tune measured by new tune monitor using damper.

## Transition and Extraction Loss

After the RF upgrades are complete, the RF voltage at transition is going to be increased by adding additional cavities. This will help reduce the losses and increase reliability. The extraction gap kicker and absorber upgrade has localised losses to the absorber and has reduced losses at extraction. These two upgrades are discussed in another paper in this workshop [9].

## LOW LEVEL RF AND INSTRUMENTATION UPGRADE

Booster has been operating since 1971 and many low level modules were developed in the 1980's and have component obsolescence issues. Upgrades to the electronics are being carefully integrated into the Booster controls.

### LLRF

New electronics modules have been commissioned that manage the phase locking of the Booster RF to the RR just before Booster extraction. The new systems provide slightly better performance and additional access and opportunities for further improvement.

A new four channel direct digital synthesis module is under development that will replace the LLRF frequency source and the analogue phase shift modules used for radial position control and paraphrasing of the rf cavities for beam capture. This module will provide more precision and flexibility to the LLRF controls.

### Dampers and Instrumentations

Booster has 8 mode dampers which damp coupled bunch modes above transition. The frontend for these analogue dampers contain obsolete components and have limited flexibility. A new digital damper card has just been completed and is undergoing initial beam tests. These new digital dampers will provide better signal to noise and gain and will be more reliable for operations.

The BPM system is going to be replaced with real time LINUX VXS and VME based systems. The new BPM system will be able to measure the beam at injection, which has 200 MHz structure, and bunched beam throughout the acceleration cycle that has 37.7 to 52.8 MHz RF structures.

## Total Loss Monitor

Fermilab uses interlocked ion chamber radiation detectors called chipmunks as an input to the radiation safety system. The chipmunk locations and trip settings are determined by the Shielding Assessment Process. Chipmunks are located outside of radiation shields and trip off the radiation safety system in the event the prescribed effective radiation dose rate limits are exceeded.

TLM (Total Loss Monitor) is being developed at Fermilab as an alternative input to the radiation safety system [10]. TLM is a long ion chamber (air-filled dielectric coaxial cable) filled with ArCO2 detector gas. The detector is mounted in the tunnel while the associated electrometer is located outside the tunnel in a service building. A single detector can cover large sections of tunnel that is hundreds of feet in length. Beam studies to characterize the TLM response under a wide variety of beam loss conditions are ongoing.

## SUMMARY

The Booster cycle rate of 15 Hz and averaging 4.3E12 protons per pulse will be completed by 2016. The beam loss has to be reduced by half compared to the present situation. The ongoing PIP beam studies along with hardware and software upgrades are critical. A successful completion of the PIP effort is a laboratory priority and essential for reaching the HEP proton delivery goals.

## REFERENCES

[1] W. Pellico et al., "FNAL - The Proton Improvement Plan (PIP)", THPME075, these proceedings, IPAC'14, Dresden, Germany (2014).

[2] I. Kourbanis, "Progress Towards Doubling the Beam Power at Fermilab's Accelerator Complex", TUOAA01, IPAC'14, Dresden, Germany (2014).

[3] K. Seiya et al., "Alignment and Aperture Scan at the Fermilab Booster", THPPP024, IPAC'12, New Orleans, USA (2012).

[4] C. S. Bhat, private communication.

[5] K Seiya et al., "Development of Cogging at the Fermilab Booster ", WEPR069, IPAC'14, Dresden, Germany (2014).

[6] C. Y. Tan, private communication.

[7] W. Marsh et al., "An application for tunes and coupling evaluation from turn by turn data at the Fermilab Booster", MOP221, PAC2011, New York, UAS (2011).

[8] N. Eddy et al, "Using the transverse digital damper as a real-time tune monitor for the Booster synchrotron at Fermilab," MOPD71, DIPAC'11, Hamburg, Germany (2011).

[9] R. Zwaska et al., "Enhancements of the Fermilab Booster to reduce losses and extend lifetime: The Proton Improvement Plan", MOXAP07, these proceedings, HB2014, Lansing, UAS (2014).

[10] T. Leveling, private communication.

# HIGH INTENSITY LOSS MECHANISMS ON THE
# ISIS RAPID CYCLING SYNCHROTRON

C.M. Warsop, D.J. Adams, B. Jones, S.J. Payne, B.G. Pine, H.V. Smith, R.E. Williamson, RAL,UK.
V. Kornilov, GSI, Darmstadt, Germany.

## Abstract

ISIS is the spallation neutron source at the Rutherford Appleton laboratory in the UK. Operation centres on a loss limited, 800 MeV, 50 Hz proton synchrotron which delivers 0.2 MW to two targets. Understanding loss mechanisms on the ISIS ring is important for optimal operation, machine developments and upgrades, as well as improving designs for future machines. The high space charge levels, combined with the low loss achieved for high power operation, makes the ring an ideal tool for studying the physics of beam loss, particularly in a fast ramping context. The ability to reconfigure the beam in storage ring mode, and ongoing developments of diagnostics and beam measurements, are allowing detailed studies of image effects, resonances, beam stability and activation. We summarise recent work and progress on these topics, comparing with theory and simulation where appropriate.

## INTRODUCTION

The ISIS facility provides neutron and muon beams for condensed matter research. High power beams are supplied by a loss limited, 800 MeV, 50 Hz proton synchrotron. Understanding and minimising beam loss in the ring are key factors in ensuring improved machine performance, optimising future machine developments, and providing the best proposals for future upgrades.

Ongoing developments and proposed upgrades to the two ISIS neutron targets, with the accompanying requirements for low loss, reliable and consistent operations at higher powers, demand improved understanding and control of loss. Proposed upgrades to the existing ring, including the 0.5 MW design using a higher energy 180 MeV injector [1], require comprehensive beam models for their design. Similarly, upgrades and the next generation short pulse neutron sources in the 2 MW regime (and beyond) all require well benchmarked codes and theory to ensure optimal, realistic, low loss designs. A detailed, experimentally verified study of high intensity beam loss mechanisms is therefore essential to underpin these plans.

The ISIS ring is a valuable tool for studying high intensity beams. The challenging operating regime of low loss with high space charge; the fast acceleration ramp – combined with a number of key beam dynamics issues discussed below, provides important opportunities for new research. The ability to run the beam in experimental storage ring mode also opens up further areas for study.

First we review losses observed on ISIS operationally, then summarise relevant R&D topics.

## HIGH INTENSITY BEAM LOSS ON ISIS

### The ISIS RCS

The ISIS synchrotron accelerates $3\times10^{13}$ protons per pulse (ppp) from 70-800 MeV on the 10 ms ramp of the sinusoidal main magnet field. At the repetition rate of 50 Hz this provides an average beam power of 0.2 MW. Charge exchange injection takes place over 130 turns, with painting in both transverse planes as the high intensity beam is accumulated and contained in the collimated acceptances of ~350 $\pi$ mm mr. The ring has a circumference of 163 m. Nominal betatron tunes are $(Q_x, Q_y)$=(4.31, 3.83), but these are varied using 2 families of 10 trim quadrupoles. The dual harmonic RF system captures and accelerates the initially unbunched beam, and allows enhanced bunching factors. The machine is harmonic number two, RF systems run at $h$=2 and $h$=4 with peak volts of 168 and 96 kV/turn respectively. Peak incoherent tune shifts of $\Delta Q\geq0.5$ are reached at about 80 MeV during bunching. Single turn extraction at 800 MeV uses a fast vertical kicker. Main loss mechanisms are associated with non-adiabatic trapping, transverse space charge and transverse instability.
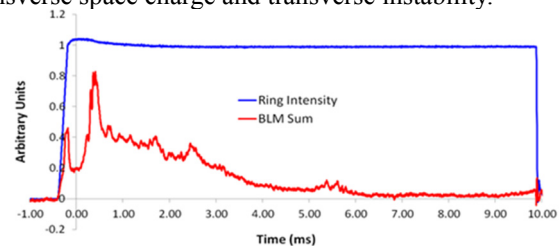


Figure 1: ISIS intensity and beam loss through the machine cycle ($2.8\times10^{13}$ ppp injected).

### Summary of Losses

The average beam power delivered by the ring is typically 160-200 kW. To allow hands on maintenance, activation has to be limited; this determines tolerable loss levels and running intensity. Figure 1 shows the circulating current and beam loss signal through the 10.5 ms machine cycle. Overall losses are <5% and concentrated at lower energy, where activation is considerably reduced. During the injection and accumulation process (-0.5−0.0 ms) losses are about 2%. During the trapping process (0.0–2.5 ms) losses are <3%, and for the rest of acceleration (2.5−10.0 ms) losses reduce to 0.5% levels, finally reaching ~0.01% at extraction.

Most loss (> ~98%) and activation is localised in 3 of the 10 super-periods, which include the injection,

collimation and extraction systems. This control is achieved with a detailed, time dependent, empirical optimisation of machine parameters. Loss distributions are monitored using the 39, 3 m long, ionisation chambers distributed around the machine circumference. Beam transformers and loss monitors are linked to a fast machine protection system that trips the beam off if losses exceed defined limits. Activation levels around most of the ring are ~10-100 µSv/hour at 1 m.
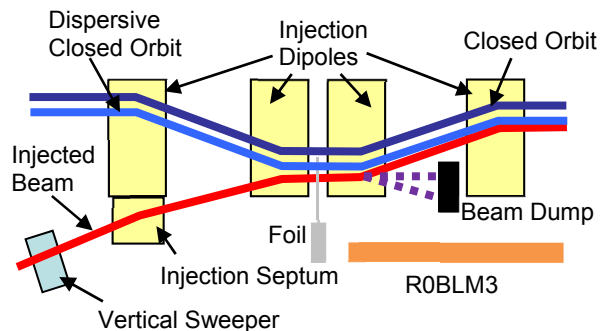


Figure 2: Schematic of the ISIS injection straight.

## Injection

The $H^-$ charge exchange injection process accumulates $3 \times 10^{13}$ ppp over 130 turns. An $Al_2O_3$ foil, of area $120 \times 40$ mm and thickness 0.5 µm, strips the beam with estimated efficiency of ~98% (see next section): most stripping products are collected on a dedicated dump (Figure 2). The beam centroid is painted in both transverse planes. Horizontally, the injection point on the foil is constant, and dispersive closed orbit motion due to the falling main magnet field varies the betatron amplitude. Vertically, a steering magnet in the injection line sweeps the vertical position at the foil (thus requiring a larger foil). The average number of foil re-circulations per proton is estimated at 30. Upgrade designs [1] reduce re-circulations substantially to ~5, by using angular vertical painting and reducing vertical foil size.
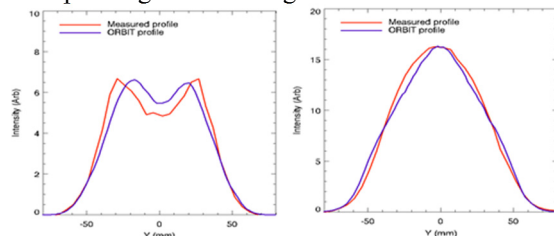


Figure 3: Simulated and measured vertical profiles after injection, left $2.5 \times 10^{12}$ ppp, right $2.5 \times 10^{13}$ ppp (red, measurement; blue, ORBIT result).

Space charge has a strong effect on the evolution of the transverse beam distributions, losses during injection and later in the cycle. Experience shows that, generally, larger amplitude, hollow painted beams give the best results. Comparisons of measured beam distributions with those from ORBIT [2] simulations have shown good agreement [3]. Results are shown in Figure 3, where the vertical beam profile after injection is shown at low and high

intensity. The effect of space charge is to "fill in" the hollow painted distributions. These studies also showed that the machine is insensitive to correlated or anti-correlated painting between the two transverse planes. There is still much to be understood about the mechanisms redistributing the particles through injection, and this will be studied in more detail as simulation models develop.
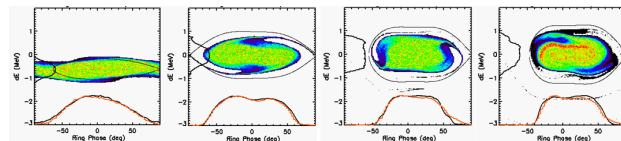


Figure 4: ORBIT simulation of the ISIS trapping process, showing ($dE$, $\phi$) space at -0.2, 0.0, 0.2, 0.5 ms.

## Longitudinal Trapping Process

The non-adiabatic, longitudinal trapping of the initially un-bunched injected beam is central to machine optimisation. In addition to the longitudinal capture, it has major effects transversely on space charge and stability via the bunching factor. Installation and optimisation of the dual harmonic RF system [4, 5] has reduced losses from ~10% to 3% levels. This allows much enhanced bunching factors, a larger longitudinal acceptance, and the ability to control bucket dynamics to optimise capture. An ORBIT simulation of typical operation with an injected intensity of $2.8 \times 10^{13}$ ppp is shown in Figure 4: orange lines show experimental data [6].

The high beam currents cause significant beam loading in the RF cavities, and a feed forward beam compensation system corrects for this in the $h$=2 systems. It is expected similar systems for the $h$=4 systems will provide benefits in the future. Major developments of high power RF systems and digital control systems [5] are also expected to allow much finer optimisation in the future, when a more efficient beam dynamics solution may be possible.

Studies with an in-house 1D code have looked at the space charge and longitudinal stability on ISIS [7]. These show that the beam significantly exceeds the Keil-Schnell-Boussard (KSB) stability criterion through injection and acceleration, by factors of ~6. However, the machine runs successfully and with low loss. This is probably explained by stabilisation due to redistributions of the beam that are small compared with other effects, and simplifications implicit in the KSB criterion. This is an important topic as KSB is often used to guide machine designs, and is the subject of planned research on ISIS.

## Transverse Space Charge

Transverse space charge peaks during the trapping process, as the beam bunches at low energy (~80 MeV). Peak incoherent tune shifts are $\Delta Q$~-0.5, with some ORBIT simulations suggesting larger shifts, see Figure 5. Transverse beam sizes peak at this time, filling the available apertures (~350 π mm mr). A key feature of the ISIS lattice is the inclusion of trim quadrupoles that allow rapid variation of tune through the cycle, and this

capability has been essential for successful operation. Examples of operational $Q$ values (corresponding to high intensity coherent tunes) are shown in Figure 6. Early in the cycle tunes are generally high to avoid integer and half integer lines, but a ramp down will be noted in $Q_y$ near 2 ms. This is required to avoid the vertical resistive-wall head-tail instability. Therefore beam is pushed over the half integer line and loss optimisation is a compromise between these two effects. The mechanisms causing loss associated with the half integer are the subject of research. In the rapid cycling, 3D context the process is complicated – no coherent quadrupole motion has been observed on the machine, but some initial ORBIT simulation results suggest it may be present. Further studies will exploit new diagnostics and simulations.
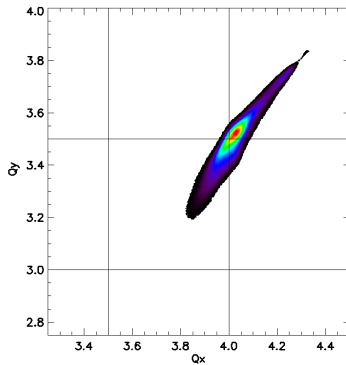


Figure 5: Incoherent tune spread from ORBIT simulations at 1 ms, intensity $2.5\times10^{13}$ ppp.
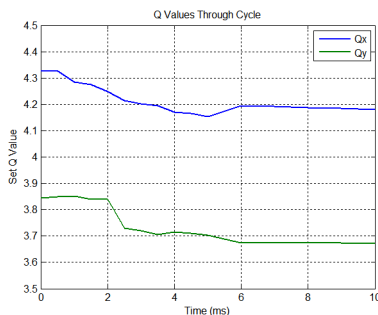


Figure 6: Programmed ($Q_x$, $Q_y$) through the ISIS cycle.

Most ISIS modelling studies have so far assumed a linear lattice, with the dominant non-linear behaviour arising from space charge. More recently, new measurements of loss whilst scanning ($Q_x$, $Q_y$) with low intensity beams [8], have revealed significant non-linear terms, Figure 7. Work is now under way to include these terms in machine simulations, and also investigate their origin with improved models and measurements of the machine lattice magnets.

The ISIS ring uses conformal, rectangular vacuum vessels that are profiled to the design beam envelopes. Whilst this has some benefits in reducing beam impedances and aiding efficient collimation, one key consequence is the generation of image driving terms and possibly enhanced losses: this is discussed in the next section.
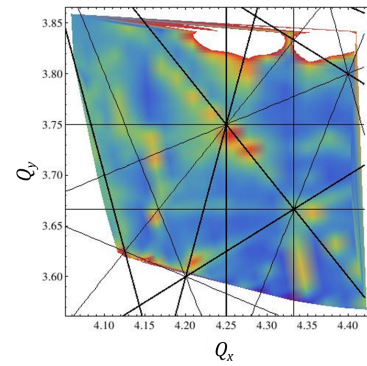


Figure 7: Measured ISIS tune map (low intensity).

Recent detailed studies of the ISIS working point for upgrade studies [1] have highlighted another consequence of these conformal vacuum vessels. As the machine tune is ramped (Figure 6) beam optics and envelopes change, and are no longer matched to the vessels, thus reducing the effective acceptance. ORBIT simulations show that whilst emittance growth reduces as $Q$ values are moved up and away from half integer resonance lines, there can also be an increase in loss that correlates with the mismatched envelope. On the real machine there is a detailed *empirical*, time dependent optimisation of many parameters, including $Q$'s, envelope harmonics and orbits, which takes these factors into account. Improvements to beam measurement and control are expected to shed more light on these effects, and potentially maximise use of aperture.

## Head Tail Instability

A head-tail instability appears vertically, at about 2 ms into the ISIS cycle. Observations suggest it is driven by the resistive wall impedance: as $Q_y$ approaches 4 growth rates increase rapidly. Before installation of the dual harmonic RF system, the instability was avoided by simply reducing $Q_y$. However, increasing intensities and longer, symmetric bunches have made the beam less stable, with the associated losses now limiting operational intensity. Experiments show an otherwise low loss, operational beam can be destabilised with a small change in bunch symmetry via a change in the phase between $h$=2 and $h$=4 RF harmonics. This is the subject of current research [9, 10]. A damper system is in development, with prototypes presently under trial.

## Acceleration and Extraction

After about 4 ms, as energy ramps, transverse space charge reduces and beam emittances damp leaving "spare" acceptance and reducing losses. However, the limited acceptance of the extraction system (280 π mm mr) requires tight control of halo. The higher activation associated with the 800 MeV beam at extraction dictates loss levels of ~0.01%. A vertical closed orbit bump is used to aid fast extraction in the last 1 ms of the cycle. This moves the beam into lower quality regions of the lattice magnets and increases the effects of

non-linearities. However, the careful control of lattice tunes (Figure 6), allows these to be avoided.

Recent upgrades to quadrupole switched-mode power supplies have improved beam control, but also introduced some interesting effects. Inadequate filtering has meant that switching frequencies have perturbed the beam as they sweep the horizontal betatron sidebands – these account for the peak in loss at 5.5 ms in Figure 1. This will be rectified with suitable modifications, but the potential for using the hardware as a tuneable, diagnostic dipole and quadrupole kicker is being explored.

## HIGH INTENSITY R&D ON ISIS

In this section research and development work to understand and reduce beam loss is summarised.

### Head-Tail Instability

This is a key topic for improving ISIS operations and also of significant interest for understanding more about the effect of space charge on beam stability [9, 10].
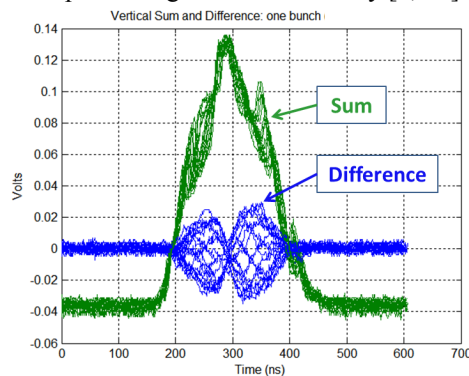


Figure 8: ISIS head-tail motion (single harmonic RF).

Some recent experiments and simulations [9, 10] of head-tail motion have concentrated on the simpler case, with just single harmonic RF operation and low intensities. Measured results have been compared with Sacherer theory and HEADTAIL [11] simulations. The mode structure observed experimentally, $m$=1, (Figure 8) does not agree with theoretical and simulation predictions, $m$=2. Growth rates suggested by theory are also much slower than those from measurements and simulations. Key next steps are investigating the driving impedance in more detail, developing more accurate simulations, and exploring limitations in the Sacherer theory, e.g. [12].

### Image Force Studies and Space Charge

The conformal, rectangular ISIS vacuum vessels give rise to image fields that can form additional driving terms leading to loss at high intensity. In particular, it is thought that offset beams due to closed orbit errors at the dominant $Q_x$=4 harmonic could be causing significant loss on ISIS [13]. This is now under detailed study [14], with development of the Set code [15] for simulation studies and investigations of expected dominant driving terms from theoretical field calculations.

### Half Integer Studies

Half integer losses are expected to have a significant effect on ISIS, but the underlying growth mechanisms are not well understood. Present studies are investigating the behaviour of coasting beams in storage ring mode, which allows investigation of the 2D, transverse resonance effect. Experiments pushing beams on to resonance show good agreement with simulations [16]. This work is allowing detailed benchmarking of codes and looking to develop models of beam loss, with the hope of controlling onset of this key resonance.
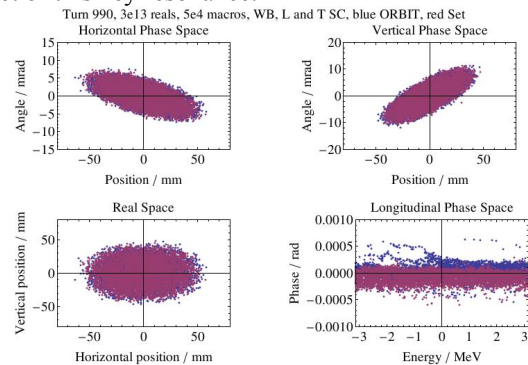


Figure 9: Set benchmarking with ORBIT.

### ISIS Code Developments

An in-house code, Set 3Di, is being developed with a particular focus on ISIS work. It includes self-consistent space charge in transverse and longitudinal planes, treatment of AG and smooth focusing lattices, injection bumps, foil scattering and image forces. Detailed benchmarking against ORBIT models (Figure 9) and ISIS is underway. The code will be a powerful tool for studying many of the topics described above.

### Modelling and Upgrade Work

Detailed ORBIT models of the ISIS ring have been developed that show good agreement with the operational machine [6]. Results of these are given above in Figures 3, 4 and 5. These well established models form the basis of upgrade designs [1].

### Activation and Foils

New FLUKA [17] models of the ISIS collimator system [18] are giving new information on activation levels and the destination of lost particles and secondary products. Comparison of predicted activation with measurements is promising, and data are being used to understand where energy is deposited to help improve machine protection. Figure 10 shows energy deposition along the collimator straight in horizontal and vertical projection.

New comprehensive studies of the $Al_2O_3$ ISIS foil have been investigating its thickness, roughness, composition and structure. Details are given in [19]. A key finding is that foils are perhaps nearer 0.50 µm in thickness rather than the 0.25 µm expected. This implies stripping efficiencies should be nearer to 99.9%, but with increased

losses due to foil scattering. The implications for ISIS operations and loss levels are being evaluated.
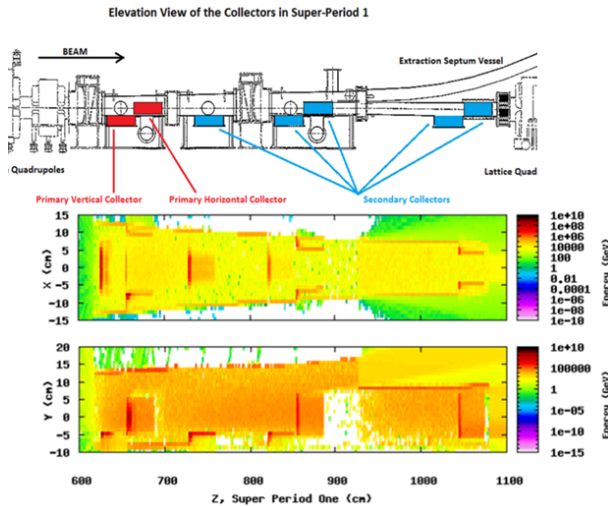


Figure 10: FLUKA simulations of ISIS collimators.

## Measurements and Diagnostics

Accurate beam measurements underpin operations and R&D work. Updates of electronics for diagnostics, new magnet power supplies, and the installation of more powerful data acquisition hardware are all allowing better beam measurement systems to be developed. New systems to determine beam optics parameters, orbits, envelopes and optimise them are being commissioned [8].
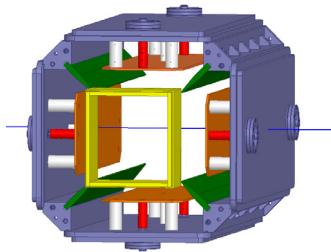


Figure 11: ISIS stripline monitor and kicker.

Research and development into new diagnostics is playing a key role, along with further studies to improve accuracy of ring profile monitors. Developments of loss monitoring, including the use of compact scintillators which can be placed within magnets, are providing enhanced protection. Damper systems and beam kickers are being developed and prototyped: Figure 11 shows a strip line kicker, due for installation next year.

## SUMMARY AND PLANS

The ISIS RCS presently runs with low and well controlled loss, but to increase intensities and maintain reliability, work is underway to improve our understanding and control of the beam. To do this we are developing diagnostics, measurement systems, simulation models, and addressing key beam dynamics issues. Designs for major upgrades depend on experimentally verified codes and theory from this work.

## REFERENCES

[1] D.J. Adams et al., Ring Simulation and Beam Dynamics Studies for ISIS Upgrades 0.5 to 10 MW, THO3LR02, Proc. HB2014.

[2] J. Galambos et al., ORBIT – A Ring Injection Code with Space Charge, THP82, Proc. PAC99.

[3] B. Jones et al., Injection Optimisation on the ISIS Synchrotron, THPP096, Proc. EPAC08.

[4] C.R. Prior, Studies of dual harmonic acceleration in ISIS, Proc. ICANS-XII, RAL Report 94-025 (1994).

[5] A. Seville et al., Progress on the ISIS Synchrotron Low Power RF System Upgrade, WEPFI063, Proc. IPAC13.

[6] D.J. Adams et al., Beam Loss Studies of the ISIS Synchrotron using ORBIT, THPPP088, Proc. IPAC12.

[7] R.E. Williamson et al., High Intensity Longitudinal Dynamics Studies for an ISIS Injection Upgrade, THO1A04, Proc. HB2012.

[8] B. Jones, et al., Progress on Beam Measurement and Control Systems for the ISIS Synchrotron, THPME181, Proc. IPAC14.

[9] V. Kornilov et al., Instability Thresholds of the Head-Tail Modes in Bunches with Space Charge, WEO1LR02, Proc. HB2014.

[10] R.E. Williamson et al., Simulations of the Head-Tail Instability on the ISIS Synchrotron, MOPAB38, Proc. HB2014.

[11] G. Rumolo et al., Electron Cloud Simulations: Beam Instabilities and Wakefields, PRST-AB V5, 121002 (2002).

[12] G.H. Rees, Interpretation of the Higher Mode, Head-Tail Motion Observed on ISIS, Particle Accelerators, V39, p159, 1992.

[13] G.H. Rees et al., Image Effects on Crossing an Integer Resonance, Particle Accelerators, V48, p251, 1995.

[14] B.G. Pine et al., Image Fields in the Rectangular Vacuum Vessels of the ISIS Synchrotron, MOPAB39, Proc. HB2014.

[15] B.G. Pine et al., Space Charge Simulations for ISIS, TH3IODN02, Proc. ICAP 09.

[16] C.M. Warsop et al., Studies of Loss Mechanisms Associated with the Half Integer Limit on the ISIS Ring, MOPAB40, Proc. HB2014.

[17] A. Ferrari et al., "FLUKA: A Multi-Particle Transport Code", CERN 2005-10 (2005), INFN/TC_05/11, SLAC-R-773.

[18] H.V. Smith et al., Activation Models of the ISIS Collectors, MOPRI115, Proc. IPAC14.

[19] H.V. Smith et al., An Overview of the Preparation and Characteristics of the ISIS Stripping Foil, MOPAB04, Proc. HB2014.

# PRESENT STATUS OF THE HIGH CURRENT PROTON LINAC AT TSINGHUA UNIVERSITY AND ITS BEAM MEASUREMENTS AND APPLICATIONS*

Q.Z. Xing#, C. Cheng, C.T. Du, L. Du, T.B. Du, H. Gong, X.L. Guan, C. Jiang, R. Tang, C.X. Tang, X.W. Wang, Y.S. Xiao, Y.G. Yang, H.Y. Zhang, S.X. Zheng, Key Laboratory of Particle & Radiation Imaging (Tsinghua University), Ministry of Education, Beijing 100084, China
W.Q. Guan, Y. He, J. Li, NUCTECH Co. Ltd., Beijing 100084, China
B.C. Wang, Northwest Institute of Nuclear Technology, Xian 710024, China
S.L. Wang, Institute of High Energy Physics, Beijing 100084, China

## Abstract

The CPHS (Compact Pulsed Hadron Source) linac at Tsinghua University, is now in operation as an achievement of its mid-term objective. The 3 MeV proton beam with the peak current of 22 mA, pulse length of 100 µs, and repetition rate of 20 Hz has been delivered to the Beryllium target to produce the neutron beam from the year of 2013. We present in this paper the development and application of the high current linac, together with the measurement of the proton and neutron beams. The beam energy of the CPHS linac will be enhanced to 13 MeV after the DTL is ready in 2015.

## INTRODUCTION

The CPHS (Compact Pulsed Hadron Source) project, which is aimed at becoming an experimental platform for education, research, and innovative applications at Tsinghua University, was launched in the year of 2009 [1]. The facility will provide the proton beam, together with the neutron beam by delivering the proton beam to bombard the Beryllium target. The designed parameters for the proton beam is 13 MeV/50 mA with the pulse length of 500 µs and repetition rate of 50 Hz. The ECR source produces the 50 keV proton beam followed by the LEBT which matches the beam into the downstream RFQ accelerator. The RFQ accelerates the beam to 3 MeV. The Alvarez-type DTL will accelerate the beam from 3 MeV to 13 MeV. The beam is matched to the DTL directly and there is no MEBT between the RFQ and DTL. The HEBT transports the beam from the DTL to the neutron target station. One uniform round beam spot on the Beryllium

target is expected with the diameter of 5 cm [2]. The facility has achieved its mid-term objective in 2013. In this paper, the development status of the CPHS linac is presented, including the proton/neutron beam measurement and application performed.

## OPERATION STATUS OF THE HIGH CURRENT 3MeV LINAC

On March 2013, the maximum transmission of the RFQ accelerator has reached 88% at 50 µs (pulse duration) /50 Hz (repetition frequency) during the commissioning [3][4]. On July 2013 the CPHS facility has achieved its mid-term objective: delivering the 3 MeV proton beam to bombard the Beryllium target [5]. As shown in Fig. 1, the 3 MeV proton beam is delivered directly from the RFQ output to the neutron target station by the HEBT. Five quadrupoles have been positioned instead of the DTL. The DTL will be ready in 2015 and the beam energy of the linac will be enhanced to 13 MeV.

Though the DTL is still in development, the CPHS facility has been in operation with the 3 MeV proton beam from 2013 until now, as shown in Fig. 2 and 3. The output current of the RFQ is relatively stable (30 mA) near the end of 2013. The total operation time in 2014 is estimated to be 500 hrs. With a reduction of the RF power of the ECR source, the peak current of the proton beam before the target has decreased to 20 mA in 2014. During the experiments which need only the proton beam, the beam is not bended by 90° and does not bombard the target.

Figure 1: Wide-angle view of the CPHS facility (from the ECR proton source to the neutron target station).
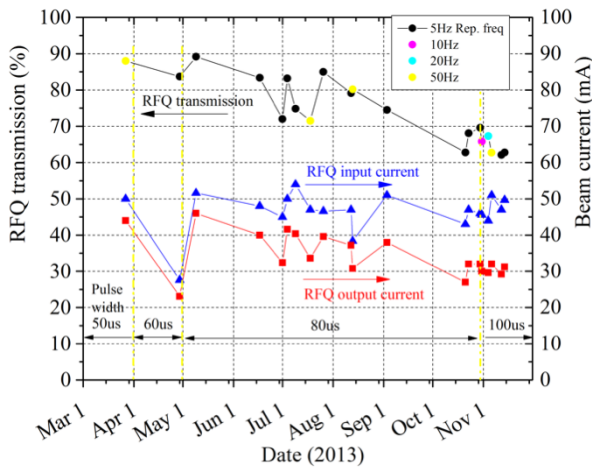


Figure 2: Operation history of the 3 MeV linac in 2013.
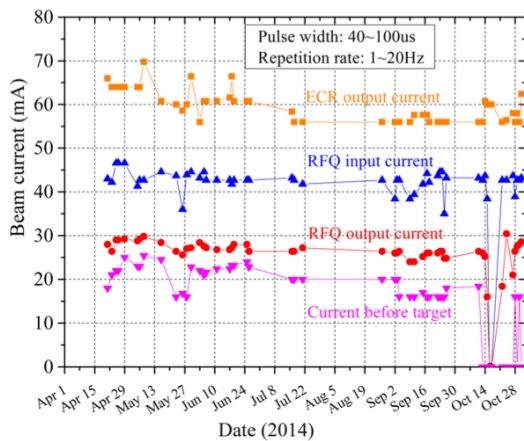


Figure 3: Operation history of the 3 MeV linac in 2014.

In 2015, the CPHS linac is aimed at reaching its designed performance, and stable operation. At the same time it will provide the proton and neutron beams to the users.

## 2D PROFILE MEASUREMENT OF THE PROTON BEAM

Based on the CT algorithm, 2D profile measurement of the proton beam is under development by the rotatable multi-wires [6]. Twenty carbon wires with the diameter of 30 μm are aligned and mounted on one board, as shown in Fig. 4. The electronics system for the measurement of the twenty wires simultaneously will be ready at the end of this year. Therefore only one wire is moved and rotated in the recent experiment and much more time is needed to finish the measurement. The first result is given in Fig. 4. The primary experiment shows that the beam is asymmetric at the measurement position and wire current near the beam centre is 0.14 mA (while the estimated value is 0.16 mA). The following challenging work on the electronics system is to measure the current which is less than 1 nA near the beam edge.
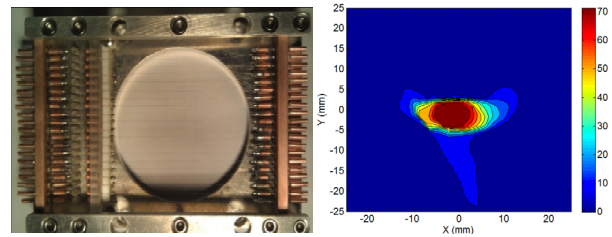


Figure 4: Rotatable multi-wires (left) and the first measurement result by only one wire (right).

## MEASUREMENT OF THE NEUTRON BEAM

The neutrons are produced by the protons bombarding the Beryllium target. The Beryllium sheet has a thickness of 1.3 mm. Presently it is modified to be mounted on one Aluminium plate after it has broken twice with the original design with the operation repetition rate of 50 Hz. Fig. 5 shows the two sides of the Beryllium target with its original design (one side is in the vacuum and bombarded by the protons and the other side is cooled by the water), from which one crack can be observed clearly at the vacuum side.



Figure 5: The vacuum side (left) and water side (right) of the Beryllium target.

Four neutron beam lines are planned in the CPHS project, among which two lines have been constructed: the neutron beam test line and neutron imaging line, as shown in Fig. 6.



Figure 6: Neutron beam test line (left) and neutron imaging line (right).

The characteristics of the neutron beam has been measured on the test line. The wavelength spectrum of the thermal neutron is shown in Fig. 7, which agrees with the simulated value within ±15%. The time structure of the

neutron with the wavelength of 1.17 Å is measured by the time-of-flight method, as shown in Fig. 8.
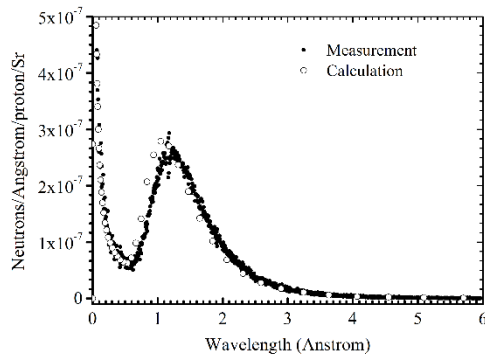


Figure 7: The wavelength spectrum of the first neutron production.
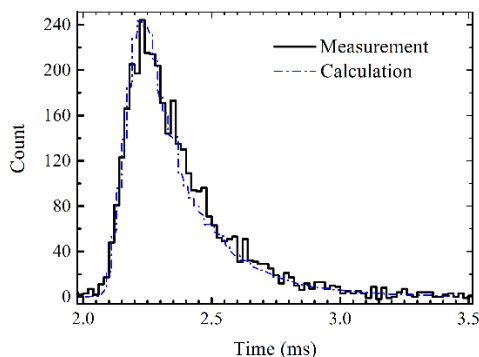


Figure 8: The time structure of the neutron with the wavelength of 1.17 Å.

## NEUTRON APPLICATION

The operation time of the CPHS facility in 2014 is estimated to be 500 hrs. More than half of the operation time is occupied by the development of neutron detectors and neutron imaging, as shown in Fig. 9.
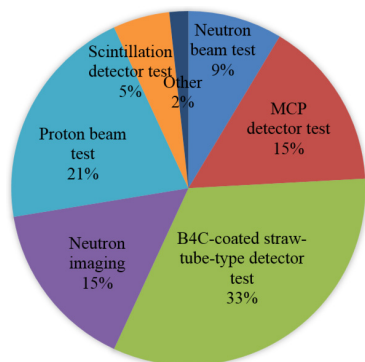


Figure 9: Time percentage of the CPHS operation for different application of the proton and neutron beam at Tsinghua University.

### Neutron Detector Development

Two kinds of the neutron detectors are developed at Tsinghua University, the $B_4C$-coated straw-tube and gadolinium-doped Micro-Channel Plate (MCP), as shown in Fig. 10. The test performed on the neutron line of CPHS

shows that the sensitive length of the straw-tube-type detector is longer than 1000 mm. The resolution of the tube module is 4 mm in the radial direction and better than 8 mm in the axial direction. The detection efficiency of the thermal neutron for single tube is larger than 7% (at 25.3 meV).
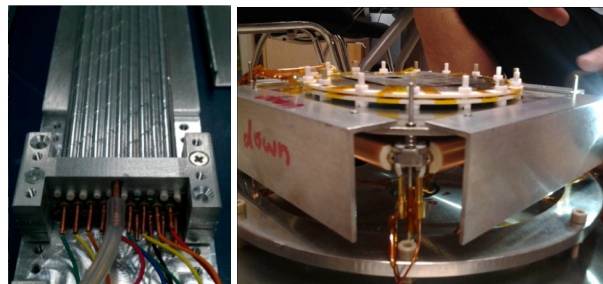


Figure 10: One $B_4C$-coated Straw-tube module (left) and one gadolinium-doped micro-channel plate (right).

### Neutron Imaging

The imaging IP board is positioned at the end of the neutron beam line. The imaging result (Fig. 11) shows that the alignment of the beam line is good because the efficient scattered neutrons are reduced sufficiently. The contribution of the gamma ray is relatively low. The picture in Fig. 11 shows that the transverse distribution of the neutron beam is rather uniform.
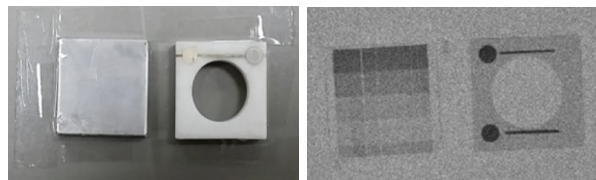


Figure 11: The test piece (left) and neutron imaging (right) after 10 hrs at the end of the neutron beam line.

## REFERENCES

[1] J. Wei et al., "The Compact Pulsed Hadron Source Construction Status", IPAC'10, Kyoto, MOPEC071, p. 633 (2010); http://www.JACoW.org

[2] Q.Z. Xing et al., "Beam Dynamics of the 13 MeV/50 mA Proton Linac for the Compact Pulsed Hadron Source at Tsinghua University", HB2012, Beijing, TUO3B05, p. 289 (2012); http://www.JACoW.org

[3] Q.Z. Xing et al., "High Power Test and Beam Commissioning of the CPHS RFQ Accelerator", IPAC'13, Shanghai, THPWO050, p. 3884 (2013); http://www.JACoW.org

[4] Q.Z. Xing et al., "CPHS Linac Status at Tsinghua University", IPAC'14, Dresden, THPME023, p. 3268 (2014); http://www.JACoW.org

[5] X.W. Wang, "Delivery of 3-MeV Proton and Neutron Beams at CPHS: A Status Report on Accelerator and Neutron Activities at Tsinghua University", Physics Procedia, to be published.

[6] L. Du et al., "Beam dynamics and experiment of CPHS linac", HB2014, East Lansing, THO2LR02 (2014)

# INITIAL COMMISSIONING OF ION BEAMS AT SPIRAL2

Patrick Bertrand, GANIL, Caen, France

*Abstract*

The official reception of the SPIRAL2 accelerator building occurred in October 2014. In parallel, the installation of the accelerator components has started in June 2013. The first part of the beam commissioning, including the ECR sources, the LEBTs and the 88 MHz RFQ should start in December, with an injection in the Linac by mid-2015. This paper describes the status of the accelerator components and installation, and the philosophy retained to commission the light and heavy ion beams at various required final energies.

## INTRODUCTION

Officially approved in May 2005, the SPIRAL2 radioactive ion beam facility at GANIL (Caen-Normandy) has been launched in July 2005, with the participation of many French laboratories (CEA, CNRS) and international partners. In 2008, the decision has been taken to build the SPIRAL2 complex in two phases: *A first one* including the accelerator, the Neutron-based research area (NFS) and the Separator Spectrometer (S3), and *a second one* including the RIB production process and building, and the low energy RIB experimental hall called DESIR [1-3]. However, in October 2013 and due to budget restrictions, the RIB production part has been postponed, and DESIR included as a continuation of the first phase.
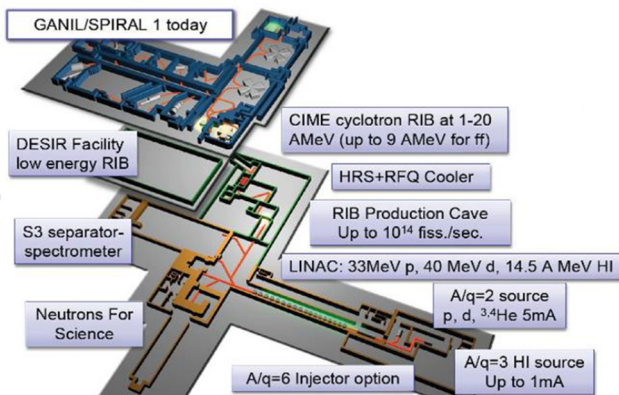


Figure 1: SPIRAL2 project layout, with experimental areas and connexion to the existing GANIL.

As recalled in Table 1, the SPIRAL2 accelerator must deal with a large variety of beams: protons, deuterons, heavy ions with $A/q<3$, ($A/q<6$ in the future). A maximum beam power of 200kW is considered for deuterons in CW mode. We notice also that the heavy ion beam intensities can go up to 1 *mA*; however, some heavy ion beams like metallic ones can also have a very small intensity, which constitutes in itself a challenge, some diagnostics having to work with a huge response range!

Table 1: Beam Specifications

| beam | P+ | D+ | ions | ions |
|---|---|---|---|---|
| A/Q | 1 | 2 | <3 | <6 or 7 |
| Max.  I (mA) | 5 | 5 | 1 | 1 |
| Min. output E (MeV/A) | 2 | 2 | 2 | 2 |
| Max output E (MeV/A) | 33 | 20 | 14.5 | 8 |
| Max. beam power (kW) | 165 | 200 | 44 | 48 |

In this paper, after giving updated information on the accelerator-NFS-S3 building and process installation, we will concentrate on our beam commissioning strategy.

## ACCELERATOR-NFS-S3 BUILDING

The construction permit of the accelerator-NFS-S3 building was obtained in October 2010. After a difficult excavation work and geotechnical/geologic studies, the first concrete started in September 2011. The building itself was officially received last October 2014 (Figure 2), and the utilities will be officially approved very soon.

During the construction, several inspections were made by the French Safety Authorities, in order to check the conformity of the building with respect to the requirements like confinement barriers, protection against earthquakes, etc...



Figure 2: Completion of the accelerator building (October 2014). The beam axis is 9.5 meters underground.

## STATUS OF THE ACCELERATOR

The building construction process has been organised in such a way, that it was possible to install progressively the process inside the building, starting by mid 2013 with the low energy beam lines and their power supply and utilities, all this in parallel with other parts of the building construction (HEBT for example). This strategy allowed us to gain about one year, but the coactivity between building and process teams, and the planning optimization appeared to be not so easy to manage, one difficulty being

the cleanliness needed for many Linac deliveries.

At present, the accelerator status of installation is the following:

The 18GHz ECR heavy ion source called Phoenix-V2 and updated to host metallic ovens, is now installed on site, together with its transport line called LEBT1.

The 2.45GHz ECR light ion source is also installed together with its transport line called LEBT2, and the main part of the merging section LEBTC line.

The 88MHz 4-vane RFQ is now assembled and aligned in the tunnel, with good vacuum tests. The bead pull is well underway, and the RFQ conditioning should occur by beginning of 2015.

The first part of the MEBT is ready to be installed and to be connected to the D-plate.

Concerning the Linac, all the cavities are qualified on vertical cryostats and tested with success. Eight low-beta cryomodules are assembled and tested, and the 4 remaining ones will be qualified and delivered at GANIL/SPIRAL2 by March 2015. Five high-beta cryomodules are qualified and ready to be installed in the tunnel, while the 2 remaining ones will be ready next December [4]. All the couplers are processed and conditioned [5], and all the warm section packages are ready to be installed. The installation of the Linac itself should start by November, waiting for the complete cleanliness of the tunnel.

All the dipoles, quadrupoles and steerers of the HEBT [6] are received and measured, and the profilers are ready to be installed. The mechanical HEBT supports are positioned, and the aluminium vacuum pipes and stainless steel diagnostic boxes are under fabrication.

All the RF amplifiers are received and tested at GANIL with a specific RF test bench, their complete installation being programmed by end of November. The cryogenic system is under final installation.

## BEAM COMMISSIONING STRATEGY AND FIRST RESULTS OBTAINED

Several years ago, we took the decision to operate the SPIRAL2 beam commissioning in 4 phases:

*First of all*, we decided to pre-install the ECR sources and low energy transport lines in two French laboratories, in order to test them *with beam* before the SPIRAL2 building availability: these successful tests were achieved by end 2012, before transportation to GANIL.

The *second phase* of beam tests concerns the injector: they will start next December at SPIRAL2/GANIL site, and will last six months, with the RFQ connected to the D-plate. We will basically reproduce the results obtained without RFQ, operate the tuning and conditioning of the RFQ, and measure the beam characteristics at RFQ exit, using the D-plate.

After dismounting of the D-plate, the *third phase* will concern the tuning of the beam with the complete MEBT, the beam tests of its fast chopper, the Linac acceleration,

and the tuning of the HEBT going to the Beam Dump.

The *fourth phase* will be the "day-1" experiment, with beam delivery for NFS physics studies by end 2015, and S3 in 2016.

### Beam pre-commissioning at LPSC Grenoble

Dedicated to heavy ions, the $18GHz$ Phoenix-V2 ECR source and its achromatic analysis beam line LBET1 have been installed at LPSC laboratory (Grenoble) during about 2 years, until June 2012 (Figure 3). The ECR source and its environment were updated these last years, to host metallic ovens developed at GANIL, and sustain 60 kV (See also [7, 8] for more details).
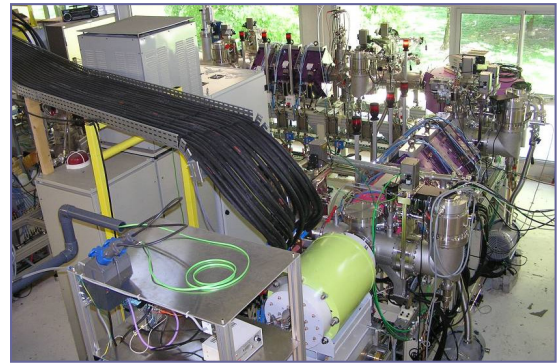


Figure 3: View of ECR source and Spiral2 LEBT1 when installed at LPSC for beam tests until mid 2012.

- Using automated optimization algorithms developed from the TRACEWIN code, we obtained 30% more than $1mA$ of $^{16}O^{6+}$ (goal for SPIRAL2), and 70µA of $^{40}Ar^{12+}$, with a good transmission (95%). Around 2mA of $^4He^{2+}$ were also achieved, which is of interest to mimic the deuteron beam and learn how to tune the Linac.

- As expected, we measured transverse emittances around 0.25 π.mm.mrad.norm.rms, with an efficient action of the hexapole corrector associated to the analysis bending magnet (Figure 4). Very similar transverse beam profiles in both pulsed and CW source mode were also obtained.
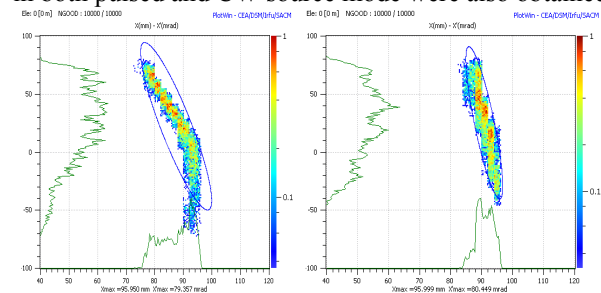


Figure 4: Horizontal dipole aberrations (left) optimized (right) tuning the hexapole ($^{16}O^{6+}$, 0.8$mA$ beam)

- The separation power of the LEBT1 line is found better than specified. (>100), which is a good sign for future Linac pure beam acceleration (Figure 5).

- We also obtained more than 20µA of $^{58}Ni^{19+}$ (Figure 6), and 48µA of $^{48}Ca^{16+}$, which is very promising [9]

In 2013, and thanks to a European contract, the LPSC

laboratory started a development of the new economical Phoenix-V3 ECR source, with a bigger plasma chamber (1.4 liter instead of 0.6), in order to increase the ion rate production, and accept new generation metallic ovens (20 mm diameter). First beams with Phoenix-V3 are expected in January 2015, using the LPSC Test bench [10].
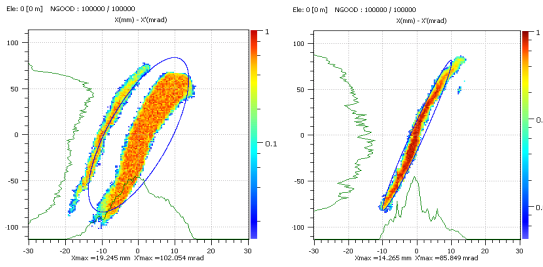


Figure 5: Beam separation of beams ($^{16}O^{3+}$ and $^{132}Xe^{25+}$) with 20*mm* (left) and 5*mm* (right) slit aperture.
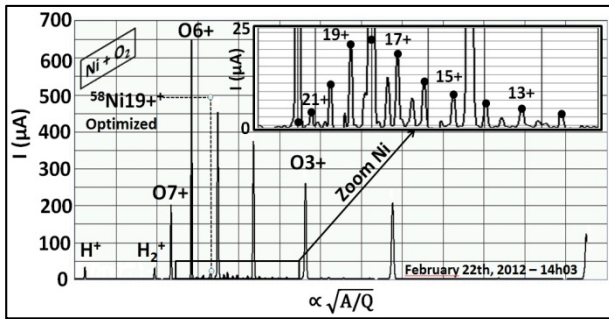


Figure 6: Spectrum optimized for $^{58}Ni^{19+}$ (~20 µA), using the Large Capacity High Temperature Oven from GANIL

### Beam pre-commissioning at IRFU/Saclay

Important results were also obtained in 2010-2012 at IRFU/Saclay, where the deuteron/proton ECR source, the transport lines LEBT2 (achromatic analysis section) and LEBC (merging transport and matching line to the RFQ) have been installed in several successive steps (Figure 7).

These results were obtained by using intensively the TRACEWIN code for the beam tuning, and by applying the "virtual accelerator concept" explained in [11].

Here are the main results obtained (see also [12]):

- First of all, the 2.45GHz permanent magnet ECR source confirmed its capability to produce a very stable and reproducible 6.7mA 40*kV* deuteron in CW or pulsed beam mode (and also down to 50*µA* in CW), with an emittance between 0.1 and 0.22 π.mm.mrad.norm.rms, depending upon the tuning of the slits and the vacuum level.

- We also verified that the set of movable LEBT slits were efficient to clean the generated halo optimally, and that we could chose the vacuum level in order to optimize the space charge compensation parameter.

- The slow chopper, developed by INFN Catania, has been tested on line and gave excellent results [13]: Transition times below 30 ns were confirmed as well as the duty cycle range from 0.1‰ to 99.99%. The device can operate up to 10 kV, up to 1 kHz. The slow chopper will be used intensively to manage the beam duty cycle.

- Automatic beam alignment and optical procedures

showed very efficient behaviors, with transverse emittance portraits and perfect RFQ matching parameters achievements: By installing at the *exact* RFQ injection point the very nice emittance-meter developed by IPHC/Strasbourg, we could measure the emittances (Figure 8) and by generating a set of $10^6$ particle reproducing them, we could check with the TOUTATIS code that the real beam should be correctly bunched and accelerated through our RFQ model (Figure 9).
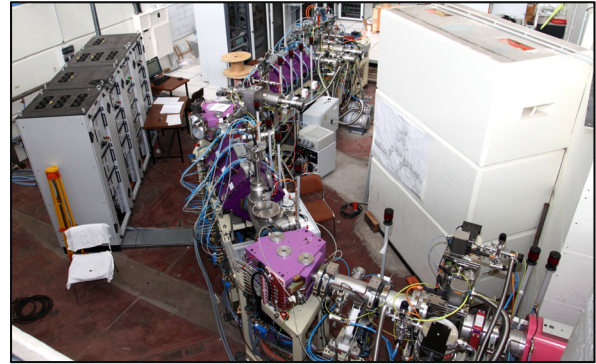


Figure 7: View of the ECR source, and LEBT2+LEBTC installed at IRFU (Saclay) for beam tests until end 2012.
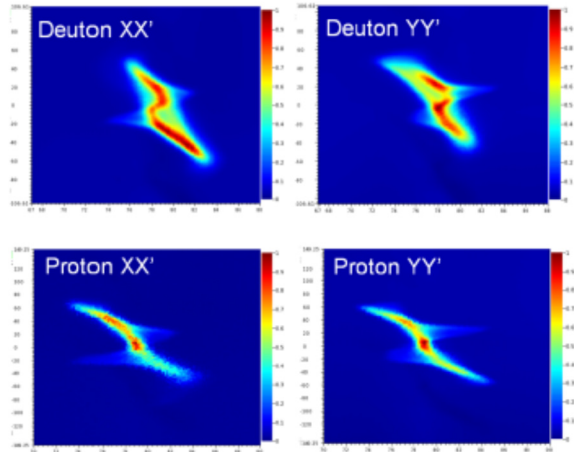


Figure 8: Deuteron and proton transverse emittances at RFQ injection point. (5*mA* in CW mode)
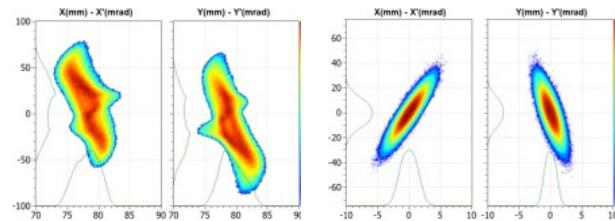


Figure 9: D$^+$ measured emittances as input for RFQ TOUTATIS acceleration, and output emittances obtained.

*Remark:* before going to the 2$^{nd}$ beam test phase, we mention that thanks to our partnership with existing accelerators (SARAF, INFIN-HH, GANIL…), we were also able to test various components like diagnostics in presence of existing beams, and to have some irradiation tests on samples to check their resistance to radiations and to validate the activation codes.

*Beam Commissioning of Injector at SPIRAL2*

As already mentioned, the two ECR sources and their associated LEBTs are now installed in the SPIRAL2 building, and we should reproduce quite easily by December 2014 the results obtained at Grenoble and Saclay respectively. The 88 MHz 4-vane RFQ has been assembled one month ago (Figure 10), with the bead pull tuning to be started. After the RFQ RF conditioning, we will enter into the complete injector beam commissioning, using the first MEBT meter, and the D-plate (Figure 11) connected after the 1st rebuncher), in the following way:



Figure 10: SPIRAL2 RFQ assembled in September 2014.



Figure 11: Assembly tests of diagnostics on D-plate

First of all, the D-plate is equipped with a set of the diagnostics: BPMs, ToF, FCT, DCCT/ACCT, harps, H-V emittance-meters...This will allow us to characterize the RFQ behaviour in terms of transmission, transverse emittances, beam profiles, energy and energy dispersion. By changing step by step the amplitude of the 1st MEBT rebuncher, and measuring the longitudinal beam length towards the end of the D-plate, we will also deduce the longitudinal emittance using the 3 gradients method.

All these measurements will be performed for the following beams successively:

- *Protons (A/Q=1)* 150μA peak, 200μs pulsed@5Hz (0.1% duty cycle), and then increase the peak current from 150μA to 5mA, with duty cycle from 0.1% to 100%
- *Helium $^4He^{2+}$ (A/Q=2)* 150μA peak, 500μs pulsed @2Hz (0.1% duty cycle),and then increase the peak

current from 150μA to 2mA, with duty cycle from 0.1% to 100%
- *Oxygen $^{18}O^{6+}$ Pencil beam* 150μA peak, 500μs pulsed @2Hz (0.1% duty cycle), and then increase the peak current from 150μA to 1mA, with duty cycle from 0.1% to 100%
- If enough time, tests with Argon, Carbon, Xenon
- Nickel $^{58}Ni^{19+}$ up to 20μA, 100% duty cycle.

The optimisation will be done by playing with the beam matching at RFQ entrance using the double solenoid, the LEBT vacuum level and the RF compensation ring, the beam input energy and alignment and the RFQ voltage. We can notice that the set of 3 horizontal-vertical slits and associated profilers installed before the RFQ entrance allow us to change the emittance homothetically.

*Remark 1:* During this *"injection phase"*, Helium beam will be used instead of the Deuteron one, because Deuterons are not allowed before having the complete authorisation given later by the French Safety authorities.

*Remark 2:* During this intermediate beam commissioning, the installation of the Superconducting Linac and of the HEBT lines and beam dump will go on in parallel, and the command/control will be achieved, with the needed high level applications.

*Full Beam Commissioning Phase with the Linac*

Once the D-plated withdrawn and the complete MEBT installed and connected to the Linac, and thanks to the knowledge acquired, to the efficiency of TRACEWIN code and to our 3D electromagnetic maps, we will pre-tune the complete 0.75MeV/u MEBT, for each beam of interest. Then we will create the SC Linac beam periodic channel step by step in the following way:

- Adjust all the quadrupoles of the linac HEBT to the Beam Dump according to the RFQ-MEBT energy,
- Tune the first cavity (amplitude & phase) using BPMs by Time of Flight measurement,
- Re-adjust all linac and HEBTs quadrupoles,
- Tune the second RF cavity,
- Operate the same way for the other 25 cavities…

The Linac tuning will be ensured by means of Beam Position Monitors (BPM) buried into the first quadrupole of each of the 19 Linac warm sections, while the beam extension monitors (BEM) installed in the 5 first warm sections [14] will allow us to tune the 3 MEBT rebunchers, in order to match the beam to the linac longitudinally.

The survey of the beam intensity and the energy will be ensured by several ACCT/DCCT devices, and a ToF system installed at the exit of the Linac ([15-17]), in the frame of the Machine Protection System [18].

The BLM scintillator detectors, developed by IFIN-HH/Bucarest and disposed around the Linac and HEBT lines, will deliver a "beam stop" signal in case of

excessive beam losses. Loss rings disposed along the HEBT vacuum pipes will also provide untimely steering information and similar beam stops signals, in order to protect the machine against beam thermal damage, together with beam energy and transmission.

### *Beam Commissioning towards NFS*

The fourth commissioning phase will consist in conducting the beam to NFS experimental hall. In the (probable) case of a first experiment based on Neutron Time of Flight, we will tune the 5mA Deuteron beam at the source, and use extensively the Fast chopper (also called "Single Bunch Selector") located along the MEBT: This device must reduce by 100 to 10000 the bunch rate in order to avoid neutron bunch overlapping effects fo physics. It is based on the superposition of a steerer magnet and 2 high impedance meander electrodes driven with high voltage pulses of opposite sign. A vacuum chamber prototype equipped with 100Ω meanders and feed-through have been constructed in collaboration with INFN-LNS and successfully tested in Catania [19]. The final device should be operational in a few months.

### *One Way to Gain Time during Future Operation*

As already mentioned we will accelerate a variety of beams with various ratios q/m, which could generate much time for each tuning in operation. One way to limit it is to make use of an important a theorem valid even in the relativistic case:

Suppose that we know the set of parameters already tuned and archived for a beam with a given $q/m$, and that we want now to accelerate a new beam with another $\hat{q}/\hat{m}$, and let define their relative difference:

$$\varepsilon = \frac{\hat{q}/\hat{m} - q/m}{q/m} .$$

Then by multiplying all the voltages and magnetic values of the machine by the factor $1/(1+\varepsilon)$, we can accelerate the beam without major difficulty (with adjustment of last cavities and HEBT fields depending on the final energy needed...). In particular *all* the phases remain unchanged!

## CONCLUSION

The beam pre-commissioning performed at IRFU/Saclay and LPSC/Grenoble was essential to validate our low energy design and simulations, and to operate many technical tests with the EPICS philosophy and our Command/Control. We enter now in the complete beam commissioning on SPIRAL2 site, which constitutes a great motivation and for all our partners and for us.

## AKNOWLEDGEMENT

## REFERENCES

[1] The scientific objectives of the SPIRAL2 project. http://pro.ganil-spiral2.eu/spiral2/what-is-spiral2/physics-case/at_download/file

[2] E. Petit, "progress of the SPIRAL2 project", IPAC 2011, San Sebastian, Spain, September 2011.

[3] P. Bertrand, R. Ferdinand, "SPIRAL2 accelerator construction progress", LINAC 2012, Tel-Aviv, Israel. September 2012.

[4] P.E. Bernaudin, "SPIRAL2 cryomodule production results and analysis", LINAC 2014, Geneva, Switzerland, September 2014.

[5] Y. Gomez et al., "Last SPIRAL2 couplers preparation and RF conditioning", SRF 2013, Paris, France, September 2013.

[6] L. Perrot et al., "HEBT lines for SPIRAL2 facility: what to do with the accelerated beams", HB2010, Morschbach, Switzerland, October 2010.

[7] J.L. Biarrotte et al., "First beams produced by the SPIRAL2 injectors", Linac 2010, Tsukuba, Japan.

[8] C. Peaucelle et al., "First A/Q=3 Beams of Phoenix V2 on the heavy low energy beam transport line of SPIRAL2", Ecris2010, Grenoble, France, Sept.2010.

[9] C. Barué et al. "Metallic beam developments for the SPIRAL2 project", ICIS 2013, Chiba, Japan, September 2013.

[10] Th. Thuiller et al, "Recent results of Phoenix V2 and new prospects with Phoenix V3", ECRIS2012, Sydney, Australia, Septemebr 2012.

[11] D. Uriot, "The virtual accelerator concept", EUROCARD2/MAX Accelerators for the driven system workshop", CERN, March 2014.

[12] D. Uriot, O. Tuske et al, J.L. Biarrotte, "Commissioning of the SPIRAL2 Deuteron injector", IPAC2013, Shanghai, China, May 2013.

[13] A. Caruso et al., "The LEBT chopper for the SPIRAL2 project", IPAC2011, San Sebastian, Spain, September 2011.

[14] R. Rovenko, "SPIRAL2 Bunch Extension Monitor", LINAC 2014, Geneva, Switzerland, September 2014.

[15] W. Le coz et al., "Progress on the beam energy monitor fot the SPIRAL2 accelerator", IBIC2014, Monterey, USA, Sept 2014.

[16] Ch. Jamet et al. "Beam intensity and energy control on the SPIRAL2 facility", LINAC 2012, Tel-Aviv, Israel. September 2012.

[17] Ch. Jamet et al, "Failure mode and effect analysis of the beam intensity control for the SPIRAL2 accelerator", IBIC2014, Monterey, USA, Sept. 2014.

[18] M-H. Moscatello, "Machine protection system for the SPIRAL2 facility", IPAC2012, New Orleans, USA, May 2012.

[19] M. Di Giacomo, A. Caruso et al., "Measurement of the first prototype of the SPIRAL2 SBS selector". IPAC2012, New Orleans, Mai 2012.

# Chromatic and Space Charge Effects in Nonlinear Integrable Optics[*]

S. D. Webb[†], D. L. Bruhwiler, and R. Kishek[‡], RadiaSoft, LLC., Boulder, CO
A. Valishev and S. Nagaitsev, FNAL, Batavia, IL
V. Danilov, ORNL, Oak Ridge, TN

## Abstract

The IOTA test accelerator is under construction at FNAL to study a novel method of advancing the intensity frontier in storage rings: nonlinear integrable optics. For particles at the design momentum, the lattice has two invariants and the dynamics is integrable. In the ideal single-particle two-dimensional case, this yields bounded, regular orbits with extremely large tune spreads. Off-momentum effects such as dispersion and chromaticity, and collective effects such as direct space charge, break the integrability. We discuss the origin of this broken integrability for both single- and many-particle effects, and present simulation results for the IOTA lattice used as a high intensity proton storage ring.

## INTRODUCTION

Future generations of intense, multi-megawatt accelerators have applications for discovery science as drivers for spallation sources, neutrino physics, and the next generation of high energy colliders. Such intense beams are prone to collective instabilities including, but not limited to: space charge driven beam halo, resistive wall instability, head-tail instability, and the various beam break-up instabilities. The physical origin of these instabilities is the constant transverse tunes in linear strong-focusing lattices. In the SNS accumulator ring, for example, it was found [1] that these instabilities did not appear for the natural chromaticity of the lattice, which was very large. It is then natural to conclude that the large tune spreads associated with these chromaticities are desirable for mitigating such instabilities.

The trouble with this is that the large chromaticities in the linear lattices will span an entire integer or more of tune space, which will cross many single-particle resonances. A more robust method is required to obtain large tune spreads without losing dynamic aperture due to single-particle dynamics. Enter the nonlinear integrable optics designed by Danilov and Nagaitsev [2], which introduce very large tune spreads while keeping the orbits regular. This work has already shown promise in preventing space charge driven beam halo [3] In this proceeding, we discuss how these invariants change in two real-machine situations: energy spread and space charge.

In the next section, we discuss how energy spread in coasting beams breaks the single-particle integrability, and how we may design the lattice to restore that integrability. How direct space charge changes a matched distribution of

the invariants is explored in the following section. We conclude with preliminary simulations of using the integrable optics to prevent resistive wall instability in an intense proton ring.

## OFF-MOMENTUM EFFECTS: CHROMATICITY & DISPERSION

The work in [2] considers purely two-dimensional particle dynamics – transverse oscillations with no energy spread. In real intense accelerators energy spread and the associated chromaticity, as well as the dispersion in the lattice, will modify the integrable Hamiltonian. Before asking the nonlinear integrable lattices to mitigate intensity-driven effects, it is important to restore the integrability which makes it so robust.

As we show in [4], a Lie operator treatment of a ring designed for integrable optics that includes off-momentum effects and nonlinear elements such as sextupoles and octupoles yields a correction to the Hamiltonian in [2] due to dispersion in the elliptic magnet sections and the lattice chromaticity. The integrable lattice factors into a product of maps:

$$\mathcal{M} = \mathcal{A}^{-1} e^{-t:\int ds \mathcal{U}(x-\delta\eta(s),y):} e^{-:h:} e^{-t:\int ds \mathcal{U}(x-\delta\eta(s),y):} \mathcal{A} \quad (1)$$

where $\mathcal{A}$ is the normalizing map, and $h$ is the Hamiltonian that generates the single turn map for the integrable optics lattice when the nonlinear elliptic potential strength is zero. Thus, $h$ includes drifts, dipoles, and quadrupoles, as well as chromaticity-correcting families of nonlinear magnets. The details of this calculation may be found in [4] and are too lengthy to include here.

The resulting Hamiltonian for the total single turn map is given, to lowest order, by:

$$\overline{\mathcal{H}} = \frac{\mu_0}{2} \left\{ [1-C_x(\delta)] \left(\overline{p}_x^2 + \overline{x}^2\right) + [1-C_y(\delta)] \left(\overline{p}_y^2 + \overline{y}^2\right) + \frac{t}{1-\delta} \int_0^{\ell_{\text{drift}}} \mathcal{U}\left(\overline{x} - \eta(s')\,\delta\right), \overline{y}\right) ds' \right\} + \ldots \quad (2)$$

where ... are higher order terms, including any nonlinear terms left over after adjusting the chromaticity. Here we have assumed a coasting beam with no synchrotron oscillations, thus $\delta$ is a constant. $\eta(s)$ is the dispersion function through the drift where the elliptic magnetic element will be placed, and $\mathcal{U}$ is the nonlinear elliptic potential from [2]. This means that the vertical and horizontal chromaticities, $C_y(\delta)$ and $C_x(\delta)$ respectively, are general functions of $\delta$. We also concluded that conventional chromaticity correction schemes – using sextupoles to correct

Computational Challenges, New Concepts and New Projects

linear chromaticity with $(2n+1)\pi$ phase advances between the sextupoles to minimize dynamic aperture loss, for example – still apply. The goal is to bring this lowest-order Hamiltonian into a form which has two invariants and thus preserves the two-dimensional integrability

The Hamiltonian in [2] derives from a self-consistent solution for free-space magnetic fields and the Bertrand-Darboux partial differential equation for Hamiltonians with a second invariant which is quadratic in the momentum. One of the fundamental assumptions going into the derivation of the Bertrand-Darboux equation is that the coefficients of the vertical and horizontal momenta must be equal. In doing see, we obtain a modification of the Hamiltonian in eqn. (22) of [2]:

$$H = (1 - C(\delta)) \left[ \frac{1}{2} \left( p_x^2 + p_y^2 + x^2 + y^2 \right) + \frac{1}{1 - C(\delta)} V(x,y) \right] \tag{3}$$

This leads us to four design principles for building a lattice ready for the nonlinear integrable optics to obtain an integrable Hamiltonian, even in the presence of energy spread:

1. Vertical and horizontal linear tunes must be equal

2. Vertical and horizontal beta functions inside the drift where the nonlinear magnet is to be placed must be equal

3. Dispersion must vanish inside this drift

4. Vertical and horizontal chromaticities must be equal

Non-dispersive sections of rings are fairly standard, and make the integral over the dispersion function into simply a multiplication by $\ell_{\text{drift}}$. The conclusion of equal chromaticities is based on the following line of reasoning.

Chromaticity correction in conventional strong-focusing linear lattices is a balancing act between having enough tune spread to Landau damp instabilities, while keeping the tune spread small enough to avoid crossing nonlinear resonances. Because the nonlinear integrable lattices already have large tune spreads, which will already cross nonlinear resonances, it is most important to keep the integrability of the unperturbed Hamiltonian so that the KAM theorem applies near these resonances. It is thus sufficient to restore the conditions required for the Bertrand-Darboux equation, specifically that the transverse momenta have the same coefficient. We can therefore adjust $C_x$ and $C_y$ until they are equal. This is actually beneficial to the dynamic aperture, as this reduces the strength required of the chromaticity-correcting nonlinear elements. It also gives us the freedom to choose whether we correct one or both chromaticities, depending on which choice will lead to the best dynamic aperture.

## SPACE CHARGE & THE INVARIANTS

We now return to study two-dimensional effects – how space charge changes the distribution of a longitudinally
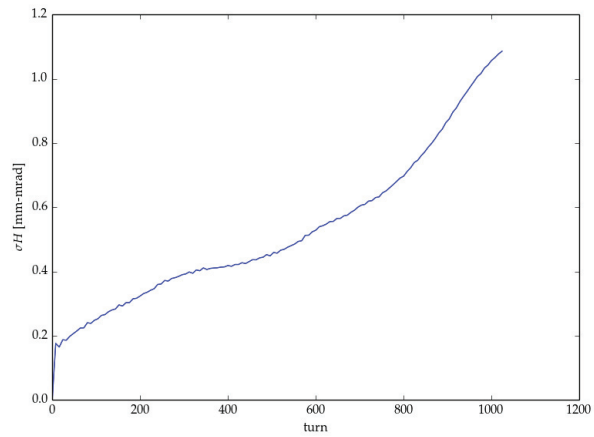


Figure 1: The r.m.s. value of $H_0$ as a function of turn.

cold beam. We consider here the distribution of the Hamiltonian, $H$, and second invariant, $I$, described in [2]. We began with a beam with an exponential distribution in $H$, viz.

$$f = \frac{N}{\varepsilon} e^{-H/\varepsilon} \tag{4}$$

where $N$ is the number of particles per unit length in the beam and $\varepsilon$ is the transverse emittance. This distribution reduces to a Gaussian distribution for a linear lattice, with $\varepsilon$ being simply the RMS emittance, equal in the vertical and horizontal. Because the elliptic potential creates strong transverse coupling, such a separation into "vertical" and "horizontal" emittance is not possible for these lattices.

The addition of space charge adds a self-consistent term to the Hamiltonian, so that the total Hamiltonian is given by

$$\mathcal{H} = H_0(J) + \mathcal{V}[f] \tag{5}$$

where $\mathcal{V}$ is the space charge potential. This has the effect of changing the invariants, and so the initial distribution will evolve. Here, $\mathcal{V}[f]$ is a functional of the phase space distribution, which can be thought of as the Green's function for the potential as a function of the charge distribution, as expressed in action-angle variables.

We use as a figure of merit the value of $H_0(p,q)$ as a function of time. The initial distribution is a delta function, $\delta(H_0 - \varepsilon)$. This function is known from [2] eqn. (22), and is analogous to the Courant-Snyder invariant for linear lattices. Thus, this bunch is analogous to a Kapchinskij-Vladimirskij distribution with emittance $\varepsilon = 15\,\text{mm} - \text{mrad}$. We therefore expect that the spread in $H_0$ should be a good indication of the beam evolution. In Fig. 1, we see that the spread in $H_0$ grows dramatically on two time scales. There is one time scale that is a handful of turns that marks a dramatic increase in $H_0$, and then a slower diffusive-like process that takes over after this.

Based on this, we would expect the bunch distribution to be expanding quite rapidly. However, this is not the case, as we see in the phase space projections from turn 712 (Fig. 2), well after the diffusion has taken hold. The
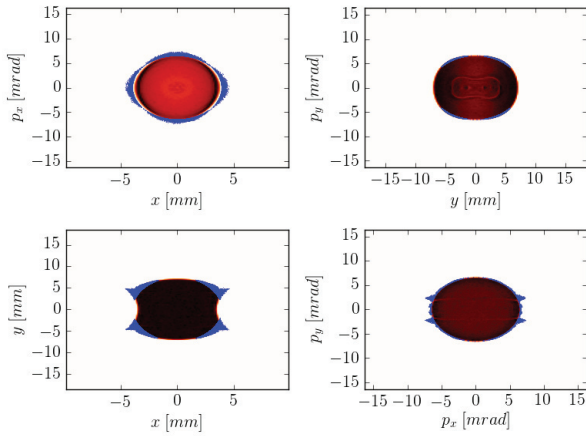
Figure 2: The transverse phase space projections after 712 turns.
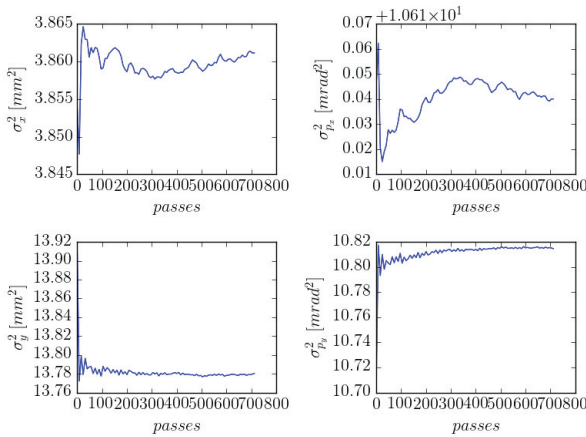


Figure 3: RMS beam size and momentum spread versus time.

initial distribution is much the same as this one, despite the RMS value of $H_0$ being 5 % of the initial $H_0$. Longer time simulations do not show a substantial departure from this distribution. Indeed, we find that variations in the RMS beam size vary at the 0.1 % level, in Fig. 3. This is contrary to our intuition based on linear optics – the beam radius is given by $\sigma_r \propto \sqrt{\beta\varepsilon}$, and therefore an increase in $\varepsilon$ should correspond to a similar increase in the beam size.

We speculate that the origin of this can be derived from a Fokker-Planck equation for diffusion in action space due to the space charge perturbation [5]. Taking the phase space distribution $f = f(J)$ as a pure function of the action, the stochasticity due to chaotic trajectories and phase mixing leads to a Fokker-Planck equation

$$\frac{\partial f}{\partial t} = \frac{\partial}{\partial J}\left\{\frac{1}{4}(\Delta t)^2\left(\frac{\partial}{\partial J}\left\langle\left(\frac{\partial \mathcal{V}[f]}{\partial \psi}\right)^2\right\rangle_\psi\right)\frac{\partial f}{\partial J}\right\} \quad (6)$$

The total Hamiltonian $\mathcal{H}$ is broken into three parts: the

single particle integrable Hamiltonian, the component of space charge that remains integrable, and the component of space charge that induces diffusion. Specifically:

$$\mathcal{H} = H_0(J) + \mathcal{V}_0[f](J) + \sum_{n \neq 0}\mathcal{V}_n[f](J)e^{in\psi} \quad (7)$$

When we generate a distribution, we are matching it to $H_0$ – tracking that distribution over many thousands of turns shows no change in the phase space distribution when current is zero. The integrable space charge component, $\mathcal{V}_0[f](J)$, represents a potential well distortion of sorts, and is the source of the rapid early filamentation that occurs over only a handful of turns. This is the origin of the abrupt growth in measured $H_0$ we see in a handful of turns in Fig. 1 The remaining terms in the space charge, varying with $\psi$, cause the diffusion we see in $H_0$ in Fig. 1.

A possible limit for space charge in the nonlinear integrable lattices may be the existence of a stable stationary solution to the Fokker-Planck equation for the phase space distribution. Thus, the figures of merit for a nonlinear integrable lattice to determine the importance of space charge could be related to the functional form of the Fokker-Planck equation, and the existence of stationary solutions. This would go a long way to explaining the stability of these beams in real space, despite their apparently poor behavior in terms of the single-particle invariant distributions.

## FUTURE WORK

Nonlinear integrable optics remains a very naïve field – it is not clear how many concepts from conventional linear lattices survive, and how they might be modified. We suggest that there are two lines of inquiry worth pursuing: how the chromatic corrections affect the dynamic aperture, and how space charge affects the distribution.

Chromatic correction schemes are designed to minimize the impact on on-energy dynamic aperture. The $\pi$ phase advances meticulously cancel terms that are not proportional to the energy offset, and the chromatic correction scheme is built around the terms, say, linear in $\delta$ for a sextupole correction. There then remains $\mathcal{O}(\delta^2)$ terms which reduce the dynamic aperture for off-energy particles. In the linear lattice case, this is avoided by avoiding the resonant lines in tune space these remaining terms generate. The nonlinear integrable optics has an enormous tune spread – this is the origin of its great robustness against parametric resonances. It is necessary to gain theoretical guidelines to how this affects the dynamic aperture. There are three specific questions in this line:

1. Where are the resonant lines for these terms in the nonlinear integrable optics?

2. What chromatic correction schemes can be used to get the equal chromaticities while minimizing the impact on dynamic aperture?

3. What is the diffusion time for particles on those resonant lines?

This requires understanding $x$ and $y$ in terms of two invariants $I_1$ and $I_2$, and their associated angle variables, to understand resonance lines and the relevant parameters for these computations. Analytical or semi-analytical results are absolutely necessary for achieving guidance here.

We have established thus far that the nonlinear decoherence prevents the onset of beam halo, and we have studied how the single-particle invariants evolve under space charge. We have seen that space charge prompts diffusion-like behavior in the $H$ and $I$ invariants, which is to be expected. What is curious is that the actual transverse profile does not change dramatically under space charge, even as the spread in the $H$ and $I$ quantities increases dramatically. Understanding this behavior is critical for moving to increasing intensity. This preliminary work suggests three additional questions in the realm of space charge:

1. How are the relevant parameters for characterizing space charge strength?

2. Is there a collective invariant consistent with space charge but different from the single-particle invariant?

3. What can be done to compensate space charge?

The suggestion here is that there are a new set of invariants $(H', I')$ which are better-preserved in the presence of space charge. This is one way to explain how the distribution in the single-particle invariants grows so rapidly, but the actual beam envelope remains relatively stable. Until the effects of space charge are fully understood, we cannot make intelligent decisions about compensation, beam transport limits, *etc.*

The current set of results are promising for implementing a working accelerator that uses the nonlinear integrable optics as a method of transporting intense beams with low loss. We have given a theoretical conclusion for handling the chromaticity. Simulations indicate high-power beams may be transported without any loss due to space charge. But our theoretical understanding of the nonlinear integrable optics in the presence of space charge remains limited. In linear lattices, envelope models yield useful parameters such as the perveance and the Laslett tune shift [6]. No such clear-cut parameters exist to characterize the effects of space charge on the nonlinear integrable optics. It is necessary to determine the relevant physics behind the space charge dynamics in these beams, and in doing so determine new figures of merit. Only then will we be able to understand the real intensity-driven limits to beam transport in the nonlinear integrable optics.

## CONCLUSIONS

We have thus discussed two new aspects of the nonlinear integrable lattices of Danilov and Nagaitsev. Through a Lie operator formalism, we were able to obtain two new design requirements for the lattices: (1) the dispersion through the drifts where the elliptic elements will be inserted must be zero, or as small as possible and (2) the vertical and horizontal chromaticities must be equal. By following these two rules, we are able to maintain single-particle integrability even in the presence of energy spread and chromatic effects. We have also studied how space charge affects the beam distribution, and have found some surprising results. While studying the distribution of the single-particle invariant $\varepsilon$, we find a large growth in the RMS spread. Our intuition from linear lattices is that this would lead to a monotonic increase in the RMS beam size. However, our study of the RMS size in the transverse plane show that the size of the beam fluctuates but is not increasing after some initial filamentation. We speculate that there are two processes at work here: a rapid filamentation due to the integrable component of the space charge potential distorting the potential well, and diffusion due to the non-integrable components of the space charge. We believe that a detailed study of this may lead to useful figures of merit characterizing the stability of beams in the presence of intense space charge effects in the nonlinear integrable lattices.

## REFERENCES

[1] V.V. Danilov, *et al.*, "Accumulation of high intensity beam and first observations of instabilities in the SNS accumulator ring", HB2014, TUAX01, p. 59 (2006).

[2] V.V. Danilov and S. Nagaitsev, "Nonlinear accelerator lattices with one and two analytic invariants", Phys. Rev. ST-Acc. Beams **13**, 084002 (2010).

[3] S. D. Webb, *et al.*, "Effects of nonlinear decoherence on halo formation", (2012), submitted for publication, arXiv:1205:7083.

[4] S.D. Webb, *et al.*, "Chromatic and Dispersive Effects in Nonlinear Integrable Optics", (2014), submitted for publication.

[5] A. J. Lichtenberg and M. A. Lieberman, *Regular and Chaotic Dynamics*, $2^{nd}$ ed., Springer-Verlag (1992).

[6] M. Reiser, *Theory and Design of Charged Particle Beams*, Wiley-VCH (2004).

# SPES BEAM DYNAMICS

A. Pisent, L. Bellan, M. Comunian, INFN-LNL, Legnaro, Italy

B. Chalykh, ITEP, Moscow, Russia

A. Russo, L. Calabretta, INFN-LNS, Catania, Italy

## Abstract

At LNL INFN is under construction a Rare Isotope Facility (SPES) based on a 35-70 MeV proton cyclotron, able to deliver two beams with a total current up to 0.5 mA, an ISOL fission target station and an existing ALPI superconducting accelerator as a post accelerator (up to 10 MeV/u for A/q=7).

In this talk will be described the elements between the production target and the experiments, like the selection system, the ECR charge breeder, the second separation system and the new CW RFQ (80 MHz, 714 keV/u, internal bunching).

The problems that have been solved during the design phase are partly common to all RIB facilities, like the necessity to have an high selectivity and high transmission for a beam of a very low intensity, plus the specific challenges related to the use of ALPI (with a reduced longitudinal acceptance) and related to the specific lay out.

At present the design phase has been finalised, and the procurement procedure for the charge breeder, the transfer lines and the RFQ are in an advanced state and will start in the next months. The main beam dynamics aspects of the transfer lines (including magnetic selections) and the linac ALPI will be discussed in detail.

## INTRODUCTION

SPES, acronym of *Selective Production of Exotic Species,* is a CW radioactive ion beam facility under construction at LNL INFN in Italy. It will produce and accelerate neutron-rich radioactive ions, in order to perform nuclear physics experiments, which will require beams above Coulomb barrier.

The main functional steps of the facility are shown in Fig.1, namely the primary beam from the cyclotron, the beam from the fission target (up to $10^{13}$ fission/second), the beam cooler, the spectrometers, the charge breeder and the accelerator, the existing ALPI with a new RFQ injector.

The use of the continuous beam from the +1 source (LIS, PIS, SIS) maximizes the RNB efficiency but needs a CW post accelerator (RFQ and ALPI); this layout also needs a charge breeder chosen to be an ECR that woks in continuous.

The energy on the transfer lines are determined by the chosen RFQ input energy ($w_{RFQ}$=5.7 keV/u); namely, all the devices where the beam is approximately stopped (production target, charge breeder and RFQ cooler) lay at a voltage:

$$eV = (A/q)w_{RFQ} \qquad (1)$$

The charge state range ($3.5 \leq A/q \leq 7$) is bounded by the RFQ field level for the upper limit and by the minimum voltage on q=1 transport line (overall space charge from the source and contaminants separations).

The beam preparation scheme satisfies various requirements:

1. the zone with worst radiation protection issues is reduced by means of the first isobar selection (resolution R=1/200).
2. after that with an RFQ cooler the beam energy spread and transverse emittance are reduced both for further separation and to cope with the charge breeder acceptance (about 5 eV).
3. HRMS and MRMS (high and medium resolution mass spectrometers, R=1/40000 and R=1/1000 respectively) are used to select the RNB (with good transmission) and to suppress the contaminants from the charge breeder source.
4. Both the HRMS and the MRMS are installed on a negative voltage platform, to decrease the beam geometrical emittance, the relative energy spread and to keep the dipole field in a manageable range (>0.1 T).
5. The 7 m long RFQ has an internal bunching and relatively high output energy; this easies the setting and allows 90% transmission into ALPI longitudinal acceptance (constraint deriving from quite long ALPI period, 4 m).
6. An external 5 MHz buncher before the RFQ will be available for specific experiments.
7. The dispersion function is carefully managed in the various transport lines; where possible the transport is achromatic, otherwise the dispersion is kept low (in particular at RFQ input D=0, D' is about 50 rad).

## Radiation Containment

RIB facilities require special radiation protection. The SPES building itself is designed in order to reduce the radiation exposure. From the beam dynamic design point of view, the separation of the nominal beam from its contaminants (nA nominal current respect to µA contaminants) in safety areas is mandatory. In this prospective, the low separation stage is placed inside radiation containment walls (see Fig. 2); at the same time such boundary conditions impose restrictions on the beam dynamics design.

As far as the HRMS is concerned, it is important to clean the nominal species from contaminants in order to reduce radioactive species implantation inside the CB.
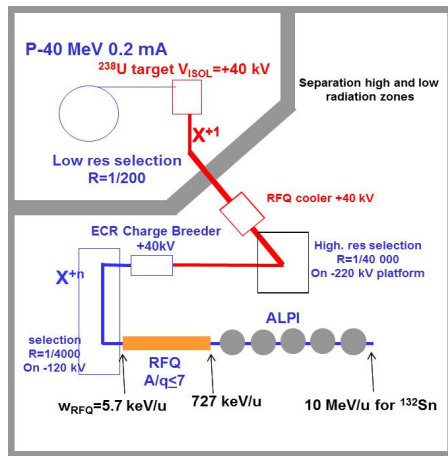
Figure 1: functional scheme of the SPES facility. There are two main areas: the 1+ line (red) and the n+ line (blue), where 1+ and n+ indicates the beam charge state.

## METHOD FOR SIMULATIONS

The main software used for the simulation is TraceWin [1] a 3D multiparticle tracker, capable of field map usage. Thus, it is possible to take into account fringe field and all non-linear effects of the line elements. Moreover, it can perform static or dynamic errors for all beam line devices.

This is useful for the complex devices like the Wien Filter and the high-resolution spectrometers, which may diverge from the linear behaviour.

The simulations will be benchmarked with different programs such as GIOS and TRACK.

Moreover, the TraceWin software with full field maps capability is ordinary used to set all beam line for the runs: this kind of commissioning was demonstrated successful for the setting of LINAC ALPI cavities [2].

## BEAM DYNAMIC SIMULATIONS

### General Layout

Figure 2 shows the actual layout of the SPES facility. The main areas are shown: the cyclotron area, the target room, the 90° magnetic, the beam cooler and HRMS spectrometer dipole zone in the new building under construction (at the right hand side); the CB and the MRMS area, the RFQ and ALPI and the experimental rooms.

The position of the new building was forced by various constraints. In particular the technological plant is placed in front of the MRMS complex and the experimental rooms. As a result the space that the RIBs have to travel from the production source to ALPI is quite long. Moreover the beam distribution line network from ALPI to the experiments in the third experimental hall have been rebuilt to leave the beam tunnel reserved to RIBs.

The layout leaves space for some additional use (low energy beam lines) and future expansions (like a new stable beam source and an EBIS charge breeder).

### Low Resolution Section

The low resolution section is the part of the line between the target and the beam cooler. The current produced by the target (up to some μA) needs to be clean from its contaminants.

Two mass spectrometers are inserted between the target and the beam cooler. The first device is the Wien Filter, which acts as a pre-mass separator with a resolution of about 1/50-1/75 in mass. The second element is a 90° magnetic dipole which achieve a separation in mass of 1/200: this resolution is sufficient in order to select the isobars.

Two focussing triplets match the Wien Filter output beam with the 90° magnetic dipole.

The selection of the isobars before the beam cooler is an important aspect because it allows the device to work in a low current regime about less than 25 nA, i.e. with reduced space charge effects. In such a way it is possible to boost the beam cooler performances: a first reasonable estimation shows the possibility to reduce the energy spread of the source down to 1 eV [3] and the transverse geometric emittance down to 10 times the input emittance [4]. The estimated transmission is about 60% [3] in the worst case.

The reference beam is chosen to be the $^{132}$Sn , extracted at 40 kV at the end of the target extraction system. With q=19 after the charge breeder i.e. A/q= 6.9, it is possible to test the maximum required electromagnetic fields of the line elements of the facility.

The input Twiss parameters used for calculations were measured during an off-line test of the target extraction system: $\alpha_{x,y}$ = -1, $\beta_{x,y}$ = 0.66 mm /π mrad. The normalized rms emittance is chosen to be $\varepsilon_{n,rms}$ = 0.007 π mm mrad, with an equivalent geometric emittance at 99% of $\varepsilon_{geo,99\%}$ = 70.18 π mm mrad.
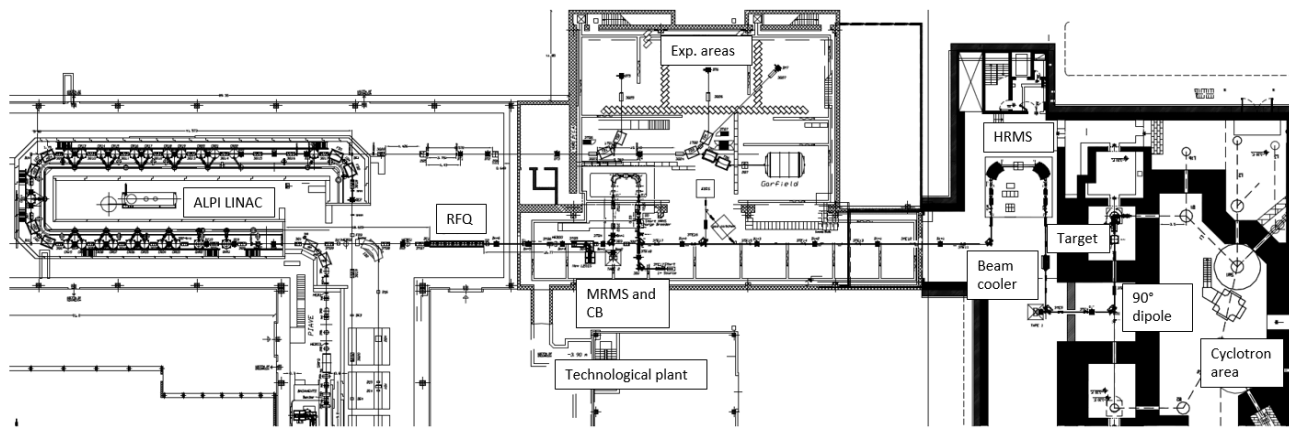
Figure 2: Full SPES layout with main areas.

The transverse spatial distribution is Gaussian-like, truncated at three sigma. As far as the longitudinal space is concerned, it follows a uniform distribution: the beam phase is included between $\pm180^0$, while the energy spread $\Delta W = \pm20$ eV. The number of macro particles simulated was $10^5$.

The first elements met by the beam after the extraction system is an electrostatic triplet. A field map of this element was calculated with COMSOL.

A horizontal defocusing quadrupole is placed before the 90˚ magnetic dipole, in order to have a better control of the resolution.

The dispersion function between the two mass spectrometers is arranged in order to maximize its value at the dipole slits, while it is matched at the entrance of the beam cooler. The multiparticle beam envelopes are shown in Fig. 3.

The magnetic spectrometer is modelled via hard edge; the curvature $R_{edge}$ of the edge angle is included with a zero-length exapole of field $A_{exa}$ using the formula expressed by Brown in [5]. The transverse emittance growth after the spectrometer is less than 7%.

Many beam species are expected to be handed, each one with its custom extraction voltage. Although, lower kinetic energy led to a larger relative energy spread term.

In order to check the resolution power of the system, different ion species (ranging from A/q=7 to A/q=4) were tested: the input for dynamic calculation was made with three beams of same emittances (i.e. 0.007 $\pi$ mm mrad), masses and Twiss parameters, separated of 0.25% in $\Delta p / p$ (i.e. 1/200 in mass). The slits at waist were left in the same position as for the reference case. The total separation is achieved.

### The High and Medium Resolution Sections

Two different spectrometers, HRMS an MRMS are provided for the SPES project. The HRMS is used to obtain the ions of interest, because it removes isobar ions coming from the source, the MRMS is used to clean the nominal beam from contaminants introduced by charge breeder.

The first separation stage is represented by HRMS placed on a 260 kV platform, this separator is constituted by six quadrupole lens, two exapole lens, two dipole and one multipole lens placed in the symmetry plane of the system to fix the high order aberration.
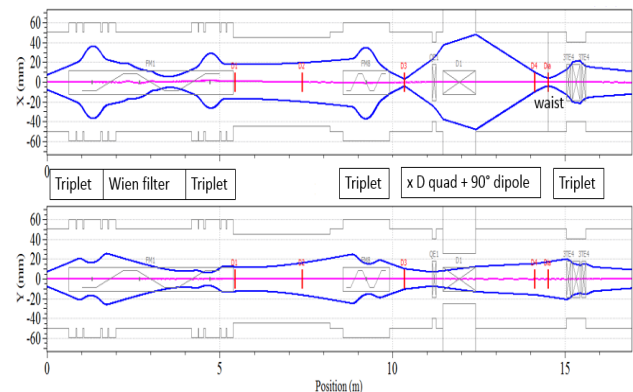


Figure 3: beam multiparticle envelopes in vertical (y) and horizontal direction (x).

The reference beam is $^{132}Sn^{1+}$ with normalized emittance in both planes equal to 0.0014 $\pi$ mm mrad. The HRMS is able to separate different isobar with $\Delta$M/M=1/20000 and $\Delta$W= $\pm$5eV (Fig. 4).
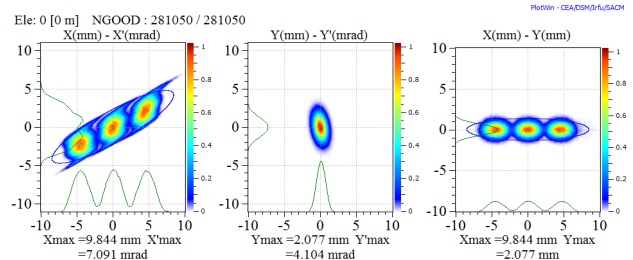


Figure 4: phase spaces at the HRMS dipole slits. The three beam separated of 1/20000 in mass.

After the charge breeder, the next spectrometer is the MRMS, placed on a 120 kV platform.

The reference beam is $^{132}Sn^{19+}$ with normalized emittance equal to 0.1 $\pi$ mm mrad in both planes. The goal in resolving power of this spectrometer is 1000 is achieved (Fig.7).
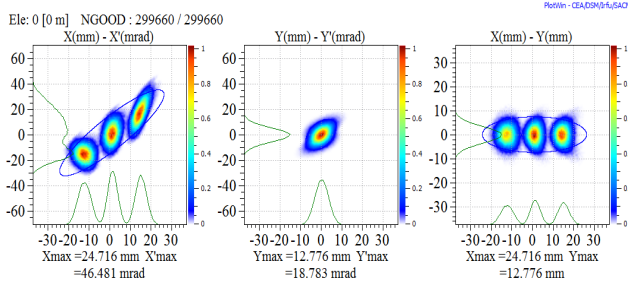


Figure 5: phase spaces at the MRMS slits. The three beam separated of 1/1000 in mass.

This separator is composed by four quadrupole lens, two dipole and one multipole lens placed in the symmetry plane of the system to fix the high order aberration.

The MRMS parameters are listed: bending angle 90˚, bending radius 0.75 m, edge angles 33.35 ˚, width ±35⁰; sextupole correction is provided by entrance and exit poleface curvature, the magnetic induction field for the test case is 0.203 T. The below Table 1 shows the mass spectrometers parameters and dipoles features.

Table 1: Medium and High Spectrometer Performances

| Parameter | MRMS | HRMS |
|---|---|---|
| Input norm. emittance rms [mm mrad] | 0.1 | 0.0014 |
| Emittance growth | 10% | 3% |
| Resolution at 99% $\Delta W = 0$ | 1/2000 | 1/60000 |
| Res. at 99% $\Delta W = \pm 5eV$ | 1/1000 | 1/20000 |

The transfer line for the MRMS connects the CB to the RFQ via MRMS. The input Twiss parameters used for the beam dynamic calculation were obtained via a simulation of the Charge Breeder extraction system; KOBRA3d, as described in [6].

The beam input is spatially Gaussian distributed, while an energy spread of $\Delta W = \pm 5$ eV is implemented. The beam charge is equal to +19 with an A/q= 6.9. The Twiss parameters and emittances are set as follows: $\alpha_{x,y}$ = -3.23, $\beta_{x,y}$ = 0.07 mm/ $\pi$ mrad; the normalized rms emittance is chosen to be $\varepsilon_{n,rms}$ = 0.1 $\pi$ mm mrad, with an equivalent geometric emittance at 99% of $\varepsilon_{geo,99\%}$ = 230.9 $\pi$ mm mrad.

The beam injection from the charge breeder extraction to the object point is given by a solenoid and a magnetic triplet. The HV platform ensures a low beam divergence and reduces the effect of the ∆W/W term. After the selection (1/1000), the beam is matched in transverse planes and dispersion to the RFQ via a magnetic dipole, a

set of triplets and two solenoids. The magnetic dipole is used in order to keep under control the dispersion generated at the MRMS.

The accelerator columns were modelled via field map, in order to take into account their focusing and defocusing effect.
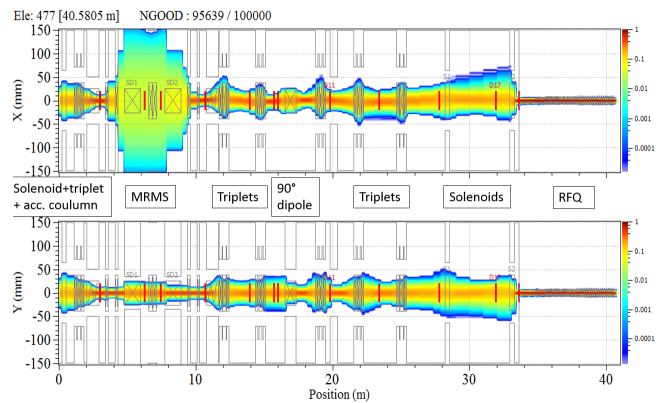


Figure 6: beam multiparticle envelopes in vertical (y) and horizontal direction (x).

An emittance growth occurs after the medium separation stage, and it is equal to 10%.

In order to check the beam transmission to ALPI, the normal conductive RFQ [7,8] were modelled via TOUTATIS. The total nominal beam losses at the exit of the RFQ are about the 7.6%. The longitudinal rms emittance at the exit of the RFQ is $\varepsilon_{long,rms}$ = 0.69 $\pi$ MeV deg, the entry kinetic energy is 760 keV, while the exit energy is 93.9 MeV.

In order to test the transfer line focusing elements sensibilities, an error study was performed. The input beam errors and the MRMS' dipole sensibilities were analysed separately. The set of error applied for the triplets are shown in Table 2.

Each error follows an independent uniform distribution between the values expressed in Table 2. 2000 runs ensure the needed statistic. The final average output longitudinal emittance at the exit of the RFQ resulted $\varepsilon_{long,rms}$ = 0.78 $\pi$ MeV deg with a standard deviation of 0.030 $\pi$ MeV deg. The resulted beam losses are shown in Fig. 9. The average losses are 7.56%, and the standard deviation is 0.98%.

Table 2: Quadrupole Magnet Errors

| Error type | Value |
|---|---|
| Translation in transverse plane | ±100 µm |
| Tilt in transverse plane | ±0.15˚ |
| Gradient error | ±0.3% |
| Multipolar component | ±0.6% |
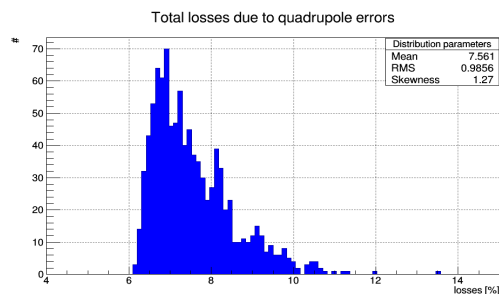
Figure 7: Total beam losses after the RFQ due to quadrupole errors define in Table 3.

**A 5 MHz buncher**, which will be coupled with a chopper system, is foreseen in order to perform certain experiments: its effect and position were studied. The voltage applied is VT= 325 V. Table 3 reports the results.

Table 3: Buncher Performances.

| Set up | transmissions | $\varepsilon_{long,rms}$ [π MeV deg] |
|--------|---------------|--------------------------------------|
| Buncher off | 92.4% | 0.69 |
| Buncher on | 40.6% | 0.16 |

### *The Acceleration Section*

The MEBT line connects the output beam from the RFQ to the LINAC ALPI. A $^{132}Sn^{19+}$ beam was simulated, with an A/q = 6.9.

The simulation was performed with the field maps of the quarter wave's cavies, in order to take into account their vertical misalignment effect on the beam. [9]

The beam can be boosted to the maximum energy with 76 QWR cavities at the maximum field. All cavities work with the maximum performance: QWR1- QWR 2=4 MV/m; CR03- CR 18=4.5 MV/m; CR 019- CR 20=6.5 MV/m. However, to reduce field of the bending magnet at the exit of structure last two cryostats from twenty should be off. The final energy in this case will be 9.04 MeV/A. Maximum limit of gradient of the quadrupole is 30 T/m. Maximum used gradient was < 25 T/m. Losses obtained in calculations are lower than 3% (mainly located at the first part of ALPI).

## CONCLUSIONS

SPES post accelerator beam design has involved the study of many critical devices, and the overall optimization to distribute the criticality. The beam transport lines from CB to ALPI are now specified and we are tendering the magnets.

The mechanical design of RFQ and HRMS will be completed during 2015, and procurement procedure will follow.
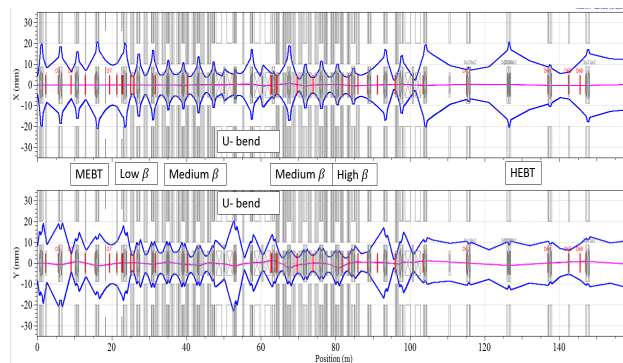


Figure 8: beam multiparticle envelopes in vertical (y) and horizontal direction (x) in the MEBT and ALPI LINAC section.
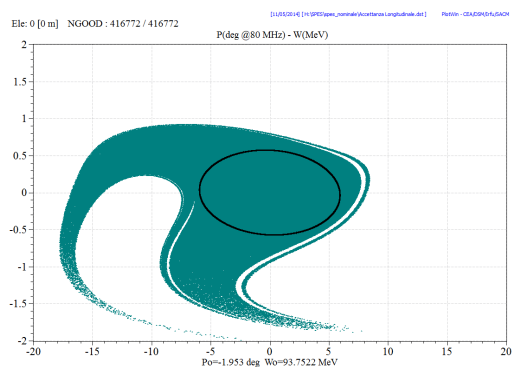


Figure 9: ALPI LINAC longitudinal acceptance.

## REFERENCES

[1] D. Uriot and N. Pichoff, "TraceWin", CEA Saclay, June 2014.

[2] M. Comunian, C. Roncolato, E. Fagotti, F. Grespan, A. Palmieri, A. Pisent, "Beam Dynamics Simulations of the Piave-Alpi Linac",IPAC2011, WEPC014.

[3] A. Nieminen et al., "Beam Cooler for Low-Energy Radioactive Ions", Nuclear Instruments and Methods in Physics Research A 469, ELSEVIER, August 2001, p. 244-253; http://www.elsevier.com

[4] M. Maggiore et al., "Plasma-beam traps and rafiofrequency quadrupole beam cooler", Review of Scientific Instruments 85, AIP publishing, November 2013.

[5] Karl L. Brown, "A First and Second Order Matrix Theory for the Design of Beam Transport Systems and Charged Particle Spectrometers", SLAC Report-75, Stanford Linear Accelerator Center, Stanford University, California (1982).

[6] Alessio Galatà, Phd thesis, University of Ferrara, in course of publication.

[7] Antonio Palmieri, "Preserving the beam quality in long RFQS on the RF side: voltage stabilization and tuning", HB2014.

[8] M. Comunian, A. Palmieri, A. Pisent, C. Roncolato "The new RFQ as RIB INJECTOR of the ALPI Linc", IPAC13, p 3812.

[9] M. Comunian, A. Palmieri, F. Grespan, "RF simulations for the QWR cavities of PIAVE-ALPI", IPAC2011, MOPC089.

# BEAM PHYSICS CHALLENGES IN RAON*

Ji-Ho Jang, Dong-O Jeon[#], Hyojae Jang, Hyung Jin Kim, Ilkyoung Shin, IBS, Daejeon, Korea
Ji-Gwang Hwang, Eun-San Kim, KNU, Daegu, Korea

## Abstract

Construction of the RAON heavy ion accelerator facility is under way in Korea. As high intensity 400 kW superconducting linac (SCL) is employed as a driver, beam physics aspects are carefully studied. The SCL is based on lattice consisting of cryomodules and quadrupole doublets. Beam dynamics studies for the RAON has progressed to cover start-to-end simulations and machine imperfection studies confirming beam loss less than 1 W/m. At present, prototyping of major components are proceeding including 28 GHz ECR ion source, RFQ, superconducting cavities, magnets and cryomodules. First article of prototype superconducting cavities have been delivered that were fabricated through domestic vendors. Prototype HTS quadrupole is under development. Progress report of the RAON accelerator systems is presented.

## INTRODUCTION

The RISP (Rare Isotope Science Project) is developing a heavy ion accelerator called RAON, and experimental facilities. One of the characteristics of RAON facility is that it will be able to supply RI beams with both IF (In-flight Fragmentation) and ISOL (Isotope Separator On-Line) methods [1,2]. The layout of the facility is given in Fig. 1.

The RAON consists of a driver linac and a post linear accelerator. The driver linac includes an injector of an ECR ion source, an RFQ, and a SCL (superconducting linac) called SCL1 and SCL2 which are separated by a 90° charge selection section. It can accelerate uranium beams up to 200 MeV/u and proton beams up to 600 MeV as summarized in Table 1. The stable ion beams with beam power up to 400 kW are delivered to the IF target and various experimental areas. The post linac is used to accelerate RI beams which are generated by the ISOL facility. A cyclotron delivers 1 mA 70 MeV proton beams to the ISOL target. The cyclotron has dual extraction ports with thin carbon foils for charge exchange extraction of H- beam. The rare isotope beams generated by the ISOL system is accelerated by a chain of post accelerators including RFQ and another superconducting linac, SCL3. The RI beams can be delivered into the low energy experimental hall or can be injected through P2DT to the SCL2 in order to accelerate to higher energy.

Construction of the RAON heavy ion accelerator facility started on December 2011. The design of the accelerator systems has progressed, and prototyping of critical components and systems have been materialized.

In this paper, the status of the RAON accelerator systems is presented along with beam dynamics design and prototyping progress.
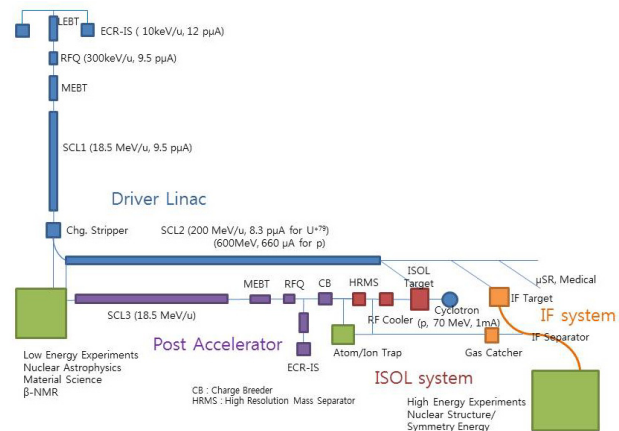


Figure 1: Layout of RAON Linac.

Table 1: Beam Specification for the Driver Linac

| Parameters | $H^+$ | $O^{8+}$ | $Xe^{54+}$ | $U^{79+}$ |
|---|---|---|---|---|
| Energy [MeV/u] | 600 | 320 | 251 | 200 |
| Current [pµA] | 660 | 78 | 11 | 8.3 |
| Power on target [kW] | >400 | 400 | 400 | 400 |

## DRIVER LINAC

### Injector

The injector of RAON driver linac consists of a 28 GHz ECR ion source, an LEBT (Low Energy Beam Transport), a 500 keV/u RFQ (Radio-Frequency Quadrupole), and a MEBT (Medium Energy Beam Transport) [1, 3].

The two-charge-state (33 and 34) uranium beams are injected into the RFQ in order to achieve the required beam power of 400 kW at the IF target. The electrostatic quadrupoles are used to focus the two charge state beams. We considered a multi-harmonic buncher and a velocity equalizer for reducing the longitudinal rms beam emittance. The beam envelope in the LEBT is shown in

Fig. 2 which is calculated by TRACK code [4].
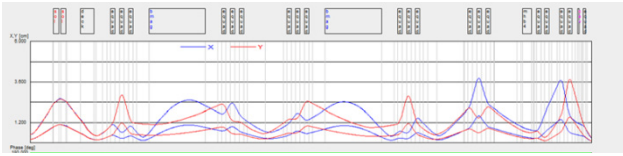


Figure 2: Beam envelope in the LEBT.

The RFQ accelerates the stable ion beams from 10 keV/u to 500 keV/u. The 81.25 MHz RFQ operates in CW mode. The design parameters are summarized in Table 2. Figure 3 shows the PARMTEQ simulation results [5]. The transmission rate becomes more than 98% and the total length is about 5 m.

Table 2: RAON RFQ Specifications

| Parameters | Value |
|---|---|
| Particles | Proton to $^{238}U^{33+,34+}$ |
| Frequency | 81.25 MHz |
| Input / Output Energy | 10 keV/u / 500 keV/u |
| Transmission | 98% |
| Peak Surface Field | 1.7 Kilpatrick |
| Operation Mode | CW |
| Length | 4.94 m |
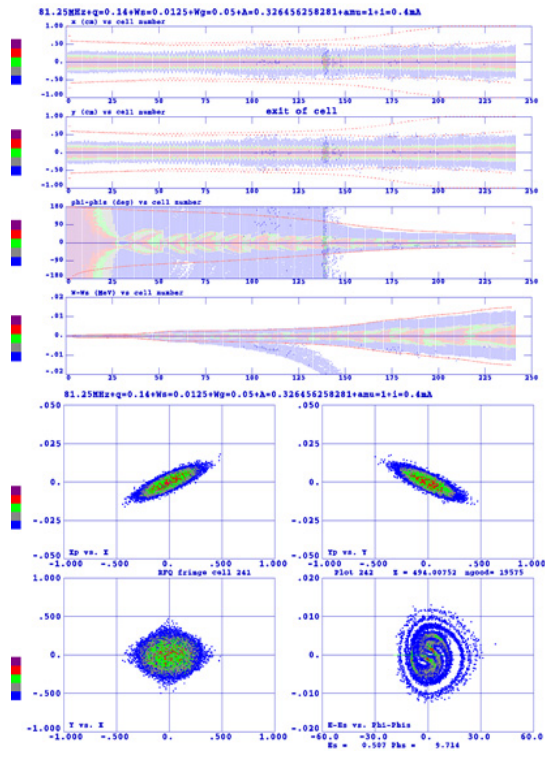


Figure 3: PARMTEQ simulation result of the RFQ.

The MEBT consists of 3 buncher cavities and 8 quadrupole magnets for longitudinal and transverse beam manipulations [1, 6]. The TRACK simulation results are given in Fig. 4 for the beam envelope and particle distributions in transverse phase spaces.

The prototype ECR ion source and the prototype RFQ of one section are finished as shown in Fig. 5 and Fig. 6. The low temperature test of the assembled superconducting magnet is in progress for the ECR ion source. The RF test of the RFQ prototype is also going on.
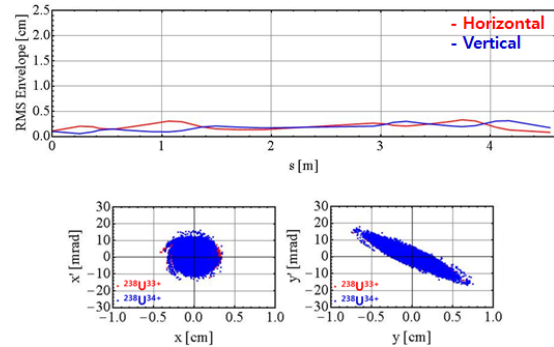


Figure 4: RMS beam envelope in RAON MEBT (upper plot) and particle distribution at the entrance of SCL (lower plot).



Figure 5: Assembled ECR superconducting magnet (left) and fabricated cryostat (right) of ECR ion source.
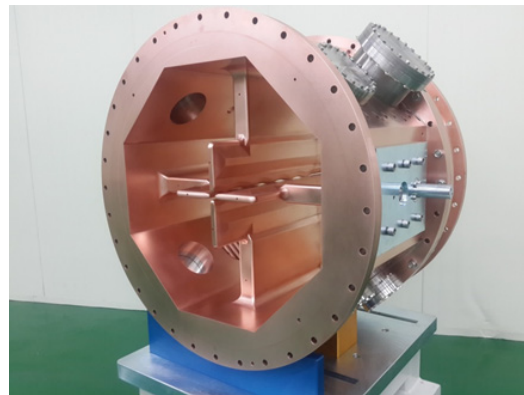


Figure 6: Fabricated RFQ prototype.

*Superconducting Linac*

The SCL of RAON driver linac consists of a low energy part of SCL1, a CSS (Charge Selection Section) and a high energy part of SCL2 [1, 7]. SCL1 uses two different type of cavities, QWR (Quarter Wave Resonator) and HWR (Half Wave Resonator), in order to accelerate uranium beams up to around 18 MeV/u. The charge stripper in CSS generates higher charge states of around 79 for the uranium beams. The CSS selects 5 charge states from 77 to 81. SCL2 uses two different type of SSR (Single Spoke Resonator) cavities, SSR1 and SSR2, in order to accelerate beams up to 200 MeV/u. The design parameters of the RAON superconducting cavities are summarized in Table 3 [7]. The energy gain in each type of cavities is given in Fig. 7 [1]. The required number of cryomodules and cavities are summarized in Table 4.

Table 3: RAON Superconducting Cavity Parameters

| Parameters | Unit | QWR | HWR | SSR1 | SSR2 |
|---|---|---|---|---|---|
| Frequency | MHz | 81.25 | 162.5 | 352 | 325 |
| $\beta_g$ | | 0.047 | 0.12 | 0.30 | 0.51 |
| Q | $10^9$ | 2.1 | 4.1 | 9.2 | 10.5 |
| $QR_s$ | $\Omega$ | 21 | 42 | 98 | 112 |
| R/Q | $\Omega$ | 468 | 310 | 246 | 296 |
| $E_{acc}$ | MV/m | 5.2 | 5.9 | 6.9 | 8.6 |
| $E_{peak}/E_{acc}$ | | 5.6 | 5.0 | 6.3 | 7.2 |
| $B_{peak}/E_{acc}$ | mT/(MV/m) | 9.3 | 8.2 | 6.63 | 7.2 |
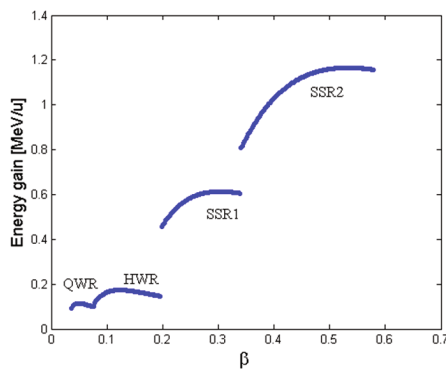


Figure 7: Energy gain in RAON SCL cavities as a function of relativistic β.

Table 4: Cavities and Cryomodules in Driver SCL Linac

| | SCL11 | SCL12 | | SCL21 | SCL22 |
|---|---|---|---|---|---|
| Cryomodule # | 22 | 13 | 19 | 23 | 23 |
| Cavity #/CM | 1 | 2 | 4 | 3 | 6 |
| Cavity Type | QWR | HWR | HWR | SSR | SSR |

The RAON superconducting linac adopts a double lattice structure with normal conducting magnets. Hence only one QWR cavity is installed in the cryomodule for reducing beam loss generated by machine imperfection. In order to avoid an envelope instability and a parametric resonance through the superconducting linac, transverse and longitudinal phase advances are set under 90 degrees and their ratios are kept about 0.8 expect small region for beam matching. For large beam acceptance, the synchronous phases of SCL cavities are ramping from lower values. The TRACK simulation result of SCL1 and SCL2 is given in Fig. 8 [8]. The rms beam size is less than 3 mm through the superconducting linac. The normalized rms emittance growth is given in Fig. 9 [8]. The transverse emttance growth is negligible and the longitudinal emttance growth is not so large.
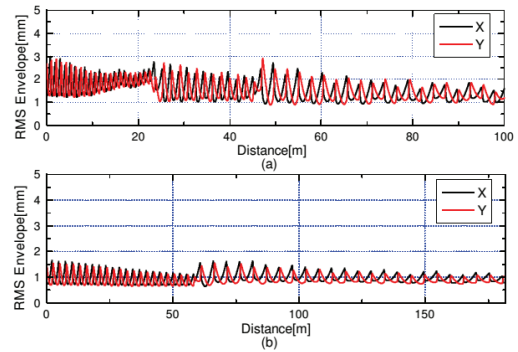


Figure 8: RMS beam envelope in RAON driver linac: (a) SCL1 and (b) SCL2.
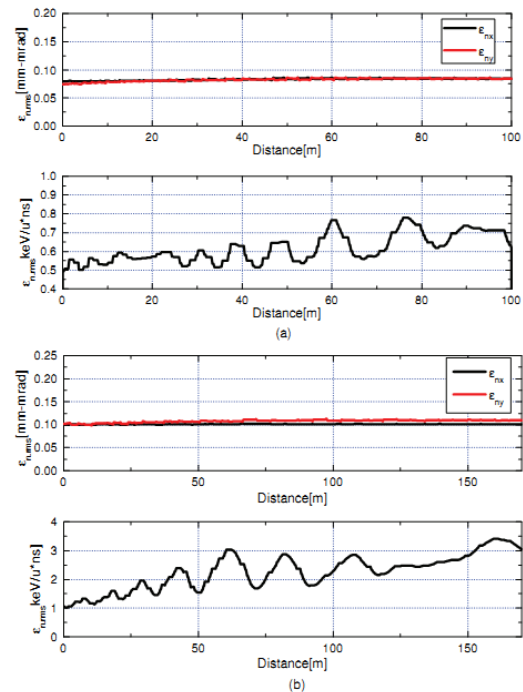


Figure 9: RMS emittance growth in the driver linac: (a) SCL1 and (b) SCL2.

The final energy of some stables ions are given in Fig. 10 at the driver linac [8].
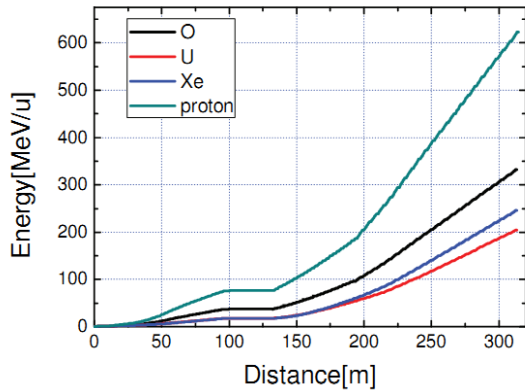


Figure 10: Final energy of stable ions in driver linac.

We used the 2nd order achromat theory [9] in the design of CSS region in order to select 5 charge states of uranium beams and reduce their emittance growth. The TRACK simulation result is given in Fig. 11 and the particle distribution in horizontal phase space at the center of the bending section is given in Fig. 12.
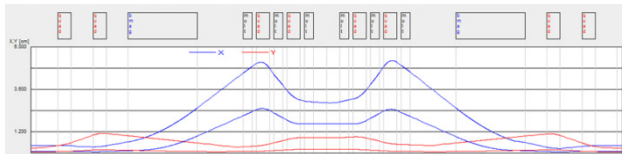


Figure 11: RMS and maximum beam envelope in charge selection section of the driver linac.
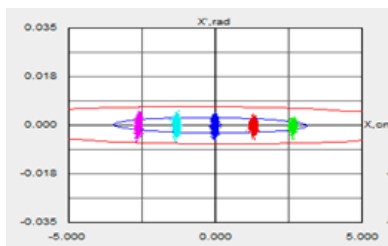


Figure 12: Particle distribution of 5 charge states at the center of charge selection section of the driver linac.

The effects of machine imperfection on beam transmission were studied [10]. The values of misalignment, amplitude and phase errors are summarized in Table 5. The result is given in Fig. 13. The upper plot of the figure shows the beam loss in unit of W/m. The loss is less than 1 W/m even without the orbit correction. The region with the beam loss higher than 1 W/m is the charge stripper region. The lower plot shows the beam center deviation under the machine imperfection.

The fabrication of the prototype SCL cavities is finished as shown in Fig. 14 and their vertical tests are in progress. The prototype cryomodules are under construction in domestic companies as shown in Fig. 15.

Table 5: Machine Imperfection of the Lattice in the RAON Driver Superconducting Linac

| Parameters | Quadrupole | Cavities |
|---|---|---|
| Displacement [mm] | ±0.15 | ±1.0 |
| Rotation [mrad] | ±5 | ±5 |
| Amplitude or field [%] | ±1 | ±1 |
| Phase [deg] | | ±1 |
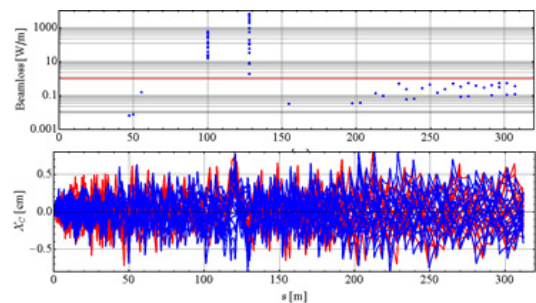


Figure 13: Beam loss and deviation of beam center due to machine imperfection.



Figure 14: Prototype of the SCL cavities: QWR(left), HWR (middle), SSR (right).



Figure 15: The prototype cryomodule for QWR (left) and HWR (right) cavities .

## POST ACCELERATOR

The post accelerator consists of an post injector and another superconducting linac, SCL3 [1]. The injector includes an 18 GHz ECR ion source, an LEBT, a 400 keV/u RFQ, and a MEBT. The ECR ion source will be used in the beam commissioning and test of the post accelerator. The LEBT matches RI beams from ISOL system into the post RFQ. The reference particle of RI beams is $^{132}Sn$ with A/q of about 8 which are generated by charge breeders in the ISOL facility. The input beam energy of the RFQ is 5keV/u and the output energy is 400 keV/u. The post MEBT includes 6 quadrupole magnets and 2 buncher cavities for beam manipulation in transverse and longitudinal directions, respectively.

The SCL3 uses the same type of QWR and HWR cavities as in the SCL1 and the lattice structure is also doublet as the SCL1 [1,8]. Fig. 16 shows the rms beam envelope in SCL3. It is less than 3 mm in almost all region of SCL3.
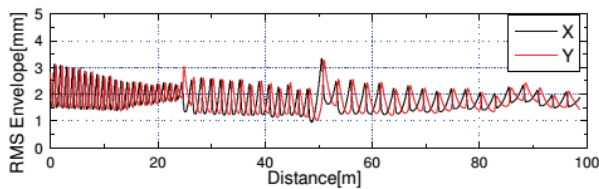


Figure 16: RMS envelope in SCL3.

The P2DT is a beam transport line between SCL3 and SCL2 for further acceleration of the RI beams. There is a charge stripper at the entrance of P2DT line and it makes Sn beams of the single charge state to 3 charge states, 45, 46 and 47. The bending angle of P2DT line is 180 degrees as shown in Fig 1. It is separated into two 90-degree bending sections. Each bending sections satisfies the 2nd order achromatic condition. TRACK simulation result is given in Fig. 17 through 180 degree bending section. The particle distribution in horizontal phase space at the center of the first 90-degree bending section is given in Fig. 18.
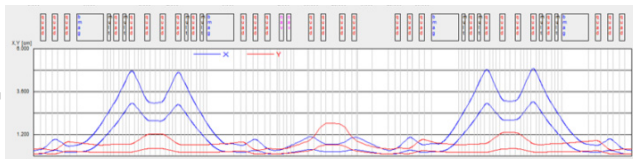


Figure 17: Beam envelope in P2DT line.
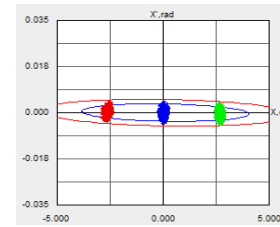


Figure 18: Particle distribution of 3 charge states at the center of the first 90-degree bending section in P2DT.

## CONCLUSION

This work summarized the beam dynamics design and the status of development of critical components in the RAON linac facilities. The optimization study of beam dynamics is in progress. The development of prototype ECR ion source and RFQ is finished. The low temperature test of the assembled superconducting magnets in the ion source and the RF test of the prototype RFQ of one section will be finished in near future. The prototype cavities for RAON SCL have been fabricated and their vertical tests are in progress. The fabrication of the cryomodules is almost finished.

## REFERENCES

[1] D. Jeon et al, J. Korean Phys. Soc. 65, 1010 (2014).

[2] D. Jeon and H.J. Kim, "Staus of the RAON Heavy Ion Accelerator Project", WEIOB03, LINAC 2014, Geneva, Switzerland (2014).

[3] I.S Hong et al, Rev. Sci. Instrum. 85, 02A709 (2014).

[4] P.N. Ostroumov, V.N. Aseev and B. Mustapha, TRACK, ANL Technical Note, Updated for version 3.7.

[5] K.R. Crandall et al, RFQ Design Codes, LA-UR-96-1839.

[6] H.J. Kim, et al, J. Korean Phys. Soc. 65, 1249 (2014).

[7] H.J. Kim et al, "Superconducting Linac for RISP", MOPP082, LINAC 2014, Geneva, Switzerland (2014).

[8] H.J. Jang et al, "Beam Dynamics Study for RAON Superconducting", MOPP080, LINAC 2014, Geneva, Switzerland (2014).

[9] K. L. Brown, "A Second-order Magnetic Optical Achromat", IEEE translation on Nuclear Physics, NS-26, p. 3490, June 1979.

[10] J.K. Hwang et al, "Estimation and Correction of the Uncontrolled Beam Loss due to the Alignment Error in the Low-Energy Linear Accelerator of RAON", May 2013, IPAC 2013, p. 2570 (2014) ; http://www.JACoW.org

# BEAM DYNAMICS STUDIES FOR THE FACILITY FOR RARE ISOTOPE BEAMS DRIVER LINAC*

M. Ikegami[†], Z. He, S.M. Lidia, Z. Liu, S.M. Lund, F. Marti, E. Pozdeyev, J. Wei, Y. Yamazaki, Q. Zhao, Y. Zhang, Facility for Rare Isotope Beams, Michigan State University, MI 48824, USA

*Abstract*

The Facility for Rare Isotope Beams (FRIB) is a high-power heavy ion accelerator facility presently under construction at Michigan State University to support nuclear physics. FRIB consists of a driver linac and experimental facility, and the linac accelerates all stable ions including uranium to kinetic energies of more than 200 MeV/u and continuous wave beam power up to 400 kW. This beam power is more than two orders of magnitude higher than the existing heavy ion linac facilities, resulting in various beam dynamics challenges for the driver linac. In this paper, we review these challenges for the FRIB driver linac and undergoing studies to address them.

## INTRODUCTION

The Facility for Rare Isotope Beams (FRIB) is a high-power heavy ion accelerator facility now under construction at Michigan State University under a cooperative agreement with the US DOE [1]. Its driver linac operates in CW (Continuous Wave) mode and accelerates all stable ions to kinetic energies above 200 MeV/u with the beam power on target up to 400 kW. This novel facility is designed to accelerate and control multiple ion species simultaneously to enhance beam power. The linac has a folded layout as shown in Fig. 1, which consists of a front-end, three Linac Segments (LSs) connected with two Folding Segments (FSs), and a Beam Delivery System (BDS) to deliver the accelerated beam to the production target. The front-end consists of two ECR (Electron Cyclotron Resonance) ion sources, a normal conducting CW RFQ (Radio Frequency Quadrupole), and beam transport lines to separate, collimate, and bunch the multiple ion charge states emerging from the ECR sources. Ion sources are located on the ground level (not shown in Fig. 1) and an extracted beam from one of two ion sources is delivered to the linac tunnel through a vertical beam drop. In the FRIB driver linac, superconducting RF cavities are exten-



Figure 1: Schematic layout for the FRIB driver linac.

sively employed. After acceleration up to 0.5 MeV/u with a normal conducting RFQ, ions are accelerated with superconducting QWRs (Quarter Wave Resonators) and HWRs (Half Wave Resonators) to above 200 MeV/u. There are two types each for QWRs ($\beta = 0.041$ and 0.085) and HWRs ($\beta = 0.29$ and 0.53). The frequency and aperture diameter for QWRs are 80.5 MHz and 36 mm respectively, and those for HWRs are 322 MHz and 40 mm respectively. We have three $\beta = 0041$ cryomodules with four cavities each and 11 $\beta = 0.085$ cryomodules with eight cavities each in LS1 (Linac Segment 1). We have 12 $\beta = 0.29$ cryomodules with four cavities each and 12 $\beta = 0.53$ cryomodules with six cavities each in LS2 (Linac Segment 2). There are 6 $\beta = 0.53$ cryomodules followed by a space to add cryomodules for future upgrade. The total number of superconducting RF cavities is 330 including those for longitudinal matching in the Folding Segments. Transverse focusing in the superconducting linac sections is provided by superconducting solenoids (8 Tesla, 20 mm bore radius). It is unique to have such large scale linac sections with low-$\beta$ superconducting RF cavities together with multi-species transport at high CW power. This poses beam dynamics challenges specific to the FRIB driver linac.

In addition to realizing high CW beam power, stringent beam-on-target requirements are imposed for the FRIB driver linac to support novel experimental program it nuclear physics. It is of essential importance at these high power levels to control and mitigate beam losses to avoid damage and excessive radio-activation of accelerator components. Detection of beam losses and halo collimation are major elements of beam loss mitigation, both of which requires careful beam dynamics considerations in their design.

In this paper, beam dynamics studies now under way in support of the FRIB driver linac are reviewed. We briefly outline five major areas and their particular challenges.

## SPACE-CHARGE EFFECTS AT LOW ENERGY FRONT-END

While the FRIB driver linac is at the frontier of CW power, its space-charge intensity is modest as high average beam power is realized by CW operation. Due to this modest intensity, space-charge effects are negligible for most of the FRIB driver linac. The exception to this in the front-end where the beam kinetic energy is low. Space-charge effects are especially important for beam transport between the ECR ion source and the first bending magnet for charge selection. Species with unwanted charge states are transported together with the (typically) two desired species in this section. This increases space-charge intensity by a factor of 15 (typical).
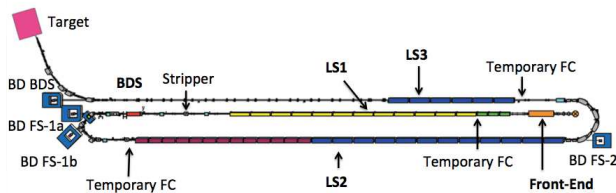
Transverse focusing is provided with two solenoid magnets in this section, and the field from the upstream one is significantly overlapped with the solenoid field of ECR ion source. The section includes a ~ 50 kV grated electro-static gap to accelerate ions to 12 keV/u. The gap field overlaps with the fringe field of the downstream solenoid magnet. These overlapped applied fields are modeled in detail with the Warp code [2] to evaluate space-charge effects and the influence of the structure of the beam emerging from the ECR sources. We are investigating the sensitivity of operating points on the initial distribution including space-charge [3]. Figure 2 shows a typical phase space distribution obtained with the Warp code. The simulations are deepening our understanding on underlying physics of transport in this section due to many species (~ 20) with space-charge, magnetized ions with large canonical angular momentum emerging from the ECR, coupled solenoid focusing with overlapping elements, and acceleration. Preliminary results are encouraging and simulations are being extended to the downstream part of the front-end to more throughly evaluate space-charge effects in the initial species separation and collimation.
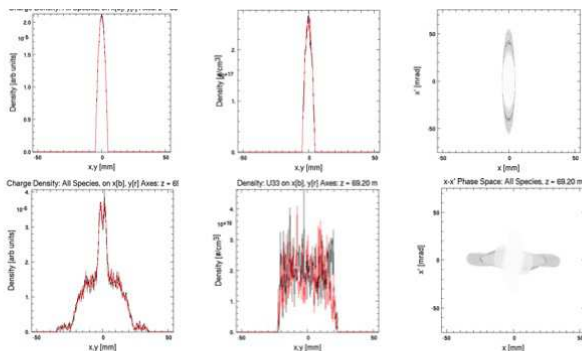


Figure 2: Typical phase-space distribution near ECR front-end obtained with the Warp code. Top: initial distribution, and bottom: distribution before entering the first bending magnet. Left: Real space beam density for all species combined, middle: that for $U^{33+}$, and right: phase space distribution for all species combined.

## MULTI-CHARGE STATE ACCELERATION

It is difficult to have sufficiently high beam intensity from ECR ion sources for some of heavy ion species. We plan to accelerate several charge states simultaneously to overcome this limitation. In the FRIB driver linac, we plan to accelerate up to two charge states before the charge stripper located after LS1, and up to five charge states after the stripper. As beam components with different charge states gain energy in the RF cavities, they undergo synchrotron oscillations with significantly different amplitudes. They also have different transverse betatron oscillations due to differences in magnetic rigidity. This necessitates a second order achromat for the arc sections in FS1 and FS2 to suppress emittance growth due to dispersion. The components with different charge

states must overlap each other both transversely and longitudinally to meet stringent on-target requirements. These requirements include the spot size containing more than 90 % of the beam of smaller than 1 mm in real space and ±5 mrad in divergence angle at the target. Also, the 95 % bunch length and energy spread should be smaller than 3 ns and ±0.5 %. This poses a significant challenge for machine tuning. There also are requirements at the stripper to minimize potential degradations in beam quality from stripping. We have confirmed by multi-particle simulation with the IM-PACT code [4] that the requirements can be met as shown in Fig. 3. Studies are now underway to identify efficient tuning methodologies. More detailed discussion on this topic will be found in [5].
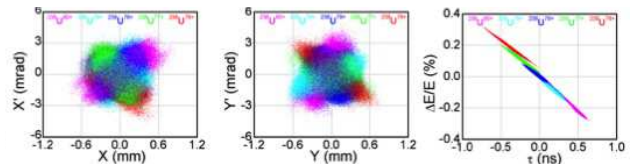


Figure 3: On-target phase space distribution for a five-charge-state uranium beam simulated with IMPACT. Left: horizontal, middle: vertical, and right: longitudinal phase-space plane. Different colors represent different charge states.

## NON-AXISYMMETRIC FIELD COMPONENT OF QUARTER WAVE RESONATORS

We adopt QWRs (Quarter Wave Resonators) in LS1 (Linac Segment 1) with superconducting solenoid magnets for transverse focusing. LS1 includes 100 QWR cavities. Non-axisymmetric field components exist in QWRs due to geometrical asymmetries. Among these non-axisymmetric components, the effect of dipole field components have been extensively studied and mitigation schemes have been developed [6, 7]. We are presently studying the effect of quadrupole components of field assymetries [8, 9]. While the quadrupole component is typically small, its effect can accumulate over a number of QWRs. Because we employ solenoid focusing in LS1 and frequently steer to compensate for misalignments, the matched beam develops significant deviations from transverse rotational symmetry about the longitudinal axis only if non-axisymmetric field components (quadrupole and higher) of QWRs are not negligible. Asymmetries between the horizontal and vertical planes induced by the quadruple field component in LS1 is shown in Fig. 4. Tuning methodologies is being studied using IMPACT code and reduced models, and mitigation schemes shall be implemented on that basis.

## BEAM LOSS DETECTION

In addition to minimizing prospects of beam losses by careful linac design, careful planning of potential fault situations is crucial. Detection of beam losses is a key to realize
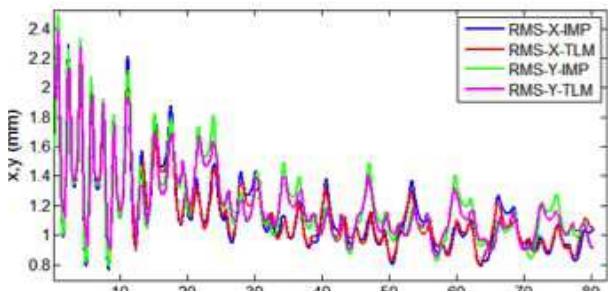
Figure 4: Horizontal and vertical plane beam envelopes in LS1 including quadrupole field components of QWRs. Blue: horizontal with the IMPACT code [4], red: horizontal with thin lens model [8], green: vertical with the IMPACT code, and magenta: vertical with a thin lens model.

high power transport while protecting the machine from damage or excessive radio-activation. Beam loss monitors detecting radiation, such as ion chambers, are widely used in various accelerators. However, it is difficult to employ these monitors to protect the low energy part of the FRIB driver linac because lost low energy heavy ions generate insufficient radiation but still can damage the machine. We plan to adopt HMRs (Halo Monitor Rings) to mitigate limitations of conventional beam loss monitors [10,11]. A HMR consists of a fixed aperture made of a thin niobium disk, and the beam current intercepted by the disk is monitored. The aperture of a HMR is supposed to be adjusted to intercept particles which will be lost downstream if there is no HMRs. A HMR will be placed in every warm section between cryomodules. A schematic for HMR is shown in Fig. 5. The
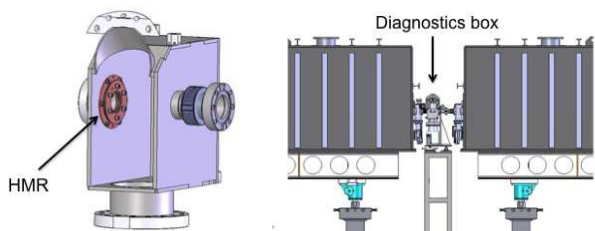


Figure 5: Halo Monitor Ring (HMR). Left: diagnostics box equipped with a HMR, and right: HMR location in diagnostics box between cryomodules.

design of HMRs requires careful beam-dynamics consideration of its aperture size and the phase advance between HMRs. We plan to adopt a similar approach to the design of the collimator system with multiple jaws although there is no intent to aggressively collimate halos with HMRs. We adjust the HMR apertures to limit the acceptance and adjust the phase advance to adequately to maximize its efficiency in capturing beam losses. An adjustable aperture HMR is not employed to avoid the risk of cavity degradation due to particulates from movable structures. Instead, we plan to secure adequate tuning margin for solenoid strength to adjust the relative aperture size to the beam size. IMPACT

simulation studies to confirm feasibility of the design and to optimize the design parameters are now underway.

## COLLIMATOR DESIGN

In the multiple charge-state acceleration in the linac, up to five charge states are selected at a charge selector placed after the charge stripper. The charge selector is located in the FS1 arc section and has two movable jaws on opposite sides to scrape the beam in the horizontal direction. Different charge states are separated horizontally at the location of charge selector due to lattice dispersion. We can select specific charge states by adjusting the edge position of the movable jaws. Each charge state at charge selector intrinsically has a halo around the beam core due to large angle scattering events in the stripper. The halos fill in space between different charge states transmitted through the charge selector and form a horizontal halo after exiting the FS1 arc section. There will also be a vertical halo due to large angle scattering. These halos could cause beam losses in the downstream sections. It is desirable to mitigate the potential risk of cavity degradation due to the halo induced beam losses over long term operation of the machine. Space is reserved in the lattice between the exit of FS1 arc and the entrance of LS2 to place a collimator system to eliminate the halos. The base design calls for two collimators each for the horizontal and vertical directions, and each collimator has two movable jaws on both sides of the beam. The feasibility of this design has been confirmed by simulations with the IMPACT code (see Fig. 6) which shows that a halo expected from the stripper can be effectively scraped while preserving core intensity. More elaborate simulations are planned to further explore possible issues involved with collimation of the stripper induced halo.
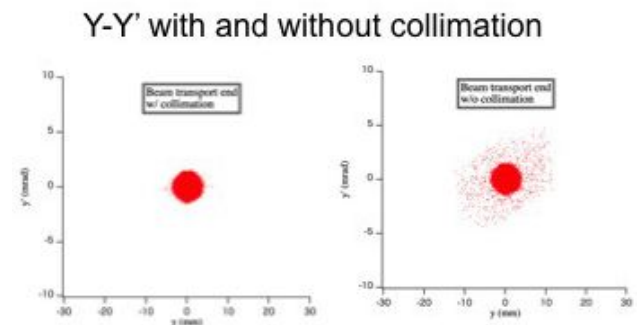


Figure 6: Simulated phase space distribution at the entrance of LS2 with (left) and without (right) halo collimation. An artificial halo is generated at the exit of FS2 arc section which covering the most part of transverse acceptance of the transport line to demonstrate the effectiveness of the collimation.

## SUMMARY

Beam dynamics studies now under way for the FRIB driver linac has been reviewed with emphasis on five areas for particular beam dynamics challenges.

Due to modest beam intensity, space charge effects are not important for most of the linac, which is a notable difference from other high power accelerators. The only exception to this is in the front-end where the beam kinetic energy is sufficiently low before the RFQ. We are developing a detailed model for the front-end utilizing the Warp code. This should aid in addressing any issues that may occur in machine commissioning and augment limited diagnostic capabilities near the sources.

To have the flux on-target, we plan to accelerate multi-charge-state beams (both from ECR sources and after a stripper) which poses tuning challenges to meet stringent beam-on-target requirements. We extensively adopt super-conducting cavities from low $\beta$ section with superconducting solenoids for transverse focusing. It also poses a specific challenge for tuning where it is required to deal with non-axisymmetric coupled beams. Careful design of tuning methodologies is one of important issues for beam dynamic studies for the FRIB driver linac.

Both detection of beam losses and halo collimation require careful consideration of beam dynamics for effective designs. For beam loss detection, the design of HMRs should be fully optimized consistent with considerations from beam dynamic simulations to mitigate the intrinsic difficulty in detecting losses of a low energy heavy ions while minimizing potential risks of adverse effects. We may need an more accurate stripper model to better evaluate the design of the halo collimator system following the stripper.

The topics which has not been covered in this paper yet having significant importance include fault studies to identify fault recovery scenarios and to optimize the MPS (Machine Protection System) design, and model-based tuning in switching ion species to realize good availability. Elaborated studies are actively conducted at FRIB on all the front.

## REFERENCES

[1] J. Wei et al., "FRIB accelerator status and challenges", LINAC'12, Tel Aviv, August 2012, p. 417.

[2] see: http://warp.lbl.gov

[3] S. Lund et al., "RMS Emittance Measures for Solenoid Transport and FRIB Front-End Simulations", MOPAB17, HB2013, East Lansing, MI, USA (2014).

[4] J. Qiang, R.D. Ryne, S. Habib, and V. Decyk, J. Comput. Phys. **163**, 434 (2000).

[5] Q. Zhao et al., "Multi-Charge-State Beam Dynamics in FRIB", TUO1LR01, HB2013, East Lansing, MI, USA (2014).

[6] A. Facco and V. Zvyagintsev, Phys. Rev. ST Accel. Beams **14**, 070101 (2011).

[7] P.N. Ostroumov and K.W. Shepard, Phys. Rev. ST Accel. Beams **4**, 110101 (2001).

[8] Z. He et al., submitted to Phys. Rev. ST Accel. Beams (2014).

[9] Z. He et al., "Beam Dynamics Influence from Quadrupole Components in FRIB Quarter Wave Resonators", MOPAB35, HB2013, East Lansing, MI, USA (2014).

[10] Z. Liu, J. Crisp, S.M. Lidia, "AC coupling studies and circuit model for loss monitor ring", To be published in Procs. of IBIC'14, TUPD21.

[11] S. Lidia et al., "Instrumentation Design and Challenges at FRIB", WEO2AB01, HB2013, East Lansing, MI, USA (2014).

# INSTABILITIES AND SPACE CHARGE*

M. Blaskiewicz[†], K. Mernick
BNL, Upton, NY 11973, USA

*Abstract*

The coherent stability problem for proton and heavy ion beams is reviewed. For all but the highest energies space charge is the dominant coherent force. While space charge alone appear benign its interaction with other impedances is less clear. The main assumptions used in calculations and their justifications will be reviewed. Transverse beam transfer function data from RHIC will be used to compare theory and experiment and some pitfalls will be discussed.

## MODELING THE TRANSVERSE FORCE

The effect of space charge on longitudinal instabilites goes back to early work on the negative mass instability [1]. Early work on coasting beam transverse instabilities included the effect of space charge as well [2]. Both these treatments used a leading order approximation with a longitudinal force proportional to the derivative of the instantaneous current and a transverse force

$$F_x = \kappa I(\tau)[x - \bar{x}(\tau, t)] \qquad (1)$$

where $\tau$ is the particle arrival time with respect to the synchronous particle, $t$ is time, $I(\tau)$ is the instantaneous current, $x$ is the transverse coordinate and $\bar{x}(\tau, t)$ is the transverse centroid position as a function of longitudinal coordinate and time. The constant $\kappa$ depends on the beam radius. There are several assumptions [3]:

1. The fields are electrostatic in the comoving frame.
2. The wavelength of perturbations in the comoving frame are long compared to the beam radius.
3. The unperturbed transverse distribution is KV, resulting in a constant density within the beam at a given $\tau$.
4. First order perturbation theory is used.
5. The fields due to boundary conditions are neglected.

For small perturbations the nonlinearities due to images do not depend on the beam dynamics and will be subsumed in a generic octupolar force. For direct space charge actual beams are generally not KV and the accuracy of Eq. (1) has been studied in [4–8] within the context of coasting beams. It was found that the nonlinearity due to direct space charge is relevant only when other forms of damping are present. Space charge enhances damping due to lattice nonlinearity if the betatron tune increases with betatron amplitude. Changing the sign results in less damping that without space charge. The tune shift with amplitude due to short strong quadrupoles has the right sign and works in both planes [9].

Figures 1 and 2 show threshold diagrams where $\Delta Q_0$ is the complex tune shift an undamped beam would have.
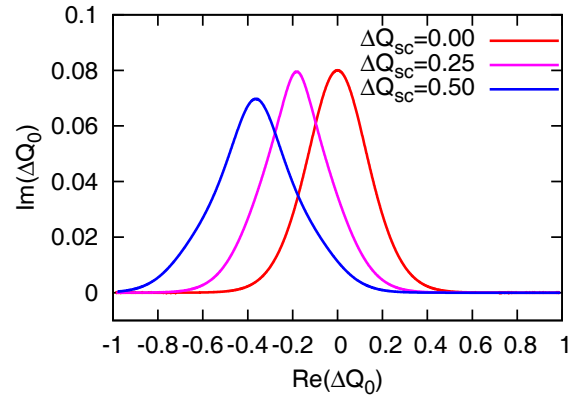


Figure 1: Threshold diagrams for tune spread due to chromatic tune spread with space charge. Average space tune shifts are quoted and the rms chromatic tune spread is 0.1.

Stable tune shifts for damped beams are below the curves. The unperturbed transverse action distribution is $F_0(J) = (3/J_0)(1 - J/J_0)^2$ and space charge is modeled as an interparticle force containing linear and cubic terms [3]. The ratio of the tune spread to the average tune shift matches that for a round gaussian beam. These solutions are for one dimensional motion and the expresion for the theshold impedance as a function of coherent beam tune is a rational function of three different dispersion integrals [5][Eq. (31)]. As is clear from the plots these effects are important if true and we go on to test them with particle tracking.
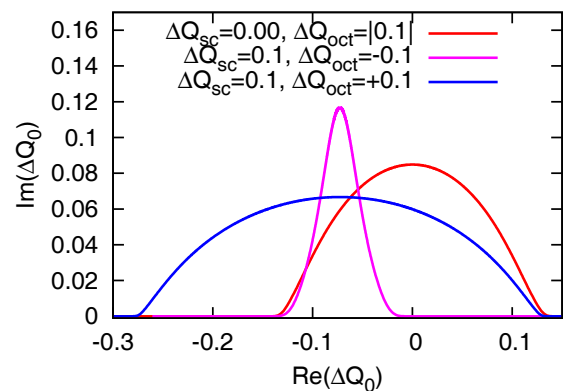


Figure 2: Threshold diagrams for tune spread due to octupoles with space charge. Average space charge and octupolar tune shifts are quoted and a chromatic tune spread of 0.01 is also included.

When both transverse dimensions are included and the space charge is modeled more accurately, certain forms of

---
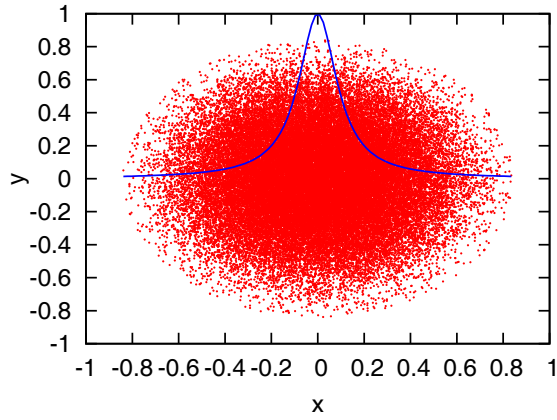
Figure 3: Initial particle distribution and space charge smoothing function used in simulations. 50,000 particles were tracked. Increasing the number of particles by a factor of 5 and increasing the update rate by a factor of 5 had no significant impact.
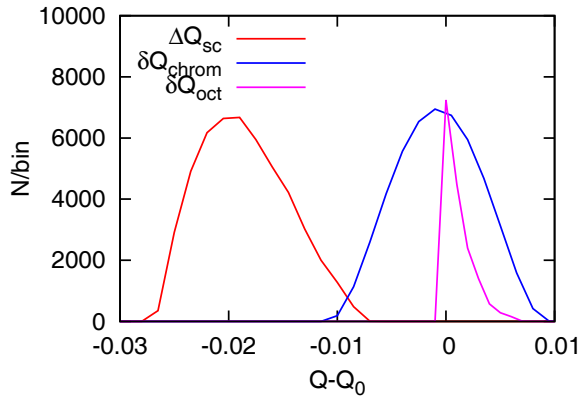


Figure 4: Tune distributions used in the tracking.

the dispersion relation have been conjectured [4, 7, 8] but reliable solutions appear to require tracking. Consider the simple model

$$\frac{dp_{xj}}{d\theta} + Q_x x_j = C_o x_j (x_j^2 + p_{xj}^2) - \delta Q_j x_j \tag{2}$$

$$+ C_{sc} \sum_{m=1}^{N_p} \frac{x_j - x_m}{\epsilon^2 + (x_j - x_m)^2 + (y_j - y_m)^2}$$

$$+ \frac{2}{N_p} \sum_{m=1}^{N_p} Im(\Delta Q_0) p_{xm} - Re(\Delta Q_0) x_m$$

$$\frac{dx_j}{d\theta} - Q_x p_{xj} = -C_o p_{xj} (x_j^2 + p_{xj}^2) + \delta Q_j p_{xj}. \tag{3}$$

In the first lines of Eq. (2) and (3) $\theta$ is the azimuth which increases by $2\pi$ each turn, $Q_x$ is the bare horizontal tune, $\delta Q_j$ is the chromatic tune shift for particle $j$ and $C_o$ characterizes the strength of the octupolar tune shift. In the second line of Eq. (2) $C_{sc}$ characterizes the strength of the space charge

force with smoothing length $\epsilon$. The third line of Eq. (2) contains the impedance like forces. For no tune spread the beam centroid oscillates with real tune $Q_x + Re(\Delta Q_0)$ and grows in amplitude by $\exp[2\pi Im(\Delta Q_0)]$ each turn. The $y$ direction has a different central tune and no $\Delta Q_0$ terms.

Figure 3 shows inital particle distributions and the smoothing fucntion used in the space charge calculations. The initial phase space distribution was matched to $(1 - x^2 - y^2 - p_x^2 - p_y^2)^2$ and 50,000 particles were tracked with 30 updates per betatron oscillation. Increasing the number of particles to 250,000 or increasing the update rate to 150 updates per oscillation had no significant effect on collective modes. Before considering detuning with amplitude we focus on the simpler chromatic tune spreads. Figure 4 shows the tune distributions for chromaticity induced tune spread and space charge tune spread. Octupolar detuning will be considered later and initially we drop space charge also, yielding purely linear equations of motion. Figure 5 shows emittance as a function of time within the stability boundary for a beam with $Im(\Delta Q_0) = 0.0002$. The magenta curve has fractional emittance growth per turn $\exp(4\pi Im(\Delta Q_0)/N_p)$ and follows from a stochastic cooling model [10].

Figure 6 shows the observed growth rate as a function of the real tune shift induced by a wall impedance. The space charge force was evaluated using a fast fourier transform convolution algorithm with a 128 by 128 grid on the beam and a double up procedure to avoid image forces. The blue and red curves in Figure 6 are the similar but when more turns are tracked instabilites can occur later. This is shown in the magenta curve. It is clear that the tracking results do not show the increased region of stability shown in Figure 1. Simulations employing octupolar damping are shown in Figure 7. As is clear from the figure the threshold value of the wall impedance depends on the number of turns tracked. While there is generally a slow, secular increase in the transverse emittance the growth rates were from data before significant emittance growth occured. Both Figures 6 and 7 show behavior typical of extended tracking with space charge. If you wait long enough things almost always go unstable. This is clearly not physical since beams persist for hours at RHIC injection energies with space charge tune shifts far in excess of the synchrotron tune. Other machines, such as the BNL AGS, can have stable beams for seconds with space charge tune shifts of order 0.2. This presents us with something of an impasse. For short runs both Figures 6 and 7 show that space charge increases the range of the stable region beyond what would be expected for a reactive impedance while longer simulations show the reverse. To make some sort of headway for bunched beams we will assume that Equation (1) is sufficiently accurate for beams of interest. While vastly reducing the theoretical and computational complexity it should be clear that this is a fairly strong assumption and that the problem of a correct transverse force model is unresolved.

Exact solutions using Eq. (1) for transverse modes of a bunched beam with constant line density within the bunch are given in appendix II of [11]. Exact longitudinal modes
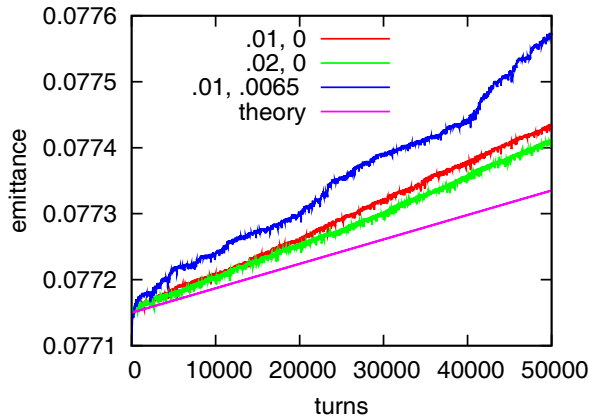
Figure 5: Emittance growth for purely linear simulations within the Vlasov stability boundary. The theory assumes all particles have imaginary tune $Im(\Delta Q_0)/N_p$ with perfect phase mixing. The blue curve is just inside the stability boundary.



Figure 6: The imaginary part of the tune seen in tracking with damping due to chromatic tune spread or frequency spread. The blue cure is the result of tracking with realistic space charge for 5000 turns and the red curve is a shifted version from tracking with no space charge. The magenta curve was obtained for tracking for 50,000 turns, no significant secular changes in the beam were observed before the instability started.

for a bunch with a parabolic current profile are given in [12] which also reduces the dispersion relation to a polynomial. The problem can also be cast as a finite eigenvalue problem [13, 14]. In the exact solutions the forces due to space charge end up being linear in the sense that the depressed tunes are just numbers, not functions of the longitudinal coordinates. The effect of space charge on transverse instabilites with smooth longitudinal profiles was studied in [3, 13–21]. The mode expansion technique was shown to be suspect in [13, 14]. It is not clear how many of the conclusions of these studies are consistent and it is certainly true that the broad conclusions presented in [14] are contradicted by [21].



Figure 7: The imaginary part of the tune seen in tracking with damping due to octupolar tune spread. The blue cure is the result of tracking with realistic space charge for 5000 turns and the red curve is from tracking with no space charge. The magenta curve was obtained for tracking for up to 50,000 turns. Data were limitied to regions where no secular changes in the beam emittance were observed before the instability started.



Figure 8: Simulation with octupolar tune spread and space charge. The points with $Re(\Delta Q_0) = -0.018$ in Figure 7 were obtained from this run. Turns 1000 though 5000 yielded $Im(Q) = 0.53 \times 10^{-4}$ while the last 1000 turns gave $Im(Q) = 1.9 \times 10^{-4}$.

In the next section we will present some beam transfer function data from RHIC in hope of providing some clarity

## BEAM TRANSFER FUNCTIONS

A beam transfer function (BTF) is obtained when a kicker is driven at a single frequency and a pickup measures the phase and amplitue of the beam response at that same frequency. One steps through frequencies and maps out the beam response [22]. Figure 9 show vertical BTF data from RHIC for polarized protons at injection. The bunches were ~ 35 ns at base and the BTFs were take near 250 MHz. The two sidebands were taken on different days and in different rings. The peaks of the BTFs were fit with a parabolic cap.
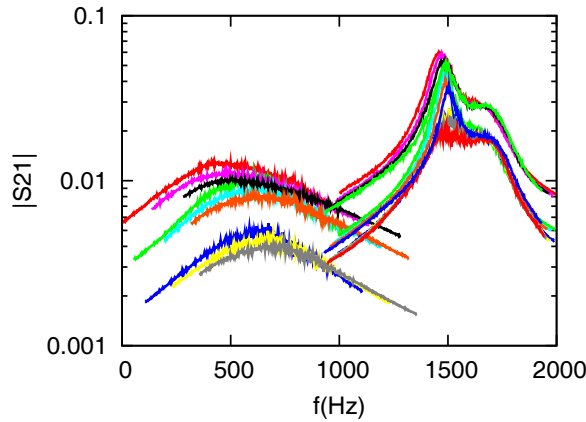
Figure 9: BTF data from RHIC near 250 MHz with protons at $\gamma = 25.5$. The average beam currents ranged from 0.3 to 1.5 A. Vertical data from the $n - Q$ sidband of the blue ring are on the left and data from the $n + Q$ vertical sideband of the yellow ring are offset to the right by 1 kHz.



Figure 11: Frequency shift of $n + Q$ vertical sideband for the yellow ring.



Figure 10: Frequency shift of $n - Q$ vertical sideband for the blue ring.
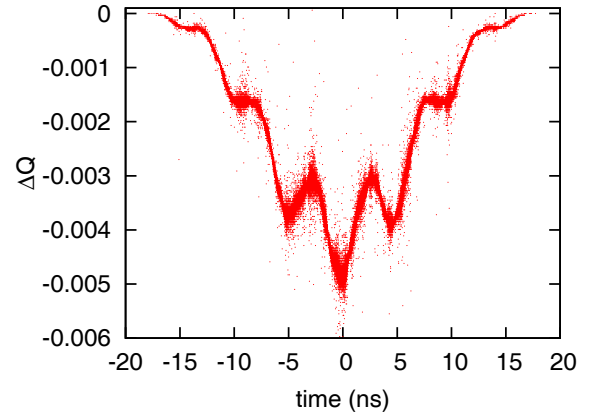


Figure 12: Space charge tune shift as a function of bunch postion used in the simulations for an average current of 1 A. The multi-hump structure is due to the admixture of 9.4 MHz and 197 MHz rf voltage.

The frequency was assumed to be a linear function of intensity and a linear drift in time was allowed for. The fitting results for the two sidebands are shown in Figures 10 and 11. The average current for a bunch is defined to be

$$I_{avg} = \frac{\int\limits_{bunch} I^2(t)dt}{\int\limits_{bunch} I(t)dt} \qquad (4)$$

The simulations assume Equation (1) is sufficiently accurate. Given this assumption any representation of collective forces that leads to Equation (1) will be acceptable. Instead of using a KV distribution and demanding a small perturbation it is much faster and more accurate to take the force on particle $j$ to be

$$F_j = C_{sc} \sum_{k=1}^{N_P} (x_j - x_k)\lambda(\tau_j - \tau_k) \qquad (5)$$

where $x_j$ and $\tau_j$ are the transverse and longitudinal coordinates of the particle kicked, and $\lambda(\tau)$ is a smoothing function. Care must be taken to keep the smoothing length small enough and the number of macroparticles ($N_p$) large enough. Figure 12 shows the incoherent space charge tune shift along the bunch and Figure 13 shows some simulated BTFs [23]. We were unable to reproduce the shoulder apparent in the $n + Q$ sideband of the data. Figures 14 and 15 show simulation results for frequency shift versus time. Agreement with the data is not good. One possible cause for the discrepancy is that the transverse emittance of the RHIC beam is a function of beam intensity. That would cause the space charge impedance to be a function of intensity. It is also likely that the broad band impedance is not the same in the two rings. Impedance measurements using kicked beams show differences by a factor of 2 [24]. We plan to take more data with both sidebands from each ring and to monitor and or control the transverse emittance.

Figure 13: Simulated BTF with $Z_{sc} = 44$ MΩ/m and $Z_{wall} = 5$ MΩ/m. The average beam currents were 1, 0.66, 0.33, 0.10 A.
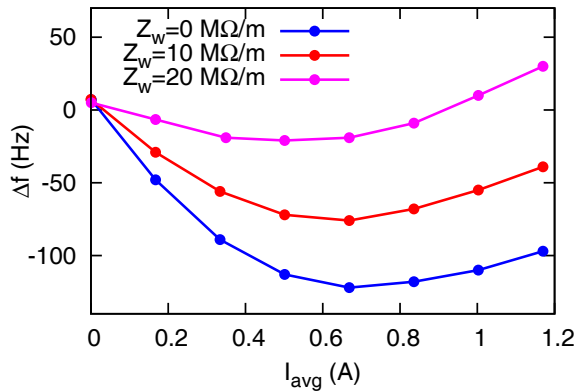


Figure 14: Simulated frequency shift of $n - Q$ vertical sideband.
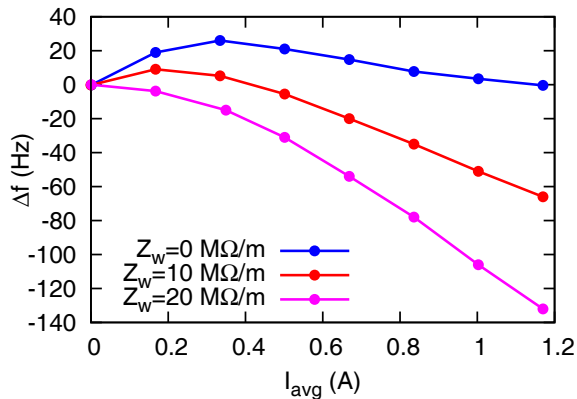


Figure 15: Simulated frequency shift of $n + Q$ vertical sideband.

## REFERENCES

[1] C.E. Nielsen, A.M. Sessler Rev. Sci. Instr. Vol. 30, p80, (1959).

[2] L.J. Laslett, V.K. Neil, A.M. Sessler Rev. Sci. Instr. Vol. 36, No. 4, p436, (1965).

[3] M. Blaskiewicz, M.A. Furman, M. Pivi, R.J. Macek PRSTAB Vol. 6, 044203 (2003).

[4] D. Mohl, H. Schonauer, *Proc. IX Int. Conf. High Energy Acc.*, Stanford, (1974) (AEC, Washington, D.C. 1974) p. 380.

[5] M. Blaskiewicz PRSTAB Vol. 4, 044202 (2001).

[6] D.V. Pestrikov NIMA Vol. 578 p65 (2007).

[7] V. Kornilov, O. Boine-Frankenheim, I. Hofmann PRSTAB Vol. 11, 014201 (2008).

[8] A. Burov, V. Lebedev PRSTAB Vol. 12, 034201 (2009).

[9] R. Baartman, in*Proceedings of the Particle Accelerator Conference (PAC97), Vancouver, Canada* (IEEE, Piscataway, NJ, 1998), p. 1415.

[10] M. Blaskiewicz, J.M. Brennan Cool13

[11] F. Sacherer CERN/SI-BR/72-5 (1972)

[12] David Neuffer *Particle Accelerators* Vol. 11, p23, (1980).

[13] M. Blaskiewicz, W.T. Weng PRE Vol. 50, No. 5, p4030 (1994).

[14] M. Blaskiewicz PRSTAB Vol. 1, 044201 (1998).

[15] A. Burov PRSTAB Vol. 12, 044202 (2009); PRSTAB Vol. 12, 109901 (2009)

[16] V. Balbekov PRSTAB Vol. 12, 124402 (2009).

[17] J.A. Holmes, S. cousineau, v. Danilov, L. Jain PRSTAB Vol. 14, 074401 (2011).

[18] V. Balbekov PRSTAB Vol. 14, 094401 (2011).

[19] V. Balbekov PRSTAB Vol. 15, 054403 (2012).

[20] V. Kornilov, O. Boine-Frankenheim PRSTAB Vol. 15, 114201 (2012).

[21] M. Blaskiewicz IPAC2012 weppr097

[22] D. Boussard, CERN 87-03, p. 416, 1987.

[23] M. Blaskiewicz, V. Ranjbar NAPAC13 (2013).

[24] N. Biancacci *et.al.* IPAC2014 p1730 (2014).

# THRESHOLDS OF THE HEAD-TAIL INSTABILITY IN BUNCHES WITH SPACE CHARGE

V. Kornilov, O.Boine-Frankenheim, GSI Darmstadt, and TU Darmstadt, Germany
C. Warsop, D. Adams, B. Jones, B.G. Pine, R. Williamson, STFC/RAL/ISIS, Oxfordshire, UK

## INTRODUCTION

Head-tail instabilities are expected to be one of the main limitations of the high-intensity operation in the future SIS100 synchrotron of the FAIR facility [1], especially for the heavy-ion bunches [2]. This instability is already beginning to limit the operation at the highest intensities in the ISIS spallation neutron source [3] at the Rutherford Appleton Laboratory in the UK. General ISIS bunch parameters, especially the space-charge conditions, are similar to the expected heavy-ion beams in SIS100, thus it might be possible to use the physical insight and the experience from the ISIS studies for anticipating the transverse stability in the SIS100 high-intensity bunches. Of particular interest is the dependence of unstable beam modes on the configuration of the RF system (single or dual harmonic), the influence of high space charge levels, the key role of the betatron tune and the determination of driving beam impedances.

## OBSERVATIONS IN ISIS

A dedicated experimental campaign of three shifts has been performed at the ISIS synchrotron in November 2013, with the primary goal to understand more about the fast losses and associated vertical oscillations around 2 ms of the ISIS cycle, see Fig. 1. These losses are a concern for the high-intensity operation and have been usually attributed to head-tail instabilities. In standard ISIS operation, a 2RF system is used. In order to be able to compare with classical theories, and to simplify the first comparisons with simulations, the most of the study was made with the 1RF ($h = 2$) operation. Approximately one-third of the measurements were done with different types of 2RF ($h = 2, 4$).
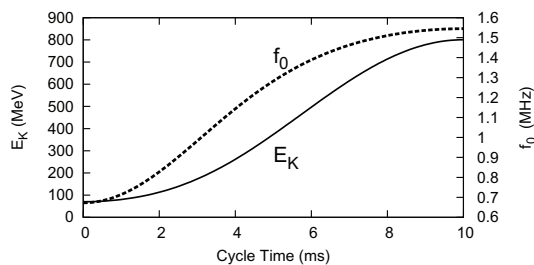


Figure 1: ISIS cycle: the proton kinetic energy (solid line) and the revolution frequency (dashed line), $C = 163.26$ m.

According to the experience at ISIS [4–6], the instability appears if the vertical tune is set closer to integer from below. The normal tune ramp at ISIS applies $Q_v = 3.85$ at 0 ms decreasing to $Q_v = 3.68$ at 10 ms, with $Q_v = 3.758$ at 2 ms. In order to focus on the operation-type instabil-
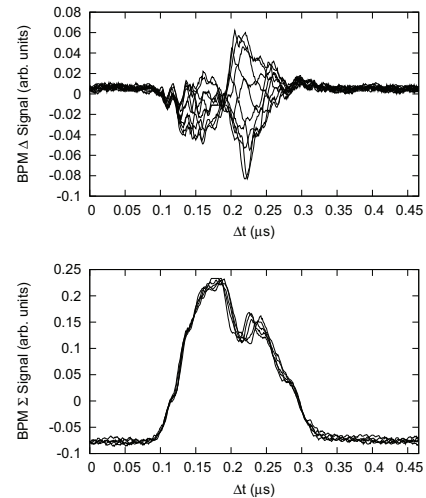


Figure 2: Consecutive bunch traces from the vertical BPM delta (top) and sum (bottom) signal of a typical instability for a 1RF bunch around Cycle Time 2 ms.
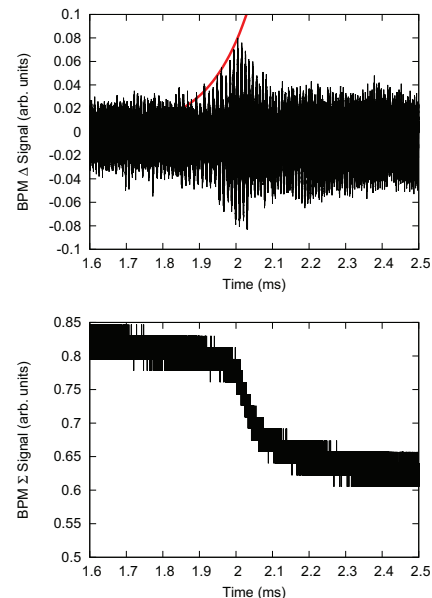


Figure 3: Time evolution of the BPM delta (top) and sum (bottom) signal for the instability from Fig. 2. The red line is an exponential with the growth time $\tau = 0.1$ ms.

ity, we have pushed the vertical tune higher around 2 ms cycle time. Once tune reaches $Q_v \approx 3.86$, reproducible strong losses and vertical collective oscillations appear. Figures 2, 3 present typical BPM signals around 2 ms. The overplotted bunch traces in Fig. 2 show a standing wave pattern

with one node, with chromaticity wiggles inside. The oscillation grows with the growth time $\tau = 0.1$ ms (Fig. 3), until it is distorted by beam losses. This proves a classical unstable $k = 1$ head-tail mode. In the majority of the recorded signals, it was hard to determine a clear growth rate, probably due to early losses. This might be attributed to large beam sizes which intentionally maximise use of aperture. More examples of the instabilities in ISIS, in 1RF and in 2RF, are given in the slides of this presentation.

For every beam and machine parameter set, an intensity scan has been performed.

The results of the intensity scans are summarized in Fig. 4. The left plot in Fig. 4 is dedicated to the 1RF instability around 2 ms (red) and around 3 ms (blue). The right plot in Fig. 4 compares different RF settings, the flat-bunch 2RF (or lengthening mode) around 2 ms, and the operation-type 2RF (stable asymmetric settings) around 2 ms. There is no instability at low intensities, which is a usual observation for collective instabilities, due to natural non-linearities in the machine optics. Hence, there is the common "bottom" thresholds. Surprisingly, it was observed that instabilities vanish above certain intensities, which we describe as "top" thresholds. This phenomenon was clearly observed and reproducible, in intensity scans upwards as well as downward.
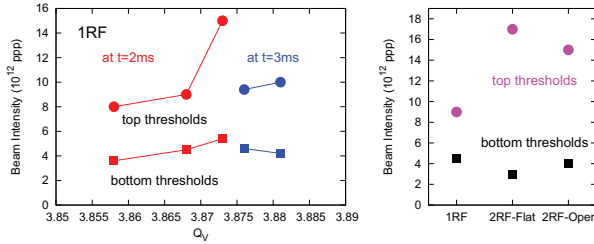


Figure 4: Summary for the intensity thresholds of the head-tail instability observed in ISIS. Beam loss and oscillations appear between the bottom and the top thresholds.

## ANALYTICAL CALCULATIONS

We use the theory of Sacherer [7] in order to identify the driving impedance and to estimate the growth rates. The center of the power spectrum is shifted by $\Delta f = f_0 Q \xi / \eta$, $\xi = -1.4, \gamma_t = 5.034$, see Fig. 5. The positive frequencies in the plot do not contribute to the instability drive, according to this theory. In the case of the ISIS bunches, with the full bunch length $t_b \approx 200$ ns around 2 ms, the head-tail modes $k = 2$ should be unstable. In order to explain the observed $k = 1$ modes, an effective bunch length $0.5 t_b$ has been assumed. The observation that the instabilities appear as the tune approaches integer from below, is a strong indication that an impedance with a Resistive-Wall frequency dependence $\mathrm{Re}(Z_\perp) \propto 1/f$ (indicated with the black line in Fig. 5) should be the driving force. However, if we assume the Resistive Thick-Wall Impedance with the pipe radius $b_{\mathrm{pipe}} = 50$ mm (i.e., overestimated impedance), much

slower instabilities than observed ($\tau < 20$ ms) are predicted, see Fig. 5.
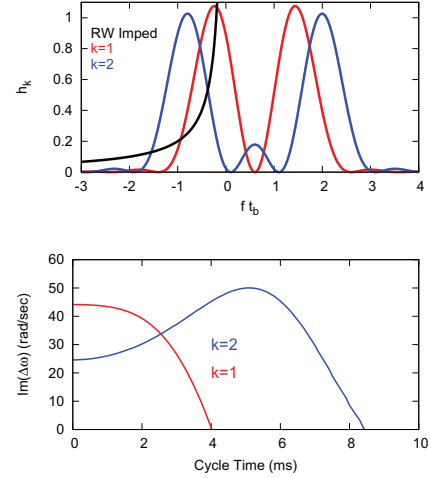


Figure 5: Calculations with the Sacherer theory for the ISIS 1RF bunches. Top: power spectrum of the head-tail modes (see [7]) and the real part of the normalized Resistive-Wall impedance in the unstable range. Bottom: the resulting growth rates.

## SPACE CHARGE AND LANDAU DAMPING

The effect of self-field space-charge on head-tail modes in bunches can be analytically solved for an airbag bunch [8]. This theory is also very useful and rather accurate for Gaussian bunches, as it was observed in particle tracking simulation [10] and in experiments in the SIS18 synchrotron at GSI Darmstadt [11]. Landau damping due to space-charge in bunches was predicted analytically in [12] and confirmed with simulation studies in [10].

The additional effect of a coherent tune shift, for example from the imaginary impedance of image charges, has been included into the airbag theory in [9],

$$\Delta Q_k = -\frac{\Delta Q_{\mathrm{sc}} + \Delta Q_{\mathrm{coh}}}{2} \pm \sqrt{\frac{(\Delta Q_{\mathrm{sc}} - \Delta Q_{\mathrm{coh}})^2}{4} + k^2 Q_s^2} , \quad (1)$$

where "+" is for modes $k \geq 0$, the notation corresponds to [11].

It is suggested that the combination of space-charge and coherent force should have an effect on Landau damping. Figure 6 shows the head-tail modes with and without a coherent tune shift, and the border of the active Landau damping area, $\Delta Q_{\mathrm{max}} = -0.23 Q_s q + k Q_s$ [11]. The lines are shifted by $(-k)$ for a better comparison. A head-tail mode is affected by Landau damping if the frequency is below damping border, the dashed line in Fig. 6. We see that the $k = 0$ mode is not damped (it is not affected by space-charge, see the left plot). The $k = 1$ mode is damped for $0 \lesssim q \lesssim 3$ without coherent force, and for $0 \lesssim q \lesssim 6$ with $\Delta Q_{\mathrm{coh}}$. The $k = 2$ mode is damped for $0 \lesssim q \lesssim 6$ without coherent force, and for $0 \lesssim q \lesssim 12$ with $\Delta Q_{\mathrm{coh}}$.
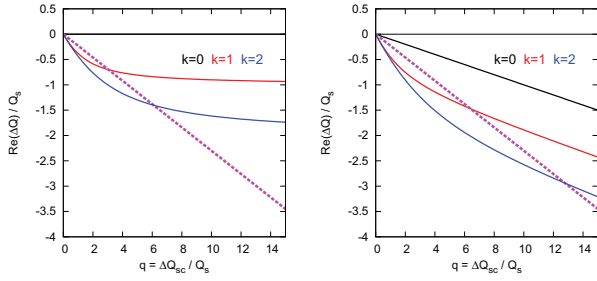
Figure 6: Effect of the image charges on the head-tail modes according to the airbag theory. Left plot: $\Delta Q_{coh} = 0$, right plot: $\Delta Q_{coh} = 0.1\Delta Q_{sc}$. The dashed line indicates the border of Landau damping.

In order to observe the modifications of Landau damping due to image charges, we consider the mode $k = 1$ and compare the areas of strong damping for different strength of the coherent forces. According to the airbag theory and the Landau damping border prediction, with $\Delta Q_{coh} = 0.1\Delta Q_{sc}$ the area of damping should be larger than for the case without image charges, see Fig. 7. For $\Delta Q_{coh} = 0.2\Delta Q_{sc}$ the coherent line remains under damping for all $q$ values considered in Fig. 7. We perform PIC simulations using the code PATRIC [13], similar to the work reported in [10], but with the coherent effect included, which varies along the bunch according to the local slice line density. The simulation results are summarized in Fig. 8. This shows a good qualitative confirmation of the effect of image charges on the space-charge induced Landau damping.
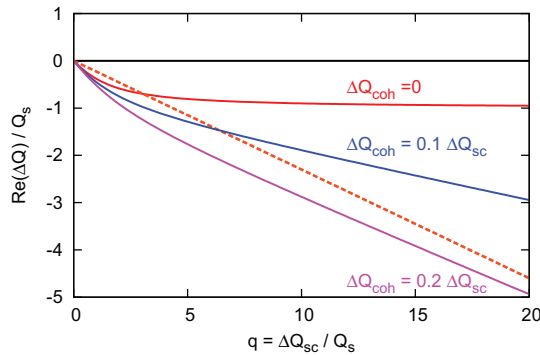


Figure 7: Effect of the image charges on the $k = 1$ head-tail mode according to the airbag theory. The dashed line indicates the border of Landau damping.

## LANDAU DAMPING IN THE ISIS BUNCHES

The parameters of the bunches in ISIS correspond to the regime of rather strong space-charge, as demonstrated in Fig. 9 with the estimations for the parameters in our 1RF experiments. The main uncertainty is associated with the transverse emittance, here we have assumed the rms
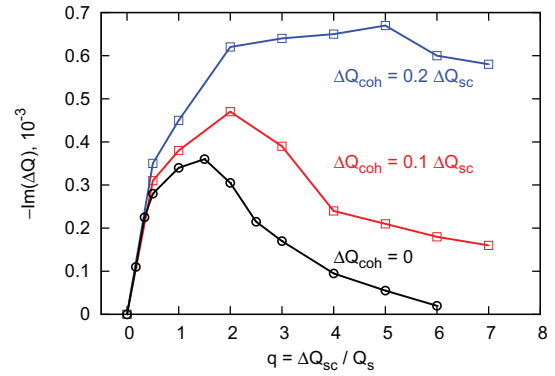
Figure 8: Damping decrement of the $k = 1$ head-tail mode obtained from the PATRIC simulations for a Gaussian (longitudinally and transversally) bunch, $Q_s = 0.01$, for different strengths of the coherent tune shift due to image charges.
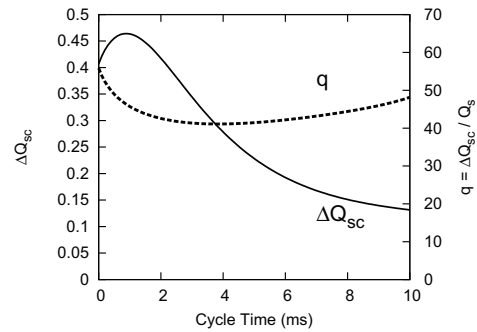


Figure 9: Space-charge tune shift and the space-charge parameter for the 1RF bunches in ISIS at the beam intensity $4 \times 10^{12}$ ppp.

non-normalized $\varepsilon = 50$ mm mrad at the start of the cycle, in the vertical plane. The space-charge parameter $q = \Delta Q_{sc}/Q_s \gg 1$ implies strong space-charge regime for the bunch head-tail dynamics [10, 12]. We can also conclude that, although the space-charge tune shifts decrease during the ramp, the space-charge parameter stays stable around $q \approx 40$ in this case.

The ISIS vacuum pipe is a rectangular, conformal, stainless steel vessel [14], see Fig. 10. The coherent tune shift due to image charges is proportional to the space-charge tune shift,

$$\Delta Q_{coh} = \Delta Q_{sc} 2\xi_{h,v} \frac{a^2}{h^2}, \qquad (2)$$

where $a$ is the beam radius, $h$ is the characteristic pipe size, and $\xi_{h,v}$ depends on the pipe geometry. For a round pipe, $h$ is equal to the pipe radius, and $\xi_{h,v} = 0.5$. For a rectangular pipe, $\xi_{h,v}$ can be calculated from analytical functions, see [15]. The results are presented in Fig. 10. The overall tune shift can be calculated as an average over the ring, $\langle 2\xi_h(s)/h^2(s)\rangle H^2 = 0.528$, and $\langle 2\xi_v(s)/h^2(s)\rangle H^2 = 1.13$, where $H = \langle h(s)\rangle = 63.42$ mm is the average pipe half-height. This results in a vertical coherent tune shift of

$\Delta Q_{\text{coh}} \approx 0.12 \Delta Q_{\text{sc}}$ for the 1RF bunch parameters with $4 \times 10^{12}$ ppp.
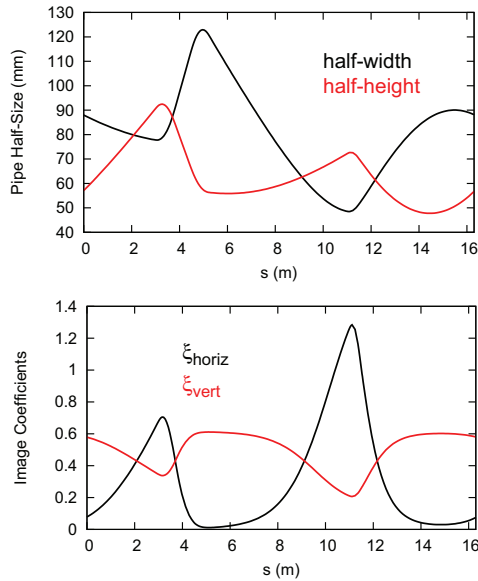


Figure 10: Top plot: half-apertures of the beam pipe in ISIS over a superperiod. Bottom plot: image coefficients for the rectangular ISIS pipe.

In order to analyse the changes in the tune shifts with the increasing beam intensity, we consider three different scenarios of the transverse emittance increase,

$$\Delta \varepsilon_\perp = k_N \frac{\Delta N_p}{N_{p0}} \varepsilon_{\perp 0}. \tag{3}$$

The case $k_N = 0$ means that the emittance does not change (most unrealistic), $k_N = 1$ implies a constant phase-space density, and $k_N = 0.5$ is an intermediate case. The space-charge tune shift is $\Delta Q_{\text{sc}} \propto N_p / \varepsilon_\perp$, thus it stays constant for $k_N = 1$ and increases linearly for $k_N = 0$, see Fig. 11. Differently, the coherent tune shift is $\Delta Q_{\text{coh}} \propto N_p$, thus it increases linearly for all the $k_N$−scenarios. As a result, the relative strength $\Delta Q_{\text{coh}} / \Delta Q_{\text{sc}}$ stays constant for $k_N = 0$ and it increases for the both $k_N = 1$ and $k_N = 0.5$. The Landau damping for the $k = 1$ mode, as predicted by our model with the airbag theory, is presented in Fig. 12. Similarly to Fig. 7, the mode is under active Landau damping if the coherent line (solid line) is below a dashed line. We see that for the unrealistic case $k_N = 0$ there is no damping, but for an increasing emittance, there is a border intensity where the head-tail mode dips into Landau damping.

## CONCLUSIONS

- Collective oscillations and beam losses have been systematically observed in ISIS around 2 ms Cycle Time for various beam and machine parameters. In most cases, it has been identified as the $k = 1$ head-tail mode with the typical growth time $\tau \approx 0.1$ ms. For 2RF operation, the mode structure can be more complicated.
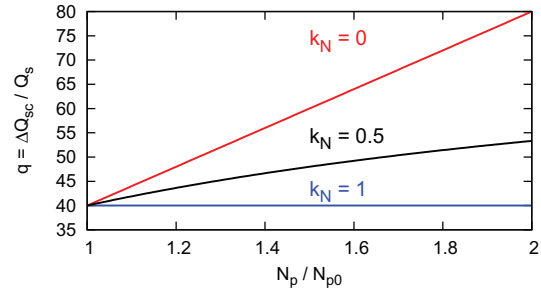


Figure 11: The space-charge parameter in the ISIS bunches for different emittance increase scenario.
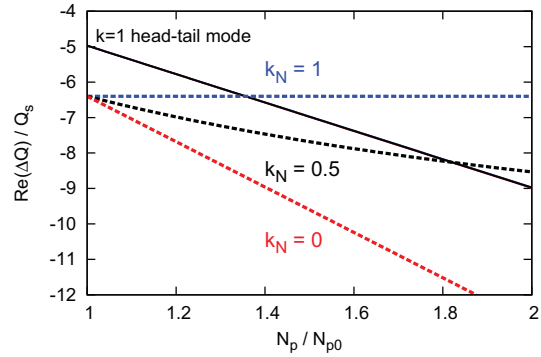


Figure 12: Illustration of the Landau damping for an increasing beam intensity. The black solid line is the coherent tune of the $k = 1$ mode. The dashed lines indicate the borders of Landau damping for different emittance increase scenario.

- With the help of the Sacherer theory, it can be concluded that the driving impedance has a Resistive-Wall type behaviour (resonant at low frequencies), because the instability appears if the vertical tune is set closer to integer from below. However, calculations with the Sacherer theory require a shorter effective bunch length in order to predict the $k = 1$ mode observed. The predicted growth rates are also much smaller than in the observations.

- Intensity thresholds have been identified for 1RF, 2RF settings, and for different driving tunes, Fig. 4. In addition to the common "bottom" thresholds, unexpected "top" intensity thresholds have been observed.

- Coherent tune shifts from the image charges modify Landau damping due to space charge in the bunches. It can be qualitatively analyzed using an airbag theory and a model for the Landau damping. Our PATRIC simulations confirm the enhanced damping due to image charges.

- Detailed calculations show that, due to a unique conformal beam pipe in ISIS, the image charges should produce strong coherent tune shifts. Additionally, the

bunches in ISIS are in a regime of rather strong space charge, $q = \Delta Q_{sc}/Q_s \approx 40$. The largest uncertainty in the ISIS experiments is due to the measurements of the transverse emittance.

- Calculations for the coherent frequency of the $k = 1$ head-tail mode and for Landau damping with different scenarios of the transverse emittance increase suggest an intensity threshold, above which the $k = 1$ mode can be stabilized. This effect is due to different development of the space-charge tune shift and the image-charge tune shift for an increasing intensity.

- Enhanced Landau damping with image charges may be achieved with a controlled transverse emittance blow-up. This has been observed in the experiments reported here. The instability in 1RF bunches around 2 ms has been cured by increasing the transverse emittance, keeping the rest of the beam parameters fixed. This observation can be interpreted as a "top" threshold in transverse emittance. It should be noted that even with the beam stabilised, the associated increase in emittance can still lead to high levels of beam loss.

- Landau damping due to space charge with the effect of image charges should be taken into account in the stability studies for SIS100. The discrepancies between the Sacherer theory and the ISIS observations imply a possibility for much faster instabilities than expected so far.

## REFERENCES

[1] FAIR Baseline Tech. Report 2006

[2] V. Kornilov, O. Boine-Frankenheim, Proc. IPAC2012, p. 2934 (2012)

[3] J W G Thomason, et al, Proc. HB2008, p. 434 (2008)

[4] G.H. Rees, Particle Accelerators **39**, pp. 159-167 (1992)

[5] C.M. Warsop, et al, Proc. HB2014, TUO3LR03 (2014)

[6] R.E. Williamson. et al, Proc. HB2014, MOPAB38 (2014)

[7] F. Sacherer, CERN-77-13, p. 198 (1976)

[8] M. Blaskiewicz, PRST-AB **1**, 044201 (1998)

[9] O. Boine-Frankenheim, V. Kornilov, PRST-AB **12**, 114201 (2009)

[10] V. Kornilov, O. Boine-Frankenheim, PRST-AB **13**, 114201 (2010)

[11] V. Kornilov, O. Boine-Frankenheim, PRST-AB **15**, 114201 (2012)

[12] A. Burov, PRST-AB **12**, 044202 (2009); V. Balbekov, PRST-AB **12**, 124402 (2009)

[13] O. Boine-Frankenheim, V. Kornilov, Proc. of ICAP2006

[14] B.G. Pine, C.M. Warsop, Proc. IPAC2011, p. 2754 (2011)

[15] K.Y. Ng, Physics of Intensity Dependent Beam Instabilities, World Scientific (2006)

# UPGRADE OF THE UNILAC FOR FAIR

L. Groening, A. Adonin, X. Du, R. Hollinger, S. Mickat, A. Orzhekhovskaya, B. Schlitt,
G. Schreiber, H. Vormann, C. Xiao, GSI, D-64291 Darmstadt, Germany
H. Hähnel, R. Tiede, U. Ratzinger, Goethe University of Frankfurt, D-60438 Frankfurt, Germany

## Abstract

The UNIversal Linear Accelerator (UNILAC) at GSI has served as injector for all ion species from protons for uranium for the past four decades. Especially its 108 MHz Alvarez type DTL providing acceleration from 1.4 MeV/u to 11.4 MeV/u has suffered from material fatigue. The DTL will be replaced by a completely new section with almost the same design parameters, i.e. pulsed current of up to 15 mA of $^{238}U^{28+}$ at 11.4 MeV/u. However, operation will be restricted to low beam duty cycles as 200 µs at 10 Hz. Since preservation of beam quality is mandatory, a regular focusing lattice, as along an Alvarez section for instance, is aimed for. A new source terminal & LEBT dedicated to operation with $^{238}U^{4+}$ is under design. The uranium sources need to be upgraded in order to provide increased beam brilliances and for operation at 2.7 Hz. Revision of the subsequent 36 MHz RFQ electrode design has started as well as the layout activities of the section providing transition from the 36 MHz section to the 108 MHz DTL.

## INTRODUCTION

GSI is currently constructing the Facility for Ion and Antiproton Research (FAIR). It aims at provision of $4\times10^{11}$ uranium ions at 1.5 GeV/u [1]. As injector for FAIR serves the existing UNIversal Linear ACcelerator UNILAC (Fig. 1) together with the subsequent synchrotron SIS18. The UNI-
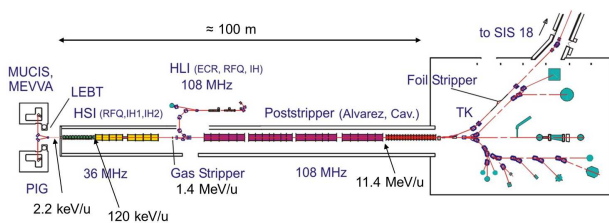


Figure 1: The UNIversal Linear ACcelerator (UNILAC) at GSI.

LAC comprises three ion source terminals. Two of them provide beams at 2.2 keV/u which are injected into an RFQ and are accelerated to 120 keV/u. It is followed by a MEBT comprising a doublet and a super lens, i.e. a 1m long RFQ that just provides longitudinal and transverse focusing without acceleration. The MEBT matches the beam into an IH-DTL. This DTL comprises 2 IH-cavities which apply the KONUS accelerating scheme [2], i.e. the design rf-phase slips from positive to negative phases. This technique allows for high effective shunt impedance and less transverse defocusing. But it provides less longitudinal focusing and requires very accurate longitudinal matching to the DTL

entrance. Transverse focusing is provided through three internal triplets per cavity. The IH-cavities operate at 36 MHz and provide acceleration to 1.4 MeV/u. Alternatively, an ECR source followed by an RFQ and one IH-cavity operated at 108 MHz can provide ions with 1.4 MeV/u as well. The 36 MHz pre-stripper DTL is followed by a stripping section, where the ion beam is intercepted by a gaseous jet of nitrogen for increase of the charge state. For instance uranium is stripped from the charge state 4+ to the charge state 28+. The subsequent post-stripper DTL comprises five Alvarez type cavities for acceleration to 11.4 MeV/u being the injection energy required by the synchrotron SIS18. The UNILAC has a high flexibility in its 50 Hz operation. Several virtual accelerators can be operated, all differing wrt to the beam they deliver, i.e. ion species, energy, pulse length, and repetition rate.

This DTL was designed in the late 1960ies and it is in operation for 40 years now. The cavities suffered from considerable material fatigue. Sparking damaged the copper surface. Especially, fast changes of the rf-duty cycles and rf-amplitudes from switching between different virtual accelerators caused rf-sparking. As a consequence, the last years saw limitations in the rf-amplitudes that could be set to the tanks. This manifested in degradation of beam quality of heaviest ions as $^{238}U^{28+}$. Additionally, the beam dynamics design did not foresee provision of intense beams, which are prone to space charge effects. The beam design parameters of the UNILAC are listed in Table 1. The age of the

Table 1: Beam Design Parameters for the Upgraded UNILAC

| Ion A/q | $\leq 8.5$ | |
|---|---|---|
| Beam Current (low duty cycle) | $128\cdot q/A$ | emA |
| Beam Current | $\approx 500\cdot q/A$ | eµA |
| Input Beam Energy | 1.4 | MeV/u |
| Output Beam Energy | 11.4 | MeV/u |
| Output Emit. (norm., tot.) hor/ver | 0.8/2.5 | mm mrad |
| Beam Pulse Length | $\leq 5000$ | µs |
| Beam Repetition Rate | $\leq 50$ | Hz |
| Rf Frequency | 108.408 | MHz |

UNILAC together with the requirement to provide reliable and intense beams for the upcoming FAIR era calls for a revision of the UNILAC, especially its post-stripper DTL. The following section will describe the envisaged upgrade measures.

## SOURCE AND LEBT

FAIR will put special emphasis on uranium beams, which are presently provided together with other heavy ions by a VARIS or MEVVA source located in the northern source terminal. The existing LEBT includes two bends which impose dispersion and hexapolar fringe fields. Additionally, operation and handling of uranium comes along with restrictions from safety requirements. For this reasons a new and dedicated uranium branch is under design as shown in Fig. 2. It is a straight LEBT comprising two quadruplets



Figure 2: The existing north and south ion source terminals and LEBT branches together with the new uranium terminal (west).

and one triplet. The source will deliver several charge states of uranium but only $^{238}U^{4+}$ is accepted by the RFQ. The fractions of other charge states (mainly 3+) are reduced by chromaticity together with an circular iris located at a beam waist of the charge state 4+. Beam envelopes from simulations along the new LEBT are plotted in Fig. 3 together with phase space distributions at the entrance to the RFQ. Simulations were done for different assumptions wrt the amount on space charge compensation (95% - 100%). The results indicate that the beam brilliance (current/emittance) could be increased by a factor of about 2 compared to the present value. Finally, the repetition rate of the source needs to be increased from 1 Hz to 2.7 Hz. This increase has been reached for ions as gold, bismuth, and lead, but for uranium further systematic investigations especially on the cathode material are required.

## RFQ

Also the RFQ suffered from sparking during operation with varying rf-duty cycles and rf-amplitudes. The attainable rf-voltages are about 10% below the required values for uranium. This leads to serious degradation of longitudinal beam quality from insufficient bunching. Additionally, the beam divergence at the RFQ exit is too large, triggering losses inside the subsequent super lens, which in consequence also has to be operated at lower voltages causing further degradation of beam quality. The design of the RFQ



Figure 3: Simulated beam envelopes along the new LEBT: Design charge state 4+ (upper), charge state 3+ (centre), and phase space distributions (4+) at the RFQ entrance (lower).

will be revised such that lower surface fields are applied at the expense of reduced acceptance.

## MEBT AND IH-DTL

The transverse and longitudinal focusing strengths of the super lens are coupled since it is an RFQ. In total the present MEBT offers just four knobs to tune its matching performance to the IH-DTL: two quadrupole gradients, one rf-amplitude, and one rf-phase. This limitation together with too low rf-amplitudes (from sparking) causes poor longitudinal matching to the KONUS IH-DTL. A new MEBT design [3] foresees two symmetric triplets and one buncher, i.e. six tuning knobs. The new MEBT layout and a compari-

son of the longitudinal matching performances are shown in Fig. 4. However, the new design foresees additional 1.4 m in length. Accordingly, the subsequent IH-cavities have to be shifted and the stripper section has to be shortened by that distance. Simulations along the MEBT and IH-DTL



Figure 4: New layout of the MEBT (upper) and longitudinal matching performances (left: old design, right: new design).

indicate that the growth of emittance could be reduced from 57/93/320% (hor/ver/long, today's design) to 54/61/65% (new design) with simultaneous increase of the overall transmission from 86% to 100%.

## ALVAREZ DTL

The beam parameters of the new post-stripper DTL are the same as for the existing one except the beam duty cycle. It will be limited to beam pulse length of 200 $\mu$s at a repetition rate of 10 Hz. The new UNILAC will serve just as an injector for the FAIR facility. Accordingly, the mixed operation between different rf-amplitudes and rf-pulse length, that caused damages at the cavity surface and limited the rf-amplitudes, will not be applied in the future.

For the type of DTL two options were initially considered: an Alvarez type and an IH type DTL. GSI has operational experience with both types. IH-DTLs offer high effective shunt impedances. This may allow to provide within the existing linac tunnel of GSI final ion energies of about 50 MeV/u (at a later upgrade stage). Such an energy opens the path to by-passing the existing synchrotron SIS18 and to inject directly into the synchrotron SIS100, which provides the final beam energy required by the FAIR users. Additionally, IH-DTLs require much less quadrupoles leading to reduction in cost. Alvarez-DTLs in turn proved to be reliable working horse accelerators. The related beam dynamics is fully understood even if considerable space charge is included. Periodic beam 3d-envelope solutions are properly defined as well as the procedure to match the incoming beam to that solution. For IH-DTLs for time being we did not find a procedure to assure matched beam transport and acceleration [4], that provides maximum mitigation of beam emittance growth from space charge.

As beam quality is of uttermost relevance for a low duty cycle injector, GSI currently plans to replace the existing post-stripper DTL with another Alvarez type DTL. The design works are at the beginning. The layout of the new cavities aims at optimization of the ratio of shunt-impedance to electric surface field. The latter shall be limited to 1.0 Kilpatrick. A new shape of drift tube plates has been found that provides 10% increase of impedance at the same surface field strength (Fig. 5). The curve does not include straight
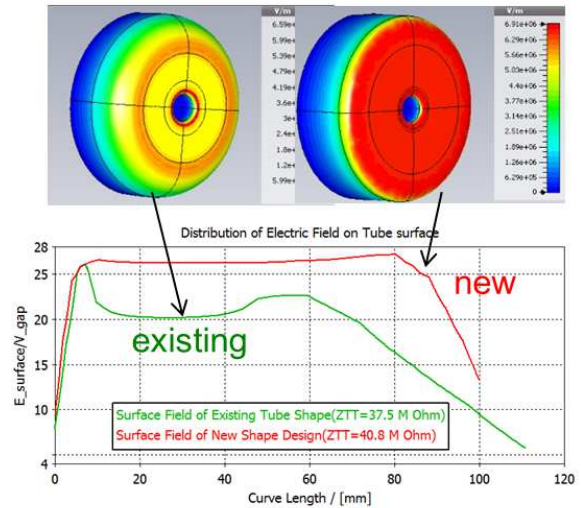


Figure 5: Comparison of the present (upper left) and new (upper right) drift tube design.
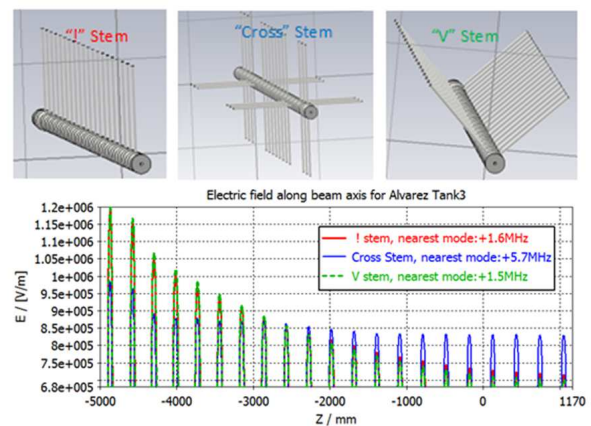


Figure 6: Several schemes of orientations of the DTL stems and their effect on the field stabilization.

sections and is defined through about 200 fixed points. This approach provides a smooth surface field distribution and should lower the multipacting rate. It does not cause significant extra cost for production nor it imposes restrictions wrt the achievable tolerances. Each drift tube along one tank will have the same end plate shape. The rf-frequency tuning of each cell is done through adoption of the drift tube length.

Stability of the accelerating field is done through well-considered orientation of the stems that keep the drift tubes.

As the drift tubes have to be provided with cooling water and electrical current for the quadrupoles, each tube is kept by two stems. It turned out that the orientation of the two stems plays a significant role in the suppression of parasitic modes as illustrated in Fig. 6. The new DTL will comprise five tanks. For each tank a maximum rf-power of 1.8 MW is available of which 0.3 MW are beam power.

Special care will be taken for proper beam envelope matching along the four inter-tank sections. These sections impose interruptions of the periodicity of the lattice inside each tank. If not being well-designed they will trigger emittance growth from mismatch. Finally, the transverse phase advance has to be increased by about 15% wrt the present layout in order to compensate for tune depression from space charge.

## REFERENCES

[1] FAIR Baseline Technical Report, Vol. 2, GSI Darmstadt, Germany, 2006, p. 335.

[2] G. Clemente et al., PRST-AB **14** 110101 (2011).

[3] H. Hähnel et al., Proc. of LINAC2014 Conf (2014).

[4] A. Orzhekhovskaya et al., Proc. of IPAC2014 Conf. (2014).

# CODE REQUIREMENTS FOR LONG-TERM TRACKING WITH SPACE CHARGE

H. Bartosik, E. Benedetto, M. Bodendorfer, V. Forte, S. Gilardoni, N. Hoimyr, A. Huschauer,
M.A. Kowalska, M. Martini, E. Metral, A. Oeftiger, B. Panzer-Steindel, F. Schmidt*, E.G. Souza,
M. Titze, R. Wasef, CERN, Switzerland; J. Amundson, V. Kapin, L. Michelotti, E. Stern,
Fermilab, USA; S.M. Cousineau, J. Holmes, A.P. Shishlo, SNS, USA; G. Franchetti, GSI, Germany;
S. Machida, RAL, UK; C. Montag, BNL, USA; J. Qiang, LBNL, USA

## Abstract

In view of the LHC Injectors Upgrade (LIU) program of
the LHC pre-accelerators LEIR [1], PSB [2], PS [3] and
SPS [4] we have started a new working group at CERN to
deal with space charge issues of these machines. The goal
is to operate with basically twice the number of particles
per bunch which will further increase the space charge tune
shifts which presently are already large. Besides obvious
remedies like increasing the injection energy we are obliged
to better understand the space charge force to optimize our
machines. To this end it has become clear that we need com-
puter models that faithfully represent the linear but also the
non-linear features of our machines. We have started close
collaborations with several laboratories around the world
to upgrade existing self-consistent space charge Particle-In-
Cell (PIC) codes for our CERN needs. In parallel we have
created a frozen space charge facility in CERN's MAD-X
code. Both types of codes are being used to study long-term
stability and to compare it with machine experiments.

## INTRODUCTION

It has been realized in 2011 that at CERN a concerted
effort was needed to study the space charge (SC) effects in
the pre-accelerators of the LHC in view of achieving a two-
fold increase of beam intensity needed to fulfill the goals of
the LIU project. To this end a SC working group has been
established to build a new team of competence in the field of
space charge effects at CERN. Students and staff members
have been won to study the 4 circular machines LEIR, PSB,
PS and SPS both with experiments and simulations. In the
meantime there is also a team to study SC effects in more
general terms.

In regular meetings [5] the machine related SC issues are
being discussed but also an educational series of talks has
been started given by experts from inside CERN and other
laboratories.

From the beginning it has been clear that one need to know
well the non-linear dynamics in conjunction with SC forces
to allow for a full understanding of emittance growth and
losses in any of the machines. Expertise is required in both
regimes and also a close collaboration with magnet experts
is mandatory to get a good modeling and measurements of
critical magnets in the rings.

The codes would need to be adapted towards an adequate
treatment of both the non-linear machine models and SC.
A decision has been made to invest into existing codes and
adapt them to CERN needs, unless we could modify CERN
codes with moderate effort. Essential is that any code would
have to pass a rigorous benchmarking test before the code
results could actually be trusted. Ease of use, flexible struc-
ture and computing performance are further critical issues
for the LIU studies. Last and not least a code benchmarking
with machine experiments is the ultimate way to give us
confidence that the whole chain from magnet modeling, the
codes and the experimental data taking are all sufficiently
well prepared and mastered so that the machines can be un-
derstood well enough to minimize the combined effect of
machine non-linearities and SC.

Intense collaborations have been initiated around the
world and we have started series of workshops [6] [1] and
collaboration meetings [7] [2] to make progress on the open
issues in the theoretical understanding and program devel-
opment.

This report is based on the outcome of those two meetings
and an outlook is given for the next steps. We concentrate
here on CERN machines where presently there is a high
demand for SC studies. Many of these discussed issues
should be of wider interest to the SC community as a whole.

We have added an Appendix about CERN's new method
to create perfectly matched 6D distribution that hasn't been
discussed anywhere before.

## CODES

In the SC field there are basically two classes of codes: on
the one hand there are the self-consistent PIC codes with 2D,
2.5D and 3D SC treatment. These codes are most relevant
over a short period at the beginning of injection when the
coherent SC are largest, the fields may be time dependent and
the dynamics are most complex. Despite these advantages
the codes tend to be slow and the results suffer from PIC
noise. On the other hand frozen SC codes are being used
over longer time ranges and when non-linear resonances
play a decisive role in conjunction with SC. These second
type of codes perform much better due to a much simpler
2D treatment of SC and they do not suffer from PIC noise.
It remains to be fully understood when either approach is
truly required and how one might combine them. To this

---

* Speaking as the representative of the CERN Space Charge working group

[1] sponsored by ICFA
[2] both co-sponsored by EuCARD-2 XBEAM

end the CERN SC working group is planning a dedicated effort to resolve these issues.

The collaboration on PIC codes concerns 3 codes: py-ORBIT [8], SYNERGIA [9] and IMPACT [10]. MADX-SC [11] has been used with a frozen SC implementation. More recently a frozen SC implementation has been added to pyORBIT [12] and is in a testing phase.

All codes are in preparation to cover the needs for the CERN accelerators of which the most relevant are:

- Time varying field

- Double RF system

- Acceleration

In particular pyORBIT, an update of the PTC-ORBIT code with a PYTHON front-end, is now ready for the CERN machines, this naturally implies that PTC is also part of pyORBIT. SYNERGIA is still in a benchmarking phase of the single particle code CHEF compared to MAD-X/PTC. IMPACT is in the process of building up the single particle part. Both pyORBIT and SYNERGIA have done most of the GSI benchmarking suite [13] and the results will be introduced into that benchmarking suite by the end of 2014.

In fact SYNERGIA has done all steps and in particular step 9 which is a long-term check over 100'000 turns of the emittance growth. To this end the standard convergence test of the emittance growth had to be carried out over the full 100'000 turns instead of just a few 1'000 turns, 71 SC kicks were needed with a grid of $64 \times 64 \times 64$. It turns out that 4 million macro-particles were needed for a successful convergence of the emittance growth. The SYNERGIA team has shown, for the first time, that a self-consistent PIC code can carry the tracking over 100'000 turns and find perfect agreement with several frozen SC codes that have also been tested in the GSI benchmarking suite. The upper graph of Fig. 1 shows the emittance growth as predicted by several frozen SC codes and in the lower graph (notice that the scales are identical) one finds basically the same curve except that the fluctuations are very small due the large number of macro particles being used.

It has been agreed that all three PIC codes should publish releases after a full benchmarking of their codes including all features required by CERN machines by the end of the year.

There has been development on the MADX frozen SC code, which has already been benchmarked in the GSI suite. In particular, the re-normalization of the sigma values (the emittance is re-calculated every turn whilst the TWISS parameters are recalculated typically every 1'000 turns) has proven essential in correctly reproducing experimental studies at the CERN PS (see below). Further work on the code is being planned in collaboration with Fermilab.

One obvious question concerning codes is their performance on various platforms. By the nature of simulating a large ensemble of macro particles all codes either operate under MPI or OPENMP to speed up the performance by
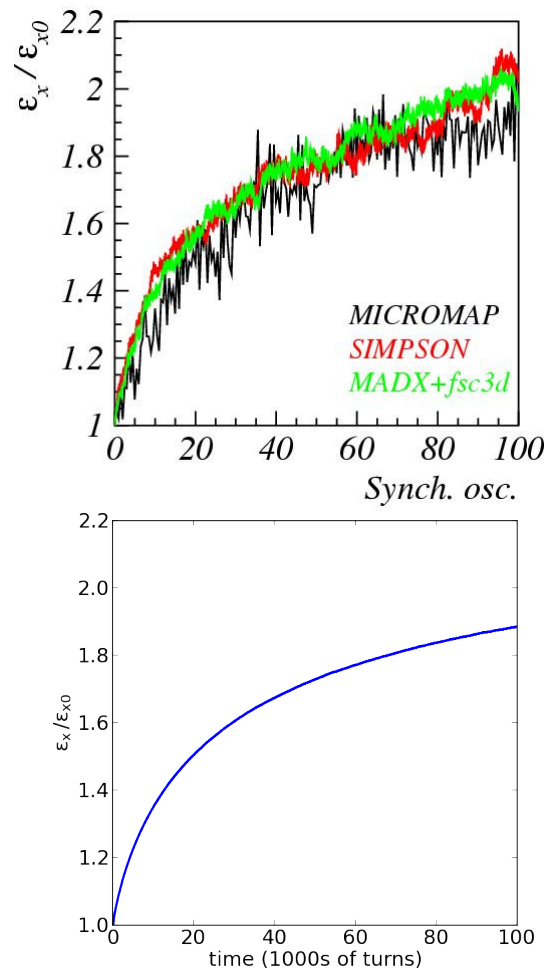


Figure 1: Emittance evolution for SIS18 over 100'000 turns performed by 3 frozen SC codes (top) and (bottom) by the PIC code SYNERGIA [9]. One complete synchrotron oscillation takes 1'000 turns.

parallelization. Nevertheless, optimization of speed must have priority throughout of the development phase of any type of code. In particular, two speed issues are important:

- Is the scalar speed optimized?

- How well does the code scale on platforms with very large number of cores?

The next step is to figure out the optimal computing system: some clusters of multicore machines, super computers with core numbers as large as 100'000 or even GPU systems.

## NOISE ISSUES

In the SC workshop in 2013 the issue of noise in PIC codes has been addressed [14] by following the motion of a few test particles in a large distribution with a PIC code. Apparently, all such test particles exhibit chaotic motion. This chaotic behavior may be weak for large amplitudes but gets stronger for smaller amplitudes. The conjecture is that since the SC force is strongest at zero amplitude, it apparently shakes

single particles erratically and proportional to its strength. The SYNERGIA team [15] has followed single particles over 100'000 turns and recorded the tunes evolution over time (see Fig.2). The analysis as described above seems valid in this long-term simulations: at the smaller amplitude the tune is changing a lot but small tune variations can even be found at larger amplitudes.
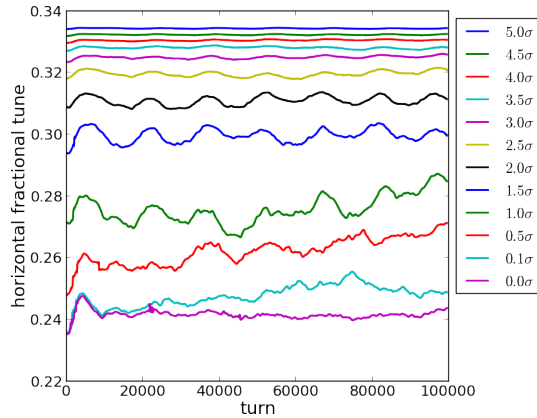


Figure 2: Evolution of the hor. tune for SIS18 calculated in a sliding 1024 turn window over 100'000 turns performed by SYNERGIA [9]. The results are shown for 12 different hor. beam sigmas ranging from 0 to 5 $\sigma$.

These findings have caused the SC community to revisit their theory of noise in PIC codes that has been studied decades ago. Struckmeier [16] reminded us that space charge effects include Intra Beam Scattering. His involved theoretical analysis leads to the conclusion that some kind of temperatures can be defined for each motion plane and that the entropy may increase when those individual temperatures are not balanced. Apparently, this holds also in PIC simulations. A team from GSI [17] has picked up from this anisotropic phenomenon and has found that in FODO structures there is an additional component of grid noise that is there even for zero anisotropy.

At SNS [18] there has been an attempt to use the FMM (Fast Multipole Method) that should in principle overcome the discretization problem that causes the grid noise. However, it turns out that anomalous pair-wise forces slip into the calculation such that effectively the noise is not reduced compared to the standard PIC codes. It was also shown that in PIC simulations for very long constant focusing channels eventually even zero amplitude particles grow in amplitude. This is an independent confirmation of the chaotic behavior of single particles in PIC simulations.

Noise in PIC simulations has also been studied at Fermilab [15]. As discussed in the section on Codes above they find good agreement for global properties like emittance growth with the frozen SC codes although all particles them selves are chaotic. The conclusion is that the individual particles mix in the distribution without actually destroying its global properties.

Lastly, there has been a more systematic numerical approach to study PIC noise [19]. A scaling law has been found

for the growth of PIC noise in 2D simulations. Tracking of noisy beams may conveniently be explained by a random walk, which shows a tendency of larger steps to the outside resulting in emittance blow-up. It has also been very instructive to see that the grid structure becomes graphically visible in the plots of the standard deviation of the electric fields.

## SC EXPERIMENTS

Various studies have been done at the PSB [20] and the PS [21] and the simulation results are starting to be convincing. At the PSB booster it could be demonstrated that good agreement between simulations (PTC-ORBIT) and experiments could be achieved for particle motion close to the $1/2$ integer resonance where large losses do occur. Precondition
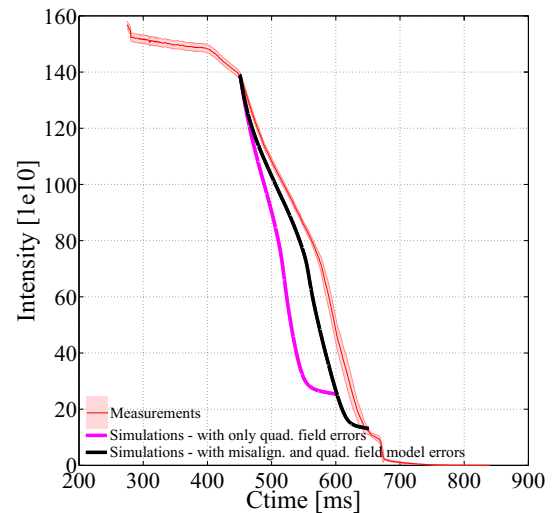


Figure 3: Intensity evolution for PSB in the vicinity of the $1/2$ integer resonance without the usual operational corrections turned on (in which case no beam loss is observed). [20]

for these nice results has been to include in the model both the measured quadrupole and misalignment errors. This is a confirmation of the strategy to complete our model evaluation before we study SC effects. An interesting theoretical side issue is the fact that the tune footprints should not use the phase advance per turn but rather the tune values (phase advance averaged over many turns) for every particle, which implies to average over full synchrotron periods.

In 2012 PS experiments have been performed in the vicinity of the coupled third order resonance $Q_x + 2 \cdot Q_y$ and in presence of SC [21]. MADX-SC simulations with frozen SC and a beam sigma re-normalization every 1'000 turns seem to be in remarkable agreement with the experiments in terms of reproducing different final beam distributions for various working points close to the normal sextupole resonance $Q_x + 2 \cdot Q_y$. Figure 4 shows the experimental results (hor. & ver. variance and particle loss) in the upper graph (errors are determined by repeated measurements) whilst the simulation results are shown in the lower graph, notice that the measurement results are shown as dashed lines to demonstrate excellent agreement except for the fact that the

horizontal integer line is not correctly reproduced in the simulations (red curve at small tunes). Additional studies are currently being carried out to investigate this effect. On
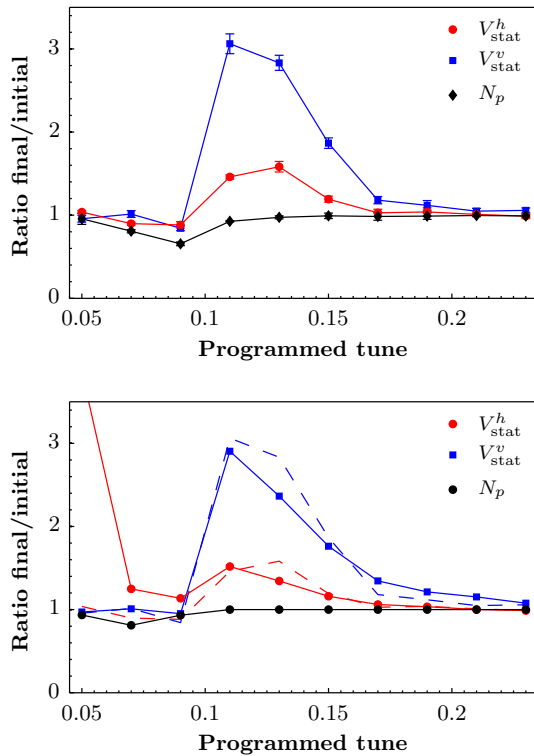




Figure 4: Horizontal & vertical variance and loss as a function of programmed tune for the 2012 PS experiment [21]. The top graph shows the experimental results whilst the lower plot shows the results of the simulations (sold lines) in comparison with the experimental data (dashed lines).

the other hand, the studies at GSI show similar results [22]. There are first indications that the beam distributions, which may be different in the 2 transverse planes, are due to the crossing of 4D fix-line structures caused by the coupled sextupole resonance [23]. Of course, the strong detuning from SC plays an important role.

A measurement campaign at the PS has shown that the resonance $4 \cdot Qy = 25$ is excited and driven by space charge [24]. Besides the integer resonance it is this $4^{th}$ order resonance that is limiting the PS performances for the production of the future high brightness beams. The symmetry of the lattice (h=50) apparently excites the structure resonance $8 \cdot Qy = 50$ which is driven by space charge. Presently a PS measurement study is under way to change the vertical integer tune such as to mitigate this structure resonance [25]. First simulations using PTC-ORBIT, IMPACT and Simpsons [25–27] have confirmed the potential of this idea.

At RHIC the MADX-SC code is being used with completely frozen SC, i.e. without re-normalization of the beam sigmas, for sub-injection energies at RHIC [28]. These simulations also included the BB effect induced by the two counter-rotating and colliding beams. Comparison with the real machine data are soon to be expected.

## CONCLUSION

The international collaboration on all relevant fronts: codes, noise and experiments is in full swing. In particular the benchmarking effort has progressed well and one of the PIC codes (SYNERGIA) has finished the GSI benchmarking suite completely. For the first time it has been demonstrated that a PIC code can be used for long-term tracking over 100'000 turns and simulating 4 million macro-particles on a 144 core machine taking 2 weeks of CPU time, thereby agreeing with the results from frozen SC codes.

Despite the fact that non-negligible PIC noise renders every macro particle in the distribution chaotic, a PIC code can nevertheless reproduce the long-term evolution of global parameters. This makes us hopeful that PIC codes will indeed be useful for storage rings over many turns which up to now has never been demonstrated.

In parallel, the theoretical analysis of PIC noise has been reviewed and extended but no remedies have yet been found to overcome the problem. In fact, even for 4 million macro-particles the noise effect can easily be seen for each individual particle.

On the other hand we are still working on getting all tools ready for the work on CERN machines and presently only PTC-ORBIT or the newest pyORBIT incarnation of the ORBIT code fulfill this requirement. The other PIC codes are still in a state of development. The plan is to have up to 3 PIC code releases ready by the end of 2014: pyORBIT, SYNERGIA and IMPACT.

The frozen SC extension MADX-SC has shown to reproduce well the beam dynamics of the PS close to the sextupole coupling resonance $Q_x + 2 \cdot Q_y$. A prerequisite is a constant re-normalization of the beam sigmas, but it remains to be seen how the unavoidable jitters of the beam sigma from turn to turn is causing some kind of noise phenomenon, albeit of a different nature than PIC noise.

## APPENDIX

Traditionally, the SC community has been using standard techniques using TWISS parameters to set-up reasonable well matched distributions. However, with the NormalForm method becoming mainstream there are now ways to achieve this in a more systematic way that will work for systems that are fully coupled in 6D. At CERN [29] we have now established the following procedure:

- Create independent 2D polar Gaussian distributions via the Box-Muller transform [30].

- Multiplied by the square root of the emittance of the horizontal, vertical and longitudinal phase space respectively.

  Eq.1 relates the emittance $\epsilon_z$ to the beam-size $\sigma_z$ and the $\beta_z$ in the longitudinal plane. The latter can be obtained by the generalized 6D TWISS parameters [31].

$$\sqrt{\epsilon_z} = \sigma_z/\sqrt{\beta_z} \qquad (1)$$

- Transform coordinates to real space via the linear NormalForm of the 6D one-turn map including BB or SC kicks [31].

- Method can be extended to higher order NormalForm and the initial distributions could be different from Gaussian.

# REFERENCES

[1] M. Bodendorfer et al., "Is Pb54+ in LEIR limited by space charge?", `https://indico.cern.ch/event/292362/timetable/#all.detailed/`

[2] E. Benedetto et al., "Space Charge in the PS Booster", `https://indico.cern.ch/event/292362/timetable/#all.detailed/`

[3] S. Gilardoni et al., "PS-LIU Space-charge related issues", `https://indico.cern.ch/event/292362/timetable/#all.detailed/`

[4] H. Bartosik et al., "Space Charge in the SPS", `https://indico.cern.ch/event/292362/timetable/#all.detailed/`

[5] `http://frs.web.cern.ch/frs/Source/space_charge/`

[6] SC-2013 joint GSI-CERN workshop held at CERN, April 2013, `https://indico.cern.ch/conferenceDisplay.py?confId=221441`

[7] SC-2013 joint GSI-CERN workshop held at CERN, April 2013, `https://indico.cern.ch/event/292362`

[8] J. Holmes, "Python ORBIT in a Nutshell", `https://indico.cern.ch/event/292362/timetable/#all.detailed/`

[9] J. Amundson et al., "SYNERGIA: Release and Benchmarking", `https://indico.cern.ch/event/292362/timetable/#all.detailed/`

[10] J. Qiang, "IMPACT: Benchmarking", `https://indico.cern.ch/event/292362/timetable/#all.detailed/`

[11] V. KAPIN, "Frozen SC Model in MADX-SC – Developments", `https://indico.cern.ch/event/292362/timetable/#all.detailed/`; V. Kapin, Fermilab and F. Schmidt, "MADX-SC Flag Description'", CERN-ACC-NOTE-2013-0036.

[12] H. Bartosik, private communication (2014).

[13] G. Franchetti, `http://web-docs.gsi.de/~giuliano/research_activity/trapping_benchmarking/main.html`

[14] F. Schmidt, "Micro-instability in space charge PIC codes", `http://indico.cern.ch/event/221441/timetable/#20130417.detailed`

[15] J. Amundson and E. Stern, "Mixing of Particles Due to Noise in SYNERGIA", `https://indico.cern.ch/event/292362/timetable/#all.detailed/`

[16] J. Struckmeier and I. Hofmann, "THE PROBLEM OF SELF-CONSISTENT PARTICLE PHASE SPACE DISTRIBUTIONS FOR PERIODIC FOCUSING CHANNELS", Part.Accel., 1992, Vol. 39, pp. 219-249; J. Struckmeier, "Space Charge Effects in Real and Simulated Charged Particle Beams - Review of the Understanding of PIC Noise", `https://indico.cern.ch/event/292362/timetable/#all.detailed/`

[17] O. Boine-Frankenheim et al., "Artificial collisions and emittance growth in computer simulations of intense beams", to be published Nucl. Inst. (2014); I. Hofmann, "GRID INDUCED NOISE in 3D PIC SIMULATION", `https://indico.cern.ch/event/292362/timetable/#all.detailed/`

[18] J. Holmes et al., "Space Charge Models for Particle Tracking on Long Time Scales — Present Thoughts", `https://indico.cern.ch/event/292362/timetable/#all.detailed/`

[19] F. Kesting, "Numerical Model and Scaling Law of PIC Noise", `https://indico.cern.ch/event/292362/timetable/#all.detailed/`

[20] V. Forte et al., "CERN PS BOOSTER SPACE CHARGE SIMULATIONS WITH A REALISTIC MODEL FOR ALIGNMENT AND FIELD ERRORS", Proc, IPAC14, Dresden (2014).

[21] G. Franchetti, S. Gilardoni, A. Huschauer, F. Schmidt and R. Wasef, "2012 PS Measurement of the coupled third order resonance in presence of SC", to be published.

[22] G. Franchetti, "Experiment in PS", `https://indico.cern.ch/event/292362/timetable/#all.detailed/`

[23] G. Franchetti and F. Schmidt "Fix-lines and stability domain in the vicinity of the coupled third order resonance", to be published.

[24] R. Wasef et al., "Space Charge effects and limitations in the CERN Proton Synchrotron", in Proc. IPAC2013, Shanghai, China, 2013.

[25] R. Wasef, "PS Experiments and Simulations", `https://indico.cern.ch/event/292362/timetable/#all.detailed/`

[26] S. Machida, "Space charge simulation for 4th order resonance", `https://indico.cern.ch/event/292362/timetable/#all.detailed/`

[27] S. Machida, "The Simpsons Program 6-D Phase Space Tracking with Acceleration", AIP conference proceedings 448, p73.

[28] C. Montag and F. Schmidt, "Recent results for RHIC with frozen SC & BB (MADX-SC)", `https://indico.cern.ch/event/292362/timetable/#all.detailed/`

[29] H. Bartosik, E.G. Souza and F. Schmidt, private communication (2014).

[30] G.E.P. Box and M.E. Muller, "A note on the generation of random normal deviates", Ann. Math. Statist. Volume 29, Number 2 (1958), 610-611.

[31] E Forest et al., "Introduction to the polymorphic tracking code: Fibre bundles, polymorphic Taylor types and 'Exact tracking'", CERN-SL-2002-044 (AP), KEK-Report 2002-3.

# STATUS OF PY-ORBIT: BENCHMARKING AND NOISE CONTROL IN PIC CODES *

J.A. Holmes, S. Cousineau, A. Shishlo, Oak Ridge National Laboratory, Oak Ridge, TN, USA

## Abstract

PY-ORBIT is a broad collection of accelerator beam dynamics simulation models, written primarily in C++, but accessed by the user through Python scripts. PY-ORBIT was conceived as a modernization, standardization, and architectural improvement of ORBIT, a beam dynamics code designed primarily for rings. Although this goal has been substantially achieved, PY-ORBIT has additional capabilities. A major consideration in high intensity beam dynamics codes, such as PY-ORBIT and ORBIT, is the simulation of space charge effects. Computational space charge simulation is, of necessity, accompanied by noise due to discretization errors, which can compromise results over long time scales. Discretization errors occur due to finite step sizes between space charge kicks, due to graininess of the numerical space charge distribution, and due to the effects of spatial grids embedded in certain solvers. Most tracking codes use space charge solvers containing some or all of these effects. We consider the manifestation of discretization effects in different types of space charge solvers with the object of long time scale space charge simulation.

## PY-ORBIT

PY-ORBIT [1] is a collection of computational beam dynamics models for accelerators, designed to work together in a common framework. It was started [2] as a "friendly" version of the ORBIT Code [3], written using publicly available supported software. Users run the code using Python scripts and the higher-level routines are in Python. The computationally intensive portions are written in C++, except for the Polymorphic Tracking Code, PTC [4], which is linked to PY-ORBIT and written in Fortran. The C++ routines and PTC are wrapped to make them available at the Python level. PY-ORBIT accommodates multiprocessing through MPI. The only additional software required by PY-ORBIT is the FFTW fast Fourier transform library [5]. The code is finding an increasing number of users and the source code is publicly available via Google Codes [1]. It is not difficult for users to develop extensions to PY-ORBIT, and it is possible for users to obtain permission to add new routines to the publicly available code. Recently, researchers at CERN and at GSI have added new methods to PY-ORBIT.

At present, PY-ORBIT is capable of performing most calculations that ORBIT does for rings and transfer lines. Many of the most widely used methods in ORBIT have been ported to PY-ORBIT and benchmarked. Single

particle tracking methods include ORBIT's native symplectic tracker, PTC tracking, and a 3D field tracker. It is planned to add the option to use linear and second order tracking by matrices from the MAD codes [6,7]. Space charge models include ORBIT's longitudinal, 2D potential and direct force methods, a full 3D (not parallel) solver, and uniform charge density 3D ellipses. A 2.5D solver has recently been added and tested by Hannes Bartosik of CERN. ORBIT's longitudinal impedance model has also been ported to PY-ORBIT, and we are now in the process of porting the transverse impedance model. Other methods that have been ported from ORBIT include injection, foil and painting, RF cavities, collimation, apertures, and many diagnostics.

Some capabilities have been developed in PY-ORBIT that are not included in the original ORBIT code. Routines have been developed for linac modeling, including RF cavities, magnets, and 3D full Particle-in-Cell (PIC) and elliptical space charge models. A detailed set of atomic physics routines has been developed for laser stripping applications, and special maps have been developed for nonlinear optics studies. One ORBIT code package that has not been ported to PY-ORBIT is the self-consistent electron cloud model.

Detailed documentation of PY-ORBIT is, at best, incomplete. In the downloaded source code there are many examples that demonstrate the use of models in scripts. Some of the methods are documented in Google Code wikis. When in doubt, the user is advised to contact one of the developers for detailed answers. Finally, some of the nice features of PY-ORBIT come from the flexibility of Python. For example, the bunch class is extendable. The basic bunch contains only the 6D coordinates of each macroparticle. It is easy, however, for the user to add various properties, such as a particle index, spin, species, ionization number, excited state, etc. Because of this flexibility, it is easy and convenient to work with PY-ORBIT.

## SPACE CHARGE MODELING OVER LONG TIMES

Particle-tracking simulations for accelerators involve following particle distributions over time. Space charge physics has been successfully incorporated into particle-tracking studies of linacs, transfer lines, accumulator rings, and rapid cycling synchrotrons (RCS). These space charge models have allowed the successful simulation of phenomena that would have been impossible otherwise. Even so, the evaluation of space charge effects is typically

the most computationally intensive part of the simulation. With the emergence of ever-higher beam intensities, it is now necessary to incorporate space charge effects into simulations of storage rings [8]. Calculations for storage rings require tracking beams for far longer times than those in linacs, accumulator rings, or rapid cycling synchrotrons. These long time scales place severe requirements on the speed and accuracy of the physics models and call for innovative methods of solution. At long time scales, there are also other effects besides space charge, such as lattice imperfections and nonlinearities, wake forces, neutral gas ionization and scattering, electron cloud interaction, intrabeam scattering, beam loss, and others, that may be critical. These effects are often relatively unimportant at short or intermediate time scales. To study them in the presence of space charge, it will be necessary to use an accurate depiction of the space charge forces.

Space charge models attempt to account for the inter-particle Coulomb force, and their evaluation requires the solution of Poisson's equation. The first issue in space charge simulation is to choose a model that contains physics sufficient to address the problem. The tools of choice in most space charge simulations are fast Poisson solvers of various dimensionalities that directly use the tracked particle distribution to obtain the space charge force. The speed of fast solvers scales as order O($\sim M$), where $M$ is the number of macroparticles. The most popular of these solvers are the PIC methods in which the particle charges are distributed to a selected set of mesh points. This is followed by the solution of the resulting potential or forces at the mesh points using fast Fourier transforms (FFTs), and then the interpolation of the forces to the particle locations. Many PIC methods are described in Refs. [9,10]. Another order O($\sim M$) method is the fast multipole method (FMM) [11], which expands the individual particle potentials as multipoles at the centers of a collection of square gridded cells containing the particles. These expansions are then shifted and accumulated through a hierarchy of coarser "parent cells" and the resulting totals are converted to Taylor series expansions as they are shifted backwards through the hierarchy of "child cells". The result is a set of local Taylor series expansions in each initial cell for the potential and force due to the particles in distant cells. The method uses pairwise force evaluations for nearby particles to eliminate grid-based discretization effects completely. The FMM solves the N-body force evaluation to machine precision when enough terms are retained in the multipole and Taylor series expansions. Even so, there are discretization effects due to the time step and the numerical particle distribution.

For long time scale calculations, the appropriate choice is usually a 2D or 2.5D transverse solver. The latter choice is necessary when transverse properties vary longitudinally along the beam or when transverse impedances are of interest. These solvers can be used in conjunction with a separate 1D longitudinal model, since longitudinal evolution typically occurs much more slowly. However, some 2.5D solvers also incorporate the longitudinal force. The above models are valid only for long bunches in which

the bunch length greatly exceeds the beam pipe radius, as is normally the case in proton storage rings. For short bunches where the longitudinal and transverse dimensions are comparable, such as those found in linacs, it is necessary to use full 3D space charge models. Computational requirements rise steeply with the dimensionality of the model, so it is important to adopt the simplest model that contains the necessary physics.

Important issues that determine the applicability of space charge models are their ability to represent the beam distribution, nonphysical effects associated with the algorithm, and their computational speed. Before discussing the pros and cons of specific approaches, it is important to consider the nonphysical effects. These effects are the result of discretization errors due to finite time step size, the coarseness of the computational particle distribution, and the use of finite spatial grids. Time discretization is a feature of any space charge simulation, regardless of beam representation. While space charge forces act continuously in classical dynamics, simulations apply them as impulses, separated by single particle transport. At the very least, it is necessary to include many space charge evaluations per betatron or synchrotron oscillation. Further discretization errors occur when the tracked particles are used directly to provide the charge/current distribution. Real accelerator bunches typically have orders of magnitude more particles than bunches used in simulations. This results in an increased graininess of the force distribution and an increased potential for large binary collisions in simulations. Both of these effects introduce noise, or diffusion, into the particle evolution. The problem of the enhanced binary collisions is often handled by introducing artificial smoothing parameters into the inter-particle force Green's functions. A final source of discretization in many PIC methods relates to the use of spatial meshes. However, because of the particle binning and force evaluation algorithms used in PIC models, gridding actually provides a smoothing of the local space charge forces. Before realizing this to be the case, we implemented an FMM solver in ORBIT in order to eliminate grid-based numerical effects. However, we discovered that, unless we introduced a smoothing parameter to the pairwise Coulomb force function, numerical diffusion was stronger than in the grid-based FFT methods. However, through the adjustment of the smoothing parameter, we were able to achieve answers and emittance growth rates comparable to those of FFT methods. Figure 1 compares RMS emittance evolution from FFT and FMM simulations with $10^5$ macroparticles for a KV distributions and a uniform focusing lattice. The period for one bare tune betatron oscillation is 50 meters, and the space charge tune shift is one third of the bare tune. The results are shown for 100 bare tune betatron oscillations, or 5000 meters. The FMM calculations are carried out alternatively with no smoothing and with an interparticle force smoothing parameter of 0.03 mm. Clearly, numerical scattering leads to emmitance growth in the unsmoothed FMM calculation, and it is necessary to include the smoothing parameter to eliminate the

scattering. The grid and binning procedures provide this smoothing in the FFT approach. The FMM approach was abandoned because it provided no physics advantage over FFT methods and also because it ran a factor of ten to fifty times more slowly on sample problems, depending on parameter settings.
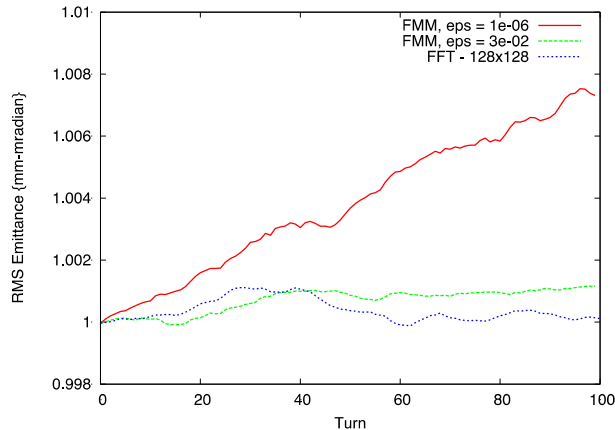


Figure 1: RMS emittance evolution for FFT and smoothed and unsmoothed FMM calculations.

In statistical and plasma physics collisions have been long characterized in terms of diffusion operators. In Ref. [12], a Fokker-Planck analysis was used to characterize entropy growth due to collisions and other stochastic processes in particle beams. More recently, this work was adapted to develop and successfully test an empirical scaling law for the collision frequency and subsequent emittance growth due to space charge in computer simulations [13]. The work in Ref. [13] was carried out for 2D space charge in FODO channels, and the results are therefore applicable to the case of PIC simulation in storage rings. From the standpoint of space charge modeling over long time scales, the essential result is that the numerical collision frequency scales as

$$\nu \propto \frac{N^2}{M}\left(1 - \frac{\Delta}{\lambda}\right)$$

Here $N$ is the beam intensity or number of physical particles, $M$ is the number of macroparticles, $\Delta$ is the macroparticle size (smoothing length or grid spacing in PIC methods), and $\lambda$ is a cutoff parameter. The collision frequency $\nu$ is directly related to the entropy and emittance growth of the beam. Thus, the rate of emittance growth increases as the square of the intensity and inversely with the number of macroparticles. The effect of finite grid or smoothing parameter size reduces the growth. Figure 2a shows the effect of grid smoothing on emittance growth for the same case as in Fig. 1, except that now the calculation is carried out for 1000 bare tune oscillations. Figure 2b shows the reduction in emittance growth due to increasing number of macroparticles.
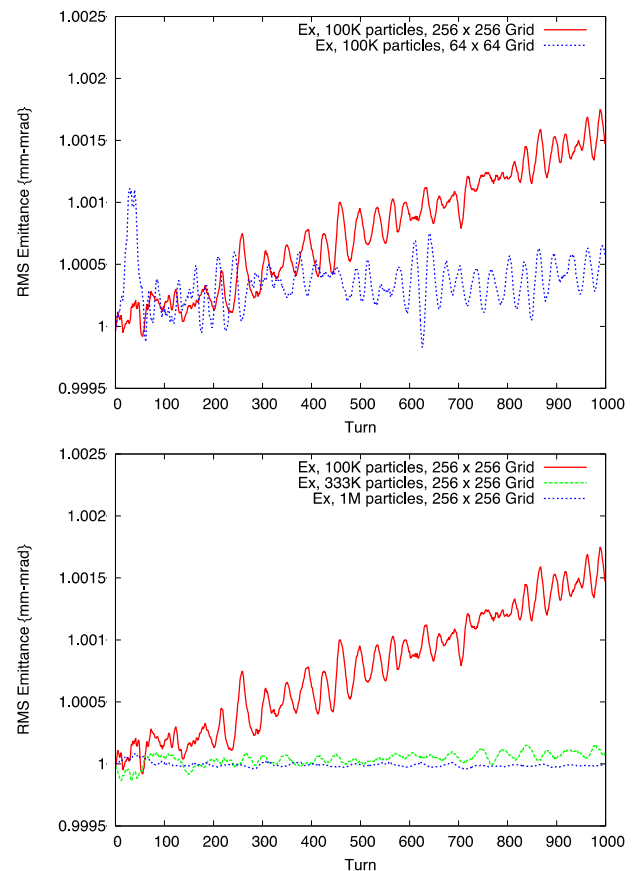


Figure 2: RMS emittance evolution for FFT PIC solver with a) two different grid sizes and b) different numbers of macroparticles.

Given the results of Ref [13], we are now prepared to consider the choice of space charge model for long time scale simulations. Direct use of the distribution of tracked macroparticles to obtain the space charge forces has been the method of choice in previous simulations of linacs, transfer lines, accumulator rings, and RCS. These methods are preferred in that they provide a faithful representation of the beam distribution, which is often complex in real accelerators. In these previous applications it was possible to use enough macroparticles $M$ to suppress the stochastic numerical emittance growth and carry out the calculation with a moderate amount of computer resources. Such simulations could typically be done on small clusters or even individual workstations. However, time scales for storage rings are orders of magnitude longer than those for linacs and small rings, and the above scaling law suggests that the number of macroparticles necessary to limit numerical emittance growth could become prohibitively large. Thus, the direct extension of PIC solution techniques to storage ring applications is likely to be extremely expensive from a computational standpoint, and may demand the use of massively powerful parallel supercomputers.

Thus we arrive at the following question: Is there any alternative to massively parallel computing for studying the effects of space charge in storage rings? The answer

may be some simplified smooth or analytic representation of the space charge force. One drawback of such an approach is that it implies a limited ability to represent the actual beam distribution. One extreme example, called the envelope or particle core model, represents the space charge distribution as a uniform ellipsoidal core that propagates according to the envelope equation. The tracked particles feel the space charge force due to the propagating core. This force is linear inside the core. Envelope models are computationally fast and easy to apply. They have been used to support theoretical studies of halo generation by mismatched beams and also the approach to the half integer resonance. One limitation of such models is that a constant emittance is specified in the envelope and thus constrains the evolution of the core. Accordingly, envelope models are simple, but far from realistic. One can envision intermediate classes of methods for handling space charge through the use of analytic or smoothed distributions, where the parameters are fitted to those of a tracked macroparticle bunch beam. Such hybrid methods could, in principle, enjoy the speed and simplicity of envelope models, have parameters that evolve with the tracked beam distribution, and eliminate the noise associated with the graininess of the particle distribution.

## BENCHMARKING OF SPACE CHARGE MODELS

As with all numerical simulation tools, it is essential to benchmark space charge routines. During its fifteen years of existence, ORBIT has been extensively benchmarked, including all its space charge models. Benchmark tests have included comparisons with analytic results, with experimental observations, and with other codes. PY-ORBIT has been thoroughly benchmarked with ORBIT as models have been completed and tested. From this standpoint, we place the same confidence in the models in PY-ORBIT that we have in ORBIT.

There are also formal benchmark tests for space charge routines. An excellent suite of benchmarks on several time scales involves space charge induced resonance trapping, and can be found in Ref. [14]. ORBIT has successfully completed eight of the nine benchmarks on this site, and the final case is under study. Some of the longer time scale tests, as posed on the site, are accompanied by significant numerically-induced emittance growth. Because of this, results in some cases are very sensitive to the parameters used in the calculation. This sensitivity is illustrated in Fig. 3, which shows the emittance evolution with resonant trapping and detrapping over one synchrotron oscillation for two initially close test particles. The particle plotted in red is trapped on both halves of the oscillation, while the blue particle escapes trapping on the second half oscillation.
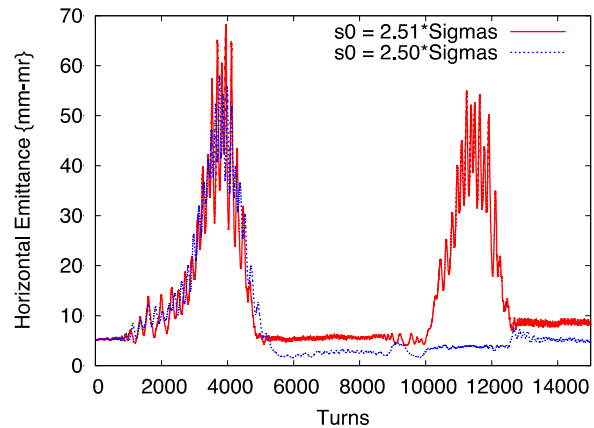


Figure 3: Emittance evolution for two nearly identical particles in resonance trapping benchmark.

## CONCLUSION

PY-ORBIT has matured to the point that it can be applied to almost all the problems accessible to ORBIT. The source code is publicly available and easy to use via Python scripts. Users are welcome to develop their own models in PY-ORBIT, either in Python for high-level models or C++ for computationally intensive routines. PY-ORBIT code is carefully benchmarked with ORBIT before being made available to the public.

In considering the choice of space charge model for a given application, the relevant issues involve representation of the beam, numerical fidelity with physics, and computational speed. For short to intermediate time scales occurring in linacs, transfer lines, accumulators, and RCS, FFT-based PIC methods of appropriate dimensionality have been the choice. For storage rings, which typically have long bunch length, 2D and 2.5D models are appropriate. For applying such models on long time scales, it is necessary to account for the effects of numerical collisionality on entropy and emittance growth. These effects were studied in Ref. [13] and a simple empirical scaling law was obtained. This law provides guidance on the necessary number of macroparticles, grid spacing, and therefore computer resources to address a given problem. If, for some applications, the necessary resources are prohibitive, it is worthwhile to consider whether a simpler, fast, analytically based approach might suffice.

Benchmarking is always an essential step in validating new code. PY-ORBIT has been carefully benchmarked with ORBIT during its development, and ORBIT has been extensively benchmarked with analytic, experimental, and other code results. Finally, sensitivity of results must be considered in any benchmarking activity, especially when long time scales are involved. If small differences in input can lead to large differences in output, and if different codes agree on this, then care must be taken on interpreting the meaning of the benchmark results.

## ACKNOWLEDGMENT

## REFERENCES

[1] Pubicly available at Google Codes by typing: svn checkout https://py-orbit.googlecode.com/svn/trunk py-orbit --username youraccount@gmail.com

[2] A. Shishlo, T. Gorlov, J. Holmes, in Proceedings of the International Computatonal Particle Accelerator Conference (ICAP 09), San Francisco, 2009.

[3] J.A. Holmes, S. Cousineau, V.V. Danilov, S. Henderson, A. Shishlo, Y. Sato, W. Chou, L. Michelotti, F. Ostiguy, in The ICFA Beam Dynamics Newsletter, Vol. 30, 2003.

[4] E. Forest, E. McIntosh, F. Schmidt, ``Introduction to the Polymorphic Tracking Code: Fibre Bundles, Polymorphic Taylor Types and "Exact Tracking"'', CERN-SL-2002-044 (AP), KEK Report 2002-3.

[5] FFTW Home Page. http://www.fftw.org

[6] H. Grote, F. C. Iselin, CERN/SL/90-13 (AP) (Rev. 5) (1996).

[7] MAD-X Home Page, http://frs.home.cern.ch/frs/Xdoc/mad-X.html

[8] Space Charge 2014, CERN, May 20-21, 2014, https://indico.cern.ch/event/292362

[9] R. W. Hockney and J. W. Eastwood, "Computer Simulation Using Particles", Institute of Physics Publishing, Bristol, 1988.

[10] J. Demmel, NSF-CBMS Short Course on Parallel Numerical Linear Algebra, especially Lectures 24-27, http://www.cs.berkeley.edu/~demmel/cs267-1995/

[11] L. Greengard and V. Rokhlin, "A Fast Algorithm for Particle Simulations", Journal of Computational Physics 73, (1987), 325.

[12] Jurgen Struckmeier, Phys. Rev. E 54, 830, (1996).

[13] O. Boine-Frankenheim, I. Hofmann, J. Struckmeier, S. Appel, Nucl. Instr. and Meth. in Phys.Research A., in press.

[14] G. Franchetti, Code Benchmarking on Space Charge Induced Trapping, http://web-docs.gsi.de/~giuliano/

# ARTIFICIAL NOISE IN PIC CODES AND CONSEQUENCES ON LONG TERM TRACKING

Kazuhito Ohmi, KEK

*Abstract*

Emittance growth and beam loss due to nonlinear space charge force has been studies using Particle In Cell simulation. Artificial noise due to macro-particle statistics sometimes presents unphysical emittance growth. Artificial noise in Particle In Cell method disturbs the accurate prediction of the emittance growth. Using a fixed periodic space charge potential is one way to study emittance growth in a first step. Frozen potential and induced resonance are discussed in this paper. While emittance growth in a presence of real noise is serious issue in accelerators. Emittance growth under tune fluctuation is discussed with relation to studies in beam-beam effects.

# INTRODUCTION

In Particle In Cell codes, space charge force is given by solving Poisson equation for macro-particles distribution mapped on grid space. Statistics of macro-particles, which cause a density modulation in the grid space, result in turn by turn fluctuation of the space charge force. Emittance conservation/growth in a periodic system is subject of our concern for the space charge effects. Artificial emittance growth caused by the fluctuation disturbs an accurate prediction, especially in long term simulation. Emittance growth in a fixed periodic potential can be discussed. In J-PARC, limitation of particle loss is very severe (1kW for the beam energy 1MW). Space charge potential is nearly determined by the core distribution. We can study emittance growth in the potential given by distribution which is initial or is fixed(frozen) at a time. Resonance and chaotic behavior in the fixed potential are subjects to be studied. It is important to study emittance growth dynamically changing potential for the next step.

Figure 1 shows evolution of $x$ and $\sigma_x$ in PIC simulation (SCTR) [1]. The space charge force is calculated turn-by-turn, where the number of macro-particle is 200,000. Fluctuations in $x$ and $\sigma_x$ are seen. The noises level is $\langle x \rangle \approx \pm 0.05$ mm ($0.5\%\sigma_{x,0}$) and $\sigma_x \approx 8.5 \pm 0.02$ mm ($0.2\%\sigma_{x,0}$). Higher order moments of the beam distribution must have similar fluctuation. Each particle experiences nonlinear force with the fluctuations in the simulation. Unphysical phenomena is seen in the simulation.
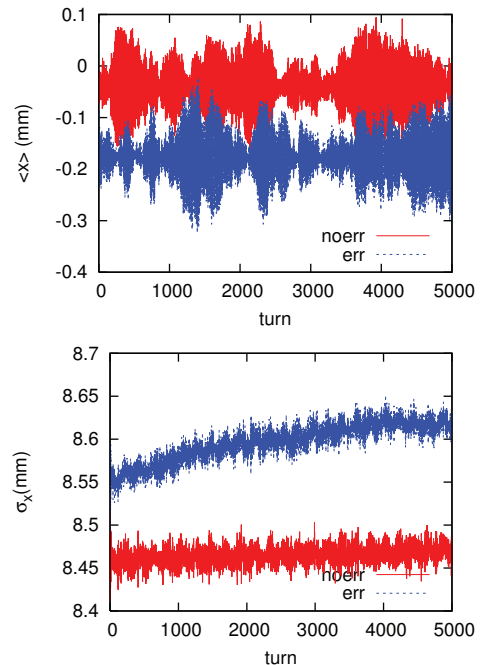


Figure 1: Evolution of x and $\sigma_x$ in Particle-In-Cell simulation (SCTR). Red and blue lines are given for lattice without and with magnet alignment errors.

# EXPERIENCES OF BEAM-BEAM INTERACTIONS IN COLLIDERS AND APPLICATION TO SPACE CHARGE EFFECTS

*Experiences of Beam-beam Interactions in Colliders*

Statistical noise in simulations is artifact, but noise in accelerator is sometimes real issue. Noise of collision offset from bunch-by-bunch feedback system degraded luminosity performance in KEKB [2]. Crab cavity is planned to be used in High Luminosity LHC. Noise in crab cavity phase and in bunch-by-bunch feedback system, which causes collision offset, has been studied in LHC [1, 3]. Theory for the noise effects was developed by G. Stupakov [4] and T. Sen et al.[5].

Potential (effective Hamiltonian) of the beam-beam interaction is expressed by

$$U(x) = \frac{N_p r_p}{\gamma_p} \int_0^\infty \frac{1 - e^{-x^2/(2\sigma_r^2 + q)}}{2\sigma_r^2 + q} dq \delta_P(s) \quad (1)$$

where $r_p$ and $\gamma_p$ are the classical radius of the proton and the relativistic factor of the beam, respectively. The potential acts once per revolution at the collision point due to the periodic delta function $\delta_P(s)$ for the circumference. The potential is expanded by Fourier series as follows,

$$U(J, \psi) = \frac{N_p r_P}{\gamma_p} \sum_{k=0}^{\infty} U_k(a) \cos 2k\psi \delta_P(s) \qquad (2)$$

The potential with an offset $\Delta x$ is given by

$$U(x + \Delta x) = U(x) + U'(x)\Delta x. \qquad (3)$$

$\Delta x$ is a random variable fluctuated turn-by-turn. Change of $J$ per collision is given for the potential by

$$\Delta J = -\frac{\partial U(x + \Delta x)}{\partial \psi} = -\frac{\partial U'}{\partial \psi}\Delta x. \qquad (4)$$

$\partial U(x)/\partial \psi$, which gives modulation of betatron motion, does not contribute emittance growth. Averaging the offset noise, diffusion of $J$ per collision is given by

$$\langle \Delta J^2 \rangle = \frac{\partial U'}{\partial \psi} \frac{\partial U'}{\partial \psi} \langle \Delta x^2 \rangle \qquad (5)$$

The Fourier expansion of the potential with respect to the offset now becomes

$$U'(J, \psi) = \frac{N_p r_p}{2\gamma \sigma_r} \sum_{k=0}^{\infty} G_k(a) \cos(2k+1)\psi, \qquad (6)$$

where

$$G_k(a) = \sqrt{a} \left[ U'_{k+1} + U'_k \right] + \frac{1}{\sqrt{a}} \left[ (k+1)U_{k+1} - kU_k \right], \qquad (7)$$

and $U'_k$ is the derivative evaluated at $a = J/(2\varepsilon)$. Diffusion of betatron amplitude is expressed by

$$\langle \Delta J^2 \rangle \approx \frac{N_p^2 r_p^2 \Delta x^2}{8\gamma^2 \sigma_r^2}$$

$$\sum_{n=-\infty}^{\infty} \sum_{k=0}^{\infty} (2k+1)^2 G_k^2 \cos[(2k+1)n\mu] e^{-|n|/\tau}$$

$$\approx \frac{N_p^2 r_p^2 \Delta x^2}{8\gamma^2 \sigma_r^2} \sum_{k=0}^{\infty} \frac{(2k+1)^2 G_k(a)^2 \sinh 1/\tau}{\cosh 1/\tau - \cos(2k+1)\mu}. \qquad (8)$$

The diffusion of betatron amplitude approximately linearly depends on its amplitude. The slope is expressed by

$$\frac{\langle \Delta J^2 \rangle}{a} = \frac{N_p^2 r_p^2}{8\gamma^2} \frac{\Delta x^2}{\sigma_r^2} \times 4.4. \qquad (9)$$

Convolution of the Eq.(9) by distribution function gives emittance growth rate and luminosity degradation as

$$\frac{\Delta L}{L} = \frac{\Delta \varepsilon}{\varepsilon} = \left( \xi \frac{\Delta x}{\sigma_r} \right)^2 \times 21.7. \qquad (10)$$

Weak-strong simulation, using frozen Gaussian colliding beam, has been done to study the effects of noise. [1] Figure 2 shows the luminosity degradation rate as function of offset noise amplitude. The rate given by formula Eq.(10) is plotted by three lines for the beam-beam tune shift values. The degradation rates agree well.
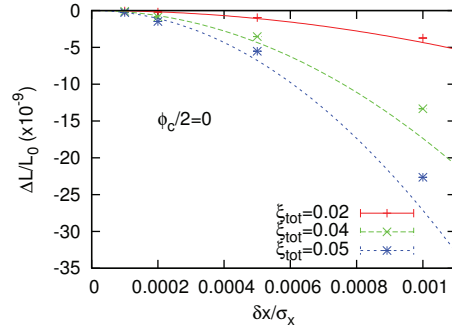


Figure 2: Diffusion rate without a crossing angle given by weak-strong simulation compared with predictions from Eq. (10).

Strong-strong simulation, in which Poisson solver is executed turn-by-turn using the particle in cell algorithm, has also been performed. Figure 3 shows the luminosity degradation rate. The agreement with formula Eq.(10) is again very well.

*Application to Space Charge Force*

The theory is applicable for space charge force. We sketch the theory. Beam distribution is assumed to be Gaussian in x-y space.

$$N\rho(x, y, z) = \frac{\lambda(z)}{2\pi\sigma_x\sigma_y} \exp\left( -\frac{x^2}{2\sigma_x^2} - \frac{y^2}{2\sigma_y^2} \right) \qquad (11)$$

where dispersion is taken into account in $\sigma_x$, $\sigma_x^2 = \beta_x \varepsilon_x + \eta_x^2(\Delta/p)^2$. Space charge force distributes along whole ring. The effective potential/Hamiltonian for one turn map is evaluated by integration of the space charge potential. Effective one turn potential ($U$) is given by

$$\prod_{i=0} \exp(-H_{i+1,i}) \exp(-U_i) = \exp(-H) \times$$

$$\prod \exp(H_{i+1,0}) \exp(-U_i) \exp(-H_{i+1,0})$$

$$= \exp(-H) \exp(-U) \qquad (12)$$

Leading order expression of $U$ is given by integration of $U_i$ with taking into account of the betatron phase,

$$U = \int ds' U(s') = \frac{\lambda_p r_p}{\beta^2 \gamma^3} \oint ds' \qquad (13)$$

$$\int_0^{\infty} \frac{1 - \exp\left( -\frac{\beta_x(s')X(s,x')}{2\sigma_x^2 + u} - \frac{\beta_y(s')Y(s,s')}{2\sigma_y^2 + u} \right)}{\sqrt{2\sigma_x^2 + u}\sqrt{2\sigma_x^2 + u}} du$$

---

[1]Simulation using frozen potential is called weak-strong simulation, and turn-by-turn simulation is called strong-strong simulation in the beam-beam society.

Figure 4: Resonance strength given by Eq.(23).
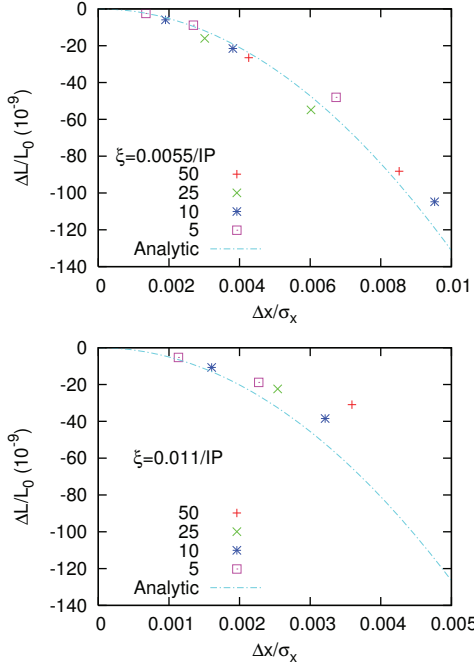
Figure 3: Diffusion rate given by strong-strong simulation compared with predictions from Eq. (10). Top and bottom are for the beam-beam tune shift 0.0055/IP and 0.011/IP, respectively.

where

$$
\begin{aligned}
X(s, s') &= \sqrt{2J_x} \cos(\varphi_x(s') + \phi_x(s)) \\
Y(s, s') &= \sqrt{2J_y} \cos(\varphi_y(s') + \phi_y(s))
\end{aligned} \tag{14}
$$

Cross terms between space charge nonlinearities and between them of space charge and nonlinear magnetic components are neglected.

The Fourier component, which correspond to resonance strength, is given by

$$
U_m(J_x, J_y) = \frac{\lambda_p r_p}{\beta^2 \gamma^3} \oint ds \int_0^\infty \frac{du}{\sqrt{2\sigma_x^2 + u}\sqrt{2\sigma_x^2 + u}}
$$
$$
\left[ \delta_{m_x 0} \delta_{m_y 0} - \exp(w_x - w_y)(-1)^{(m_x + x_y)/2} \right.
$$
$$
\left. I_{m_x/2}(w_x) I_{m_y/2}(w_y) e^{-im_x \varphi_x - im_y \varphi_y} \right]. \tag{15}
$$

where $H$ and $U$ are one turn effective Hamiltonian of lattice transformation and space charge force, respectively.

The diffusion rate due to offset noise for the space charge potential Eqs.(13) and (23) is estimated by Eq.(8). Figure 4 shows the Fourier component/resonance strength for horizontal betatron phase as function of betatron amplitude. It is seen that lower component $U_{40}$ is dominant. Diffusion rate due to the noise is evaluated by Eqs.(6) and (7) using $U_k$ and $U_k'$ evaluated by Fig.4.

## Tune Fluctuation due to Ripple in J-PARC MR

We discuss effects of realistic noise in space charge dominant machine, J-PARC Main Ring. Tune modulation

due to ripple of power supply has been observed around $\delta\nu \approx \pm 0.01$ with 50Hz in J-PARC MR,. Diffusion of $J$ for tune modulation is evaluated by similar formula as the offset noise as follows,

$$
\langle \Delta J^2 \rangle \equiv \frac{\langle (J(N) - J(0))^2 \rangle}{N} \tag{16}
$$

$$
= \frac{1}{N} \sum_{i=0}^{N} \sum_{j=0}^{N} \frac{\partial U_i}{\partial \psi} \frac{\partial U_j}{\partial \psi} \langle \Delta \psi_i \Delta \psi_j \rangle. \tag{17}
$$

One summation is replaced by $N$, then another is expressed by summation of correlation of the noise.

$$
\langle \Delta J^2 \rangle = \sum_{n=-\infty}^{\infty} \frac{\partial U_\ell}{\partial \psi} \frac{\partial U_{\ell+n}}{\partial \psi} \langle \Delta \psi_\ell \Delta \psi_{\ell+n} \rangle. \tag{18}
$$

The correlation is expressed by

$$
\langle \Delta \psi_\ell \Delta \psi_{\ell+n} \rangle = 4\pi^2 \Delta \nu^2 e^{-|n|/\tau_c} \tag{19}
$$

where the correlation time is 50Hz, $\tau_c = 4,000$ turns (C=1567m). The diffusion rate of the betatron amplitude is expressed by,

$$
\langle \Delta J^2 \rangle = 8\pi^2 \Delta \nu^2 \sum_{k=0}^{\infty} k^2 U_k^2 \frac{\sinh 1/\tau_c}{\cosh 1/\tau_c - \cos 4\pi k\nu} \tag{20}
$$

The diffusion rate is evaluated by $U_m \sim 10^{-7}$ m at $J \sim 4\varepsilon$ in Fig. 4.

$$
\sqrt{\langle \Delta J^2 \rangle} \sim 5.6 \times 10^{-10} \text{m at } J \sim 4\varepsilon = 40 \times 10^{-6} \text{m} \tag{21}
$$

The beam loss is evaluated by convolution of the beam distribution and diffusion rate as function of $J$.

The magnet ripple should cause fluctuations not only tune but also beta function and dispersion; that is beam size fluctuate turn-by-turn. In this approach, treatment of resonance is not sufficient. Synchrotron motion may be also important. These effects are discussed in the future.

## FROZEN MODEL IN SCTR CODE

SCTR code has developed to study space charge effects in J-PARC. The code is based on the ordinary Poisson

solver using particle in cell algorithm. Basically potential for space charge force is calculated every 1-2 meter ($< \beta_{xy}$) interval. The potential can be frozen and recalculated any time. The potential, which is represented by spline functions, is stored every points with 1-2 m interval.

Figure 5 shows dipole motion and beam size evolution in frozen mode (green) compared with those of non-frozen mode (blue). Dipole motion seen in non frozen mode is larger than that in frozen mode. It is difficult to say whether the motion in nonfrozen motion artifact, it enhances emittance growth in the simulation. Beam size in non-frozen model increase faster, but the difference is not remarkable. No quadrupole oscillation in non-frozen model is seen.
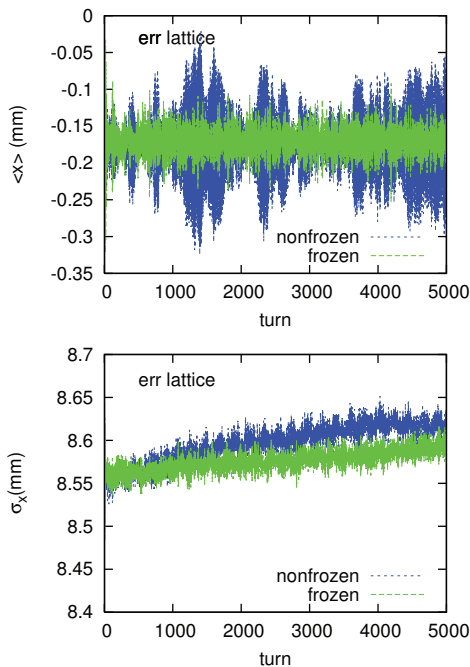


Figure 5: Dipole motion and beam size evolution in frozen mode. Green and blue lines are given by frozen and non-frozen modes, respectively.

Remarkable difference is seen in hallo distribution and beam loss. Comparison of frozen/non-frozen model was performed and presented at PAC07 [1], for example. Figure 6 shows the difference of frozen/non-frozen simulation. Red and magenta lines depict beam-loss for frozen model with $128 \times 128$ grid, 160k macro-particles and $64 \times 64$ grid, 40k macro-particles, respectively. The beam loss is independent of grid size/number and macro-particle number. Green and blue lines depict beam-loss for non-frozen model with $128 \times 128$ and $64 \times 64$ grid for 160k macro-particles, respectively. Cyan line depicts beam loss $64 \times 64$ grid for 40k macro-particles. Beam statistics strongly affect the beam loss in non-frozen model. This beam loss is artifact and should be more remarkable for high tune shift as is also seen in the beam-beam studies.

The frozen model is merit for computation performance using many processors. For PIC simulation, grid informa-
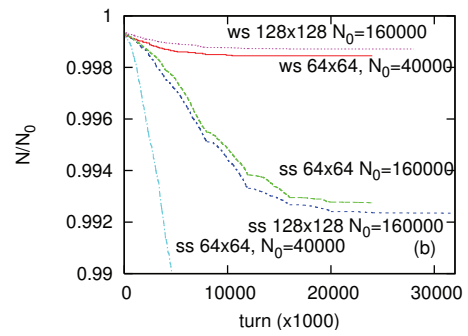
Figure 6: Evolution of beam loss in frozen and non-frozen model.

tion must communicate between processors. The communication is necessary only when potential is recalculated in frozen model. Thus parallel computation using $> 1000$ processors is performed without performance loss. Figure 7 shows beam distribution during fully acceleration of J-PARC RCS 0.4GeV to 3GeV (top) and MR 3GeV to 30 GeV (bottom) [6].
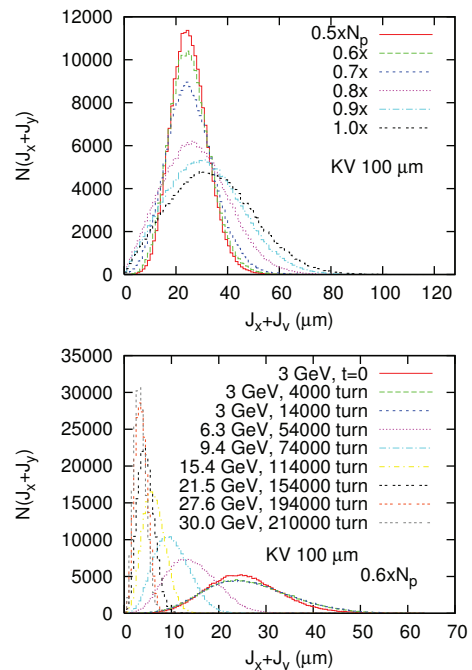


Figure 7: Evolution of the beam distribution during acceleration of J-PARC RCS(top) and MR(bottom).

## Simulation for Choice of Operating Point in J-PARC MR

The frozen simulation is used for choice of operating point in J-PARC MR. MR has been operated at $(\nu_x, \nu_y) = (22.40, 20.75)$. Figure 8 shows beam loss map in the tune area, $22.0 < \nu_x < 22.5$ and $20.5 < \nu_y < 21.0$. Green area corresponds to the loss less than $\Delta N/N_0 < 10^{-4}$ in 5,000

turns. Wide green space is seen for the case without lattice errors in left picture. When errors are taken into account, sum x-y linear coupling resonance $\nu_x + \nu_y = 43$ clearly degrades beam loss. Dominant error is rotation of quadrupole magnets. Sum resonance component of x-y coupling is corrected, then the beam loss is recovered partially as shown in right picture.
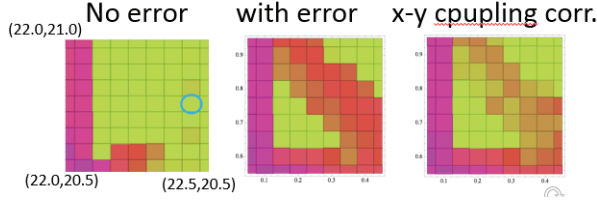


Figure 8: Beam loss map near present operating point. Loss of green mark is $\Delta N/N_0 < 10^{-4}$, in 5000 turns.

Beam loss map is obtained in wider area $20.0 < \nu_x < 23.0$ and $20.0 < \nu_y < 22.0$ as shown in Figure 9. Several good operating point are seen around $(\nu_x, \nu_y) = (21.38, 21.40)$ and $(20.9, 20.88)$. $(22.38, 22.40)$ is also good though it is out of the area. It is possible to study at injection energy in the area, but is hard for magnet strength at the top energy. Figure 10 shows the beam loss evolution at three operating points. Lattice error is taken into account in this simulation. At present operating point, coupling resonance is severe. but is somewhat recovered by correction using skew quadrupole magnets. For $(21.38, 21.40)$ and $(22.38, 22.40)$, degradation due to lattice error is not severe. The beam loss is far less than present point. Another motivation of choosing the operating point $\nu_x \approx \nu_y$ is better integrability due to angular momentum conservation in x-y motion [7, 8]. Beam test is being done for $(21.38, 21.40)$ and $(22.38, 22.40)$ in Nov 2014 [9].
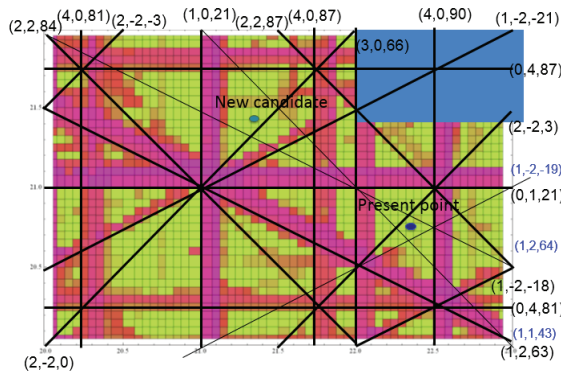


Figure 9: Beam loss map wide tune area, $20 < \nu_x < 23$, $20 < \nu_y < 22$. Lattice error is not taken into account; wiout and with coupling correction. Loss of green mark is $N/N_0 < 10^{-4}$ in 5,000 turns.
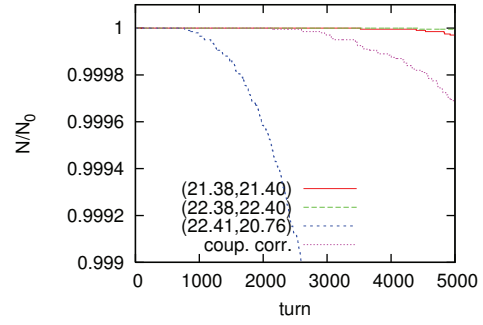


Figure 10: Beam loss at operating points (21.38,21.40), (22.38,22.40) and (22.40,20.75). Lattice error is taken into account.

## EVALUATION OF RESONANCE WIDTH IN THE FROZEN POTENTIAL

In the frozen model, emittance growth is caused by chaotic diffusion near resonances. Resonances induced by the potential in the frozen model can be evaluated analytically, for example in Gaussian distribution.

Phase space structure near resonances are characterized by the resonance width. It is determined by their strength and tune slope for amplitude as follows,

$$\Delta J_x = 2\sqrt{\frac{U_{m_x,0}}{\Lambda}} \qquad \Lambda = \frac{\partial^2 U_{00}}{\partial J_x^2}. \qquad (22)$$

The resonance width is estimated for Gaussian distribution by analytic method, The tune slope $\partial^2 U_{00}/\partial J_x^2$ is induced by space charge potential. That of space charge is dominant for that of nonlinear magnets as shown later. The tune slope is evaluated by $U_{00}(J_x, J_y)$ in Eq.(23).

$$U_{00}(J_x, J_y) = \frac{\lambda_p r_p}{\beta^2 \gamma^3} \oint ds \int_0^\infty \frac{d\eta}{\sqrt{2+\eta}\sqrt{2r_{yx}+\eta}}$$
$$(1 - e^{-w_x - w_y} I_0(w_x) I_0(w_y)). \qquad (23)$$

where $r_{yx} = \sigma_y^2/\sigma_x^2$ and

$$w_x = \frac{\beta_x J_x/\sigma_x^2}{2+\eta}. \qquad w_y = \frac{\beta_y J_y/\sigma_y^2}{2+\eta/r_{yx}}. \qquad (24)$$

$$\frac{\partial}{\partial J_x} = \frac{\beta_x/\sigma_x^2}{2+\eta}\frac{\partial}{\partial w_x}. \qquad \frac{\partial}{\partial J_y} = \frac{\beta_y/\sigma_x^2}{2r_{yx}+\eta}\frac{\partial}{\partial w_y}. \qquad (25)$$

The tune shift is given by derivative of $U_{00}$ for $J_{xy}$ as follows,

$$2\pi\Delta\nu_x = -\frac{\partial U_{00}}{\partial J_x}$$
$$= -\frac{\lambda_p r_p}{\beta^2 \gamma^3} \oint ds \frac{\beta_x}{\sigma_x^2} \int_0^\infty \frac{e^{-w_x - w_y} d\eta}{(2+\eta)^{3/2}(2r_{yx}+\eta)^{1/2}}$$
$$[(I_0(w_x) - I_1(w_x))I_0(w_y)], \qquad (26)$$

$$2\pi\Delta\nu_y = -\frac{\partial U_{00}}{\partial J_y}$$

$$= -\frac{\lambda_p r_p}{\beta^2\gamma^3}\oint ds\,\frac{\beta_x}{\sigma_x^2}\int_0^\infty \frac{e^{-w_x-w_y}d\eta}{(2+\eta)^{1/2}(2r_{yx}+\eta)^{3/2}}$$
$$[I_0(w_x)(I_0(w_y)-I_1(w_y))].\qquad(27)$$

The tune slope is given by second derivative of $U_0$ as follows,

$$\frac{\partial^2 U_{00}}{\partial J_x^2} = -2\pi\frac{\partial\nu_x}{\partial J_x}\qquad(28)$$

$$= \frac{\lambda_p r_p}{\beta^2\gamma^3}\oint ds\,\frac{\beta_x^2}{\sigma_x^4}\int_0^\infty \frac{e^{-w_x-w_y}d\eta}{(2+\eta)^{5/2}(2r_{yx}+\eta)^{1/2}}$$
$$\left[\left\{\frac{3}{2}I_0(w_x)-2I_1(w_x)+\frac{1}{2}I_2(w_x)\right\}I_0(w_y)\right],$$

$$\frac{\partial^2 U_{00}}{\partial J_x^2} = -2\pi\frac{\partial\nu_x}{\partial J_y} = 2\pi\frac{\partial\nu_y}{\partial J_x}$$

$$= \frac{\lambda_p r_p}{\beta^2\gamma^3}\oint ds\,\frac{\beta_x\beta_y}{\sigma_x^4}\int_0^\infty \frac{e^{-w_x-w_y}d\eta}{(2+\eta)^{3/2}(2r_{yx}+\eta)^{3/2}}$$
$$[(I_0(w_x)-I_1(w_x))(I_0(w_y)-I_1(w_y))],\qquad(29)$$

$$\frac{\partial^2 U_{00}}{\partial J_y^2} = -2\pi\frac{\partial\nu_y}{\partial J_y}\qquad(30)$$

$$= \frac{\lambda_p r_p}{\beta^2\gamma^3}\oint ds\,\frac{\beta_y^2}{\sigma_x^4}\int_0^\infty \frac{e^{-w_x-w_y}d\eta}{(2+\eta)^{1/2}(2r_{yx}+\eta)^{5/2}}$$
$$\left[I_0(w_x)\left\{\frac{3}{2}I_0(w_y)-2I_1(w_y)+\frac{1}{2}I_2(w_y)\right\}\right],$$

where $I_0(x)' = I_1(x)$, $I_0(x)'' = (I_0(x)+I_2(x))/2$ are used.

Figure 11 shows tune spread ($\Delta\nu_{x,y}(J_x,J_y)$), slope ($\partial^2 U_0/\partial J_x^2$), 4-th order resonance strength ($U_{4,0}$) and its width due to space charge force. The resonance width is visible size, $0.2\varepsilon$, when $J_R=\varepsilon$.

Resonances and tune spread/slope are also induced by nonlinear magnets. One turn map is expanded by 12-th order polynomials. Taking at phase independent term, $H_{00}$ is obtained as

$$
\begin{aligned}
H_{00}(\boldsymbol{J}) =\ & 3.43103\times10^{14}J_x^6 + 7.36914\times10^{14}J_x^5 J_y + 7.17029\times10^{11}J_x^5 + 2.34124\times10^{15}J_x^4 J_y^2 \\
& + 1.70991\times10^{12}J_x^4 J_y + 1.43961\times10^8 J_x^4 + 4.48931\times10^{15}J_x^3 J_y^3 + 2.20917\times10^{12}J_x^3 J_y^2 \\
& + 2.50211\times10^8 J_x^3 J_y + 613899.J_x^3 + 3.33998\times10^{15}J_x^2 J_y^4 + 1.79716\times10^{12}J_x^2 J_y^3 \\
& + 7.07531\times10^8 J_x^2 J_y^2 + 809323.J_x^2 J_y + 1095.71 J_x^2 + 7.58773\times10^{14}J_x J_y^5 \\
& + 5.7438\times10^{11}J_x J_y^4 + 4.55828\times10^8 J_x J_y^3 + 650655.J_x J_y^2 + 2096.06 J_x J_y \\
& + 4.11283\times10^{13}J_y^6 + 4.00294\times10^{10}J_y^5 + 5.3027\times10^7 J_y^4 + 79924.4 J_y^3 + 1106.98 J_y^2
\end{aligned}
$$
$$(31)$$

Figure 12 shows the tune shift and slope. Typical tune slope is $\partial^2 H_{00}/\partial x^2 = 1000\sim3000$. This value is similar for $U_{00}$ at $J_x=3^2\varepsilon$, namely tune slope of space charge is dominant for that of lattice nonlinearity at $J < 9\varepsilon(3\sigma)$, vice versa.

Resonance strength due to lattice nonlinearity is obtained by the one turn map. Table 1 shows the resonance
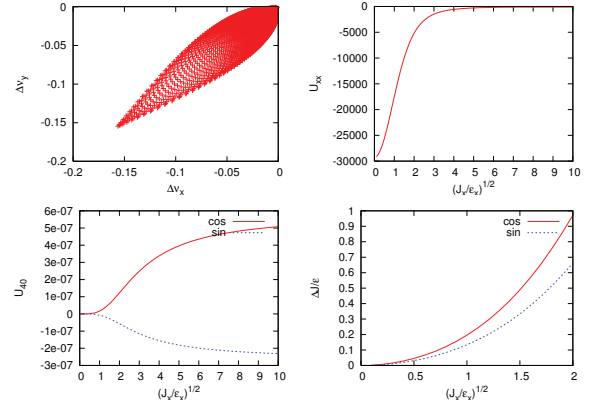


Figure 11: Tune spread ($\Delta\nu_{x,y}(J_x,J_y)$), slope ($\partial^2 U_0/\partial x^2$), 4-th order resonance strength ($U_{4,0}$) and its width due to space charge force as function of $J_R$.

Table 1: Resonance width Under the Tune Slope Eq.(31)

| mx | my | Jx | Jy | \|G\| | B0 | B | BR |
|---|---|---|---|---|---|---|---|
| 1 | 0 | 3.6E-05 | 0.0E+00 | 4.84E-08 | | 1.88E-07 | 1.86E-07 |
| 2 | 0 | 3.6E-05 | 0.0E+00 | 2.47E-08 | | 4.55E-08 | 4.66E-08 |
| 1 | 1 | 1.8E-05 | 1.8E-05 | 1.28E-25 | | 1.67E-26 | 4.01E-09 |
| 0 | 2 | 0.0E+00 | 3.6E-05 | 5.55E-09 | | 3.91E-09 | 2.69E-09 |
| 3 | 0 | 3.6E-05 | 0.0E+00 | 5.46E-08 | | 1.29E-07 | 1.32E-07 |
| 2 | 1 | 1.8E-05 | 1.8E-05 | 2.09E-25 | | 1.42E-26 | 1.42E-07 |
| 2 | -1 | 1.8E-05 | 1.8E-05 | 2.16E-25 | | 4.52E-27 | 7.96E-08 |
| 1 | 2 | 1.8E-05 | 1.8E-05 | 4.66E-08 | | 1.78E-07 | 1.83E-07 |
| 1 | -2 | 1.8E-05 | 1.8E-05 | 1.48E-07 | | 2.72E-07 | 2.72E-07 |
| 0 | 3 | 0.0E+00 | 3.6E-05 | 1.42E-25 | | 1.59E-26 | 1.10E-07 |
| 4 | 0 | 3.6E-05 | 0.0E+00 | 2.50E-07 | | 2.51E-07 | 2.51E-07 |
| 3 | 1 | 1.8E-05 | 1.8E-05 | 1.93E-26 | | 2.52E-27 | 6.80E-09 |
| 3 | -1 | 1.8E-05 | 1.8E-05 | 1.61E-26 | | 4.97E-27 | 7.04E-10 |
| 2 | 2 | 1.8E-05 | 1.8E-05 | 2.49E-08 | | 5.90E-09 | 5.58E-09 |
| 2 | -2 | 1.8E-05 | 1.8E-05 | 1.27E-08 | | 8.40E-09 | 8.03E-09 |
| 1 | 3 | 1.8E-05 | 1.8E-05 | 2.52E-26 | | 5.66E-27 | 3.56E-09 |
| 1 | -3 | 1.8E-05 | 1.8E-05 | 1.63E-26 | | 1.10E-26 | 8.42E-10 |
| 0 | 4 | 0.0E+00 | 3.6E-05 | 1.20E-08 | | 1.45E-08 | 1.42E-08 |

width determined by resonance strength up to 4-th and the tune slope, Eq.(31). The width is reduced by space charge slope in Fig.11 depending on the resonant amplitude $J_R$.

In simulation with the frozen model, resonance width is seen in the phase space plot. Figure 13 shows the $x$ phase space plot for parabolic (top) and Gaussian (bottom) beam, and compared with analitical estimate. Left and right plots is given for ideal and error lattices, respectively, at $(\nu_x,\nu_y)=(21..38,21.40)$. 4-th order resonance is seen in parabolic, but not in Gaussian in ideal lattice. It is seen in Gaussian beam for error lattice. The 4-th order resonance is somewhat weaker than the previous estimation in Fig.11.

Figure 14 shows $x$ phase space plot at $(\nu_x,\nu_y)=(22..41,20.80)$. Top and bottom plots are for parabolic and Gaussian beam, respectively. Left and right are for ideal and error lattice, respectively. 3rd order resonance is seen. Separatrix structure of 3rd order resonance is destroyed in the error lattice. We guess this is due to x-y linear coupling

**Computational Challenges, New Concepts and New Projects**
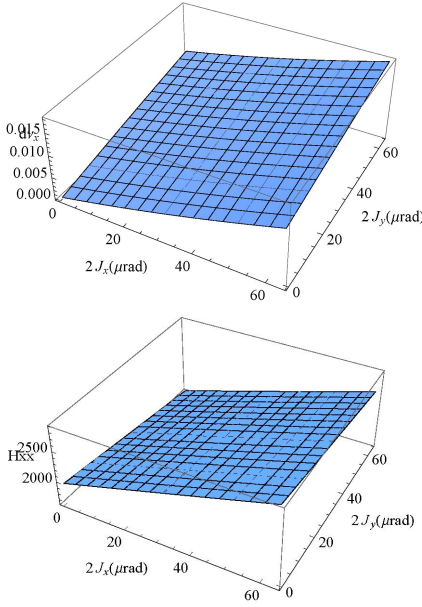
Figure 12: Tune spread, $\partial^2 H_{00}/\partial x^2$ induced by lattice nonlinearity.
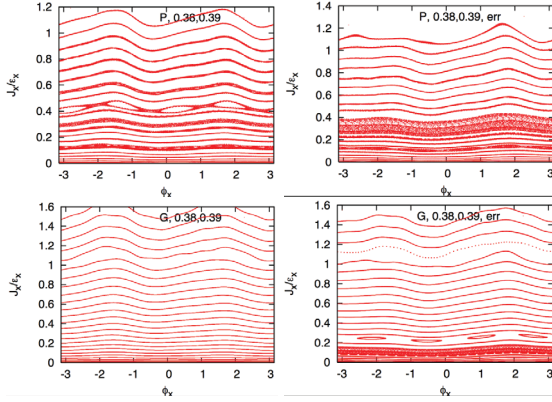


Figure 13: Phase space plot given by frozen model simulation for parabolic (top) and Gaussian (bottom) beam at $(\nu_x, \nu_y) = (21..38, 21.40)$. Left and right plots are for ideal and error lattices, respectively.

resonance $(\nu_x + \nu_y = 43)$. The two resonances excited simultaneously in this point.

## TOY MODEL WITH THE TUNE SLOPE AND RESONANCE STRENGTH

We study a model with a given tune slope and resonance strength. This is an example of Hamiltonian,

$$H = \mu_0 J + \left( J + \frac{e^{-2aJ}}{2a} \right) + bJ \cos m\phi \qquad (32)$$

The tune shift is given by

$$\mu = \frac{\partial H}{\partial J} = \mu_0 + (1 - e^{-2aJ}). \qquad (33)$$
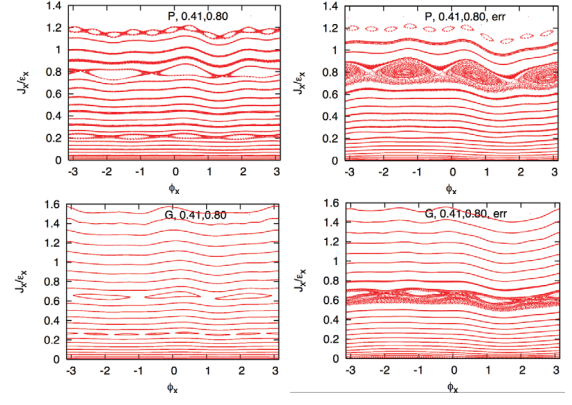


Figure 14: Phase space plot at $(\nu_x, \nu_y) = (22..41, 20.80)$. Top and bottom plots are for parabolic and Gaussian beam, respectively. Left and roght are for ideal and error lattice, respectively.

For small amplitude tune shift $2aJ$, where $a > 0$. The tune slope is given by

$$\frac{\partial^2 H}{\partial J^2} = 2a e^{-2aJ}. \qquad (34)$$

Half width of the resonance is expressed by

$$\Delta J = \sqrt{\frac{2bJ_R}{ae^{-2aJ_R}}}. \qquad (35)$$

Symplectic integration is performed by $H(J, \phi)$ as follows,

$$
\begin{aligned}
J_{n+1} &= \frac{J_n}{1 - bm \sin m\phi_n} \qquad (36) \\
\phi_{n+1} &= \phi_n + \mu + (e^{-2aJ_{n+1}} - 1) + b \cos m\phi_n
\end{aligned}
$$

where $J_n$ and $\phi_n$ are those of $n$-th turn.

We study two cases of parameters,

- $a = 0.5$, $b = 0.002$, $m = 4$, $\mu = 2\pi \times 0.203$

- $a = 0.5$, $b = 0.0002$, $m = 4$, $\mu = 2\pi \times 0.203$

The resonance widths are given as (1) $\Delta J = 0.07$ and (2) $=0.02$. The betatron amplitude, where the resonance hits, is $J_R = 0.38$.

The model is tracked using the two sets of parameters. Figure 15 shows phase space trajectories. 4-the order resonance is seen, and their position $(J_R)$ and widths agree with the formula, Eqs.(33) and (35)

Tune spread area modulates due to synchrotron oscillation. To study the effect, the strength of tune shift term $a$ is made a modulation as

$$a = \frac{a_0}{2}(1 + \cos 2\pi\nu_s n). \qquad (37)$$

The resonant amplitude move to larger amplitude for small $a$. The model does not match to space charge force in this
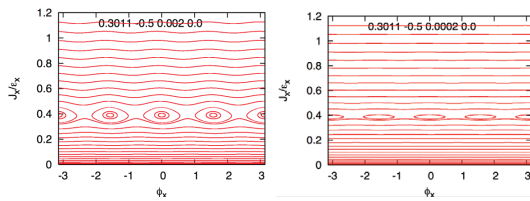
Figure 15: Phase space trajectory for the model map, Eq.(36). Left and right plots correspond to parameters (1) and (2), respectively.

point. This model should be improved in the future. Figure 16 shows phase space plot taking into account of the effective synchrotron motion. Chaotic area drastically increases due to the synchrotron motion. Figure 17 shows the emittance growth of the model with Eqs.(36) and (37). We can see the emittance growth depending on the resonance width.
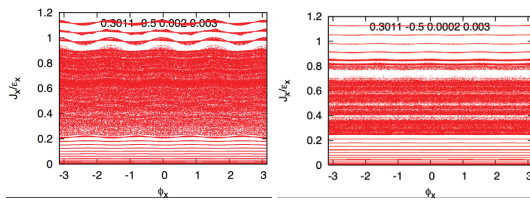


Figure 16: Phase space trajectory for the model map taking into account of effective synchrotron motion, Eqs.(36) and (37). Left and right plots correspond to parameters (1) and (2), respectively.
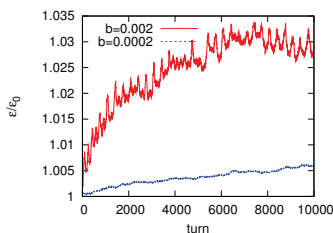


Figure 17: Emittance growth of the model with Eqs.(36) and (37).

## SUMMARY

Noise of PIC simulation induces artificial emittance growth. While collision offset noise in colliders, which is similar situation in computer simulation, is real issue. Noise of power supply ripple in J-PARC can be treated similar way.

To avoid noise frozen model is used as cross check of ordinary non-frozen model simulation. The model is limited to study incoherent emittance growth. Tools to study the incoherent resonance effect is being prepared. Simple toy model was executed to understand resonance phenom-

ena. Synchrotron motion is important for emittance growth combined with the resonances.

Complex accelerator system with complex space charge effects may be represented by simple several lines of Hamiltonian, though simple accelerator system with fundermental space charge effect is complex.

The author thanks fruitful discussions with Drs. H. Harada, S. Igarashi, A. Molodozhentsev and Y. Sato.

## REFERENCES

[1] K. Ohmi et al., "Beam-beam effect with an external noise in LHC", PAC07.

[2] K. Ohmi, proceedings of PAC05, TPPP004.

[3] S. Paret, J. Qiang, Proceeding of Bbeam-beam 2013, CERN.

[4] G. Stupakov, SSCL-560 (1991).

[5] T. Sen and J.A. Ellison, Phys. Rev. Lett. 77, 1051 (1996).

[6] K. Ohmi et al., proceedings of HB2010, WEO1A04.

[7] V.V. Danilov, E.A. Perevedentsev, "An approach to integrability in round colliding beams," Proc. Advanced ICFA Beam Dynamics Workshop on Beam Dynamics Issues for e+e- Factories, Frascati, 321 (1997).

[8] K. Ohmi and K. Oide, Phys. Rev. ST-AB 10, 014401 (2007).

[9] Y. Sato et al., proceedings of HB2014.

# INSTRUMENTATION DESIGN AND CHALLENGES AT FRIB*

S. Lidia[#], Facility for Rare Isotope Beams, Michigan State University, East Lansing, MI, USA

*Abstract*

The Facility for Rare Isotope Beams (FRIB) will use a superconducting linear accelerator to extend the heavy ion intensity frontier for ion species from protons to uranium. The unique design of the twice-folded linac, coupled with the 5 orders of range of beam intensities present new challenges for instrumentation, and machine protection systems. Multi-charge state beams in the low energy linac and dispersive arc regions add complexity to instrumentation systems used for longitudinal tuning and transverse orbit optimization. Beam loss monitoring systems must distinguish losses from the three parallel linac segments sharing the same enclosure. Finally, quick response to abnormal conditions is required to prevent catastrophic damage to beam line components from the high power, heavy ion beams. We present an overview of beam diagnostic systems and detection networks required for the safe tuning, operation, and maintenance of FRIB.

## FRIB FACILITY OVERVIEW

Facility for Rare Isotope Beams (FRIB) is a high-power, high-brightness, heavy ion facility under construction at Michigan State University under cooperative agreement with the US DOE [1]. The linac will accelerate ions to energies above 200 MeV/u, with up to 400 kW of beam power on target. The linac facility, shown in Fig. 1, consists of a Front End, three Linac Segments (LSs) connected by two Folding Segments (FSs), and a Beam Delivery System (BDS) leading to the production target [2].

The front-end consists of two ECR (Electron Cyclotron Resonance) ion sources, a normal conducting CW (continuous wave) RFQ (Radio Frequency Quadrupole) linac, and beam transport lattices. Ion sources are located on the ground level and beam from one of two ion sources is delivered to the linac tunnel through a vertical beam drop. An electrostatic chopper upstream of the vertical beam drop is the primary control of the time structure and duty cycle of the ion beam. A multi-harmonic buncher (MHB) precedes the RFQ and impresses the initial 80.5 MHz RF time structure on the beam. The front end is shown schematically in Fig. 2.
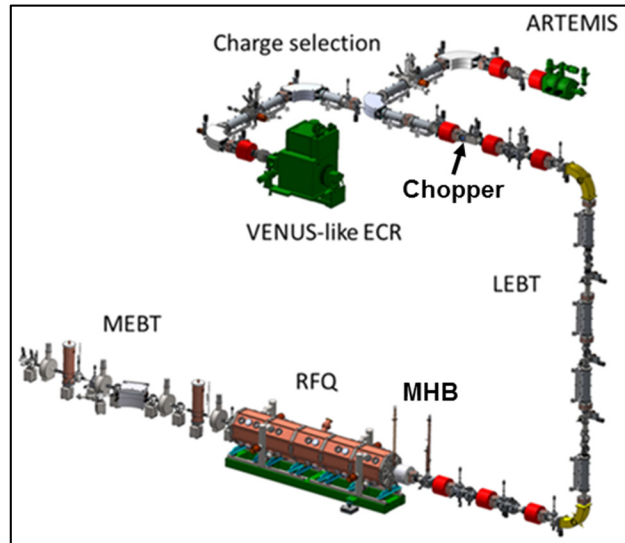


Figure 2: Front end schematic layout.

This paper will first discuss the requirements and specifications of the beam instrumentation systems necessary for FRIB commissioning and operation. Then specific challenges and issues will be presented, along with proposed solutions, which arise from the unique design and operation of this facility.
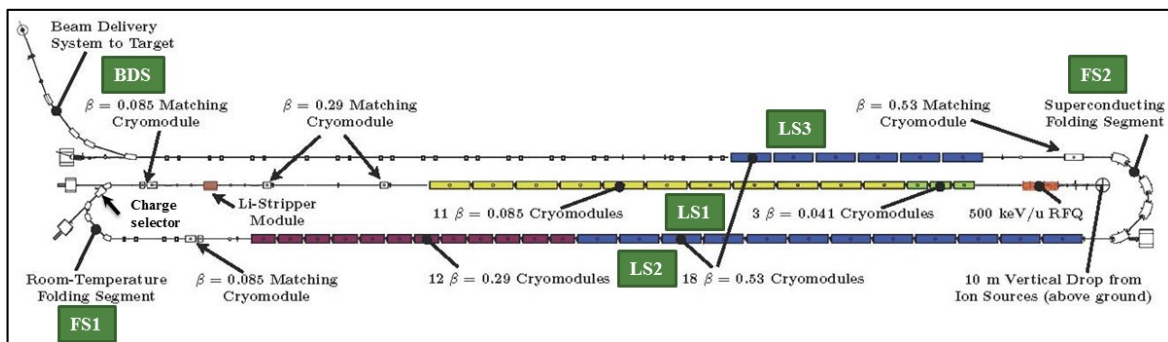


Figure 1: FRIB drive linac schematic layout.

## OVERVIEW OF BEAM DIAGNOSTIC INSTRUMENTATION

The suite of beam instrumentation systems is designed to facilitate initial commissioning and tuning activities

preceding user operations, and then to monitor beam transport and acceleration function, and to provide sensors for machine protection during operations. Diagnostic systems will be provided to continuously measure beam position and orbit deviations, beam current and transmission at several points, and beam loss induced radiation fields. On-demand diagnostics will produce measurements of beam phase space densities, bunch duration, 1-D beam profiles and 2-D transverse (x-y) or hybrid (x-z) distributions. Time of flight measurements using a dense network of beam position monitors will enable phase and amplitude tuning of the linac sections [3].

### Beam Modes

The FRIB linac is designed to support multiple operating modes with varying time structure and peak intensity of the ion beams. These modes can be grouped into four general categories:

- Short pulse (<5 – 50 μs), low duty cycle (< ~1 Hz), varying intensity (50 to 650 μA)
- Moderate pulse length (~0.01 s to s), low duty cycle (< ~1 Hz to 5% duty factor), nominal intensity (3 – 10 pμA)
- Approximately CW (50 μs gap @ 100 Hz), low to nominal intensity (<10 to 400 kW)
- Dynamic ramp to high power (variable intensity, pulse duration, and repetition rate) to slowly increase the target temperature (~10 minutes)

Several modes used for commissioning the front end and fragment separator lack quantitative definition, but may be mapped to one of the other categories. These modes exhibit a wide range in intensity (2 – 650 eμA for Front End commissioning, and 0.0001–30 pnA for fragment separator commissioning and secondary beam development).

### Overall Requirements and Sensitivities

To meet the demands of the FRIB experimental systems, stringent requirements on the linac driver and beam delivery system are imposed. These are summarized in Table 1.

Table 1: Required beam parameters at target for five-charge-state Uranium

| Parameter | Value | Required (% beam) |
|---|---|---|
| Beam spot size | 1 mm | ≥ 90% |
| Angular spread | ±5 mr | ≥ 90% |
| Bunch duration | 3 ns | ≥ 95% |
| Energy spread | ±0.5% | ≥ 95% |

### Front End

The instrumentation package in the Front End section will enable selection and tuning of two charge states for simultaneous production, acceleration and transport to the first linac segment, while maintaining beam quality. Each source line (Fig. 2) will include a diagnostic station, capable of intercepting up to 300 W of continuous beam

power, which includes (i) horizontal and vertical charge-selecting slits; (ii) a Faraday cup; (iii) view screen and optics; and (iv) horizontal and vertical Allison scanners.

The LEBT beamline contains the electrostatic, deflecting mode chopper and Faraday cup monitor for the deflected beam, followed by collimating apertures. A sequence of 1-D profile monitors and pepperpot emittance monitor analyze the beam quality and ensure that the transport lattice and beam distribution are well matched. Following the multi-harmonic buncher and velocity equalizer [3], a stripline fast Faraday cup [4] will be utilized to monitor the longitudinal distribution prior to injection to the RFQ.

Beam current monitors (BCMs, ACCT-type [5]) continuously monitor the beam transmission through the RFQ and at the exit of the MEBT. A 50 μs, 100 Hz current notch or beam gap is imposed by the chopper so that the current baseline can be periodically recovered with the ACCTs. Beam position monitors (BPMs), tuned to a harmonic of the 80.5 MHz cavity frequency, are introduced following the RFQ. Nearly all BPMs in the FRIB lattice use 20-mm diameter, capacitively-coupled buttons to sense beam excursions [6].

### Linac Segments

The first linac segment (LS1) accelerates the two-charge-state ion beam from 500 keV/u to 16 MeV/u. Beam position monitors are placed both in the cryogenic assembly between superconducting solenoids and RF cavities (Fig. 3), as well as in the warm sections between cryomodules (Fig. 4). In the remaining two linac segments (LS2 and LS3), BPMs are placed in the warm sections between cryomodules.
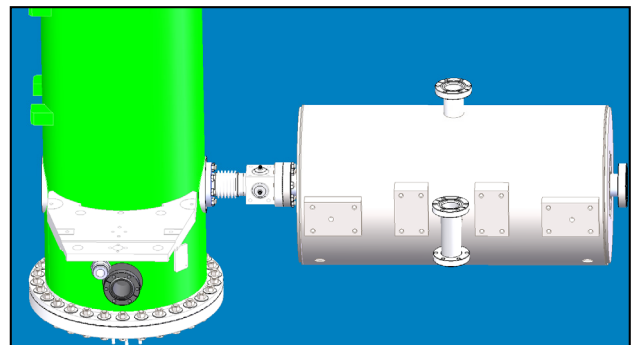


Figure 3: Cryogenic BPM installed between solenoid and cavity in LS1.

Beam current monitors are installed along each straight arm in the folded linac. These are Bergoz AC current transformers (ACCTs) with ~300 kHz high frequency cutoff, and 100 ms droop (*L/R*) time constant. The positions of the unshielded current monitors have been optimized to limit the DC magnetic field

Loss (or Halo) Monitor Rings [7][8] are installed in the warm sections between cryomodules. These niobium rings have apertures that closely match the physical apertures of the cryomodules. They are capacitively-coupled to the

electrical ground of the diagnostic box and provide a measurement of intercepted current whether from halo scraping or transverse excursions of the beam core.
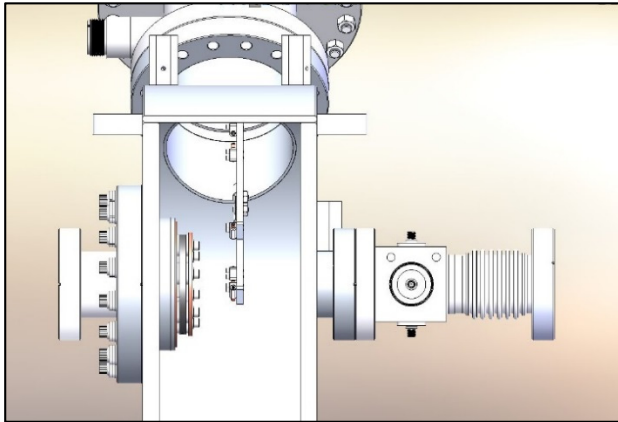


Figure 4: Warm section diagnostic box, with wire profile monitor (PM), BPM, and loss monitor ring (LMR). The profile monitor (shown) is absent in stations connecting cryomodules.

External beam loss monitors (ionization chambers and scintillator-PMT-based, moderated neutron detectors) will be placed along the high energy side of LS2 and along LS3 for prompt detection of x-rays and gammas, and for more sensitive detection of neutron fluxes.

### Folding Segments

The low energy (~16 MeV/u) Folding Segment 1 serves several purposes: (i) to provide a warm magnet transport lattice to connect LS1 to LS2; (ii) to strip the two-charge-state ion beam into many charge states, followed by; (iii) selecting up to five charge states for transport and insertion in LS2; and, finally, (iv) to provide a straight-ahead beam dump line for commissioning and tuning LS1. A second beam dump in FS1 is provided to facilitate tuning of the charge state selector and optics. The high energy (~150 MeV/u) Folding Segment 2 provides a superconducting magnetic transport lattice to connect LS2 to LS3, as well as a straight ahead beam dump for LS2 commissioning and tuning.

The basic instrumentation suite includes beam position monitors, transverse profile monitors, and beam current monitors. The charge stripper imposes constraints on the impinging beam distribution to limit the growth in energy spread and beam emittance. A Feschenko-type bunch shape monitor [9] will be used to monitor the transverse and longitudinal bunch profile, enabling upstream tuning to match the stripper admittance.

### Beam Delivery System

The final transport lattice which comprises the Beam Delivery System (BDS) serves to deliver the multi-charge-state beam to the target with parameters given in Table 1, for example. The beam instrumentation design includes beam position, transverse profile, and beam current monitoring. A full energy (200 MeV/u), straight ahead beam dump is used for commissioning and tuning of LS3 and the linac-to-BDS transport line, but is not rated for full beam power.

## CHALLENGES FOR BEAM INSTRUMENTATION

FRIB employs a superconducting linac to accelerate the high power, high brightness hadron beam. As such, it shares operational issues with other facilities (SNS, ESS, RHIC, LHC, JPARC, etc.) with regards to power handling and cleanliness of components, restrictive access to the beam line and prohibitions against actuated diagnostics near cryomodules, etc. Several other challenges for beam instrumentation are introduced in the FRIB case due to the low energy of the heavy ion beams, the folded linac geometry, and the requirement to transport multiple charge states simultaneously.

### Low-Beta Beam Position Monitoring

The relatively low velocity of the ion beams in the drive linac has implications for accurate beam position monitoring. With low β, the electric field lines spread out resulting in longer, slower image current, and reduced high frequency content. This effect depends on the proximity to the button and produces a position- and velocity-dependent frequency response [6][10][11].

Shafer's analysis of low-β beam pickups [11] identified a correction factor determine position. With BPM buttons $A$ and $B$ centered on the midplane (with separation $D$), the beam position is estimated as

$$\Delta x \cong \frac{1}{1+G}\frac{D}{\pi}\frac{A-B}{A+B}, \quad (1)$$

where

$$G = 0.0347\left(\frac{\omega}{\beta c}\frac{D}{\gamma}\right)^2 - 0.00181\left(\frac{\omega}{\beta c}\frac{D}{\gamma}\right)^3. \quad (2)$$
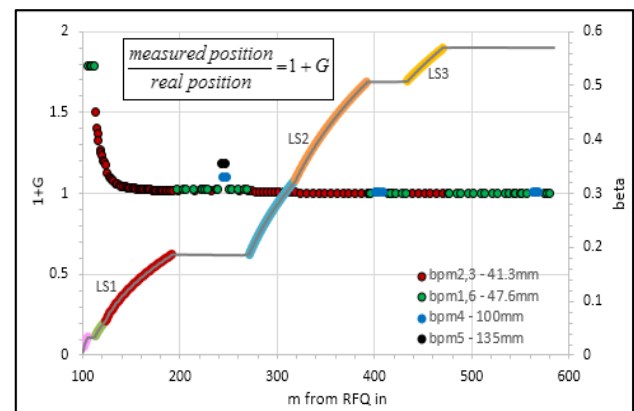


Figure 5: Linear correction factor for low-β. [6]

The linear correction factor for the FRIB BPMs are shown in Fig. 5. The effect is pronounced for position measurements in the MEBT, the lower energy region of LS1, and the large dispersion region of FS1 which requires large aperture BPMs.

*Multiple Charge State Beams*

The acceleration, transport and delivery of a multiple charge state composite beam presents particular complications to the beam instrumentation design and functionality for establishing the machine tune. Representative ion species for FRIB are listed in Table 2, where Q1 is the beam charge state in the Front End and LS1, and Q2 is the beam charge state following the stripper and charge selector in FS1. In the case of Uranium, two charge states are transmitted to the stripper, with five states selected for additional acceleration and target delivery.

Table 2: Representative Ion Species in FRIB

| Ion Species | A | Emax (MeV/u) | Q1 | Q2-center | Q2-spread |
|---|---|---|---|---|---|
| U | 238 | 200 | 33, 34 | 78 | 76-80 |
| Xe | 136 | 242 | 24 | 51 | 50-52 |
| Kr | 86 | 262 | 17 | 35 | 35 |
| Ca | 48 | 268 | 12 | 20 | 20 |
| Ar | 36 | 318 | 10 | 18 | 18 |
| O | 16 | 319 | 3 | 8 | 8 |

From a beam dynamics perspective, the effect of multiple charge states is homologous to a momentum spread: $\Delta Q/Q \sim \Delta p/p$. In the case of Uranium beams, the charge state spread ($\Delta Q/Q$) is ~3% before the stripper and ~6% following the selector. Differential focusing and acceleration is required to remove different charge-state-induced phase space offsets.

Uranium beams undergoing low energy acceleration in LS1 will execute synchrotron oscillations. Due to the large $\Delta Q/Q$ separation between charge states they will orbit about different stable phase points. The result is an overall oscillation in the longitudinal emittance (Fig. 6).

The challenge to beam instrumentation is to spatially resolve the phase dispersion of the two charge states along the linac. This can be accomplished by utilizing the network of BPMs and measuring phase differences between the fundamental and 3rd harmonic of the bunch frequency, for example.

A separate issue with multi-charge state beams arises in FS1 due to dispersion. Figure 7 shows the effect near the position of maximum dispersion for the ideal lattice case. Here, the beam distribution at the BPM following the charge selector is dispersed horizontally by up to ~80 mm. A large (150 mm) aperture, elliptical, split plate BPM design (Fig. 8) provides a larger linear response regime [12].
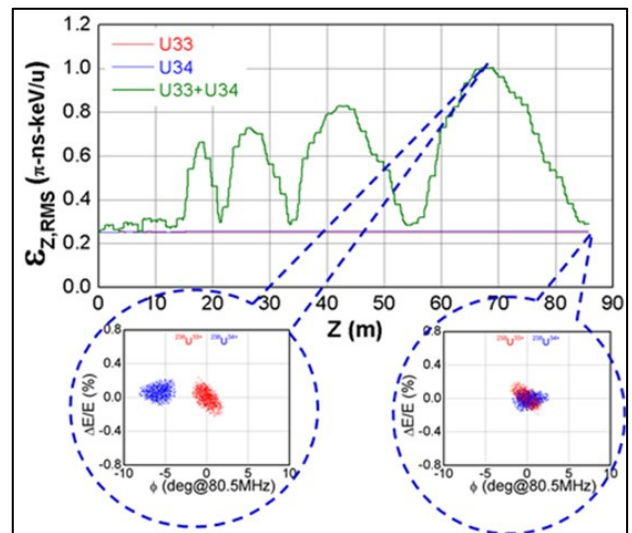


Figure 6: Longitudinal emittance evolution of two-charge-state beam in LS1
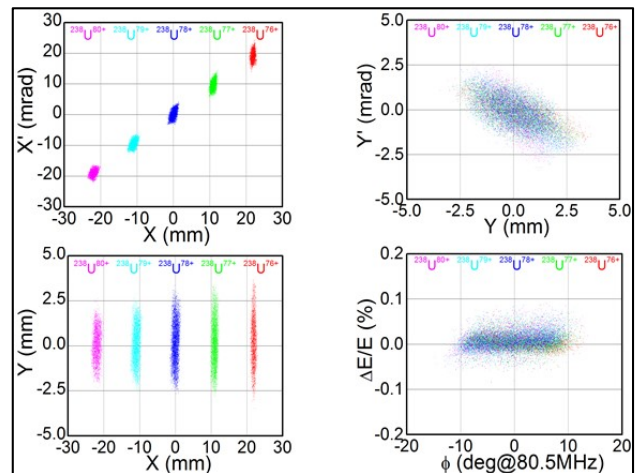


Figure 7: Five-charge-state beam dispersion in FS1.

*Large Dynamic Range of Beam Intensity*

The previously discussed beam modes define the range of conditions that the beam instrumentation must serve. Beam instrumentation is required to detect beam currents ranging from ~1 mA to ~1 µA, with bandwidths sufficient to provide sensitivity over orders of magnitude in duty cycle or pulse duration (CW to 50 µs pulse duration at 1 Hz). Additional operating modes (albeit a small fraction of the operating schedule) require lower peak intensities and average beam power. The baseline resolution requirements for the diagnostic systems assumes CW operation with 100 µA beam current. Operationally, for reduced average beam currents, longer integration or averaging times may be used to restore resolution. In the extreme case of ion beam fluxes ~100 pfA, intercepting diagnostics may be utilized with long integration times to acquire flux density information on the transported beams.
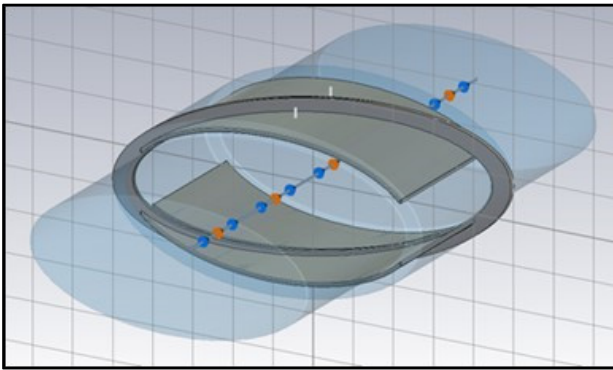
Figure 8: Large aperture, elliptical, split-plate BPM in FS1.

## Machine Protection Issues

The high power and brightness, and short (< mm) Bragg range of the FRIB heavy ion beam places critical importance on the fast protection system to detect and mitigate against prompt beam losses [13]. The performance and lifetime of sensitive superconducting cavity surfaces can be affected by small losses (< 1 W/m) occurring over long durations.

The twice-folded geometry of the FRIB linac places the high energy linac segment in close proximity to the low energy linac segment. Traditional loss monitors, eg. ionization chambers and scintillation-based neutron detectors, will be unable to differentiate the low-amplitude loss signals arising in LS1 from the high-amplitude signals generated in LS3 due to radiation cross-talk [14]. Additional x-ray background sources originating from the RF cavities themselves can also overwhelm the relatively low-amplitude beam-generated signals in the low energy linac modules.

Table 3: FRIB Beam Loss Detection Layers

| | | LS1 | FS1 | LS2 low energy | LS2 high energy | FS2 | LS3 | BDS |
|---|---|---|---|---|---|---|---|---|
| Fast Loss | Primary | DBCM | DBCM | DBCM | DBCM | DBCM | DBCM | DBCM |
| < 35 μs | Secondary | HMR | HMR | HMR | BLM | BLM | BLM | BLM |
| | Tertiary | | | | HMR | HMR | HMR | |
| Slow loss | Primary | HMR/Temp | HMR | HMR/Temp | BLM | BLM | BLM | BLM |
| > 100 ms | Secondary | HMR/Temp | | HMR/Temp | HMR/Temp | HMR | HMR/Temp | |
| | Tertiary | Cryo | | Cryo | HMR/Temp | | HMR/Temp | |
| | | | | | Cryo | | Cryo | |

The loss monitor network scheme for FRIB is shown in Table 3. Fast and slow losses, in each segment of the accelerator chain, are separated, and the primary as well as backup detection schemes are indicated. The primary fast detection schemes are based on direct monitoring utilizing differential beam current monitors (DBCMs) [15]. Secondary radiation monitoring appears only as the primary beam energy increases to a suitable production threshold. The slow loss schemes are based on time averaged loss ring monitoring as well as thermal drift monitoring in cryomodules.

## SUMMARY

The beam instrumentation design for the FRIB linac has been presented, and has been shown to satisfy the requirements for measuring and tuning of the expected high power, high brightness hadron beams. Issues and challenges to beam instrumentation specific to the FRIB linac facility have been described, and proposed solutions presented.

## REFERENCES

[1] J. Wei, et al., "FRIB accelerator status and challenges", LINAC'12, Tel Aviv, August 2012, p. 417; http://www.JACoW.org

[2] F. Pellemoine, et al., "Development of a production target for FRIB: therm-mechanical studies", J. Radioanal Nucl Chem, DOI 10.1007/s10967-013-2623-7.

[3] Q. Zhao, et al., "FRIB accelerator beam dynamics design and challenges", Proceedings of HB2012, Beijing, China, WEO3B01; http://www.JACoW.org

[4] A. Dainelli, et al., Nucl. Instrum. Methods Physics Res. **A382** (1996) 100.

[5] http://bergoz.com/

[6] O. Yair, et al., "FRIB beam position monitor pick-up design", *Proceedings of IBIC2014*, Monterey, USA, TUPF16; http://www.JACoW.org

[7] Z. Liu, et al., "A new beam loss detector for low-energy proton and heavy-ion accelerators", Nucl. Instrum. Methods Physics Res. **A767** (2014), 262.

[8] M.-H. Moscatello, et al., "Machine protection system for the SPIRAL2 facility", *Proceedings of IPAC2012*, New Orleans, USA, WEPPD044; http://www.JACoW.org

[9] Feschenko A.V., Ostroumov P.N. "Bunch Shape Measuring Technique and Its Application For an Ion Linac Tuning", *Proc. of the 1986 Linear Accelerator Conference*, Stanford, 2-6 June, 1986, pp. 323-327.

[10] A. Lunin, et al., "Development of a low-beta button BPM for the PXIE project', *Proceedings of IBIC2013*, Oxford, UK, TUPC14; http://www.JACoW.org

[11] R.E. Shafer, "Beam position monitor sensitivity for low-β beams", AIP Conf. Proc. **319** (1994).

[12] E. Schulte, in *Beam Instrumentation*, J. Bosser (ed.), CERN-PE-ED 001-92.

[13] S. Lidia, "Diagnostics for high power accelerator machine protection systems", *Proceedings of IBIC2014*, Monterey, USA, TUIYB1; http://www.JACoW.org

[14] Z. Liu, et al., "Beam loss monitor system for the low-energy heavy-ion FRIB accelerator", *Proceedings of IBIC2013*, Oxford, UK, MOPC46; http://www.JACoW.org

[15] W. Blokland, C. Peters, "A new differential and errant beam current monitor for the SNS accelerator," *Proceedings of IBIC2013*, Oxford, UK, THAL2; http://www.JACoW.org

# BEAM LOSS MECHANISMS, MEASUREMENTS AND SIMULATIONS AT THE LHC (QUENCH TESTS)

M. Sapinski, CERN, Geneva, Switzerland

## Abstract

Monitoring and minimization of beam losses is increasingly important for high-intensity and superconducting machines. In the case of the LHC, the collimation system is designed to absorb the energy of lost particles and confine the main multi-turn losses to regions without sensitive equipment. However many loss mechanisms produce local loss events which can be located elsewhere in the machine. A beam loss monitoring system, covering the whole machine circumference is therefore essential, and is used for both machine protection and diagnostics. In order to fully understand the measured signals and set-up the beam abort thresholds, extensive simulation work is required, covering particle tracking in the accelerator and the generation of the particle showers created by the lost particles. In order to benchmark these simulations and verify beam-abort thresholds, special tests have been performed where beam losses are provoked in a controlled manner over a wide range of duration. This work summarizes the experience in understanding beam losses in the LHC during Run 1.

## INTRODUCTION

When the beam particles deviate from their optimal trajectory and hit the vacuum chamber or if they interact with objects inside the vacuum chamber (rest gas molecules, dust) they are usually lost from the beam. These beam losses are a natural aspect of every machine operation. Their effects are: decrease of beam intensity and lifetime, activation and radiation damage of accelerator elements. In case of catastrophic losses, when unexpectedly large fraction of the beam is lost in the area which is not designed to accept such a loss, their may lead to a damage of the vacuum chamber and other machine elements.

In case of superconducting accelerator the beam losses heat up the magnet coils and may lead to a sudden transition to normal-conducting state called a *quench*. In LHC the total energy stored in a circulated beam reaches 392 MJ while the quench level is only about a few mJ/cm$^3$, therefore a loss of about $10^{-10}$ of the total beam intensity on superconducting magnet aperture may heat up the coil above transition temperate and quench the magnet.

The most obvious way to quantify the beam losses is a decrease rate of the beam current, measured typically in loss of particles per turn, per second or per a given phase of the machine cycle. This measurement is done using beam current transformers.

Another loss quantification is the beam power lost in a given location, for instance on a collimator or along the beam chamber. In case of LHC primary collimators only a small fraction ($\sim$ 2%) of the impacting beam power is deposited in the graphite jaw. The rest is deposited in the downstream collimators and absorbers. In order to allow hands-on intervention on beamline elements the activation must be limited and therefore the regular losses should be kept at the level below 1 W/m.[1]

Finally the beam losses are measured by Beam Loss Monitors (BLM) using radiation units, for instance Grays. This way of loss quantification is usually used in protection-related studies, for instance assessing the damage or quench potential of the losses. It is related to the energy density deposited inside accelerator components.

These various quantifications of beam losses are related. For instance a single proton lost in LHC generates BLM signal between $10^{-12}$ and $10^{-10}$ Gy.

This paper describes the beam losses in LHC and concentrates on a special case of controlled loss experiments called quench tests. They were analyzed and simulated with unprecedented precision using state-of-art techniques.

## BEAM LOSS MECHANISMS AND TIMESCALES

Beam losses are often divided into normal and abnormal. The normal losses are those which cannot be avoided, for instance losses due to luminosity debris or due to particle diffusion from beam core to the halo which are usually caught on the collimation system. The beam instabilities due to operational variations, for instance tune change during the squeeze or ramp, are also producing normal losses. In LHC the average intensity lost during a fill, between capture and start of physics is about 3.5%. Table 1 shows the distribution of losses between various phases of the machine cycle.

Table 1: Beam Losses During Various Phases of Machine Cycle During Luminosity-production Year 2012 [1]

| phase | average | maximum |
|---|---|---|
| RF capture | 0.5% | 2% |
| ramp | 1.2% | 15% |
| squeeze+adjust | 1.7% | 10% |

Abnormal losses happen due to malfunction of accelerator equipment, for instance spurious discharge of the kicker magnets or dust particles falling into the beam. The last ones, called colloquially Unidentified Falling Objects (UFO), are of special concern in LHC, because they can provoke magnet quenches compromising machine operation at 6.5 TeV.

It is convenient to classify beam losses according to their duration:

---

[1] This value is applicable for a beamline shielded with magnets.

- Ultra-fast losses developing in less then three machine turns (270 µs) are usually linked to injection or dump; only passive protection systems (absorbers, collimators) can protect from effect of those losses; the quench level of superconducting magnets in this timescale is determined by heat capacity of a dry cable.
- Very fast losses developing up to millisecond are typically UFO losses; in this timescale the BLM system allows to prevent magnet quenches; the quench level is driven by heat transfer to the superfluid helium inside the cable.
- Fast losses, up to several seconds can be due to various mechanisms, for instance RF trips or powering failures; there are multiple protection systems active in this timescale; heat capacity of helium inside the cable is saturated, the heat transfer outside coil starts to play important role.
- Slow losses, longer than several seconds are typically collimation and luminosity losses; in addition to protection systems the time is long enough for human reaction; quench limit is determined by the heat transfer to the cryogenic system.

## MEASUREMENT TECHNIQUES

The beam particles, when interacting with accelerator material, produce showers of secondary particles which can usually be detected by radiation detectors. In LHC the BLM system uses ionization chambers [2] installed on the outside of the magnets cryostats. The current from the chambers is converted to frequency and this signal is send to the surface card performing real-time data analysis. This scheme allows for the $10^9$ dynamic range of the measured current.

As BLMs are situated in the radially peripheral part of the shower, they cannot be used to determine loss pattern with accuracy better than 1-2 meters. Semiconductor detectors have been installed on the cold mass of some of the LHC magnets in order to better corelate the energy deposition in the magnet coil with BLM signal (see Fig. 1 and 2). It is planned to install those detectors inside the cold mass, very close to the coils [3]. They operate at temperature of 2 K and must withstand dose of several MGy.
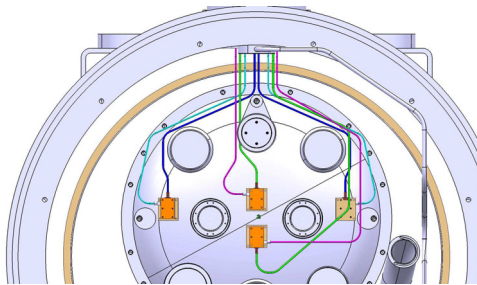


Figure 1: Drawing of cryogenic BLMs installed on the helium vessel of LHC main dipole.

The advantage of semiconductor detectors is their speed which allows for nanosecond resolution in comparison to ion-
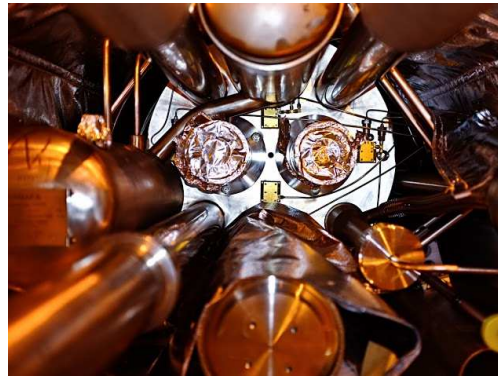


Figure 2: A photo of an installation of cryogenic BLMs on the magnet cold mass.

ization chambers with only about 40 µs resolution. Therefore the diamond detectors are installed behind the collimators, what allows for measureing bunch structure of the beam losses.

In some cases the beam losses are assessed measuring activation of machine elements in the intermissions of normal operation.

## BEAM LOSS EXPERIMENTS

The beam losses are present in daily operation of most machines. Both, the normal and abnormal losses, limit the machine performance. For instance the debris due to luminosity production may generate losses exceeding the steady-state quench limit and therefore determine the maximum allowed instantaneous luminosity. UFO losses may lead to quenches of main ring magnets so frequent, that the recovery time (about 8 hours per quench) will not allow for an efficient operation. In order to understand better the limits imposed by quench phenomena a series of experiments, called beam-induced quench test, have been performed. The goals of the experiments are:

- Assessment of the machine performance limits due to magnet quenches.
- Determination of beam-induced quench levels.
- Validation of the BLM quench-preventing beam-abort thresholds.

The quench tests have been performed first time with Tevatron magnets in 1980 [4]. The first beam-induced quenches in LHC took place in 2008 [5]. In the year 2010 the UFO losses were observed for the first time. This was also the year when a total energy stored in the beam increased well above safe beam limits of about 1 MJ. To address these two aspects quench tests with a wire scanner [6] and with dynamic orbit bump [7] were performed.

In 2011 two new types of quench tests were performed. The first type was a steady-state test with collimators with a goal to identify the improves the collimation system needed for high luminosity run [8]. The second one was devoted to investigation of ultra-fast losses with beam energies above injection and was performed by splashing an injected bunch

on a collimator in front of magnet with increased coil current corresponding to high beam energy [9].

The year 2012 was devoted to luminosity production therefore no quench tests were performed, although an effort to prepare ones has started. This effort was concluded with a 48-hour quench test campaign in February 2013 right after the end of Run 1. During this campaign the four tests were executed, some being an extension of previous tests, other presenting a new approach to controlled beam loss generation.
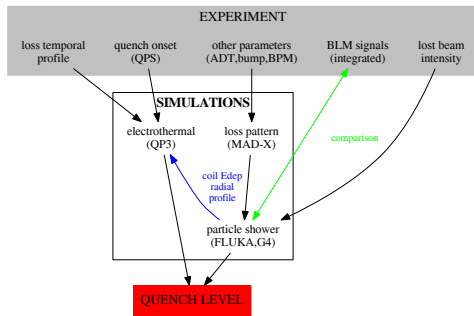


Figure 3: Quench test analysis scheme.

Figure 3 presents the analysis scheme of a typical quench test. The most important experimental measurements are the time structure of the losses the BLM signals and the amount of the lost beam intensity. Typical result of the experiment is shown in Fig. 4 for UFO-timescale test. Three simulations are needed to analyze the experiment. The particle tracking code is used to reconstruct the loss pattern on the aperture. Result of this code, together with lost intensity from the experiment, are fed to a particle shower simulation which produces BLM signals and energy density deposition in the coil. The BLM signals are compared with experimental values and general agreement gives confidence into values of energy deposition in the coil. Finally electro-thermal simulations are preformed.[2] The two quench levels: from electro-thermal and particle shower simulations, are compared. An agreement means that the quench level is correctly modelled and can be extrapolated to different magnet currents and loss duration. Because of significant uncertainties in the experiment and the simulations an agreement within factor 2 is regarded as good.

## LOSS PATTERN SIMULATIONS

In LHC the global loss patterns are well understood. They occur on collimator system and follow the collimation hierarchy. The leakage to the cold sectors is well controlled and is about $3 \cdot 10^{-4}$. In Fig. 5 the measurement and the simulations of the loss maps are shown. The program used to perform these simulations, called SixTrack [10], tracks the particles, which underwent the first scattering in collimators, over several turns until they are lost in the collimation system

---

[2] Because of the dependence of the electro-thermal simulations from energy gradient in the coil the two analysis branches are not independent.
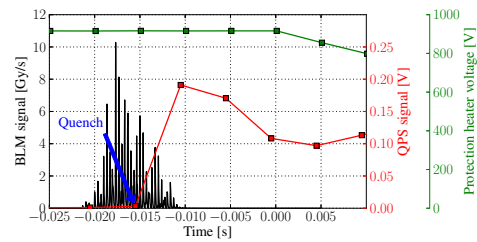


Figure 4: Result of 5 ms quench test. The BLM signal (black line) shows particular, spiky structure. The resisitive voltage on the coil (red line) indicates the quench onset 5 ms after beginning of the loss.

or on cold aperture. The agreement between measured and simulated loss patterns is very good.
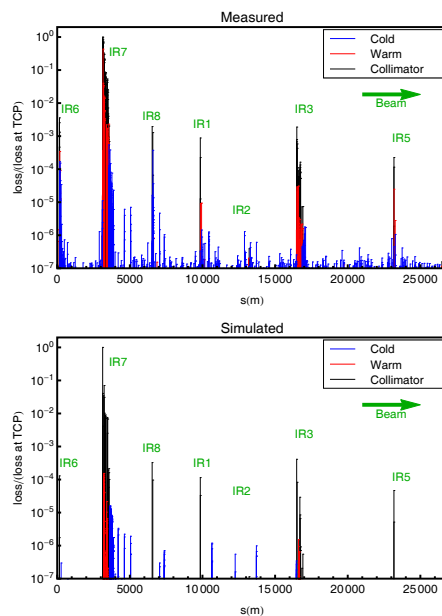


Figure 5: Beam loss distribution measured by the BLM system during qualification loss map (upper) and simulation (bottom). Reproduced from [11].

A cause for a local loss in the cold section can be UFO event, accidental orbit bump or a leak from the collimation system. A loss pattern in such case is affected by machine optics, beam dynamics, oscillations and roughness of the vacuum chamber surface.

A direct measurement of the loss pattern is limited by the accuracy of the BLM system which is defined by the longitudinal development of the shower. Better accuracy can only be attempted by a precise beam position and emittance measurement and by beam trajectory modelling. An example of such procedure is shown in Fig.6. In this experiment an injected beam was kicked with large vertical angle (750 μrad) and hit a main dipole magnet leading to a quench. The beam emittance has been measured in SPS and the trajectory has been measured by BPMs. The MAD-X modelling of previous shot with smaller angle (80 μrad) shows very good

agreement with BPM readings. This allows to trust the large kick trajectory modelling and estimation of the loss profile.
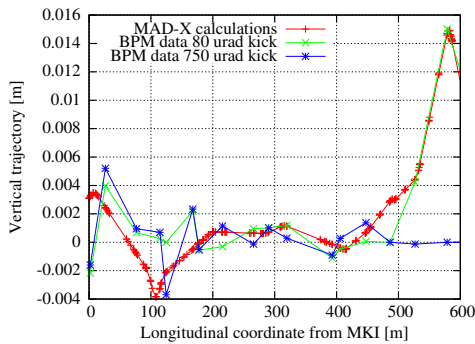


Figure 6: Beam trajectory in case of large kick event (see text). Courtesy of C. Bracco.

The above experiment features particularly large beam impact angle, but for most of the losses on the vacuum chamber this angle is much smaller. In Fig. 7 a strict correlation between distance of the lost proton from a centre of lattice quardupole magnet and the impact angle is shown. The angle reaches minimum close to the magnet center.
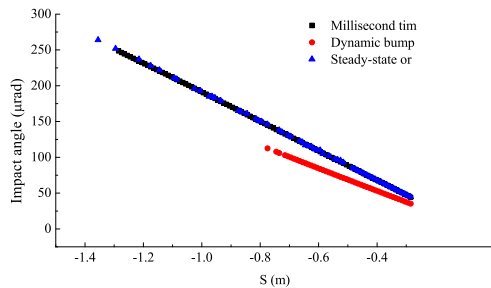


Figure 7: Correlation between proton impact angle and the loss position along main quadrupole magnet [12]. Courtesy of V. Chetvertkova.

A consequence of such small impact angles is a sensitivity of the loss pattern to the surface roughness. Even a small variation from a perfect surface (e.q. $30\,\mu\mathrm{m}$, as shown in Fig. 8) can significantly affect the loss distribution.
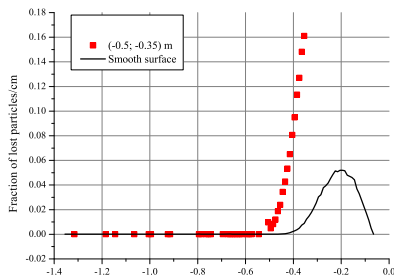


Figure 8: Influence of a hypothetical deviation from perfect surface on loss pattern [12]. Courtesy of V. Chetvertkova.

## PARTICLE SHOWER SIMULATIONS

Particle shower simulations are needed to assess the effect of the beam loss on accelerator equipment and to reproduce the BLM signals. Typically the input to the particle shower simulations is the loss pattern, obtained from tracking code.

The results of the particle shower simulations must be normalized to the amount of lost particles in order to be compared with the values of measured BLM signals. The agreement of the BLM signals enhances confidence to the results of the simulations of the energy deposited in the coils, which cannot be measured. The ratio of the BLM signals to the energy density in the coil gives a base to the protection function of the BLM system. Because the particle shower is small in the first centimeters of its development (coil) and grows downstream (BLM), the relation between the BLM signal and the energy in the coil depends on the scale of the losses.

In Fig. 9 the dependence of the BLM threshold, which is proportional to the ratio between BLM signal and energy deposit in the superconducting coil, is shown as a function of the longitudinal spread of the loss. This curve explains why even a small deformation of the vacuum chamber wall leading to concentration of losses in one location can affect significantly the energy deposit in the magnet coil leaving the BLM signal unchanged.
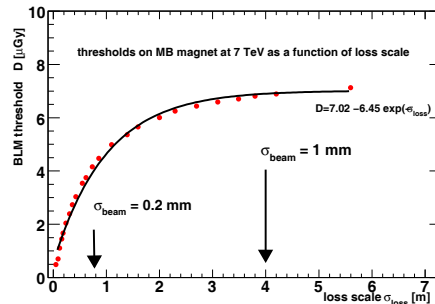


Figure 9: Dependence of the ratio of BLM signal to energy density deposited in the coil in function of loss length [13].

Figure 10 shows a quench test in which a particular good agreement between FLUKA simulations and measurements of the BLM signals was achieved. In most tests the agreement was much better than a factor 2, especially for the monitors with the highest signals.
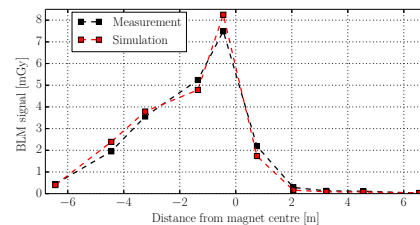


Figure 10: Measured and simulated BLM signals in case of 5 ms quench test. Courtesy N. Shetty [14].

## ELECTRO-THERMAL SIMULATIONS

One of the beam loss effects is heating of the accelerator elements, for instance the magnet coils. To estimate the temperatures the heat transfer must be taken into account. This is particularly interesting in case of superconducting magnets, because of complex heat transfer mechanisms to superfluid helium. The electro-thermal codes allow for estimation of the coil temperature in the presence of heating from the beam loss and cooling mechanisms. They also estimate the energy deposit at which the magnet quenches. The code used to simulate quench tests is QP3 [15]. Input to the code are Rutheford cable parameters (amount of superconductor, type of insulation), the amount of liquid helium in the cable, the current density and shapes of the radial (from patricle shower simulations) and temporal (from experiment) distributions of energy density in the coil. The program performs iterative search for a minimum energy deposition causing the quench.

Results of the quench level determination for selected quench tests are presented in Table 2. In most cases the quench levels agree within factor 2. Only in case of 5 ms loss the disagreement is wors. The discrepancy is attributed to spiky structure of the loss obtained in this experiment (see Fig. 4), which is not simulated in QP3.

Table 2: Quench Levels for Selected Tests

| timescale | $E_{beam}$ | Part. Shower | El.-Thermal. |
|---|---|---|---|
| ns | 450 GeV | $\leq 36$ mJ/cm$^3$ | 38 mJ/cm$^3$ |
| $\sim 5$ ms | 4 TeV | 250 mJ/cm$^3$ | 58 mJ/cm$^3$ |
| $\sim 5$ s | 4 TeV | $> 50$ mW/cm$^3$ | 115mW/cm$^3$ |
| $\sim 5$ s | 4 TeV | 208 mW/cm$^3$ | 180mW/cm$^3$ |
| 20 s | 4 TeV | 41 mW/cm$^3$ | 70 mW/cm$^3$ |

Due to uncertainties in magnetic field value, liquid helium contribution and additional stress due to cable bending the estimation of quench limit in the ends of the magnets is less accurate. Unfortunately many realistic beam loss scenarios foresee the maximum energy deposit in these regions.

## CONCLUSION

The main conclusions which can be drawn from the beam-induced quench tests performed during LHC Run 1 are:

- The experiments should involve an attempt where one of the parameters, is below the quench; this allows for determination of the quench level range.
- For fast tests the synchronization of the BLM and QPS signals are crucial for test analysis.
- BLMs cannot resolve the local loss pattern; even a small surface roughness may result in a loss pattern giving significantly different energy deposition in the coil.
- Parametric study of simulation parameters is very important to understand the sources of uncertainties on the quench test results.
- Transverse damper, used in various excitation modes, is a very good tool to generate controlled losses.

- Particle tracking is often more uncertain than particle shower simulations and probably requires more conceptual development.
- The maximum of energy deposition often takes place in complex regions of the magnets where both, the particle shower and electro-thermal simulations give more uncertain results.

## REFERENCES

[1] G. Papotti et al., *Beam Losses through the Cycle*, Proceedings of the 2012 Evian Workshop on LHC Beam Operation

[2] http://cern.ch/blm

[3] C. Kurfuerst, *Cryogenic Beam Loss Monitoring for the LHC*, CERN-THESIS-2013-232

[4] R. Dixon, N.V. Mokhov, A. VanGinneken, *Beam Induced Quench Study of Tevatron Dipoles*, Fermilab FN-327

[5] M. Sapinski et al., *Beam-induced quenches of LHC magnets*, Proceedings of IPAC13, THPEA045

[6] M. Sapinski et al., *LHC magnet quench test with beam loss generated by wire scan* , Proceedings of IPAC11, WEPC173

[7] A. Priebe et al., *Beam-induced Quench Test of LHC Main Quadrupole*, Proceedings of IPAC11, WEPC172

[8] D. Wollman et al., *Collimation Losses in the DS of IR7 and Quench Test at 3.5 ZTeV*, CERN-ATS-2011-042 MD

[9] Ch. Bracco et al., *Experiments on the Margin of Beam Induced Quenches for LHC Superconducting Quadrupole Magnet*, Proceedings of IPAC12, MOPPC004

[10] G. Robert-Demolaize, R. Assmann, S. Redaelli, and F. Schmidt, Proceedings of the 21st Particle Accelerator Conference, 2005 (IEEE, Piscataway, NJ, 2005), p. 4084.

[11] R. Bruce et al., *Simulations and measurements of beam loss patterns at the CERN Large Hadron Collider*, Phys. Rev. ST Accel. Beams **17**, 081004 (2014)

[12] V. Chetvertkova et al., *MadX Tracking Simulations to Determine the Beam Loss Distributions for the LHC Quench Tests with ADT Excitation*, Proceedings of IPAC14, THPRI094

[13] M. Sapinski, B. Dehning, A. Priebe, *Simulation of Beam Loss in LHC MB Magnet and Quench threshold test*, CERN-LHC-Project-Note-422

[14] N. Shetty et al., *Energy Deposition and Quench Level Calculations for Millisecond and Steady-state Quench Tests of LHC Arc Quadrupoles at 4 TeV*, Proceedings of IPAC14, MOPRO019

[15] A. Verweij, *QP3: Users Manual*, CERN EDMS 1150045, 2008

# BEAM INSTRUMENTATION AT THE 1 MW PROTON BEAM OF J-PARC RCS

K. Yamamoto[#], N. Hayashi, K. Okabe, H. Harada, P. K. Saha, M. Yoshimoto, S. Hatakeyama,
H. Hotchi, Y. Hashimoto and T. Toyama, J-PARC Center, Tokaimura, Japan

## Abstract

Rapid Cycling Synchrotron(RCS) of Japan Proton Accelerator Complex(J-PARC) is providing more than 300 kW of proton beam to Material and Life science Facility(MLF) and Main Ring(MR). Last summer shutdown, a new ion source was installed to increase output power to 1 MW. In order to achieve reliable operation of 1 MW, we need to reduce beam loss as well. Beam quality of such higher output power is also important for users. Therefore we developed new monitors that can measure the halo with higher accuracy. We present beam monitor systems for these purposes.

## INTRODUCTION

The 3 GeV rapid cycling synchrotron (RCS) at the Japan Proton Accelerator Research Complex (J-PARC) is a high-intensity proton synchrotron. It delivers an intense proton beam to the target for neutron production in the Materials and Life Science Experimental Facility (MLF) as well as to the Main Ring (MR) synchrotron at a repetition rate of 25 Hz[1]. The RCS commissioning started since 2007, and output beam power was gradually increased. So far, RCS is providing about 300 kW of proton beam to MLF and MR[2]. Last summer shutdown, we installed a new ion source and radio frequency quadrupole linac to achieve designed output power of 1 MW[3]. In the beam commissioning of October 2014, we achieved 770 kW output with acceptable beam loss[4].

In order to achieve reliable operation of 1 MW, we need to reduce beam loss as well. Beam quality of such higher output power is also important for users. Therefore we developed new monitors that can measure the halo with higher accuracy. At first we present beam monitor systems which are used for the beam commissioning to establish higher power operation. Next we introduce some new monitors to measure the beam halo with higher accuracy and to achieve higher reliability.

## REGULAR MONITORS FOR BEAM COMMISSIONING

The monitor system is important to conduct the beam commissioning. Figure 1 shows RCS parameters and the monitor location. Some parameters of regular monitors are written in a reference[5].

### Beam Position Monitor (BPM)

We prepared 54 BPMs (Normal BPM) to measure a beam orbit in the RCS. Since the physical aperture of the RCS is too large (more than 250mm), it is difficult to

ensure the linear response. In order to clear this issue, we chose the diagonal cut electrode[6]. Figure 2 shows the 3-D model of the BPM head. Three BPMs (ΔR-BPM), which are installed in the arc section of the large dispersion function, are used for RF radial feedback system. We also have extra two BPMs (324BPM) which can detect 324 MHz frequency signal. 324 BPM are used to obtain the information of the injection beam[7].

The normal BPM system has two operation modes. The one mode, so-called "COD mode", is to record the averaged beam position of each 1 ms by the full 25 Hz repetition. The other is to store the whole waveform data of all BPMs for further analysis, like turn-by-turn position calculation (not 25Hz but 1 shot per several seconds).

The position accuracy is estimated to be about 0.5 mm using a newly developed Beam Based Alignment method[8].
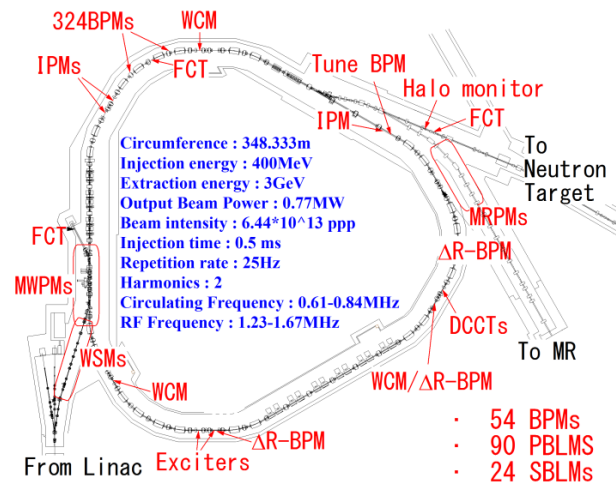


Figure 1: Monitor Layout and RCS parameters.
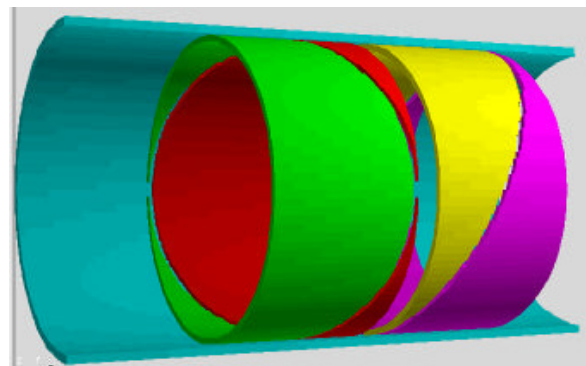


Figure 2: 3-D model of the diagonal cut electrodes.

_____
#kazami@post.j-parc.jp

## Tune Measurement

Transverse betatron tune is one of the important parameter for a synchrotron. To measure the tune value, two exciters and one tune BPM are prepared. Tune BPM has four electrodes for horizontal and vertical tune measurement. Vertical exciter has two electrodes at top and bottom in the vacuum chamber, and horizontal exciter has two electrodes at left and right side in the vacuum chamber. A longitudinal length of exciter electrode is 586mm and an arc length is 200mm. RF amplifiers for the exciters can drive 1 kW RF, and its frequency range is from 100 kHz to 7 MHz. The signal from tune BPM is analyzed by a real time spectrum analyzer and the data is stored in PC. Figure 3 shows the measured and calculated tune during acceleration.
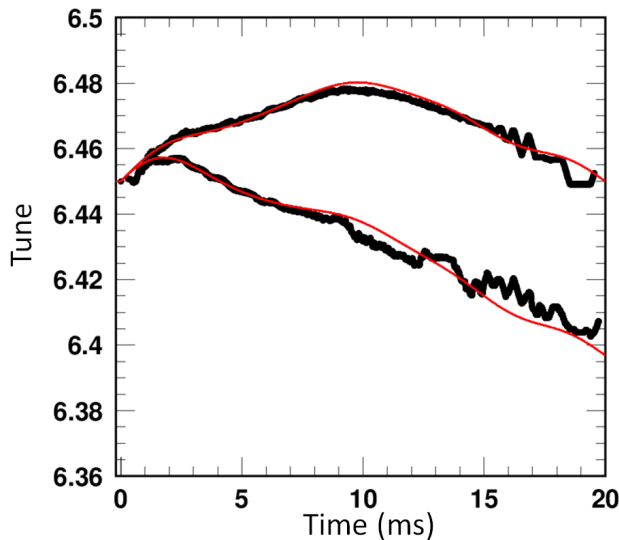


Figure 3: measured and calculated tune during acceleration. Black:measured, Red:calculated

## Current Transformer (CT)

We have two DCCTs to measure the beam current during whole acceleration process. First DCCT was purchased from Bergoz[9], and second one was developed. Second DCCT is made by the FINMET. In both DCCT, Dynamic range is from 150 mA to15 A and the bandwidth is DC to 20kHz. Those inner diameters are 380mm. The accuracies are about 1%.

Three fast CT (FCT) are installed. Those are made by the FINMET. The number of the coil turn is 20 and bandwidth is 2 kHz to10 MHz. Two FCT are used to phase detection for RF, and one FCT measures and limits the beam current to the injection dump[10].

The Wall Current Monitos (WCM) are used to measure the longitudinal profile of the beam. We have three WCS. The shunt impedances of WCM is 0.1 ohm (10 ohm*100 para). We can also obtain the longitudinal tomography by the WCM data.

## Beam Loss Monitor (BLM)

We prepared two kind of BLM. One is the proportional counter (PBLM) and the other is a plastic scintillator connected on a photo multiplier tube (SBLM).

The filling gas of PBLM is Ar-Co2 mixture, and it was purchased from Toshiba Electron Tube Co., Ltd[11]. A total of 90 PBLMs were set up all over the accelerator beam line. These PBLMs are connected with the machine protection system (MPS) and it is always checking that the integration of PBLM signal is not over a preset value. Integration values are also archived at all times and we can check it when some interlock alerted.

SBLM has good time resolution (FWHM is less than 100ns) and its wave form data is used for a comparison between the experiment and simulation. So far, the time structure and the amount of the beam loss are well in agreement with the simulation.

## Ionization Profile Monitor (IPM)

In order to measure the transverse beam profile during the acceleration period, we installed three IPMs as a non-destructive beam monitor. Two IPMs are installed in the dispersive arc section, and one IPM is installed dispersion-free extraction straight insertion.

From the beam test, it found that the external electric field was distorted and the measured beam profile on the ion collection mode was also shrunk to a half [12]. We replaced the electrode, resisters, Micro Channel Plate (MCP) and anode plate. Figure 4 shows New MCP and anode plate. After that the electric field becomes uniform and we can take an beam profile with enough accuracy[13].

Figure 5 shows the IPM measurement result of the injection beam.
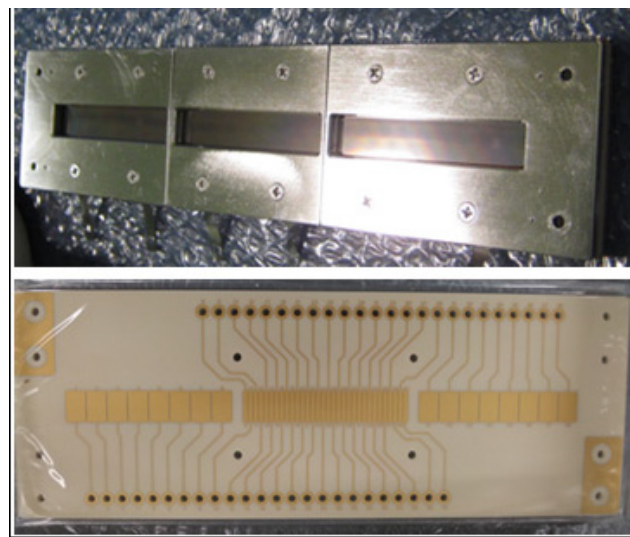


Figure 4: New MCP and anode plate.

## Wire Monitors (WSM, MWPM, MRPM)

The destructive profile monitors, Wire Scan Monitors (WSM)[14], Multi Wire Profile Monitors (MWPM)[15]

and Multi Ribbon Profile Monitors (MRPM)[16] are used at the Linac - 3 GeV RCS Beam Transport (L3BT) line, 3 GeV RCS -50 GeV main ring Beam Transport (3-50BT) line and injection line of RCS. These monitors detect the secondary electron emission from the wires or ribbons. Further information of these monitors is in references.

The MWPM7, which installed in the injection dump line, was used not only to measure the profile, but also to measure the amount of $H^0$ and $H^-$ unstripped particles. Measurement results are shown in reference[17].
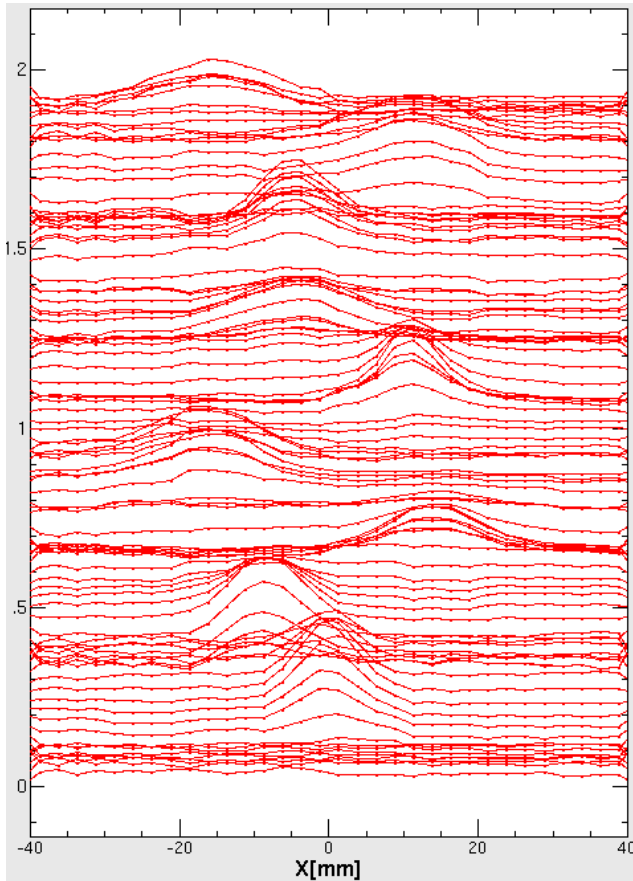


Figure 5: IPM measurement result of the injection beam.

# NEW MONITORS FOR FURTHER SAFETY/QUALITY OF THE BEAM

## Monitors for Safety/Stable Operation

The radiation leak accident was happened in the hadron experimental hall at J-PARC on May 23, 2013. The accident was caused by a target sublimation due to an abnormal beam extraction from the main ring[18]. From this accident, we think we have to improve the monitoring systems and interlocks to prevent and rapidly detect the radiation leakage. In the RCS, we installed two new systems. First one is the real time monitoring system of the beam profile on the mercury target. In this system, we can check the beam profile on the mercury target by multi wire monitor when some interlock alerts. Figure 6 shows the measured profile on the mercury target. Second new

system is fast interlock of linac CT. In this new interlock, the beam is stopped immediately when the beam current exceed the limit.

These new systems provide us more safety and stable operation.
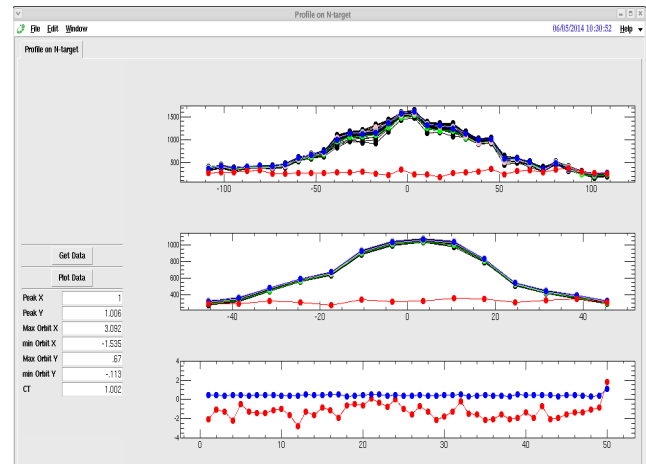


Figure 6: The beam profiles on the mercury target.

## Injection Beam Halo Monitors

The halo of the injection beam is a source of the beam loss in RCS. We tested two kind of monitors to measure the injection beam halo[19]. The one is the Vibration Wire Monitor (VWM), and the other is the monitor by using the L3BT scrapers, SBLM and CT.

The VWM was purchased from Bergoz. The principle of the VWM is to detect the eigen frequency shift that induced by the temperature rise due to the beam hitting of the wire. The wire is made by sus316L and its diameter is 0.1mm. We tested VWM to measure injection beam profile, but we cannot take data at some frequency regions. We think perhaps electric circuit has some problem and now we try to improve it.

The schematic of the halo monitor system by L3BT scraper is shown in Figure 7. The L3BT scrapers are located downstream in the linac. The J-PARC linac accelerates negative hydrogen beam for the charge-exchange injection of RCS. The L3BT scraper removes two electrons from the negative hydrogen, and scraped halo beam that was converted to the proton is transported to the 100 deg. dump. Therefore we can measure the amount of the scraped halo beam by the SBLM located near the scraper. A beam current of the scraped halo beam is also measured by the CT at the 100 deg. dump line. This system has two advantages. The first advantage is the redundancy by two kind of monitors which measures in another principle. The second advantage is absolute value measurement by the CT. In the usual case, the amount of the halo is measured as a relative value of the amount of the core beam. But this system can directly measure the amount of the halo. Figure 8 shows the measurement result of this system. Measured results are consistent, and the SBLM and the CT are able to detect

the halo of ten to the minus fourth power order of magnitude to the core beam.
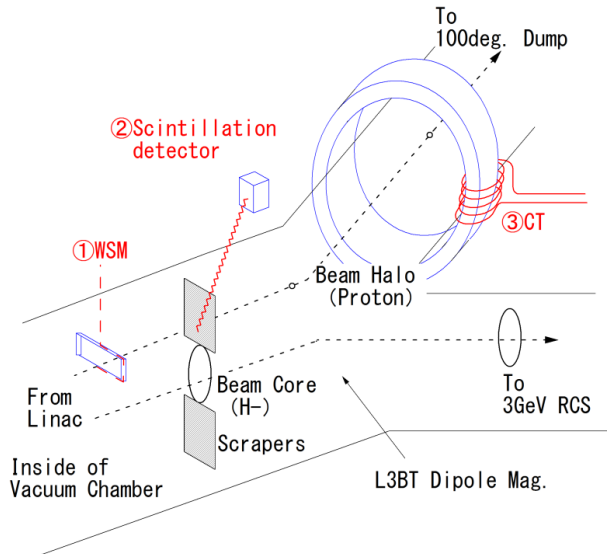


Figure 7: Schematic of the monitor system by the L3BT scraper.
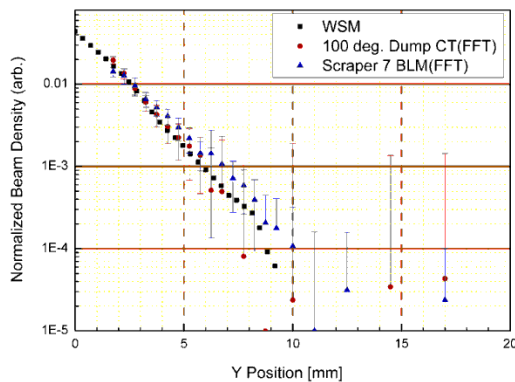


Figure 8: Measurement results of the monitor system by the L3BT scraper.

*Extraction Beam Halo Monitors*

Two kinds of monitors were developed to reduce the beam loss of MR by the halo of the RCS extraction beam.

The first one, Optical Transition Radiation (OTR) monitor, is installed in the 3-50 BT line. To achieve a large dynamic range, a multi-screen system is adopted. By using this system, the halo of ten to the power of minus six to the peak of beam core can be observed[20].

The second monitor is similar to L3BT scraper system. This system consists of a wire type beam scraper and some beam loss monitors. To use some kinds of SBLM with different sensitivities, it has wide dynamic range. Beam profile including both of the beam core and halo can be measured.

Measurement results are shown in references[21][22].

*Delayed Proton Monitor for μ-e Conversion Measurement*

DeeMe (Direct electron emission measurement for Mu-e conversion) experiment, proposed at MLF, is planned to find μ-e conversion process on the muon production target[23]. In order to distinguish the μ-e event signal from a background, the number of delayed protons (we call such delayed proton "after-proton") that come after hundreds of nanoseconds from the main beam should be less than ten to the power of minus eighteen order of magnitude. This corresponds that only few after-protons are allowed within 1 hour operation. Figure 9 shows the measurement time window of DeeMe. It is impossible to measure such slight protons by an ordinary monitor. Thus, in order to develop a new measurement system for the background evaluation, we considered what particle becomes the after-proton.
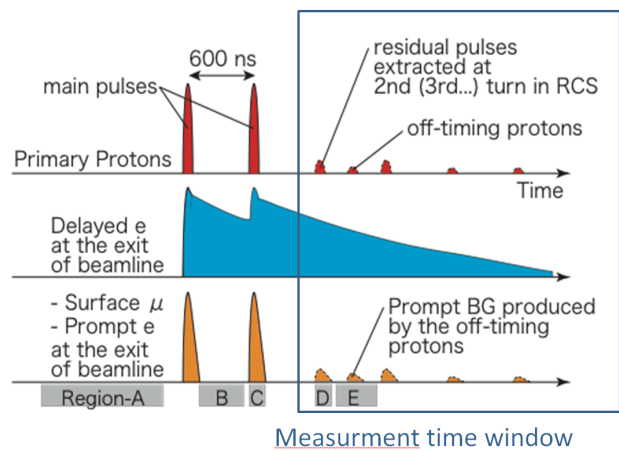


Figure 9: Measurement time window of DeeMe.

If the after-proton exists, the proton have to remain after extraction of the two main bunches and it needs to extract without the pulse kicker magnetic fields. This fact means that the after-proton must have extremely larger emittance than the normal beam. Orbit calculation result indicated that the protons with 2500 πmm-mrad. emittance can partially extract, and some particles hit the branch chamber in that case. Therefore we can detect the existence of the after-proton by monitoring the protons that are scattered at the branch chamber.

We simulated scattered proton trajectories by G4Beamline code[24]. Here we assumed from 324π to 5000π mm-mrad. emittance uniform beam. Figure 10 shows the geometry and the proton trajectories in the simulation. The simulation result showed that the ratio of the number of the proton that hit the outside scintillators (two green plates in Fig. 10) to the number of the proton that pass through the 3NBT line is 0.025. We set up two SBLMs like the simulation model, and measured the scattered protons. Measurement was carried out from Mar. 7, 2013 to May 25, 2013. During this operation period, the total coincident counts in the time window are 87. On the other hand, total extracted protons are

$3.13*10^{21}$. By using these values, we can obtain the after-proton rate of $1.1*10^{-18}$. This almost satisfies the requirement.
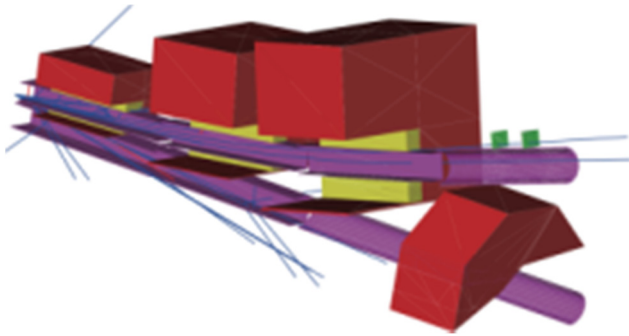


Figure 10: simulation result of after-proton.

## CONCLUSION

We demonstrated 770 kW beam in October 2014. Since regular monitors worked well, so far we understand the characteristics of the beam. Since regular monitors worked well, so far we understand the characteristics of the beam. To establish further stable and safety operation, some monitors and interlocks are improved. To reduce the beam loss, high sensitive halo monitors are developed.

## REFERENCES

[1] Y. Yamazaki ed., "Technical design report of J-PARC", KEK Report 2002-13; JAERI-Tech 2003-44

[2] K.Yamamoto et al., "Residual doses by 400 MeV injection energy at J-PARC rapid cycling synchrotron", Proc. IPAC'14, THPME063, (2014).

[3] K.Yamamoto, "The path to 1 MW at J-PARC, including 400 MeV linac improvement, RCS improvements, and plans for front end upgrades", Proc. ICANS XXI, ABT-01, (2014).

[4] H. Hotchi, "Lessons from 1-MW Proton RCS Beam Tuning", in these proceedings, (2014).

[5] N. Hayashi et al., "Beam instrumentations for the J-PARC RCS commissioning", Proc.EPAC'08, TUPC034, (2008).

[6] N. Hayashi et al., "The Beam Position Monitor System of the J-PARC RCS", Proc.EPAC'08, TUPC035, (2008).

[7] N. Hayashi et al., "Performance of injection beam position monitors in the J-PARC RCS", Proc. IBIC'13, WEPC19, (2013).

[8] N. Hayashi et al., "Beam position monitor system of J-PARC RCS", Nucl. Instrum. Meth A 677(2012), p. 94-106

[9] Bergoz, BDCCT-S-380-H.

[10] P.K. Saha. et. al., "State of the art online monitoring system for the waste beam in the rapid cycling synchrotron of the Japan Proton Accelerator Research Complex", Phys. Rev. ST Accel. Beams 14, 072801 (2011).

[11] Toshiba Electron Tube Co., Ltd. http://www.toshiba-tetd.co.jp

[12] K. Satou et al., "IPM systems for J-PARC RCS and MR", Proc.HB2010, WEO1C05, (2010).

[13] H. Harada et al., "Ionization Profile Monitor (IPM) of J-PARC 3-GeV RCS", Proc. IPAC'13, MOPME021, (2013).

[14] A. Miura et al., "Operational Performance of wire scan monitor in J-PARC Linac", Proc. IPAC'10, MOPE021, (2010).

[15] S. Hiroki et al., "Multi-wire profile monitor for J-PARC 3 GeV RCS", Proc. EPAC'08, TUPC036, (2008).

[16] Y. Hashimoto et al., "Multi-Ribbon Profile Monitor Using Carbon Graphite Foil for J-PARC", Proc.HB2010, WEO2A01, (2010).

[17] P. K. Saha et al., "Advanced uses of a current transformer and a multi-wire profile monitor for online monitoring of the stripper foil degradation in the 3-GeV RCS of J-PARC", Proc. IBIC'13, MOPF15, (2013).

[18] T. Koseki, "Present Status of J-PARC - after the Shutdown due to the Radioactive Material Leak Accident-", Proc. IPAC'14, THPME061, (2014).

[19] K. Okabe et al., "Feasibility studies of a vibration wire monitor and a halo scraper in the J-PARC L3BT", J. Korean Phys. Soc., **63**, p.1379 (2013).

[20] Y. Hashimoto et al., "A development of high sensitive beam profile monitor using multi-screen", Proc. IBIC'13, MOPF15, (2013).

[21] Y. Hashimoto et al., "Two-dimensional and wide dynamic range profile monitor using OTR /fluorescence screens for diagnosing beam halo of intense proton beams", in these proceedings, (2014).

[22] M. Yoshimto, et. al., "Beam halo measurement using a combination of a wire scanner type beam scraper and some beam loss monitors in J-PARC 3-GeV RCS", in these proceedings, (2014).

[23] Y. Nakatsugawa, "Experimental Search for ·-e Conversion in Nuclear Field at J-PARC MLF H-Line", Proc. NuFact2013, (2013).

[24] http://www.muonsinternal.com/muons3/G4beamline

# BEAM DIAGNOSTIC CHALLENGES FOR
# HIGH ENERGY HADRON COLLIDERS

E. B. Holzer*, CERN, Geneva, Switzerland

## Abstract

Two high energy hadron colliders are currently in the operational phase of their life-cycle, RHIC and LHC. A major upgrade of the LHC, HL-LHC, planned for 2023 aims at accumulating ten times the design integrated luminosity by 2035. Still further in the future, studies in the frameworks of the Future Circulating Collider (FCC) and the Super Proton Proton Collider (SppC) are investigating machines with a center-of-mass energy of up to 100 TeV and with up to 100 km circumference. The existing machines already pose considerable diagnostic challenges, which will become even more critical with any increase in size and energy. Cryogenic environments lead to additional difficulties for diagnostics and further limit the applicability of intercepting devices, making non-invasive profile and halo measurements essential. The sheer size of these colliders requires the use of radiation tolerant read-out electronics in the tunnel and low noise, low loss signal transmission. It also implies a very large number of beam position and loss monitors, all of which have to be highly reliable. To fully understand the machine and tackle beam instabilities, bunch-by-bunch and intra-bunch measurements become increasingly important for all diagnostic systems. This contribution discusses current developments in the field.

## INTRODUCTION

The Relativistic Heavy Ion Collider (RHIC) is operating since the year 2000. It accelerates various ion species for symmetric and asymmetric collisions. Furthermore, it has the unique capability of colliding high energy polarized protons to study the spin structure of the proton. The Large Hadron Collider (LHC) is operational since 2009, mostly running p-p collisions, and for four weeks per operational year Pb-Pb or p-Pb collisions. While the maximum RHIC beam energy is 100 GeV/n for ions and 255 GeV for protons, the LHC was running at 3.5 and 4 TeV and is scheduled to run at 6.5–7 TeV beam energy in the coming years. The average beam current at RHIC is well above 100 mA for almost all ions, while at LHC it is around half an Ampere for proton, but much lower for lead ions. The peak luminosity as well as the integrated luminosity per year for heavy ion collisions at LHC is considerably lower than at RHIC. With its proton luminosities, on the other hand, LHC is unmatched with $7.7 \times 10^{33}$ cm$^{-2}$s$^{-1}$. Table 1 (top) gives an overview of RHIC and LHC parameters. The estimated performance is shown for the LHC Run2, which starts in 2015 after the current long shutdown 1 (LS1), and for the planned luminosity upgrade HL-LHC (High Luminosity LHC). HL-LHC is scheduled for Pb ions for 2020, at the start of Run3, and

* barbara.holzer@cern.ch

for protons for 2025, at the start of Run4. LHC beam instrumentation experiences during Run1 and challenges for Run2 are discussed in [1] and [2] respectively.

Looking still further in the future, there are currently two studies for hadron colliders, the FCC-hh and the SppC. Bother studies include as a potential intermediate step an electron-positron collider in the same tunnel, called FCC-ee and Circular Electron-Positron Collider (CEPC) respectively. The FCC-hh study considers p-p, Pb-Pb and p-Pb collisions, the SppC p-p collisions. With an envisaged circumference of 80 or 100 km the FCC is somewhat larger than the SppC with 50–70 km. Physics start date (2035–2042), beam energy (25–50) TeV/n and beam current (≈0.5 A) are rather comparable. Table 1 (bottom) summarizes parameters under consideration.

## STORED ENERGY

The energy stored in one LHC beam has reached the record level of 140 MJ during the 4 TeV run. 362 MJ are expected at 7 TeV, 694 MJ at HL-LHC and even 8 GJ for FCC-hh. 10 GJ will be contained in the LHC magnets at 7 TeV. Already one LHC pilot bunch of $5 \times 10^9$ is close to damage limits at 7 TeV. The machine protection system is vital for the survival of these colliders, and must be integrated with the machine design. A dependability analysis comprises reliability, availability, maintainability and safety. It yields the allowed budgets for each subsystem in terms of: probability of component damage due to malfunctioning; downtime due to false alarms; and downtime due to maintenance. There is an inherent conflict between these budgets. By reducing the damage probability (increasing protection) the machine availability will go down due to increased numbers of false dumps and maintenance time. Several beam instrumentation systems are/will be part of machine protection, e. g. beam loss measurement (BLM), beam position measurement (BPM) at critical locations, and a fast measurement of the beam current change.

### Beam Cleaning and Losses

The collimation system gets increasingly complex with increasing beam energy and brightness. At the LHC there are already more than 100 collimators installed. At the same time the tolerance for collimator set-up becomes tighter. LHC has installed 18 new collimators with embedded BPM buttons at the tapered ends of both collimator jaws, retracted by 10.6 mm from jaw surface. The new design was successfully tested at the CERN SPS. The readout is via a newly designed compensated diode peak detector electronics. It achieves an excellent resolution of less than 100 nm for centered beams [3]. With this system the collimator alignment will take less than 20 s with an achieved tolerance

Table 1: High Energy Hadron Colliders, Top: Current, Bottom: Studies (Parameters under Consideration)

|  |  | Circum-ference [km] | Physics Start | Maximum Beam Energy [TeV/n] | Average Beam Current [mA] | Peak Luminosity [cm$^{-2}$s$^{-1}$] |
|---|---|---|---|---|---|---|
| **RHIC** (Brookhaven) | pp pol. | 3.8 | 2001 | 0.255 | 257 | $2.1\times10^{32}$ |
|  | AuAu |  | 2000 | 0.1 | 145 | $8.4\times10^{27}$ |
| **LHC** (CERN) | pp | 26.7 | 2009 | 3.5–4 | 400 | $7.7\times10^{33}$ |
|  | pp |  | 2015 | 6.5–7 | 580 | $1–2\times10^{33}$ |
|  | PbPb (pPb in 2012) |  | 2010 | 1.38 | 6.8 | $0.5\times10^{33}$ |
|  | PbPb |  | 2015 | 2.76 | 7.4 | $1\times10^{33}$ (lev.) |
| **HL-LHC** (CERN) | pp | 26.7 | 2025+ | 7 | 1200 | $5\times10^{34}$ (lev.) |
|  | PbPb |  | 2020 | 2.76 | 22 | up to $7\times10^{33}$ |
| **FCC-hh** | pp | 100 (80) | 2035–2040+ | 50 | 0.5 | $5\times10^{34}$ (lev.) |
| **SppC** | pp | 50–70 | 2042+ | 25–45 | 0.4–0.5 | $2–3\times10^{35}$ |

of 10 $\mu$m [4]. It can be done in parallel for all equipped collimators and without touching the beam. The set-up is two orders of magnitude faster than with the BLM method, where the center of the beam is found by scraping into its tails. The validation of the correct collimator positioning requires the measurement of 'loss maps' with controlled beam blow-up in dedicated low intensity fills, where the leakage of collimation losses into the rest of the machine is measured with the BLM system. The embedded BPMs make constant monitoring of beam to jaw position possible. Hence, tighter collimator settings due to reduced safety margins allow for smaller $\beta^*$ at the experiments, resulting in higher luminosity. As the intensities increase, uncontrolled losses of even the beam halo have to be avoided. Beam size measurements have to evolve in terms of dynamic range to monitor the halo and aid in understanding the mechanisms of its formation. Details of halo monitoring are discussed in this workshop [5] and in previous workshops and schools [6–8].

Beam loss monitoring is one of the key systems in machine protection. When potentially dangerous levels of losses are detected the beam is safely aborted. A system with individual, localized loss monitors is best suited for time and position resolution. On the other hand, all loss locations can not necessarily be predicted at the design stage of an accelerator. At the LHC about one third of the BLMs had to be relocated during LS1, to cover the circumference of the machine more uniformly. During beam operation previously unconsidered beam losses, dubbed 'UFO' losses, had appeared in high numbers all along the machine, also in the cold dipole magnets which had not been equipped with BLMs during Run1. These losses are believed to be caused by beam - dust interactions. Simulations and measurements suggest that at 7 TeV they can quench a magnet. Long, distributed loss monitors would avoid holes in the protection system. The number of monitors and readout channels could be significantly reduced, also reducing the cost. Optical loss monitoring based on the Cherenkov effect in fibers, or indi-

vidual crystals, is insensitive to synchrotron radiation, which will be copious in machines like the FCC-hh. Noise due to electromagnetic interference can be avoided with optical measurements. At the LHC, significant losses anywhere in the machine are always visible as well at the collimators. At this location the timing of the loss is resolved by a bunch-by-bunch loss measurement, using diamond BLMs with few ns time resolution. To be able to use fiber loss monitors for machine protection, further R&D work is required, in particular for absolute measurements and position and time resolution.

## NON-INVASIVE TRANSVERSE PROFILE MEASUREMENTS

Practically all measurements have to be non-invasive to the beam. This is a particular challenge for transverse profile/emittance measurement. Most non-invasive devices are affected by systematic effects which increase in magnitude with higher brightness and/or smaller physical beam sizes, and often require cross calibration. Absolute profile measurements are nevertheless possible, at least theoretically, with detailed study, and correction procedures. At LHC to date the wire scanner is the only means of absolute beam size measurement. All other profile measurements have to be calibrated against the wire scanner. At injection energy, 450 GeV, a full injection batch of 288 proton bunches will break the wire, the operational limit is about $2.7 \times 10^{13}$ protons. At top energy the limit of $2.7 \times 10^{12}$ corresponds to about 20 bunches [9]. At this energy quenching of an adjacent cold magnet limits the beam intensity. The crossover of these two regimes was calculated to be around 4 TeV. Wire aging is dominated by sublimation. A dedicated low intensity run is required to calibrate the other profile/emittance measurements. In addition to the systems mentioned below, other promising or proven devices for (quasi) non-invasive measurements are electron beam scanners, gas screen or gas pencil beams.

**Instrumentations and Beam Material Interactions**

## Ionization Profile Monitors (IPM)

RHIC and LHC are equipped with IPMs for both beams and both planes.

IPM measurements in RHIC date back to 1999. After successive design improvements, a new design was put into operation in 2008. The improvements included shielding from upstream losses and electron cloud, increased homogeneity of the electric field, fast signal gating to reduce aging of the multichannel plate (MCP) and shielding the readout electronics, including the MCP, from the beam's image current by putting them in a Faraday cage. Electrons from beam–rest gas interactions are accelerated towards the MCP by an electric field, and guided by a magnetic field, parallel to the electric field. The signal is amplified in the MCP and collected on an anode consisting of 64 strips oriented parallel to the beam axis. Remaining systematic effects could be traced to offset and gain variations between the readout channels and imprecise knowledge of the beam beta functions. A set of calibration measurements, scanning the beam position over the active detector region was used to determine channel offsets. Then, an elaborate calibration procedure for each individual channel gain, described in [10], was performed on the offset corrected profiles, whereby the best gain value was found by minimizing the $\chi^2$s of the Gaussian profile fits. Measurements of the beta functions at the monitor locations for Au-Au at store energy revealed a deviation of the optics model of +8% to -36%. All the corrections applied, absolute emittance measurements are achieved. This could be demonstrated by excellent agreement between horizontal and vertical emittances of both beams under optimized 3D stochastic cooling and by an agreement within 15% with the emittances measured by the experiments STAR and PHENIX [11].

The LHC IPM uses injected Ne gas for signal enhancement and a magnetic guide field of 0.2 T. The electrons created in the beam–gas interactions are accelerated towards an MCP and amplified. A radiation hard camera acquires the optical signal from a phosphor screen behind the MCP [12]. The monitor was primarily designed for the Pb beams, which emit very little synchrotron light at injection energy. The IPM works well in all Pb conditions. The proton profile agrees with wire scanner measurements only at 450 GeV. As the energy increases and the beam size shrinks, the profile is broadened by the space charge of the bunch. This distortion eventually dominates the measurement. Simulations show that increasing the magnetic field to 1 T would solve this problem, but it was not possible to install such a magnet during LS1. Efforts are undertaken to develop a deconvolution algorithm for profile reconstruction [13].

## Beam Gas Vertex Monitor (BGV)

The LHCb experiment performed special runs with gas injection to measure 3D beam profiles for absolute luminosity determination during Run1. The inelastic beam gas interactions were reconstructed using the LHCb vertex detector [14]. Based on this concept, the BGV is developed in collaboration with LHCb (CERN), EPFL Lausanne (Switzerland) and RWTH Aachen (Germany) [15]. It uses the LHCb monte-carlo and track reconstruction framework as well as scintillating fiber tracking detectors with SiPMs readout developed for the LHCb vertex detector upgrade [16]. The BGV is being designed to measure absolute values of beam position, angle, profile and relative bunch populations during all of the LHC cycle, unlike the vertex detectors of the experiments, which can only operate during stable beams. It applies a controlled Neon gas pressure bump for sufficient event rate. A prototype is currently being installed at the LHC. The final specifications are to provide within one minute 5% accuracy on the relative bunch width measurement and 2% accuracy on the absolute average beam width. The prototype was designed for providing the same 5% accuracy on the relative bunch width measurement but with an increased measurement interval of five minutes and a relaxed 10% accuracy within one minute.

## LHC Synchrotron Light Monitor

At top energy, the imaging of the synchrotron light will be dominated by diffraction. Even with the newly chosen UV wavelength of 250 nm, the contribution from diffraction is estimated to be around 250 $\mu$m compared to a beam size of 180 $\mu$m. Absolute beam size measurement will be very challenging in these conditions. Therefore, interferometric measurement will be performed in parallel, using a new optical line which was designed in collaboration with KEK (Japan), SLAC (US) and CELLS-ALBA (Spain) [17]. This technique is based on diffraction rather than being limited by it. The beam size can be inferred from the visibility of the interference pattern.

## Transverse Schottky Measurements

Both RHIC and LHC are equipped with a Schottky system to measure transverse beam parameters. The RHIC detector is a high frequency cavity operated at 2.07 GHz. At CERN a slotted waveguide pick-up operates at 4.8 GHz. The operating frequency has to be high enough for the coherent signals not to dominate the measurements, and low enough that the bands do not overlap. The readout consists in both cases of several stages of filtering, amplification and down-mixing. The CERN system has 25 ns gating for individual bunch measurements, while the RHIC cavity can only provide averaged results.

The RHIC cavity has also been used for completely non-invasive transverse beam size measurements [18]. In this method the cavity is moved transversely to the beam in a range of a few cm, recording the signals at each position. The power measured in the Schottky band around the revolution harmonics (excluding the sharp coherent peak) is compared to the sum of the power in the two betatron side-bands. The first one is proportional to the square of the distance of the orbit from the center of the cavity. The second one is independent of this distance, but proportional to the square of the rms beam size. Hence, an absolute value of the rms beam size can be derived for these measurements. The uncertainty

on the emittance measurement reported is 2009 was 20 %. A noticeable reduction in this uncertainty could be possible by using the measured beta function rather than the model and improving the algorithm for extracting the power from the spectrum. Also the improved orbit stability, due to the correction for the 10 Hz triplet vibrations, should reduce the systematic error.

The LHC system aims to provide on-line chromaticity and bunch-by-bunch tune measurements. These measurement were achieved during Run1 for ion beams, where the power in the Schottky bands scales with the square of the ion charge. Proton measurements on the other hand were plagued by large coherent signals at the revolution frequency band and at the betatron bands. The controlled longitudinal beam blow up during the proton ramp makes the signal disappear completely. During LS1, the pick-up design has been modified to avoid deformations, which were seen in Run1. The read-out system will be improved as well.

## MACHINE SIZE, RADIATION AND CRYOGENIC TEMPERATURES

The increase in machine length in itself poses considerable challenges for beam instrumentation, and in particular for the BLM and BPM systems. The number of their monitors increases in proportion to the number of optics cells. The cost increases, but also system maintenance and availability becomes increasingly challenging. More data is produced by the instruments, which needs to be extracted, logged, monitored, analyzed and made available for various online and offline applications. Because of the long distances involved, to keep electromagnetic interferences small, the front-end read-out electronics is often positioned in the accelerator tunnel, close to the instrument. In this case it has to be radiation tolerant, which considerably complicates design and production. To transport the signal to the surface requires low noise, low loss signal transmission. Optical signal transmission and optical diagnostic techniques are preferable in such conditions.

Collimation regions, the vicinity of the interaction points, regions of beam injection and beam extraction have particularly high levels of radiation. This poses i. a. a problem for beam loss monitoring, as a typical loss monitor cannot distinguish between a beam loss and other sources of radiation.

A cryogenic environment makes beam monitoring considerably more complex. BPMs and certain BLMs need to be installed inside the cryostat. Again, this calls for very high dependability of the systems. By placing the loss monitor inside the cryostat, it is closer to the loss location and at the same time shielded from other radiation source. This way it can protect the magnet from quenching due to beam loss even in high radiation areas. Three different technologies are investigated at CERN, liquid helium, silicon and diamond. Prototypes have been installed in the LHC during LS1.

## IMPROVING THE PERFORMANCE

New machines with higher energy and brightness require several beam instrumentation systems to improve in performance, e. g. BPM stability, resolution and precision for fast feedback systems and transverse damping. The same holds for pushing existing machines to higher luminosities. The colliders crucially depend on feed-back systems, on systems which damp beam instabilities and/or on beam cooling. RHIC's orbit, tune and coupling feed-backs were a key to higher luminosities, polarization and integrated luminosity/uptime [19]. During Run1, LHC used an orbit feed-back and during certain periods of the cycle also a tune feed-back. Bunch-by-bunch and intra-bunch measurements are required to diagnose, and eventually avoid, beam instabilities. This section collects a number of recent instrumentation improvements and some which are planned for the near future.

### Intra-Bunch Measurements

A new Multiband Instability Monitor (MIM) for the LHC is being developed [20]. It uses a broadband stripline pick-up. 16 narrow frequency bands spaced by 400 MHz, covering the frequency range of 0.4–6.4 GHz, are individually monitored. When a bunch starts to oscillate, it's frequency spectrum changes to reflect the oscillation modes of the bunch. The amplitude and phase information of these 16 frequencies might, at a later stage, be used to reconstruct the intra-bunch motion in the time domain. For the time being it is planned to use the MIM to trigger the high rate acquisitions of other systems which can measure instabilities, e. g. the transverse damper system, bunch-by-bunch emittance and intensity measurements and the head-tail monitor. The head-tail monitor shares the same pick-up and uses a wideband oscilloscope to measure in the time domain. The higher sensitivity of the MIM should allow to detect sub-micron oscillations.

### Wall Current Transformer (WCT)

A new fast beam current transformer has been developed at CERN for Run2. It aims to improve the bunch-by-bunch resolution, and remove the dependency on beam position and bunch length observed during Run1 [21]. It is designed for a bandwidth of up to $\approx$100 MHz, for a position dependence of less than 0.1 %/mm and for a bunch length dependence of 0.1 %.

### Electron Back-Scattering Detector (eBSD)

To attain higher polarized proton luminosities in RHIC, partial compensation of the beam-beam effect is planned with the help of electron lenses [22]. A low energy ($\approx$6 keV) and high intensity ($\approx$1 A) electron beam moving in the opposite direction is mixed with the proton beam over a 2 m long interaction region within a field of $\approx$6 T. The two beams are approximately $300\mu$m rms and their centers need to be aligned to less than 30–50$\mu$m. The eBSD [23] is a new measurement device for the precise alignment of the two beams. It was successfully commissioned in 2014 with ion

beams. Back-scattered electrons are intercepted by a small plastic scintillator in the vicinity of the electron gun. A 1.2 m long light-guide leads to a magnetically shielded photomultiplier tube. An automatic procedure aligns the two beams by maximizing the eBSD counting rates. The alignment is based on a program for maximizing luminosities at the RHIC experiments. An eBSD could possibly be used for hollow electron lens alignment [24]. A hollow electron lens is considered as an option for beam collimation for HL-LHC in the framework of the LARP collaboration.

## WAKEFIELDS AND RF HEATING

In order to limit beam instabilities, the impedance budgets are very strict, in particular for numerous devices like the BPMs. Also for the survival of the instrument a careful management of the beam induced wake functions is crucial. Several LHC system suffered strong heating during Run1 [25]. Injection kickers and forward physics experiments overheated. The beam screen of the injection protection system deformed. RF contact fingers at magnetic interconnects and the extraction mirror of the synchrotron light monitor were heated to the point of failure [26]. The redesigned extraction mirror couples much less to the beam, and the heat dissipation via conduction and radiation should now be sufficient. By installing a camera in the RHIC polarimeter, strong RF heating was discovered at the ends of the thin carbon wire when well outside the beam and even in parking position, explaining the frequent wire breakages [27]. The addition of field-intercepting "fins" have been shown to reduce the heating.

All new instruments installed on the beam have to be validated by EM simulations and/or laboratory test. The incorporation of temperature sensors will be advisable for certain devices. Heating effects can often be observed indirectly by vacuum degradation, increased beam losses or degraded performance of the device. Possibilities for mitigation include: design changes to reduce the build-up of wake fields; adding ferrites to absorb the RF power given there is sufficient cooling for the ferrites; or using multi-mode couplers to extract the power and dissipate it outside of the beam vacuum.

## ACKNOWLEDGMENT

## REFERENCES

[1] R. Jones, "The Beam Instrumentation and Diagnostics Challenges for LHC Operation at High Energy", IBIC2014, Monterey, CA USA (2014).

[2] R. Jones, "First Years Experience of LHC Beam Instrumentation", IPAC2011, San Sebastian, Spain, (2011).

[3] M. Gasior et al., "BPM electronics based on compensated diode detectors - results from development systems", BIW12, Newport News, USA (2012).

[4] G. Valentino et al., "Development and Beam Tests of an Automatic Algorithm for Alignment of LHC Collimators with Embedded BPM", THPFI063, IPAC2013, Shanghai, China (2013).

[5] K. Wittenburg, "Beam Diagnostics for the Detection and Understanding of Beam Halo", *These Proceedings*, HB2014, East Lansing, USA (2014).

[6] Workshop on Beam Halo Monitoring, SLAC, USA (2014), `https://portal.slac.stanford.edu/sites/conf_public/bhm_2014/Pages/default.aspx`

[7] K. Wittenburg, "Beam Halo and Bunch Purity Monitoring", CAS on beam Diagnostics, Dourdan, CERN-2009-005 (2009).

[8] 29th ICFA Advanced Beam Dynamics Workshop on Beam Halo Dynamics, Diagnostics, and Collimation, HALO'03, Montauk, Long Island, New York (2003).

[9] M. Sapinski et al., "Carbon Fiber Damage in Particle Beam", HB2010, Morschach, Switzerland, (2010).

[10] R. Connolly et al., "Summary of experience with IPM measurements at BNL-RHIC", 9th DITANET Topical Workshop on Non-Invasive Beam Size Measurement for High Brightness Proton and Heavy Ion Accelerators, CERN, Switzerland (2013), `https://indico.cern.ch/event/229959/`

[11] M. Minty et al., "Absolute Beam Emittance Measurements at RHIC using Ionization Profile Monitors", IBIC2014, Monterey, CA USA, MOPF09 (2014).

[12] M. Sapinski et al., "The first experience with the Beam Gas Ionization Monitor", IBI2012, Tsukuba, Japan, (2012).

[13] M. Sapinski et al., "Investigation of the Effect of Beam Space-charge on Electron Trajectories in Ionization Profile Monitors", *These Proceedings*, HB2014, East Lansing, USA (2014).

[14] LHCb Collaboration, J. Instrum. 7 P01010 (2012).

[15] P. Hochev et al., "A Beam Gas Vertex detector for beam size measurement in the LHC", IPAC14, Dresden, Germany (2014).

[16] M. Ferro-Luzzi, Nucl. Instrum. Methods Phys. Res., Sect. A 553, 388 (2005).

[17] G. Trad, "A Novel Approach to Synchrotron Radiation Simulation", IPAC14, Dresden, Germany, (2014).

[18] K. A. Brown et al., "Measuring transverse beam emittance using a 2.07 GHz movable Schottky cavity at the Relativistic Heavy Ion Collider", Phys. Rev. ST Accel. Beams 12, 012801 (2009).

[19] M. Minty et al., "Precision Beam Instrumentation and Feedback-Based Beam Control at RHIC", IPAC11, San Sebastian, Spain, MOPO022 (2011).

[20] R. Steinhagen, "A Multiband-Instability-Monitor for High-Frequency Intra-Bunch Beam Diagnostics", IBIC13, Oxford, UK, (2013).

[21] J.-J. Gras et al., "Optimization of the LHC Beam Current Transformers for Accurate Luminosity Determination", IPAC11, San Sebastian, Spain, (2011).

[22] W. Fischer et al., "First Experience with Electron Lenses for Beam-Beam Compensation in RHIC", IPAC2014, Dresden, Germany, TUYA01, (2014).

**ISBN 978-3-95450-173-1**

[23] P. Thieberger et al., "The Electron Backscattering Detector (eBSD), a new tool for the precise mutual alignment of the electron and ion beams in electron lenses", IBIC2014, Monterey, CA USA, MOPD02, (2014).

[24] P. Thieberger et al., "Scattered electrons as possible probes for beam halo diagnostics", Workshop on Beam Halo Monitoring, SLAC, USA (2014), for url see [6].

[25] B. Salvant et al., "Update on Beam Induced RF Heating in the LHC", TUPME032, IPAC13, Shanghai, China (2013).

[26] F. Roncarolo et al., "Electromagnetic coupling between high intensity LHC beams and the synchrotron radiation monitor light extraction system", IPAC13, Shanghai, China (2013).

[27] H. Huang et al., "RHIC p-Carbon polarimeter target lifetime issue", IBIC2014, Monterey, CA USA (2014).

# EMITTANCE TRANSFER IN LINACS

L. Groening, X. Chen, M. Maier, O.K. Kester, GSI, D-64291 Darmstadt, Germany

M. Chung, Ulsan National Institute of Science and Technology, Ulsan 698-798, Republic of Korea

## Abstract

Flat beams feature unequal emittances in the horizontal and vertical phase space. Such beams were created successfully in electron machines by applying effective stand-alone solenoid fringe fields in the electron gun. This contribution is an extension of the method to ion beams and on the decoupling capabilities of such a round-to-flat adaptor. The beam line provides a single-knob tool to partition the horizontal and vertical rms emittances, while keeping the product of the two emittances constant as well as the transverse rms Twiss parameters ($\beta_{x,y}$ and $\alpha_{x,y}$) in both planes. This single knob is the solenoid field strength. The successful commissioning of the set-up with beam will be presented as well.

## INTRODUCTION

Transformation of a round beam (equal transverse emittances) to a flat beam (different transverse emittances) requires changing the beam eigen-emittances. The eigen-emittances are defined through the beam second moments as

$$\varepsilon_1 = \frac{1}{2}\sqrt{-tr[(CJ)^2] + \sqrt{tr^2[(CJ)^2] - 16det(C)}} \quad (1)$$

$$\varepsilon_2 = \frac{1}{2}\sqrt{-tr[(CJ)^2] - \sqrt{tr^2[(CJ)^2] - 16det(C)}}, \quad (2)$$

where

$$C = \begin{bmatrix} \langle xx \rangle & \langle xx' \rangle & \langle xy \rangle & \langle xy' \rangle \\ \langle x'x \rangle & \langle x'x' \rangle & \langle x'y \rangle & \langle x'y' \rangle \\ \langle yx \rangle & \langle yx' \rangle & \langle yy \rangle & \langle yy' \rangle \\ \langle y'x \rangle & \langle y'x' \rangle & \langle y'y \rangle & \langle y'y' \rangle \end{bmatrix} \quad (3)$$

and

$$J = \begin{bmatrix} 0 & 1 & 0 & 0 \\ -1 & 0 & 0 & 0 \\ 0 & 0 & 0 & 1 \\ 0 & 0 & -1 & 0 \end{bmatrix}. \quad (4)$$

Linear transport elements as drifts, quadrupoles, dipoles, and rf-gaps do not change neither the beam rms emittances nor the eigen-emittances. Solenoids, skew quadrupoles, and -dipoles change the rms emittances through x-y coupling. But they do not change the eigen-emittances. This is often expressed by the simplecticity criterion for the transport matrix $M$ representing the transport element [1]

$$M^T J M = J. \quad (5)$$

A matrix $M$ satisfying the above criterion, is called symplectic and the eigen-emittances of a beam being transported by $M$ remain constant. Beam particle coordinates are expressed by displacements x and y in space and by the respective

derivatives x' and y' w.r.t. the longitudinal coordinate s. The matrix of a solenoid fringe field reads as

$$M_F = \begin{bmatrix} 1 & 0 & 0 & 0 \\ 0 & 1 & k & 0 \\ 0 & 0 & 1 & 0 \\ -k & 0 & 0 & 1 \end{bmatrix} \quad (6)$$

with $k = \frac{B}{2(B\rho)}$. $B$ is the solenoid on-axis magnetic field strength and $B\rho$ is the beam rigidity. $M_F$ does not satisfy Equ. 5 and changes the eigen-emittances. However, it leaves constant the 4d rms emittance defined as the square root of the determinant of $C$ from Equ. 3.

Stand-alone fringe fields do not exist since magnetic field lines are closed. Effective stand-alone fringe fields act on the beam if the beam charge state is changed in between the fringes of the same solenoid. This is the case for rf-guns [2,3] (free electron creation inside solenoid), extraction from an Electron-Cyclotron-Resonance ion source [4] (ionisation inside the solenoid), and for charge state stripping inside a solenoid [5]. Further discussion of symplecticity of fringes shall be avoided here and we refer to [6] instead. We just point out that changing the ion beam charge state is equivalent to cancelling the stripped-off electrons from the system. This cancellation is a non-symplectic action and conservation of the eigen-emittances within the remaining subsystem cannot by assumed in general.

In this report we assume that an effective fringe field (Equ. 6) coupled an initially round & decoupled beam. The second moments matrix of this beam at the entrance to that fringe is given by

$$C_1' = \begin{bmatrix} \varepsilon\beta & 0 & 0 & 0 \\ 0 & \frac{\varepsilon}{\beta} & 0 & 0 \\ 0 & 0 & \varepsilon\beta & 0 \\ 0 & 0 & 0 & \frac{\varepsilon}{\beta} \end{bmatrix}, \quad (7)$$

where $\varepsilon$ is the rms emittance in both transverse planes and $\beta$ is the rms beta function.

The report is organized in the following: in the first section we repeat parts of references [7] and [8], i.e. decoupling of the beam using a generic decoupling beam line. The subsequent section treats the extension of the generic case to any decoupling beam line. Finally, we report on successful experimental demonstration of one-knob emittance transfer.

## DE-COUPLING FOR THE GENERIC CASE

The beam second moment matrix after passing the fringe field of Equ. 6 is

$$C_2' = M_F C_1' M_F^T = \begin{bmatrix} \varepsilon_n R_n & -k\varepsilon_n\beta_n J_n \\ k\varepsilon_n\beta_n J_n & \varepsilon_n R_n \end{bmatrix}, \quad (8)$$

where

$$\varepsilon_n = \sqrt{\varepsilon\beta(\frac{\varepsilon}{\beta} + k^2\varepsilon\beta)}, \quad \beta_n = \frac{\beta\varepsilon}{\varepsilon_n}, \qquad (9)$$

introducing the 2×2 sub-matrices $R_n$ and $J_n$ as

$$R_n = \begin{bmatrix} \beta_n & 0 \\ 0 & \frac{1}{\beta_n} \end{bmatrix}, \quad J_n = \begin{bmatrix} 0 & 1 \\ -1 & 0 \end{bmatrix}. \qquad (10)$$

Inter-plane coupling is created and the rms emittances and eigen-emittances after the fringe read

$$\varepsilon_{x,y} = \varepsilon_n, \quad \varepsilon_{1,2} = \varepsilon_n(1 \mp k\beta_n). \qquad (11)$$

The parameter $t$ is introduced to quantify the interplane coupling. If $t$ defined as

$$t = \frac{\varepsilon_x\varepsilon_y}{\varepsilon_1\varepsilon_2} - 1 \ge 0 \qquad (12)$$

is equal to zero, there are no inter-plane correlations and the beam is fully decoupled.

Obtaining this result we neglected the finite solenoid length, i.e. its central longitudinal field. Tracking simulations using 3D-field maps of finite solenoids confirmed that this omission is justified [9].

As shown for instance by Kim [7] the beam represented by Equ. 8 is decoupled through a beam line formed by an identity matrix in the $x$-direction and an additional 90° phase advance in $y$-direction

$$R_q = \begin{bmatrix} I_n & O_n \\ O_n & T_n \end{bmatrix}. \qquad (13)$$

Here the 2×2 sub-matrices $O_n$, $T_n$ and $I_n$ are defined as

$$O_n = \begin{bmatrix} 0 & 0 \\ 0 & 0 \end{bmatrix}, \quad T_n = \begin{bmatrix} 0 & u \\ -\frac{1}{u} & 0 \end{bmatrix}, \quad I_n = \begin{bmatrix} 1 & 0 \\ 0 & 1 \end{bmatrix}. \qquad (14)$$

If the quadrupoles are tilted by 45° the 4×4 transfer matrix can be written as

$$\overline{R} = R_r R_q R_r^T = \frac{1}{2}\begin{bmatrix} T_{n+} & T_{n-} \\ T_{n-} & T_{n+} \end{bmatrix}, \qquad (15)$$

where

$$R_r = \frac{1}{\sqrt{2}}\begin{bmatrix} I_n & I_n \\ -I_n & I_n \end{bmatrix}, \quad T_{n\pm} = T_n \pm I_n. \qquad (16)$$

The beam matrix $C_3'$ after the decoupling section is

$$C_3' = \overline{R}C_2'\overline{R}^T = \begin{bmatrix} \eta_+\Gamma_{n+} & \zeta\Gamma_{n-} \\ \zeta\Gamma_{n-} & \eta_-\Gamma_{n+} \end{bmatrix}, \qquad (17)$$

and the 2×2 sub-matrices $\Gamma_{n\pm}$ are defined through

$$\Gamma_{n\pm} = \begin{bmatrix} u & 0 \\ 0 & \pm\frac{1}{u} \end{bmatrix}, \qquad (18)$$

with

$$\eta_\pm = \frac{\varepsilon_n}{2}(\frac{\beta_n}{u} + \frac{u}{\beta_n} \mp 2k\beta_n) \qquad (19)$$

and

$$\zeta = \frac{\varepsilon_n}{2}(-\frac{\beta_n}{u} + \frac{u}{\beta_n}). \qquad (20)$$

Assuming that this beam matrix is diagonal, its $x$-$y$ component vanishes

$$\zeta\Gamma_{n-} = O_n \qquad (21)$$

solved by

$$u = \pm\beta_n, \qquad (22)$$

where the positive sign indicates that $\varepsilon_x$ is made equal to $\varepsilon_1$ by decoupling and the negative sign means that $\varepsilon_y$ is made equal to $\varepsilon_1$. We calculate the final rms emittances obtaining

$$\varepsilon_{x,y} = |\varepsilon_n(1 \mp k\beta_n)|. \qquad (23)$$

For a given effective solenoid fringe field strength $k$, the corresponding quadrupole gradients may be determined using a numerical routine, such that finally the rms emittances are equal to the eigen-emittances. If these optimized gradients are applied to remove interplane correlations produced by a different fringe strength $k_1$, the resulting rms emittances and eigen-emittances at the exit of the decoupling section are calculated as

$$\varepsilon_{x,y} = \frac{\varepsilon_n(k_1)}{2}\left|\frac{\beta_n(k_1)}{\beta_n(k_0)} + \frac{\beta_n(k_0)}{\beta_n(k_1)} \mp 2k_1\beta_n(k_1)\right| \qquad (24)$$

and

$$\varepsilon_{1,2} = \varepsilon_n(k_1)|1 \mp k_1\beta_n(k_1)| \qquad (25)$$

with the parameter

$$t = \frac{\varepsilon^2\beta^2}{\frac{\varepsilon}{\beta}(\frac{\varepsilon}{\beta} + k_0^2\varepsilon\beta)}\frac{(k_1^2 - k_0^2)^2}{4}. \qquad (26)$$

In the same way the rms Twiss parameters of a beam coupled by $k_1$ but decoupled by $\overline{R}(k_0)$ are found from Equ. (17) as

$$\tilde{\alpha}_x = \tilde{\alpha}_y = 0, \quad \tilde{\beta}_x = \tilde{\beta}_y = \beta_n(k_0), \qquad (27)$$

showing that the rms Twiss parameters after decoupling do not depend on the coupling solenoid fringe strength $k_1$ if the decoupling section was set assuming a coupling strength $k_0$. We stress the very convenient feature of the generic decoupling line $\overline{R}$: once a decoupling set of gradients has been found for the fringe field strength $k_o$, these gradients will practically decouple also beams coupled by a different strength $|k_1| \le |k_0|$. This is shown in Fig. 1, which was originally presented in [8]. Moreover, the Twiss parameters $\beta$ and $\alpha$ at the exit of the generic beam line $\overline{R}$ do not depend on the fringe strength. These two features enormously facilitate the design and operation of such a round-to-flat adapter.
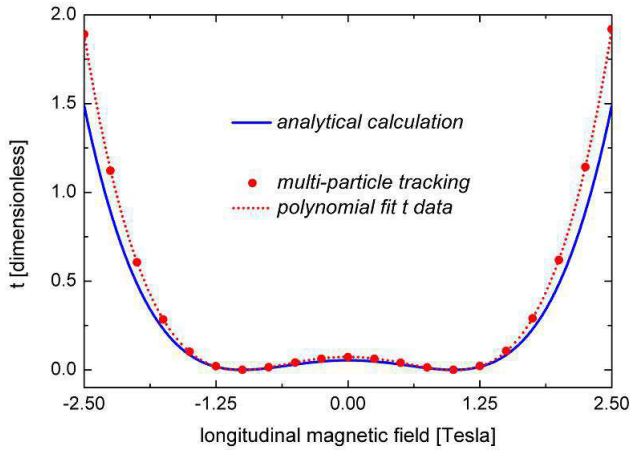
Figure 1: The coupling parameter $t$ at the exit of the generic beam line $\overline{R}$ as a function of the solenoid field causing the fringe field strength $k_1$ (blue line). The figure is taken from [8] and $k_0$ corresponds to 1.0 T. The dependency is described by Equ. 26.

## DECOUPLING FOR THE GENERAL CASE

In the previous section we derived the following ensemble $\mathcal{P}$ of properties of the generic decoupling line $\overline{R}$ of Equ. 15:

- $t$ at the exit scales as $(k_1^2 - k_0^2)^2$, where $k_o$ is the assumed fringe strength and $k_1$ is the strength actually applied for the coupling. $t << 1$ holds over a wide range of $k_1$ (Equ. 26 and Fig. 1 with $B \sim k_1$).

- the exit Twiss parameters $\beta_x$, $\alpha_x$, $\beta_y$, $\alpha_y$ do not depend on the actual fringe strength $k_1$ (Equ. 27).

- the only quantity considerably changed through the fringe strength is the transverse rms emittance partitioning $\varepsilon_x/\varepsilon_y$ (Equ. 24).

It must be stressed that these properties hold for both signs in Equ. 22. However, [8] found by various tracking simulations with TRACK [10] as well as by applying the matrix formalism, that $\mathcal{P}$ seems to hold for any beam line $M_D$ that provides decoupling of a round beam previously coupled through a stand-alone solenoid fringe field. This feature was not understood in [8].

Instead it can be understood through the procedure being illustrated in Fig. 2. Suppose there is any arbitrary beam line $M_D$ that provides decoupling. This beam line includes x-y coupling linear elements. We prolong $M_D$ by a beam line represented by the matrix

$$A = \begin{bmatrix} A_x & O_n \\ O_n & A_y \end{bmatrix} \qquad (28)$$

with the 2×2 sub-matrices $A_x$ and $A_y$. $A$ must not include any x-y coupling element.

The resulting total beam line is the product $AM_D$. We choose for the non-coupling line $A = \overline{R}M_D^{-1}$ such that $\overline{R} = AM_D$.
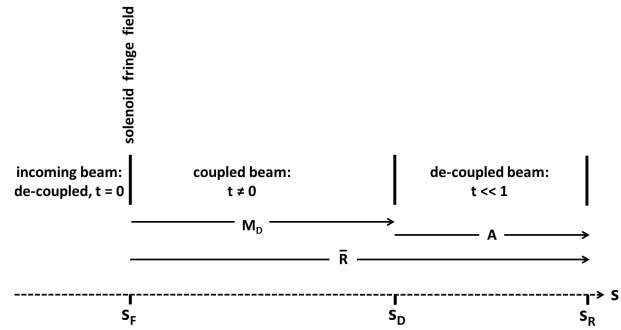


Figure 2: Extension of the decoupling features of the generic beam line $\overline{R}$ to any decoupling beam line $M_D$. $S_F$ denotes the location of the initially coupling stand-alone solenoid fringe field. The arbitrary decoupling beam line $M_D$ ends at $S_D$, and the generic beam line $\overline{R}$ ends at $S_R$. The beam line $A$ does not include any x-y coupling element.

Care is to be taken in choosing the right sign at Equ. 22 in the construction of $\overline{R}$. This is to assure that both, $M_D$ and $\overline{R}$, reduce $\varepsilon_x$ to the same of the two eigen-emittances. Choosing the wrong sign, $A$ gets an emittance exchange beam line that includes coupling elements. As shown above, at the exit of $\overline{R}$ the properties $\mathcal{P}$ hold. From the exit of $\overline{R}$ the Twiss parameters $\varepsilon$, $\beta$, and $\alpha$ (in both planes) are transported backwards to $S_D$ by applying $A^{-1}$ being aware that $\alpha$ and $\beta$ do not depend from the fringe strength. As $A$ does not include any x-y coupling element, neither does $A^{-1}$. Accordingly, the back-transformed Twiss parameters at $S_D$ also do not depend on the fringe strength. The same way the invariance of the Twiss parameters w.r.t. the fringe strength is kept through the back-transportation by $A^{-1}$, the weak dependence of $t(k_1)$ is back-transported & preserved through $A^{-1}$. Since $A^{-1}$ is non-coupling, it preserves $t$. In other words, the properties $\mathcal{P}$ at the exit of $\overline{R}$ are preserved during back-transportation by $A^{-1}$. As a consequence the properties $\mathcal{P}$ hold also at the exit of the arbitrarily chosen decoupling beam line $M_D$.

## EXPERIMENTAL DEMONSTRATION

The EMitance Transfer EXperiment (EMTEX) was installed [11] last year along the transfer channel from GSI's UNIversal Linear ACcelerator (UNILAC) to the synchrotron. Figure 3 shows the set-up starting with two doublets to match
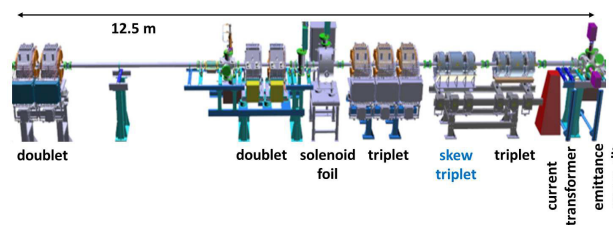


Figure 3: Beam line of EMTEX (Emittance Transfer Experiment).

the beam to the entrance of the short solenoid, which provides inter-plane coupling. The foil can be moved into the solenoid center. Stripping in the foil causes the entrance and exit fringe fields to act differently on the beam. Together with the fact that the solenoid is sufficiently short, this set-up provides for an effective stand-alone solenoid fringe field modelled through Eq. 6. After the solenoid the coupled beam is matched by a triplet to the skew triplet that provides decoupling. Another regular triplet re-matches the beam for further transport. It is followed by a slit-grid beam emittance meter which allows for measuring the phase space distribution in the horizontal and vertical planes.

For the experiment a low intensity beam of $^{14}N^{3+}$ at 11.4 MeV/u was used. First, all EMTEX magnets were turned off and the stripping foil was removed from the solenoid. Full beam transmission was assured by using beam current transformes installed in front of and behind EMTEX. In order to assure that the beam in front of EM-TEX does not exhibit already some inter-plane correlations, its image was observed using a fluorescence screen. The image was observed under variation of a quadrupole being installed in front of the screen. The quadrupole strength was varied to deliver a large spectrum of beam spot aspect ratios. Considerable inter-plane correlations would have manifested through tilted beam images. As only upright images were observed, it was assumed that no inter-plane correlations are present at the entrance to EMTEX.

In the following step, beam emittances were measured in both planes at the exit of EMTEX. The obtained Twiss parameters together with the settings of the first two doublets were used to determine the beam Twiss parameters at the entrance to the first doublet of EMTEX. A horizontal (vertical) rms emittance of 1.04 (0.82) mm mrad was measured. Both doublets were set to provide a small beam with double waist at the location of the foil. The foil (carbon, 200 $\mu$g/cm$^2$, 30 mm in diameter) was moved into the solenoid. The measured beam current transmission increased by a factor of 2.3 as expected from charge state stripping of the beam from 3+ to 7+. Beam phase probes behind EMTEX were used to detect eventual beam energy loss induced by the foil. Within the resolution of the probes we assume that energy loss is close to the calculated value of 0.026 MeV/u from the ATIMA code [12]. The same code was used to calculate the mean angular scattering of 0.474 mrad per plane. After determining all required input parameters the solenoid field was set to 0.9 T. Applying a numerical routine the three triplets behind the solenoid were set to decouple the beam and to provide for a beam with small vertical and large horizontal emittance together with full transmission through the entire set-up. These gradients were set and full beam transmission was preserved. Just very few steering was needed to re-center the beam in the emittance meter. This was required due to slight misalignment of the solenoid axis w.r.t. the beam axis. For the setting mentioned above both transverse emittances were measured. Afterwards the solenoid field was reduced stepwise to 0 T. The solenoid field $B_i$ was set by following the remanence-mitigating path

$B_{i-1} \rightarrow B_{max} \rightarrow 0\ T \rightarrow B_i$. All quadrupole gradients were kept constant. For each solenoid setting full transmission was preserved and both emittances were measured.
Figure 4 plots the measured rms emittances behind EMTEX as functions of the solenoid field strength. With increas-
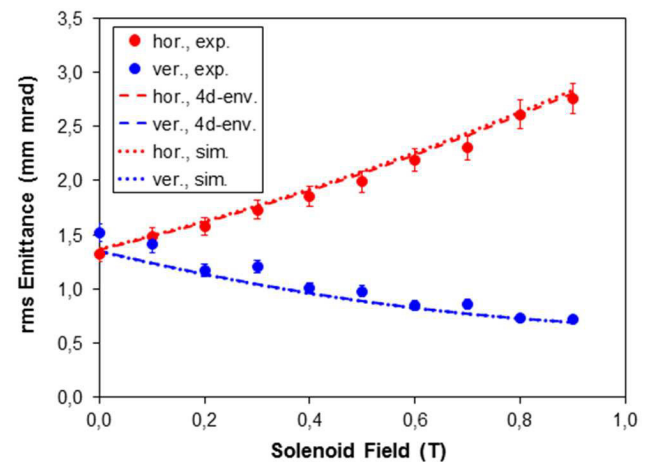


Figure 4: Vertical (blue) and horizontal (red) rms emittances at the exit of the EMTEX beam line as functions of the solenoid field strength. All other settings were kept constant. Shown are results from measurements (dots), from application of the 4d-envelope model for coupled lattices (dashed), and from tracking simulations (dotted).

ing solenoid field the vertical emittance decreases while the horizontal increases. The product of the two emittances remains constant within the precision of the measurement. This behaviour is in full agreement to theoretical predictions from [8] and to tracking simulations with TRACK [10] using magnetic field maps. It is also in agreement with calculations that apply the recently developed 4d-envelope model for coupled lattices [13–16]. The observed emittance separation under variation of the solenoid field only, confirms that EMTEX is an one-knob tool for adjustable emittance partitioning.

Figure 5 displays measured phase space distributions as functions of the solenoid field strength. It demonstrates that the shapes of the occupied areas in phase space and espe-
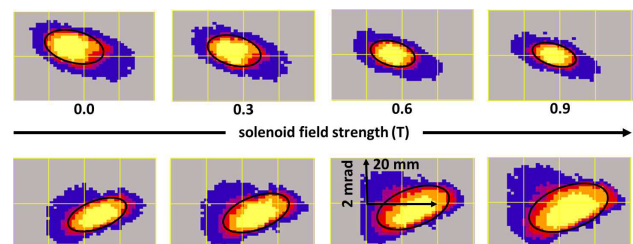


Figure 5: Vertical (upper) and horizontal (lower) phase space distributions measured at the exit of the EMTEX beam line as functions of the solenoid field strength. All other settings were kept constant. Black ellipses indicate the 4×rms ellipses.

cially the shapes of the corresponding 4×rms ellipses do not depend on the solenoid field strength within the resolution of the measurement. Also this experimental result is in full agreement to the observation from simulations reported in [8] and to the properties of EMTEX derived previously. These references assume a beam with exactly equal transverse emittances at the entrance of EMTEX. The beam emittances in the experiment differed by 23% from each other. However, the quasi-invariance of the final ellipse shapes is in excellent agreement with the 4d-envelope model and with tracking simulations also for the presented experiment. Accordingly, the experimental data also confirm that EMTEX is a one-knob emittance partitioning tool that preserves the beam envelope functions $\beta$ and $\alpha$ at its exit, if the initial beam emittances are similar. This feature makes it obsolete to re-match the envelopes as a function of the desired emittance partitioning once the partitioning is completed.

The emittance partitioning is given by the solenoid field strength. As shown in [8], inversion of the solenoid field swaps the behaviours of the emittances displayed in Fig. 4, i.e. for negative solenoid field strengths the vertical emittance increases and the horizontal one decreases with the field strength. This could not be tested experimentally, since the solenoid power converter was uni-polar. However, inversion of the solenoid field strength is fully equivalent to inversion of the skew quadrupole gradients, while keeping all other gradients and the solenoid field constant. Inversion of the skew gradients corresponds to rotation of the skew quadrupoles by 90° , i.e. to swapping the transverse planes. Accordingly, the sense of emittance partitioning is inverted for inverted skew gradients. This was verified experimentally as shown in Fig. 6. Also for inverted skew quadrupole
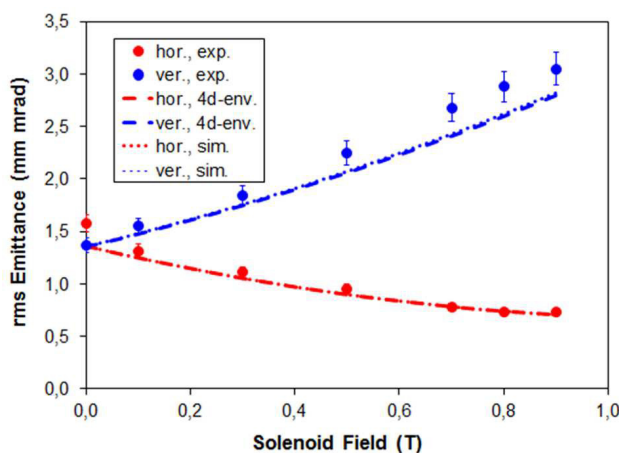
gradients, preservation of the orientations and shapes of the measured phase space distributions was observed. Just the sizes of the corresponding 4×rms ellipses changed with the solenoid field strength. For inverted skew quadrupoles the agreement to theory and to simulations is still good but slightly worse than for the case shown in Fig. 4. Additionally, for a given solenoid field value the horizontal emittance values shown in Fig. 6 are not exactly equal to the vertical emittance values shown in Fig. 4. According to theory they should be equal. However, the differences are very small. We attribute them to remanence effects in the solenoid and in the bi-polar skew triplets.

## REFERENCES

[1] A.J. Dragt, Phys. Rev. A **45**, 4 (1992).

[2] R. Brinkmann, Y. Derbenev, and K. Flöttmann, Phys. Rev. ST Accel. Beams **4**, 053501 (2001).

[3] D. Edwards, H. Edwards, N. Holtkamp, S. Nagaitsev, J. Santucci, R. Brinkmann, K. Desler, K. Flöttmann, I. Bohnet, and M. Ferrario, in *Proceedings of the XX Linear Accelerator Conference, Monterey, CA,* edited by A. Chao, e000842 (2000).

[4] P. Bertrand, J.P. Biarrotte, and D. Uriot, in Proceedings of the 10th European Accelerator Conference, Edinburgh, Scotland, edited by J. Poole and C. Petit-Jean-Genaz (Institute of Physics, Edinburgh, Scotland, 2006).

[5] L. Groening, Phys. Rev. ST Accel. Beams **14**, 064201 (2011).

[6] C. Baumgarten, Nucl. Instrum. & Methods **A 735**, p. 546 (2014).

[7] K.-J. Kim, Phys. Rev. ST Accel. Beams **6**, 104002 (2003).

[8] C. Xiao, L. Groening, O. Kester, H. Leibrock, M. Maier, and C. Mühle, Phys. Rev. ST Accel. Beams **16**, 044201 (2013).

[9] C. Xiao, L. Groening, and O. Kester, Proceedings of the 52nd ICFA Advanced Beam Dynamics Workshop, Beijing, PR China, edited by J. Wang (Institute of High Energy Physics, Beijing, PR China, 2012).

[10] P. Ostroumov, TRACK version-37, user manual, http://www.phy.anl.gov/atlas/TRACK/

[11] M. Maier, L. Groening, C. Mühle, I. Pschorn, P. Rottländer, C. Will, C. Xiao, and M. Chung, Proceedings of the 5th International Particle Acceleratore Conference, Dresden, Germany, edited by C. Petit-Jean-Genaz (CERN, Geneva, Switzerland, 2014).

[12] http://web-docs.gsi.de/weick/atima/

[13] Hong Qin, Moses Chung, and Ronald C. Davidson, Phys. Rev. Lett. **103**, 224802 (2009).

[14] Hong Qin, Ronald C. Davidson, Moses Chung, and Joshua W. Burby, Phys. Rev. Lett. 111, 104801 (2013).

[15] Hong Qin, Ronald C. Davidson, Joshua W. Burby, and Moses Chung, Phys. Rev. ST Accel. Beams **17**, 044001 (2014).

[16] Moses Chung, Hong Qin, Lars Groening, Ronald C. Davidson, and C. Xiao, *Beam Envelope Calculations in General Linear Coupled Lattices*, submitted to Phys. Plasmas.

Figure 6: Vertical (blue) and horizontal (red) rms emittances at the exit of the EMTEX beam line as functions of the solenoid field strength. All other settings were kept constant. Shown are results from measurements (dots), from application of the 4d-envelope model for coupled lattices (dashed), and from tracking simulations (dotted). W.r.t. Fig. 4 the gradients of the skew quadrupoles are inverted.

# MEASUREMENTS OF BEAM HALO DIFFUSION AND POPULATION DENSITY IN THE TEVATRON AND IN THE LARGE HADRON COLLIDER*

G. Stancari[†], Fermilab, Batavia, IL 60510, USA

## Abstract

Halo dynamics influences global accelerator performance: beam lifetimes, emittance growth, dynamic aperture, and collimation efficiency. Halo monitoring and control are also critical for the operation of high-power machines. For instance, in the high-luminosity upgrade of the LHC, the energy stored in the beam tails may reach several megajoules. Fast losses can result in superconducting magnet quenches, magnet damage, or even collimator deformation. The need arises to measure the beam halo and to remove it at controllable rates. In the Tevatron and in the LHC, halo population densities and diffusivities were measured with collimator scans by observing the time evolution of losses following small inward or outward collimator steps, under different experimental conditions: with single beams and in collision, and, in the case of the Tevatron, with a hollow electron lens acting on a subset of bunches. After the LHC resumes operations, it is planned to compare measured diffusivities with the known strength of transverse damper excitations. New proposals for nondestructive halo population density measurements are also briefly discussed.

## INTRODUCTION

Understanding particle losses and beam quality degradation is one of the fundamental aspects in the design and operation of accelerators. From the point of view of machine protection, losses must be absorbed by the collimation system to avoid damaging components. Beam lifetimes and emittance growth determine the luminosity of colliders. Knowledge of the machine aperture (physical and dynamical) and of the mechanisms that drive particle loss is essential.

The LHC and its planned luminosity upgrades (HL-LHC) represent huge leaps in the stored beam energy of colliders. In 2011, the Tevatron stored a beam of 2 MJ at 0.98 TeV, whereas the LHC reached 140 MJ in 2012 at 4 TeV. The nominal LHC will operate at 362 MJ at 7 TeV in 2015, and the HL-LHC project foresees that around 2023 the machine will store proton beams of 692 MJ.

No scrapers exist in the LHC for full beam at top energy. Moreover, the minimum design HL-LHC lifetimes (about 0.2 h for slow losses during squeeze and adjust) are close to the plastic deformation of primary and secondary collimators.

Halo populations in the LHC are not well known. Collimator scans [1, 2], van-der-Meer luminosity scans [3], and losses during the ramp [4] indicate that the tails above $4\sigma$ (where $\sigma$ is the transverse rms beam size) represent between 0.1% and 2% of the total population, which translates to megajoules of beam at 7 TeV. Quench limits, magnet damage, or even collimator deformation will be reached with fast losses [5]. In HL-LHC, these fast losses include crab-cavity failures, which generate orbit drifts of about $2\sigma$ [6].

Hence, the need arises to measure and monitor the beam halo, and to remove it at controllable rates. For HL-LHC, beam halo monitoring and control are one of the major risk factors for operation with crab cavities. Hollow electron lenses were proposed as an established and flexible tool for controlling the halo of high-power beams [7].

The dynamics of particles in an accelerator can be quite complex. Deviation from linear dynamics can be large, especially in the beam halo. Lattice resonances and nonlinearities, coupling, intrabeam and beam-gas scattering, and the beam-beam force in colliders all contribute to the topology of the particles' phase space, which in general will include regular and chaotic regions, and resonant islands. In addition, various noise sources are present in a real machine, such as ground motion (resulting in orbit and tune jitter) and ripple in the radiofrequency and magnet power supplies. As a result, the macroscopic motion can acquire a stochastic character, which can be described in terms of particle diffusion [8–12].

Calculations of lifetimes, emittance growth rates, and dynamic aperture from various sources are routinely performed in the design stage of all major accelerators, providing the foundation for the choice of operational machine parameters. Experimentally, it was shown that beam halo diffusion can be measured by observing the time evolution of particle losses during a collimator scan [13]. These phenomena were used to estimate the diffusion rate in the beam halo in the SPS at CERN [14, 15], in HERA at DESY [13], and in RHIC at BNL [16]. An extensive experimental campaign was carried out at the Tevatron in 2011 [17–19] to characterize the beam dynamics of colliding beams and to study the effects of the novel hollow electron beam collimator concept [20]. Following the results of the Tevatron measurements, similar experiments were done in the LHC [2, 21].

In this paper, we review some of the present and future experimental methods to estimate beam halo populations, with a discussion of their systematic effects. We also survey the experimental data on the dynamics of the beam halo, with a discussion on the relationship between diffusivities and population densities.

# HALO POPULATION DENSITY

## Collimator Scans

The dynamics of the beam halo was studied experimentally with collimator scans [13] at the Fermilab Tevatron proton-antiproton collider in 2011. The main motivation was to observe the effect on diffusion of beam-beam forces and of the novel hollow electron beam collimator [20]. The same data was used to estimate halo populations beyond about $7\sigma$. Lower amplitudes could not be reached because of the minimum size of the collimator steps and of the safety thresholds of the beam loss monitors.

In the Tevatron, 36 proton bunches (identified as P1–P36) collided with 36 antiproton bunches (A1–A36) at the center-of-momentum energy of 1.96 TeV. There were 2 head-on interaction points (IPs), corresponding to the CDF and the DZero experiments. Each particle species was arranged in 3 trains of 12 bunches each, circulating at a revolution frequency of 47.7 kHz. The bunch spacing within a train was 396 ns, or 21 53-MHz rf buckets. The bunch trains were separated by 2.6-$\mu$s abort gaps. The synchrotron frequency was 34 Hz, or $7 \times 10^{-4}$ times the revolution frequency. The machine operated with betatron tunes near 20.58. Protons and antiprotons shared a common vacuum pipe. Outside of the interaction regions, their orbits wrapped around each other in a helical arrangement. Therefore, bunch centroids could be several millimeters away from the physical and magnetic axes of the machine. Beam intensities and bunch lengths were measured with a resistive wall monitor. Transverse beam sizes were inferred from the recorded synchrotron light images.

All collimators were retracted except one. The collimator of interest was moved in or out in small steps, and the corresponding local loss rates were recorded as a function of time. A detailed description of the Tevatron collimation system can be found in Ref. [22].

Collimator scans were also used to estimate halo populations in the LHC at 4 TeV. The experiments were described in Refs. [2, 21]. The goal of these experiment was to measure both halo populations and diffusivities under the same conditions. One nominal bunch ($1.15 \times 10^{11}$ protons) per beam was used. The study started with squeezed, separated beams. Orbit stabilization was turned off. The primary and secondary collimators in the IR7 region were retracted from their nominal settings of $4.3\sigma$ and $6.3\sigma$ respectively to a half gap of $7\sigma$. The jaws of a vertical and a horizontal primary collimators were moved in small steps. The collimators were selected from different beams to be able to perform the scrapings in parallel without inducing cross-talk in the loss-monitor signals. The jaws were moved after waiting for the beam losses from the previous step to reach a steady-state (approximately every 10 to 40 seconds). The jaws were left for a few minutes in the beam after they had reached their final inward position, to allow the losses to stabilize. Subsequently, the jaws were moved out in small steps, again after waiting for the transient to decay. The procedure of inward and outward steps was then repeated after bringing the beams into collision.

In the approximation of static beam distributions, the beam densities can be calculated from the measured intensity loss during a short interval (4 s in this case) centered around the collimator movement. The results are shown in Figure 1 (solid black lines). Similar results are obtained by integrating the calibrated losses over the same short interval (Figure 1, dashed black lines). For comparison, a Gaussian core with the measured beam emittance is also shown in Figure 1 (gray line). Tail populations beyond $4\sigma$ are reported in Table 1. It is interesting to note the depletion in the case of collisions compared with separated beams.

Scans with primary collimators in a dispersive region of the LHC were used to estimate the population of the off-momentum halo and of the abort gap [23]. Tails of about 0.5% were observed at a relative momentum deviation above $1 \times 10^{-3}$.

## Other Estimates

An estimate of the beam distribution can be obtained with van-der-Meer luminosity scans [3, 6]. The two colliding beams are displaced with respect to each other, and the luminosity is recorded as a function of separation. With this technique, it was observed that the luminosity curve is well described by a double Gaussian, and that the beam population above $4\sigma$ was of the order of 0.1%.

Losses during the LHC acceleration ramp, as the collimator settings are tightened, also give indications of the magnitude of beam tails [4]. On average, 1% of the beam was above $6\sigma$ and was lost during the ramp in 2012.

## Nondestructive Beam Halo Diagnostics

Halo monitoring is clearly a high priority for high-power machines. A true halo monitor should provide a real-time, 2-dimensional transverse beam distribution. This requires a response time of a few seconds, and a dynamic range of the order of $10^6$.

In the LHC, it is planned to use synchrotron radiation as diagnostic phenomenon [24]. Dynamic range can be achieved with the coronagraph technique [25] (perhaps replacing the stop with a neutral filter), or more simply with a set of state-of-the-art digital cameras.

A new kind of detector was recently developed for the RHIC electron lenses [26]. It was shown that the rate of electrons backscattered towards the gun by Coulomb collisions with the circulating ions is a sensitive probe of the overlap between the two beams. Although a 2-dimensional reconstruction would require some kind of scanning of the electron beam, the method is based on scintillator counters and has a wide dynamic range. It is a promising means to continuously monitor the halo, especially in conjunction with a hollow electron lens.
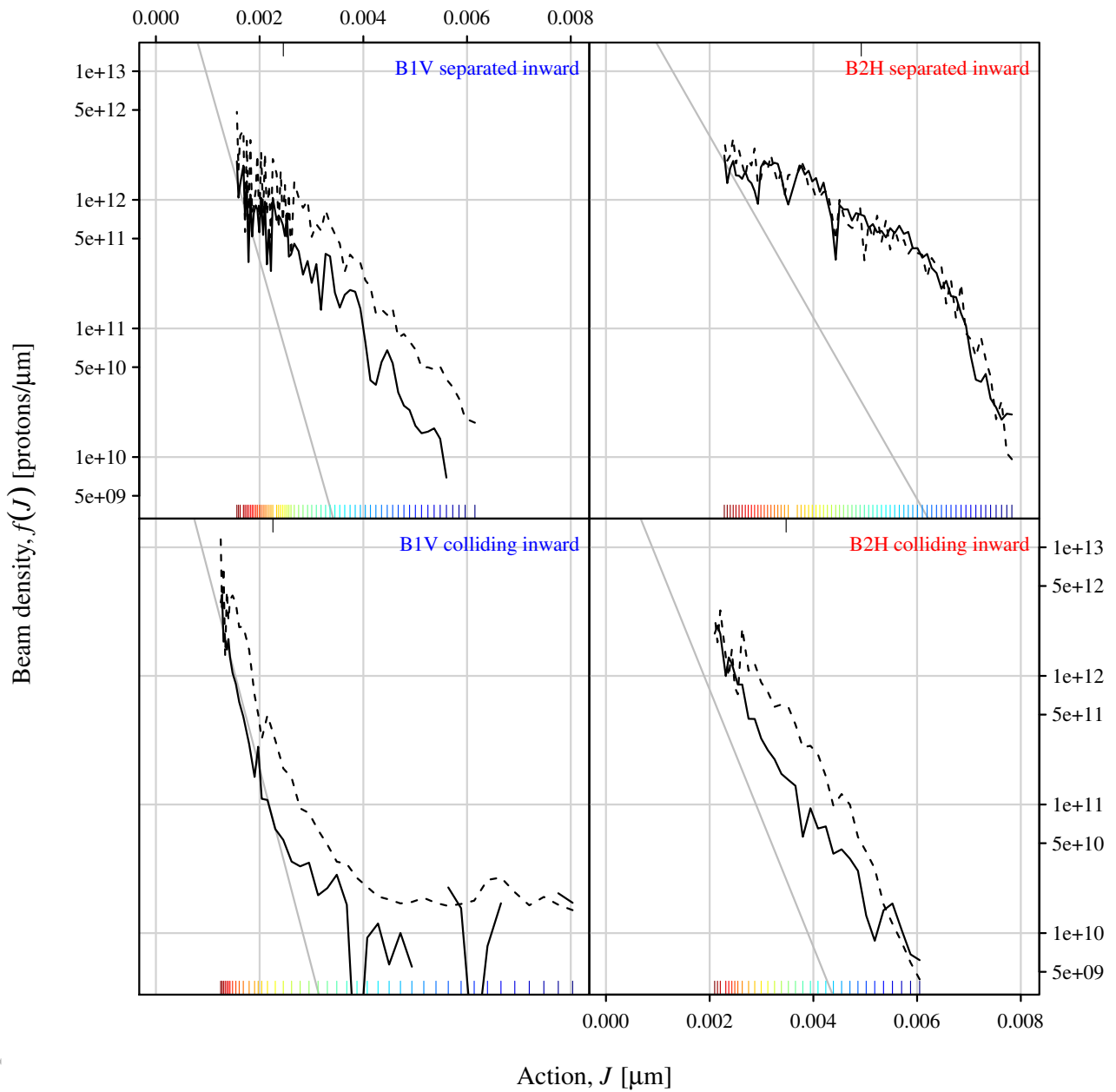
Figure 1: Measured beam halo distributions during the inward collimator scans in the LHC at 4 TeV, as a function of collimator position in units of action $J \equiv x_c^2/(2\beta)$, where $x_c$ is the half gap and $\beta$ is the local amplitude lattice function: from total intensity loss (solid black); from integrated loss-monitor rates (dashed black). The gray line denotes a Gaussian core with the measured beam emittance. The colored vertical tick marks indicate the collimator positions. The 2 left plots refer to the vertical scraping of beam 1 with separated and colliding bunches; the 2 right plots are for beam 2 in the horizontal plane.

Table 1: Estimates of Halo   opulation in the LHC at 4 TeV with Collimator Scans.

| Data set | Beam | Plane | Collisions? | Action $J$ corresponding to $4\sigma$ [$\mu m$] | Tail population beyond $4\sigma$ [$10^8\ p$] | [%] |
|---|---|---|---|---|---|---|
| 1 | B1 | V | N | 0.00246 | 8.2 | 0.58 |
| 2 | B1 | V | Y | 0.00226 | 1.6 | 0.13 |
| 3 | B2 | H | N | 0.00492 | 8.5 | 0.86 |
| 4 | B2 | H | Y | 0.00347 | 2.4 | 0.35 |

## HALO DIFFUSIVITY

Halo diffusivities can also be measured with collimator scans [13]. All collimators except one are retracted. As the collimator jaw of interest is moved in small steps (inward or outward), the local shower rates are recorded as a function of time. Collimator jaws define the machine aperture. If they are moved towards the beam center in small steps, typical spikes in the local shower rate are observed, which approach a new steady-state level with a characteristic relaxation time. When collimators are retracted, on the other hand, a dip in loss rates is observed, which also tends to a new equilibrium level.

We consider the evolution in time $t$ of a beam of particles with density $f(J,t)$ described by the diffusion equation $\partial_t f = \partial_J (D \partial_J f)$, where $J$ is the Hamiltonian action and $D$ the diffusion coefficient in action space. The particle flux at a given location $J = \bar{J}$ is $\phi = -D \cdot [\partial_J f]_{J=\bar{J}}$. During a collimator step, the action $J_c = x_c^2/(2\beta_c)$, corresponding to the collimator half gap $x_c$ at a ring location where the amplitude function is $\beta_c$, changes from its initial value $J_{ci}$ to its final value $J_{cf}$ in a time $\Delta t$. In the Tevatron, typical steps in half gap were 50 $\mu m$ in 40 ms; smaller steps (10 $\mu m$ in 5 ms, typically) were possible in the LHC. In both cases, the amplitude function was of the order of a hundred meters. It is assumed that the collimator steps are small enough so that the diffusion coefficient can be treated as a constant in that region. If $D$ is constant, the local diffusion equation becomes $\partial_t f = D \partial_{JJ} f$. With these definitions, the particle loss rate at the collimator is equal to the flux at that location: $L = -D \cdot [\partial_J f]_{J=J_c}$. Particle showers caused by the loss of beam are measured with scintillator counters or ionization chambers placed close to the collimator jaw. The observed shower rate is parameterized as $S = kL + B$, where $k$ is a calibration constant including detector acceptance and efficiency and $B$ is a background term which includes, for instance, the effect of residual activation. Under the hypotheses described above, the diffusion equation can be solved analytically using the method of Green's functions, subject to the boundary condition of vanishing density at the collimator and beyond. Details are given in Ref. [27]. By using this diffusion model, the time evolution of losses can be related to the diffusion rate at the collimator position. With this technique, the diffusion rate can be measured over a wide range of amplitudes.

Some of the results of measurements in the Tevatron were presented in Refs. [17–19]. Experiments in the LHC were reported in Ref. [2]. It was shown that the value of the diffusion coefficient near the core is compatible with measured emittance growth rates. The effect of collisions in both the Tevatron and in the LHC was clearly visible. In the Tevatron, diffusion enhancement in a specific amplitude region due to a hollow electron lens was observed. During the next run in 2015, we propose to measure halo diffusion in the LHC as a function of excitation strength in the transverse dampers, to provide a further test of the accuracy of the technique.

## DISCUSSION AND CONCLUSIONS

Extracting beam distributions from collimator scrapings requires some care. The underlying assumption is that the beam distribution is static or that, if there is beam diffusion, it is independent of amplitude. In reality, the diffusion rate increases with betatron amplitude. Neglecting this fact results in overestimating the tails, and may explain in part the discrepancy between slow and fast scrapings in Ref. [1]. Another systematic effect is introduced by using a loss-monitor calibration that is independent of collimator position.

Van-der-Meer scans are used to measure the effective beam overlap and the absolute calibration of luminosity. Extracting from them a beam distribution and a halo population requires further hypotheses. The assumption that the two beams are identical introduces a systematic uncertainty.

It may be possible to get more accurate estimates of halo populations by taking into account the relationship between population density, diffusivity, and instantaneous loss rates from the diffusion model.

As an example, for simplicity, let us consider the Gaussian core of a beam with root-mean-square (rms), unnormalized emittance $\varepsilon$. In action coordinates, this translates into an exponential density $f_G(J,t) = (N/\varepsilon) \cdot \exp[-J/\varepsilon]$. Let's further assume a constant intensity decay, $N(t) = N_0 \exp(-\lambda t)$, and a constant emittance growth rate: $\varepsilon = \varepsilon_0 \exp(\gamma t)$. By multiplying the diffusion equation by $J$ and integrating, one obtains a relationship between the emittance growth, the diffusion coefficient, and its gradient $D' \equiv \partial_J D$: $\gamma = 2\langle (D/\varepsilon - D') \cdot J \rangle / \varepsilon^2$, where $\langle \rangle$ indicates an average over the distribution function. Moreover, by substituting the Gaussian form of the density $f_G$ directly into the diffusion equation, one obtains a first-order differential equation for the diffusion coefficient:

$$D' - D/\varepsilon + \gamma \cdot J - (\lambda + \gamma)\varepsilon = 0 \qquad (1)$$

It can be solved by imposing a null flux at the origin. This results in explicit forms for the diffusion coefficient as a function of action:

$$D(J) = \gamma \varepsilon J + \lambda \varepsilon^2 \left[ \exp\left(J/\varepsilon\right) - 1 \right] . \qquad (2)$$

In other words, an exponentially increasing diffusion coefficient is necessary to produce a Gaussian beam distribution. In more realistic cases ($D$ increasing as a power of $J$), beam tails are inevitable.

These relationships can be used to test the stochastic model of halo dynamics and, if it is verified, to provide more accurate measurements of halo populations, which take diffusivity into account. One of the advantages of collimator scans is that they allow a simultaneous measurement of losses, drift velocities, and diffusivities as a function of betatron amplitude.

## ACKNOWLEDGMENTS

## REFERENCES

[1] F. Burkart, Ph.D. Thesis, Goethe Universität, Frankfurt am Main, Germany, CERN-THESIS-2012-046 (2012).

[2] G. Valentino et al., Phys. Rev. ST Accel. Beams **16**, 021003 (2013).

[3] The CMS Collaboration, CMS-PAS-EWK-11-001 (2011).

[4] S. Redaelli et al., in Proceedings of the 2013 International Particle Accelerator Conference (IPAC13), Shanghai, China, May 12–17, 2013, p. 978.

[5] R. Schmidt et al., in Proceedings of the 2014 International Particle Accelerator Conference (IPAC14), Dresden, Germany, June 15–20, 2014, p. 1039.

[6] B. Yee-Rendon et al., Phys. Rev. ST Accel. Beams **17**, 051001 (2014).

[7] G. Stancari et al., FERMILAB-TM-2572-APC, arXiv:1405.2033 [physics.acc-ph], CERN-ACC-2014-0248 (2014).

[8] A. J. Lichtenberg and M. A. Lieberman, *Regular and Chaotic Dynamics* (Springer-Verlag, New York, 1992), p. 320.

[9] T. Chen et al., Phys. Rev. Lett. **68**, 33 (1992).

[10] A. Gerasimov, FERMILAB-PUB-92-185 (1992).

[11] F. Zimmermann, Part. Accel. **49**, 67 (1995); SLAC-PUB-6634 (1994).

[12] T. Sen and J. A. Ellison, Phys. Rev. Lett. **77**, 1051 (1996).

[13] K.-H. Mess and M. Seidel, Nucl. Instr. Meth. Phys. Res. A **351**, 279 (1994); M. Seidel, Ph.D. Thesis, Hamburg University, DESY 94-103 (1994).

[14] L. Burnod, G. Ferioli, and J. B. Jeanneret, CERN-SL-90-01 (1990).

[15] M. Meddahi, Ph.D. Thesis, Université de Paris VII, Paris, France, CERN-SL-91-30-BI (1991).

[16] R. P. Fliller III et al., in Proceedings of the 2003 Particle Accelerator Conference (PAC03), Portland, Oregon, USA, May 12–16, 2003, p. 2904.

[17] G. Stancari et al., in Proceedings of the 2nd International Particle Accelerator Conference (IPAC11), San Sebastián, Spain, September 4–9, 2011, p. 1882, FERMILAB-CONF-11-411-AD-APC.

[18] G. Stancari et al., in Proceedings of the 52nd ICFA Advanced Beam Dynamics Workshop on High-Intensity and High-Brightness Hadron Beams (HB2012), Beijing, China, September 17–21, 2012, p. 466, arXiv:1209.5380 [physics.acc-ph], FERMILAB-CONF-12-506-AD-APC.

[19] G. Stancari et al., in Proceedings of the ICFA Mini-Workshop on Beam-Beam Effects in Hadron Colliders (BB2013), CERN, Geneva, Switzerland, March 18–22, 2013, CERN-2014-004, p. 83, arXiv:1312.5007 [physics.acc-ph], FERMILAB-CONF-13-054-APC.

[20] G. Stancari et al., Phys. Rev. Lett. **107**, 084802 (2011).

[21] G. Valentino et al., CERN-ATS-Note-2012-074-MD (2012).

[22] N. Mokhov et al., J. Instrum. **6**, T08005 (2011).

[23] D. Mirarchi et al., CERN-ACC-NOTE-2014-0061 (2014).

[24] H. Schmickler, private communication (2014).

[25] T. Mitsuhashi, in Proceedings of the 7th European Workshop on Beam Diagnostics and Instrumentation for Particle Accelerators (DIPAC05), CERN, Geneva, Switzerland, June 6–8, 2005, p. 7.

[26] P. Thieberger et al., in Proceedings of the 2014 International Beam Instrumentation Conference (IBIC14), Monterey, California, USA, September 14–18, 2014, MOPD02.

[27] G. Stancari, FERMILAB-FN-0926-APC, arXiv:1108.5010 [physics.acc-ph] (2011).

# STATUS OF PREPARATIONS FOR A 10 MICROSECOND LASER-ASSISTED H⁻ BEAM STRIPPING EXPERIMENT

S. Cousineau, A. Aleksandrov, V. V. Danilov, T. Gorlov, Y. Liu, A. Menshov, M. Plum, A. Rakhman, A. Shishlo, ORNL, Oak Ridge, Tennessee, TN, USA

N. Luttrell, F. Garcia, University of Tennessee, Knoxville, TN, USA

David Johnson, Fermilab, Batavia, Illinois, IL, USA

Y. Wang, University of Alabama, Huntsville, AL, USA

Y. Takeda, High Energy Accelerator Research Organization, Tsukuba, Japan

## Abstract

At the Spallation Neutron Source accelerator preparations are underway for a 10 us laser-assisted H-stripping experiment. This is a three orders of magnitude increase in pulse duration compared the to initial 2006 proof of principle experiment. The focus of the experiment is the validation of methods that reduce the average laser power requirement, including laser-ion beam temporal matching, ion beam dispersion tailoring, and specialized longitudinal and transverse optics. In this presentation we report on the status of preparations and the anticipated schedule for the experiment.

## INTRODUCTION

Many high intensity hadron synchrotrons accumulate beam through the process of charge exchange injection, whereby an H⁻ ion is converted to a proton via passage through a thin carbon foil that strips the two electrons. This method has been demonstrated to work for beam powers up to 1.4 MW. However, the survivability of the carbon stripper foils beyond the 1.4 MW level is unknown. Evidence of foil damage including tears, curls, and bracket melts, is routinely observed at high power hadron facilities such as the Spallation Neutron Source (SNS) [1]. The damage is exponentially worse with increasing beam powers. Although there are a number of research programs dedicated to improving foil durability [2], currently there is no viable alternative technology to replace the foils once the power limit is reached.

Beyond the issue of foil survivability, there is also the problem of beam scattering in the foil. This leads to emittance dilution and more importantly, beam loss and radiation. At the SNS and similar accelerators, the injection region is the hottest area of the accelerator.

The idea of using a laser and two magnets to replace the carbon foil in the charge-exchange process was proposed almost three decades ago. In this scenario the first, loosely bound electron is Lorentz stripped from the ion using a magnetic field. Because the second, more tightly bound electron cannot be stripped with a conventional magnet, a laser is used to resonantly excite the electron to a more loosely bound state (typically n=3 or n=4), whereby it can be Lorentz stripped with a second magnet, resulting in a proton. Figure 1 illustrates the concept.
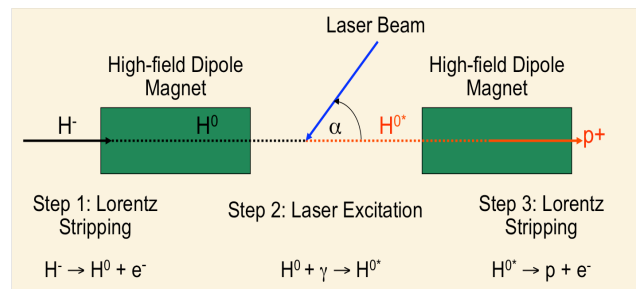


Figure 1: The laser stripping concept.

This method was successfully demonstrated in a 2006 proof of principle experiment at the SNS, where 90% stripping of a 6 ns, 900 MeV H⁻ beam was accomplished using a 355 nm laser and two magnets. Unfortunately, a straightforward scaling of this experiment to the full SNS duty cycle would require ~600 kW of average laser power, which is not feasible. Rather, it is necessary to reduce the average laser power requirement through laser and ion beam manipulations [3,4].

At SNS, preparations are underway for the next laser stripping experiment. The goal of the experiment is to achieve 90% stripping efficiency of a 5-10 us, 1 GeV H⁻ beam. The central theme of the experiment is the validation of methods used to reduce the required average laser power. For a future operational system that would strip millisecond-level pulses, these methods would be employed along with a power recycling optical cavity. The recycling cavity is under development in the laser lab at SNS, but is not part of the current stripping experiment.

This paper describes the configuration for the 10 us experiment, the work underway to prepare the ion and laser beam parameters, and the schedule.

## EXPERIMENTAL CONFIGURATION AND HARDWARE

Four primary goals drove the design of the experimental configuration:

1) Achieve high efficiency stripping.
2) Protect the laser.
3) Prevent disruptions to production beam operations.
4) Provide schedule flexibility for the experiment.

The final design, based on these goals, is described below.

### Interaction Point Location

The experiment will take place in the SNS High Energy Beam Transport (HEBT) line, which transports the beam from the end of the superconducting linac (SCL) to the ring, and contains a 90° bend. The desired ion beam optics, described in a forthcoming section, necessitates that the interaction point be located downstream of the bend. Beyond this consideration, it is convenient to have several independently powered upstream quadrupoles for tuning flexibility, and it is also preferable to be located in a low radiation region. The final location of the interaction point (IP) that satisfies these objectives is near the end of the HEBT between a pair of quadrupoles (QH28 and QV29). One disadvantage of this location is that most of the diagnostics that will be used to measure and configure the beam parameters are ~30-40 meters upstream, requiring the use of models to predict the optics at the IP. To partially address this issue, a pair of additional wirescanner will be added – one at the interaction point, and another one a few meters downstream of the IP.

### Laser Remote Placement

Two options were considered for the location of the laser station: 1) In the tunnel adjacent to the IP, and 2) in the ring service building, approximately 70 meters from the IP. Obviously, from the standpoint of the laser optics, the first option is far simpler. However, placing the laser in the tunnel introduces a host of other problems, all stemming from the need to protect the laser from radiation damage. Loss of the high power UV laser due to radiation exposure would represent a single-point failure for the entire experiment, and as such, the laser cannot be left in the tunnel during production beam operations. The in-tunnel scenario would require installing the laser, performing the experiment, and then removing the laser all during a dedicated accelerator physics study period. The longest accelerator physics blocks of time are associated with the start up periods following the twice-annual maintenance outages. Experience has shown that this time often evaporates the wake of equipment turn-on issues.

Due to the restrictive schedule logistics associated with the in tunnel option, the decision was made to place the main laser outside of the tunnel, in the ring service building. The UV laser will be transported ~70 m from the ring service building to a small final focusing table adjacent to the IP. This configuration provides flexibility for the experimental schedule while also protecting the laser. Underlying concerns regarding the laser power loss in transport and the laser pointing stability have been investigated this past year and will be discussed later in this document.

### Experimental Station

The experimental station contains the IP, windows to accommodate entrance and exit of the laser, diagnostics at the IP and downstream of the IP, and two dipole magnets to strip the electrons. A drawing of the experimental station is given in Figure 2 below.

The two stripping magnets that convert H- to $H^0$ upstream of the IP, and then $H^0*$ to p+ downstream of the IP have unique design requirements. First, the field gradient must be large in order to minimize the induced angular spread in the beam from the probabilistic nature of the stripping. In addition, the magnetic field must not be present during nominal beam operations. The final design of the magnet that meets these requirements is a Halbach cylindrical array with 1.2 T peak field and 40 T/m field gradient, arranged with opposite polarity on either side of the IP in order that there should be approximately zero field at the IP. Due this arrangement and the charge state change between the magnets, a cumulative kick of ~17 mrad will be imparted to the beam. To compensate, corrector magnets have been placed on the outside of each stripper magnet. The stripper-corrector magnet pairs will be mounted on actuators for remote insertion and retraction from the beam pipe. The design of the magnet is described in more detail in [5].

The experimental station contains one pair of optical ports for entrance and exit of the laser, and second pair for viewing and for flexibility in the laser placement. In order to reduce the laser power density on the exit window to prevent breakage, a defocusing lens is located between the IP and the exit window.

While most of the diagnostics used to prepare the beam will be 30-40 m upstream of the IP, the experimental station will contain a dual-plane wirescanner at the location of the IP to verify the beam size, and a BCM just downstream of the IP to measure the stripped beam fraction. In addition, the second wirescanner will be placed downstream of the next quadrupole to assist in the ion beam optics tune up.
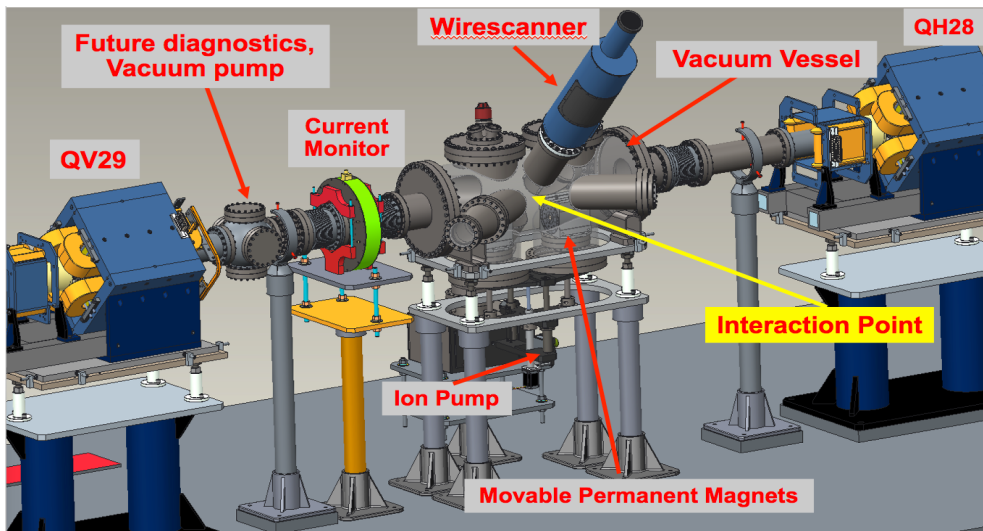
Figure 2: The final design of the experimental station.

## PARAMETER REALIZATION EFFORTS

The central theme of this experiment is the validation of methods for reducing the required average laser power. These methods, described below, involve placing the ion beam in an off-nominal Twiss configuration, and temporally matching the laser and ion beam. Altogether, these methods reduce the required average laser power from 600 kW to 50 W.

### Laser Configuration

Obviously, a significant savings in laser power can be realized by having the laser on only when beam is present. The SNS beam has a 402.5 MHz microstructure and a nominal 6% duty factor; the duty factor for this experiment is even lower. The laser system for the experiment is a frequency tripled, master oscillator power amplification (MOPA) scheme. The 355 nm final laser wavelength preserves the choice of the n=3 H⁻ excited state that was used in the initial proof of principle experiment. The laser has been demonstrated to operate in burst mode with 10 us, 10 Hz macrostructure, and 402.5 MHz, 30 – 55 ps microstructure, identical to the ion beam parameters for the experiment. The laser scheme and measured microstructure are shown together in Figure 3.

A major concern with the remote placement of the laser was the amount of power loss in transport, and whether enough laser power would be available at the IP to provide 90% stripping. Answering this question involved separate efforts to measure the total available UV laser power, and to measure the power loss on the windows, the mirrors, and in air.

Because it is not possible to directly measure picosecond level UV laser pulses, an optical correlator was developed to perform the measurement [6]. Using this device, the final power measurements gave laser powers in the range of 1.35 – 2 MW for micropulses lengths of 30 – 55 ps (FWHM), with power varying inversely to pulse length.
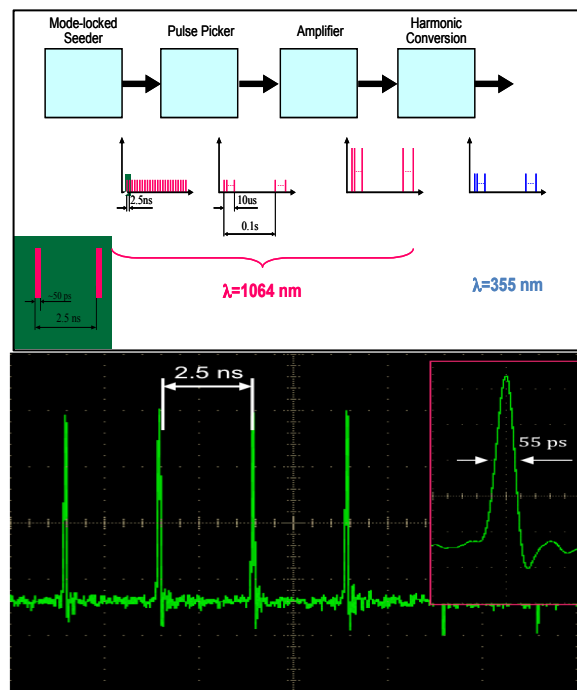


Figure 3: (Top) Laser amplification scheme. (Bottom) Laser microstructure measurement.

To estimate the laser power loss in transport, an eight meter, four-mirror mock up of the transport line was set up in the laser lab. The mirror loss was measured independently to be < 1 % per reflection. The laser was cycled through six iterations of the loop for a total of 48 meters of transport. The power loss was measured on every cycle and the results were extrapolated to 70 m, the estimated transport line length. The final estimates predict 1/3 of the laser power will be lost in transport, due primarily to Fresnel diffraction at the aperture and higher order mode losses, which diminishes with distance. Given the initial laser power measured with the optical correlator, the remaining available laser power at

the IP should be sufficient to support 90% efficient H⁻ stripping.

Finally, the last major concern with the laser transport line is the pointing stability due to mechanical vibrations and temperature drift. One mirror on the laser table will be driven with a pair of Piezoelectric actuators to provide compensation for slow drifts on the order of 1 Hz or slower. Experience with the laser-based beam diagnostics systems in the SNS SCL/HEBT tunnel indicates that this feedback control should provide sufficient laser beam pointing stability for the laser-ion beam interaction.

### Ion Beam Optics

The ion beam Twiss parameters in both the transverse and longitudinal planes can be configured to provide savings in the laser power budget. First, it is necessary to squeeze the bunch longitudinally to maximize the laser-ion beam cross section. The nominal micropulse length in the SNS HEBT is ~150 ps. For full overlap with the laser beam, this experiment requires that the micropulse length be ≤ 25 ps. The last few cavities in the SCL can be used to manipulate the bunch length, and a bunch shape monitor (BSM) in the HEBT, capable of measuring picosecond-level micropulses, is used to measure the length.

A complicating factor is the space charge of the bunch, which causes expansion of the micropulses between the end of the SCL and the IP, to the level of about 1 degree of length per milliamp of current. In an operational system, dedicated cavities would be located just upstream of the IP such that this was not an issue. However, for the current experiment the beam current will be limited to 1 – 5 mA for this reason. At these currents the microbunch lengths of $\sigma_l < 25$ picoseconds have been routinely configured, as shown in Figure 4.
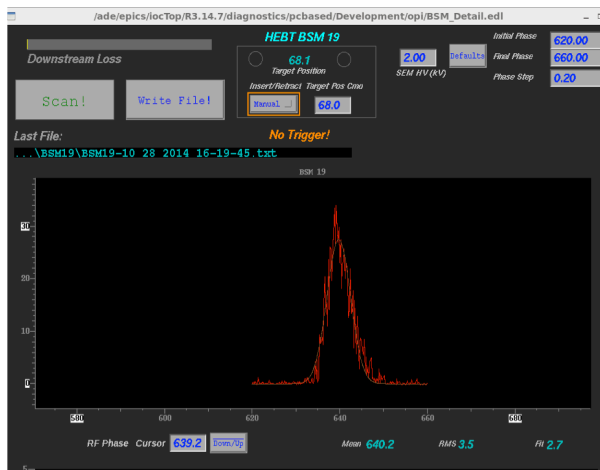


Figure 4: BSM measurement of a 22 ps microbunch.

In the transverse plane, the goal is to minimize the excitation frequency spread and maximize the cross section for interaction with the laser. First, dispersion tailoring can be used to eliminate the transition frequency spread due to beam energy spread [2]. This method

capitalizes on the fact that the required laser frequency for excitation in the rest frame is a combination of the particle energy and the angle between the ion beam and the laser, as shown below:

$$f_{\text{rest frame}}(1 \rightarrow 3) = \gamma_n (1 + \beta_n \cos(\alpha_n)) f_{\text{beam frame}}$$

Conceptually, the idea is to set the dispersion derivative such that each combination of particle energy $\gamma_n$ and angle $\alpha_n$ yields the same value of the laser frequency in the ion beam rest frame. For the SNS 1 GeV beam, this scenario corresponds to a dispersion function with values D=0 and D'=-2.6 at the IP. Given the upstream arc and the large number of independently powered quadrupoles, this is readily accomplished and has been demonstrated on multiple occasions.

After dispersion tailoring, the residual transition frequency spread is due to transverse divergence of the beam. Since the experiment will be conducted in the x-z plane, it will be advantageous to eliminate this spread by having $\alpha_x = 0$ at the IP. Finally, to maximize the cross section of the laser with the ion beam, the vertical size should be as small as possible.

Experiments conducted over the last year have demonstrated all of the required Twiss parameters separately, with best measured shown below in Table 1 below. The details of these measurements are available in [7], in these proceedings. For the moment, the Twiss parameters are fit at location 30 m upstream of the IP, which introduces the possibility of propagate error. The measurements will be repeated when the experimental station wirescanners are installed. In the near future, efforts will focus on simultaneous demonstration of all ion beam parameters.

Table 1: Measured Ion Beam Optics Parameters

| Parameter | Measured Value |
|---|---|
| $\sigma_l$ | 22.3 (picoseconds) |
| D, D' | 0 (meters), -2.4 (radians) |
| $\alpha_x$ | 0 (radians) |
| $\sigma_y$ | 0.1 (mm) |

## FINAL SIMULATIONS

In recent simulations done with the pyORBIT code [8] which include all the measured parameters, the stripping efficiency was calculated versus the laser radius and divergence [6]. The results are shown in Figure 5. While there is a region of very high stripping efficiency, it is yet unknown if the laser density for these parameters exceeds the damage threshold of the defocusing lens. This is currently under investigation.
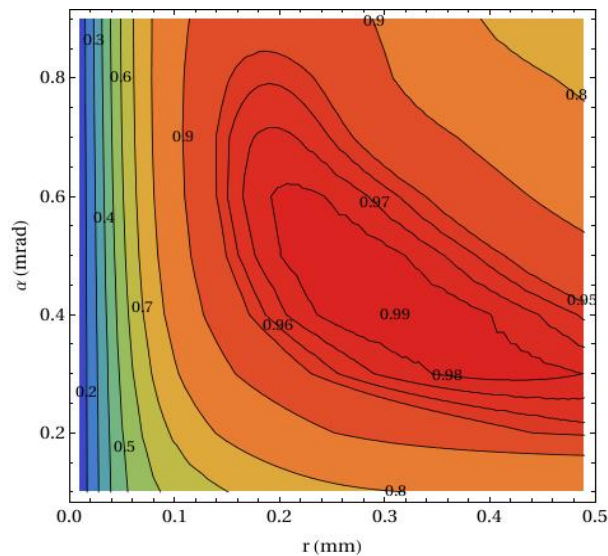
Figure 5: Simulated laser stripping efficiency versus laser radius and divergence.

## SCHEDULE

This project has been planned over a 3 year time period, with an end date of May 2016. The primary focus of the first year was to choose the interaction point location, decide on the laser placement, and verify the ion and laser beam parameters. This work is complete. During the second year, the design of the stripping magnets and the experimental vessel was completed; they are now being manufactured with expected delivery dates in mid-winter. The diagnostics hardware are complete and ready for installation. The laser transport line design has just begun.

Installation of the diagnostics will commence in winter of 2015; the experimental vessel and stripping magnets will be installed in summer 2015; the transport line will be installed, along with the final optics table, in either summer of 2015 or winter of 2106. The first stripping experiments will commence in spring of 2016.

## ACKNOWLEDGMENT

## REFERENCES

[1] M. Plum et al., PRSTAB **14**, 030101 (2011).

[2] I. Sugai, D. Gilliam, and A. Stolarz, *Nuclear Instruments and Methods A*, vol. 590, no. 1-3, pp. 1-238, 2006.

[3] V. Danilov et al., PRSTAB **6**, 053501 (2003).

[4] V. Danilov et al., PRSTAB **10**, 053501 (2007).

[5] A. Aleksandrov and A. Menshov, "Magnet Design for SNS Laser Stripping Experiment," Proceedings of IPAC14, Dresden (2014).

[6] A. Rakhman et al, *Applied Optics*, Vol. 53, No. 31 (2014).

[7] T. Gorlov, V. Danilov, A. Shishlo, PRSTAB **13** 050101 (2010).

# THE PARTICLE-IN-CELL CODE BENDER AND ITS APPLICATION TO NON-RELATIVISTIC BEAM TRANSPORT

D. Noll[*], M. Droba, O. Meusel, U. Ratzinger, K. Schulte, C. Wiesner
Institute of Applied Physics, Goethe University Frankfurt am Main

## Abstract

A new non-relativistic, electrostatic Particle-in-Cell code named bender has been implemented to facilitate the investigation of low-energy beam transport scenarios. In the case of high-intensity beams, space-charge compensation resulting from the accumulation of secondary particles – electrons for positively charged ion beams – is an important effect. It has been shown, that the distribution of compensation electrons can have a significant influence on the beam and lead to an emittance growth. To improve the understanding of the dynamics of the compensation and the resultant self-consistent steady state, ionization of residual gas as well as secondary electron production on surfaces have been implemented and used to study a number of test systems. We will present first results of these compensation studies as well as further applications of the code, among them the chopper section of the future FRANZ facility [1].

# IMPLEMENTATION

The Particle-in-Cell [2] code bender is written in the C++ language and uses MPI for parallelisation. It reads input files in an XML-style format. All numerical values in this file are affixed with units. The output of the code can be configured to include particle distributions and losses, field and potential distribution and single particle tracks, as required.

External fields can either be loaded from data exported from tools like the CST Suite or Opera, calculated numerically via either the solution of Laplace's equation on a lattice or from the Biot-Savart law by integrating the current flow through wires defined by analytic expressions, or calculated from several available field models, including multipole field distributions and several solenoid field models.

For use as boundaries for either particle movement or the Poisson solver, various geometric primitives like planes, tubes and plates are implemented. For more complex geometries, an import from STL files is available.

All geometric objects in the code can then be transformed by one or multiple affine transformations, which allows objects like fields, geometric objects, monitors and even poisson solvers to be placed in the simulation "space" at will.

To simulate dc beams, a fixed number of particles, spread out over $v_{beam}\Delta t$, are inserted in every time step, continuously building up the beam volume.

## Field Solvers

The code provides three solvers for Poisson's equation.

For problems requiring either non-equidistant grid spacing or geometrically complex boundary conditions, there is

---

* noll@iap.uni-frankfurt.de

a cartesian solver using a Shortley-Weller finite-difference stencil [3]

$$\frac{\varphi_{i-1,j,k}}{\Delta_- (\Delta_+ + \Delta_-)} - \frac{\varphi_{i,j,k}}{\Delta_+ \Delta_-} + \frac{\varphi_{i+1,j,k}}{\Delta_+ (\Delta_+ + \Delta_-)}$$
$$+ \text{other dir.} = -\frac{\rho_{i,j,k}}{2\epsilon_0} + O(\Delta^3), \qquad (1)$$

where $\Delta_\pm$ are the distances to either the neighbouring grid points or a grid boundary. Dirichlet, Neumann and periodic boundary conditions on the grid boundaries can be considered. The grid can be distributed among processors in blocks in all directions, which allows bent geometries to be followed without wasting memory on inactive regions. An example is shown in Fig. 1.

On initialisation of the solver, all processors calculate the positions and the sizes of boundary surfaces with their neighbours. In a second step, intersections between the grid lines and the boundary objects given for the solver are calculated in multiple passes over each direction. In the first of the three passes, grid points not contained in any boundary object are assigned a global index. When an intersection with an object is found on the line between two grid points, its position is stored for the respective active grid point using its index. In a third step, the geometric information gathered is communicated in the bounding areas found in the first step.

After mesh generation, a sparse matrix for the potential on the grid points is constructed using Eq. (1). To solve this matrix, the PetSc library [4] is used. After the solution process, to be able to calculate the electric field in the region between the grid portions local to two processors, potential
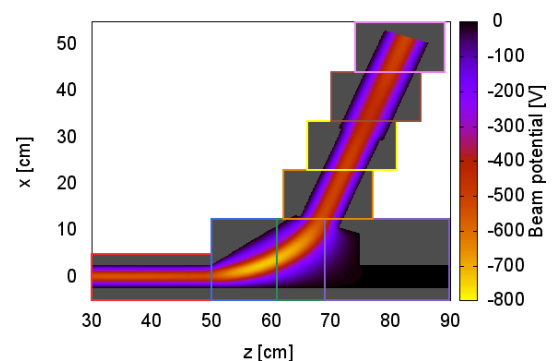


Figure 1: Example of a calculation of electric potential of a guided electron beam on 16 processors. The coloured rectangles show the grid portions on each processor. Each domain is additionally split in vertical direction. The grey portions of the grid are disabled on each processor, the white portions are not considered by any processor.

values from the neighbouring processors are required and are therefore communicated.

For simulations of radially symmetric systems, the code includes an rz finite difference solver also using the PETSc library. In the case only a rectangular grid with equidistant spacing is required, a 3d xyz solver using Fourier's method implemented using the FFTW library [5] can be used. Both of these solvers allow for Dirichlet, Neumann or periodic boundary conditions and can be distributed among processors in longitudinal direction.

All three solvers don't require particles to be local to their grid portions. However, when requested, particles can be distributed among processors according to each processors portion of the grid, reducing the amount of communication in the field accumulation step.

*Particle Pusher*

Bender implements various algorithms for integration of particle motion, among others one using the standard RK4 integration algorithm and a symplectic Euler integrator. The (non-relativistic) algorithm used in the simulations presented below is

$$r_{i+1} = r_i + \frac{\Delta t}{m} \left( p_i + \Delta p_i \right)$$

$$p_{i+1} = p_i + A_{i+1}^{-1} \left( p_i + \Delta p_i + \frac{q\Delta t}{2} E_{i+1} \right)$$

$$\Delta p_{i+1} = \frac{q\Delta t}{2} E_{i+1} + \lambda p_{i+1} \times B_{i+1},$$

where $r_i$ and $p_i$ are the particles position and momentum in the $i$'th step, $q$ and $m$ its charge and mass, $\Delta p$ was defined to avoid recalculation between adjacent time steps, $\lambda = q\Delta t / (2m)$ and

$$A_i = \begin{pmatrix} 1 & -\lambda B_i^z & \lambda B_i^y \\ \lambda B_i^z & 1 & -\lambda B_i^x \\ -\lambda B_i^y & \lambda B_i^x & 1 \end{pmatrix}.$$

The implementation was compared to several analytically solvable test cases and showed second order accuracy as well as long time energy conservation.

## SPACE CHARGE COMPENSATION

Two processes lead to the production of electrons in positive low-energy ion beams: impact ionisation of residual gas atoms and molecules and secondary particle production due to the impact of particles on the beam pipe. These electrons can then be trapped inside the beams positive potential, reducing it until a steady-state is produced.

The amount of electrons produced per meter per second by a beam of energy $E$, current $I$ in a homogeneous residual gas background of pressure $p$ and temperature $T$ is given by

$$\nu = \frac{Ip\sigma(E)}{ekT},$$

where $\sigma(E)$ is the total proton impact ionisation cross section. For $I = 100\,\text{mA}$, $E = 120\,\text{keV}$ protons on $p = $

$1 \times 10^{-3}\,\text{Pa}$, T=300 K $N_2$, $\nu = 8 \times 10^{15}$ electrons/s/m are produced. The energy of most of these electrons is not large enough for them to cause additional ionisation. However, in high-intensity beams, the space charge potential can be high enough for electrons to gain sufficient energy to ionise additional gas molecules.

Secondary electron production on surfaces for protons is in the order of a few electrons per impact, depending on energy, impact angle and surface composition. Thus, if significant portions of the beam (0.6 % for the parameters given above) are lost, this mechanism dominates residual gas ionisation. However, since these electrons are created at zero potential, it is unclear if they are able to remain in the system for long times.

For the simulation, Argon was considered as a residual gas, as a compromise between absolute value – lower cross section meaning longer simulation time –, complexity of the residual gas ions – for $H_2$ for example, $H_2^+$ and $H^+ + H^0$ are produced–, and data availability.

Ionising collisions were implemented in bender using the Null-collision method [6]. Argon is considered as an homogeneously distributed ideal gas. Single-differential cross section data for proton impact ionisation were taken from [7]. Electron impact cross section data is calculated from the Binary-Encounter-Bethe-model [8]. The velocities of the freed electrons are then distributed isotropically. Under the assumption, that the remaining, very low-energy ion travels in the direction of the projectile, the deflection angle of the projectile and the energy of the residual gas ion can be calculated from energy and momentum conservation.

*Compensation Without Magnetic Fields*

Initially a system without any magnetic focussing elements was investigated. A 100 mA, 120 keV beam with an emittance of 100 mm mrad was matched through a 50 cm drift section in a way, that avoids particle losses at 0 % to 100 % compensation. The section is bounded by two repeller
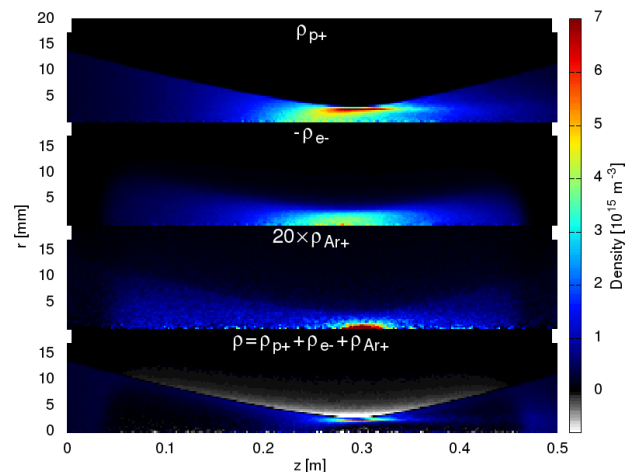


Figure 2: Proton, electron, residual gas ion and total charge densities for the simulation of a 50 cm long drift system.
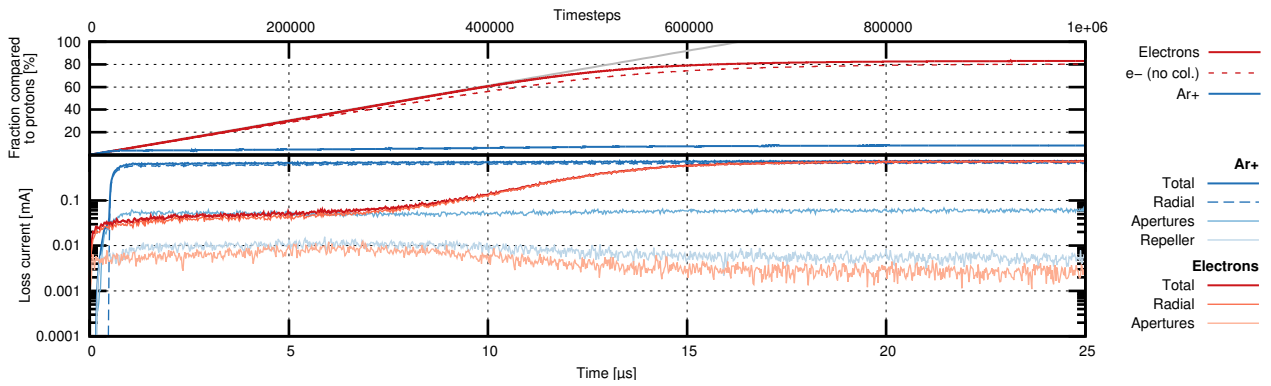
Figure 3: Global compensation degree and particle losses from the compensation simulation of a 50 cm drift. The compensation degree is plotted for two simulations – one including electron impact ionisation and one with just proton impact ionisation ("no col."). Particle losses are registered on the repeller electrodes at the end of the system and on the beam tube in radial direction. Some ions as well as a small amount of electrons created inside the repeller are accelerated out of the simulation volume longitudinally through the repeller apertures.

electrodes at $-1.5\,\text{kV}$ potential to trap electrons longitudinally.

Simulation runs were made using either the rz- oder the fast fourier poisson solver, on a grid of either $\Delta r = 0.1\,\text{mm}$, $\Delta z = 0.2\,\text{mm}$ or $\Delta x = \Delta y = 0.4\,\text{mm}$, $\Delta z = 1.7\,\text{mm}$. The time step used was $\Delta t = 25\,\text{ps}$. On 12 processors of the "Fuchs" cluster [9] using the rz solver and 50 macroparticles inserted per step, simulation time is about 1 day for $25\,\mu\text{s}$.

Figure 3 shows the global compensation degree during built-up of compensation. For the first $10\,\mu\text{s}$, the compensation degree follows

$$\eta_{\text{comp}}(t) = \frac{v_{\text{beam}}e}{I} \nu t,$$

which means, that only a negligible amount of electrons is able to escape the confinement.

After the initial linear increase, at about 7 ns, the potential is sufficiently reduced for electrons to start escaping. After 17 ns the electron loss current – almost exclusively in radial direction – equals the current of residual gas ions. At this point, an equilibrium is reached, with a global compensation degree of 80.7 %. The introduction of electron impact ionisation increases this value to 83.3 %.

The argon ions produced by ionisation are constantly accelerated out of the system radially. The amount of ions in the system slowly increases during the built-up, due to the decrease in space charge potential. In the steady-state, argon ions are responsible for an additional positive charge of 8 % of the beams charge.

The densities in the steady-state of the system are shown in Fig. 2.

It was found, that the electron velocities at a given longitudinal position follow a Gaussian profile. This would suggest that the system is in a thermodynamic equilibrium. The temperature is neither isotropic, $T_x \approx T_y \neq T_z$, nor is it equal everywhere in the system. Table 1 shows the plasma parameters for the electrons at the position of the beams focus.

Table 1: Plasma Parameters of Compensation Electrons at $z = 28\,\text{cm}$

| | | | | | |
|------|---------------------|----------|-------------|------|-----|
| $T_x$ | 34.1 | eV | $\lambda_d$ | 0.7 | mm |
| $T_y$ | 33.7 | eV | $\omega_p$ | 0.5 | GHz |
| $T_z$ | 48.1 | eV | $\ln \Lambda$ | 16.6 | |
| $n_e$ | $3.9 \times 10^{15}$ | m$^{-3}$ | | | |

For such a system, a self-consistent solution of the Poisson-Boltzmann equation given in 1d under the assumption of a radially symmetric and longitudinally homogeneous system

$$\frac{1}{r}\frac{\text{d}}{\text{d}r}\left(r\frac{\text{d}\varphi(r)}{\text{d}r}\right) = -\frac{1}{\epsilon_0}\left(\rho_{\text{beam}}(r) - \rho_e(r)\right),$$

$$\rho_e(r) = \rho_0 \exp\left\{-\frac{e\varphi(r)}{kT}\right\} \qquad (2)$$

should provide the spatial distribution of the compensation electrons. $\rho_0$ can be determined by setting the total electron charge to a fraction $\eta_{\text{comp}}$ of the beams total charge,

$$\int_0^R \text{d}r\, r\, \rho_{\text{beam}}(r) = \rho_0 \eta_{\text{comp}} \int_0^R \text{d}r\, r\, \rho_e(r). \qquad (3)$$

Figure 4 shows the solution of Eq. (2) and (3) in comparison to the bender solution. Except for an excess of electrons close to the axis – probably a result from the presence of the residual gas ions – the simulation agrees very well to the simple 1d theory. In general, this means that for finite electron temperatures even at 100% space charge compensation, there is some remaining space charge force on the beam.

The source of the thermal distribution is yet unclear, and could be a result of (numerical) noise in the particle distributions. In a physical system with the parameters given in Tab. 1, particles should relax to a thermal distribution due to Coulomb collisions on a timescale of [10]

$$\tau_{ee} = 3\pi(2\pi)^{1/2}\frac{\epsilon_0^2(kT)^{3/2}}{n_e e^4 m^{1/2} \ln \Lambda} \approx 0.5\,\text{ms}.$$
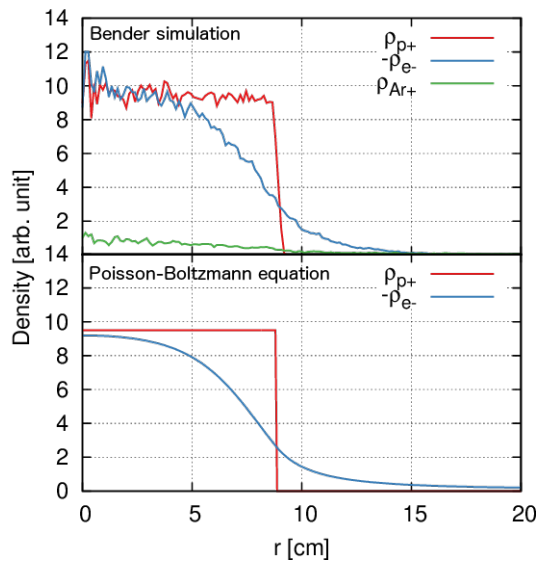
Figure 4: Radial electron distribution at $z = 10$ cm from the solution of the Poisson-Boltzmann equation (2) in comparison to the bender simulation for the drift system using the fast fourier solver. $\eta = 90.6\,\%$ and $T = 22.9$ eV.

In the simulation however, a thermal electron distribution can be observed as early as a µs. So far, we have found no significant dependance of the resulting temperatures on simulation parameters, except for the choice of solver geometry. Comparing simulations done using the Fourier solver to the 2d rz-case, the latter shows an excess of electrons with low absolute velocities.

## Simulation of a Two-solenoid LEBT

As a next step, simulation runs for a two-solenoid beam transport section using the rz solver were made. The 1.6 m long section includes two 25 cm long solenoids at 0.7 T to match the beam without any losses.

In these simulations, no steady-state was reached. Especially in the fringe field regions of the solenoid near the axis, low-energy electrons and residual gas ions accumulate, leading to a linear increase in the number of particles for these species. This spurious accumulation of residual gas ions near the axis was also found in the 2d simulations made for the drift section, where it does not grow indefinitely however. It is noticeably absent in the simulations made using the 3d fast fourier solver. Several ways to ameliorate the situation such as incorporating the dynamics of the background gas (either dynamically or by including a fixed profile) or including recombination have been suggested.

As for the case of the simple drift, a double layer forms at the edge of the beam in between the two solenoids. In the center of the solenoids however, electrons are strongly bound to the field lines. Thus the size of the double layer is greatly reduced there.

# SIMULATION OF THE FRANZ E×B CHOPPER

The E×B chopper concept, designed for high-repetition chopping of a 50 mA, 120 keV proton beam at the Frankfurt Neutron Source FRANZ [11], uses magnetostatic deflection to safely dump the unwanted beam fraction, which is compensated for short periods of time by a voltage pulse to two deflection plates to provide short beam pulses in forward direction. The copper was successfully commissioned using a low-energy helium beam [1]. The layout is shown in Fig. 5.
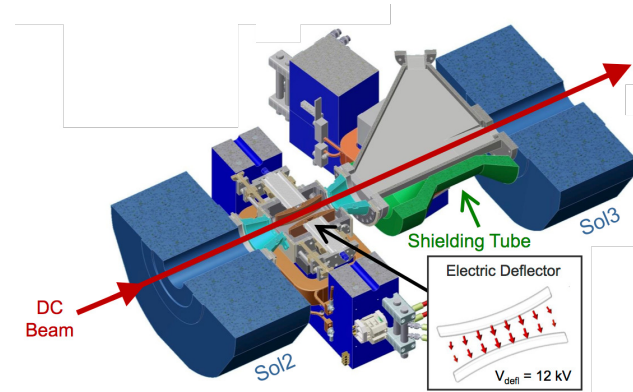


Figure 5: Layout of the E×B chopper located between solenoid 2 and 3 of the FRANZ low-energy beam transport section.

Magnetic and electric fields were simulated using the CST Suite and imported into bender. There is some magnetic flux from and to the H-type dipole magnet, which provides static beam deflection, into the adjacent solenoid magnets, which are used to match the beam to the chopper and the chopped beam to the following RFQ. To capture this effect in the simulation and still be able to independently adjust field levels, each magnet was simulated in the whole setup but with every other magnet turned of.

First, single particle tracking using bender was used to understand the distortions produced by the crossed electric and magnetic field configuration [12]. After optimisation of the field geometry, simulations including space charge of the 50 mA proton beam were made. In addition to the proton beam, the simulation includes 5 mA of $H_2^+$ and 5 mA of $H_3^+$ ions produced by the ion source. The input distribution at the start of the section were taken from 2D matching simulations of the LEBT. The voltage pulse on the deflection plates was taken from measurements of the pulse generator.

The geometry of the chopper system was included in the solution of the electric field of the proton beam. Simulations were made using a mesh of 2.5 mm in each direction distributed on 10-20 processors of the CSC cluster "Fuchs" [9].

Figure 6 shows the particle distribution at a time step during the fall time of the voltage pulse. The beam is swept over an aperture of 20 mm radius. Both the $H_2^+$ and the $H_3^+$ ions are deflected too strongly, so that only particles in the flanks of the pulse are transmitted into the following section.
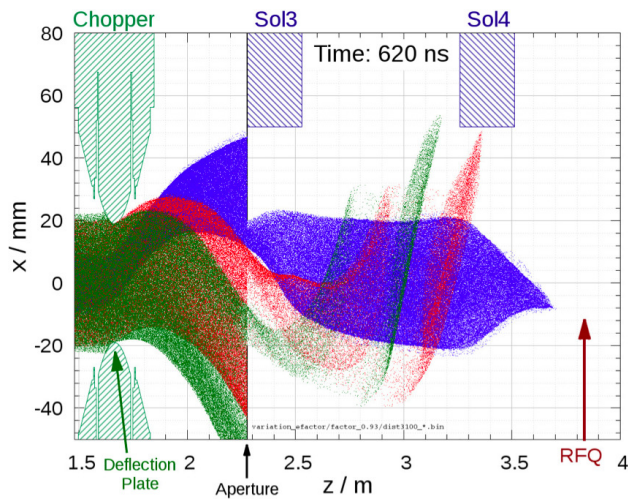
Figure 6: Snapshot of the chopper simulation, 50 mA proton beam (blue), 5 mA $H_2^+$ (red) and 5 mA (green).

Transmission of the proton beam through the aperture is, by design, 100%.

Simulations show, that the design flat-top pulse length of 50 ns can be reached with low beam offset below ±0.3 mm. The total pulse length is 350 ns. A large fraction of the pulse flanks has considerable position offset and will be collimated at the RFQ entrance. However, it was found, that the long pulse length compared to the flat top helps to mediate the effect of longitudinal broadening of the pulse by space charge forces compared to (theoretical) pulses of more step-wise distribution.

## CONCLUSION AND OUTLOOK

The dynamics of space charge compensation has been studied for some geometrically simple systems using a Particle-in-Cell code developed at IAP. For a system without any magnetic field, a thermal distribution of compensation electrons has been found. Furthermore, the code has been used extensively for the investigation of the E×B chopper concept including space charge.

Additionally, bender is in use for several other projects, including simulation of beam injection into a figure-8 storage ring [13], beam dynamics in CH cavities, simulation of electron beams in an electron lens for the IOTA ring at Fermilab [14] and simulation of plasma dynamics in Gabor lenses [15].

## REFERENCES

[1] C. Wiesner et al., Experimental Performance of an E×B Chopper System, Proc. of IPAC 2014, THPME015 (2014).

[2] C. K. Hockney, A. B. Langdon, Plasma Physics via Computer Simulation, CRC Press (2004).

[3] G. H. Shortley, R. Weller, The Numerical Solution of Laplace's Equation, J. Appl. Phys. 9, 334 (1938).

[4] S. Balay, S. Abhyankar, M. F. Adams, J. Brown, P. Brune, K. Buschelman, V. Eijkhout, W. D. Gropp, D. Kaushik, M. G. Knepley, L. C. McInnes, K. Rupp, B. F. Smith, H. Zhang, PETSc Web page, http://www.mcs.anl.gov/petsc

[5] M. Frigo, S. G. Johnson, The Design and Implementation of FFTW3, Proceedings of the IEEE 2005, 93, 2, Special issue on "Program Generation, Optimization, and Platform Adaptation"(2005).

[6] V. Vahedi, M. Surendra, A Monte Carlo collision model for the particle-in-cell method: applications to argon and oxygen discharges, Computer Physics Communications 87, 1-2, p. 179-198, 1995.

[7] M. E. Rudd, Y.-K. Kim, D. H. Madison and T. J. Gay, Electron production in proton collisions with atoms and molecules: energy distributions, Reviews of Modern Physics 64, 2, p. 441 (1992).

[8] Y.-K. Kim and M. E. Rudd, Binary-encounter-dipole model for electron-impact ionization, Phys. Rev. A 50, 5, p. 3954 (1994).

[9] Center for Scientific Computing Cluster "Fuchs", http://hhlr.csc.uni-frankfurt.de/

[10] R. J. Goldston, P. H. Rutherford, Introduction to Plasma Physics, Institute of Physics Pub. (1995).

[11] C. Wiesner et al., Proton Driver Linac for the Frankfurt Neutron Source, AIP Conf. Proc. 1265, 487 (2010).

[12] C. Wiesner et al., Chopping High Intensity Proton Beams Using a Pulsed Wien Filter, Proc. of IPAC 2012 (2012).

[13] Droba, M., Ates, A., Meusel, O., Niebuhr, H., Noll, D., Ratzinger, U., Wagner, J., Simulation Studies on Beam Injection Into a Figure-8 Type Storage Ring, Proc. of IPAC2014, TUPRO045(2014).

[14] G. Stancari, Applications of electron lenses: scraping of high-power beams, beam-beam compensation, and nonlinear optics, arXiv 1409.3615 (2014).

[15] K. Schulte et al., Space-Charge Compensation of Intense Ion-Beams by Nonneutral Plasma Columns, Proc. of HB2014, MOPAB19 (2014).

# NOISE AND ENTROPY IN NON-EQUIPARTITIONED PARTICLE BEAMS

I. Hofmann and O. Boine-Frankenheim

GSI Helmholtzzentrum für Schwerionenforschung GmbH, Planckstr.1, 64291 Darmstadt, Germany
Technische Universität Darmstadt, Schlossgartenstr.8, 64289 Darmstadt, Germany

## Abstract

The numerical noise inherent to particle-in-cell (PIC) simulation of 3d high intensity bunched beams in periodic focusing is explored on the basis of the rms entropy model by Struckmeier and of simulations with the TRACEWIN code using linac relevant parameters. Starting from noise in a matched equilibrium beam and its dependence on grid and particle number we explore the relevance of this noise under dynamical situations. The cases under study are fast emittance exchange; an initially mismatched beam; slow crossing through space charge structure resonances. We find that an effect of the equilibrium noise can be retrieved in a dynamical case, if the process is evolving sufficiently slowly.

## INTRODUCTION

In this paper we deal with the numerical noise generated by the discreteness of the spatial grid used for the Poisson solver as well as the effect of artificial collisions due to using highly charged super-particles. In simulation of extended plasmas this type of noise received attention since the 1970's, when interest in this field was growing in parallel with the performance of numerical computation.

More recently, the interest has revived to get a quantitative understanding of this noise in the field of high intensity beam simulation, where numerical noise may play a role for long-term simulation. In this context new interest was found in the analytical modelling of noise and the associated entropy growth based on the rms entropy model by Struckmeier [1, 2]. It is based on second order moments of the Vlasov-Fokker-Planck equation and assumes that collisional behaviour and temperature anisotropy can drive rms emittance growth, which is used to define an rms entropy growth. The associated noise and entropy growth in 2d beams - the transverse 4d phase space - is studied in a recent paper by Boine-Frankenheim et al. [3]. A companion paper by Hofmann et al. [4] deals with the rms entropy model and noise in 3d short bunches - in 6d phase space - with particular emphasis on linear accelerator applications. Some results of the latter are reviewed in the following section.

## REVIEW OF ENTROPY AND NOISE THEORY

The basic equation for the rms entropy growth is based on the idea that the change of the six-dimensional rms emittance defined as product of individual plane rms emittances, $\epsilon_{6d} \equiv \epsilon_x \epsilon_y \epsilon_z$, is a suitable measure for rms entropy growth, hence the system noise. The resulting relative change of rms emittance is given by:

$$\frac{1}{k}\Delta S = \frac{\Delta \epsilon_{6d}}{\epsilon_{6d}} = \Delta s \frac{k_f^\star}{3} \ (I_A + I_{GN}) \tag{1}$$

with a term related to temperature anisotropy,

$$I_A \equiv \left( \frac{(T_x - T_y)^2}{T_{xy}} + \frac{(T_x - T_z)^2}{T_{xz}} + \frac{(T_y - T_z)^2}{T_{yz}} \right), \tag{2}$$

$k^\star$ the dynamical friction coefficient and $I_{GN}$ describing an offset explained as grid noise in connection with the periodic focusing (see Ref. [4]).

We consider a periodic FODO lattice of 1000 cells with symmetrically arranged rf kicks. The zero current phase advance per cell of this lattice is assumed to be $k_0 = 60°$ in $x, y, z$ with equal emittances in all three directions. The beam is matched for a Gaussian distribution and the current is chosen such that the tune depression is $k/k_0 \approx 0.55$. The envelopes obtained with the TRACEWIN code are shown in Fig. 1:
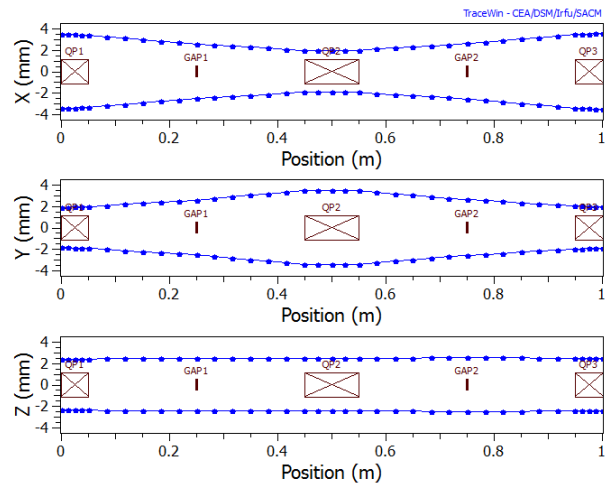


Figure 1: Basic cell of periodical FODO lattice with rf gaps.

The alternating focusing causes a strong modulation and local imbalance of "temperatures". According to Eq. 2, with more details in Ref. [1], this purely collisional effect is as source of entropy growth, which is amplified by grid heating effects Ref. [4]. Following Ref. [4], results for the relative growth of $\epsilon_{6d}$ are shown in Fig. 2 as function of $n_c$ and for different $N$. The $n_{cx,y,z}$ are understood as half number of cells between the maximum grid extent values of $\pm 3.5\sigma$. Beyond, the mesh is replaced by an analytical continuation for the space charge potential based on a Gaussian core of identical rms size. We note that the number of space charge
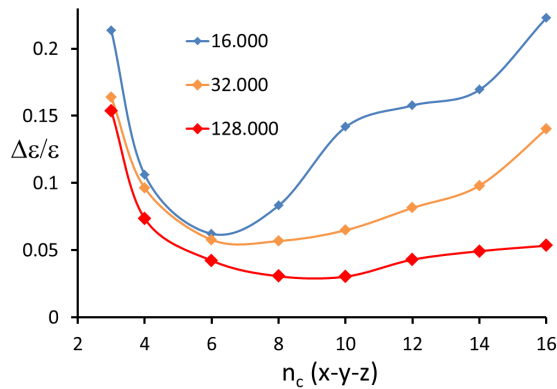
Figure 2: Relative growth of $\epsilon_{6d}$ in FODO lattice of Fig. 1 for $N$=16.000/32.000/128.000, as function of the number of grid cells in $x, y, z$.

steps per lattice cell has been chosen here as 15 (10/m in TRACEWIN). Also, the option "linear interpolation" (on the grid) is chosen.

Note that $n_c = 7$ implies only two grid points per $1\sigma$ of the Gaussian profile. This can explain the steeply rising noise or "grid heating" for less resolution, with only small differences between numbers of particles. All three cases show that an *optimum value of $n_c$ exists*, where the noise is minimum. It is the higher the larger $N$. The increase of $\Delta\epsilon_{6d}/\epsilon_{6d}$ above the optimum $n_c$ is most pronounced for the case $N$=16.000, where an estimate shows that the number of simulation particles per grid cell is only as low as approximately 1 for $n_c = 16$, which explains the strong rise of the noise. It is also seen that large $N$ is efficient only if the grid resolution is sufficiently large. For $N$=128.000 the gentle increase of the noise when rising above $n_c = 10$ might be indicative of an increase of the Coulomb logarithm with higher resolution of the colliding charges.

In summary, for $N \approx 10^5$ and a matched equilibrium beam at moderate space charge tune depression of about 50% an optimum $n_c \approx 8...10$ exists. In the following we explore to what extent the initial equilibrium noise level is relevant for describing dynamical situations driven by mismatch or resonances. This is obviously a complex discussion, and the following examples can only be a first attempt.

## EMITTANCE EXCHANGE AND NOISE

In linear accelerators it is understood that collision effects between real particles play no role, and emittance exchange can only occur due to resonant processes. For our discussion of simulation beams and the understanding of noise, it is nonetheless of interest to first explore the role of grid and collision noise in a case of anisotropy, but unaffected by resonances.

### Grid and Collision Noise

Anisotropy as source of emittance exchange can be studied by choosing initially different emittances. We consider a Gaussian distribution function, $N = 16.000$, and compare small and larger values of $n_c$. In the first example of Fig. 3 we assume $n_c = 10$. An initial anisotropy with
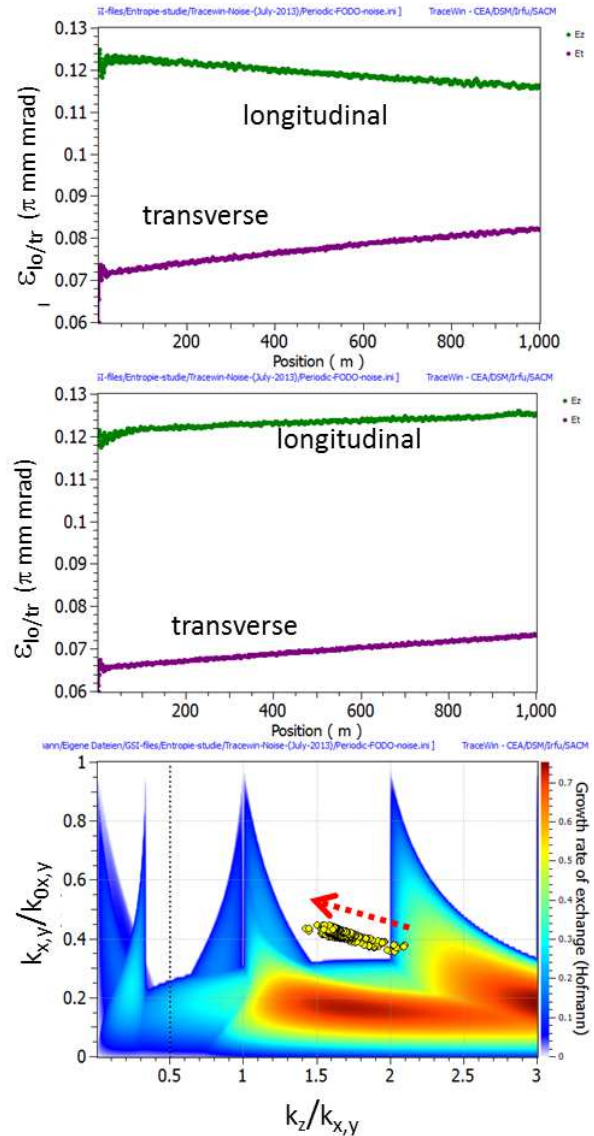


Figure 3: Rms emittances for $n_c = 10$ (top) and $n_c = 3$ (center); and stability chart (bottom, colour scale indicating theoretical rates of emittance change) for grid resolution $n_c = 10$.

$\epsilon_z/\epsilon_{x,y} = 2$ is assumed for zero current phase advances $k_{0x,y,z} = 52°/52°/60°$, with corresponding initial space charge depressed tunes of $k_{x,y,z} \approx 21°/21°/37°$. The slight splitting of zero current tunes between $z$ and $x, y$ is chosen in the example to avoid the resonant coherent emittance exchange by the $k_z/k_{x,y} \approx 1$ resonance. The pronounced collisional effect leads to a shrinking longitudinal emittance, while the transverse emittance (average of $\epsilon_x$ and $\epsilon_y$) grows.

It is expected from collisional behaviour - and consistent with Eq. 1 that the different temperatures of the ensemble relax towards an equipartitioned equilibrium. Note that the footprint of tunes in the bottom chart of Fig. 3 is taken over the 1000 periodic cells and entirely in the resonance-free region (few points exceeding $k_z/k_{x,y} = 2$ are caused by jitter only). The dashed (red) arrow in this chart marks the time evolution along the lattice.

Following Fig. 2, the noise level for a poor grid resolution $n_c = 3$ is close to that for $n_c = 10$ - only about 30% higher. The corresponding result - with parameters otherwise identical with Fig. 3 - is shown in the bottom graph of Fig. 3. This case is dominated by grid heating to the effect that all emittances increase. The increment of $\epsilon_{6d}$ is about comparable. This indicates the different nature of noise from grid heating and collisional heating in particular for anisotropic beams.

*Resonant Exchange and Noise*

Here we take again $\epsilon_z/\epsilon_{x,y} = 2$, but remove the splitting of tunes and assume $k_{0x,y,z} = 60°/60°/60°$, with corresponding $k_{x,y,z} \approx 26°/26°/35°$. We first use the larger $N = 10^5$ to keep collisions at a low level and assume $n_c = 6$, which is close to the bottom noise level of Fig. 2. Results are shown in the top of Fig. 4. It is noted that a rapid partial emittance exchange occurs during less than the first 20 cells. It is caused by the $k_z/k_{x,y} = 1$ resonance, which is driven by the space charge octupole [5]. This process is so fast that a noise effect should not be expected. This is confirmed by a comparison with the same calculation carried out with $N$ as low as $10^3$ in the center of Fig. 4. In spite of the much stronger noise effect for $N = 10^3$ the fast resonant exchange is practically unchanged and thus not influenced by the noise. It is followed by a collisional emittance exchange until complete equipartition and, beyond this point, a continuing growth of both emittances.

## INITIALLY MISMATCHED BEAMS

Here we refer to mismatch as one of the sources of halo formation and beam loss in high current linacs. In the following example we assume parameters (before mismatch) as for Fig. 2, with $N = 10^5$ and a large initial envelope mismatch by a factor $MM = 1.6$ in all planes. It is known that under the repeating action of mismatch oscillations particles are resonantly driven into a beam halo. In Fig. 5 we show the resulting 99.9% emittances in $x, y, z$ (top) and $\epsilon_{6d}$ (center) for a case with $n_c = 6$, which indicates the rapid conversion of mismatch into a halo population within about 50 periods. As quantitative measure for the transport into the halo region we also plot the percentage of particles, which are detected outside a radius of 5 mm after period 1000 (MM=1.6 and MM=1.2/1.2/1.6), where this radius marks the beam edge (99.9% of particles) in the absence of mismatch (MM=1). The percentage of particles into halo is seen to be practically insensitive to the grid resolution - even for the strong grid heating case $n_c = 3$. This is not unexpected in view of the rapid halo formation process. The early behaviour of
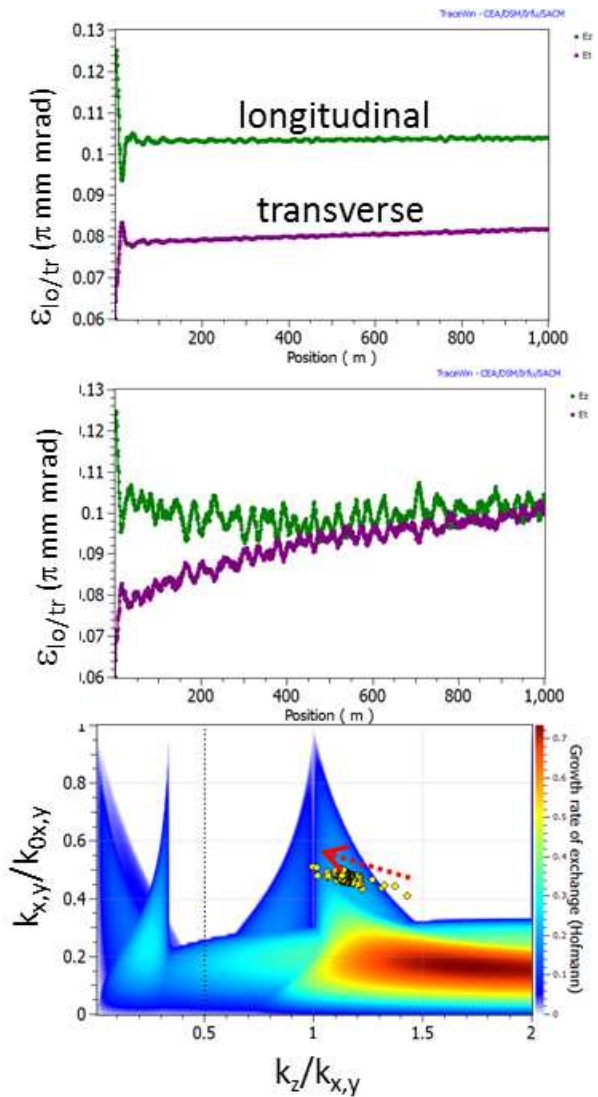


Figure 4: Resonant case: rms emittances for $N = 10^5$ (top) and $N = 10^3$ (center); and stability chart (bottom, for $N = 10^5$).

$\epsilon_{6d}$ is dominated by the coherent mismatch oscillations and becomes noise- or entropy-like only after about 200 cells.

## RESONANCE DRIVEN EMITTANCE GROWTH

In contrast with the preceding examples of "fast processes" we study here the behaviour for slow resonant processes by relatively slow crossing of low order resonances driven by space charge multipoles.

### $90° \to 60°$ *Tune Scan*

For a beam as used in Fig. 2 and with $N = 10^5$ we now assume a tune scan from $k_{0x,y,z} = 90°/90°/60°$ to $k_{0x,y,z} = 60°/60°/60°$ over 500 cells between cell 100 and 600 as shown in Fig. 6. Note that this scan leads to a scan of the rms value $k_{x,y}$ from approximately $55° \to 35°$. We note
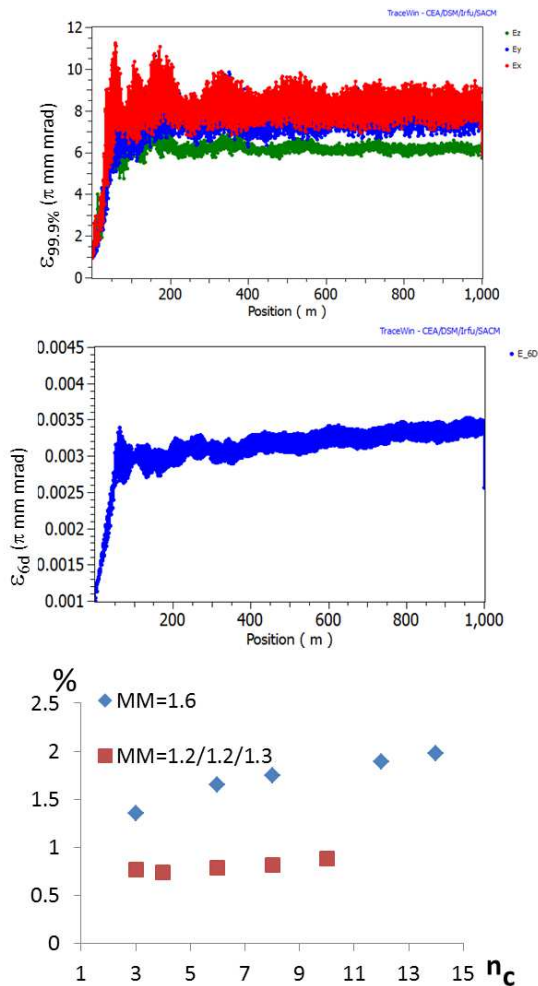
Figure 5: Mismatch action (MM=1.6) on $\epsilon_{99.9\%}$ (top), $\epsilon_{6d}$ (center) and percentage of particles into halo ($R > 5$ mm) as function of $n_c$ (bottom).





Figure 6: $x$-density probability (top) and percentage of particles into halo ($R > 5/10$ mm) as function of $n_c$ (bottom), for $n_c = 7$.

that the rms value of $k_{x,y}$ is crossing the value 45° at about cell 300. This indicates the center of a resonant stopband due to $4 \times 45 = 180$, possibly also $8 \times 45 = 360$ (see also Ref. [6]), for which there is an indication in the density probability plot. In Fig. 6 we show the $x$-density probability as well as the halo percentage into $R = 5$ and $R = 10$ mm apertures.

Comparing with the case $N = 128.000$ in Fig. 2 we suggest that the grid heating regime for small $n_c$ is reflected in the halo percentage. However, in the region $6 \leq n_c \leq 10$ the (collisional) noise is practically not increasing, while the halo percentage rises by almost a factor of 3 ($R = 5$ mm). This rise is nearly unchanged, if we increase N to $10^6$.

This result seems to indicate that for a slowly occurring resonance crossing the constancy of the noise level in equilibrium - with regard to rising $n_c$ - is not a guarantee that the percentage of particles into the halo is properly described by the simulation. Instead, it seems that a larger $n_c$ and thus higher accuracy in space charge potential calculation gives a more reliable prediction of the halo population.

## 90° *Stop-Band Crossing*

A much stronger type of space charge resonance occurs in the vicinity of the 90° stop-band. The condition $4 \times 90 \approx 360$° gives rise to resonance with the space charge pseudo-octupole as was shown experimentally [7], whereas theoretically also the so-called envelope instability (with $2 \times 90° \approx 180°$) might occur near this condition [6]. This crossing is realized in the simulation by a scan from $k_{0x} = 105° \rightarrow 88°$ during 1000 cells and fixed $k_{0y,z} = 105°/60°$ as shown in Fig. 7 for $N = 128.000$ and $n_c = 6$. The initial (rms) depressed tunes are $k_{x,y,z} = 91.5°/91.5°/49°$. The 4-th order resonance results in trapping of particles in four islands. This process becomes visible already after the first few cells and leads to their increasing separation from the core. Their separation as well as their rotation in the $x - x'$ phase are also identified in the $x$-density profile.

Increasing the grid resolution to $n_c = 12$ we have found, however, a significant deviation. There is no longer a void between core and islands, and more particles get extracted from the core. The $x - x'$ plot at 570 m actually indicates a strong presence of an envelope mode, which breaks the four-fold symmetry in the previous example. We attribute it to the envelope instability, which - surprisingly - was not found in the simulation with $n_c = 6$. The associated core oscillation is also visible in the $x$-density profile. We found that plotting $\epsilon_{x,53\%}$, the emittance of an ellipse including
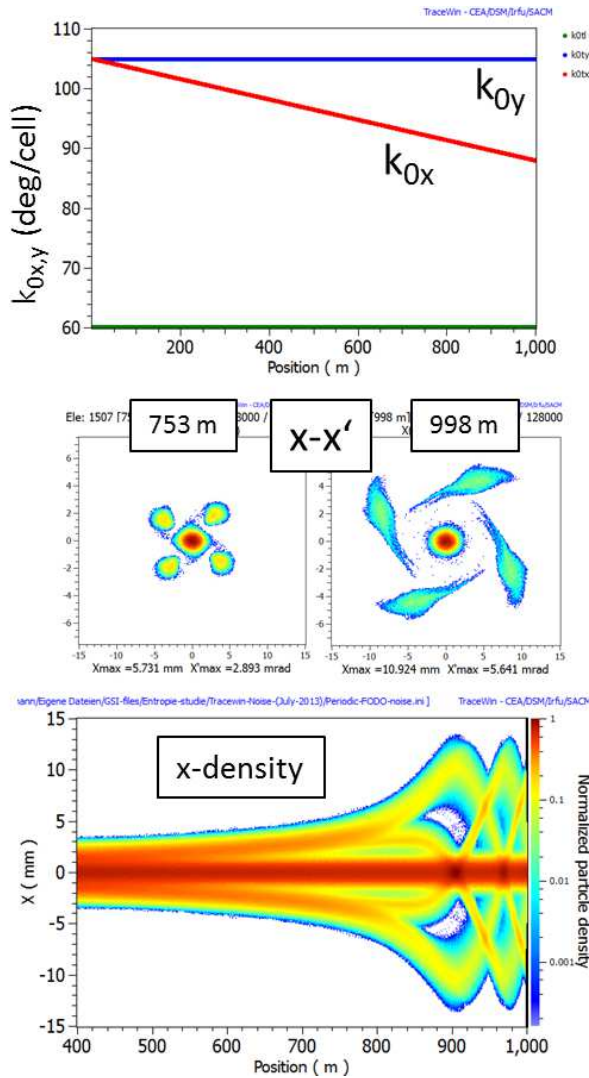
Figure 7: Tune scan (top), $x - x'$ phase space plots (center) and $x$-density profile (bottom) for $n_c = 6$.
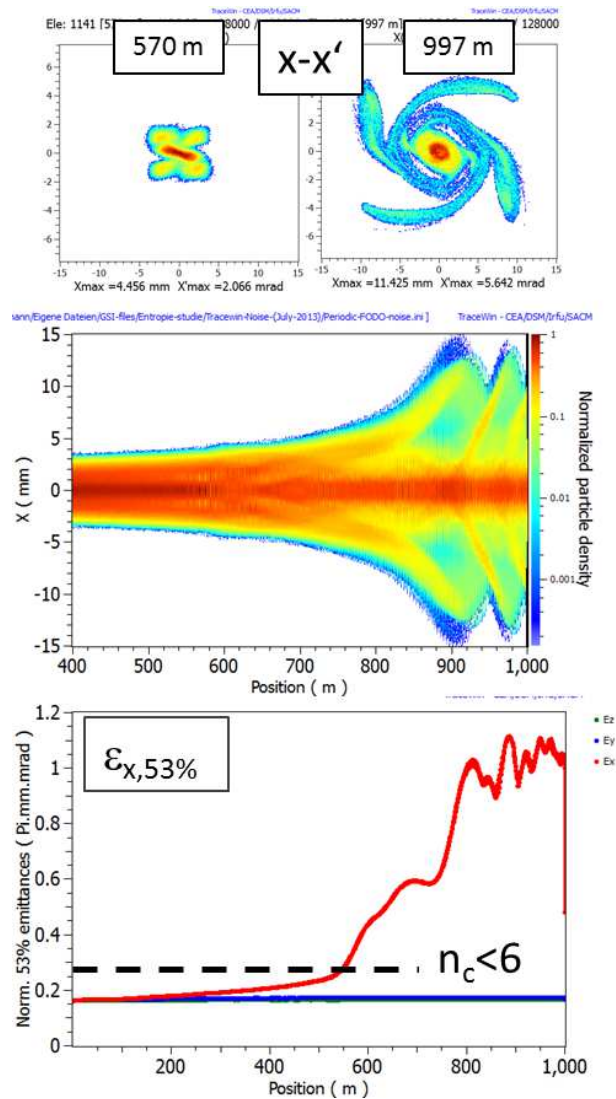


Figure 8: $x - x'$ phase space plots (top), $x$-density profile (center) and $\epsilon_{x,53\%}$ for $n_c = 12$.

53% of the particles, is a practical measure as it is chosen to include a fraction of particles trapped in the islands. Results as function of $n_c$ and for different $N$ are summarized in Fig. 9 in terms of the growth in $\epsilon_{x,53\%}$, including cases, which have been evaluated only until cell 600. The results indicate a "jump" in the behaviour for $n_c > 6$, independent of $N$. Apparently the additional feature occurs only subsequent to the development of the islands and thus becomes visible beyond approximately 600 cells. We cannot at present explain this behaviour as it is not obvious why a lower order resonance mode - the envelope mode - should appear only for higher $n_c$. A possible explanation might be the degradation of grid resolution in the core, while the grid cells grow with increasing distance of the islands from the center. Also, the envelope instability is growing exponentially from noise level - assuming an initially envelope matched beam - which makes this a noise sensitive process.

## CONCLUSION

We have explored the validity of the 6d rms emittance concept as measure for beam entropy growth driven by grid *and* collision induced noise, in particular under dynamical conditions beyond equilibrium. We find that noise only matters for sufficiently slow processes - fast emittance exchange or mismatch evolution is insensitive to it. For slow resonances, on the other hand, the equilibrium noise optimum at moderate resolution is not necessarily sufficient. In our examples higher grid resolution appears advantageous to resolve complex higher order resonance behaviour. These examples justify more work to be done in order to develop practically useful guidelines.
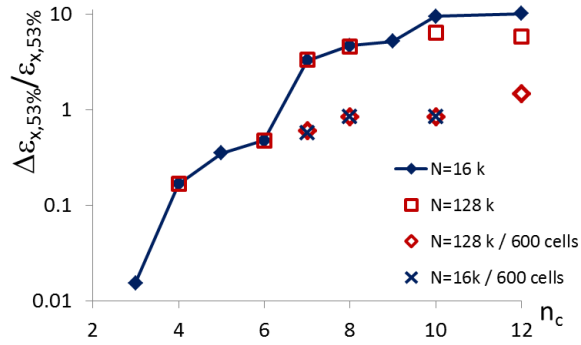
Figure 9: Comparison of maximum values of $\epsilon_{x,53\%}$ for different $N$ as function of grid resolution.

# REFERENCES

[1] J. Struckmeier, Phys. Rev. E 54, 830 (1996).

[2] J. Struckmeier, Phys. Rev. ST Accel. Beams 6, 034202 (2000).

[3] O. Boine-Frankenheim, I. Hofmann, J. Struckmeier and S. Appel, Nuclear Instruments and Methods in Physics Research A 770, 164 (2015.)

[4] I. Hofmann O. Boine-Frankenheim, to be published in Phys. Rev. ST Accel. Beams (2014).

[5] I. Hofmann, G. Franchetti, O. Boine-Frankenheim, J. Qiang, and R. D. Ryne, Phys. Rev. ST Accel. Beams 6, 024202 (2003).

[6] I. Hofmann, L.J. Laslett, L. Smith and I. Haber, *Part. Accel.* **13**, 145 (1983).

[7] L. Groening et al., Phys. Rev. Lett. **102**, 234801 (2009).

# RADIO FREQUENCY QUADRUPOLE FOR LANDAU DAMPING IN ACCELERATORS: ANALYTICAL AND NUMERICAL STUDIES

A. Grudiev, K. Li, CERN, Geneva, Switzerland
M. Schenk, University of Bern, Bern, Switzerland

*Abstract*

It is proposed to use a radio frequency quadrupole (RFQ) to introduce a longitudinal spread of the betatron frequency for Landau damping of transverse beam instabilities in circular accelerators. The existing theory of stability diagrams for Landau damping is applied to the case of an RFQ. As an example, the required quadrupolar strength is calculated for stabilizing the Large Hadron Collider (LHC) beams at 7 TeV. It is shown that this strength can be provided by a superconducting RF device which is only a few meters long. Furthermore, the stabilizing effect of such a device is proven numerically by means of the PyHEADTAIL macroparticle tracking code for the case of a slow head-tail instability observed in the LHC at 3.5 TeV.

## INTRODUCTION

In accelerators, the effect of Landau damping [1] provides a natural stabilizing mechanism against collective instabilities if the particles in the beam have a small spread in their natural (betatron or synchrotron) frequencies, see for example [2] and references therein. If the spread introduced by non-linearities naturally present in an accelerator is too small, a dedicated non-linear element is added to the system. For example, in LHC [3], 84 focusing and 84 defocusing (arranged in 16 families – two per sector), 0.32 m long superconducting magnetic octupoles is used to introduce a betatron frequency spread for Landau damping of the dipole modes. The LHC octupoles have been successfully used to stabilize the beams up to the energy of 4 TeV at which LHC has been operated so far [4]. The effect of the transverse spread however, reduces as the transverse geometrical beam emittance decreases at higher energies due to adiabatic damping.

Recently [5], it has been proposed to use an RFQ to introduce a longitudinal spread of the betatron frequency for Landau damping of the transverse collective oscillations. The basic idea is to use the harmonic dependence of the quadrupolar focusing strength of the RFQ on the longitudinal position of the particles in the bunch. It has been shown that in high energy accelerators, the longitudinal spread is more effective than the transverse one due to the longitudinal emittance of the beam being much larger than the transverse one. The higher efficiency of the longitudinal spread for Landau damping allows for a compact, only a few meters long, RF device based on several 800 MHz superconducting cavities operating in a TM quadrupolar mode to provide the same functionality as the LHC octupoles whose total length is about 56 m. In this paper, the work presented in [5] is summarized and the first results on the implementation of the RFQ in the PyHEADTAIL macroparticle tracking code and on the simulation of its stabilizing effect on a slow transverse head-tail instability observed in LHC at 3.5 TeV [4] are reported.

## RFQ FOR LANDAU DAMPING

For an ultra-relativistic particle of charge q and momentum $p$ traversing an RFQ along the $z$-axis at the time moment $t$, the transverse kick in the thin-lens approximation is given by

$$\Delta \mathbf{p}_\perp = p k_2 (-x\mathbf{u}_x + y\mathbf{u}_y)\cos\omega t, \qquad (1)$$

where $\omega$ is the RFQ frequency, $\mathbf{u}_\alpha$ is the unit vector along the $\alpha$ coordinate and $k_2$ is the amplitude of the normalised integrated quadrupolar strength

$$k_2 = \frac{q}{pc}\frac{1}{\pi r}\int_0^{2\pi}\left\|\int_0^L (E_x - cB_y)e^{j\omega z/c}\,dz\right\|\cos\varphi\,d\varphi, \qquad (2)$$

where $c$ is the speed of light, $L$ is the length of the RFQ and $[r, \varphi, z]$ are cylindrical coordinates. Assuming that the bunch centre ($z = 0$) passes the thin-lens RFQ at $t = 0$, the substitution $t = z/c$ gives the dependence of the quadrupolar strength along the bunch. Substituting this dependence in the expression for the betatron frequency shift due to quadrupolar focusing yields the expression for the variation of the betatron frequency (so-called detuning) along the bunch

$$\Delta\omega_{x,y} = \pm\beta_{x,y}\frac{\omega_0}{4\pi}k_2\cos(\omega z/c), \qquad (3)$$

where $\omega_0$ is the revolution frequency and $\beta_{x,y}$ are the horizontal and vertical beta functions, respectively. Taking into account that $\cos\omega z/c$ can be approximated as $\sim 1-(\omega z/c)^2/2$ for small arguments and $<z^2> = \sigma_z^2 J_z/\varepsilon_z$ after averaging over the synchrotron period $T_s$, one can derive the expression for the variation of the betatron frequency in terms of the longitudinal action $J_z$

$$\langle\Delta\omega_{x,y}\rangle_{T_s} \approx \pm\beta_{x,y}\frac{\omega_0}{4\pi}k_2\left[1 - \frac{1}{2}\left(\frac{\omega\sigma_z}{c}\right)^2\frac{J_z}{\varepsilon_z}\right], \qquad (4)$$

where $\sigma_z$ and $\varepsilon_z$ are the RMS bunch length and the longitudinal emittance, respectively. Equation (4) is composed of two terms. The first one is a constant betatron frequency shift which, if necessary, can be compensated by a static magnetic quadrupole. The second term describes the incoherent spread required for Landau damping. It is used to estimate the integrated quadrupolar strength amplitude needed to stabilize a transverse instability with a coherent betatron frequency shift $\Delta\Omega^{coh}_{x,y}$ according to the following condition

$$\beta_{x,y}\frac{\omega_0}{8\pi}k_2\left(\frac{\omega\sigma_z}{c}\right)^2 > \left|\Delta\Omega_{x,y}^{coh}\right|, \qquad (5)$$

which is based on applying the generalized theory of stability diagrams for Landau damping [6] to the case of an RFQ.

According to the Panofsky-Wenzel theorem [7], an RFQ also causes a change of the longitudinal momentum depending on the transverse and longitudinal coordinates of a particle in the bunch. This leads to a transverse spread in the synchrotron frequency. However, for the LHC, this transverse spread is found to be negligible compared to the longitudinal spread due to the large difference between the transverse and longitudinal emittances.
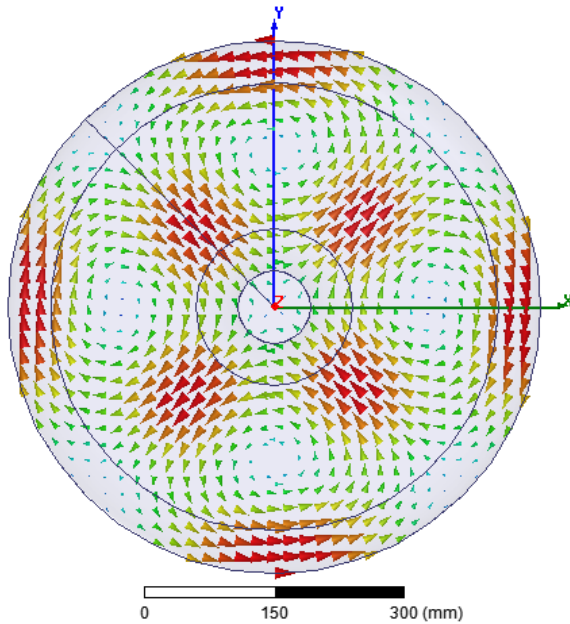


Figure 1: Magnetic field distribution in the transverse plane of the TM quadrupolar mode cavity of the RFQ.

For illustration, a design of an RFQ device with the same functionality as the LHC octupoles has been proposed. From Eq. (5), the required quadrupolar strength is expressed as

$$k_2 = \frac{2}{\pi}\frac{\left|\Delta\Omega_{x,y}^{coh}\right|}{\omega_0\beta_{x,y}}\left(\frac{\lambda}{\sigma_z}\right)^2.$$

Its value $k_2 = 1.4\cdot10^{-5}$ m$^{-1}$, required for Landau damping of a coupled bunch mode with the coherent betatron frequency shift of ~$0.0002\omega_0$, is calculated for nominal beam parameters of the LHC at 7 TeV [3]: $\sigma_z = 0.08$ m and beta functions of 200 m at a potential location in IR4 near the main RF system. An RFQ wavelength of $\lambda = 0.375$ m, i.e. RFQ frequency of 800 MHz is chosen, which is the second harmonic of the main RF frequency and for which the bunch still fits in the RFQ bucket as $4\sigma_z = 0.32$ m $< \lambda$. On the other hand, the normalised quadrupolar strength of a cylindrical 800 MHz 0.15 m long pillbox cavity operating in a TM quadrupolar mode is calculated from the complex electromagnetic field map

obtained numerically using the code HFSS [8]. In Fig. 1, the distribution of the magnetic field in the transverse plane of the cavity is shown for illustration. The strength value per cavity is determined to be $k_2 = 6\cdot10^{-6}$ m$^{-1}$, given the maximum values of 46 MV/m and 120 mT for respectively the electric and magnetic fields on the cavity surface. Taking this value as a maximum that can be achieved in one cavity due to limitations on the surface fields coming from an RF superconductivity quench or an electrical discharge in vacuum [9], the total number of cavities needed can be determined to be three. Adding the same factor two margin as for the LHC octupoles, we conclude that six cavities with a total active length of less than a meter can provide the same Landau damping as the 56 m of LHC magnetic octupoles at a nominal current of 500 A. The whole RFQ device, including the RF power couplers and the coupler for lower, same and higher order parasitic modes suppression could be integrated in a single few meters long cryostat.

## NUMERICAL STUDIES AND RESULTS

The performance of an RFQ with the design parameters given in the previous section is evaluated numerically for the LHC by means of PyHEADTAIL, a macroparticle tracking code under development at CERN and successor of the well-established HEADTAIL code [10]. Amongst others, this software allows to study the formation of collective instabilities in circular accelerators and to evaluate appropriate methods for their mitigation.

The PyHEADTAIL model assumes linear periodic transport from one section to another along the accelerator ring in the transverse and longitudinal planes. All the impedances are lumped in a single point where they are adequately weighted by the corresponding beta functions. Macroparticle bunches are initialised and tracked through the ring via the concatenation of linear periodic maps and wakefield kicks. After each linear transport, the effect of chromaticity, i.e. the variation of the betatron tune with the relative momentum deviation $\Delta p/p$, is applied by changing the individual phase advance of every single macroparticle in the bunch (incoherent detuning). The amplitude detuning caused by magnetic octupoles [11] possibly installed in the accelerator as well as the detuning introduced by an RFQ (Eq. (3)) are implemented in the same manner.

For the numerical study, an LHC case was identified for which experimental data are available to make direct validation of the simulation results possible. The chosen study case is a single-bunch horizontal slow head-tail instability, which has been observed during LHC commissioning at an energy of 3.5 TeV [4]. It has been shown experimentally that this instability is fully suppressed by means of the magnetic octupoles installed in the LHC. These devices have the sole purpose of introducing an incoherent betatron tune spread for beam stabilization through the process of Landau damping [11]. The octupolar strength, and hence the tune spread, are controlled by the electric currents $I_f$ and $I_d$ in the focusing

and defocusing octupole magnets, respectively. Experiments have shown that the threshold value for the mitigation of the abovementioned instability lies between $I_d = -I_f = 10$ A and $I_d = -I_f = 20$ A.

Before studying the RFQ, the experimentally observed beam stabilization achieved using the octupole magnets and the threshold values for $I_f$ and $I_d$ are reproduced with PyHEADTAIL simulations. The LHC machine and beam parameters used for this study are summarized in Tab. 1. The wakefield kicks are calculated from wake tables computed from the latest version of the LHC impedance model [12]. To simplify the analysis, only the dipolar wake components are considered. It has been verified that including the quadrupolar terms does not significantly change the outcome of the simulations. Due to the comparatively low growth rate of the observed instability with rise times of the order of several seconds, the bunch is tracked over a total number of 300 000 turns which corresponds to a time range of 27 s in the LHC. The bunch is composed of one million macroparticles which was shown from convergence studies to be sufficient to yield accurate results.

Table 1: Main Parameters Used in the PyHEADTAIL Simulations to Reproduce the Experimental Observations Made in LHC.

| Parameter | | Value |
|---|---|---|
| Beam energy | $E$ | 3.5 TeV |
| Beam intensity | $N_b$ | $1.05 \cdot 10^{11}$ p/b |
| RMS bunch length | $\sigma_z$ | 0.06 m |
| Norm. horizontal emittance | $\varepsilon_x$ | 3.75 μm |
| Horizontal chromaticity | $Q'_x$ | 6 |
| Nb. of macroparticles | | $10^6$ p/b |
| Nb. of turns | | $3 \cdot 10^5$ turns |
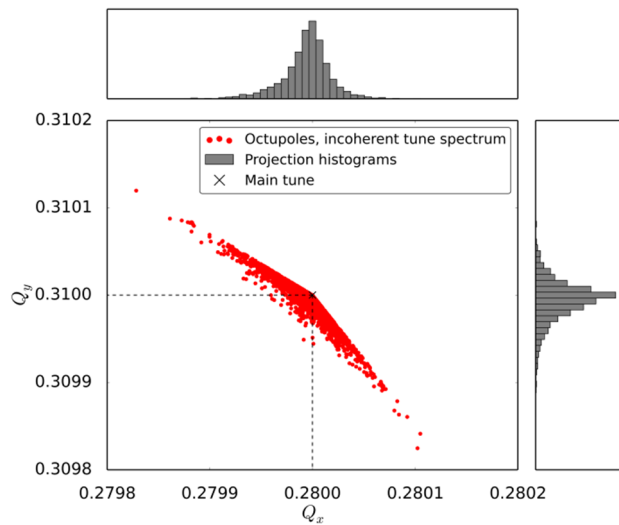


Figure 2: Incoherent betatron tune spectrum $Q_y$ vs. $Q_x$ (tune footprint) introduced by the presence of the LHC octupole magnets at $I_d = -I_f = 20$ A and using the beam parameters given in Tab. 1.

Figure 2 shows the incoherent betatron tune spectrum originating from amplitude detuning caused by the LHC octupole magnets at an electric current of $I_d = -I_f = 20$ A and using the machine and beam parameters defined in Tab. 1. The spectrum is obtained from PyHEADTAIL simulations incorporating purely linear betatron and synchrotron motion together with the detuning effect of the LHC octupole magnets. The spectral analysis is performed using the SUSSIX code [13]. The shape and distributions of the betatron tune spectrum can be fully understood from the amplitude detuning formula given in [11].
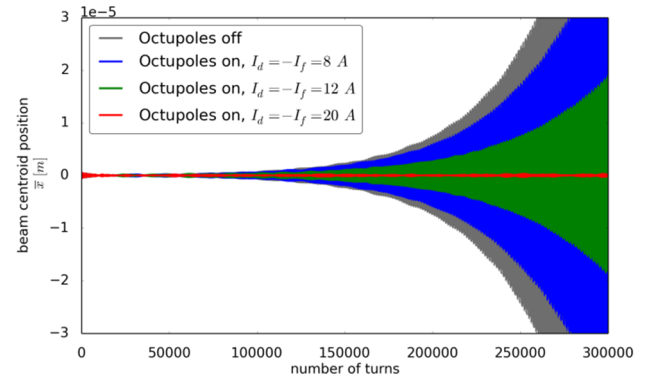


Figure 3: Horizontal beam centroid position vs. number of turns as obtained from PyHEADTAIL using the parameters in Tab. 1. Results are shown for various electric currents in the LHC octupole magnets.

Figure 3 shows the outcome of the PyHEADTAIL simulations using the parameters in Tab. 1. The horizontal bunch centroid position versus the number of turns is plotted for four different values of the electric currents $I_f$ and $I_d$ in the octupole magnets. In case the octupoles are switched off (grey curve), a very clean instability is seen with an exponential amplitude growth of the horizontal bunch centroid motion. The frequency analysis of this motion reveals a mode $m = -1$ instability, in agreement with what has already been determined from experimental data [4]. As can be seen in Fig. 3, starting from electric currents of $I_d = -I_f = 8$ A (blue) in the octupole magnets, the growth rate of the instability decreases. This is a result of Landau damping setting in, i.e. the incoherent betatron tune spectrum introduced by the octupole magnets becomes wide enough to overlap with the frequency of the coherent (unstable) mode. At values of $I_d = -I_f = 8$ A and $I_d = -I_f = 12$ A (green) however, Landau damping is not yet sufficient to fully suppress the instability. This can only be achieved when setting the electric currents to a value of $I_d = -I_f = 20$ A (red) or higher. The stabilization threshold has been cross-checked with stability diagram theory for magnetic octupoles, yielding $I_d = -I_f = 18$ A.

The excellent agreement of the results obtained from experimental data, PyHEADTAIL simulations and stability diagram theory proves a solid understanding of the observations made. The fact that the instability is cured unambiguously through the process of Landau damping makes it an ideal case to study the effect of an

RFQ on beam stabilization. In the following, the incoherent betatron tune spectrum originating from the presence of an RFQ is shown and explained first. Afterwards, the octupole magnets used to obtain the results presented in the previous paragraphs are replaced by an RFQ to evaluate its performance in comparison.
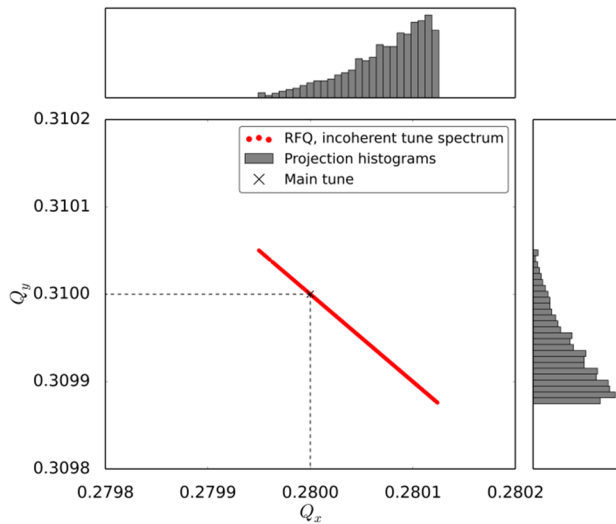


Figure 4: Incoherent betatron tune spectrum $Q_y$ vs. $Q_x$ (tune footprint) introduced by the presence of an RFQ at a strength of $k_2 = 7.8 \cdot 10^{-6}$ m$^{-1}$ and using the beam parameters given in Tab. 1.

Similarly to octupole magnets, the detuning caused by an RFQ leads to an incoherent betatron tune spectrum with a certain spread and distribution characteristic for the chosen parameters of the beam and of the device and its location in the accelerator. An example is shown in Fig. 4 for the machine and beam parameters given in Tab. 1. The beta functions at the location of the RFQ are chosen to be 200 m for reasons explained in the previous section. The RFQ frequency is fixed to 800 MHz. The shape and distributions of the betatron tune spectrum can be understood from the detuning formula in Eq. (4). First, as opposed to what is observed when using magnetic octupoles (Fig. 2), the tune shifts $\Delta Q_x$ and $\Delta Q_y$ induced by an RFQ are fully correlated as there is only one independent variable $J_z$. The tune shift ratio $\Delta Q_y/\Delta Q_x$ is defined by the negative ratio of the beta functions $-\beta_y/\beta_x$ at the location of the RFQ. Second, compared to the spectra resulting from magnetic octupoles, the projection histograms in Fig. 4 show much more asymmetric distributions with the betatron tunes of the majority of macroparticles shifted away from the original main tune of the accelerator (black dashed lines). This asymmetry is expected for the case where $\lambda > \sigma_z$, i.e. the approximation in Eq. (4) holds. Since the longitudinal phase space distribution is chosen to be Gaussian and centred about zero longitudinal action $J_z = 0$, a large fraction of the particles in the beam experience only the constant betatron tune shift, i.e. the first term in Eq. (4). On the other hand, there is only a small number of particles with a large longitudinal action $J_z$ whose tune shift is

dominated by the second term in Eq. (4). In case the approximation does not hold, i.e. if $\lambda \leq \sigma_z$, the incoherent tune spectrum will become more symmetric and uniform.

Figure 5 shows the horizontal bunch centroid position versus the number of turns with and without the presence of the RFQ. Similarly to what has been found for the octupole magnets in Fig. 3, starting from an RFQ strength of $k_2 = 6.2 \cdot 10^{-6}$ m$^{-1}$ (blue), the growth rate of the instability decreases, indicating the presence of Landau damping. Again, at moderate RFQ strengths of $k_2 = 6.2 \cdot 10^{-6}$ m$^{-1}$ and $k_2 = 6.8 \cdot 10^{-6}$ m$^{-1}$ (green), Landau damping is not sufficient to prevent the instability from evolving. Only by increasing the strength to a value of $k_2 = 7.8 \cdot 10^{-6}$ m$^{-1}$ or higher, the instability can finally be fully damped. At the given beam energy of 3.5 TeV, this strength can be provided by a single superconducting cavity of the kind described in the previous section. A comparison of the simulation outcomes presented in Fig. 3 and 5 shows that similarly to octupole magnets, an RFQ can indeed be used for beam stabilization through Landau damping.
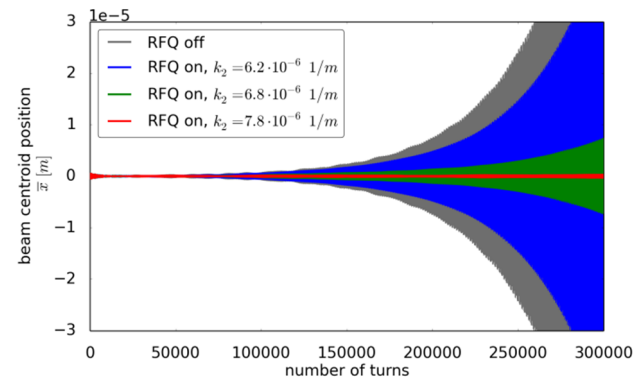


Figure 5: Horizontal beam centroid position vs. number of turns as obtained from PyHEADTAIL using the parameters in Tab. 1. Results are shown for various strengths $k_2$ of RFQ cavities operating at 800 MHz.

## CONCLUSION

It has been shown that an RF quadrupole introduces a longitudinal spread of the betatron frequencies which can be used for Landau damping of the transverse coupled bunch instabilities. As an example, the required strength of the RFQ providing the same functionality as the LHC magnetic octupoles has been calculated. Furthermore, a possible implementation of the RFQ using a set of superconducting cavities in one few meters long cryostat has been shown. To evaluate numerically the performance of such a device and its effect on the stabilization of transverse beam instabilities, the macroparticle tracking code PyHEADTAIL has been used. A thoroughly analysed and well-understood LHC case at 3.5 TeV served to prove numerically that the RFQ can, similarly to octupole magnets, generate the necessary incoherent betatron tune spread to provide sufficient Landau damping to fully stabilize the beam.

## ACKNOWLEDGMENT

The authors are grateful to E. Métral for his interest in this work and enlightening discussions about the physics of Landau damping.

## REFERENCES

[1] L. D. Landau, J. Phys. USSR 10, 25 (1946).

[2] A. W. Chao, Physics of Collective Beam Instabilities in High Energy Accelerators (John Wiley & Sons, New York, 1993).

[3] "LHC Design Report", CERN-2004-003, 2010.

[4] E. Métral, B. Salvant and N. Mounet, "Stabilization of the LHC Single-Bunch Transverse Instability at High-Energy by Landau Octupoles", in Proceedings of IPAC11, San Sebastian, Sept. 2011, p.775; CERN-ATS-2011-102, 2011.

[5] A. Grudiev, Phys. Rev. ST Accel. Beams 17, 011001 (2014).

[6] J. S. Berg and F. Ruggiero, "Stability Diagrams for Landau Damping", in Proceedings of PAC97, Vancouver, May 1997, p.1712; LHC Project Report 121, 1997.

[7] W. K. H. Panofsky and W. A. Wenzel, Rev. Sci. Instrum. 27, 967 (1956).

[8] Ansys HFSS, http://www.ansys.com/

[9] H. Padamsee, J. Knobloch and T. Hays, RF Superconductivity for Accelerators (John Wiley & Sons, New York, 1998).

[10] G. Rumolo and F. Zimmermann, Phys. Rev. ST Accel. Beams 5, 121002 (2002).

[11] J. Gareyte, J. P. Koutchouk and F. Ruggiero, LHC project report No. 91, 1997.

[12] N. Mounet et al, "Impedances and instabilities", Proceedings of the 5th Evian workshop on LHC beam operation (2014).

[13] R. Bartolini and F. Schmidt, CERN-SL-Note-98-017.

# NEW PSB H⁻ INJECTION AND 2 GeV TRANSFER TO THE CERN PS

W. Bartmann, J.L. Abelleira, B. Balhan, E. Benedetto, J. Borburgh, C. Bracco, C. Carli, V. Forte,
S. Gilardoni, G.P. Di Giovanni, G. Gräwer, B. Goddard, K. Hanke, M. Hourican, A. Huschauer,
M. Meddahi, B. Mikulec, G. Rumolo, L. Sermeus, R. Steerenberg, G. Sterbini, Z. Szoke,
R. Wasef, Y. Wei, W. Weterings, CERN, Geneva, Switzerland

## Abstract

At CERN Linac4 is being commissioned as first step in the LHC injector upgrade to provide 160 MeV H⁻ ions. In order to fully deploy its potential, the PSB conventional multiturn injection will be replaced by a charge exchange injection. An expected brightness improvement of about a factor 2 would then be difficult to digest at PS injection due to space charge. Therefore the transfer energy between PSB and PS will be increased at the same time from 1.4 to 2 GeV. This paper describes the new PSB injection system and the status of its test stand. Modifications of the PSB extraction and recombination septa and kickers in the transfer line are shown. A new focussing structure for the transfer lines to match the horizontal dispersion at PS injection and the design of a new Eddy current septum for the PS injection are presented.

## MOTIVATION

The described CERN PS Booster (PSB) upgrades - undertaken within the LHC injector upgrade (LIU) - aim at providing brighter beams for the LHC after Long Shutdown 2 (LS2) and at preparing the beams for the High Luminosity upgrade of LHC (HL-LHC) in Long Shutdown 3 (LS3).

The upgrade of the PSB injection has two main ingredients. Linac4 will provide beams at 160 MeV instead of the present beam energy of 50 MeV from Linac2. Considering the present incoherent space charge tune shift as acceptable, the intensity which can be accumulated during the multi-turn injection process can be doubled within a given emittance [1].

The second important upgrade at injection is the change from a conventional multi-turn injection of protons from Linac2 to a charge exchange injection of H⁻ from Linac4. The injection of H⁻ onto an already occupied phase space area allows to better tailor the brightness of the various beams used in the CERN accelerator complex. In addition, the conventional multi-turn injection process is inherently loss dominated due to the exploitation of a septum (40% loss with respect to delivered intensity by Linac2). The septum width together with the available aperture at PSB injection also limits the number of injection turns to about 13. The new H⁻ injection will allow to significantly reduce the losses per injection turn to the order of a few percent, dominated by the stripping efficiency of the foil.

In Figures 1 and 2 the brightness limitations before and after the upgrades are compared for the standard production of the 25 ns LHC beam in the LHC injector chain [2] . Before the upgrades of its injection system, the PSB represents the

limit in brightness of the LHC beams. After upgrading the PSB with the potential factor two gain in brightness, the injection into the PS would replace the PSB as the brightness bottleneck in the accelerator chain. Thus, an increase of the PS injection energy from 1.4 to 2.0 GeV is foreseen, which shall give the possibility to increase the brightness by about 60% at PS injection. In order to reach the HL-LHC beam requirements for after LS3, also upgrades concerning the SPS beam loading are required [2].
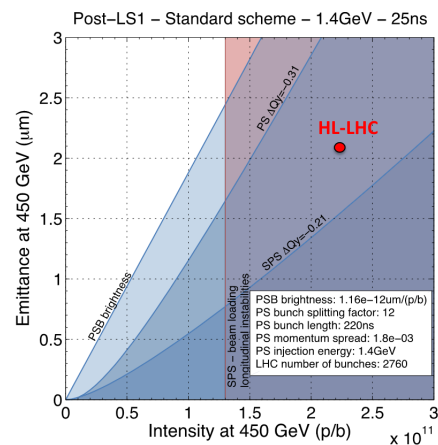


Figure 1: Emittance as a function of intensity at SPS extraction for LHC beams after LS1.
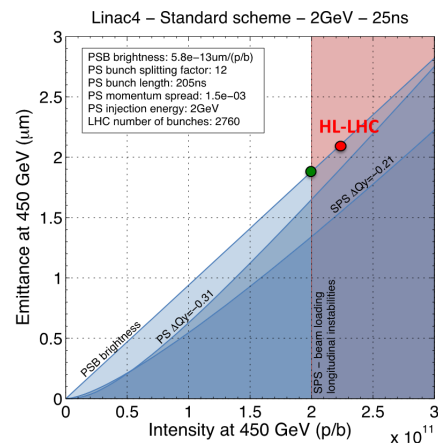


Figure 2: Emittance as a function of intensity at SPS extraction for LHC beams with the foreseen upgrades of the LHC injectors after LS2.

# PSB H⁻ INJECTION

Presently the PSB injection performs first a splitting of the Linac pulse into 4 beam lines which are vertically separated. Further downstream these 4 beams are horizontally injected into the 4 rings over several turns deploying a septum magnet and a varying orbit bump. The present 50 MeV beam pulse from Linac2 is deflected vertically along the pulse with different kick strengths separated by 100 ns from a staged kicker system. The kicker system consists of 5 terminated magnets which are energised by 5 PFN type generators operating at 28 kV. The first part of the pulse is not deflected and dumped on a so-called head dump within the vertical septum magnet tank. The flat part of the Linac pulse is then separated by the kickers into 4 beamlets which are deflected by a vertical steerer and three septum magnets onto the vertical position of the PSB rings 1,2 and 4. The beam for ring 3 is deflected only by the vertical steerer and passing in between the septa without further deflection. The end of the pulse sees the maximum deflection of the kicker system and is dumped on the tail dump. The parts of the pulse which overlap with the kicker rise-time are intercepted by scrapers protecting the septum coils. However, these losses are about three orders of magnitude smaller than the losses during the multiturn injection process in the horizontal plane deploying a varying bump and a septum magnet where about 40% of the injected beam is lost.

The future kicker system has to cope with a 160 MeV H⁻ beam which means an increase of a factor 1.9 in magnetic rigidity. In order to reach the required increase in integrated magnetic field, the magnets are short circuited inside the vacuum vessel. Since not only the beam rigidity but also the possible number of injected turns will be increased and consequently the required kicker pulse length, the beam pulse from Linac4 will not be continuous but chopped to provide gaps for the kicker field to rise. This allows for rise-times of up to 2 $\mu$s without risking to sweep this part of the beam over the downstream vertical septa allowing scrapers to be omitted. The PSB straight section occupied presently
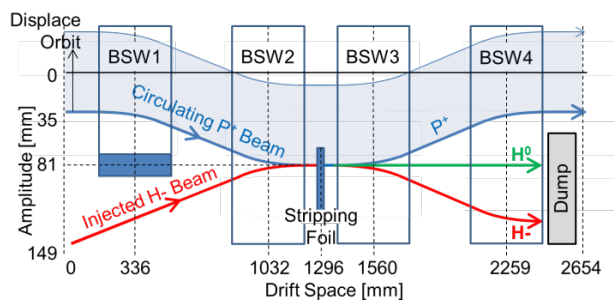


Figure 3: Configuration of the injection straight section.

by the horizontal injection septa, injection instrumentation and one of the painting bumpers will be used to install a 4 magnet chicane bump, a foil handling system and related instrumentation within a length of 2.564 m, Fig. 3. A dump taking care of partially stripped or unstripped particles is

placed directly downstream of the fourth chicane magnet. This dump is fully made of metallic components to reduce as much as possible the number of interventions and thus, the integrated radiation dose for personnel.

A chicane bump displaces the beam by a constant 46 mm at the foil location, while a painting bump is used to vary horizontally the orbit and angle offset of the beam at the foil in order to paint in transverse phase space. Figure 4
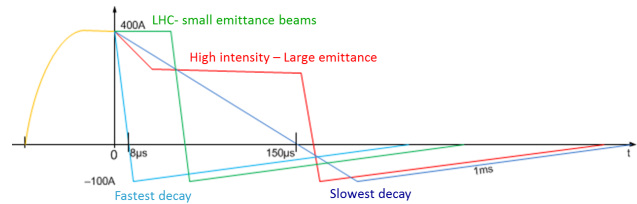


Figure 4: Current decay in painting bumpers for different beam types.

shows the current decay in the painting magnets for LHC and high intensity beams, one turn corresponds to about 1 $\mu$s. The minimum number of required turns is defined by the longitudinal painting, which requires about 40 turns [3]. The maximum number of turns depends on the current delivered by the Linac4 source. For the nominal source current of 80 mA, a maximum number of about 100 turns is sufficient to reach the required target intensities. In case of 50 mA source current, the number of required turns will increase to 150 which is the maximum possible pulse length for all injection equipment. The transverse painting is optimised for each
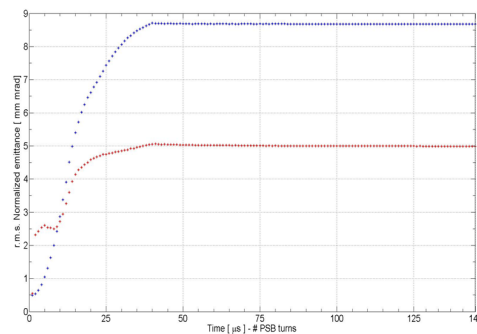


Figure 5: Horizontal (blue) and vertical (red) emittance evolution for ISOLDE fixed target beam during painting.

beam type. In case of LHC beams, no transverse painting is taking place and only foil scattering is contributing to emittance blow-up [4]. For high intensity beams, Fig. 5 and Fig. 6, the painting bump is reduced very quickly at the beginning to move the injected beam away from the centre of transverse phase space. When the injected beam has reached the outer part of phase space an almost constant plateau of the painting function with variable length is used to reach the required number of injection turns.

After injection the chicane bump is reduced to zero within 5 ms. The varying bump height during the decay generates a
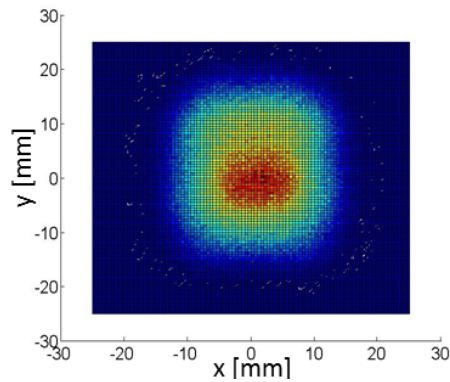
Figure 6: Real space intensity distribution of ISOLDE fixed target beam.



Figure 8: Cross section of the stripping foil unit design with the foil exchange mechanism and a beam observation system (BTV).

detuning of the machine. Two options of compensation were studied, bending magnets with rectangular or sector edge shape, with active or passive compensation. Even though at injection there is higher risk to cross a vertical resonance line, bending magnets with rectangular edge shape were chosen together with an active compensation of the varying edge focussing by trim power supplies. Also in case of sector bends vertical edge focussing cannot be avoided due to the varying beam angle with respect to the magnet edge during painting and the values of the betatron functions at the trim quadrupoles favour a correction of the vertical detuning [5]. Also multipole perturbations generated by Eddy currents induced by the varying chicane field in the vacuum chamber can be compensated [6].

*Test Stand*

The new injection equipment will be tested prior to commissioning in two test stands to be installed in Linac4. One setup concerns a permanent installation of the $H^-$ stripping foil [7], Fig. 7. It is foreseen to measure the stripping efficiency at the percent level by measuring the beam current before and after the foil with a current measurement resolution of 0.1 mA. A rough estimation of the emittance growth due to foil scattering could be obtained by measuring beam profiles with SEM grids. The rigidity of foils and the foil holding mechanism can be tested as a function of many mechanical cycles. The foil control system and the foil–screen interference interlock shall be commissioned. The operation of this test stand shall start autumn 2015. The second test
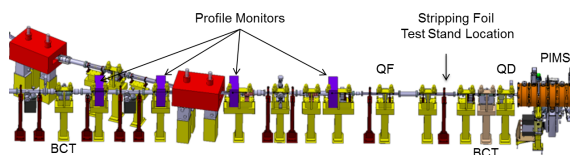


Figure 7: Layout of stripping foil test stand between Linac4 PI-Mode Structure (PIMS) and main dump.

stand includes a temporary installation of half of the future PSB $H^-$ injection chicane in the transfer line between Linac4
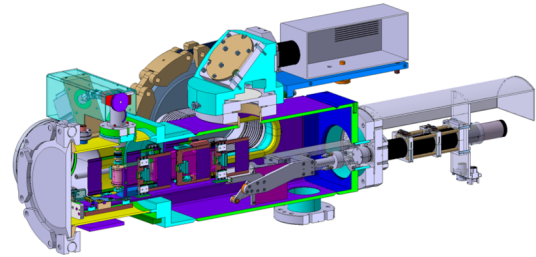
and PSB. The equipment inventory includes a stripping foil and screen unit, Fig. 8, two chicane magnets with the internal dump and the $H^0/H^-$ current monitor. In addition there will be diamond and ionisation chamber beam loss monitors, beam current transformers, an additional screen and an external dump, Fig. 9. The full installation will be enclosed by two vacuum valves. The aim of this test is to
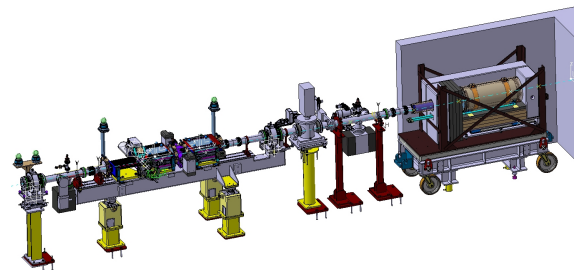


Figure 9: Layout of second test stand in the Linac4 transfer line with the external dump. Courtesy Jerome Humbert.

measure more precisely the stripping efficiency deploying an $H^0/H^-$ current monitor. The powering and controls of two chicane magnets will be tested for current stability and interlocking. The aperture, temperature and pressure behaviour of the internal $H^0/H^-$ dump will be measured. Diamond loss monitors should allow to measure secondary particles close to the internal dump which allows to evaluate operational conditions with respect to foil degradation. These tests are foreseen to take place in 2016.

## PSB-PS 2 GeV TRANSFER

The 2 GeV upgrade is required to keep the incoherent space charge tune shift at PS injection below 0.31. The higher injection energy is also beneficial for beams where brightness is not the figure of merit, like high-intensity fixed target (FT) beams. Those beams generate losses during the injection process which can be reduced due to the smaller beam size at 2 GeV. In order to further reduce the losses generated by these beams, the transfer between PSB and PS will be upgraded such that beams with different destinations in the accelerator chain can be transferred with dedicated
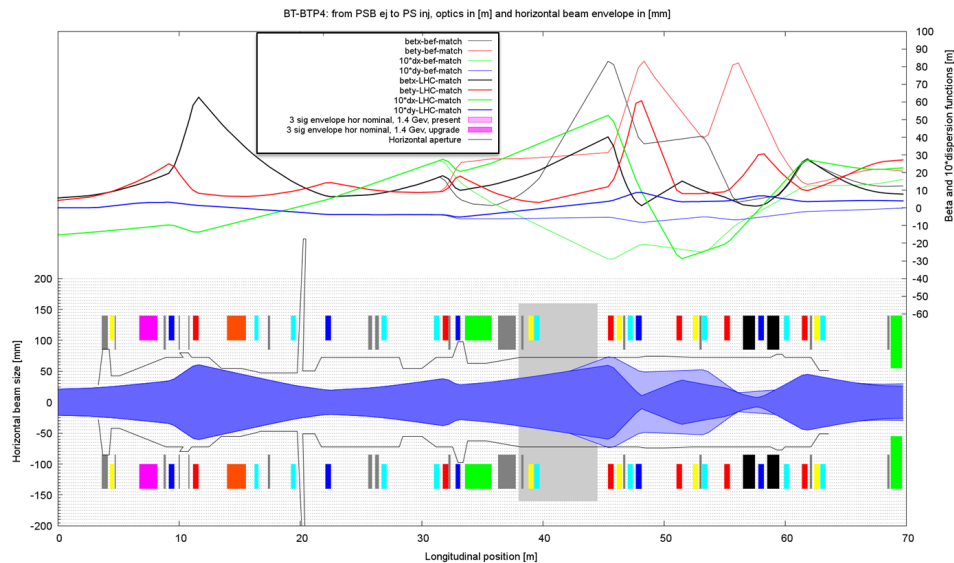
Figure 10: Optics functions from PSB ring 4 extraction to PS injection in the top part; present optics (thin lines) and proposed high-intensity FT beam optics for the upgrade (thick lines). The bottom part shows the horizontal 3 $\sigma$ beam envelope for the present optics in light and for the proposed optics in dark shade. The grey line represents the physical aperture.

optics settings in the transfer line, so called pulse-to-pulse modulated operation. This flexibility in optics settings requires to partly replace quadrupoles in the transfer line with a laminated yoke design. These quadrupoles are not only replaced but also re-arranged such that the present mismatch in horizontal dispersion at PS injection can be suppressed. Thus, a source of emittance blow-up in the LHC beam production can be removed. Due to the small emittance of LHC beams, the beam fits nicely in the line aperture. The main difficulty in matching the optics for these beam types lies in keeping the minimum beam size at least at the level of the present optics to avoid space-charge effects in the line due to the increased brightness with Linac4 beams after the PSB upgrades.

In contrary to the LHC beams which are aimed to be produced with highest possible brightness, the high-intensity FT beams should be delivered with highest possible intensity – as long as they can be produced at an acceptable loss level. Due to the linear brightness behaviour of the PSB, the high intensity beams have large emittances. Thus, a dedicated optics for the FT beams aims at reducing the beam size in the separation wall between PSB and PS where a particularly long distance between quadrupoles leads to naturally high beam sizes, Fig. 10. Also at the PS injection septum the beam size was optimized with respect to the available aperture. This FT optics leads to modifications of the PS injection optics which requires additional quadrupoles in the PS.

### Hardware Upgrades

All beam transfer elements between PSB extraction and PS injection have to be upgraded to cope with 2 GeV beam rigidities, while still accepting 1.4 GeV beam envelopes. For the PSB extraction kicker the operating voltage can be increased by 30%, but this will drive the field in the ferrite of the end cells 10% above the saturation limit. Measurements of the kick linearity have to be performed to validate the existing kicker for 2 GeV.

For the first recombination kicker it is foreseen to build a spare tank equipped with new magnets, install the new unit and keep the old tank as a full spare. In the second recombination kicker system, the magnets are charged with the pulse forming line. The required voltage for 2 GeV is very close to the magnet breakdown limit which means that voltage conditioning of the magnets will be necessary. In case of voltage breakdown problems, a system configuration as for the first recombination kicker will have to be adopted.

The PSB extraction septa will have a reconfigured cooling circuit and an increased bus-bar cross section to cope with the increased Joule heating for the higher required current. The recombination septa magnets will be rebuilt within the same vacuum vessels. The instrumentation presently installed inside the septa tanks will be removed and make space for longer magnets. The cross section of these magnets can remain the same [8].

The hardware of the PS injection has to be upgraded for both, kicker and septum systems. Presently the septum shares a short straight section in the PS with an injection bumper magnet. This bumper will be integrated next to the septum in the same vacuum tank. This allows increasing the septum length to deal with the 30% increase in rigidity.

Instead of a pulsed direct drive septum as presently used, an Eddy current septum option is being studied. Also the bumper shall be of an Eddy current design, Fig. 11. The improved robustness of the septum blade in case of an Eddy current septum will be at the expense of a more complicated powering scheme. The effect from the much slower decaying
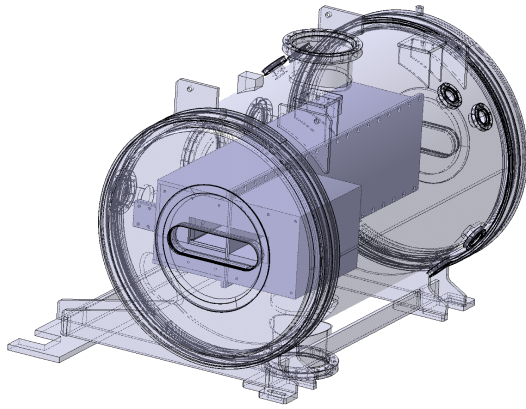
Figure 11: Assembly of PS injection Eddy current septum and bumper magnet in common vacuum vessel.

Eddy current field with respect to the main field onto the orbiting beam is studied together with an optimisation of the injection bump. Particular attention is required for the powering of the under vacuum injection bump magnet. Due to the different magnet and powering design compared to the remaining four bumper magnets, the injection bump may not be perfectly closed and generates a beating of the machine orbit during the injection process of a few hundred turns. Measurements were performed to estimate the acceptable orbit deviation and relate this value to a maximum delay of the under vacuum bumper with respect to the bumper magnets outside vacuum. The delay of one injection bumper
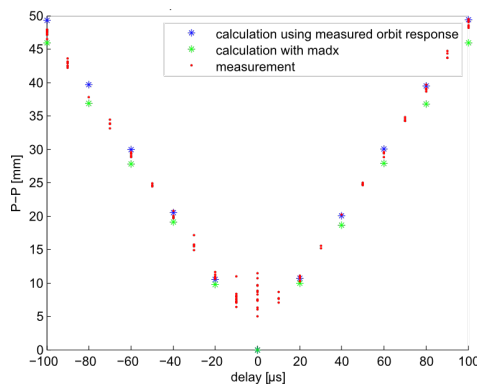


Figure 12: Peak-to-peak orbit variation for different delays of one injection bumper. Measurement of beam position in the ring (red), calculated beam position using real orbit response from four bumpers (blue) and MADX simulation (green).

was changed in steps of 10 $\mu$s and the peak-to-peak orbit variation recorded from turn-by-turn position monitors. The same situation was simulated with MADX. Figure 12 shows a good agreement between measured and simulated data. For delays within $\pm 20\mu$s the measurement is dominated by the injection kicker flattop ripple.

The present PS injection kicker system allows to inject LHC beams also at 2 GeV by short-circuiting the magnets. However, this increases the kicker flattop ripple by about 10% compared to the terminated mode. Also, high-intensity

beams cannot be injected with short circuit mode due to their shorter bunch spacing. For the upgrade it is foreseen to either install a second kicker system $180^o$ downstream of the present injection kicker to compensate for the remaining kick due to the increased beam rigidity, or to rebuild the existing kicker system for the future rise-time and kick requirements.

## SUMMARY

In order to fully deploy the beam brightness potential from Linac4 H$^-$ beams at 160 MeV, major upgrades of the beam transfer systems for PSB and PS are foreseen in LS2. The conventional multi-turn injection system of the PSB will be replaced by a charge exchange injection system. This shall significantly reduce the losses at injection and allow for more flexibility in tailoring target emittances for different beam types. Preparations for a test stand to validate the required equipment are ongoing with the aim for measurements in 2016.

In order to digest the beams from Linac4 and PSB, the PS requires an increase in injection energy to reduce space charge detuning. Consequently, all beam transfer elements between PSB extraction and PS injection will be upgraded for 2 GeV beams. The focussing structure in the transfer line between PSB and PS will be modified in order to provide dedicated optics settings for high brightness LHC and high intensity fixed target beams.

## REFERENCES

[1] K. Hanke et al., "PS Booster Energy Upgrade Feasibility Study First Report " CERN, Geneva, Switzerland, 2010 `https://edms.cern.ch/document/1082646/3`

[2] G. Rumolo et al., "Protons: Baseline and Alternatives, Studies Plans" LHC Performance Workshop, Chamonix, 2014, `https://indico.cern.ch/event/315665/session/5/contribution/21/material/paper/0.pdf`

[3] C. Bracco et al., "PSB injection: Beam Dynamics Studies" LIU Day, CERN, Geneva, Switzerland, 2014, `https://indico.cern.ch/event/299470/session/1/contribution/8/material/slides/0.pptx`

[4] E. Benedetto et al., "Transverse Emittance Preservation Studies for the CERN PS Booster Upgrade", THO4LR05, Proc. HB2014, East Lansing, USA (2014).

[5] M. Aiba et al., "Assessment of CERN PSB Performance with Linac4 by Simulations of Beams with Strong Direct Space Charge Effects" Proceedings of IPAC'10, Kyoto, Japan.

[6] E. Benedetto et al., "Detailed Magnetic Model Simulations of the H$^-$ Injection Chicane Magnets for the CERN PS Booster Upgrade, including Eddy Currents, and Influence on Beam Dynamics", TUPRI027, IPAC'14, Dresden, Germany (2014).

[7] W. Weterings et al., "The Stripping Foil Test Stand in the Linac4 Transfer Line", INTDS14, JRNC-D-14-00919, to be published.

[8] J.L. Abelleira et al., "Progress in the Upgrade of the CERN PS Booster Recombination", MOPAB02, Proc. HB2014, East Lansing, USA (2014).

# LONG-TERM BEAM LOSSES IN THE CERN INJECTOR CHAIN

S. Gilardoni, G. Arduini, H. Bartosik, E. Benedetto, H. Damerau, V. Forte, M. Giovannozzi,
B. Goddard, S. Hancock, K. Hanke, A. Huschauer, M. Kowalska, M. J. McAteer, M. Meddahi,
E. Métral, B. Mikulec, Y. Papaphilippou, G. Rumolo, E. Shaposhnikova, G. Sterbini, R. Wasef
CERN, Geneva, Switzerland

## Abstract

For the production of the LHC type beams, but also for the high intensity ones, the budget allocated to losses in the CERN injector chain is maintained as tight as possible, in particular to keep as low as possible the activation of the different machine elements. Various beam dynamics effects, like for example beam interaction with betatronic resonances, beam instabilities, but also reduced efficiency of the RF capture processes or RF noise, can produce losses even on a very long time scale. The main different mechanisms producing long term losses observed in the CERN injectors, and their cure or mitigation, will be revised.

## INTRODUCTION

The three synchrotrons forming the CERN LHC injector chain, namely the PSB (PS Booster), the PS (Proton Synchrotron) and the SPS (Super Proton Synchrotron), were built in laps of time of about 20 years with the goal of providing the largest variety of beams to the physics user community, thus leading to the implementation of very versatile machines. The PS was built as a sort of prototype machine in the late 50s and it is the first proton synchrotron with strong focusing ever operating [1]. The PSB was built to increase the PS injection energy from the 50 MeV of the Linac1 to 800 MeV. Then in the course of the CERN history, the extraction energy was increased first to 1 GeV, then to 1.4 GeV [2] and finally it will be upgraded to 2 GeV [3], with the goal of reducing the effect of direct space charge at PS injection. For the very same reason, the injection energy of the PSB is going to be increased from the 50 MeV of the proton Linac2 to the future 160 MeV provided by the H$^-$ Linac4. The last in the chain, the SPS, was built to produce high intensity beams for fixed target physics [4], but then was transformed first into a proton-antiproton collider, then − as the PS − into a lepton injector for LEP, and finally − as the PSB and the PS − is today operating as LHC injector.

All the three machines are producing two main families of beam types: high brightness beams for the collider, high intensity beams either for the following machine or for fixed target local users. The goal of this paper is to present a review of the loss mechanisms identified and eventually limiting the production of these two categories. Special attention will be given to the losses appearing on very long time scale, up to few hundreds ms or few thousand turns, considering that the synchrotrons magnetic cycles last few seconds. Some details are also given to the injection and extraction processes and related losses.

### LHC Beam Production Schemes

The LHC collider operates for luminosity production with two different bunch spacing, either 50 ns or 25 ns, the latter being the nominal configuration. The role of the injectors in the beam production is as follows: the PSB defines the initial transverse emittances, the PS the bunch spacing whereas in the SPS, on top of adapting the bunch length to the longitudinal acceptance of the LHC, tails in the transverse plane are scraped to avoid eccessive losses during the LHC filling process.

The production of the 25 ns bunch spacing beam is realized as follows. Linac2, or Linac4 in the future, fills each of the 4 PSB rings into $h$=1+2 bucket. Each PSB bunch is injected to the PS on $h = 7$ and after 1.2 s, the PS receives two other PSB bunches. A first acceleration takes place up to 2.5 GeV, where the bunches triple split. Eighteen bunches are accelerated up to 26 GeV/$c$ on $h$=21 where two consecutive double splittings produce the final bunch spacing of 25 ns creating a batch of 72 bunches. The 50 ns spacing is realised by eliminating the last splitting. Prior to the transfer to the SPS, the bunches are rotated in the longitudinal plane to reduce the total bunch length to about 4 ns. Up to five consecutive batches of 72 bunches can be injected in the SPS at 26 GeV/$c$, and accelerated to 450 GeV/$c$ to be delivered to the LHC. The longitudinal emittance is increased in the PS and SPS to reduce longitudinal instabilities, whereas transverse scraping is done in the SPS before reaching the extraction energy to eliminate tails. Besides the classical production scheme, alternative ones were proposed to overcome the current brightness limitation of the PSB. One realised during the 2012 run is BCMS (Batch Compression Merging and Splittings). It comprises the injection of 2×4 bunches on the 9th harmonic in the PS, batch compression from $h$=9 to $h$=14, bunch merging followed by a triple splitting all done at low energy instead of the triple splitting only. These evolved RF gymnastics are performed at an intermediate kinetic energy to avoid transverse emittance blow up due to space charge and to relax the requirements on the longitudinal emittance at injection. The resulting 12 bunches are accelerated to the extraction flat top where two bunch splittings occur to obtain the final 25 ns bunch spacing as for the nominal scheme. The advantage with respect to the traditional scheme results from the smaller splitting factor of the PSB bunches (6 instead of 12). Before extraction to the SPS, 25 ns spaced bunches can have the same intensity in only half of the transverse emittance. Typical beam parameters realised for the 25 ns beam and expected after the injector upgrade within the LIU (LHC Injector Upgrade)

Table 1: Proton Beam Parameters for LHC and Neutrino Production Beams. The asterisk (*) indicates that feasibility including operational viability (especially in the PS) remains to be demonstrated.

|  | Operation | | Record | | After LIU (2020) | |
| --- | --- | --- | --- | --- | --- | --- |
|  | | | | | Aim | Study |
|  | LHC | CNGS | LHC | CNGS | LHC | post-CNGS |
| SPS beam energy [GeV] | 450 | 400 | 450 | 400 | 450 | 400 |
| Bunch spacing [ns] | 50 | 5 | 25 | 5 | 25 | 5 |
| Bunch intensity [$10^{11}$] | 1.6 | 0.105 | 1.3 | 0.13 | 2.5 | 0.17 |
| Number of bunches | 144 | 4200 | 288 | 4200 | 288 | 4200 |
| SPS beam intensity [$10^{13}$] | 2.3 | 4.4 | 3.75 | 5.3 | 6.35 | 7.0(*) |
| PS beam intensity [$10^{13}$] | 0.6 | 2.3 | 1.0 | 3.0 | 1.95 | 4.0(*) |
| PS cycle length [s] | 3.6 | 1.2 | 3.6 | 1.2 | 3.6 | 1.2/2.4(*) |
| SPS cycle length [s] | 22.8 | 6.0 | 21.6 | 6.0 | 21.6 | 6.0/7.2 |
| PS momentum [GeV/c] | 26 | 14 | 26 | 14 | 26 | 14 |

program [5], together with the ones for the high intensity beams, are presented in table 1.

### High Intensity Beam Production Schemes

High intensity multi-bunch beams for fixed target physics at the SPS were regularly produced until 2012, in particular for the CNGS (CERN Neutrinos to Gran Sasso) [6] experiment now concluded. Table 1, summarises the last beam performances and the study case for a Laguna [7]-type high-intensity neutrino production beam. Two bunches per PSB ring, operating on $h=2$, are injected in the PS into buckets at harmonic $h=8$. After a first acceleration, a double bunch splitting takes place at 3.5 GeV/$c$ and acceleration to the final 14 GeV/$c$ extraction momentum is done on $h = 16$ harmonics. Finally, prior to extraction, the beam is debunched to allow imposing a 200 MHz structure before extraction for the recapture in the SPS. The extraction is realised on five consecutive turns, either using the so called CT [8, 9] (Continuous Transfer) technique or, in the near future, using the MTE (Multi-Turn) extraction [10]. Thus, two consecutive 1.2 s long PS cycles, with 5-turn extraction each, are used to fill the 10/11th of the SPS circumference. In the SPS, after re-capture at 14 GeV/$c$, the beam is accelerated up to 400 GeV, thus crosses transition at about 22.8 GeV and in the case of the CNGS, the machine is emptied on two consecutive extractions of about half machine separated by 46 ms.

The injector complex is also producing high intensity beams delivered at low energy either by the PSB or by the PS. The maximum intensity produced by the PSB, about $10^{13}$ p per ring, is delivered to the ISOLDE target for rare isotope production [11]. In this case the PSB takes the maximum current deliverable by the Linac2 per ring. For the PS, a single bunch high intensity beam used for the nTOF experiment is delivered to a lead target to study the interaction of neutrons with different materials [12].

## LOSSES FOR LHC BEAMS

The double injection in the PS is needed to maximize the number of bunches after the longitudinal splitting, requir-

ing also very high intensity injected in the PSB. Every PSB bunch is split up to 12 times to get finally 72 bunches at 25 ns spacing at PS extraction. This requires Linac2 to inject a high intensity beam with a limited brillance, due to the multi-turn injection process and large space-charge. The direct space-charge tune shift in the PSB, considering the typical LHC beam parameters, can be as large as ($|\Delta Q_x|$=0.51, $|\Delta Q_y|$= 0.61) [13]. Clearly, a certain number of resonances is crossed during the injection process: being the injection on a non-zero dB/dt , the effect on the beam is reduced. The tunes at injection are about $Q_x \approx 4.4$ and $Q_y \approx 4.5$, to reduce the interplay between the beam and the integer resonance. During acceleration the working point is moved dynamically towards the design value of about $Q_x = 4.17$ and $Q_y = 4.23$, thanks to the reduction of the indirect space-charge neck tie. A very detailed study of space charge effects can be found in [14] and the discussion on emittance preservation is presented in [15], whereas resonance compensation studies can be found in [16]. Once the first batch is injected into the PS, there is a 1.2 s long waiting time on the PS flat bottom before the second injection. During this period the beam has a very large tune spread induced by the direct space charge, in the vertical plane up to |0.3|, while the synchrotron period is of the order of 1 ms and the chromaticity is very large (-0.8, -1) and uncorrected. The beam, due to the synchrotron motion, crosses several times the integer and the $4q_y$=1 resonance, creating transverse emittance increase and beam losses. While the presence of the integer is pretty obvious, the fourth order resonance seems to be the result of the coupling of space-charge with one of the structure resonances, either the $4Q_y$=25 or $8Q_y$=50, being the machine tune 6.25 and the machine periodicity either 25 or 50 [17–19]. The space charge limitation is reduced, for the fourth time in the PS history, with the future increase of the injection energy, this time from 1.4 GeV to 2 GeV. Other techniques like breaking the symmetry of the lattice as proposed in [18], or fully coupling the horizontal and vertical plane to create vertical dispersion, or using flat bunches (both described in [13]), are under investigation to create some margin for the space charge limit.

Headtail instabilities of mode 5 or 6 also appear during the long injection flat bottom. They are currently cured by introducing linear coupling by dedicated skew quadrupoles and forcing the tune close to the coupling resonance [20]. This solution, however, firstly creates round beams, secondly forces the transverse working point in a well defined region. In the future, the transverse damper [21] will be probably preferred to the linear coupling, adding some flexibility to the choice of the working point. A chromaticity correction will be also introduced, to reduce the frequency range at which the damper has to act, but also to eventually mitigate the losses due to space charge coming from the multiple crossing of the betatronic resonances due to the synchrotron motion.

After the triple splitting, the beam is accelerated and right after transition crossing, coupled bunch longitudinal instabilities are observed [22]. The consequences are beam losses and a significant variation of longitundinal emittance, intensity and bunch length along the extracted batch. This lack of reproducibility is an issue, creating capture losses up to 1-2% in the SPS. This limitation should be eliminated thanks to the use of a longitudinal damper, a function provided by a newly installed Finemet© cavity [23]. Electron cloud is regularly observed on the extraction flat top, even if there is no evident sign that the beam quality is affected. There is instead a clear horizontal instability appearing, together with electron cloud, if the bunches are shorter than nominal or if the beam is kept artificially in the machine 50 ms longer than necessary [24, 25]. In case this becomes a limitation for the future beams, it was shown that the transverse damper can effectively delay the instability by about 10 ms [21] or eventually the adjustment of the bunch length at extraction by a reduction of the cavity voltage might be beneficial [25]. Close to the extraction, the bunches are rotated longitudinally to fit the bucket length of 5 ns of the SPS. Despite the fact that the beam transfer is bunch-to-bucket, the bunch rotation can create long tails in dp/p, that are not properly recaptured in the 200 MHz bucket of the SPS. Losses are thus observed during the capture process, as presented in [26]. The cure in this case would be the increase of the voltage available for the 40 MHz system used for the first bunch shortening [26]. Once the beam is transferred, the first limitations appearing in the SPS cames again from the long waiting time at flat bottom due to the multiple injections (up to 5 from the PS), followed by the lack of RF power during acceleration and at flat top. Space-charge is limiting the maximum brightness at injection, bounding for the moment the maximum acceptable direct space-charge tune shift to about $\Delta Q_x$ = -0.11 and $\Delta Q_y$=-0.20 [5].

Transverse Mode Coupling Instability (TMCI) used to limit significantly the maximum intensity of the single bunch beams to 1.6×$10^{11}$ p/b for a longitudinal emittance of 0.35 eVs. The introduction of a new special optics, changing $\gamma_{tr}$ from 22.8 to 18 and thus increasing the slip factor $\eta = 1/\gamma_{tr}^2 - 1/\gamma^2$ all along acceleration, pushed the TMCI limit at 4.5×$10^{11}$ p/b [27], well beyond the needs even of the future HL-LHC type beams. Another major limitation of

the SPS could be caused by electron cloud effects resulting in pressure rise, beam instabilities, emittance growth and losses. It is commonly accepted that either scrubbing, or coating with aC [28] all or a part of the vacuum chambers, or a combination of both will solve the electron cloud issue [5]. Recent studies proved that the scrubbing can be improved by using a special doublet beam, where the beam is composed of trains of 2 bunches spaced by 5 ns and these doublets are in turn separated by 20 ns. Experiments and simulations showed a net improvement of the secondary emission yield threshold with respect to the nominal 25 ns beam used for the scrubbing [5]. During the acceleration, done with the 200 MHz system alone, the beam becomes longitudinally unstable for an intensity of about 2-3 ×$10^{10}$ p/b, well below the performances required for the LHC beam production. This instability is mitigated by the 800 MHz RF system operating in bunch-shortening mode and a significant controlled longitudinal emittance blow up from 0.35 eVs to 0.5 eVs done with the 200 MHz system. On top of that, there is a clear lack of RF power available to maintain the high intensity bunches sufficiently short, of the order of 1.5 ns, to be transferred to the LHC 400 MHz system and without causing capture losses in the collider. The solution proposed to overcome this limitation is the upgrade of the 200 MHz system, with an increase of the available RF power by at least a factor of 2 obtained by increasing the number of cavity modules and by rearranging sections to reduce the impedance by about 20%. Once the full upgrade of the 200 MHz system will take place the maximum available power for the 2 longest (4 sections) cavities would be instead about 1.6 MW, bringing the maximum intensity per bunch up to 2.0×$10^{11}$ p/b for 25 ns without any performance degradation [23, 29, 30] in the hypothesis that no new beam instabilities would appear in the new working regime.

## LOSSES FOR HIGH INTENSITY BEAMS

The losses during the CNGS-like beam production are particularly concentrated in the PS and the SPS. The PSB, designed with the margin necessary to produce high intensity beams, does not suffer from any particular limitations. A detailed analysis of source of losses and impact on the different machine devices can be found in [31], whereas a more specific work related to the PS can be found in [32]. A report on the most recent intensity record realised by the injectors complex can be found in [33]. The PSB injection from the Linac2 causes losses of the order of 30-40%, not unusual as result of the transverse painting and longitudinal adiabatic capture. They are considered acceptable because limited at 50 MeV, with a very good beam transmission up to extraction. The H$^-$ injection scheme and chopping from Linac4 will greatly improve injection losses to only few percents. Small losses are observed during the fast extraction process in correspondence to the extraction septum. The transverse damper is always active during acceleration to avoid the development of a headtail instability [34]. Once the beam is injected into the PS, in a bunch-to-bucket transfer,

large transverse beam losses of the order of 5% are observed during the first few ms. The results of studies realized in past years [35,36] proved that the high beam losses observed during the first few hundred turns are related to two different mechanisms. Losses appearing during the first few turns are caused by a too small aperture of the injection septum, considering the transverse emittances that the PSB can deliver at 1.4 GeV. Losses appearing on a longer time scale, few hundred turns, are caused by intra-bunch injection oscillations, resulting from the effect of indirect space combined with the presence of unavoidable injection errors.This mechanism is enhanced by the fact that the PSB is composed of 4 vertically superposed rings, and that the 8 bunches can feature 4 different trajectories. Furthermore, the presence in the PS of the horizontal injection bump reduces also the available aperture for about 500 turns while the beam is oscillating in the vertical plane. It was experimentally proved that the injection oscillations can be effectively eliminated by the transverse damper, as described in [36,37]. The accelerating RF system of the PS is composed of ferrite loaded cavities tunable from 2.8 MHz to 10 MHz which was installed in the early 1970s [38]. Longitudinal losses were identified during acceleration for intensities beyond $3.5 \times 10^{13}$ p/b, in particular at transition crossing, where the RF-phase jump takes place. A single bunch transverse instability at transition crossing, a vertical TMCI, appears for single bunch intensities of about $6 \times 10^{12}$ p/b and causes losses of the order of few percent [35,39]. TMCI appears as an intrabunch vertical oscillation with a central frequency of 700 MHz driven by a broadband impedance source. This frequency range is well beyond the capabilities of the existing transverse damper, whose bandwidth is limited today to about 23 MHz. According to preliminary results [40], the driving impedance has been identified as generated by the several kickers installed in the PS ring. Currently the solution adopted to avoid this instability is a significant increase of the longitudinal emittance [41]. Losses at extraction, taking place on few turns, are due to the CT extraction technique [8]. The horizontal fractional tune is set to 0.25, and the beam is cut in 5 equally populated slices on 5 consecutive turns by shaving it with an electrostatic septum. Each portion of the beam cut by the septum is extracted in one turn. Losses appearing during the shaving process and dispersed along the entire machine circumference are due to the interaction with the beam and the blade of the electrostatic septum [9]. About 10% of the total circulating intensity is lost, causing significant machine activation. A new extraction technique, MTE [10], should definitely replace during the 2014 run the CT extraction, thus reducing significantly the losses at the extraction, from a maximum of 10% to about 1-2%, as proven during a brief part of the CNGS run [42]. The MTE extraction is based on beam trapping in stable islands of the transverse phase-space [10]: the beam is split in five beamlets by crossing of a fourth-order resonance and, once sufficiently separated in the horizontal plane, each beamlet is extracted on five consecutive PS turns. The adiabaticity of the trapping process requires a long extraction flat top. The

losses during the MTE extraction are produced, as expected, by the fact that the beam has to be transferred de-bunched from the PS and SPS. A portion of the beam intercepts the blade of the extraction septum during the kicker rise time causing unavoidable losses. A passive device, called dummy septum, was installed in 2013 to protect the extraction septum by intercepting these particles in the straight section before the extraction point [43]. The commissioning of the device should be concluded by the end of 2014. The beam is then transferred at 14 GeV/$c$ to the SPS with a double batch injection, with observed losses up to 10%. Injection losses are both transverse and longitudinal. Considering the transverse plane, the CT extraction cannot produce 5 equally populated slices with the same transverse emittances [10]. If on one side, the horizontal transverse emittance is reduced by the extraction process by a factor of three and becomes significantly smaller than the vertical, on the other side it is very difficult to have a unique optics to minimise the mismatch at SPS injection of the 5 slices [44]. An emittance exchange section is installed in the transfer line between the PS and the SPS to take advantage of the smaller horizontal emittance resulting from the CT extraction, and transforming it into the vertical being the SPS mechanical aperture smaller in the vertical plane. On top of this, fast kickers are installed in the same line to correct the trajectory of each beam portion, as described in [45], and thus minimise injection oscillations that might be different depending on the PS extracted turn. The SPS transverse damper has to be active since the beginning to reduce the injection oscillations which are clearly PS-turn dependent and a transverse coupled bunch instabilities caused by resistive wall (dipole modes) [46]. Longitudinal losses are observed already at injection. Certainly one of the main causes is the fact that the transfer between PS and SPS is not bunch-to-bucket. In the SPS, the recapturing process has some inefficiencies, causing losses also during the second PS injection. The capture is done using the main 200 MHz system at 800 kV, which gives the best beam transmission. A part of the un-captured beam is filling the empty gap between two PS injections, i.e. the 1/11th of the machine left empty on purpose for the rise time of the extraction kickers. A first fraction of this beam is lost at the beginning of the acceleration, the second unfortunately eventually at high energy if not properly cleaned by the transverse damper used as abort cleaning device. Transition crossing is another critical moment in the accelerating cycle in the SPS, where the usual phase jump occurs but no gamma transition scheme is implemented as in the PS. Typical losses through transition at high intensity were around 7% for settings not optimised for very high intensities. During past operation, the maximum available voltage was used due to uncontrolled emittance blowup during transition crossing and any voltage reduction led to beam losses. A careful adjustment of the voltage program of the 200 MHz cavities and of the one-turn-delay feedback system could improve the situation, but this requires continuous monitoring of the longitudinal beam parameters, depending also on the beam quality received from the PS. Slow losses

were observed also during acceleration after transition. A review of the longitudinal studies for the preparation of the CNGS production can be found in [47]. The improvements proposed to reduce longitudinal losses are: a) realise a separate capture of each PS batch in the SPS (possible due to large bandwidth of the main 200 MHz TW RF system) that would allow voltage capture modulation (0.8 MV increased to 2.5 MV); b) implement a variable gain of 1-turn-delay feedback and upgrade of the frequency range of the feed-forward system below transition energy. All of these will be realised in 2020 in the framework of the LHC Injector Upgrade Program. The 800 MHz upgrade will place in 2014, with a new feed-forward and feed-back system and could be used to improve the longitudinal Landau damping.

# REFERENCES

[1] E. Regenstreif, CERN-59-29

[2] S. Gilardoni, D. Manglunki (eds.), CERN-2013-005, pag. 7

[3] M. Giovannozzi et al., "Possible improvements to the existing pre-injector complex in the framework of continued consolidation?, Chamonix 2010 LHC Performance Workshop.

[4] VV.AA., "The 300 GeV program", CERN-1050-E

[5] H. Bartosik, "Can we ever reach the HL-LHC requirements with the injectors (LIU)?", in RLIUP: Review of LHC and Injector Upgrade Plans, CERN-2014-006

[6] K. Elsener (ed.), CERN-AC-Note (2000-03)

[7] A. Rubbia, J. Phys. Conf. Ser. 408, 012006 (2013).

[8] C. Bovet et al., "The fast shaving ejection for beam transfer from the CPS to the CERN 300 GeV machine", PAC'73, San Francisco, CA, USA, p. 438.

[9] J. Barranco, S. Gilardoni, Phys. Rev. ST Accel. Beams 14 (2011) 030101

[10] M. Giovannozzi (ed.), CERN-2006-11

[11] http://isolde.web.cern.ch

[12] https://ntof-exp.web.cern.ch/ntof-exp/

[13] G. Rumolo et al., "Expected Performance in the Injectors at 25 ns without and with Linac4", in RLIUP: Review of LHC and Injector Upgrade Plans, CERN-2014-006

[14] V. Forte et al.,"CERN PS Booster Space Charge Simulations with a Realistic Model for Alignment and Field Errors", IPAC'14, Dresden, Germany, TUPRI029

[15] E. Benedetto et al., "Transverse Emittance Preservation Studies for the CERN PS Booster Upgrade", these proceedings

[16] P. Urschütz, CERN-THESIS-2004-43

[17] R. Wasef et al.,"Space Charge effects and limitations in the CERN Proton Synchrotron", IPAC'13, Shanghai, China

[18] R. Wasef, "PS Experiments and Simulations", https://indico.cern.ch/event/292362/timetable/#all.detailed/

[19] S. Machida, "Space charge simulation for 4th order resonance", https://indico.cern.ch/event/292362/timetable/#all.detailed/

[20] E. Métral et al., "Simulation Study of the Horizontal Head-Tail Instability Observed at injection of the CERN Proton Synchrotron", PAC'07, Albuquerque, NM, USA, FRPMN074

[21] G. Sterbini et al., "Beam-based performance of the CERN PS transverse feedback", these proceedings

[22] L. Ventura, CERN-THESIS-2013-191

[23] M. A. Angoletta et al., "Upgrades of the RF Systems in the LHC Injector Complex", these proceedings

[24] R. Steerenberg et al., LHC Project Report 1034

[25] G. Iadarola et al., "Electron Cloud Studies for the Upgrade of the CERN PS", IPAC'13, Shanghai, China, WEPEA013

[26] H. Timko et al., Phys. Rev. ST Accel. Beams 16 (2013) 051004

[27] H. Bartosik, CERN-THESIS-2013-257

[28] C. Yin Vallgren, et al., Phys. Rev. ST Accel. Beams 14, 071001 (2011)

[29] E. Shaposhnikova et al., "Upgrade of the 200 MHz RF system in the CERN SPS for future high intensity beams", IPAC'11, San Sebastián, Spain, MOPC058

[30] T. Argyropoulos et al., "Other Means to Increase the SPS 25 ns Performance - Longitudinal Plane", Chamonix 2014 LHC Performance Workshop

[31] G. Arduini et al., Beam Losses and Radiation Working Group, http://blrwg.web.cern.ch/blrwg/

[32] L. Bruno et al., CERN-ATS-2011-007

[33] E. Shaposhnikova et al.,"Recent Intensity Increase In The Cern Accelerator Chain", CERN-AB-2005-029

[34] D. Quatraro, CERN-THESIS-2011-103

[35] S. Aumon, CERN-THESIS-2012-261

[36] A. Huschauer et al., paper submitted to PRSTAB

[37] A. Blas et al., CERN-ACC-2013-0215

[38] H.-Ch. Grassmann, R. Jankovsky, W. Pirkl, "New RF System for the 28 GeV Proton Synchrotron at CERN", Siemens Review, 44, 1977, p. 166.

[39] E. Métral, "Fast High-Intensity Single-Bunch Transverse Coherent Instability in Synchrotrons due to a Broad-Band Resonator Impedance", CERN-PS-2001-035-AE

[40] M. Migliorati, private communication

[41] R. Cappi et al.,"Beam Breakup Instability in the CERN PS near Transition", EPAC'00, Vienna, Austria (2000).

[42] E. Benedetto et al., "Results from the 2009 Beam Commissioning of the CERN Multi-Turn Extraction", IPAC'10, Kyoto, Japan, THOBMH02

[43] C. Bertone et al.,"Studies and implementation of the PS dummy septum to mitigate irradiation of magnetic septum in straight section 16", CERN-ACC-2014-0043

[44] G. Arduini et al.,"TT2/TT10 transfer line studies for the 14 GeV/c continuous transfer", PS-Note-99-08 (CA) and SL-Note-99-013 (MD), (1999)

[45] A. Franchi et al., CERN-AB-Note-2008-005.

[46] W. Höfle, "Transverse damping and fast instabilities", CERN-OPEN-99-060

[47] T. Bohl et al.,"RF studies of the high intensity CNGS beam in the SPS", AB-Note-2005-034-MD.

# RECENT DEVELOPMENT IN THE MITIGATION OF LONG TERM HIGH INTENSITY BEAM LOSS

G. Franchetti, S. Aumon, F. Kesting, H. Liebermann, C. Omet, D. Ondreka, R. Singh, GSI
S. Gilardoni, A. Huschauer, F. Schmidt, R. Wasef, CERN

Long term beam loss are due to the presence of several factors, but lattice nonlinearities and high intensity certainly rank among the main causes for long term beam loss. Experimental and numerical studies have shown that periodic resonance crossing induced by space charge in a bunched beam is a deleterious effect for beam survival [1, 2]. Given the complexity of the topic, the studies in the past have been focused to investigate one dimensional resonances, for example in Ref. [1] the resonance was $4Q_x = 25$, while in Ref. [2] the resonance was $3Q_x = 13$. The underlying mechanism leading to beam loss is explained, in this case, in terms of instantaneous stable islands in a two-dimensional phase space and their crossing the particles orbits. This mechanism was studied in details in Ref. [3].

Studies for SIS100 have shown, however, that in the injection scenario of the uranium ions, random components of magnets nonlinearities excite a significant web of resonances including coupled resonances [4]. One of the simpler of the nonlinear coupled resonances is the $Q_x + 2Q_y = N$. Although the mechanism of the beam loss remains the same (the periodic resonance crossing induced by space charge), the details of the mechanism have never been, in this case, studied. The reason for that is in the complexity of the 4-dimensional coupled motion, which poses an extraordinary challenge to disentangle the dynamics. While for 1-dimensional resonances the mechanism is relatively well understood, for 2-dimensional resonances it remains still unraveled.

In this context, within the collaboration between CERN and GSI, in 2012 a new experimental campaign in the CERN-PS for investigating the resonance $Q_x + 2Q_y = 19$ has been undertaken. The results of measurements collected in a scan of beam intensity/profiles versus tunes have shown puzzling features: when the space charge tune-spread overlaps the third order resonance an asymmetric beam response is found: in one plane we find halo, whereas in the other plane a core growth takes place. In Fig. 1 we show a plot with the beam profiles resulting from the space charge tune spread overlapping with the third order resonance, the tunes of the measurement are reported on the picture, the tune-shift is $\Delta Q_x \simeq -0.046, \Delta Q_y \simeq -0.068$. The asymmetry of the profile is quite evident and shows that a new and more complex dynamics is driving the beam halo formation. The details of these measurements will be part of a dedicated article.

The explanation of this beam profile shape have to be searched into the effects created by the 4D coupled dynamics. In this scenario the analogous of the fix points become the fix-lines [5]. These extended closed lines play a similar role as the fix points for the crossing of the 1D resonances. The description of this dynamics is beyond the purpose of this
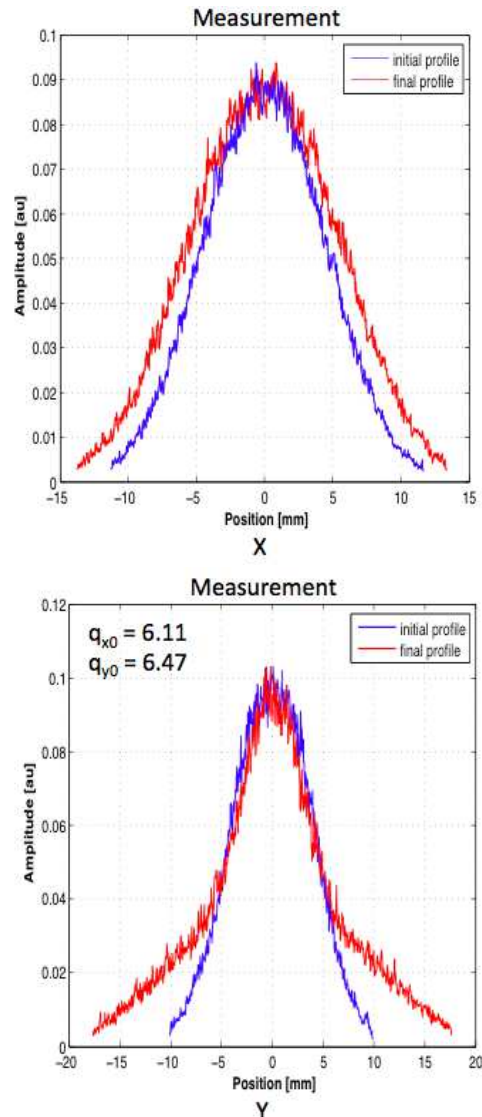
Figure 1: Beam profiles after 1 second storage of the beam in the CERN-PS. The asymmetry of the beam response is evident.

proceeding, a full study for the case of single particle is part of a future work [6].

If the halo edge is exceeding the beam pipe, long term beam loss is unavoidable. While the issue of the self-consistency during a substantial change of the space charge intensity is of relevance, practically this scenario is not really foreseen in practical operation in order to avoid significant machine or collimators damage.

The relevant issue is therefore if a strategy that allows to mitigate beam loss in a conventional operational scenario

can really be effective over long term storage of a high intensity bunched beam. Past numerical studies have shown that resonance compensation is certainly a way to attack the problem, and simulations using a *frozen space charge* model has shown a beneficial effect of the resonance compensation [4, 7, 8]. From the fundamental point of view, however, it remains to be established if this procedure can be operated in a real high intensity bunched beam.

In the common practice, resonance compensation is understood as the creation of an artificial driving term that counteract the driving term created by the machine non-linearities. The effectiveness of the procedure relies on the assumption that a resonance is excited mainly by a single harmonics. While this assumption may prove to work decently in standard operational regimes, it is not obvious what are the consequences of a periodic resonance crossing induced by space charge.

For these reasons in parallel with the CERN experimental effort, at GSI a campaign for testing the effectiveness of a resonance compensation in presence of space charge has been undertaken.

We have proceeded as follows. First we have measured the resonance chart of the SIS18, and afterwards we implemented a compensation of a third order resonance. On the best compensation we could achieve we explored the robustness of the mitigation scheme for moderately intense bunched beams.

## ASSESSMENT OF RESONANCES IN SIS18

The campaign started with an assessment of the resonance chart of SIS18 after its return to operation from the shutdown. In Fig. 2 it is shown the resonance chart of SIS18 after the re-alignment of the SIS18 magnets operated during the May/June shutdown. The apparent mismatch of some of the resonance lines with the theoretical solid lines is due to small systematic tune-shifts present in the machine model used by the control system. Most of the resonances in the picture are weaker than they were before the re-alignment, which speaks for a beneficial effect of the machine re-alignment. The linear coupling resonances are significantly mitigated, in particular the line $Q_x - Q_y = 1$ is weakened. However, the benefit of the magnets re-alignment is not completely obvious: the machine has now a new third order resonance before not present, which is the line $3Q_y = 10$. The third order resonance $Q_x + 2Q_y = 11$ appears stronger, as well as the half integer $2Q_y = 7$.

## THIRD ORDER RESONANCE MITIGATION

The third order resonance $Q_x + 2Q_y = 11$ is of particular interest because a similar resonance will affect the SIS100 for the preliminary working point for ions (example for the uranium beam scenario at the working point $Q_x = 18.84, Q_y = 18.73$) and fast extraction. The same type of resonance was investigated in the CERN-PS campaign.
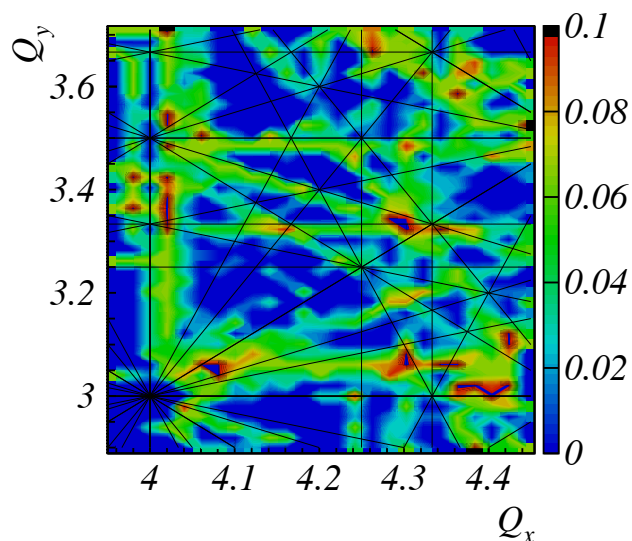


Figure 2: Resonances of SIS18 measured on the 16/7/2014 after the magnets re-alignment. This picture have been obtained by using SISMODI control system.

The major effort of the experimental campaign was to compensate this resonance line and verify the robustness of the compensation for a bunched beam in a SIS100 "type" scenario, i.e. a bunched beam stored for 1 second at injection energy.

First, the resonance strength was assessed by measuring the beam loss while the resonance is crossed in 1 second from $Q_y = 3.45$ to $Q_y = 3.35$. The horizontal tune was kept fix to $Q_x = 4.2$. We used a coasting beam with an intensity low enough to prevent space charge effects; in fact, for $2 \times 10^8$ ions of $U^{73+}$, the tune-shift is $\Delta Q_x \simeq -2.5 \times 10^{-3}, \Delta Q_y \simeq -5 \times 10^{-3}$. The injected beam is chosen to completely fill the transverse acceptances of SIS18, thus emphasizing the beam loss due to resonances. Throughout the resonance crossing the beam was always kept coasting. Figure 3 top shows the beam survival during the crossing of $Q_x + 2Q_y = 11$ in 1 second for the un-compensated machine: only $\sim 35\%$ of the beam survives. The stop-band is found in the range $450 \div 750$ ms, which corresponds to $Q_y = 3.375 \div 3.405$ because of the linear tune ramp.

The effort for compensating this resonance is based on creating a controlled driving term by using the normal sextupoles of SIS18. They are set to act against the driving term created by the "natural machine errors". The driving term is identified by its strength $\Lambda$ and by an angle $\alpha$. The pair $(\alpha, \Lambda)$ allows the complete determination of the strengths of two arbitrary sextupoles through the machine optics, which is supposed to be completely known. For the experiment we used the sextupoles GS05KS3C, GS07KS3C. Figure 3 center shows the effect of the two sextupoles in terms of beam survival as function of $\alpha$ for the strength of the driving term of $\Lambda = 0.002$. (the units of $\Lambda$ are of integrated sextupole strength, as used in the LSA setting generation system, which we used in replacement of the SISMODI). This picture shows a peculiar feature of the power supply

of the SIS18 sextupoles. In fact, the attempt of correcting the resonance by using a too small $\Lambda$, has set small currents to the two correcting sextupoles. In this situation the power supply system is not able to resolve these small currents, and set therefore some threshold current. The resulting effect appears as a discontinuous beam survival at $\alpha \simeq 20, 170$ degree. This feature certainly becomes a limitation for compensating a resonance at low machine rigidity.

Fortunately the rigidity of the $U^{73+}$ at 11.4 MeV injection energy is high enough to prevent this situation. The third order coupled resonance is in fact better compensated for a different strength of the correcting driving term, namely for $\Lambda = 0.025$. For this strength the angle of $\alpha \sim 270$ degree yields the best performance, improving the beam survival from $\sim 35\%$ to $\sim 85\%$. This result is shown in Fig. 4 bottom. A better optimization of the compensation was not reached, and the reasons for this were beyond the beam time available: this would require an ORM analysis and verification of the SIS18 optics, with especial attention to the sextupole correctors used.

## EFFECT OF HIGH INTENSITY BUNCH DYNAMICS

The effectiveness of the best resonance compensation achieved was tested with a bunched beam with a moderate intensity. The beam was injected, bunched, and stored for 1 second keeping the machine tunes fixed (standard operation mode). We explored the bunched beam survival for several working points $Q_y$, keeping $Q_x = 4.2$ at each measurement. The beam intensity allowed a moderate space charge tunes-shift of $\Delta Q_y \simeq 0.05$ corresponding to $6.5 \times 10^8$ ions of $U^{73+}$ present in the machine before bunching. This tune-spread is not significantly affected by the chromaticity because the momentum spread of the beam at injection is $(\delta p/p)_{rms} \simeq 7.5 \times 10^{-4}$, which for the natural chromaticity yields a maximum tune spread of $(\delta Q_y)_{max} \simeq \pm 0.0072$. Hence the space charge remains the dominant effect. The same argument shows that the effect of the dispersion enlarges/reduces particles amplitudes of $\sim 6$ mm, which compared with full machine acceptance, becomes of minor relevance.

The results of this scan are shown in Figure 4. The red markers show the beam survival without correction. We identify three "valleys" corresponding to the effect of three resonances: the half integer $2Q_y = 7$, the third order coupled resonance $Q_x + 2Q_y = 11$, and the third order one dimensional resonance $3Q_y = 10$. If we set the tune at the edge of the resonance stop-band at $Q_x = 3.405$, the impact on beam survival is dramatic: in 1 second only $\sim 10\%$ of the beam survives, whereas in absence of periodic resonance crossing due to space charge, the survival on this working point is of 100%.

The blue markers in Fig. 4 show the very same measurements with the two correcting sextupoles activated for the best correction of $Q_x + 2Q_y = 11$ at $\alpha = 270$ degree (Fig. 3 bottom). The result is that the partial resonance compen-
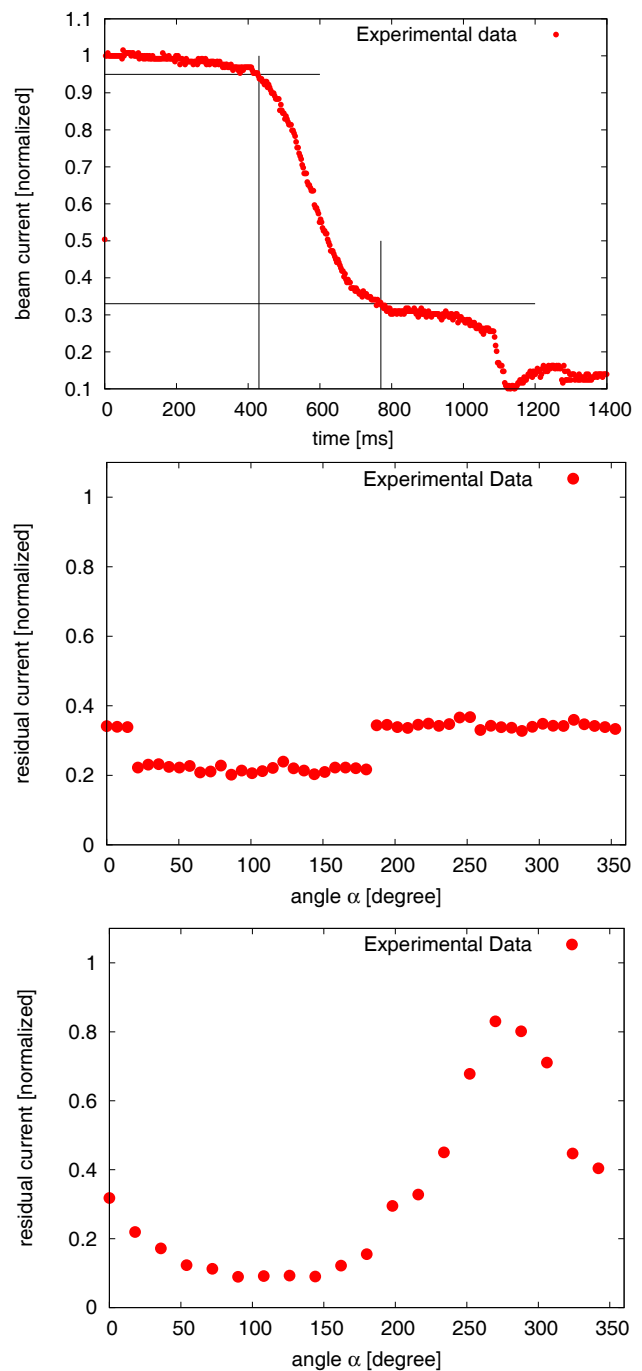
Figure 3: Top: beam survival by crossing the resonance $Q_x + 2Q_y = 11$ in 1 second. The survival is $\sim 35\%$. Center: effect of the power supply, note the discontinuity of beam survival at $\alpha = 20, 170$ degree for a small driving term. Bottom: best compensation for $\Lambda = 0.025$ at $\alpha = 270$ degree.

sation still yields an advantage to mitigate the beam loss induced by the periodic resonance crossing over 1 second storage. The blue markers yield a beam survival of $\sim 70\%$ in the range $3.415 < Q_y < 3.46$ except for the new valley appearing at $Q_y = 3.43$. The advantage is evident for $Q_y = 3.42$ where beam survival goes from $\sim 30\%$ to $\sim 75\%$.
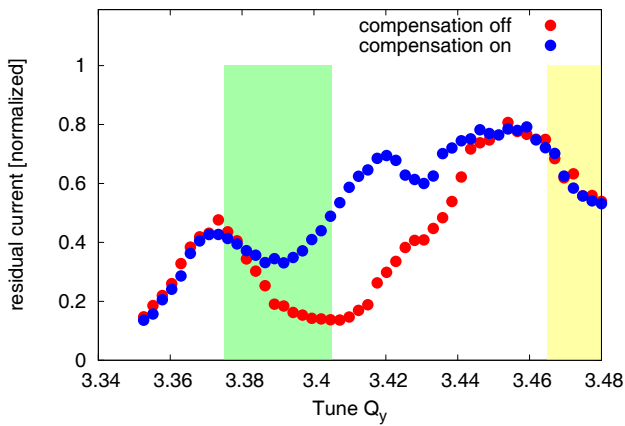
Figure 4: Beam survival for a bunched beam stored for 1 second. The green curve is obtained for a partially compensated third order resonance, whereas the red curve is measured for the naked machine.

At the tune $Q_y \simeq 3.43$ there is a slight discontinuity in the red curve. This indicate the presence of a higher order resonance. This resonance appear clear in the measurement with the resonance compensation activated (a new valley in the beam survival appears). We have no information on the nature of this resonance, except of its weak strength.

Interestingly we also observe that the compensation here implemented does not affect the other two resonances shown in Fig. 4. In fact in $3.35 < Q_y < 3.37$ and in $3.45 < Q_y < 3.48$ green and red markers fully overlap, showing that the compensating method really affects only this specific resonance. Other resonances far away from the investigated area might be excited by this compensation scheme, but this is not part of this study.

## CONCLUSION

The measurements and the results obtained in this campaign allow to conclude that

1 The technique used to compensate the resonance seems a promising tool for a first order compensation. The implementation of this "fast" technique completely relies on the feature of the new settings generation system (LSA) for automatizing the data acquisition process.

2 The experimental evidence shows that the resonance compensation for a third order resonance allows to mitigate the beam loss due to the effect of moderate space charge in bunched beams stored for 1 second.

The physics case, and further details on these measurements will appear in dedicated studies.

## OUTLOOK

Although the results are encouraging, the following issues remain to be investigated:

1 We have no clear evidence of why we cannot compensate completely the resonance. This may lay in the imperfect knowledge of the optics at the location of the sextupole correctors, or due to other unknown details

of the machine. In addition we have got evidences that different pairs of sextupoles excited to create the same driving term do not produce the same beam survival. All these discrepancies require further investigations to consolidate the method and/or to improve it.

2 The verification with the bunched beams was made with a relatively low intensity $\Delta Q_y \simeq 0.05$. The space charge tune-shift here obtained do not compare with that foreseen in the SIS100 scenario, which is expected to be a factor 4 larger. Further measurements on a single third order resonance with more intense beam have to be foreseen to consolidate this first findings.

3 Further experimental studies on half integer, and linear coupling, as well as on the 4th order 1 and 2 dimensional resonances will be carried out as well.

## ACKNOWLEDGMENT

## REFERENCES

[1] G. Franchetti, I. Hofmann, M. Giovannozzi, M. Martini, E. Métral, Phys. Rev. ST Accel. Beams **6**, 124201 (2003); E. Métral, G. Franchetti, M. Giovannozzi, I. Hofmann, M. Martini, R. Steerenberg, Nucl. Instr. and Meth. A 561, (2006), 257-265.

[2] G. Franchetti, O. Chorniy, I. Hofmann, W. Bayer, F. Becker, P. Forck,T. Giacomini, M. Kirk, T. Mohite, C. Omet, A. Parfenova, P. Schuett, Phys. Rev. ST Accel. Beams **13**, 114203 (2010).

[3] G. Franchetti and I. Hofmann, Nucl. Instr. and Meth. A **561**, (2006), 195-202.

[4] Mitigation of Space Charge and Nonlinear Resonance Induced Beam Loss in SIS100 G. Franchetti, S. Sorge, Proc. of IPAC2011, S. Sebastian, Spain. MOPS002. p. 589.

[5] F. Schmidt, "Untersuchungen zur dynamischen Akzeptanz von Protonenbeschleunigern und ihre Begrenzung durch chaotische Bewegung", PhD thesis, DESY HERA 88-02 (1988).

[6] G.Franchetti, F. Schmidt to be published soon.

[7] Effect of self-consistency on space charge induced beam loss G. Franchetti, S. Sorge, Proc. of IPAC2013, Shanghai, China. TUME001. pag. 1556.

[8] Effect of self-consistency on periodic resonance crossing G. Franchetti, Proc. of HB2012, Beijing, China, 2012. WEO1C01. pag. 429.

# SIMULTANEOUS ACCELERATION OF RADIOACTIVE AND STABLE BEAMS IN THE ATLAS LINAC*

B. Mustapha[#] and P.N. Ostroumov, ANL, Argonne, IL 60439, USA
A.A. Perry, ANL and IIT, Chicago, IL 60616, USA
M.A. Fraser, CERN, Geneva, Switzerland

## Abstract

ATLAS is now the only US DOE National User Facility for low-energy heavy-ion stable beams. With the recent commissioning of the Californium Rare Isotope Breeder Upgrade (CARIBU), ATLAS is now also used to accelerate radioactive beams. The demand for both stable and radioactive beam time is already exceeding two to three times the 5500 hours delivered by ATLAS every year. The time structure of the EBIS charge breeder to be installed next year for CARIBU beams is such that less than 3% of the ATLAS duty cycle will be used for radioactive beams. Being a CW machine, ~ 97% of the ATLAS cycle will be available for the injection and acceleration of stable beams without retuning. This simultaneous acceleration is possible for stable and radioactive beams with charge-to-mass ratios within 3%. We have developed a plan to upgrade ATLAS for this purpose to be implemented over the next few years, where two to three beams could be delivered simultaneously to different experimental areas. The upgrade concept will be presented along with the recent studies and developments done in this direction.

## THE ATLAS FACILITY AND RECENT UPGRADES

The Argonne Tandem Linear Accelerator System (ATLAS) was the first superconducting linac for ion beams in the world [1]. It has been operating and delivering ion beams for over thirty years at different capacities. Over the same period, ATLAS has undergone several upgrades [2]. The most recent are CARIBU [3] and the Efficiency and Intensity upgrade [4].

CARIBU uses a Californium fission source to produce radioactive daughter nuclei which are collected, separated and then cooled to form a beam. An ECR charge breeder [5] is used to increase the charge state of these beams for injection and acceleration in ATLAS.

The Efficiency and Intensity upgrade consisted of a new RFQ [6] and a new superconducting module [7]. The RFQ replaced the first three superconducting cavities of the Positive Ion Injector (PII) to avoid deterioration of the beam quality due to fast acceleration of low energy beams. The RFQ uses the existing multi-harmonic buncher (MHB) as a pre-buncher. Two notable features of the ATLAS RFQ are trapezoidal modulations in the accelerating section and

a compact output matcher to produce an axis symmetric beam for direct beam injection into PII which uses solenoidal focusing [8]. The new cryomodule replaced three old modules with split-ring resonators [9]. The split-ring cavities are known to cause beam steering which results in beam loss and the subsequent quench of solenoids. The new cryomodule is made of 7 quarter-wave resonators (QWR) and 4 superconducting solenoids. The QWRs were designed and built with steering correction [10]. The new module should be able to accelerate 10 to 100 times higher intensity stable beams without significant beam loss.

Both the new RFQ and cryomodule have been recently commissioned and are now being used for routine ATLAS operations. Following this upgrade, the transmission has improved by 50 to 100% for all beams accelerated in ATLAS [11]. The overall transmission is now routinely over 80%, which is dictated by the MHB used to produce a small longitudinal emittance for more efficient beam transport and acceleration in ATLAS [12]. Figure 1 shows the current layout of ATLAS after the recent upgrades.

## THE NEED FOR MULTI-USER CAPABILITIES AT ATLAS

ATLAS is now the only US DOE National User Facility for low-energy heavy-ion stable beams delivering upward of 5500 hours of beam-on-target every year. With CARIBU online, ATLAS is also being used for the acceleration of radioactive beams, which often require longer beam time for experiments due to their lower intensity. In the past two years, the demand for ATLAS beam time has more than doubled and with longer radioactive beam run periods, less and less users will be served, especially stable beam users. Therefore the need for a multi-user capability is significant at ATLAS in order to satisfy more users and maximize the scientific output of the ATLAS facility.
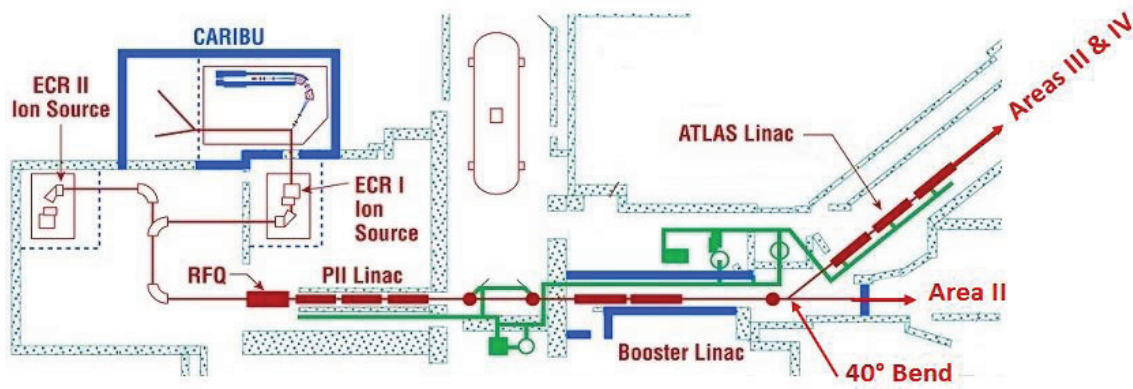
Figure 1: Current layout of the ATLAS facility showing CARIBU, the ECRs, the RFQ and the three linac sections; PII, Booster and ATLAS. It also shows the beam lines leading to the different experimental areas II, III and IV.

# THE EBIS CHARGE BREEDER AND SIMULTANEOUS ACCELERATION OF RADIOACTIVE AND STABLE BEAMS

With the installation of the recently commissioned CARIBU EBIS charge breeder [13] in 2015, it will be possible to simultaneously accelerate one radioactive and one stable beam in ATLAS. The EBIS produces a 10 µs to 1 ms beam pulse up to a 30 Hz repetition rate, that is about 3% of the duty cycle. ATLAS, being a CW machine, enables the possibility of injecting stable beams during the remaining 97% of the duty cycle. Considering the fact that a stable beam with a charge-to-mass ratio close to that of the CARIBU beam is usually used as a guide beam to tune the linac, it would be straightforward to inject any stable beam with a charge-to-mass ratio within 3% without retuning the machine. Figure 2 shows the proposed time structure of the ATLAS beam for the simultaneous acceleration of one radioactive beam from CARIBU EBIS and one stable beam from the ECR ion source. The proposed operation scheme is 3% for radioactive beam, 96% for stable beam and 1% for switching between the two beams.
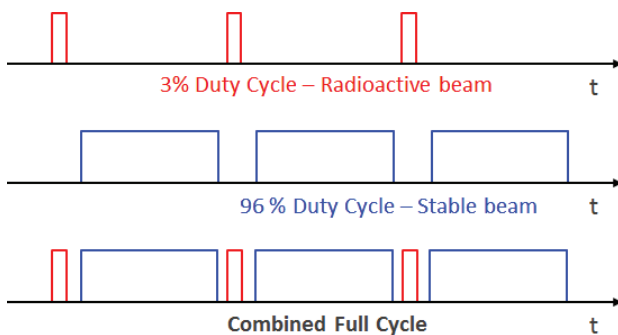


Figure 2: Time structure for the proposed simultaneous acceleration of radioactive and stable beams in ATLAS. 3% duty cycle for the radioactive beam (top), 96% for the stable beam (middle) and 1% for switching between beams to combine them into the full cycle (bottom).

The CARIBU beam mass numbers range from 80 to 170 with atomic numbers from 30 to 70. The highest charge-to-mass ratio that they could be ionised to is ¼. Considering that ATLAS accelerates beams with charge-to-mass ratios equal to or higher than 1/7, the useful range for the multi-user capability is $1/7 < q/A < 1/4$. Higher q/A ($\sim 1/3$) could be achieved by operating the EBIS with longer breeding times and a 10 Hz repetition rate, which would also lead to a 10% (radioactive beam)-90% (stable beam) operation scheme.

## A MODIFIED LEBT FOR TWO BEAM INJECTION

Figure 3 shows a preliminary layout for a modified low-energy beam transport (LEBT) line for the injection of two beams; one radioactive from the CARIBU EBIS and one stable from the ECR [14]. As shown on the figure, both the EBIS and ECR have their own high-voltage platform which could be adjusted independently to match the required RFQ injection velocity. The main components of the new LEBT are a pulsed electrostatic deflector and an achromat. The deflector is turned off when injecting the beam from EBIS and turned on when injecting from the ECR. When the deflector is off, the DC beam from the ECR is stopped. The proposed achromat is made of four 45° bending magnets with a dispersive middle plane for further purification of the EBIS beam. An option with two 90° magnets is being considered for higher resolution. The achromatic property is essential for the transport of beams with different charge-to-mass ratios and to minimize any emittance growth from the energy spread.
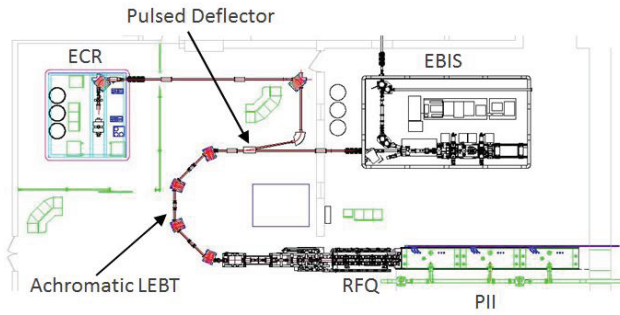
Figure 3: Layout for a new LEBT including a pulsed electrostatic deflector to inject either an EBIS or an ECR beam, and an achromat made of four 45° magnets.

## EXTRACTION OF ONE BEAM AFTER THE BOOSTER

Following the injection, the two beams are accelerated in the RFQ, PII and Booster in different time periods of the duty cycle as shown in Figure 2. After the Booster, a beam could be either injected into ATLAS for further acceleration using the 40-degree bend area to serve the experimental areas III and IV as shown in Figure 1, or sent straight through to experimental area II at the Booster energy. At this time, the 40-degree bend area is made of DC magnets and it is not achromatic. We propose to modify it for pulsed extraction of one of the beams to experimental area II while the second beam is injected in the ATLAS section of the linac for further acceleration. At the same time, the injection line could be made achromatic. Figure 4 shows the Booster-to-ATLAS injection line modified to be achromatic, while Figure 5 shows a pulsed achromatic chicane to be placed under the ATLAS main beam line for the extraction of one of the beams to experimental area II. The two main components of the extraction line are a 5° pulsed kicker magnet and a 15° septum magnet for a total of 20° beam deflection under the ATLAS line. The rest of the chicane is made of three 20° regular magnets. An option using a Lambertson magnet instead of the septum is being investigated.



Figure 4: Top view of the 40-degree bend area modified to be achromatic for the transport of beams with different charge-to-mass ratios.



Figure 5: Side view of the vertical chicane to be placed under the ATLAS main line for the extraction of one of the beams after the Booster to send to experimental area II. The achromatic chicane is made of a kicker and a septum magnet followed by three 20° regular magnets.

## EXAMPLES OF SIMULATNEOUS RADIOACTIVE AND STABLE BEAMS

Simultaneous multiple charge state acceleration was first demonstrated at ATLAS [15]. The acceptance in the charge-to-mass ratio is about 3%. Figure 6 shows an example of simultaneous two-beam injection and acceleration in ATLAS. In this case, the radioactive beam is $^{132}Sn^{27+}$ from the CARIBU EBIS and the stable beam is $^{48}Ca^{10+}$ commonly produced in an ECR source. The figure shows combined phase space plots for the two beams at different stages of injection and acceleration ending at the Booster with an energy of 5.9 MeV/u, where one of the beams will be extracted. In this case, the $^{48}Ca$ beam is extracted to send to experimental area II while the $^{132}Sn$ beam is injected for further acceleration into the ATLAS section of the linac up to an energy of 10 MeV/u for experimental area III or IV [14].

Similar examples of possible simultaneous stable and radioactive beams are listed on Table 1. The table shows that for every stable beam, multiple candidates for the radioactive beams could be accelerated simultaneously and vice versa, which adds a much needed flexibility in the scheduling of beam time. It is also important to note that by adjusting the breeding time of the EBIS, the charge state distribution of any radioactive beam could be adjusted to match the closest stable beam of interest.
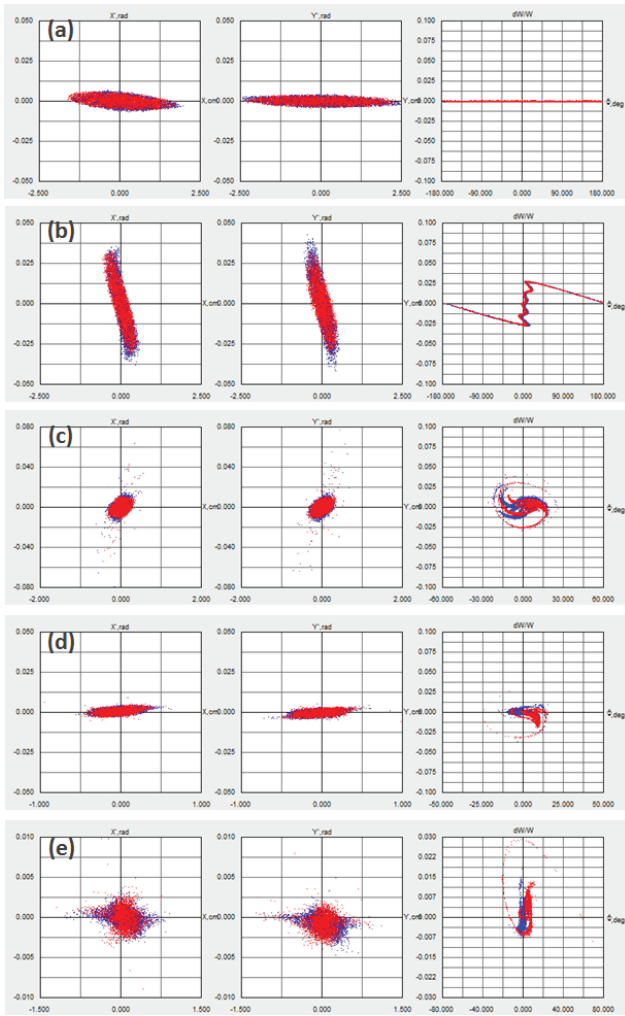
Figure 6: Phase space plots for the simultaneous injection and acceleration of the radioactive beam $^{132}Sn^{27+}$ (red) and the stable beam $^{48}Ca^{10+}$ (blue) at the LEBT (a), in front of the RFQ (b), at the RFQ exit (c), at the end of PII (d) and Booster (e).

Table 1: Examples of radioactive and stable beams that could be simultaneously accelerated in ATLAS.

| q/A | Stable beams | Radioactive beams |
|---|---|---|
| 0.25 | $^{20}Ne^{5+}, ^{28}Si^{7+}, ^{36}Ar^{9+}$ | $^{84}Se^{21+}, ^{88}Kr^{22+}, ^{92}Sr^{23+}$ |
| 0.24 | $^{50}Ti^{12+}$ | $^{101}Zr^{24+}, ^{105}Ru^{25+}, ^{117}Cd^{28+}$ |
| 0.23 | $^{48}Ti^{11+}, ^{56}Fe^{13+}, ^{74}Ge^{17+}$ | $^{92}Kr^{21+}, ^{105}Nb^{24+}, ^{109}Tc^{25+}$ |
| 0.22 | $^{40}Ca^{9+}, ^{102}Ru^{23+}, ^{120}Sn^{27+}$ | $^{89}Br^{20+}, ^{112}Rh^{25+}, ^{139}Xe^{31+}$ |
| 0.20 | $^{40}Ar^{8+}, ^{60}Ni^{12+}, ^{90}Zr^{18+}$ | $^{85}Se^{17+}, ^{110}Mo^{22+}, ^{124}In^{25+}$ |
| 0.19 | $^{132}Xe^{25+}$ | $^{137}I^{26+}, ^{153}Pr^{29+}, ^{165}Tb^{31+}$ |
| 0.17 | $^{80}Se^{14+}$ | $^{91}Kr^{16+}, ^{97}Zr^{17+}, ^{109}Ru^{19+}$ |
| 0.15 | $^{180}Hf^{27+}, ^{197}Au^{29+}, ^{238}U^{37+}$ | $^{100}Sr^{15+}, ^{101}Y^{15+}, ^{107}Nb^{16+}$ |

# STAGING OF THE PROPOSED ATLAS MULTI-USER UPGRADE

The proposed ATLAS multi-user upgrade could be implemented in three stages starting with two beams at different energies and ending with three beams with more flexible output energies serving three different experiments simultaneously. The last stage would also deliver much higher intensity stable beams with the possibility of accelerating multiple charge state radioactive beams to increase their intensities. The different stages of the proposed upgrade are described below.

## Stage I

This stage is essentially the one described above. It will allow the simultaneous acceleration of two beams; one radioactive from CARIBU EBIS and the other stable from the ATLAS ECR. Both beams are accelerated simultaneously up to the Booster energy. Then one of the beams is extracted to be sent to experimental area II while the second is injected for further acceleration in the ATLAS section of the linac up to the full ATLAS energy for delivery to experimental area III or IV. This first stage will require the installation of:

- The CARIBU EBIS charge breeder, which will happen independently next year.
- A pulsed electrostatic deflector to inject the EBIS and ECR beams in different time periods of the ATLAS cycle as shown in Figure 2.
- A new achromatic LEBT for the transport of beams with different charge-to-mass ratios without emittance growth.
- A pulsed switchyard after the Booster for the extraction of one beam while the second is injected into the ATLAS section of the linac. A kicker and septum magnets are required for an achromatic vertical chicane to be placed under the main ATLAS beam line to serve experimental area II.
- Eventually, a new transport line to deliver the beam extracted at the Booster to experimental areas III and IV in addition to area II.

In this first stage, it will not be possible to accelerate the two beams to the full ATLAS energy for two main reasons: first because the 40-degree bend area is not achromatic and thus not suited for multiple beam injection, and second because the ATLAS section of the linac still have split-ring resonators which can cause significant beam steering and beam loss especially when injecting beams with different charge-to-mass ratios.

## Stage II

This second stage will allow the simultaneous acceleration of two beams, one radioactive and one stable, to the full energy of ATLAS. It will also allow for the acceleration of high-intensity stable beams to the full energy in the ATLAS section of the linac which was limited by the steering in the split-ring resonators. High-intensity stable beams are much needed for the production of a different class of radioactive beams using the future

Argonne Inflight Radioactive Isotope Separator (AIRIS) [16]. This stage will require:

- The modification of the 40-degree bend area to be achromatic for the transport and injection of beams with different charge-to-mass ratios.
- Replacing the three remaining split-ring resonator cryomodules with at least one new QWR module, similar to the one installed recently. Adding a second QWR module similar to the energy-upgrade cryomodule is also recommended.
- Pulsed switchyards downstream of ATLAS to send the beams to different experimental areas
- Reconfiguring and adding new shielding to accommodate higher intensity beams in ATLAS.

It is important to note, that the first 72 MHz - $\beta \sim 0.77$ QWR cryomodule replacing the split-ring resonators would produce the same beam energies available now at ATLAS while enhancing their intensity for the production of radioactive beams in AIRIS. A second 109 MHz – $\beta \sim 0.15$ QWR cryomodule similar to the energy-upgrade cryomodule [17], would boost the energy of ATLAS beams up to 20 MeV/u for the heavier ions and 30 MeV/u for the lighter ones, which would further enhance the production of radioactive beams in AIRIS from higher cross sections of several production channels [18].

### Stage III

This last stage will allow the simultaneous acceleration of three beams, one radioactive and two stable, to either the Booster energy or the full ATLAS energy to serve three experimental areas simultaneously. Higher intensity stable beams will be produced in a new superconducting (SC) ECR ion source and multiple charge states of radioactive beams will be combined to at least double their intensity. This last stage will require:

- Replacing one of the existing ECRs with a new high-performance SC ECR source.
- Developing and installing a beam chopper system in the LEBT to inject two stable beams with close q/A ratios into two separate RF buckets.
- Modifying the injection for multiple-charge-state radioactive beams from CARIBU EBIS.
- Developing and installing two RF switchyards for areas II and III.
- Modifying the experimental beam lines to allow the transport of multiple-charge-state and larger emittance beams.

## SUMMARY

With the CARIBU EBIS installation next year, it will be possible to simultaneously accelerate radioactive and stable beams in ATLAS. This could significantly increase the available beam time to satisfy the increasing demand from the users. The overlap in charge-to-mass ratio between stable and radioactive beams is significant and should allow for a much needed flexibility in beam scheduling.

We have presented a detailed plan to upgrade ATLAS with multi-user capabilities which could be implemented in

three stages. The first stage is at low cost by adding a pulsed injection and extraction for simultaneous two- beam acceleration, which could be implemented in two years. The second stage will replace the remaining split-ring resonators with one or two QWR cryomodule and adds a pulsed switchyard after ATLAS, allowing two- beam acceleration to the full ATLAS energy. The third and last stage will install a new SC ECR for higher intensity stable beams and the simultaneous multiple-charge-state acceleration of radioactive beams. With the completion of this upgrade, three beams could be accelerated and delivered to three different experimental areas simultaneously.

## REFERENCES

[1] "The Argonne Superconducting heavy-ion linac", L.M. Bollinger et al, Proceedings of the Conference on Proton Linear Accelerators, Chalk River, Ontario, 14-17 September 1976, AECL-5677, p95 (1976).

[2] "Superconducting Low-Velocity Linac For The Argonne Positive-Ion Injector", K.W. Shepard et al, Proceedings of the 1989 IEEE Particle Accelerator Conference, Chicago, Illinois, March 20-23, 1989, IEEE Publishing Vol. 2, p974 (1989).

[3] "Radioactive beams from gas catchers: The CARIBU facility", G. Savard et al., Nucl. Instr. Meth. B 266,4086 (2008).

[4] "Completion of Efficiency and Intensity Upgrade of the ATLAS Facility", P.N. Ostroumov et al, Proceedings of the 2014 Linear Accelerator Conference (LINAC-14), Geneva, Switzerland, August 31 - September 5, 2014.

[5] "Improved charge breeding efficiency of light ions with an electron cyclotron resonance ion source", R. Vondrasek et al, Rev. Sci. Instrum. **83**, 113303 (2012).

[6] "Development and beam test of a continuous wave radio-frequency quadrupole accelerator", P.N. Ostroumov et al, Phys. Rev. ST–AB 15 (2012) 110101.

[7] "Commissioning of the 72 MHz Quarter-Wave Cavity Cryomodule at ATLAS", M.P. Kelly et al, Proceedings of the 2014 Linear Accelerator Conference (LINAC-14), Geneva, Switzerland, August 31 - September 5, 2014.

[8] "A full three-dimensional approach to the design and simulation of a radio-frequency quadrupole", B. Mustapha et al, Phys. Rev. ST–AB 16 (2013) 120101.

[9] "Split-ring Resonator for the Argonne Superconducting Heavy-ion Booster", K.W. Shepard et al, IEEE Trans. Nucl. Sci. NS-24, p1147 (1977)

[10] "Electro-Magnetic Optimization of a Quarter-Wave Resonator", B. Mustapha and P.N. Ostroumov, Proceedings of the XXV Linear Accelerator Conference (LINAC-10), Tsukuba, Japan, September 12-17, 2010

[11] "Improved beam characteristics from the ATLAS upgrade", C. Dickerson et al, this conference.

[12] "A Driver Linac for the Advanced Exotic Beam Laboratory: Physics Design and Beam Dynamics Simulations", B. Mustapha P. N. Ostroumov and J. A.

Nolen, Proceedings of PAC-07 Conference, Albuquerque, New Mexico, June 25-29, 2007, p1601.

[13] "First Charge Breeding Results at CARIBU EBIS", S. Kondrashev et al, Proceedings of the 12th International Symposium on Electron Beam Ion Sources and Traps (EBIST-2014), East Lansing, Michigan, USA, May 18-21, 2014.

[14] "Proposal for Simultaneous Acceleration of Stable and Unstable Ions in ATLAS", A. Perry et al, Proceedings of the 2013 North American Particle Accelerator Conference (NA-PAC-2013), Pasadena, CA, September 29 - October 4, 2013.

[15] "Simultaneous Acceleration of Multiply Charger Ions through a Superconducting Linac", P. Ostroumov et al, Physical Review Letters 86, 2798 (2001).

[16] "Argonne In-flight Radioactive Ion Separator", S. Manikonda et al., Proceedings of HIAT-2012, Chicago, IL, USA.

[17] "The ATLAS Energy Upgrade Cryomodule", J. D. Fuerst, Proceedings of SRF 2009, Berlin, Germany.

[18] C. Hoffman (PHY/ANL), private communication

# EXPERIENCE WITH STRIPPING HEAVY ION BEAMS

H. Okuno, RIKEN Nishina Center for Accelerator-based Science, Wako, Japan

## Abstract

Charge strippers play a critical role in many high-intensity heavy ion accelerators. Recent progress on accelerator technology make charge strippers so critical that traditional carbon foils can easily reach the limit of their application due to their short lifetime. In fact, three major heavy ion accelerator facilities (GSI, MSU/ANL, and RIKEN) have extensively studied alternatives to carbon foils to realize high-intensity acceleration of very heavy ions such as uranium. For example, the liquid lithium stripper was developed at MSU/ANL, and the helium gas stripper and rotating beryllium disk stripper were developed at the RIKEN radioactive-isotope beam factory (RIBF). The RIBF two strippers greatly contributed to the increase in the uranium beam intensity. However, we believe the Be disk stripper will reach its limit in near future due to its large deformation and requires further development for the RIKEN RIBF intensity upgrade program.

## INTRODUCTION TO CHARGE STRIPPERS

The production of high-intensity radioactive-isotope (RI) beams is one of the important applications of heavy ion accelerators. The three major heavy ion accelerator facilities (RIKEN, MSU/NSCL, and GSI) are each operating or constructing facilities (Radioactive-Isotope Beam Factory (RIBF) [1], the Facility for Rare Isotope Beams (FRIB) [2], or the Facility for Antiproton and Ion Research (FAIR) [3], respectively) to produce high-intensity RI beams using in-flight fission or projectile fragmentation of accelerated uranium ions in order to explore inaccessible regions of the nuclear chart. These facilities adopted different accelerator schemes, such as cyclotrons for RIBF, superconducting linear accelerators (linacs) for FRIB, and synchrotrons for FAIR. However, all facilities begin the acceleration with low charge state ions from the ion source and strip their charge once or twice during acceleration to increase the energy gain or decrease magnetic rigidity.

After passing through a stripper thick enough to reach a charge equilibrium, the charge state is an increasing function of projectile energy. Figure 1 shows the equilibrium charge state of uranium ions in solid as a function of projectile energy. In this study, we focus on charge strippers for uranium ion acceleration because these strippers encounter the most difficult problems due to largest heat deposits and heaviest radiation damage. The lines in Fig. 1 show the paths of the charge states at the three facilities. To increase the charge from 4+ to 28+, FAIR uses an $N_2$ gas stripper at 1.4 MeV/u because the acceleration of the low charge state to 28+ is essential for reducing space charge forces in the pulsed operation. To increase the charge from 33.5+ to 78+ on average, FRIB uses a liquid lithium stripper at 17 MeV/u. About 80% of the input ions can be gathered

using multi-charge-acceleration technique. Finally, RIBF adopted two-step charge stripping at 11 MeV/u and 51 MeV/u to increase the charge from 35+ to 86+. We identify the following requirements for charge strippers:

- High charge state,
- High stripping efficiency,
- Small energy spread,
- Long lifetime,
- Good stability.

A high charge state is required to reduce the total accelerating voltage and cost. In this sense, solid or liquid strippers are preferred because the density effect provides about 20% higher charge states compared to gas strippers. Suppression of electron capture in low-Z materials is another method for obtaining a higher charge state [4]. This suppression comes from the slow velocity of electrons in low-Z materials, and the resulting stripping efficiency should be high. The typical stripping efficiency of a charge stripper is around 10–30%. Using too many strippers decreases beam intensity to zero. In some cases, the shell effect aids the high stripping efficiency. Moreover, the energy spread after the beam passes through the stripper should be small. There are the main two causes for the energy spread: non-uniformity in the stripper thickness, and straggling charge state energy arising from the fluctuation of charge states in the material [5]. The lifetime of the charge stripper should be long. In particular, lifetime-related problems are critical to high-power beam operation. Finally, good stability contributes to the stable operation of the accelerator complex.
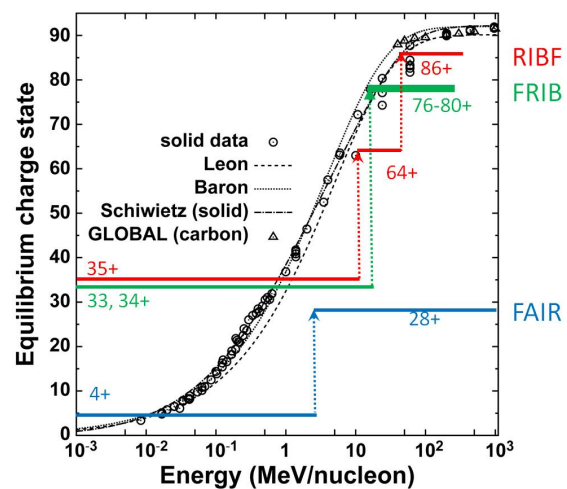


Figure 1: Charge evolutions in uranium acceleration for FAIR, FRIB, and RIBF as a function of projectile energy with an equilibrium charge state.

# RESEARCH AND DEVELOPMENT (R&D) RESULTS FOR FRIB AND RIBF

This section describes the R&D results on the charge strippers for FRIB and RIBF to show how the requirements discussed in the previous section can be fulfilled.

## Liquid Lithium Stripper at FRIB

The FRIB liquid lithium charge stripper was developed in collaboration with Argonne National Laboratory (ANL) [6]. The charge stripper module primarily consists of a vacuum chamber to produce thin liquid film and a compact electromagnetic pump. The length of the module is 2 m in the beam line. This stripper is used for electron stripping light ions to uranium at 17 MeV/u. The designed maximum power deposition is 30 kW/mm$^3$. A round lithium jet from nozzle is impacted on the edge of the deflector to produce films as thin as 10 $\mu$m. The velocity of the lithium liquid is 50 m/s, and the temperature is approximately 200°C. The electromagnetic pump makes lithium flow in a helical tube using coupling between the radial field from a permanent magnet and current in the axial direction. The experimental work was performed with low-energy proton beams from the Low-Energy Demonstration Accelerator (LEDA) source at the Los Alamos National Laboratory (LANL). The beam was deposited on the liquid lithium film with a power density deposition similar to the maximum expected at FRIB when accelerating 400 kW of uranium. The film was not perturbed at the beam impact point as shown in Fig. 2. To test the stability and reliability of the charge stripper, FRIB will construct the charge stripper module within the next 6 months using continuous flow.
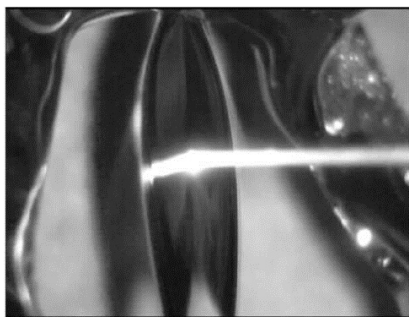


Figure 2: A photo of the high speed lithium film being impacted by a 70 keV, 300 W proton beam.

## Charge Strippers at RIBF

Figure 3 shows the acceleration scheme for uranium ion beam at RIBF. The 35+ ions from the 28 GHz superconducting electron cyclotron resonance (SC-ECR) ion source [7] are accelerated using four ring cyclotrons: RIKEN Ring Cyclotron (RRC), fixed-frequency ring cyclotron (fRC), intermediate-stage ring cyclotron (IRC), and superconducting ring cyclotron (SRC). The two charge strippers are installed at 11 MeV/u and 51 MeV/u to enhance the charge state

from 35+ to (64+/71+) and from (64+/71+) to 86+, respectively. After 2006, our continuous efforts greatly increased the uranium beam intensity from 0.03 pnA to 25 pnA. In particular, the new injector with 28 GHz SC-ECR was commissioned in 2011 [8]. Figure 4 shows the beam intensity of uranium ion at the exit of SRC, which was the last ring cyclotron in 2007. Even when the beam intensity is about one-ten-thousand of the goal intensity of 1 p$\mu$A, this decrease in the beam intensity clearly shows the degradation of the conventional carbon foil used as the first stripper, which motivated us to begin extensive R&D studies.
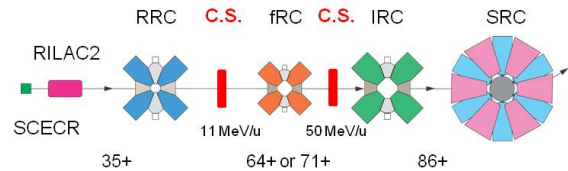


Figure 3: Acceleration scheme for uranium beams using two strippers.
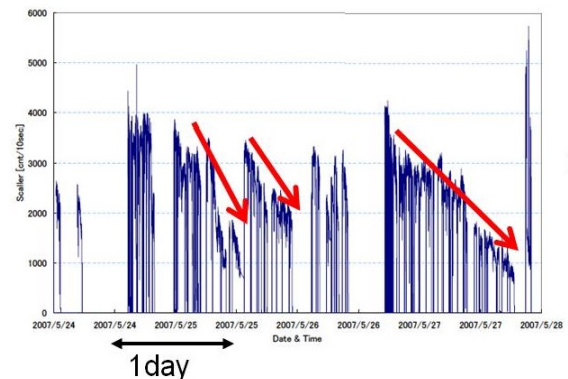


Figure 4: The current trend at the exit of SRC in 2007.

In our R&D for the first stripper, we consider both foils and gas strippers in parallel. We first considered rotating cylinder foils with large carbon foils to expand the irradiation area. The first test failed catastrophically, and the foil broke in 3 min. However, from measurements, we identified the importance of the slow cylinder rotation and the robustness of the carbon nanotube (CNT) foils. Finally, we found that slowly rotating CNT-based foils can survive for a long time, as shown in a user run in 2011 [9]. We further studied a gas stripper, which measured equilibrium charge states in $N_2$ and Ar gas, using a small gas cell with a differential pumping system [10]. The charge states in these materials are far below the acceptable charge states for fRC. However, we suggested that low-Z gases can increase the charge state [4]. The experimental results of the cross-sectional measurements for electron-loss and electron-capture using the small gas cell were promising and encouraged us to make prototypes to measure fundamental data such as the evolution of the charge state and the energy spread after the stripper [11]. Finally, we determined that the helium gas stripper practical

even though some technical issues remained. In particular, the most challenging issue is the sufficient confinement of the thick helium gas in order to reach charge equilibrium. However, we realized the helium gas stripper for practical operations after overcoming the confinement issue [12], and it has been working well since November 2012.

Figure 5 and 6 illustrate the fundamental data for the charge evolution and energy spread of the uranium ion after the stripper. Figure 5 clearly shows higher charge states in He gas than those in Ar and Ne. Here, we note that the charge reaches equilibrium slowly in He gas compared to other gases because the electron-loss cross-section is proportional to the square of the atomic number, resulting in a smaller cross-section in He than that in other gases. The obtained equilibrium charge states are consistent with the cross-section measurements that show significant charge-state enhancement in He gas compared to that in the reference $N_2$ gas [4]. Figure 6 shows the energy spread of the uranium ion. Charge state straggling is dominant in He gas, while non-uniformity is dominant in carbon foils. The red circled points show the energy spread in the operational points. In real operations, a smaller energy spread can be expected in He than that in fixed carbon foils. Moreover, when rotating strippers are used, an additional energy spread occurs due to non-uniformity in large carbon foils. Figure 7 shows the jitter of beam timing after the He stripper and rotating carbon foil, and the periodic behavior shows the non-uniformity of the thickness distribution in the large foil.



Figure 6: Obtained energy spread for He and carbon-foil strippers as a function of the target thickness.
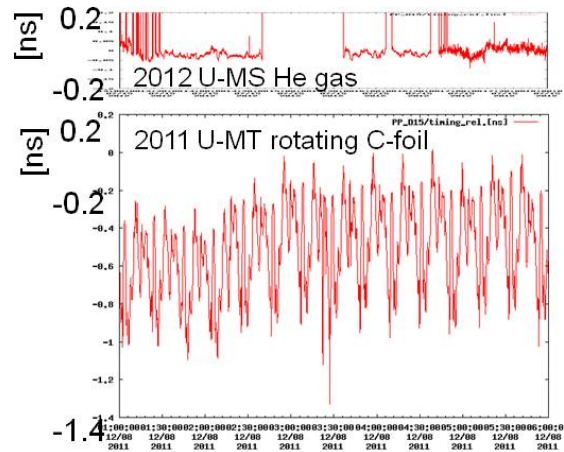


Figure 7: Jitter of the beam timing after the He gas stripper and the rotating carbon-foil stripper.



Figure 5: Measured and calculated charge-state evolution for He, Ne, and Ar.

There was little R&D activity for the second stripper before the new injector system was commissioned because the foil temperature can be kept low in low-intensity beams. After the new injector operation began, the lifetime of the fixed carbon foil became as short as 5–10 h due to high temperatures of the foils. We then tested Be, Ti, and C wheel strippers. Figure 8 shows the measured charge distribution after the Be and Ti wheel strippers. The charge-state distribution after the Be stripper is similar to that after the fixed carbon foil stripper, reaching a maximum at charge state of

86+. However, the charge state after the Ti wheel stripper is low. The charge distribution after the carbon wheel could not be measured because of the poor uniformity of thickness. The energy distribution after the disks was measured by a scintillation counter placed downstream of the second stripper. The data shows that energy width after fixed carbon foil, Ti disk, and Be disk are comparable, while rotating carbon disk had a very broad distribution. Based on the fundamental data, we decided to use the Be disk [13]. We had also measured the charge distribution in gas. However, the mean charge after the $N_2$ and He gases was more than three times lower than that after the carbon foil. The lowest acceptable charge state is 86+ for the last cyclotron, but we could not achieve a sufficiently high charge state in gas.

## OPERATIONAL EXPERIENCES AT RIBF

Table 1 lists the charge strippers adopted for user runs after extensive R&D studies. In 2011, to accept the increasing beams, we used large rotating CNT-based foils, which greatly contributed to the extraction of a 2.4-pnA uranium beam from SRC. In 2012, we replaced the carbon-foil-based system with the He gas stripper and the Be disk stripper. The fRC was modified to increase the bending power to accept 64+ for this replacement. These new charge stripping sys-
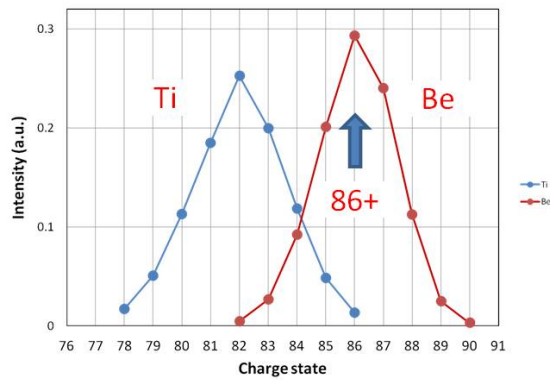
Figure 8: Charge distributions of the uranium ion at 51 MeV/u after rotating Be and Ti disks.

Table 1: Charge Strippers Used during User Runs at RIBF

| Year | Q1 | 1st C.S. | Q2 | 1st C.S. | Q2 | Iext. (pnA) |
|------|----|----------|----|----------|-----|-------------|
| 2007-2009 | 35 | C-foil | 71 | C-foil | 86 | 0.8 |
| 2011 | 35 | Rotating CNT -SDC foil | 71 | C-foil | 8+ | 2.4 |
| 2012- | 35 | He gas | 64 | Rotating Be disk | 86 | 15-25 |

tems greatly contribute to the extraction and stable supply of 15-pnA and 25-pnA uranium beams from 2012 to 2014. Figure 9 shows the helium gas stripper [12], where 7 kPa of He gas can be accumulated over a cell length of 50 cm. The total thickness of He is 0.7 mg/cm$^2$. Using 21 pumps, about 430 m$^3$/day of He gas can be circulated. The five stage differential pumping allows eight order pressure reduction. The resulting beam aperture is greater than 10 mm. The stripper has a unique recycling system wherein gas leaking through through the orifices in the gas cell is evacuated by mechanical booster pumps (MBPs) and directly returned to the gas cell chamber. Moreover, this system does not have problems with oil contamination because the MBP is effectively oil free. This system was utilized in real operations beginning in November 2012. In practical operations, we were concerned that the target thinning caused by the heat load due to uranium beams will determine the application limit of gas stripper. We measured the time-of-flight (TOF) of U$^{64+}$ beams as a function of the beam intensity using phase probes during the operation. Figure 10 shows the time difference of the ions. A large time difference indicates the early arrival of the ion, which further indicates target thinning due to increasing gas temperature. The beam intensity at the gas stripper is around 0.6 p$\mu$A at maximum, which corresponds to an energy deposit of 50 W. The data shows that the increase in temperature is about 15 K which does not affect on beam operation so much, suggesting that that gas is not heated as expected. We believe some suppression
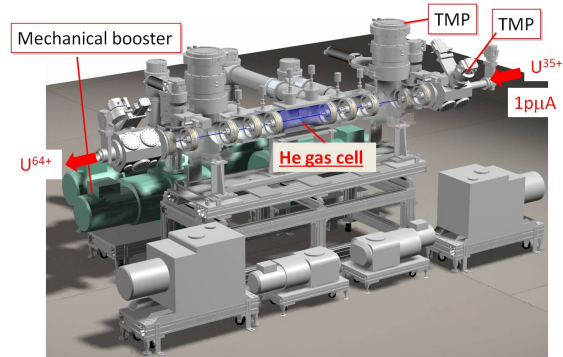


Figure 9: Cross-sectional view of the newly constructed recirculating He gas stripper.

mechanism of the heat efficiency exists. We will perform a spectroscopic study of the mechanism in the near future. The second concerning point is impurity because the practical stripper recycles the helium gas where impurity could easily be contained. The effect of impurity (air, water, hy-
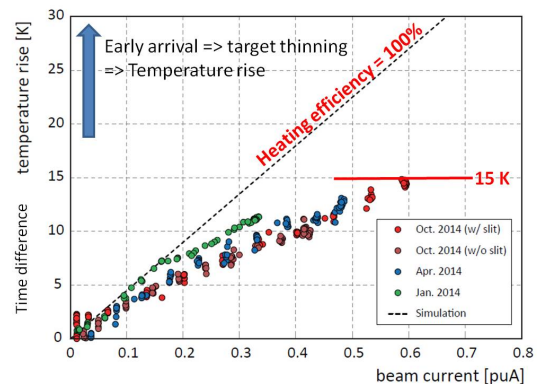


Figure 10: Time difference in ion arrival from the He gas stripper as a function of the beam current. Time difference of 1 ns corresponds to a temperature rise of 22 K.

drocarbon) on the charge state can be large for the low-Z gas stripper because the capture cross-section is proportional to $Z^{4.2}$. The level of impurity must be less than 100 ppm to avoid affecting the charge state. Thus, the charge state in the gas is very sensitive to impurities. Charge states with recycled helium are compared to the charge evolution obtained in Fig. 6; no significant difference could be identified.

As discussed previously, Be rotating disks were used for the second stripper. The rotating disk module can provide rotation speeds of about 1000 rpm at maximum and 60 times the irradiation area of the beam spots [14]. Figure 11 shows the disk before, during, and after irradiation. The disk thickness is 0.1 mm, and the heat load on the stripper is around 90 W. The Be disk survived more than one month of beam irradiation although the disk was severely deformed [13]. Beryllium is ductile above 400°C and brittle below 400°C. Thus, the deformation is a result of thermal cycle properties and has an effect on the beam quality after the stripper. In fact, beam loss occurs in the operation due to fluctuation of

Table 2: Candidates for Second Charge Strippers at RIBF

| Material | Status/Merits | Demerits | Future work |
|----------|---------------|----------|-------------|
| $CH_4$ (gas) | Experience in RIBF | Combustible | Charge state |
| Be (solid) | Experience in RIBF | Large deformation | Improvement of structure |
| C (solid) | Experience in RIBF | Poor uniformity in thickness | New material |
| SiC (solid) | Heat resistant | Low charge | Charge state |
| Li (liquid) | Experience in FRIB/ANL and BNCT | Combustible | Study using water |

the beam after the second stripper as a result of the large disk deformation.
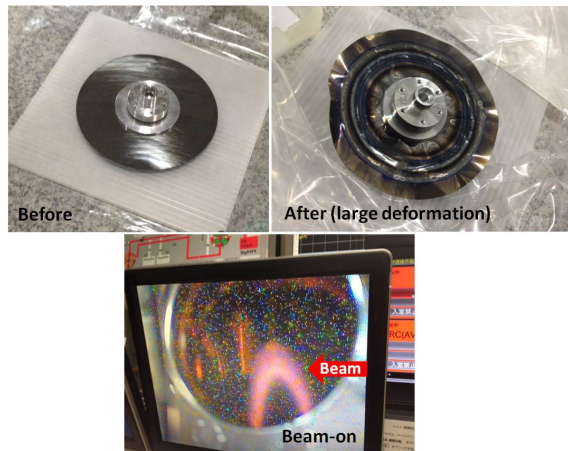


Figure 11: The Be disk stripper before, during, and after beam irradiation.

## OUTLOOK AND SUMMARY

The Be disk will reach its application limit in the near future due to its large deformation, and we need a stripper that can survive beam irradiation with 2–3 times the present beam intensity to realize 100 pnA at the SRC exit, which is our goal intensity. Furthermore, more extensive R&D studies will be performed because the charge stripper is highly important to the future goal intensity. Figure 12 explains a proposed upgrade plan. The present scheme for the uranium beam uses two charge strippers to breed the charge from 35+ to 64+ and from 64+ to 86+. Only 5% of the initial beam reaches the final accelerator with two-step charge stripping. In essence, our upgrade plan disregards the first stripper to increase the beam intensity by a factor of five and to improve the beam quality. Moreover, the present fRC should be replaced with a superconducting fRC to increase the bending power for an acceptance of 35+. As a result, the load to the charge stripper will be more severe. We will test the candidates listed in Table 2, including methane gas, beryllium with an improved structure, carbon disks with good uniformity, silicon carbide, liquid lithium, and oil.

In summary, the charge stripper is a key issue for heavy ion accelerators with high intensity. The liquid Li strip-
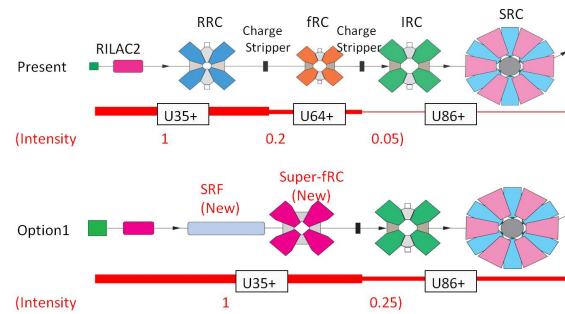


Figure 12: Acceleration scheme for optional intensity upgrades using the present plan.

per research is continuing successfully at FRIB. Moreover, the helium gas stripper solved the bottle-neck problem in uranium acceleration, and the Be wheel was successfully applied for the second stripper. For further intensity upgrade, we need to continue research for the second stripper ($CH_4$ gas, C, Be, SiC, and liquid Li).

## REFERENCES

[1] Y. Yano, Nucl. Instrum. Methods Phys. Res., Sect. B 261 (2007) 1009.

[2] J. Wei et al., Proc. Linac Conference, Tel Aviv (2012), pp. 417.

[3] O. Kester, IPAC13, Shanghei (2013), TUXB101.

[4] H. Okuno et al., Phys. Rev. ST Accel. Beams 14 (2011) 033503.

[5] H. Weick et al., Phys. Rev. Lett. 85 (2000) 2725.

[6] J. Nolen and F. Marti, Rev. Accel. Sci. Technol. 6 (2013) 1–16.

[7] Y. Higurashi et al., Rev. Sci. Instrum. 83 (2012) 02A308.

[8] K. Yamada et al., IPAC'12, New Orleans (2012) TUOBA02.

[9] H. Hasebe et al., INTDS12, Mainz, (2012).

[10] H. Kuboki et al., Phys. Rev. ST Accel. Beams 13 (2010) 093501.

[11] H. Imao et al., Phys. Rev. ST Accel. Beams 15 (2012) 123501.

[12] H. Imao et al., IPAC13, Shanghai (2013) THPPA01 & TH-PWO038.

[13] H. Hasebe et al., INTDS2014, Odaiba (2014).

[14] H. Ryuto et al., (2004) Cyclotrons'04, Yoyogi (2004) 19P24.

# PRESERVING BEAM QUALITY IN LONG RFQS ON THE RF SIDE: VOLTAGE STABILIZATION AND TUNING

Antonio Palmieri INFN-LNL, Legnaro (PD), Italy

## Abstract

RFQs are the injectors customarily used in modern linacs and the achievement of a high beam transmission for a RFQs is of paramount importance in case of both high intensity linacs and RIBs facilities. This calls for an accurate control of the longitudinal inter vane voltage along the four structure quadrants (field stabilization), in order to keep its deviation from nominal value as low as possible (a few %, typically). In particular, for long RFQs (in which the structure length can be significantly higher than the RF wavelength), this aspect is more challenging, since the effect of a perturbation (e.g. due to mechanical errors and/or misalignments) on the nominal RFQ geometry has a major impact on voltage. This paper describes and analyses these issues, as well as the methods used to tackle them.

## INTRODUCTION

In some important cases, the achievement of a high beam transmission (>95%) for a RFQ is a key issue for the proper operation of the overall facility in which the RFQ is included. This is particularly true in the cases of high intensity proton and/or deuteron RFQs (avg. beam power > 10 kW) and in the case of RIB acceleration. In the first case, the high space charge at low energy induces beam losses giving rise to the structure activation with the production of neutrons, (p-Cu and d-d reactions), and the loss control has to be compliant with a hands-on maintenance of the machine. In the second case, the RIB current loss can jeopardize the quality of the outcomes of Nuclear Physics experiments, while lost RIBs in the RFQ can give rise to high-lifetime decay products, which can undergo implantation reactions in the RFQ body.

These circumstances call for the adoptions of some adjustments in beam dynamics design and some stricter constraints on mechanical and electromagnetic parameters.

One of the adjustments is the accurate control of the longitudinal behavior of the inter-vane voltage along the four quadrants of the structure, and of voltage disuniformities among the quadrants with deviations from the nominal values that shall not exceed a few %. For instance, the following table lists these constraints for the RFQs being developed at LNL, namely the IFMIF RFQ [1], the TRASCO RFQ [2] and the SPES RFQ [3]. All of these RFQs have been designed for CW operation.

Table 1: RFQs Developed at LNL: Main Parameters

|  | **TRASCO** | **IFMIF** | **SPES** |
|---|---|---|---|
| status | Constructed | Construction in progress | Developing |
| f [MHz] | 352.2 | 175 | 80 |
| l [m] | 7.13 | 9.8 | 7.2 |
| $R_0$[mm] | 2.93-3.07 | 4.13-7.10 | 5.27-7.86 |
| $\rho/R_0$ | 1 | 0.75 | 0.76 |
| Ib [mA] | 30 | 125 | 1e-6 |
| V[kV] | 68 | 79-132 | 64-86 |
| W [MeV/u] | 5 | 5 | 0.727 |
| E.M. segments | 3 | 1 | 1 |
| Mech. modules | 6 | 18 | 6 |
| dV/V range | ±1% | ±2% | ±3% |
| $Q_0$ | 8000 (20% margin) | 12000 (25% margin) | 16000 (20% margin) |
| RF power [kW] | 800 (20% margin) | 1250(25% margin) | 120(20% margin) |

In order to understand the causes of these voltage deviations, it should be pointed out that the effect of a perturbation (e.g. due to mechanical errors and/or misalignments) on the nominal geometry in a four-vane RFQ provokes a mixing of the operating $TE_{210}$ mode (Quadrupole mode) with neighboring quadrupole $TE_{21n}$ and $TE_{11n}$ dipole modes. Now, if the overall RFQ length l is significantly greater than the wavelength $\lambda$, the eigenfrequencies $f_n$ of the neighbouring modes can be very close to the operational one, i.e. $f_0$, thus enhancing the perturbation effect. The measures that are undertaken to tackle this issue consist in the "stabilization" and "tuning". In particular, the RFQ stabilization involves actions that can be taken before knowing the actual RFQ voltage profile (i.e. in the design phase), namely: 1) The usage of coupling elements (resonant coupling) [4] this method consists in dividing the RFQ in N resonantly coupled segments and has the advantage of increasing the frequency spacing between the $f_0$ and the frequencies of the other quadrupole modes. This method is used mainly in RFQs with $L/\lambda > 6$ [5, 6, 7], 2). The usage of stabilizing devices for the dipole modes (dipole stabilizers or DSRs) [8]: this method consists in inserting longitudinal bars in the RFQ volume in correspondence of the end-cells and coupling cells, which do not perturbate

the quadrupole mode, but shift the dipole frequencies and create a "dipole-free region in the neighbourhood of the $f_0$ frequency. The RFQ tuning, indeed, consists in those actions that, starting from the actual knowledge of the voltage along z, and of the frequency in the real RFQ (typically by measurements), allow the attainment of the voltage specifications at the target frequency. In the following, this aspect will be analyzed in detail. The analysis will be carried out for four-vane RFQs only, and in particular for the RFQs developed at LNL.

# RFQ CIRCUIT MODELING

A four vane RFQ can be modelled with a five conductor (the four electrodes E1, E2, E3 and E4 plus a "virtual" ground) transmission line, whose infinitesimal element of length dz is shown in Figure 1[9]. This topology is similar to the four-conductor line used in [10]. In such circuit the $L_{si}$ (i=1,..,4) are the inductances associated with the longitudinal current flow along the vanes, $L_i$ and $C_i$ are respectively the inductances (integrated in length) associated with the flux of magnetic field through the RFQ cross-section and the intra-vane capacitances (per unit length). $C_a$ and $C_b$ are the capacitances (per unit length) between opposite vanes.
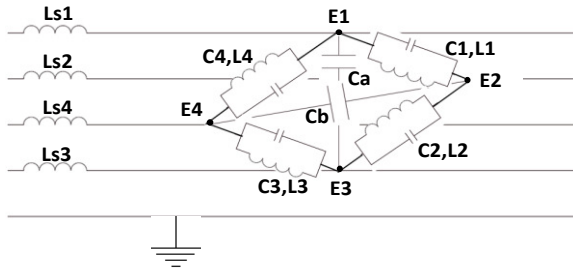


Figure 1: The RFQ equivalent transmission line.

In the ideal RFQ ($C_i$=C, $L_i$=L and $C_a$=$C_b$, i=1,..,4), by defining $\omega_0^2 = 1/LC$ and $h = C_a/C$, the line equations can be written as follows, where $U_i$ are the inter-vane voltages ($U_i$=$E_{(i\,mod\,5)+1}$- $E_i$).

$$\frac{d^2\underline{U}}{dz^2} = \left(-\frac{\omega^2}{c^2} + \frac{1}{c^2}\underline{\underline{C}}^{-1}\underline{\underline{L}}\right)\underline{U} \quad (1)$$

Here $\underline{\underline{A}} = \underline{\underline{C}}^{-1}\underline{\underline{L}}$ is a 4x4 circulant matrix defined by the vector $\underline{\Omega}^2=(\omega_0^2/4)[1+2/(1+h),-1,-(1-h)/(1+h),-1]$.The eigenvalues of **A** are proportional to the quadrupole TE$_{21}$ and dipole TE$_{11}$ frequencies ( $f_q = f_0$ and $f_d = f_0/\sqrt{1+h}$ ), plus a zero eigenvalue corresponding to the "monopole mode" the only goal of which is to guarantee the voltage consistence of $U_1+U_2+U_3+U_4=0$. A transformation between modal voltage vector $\underline{\hat{U}} = U_q\hat{e}_q+U_m\hat{e}_m+U_{d1}\hat{e}_{d1}+U_{d2}\hat{e}_{d2}$ and vane voltage vector $\underline{U}$ is therefore established. Moreover, this transformation decouple the transmission line in three independent equivalent lines, corresponding to the Q and the two D modes, with longitudinal wave number

$\gamma = (1/c)\sqrt{\omega^2 - \omega_c^2}$ where $\omega_c$ can be $\omega_q$ or $\omega_d$. If boundary conditions for the RFQ U'(0)=U'(l)=0 @f=,$f_{q0}$ are assigned via a resonant lumped LC element (End-cell) [8], longitudinal quadruople and dipole eigenfrequencies $f_{q0}$, $f_{q1}$,…$f_{qn}$,… $f_{d0}$, $f_{d1}$, …$f_{dn}$,…and orthonormal eigenvectors $\underline{\phi}_{qn} = \phi_{qn}\hat{e}_1$ , $\underline{\phi}_{d1n} = \phi_{dn}\hat{e}_3$ $\underline{\phi}_{d2n} = \phi_{dn}\hat{e}_4, n \in N_0$ can be determined.

# PERTURBATION ANALYSIS

In case of geometric errors in the RFQ vane and/or vessel profiles, a perturbative term $\underline{\underline{\delta A}}$ appears. From the purely geometrical point of view, this term is due to capacitance perturbations $\underline{\underline{\delta C}}$ (i.e. due to mean aperture $R_0$ deviations from the nominal value) and/or inductance perturbations $\underline{\underline{\delta L}}$ (i.e electrode height H or tank radius deviations). In this case, the perturbed operator reads

$$\underline{\underline{\delta A}} = c^{-2}\delta\left(\underline{\underline{C}}^{-1}\underline{\underline{L}}\right) = c^{-2}\left(\underline{\underline{C}}^{-1}\underline{\underline{\delta L}} - \underline{\underline{C}}^{-1}\underline{\underline{\delta C}}\underline{\underline{A}}\right)$$

and, in the modal basis,

$$\underline{\underline{\delta k}}^2 = c^{-2}\underline{\underline{S}}^{-1}\underline{\underline{C}}^{-1}\left(\underline{\underline{\delta L}} - \underline{\underline{\delta C}}\underline{\underline{A}}\right)\underline{\underline{S}} .$$

**S** being the eigenvector matrix. Therefore it is possible to write the explicit expression of the perturbed voltage of the RFQ as follows: $\underline{U} = U_0\underline{\phi}$, with

$$\underline{\phi} = \underline{\phi}_{q0} + \delta\underline{\phi} = \underline{\phi}_{q0} + \sum_{n=1}^{\infty}a_{qn}\underline{\phi}_{qn} + \sum_{n=0}^{\infty}a_{d1n}\underline{\phi}_{d1n} + \sum_{n=0}^{\infty}a_{d2n}\underline{\phi}_{d2n}$$

where

$$a_{qn} = \frac{-\omega_0^2}{4(\omega_0^2 - \omega_{qn}^2)}\int_0^\ell \varphi_{q0}\varphi_{qn}(\frac{\delta C_{QQ}}{C} + \frac{\delta L_{QQ}}{L})dz \quad n \in N$$

$$a_{d1n,d2n} = \frac{-\sqrt{2}\omega_0^2}{4(\omega_0^2 - \omega_{dn}^2)}\int_0^\ell \varphi_{q0}\varphi_{dn}(\frac{\delta C_{Qd1,Qd2}}{C} + \frac{\delta L_{Qd1,Qd2}}{L})dz \quad n \in N_0$$

with

$$\delta C_{QQ} = \sum_i \delta C_i \quad \delta L_{QQ} = \sum_i \delta L_i$$

$$\delta C_{Qd1} = \sqrt{2}(\delta C_1 - \delta C_3)/(1+h), \delta C_{Qd2} = \sqrt{2}(\delta C_4 - \delta C_2)/(1+h)$$

$$\delta L_{Qd1} = \sqrt{2}(\delta L_1 - \delta L_3), \delta L_{Qd2} = \sqrt{2}(\delta L_4 - \delta L_2)$$

The perturbed quadrupole frequency is:

$$\Delta\omega_0 \cong -c^2/2\omega_0\left\langle\hat{U}_{q0}\left|\underline{\underline{\delta k}}^2\right|\hat{U}_{q0}\right\rangle .$$

The term $(\omega_0^2- \omega_n^2)/\omega_0^2$ is proportional to $(\lambda/l)^2$ and therefore, the longer the RFQ, the more important is the perturbation effect. Moreover, it is evident that a key parameter is the dependence of the $\delta L$'s and $\delta C$'s on the geometric errors in the RFQ, which cause a variation of the local cut-off frequency $f_0$ for the Q mode $\delta f_0$=−$(1/2(f_0/C)\delta C+1/2(f_0/L)\delta L$. In particular, it has to be taken into account that the C depend mainly on $R_0$ and $\rho$, while L depend mainly on the upper RFQ wall height (or tank radius) H and on the electrode thickness $W_b$. Therefore it is possible to write that $\delta C_i$=$\alpha_{R0}\delta R0+\alpha_\rho\delta\rho$ and $\delta L_i$=$\alpha_H\delta H+\alpha_{Wb}\delta W_b$, and equivalently that $\delta f_0$=$\chi_{R0}\delta R0+\chi_\rho\delta\rho+$=$\chi_H\delta H+\chi_{Wb}\delta W_b$. On the other hand, it should be observed that, while $\chi_\rho$ depends only on

construction accuracy (±10-20 μm is the state of the art), $\chi_{R0}$ depends on electrode positioning (errors of ±100 μm can occur), due to alignment and/or brazing. As for the inductive terms, their sensitivities $\chi_H$ and $\chi_{Wb}$ turn out to be one order of magnitude lower than the corresponding capacitive ones. These parameters, obtained via 2D and 3D simulations are listed in Table 2.

Table 2: Frequency Sensitivities W/O Geometric Deviations for the RFQs Developed at LNL (per Quadrant)

|  | TRASCO | IFMIF | SPES |
|---|---|---|---|
| $\chi_{R0}$[MHz/mm] | 40 | 7.6 to11.8 | 2.7 to 3.5 |
| $\chi_{\rho}$ [MHz/mm] | -30 | -3.6 to7-5.3 | -3.2 to -2.2 |
| $\chi_H$ [MHz/mm] | -3.2 | -0.9 | -0.13 |
| $\chi_{Wb}$[MHz/mm] | 2.0 | 0.55 | 0.16 |

With these values it is possible to analyze the effect of a perturbation on the quadrupole $TE_{210}$ voltage profile. As a first example, the misalignment of one electrode will be considered on a 9.9 m un-segmented RFQ with constant U and $R_0$ operating at 175 MHz with ideal boundary conditions for the Q mode with $\chi_{R0}$=7.6 MHz/mm. In particular, in case one electrode is displaced of $\delta R_0$=0.05 mm away from beam axis for all z in the interval [$a$, $l/2+a$] with respect to its nominal position and with $a$ varying in the interval [$0, l/2$], a corresponding perturbation of the capacitances $C_1$ and $C_4$ occurs. As expected, the perturbed voltages are proportional to $\Delta R_0$ and the Q component scales as $(\lambda/l)^2$ The diagram is shown in Figure 2 for the case of Q and D components.
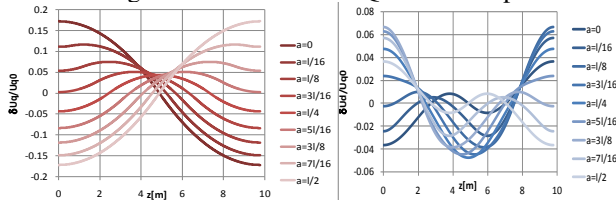


Figure 2: The voltage perturbations (Q component, left, D component, right).

Already from this example it is possible to notice that, only with electrode misalignments in the order of tenth of μm, the voltage specifications are not met, and the RFQ stabilization mechanisms alone are not able to meet the requirements.

## TUNERS AND TUNING RANGE

In order to meet the requirements, it is necessary to use a system of $N_T$ slug tuners per quadrant. Tuners are metallic cylinders of radius a placed on the upper walls of the RFQ and inserted for a depth h in the cavity volume, which compensate the geometric variation in capacitive region with corresponding variations in the inductive region. Figure 3 shows the tuners for the TRASCO RFQ.
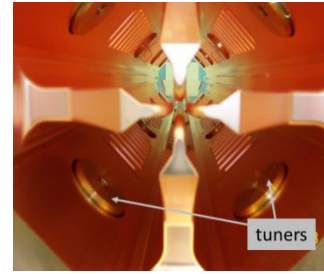


Figure 3: Tuners inserted in the TRASCO RFQ.

A tuner placed in the position $z_i$ (i=1,..,NT) varies both the local cut-off frequency for any z in the interval

[$z_i$-a,$z_i$+a], and global resonant frequency according to the relationships (for h>0)

$$\delta fq_0(z_i) =\chi_{t2D}h_i \; \delta f_0=\chi_{3D}h$$

Therefore, if the function $\delta fq_{0j}(z)\approx-+1/2 \; \delta C_j(z)/C$, (j=1,..,4) is known, by setting the tuner heights $h_i$ in such a way that $\delta L_j(z_i)=-(L/C) \; \delta C_j(z_i)$ it is possible to compensate the capacitance and therefore the voltage perturbation. The basic idea is that the tuning range (the frequency interval that can be spanned by the tuners) defined as $\Delta f_{TR}=4N_T\chi_{3D}(h1+h2)$, should correct frequency (local and global) shifts induced by the maximum $\delta R_0$ error to be expected. It should be noticed that, since the overall frequency perturbation is due to terms coupled with operating mode, it is not compensated by the previous relationships. As an empiric rule, half of the tuning range is employed for $f_0$ correction and the other half for voltage correction. Typically, the tuning range is expected to be symmetric about the operational frequency $f_0$, i.e. $\Delta f_{TR}$ =[$f_0 - \Delta f_{TR}$ /2, $f_0 + \Delta f_{TR}$ /2] corresponding to [0, h1+h2]. This is due to the fact that, if h<0, the tuner sensitivity decays exponentially. In particular, this implies that $f_0$ is higher than the average cut-off frequency for the $TE_{210}$ mode of the RFQ $f_{q0}$ of an amount equal to $\Delta f_{TR}$/2.

An unwanted but unavoidable effect of tuners is the increase in power consumption. An estimation of such effect can be done by considering the case of maximum h1+h2 and calculating the dissipated power on the tuners $\Delta P$ (with a factor 2 safety margin). This extra power has to be considered when dimensioning the RF system, too. Table 3 lists a comparison for the tuning ranges of the RFQs developed at LNL.

Table 3: Tuning Ranges for the RFQs

|  | TRASCO | IFMIF | SPES |
|---|---|---|---|
| NT | 96 | 88 | 96 |
| a [mm] | 24.5 | 44.5 | 44.5 |
| ΔR0 range[mm] | ±0.05 | ±0.1 | ±0.2 |
| Δf range[MHz] | ±1 | ±1 | ±0.5 |
| h1+h2 range[mm] | [-10, 10] | [-15, 30] | [0,80] |
| ΔP/P0 [%] | 4 | 7 | 8 |

## PERTURBATION SYNTHESIS AND TUNING ALGORITHM

The basic idea of perturbation synthesis is that the capacitance (or inductance) perturbative terms can be spanned in series of the quadrupole and dipole eigenfunctions $\varphi_{qm}$ and $\varphi_{dm}$ Therefore, coefficients $b_{qm}$, $b_{d1m,d2m}$ exist such that:

$$\delta C_{QQ} = \sum_{m=1}^{NQ} b_{qm}\varphi_{qm}, \quad \delta C_{Qd1,Qd2} = \sum_{m=0}^{Nd1,Nd2} b_{d1m,d2m}\varphi_{dm}$$

where NQ, Nd1 and Nd2 are the number of harmonics used. Now, provided that the measured perturbed components $\Delta U_q$, $U_{qd1}$ and $U_{qd2}$ can be spanned in series of RFQ eigenfunctions as follows,

$$a_{qn} = \int_0^1 \Delta U_q \varphi_{qn} dz \ n \in N, \ a_{d1n,d2n} = \int_0^1 U_{qd1,qd2}\varphi_{dn} dz \ n \in N_0$$

The substitution of the above expression in the perturbative voltage development leads to the following matrix equations, from which the unknown coefficient $b_{qm}$, $b_{d1m,d2m}$ can be obtained

$$\mathbf{C}^{(q)}\mathbf{b}_q = \mathbf{a}_q, \ \mathbf{C}^{(d)}\mathbf{b}_{d1} = \mathbf{a}_{d1}, \ \mathbf{C}^{(d)}\mathbf{b}_{d2} = \mathbf{a}_{d2}$$

The $N_T x4$ matrix **$\underline{\delta h}$** of tuner heights can be transformed into the modal function basis, thus obtaining the three vectors of $N_T$ elements $\delta h_Q$, $\delta h_{d1}$, $\delta h_{d2}$ Such vectors can be multiplied by appropriate gain parameters $g_Q$, $g_{d1}$ and $g_{d2}$, in order to speed up the tuning convergence process. For example, let us consider the case of the SPES RFQ with two electrodes displaced of 0.2 mm, $R_0$=5.8 mm, $\chi_{R0}$=3.5 MHz/mm. This leads to a frequency shift of 150 kHz and Q [D] perturbations on nominal voltage of ±10% [±20%]. With the usage of 24 regularly spaced tuners per quadrant ($\Delta z_T$=l/24), the tuning algorithm is implemented with $g_Q$=$g_{d1}$=$g_{d2}$ 3.5, $N_q$=$N_d$=2. In this case, the tuner depth profiles which reduce all perturbative components within ±2% are shown in Figure 3. The tuning range is able to compensate the effect of such perturbation, but, at the same time, it saturates for z<2m. This is an indication of the relationship between the $\delta R_0$ and h1+h2 ranges.
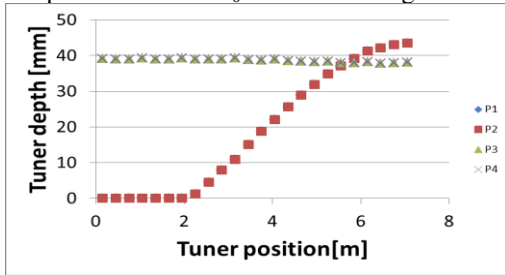


Figure 4: Tuner depths vs position for SPES RFQ (test case).

Due to the discreteness of tuner positions, the tuning procedure scheme is iterative and some iterations are needed in order to converge up to the attainment of the specifications. The tuner spacing should be kept as uniform as possible although, in principle, tuner periodicity is broken by the presence of vacuum ports,

couplers etc. In fact, if the same exercise of Figure 4 is repeated for a set of tuners spaced in six groups of four tuners with $\Delta z_T$=l/48, and with a tuner free zone of 5l/48 between each set, the Q component lies within ±4% with the same tuner height range.

An interesting spin-off of this analysis consists in the identification of the water variation temperature to be applied to the RFQ vessel in case of a detuning during high power operations. The RFQ frequency is controlled by varying the temperature difference between vanes and vessel $T$-$T_v$. Now, if one of the two temperatures (i.e. vane) is kept constant and N independent cooling circuits are foreseen for the vessel, each l/N long subdivision of the RFQ can act as a tuner. The case of IFMIF RFQ, with N=3 (3 supermodules) $T_v$=15ºC, $\partial f/\partial(T$-$T_v$)=16kHz/°C, T=22°C is an example. Let us suppose that some detuning occurs due to thermal-induced deformation at RFQ extremities ($\Delta R_0$=0.1 mm to 0 mm in the first and last 20 cm of the cavity): such effects were observed for instance in the High Power Testing of TRASCO RFQ . In Figure 5 it is possible to see the comparison between untuned and tuned voltage: the temperature variations needed to tune the voltage were +0.9ºC in Supermodules 1 and 3 and -1.8C in Supermodule 2.
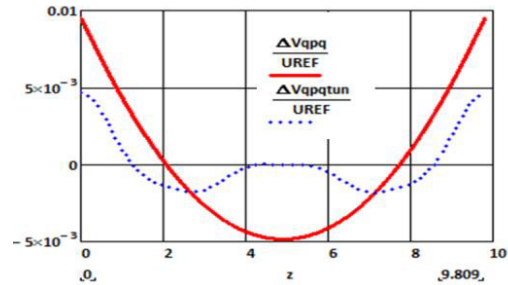


Figure 5: Estimation of Voltage tuning with water temperature variation: untuned [tuned] $\delta U_q/U_{q0}$ (solid curve) [(dotted curve)].

## EXPERIMENTAL RESULTS

The methods described in this paper were experimentally tested on the TRASCO and IFMIF RFQs. In particular, the following set-ups were measured: 1) The first 2.36 m module of the TRASCO RFQ, used for high power testing [2], 2) the 9.9 m full-scale aluminium model of the IFMIF RFQ [11,12], and 3) the 2m IFMIF RFQ (3 modules (16th ,17th and 18th ) out of 18 + 1 39 cm RF plug) to be used for the High Power tests. The functions $U_i(z)$ were measured with the Bead Pulling technique, with dielectric bead in case 1), magnetic bead in case 3) and both in case 2). If a metal bead is used, the presence of the tuners strongly affects the phase acquisition. Therefore, the raw phase data need to be properly interpolated in order to get rid of the tuner-induced bumps. The available tunable dummy devices are: a) Tunable end-cell: the proper boundary condition is obtained by varying the end-plate thickness, b) Tunable DSRs (case 1 only): the attainment of the dipole-free

region is obtained by varying the length of the rods at both RFQ ends (Figure 6), c) Dummy aluminium tuners.

The initial step in the tuning consists of experimentally determining the optimum thickness of the End Cell and DSR lengths. The tuning algorithm is then applied to the dummy tuners. Finally, the coupling dummy loop(s) is included in order to verify its effects on the voltage uniformity and final end plates are mounted: copper tuners are machined to length and replaced in batches (4 batches in case 1, and 3 batches in case 3), in order to perform minor correction to the tuner heights if needed (Figure 7).
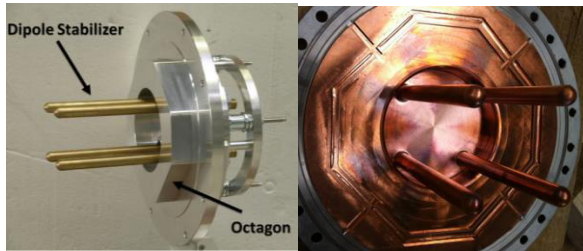


Figure 6: Tunable (left) and final (right) end cell equipped with DSRs used for the TRASCO RFQ High Power Tests. The inserted thickness of the end plate (octagon) is visible.



Figure 7: Dummy (left) and copper tuners brazed and to be machined to length (right) for the IFMIF RFQ.

The results of tuning procedure are summarized in Table 4. In particular, it should be considered that the tuning results in the $3^{rd}$ column do not include the RF plug.

Table 4: Summary of Tuning Procedures

|  | **TRASCO** | **IFMIF Al model** | **IFMIF High Power test** |
|---|---|---|---|
| Tuner heights | [-4.8,11.5] | [11.2, 18.2] | [-14.7, 12.2] |
| $\delta Uq/U_0$ [%] untuned (tuned) | +12/-15 ($\pm 1$) | -21/+22 ($\pm 2$) | -8/+3 (-0.5,+1.0) |
| $U_{qd1}/U_0$ [%] untuned (tuned) | -10/+4 ($\pm 1$) | $\pm 3$ ($\pm 2$) | -0.3/+0.9 (0, 0.8) |
| $U_{qd2}/U_0$ [%] untuned (tuned) | -7/+17 (-1/+2) | -1/+3 ($\pm 2$) | 0.3/0.9 (0.2/0.8) |

Here, "untuned" means that all the tuners were set at half of their range. In the case of IFMIF Al model, the fact that the tuners are not regularly spaced provokes the large perturbation for the Q mode. Fig. 8 shows the comparison between measured voltage $\Delta Uq/U_0$ (red curve) and the same quantity obtained with perturbative analysis (blue curve), in the untuned case for the IFMIF RFQ Aluminium model.
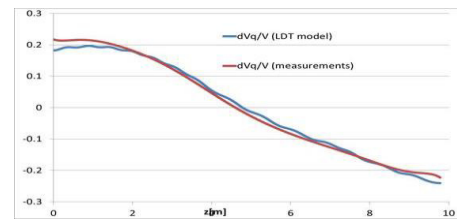


Figure 8: $\delta Uq/U_0$: measured data (red curve) vs Perturbation Analysis forecasts (blue curve).

Finally, Figure 9 shows the final tuning results for the TRASCO and IFMIF High Power Test RFQs.
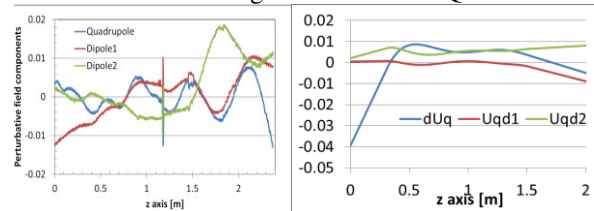


Figure 9: $\delta Uq/U_0$ obtained for TRASCO (left) and IFMIF (right) RFQs.

## CONCLUSIONS AND PERSPECTIVES

The analysis proved useful in the design phase of the RFQ. The identification of the needed tuning margins and experimental results confirmed the adopted approach. The next steps include the tuning of the final structures considered in this paper and the analysis on the effects of "real" RFQ voltage profile on beam dynamics parameters.

## ACKNOWLEDGMENTS

## REFERENCES

[1] M. Comunian, A. Pisent, IPAC 2011 p.670
[2] E. Fagotti et al, LINAC 2012, p.828
[3] M. Comunian et al. LINAC 2012, p. 951
[4] L. Young, LINAC 90, p.530
[5] L. Young et al., LINAC 98 p.270
[6] E. Fagotti et al., LINAC 2008
[7] O. Piquet et al., IPAC 2014
[8] F. Grespan et al., Nuclear Instruments and Methods in Physics Research A 582 (2007) 303–317
[9] A. Palmieri et al, IPAC 2010 p. 606.
[10] A. France, IPAC 2014 p. 34
[11] A. Palmieri et al, IPAC 2010 p. 609.
[12] A. Palmieri et al, LNL Annual Report 2012

# H- BEAM OPTICS FOR THE LASER STRIPPING PROJECT

T. Gorlov, A. Aleksandrov, S. Cousineau, V. Danilov, M. Plum, ORNL, Oak Ridge, TN, USA

## Abstract

Successful realization of the laser stripping experiment depends on the correct tailoring of the H- bunch and the laser beam. H- beam preparation is a challenging task, with the requirement to tune up about 10 parameters simultaneously in situ, taking into account the live state of the accelerator. This makes a huge technological difference compared to the foil stripping method. In this paper, we present our experience and our methods of tuning the H- beam.

## INTRODUCTION

We prepared an experiment to demonstrate laser assisted stripping of a 10 microsecond H- beam at the Spallation Neutron Source (SNS) accelerator. The general up-to-date information about the status of the project can be found in [1, 2]. More information about the history and background can be found in [3, 4]. The new experiment expects to achieve more than 90% stripping efficiency. This requires an experimental station including routine hardware, magnets [5], and beam instrumentation. The most important scientific aspect for successful realization of the experiment is the tuning of the laser beam and the H- beam at the interaction point. The recent work about the laser system can be found in [6]. In this present paper, we present a theory and experimental methods of tuning the H- beam.

The first big challenge of beam tuning is that all of the H- beam parameters, such as Twiss parameters and the dispersion functions, must be tuned simultaneously for high efficiency stripping. Laser tuning is a large, separate work and is based on the H- beam parameters. This factor makes the method of laser stripping injection much more difficult compared to the foil stripping injection. Another particular difficulty is that the SNS accelerator has not been developed for this sort of experiment, and beam tuning and manipulation is limited and not optimized. The location of the experiment has been chosen taking into account maximum beam flexibility at the interaction point (Figure 1).
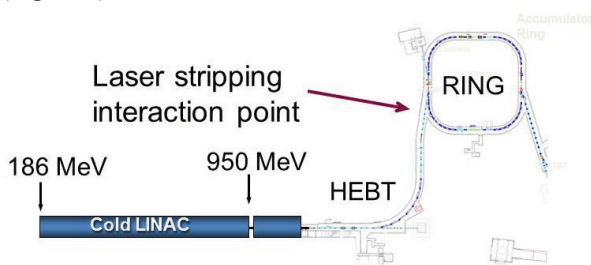


Figure 1. Location of the laser stripping experiment at SNS.

In this paper we will discuss various methods of H- beam parameter tuning for the laser stripping experiment.

## INTERACTION BETWEEN H⁰ AND LASER BEAM

After $H^- \rightarrow H^0 + e^-$ stripping by the first stripping magnet, the $H^0$ bunch interacts with the laser beam at the interaction point (Figure 2), which provides excitation of
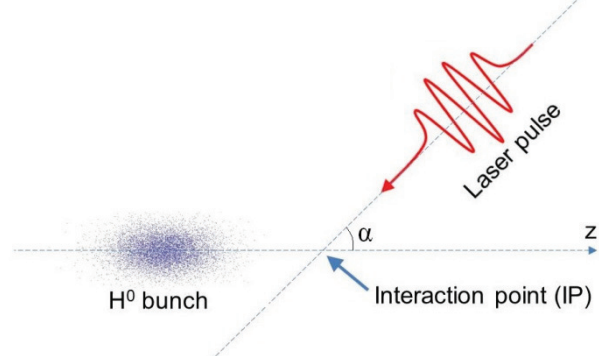


Figure 2. Interaction of $H^0$ beam with the laser beam.

$H^0$ from the first ground state to the third excited state. The beam energy is supposed to be 1 GeV in the experiment and incidence angle $\alpha$ between laser and $H^0$ beam, which can be calculated from Equation (1) [3]:

$$\lambda_0 = \frac{\lambda}{\gamma(1 + \beta \cos \alpha)} \tag{1}$$

where $\gamma$ and $\beta$ are relativistic factors of a bunch. This formula gives most optimal resonant conditions for $H^0$ beam excitation. This formula gives $\alpha = 39.33^0$ for $T_{H0} = 1$ GeV. The theory of laser stripping excitation [3] shows that each particle of the $H^0$ beam should interact with the laser beam in a proper way (it must have proper energy, angle, and position). In this way, Twiss parameters of the $H^0$ bunch must be properly tuned for high efficiency excitation.

## TRANSVERSE BEAM OPTICS

Transverse beam parameters can be defined at least by three vertical $\{\alpha_y, \beta_y, \varepsilon_y\}$, and three horizontal $\{\alpha_x, \beta_x, \varepsilon_x\}$ Twiss parameters plus dispersion and its derivative. The laser stripping location point (see Figure 1) has a large number of "knobs" to control these parameters.

### Transverse Emittances

Equation (1) can be considered as a perfect resonant condition for particle excitation, although the whole bunch has some angular spread depending on emittances $\varepsilon_x$, $\varepsilon_y$. The default non-normalized emittances during SNS production is about 0.3 $\pi$ mm × mrad for the vertical and the horizontal plane. This number can be reduced to 0.1 $\pi$ mm × mrad and smaller with the help of LINAC apertures. In addition to the angular spread, small

transverse emittances allow the achievement of a small transverse size that improves the overlap between the small laser beam and the $H^0$ beam.

### Tuning of Transverse Twiss Parameters

The SNS accelerator has a large number of quadrupoles to manipulate the beam at the interaction point. There is a big question that has been studied empirically: what should be the optimal number of quadruples upstream of the interaction point? On one hand, a small number of quadrupoles gives limited flexibility to manipulate the beam. On the other hand, a large number of quadrupoles provide better flexibility to control beam parameters but involve a very long part of the accelerator and make it difficult to provide a good agreement with a model. After some empirical study, we decided to take last 7 upstream quadrupoles Quad20–Quad26 for tuning the transverse beam parameters. The method follows these three stages:

1) We measure more than three vertical and horizontal beam profiles to determine Twiss parameters at the beginning of Quad20.
2) We run an application that optimizes Twiss parameters at the interaction point and generates a number of Quad20–Quad26 solutions (Figure 3).
3) We select the most optimal solution with the best combination of $H^0$ bunch parameters.

The application defines goals parameters at the interaction point and gives multiple solutions for this interaction point. Then we set up quadrupoles for the selected solution from the table. Different Twiss parameters have a different role at the interaction point.

### Vertical and Horizontal Size

As a rule, the laser beam has a small transverse size and a large power density. For this reason, the vertical size of

the $H^0$ beam should be small enough to provide good overlap with the laser beam. Solutions in Figure 3 show that we can tune the beam with vertical root-mean-square (rms) size < 0.1 mm. Figure 4 shows that the predicted vertical size agrees with the measurement.
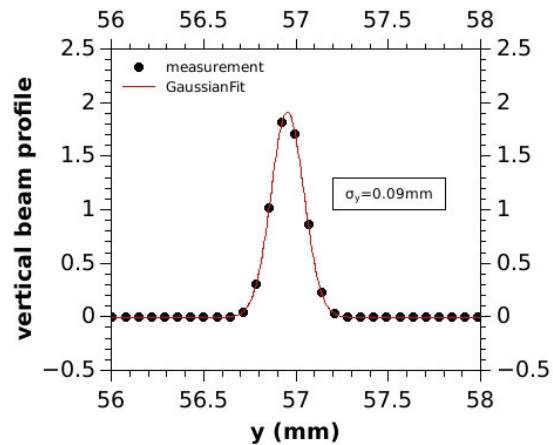


Figure 4. Example of vertical beam profile measured with the wire scanner for one of beam tuning.

The final vertical size is an important parameter to know prior to the experiment because it defines the laser beam size to be adjusted. The horizontal size is not as important as the vertical size because the laser shoots in a horizontal plane. However, the horizontal transverse size is still important and should be smaller than about 2 mm. The horizontal beam size also correlates with the horizontal angular spread, which is much more important (see the "Horizontal angular spread" section below).
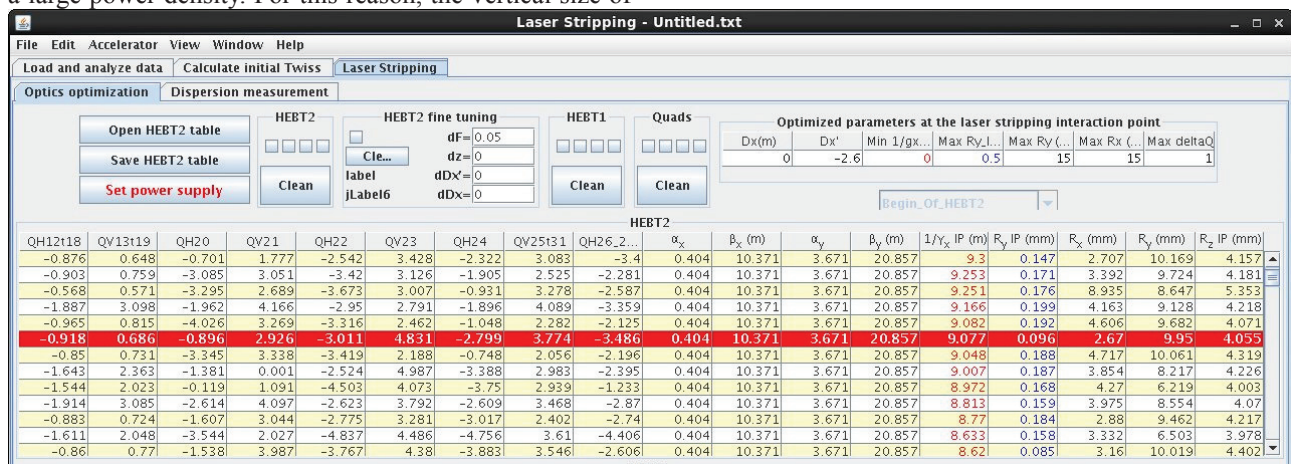


Figure 3. Screenshort of the application with an example of generated solutions for laser stripping.

### Maximum Beam Size

The "$R_x$" and "$R_y$" columns in Figure 3 show the maximum transverse beam size along the Quad20–Quad26 that should be small enough (less than 10 mm) to prevent beam losses in a vacuum chamber.

### Horizontal Angular Spread

The horizontal angular beam spread is considered to be one of the main impacts for resonant excitation (1) and it should be as small as possible for more excitation efficiency. In a simple model, the rms angular spread is proportional to Twiss parameter $\gamma^{1/2}$ where $\gamma = (1 + \alpha^2)/\beta$.

In this way $1/\gamma$ should be as big as possible (see the corresponding column in Figure 3). A bigger value of $1/\gamma$ leads to a bigger horizontal beam size and produces a worse result. The empirical study shows that the optimal value should be about 10.

### Horizontal Dispersion Function

Bending magnets of SNS accelerator (see Figure 1) give extra flexibility to manipulate the horizontal dispersion function at the interaction point, which would be zero in pure LINAC configuration. Horizontal beam size depends on $D_x$ function that must be zero at the interaction point to keep the horizontal size smaller.

### Horizontal Dispersion Derivative Function

This is probably the most interesting parameter from the point of view of laser stripping theory. Equation (1) gives the perfect resonant condition incidence angle-energy relation for the $H^0$ particle. The laser cannot be adjusted perfectly for all beam particles because of its angular-energy spread, but the resonant condition can be significantly improved by introducing correlation according to (1) between angle-energy for particles in the bunch. The parameter of dispersion derivative $D_x'$ is responsible for the correlation and it can be adjusted due to the SNS dipole bending magnets. Optimal $D_x'$ can be calculated from the following equation:

$$D_x' = \frac{\dfrac{\lambda}{\lambda_0} - \dfrac{m}{m+T}}{\sqrt{2\dfrac{\lambda}{\lambda_0}\dfrac{T}{m} - \left(\dfrac{\lambda}{\lambda_0} - 1\right)^2}} . \qquad (2)$$

$D_x' = 2.6$ for $T = 1$ GeV $H^0$ beam energy, $\lambda_0 = 102.5$ nm, $\lambda = 355$ nm, $m_{H0} = 0.938$ GeV (mass of $H^0$). $D_x$ is defined as $-\Delta x/(\Delta p_z/p_z)$. The sign of $D_x'$ is important and depends on the frame and the laser beam direction. It should be $-2.6$ in our definitions.
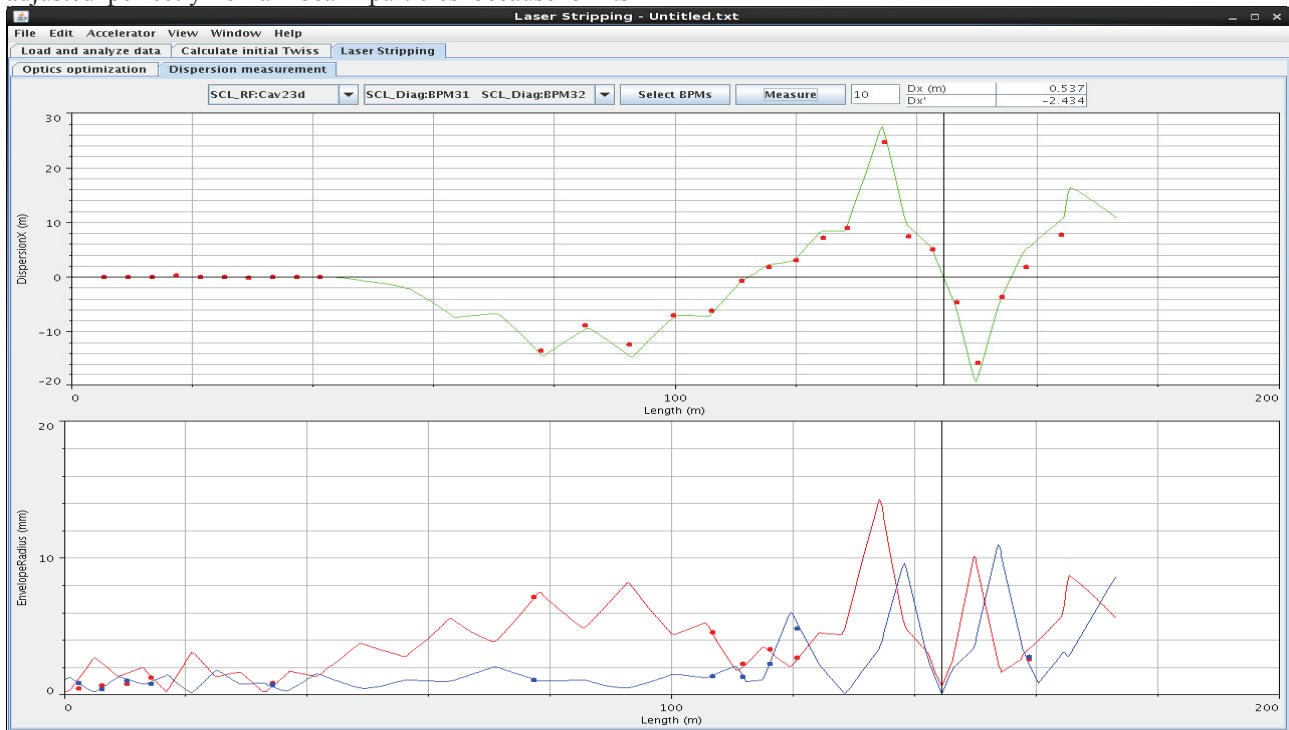


Figure 5. Laser stripping experimental tuning of transverse parameters for laser stripping.

### Experimental Tuning of Transverse Beam Parameters

Figure 5 presents an example of tuning transverse parameters for laser stripping at the interaction point. The lower picture presents the vertical and horizontal size of the beam (solid lines for a model and a point for experimental measurements with the help of a wire scanner). The upper plot shows the dispersion function. It can be seen that the model agrees with the experimental measurements—at least at the vicinity of the interaction point—five wirescanners to the left and one wirescanner from the right. The laser stripping parameters at the interaction point can be measured after wire scanner installation for the experiment.

### Fine Tuning of Transverse Beam Parameters

The parameters, $r_x$, $r_y$, $D_x$, $D_x'$, measured at the interaction point, can be different from the model; for example, $D_x = 0.5$ m instead of 0.0 m and $D_x' = -2.43$ instead of $-2.6$ (see Figure 5). The application (Figure 3) has an option for a small correction of the parameters. After a satisfied solution has been chosen and the parameters at the interaction point have been measured, this function changes the parameters for a small value without changing other ones. In this way, there is a chance to correct the parameters for better efficiency.

## LONGITUDINAL BEAM OPTICS

The laser beam has micropulse duration of 55 ps FWHM [6]. In this way, it is obvious that the $H^0$ micropulse should be comparable to the laser pulse for good overlap. Calculations [7] show that the longitudinal rms size of the $H^0$ should be 3 degrees (25ps FWHM) or smaller in terms of 805 MHz frequency. Measurements of the default beam at the interaction point gives 10–20 degrees (see Figure 6).
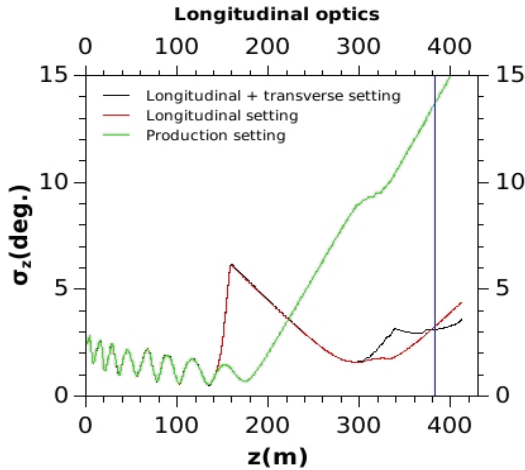


Figure 6. Longitudinal beam size for different cavity settings.

Previous work [7] presents a detailed theoretical and experimental study of the bunch shortening. In this paper, Figure 6 shows that a shortened bunch between 300 m and 380 m has an extraordinary significant jump in bending magnets when the quadrupoles are adjusted for transverse laser stripping tuning. The last column of the table in Figure 3 presents the approximate longitudinal beam size, which is important when selecting the optimal solution for laser stripping. Calculations show that it's acceptable to have solution with 4 degrees maximum longitudinal size. Figure 7 presents the space charge effect on the longitudinal beam size.
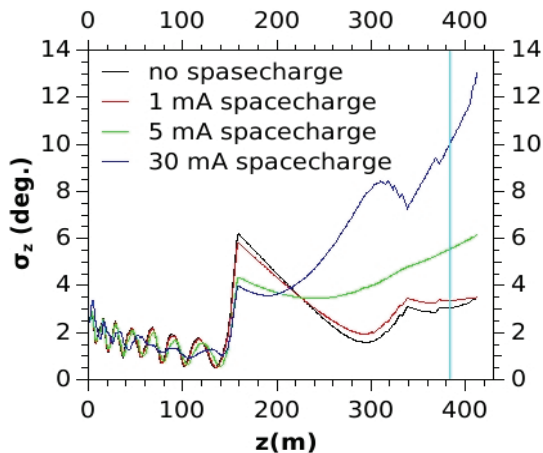


Figure 7. Space charge effect.

The average current of $H^-$ minipulse should not exceed 1 mA for the laser stripping experiment.

## LASER STRIPPING EFFICIENCY

The laser stripping efficiency calculation must be based upon bunch parameters achieved in an experiment. At this time, independent transverse and longitudinal beam parameters have been achieved separately and can be used to generate a realistic beam for an efficiency estimate. We do it in the following way: The laser stripping application in Figure 3 has been developed for online beam tuning. It is based on a linear envelope model and is written for a fast solution of the bunch optimization.

1) We take parameters of quadrupole fields and input emittance and insert them into the PyOrbit [8] accelerator program together with the longitudinal bunch shortening cavity configuration.
2) After tracking the particle beam, we obtain the $H^0$ particle bunch at the laser stripping interaction point.
3) We use the $H^0$ bunch for the laser stripping application also written in the PyOrbit code to calculate laser stripping efficiency.

We used 10,000 particles for $H^0$ bunch simulations. The example of longitudinal phase space distribution is shown in Figure 8.
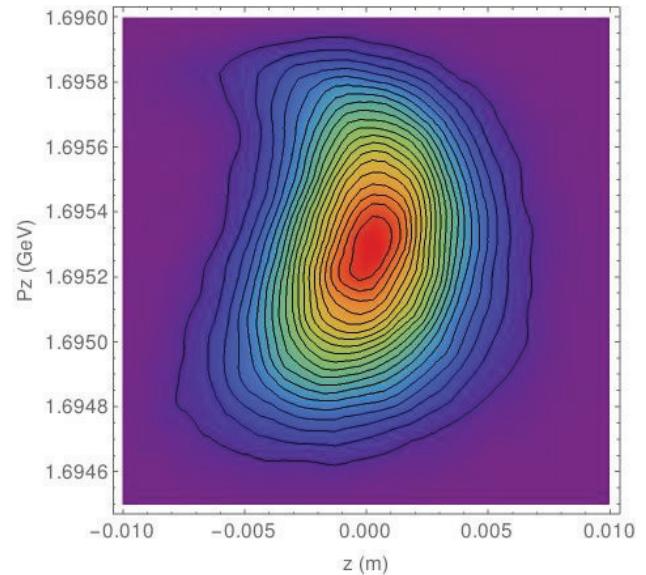


Figure 8. Longitudinal phase space of $H^0$ bunch at the interaction point generated by the PyOrbit code.

Figure 8 clearly demonstrates non-Gaussian behavior of the bunch. We used the round Gaussian laser beam for simulations (Figure 9).
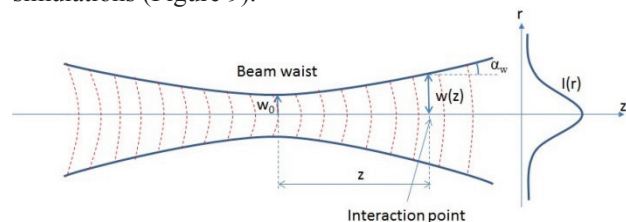


Figure 9. The round Gaussian laser beam for laser stripping simulations.

The laser beam is defined by fixed parameters of Peak power = 0.8 MW, and longitudinal pulse width FWHM = 55 ps. The variable laser beam parameters at the excitation point w and $\alpha_w$ = dw/dz is replaced by the beam radius of power density r = 0.5 w and the radius slope $\alpha_r$ = 0.5 $\alpha_w$. Figure 10 presents laser stripping efficiency as a function of r and $\alpha_r$.
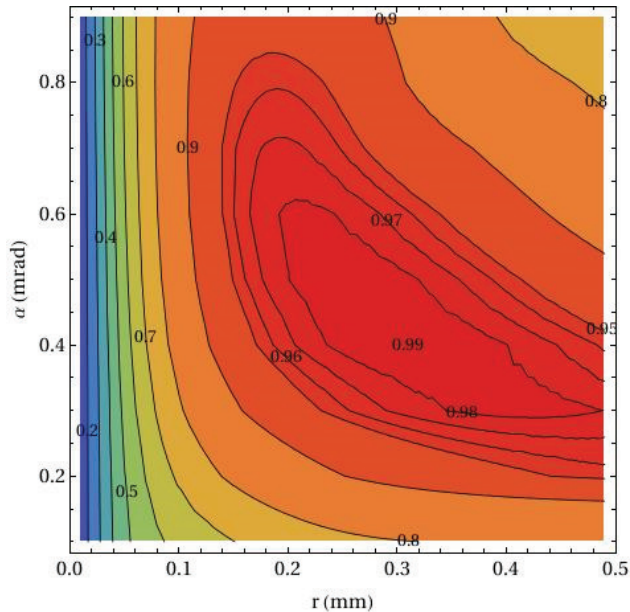


Figure 10. Laser stripping efficiency as a function of the variable laser beam parameters of the radius and its divergence.

The peak of this plot has a single point with 99% of excitation efficiency for r ≈ 0.3mm and $\alpha_r$ ≈ 0.4 mrad. This picture is important for the design of a laser system because tuning a laser beam optics is not as flexible as an H⁻ beam optics and must be known in advance. It should be noted that this is just up-to-date study of laser stripping efficiency; final calculations can be done only after diagnostics are installed at the interaction point and after the final beam tuning is done for 1 GeV beam.

Figure 9 schematically represents interaction point z and beam divergence α with a positive sign while the real experimental interaction point will have a negative sign and convergence for technical simplicity. Figure 10 has symmetry relatively to beam divergence α.

## SUMMARY

- Transverse and longitudinal tuning of the H⁻ beam has been studied separately and satisfactory beam parameters have been achieved.
- As a next step, it would be good to make simultaneous experimental tuning of transverse and longitudinal beam parameters.
- A lot of empirical methods and parameter tuning have been learned during the study of H⁰ beam optics in spite of the existing straightforward models of beam dynamics.
- An application for online laser stripping H⁻ beam tuning has been developed. Real beam tuning functions, such as a beam correction, have been implemented into the application.
- Calculations show that a bunch with the achieved longitudinal and transverse parameters would give 99% laser stripping efficiency.

## ACKNOWLEDGMENT

## REFERENCES

[1] S. Cousineau et al., "Status of preparation for a 10 microsecond laser-assisted H⁻ beam stripping experiment", IPAC14, Dresden, Germany (2014).
[2] S. Cousineau et al., "Status of Preparation for a 10 us H⁻ laser Assisted Stripping Experiment", HB2014, East Lansing, Michigan, USA.
[3] V. Danilov et al., PRSTAB, 6, 053501(2003).
[4] V. Danilov et al., PRSTAB 10, 053501 (2007).
[5] A. Aleksandrov and A. Menshov, "Magnet Design for SNS Laser Stripping Experiment", IPAC14, Dresden, Germany (2014).
[6] Y. Liu et al.,"Laser System for the SNS Laser Stripping Experiment," IPAC14, Dresden, Germany. (2014).
[7] T. Gorlov et al., "Longitudinal bunch shortening for the laser stripping project", IPAC14, Dresden, Germany (2014).
[8] http://code.google.com/p/py-orbit/

# BEAM DYNAMICS AND EXPERIMENT OF CPHS LINAC *

L. Du[#], C.T. Du, X.L. Guan, C.X. Tang, R. Tang, X.W. Wang, Q.Z. Xing, S.X. Zheng, Key
Laboratory of Particle & Radiation Imaging (Tsinghua University), Ministry of Education, Beijing
100084, China
M.W. Wang, Northwest Institue of Nuclear Technology, Xian, China

## Abstract

We present, in this paper, the present beam dynamics simulation results and experiments of the 3 MeV high current proton linac for the Compact Pulsed Hadron Source (CPHS) at Tsinghua University. The beam dynamics simulations of the recent status of the linac have been done, which helps the operation. Facility used for 2D beam profile measurement which is based on the CT algorithm with rotatable multi-wires, is under development. Some other experiments such as beam position measurement will also be introduced below.

## INTRODUCTION

The Compact Pulsed Hadron Source (CPHS) project at Tsinghua University was launched in the year of 2009 [1], whose layout is shown in Figure 1. The final expected parameters of the CPHS linac are: beam energy to be 13 MeV, beam current to 50 mA, repetition rate to be 50 Hz and pulse length to be 500 μs.
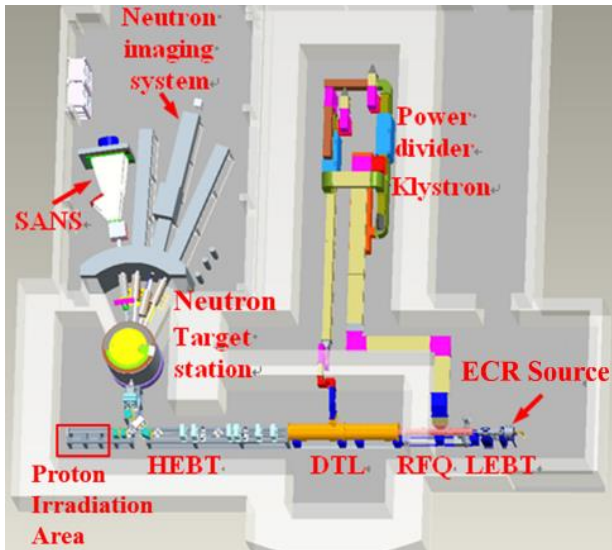


Figure 1: Layout of CPHS project.

So far, CPHS has achieved its mid-term objective: delivering the 3 MeV proton beam to bombard the Beryllium target [2]. Figure 2 shows the status of CPHS linac facility at Tsinghua University recently, which contains one ECR Ion Source (IS), one Low Energy Beam Transport line (LEBT), one 4-vane Radio Frequency Quadrupole (RFQ) accelerator, and one High Energy Beam Transport line (HEBT) [3].
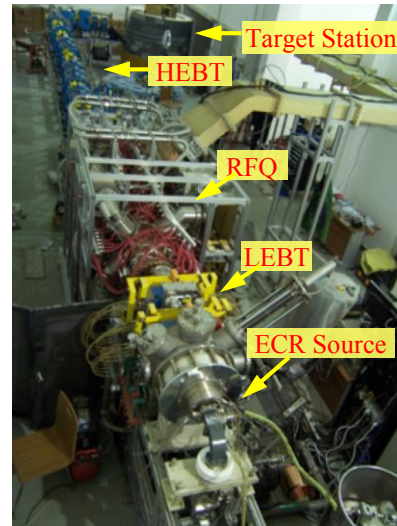
Figure 2: CPHS linac facility and the target station.

Figure 3 shows the operation status of the CPHS linac in 2014. The transmission rate of the RFQ is 70% recently, which is lower than the designed value of 97% and primary experimental value of 88% (with input peak current of 50mA at 50 μs /50 Hz). The reason may come from the unmatched beam from the LEBT, or the deformation of the RFQ cavity. Therefore, the linac will be inspected separately to solve the problem in the next stage.
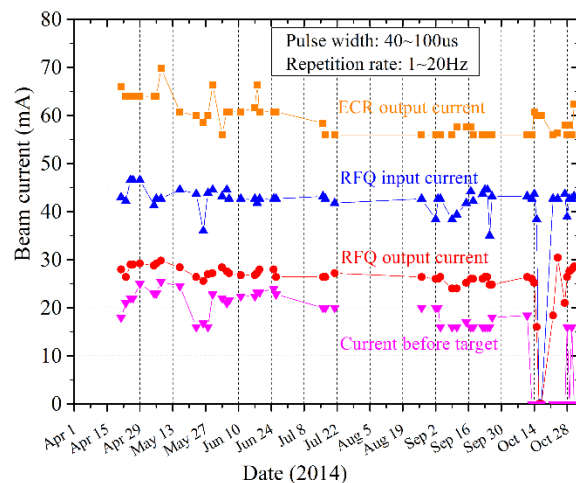


Figure 3: Operation history of the 3 MeV linac in 2014.

In this paper, the beam dynamics simulation results of the recent status of the CPHS linac are presented. Experiments such as beam profile measurement and beam position measurement are introduced.

## BEAM DYNAMICS SIMULATION

The beam dynamics simulation mainly focus on the Low Energy Beam Transport line and 4-vane Radio Frequency Quadrupole accelerator, which are the main part of the CPHS linac. The simulation of the LEBT is taken by Trace3D [4], TRACK [5] and TraceWin [6], and the field of the solenoid is calculated by Possion/ Superfish [7], as shown in Figure 4 [8]. The distribution at the end of the LEBT is imported directly to the RFQ entrance, then the beam dynamics simulation is accomplished by Toutatis/ TraceWin [9].
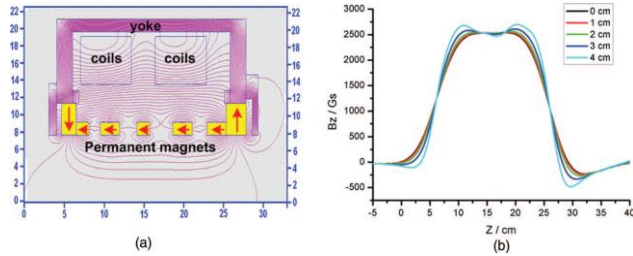


Figure 4: Solenoid and its field distribution in CPHS LEBT.

The beam information calculated by TraceWin at the LEBT entrance, RFQ entrance and RFQ end is shown respectively in Figure 5~Figure 7. These results show a nice beam in the RFQ. Figure 8 presents the beam envelop in the structures.



Figure 6: Beam information at the RFQ entrance.
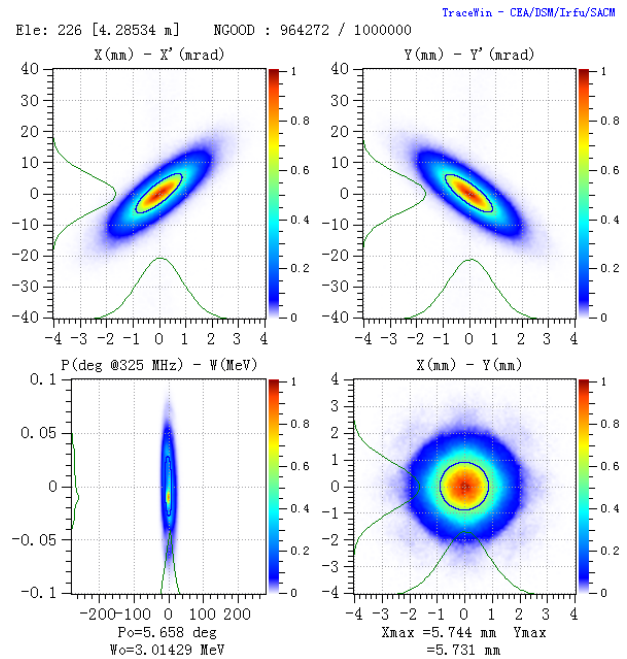


Figure 7: Beam information at the RFQ end.



Figure 5: Beam information at the LEBT entrance.
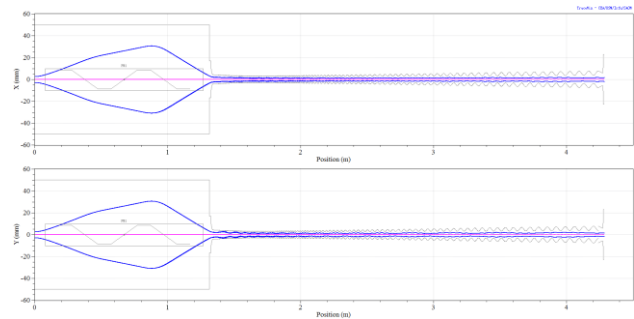


Figure 8: Beam envelop in the LEBT and RFQ.

## BEAM PROFILE MEASUREMENT

2D beam profile measurement is under development based on the Computed Tomography (CT) algorithm with rotatable multi-wires. Twenty carbon wires with the diameter of 30 μm are aligned and mounted on one stainless steel frame, as shown in Figure 9 and Figure 10.

The current signal is obtained from the Secondary Electron Emission [10] and then amplified by a set of electronics system. Then Total Variation Algebraic Reconstruction Techniques (TV-ART) CT Algorithm is used to rebuild the image of the beam profile.
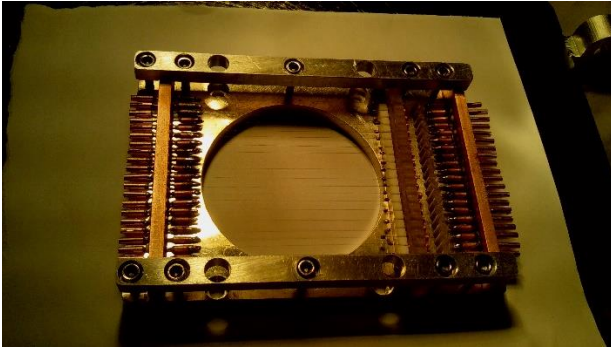


Figure 9: Rotatable multi-wires.



Figure 10: 2D beam profile measurement system.

The primary experiment shows that wire current near the beam centre is 0.3 mA (while the estimated value is 0.4 mA). The beam is unstable day by day at the measurement position. Figure 11 shows one of the 1D distribution measured by the wires, in which the "halo" can be seen clearly.
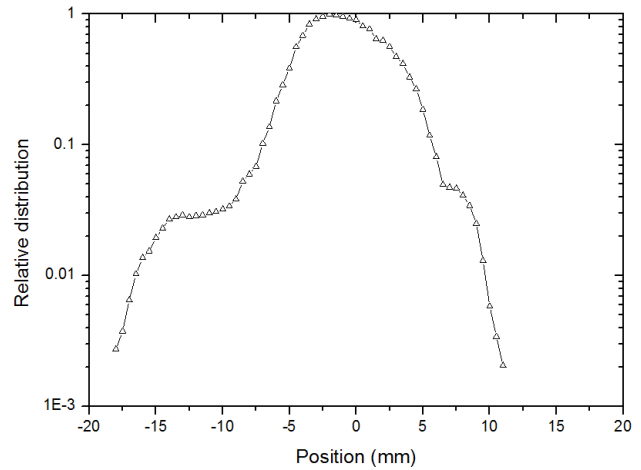


Figure 11: 1D distribution measured by the wires.

Figure 12 shows the rebuilding result with data of five directions. Streak artifacts can be seen in the image. When the angular sampling increase to 17, the image become quite well, as shown in Figure 13. To avoid the thermal emission of the wire, the pulse width is decreased to 40 μs while the beam profile measurement.
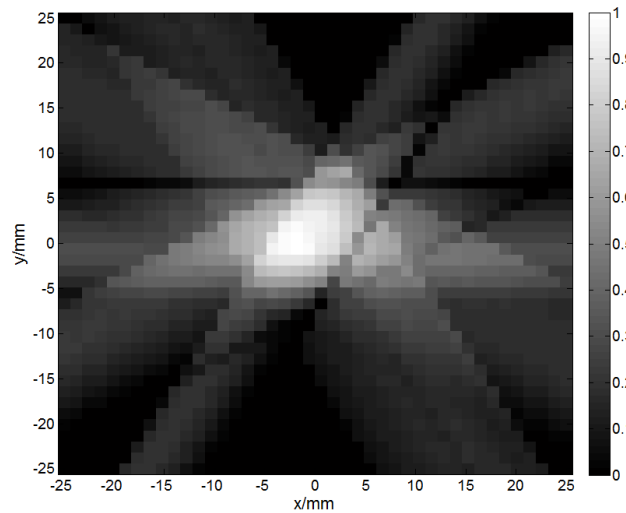


Figure 12: Rebuilding image of five directions.
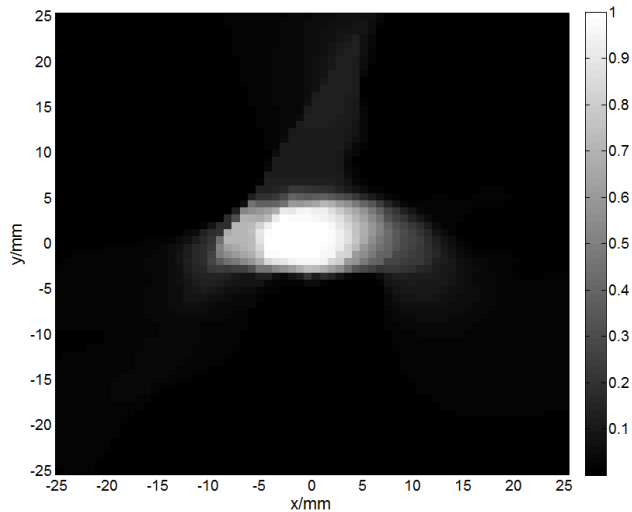
Figure 13: Rebuilding image of 17 directions.

The following challenging work on the electronics system is to measure the current which is less than 1 nA near the beam edge.

## BEAM POSITION MEASUREMENT

The CPHS beam position measurement system is formed by several button-type BPMs and a hadron phase & position processor- Libera Single Pass H.

The button-type BPM, which have one button in each of the four directions, is showed in Figure 14 and Figure 15.
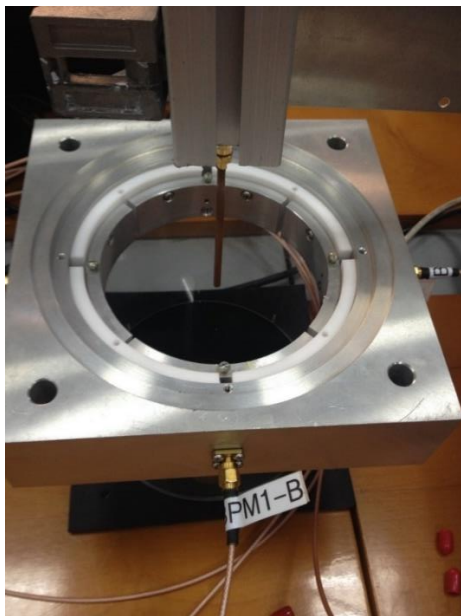


Figure 14: The button-type BPM in test.



Figure 15: The button-type BPM on the beam line.

The output signals from the four ports of the BPMs are imported into Libera through a 20 dB amplifier. IQ sample signals can be obtained by using the method of undersampling and digital orthorhombic demodulation. These signals are used to calculate the amplitude and phase. The value of the particle energy can be obtained from the phase information of two BPMs. Figure 16 and Figure 17 respectively show the transverse position signal and the longitudinal phase signal displayed in Libera, from which we can conclude that the beam center is 2 mm above the beam channel and 2 mm on the right of the beam channel.
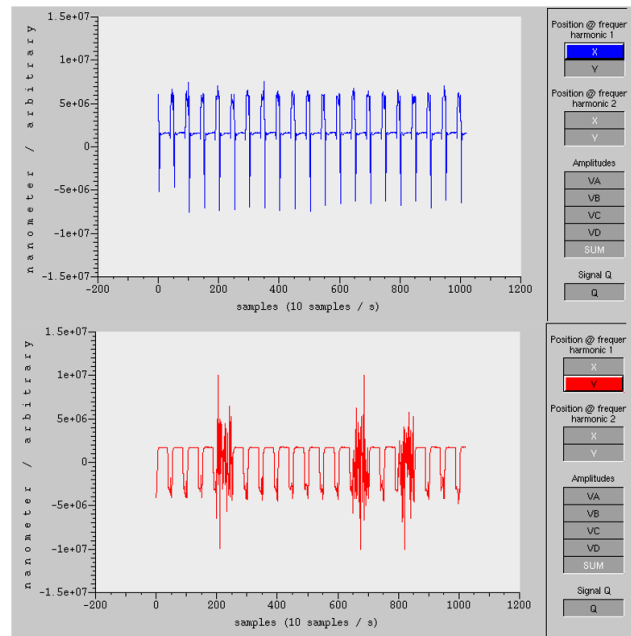


Figure 16: The transverse position signal displayed in Libera.
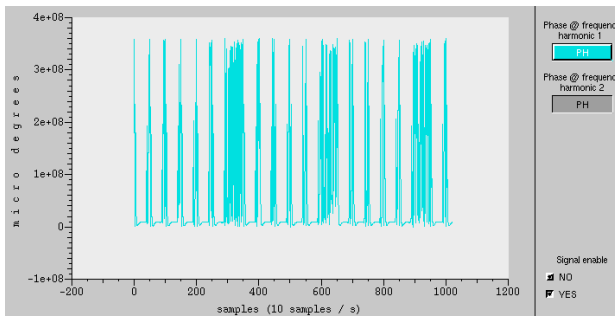
Figure 17: The longitudinal phase signal displayed in Libera.

At present, the measurement resolution of transverse position is 180 μm and the measurement resolution of phase is 0.6 degree.

## CONCLUSION

The operation notes and beam dynamic results show that there are some problems to be solved. The experiments on the linac are proceeding quite well. The next stage of CPHS linac is the transformation of the low-energy part including Ion source, LEBT and RFQ and the upgrade of the whole linac system.

## ACKNOWLEDGEMENT

The authors would like to thank Nanuopa Co. Ltd. for the manufacture of rotatable multi-wires.

## REFERENCES

[1] J. Wei et al., "The Compact Pulsed Hadron Source Construction Status", IPAC'10, Kyoto, MOPEC071, p. 633 (2010); http://www.JACoW.org

[2] X.W. Wang, "Delivery of 3-MeV Proton and Neutron Beams at CPHS: A Status Report on Accelerator and Neutron Activities at Tsinghua University", Physics Procedia, to be published.

[3] Q.Z. Xing et al., "Present Status of the 3MeV Proton Linac at Tsinghua University", LINAC'14, THPP137; http://www.JACoW.org

[4] K.R. Crandall, et al., "TRACE 3-D Documentation", LAUR-97-886.

[5] V.N. Aseev, et al., "TRACK: The New Beam Dynamics Code", PAC'2005, Knoxville, May 2005, p. 2053 (2005), http://www.JACoW.org

[6] D. Uriot, N. Pichoff, "TraceWin, Documentation", internal report CEA/DSM/DAPNIA/SEA/2000/45.

[7] J. Billen, et al., "Poisson/Superfish", LA-UR-96-1834.

[8] Y. Yang, "A low energy beam transport system for proton beam", Rev. Sci. Instrum. 84, 033306 (2013).

[9] R. Duperrier, "TOUTATIS, a radio frequency quadrupole code", Phys. Rev. Special Topics Acc. & Beams, december 2000.

[10] E.J. Sternglass, The Physical Review, Second Series, Vol. 108, No. 1; OCTOBER 1, 1957.

# CATALOGUE OF LOSSES FOR THE LINEAR IFMIF PROTOTYPE ACCELERATOR

N. Chauvin*, P.A.P. Nghiem, D. Uriot, CEA, IRFU, F-91191 Gif-sur-Yvette, France
M. Comunian, INFN/LNL, Legnaro, Padova, Italy
C. Oliver Amoros, CIEMAT, Madrid, Spain

## Abstract

One of the activities of the EVEDA (Engineering Validation and Engineering Design Activities) phase of the IFMIF (International Fusion Materials Irradiation Facility) project consists in building, testing and operating, in Japan, a 125 mA/9 MeV deuteron accelerator, called LIPAc, which has been developed in Europe.

For the accelerator safety aspects, a precise knowledge of beam loss location and power deposition is crucial, especially for a high intensity, high power accelerator like LIPAc. This paper presents the beam dynamics simulations allowing to estimate beam losses in different situations of the accelerator lifetime: starting from scratch, beam commissioning, tuning or exploration, routine operation, sudden failure. Some results of these studies are given and commented. Recommendations for hot point protection, beam stop velocity, beam power limitation are given accordingly.

## INTRODUCTION

For a high power megawatt class accelerator, any loss, even a tiny proportion of the beam, can be harmful. A careful and detailed loss study is thus necessary for various loss scenarios. That should be analysed for all the different stages of the accelerator lifetime, from its starting up, beam commissioning through routine operation, as well as for the various accidental breakdowns. Such a catalogue will be useful, or even necessary in the definition of safety procedure, limitations and recommendations, aiming at protecting personnel or facilities.

The linear IFMIF prototype accelerator (LIPAc) is being constructed in Europe and will be assembled in Japan [1]. This machine aims at accelerating a 125 mA D$^+$ continuous beam at 9 MeV. The general layout of LIPAc is recalled in Fig. 1, where beam energy and power for each subsystem are also given (for more details see Ref. [2]).

The LIPAc very high continuous beam intensity implies that almost the whole accelerator is concerned by a high power beam which ranges from 0.012 to 1.125 MW. It is common to consider that it is safe enough to use the lowest duty cycle and the lowest beam intensity during beam commissioning or during accelerator tests and exploration. But in the present case, as the ion source is optimised to provide a 140 mA continuous beam, the lowest duty cycle for which the beam is still stable is a few $10^{-3}$. Indeed, 1 ms is a typical time scale for the ECR source plasma to be established and for the extracted beam to reach a steady state. Furthermore,

the nominal beam intensity implies a very high space charge regime. So, any beam tuning with too low intensity will not be representative of the nominal conditions because of much lower space charge effects. Thus, the ability to lower the beam power is considerably limited. In the same way, a beam stop system is foreseen in the LEBT to shut off the beam in an accidental case in less than 10 µs. It is not sure that such a machine protection system is fast enough for a MW beam power.

This paper will mainly focus on the protocol and methodology that has been employed to simulate different loss situations; then, some results are presented and discussed in a few loss scenarios and finally, consequences on safety measures are drawn.

## LOSS STUDY PROTOCOL

In the following, the losses are given in power deposition (Watt). They are obtained with the nominal (maximum) current of 125 mA, continuous wave. From that, losses can be reduced if needed, by reducing consequently the duty cycle and even the current if necessary. Theoretically, because space charge effects decrease with intensity, losses at lower current are less than what can be inferred by a linear relation. But as a precaution, it is wise to deduce losses at lower current with a simple linear transformation.

The double issue is to define as exhaustively as possible all the typical loss situations in the accelerator lifetime and to define the procedure to simulate and estimate them. The following stages have been identified: (A) Ideal machine; (B) Starting from scratch; (C) Beam commissioning, tuning, exploration; (C) Routine operation; (E) Sudden failure.

### Situation A: Ideal Machine

"Ideal" means here nominal machine parameters and tunings, without any error. That should correspond, on the real machine, to a completely satisfying situation, if all the accelerator components would be perfectly fabricated and aligned, or else corrected at the source, and the beam would have been tuned. Losses in such conditions should be minimum; we cannot hope to have less. These are minimum and permanent losses that have to be withstood. It is very unlikely, (although highly desirable!) that this situation will occur on the real machine. At least, this situation is an optimal reference case that can be used as a comparison to the other scenarios described in the following subsections. The losses are obtained by a start-to-end simulation without any error for the nominal tuning [3].

---

* Nicolas.Chauvin@cea.fr
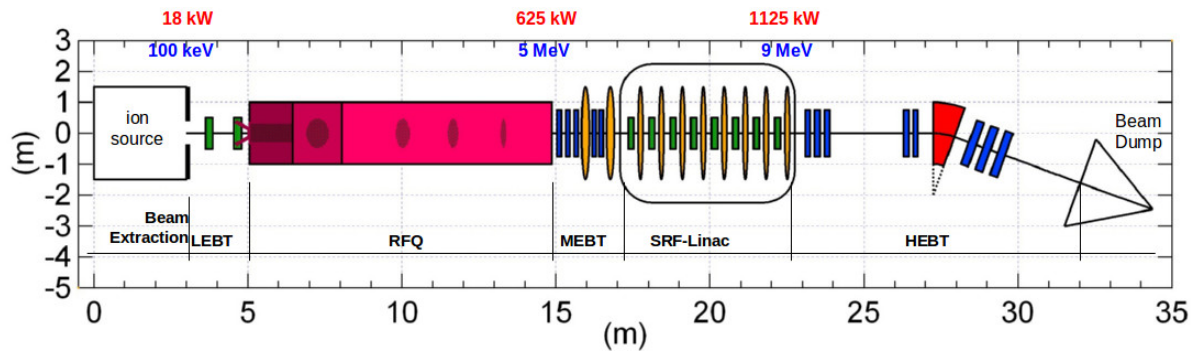
Figure 1: LIPAc general layout.

## Situation B: Starting From Scratch

In this condition, no correction has yet been applied, while we can expect that: (1) The accelerator components have been fabricated and aligned as specified, within the already defined tolerance ranges. (2) The tunable parameters (accelerating and focusing fields and gradients) are set at their optimised values given by beam dynamics simulation. We must however expect that the real beam behaviour is not exactly the same as the simulated one (the IFMIF very high space charge regime has never been experimentally observed). This theory-reality difference can be roughly estimated as equivalent to field and gradient variations in a $\pm 10\%$ range of their nominal values, according to the beam dynamics optimization results obtained in different working configurations since the beginning of the project.

Losses when starting from scratch can thus be estimated by performing a start-to-end error study without any correction. Two kinds of "errors" can be applied: mechanical end alignment errors randomly distributed within tolerances and tunable parameter errors randomly distributed within a $\pm 10\%$ range of their nominal values. Tolerance values, including static and dynamic ones, are discussed and presented in Refs. [2, 3].

## Situation C: Beam Commissioning, Tuning, Exploration

This occurs during beam commissioning or whenever the beam operation is not as satisfying as expected so that a beam tuning is necessary. Besides, experiments requiring an exploration around a nominal setting can be desirable for beam physics purposes.

However, the induced beam losses can be calculated in the same way as in the "B" case; we can assume mechanical errors within tolerances and tunable parameter variations of about $\pm 10\%$. The only difference is that now the beam trajectory is corrected.

## Situation D: Routine Operation

This situation happens when the beam characteristics are satisfying, i.e., as expected with all the parameters, mechanical and tunable parameters, as specified within tolerances

and the trajectory corrected. Losses can thus be calculated by performing an error study with trajectory correction.

## Situation E: Sudden Failure

These accidental situations are not easy to be exhaustively studied, especially when a combination of different failures can lead to more important losses than an individual failure. Reflections and analysis should be carried out for each subsystem to detect what is the worst case, what is the main affected location or equipment, when one tunable parameter (gradient, field, phase, RF power, pressure ...), or a given combination of them, are suddenly switched off. But attention should also be paid to detect if there is an intermediate case which can induce more losses, for example, in the transition from the nominal value to zero for specific field or gradient.

In this work, only two cases are studied: failure of individual components and global failure of all the components at once, from 110% to 0% of their nominal values. This can be due, for example, to power supply failures that accidentally provide a larger power or that can be suddenly switched off, making the fields or gradients returning progressively to zero.

# BEAM LOSS SIMULATION RESULTS

Start-to-end LIPAc simulations with $10^6$ macro-particles have been thoroughly carried out with the TraceWin code [4]. The error studies have also been performed with TraceWin, by tracking $10^6$ macro-particles in 500 through different linacs, each with different random errors that are uniformly distributed.

Due to lack of space, all the obtained results will not be presented here. As the simulation results for situation A and D can be found in previous works [2, 3], they will not be exposed in the present paper.

## Beam Losses During Beam Commissioning, Tuning or Exploration

As discussed above, loss probabilities are calculated from results of an error study with mechanical errors randomly distributed within tolerances and tunable parameter (field, gradients) errors randomly distributed within $\pm 10\%$ of their
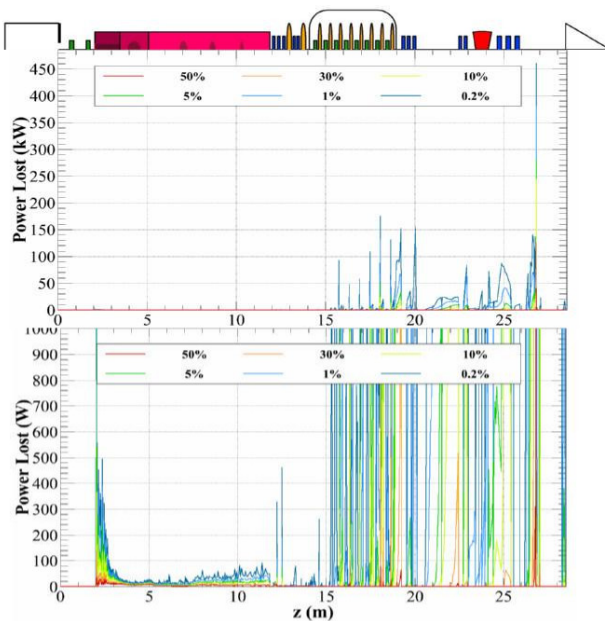
Figure 2: Beam power loss probabilities during beam commissioning, tuning or exploration, for a full-power beam (statistics over 500 machines). The bottom figure is a zoom of the top one toward the low power losses.

nominal values. Here, the beam trajectory are corrected. The correction scheme relies on steering coils (H and V) associated with downstream beam position monitors (H and V). In the LEBT, steerers are located inside the two solenoids. Then, 4 steerers and BPMs are located in the MEBT, 8 in the SRF-linac (at each lattice) and 6 in the HEBT.

Simulations are performed for the nominal 125 mA c.w. beam current. Once losses are known, a proportional calculation will give the maximum acceptable duty cycle or current at starting to avoid harmful losses. Loss probabilities along LIPAc are given in Fig. 2.

*Beam Losses in Case of Sudden Failure*

Due to the number of distinct accelerator components and their different nature in the low-energy section (from the source until the end of the RFQ, $E \leq 5$ MeV) and in the high-energy section (from the MEBT, $E \geq 5$ MeV), the loss studies are performed separately for each of them. Nevertheless, even in the case of a failure in the low energy section, the beam has been tracked (and the losses have been recorded) all along the LIPAc.

Power deposition due to beam losses are given in Fig. 3 in the case of sudden failure of the Solenoids of the LEBT and the RFQ voltage.

When all the low-energy part suddenly fails, losses occur mainly at the end of the LEBT and at the RFQ entrance. When the solenoid magnetic fields move around ±5% of their nominal values, the beam is either not focused enough to pass through the injection cone or is so mismatched that it
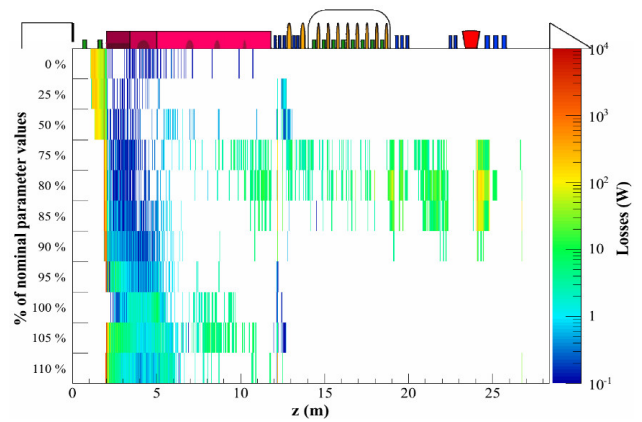
Figure 3: Beam power lost in case of sudden failure of the low energy part (LEBT solenoids and RFQ voltage) at once.

is lost in the first RFQ section. It can be noted that this case is less harmful than that of RFQ failure alone where more important losses occur in the sections downstream the RFQ.

## CONCLUSION

Beam dynamics simulations have been performed in order to estimate beam losses during different stages of the LIPAc lifetime. More detailed explanation of this work as well as extensive simulation results for all the stages of the accelerator lifetime that have been identified can be found in [5].

The catalogue of losses is meant to be a starting point for assessing all the accelerator safety aspects. Losses should concern all the accelerator sections by the identified hot points to be protected (facing beam equipment and diagnostics). The impact of those results on almost all the accelerator sub- systems shows the importance of setting up such a catalogue of losses for a high power accelerator or at least the high power part of an accelerator, where the beam power reaches more than hundreds of kW.

The protocol of loss studies presented in this article can likely be applied to any accelerator, by appropriately adjusting the numerical values used here.

## REFERENCES

[1] A. Mosnier et al, "Present Status and Developments of the Linear IFMIF Prototype Accelerator (LIPAc)", THPPP075, Proc. of IPAC 2012, New Orleans, USA (2012).

[2] P.A.P. Nghiem et al, *Nucl. Instru. Meth. Phys. Res.* A **654**,63-71, (2011).

[3] N. Chauvin et al, "Start-to-end Beam Dynamics Simulations for the Prototype Accelerator of the IFMIF/EVEDA Project", MOPS026, Proc. of IPAC 2011, San Sebastiàn, Spain, (2011).

[4] http://irfu.cea.fr/Sacm/logiciels/index.php.

[5] P.A.P. Nghiem et al, *Laser and Particle Beams* **32**,461–469, (2014).

# ECRIS DEVELOPMENTS TOWARDS INTENSE HIGH BRIGHTNESS HIGHLY-CHARGED ION BEAMS *

L. Sun[#], W. Lu, Y. Yang, X. Fang, Y. C. Feng, W. H. Zhang, J. W. Guo, X. Z. Zhang, C. Qian, H. W. Zhao

IMP/CAS, Lanzhou, 730000, China

## Abstract

To meet the increasing needs of modern heavy ion accelerators, ECR ion source must be developed to deliver high intensity high brightness high charge state ion beams, in terms of accelerator output power and beam transmission efficiency. With the success in several laboratories on fully superconducting ECR ion source development, the performance of highly charged heavy ion beams have been greatly enhanced. For instance, $U^{33+}$ intensity had been doubled in 2011 by VENUS source at LBNL. This paper will present the development work at IMP towards high performance ECR ion source. Recent high intensity bismuth results will be given, such as 710 eμA $Bi^{30+}$ with SECRAL source. The first room temperature ECR ion source using evaporative cooling technique will also be reviewed. And the discussion of ECRIS beam extraction and the transmission beam line elements on ion beam quality will also be presented in this paper.

## INTRODUCTION

Since been used as preinjectors for heavy ion accelerators about 30 years ago, Electron Cyclotron Resonance (ECR) ion source has been an indispensable machine to provide intense CW or long pulse (~ms) highly charged ion beams. The development of nuclear research strongly demands the modern heavy ion accelerators to be constructed or under construction to be capable of delivering high power heavy ion beams on the targets. To make the accelerators cost efficient, and achieve the design goal, intense highly charged heavy ion beams must be provided in the front end section. The FRIB project under construction at MSU campus needs 13 pμA $U^{33+ \& 34+}$ beam from the ion source and a dedicated achromatic transmission line and the successive matching beam line for downstream RFQ [1]. The SPIRAL 2 project going on at GANIL laboratory, eventually 1 emA $Ar^{12+}$ is expected to be delivered from the ion source to reach the goal of 1 emA heavy ion beam with the M/Q =3 for M≤36 [2]. And the RIKEN RIBF project also demands 15 pμA $U^{35+}$ eventually [3]. For the upgrade programme at IMP, the HIRFL facility needs the ion source being capable of producing very high charge state heavy ion beams with sufficient beam intensities, such as 100 eμA $Xe^{31+}$ and $U^{41+}$. All these facilities have made ECR ion sources in the baseline design to reach the desired parameters, due to the features of its high capacity

of intense high charge state heavy ion beam production. Fundamentally, the front end beam properties are determined by the ion source performance and the successive low energy beam transmission (LEBT) line design. The intrinsic properties have big impact on its output beam quality, which should be taken care of during the ion source and its LEBT design. A high performance ECR ion source injector front end should be an optimum design of both the ion source and the matching LEBT line, which enables the front end section to be capable of providing high brightness ion beam with sufficient beam intensity. In the following contents, the production of intense heavy ion beams with an ECR ion source will be generally reviewed, and the features of the ECR ion source LEBT line will also be discussed in terms of beam quality.

## INTENSE BEAM PRODUCTION WITH MODERN ECR ION SOURCES
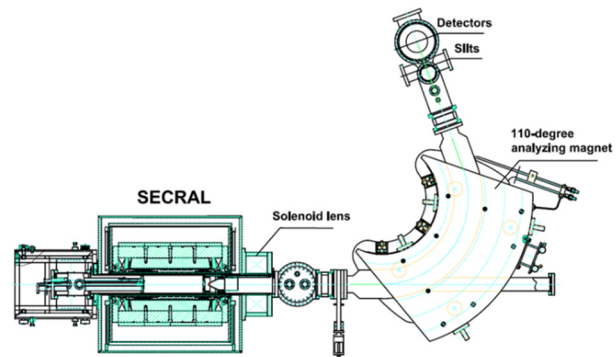


Figure 1: SECRAL ion source and LEBT layout.

ECR ion source is a kind of magnetic confined plasma machine, which was actually developed based on plasma fusion device [4]. Plasma electrons are heated through ECR heating to high energy by coupled microwave power with the frequency in the range of 2.45 GHz to 28 GHz. The plasma is confined by a strong nested so-called mini-B magnetic field configuration, which is the superposition of an axial mirror field and a radial multiple field (normally a hexapole field). Hot electrons are confined at the centre of the nested field and the HCIs, which are produced by stepwise ionization while they are confined in the plasma, are trapped by the space charge established by the electrons inside the plasma. The lost ions that enter the extraction region will be accelerated by the applied HV potential to form intense mixed ion beams. HCI beams in the extracted mixing beam can be separated with an analyser dipole magnet. Normally, a solenoid is used to focus the extracted intense beams to match the downstream elements. Fig. 1

gives the LEBT line layout of SECRAL source. Electro-static lens is an alternative option for the purpose of beam focusing, such as the LEBT line of SuSi at MSU [5].

## Ion Source Development

As ECR ion source is a magnet confined microwave heating plasma machine, its features could be generally de-scribed with the knowledge of under dense plasma. ECR source researchers have summarized the machine's perfor-mance with semi-empirical laws, i.e. extracted ion beam with charge state of $q$ is determined by

$$I_i^q = \frac{1}{2} \frac{n_i^q q e V_{ex}}{\tau_i^q},$$

where $n_i^q$ is the incident ion density, $V_{ex}$ is the effective vol-ume of the ion with charge state $q$, $\tau_i^q$ is the average con-finement time of the ion with charge state $q$, and the factor *1/2* means that the magnetic configuration of an ECRIS has two symmetrical ends while the ion beam is extracted on one side only. From the formula above, it is easy to see that high charge state ion beam production in an ECR ion source is a compromise of ion creation and loss. Therefore, the source parameters need to be optimized for best perfor-mance during operation. The most efficient way to increase the beam output is to increase the ion density and enhance the efficient plasma volume. According to the knowledge of microwave heating plasma, the higher the incident mi-crowave frequency $\omega_{ecr}$, the more beam could be achieved, i.e. $I_i^q \propto \omega_{ecr}^2$. For this reason, modern ECR ion sources are mostly working in the frequency range of 14~28 GHz. Since sufficient magnetic confinement is essential for the production of highly charge ions, the higher the frequency adopted, the stronger the magnetic fields are required. Therefore, when coming to the gyrotron frequency ($f > 20$ GHz), superconducting technique is incorporated.
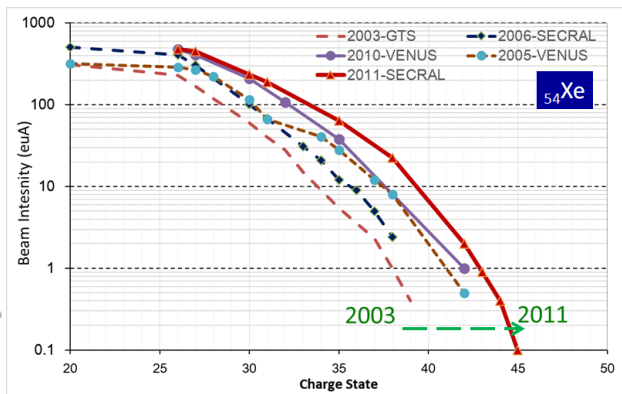


Figure 2: Xenon ion beam intensities evolution from 2003 to 2011 with the contribution of advanced sources.

Two kinds of configurations are utilized in the magnet design of fully superconducting ECR ion sources, i.e. the conventional structure, such as VENUS/LBNL [6], SERSE/INFN [7], SuSi/MSU [5] and SCECRIS/RIKEN [3], and the one with the unique reversed structure, or SECRAL design [8]. There are many pros and cons in the design of each technical solution, however either of them can provide good enough magnetic confinement to the

plasma created therein, which guarantees sufficiently good source performance. With the contributions from the mod-ern ECR ion sources, especially those from fully supercon-ducting ECR ion sources, beam results are enhanced obvi-ously. Fig. 2 provides xenon beam results evolution be-tween 2003 and 2011. Apparently, either the beam intensi-ties or the beam charge states have been boosted enor-mously over the time. And the evolution is still going on with the ECR ion source technology advancement.
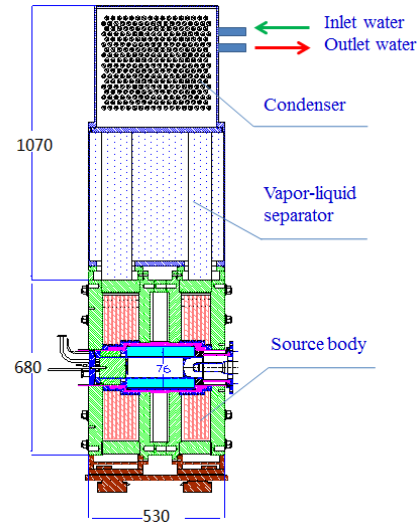


Figure 3: Schematic plot of LECR4 ion source.

Since superconducting technology is costly, challengea-ble and time consuming solution towards intense high charge state ion beam production, we are investigating into alternative technical solution of magnet design for an EC-RIS to achieve similar beam performance that a supercon-ducting ECR ion source can make at 18 GHz. Evaporative cooling technology has been applied in many high-power, high current density devices, such as Three Gorges Power Station in China. Evaporative cooling technology is a new efficient heat transfer method, which utilizes phase-change heat transfer mode to achieve the cooling for heating equip-ment. The coolant absorbs the latent heat of vaporization to cool the heating parts. The coolant can generally keep under a boiling point of 40-60℃, and the temperature of heating parts can be controlled under an ideal situation. On the other hand, the insulation of coolant can surely lead to a direct contact between electrified parts and evaporative coolant, therefore the coils can be immersed in the liquid coolant [9]. The heat transfer is very efficient and reliable. The typical adventures of such a technology to be utilized in an ECR ion source are (in comparison with traditional room temperature ECR ion source using deionized water cooled pancake coils):

- High pressure (in the range of 20 kg/cm²) deionized water free.
- Higher current density in the coils.
- Sufficiently high axial field confinement for 18 GHz operation.

Based on this concept, the first ECR ion source named

LECR4 (Sectional plot shown in Fig. 3) has been successfully constructed at IMP [10], which can produce the best results in comparison with other high performance room temperature ECR ion sources such as GTS/Grenoble [11], and even close to the best results that an superconducting ECR ion source optimized to 18 GHz (as indicated in Table 1). This new results provide an alternative option for the development of an ECR ion source that has the similar performance of a fully superconducting ECR ion source working at 18 GHz.

Table 1: First Beam Results of LECR4 at 18 GHz

| $f$ (GHz) | | SECRAL *18* | GTS *18* | LECR4 18 |
|---|---|---|---|---|
| $^{16}O$ | $6^+$ | 2300 | 1950 | 1970 |
| | $7^+$ | 810 | | 438 |
| $^{40}Ar$ | 8+ | | 1100 | 1717 |
| | $9^+$ | 1100 | 920 | 1075 |
| | 11+ | 810 | 510 | 503 |
| $^{129}Xe$ | 20+ | 505 | 310 | 293 |
| | 23+ | | | 143 |
| $^{209}Bi$ | 28+ | 214 | | 118 |
| | 30+ | 191 | | 78 |
| | 32+ | | | 51.5 |

## Intense Beam Production

As shown in Fig. 2, a state of the art ECR ion source has already produced very intense highly charged gaseous ion beams. But practically, most of the ion beams that the experimenters demand are from solid elements. For the case of solid material or metallic ion beam production, special instrument is needed to produce sufficient vapor of incident material that could be delivered and ionized by the hot ECR plasma. Typical techniques such as plasma insertion, plasma sputtering, MIVOC and micro-oven have been used, however with regard to long term service with intense highly charged ion beams, for instance >10 pµA $U^{34+}$, micro-oven is the only workable solution. 4 types of micro-ovens have been designed and tested in ECR ion source laboratories, i.e. resistor oven with the highest operating temperature of 1600º C but moderate material loading capacity, low temperature oven incorporating cartridge heaters with the highest operating temperature of 800º C and much larger material loading capacity, high temperature resister oven that could reach the temperature of 2000º C mainly designed for refractory material ion beam production and the inductive heating oven that could also reach the temperature up to 2000º C but with a much complicated auxiliary power system.

Traditional resister heating oven has been widely adopted in ECR ion source laboratories for many years. It is a quite matured technique to serve tens of eµA ion beams production from moderate melting temperature solids. For very refractory ion beam production, such as uranium, traditional oven is not suitable for the application. A high

electrical current driven resister heating oven has been developed in LBNL [12], which utilizes resistively-heated refractory metal enclosures, normally of the material of Re, Mo, W or Ta. The nominal excitation current is up to 400 A. The off-line test of this kind of oven has reached a temperature up to 2300℃. However, during operation, the oven is located off-axis near the ion source injection field peak, where exists a very strong magnetic field up to 4 T (for VENUS) contributed from both the solenoids and the sextupole magnet. Therefore, Lorentz forces from different directions act upon the oven during operation. When very high temperature needed, high electrical current is energized in the oven, which makes the Lorentz forces even stronger. As most of the metals will soften at high temperature, the high Lorentz force will twist the oven and eventually destroy the oven. After years' research and upgrade, the LBNL researchers have developed a more durable oven that can work under high field with sufficiently high temperature for about one week or even longer. With this oven, recorded uranium beam intensities were made with VENUS in 2011, as shown in Fig. 4. Based on the same design, a high temperature oven has also been recently developed in RIKEN and been used for routine operation [13].
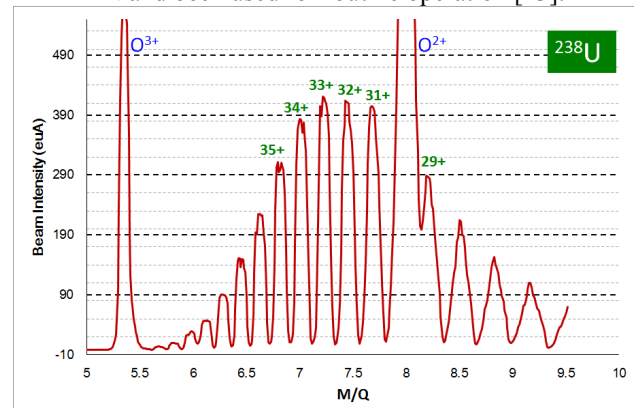


Figure 4: Spectrum from VENUS when 440 eµA $U^{33+}$ produced at 28 GHz.

A DC current driven high temperature oven as discussed above can't avoid the strong Lorentz forces when used for operation in an ECR ion source. As for the 4th generation ECR ion source working at the frequency higher than 40 GHz, the field at the oven location is even higher (proportional to the working frequency), which indicates that much stronger Lorentz force will be applied to the oven. For this reason this type of high temperature oven might not be applicable to the future needs. An alternative solution is based on the traditional inductive heating technique that has been widely used in industrial processing of metal materials. At NSCL/MSU, a micro-oven based on inductive heating technique has been developed and used in routine operation for refractory ion beam production (Fig. 5). This oven technique can definitely avoid the Lorentz forces problem. But it utilizes 1~2 kW RF power in the frequency range of ~100 kHz, the power coupling between the RF generator and the oven susceptor needs professional design and fabrication. Additionally, working at the temperature below 2000℃, the oven is reliable and stable, but at higher

temperature the furnace heat insulator degrades very quickly and the oven can't hold the temperature thereafter. Nevertheless, with new furnace heat insulator materials utilized, this type oven may sustain the long term operation at the temperature up to 2300℃.



Figure 5: Picture of an inductive heating oven developed at NSCL/MSU.

For very intense solid material ion beam production, a vapour pressure up to $10^{-1}$ mbar is needed from the oven. To sustain such a working condition for a very long time, the oven loading capacity must be high enough. For this reason, a kind of oven utilizing cartridge heaters has been designed and fabricated at IMP based on the LBNL concept. Another advantage of this type of oven is the precise control of the temperature rise, since the temperature control of the oven is realized through cartridge power control, and the temperature rise is quite slow. For the solid material that needs the temperature below 700℃, such as Ca, Bi, Pb and etc., this oven is a very applicable technical approach. With this type of oven installed, recorded bismuth beam intensities have been produced in 2014. Working at 4.74 kW@24 GHz + 1.4 kW@18 GHz, 710 eμA $Bi^{30+}$ and 680 eμA $Bi^{31+}$ have been obtained at the faraday cup [14]. Fig. 6 gives the spectrum when 710 eμA $Bi^{30+}$ produced. The present results seems to be still limited by oven output of Bi vapour and ion source conditioning at high power.
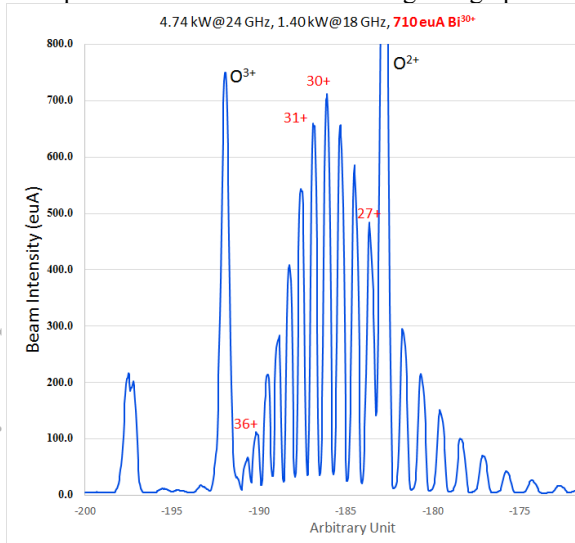


Figure 6: Spectrum optimized for 710 eμA $Bi^{30+}$.

## Intense Beam Emittance

In general, two issues are essential for ion beams injected to an accelerator, i.e. beam intensity and beam brightness. High power accelerators need very intense ion beams, while optimal brightness can guarantee the transmission of ion beam with less losses. With the increase of ion beam extracted from an ECR ion source, beam quality will deteriorate as a cause of more severe space charge effect. It is worth checking the beam emittance evolution with the increase of beam intensity. With SECRAL source, the beam emittance was measured with Alison type scanners. Fig. 7 shows the horizontal and vertical normalized rms emittances measured for $Bi^{31+}$ intensity from 100 eμA to 600 eμA. Error bars are not given here, which should be in the range of ±10% [15]. According to the study, the emittances do not deteriorate dramatically with the beam intensity increase.
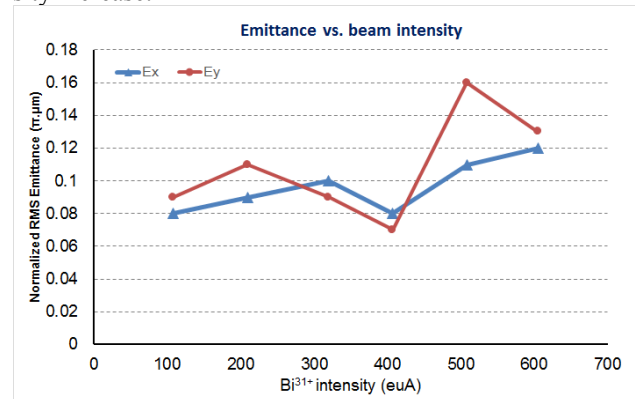


Figure 7: $Bi^{31+}$ beam emittance variation with the increase of beam intensity.

## ECR LEBT AND BEAM QUALITY

### Ion Beam from an ECR Ion Source

In an ECR ion source, the ions are produced in a superimposed field of axial mirror field and radial sextupole field, which makes the ions have inhomogeneous spacial distribution at the ion source extraction that is reflected by the triangle tracks at the both ends of the ion source. Fig. 8 provides the triangle image created at SECRAL plasma electrode.

### Ion Source Extraction Field

As shown in Fig. 9, when ion beam extracted, it will experience a hemi-solenoidal field. Provided that the extracted beam is a symmetrical one, we have the initial σ matrix:

$$\sigma_0 = \varepsilon \begin{pmatrix} \beta & -\alpha & 0 & 0 \\ -\alpha & \gamma & 0 & 0 \\ 0 & 0 & \beta & -\alpha \\ 0 & 0 & -\alpha & \gamma \end{pmatrix},$$

and the hemi solenoid transport matrix assumed to be:

$$R_{exit} = \begin{pmatrix} 1 & 0 & 0 & 0 \\ 0 & 1 & k & 0 \\ 0 & 0 & 1 & 0 \\ -k & 0 & 0 & 1 \end{pmatrix},$$

Therefore, the extracted beam final σ matrix will be:

$$\sigma_s = R_{exit}\sigma_0 R_{exit}^T = \varepsilon \begin{pmatrix} \beta & -\alpha & 0 & k\beta \\ -\alpha & k^2\beta+\gamma & -k\beta & 0 \\ 0 & -k\beta & \beta & -\alpha \\ k\beta & 0 & -\alpha & k^2\beta+\gamma \end{pmatrix}$$

where $\alpha$, $\beta$ and $\gamma$ are beam Twiss parameters, $\varepsilon$ is the beam initial emittance, $k=B_s/B\rho$, $B_s$ is the extraction field, and $B\rho$ is the ion rigidity. Obviously, the hemi solenoid field introduces a coupling between the horizontal and vertical coordinates, and causes beam emittance growth. As discussed above, the extracted beam is actually asymmetric which will induce more severe coupling and beam emittance deterioration.



Figure 8: Plasma bombardment images on plasma electrode.
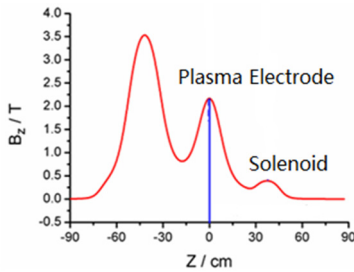


Figure 9: SECRAL axial field distribution, and ion beam extraction started from plasma electrode.

Solenoid lens can provide very efficient pre-focusing of the beam extracted from an ECR ion source in a short transmission length. Compared with an electrostatic lens, it will not destroy the space compensation in the source extraction region. The matrix operations of a solenoid in beam optics tell us that for an axisymmetric and un-coupled beam, a solenoid will only have focusing effect, without any additional transverse coupling. However, if a coupled beam transmits through a solenoid, the coupling effect will become more severe, transverse emittance will transfer between the horizontal and vertical directions, and the polarity of the solenoid field will have obvious impact on the beam quality. Fig. 10 shows the experiment and simulation results done with SECRAL transmission beam line. For modern high intensity heavy ion facilities, linac accelerators are common choice for the injector design, which normally has symmetric transverse acceptance. If the beam coupling dominates the beam quality deterioration, emittances at horizontal and vertical directions will be quite different, and high beam loss will be seen at the injection region. Some decoupling solutions should be adopted for the purpose.
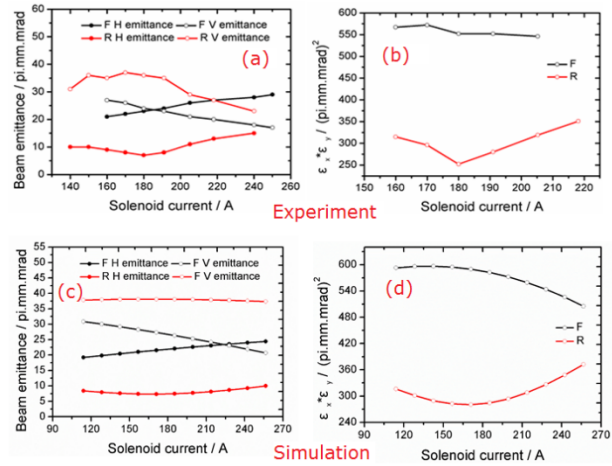


Figure 10: Experiment (a, b) and simulation (c, d) results to understand the beam coupling with SECRAL ion source and LEBT.

*Dipole Magnet Design*

Dipole magnet is an essential part in the LEBT design for an ECR ion source system. It will determine the downstream beam quality and quantity. Most of the analyser magnet has double focusing structure to have beam focusing in both vertical and horizontal directions. As the design of SECRAL LEBT line, one solenoid lens is used in the ECR beam line which can't control the beam envelope and divergence simultaneously at the entrance of the dipole magnet. Therefore, a large magnet gap is favoured to provide the highest beam acceptance, and it also can minimize the high order aberration induced to the large envelope beams. And essentially, the mass resolution should be high enough, especially when very highly charged heavy ion beams are desired, and normally a $\Delta m/m = 1/100$ resolution is desired.
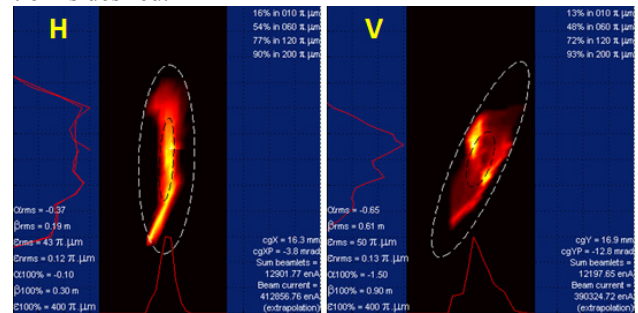


Figure 11: Beam emittances in Horizontal (left) and Vetical (right) directions: $\varepsilon_{h.rms}=0.12$ $\pi.\mu m$, $\varepsilon_{v.rms}=0.13$ $\pi.\mu m$. $\alpha_{h.rms}= -0.37$, $\alpha_{v.rms}= -0.65$.

A normal dipole design will have sextupole field component in the vertical plane at the magnet entrance and exit, and in the horizontal plane along the beam trace. The sextupole component causes obvious beam aberration, and consequently beam emittance increase. Fig. 11 is the beam emittance plot from SECRAL source. Since sextupole component field increases quadratically from the center beam trace, the larger envelop beams may see stronger sextupole components, and therefore more severe aberration. Two applicable technical solutions can solve the problem,

i.e. a well-trimmed dipole magnet, or external compensation with sextupole magnet. The first option is a very straightforward method. By accurate calculation and simulation, the magnet can be designed to correct the sextupole components in both vertical and horizontal planes. Technically, the magnet edges need to be carefully shaped, and the pole surfaces need to be trimmed to have smoothly varying shape to produce a desired quadratic terms. This technical approach is very time consuming and expensive. The VENUS [16] and SuSI [17] analyser magnets are using this concept. An alternative and cheap solution is to add an external sextupole magnet to generate a reversed sextupole field against the one induced by the dipole magnet so as to cancel the sextupole magnet negative effect and reduce the aberration. Recently a sextupole magnet has been built and installed to the SECRAL LEBT dipole magnet exit to investigate the feasibility. Meanwhile the code simulation already indicates that the design is very effective to reduce the aberration and improve the beam quality [18].

### Space Charge

Space charge has been discussed in many presentations about the negative effect induced. For most of the ECR ion sources in operation, the total extracted ion beam is no more than 4 emA, which will not give much space charge influence. While for the very intense beam production, for example, when more than 400 e$\mu$A U$^{33+}$ produced with VENUS and 700 e$\mu$A Bi$^{30+}$ produced with SECRAL, the total extraction beam was over 10 emA, and the space charge effect will dominate the beam quality issues. According the recent research results from NSCL/MSU with a space charge detector, the space charge compensation ratio at the source extraction region is about 70% [19]. Thus, for a 10 emA total beam extraction, 3 emA space charge will have influence on incident ion beam quality. There're several negative effects the space charge will affect the beam transmission, i.e. beam aberration and emittance growth, decrease of momentum resolution of the Q/A selector system which is discussed in Ref. 20 in details.

## CONCLUSION

To meet the needs of future heavy ion accelerators, ECR ion sources have been developed to produce very intense highly charged ion beams, such as 400 e$\mu$A U$^{33+}$ and 700 e$\mu$A Bi$^{30+}$, but the beam quality is another issue which needs a systematic consideration of the design from the ion source to the downstream LEBT line, so as to minimize the emittance growth and beam quality degradation, therefore to guarantee injection to the post accelerator with high enough beam intensity and brightness. In terms of the several high intensity projects under construction and to be started in next 5 years, such as FRIB, SPIRAL 2, and HIAF (50 p$\mu$A U$^{34+}$ needed) and etc., intense beam extraction and transmission is very critical and challengeable research topic for the ECR ion source researchers to take on, other than the high performance ECR ion source development. Higher frequency next generation ECR ion source could be built in 10 years, however, to produce very intense highly charged beams from solid materials especially those from refractory ones, oven is a real challenge as a supporting technology.

## REFERENCES

[1]  E. Pozdeyev, N. Bultman, G. Machicoane, G. Morgan, X. Rao, and Q. Zhao, "Status of The FRIB Front End", PAC'13, Pasadena, USA, Sept. 2013, p.734 (2013) ; http://www.JACoW.org

[2]  R. Ferdinand, "The SPIRAL 2 Superconducting Linac", PAC'09, Vancouver, Canada, May 2009, p.4281 (2009); http://www.JACoW.org

[3]  T. Nakagawa et al., Rev. Sci. Instrum. 81, 02A320 (2010) .

[4]  R. Geller, Electron Cyclotron Resonance Ion Sources and ECR Plasmas, (Institute of Physics Publishing, Bristol and Philadelphia, 1996), 364.

[5]  L. T. Sun et al., "Intense Beam Production with SuSI", ECRIS'10, Grenoble, France, Aug. 2010, p.4 (2010); http://www.JACoW.org

[6]  D. Leitner et al., Rev. Sci. Instrum. 77, 03A302 (2006).

[7]  S. Gammino et al., "Comparison of Operations of The SERSE Ion Source at 18 and 28 GHz", Proceedings of PAC'01, Chicago, June 2001, p.2409 (2001); http://www.JACoW.org

[8]  H. W. Zhao et al., Rev. Sci. Instrum. 77, 03A333 (2006).

[9]  B. Xiong et al., Rev. Sci. Instrum. 85, 02A913 (2014).

[10]  W. Lu et al., Rev. Sci. Instrum. 85, 02A926 (2014).

[11]  D. Hitz et al., Rev. Sci. Instrum. 75, 1403 (2004).

[12]  T. Loew, S. Abbott, M. Galloway, D. Leitner, C. M. Lyneis, "Design of a High Temperature Oven for An ECR Source for The Production of Uranium Ion Beams", PAC'07, Albuquerque, New Mexico, USA, June 2007, p.1742 (2007); http://www.JACoW.org

[13]  J. Ohnishi, Y. Higurashi, M. Kidera, K. Ozeki and T. Nakagawa, Rev. Sci. Instrum. 85, 02A941 (2014).

[14]  L. Sun et al., "Status Report of SECRAL II Ion Source Development", ECRIS'14, Nizhny Novgorod, Russia, Aug. 2014, TUOMMH03 (to be published); http://www.JACoW.org

[15]  Y. Cao et al., Rev. Sci. Instrum. 77, 03A346 (2006).

[16]  M. Leitner, S. R. Abbott, D. Leitner, C. Lyneis, "A High Transmission Analyzing Magnet for Intense High Charge State Beams", ECRIS'02, Jyväskylä, Finland, June, 2002, p.32 (2002).

[17]  P. A. Závodszky et al., High Energy Physics and Nuclear Physics, 31 (S1), 18 (2007).

[18]  Y. Yang et al., Rev. Sci. Instrum. 85, 02A719 (2014).

[19]  D. Winklehner, D. Leitner, D. Cole, G. Machicoane, and L. Tobos, Rev. Sci. Instrum. 85, 02A739 (2014).

[20]  Y. Yang et al., Rev. Sci. Instrum. 85, 083301 (2014).

# THE KICKER IMPEDANCE AND ITS EFFECT ON THE RCS IN J-PARC

Y. Shobuda, P. K. Saha, T. Toyama, M. Yamamoto, J-PARC Center, Ibaraki, JAPAN
Y. H. Chin and Y. Irie, KEK, Ibaraki, JAPAN

## Abstract

Measurements demonstrate that the kicker impedance dominates along the RCS. Based on a newly developed theory, the impedance is measured by observing the beam-induced voltages at the ends of power cable of the kicker. Toward one mega-watt goal, it is essential to take advantage of tune manipulations and the space charge damping effect. A reduction scheme of the kicker impedance is proposed to pursue the ultimate goal at the RCS.

## INTRODUCTION

There are the accelerators aiming at producing mega-watt class beams in the world [1, 2]. One of such facilities is the 3GeV rapid cycling synchrotron (RCS) in Japan Proton Accelerator Research Complex (J-PARC) [1]. In order to extract the high intensity beams from the RCS, eight distributed type kicker magnets are installed in the RCS [3].

On the other hand, in order to steadily circulate the high intensity beams in the RCS, it is important to precisely estimate the coupling impedances along the ring. In the RCS, the coupling impedance has been lowered except the kicker impedance [4]. When we apply Sacherer's formula [5], the beam should become unstable around 100 kW, where the chromaticity $\xi$ is fully corrected in the entire energy. Accordingly, it has been concerned that the kicker impedance disturbs realizing the high intensity beam in the RCS.

Contrary to our expectation, the beam at last becomes unstable beyond about 300 kW with the fully chromaticity correction. This means that a significant gap exists between the theoretical prediction and the measurement results.

The situation has goaded us to review the estimation of the kicker impedance from theoretical and experimental points of view. In the process, the authors have found that the causality condition is not satisfied in Nassibian's formula [6, 7] describing the impedance of the kicker where all terminals are connected to the matched resistors.

Accordingly, a theory has been developed to estimate the kicker impedance. The theory describes the impedance, where the terminals of the kicker magnet are connected to the power cables [8] as well as to the matched resistors [9]. The theoretical results well reproduce the measurement results by using the standard wire-measurement scheme [10]. Moreover, the theory successfully relates the beam-induced voltages at the ends of the cables to the kicker impedance. One advantage of developing the theory is to enable to find the kicker impedance by letting a beam pass through the kicker and by measuring the beam-induced voltages at the ends of the cables.

At the same time, simulation studies have been progressing. The beam simulation code ORBIT, which is originally developed in SNS [2] for storage rings, has been upgraded by

J. Holmes in order to incorporate the Lorentz-$\beta$ dependence of the kicker impedance into the code. The precise estimation of the impedance brings the code into action, especially in the serious condition as in the RCS.

Before we discuss a strategy to accomplish one mega-watt beam, let us review how to produce the kicker impedance from the beam-induced voltage.

## KICKER IMPEDANCE
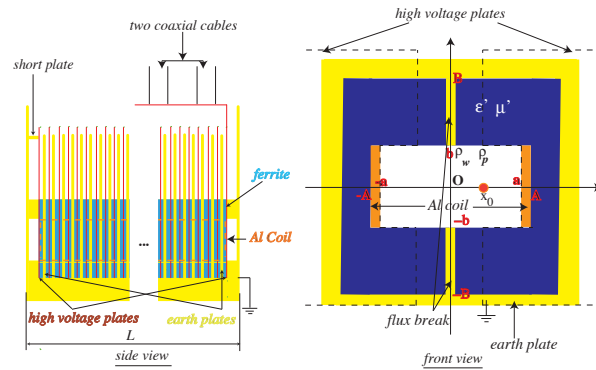


Figure 1: A schematic picture of the kicker magnet.

A schematic picture of the kicker magnet is shown in Fig. 1. The kicker magnet has four terminals at the corners. The right front and the left back terminals of the kicker are terminated by the short plates, respectively. The short plates double the excitation current by superposing the forward and backward currents, when a beam is extracted from the RCS. The right back and the left front terminals are connected to two-parallel coaxial cables, respectively.

The formulae of the kicker impedances are described as follows,

$$Z_L = Z_L^{(0)}(x_0 = x = 0) + Z_L^{(1)}(x_0 = x = 0)$$
$$+ Z_L^{(crr)}(x_0 = x = y = 0)$$
$$\simeq Z_L^{(0)}(x_0 = x = 0) + Z_L^{(crr)}(x_0 = x = y = 0), \quad (1)$$

$$Z_x = \left. \frac{\partial^2 Z_L(x_0, x, y = 0)}{k \partial x_0 \partial x} \right|_{x_0 = x = 0}$$

$$\simeq \left. \frac{\partial^2 Z_L^{(1)}(x_0, x, y = 0)}{k \partial x_0 \partial x} + \frac{\partial^2 Z_L^{(crr)}(x_0, x, y = 0)}{k \partial x_0 \partial x} \right|_{x_0 = x = 0}, \quad (2)$$

where $Z_L$ and $Z_x$ are the longitudinal and the horizontal impedances, respectively, $x_0$ and $x$ are the horizontal positions of the source and the witness particles, respectively,

and $k$ is wavenumber. The impedances $Z_L^{(0)}$ and $Z_L^{(1)}$ are approximated in low frequency region : $f < c\beta/(2\pi L)$ as

$$Z_L^{(0)}(x_0, x) = 2 \sum_{m=1}^{\infty} (-(-1)^m + 1 + \cos \frac{m\pi(\rho_p + a)}{2a}$$

$$- \cos \frac{m\pi(-\rho_p + a)}{2a}) \frac{\sin \frac{m\pi(x+a)}{2a}}{m\pi}$$

$$\times [\frac{c\beta\theta_1 Z_{c,c}(e^{j(k+\omega\theta_1)L} - 1)F_3}{q(1 + c\beta\theta_1) \cosh \sqrt{\frac{m^2\pi^2}{4a^2} + \omega^2\theta_1^2 - k^2\beta^2}b}$$

$$+ \frac{c\beta\theta_1 Z_{c,c}(e^{j(k-\omega\theta_1)L} - 1)F_4}{q(1 - c\beta\theta_1) \cosh \sqrt{\frac{m^2\pi^2}{4a^2} + \omega^2\theta_1^2 - k^2\beta^2}b}$$

$$+ \frac{j\omega L M_+}{\cosh \sqrt{\frac{m^2\pi^2}{4a^2} + \frac{k^2}{\gamma^2}}b}], \tag{3}$$

$$Z_L^{(1)}(x_0, x) = -2 \sum_{m=1}^{\infty} (-(-1)^m - 1 + \cos \frac{m\pi(\rho_p + a)}{2a}$$

$$+ \cos \frac{m\pi(-\rho_p + a)}{2a}) \frac{\sin \frac{m\pi(x+a)}{2a}}{m\pi}$$

$$\times [\frac{\omega\theta_3 Z_{c,d}(e^{j(k+\omega\theta_3)L} - 1)F_1}{q(k + \omega\theta_3) \cosh \sqrt{\frac{m^2\pi^2}{4a^2} + \omega^2\theta_3^2 - k^2\beta^2}b}$$

$$+ \frac{\omega\theta_3 Z_{c,d}(e^{j(k-\omega\theta_3)L} - 1)F_2}{q(k - \omega\theta_3) \cosh \sqrt{\frac{m^2\pi^2}{4a^2} + \omega^2\theta_3^2 - k^2\beta^2}b}$$

$$- \frac{j\omega L M_-}{\cosh \sqrt{\frac{m^2\pi^2}{4a^2} + \frac{k^2}{\gamma^2}}b}], \tag{4}$$

$$Z_L^{(crr)}(x_0, x, y = 0) = -\frac{L_f}{a} \sum_{m=1}^{\infty} (E_m^\gamma$$

$$- \frac{jkZ_0 \tanh k_{xm}b \sin k_{xm}'(x_0 + a)}{2\beta\gamma^2 k_{xm}}) \sin \frac{m\pi}{2a}(x + a), \tag{5}$$

$$E_m^\gamma = \frac{1}{\left\{ \frac{k_{xm}'^2}{k_{xm}^2} - \frac{[1 - \frac{\mu' k_{ym}' \tanh k_{ym}'(b-B) \tanh k_{xm}b}{\gamma^2(1-\beta^2\epsilon'\mu')k_{xm}}]}{[1 - \frac{1}{\gamma^2(1-\beta^2\epsilon'\mu')}]} \right.}$$

$$\times \frac{[1 - \frac{\epsilon' k_{ym}' \frac{\cosh k_{ym}'(b-B)}{\tanh k_{ym}'(b-B)}}{\gamma^2(1-\beta^2\epsilon'\mu')k_{xm} \sinh k_{xm}b}]}{[1 - \frac{\mu'\epsilon'}{\gamma^2(1-\beta^2\epsilon'\mu')}]} \right\}$$

$$\times \frac{jkZ_0}{2\beta\gamma^2 k_{xm}} \left\{ \frac{k_{xm}'^2 \tanh k_{xm}b \sin k_{xm}'(x_0 + a)}{k_{xm}^2} \right.$$

$$- \frac{(1 - \frac{\mu' k_{ym}' \tanh k_{ym}'(b-B)}{\gamma^2(1-\beta^2\epsilon'\mu')k_{xm}}) \frac{\sin \frac{m\pi}{2}}{\tanh k_{xm}b}}{(1 - \frac{1}{\gamma^2(1-\beta^2\epsilon'\mu')})(1 - \frac{\mu'\epsilon'}{\gamma^2(1-\beta^2\epsilon'\mu')})}$$

$$\times [\frac{(1 - \frac{\epsilon' k_{ym}' \tanh k_{xm}b}{\gamma^2(1-\beta^2\epsilon'\mu')k_{xm} \tanh k_{ym}'(b-B)}) \sin k_{xm}'(x_0 + a)}{\sin \frac{m\pi}{2}}$$

$$- \frac{2C_r(x_0)[\cosh k_{ym}'(b - B) - 1]}{k_{ym}' \sinh k_{ym}'(b - B) \cosh k_{xm}b}] \right\}, \tag{6}$$

$$M_- = \frac{(M^r(x_0) - M^l(x_0))}{2(1 - c^2\beta^2(L_k - M_b)C_k)}, \tag{7}$$

$$M_+ = \frac{(M^r(x_0) + M^l(x_0))}{2(1 - c^2\beta^2(L_k + M_b)C_k)}, \tag{8}$$

$$\theta_1 = \sqrt{(L_k + M_b)C_k}, \theta_3 = \sqrt{(L_k - M_b)C_k}, \tag{9}$$

$$Z_{c,d} = \sqrt{\frac{L_k - M_b}{C_k}}, Z_{c,c} = \sqrt{\frac{L_k + M_b}{C_k}}, \tag{10}$$

$$k_{xm}' = \frac{m\pi}{2a}, k_{xm} = \sqrt{k_{xm}'^2 + \frac{k^2}{\gamma^2}}, \tag{11}$$

$$k_{ym}' = \sqrt{k_{xm}'^2 + k^2(1 - \epsilon'\mu'\beta^2)}, \tag{12}$$

$$C_r(x_0) = -\frac{1}{2(B - b)}(1 - \frac{M^r(x_0) + M^l(x_0)}{L_k + M_b}), \tag{13}$$

where $C_k$ is the capacitance per a unit length of the kicker, $L_k$ and $M_b$ are the self and the mutual inductances per a unit length of the coils, $M^r(x_0)$ and $M^l(x_0)$ are the induction coefficients per a unit length between the beam and the right and the left coils, respectively, $\beta$ and $\gamma$ is the Lorentz-$\beta$ and $\gamma$, respectively, and $L_f$ is the total length of the ferrite in the magnet. The functions $F_1(\omega), F_2(\omega), F_3(\omega)$ and $F_4(\omega)$ are obtained by solving the boundary conditions:

$$(Z_{c,d} - Z_{cable})F_1 - (Z_{c,d} + Z_{cable})F_2$$
$$- (Z_{c,c} - Z_{cable})F_3 + (Z_{c,c} + Z_{cable})F_4$$
$$= -(M_- + M_+)qc\beta - Z_{cable}qC_kc^2\beta^2(M_- + M_+), \tag{14}$$
$$- Z_{c,d}F_1 + Z_{c,d}F_2 - Z_{c,c}F_3 + Z_{c,c}F_4$$
$$= qc\beta(M_- - M_+), \tag{15}$$
$$Z_{c,d}e^{j\omega\theta_3 L}F_1 - Z_{c,d}e^{-j\omega\theta_3 L}F_2$$
$$- Z_{c,c}e^{j\omega\theta_1 L}F_3 + Z_{c,c}e^{-j\omega\theta_1 L}F_4$$
$$= -(M_- + M_+)qc\beta e^{-j\omega\frac{L}{c\beta}}, \tag{16}$$
$$- (Z_{c,d} + Z_{cable})e^{j\omega\theta_3 L}F_1 + (Z_{c,d} - Z_{cable})e^{-j\omega\theta_3 L}F_2$$
$$- (Z_{c,c} + Z_{cable})e^{j\omega\theta_1 L}F_3 + (Z_{c,c} - Z_{cable})e^{-j\omega\theta_1 L}F_4$$
$$= (M_- - M_+)qc\beta e^{-j\omega\frac{L}{c\beta}}$$
$$- Z_{cable}(M_- - M_+)qC_kc^2\beta^2 e^{-j\omega\frac{L}{c\beta}}, \tag{17}$$

where

$$Z_{cable} = \frac{1}{2}\sqrt{\frac{L_{cable}}{C_{cable}}} \times$$

$$[\frac{1 + \frac{-\sqrt{\frac{L_{cable}}{C_{cable}}} + 2R_T}{\sqrt{\frac{L_{cable}}{C_{cable}}} + 2R_T}e^{-j\omega 2\sqrt{C_{cable}L_{cable}}l_{cable}}}{1 + \frac{-\sqrt{\frac{L_{cable}}{C_{cable}}} + 2R_T}{-\sqrt{\frac{L_{cable}}{C_{cable}}} - 2R_T}e^{-j\omega 2\sqrt{C_{cable}L_{cable}}l_{cable}}}], \tag{18}$$

$$L_{cable} = \frac{R_{cable}}{j\omega} + \mathcal{L}_{cable}, C_{cable} = \frac{G}{j\omega} + \mathcal{C}_{cable}, \tag{19}$$

$\mathcal{L}_{cable}$ is the inductance per a unit length of the cable, $\mathcal{C}_{cable}$ is the capacitance per a unit length of the cable, $R_{cable}$ is the

resistivity per a unit length of the inner and outer conductors in the cable and $G$ is the admittance per a unit length of the insulator between the conductors. Equation (18) deals with the case that two-parallel cables are connected at the end and terminated with the device having the impedance $R_T(\omega)$ (if the terminal is open as in the present kicker, $R_T$ is identical to infinity.).
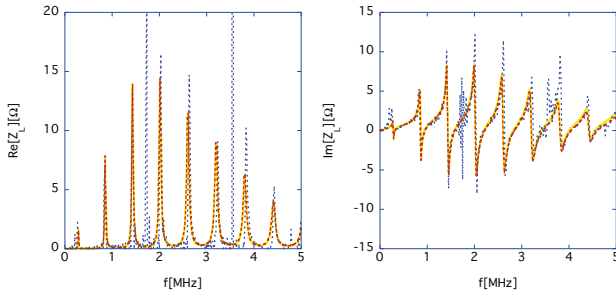


Figure 2: The theoretical (red) and the measurement (blue) results of the longitudinal impedance $Z_L$ for $\beta = 0.54$ and the theoretical one for $\beta = 0.97$ (yellow).
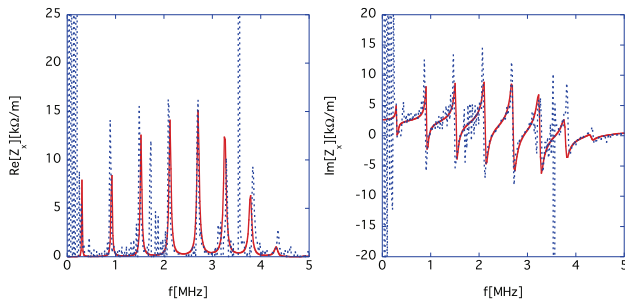


Figure 3: The theoretical (red) and the measurement (blue) results of the horizontal impedance $Z_x$ for $\beta = 0.54$.

The impedance is theoretically calculated by solving the functions $F_1(\omega), F_2(\omega), F_3(\omega), F_4(\omega)$ in terms of the coupling factors $M_-$ and $M_+$. On the other hand, the functions $F_1(\omega), F_2(\omega), F_3(\omega), F_4(\omega)$, and the coupling factors $M_-$ and $M_+$ can be determined as the function of the beam-induced voltages at the ends of cables by relating the boundary conditions to those for the cables [8].

The impedances are measured by letting an injection beam from LINAC pass through the kicker once and extracting it from the RCS immediately. The theoretical and the measured results by using the beam with $\beta = 0.54$ are shown in Figs. 2 and 3. The theoretical results (red) well reproduce the measurement results (blue). The artificial sharp peaks appear in the measured results at $n/\Delta t$, where $n$ is integer, $\Delta t (\simeq 560\text{ns})$ is the pulse length of the beam, because they are singular points in the Fourier transform of the pulse beam. The agreement between the theoretical result and the measurement one using the beam (not a wire) significantly enhances the reliability of the estimation of the kicker impedance at the RCS.

The theoretical results for $\beta = 0.97$ are shown in the yellow lines in Figs. 2 and 8, as well. The comparison between the results for $\beta = 0.54$ and the ones for $\beta = 0.97$ shows that the longitudinal impedance has little dependence on $\gamma$ factor, while the horizontal one is roughly proportional to $\beta$. In general, the impedance for a non-relativistic beam tends to be smaller than that for a relativistic one. However, the longitudinal wakes are excited by the beam like cosine function [11], and they are nearly constant at low frequency during the beam passage. Consequently, the longitudinal impedance has little dependence on the $\gamma$ factor at low frequency. This means that the beam tends to be more unstable horizontally than longitudinally, as it becomes relativistic.

Now, let us discuss the strategy to achieve one mega-watt goal at the RCS.

## SIMULATION/MEASUREMENT RESULTS AND THE STRATEGY TO ACHIEVE ONE MEGA-WATT GOAL AT THE RCS
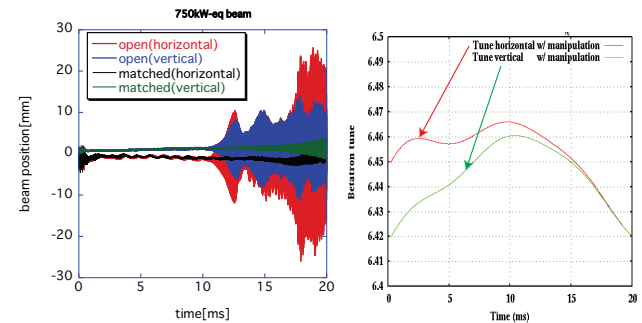


Figure 4: The left figure shows the measured beam positions of 750 kW beam for the different terminal conditions, where $\xi$ is fully corrected in the entire energy. The right figure depicts the tune behavior in the measurements.

Let us start demonstrating that the kicker impedance dominates among the RCS impedance sources. The kicker impedance is minimized by connecting matched resistors to all terminals of the cables. The procedure eliminates the spike structures in Figs. 2 and 3 by absorbing the beam-induced current into the matched resistors [8, 12]. Figure 4 shows the measured beam positions for 750 kW equivalent beam, where the chromaticity $\xi$ is fully corrected in the entire energy. When the terminals are open, the vertical motion (blue) becomes unstable accompanied with the horizontal motion (red), because the horizontal and vertical tunes merge during the acceleration. The black (horizontal) and green (vertical) lines demonstrate that the resistors remarkably suppress the beam growth rate, compared with the red and blue lines. Now, it is obvious that the kicker impedance substantially determines the preferable tune to increase the beam intensity.

Figure 5 shows simulation results for one mega-watt beam (the r.m.s size of momentum spread ($\Delta p/p$) of the injection beam from LINAC is assumed to be 0.025%.). The results is obtained with the condition that the chromaticity $\xi$ is corrected only at the injection energy. Even in the condition, the left figure predicts the beam instability, where the tunes
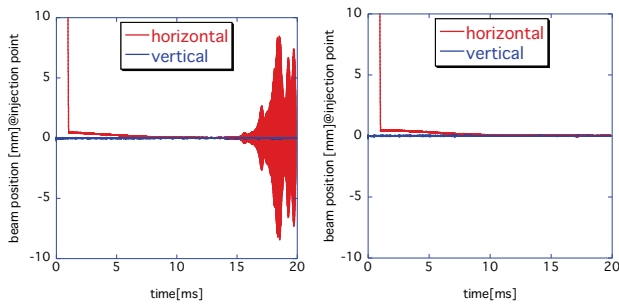
Figure 5: 1 MW simulation results, where the chromaticity $\xi$ is corrected only at the injection energy. In the left figure, the tunes $\nu_x = 6.45$ and $\nu_y = 6.42$ are fixed during the acceleration. In the right figure, the tunes change as in the right figure of Fig. 4.

$\nu_x = 6.45$ and $\nu_y = 6.42$ are fixed during the acceleration time. Nevertheless, the right figure of Fig. 5 shows that the beam instability can be avoided, if the tunes are manipulated as in the right figure of Fig. 4.
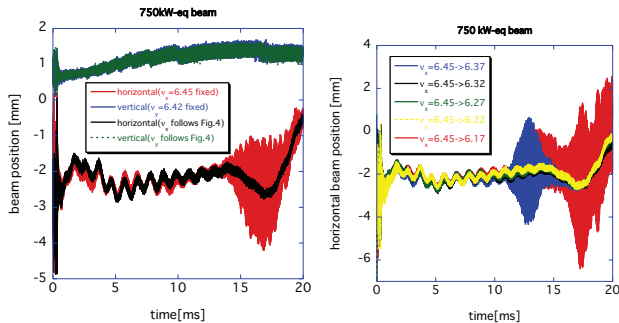


Figure 6: Measurement results of 750 kW beam, for the different tune manipulations, where the chromaticity $\xi$ is corrected only at the injection energy.

The availability of the tune manipulation is demonstrated by using 750 kW equivalent beam and the injection beam with $\Delta p/p = 0.18\%$. In the left figure of Fig. 6, the beam instability shown by the red and the blue lines (the tunes are fixed) is stabilized to be the black and the green lines by the tune manipulation (the right figure of Fig. 4). The beam with the fixed tunes becomes unstable only in the horizontal direction, because the horizontal tune and the vertical one are isolated in the case.

Several tune manipulations are experimentally challenged by gradually decreasing the tunes toward the extraction time. The right figure of Fig. 6 shows the results. Three tracking patterns ($\nu_x = 6.32, 6.27$ and $6.22$ at the extraction time) seem promising to achieve the high intensity goal.

Only tune manipulations may be insufficient to accomplish one mega-watt beam. In that case, we actively make use of the damping effect due to space charge. In the accelerator covering the intermediate energy region such as the RCS, the smaller bunching factor (average current/peak current) especially around the low energy region causes the beam stabilization by expanding the tune spread [13]. This is

realized by reducing the momentum spread of the injection beam.

To demonstrate the scheme, let us prepare for the LINAC beam with two momentum spreads (0.08% and 0.18%). The left figure of Fig. 7 shows the measured bunching factor of the beams accumulating the injection beams with the different $\Delta p/p$. The injection beam with the smaller momentum spread creates the smaller bunching factors for the RCS beam. The right figure of Fig. 7 shows the corresponding RCS beam behaviors, where $\nu_x = 6.45$ and $\nu_y = 6.42$ are fixed during the acceleration, while the chromaticity $\xi$ is corrected only at the injection energy. The beam with the smaller bunching factor is stabilized, as expected.
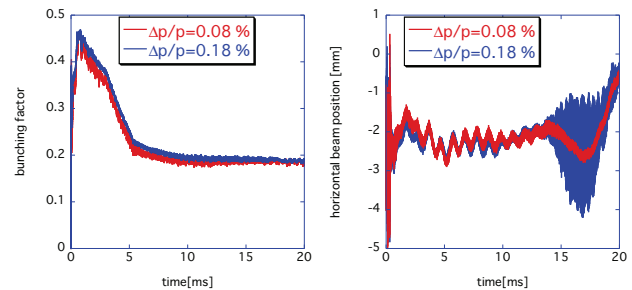


Figure 7: The measured bunching factors (left) and the horizontal beam positions for 750 kW beam (right).

In the routine operation of RCS, the sextupole magnets are turned off, and the voltage with the second harmonic RF as well as the one with the fundamental harmonic RF is excited during the injection period. In order to mitigate the space charge effect, the longitudinal painting is performed by applying the phase sweep of the second harmonic voltage (typically $-100$ degree) relative to the phase of the fundamental one, and by adequately superposing the voltage with second harmonic to the one with the fundamental harmonic in order that the injection beam feels momentum offset (typically $-0.2$ %) relative to the center of the RF-bucket (In Figs. 4-7, the phase sweep and the momentum offset are set to $-100$ degree and $-0.2$ %, respectively.).

On the other hand, the present strategy to achieve one mega-watt beam is to make maximum use of the tune manipulation combined with the space charge damping effect. When the damping effect is insufficient in reality, the bunching factor will be made lowered by activating the second harmonic voltage without the phase sweep, neither the momentum offset during the injection period.

## A REDUCTION SCHEME OF THE KICKER IMPEDANCE

In order to pursue the higher intensity beam, there is no way except reducing the kicker impedance itself. In order to reduce the impedance, main idea is to insert a resistor between the coaxial cable and PFN (pulse forming network). However, the resistor has to be isolated from PFL to ensure twice excitation current due to the superposition of the forward and backward currents to extract beams, while it needs
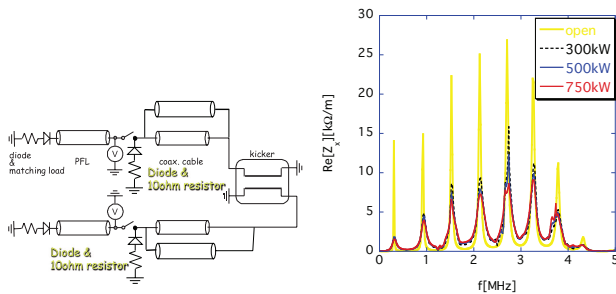
Figure 8: The terminal conditions of kicker cables (left), and the intensity dependence of the impedance at $\beta = 0.97$ (right).

to be seen by the beams to absorb the beam-induced current. A mechanism is needed to isolate the damping resistor from the pulse current from PFL. From a mechanical point of view, the easiest way is to insert a diode in front of the resistor, as in the left figure of Fig. 8.

Requirement to real diodes is that the reverse voltage $V_R$ must have at least 40 kV or higher. The most significant concern is whether the beam-induced current flows the diode having the such high reverse voltage. In order to substantially reduce the impedance of the diode, four diodes with $V_R = 65$ kV (MD04SNKJ [14]) connected in parallel are connected to the resistor.

Now, let us observe the kicker impedance. The conventional wire method cannot measure the impedance of the kicker with the diodes. This is because the measurement is basically done in frequency domain by using weak currents with Network Analyzer.

However, it is now possible to indirectly (not directly as in sec.2) find it by measuring the behavior of $R_T$ (of the diode plus resistor) in Eq.(18) for the high intensity beam. The results are shown in the right figure of Fig. 8. The impedance becomes lower as the beam intensity is higher, because the diode becomes more conductive for higher current and the terminal impedance $R_T$ approaches the characteristic impedance of the kicker. The scheme successfully makes the present kicker impedance halved or less.

## SUMMARY

The measured beam-induced voltage at the ends of the kicker cables is successfully transformed to the kicker impedance. The measurement enhances the reliability of the estimation of the kicker impedance, so that it is incorporated into the input of ORBIT.

In order to achieve high intensity beams, it is effective to utilize tune manipulations and the space charge damping effect. In other words, it is preferable that the momentum spread of the injection beam is as small as possible.

The measurements of the terminal impedance $R_T$ at the ends of the kicker cables by the beam-induced voltage/current demonstrate that the kicker impedance can be halved or less by attaching the resistors combined with four diodes in parallel there.

## REFERENCES

[1] http://j-parc.jp/index-e.html

[2] http://neutrons.ornl.gov/facilities/SNS/status.shtml

[3] J. Kamiya *et al*, 'Performance of extraction kicker magnet in a rapid cycling synchrotron', PRST Accel. and Beams **12**, 072401 (2009).

[4] Y. H. Chin *et al*, 'Impedance and beam instability issues at J-PARC rings', in the Proceedings of HB2008, Nashville, Tennessee, WGA01-1, (2008).

[5] B. Zotter and F. Sacherer, in *1st International School of Particle Accelerators "Ettore Majorana" - Theoretical aspects of the behaviour of beams in accelerators and storage rings* , Myrtle Hildred (ed.), 175, (1977).

[6] G. Nassibian, CERN/PS 84-25 (BR) (1984).

[7] K. Y. Ng, AIP Conference Proceedings **184**, 472 (1989).

[8] Y. Shobuda *et al*, 'Measurement scheme of kicker impedances via beam-induced voltages of coaxial cables', NIMA **713**, 11, 52-70, (2013).

[9] Y. Shobuda *et al*, 'Analytical approach to evaluate coupling impedance of traveling kicker magnets', NIMA **691**, 11, 135-151, (2012).

[10] *Handbook of Accelerator Physics and Engineering*, ed. A. W. Chao and M. Tigner (1999).

[11] A. W. Chao, *Physics of collective beam instabilities in high energy accelerators*, (Wiley, New York, 1993).

[12] Y. Shobuda *et al*, 'A trial to reduce the kicker impedance of 3-GeV RCS in J-PARC', in the Proceedings of IPAC2013, Shanghai, China, 1742, (2013).

[13] Y. Shobuda *et al*, 'Mitigation of beam instability due to space charge effects at 3GeV RCS in J-PARC', in the Proceedings of IPAC2011, San Sebastian, Spain, MOPS004, (2011).

[14] http://www.origin.co.jp/

# RING SIMULATION AND BEAM DYNAMICS STUDIES FOR ISIS UPGRADES 0.5 TO 10 MW

D.J. Adams, B. Jones, B.G. Pine, C.R. Prior*, G.H. Rees*, H.V. Smith, C.M. Warsop,
R.E. Williamson, ISIS and *ASTeC, Rutherford Appleton Laboratory, STFC, UK

## Abstract

Various upgrade routes are under study for the ISIS spallation neutron source at RAL in the UK. Recent work has concentrated on upgrading the injector, increasing injection energy from 70 to 180 MeV, and studying the challenging possibility of reaching powers up to 0.5 MW in the existing 800 MeV RCS. Studies for the longer term are exploring the possibilities of a 5 MW, 3.2 GeV RCS that could form part of a new stand-alone 10 MW next generation "ISIS II" facility. A central part of these ring studies is the use of computer simulations to guide designs, for example optimising the injection painting configuration and providing an indication of expected loss levels. Here we summarise the computer models used, indicate where benchmarking has been possible, describe optimisations and results from studies, and outline the main uncertainties. Understanding the limitations in high power RCS accelerators is an important part of determining optimal facility designs for the future.

## INTRODUCTION

A range of ISIS upgrade routes is now under study, a lower beam power regime of 0.5 MW, and a higher power regime from 1 MW upwards. A key factor determining the optimal beam power for future short pulse spallation sources will be the results of ongoing target and moderator studies, which are working to optimise the brightness of neutron beams for the user.

In the lower power regime, an upgrade replacing the existing 70 MeV ISIS linac with a new 180 MeV injector is the favoured route. This could potentially boost powers to 0.5 MW and also address obsolescence issues with the present linac. This paper summarises the design of the beam dynamics for the existing ISIS RCS with the new 180 MeV injector.

For the higher power routes, a new stand alone option ("ISIS II") is the favoured route, with an initial beam power of 1 - 2 MW, capacity for multiple targets and further upgrade routes to 5 or even 10 MW. Studies are presently concentrating on a "base-line" option, consisting of an 800 MeV H⁻ linac and a 3.2 GeV RCS, which has been studied in some detail [1]. Such a design would have the potential for 2 – 5 MW with a single ring, and 10 MW with two stacked rings. Understanding the limitations and optimising parameters for this 3.2 GeV RCS are thus an important step in identifying the best designs. Other options, (e.g. FFAGs), will have to compare favourably with this base-line. Initial results from 1D and 3D simulations of the 2 - 5 MW, 3.2 GeV RCS are also presented below.

## 180 MEV INJECTION UPGRADE

The main potential benefits to the synchrotron of a new higher energy linac, chopper and energy ramping injection line are reduced transverse space charge and more flexible, optimised transverse and longitudinal injection systems.

Currently a 70 MeV, 25 mA H⁻ linac provides a pulse length of 200 µs for injection into the RCS. Beam is accumulated via charge exchange through a foil centred in a 4-magnet, symmetric, horizontal bump, with 45 mr deflections. Beam is painted dispersively in the horizontal plane, exploiting orbit motion due to the falling main magnet field. Vertically a sweeper magnet paints the position at the foil. About $3\times10^{13}$ protons per pulse (ppp) are accumulated over 130 turns. Transverse acceptances are collimated at ~$350\,\pi$ mm mr using an adjustable collector system.

The DC accumulated beam is non-adiabatically trapped into two bunches by the ring dual harmonic RF (DHRF) system. The RF system consists of 10 ferrite tuned cavities, with peak design voltages of 168 and 96 kV/turn for the $h$=2 and 4 harmonics respectively. Nominal betatron tunes are $(Q_x, Q_y)$=(4.31, 3.83), with peak incoherent tune shifts of ~0.5. Intensity is loss limited: the main mechanisms are longitudinal trapping, transverse space charge and stability. Single turn extraction uses a fast vertical kicker and septum.

Most of the existing ring would remain unchanged for the upgrade. However, a new injection straight with higher field bump magnets and new injection beam dumps would be required. Also the ring collimation system would need modifications to intercept beam losses at higher energies. To facilitate hands on maintenance machine activation levels would be kept at existing levels.

### Transverse Space Charge and Stability

Reduction of transverse space charge with increasing injection energy is expected to scale as $\beta^2\gamma^3$ allowing the existing injection intensity of $3\times10^{13}$ ppp at 70 MeV (0.2 MW) to be raised to $8\times10^{13}$ ppp (0.5 MW). This simple scaling law gives basic guidance, but detailed assessment and simulations with the in-house code Set [2] confirm that these intensities are the upper limit, which depend on achieving optimal bunching factors, emittances and working points. The smaller energy ramp, 180 - 800 MeV, also reduces emittance damping, which will require a small increase in the extraction system acceptance [2]. Instabilities are one of the major concerns with the most obvious problem being resistive-wall head-tail already observed on ISIS [3]. This is presently avoided by lowering $Q_y$. The growth rate can be expected

to scale strongly with intensity, and lowering $Q_y$ further will tend to increase loss associated with the half integer resonance. The development of a damping system is expected to resolve this issue [4].

### Injection Scheme Specification

The new injection system assumes a linac beam current of 43 mA and a chopping duty cycle of 70% which requires 500 µs (~500 turns) to accumulate $8 \times 10^{13}$ ppp. There is some freedom in selecting the timing of injection with respect to the main magnet field minimum: on the falling edge, symmetrically, or the rising edge.

The ring injection straight geometry is based on the existing design but the injection point is moved from the inside of the ring to the outside. This reduces the injection beam line complexity, and also the impact on ISIS operations, by making construction of all components (excluding the ring injection straight) independent of the existing machine. The new injection foil would be graphite of thickness 200 µg/cm$^2$ and have an expected stripping efficiency of >99.75% [5]. A schematic of the layout is shown in Figure 1.
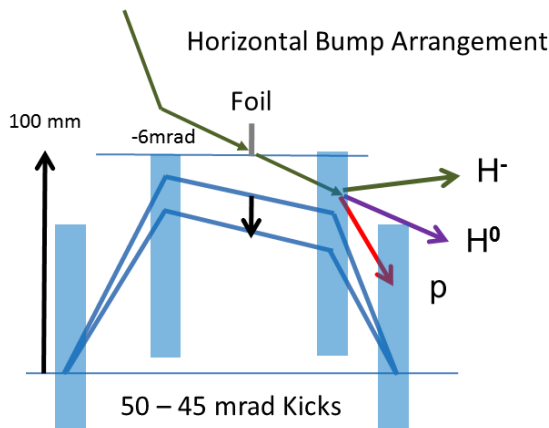


Figure 1: Schematic of injection straight.

A basic design principle has been to include as much flexibility in the beam parameters as possible, within the constraints of achieving practical hardware designs. With this in mind, transverse painting schemes allow for centroid amplitudes in the range 60 - 200 $\pi$ mm mr in both planes, with free choice of correlation schemes. The beam must be accumulated and accelerated within maximum emittances of ~300 $\pi$ mm mr to stay within the acceptance of the ring collimators and extraction system.

Longitudinal injection control is enhanced with the use of a chopper, with the aim to maximise the bunching factors (>0.4). The chopper requires timing modulations to track the injection line energy ramping, ±1 MeV, and varying beam revolution frequency in the synchrotron. RF requirements are limited to the peak design voltages of 168 and 96 kV/turn for the $h$=2 and 4 harmonics respectively. To facilitate hands on maintenance, loss levels of less than ~0.1% are required. These must be controlled, i.e. localised in the injection and collimator straights.

### Transverse Painting and New Injection Straight

The injection point in the new design is on the outside of the ring, at a horizontal displacement of 100 mm and angle of 6 mr with respect to the ring central axis. Capability for centroid painting in the range 60 - 200 $\pi$ mm mr in both planes is included.

The beam is painted horizontally using a combination of dispersive painting (injection energy mismatch to ring synchronous energy) and changing the local bump amplitude and angle at the foil. Dispersion at the foil is 2 m, 0.37 mr providing typical painting amplitudes 0 - ±10 mm and angles ±2 mr for a ±1 MeV variation in injection energy. The bump deflection angles are constrained to the range 45 - 50 mr providing a local displacement and angle at the foil 70±5 mm, ±10 mr respectively. The lower bound, 45 mr, conserves the position of the H$^0$ beam dump. The upper bound of 50 mr is considered the maximum deflection angle achievable in a magnetic design [6].

Vertical painting is achieved by varying the injection angle, 2 - 6 mr, at a constant displacement with respect to the ring central orbit of 20 mm. Beam parameters on the foil are controlled by two upstream steering magnets per plane in the transport line, which are programmed through the injected pulse. Horizontal and vertical phase space plots of the full painting amplitudes, 60 - 200 $\pi$ mm mr, are shown in Figure 2. The corresponding bump magnet angular deflections for injection symmetrically about field minimum and a schematic of the real space layout are also shown.
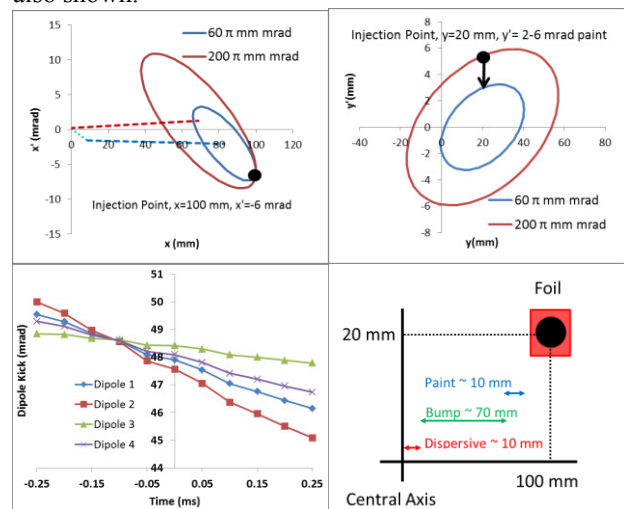


Figure 2: Transverse phase space (top), bump angular deflections over injection and real space layout (bottom).

Magnetic models of the injection straight using OPERA [7] have been used to track injection trajectories of the H$^-$, H$^0$ and protons to confirm beam dump positions and aperture clearances [5].

Vertical painting schemes are unconstrained for any injection timing. However, increasing or decreasing horizontal painting amplitudes for correlated, constant and anti-correlated schemes can only be achieved for

injection symmetrically about field minimum. Therefore, symmetric injection timing is the preferred choice.

*Longitudinal Painting and Acceleration*

The basic viability of accelerating $8\times10^{13}$ ppp ($4\times10^{13}$ per RF bucket) with the existing RF system has been confirmed by simulating the acceleration of an invariant Hofmann-Pedersen (HP) distribution [8, 9] taking into account space charge. If no further RF capacity is available this defines an upper limit to the painted longitudinal emittance for multi-turn injection as emittance increases during injection are inevitable. Therefore, given the chopping duty factor, an energy painting amplitude was chosen to accumulate a beam within that emittance. It is also noted that beam stability measured using the Keil-Schnell-Boussard (KSB) criterion [10] is strongly dependent on the energy spread of the beam. Within these constraints the painting amplitude as a function of time was chosen, alongside the RF phases, to paint the beam as close to a HP as possible.

The proposed painting scheme is an optimisation of previous longitudinal simulations [8], injecting symmetrically about the main magnet field minimum (-0.25 – 0.25 ms) with the injection energy sweeping non-linearly between 181.2 and 182.2 MeV. This is combined with a non-linear RF steer to paint the beam in energy from the centre of the RF bucket to 1.3 MeV off axis. The maximum injected momentum spread available from the injector design, $1.0\times10^{-3}$ is used. RF volts are held constant at 74 and 55.5 kV per turn for $h$=2 and $h$=4 respectively through injection, and the phase between them is varied to maximise the bunching factor, and emittance by maintaining a stationary bucket. A schematic of the process is shown in Figure 3.
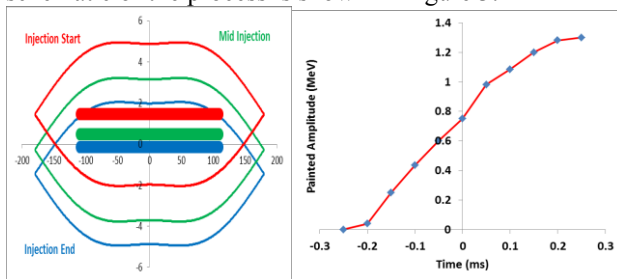


Figure 3: Longitudinal phase space painting of beam and RF bucket (left), with painting amplitudes (right).

Parameters through acceleration peak at 157.3 and 115.5 kV per turn for $h$=2 and $h$=4 respectively with the phase between the two systems varying between 9 and -64°. Second harmonic voltages are slightly above current ISIS limits to reduce losses inferred from 3D studies detailed in the next section.

The longitudinal simulation results of this injection scheme, using an in-house 1D code [8], are summarised in Figure 4. They show a well-controlled beam with bunching factors >0.4 and stability parameter [8] peaking just above 1. Options for increasing gap volts and dealing with the additional beam loading due to high intensity beams are currently under study.
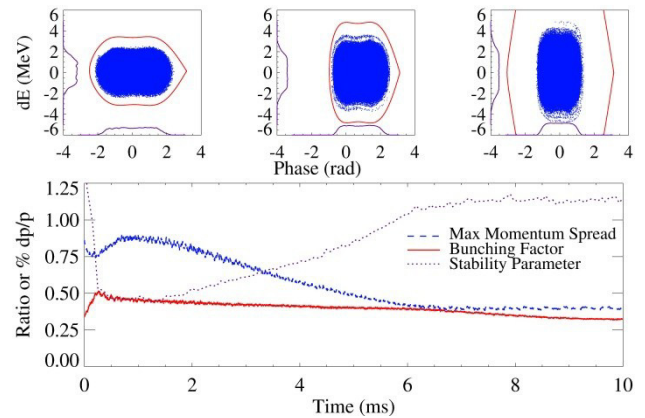


Figure 4: Phase space at the end of injection, 5 and 10 ms (top), evolution of bunching factor, stability parameter, peak dp/p for proposed injection scheme (bottom).

*The ORBIT 3D Model*

3D simulations of injection and acceleration use the ORBIT code [11] with modifications to allow RF bucket offsets. The ISIS ring is described using linear transfer matrices generated in MAD [12]. Injection dipoles are modelled using horizontal kicks which are dynamic during injection and then reduced to zero over 100 µs. The foil is modelled as a square, 11x11 mm, corresponding to the size of the injected beam at 3.33 sigma. Beam vacuum vessels and collimators are included. Space charge is simulated with the 3D space charge routine using a transverse grid of 128x128 and 64 longitudinal bins. Half integer driving terms are included by using quadrupole errors in the MAD model at expected levels for machine errors. Coherent instabilities are not included. A single bunch is modelled.

This simulation is based on the model benchmarked against the present ISIS machine [13] where comparisons with measurements of longitudinal profiles and beam losses showed reasonable agreement. The model has also shown good agreement with measured transverse profiles though injection [14].

Convergence tests show 5 M macro particles produce beam loss results at 0.1% levels with a deviation of 0.001%. Emittance evolutions change by 2% between 2.5 and 5 M particles. Random seed tests show deviations within these limits. Hence 5 M particles are used for final simulation results.

*Injection Painting Amplitudes*

The aim of the 3D painting process is to establish a stable beam distribution of $8\times10^{13}$ ppp ($4\times10^{13}$ per bucket) within machine acceptances and minimal losses. Non-linear space charge forces lead to complicated dependencies on painted centroid emittances, tune, and bunching factors. Therefore, to identify viable working parameters a set of ORBIT scans was performed, monitoring emittance over 1000 turns for different painting conditions. For each scan centroid emittances were constant through injection. The set of scans explored the effects of varying the centroid emittances in both

planes from 60 - 110 $\pi$ mm mr. In all cases the injected beam un-normalised RMS emittance was 0.46 $\pi$ mm mr.

The results, the evolution of 99% emittances for selected painting cases, are shown in igure 5. The aim was to produce the lowest emittance, stable beam on turn 1000 with minimal beam loss. Final results indicated painting amplitudes for centroid emittances of $(\varepsilon_{xc}, \varepsilon_{yc})$=(100, 65-75) $\pi$ mm mr produced beams with 99% emittances of $(\varepsilon_{x99\%}, \varepsilon_{y99\%})$=(343, 242) $\pi$ mm mr. This is easily accommodated within the collimated acceptance of the ring $(\varepsilon_{collx}, \varepsilon_{colly})$≈(400, 322) $\pi$ mm mr. The resulting distributions are shown in Figure 6.
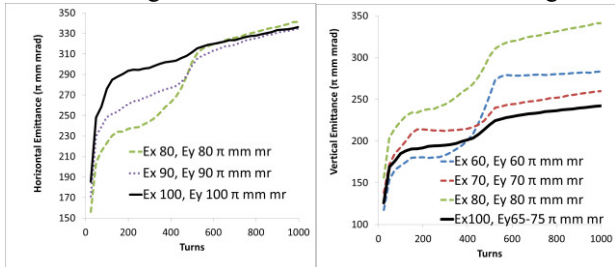


Figure 5: Emittance evolution for varying centroid painting amplitudes.
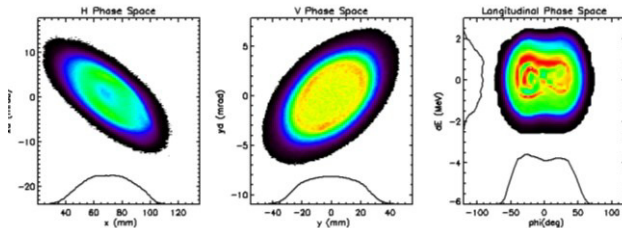


Figure 6: Phase space plots at the end of injection for optimised painting.

The foil produced 3.7 re-circulations per injected proton for the best case. Foil temperatures peak at 1657 K for 50 Hz machine operation [5] which is within safe operating temperatures.

## Working Point and Envelope Errors

A main loss mechanism in the upgrade is expected to be related to half integer loss – particularly if head-tail instability forces a reduction in $Q_y$ [15]. Therefore effects of working point and representative quadrupole driving term (DT) errors were studied with ORBIT.

Simulations were run with a nominal beam for two working points, the design $(Q_x, Q_y)$=(4.31, 3.83) and a raised $(Q_x, Q_y)$=(4.41, 3.93), and with representative quadrupole DTs on and off. Collimators were placed at 100% acceptance and normal apertures included. For each case evolution of 99% emittance and beam loss were recorded.

Evolution of emittances are shown in Figure 7 with the total loss indicated in the legend. It can be seen that adding the error term increases emittance and total loss at both working points. As expected, moving the working point up, away from resonance, reduces growth with and without driving terms but surprisingly does not reduce losses.

Whilst behaviour of emittances was as expected, beam loss levels were complicated by an additional effect due to the conformal ISIS vacuum vessels. Around most of the machine, apertures are matched to the design envelope, and working point, of the lattice: this is included in the ORBIT model. Once the tune is changed, the mis-match with the aperture effectively reduces the useful acceptance. These simulations demonstrated that, while losses were low, it was an important effect, with loss location correlating with expected ripple in the beta function. Therefore, the higher losses at the higher $Q$ suggest the design working point may be better. This important, if subtle, effect and possible remedies will be studied further.
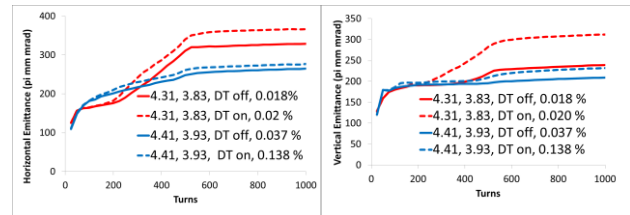


Figure 7: Emittance evolution at 99% occupancy with varying Q and harmonic envelope errors.

## ORBIT Results Summary

Studies in the previous section have guided optimisations to a workable solution. An injection painting parameter set has been found based on transverse painting amplitudes in the horizontal and vertical planes of 100, 65 - 75 $\pi$ mm mr respectively. This incurs 3.7 foil re-circulations equating to a maximum foil temperature of 1657 K. Longitudinally a chopper with 61% duty cycle, painted amplitude 0 - 1.3 MeV and choice of RF parameters show good control with bunching factors at the end of injection 0.51 and >0.4 for the remainder of acceleration. Simulations with 5 M macro particles suggest losses of 0.082% when collimators are inserted at 80% of the aperture.

Whilst the simulation produces a loss of <0.1%, this result will not reflect an accurate machine performance. At this stage the result suggests a plausible and workable design. Future studies to refine the design involve inclusion of non linear optics, impedances and magnet errors.

## MULTI MW UPGRADE RING STUDIES

### Multi MW Ring

Plans for an accelerator complex capable of producing 2 - 10 MW beams centre on the use of an 0.8 - 3.2 GeV RCS [1]. This lattice design is based on a 5 super period, 370 m circumference ring, optimised for low loss multi turn injection through a foil located in the middle of an 8° dipole operating at 30 Hz (2 MW). Transverse injection painting is dispersive in the horizontal plane and uses 4 local ring bump magnets in the vertical plane for accumulation of $1.3\times10^{14}$ protons. The beam is chopped longitudinally, trapped and accelerated with a $h$=4 single harmonic RF system. Increasing the repetition rate to

50 Hz and intensity to $2.0 \times 10^{14}$, provides an upgrade path to 5 MW. Two such rings, stacked, could then provide 10 MW.

The initial 30 Hz option has undergone some initial studies and results are given below. This design assumes a linac current of 57 mA with chopping duty factor ~50%, injecting over 800 μs (550 turns) starting 400 μs before magnetic field minimum.

### 1D Design and Results

Initial calculations for RF parameters are centred on the voltage required to remain synchronous with the main magnet field and overcome longitudinal space charge forces. The induced longitudinal space charge voltage will never exceed 40% of the applied RF voltage [9]. This determines an RF accelerating voltage profile.

The basic viability of accelerating $1.3 \times 10^{14}$ ppp ($3.25 \times 10^{13}$ per bucket) with these parameters has been tested using an in-house longitudinal particle tracking code [11] including space charge and a measure of beam stability using the KSB criterion [10]. A HP distribution [9] created at main magnet field minimum accelerated stably with no filamentation or beam loss.

Preliminary longitudinal simulations (see Figure 8) have shown that the requisite intensity can be accelerated within the design specifications. RF volts are held constant at 100 kV per turn through injection and peak at 450 kV per turn mid-cycle. The injected beam energy and RF steer are used to paint the injected beam linearly from the centre of the RF bucket to 2.1 MeV off axis.

However, as also shown in Figure 8, the stability criterion is broken towards the end of the acceleration cycle (>15 ms). Further simulations and analytical calculations are required to meet this criterion, optimise longitudinal painting and hence define the RF system requirements.
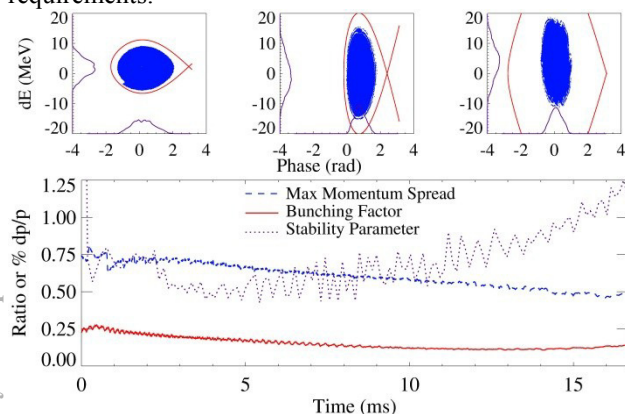


Figure 8: Phase space at the end of injection, 8.33 and 16.67 ms and evolution of bunching factor, stability parameter [8] and maximum dp/p.

### 3D Design and Results

The ring acceptance has been designed to accomodate a maximum unnormalised accumulated beam emittance of $135 \, \pi$ mm mr in each plane. Painting studies suggest anti-correlated painting with centroid emittances 60 - 40

and $50 - 70 \, \pi$ mm mr in the horizontal and vertical planes respectively produce reasonable beam distributions with 99% emittance of 147 and $150 \, \pi$ mm mr. This requires ±2.5 MeV control in injection energy and up to 32 mr deflection angles on local steering magnets. Beam distributions produced by ORBIT simulations at the end of injection are shown in Figure 9. Results look promising but many further studies are planned.
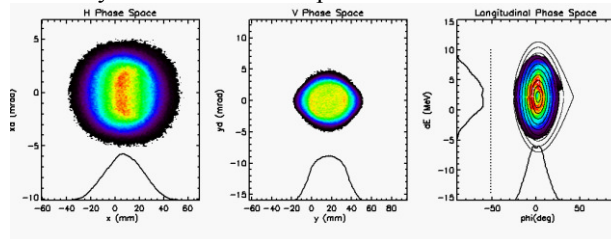


Figure 9: Phase space at the end of injection.

## REFERENCES

[1] G.H. Rees, "Linac, Beam Line and Ring Studies for ISIS Upgrades", ASTeC internal report GHR1, (2009).

[2] B.G. Pine, "An Assessment of Transverse Dynamics for the 180 MeV Injection Upgrade for ISIS", internal report.

[3] R.E. Williamson et al., "Simulations of the Head-Tail Instability on the ISIS Synchrotron", MOPAB38, HB2014, to be published.

[4] S.J. Payne, "Strip Line Monitor Design for the ISIS Proton Synchrotron Using the FEA Program HFSS", IBIC2013, UK, pp. 435 – 437 (2013).

[5] B. Jones et al., "Injection and stripping foil studies for a 180 MeV injection upgrade at ISIS", HB2012, China (2012).

[6] A.J. McFarland, "21kA Pulsed Dipole Power Supply Design for the 180MEV Injection System Upgrade studies at ISIS", IET Conf. Pub.Volume 2009 Issue CP553.

[7] Opera Vector Fields, www.cobham.com

[8] R.E. Williamson et al., "High Intensity Longitudinal Dynamics Studies for an ISIS Injection Upgrade", HB2012, pp. 492-496 (2012).

[9] A. Hofmann, F. Pedersen, "Bunches with Local Elliptic Energy Distributions", IEEE Trans. Nucl. Sci., 26-3, p.3526 (1979).

[10] D. Boussard, "Observation of Microwave Longitudinal Instabilities in the CPS", CERN Report CERN-LAB II/RF/Int./75-2 (1975).

[11] J.A. Holmes, "ORBIT Beam Dynamics Calculations for High Intensity Rings", EPAC02, France (2002).

[12] The MAD Program Version 8.16. Hans Grote. CERN/SL/90-13 (AP) Rev 4.

[13] D.J. Adams et al., "Beam Loss Studies of the ISIS Synchrotron using ORBIT", IPAC12, USA (2012).

[14] B. Jones et al., "Injection Optimisation on the ISIS Synchrotron", EPAC08, Italy (2008).

[15] C.M. Warsop et al., "High Intensity Studies on the ISIS Synchrotron, Effects of Half Integer Resonance", HB2010, Switzerland, (2010).

# RECENT RESULTS ON BEAM-BEAM EFFECTS IN SPACE CHARGE DOMINATED COLLIDING ION BEAMS AT RHIC*

C. Montag, BNL, Upton, NY 11973, USA

## Abstract

To search for the critical point in the QCD phase diagram, RHIC has been colliding gold ions at a variety of beam energies ranging from 2.5 GeV/n to 9.8 GeV/n. During these low energy operations below the regular injection energy, significant lifetime reductions due to the beam-beam interaction in conjunction with large space charge tune shifts have been observed. Extensive simulation studies as well as beam experiments have been performed to understand this phenomenon, leading to improved performance during the 7.3 GeV run in FY2014.

## INTRODUCTION

The Relativistic Heavy Ion Collider RHIC was designed to collide beams of fully stripped Au ions at a top energy of 100 GeV/nucleon. To search for the critical point in the QCD phase diagram, center-of-mass energies in the range from 5 to 20 GeV per nucleon pair are required, which extends far below the nominal RHIC injection energy of 9.8 GeV/nucleon. At such low energies, the space charge tune shift becomes significant, and typically exceeds the beam-beam tuneshift by an order of magnitude [1].

When RHIC operated at beam energies of 3.85 and 5.75 GeV/nucleon in 2010, a significant reduction in beam lifetime due to the beam-beam interaction was observed, as illustrated in Figure 1. During that entire physics run, the working point was set at $(Q_x, Q_y) = (28.13, 29.12)$ as the result of a brief tune scan.
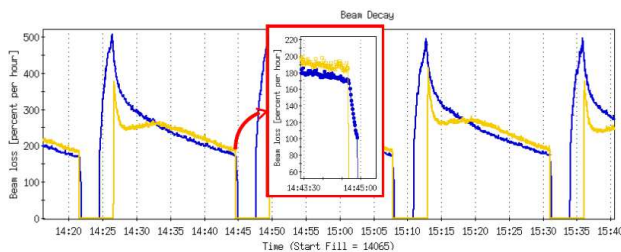


Figure 1: Beam decay rates during several Au beam stores at 5.75 GeVnucleon beam energy. The Blue beam decay rate improves dramatically as soon as the Yellow bean is dumped at the end of each store (see insert). Note that the algorithm to calculate the beam decay rate from the measured beam intensity has a time constant of 20 sec. Hence, the actual drop in instantaneous beam decay is even more dramatic than suggested by the picture.

To gain a better understanding of beam-beam effects in space charge dominated colliding ion beams, extensive sim-

ulations have been performed. In the following sections, we describe the simulation methods and present results on emittance growth as well as frequency map analysis and diffusion studies.

## TRACKING MODELS

Space charge simulations tend to be very CPU-time consuming due to the frequent recalculations of the particle distributions and associated electro-magnetic fields. However, in the particular problem under study here, we can take advantage of the fact that the evolution of the particle distribution is comparatively slow, as indicated by the experimentally observed beam decay of several hundred percent per hour, which is equivalent to a beam lifetime of tens of minutes. Since typical simulations track particles only over a number of turns that corresponds to seconds in real beamtime, we can therefore assume that the particle distribution remains constant in amplitude space over the course of the simulation. This approach, which is similar to the weak-strong method of beam-beam simulations, significantly speeds up the simulation. In addition, since re-calculating the electro-magnetic fields from the actual particle distribution is avoided, no artificial noise due to the limited number of particles is introduced into the simulation. Furthermore, since the space charge kicks do not depend on the actual distribution of test particles, we can apply methods such as frequency map analysis or action diffusion that require special, non-realistic distributions.

Two different accelerator models are used for tracking, a simplified "toy model", and the realistic RHIC lattice. The simplified model consists of 11 FODO cells. The quadrupoles are modeled as thin lenses, while the dipoles in this "ring" are just drifts, i.e. their bending radius is infinite. 10 of these FODO cells are identical, while in the 11th cell the quadrupole strengths are increased by 3 percent to break the periodicity of the lattice. The phase advance per FODO cell is approximately 108 degrees, depending on the exact working point. In the center of one of the drifts of the 11th cell a beam-beam kick is applied. The drift spaces ("dipoles") are subdivided into 32 slices of equal length each; at the end of each slice a space charge kick is applied according to the local $\beta$-functions and the beam emittance, which is assumed to be constant. The tune is adjusted using all quadrupoles simultaneously. The space charge tune shift in this model is set to $\xi_{sc} = -0.05$, while the beam-beam tune shift is set to $\xi_{bb} = -0.003$. In cases without beam-beam interaction, the space charge tune shift is set to $\xi_{sc} = -0.053$; this ensures that the total tune shift is identical in both cases.

The large number of defocusing space charge and beam-beam kicks modifies the optics, and therefore the $\beta$-functions at each kick location, while the kicks themselves depend on the local RMS beam sizes and therefore the actual $\beta$-functions. In a first step, the self-consistent $\beta$-functions in the presence of (linearized) space charge and beam-beam kicks are determined. Using this information, in the second step test particles are tracked and the appropriate space charge and beam-beam kicks are applied at each slice, depending on the local RMS beam sizes.

The second approach uses the MADX-SC program to model space charge in the real RHIC lattice. Space charge kicks are applied at each quadrupole, while beam-beam collisions are modeled at IPs 6 and 8. Multipole errors are added to each dipole and each quadrupole based on measurements on a single spare dipole and a single spare quadrupole at a field strength corresponding to 2.5 GeV/nucleon Au ions. Since this model had been benchmarked against dynamic aperture measurements with 5.86 GeV protons, which have the same rigidity and therefore use the same lattice as 2.5 GeV/nucleon Au ions, measured beam parameters for 5.86 GeV protons are used throughout the study. Table 1 lists the relevant beam parameters used in this study.

Table 1: Beam Parameters for the MADX-SC RHIC Tracking Model

| | |
|---|---:|
| beam energy [GeV] | 5.86 |
| bunch intensity | $4 \cdot 10^{10}$ |
| transverse rms emittance [mm mrad] | 0.16 |
| $\beta^*$ [m] | 10 |
| $\sigma_{\mathrm{IP}}$ [mm] | 1.3 |
| RMS bunch length [m] | 3.0 |
| space charge tune shift | -0.065 |
| beam-beam tuneshift per IP | -0.005 |

## RESULTS

Most of the tracking studies were performed using the simplified "toy" model. As a first step, a tune scan was performed along a parallel to the coupling resonance, from $(Q_x, Q_y) = (3.09, 3.08)$ to $(3.35, 3.34)$, and the emittance growth rate was determined by tracking 1000 particles over 20000 turns and fitting a straight line to the turn-by-turn 4D emittance data. The number of slices, and therefore space charge kicks, per drift was set to 8, 16, and 32, respectively, to determine the necessary number of slices. This study resulted in the number of slices set to 32 throughout the entire tracking study.

Adding the beam-beam kick leads to an additional breaking of the periodicity of the lattice. To ensure that the observed emittance growth is indeed caused by the nonlinear nature of the beam-beam force and not due to broken periodicity, we compare the results obtained with the nonlinear beam-beam kick with those using only the linearized part of the beam-beam force. As Figure 2 demonstrates, the observed emittance growth is indeed dominated by the nonlinearity of the beam-beam kick. With the nonlinear
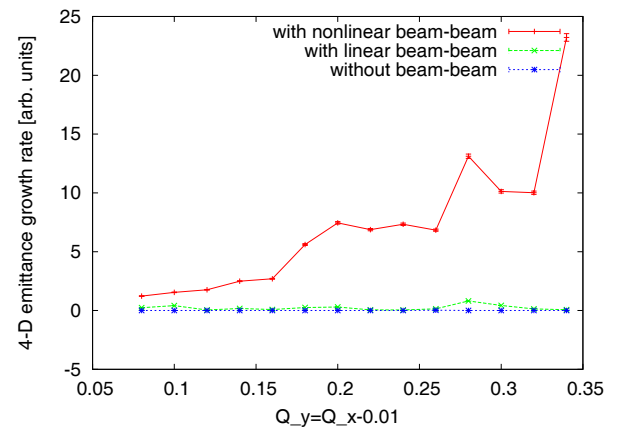


Figure 2: Emittance growth rates during a tune scan with a nonlinear (red) and a linearized (green) beam-beam kick in addition to the nonlinear space charge kicks. The blue line corresponds to the case without any beam-beam interaction.

beam-beam kick added, tunes close to the integer exhibit the smallest emittance growth, while the emittance growth rate increases almost monotonically with the distance from the integer. Without the beam-beam kick, no emittance growth is observed within the error bars of the linear fit at any working point during the scan, which is in qualitative agreement with experimental observations of beam lifetime.

To provide a better understanding of the underlying mechanism causing the emittance growth in the presence of the beam-beam interaction, the method of frequency map analysis was used. For this purpose, a single test particle was tracked over 1024 turns, and the tune for the first and last 512 turns was determined to high precision using an interpolated FFT technique [2]. As Figure 3 shows for the FY2010 fractional working point $(Q_x, Q_y) = (.13, .12)$, the presence of the beam-beam interaction results in a significant enhancement of tune diffusion, especially along the coupling resonance $Q_x = Q_y$. A similar picture is obtained at the near-integer working point $(Q_x, Q_y) = (.09, .08)$, as shown in Figure 4.

Comparing these two working points in amplitude space yields similar results, Figure 5, with the near-integer working point showing slightly higher tune diffusion at smaller amplitudes. This is surprising insofar as the tune scan (Figure 2) indicates a significantly smaller emittance growth at these tunes.

All results presented so far are obtained in a purely linear lattice, with the space charge and beam-beam forces being the only non-linearities. This limitation is overcome by tracking in the realistic RHIC lattice with its known non-linearities, both from lattice sextupoles and multipole errors. Comparing tune diffusion in the RHIC lattice for the FY2010 working point, $(Q_x, Q_y) = (.13, .12)$, and the near-integer working point $(Q_x, Q_y) = (.095, .085)$ shows higher tune diffusion at smaller amplitudes at the near-integer working point than at $(.13, .12)$, see Figure 6. This is in stark contrast to experimental results obtained during beam experiments in previous years as well as during FY2014 which showed

**Computational Challenges, New Concepts and New Projects**
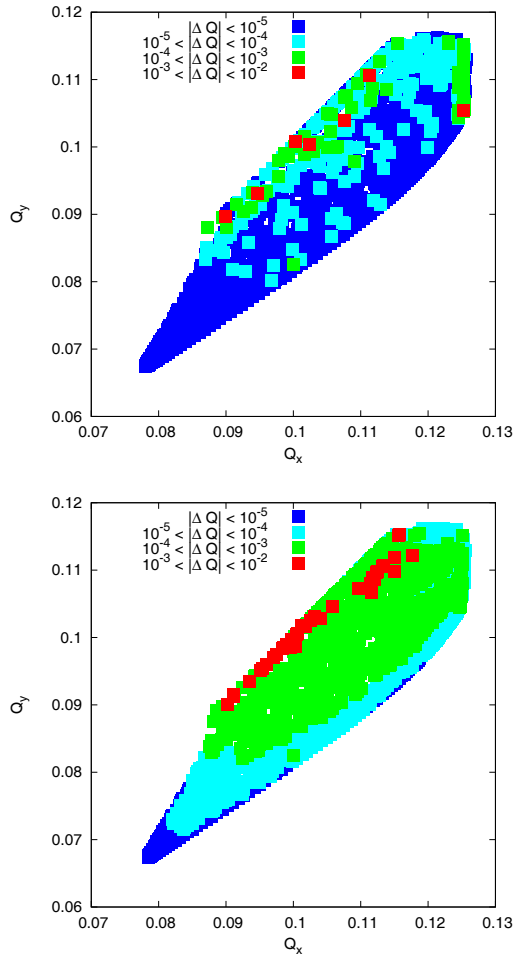
Figure 3: Tune footprints in the "toy" model without (top) and with (bottom) beam-beam interaction, for a working point of $(Q_x, Q_y) = (.13, .12)$.
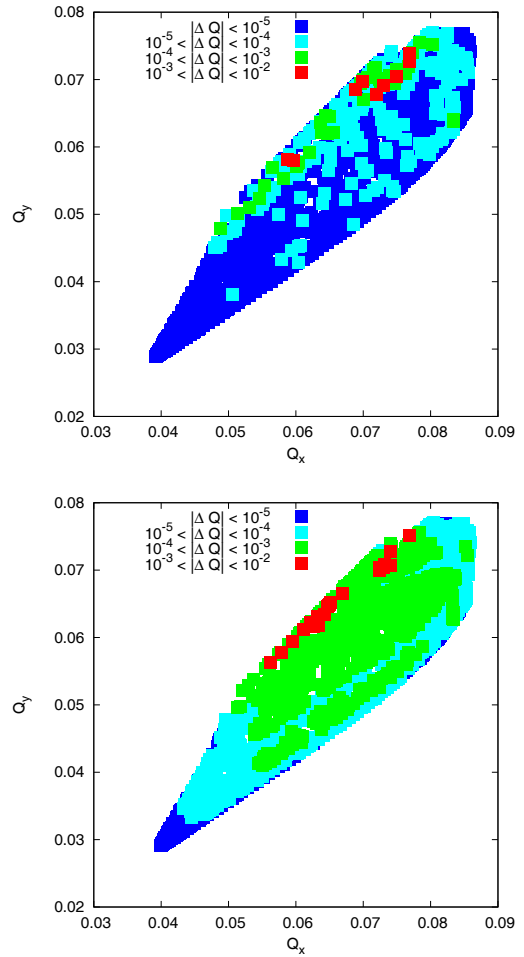


Figure 4: Tune footprints in the "toy" model without (top) and with (bottom) beam-beam interaction, for a working point of $(Q_x, Q_y) = (.09, .08)$.

improved beam lifetime in collisions at the near-integer working point [3, 4]. Dynamic aperture simulations qualitatively agree with this experimental result as well.

The fact that those areas with enhanced diffusion correspond to particles on or near the linear coupling resonance $(Q_x = Q_y)$ leads to the suspicion that at least on this particular resonance tune diffusion does not necessarily indicate amplitude diffusion. To prove this theory, we perform a tune scan on the linear coupling resonance and record the emittance growth as a function of tune, using our "toy" model. As Figure 7 shows, there is still no emittance growth without beam-beam interaction.

If we now perform a frequency map analysis at the working point $(Q_x, Q_y) = (.08, .08)$, we notice very strong tune diffusion even at small amplitudes, as depicted in Figure 8. The fact that this tune diffusion does not translate into emittance growth proves that frequency map analysis is misleading when studying beam-beam effects in space charge dominated ion beams. Instead of tune diffusion, we therefore study amplitude diffusion.

We define the amplitude diffusion coefficient as [5]

$$D(J_x, J_y) = \lim_{N \to \infty} \frac{\sigma_{J_x}^2(N) + \sigma_{J_y}^2(N)}{N}, \quad (1)$$

where $N$ denotes the number of turns and $\sigma_{J_x}(N), \sigma_{J_y}(N)$ the rms action spread at turn $N$ of a set of particles launched at identical horizontal and vertical action values $J_x, J_y$ in phase space.

At regular intervals in the $(J_x, J_y)$ space, we launch 100 particles of equal action $J_{x,i}, J_{y,i}$ in phase space and track them over 10000 turns. After each turn $N$, we calculate the RMS action spread

$$J_{\text{RMS}}(N)^2 = \langle (J_i(N) - \langle J(N) \rangle)^2 \rangle \quad (2)$$
$$= \langle (J_{x,i}(N) - \langle J_x(N) \rangle)^2$$
$$+ (J_{y,i}(N) - \langle J_y(N) \rangle)^2 \rangle \quad (3)$$

and perform a linear fit

$$J_{\text{RMS}}(N)^2 = a + bN \quad (4)$$
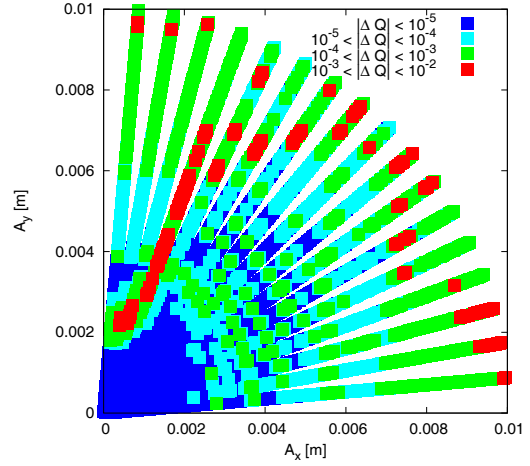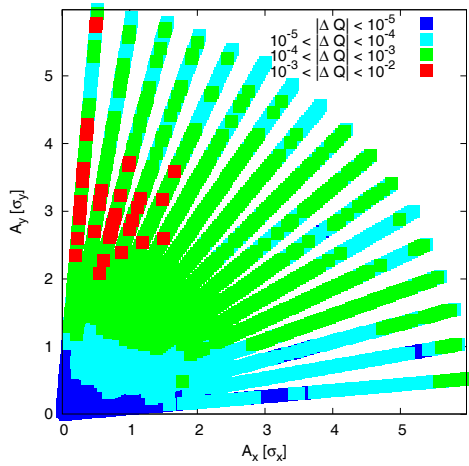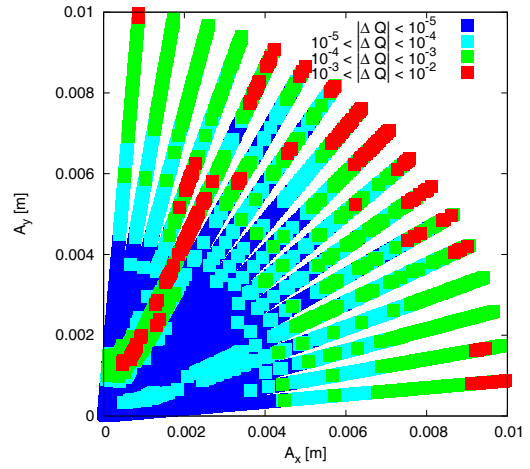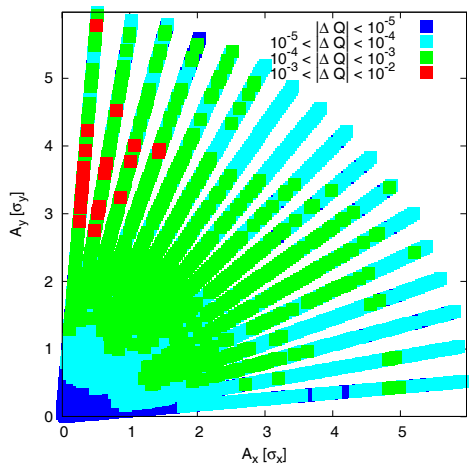
Figure 5: Tune diffusion at two working points, in amplitude space. Top: $(Q_x, Q_y) = (.09, .08)$. Bottom: $(Q_x, Q_y) = (.13, .12)$.



Figure 6: Tune diffusion in the RHIC lattice with beam-beam interaction, in amplitude space. Top: $(Q_x, Q_y) = (28.095, 30.085)$. Bottom: $(Q_x, Q_y) = (28.13, 30.12)$.

to determine the diffusion coefficient

$$D(J) = \lim_{N \to \infty} \frac{\sigma_J^2(N)}{N} = b. \quad (5)$$

As Figure 9 shows, the diffusion coefficient $D(J)$ at amplitudes below $4\sigma$ is larger the further away from the integer the working point is chosen. This result is consistent with the emittance growth data obtained using the same tracking model, shown in Figure 2. Since only 1000 particles were tracked to obtain those emittance growth data, amplitudes beyond $4\sigma$ are irrelevant because the probability of any one of those 1000 particles being launched at such large amplitudes is extremely small.

## DISCUSSION

Simulation studies in the "toy" model show that emittance growth rates due to the beam-beam interaction in space charge dominated ion beams increase with the distance of the working point from the integer resonance, which is in agreement with lifetime observations in RHIC. However, this observation is not supported by frequency map analysis
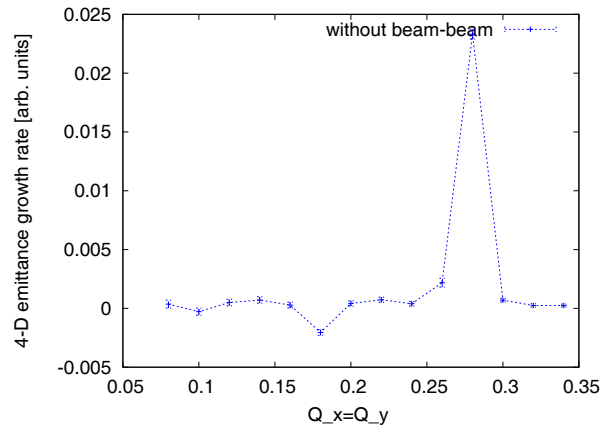


Figure 7: Emittance growth rates without beam-beam interaction on the coupling resonance as a function of tune.

in the same tracking model, thus indicating that tune diffusion studies are not suitable for an understanding of the underlying dynamics. Amlitude diffusion simulations, on the other hand, agree with emittance growth simulations and experimental observations of beam lifetime.

Computational Challenges, New Concepts and New Projects
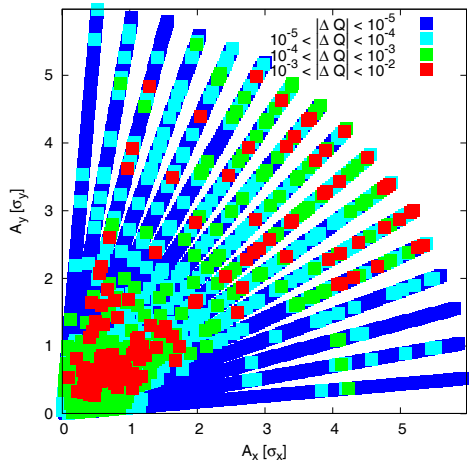
Figure 8: Tune diffusion on the coupling resonance without beam-beam interaction, in amplitude space. $(Q_x, Q_y) = (.08, .08)$.

## REFERENCES

[1] A. Fedotov et al., "Beam Lifetime and Limitations during Low-energy RHIC Operation", Proc. PAC'11

[2] A. Bazzani et al., Part. Accel. **52**, 147 (1996)

[3] C. Montag and A. Fedotov, "Beam-Beam Effects in Space Charge Dominated Ion Beams" Proc. Beam-Beam 2013, CERN-2014-004

[4] C. Montag et al., "RHIC Performance During the 7.5 GeV Low Energy Run in FY 2014" Proc. IPAC 2014

[5] N. Abreu et al., C-A/AP/346
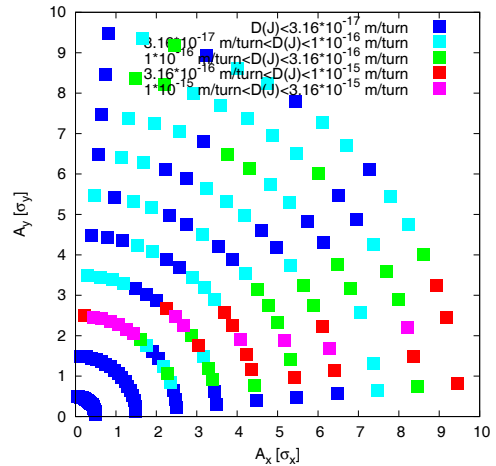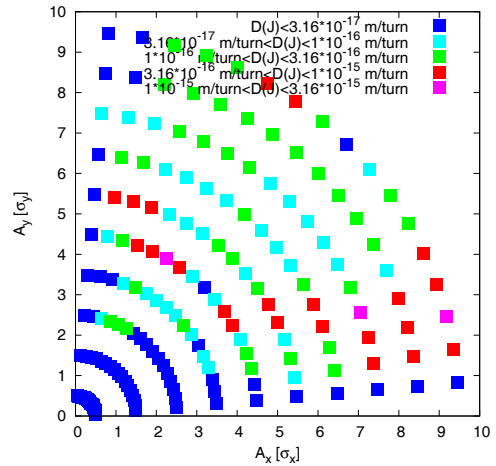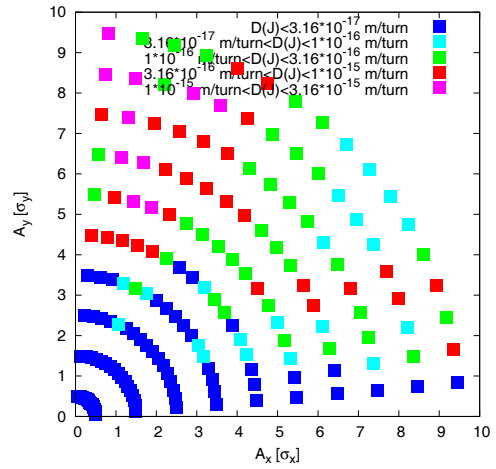
Figure 9: Amplitude diffusion with beam-beam interaction in the "toy" model at the near-integer working point $(Q_x, Q_y) = (.095/.085)$ (top), the FY2010 working point $(.13, .12)$ (center), and the RHIC high energy ion working point $(.23, .22)$ (bottom).

# PERFORMANCE OF TRANSVERSE INTRA-BUNCH FEEDBACK SYSTEM AT J-PARC MR

Y. H. Chin, T. Obina, M. Okada, M. Tobiyama, T. Toyama, KEK, Ibaraki, Japan

K. Nakamura, Kyoto University, Kyoto, Japan

Y. Shobuda, JAEA, Ibaraki, Japan

## Abstract

A new broadband (~100MHz) feedback system has been developed for suppression of intra-bunch oscillations and reduction of particle losses at the J-PARC Main Ring (MR). A new BPM has been designed and fabricated, based on Linnecar's exponential coupler stripline type, for a flatter and wider frequency response. The design and performance of the new BPM as well as preparation of a newly installed exciter and power amplifier is presented. We also report beam test results of suppression of horizontal intra-bunch oscillations at 3 GeV with the bunch length of 150-200 ns. Simple simulations results without wake fields and the space-charge effects qualitatively reproduce the experimental results of the intra-bunch FB system.

## INTRODUCTION

The J-PARC is composed of three proton accelerators: the 400MeV linear accelerator (LINAC), the 3 GeV Rapid Cycling Synchrotron (RCS), and the Main Ring (MR) Synchrotron. The main parameters are listed in Table 1. At the J-PARC MR, transverse instabilities have been observed during the injection and at the onset of the acceleration. The present narrowband bunch-by-bunch feedback system (BxB FB) is effectively suppressing these transverse dipole oscillations, allowing to attaining the 230 kW beam power [1]. But the BxB feedback system can damp only the center of mass motions of the whole bunches. Even with the BxB feedback system on, internal bunch oscillations have been still observed, which is causing additional particle losses [2]. To suppress intra-bunch oscillations, a more wideband and elaborate feedback system (named the intra-bunch feedback system) has been developed [3].

## INTRA-BUNCH FEEDBACK SYSTEM

Figure 1 shows the schematic of the new intra-bunch feedback system. It is composed mainly of three components: a BPM, a signal processing circuit (iGp12) and kickers. It divides each bucket to 64 slices and acts on each slice as if it is a small bunch (bunch-let) in a narrow band feedback system. The signal processing circuit detects betatron oscillation of each bunch slice using signals from the BPM and calculates feedback signals. These feedback signals are sent to the kickers through the power amplifiers. The new system and its set-up are similar to those of the current BxB feedback system. The main improvement is that each component now has a (64 times) wider frequency sensitivity than the one for the

BxB feedback system. The intra-bunch feedback system has been installed at the D3 building, while the current BxB feedback system is still operational at the D1 building.

Table 1: Main Parameters of J-PARC Main

| Circumference | 1568m |
|---|---|
| Injection Energy | 3GeV |
| Extraction Energy | 30GeV |
| Repetition Period | 2.48s |
| RF Frequency | 1.67-1.72 MHz |
| Number of Bunches | 8 |
| Synchrotron Tune | 0.002-0.0001 |
| Betatron Tune (Hor./Ver.) | 22.41/20.75 |
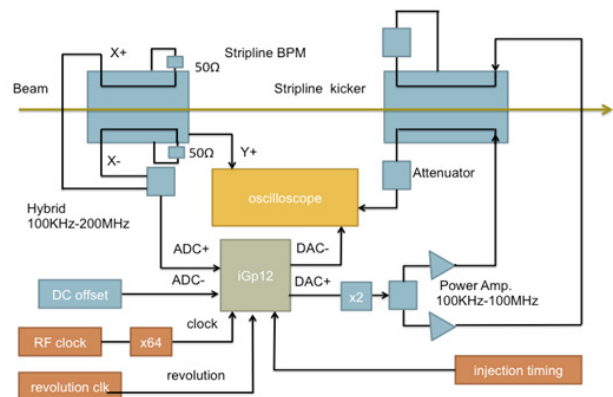


Figure 1: Schematic of the intra-bunch feedback system.

## BPM

The new stripline BPM has been designed and fabricated based on Linnecar's electrode design [4] (see Fig. 2). It is equipped with the exponentially tapered electrodes which, in principle, allow a flatter and wider frequency response (the green line in Fig.3) than the conventional rectangular ones (the blue line in Fig.3). The diameter of the beam pipe is 147mm, and the length of the electrodes is 300mm. The electrodes are placed 67mm from the center of the beam pipe. The height of the electrodes from the chamber surface needs to be gradually reduced (proportional to its width) toward their tips for the impedance matching. The BPM characteristics were measured by the stretched wire method. The measured frequency response is shown by the red line in Fig. 3. It can be seen that the new BPM has a good frequency response up to 1GHz. The position sensitivity is also measured and it is found to be fluctuating around 0.027 by 0.002.
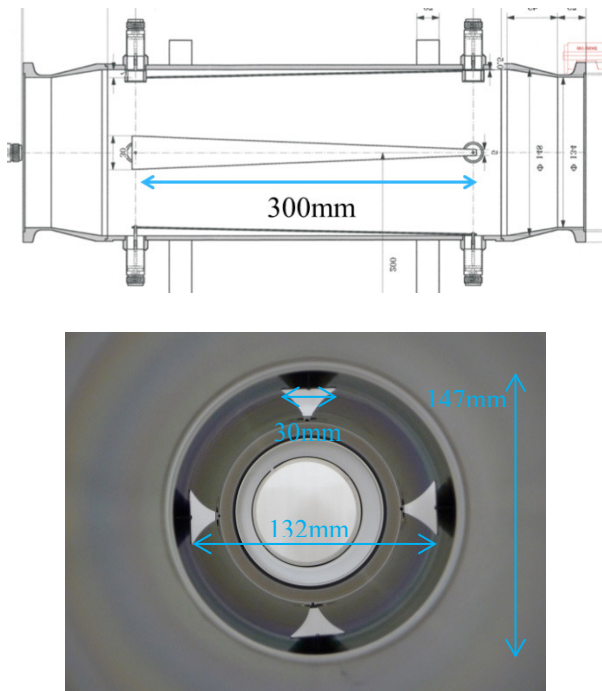
Figure 2: Side (top) and front (bottom) views of BPM.
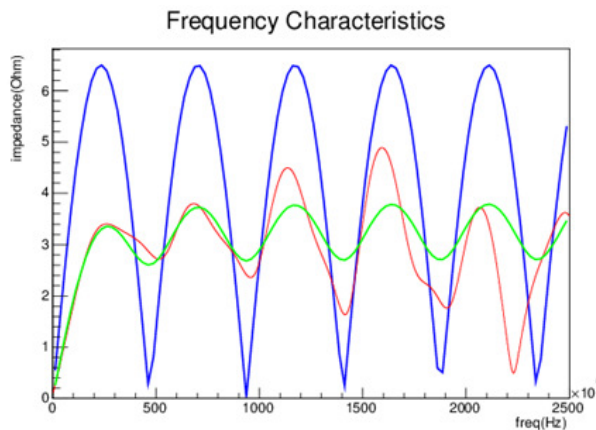


Figure 3: Theoretical and measured frequency responses of BPMs.

## Stripline Kickers and Power Amplifiers

The new stripline kickers were also fabricated (see Fig. 4). The electrodes are 750mm long and they are put on the circle of the diameter 140mm. They are coated with the Diamond Like Carbon (DLC) to suppress the multi-pactoring effect, which may be serious when the kickers are used for slow extraction. The power amplifiers have 3kW capability. Their bandwidth is 100kHz-100MHz, which limits the bandwidth of the whole system now. The kick angle at 3 GeV when used with the two 3kW amplifiers is estimated to be 3.5μrad at DC.

## Signal Processing by iGp12

We adopt the iGp12 signal processing module developed by Dimtel Inc. [5]. It samples BPM signals (through the hybrid coupler) at the rate of 64th harmonic

of the RF frequency (~100MHz). It divides each RF bucket into 64 bins (slices). It extracts betatron oscillation signals by using the n-tap FIR (n≤16, n=8 is used) filter on each slice, and feedbacks kick signals to each slice. As seen in Fig.3, the frequency characteristic of the BPM is approximately linear in the low frequency region (up to 200MHz). Thus, the beam position can be reconstructed by integrating the differentiated signals from the BPM.
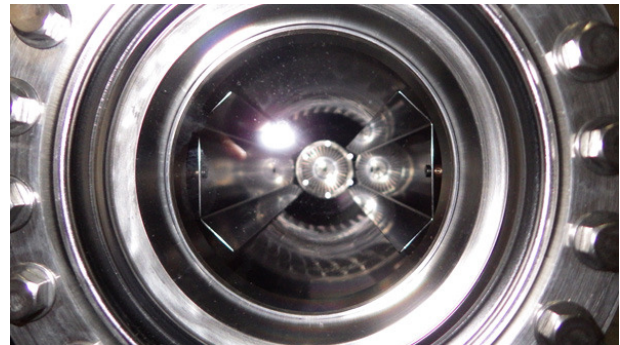


Figure 4: The front view of the horizontal stripline kicker.

## BEAM TESTS AT 3 GeV DC MODE

### Beam Conditions

The first beam test was done in May 2014 with a single bunch of $2.7\times10^{12}$ ppp at the energy of 3GeV. This beam intensity is 1/5 of the maximum intensity of MR at present. The main beam parameters are as follows: the bunch length is 150-200ns, the chromaticities are $\xi_x$=+0.5 and $\xi_y$=+1.2, and the synchrotron tune is $\nu_s$=1.7×10$^{-3}$. First, we applied the intra-bunch feedback system to the horizontal oscillations at the injection, while the vertical BxB FB system is always turned on (when it is tuned off, a large amount of particle losses prevents the testing).

### Reduction of Horizontal Oscillations

Figure 5 shows the 3-D view of the time evolutions of the oscillation amplitude of the horizontal dipole moment in the following three conditions: (top) both the intra-bunch and the BxB FB systems are off, (middle) only the BxB FB system is on, and (bottom) only the intra-bunch FB system is on. The X-and Y-axes show the oscillation amplitudes of the bunch-slices and the revolution turn, respectively. The large horizontal oscillations are excited around the 262th turn due to the mismatching field of the injection kicker magnets. The horizontal oscillation decays even without the feedback systems, indicating that it is not instability. It can be clearly seen that the intra-bunch FB system damps the horizontal oscillations much quicker than the BxB FB system.

The slow change of the dipole moment amplitude (300 turns) is due to the change in the longitudinal profile of the bunch, not the horizontal oscillation amplitude itself. A possible cause of this longitudinal profile change is a quadrupole oscillation of the bunch in the longitudinal phase space due to mismatching between the bunch and the bucket shapes.

Title: RUN54_2014−05−07−13−36−33 3GeV DC H:BxB Off IB Off, V:BxB On



Title: RUN54_2014−05−07−14−27−45 3GeV DC H:BxB On IB Off, V:BxB On



Title: RUN54_2014−05−07−14−10−10 3GeV DC H:BxB Off IB On, V:BxB On



Figure 5: Time evolutions of the horizontal dipole moment after excited at 262th turn. (Top) Both the intra-bunch and BxB FB systems are off. (Middle) Only the BxB FB system is on. (Bottom) Only the intra-bunch FB system is on.

Figure 6 shows Fourier transforms of the horizontal oscillations of the bunch slices shown in Fig. 5: (top) all FB systems off, (middle) only BxB FB system on, and (bottom) the only intra-bunch FB system on. The Y-axis is the frequency. Even when the BxB FB system is on, the betatron sidebands are clearly visible at around 76kHz. But, they disappear when the intra-bunch FB system is turned on.

Figure 7 shows the evolution of the bunch signals at every 100 turns after the large perturbation at the 262th turn. In each plot, signals are superimposed on 10

consecutive turns. It can be seen in the bottom figure that the intra-bunch oscillations are almost completely damped by the intra-bunch FB system after the first 100 turns.

Title: RUN54_2014−05−07−13−36−33 3GeV DC H:BxB Off IB Off, V:BxB On



Title: RUN54_2014−05−07−14−27−45 3GeV DC H:BxB On IB Off, V:BxB On



Title: RUN54_2014−05−07−14−10−10 3GeV DC H:BxB Off IB On, V:BxB On



Figure 6: FFT of horizontal dipole moment amplitude.

## SIMULATIONS

We made very simple simulations to see if they can qualitatively reproduce the experimental results of the intra-bunch FB system. Macro particles of 6400 are used. Wake fields, space charge effects and nonlinear effects are not included in these simulations. We plan to add more effects such as wake fields, the space charge and the multi-bunch effects for more accurate evaluations in future.
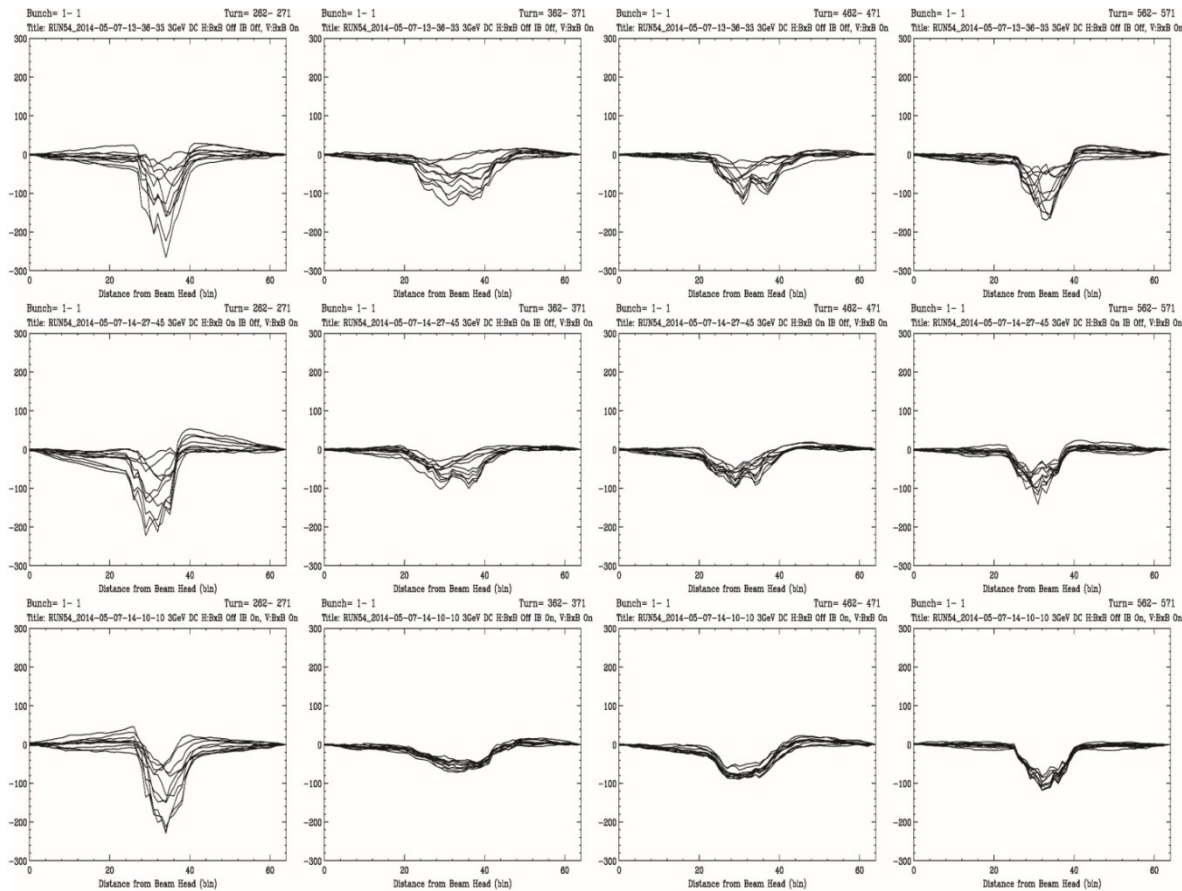
Figure 7: Time evolution of the bunch signals at every 100 turns after the large perturbation at the 262th turn. In each plot, signals are superimposed on 10 consecutive turns. (Top) Both the intra-bunch and the BxB FB systems are off. (Middle) Only the BxB FB system is on. (Bottom) Only the intra-bunch FB system is on. The 1st row corresponds to 262th turn, the 2nd row to 362th turn, the 3rd row to 462th turn, and the 4th row to 562th turn, respectively.

Figure 8 shows the time revolution of center slice of the bunch. The left figures are for experimental results and the right ones are for simulations. It can be clearly seen that the intra-bunch FB system damps oscillations faster than the BxB FB system. This tendency qualitatively agrees with the experiments. At the maximum gain configuration, the damping time is about 2000 turns and 40 turns when only the BxB FB is on and when only the intra-bunch FB is on, respectively. The experimental results when both the feedback systems are turned off shows damping of signals, indicating the existence of additional damping mechanisms, such as non-linear effects or wake fields. More elaborate simulation models are needed for accurate evaluations.

## INTERNAL MOTIONS

In Fig. 9, the delta signal motions are plotted every 5 turns after the 200th turn from the perturbation kick. In simulations, arbitrary offsets are added to match with the initial perturbations of the experiment. Good qualitative agreements are seen between the simulations and the experiments.

## CONCLUSIONS

The first beam test successfully demonstrates that the new intra-bunch FB system is quite effective to suppress intra-bunch oscillations. Simple simulations results without wake fields nor the space-charge effects qualitatively reproduce the experimental results of the intra-bunch FB system. However, the horizontal oscillations presented in this paper are merely incoherent oscillations caused by the kicker mismatching field. More serious instabilities and resulting particle losses are observed on the vertical plane during the injection and at the onset of acceleration (when $\xi_y$=-0.3). They can be, however, suppressed by setting the vertical chromaticity to $\xi_y$=-3.2, although a smaller (slightly negative) vertical chromaticity is preferable for operational purposes. Preliminary beam tests on the vertical instabilities suggest that the new intra-bunch feedback system helps in stabilizing the beam against occasional bursts of large particle losses. More testing and tuning of the system are under way. The intra-bunch FB system is now used in routine operation at J-PARC MR. The beam loss at the injection is reduced from 350W to 170W.

# REFERENCES

[1] Y. Kurimoto et al., "Bunch by bunch feedback system in J-PARC MR", DIPAC2011, Hamburg, May 2011, p482 (2011).

[2] Y. H. Chin et al., "Analysis of transverse instabilities observed at J-PARC MR and their suppression using feedback systems" NA-PAC2013, Pasadena, September-October 2013, p.27 (2013).

[3] K. Nakamura et al., "Transverse intra-bunch feedback in the J-PARC MR", IPAC14, Dresden, June 2014, p.2786 (2014).

[4] T. Linnecar, "The high frequency longitudinal and transverse pick-ups used in the SPS", CERN-SPS/ARF/78-17 (1978).

[5] Dimtel, Inc., San Jose, USA, http://www.dimtel.com
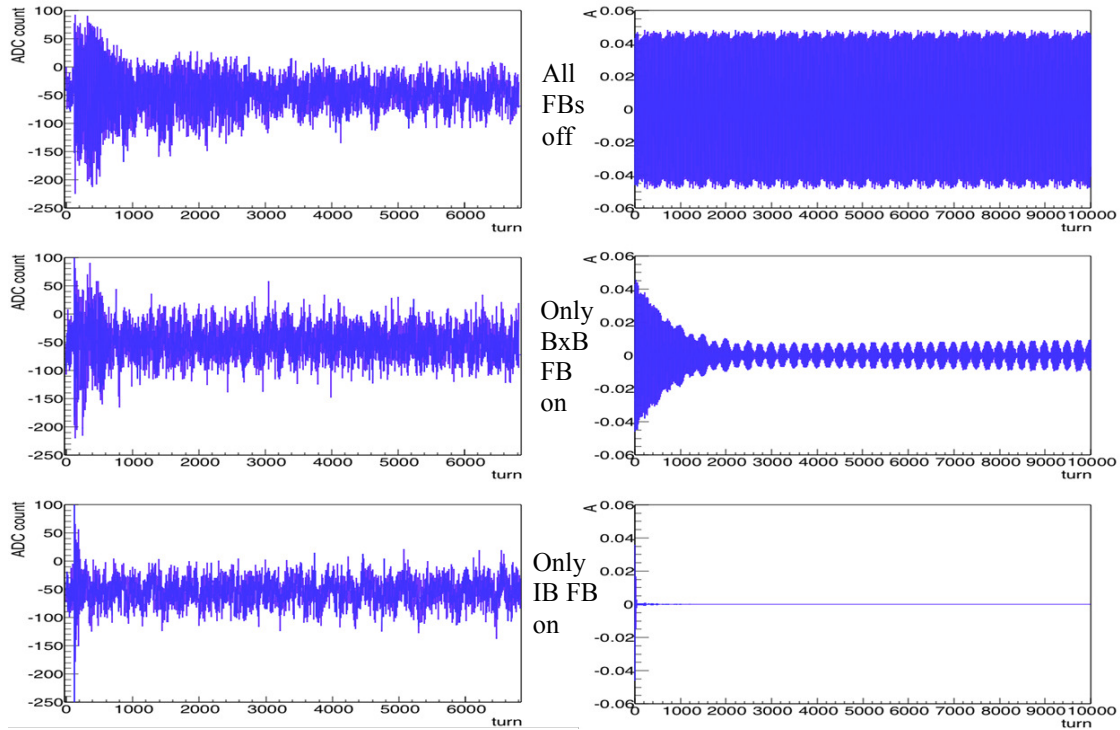
Figure 8: Time revolution of the center slice of the bunch (the 30th slice). The left figures are the experimental results (Top: all FBs off, Middle: only BxB FB on, Bottom: only intra-bunch FB on) and the right ones are the simulations (Top: all FBs off, Middle: only BxB FB on, Bottom: only intra-bunch FB on).
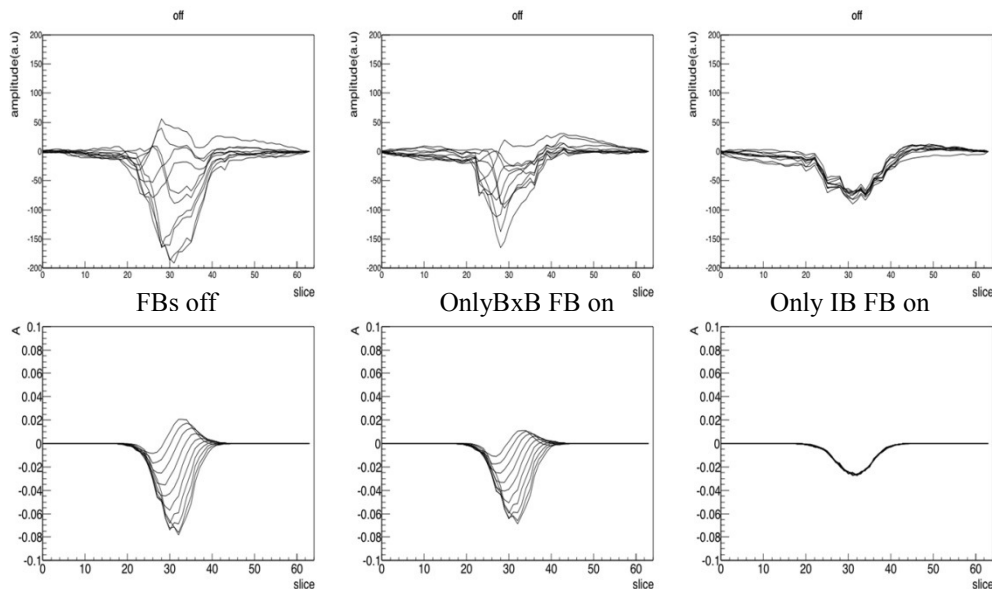


Figure 9: The delta signal motion around 250th turn after a perturbation kick. The top figures are for the experimental results (Left: all FBs off, Middle: only BxB FB on, Right: only intra-bunch FB on) and the bottom ones are for the simulations (Left: all FBs off, Middle: only BxB FB on, Right: only intra-bunch FB on).

# DYNAMIC CORRECTION OF EXTRACTION BEAM DISPLACEMENT BY FIELD RINGING OF EXTRACTION PULSED KICKER MAGNETS IN THE J-PARC 3-GEV RCS

H. Harada[#], P.K. Saha, F. Tamura, S. Meigo and H. Hotchi

J-PARC Center, KEK & JAEA, Tokai-mura, Naka-gun, Ibaraki-ken, Japan

## Abstract

The 3-GeV rapid cycling synchrotron (RCS) of J-PARC is designed for a high-intensity output beam power of 1MW. The RCS is extracted two bunches by using eight pulsed kicker and three DC septum magnets with 25Hz repetition. The extracted beam is simultaneously delivered to the material and life science experimental facility (MLF) as well as the 50-GeV main ring synchrotron (MR). The kicker magnets have the ringing of flat-top field and the ringing causes the position displacement. The displacement is big issue because it causes an emittance growth of the extracted beam directly. In the beam tuning, we performed a timing scan of each kicker magnet by using a shorter pulse beam in order to understand the characteristics of ringing field. We then carefully optimized the trigger timings of each kicker for the ringing compensation. We have successfully compensated the extracted beam displacements to (min., max.) = (−1.1 mm, +0.6 mm) as compared to (−14 mm, +10 mm) with no ringing compensation. The procedure for ringing compensation and experimental results are reported in this paper.

## INTRODUCTION

The Japan Proton Accelerator Research Complex (J-PARC) is a multipurpose proton accelerator facility [1,2], comprising three accelerator facilities that are a 400-MeV LINAC, a 3-GeV rapid cycling synchrotron (RCS), and a 50-GeV main ring synchrotron (MR), and three experimental facilities that are a materials and life science experimental facility (MLF), a hadron experimental hall, and a neutrino beam line to Kamioka. In this chain of accelerators, the RCS has two functions as a proton driver to produce pulsed muons and neutrons at the MLF and as an injector to the MR, aiming at 1-MW output beam power. The RCS was beam-commissioned in October 2007 and the output beam power has been steadily increasing following progressions in the beam tuning, hardware improvements and the realistic numerical simulations [3,4,5]. After the LINAC had been upgraded output energy from 181 to 400-MeV by installation of ACS linac section in 2013 summer-autumn maintenance period, the RCS has successfully achieved output beam power of 300-kW for user operation and demonstrated 550-kW equivalent intensity with beam loss mitigation in our beam study [6]. In 2014 summer maintenance period, the Ion Source (IS)

#hharada@post.j-parc.jp

and RFQ in LINAC were replaced in order to upgrade a peak current from 30 to 50 mA. After upgrading the peak current from LINAC, the RCS started a beam tuning of the designed 1-MW intensity in October 2014. In first trial of the designed 1-MW intensity, we achieved 770-kW equivalent intensity [7]. In higher intensity beams, the trip of RF power supplies was happened. In December 2014 and January 2015, we will retry a beam tuning of 1-MW intensity after the treatment for the RF issue.

As shown in Fig. 1, the RCS extraction system consists of eight pulsed kicker magnets and three DC septum magnets. The extracted beam of two bunches is simultaneously delivered to MLF and MR with a repetition rate of 25 Hz. The pulsed kicker magnet has a ringing of flat-top field and the ringing causes position displacements to the extracted beam for horizontal plane. In this paper, the configuration and field ringing of kicker magnet are introduced and the effect on extracted beam is mentioned. The measured beam displacements by kicker timing scan and the procedure for kicker ringing compensation are reported. Finally, the results of the compensation are described.
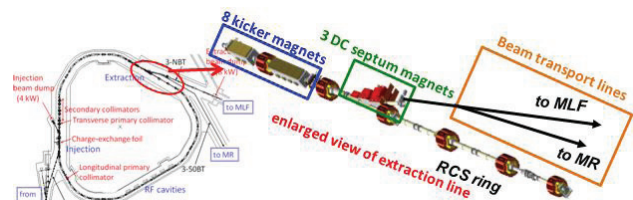


Figure 1: RCS and extraction line

## EXTRACTION KICKER MAGNET

The detail configuration and field measurement of extraction kicker magnet and power supply have already been described in reference [8]. In this section, the configuration and measured magnetic field are briefly introduced.

### Configuration

Kicker magnet consists of twin-C distributed Ferrite core with twenty units and two conductors in vacuum and the power source consists of two Thyratrons, PFN & loading cables and matching registers. Schematic diagram of kicker magnet system is shown in Fig. 2. Kicker magnet as shown in Fig. 2 is driven by two Thyratrons via two conductors. Operation charging voltage of Thyratron is 60 kV and exciting current of magnet by two Thyratrons is 6

kA. As shown in Fig. 2, two conductors have exciting current in the opposite direction. The eight kickers have three types (S:3, M:2 and L:3), which are identified by vertical aperture gap of 153 mm (S: Nos.1, 7 and 8), 173 mm (M: Nos.2 and 6) and 199 mm (L: Nos. 3, 4 and 5).
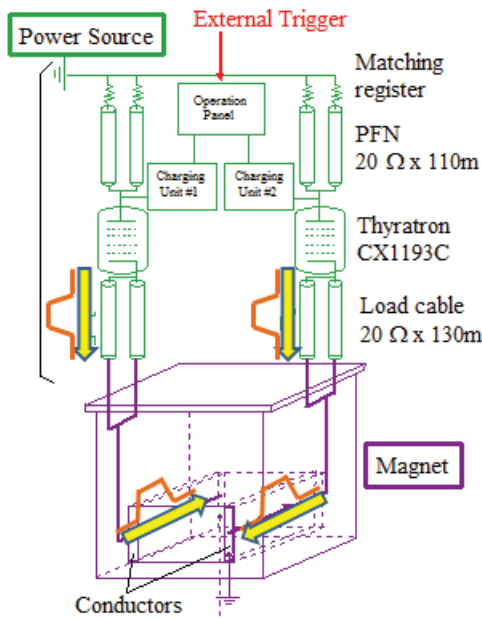


Figure 2: Schematic diagram of kicker system

## *Measured magnetic field and ringing field*

Twin-C core and calculated magnetic fields of kicker in the conditions of one (upper graph) and both (lower graph) side excitations are shown in Fig. 3. The measured fields are shown in Fig. 4. The measured fields in the condition of right and another left side excitation are A and B as shown by the upper graph in Fig. 4, respectively. Field C is the summed field of both A and B. Field D in Fig. 4 is the measured field in the condition of both side excitations. Field C is a good agreement with D. So, field D is created by combination of field A and B. It was found that the disturbance of the flattop as shown by the lower graph in Fig. 4 is caused by two reasons. One is the impedance mismatch between load cables and corresponding magnet and it is shown in the measured field A. The other is the effect of the magnetic field induced by the penetrated magnetic flux from the opposite side of the ferrite core and it is shown in the measured field B. As a result, the flattop of the kicker magnetic field showed a ringing structure such as measured filed D.

## EXTRACTION BEAM QUALITY

The ringing field causes the different beam center position between two bunches and the beam displacements in first bunch. So, the flattop uniformity of the kicker magnetic field affects a quality of the extracted beam directly. In a first beam commissioning of the RCS, the required flatness of the flattop is 2% in the time length of 840 nsec in order to extract the two bunches as compared with the measured field flatness of 6%. In order to

compensate the distortion, the timing adjustment of the each kicker magnet was attempted. The timing of four out of eight kickers was modified to cancel out the peaks and valleys of the flattop. The trigger timing of first group (Nos. 1, 3, 5, and 7 kickers) was fixed. On the other hand, the trigger timing of second group (Nos. 2, 4, 6, and 8 kickers) was delayed for about 130 nsec. This delay condition calls as "reference delay". The flatness of 2% was achieved in the time length of 850 nsec, which satisfies the requirement in first beam commissioning. These results have already discussed in reference [9].
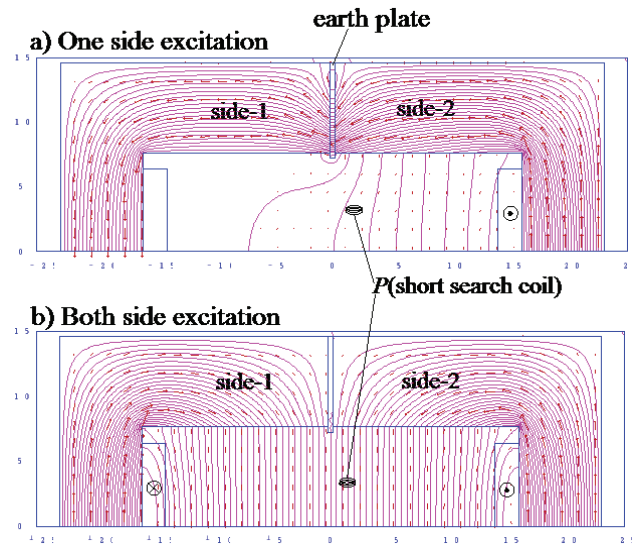


Figure 3: Calculated field and twin-C core of kicker. One side excitation case : a); both side excitation case : b). *P* is a short search coil position in field measurement.
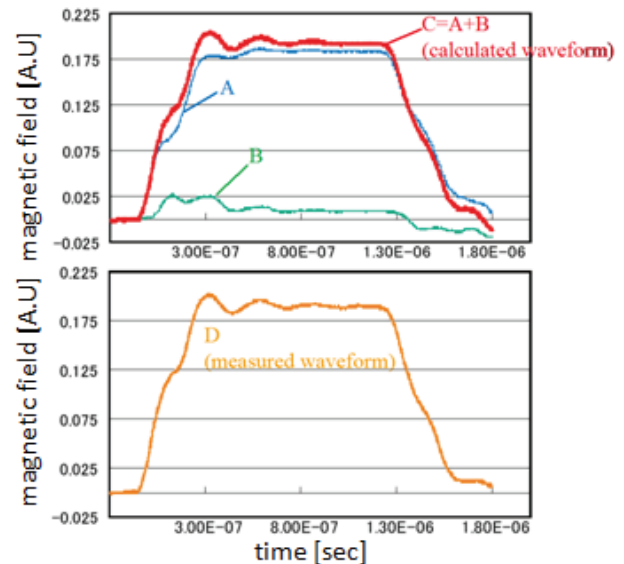


Figure 4: Time structures of measured magnetic field. Filed A and B in the upper graph are the measured fields in right and left side excitation. Field C in the upper is the summed field of both A and B. Field D in the lower is the measured field in condition of both side excitations.

*Beam displacement measurement caused by kicker field ringing*

In a user operation up to June 2013, eight kickers have been operated in trigger timing delay of 130 nsec between first and second kicker group. A higher quality of extracted beam is required in a stage of beam tuning for high intensity in order to reduce the shock wave at a neutron target and the emittance growth of MR injection beam. To understand the flattop uniformity on total field of kickers, the uniformity was measured as beam position displacements by using a shorter pulsed-beam and trigger timing scan of entire kickers. The beam bunch length of 30 nsec is shorter than normal one of 150-200 nsec in order to measure the ringing structure. The measured beam displacement $\Delta x$ is shown in Fig. 5. Fortunately, there was no much deference of beam center positions between first and second bunches. However, the measured beam displacements in first bunch was a range from $-5.5$ mm to $+3.3$ mm, corresponding to $-1.6\%$ and $+0.75\%$. As the result, the ringing cannot be compensated by only simple trigger delay of 130 nsec between two groups. So, it is very important to directly measure the time structure of beam displacement by trigger timing scan with shorter pulsed beam for understanding the effect on kicker ringing.

In order to further compensate the kicker ringing, the trigger timing of each kicker must be optimized. However, the time structure of kicker ringing is not simple. In fact, eight kickers consist of three types with different core gap corresponding to strength of magnetic field and each kicker has different betatron phase-advances. Therefore, it is very important to understand the effect on the beam position and the ringing structure kicker-by-kicker. And then, the trigger timing of each kicker should be optimized by the beam-based data for the ringing compensation.

*Beam-based position displacement response measurement kicker-by-kicker*

The beam-based measurements of beam displacement response kicker-by-kicker were performed by using a shorter pulsed-beam and trigger timing scan of single kicker. The trigger timing of a single kicker was swept kicker-by-kicker and the timing of other seven kickers was fixed where the extracted beam position was measured by BPM at the extraction beam transport line. Each data of the trigger timing scan for eight kickers (Nos.1 to 8) is shown in Fig.6. The time structure of each ringing was clearly measured and the different structure between each kicker was understood well. To check whether these data is right or not, we measured the beam displacements by entire timing scan in the other condition that timing delays of Nos.1, 4, 7 and 8 are 10, 35, 10 and $-10$ nsec. The measured beam displacements by entire timing scan were compared with the calculated ones based on scan data kicker-by-kicker for two data of different timing delay. The compared results are shown in Fig. 7. The calculated beam displacements based on scan data kicker-by-kicker is a good agreement with the measured ones by entire trigger timing scan. So, we can discuss with timing optimization

of each kicker based on scan data kicker-by-kicker for the ringing compensation
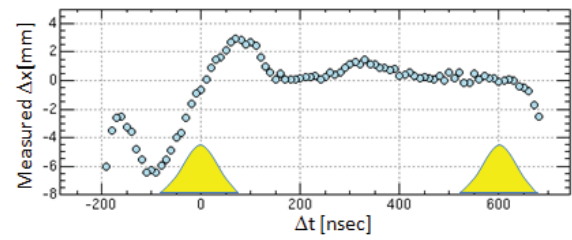


Figure 5: The measured beam displacement $\Delta x$ (dots of light blue) by trigger timing scan of entire kickers and normal two bunched beams (yellow). Left and right bunches are first and second ones, respectively.
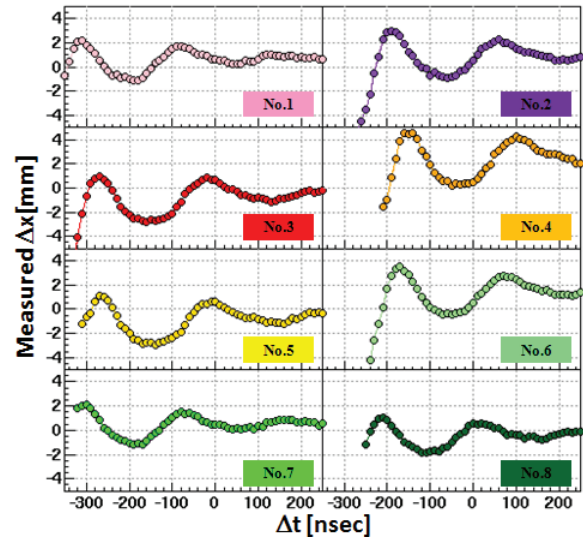


Figure 6: The measured beam displacement $\Delta x$[mm] by trigger timing scan of $\Delta t$[nsec] kicker-by-kicker. $\Delta t$ of 0 is bunch center of first bunch.
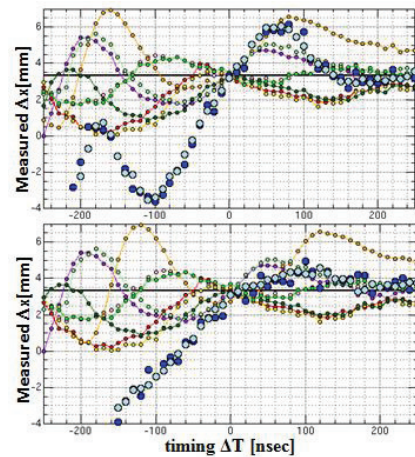


Figure 7: The calculated beam displacements (blue dots) based on scan data kicker-by-kicker and the measured beam displacements (light blue dots) by entire trigger timing scan of eight kickers. $\Delta t$ of 0 is bunch center of first bunch. The upper and lower graphs are the calculated and measured displacements for different timing delays kicker-by-kicker in the upper graph is fixed.

*Trigger timing optimization of each kicker for the ringing compensation*

Search of the optimized kicker's trigger timing were performed based on timing scan data kicker-by-kicker. The time structure of each kicker ringing is not simple and we could not adapt a beautiful method such as "least-square method" for optimization of trigger timing kicker-by-kicker. So, we tried to search the trigger timing of each kicker for further ringing compensation by "brute force method". The trigger delays of each kicker for reference delay (1) and optimized delay from reference one (2) are described in Table 1. Beam displacements in the case of no trigger delay (0), reference delay (1) and optimized delay (2) are shown in Fig. 8. In first bunch length, (min., max.) of beam displacements with trigger delay of (0) and (1) are (−14 mm, +10 mm) and (−5.5 mm, +3.2 mm), respectively. After the optimization of trigger delay that is (2), (min., max.) of beam displacements are (−1.1 mm, +0.6 mm). As the result, we have successfully achieved to compensate further the beam displacement of extracted first bunch from (−5.5 mm, +3.2 mm) of reference delay to (−1.1 mm, +0.6 mm) of optimized delay, corresponding to the field distortion degree of (−0.28%, +0.15%).

The extracted beam profile of first and second bunch for trigger delays of (0) to (2) were measured by a multi wire profile monitor at the extraction beam transport line for confirming the optimization of trigger delay kicker-by-kicker. These measured beam profiles and fitted Gaussian functions are shown in Fig. 9. The center position displacements of measured beam profiles between first and second bunch made no differences among three timing delay patterns. On the other hand, the measured beam width of first bunch in trigger delay patterns of (0) and (1) is wider than that of second bunch. But, the fitted width $\sigma_x$ of the measured beam profile for first bunch after the optimization of timing delay (2) kicker-by-kicker was a good agreement with the width for second bunch.

The extracted beam displacements caused by the kicker field ringing were compensated well and the good beam quality of extraction beam was successfully achieved by using the timing scan data kicker-by-kicker. So, our procedure fills the role for compensation of the kicker field ringing as a good example.

Table 1: Trigger Delay Kicker-by- Kicker

| Kicker | Trigger delay $\Delta t$ (1) | Trigger delay $\Delta t$ (2) |
|--------|------------------------------|------------------------------|
| No.1   | 0 nsec                       | 60 nsec                      |
| No.2   | 0 nsec                       | -20 nsec                     |
| No.3   | 0 nsec                       | 50 nsec                      |
| No.4   | 0 nsec                       | 30 nsec                      |
| No.5   | 0 nsec                       | 200 nsec                     |
| No.6   | 0 nsec                       | -30 nsec                     |
| No.7   | 0 nsec                       | 50 nsec                      |
| No.8   | 0 nsec                       | -40 nsec                     |
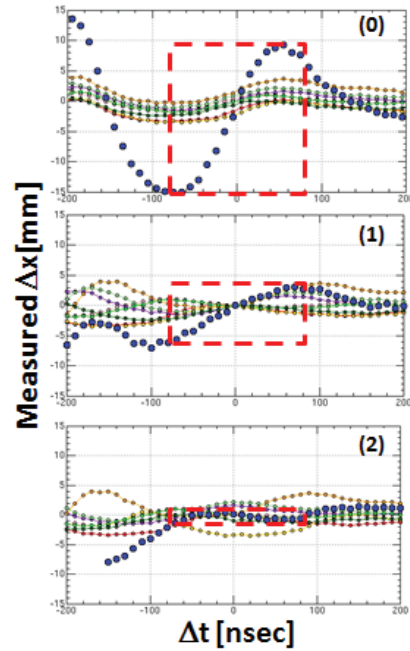


Figure 8: Beam displacements (blue dots) with no compensation (upper graph), compensation by reference delay (center graph) and compensation by optimized delay (lower graph) in the region of first bunch. Rectangle of red dash line is first bunch length.
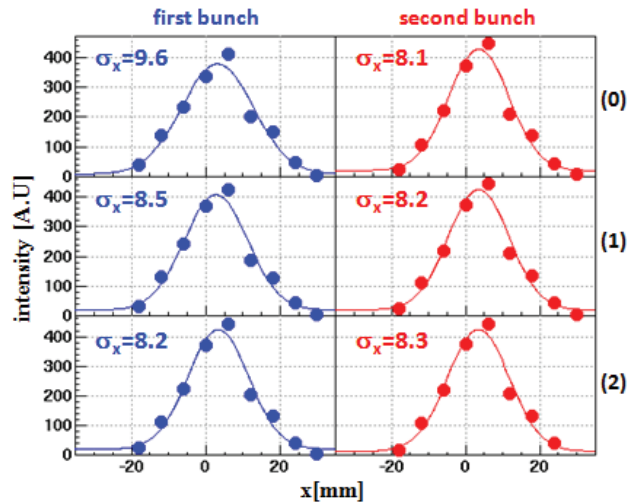


Figure 9: The measured beam profile of extracted first (left) and second bunch (right). Upper, center and lower graphs are the measured beam profile in the trigger delay patterns of (0), (1) and (2), respectively. Lines are fitted Gaussian functions and $\sigma_x$[mm] is analyzed one sigma by the function.

## EXTRACTION BEAM STABILITY

We found that it is very important to keep the trigger delay kicker-by-kicker for extraction beam quality. However, there is a gradual change in Thyratron condition where Thyratron output timing has a drift over a period of minutes by lifetime or bad condition of Thyratron. In fact, the extracted beam in a user operation caused the beam displacement of more than 25 mm when Thyratron output has had a drift. Therefore, online monitor system of output current for all Thyratrons were developed. In the system, output current Thyratron-by-Thyratron was monitored and the output timing was analyzed online. If Thyratron output timing has a difference of more than |10| nsec from a reference one, the output timing is automatically corrected by the trigger timing. We have achieved to keep the extraction beam stability for beam delivering to the MLF and the MR.

## CONCLUSION

The J-PARC 3-GeV RCS is extracted two bunched beam as high-intensity proton beam by using eight pulsed kicker and three DC septum magnets with 25Hz repetition. The extracted beam is simultaneously delivered to MLF as well as the 50-GeV MR. The kicker magnets have the ringing of flat-top field caused by the magnet configuration and the ringing causes the beam position displacement of the extraction beam. The displacement is big issue because it causes an emittance growth of the extracted beam directly.

In a first beam commissioning started since October 2007, the required flatness of the flattop is 2% in the time length of 840 ns in order to extract the two bunches as compared with the measured field flatness of 6%. For compensation of the kicker ringing, eight kickers had in trigger timing delay of 130 nsec between first (Nos.1, 3, 5 and 7) and second kicker group (Nos.2, 4, 6 and 8). The flatness of 2% was achieved in the time length of 850 nsec In order to understand the flattop uniformity or the ringing structure by total field of kickers, the uniformity was measured as beam position displacements by using a shorter pulsed-beam of 30 nsec and trigger timing scan of entire kickers. In the region of first bunch length, we found that (min., max.) of beam displacements were (−5.5 mm, +3.2 mm), corresponding to the field distortion degree of (−1.6%, +0.75%).

In a user operation up to June 2013, eight kickers have been operated in the trigger timing delay. However, a higher quality of extracted beam is required in a stage of beam tuning for high-intensity operation in order to reduce the shock wave at a neutron target and the emittance growth of MR injection beam. Therefore, it is necessary to further compensate the effect on the kicker ringing. In order to further compensate the kicker ringing, the beam-based measurements of beam position displacement response kicker-by-kicker were performed by using a shorter pulsed-beam and trigger timing scan of single kicker. After that, search of the optimized kicker's trigger timing were performed based on the timing scan data kicker-by-kicker. As the result of trigger-timing optimization, we have successfully achieved to compensate further the beam displacement of extracted first bunch from (−5.5 mm, +3.2 mm) to (−1.1 mm, +0.6 mm), corresponding to the field distortion degree of (−0.28%, +0.15%). Additionally, the beam width of the measured beam profile for first bunch was a good agreement with the width for second bunch. The extracted beam displacements caused by the kicker field ringing were compensated well and the good beam quality of extraction beam was successfully achieved by using the timing scan data kicker-by-kicker.

For extraction beam stability, online monitor and automatic correction system for Thyratrons output timing were developed. We have achieved to keep the extraction beam stability for beam delivering to the MLF and the MR.

We have achieved to keep the extraction beam quality and stability without improvement of kicker magnet devices and new installation of correction magnet. Our procedure fills the role for compensation of the kicker field ringing as a good example.

## REFERENCES

[1] High-intensity Proton Accelerator Project Team: JAERI Report No. JAERI-Tech 2003-044.

[2] High-intensity Proton Accelerator Project Team: KEK Report No. 202-13.

[3] H. Hotchi et al., Phys. Rev. ST Accel. Beams 12, 040402 (2009).

[4] H. Hotchi et al., Phys. Rev. ST Accel. Beams 15, 040402 (2012).

[5] H. Harada et al., Proc. HB2012, Beijing, China, p. 339 (2012).

[6] H. Hotchi et al., Proc. IPAC'14, Dresden, Germany, p. 899 (2014).

[7] H. Hotchi et al., "Lessons from 1-MW Proton RCS Beam Tuning", these proceedings, HB2014, East Lansing, USA, 2014.

[8] J. Kamiya et al., IEEE Trans. Appl. Supercond., 16, 1362 (2006).

[9] J. Kamiya et al., Phys. Rev. ST Accel. Beams 12, 072401 (2009).

# PULSE-TO-PULSE TRANSVERSE BEAM EMITTANCE CONTROLLING FOR MLF AND MR IN THE 3-GeV RCS OF J-PARC

P.K. Saha*, H. Harada, H. Hotchi and T. Takayanagi

J-PARC Center, KEK & JAEA, Tokai-mura, Naka-gun, Ibaraki-ken, Japan

## Abstract

The 3-GeV RCS (Rapid Cycling Synchrotron) of J-PARC (Japan Proton Accelerator Research Complex) is a MW-class proton beam source for the muon and neutron production targets in the MLF (Material and Life Science Experimental Facility) as well as an injector for the 50-GeV MR (Main Ring). The RCS has to meet not only the beam power but also to ensure two different transverse sizes of the extracted beam for the MLF and MR, especially at high intensity operation. Namely, a wider one for the MLF in order to reduce damage on the neutron production target, while a narrower one for the MR in order to ensure a permissible beam loss in the beam transport line of 3-GeV to the MR and also in the MR. We proposed a pulse-to-pulse direct control of the transverse injection painting area so as to ensure a desired extracted beam emittance. For that purpose, RCS injection system was carefully designed for changing painting area between MLF and MR very accurately. The extracted beam profiles for the MR are measured to be sufficiently narrower than those for the MLF and also shown to be consistent with numerical beam simulation results. The system is already in service and plays an important role even at the present 300 kW beam operation. It is thus one remarkable progress on the RCS design goal to confirm that the beam parameters can be dynamically controlled and delivered as requested by the users even in simultaneous operation. A detail of the design strategy, painting process as well as experimental results are presented.

## INTRODUCTION

The 3-GeV Rapid Cycling Synchrotron (RCS) of Japan Proton Accelerator Research Complex (J-PARC) is designed for a beam power of 1 MW [1]. A total of $8.33 \times 10^{13}$ protons in two bunches is accelerated to 3 GeV at a repetition rate of 25 Hz and simultaneously delivered to the neutron and muon production targets in the MLF (Material and Life Science Experimental Facility) as well as to the MR (50-GeV Main Ring synchrotron). Figure 1 shows a schematic view of the RCS, which is a three-fold symmetric lattice having a circumference of 348.333 m. The injected beam energy is recently upgraded to the designed 400 MeV from the 181 MeV so far. The RCS beam power at present for the operation is 300 KW, while a beam power of nearly 800 kW with sufficiently low loss has already been demonstrated in a recent beam study [2]. A pattern dipole magnet named Pulse Bending magnet (PB) located downstream of the RCS extraction beam transport (BT) line is used to switch the beam destination to the MR

* E-mail address: saha.pranab@j-parc.jp
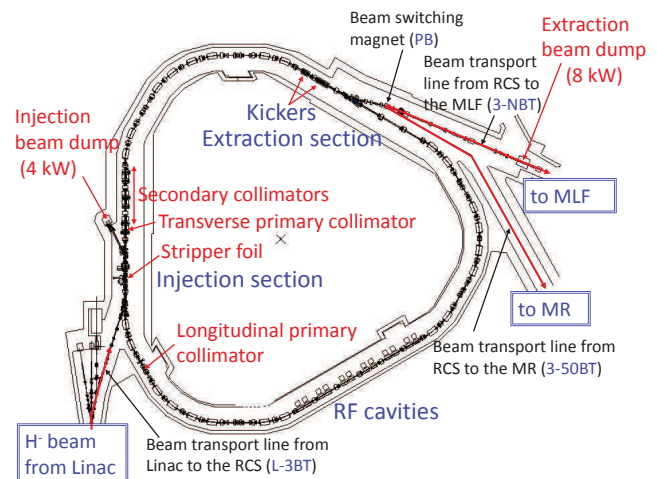
Figure 1: Schematic view of the 3-GeV RCS of J-PARC. Extracted beam is simultaneously delivered to the MLF and MR at a repetition rate of 25 Hz. A pattern dipole magnet named Pulse Bending magnet (PB) located downstream of the RCS extraction line acts as a switching magnet for changing beam destination MLF to MR.

according to the operation strategy. At present for the MR with fast extraction operation, RCS beam delivery ratio to the MLF and MR is typically 9:1.

However, RCS design goal is not only to achieve the beam power but also to ensure specific requirements of each downstream facility. One such an issue, especially at high intensity operation is to control transverse emittance of the extracted beam pulse-to-pulse between MLF and MR even in simultaneous operation. Namely, a wider transverse beam distribution for the MLF in order to reduce damage on the neutron production target, while a narrower one for the MR in order to ensure a permissible beam loss in the BT of 3-GeV RCS to the MR (3-50BT) as well as in the MR. The BT of RCS to the MLF targets named 3-NBT has the aperture of $324\pi$ mm mrad, same as the RCS primary collimator but 3-50BT and MR designed apertures are much smaller, $120\pi$ mm mrad and $81\pi$ mm mrad, respectively. In order to realize such a requirement, we proposed pulse-to-pulse direct control of the transverse painting area during multi-turn $H^-$ charge-exchange injection process in the RCS so as to ensure a desired transverse beam profile or in other words, a desired transverse emittance of the extracted beam. The designed injection painting area in the RCS for the MLF and MR are 216 and $144\pi$ mm mrad, respectively. The RCS injection system was carefully designed for varying both hor-

izontal and vertical painting areas pulse-to-pulse between MLF and MR and has also been experimentally verified through beam studies. At the present 300 kW operation of the RCS, the transverse painting areas for the MLF and MR are chosen to be 100 and $50\pi$ mm mrad, respectively.
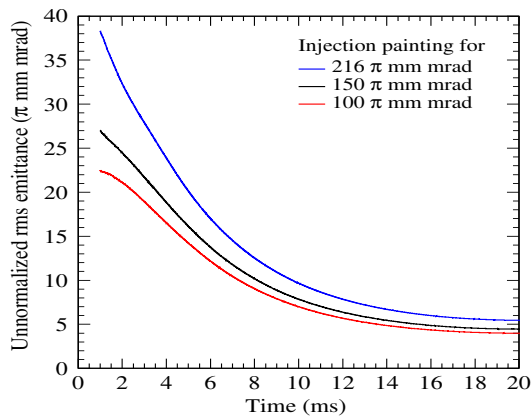


Figure 2: Estimated damping of the transverse rms horizontal emittance and dependence on the injection painting area for a beam power of 350 kW. A smaller painting area gives comparatively a smaller emittance of the extracted beam.

Figure 2 shows numerical results for expected transverse rms emittance damping and dependence on the injection painting areas of 216, 150 and $100\pi$ mm mrads as shown by blue, black and red lines, respectively. The painting emittance values are 99.7% emittance values for all cases. In this simulation injected beam energy was 181 MeV and a beam power of 350 kW at the extraction energy of 3 GeV was considered, where a full 3-D space charge effect was taken into account. It can be easily seen that a smaller initial painting area guaranties comparatively a smaller emittance of the extracted beam. One can expect nearly 25% reduction of an rms emittance for an injection painting area of $100\pi$ mm mrad as compared to that of $216\pi$ mm mrad.

## RCS INJECTION SCHEME AND TRANSVERSE PAINTING PROCESS

Figure 3 shows a layout of the RCS injection area. The $H^-$ beam from the LINAC is stripped to $H^+$ by the 1st stripped foil placed in the middle of 4 injection chicane magnets, also called shift bump magnets (SB), and is injected into the RCS. The transverse injection painting in the horizontal direction are performed by 4 painting bump magnets named PBH. The first two of them (PBH1~2) are place in the upstream of the SB, while the rest two (PBH3~4) are place at the downstream of the SB. The two vertical painting bump magnets (PBV1,2) are placed at the LINAC to the RCS injection beam transport (L-3BT) line. In the original design, two pulse steering magnets named PSTR1 and PSTR2 are used for changing painting area MLF to MR in the horizontal direction but recently with upgraded power supplies of the PBHs, it has also been successfully done by using only PBHs.

Figure 4 shows a schematic view of the RCS transverse injection painting process for horizontal and vertical planes in the upper and lower plots, respectively. The painting area is considered to be the design maximum of $216\pi$ mm mrad for both planes as shown by the bigger ellipses (black), where a typical injected beam emittance is considered to be $4\pi$ mm mrad (blue). In the horizontal direction, the position and angle (x and x') of the injected beam center is matched to a closed orbit offset made by the SBs together with PBHs. The horizontal phase space painting is performed by varying the closed orbit by the PBHs during 0.5 ms injection period as shown by the arrow [3, 4]. The SBs are then linearly ramped down to zero so as to move the closed orbit to the ring center. In the vertical direction, however, injected beam angle (y') at the foil is directly swept by the PBVs. As shown in the figure the vertical angle of the injected beam can be swept either center-to-outside or outside-to-center in the circulating phase space for so-called correlated or anti-correlated painting.

## METHODS FOR SWITCHING PAINTING AREA BETWEEN MLF AND MR

In this section, two methods for changing injection painting area pulse-to-pulse between MLF and MR, especially for the horizontal direction are described. A change of the painting area between MLF and MR in the horizontal direction is originally performed by using PSTR magnets but recently it has also been realized by using only PBHs because of their upgraded power supplies.

### Switching Horizontal Painting Area by PSTRs

Figure 5 shows a schematic view of changing transverse painting area between MLF and MR. The design painting areas for the MLF and MR are considered to be $216\pi$ mm mrad and $144\pi$ mm mrad as shown by the black and red ellipses, respectively. In order to change painting area from MLF to MR in the horizontal direction, PSTR magnets are used to change only angle of the injected beam to a smaller value by keeping its position same as that for the MLF. This is because a change of the both position and angle for a smaller painting area needs to move the foil further inside in the horizontal direction. That will significantly increase the foil hits of the circulating beam for the MLF. It is therefore a big issue for the corresponding foil scattering beam loss as well as foil lifetime as 90% of the beam is delivered to the MLF. The injected beam orbit, painting for the MLF is fixed by two DC septa, while two PSTRs are additionally used to control the injected beam orbit in such a way to realize a smaller painting area for the MR. The black and red arrows shows the amplitude and direction of closed orbit variation for the corresponding painting area performed by the PBHs. It has also to be mentioned that the chicane bump offset for the MLF and MR should be changed and it is about 11% higher for the later case. A further detail of the designed strategy as well as experimental results can be found in our separate article [5].
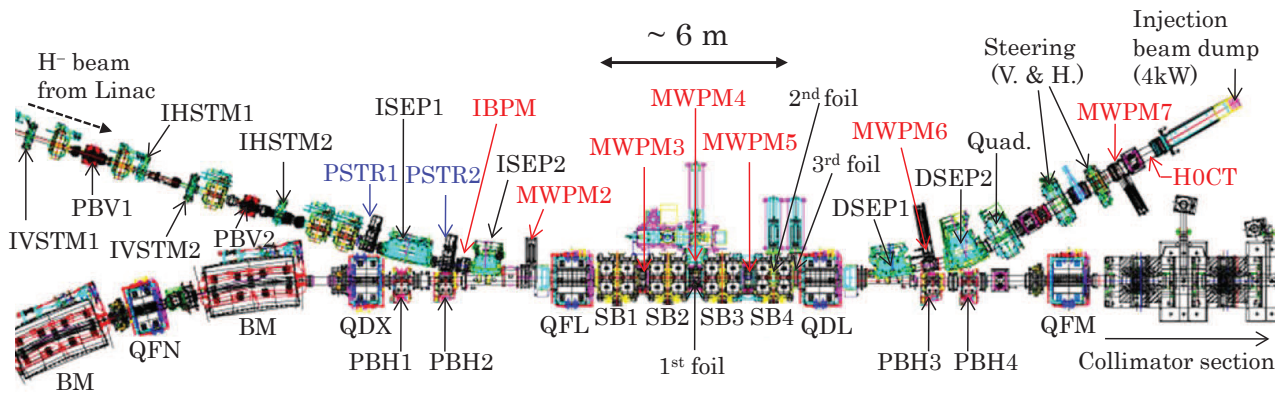
Figure 3: Layout of RCS injection area. The SB1~4 are the injection chicane magnets. The PBH1~4 and PBV1~2 (injection line) are used for transverse injection painting in the horizontal and vertical directions, respectively. The two pulse steering magnets named PSTR1 and PSTR2 (injection line) are used to control horizontal phase space coordinates of the injected beam at the 1st stripper foil in order to change horizontal painting area between MLF and MR. The PBVs are used for controlling vertical angle of the injected beam for changing vertical painting area between MLF and MR.
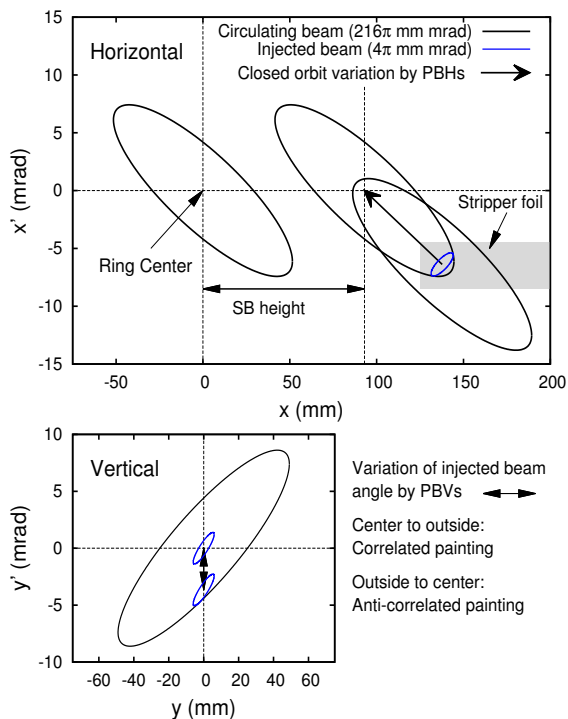


Figure 4: Schematic view of the transverse painting process in the horizontal (top) and vertical direction (bottom). A controlled closed orbit is variation is done by using PBHs for horizontal painting, while injected beam angle itself is sweeped in the vertical phase space for vertical painting.
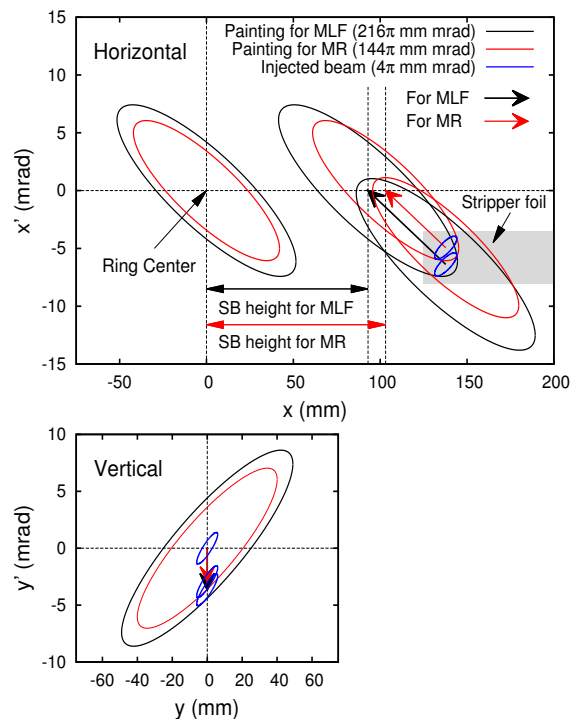
Figure 5: Schematic view of switching painting area between MLF and MR. The PSTRs are used to change angle of the injected beam by keeping its position unchanged at foil in the horizontal direction, while PBVs are used to control size of the injected beam angle in the vertical direction.

As for the vertical direction, a painting area pulse-to-pulse between MLF and MR, however, is changed by controlling the size of the injected beam angle at the foil by using two vertical painting magnets, PBV1,2. A typical case for correlated painting is shown.

*Switching Horizontal Painting Area by PBHs*

In stead of PSTRs, horizontal painting magnets PBHs are only used in this method for switching horizontal painting area MLF to MR. Figure 6 shows a demonstration such a process which has also been successfully introduce in the recent beam studies. In this case, injected beam position and angle are both kept same for both MLF and MR but PBHs

patterns are carefully controlled for a particular closed orbit variation so as to realize a desired painting area. As the closed orbit variation at the end of injection determines the painting area, its amplitude for the MR painting is controlled as shown by the red arrow.

Figure 7 shows typical current patterns for the first painting magnets (PBH1). The solid black and red curves are typical patterns for 216 and $144\pi$ mm mrad painting area, where initial closed orbit offsets at the foil are different. However, in this method initial closed orbit offset is kept same and thus the current at the starting of $144\pi$ mm mrad is matched to that of $216\pi$ mm mrad by adding an offset between these two currents at start as shown by the red dotted curve. In stead of current being zero at the end, there has thus an offset at the end of injection, which determines the painting area for the MR. At present PBHs patterns are kept flat further 0.05 ms after injection is finished and then linearly ramped down to zero by another 0.35 ms. One big advantage with this method is that the painting area is changed by using only PBHs and injected beam orbit for both MLF and MR can be kept same. The chicane bump height is also same for both MLF and MR painting. The partially stripped and un-stripped waste beam orbits are can be thus kept same. However, an extra foil hits after the injection due to remaining offset of the PBHs can be considered as one small issue. In the vertical direction the procedure is same as done in the previous method.



Figure 7: Typical PBH current patterns for different painting areas. The dotted line is a typical patterns for changing horizontal painting area MLF to MR by using only PBHs.



Figure 6: Schematic view of switching horizontal painting area by using only PBHs.

## EXPERIMENTAL RESULTS

In order to verify a dependence of the extracted beam profiles on the RCS injection painting area, experimental studies were carried out for both 181 MeV and recently upgraded 400 MeV injection energies.

### Measurement of Extracted Beam Profiles by Changing Horizontal Painting Area by PSTRs

The experimental study by using PSTRs were carried out at 181 MeV injection. For simplicity, transverse injection

painting applied only for the horizontal direction and was 150 and $100\pi$ mm mrad for the MLF and MR, respectively. The extracted beam profiles were measured by a Multi-wire Profile Monitor (MWPM) placed in the 3-NBT. Figure 8 shows the measured (solid red circles) and simulated (lines) horizontal extracted beam profiles for MLF (top) and MR (bottom) for an equivalent beam power of 350 kW. As expected, the width of the extracted beam profile for the MR painting is measured to be narrower as compared to that of MLF painting and is also quite consistent with corresponding simulation results. The simulation was performed by using ORBIT code [6, 7].
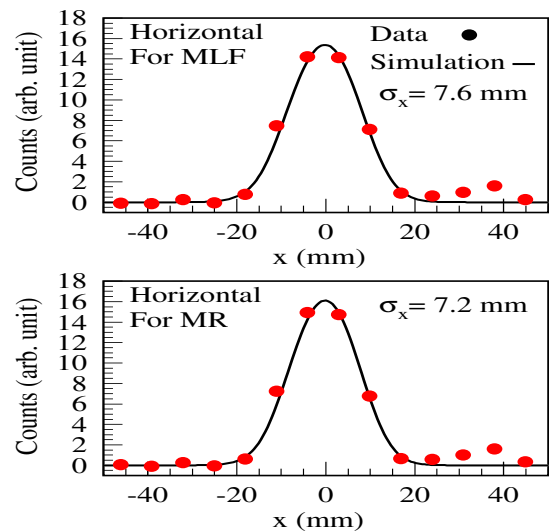


Figure 8: Comparison of horizontal extracted beam profiles for the MLF 150 and MR $100\pi$ mm mrad injection painting applied for only in the horizontal direction. The equivalent beam power was 350 kW, where red solid circles are the measured data by MWPM and lines are the corresponding simulation results. The profile width for a smaller injection painting area for the MR is confirmed to be narrower as compared to that for a larger one for the MLF.

*Measurement of Extracted Beam Profiles by Changing Horizontal Painting Area by PBHs*

Figure 9 shows comparisons of both horizontal and vertical extracted beam profiles between MLF and MR. The painting area between MLF and MR was changed by using PBHs and PBVs for the horizontal and vertical directions, respectively. In this experiment, the injected beam energy was 400 MeV and the extracted beam intensity was $4.6 \times 10^{13}$ ppp (550 kW equivalent). The painting area for the MLF and MR was chosen to be 100 and $50\pi$ mm mrad, respectively. The top two figures are for comparison in the horizontal direction, while bottom two figures are those for the vertical direction. The measured profiles are plotted with red solid circles, where lines are corresponding beam simulations. Here also extracted beam profiles for the MR painting is measured to be significantly narrower as compared to those for the MLF painting even for an equivalent beam power of 550 kW. The simulation results are also found to be almost consistent with measured ones.
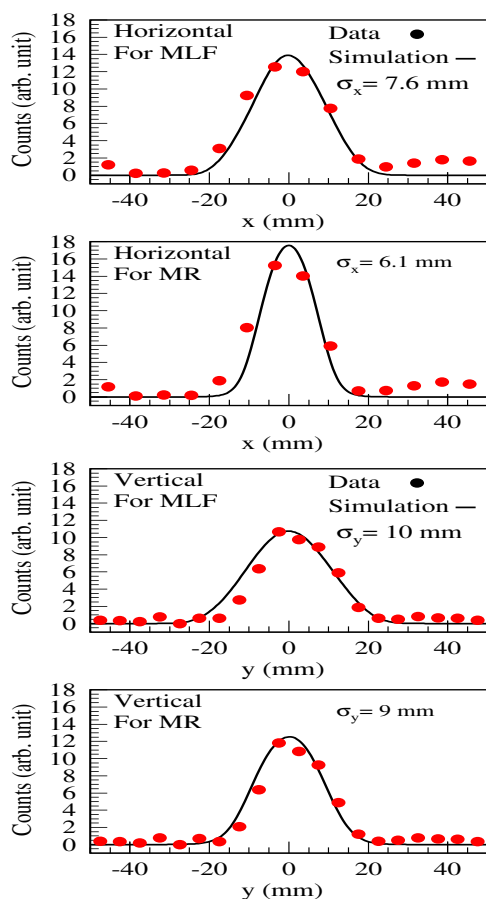


Figure 9: Comparison of the horizontal (top two) and vertical (bottom two) extracted beam profiles for the MLF 100 and MR $50\pi$ mm mrad injection painting applied for both horizontal and vertical directions. In this case painting area between MLF to MR was changed by the PBHs and PBVs for the horizontal and vertical directions, respectively. The beam profile widths for the MR are obtained to be narrower than those for the MLF.

## SUMMARY

In order to control extracted beam emittance pulse-to-pulse in simultaneous operation, a direct control of the transverse injection painting is proposed and has also been successfully demonstrated through experimental studies. The extracted beam profiles for a smaller injection painting area for the MR are measured to be significantly narrower as compared to those for a larger painting area for the MLF. Two independent methods, especially for changing painting area in the horizontal direction are considered and also successfully applied in the experimental studies. The corresponding numerical simulation results are also found to be consistent with measurements. The system is already in service even at the present RCS operation with 300 kW beam, where transverse painting area for the MLF and MR are fixed to be 100 and $50\pi$ mm mrad, respectively. It is thus confirmed that in a multi user machine beam parameters can be dynamically controlled and delivered as requested by the users even in simultaneous operation. The present principle can be applicable to any similar multi user machine for controlling beam emittances in a pulse-to-pulse mode.

## REFERENCES

[1] High-intensity Proton Accelerator Project Team, " Accelerator Technical Design Report for J-PARC", JAERI-Tech 2003-044 and KEK Report 2002-13.

[2] H. Hotchi et al., "Lessons from 1-MW Proton RCS Beam Tuning", in this proceeding, MOXLR02, HB2014, East Lansing, MI, USA (2014).

[3] P.K. Saha et al., "Direct observation of the phase space footprint of a painting injection in the Rapid Cycling Synchrotron at the Japan Proton Accelerator Research Complex" Phys. Rev. ST Accel. Beams 12, 040403 (2009).

[4] H. Hotchi et al., "Beam loss reduction by injection painting in the 3-GeV rapid cycling synchrotron of the Japan Proton Accelerator Research Complex"Phys. Rev. ST Accel. Beams 15, 040402 (2012).

[5] P.K. Saha et al., "Beam emittance control by changing injection painting area in a pulse-to-pulse mode in the 3-GeV Rapid Cycling Synchrotron of Japan Proton Accelerator Research Complex", Phys. Rev. ST Accel. Beams 16, 120102 (2013).

[6] J.A. Holmes, "Recent Enhancements to the ORBIT Code", in the Proceedings of IPAC2010, Kyoto, Japan, 1901 (2010).

[7] P.K. Saha et al., "ORBIT Beam Simulation Progress in the 3-GeV Rapid Cycling Synchrotron of J-PARC", in the Proceedings of IPAC2013, Shanghai, China, 521 (2013).

# MODELING AND FEEDBACK DESIGN TECHNIQUES FOR CONTROLLING INTRA-BUNCH INSTABILITIES AT CERN SPS RING [*]

C. Rivetta[†], J. Fox, O. Turgut , SLAC, Menlo Park, California, USA
W. Hofle, K. S. B. Li, CERN, Geneva

## Abstract

The feedback control of intra-bunch instabilities driven by electron-clouds or strong head-tail coupling (transverse mode coupled instabilities MCI) requires bandwidth sufficient to sense the vertical position and apply multiple corrections within a nanosecond-scale bunch. These requirements impose challenges and limits in the design and implementation of the feedback system. This paper presents model-based design techniques for feedback systems to address the stabilization of the transverse bunch dynamics. These techniques include in the design the effect of noise and signals perturbing the bunch motion. They also include realistic limitations such as bandwidth, nonlinearities in the hardware and maximum power deliverable. Robustness of the system is evaluated as a function of parameter variations of the bunch.

## INTRODUCTION

The feedback control of intra-bunch instabilities induced by electron-cloud (ECI) or strong head-tail interaction (transverse mode coupled instabilities - TMCI) requires enough bandwidth to sense the vertical position motion and apply correction fields to multiple sections of a nanosecond-scale bunch. Through the US LARP-CERN collaboration a wide-band feedback system is under research and development to control these intra-bunch instabilities. The effort is motivated by the plans to increase the beam current in the Super Proton Synchrotron (SPS) as part of the HL-LHC upgrade.

The feedback controller is implemented based on a digital reprogrammable processing channel, sampling the transverse bunch motion at a rate of 4 GS/s. The approach followed to design the controller is to consider the bunch dynamics as a multi-input multi-output system (MIMO). This conception arise because the multiple samples (multi-input) measuring the transverse motion across the bunch are used input to generate the multiple output samples that defines the control signal driving the kicker device.

During the first part of this development, the feedback control system is using a bank of finite-impulse response (FIR) filters to conduct MDs at CERN SPS ring during January 2013. In this bank, a filters are used to process individually each sample of the input signal. This planning was followed, in part, because of the simplicity of the filter implementation and the definition of its parameters and the limitations imposed by the hardware installed in the machine. The band-width of the existent kicker is about 160 MHz, limiting the effective feedback control on a 3.2ns bunch length to the first side-band around the betatron tune. Additionally, the setting of the Q26 lattice in the machine defined the fractional betatron frequency $\omega_\beta = 0.185$ and the fractional synchrotron frequency $\omega_s = 0.0059$ and the phase lag of the FIR filter was not a limitation to damp the transverse bunch dynamics corresponding to the barycentric and head-tail motions [1].

In the second stage of this development, new strip-line kickers with wider bandwidth were installed in the SPS ring and a slotted-coaxial kicker is under development [2,3]. That potentially will define a true wide-band feedback channel able to drive multiple intra-bunch modes. A new challenge in the design of the feedback controller exists due to the re-definition of the SPS lattice from the Q26 to the Q20 optics [4,5]. The new optics in the machine sets a fractional synchrotron frequency $\omega_s = 0.0170$, spreading out the frequency of the satellite bands around the betatron frequency $\omega_\beta = 0.185$. In [6], the design of a controller based on a bank of infinite-impulse response (IIR) filters is analyzed to stabilize the intra-bunch dynamics corresponding to the new Q20 optics. In that pre-design, the phase of the filters is kept almost constant in the frequency range corresponding to the fractional betatron tune and its dominant side-bands ($f_\beta \pm n f_s$). That design uses the bunch dynamics model to define the fundamental parameters of the controller and test the stability and performance robustness of the controller. It does not incorporate specifically the model into the design of the controller.

This paper addresses another methodology for the controller design to stabilize the intra-bunch dynamics of the beam at SPS with Q20 optics. The model of the intra-bunch dynamics is included intrinsically in the controller design providing the maximum information of the bunch modes to be stabilized. This realization gives higher order controllers respect to the FIR/IIR filter banks. In this paper we design a full model-based controller to stabilize the dominant bunch modes, analyze different controller options comparing the stability and performance robustness of the system when the betatron and synchrotron frequency are changed and the initial modal instability (growth rates) are varied. Based on this full controller, simplified versions or reduced order controllers has to be evaluated. The study of these reduced controllers is attractive to simplify the firmware implementation and the setting of the controller parameters in real-time operation.

## FEEDBACK SYSTEM

The first requirement for the controller is to stabilize the intra-bunch dynamics driven by electron cloud and strong head-tail instabilities. Additionally, the feedback system has to be robust to parameter changes in the beam dynamics and different operation conditions of the machine. The controller has to have enough dynamic range to keep the stability-performance of the system for a maximum set of beam transient conditions. Given the conditions that the open loop system is unstable and the feedback channel has delay, it could exist a combination of fast unstable dynamics and long delay in the system that makes the controller unfeasible. The bandwidth of the controller has to be limited to minimize the effect of the receiver noise in the saturation of the power stage. Additionally, the filter has to be able to reject signal perturbations that affects the performance of the feedback system. Feedback control model-based design techniques allows to assess the system stability and address the system performance including in the controller design the rejection to noise and perturbations.

The architecture of the feedback control channel prototype implemented for this application is based on a digital reprogrammable system, sampling the transverse bunch motion at a rate of 4 GS/s. A single bunch controller has been developed to explore new technology and control techniques and it is planned to expand this prototype to allow multibunch control. The implementation of this system is based on a reconfigurable FPGA and ADC/DAC operating at 4 GS/s. The system is synchronized with the SPS RF clock and is able to perform diagnostic functions, set feedback parameters and record the bunch motion at selected intervals [7]. A general block diagram of the proposed hardware is depicted in Fig. 1. Analog equalization of the pick-up and cable transfer function is included in the feedback channel. The controller is programmable and has the flexibility to implement FIR / IIR filter banks or more complex control topologies based on the bunch model dynamics.
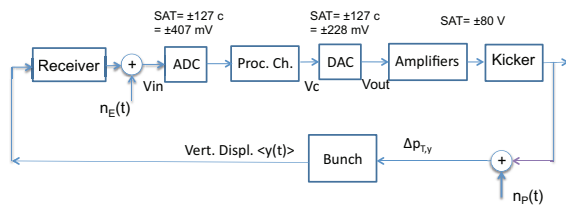


Figure 1: Block diagram control feedback system.

## MODEL-BASED CONTROLLERS

During the last decades, research in the feedback control area filled the gap between the classic and modern control theory, including in the controller design the information of the system model, its parameter variations, perturbation and noise to access the stability and performance of the closed loop feedback. [8]. There exists several options to include the bunch model in the design of the controller. We follow

in this paper the one based on the observer technique, which is described by the block diagram depicted in Fig. 2.
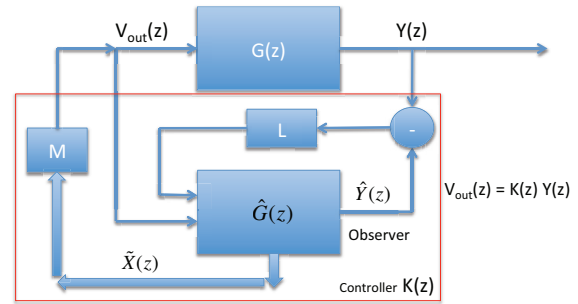


Figure 2: Block diagram model-based controller.

Defining by $G(z)$ the transfer function matrix in $\mathcal{Z}$-domain between the vertical motion of the multiple samples of the bunch $Y(z)$ and the control signal $V_{out}(z)$, the idea is to create an observer based on the bunch dynamical model $\tilde{G}(z)$ and the processed error signal $L(Y(z) - \tilde{Y}(z))$. This observer will allow to estimate in real-time the internal states $X$ of the system that are not included directly in the system output $Y(z)$. The feedback control will generate the correction signal $V_{out}(z) = -M\tilde{X}(z)$ based on the gain matrix M. The controller is defined by the transfer function matrix $K(z)$, such that $V_{out}(z) = K(z)Y(z)$ includes the dynamic model of the bunch and has to gain matrices $L$ and $M$ to adjust the system specifications and robustness.

In this approach is critical the knowledge of the bunch dynamical model. This can be obtained via analytical methods, where the model can include parameter variations based on the different operation conditions of the machine or estimated via identification techniques. The last option is under research and uses the correlation between an injected signal to perturb the bunch and the vertical displacement as response to that excitation [9]. This technique not only is useful to estimate the bunch dynamical model to design the controller but also can be used as diagnostic tool to extract bunch and machine parameters during operation.

Let us assume that the relationship between input-output, $G(z)$, can be represented by a realization in state space $\tilde{G} = \{A, B, C, D\}$. The model of the observer can be expressed as;

$$\tilde{x}(k+1) = A\tilde{x}(k) + Bv_{out}(k) + v(k)$$
$$\tilde{y}(k) = C\tilde{x}(k) + Dv_{out}(k)$$

where $\tilde{y}(k)$ and $\tilde{x}(k)$ are the estimated outputs and internal states of the system, respectively and $v_{out}(k)$ and $v(k)$ are input signals. The matrix $D$ is equal to zero for strictly proper transfer function representations (general physical systems). Then, if $v(k)$ is proportional to the error between the measured and the estimated outputs

$$v(k) = L(y(k) - \tilde{y}(k)) = L(y(k) - C\tilde{x}(k)) \text{ and}$$
$$\tilde{x}(k+1) = (A - LC)\tilde{x}(k) + Bv_{out}(k) + Ly(k) \quad (1)$$

The control signal $u(k)$ is equal to $v_{out}(k) = -M\tilde{x}(k)$, replacing into (1)

$$\tilde{x}(k+1) = (A - LC - BM)\tilde{x}(k) + Ly(k)$$
$$v_{out}(k) = -M\tilde{x}(k)$$

This is the state space representation of the controller with input $y(k)$, output $v_{out}(k)$ and dynamics defined the eigenvalues of the matrix $A - LC - BM$. The control transfer function can expressed in $\mathcal{Z}$-domain by the matrix $K(z)$

$$V_{out}(z) = K(z)Y(z) = -M(z\mathbf{I} - (A - LC - BM))^{-1}LY(z)$$

The order of the controller is defined by the order of the model representing the system (size of the matrix A). The characteristics of the controller and the closed loop system are defined by the gain matrices $M$ and $L$. There exists several techniques to calculate the gain matrices based upon the system specifications, external perturbations and system uncertainties. In general the number of unknown in the gain matrices is larger than the number of specifications and restrictions imposed to the design. Formulations to calculate the matrix parameters are posed as optimization problems where the system specifications and restrictions are included in the cost function.

In our case, we are designing a stabilizing feedback system or damper. Assuming we do not want to affect the frequency of each bunch mode, the final location of the dominant bunch eigenvalues can be assigned. If the dynamics of the observer is designed such that it is faster than the bunch dynamics, the gain matrices can be evaluated separately where the matrix $M$ adjusts the final position of the dominant bunch eigenvalues and the gain matrix $L$ defines the dynamics of the observer. In the pre-design presented as example in this paper, the dominant bunch modes are damped to the similar rates and two cases are evaluated for the dynamics of the observer. Those cases are compared taking into account the transient response and dynamic range of signals, the robustness of the final system to parameter variations, e.g. variation of the betatron and synchrotron tunes, different unstable modes, etc.

## DESIGN OF THE CONTROLLER

Let us assume the bunch dynamical model captures the six dominant modes whose eigenvalues are $\lambda_k = \pm i\,(\omega_\beta + k\omega_s)$ for $k = ..., -6, ..., 0, ..., +6, ....$ The controller is designed such that the final magnitude for those dominant eigenvalues $\lambda_k = -\sigma \pm i(\omega_\beta + k\omega_s)$ are: $\lambda_0 = -0.027 \pm i\,2\pi\,0.185$ and $\lambda_k = -0.019 \pm i\,2\pi\,(0.185 + k\,0.017)$ for $k = -6, ..., 0, ..., +6$. Two controllers are presented and their difference depends of the magnitude of the gain matrix $L$. In one case, labeled: *Design 1*, the eigenvalues of the controller are complex conjugated while in the *Design 2* the eigenvalues are real or complex conjugated with minimum imaginary components.

### Results

Some results of those designs are depicted in Figs. 3 to 8. In Fig. 3 the response of the vertical motion of the multi-

ple slices of the bunch is depicted when the vertical initial offset of the bunch is 1mm and the controller corresponds to *Design 1*. Similarly, Figs. 4 and 5 show the estimated outputs by the observer and the control signals for that case. Figs. 6, 7 and 8 depict the same transient for the controller labeled *Design 2*. It is possible to observe that the initial transient response is more aggressive in the *Design 2* controller requiring more dynamic range in the amplifier driving the kicker. Additionally, because the difference between both controllers is mainly in the dynamics of the observer (definition of gain matrix L) and the dominant dynamics in closed loop of the system is almost the same (definition of gain matrix M, setting of dominant eigenvalues $\lambda_k$), the transient response only differs in the first revolutions. During this period, the observer response transitions from the initial state toward the estimated output signal.
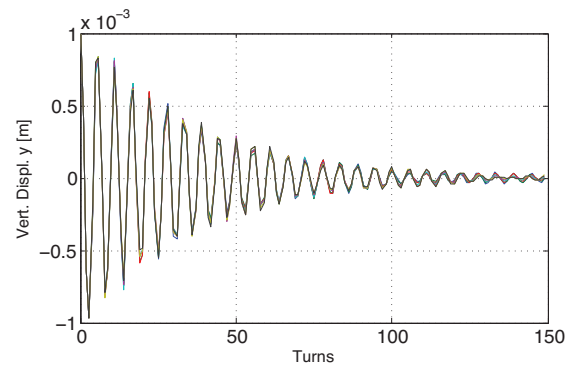


Figure 3: vertical displacement - *Design 1* controller
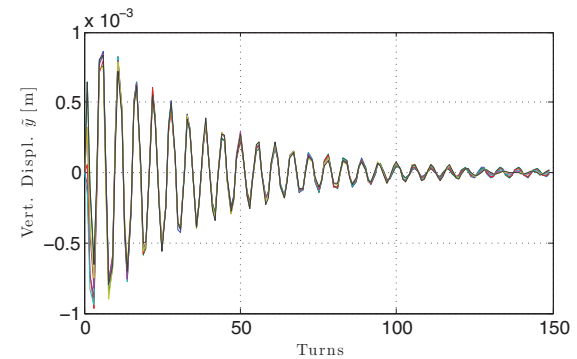


Figure 4: observer output - *Design 1* controller

It is important to evaluate the effect on the final stability and performance of the system if the beam parameters are changed while the controller is kept with its design based on the nominal parameters of the bunch. To analyze that impact, the betatron and synchrotron frequencies are changes as well as the bunch is assumed unstable and quantified by the growth rate per mode. Both designs have similar robustness characteristics and a summary of the results follows. If the betatron frequency is changed keeping the synchrotron frequency constant and assuming that the damping is null for all the modes, the system reaches the stability
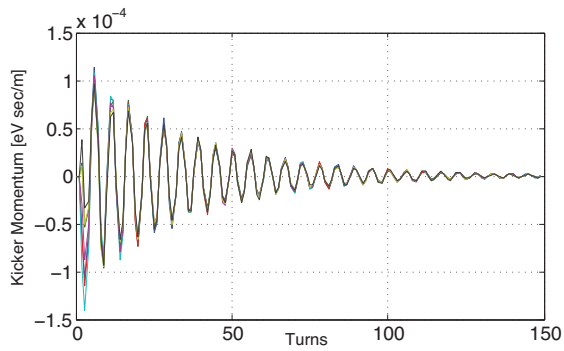
Figure 5: control signal - *Design 1* controller
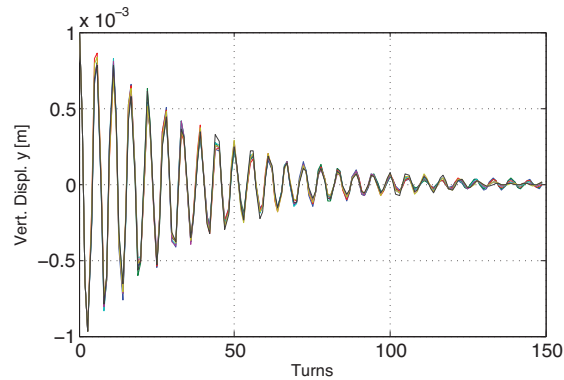


Figure 6: vertical displacement - *Design 2* controller
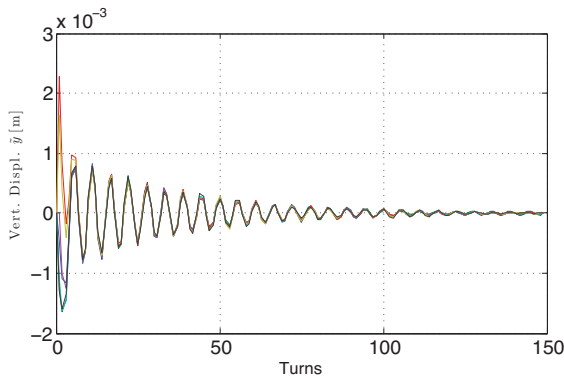


Figure 7: observer output - *Design 2* controller
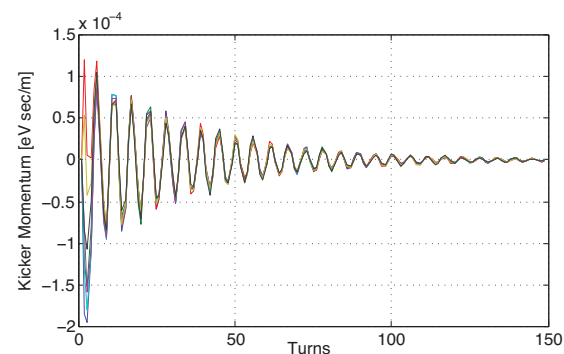


Figure 8: control signal - *Design 2* controller

limits operating in closed loop if either $\omega_\beta < 0.85\,\omega_{\beta 0}$ or $\omega_\beta > 1.2\,\omega_{\beta 0}$, where $\omega_{\beta 0} = 2\pi\,0.185$ is the nominal value. This limit is mainly defined by the instability of the high order modes. Similarly, it is possible to evaluate the effect of changes in the synchrotron frequency. In this case, the system reaches the stability limits operating in closed loop if either $\omega_s < 0.7\,\omega_{s0}$ or $\omega_s > 1.3\,\omega_{s0}$, where $\omega_{s0} = 2\pi\,0.017$ is the nominal value.

An important parameter to analyze with this controller is the maximum growth rate or instability that is possible to damp assuming that the kicker amplifier or any other limitation in the feedback channel does not reach its maximum dynamic range. To study this point, two cases of unstable beam were considered. In one case the growth rate for all the modes was assumed the same, while in the other case, only one mode was assumed unstable and the others remained with zero damping. In the case that all the modes are unstable, the designed controller is able to stabilize bunches with growth rates $\sigma \leq 0.03 - 0.035$ 1/turns. For individual modes unstable, the maximum growth rate that the controller can damp per mode are summarized in table **??**.

Table 1: Maximum Growth Rate possible to stabilize

| Mode | Growth Rate |
|------|-------------|
| 0 | $\sigma = 0.05$ 1/turns |
| $\pm 1$ | $\sigma = 0.05$ 1/turns |
| $\pm 2$ | $\sigma = 0.05$ 1/turns |
| $\pm 3$ | $\sigma = 0.04$ 1/turns |
| $\pm 4$ | $\sigma = 0.04$ 1/turns |
| $\pm 5$ | $\sigma = 0.04$ 1/turns |
| $\pm 6$ | $\sigma = 0.04$ 1/turns |

### Remarks about this pre-design

The model-based design technique defines controllers with an order equal to the model used. In general, it is a high order controller. As a MIMO controller, this topology links all the measured variables to calculate each sample of the correction signal $v_{out}(k)$. This issues can limit the implementation and processing in the reconfigurable FPGA due to time involved in the multiple arithmetic operations. It will be important to consider simplified or reduced controllers based on this model-based technique and evaluate the impact on the stability and performance robustness of the system when it is compared with the respect the full-order controller evaluated in this design.

Using this design methodology, where the controller incorporates as much as possible information about system to stabilize, it makes relatively straightforward to incorporate the specification in the design process. As disadvantage, some designs could be sensitive to parameters variations if the model used does not take into account such parameter variations, uncertainties and un-modeled dynamics.

As a final remark, the design requires of the reduced bunch dynamical model. Analytical models of the bunch dynamics can be used incorporating realistic parameters for their

description. Another option is to evaluate the model in real-time based on measurements in the machine. Identification techniques allows to quantify a reduced model base on the response of the vertical motion of the bunch to signals designed to perform a successful identification. Part of the research in this project is focus on evaluating this techniques to extract the bunch reduced model [9].

## CONCLUSIONS

A pre-design of a controller to mitigate the intra-bunch instability has been studied showing good results. This model-based design controller includes in the observer a model of the bunch with multiple modes ($k = -6, ..., 0, ..., +6$). In the design, the location of the dominant eigenvalues of the closed loop system was set to provide satisfactory damping to those dominant bunch modes. This controller topology renders high order systems requiring large processing power.

Future work includes to test the controller performance using more realistic bunch simulators as HeadTail or CMAD. Additionally, the effort will be focused on reducing the order of the controller, balancing the performance, processing power and complexity requirements. These controllers will be compared with the IIR bank filters to define the best option to implement in the FPGA.

## ACKNOWLEDGMENT

## REFERENCES

[1] C. H. Rivetta et al., " Control of Intrabunch Dynamics at CERN SPS Ring Using 3.2GS/s Digital Feedback Channel", FROAA3, NA-PAC' 13 Pasadena, USA (2013).

[2] J. M. Cesaratto et. al., "SPS Wideband Transverse Feedback Kicker: Design Report", SLAC-R-1037 (2013).

[3] J. M. Cesaratto et. al., "A Wideband Slotted Kicker De- sign for SPS Transverse Intra-Bunch Feedback" , WEPME61, IPAC'13, Shanghai, China (2013).

[4] H. Bartosik et al., " Experimental Studies with Low Transition Energy Optics in the SPS IPAC'11 San Sebastian, Spain (2011).

[5] H. Bartosik et al., "Impact of LowTransition Energy Optics to the Electron Cloud Instability of LHC Beams in the SPS IPAC'11 San Sebastian, Spain (2011).

[6] C. H. Rivetta et al., " Feedback System Design Techniques for Control of Intrabunch Instabilities at the SPS", TUPRI086, IPAC'14, Dresden, Germany (2014).

[7] J. D. Fox et al., "A 4 GS/s Feedback Processing System for Control of Intra-Bunch Instabilities", IBIC13, Oxford, UK (2013).

[8] S. Skogestad, I. Postlethwaite, *Multivariable Feedback Control, Analysis and Design*, (New York: John Wiley & Sons, 2001).

[9] O. Turgut et al., "Identification of Intra-Bunch Transverse Dynamics for Feedback Control Purposes at CERN Super Proton Synchrotron", *These Proceedings*, HB2014, East Lansing, USA (2014).

# LONGITUDINAL MICROWAVE INSTABILITY IN A MULTI-RF SYSTEM

T. Argyropoulos, CERN, Geneva, Switzerland

## Abstract

The longitudinal microwave instability is observed as a fast increase of the bunch length above some threshold intensity. Recently, this type of instability was seen for a single proton bunch at high energies in the CERN SPS and is proven to be one of the limitations for an intensity increase required by the HL-LHC project. In this paper a theoretical approach to the analysis of the microwave instability is verified by particle simulations. The study is applied to the SPS and is based on the current SPS impedance model. Finally, the effect of the 4th harmonic RF system on the microwave instability threshold is investigated as well.

## INTRODUCTION

There is a very wide range of phenomena in high-intensity circular accelerators that is called by the same name "microwave ($\mu w$) instability". Usually, but not always, an instability is called $\mu w$ if

$$f_r \tau \gg 1, \tag{1}$$

where $\tau$ is the bunch length and $f_r = \omega_r/(2\pi)$ is the resonant impedance frequency. In proton accelerators $\mu w$ instability is observed as a fast increase of the bunch length and thus of the longitudinal emittance $\varepsilon_l$. This bunch lengthening can be distinguished from the bunch lengthening due to potential well distortion by a change in the slope of bunch length versus intensity. The break point where the slope changes is considered as the instability threshold.

The operation of the CERN SPS in the past was limited by $\mu w$ instability. At that time, measurements with long bunches and RF off had allowed the dominant resonant impedances with high $R_{\rm sh}/Q$ to be seen as peaks in the unstable beam spectrum [1], where $R_{\rm sh}$ is the shunt impedance and $Q$ the quality factor. Most of the impedance sources were identified and it was proved, both by measurements and simulations, that the pumping port impedance was the main source of instability. Consequently, shielding these devices led to a significant improvement of the beam stability [2].

Today, the SPS is used as the LHC injector where particles are accelerated by the main 200 MHz RF system. In addition to that, for proton beams, a 4$^{\rm th}$ harmonic RF system (800 MHz) operated in bunch shortening mode (BSM) is used for beam stability (Landau damping). During measurements in 2012, before long shutdown 1 (LS1), a stable LHC proton beam (4 batches of 72 bunches each) with a bunch spacing of 25 ns and a bunch intensity of $N_b = 1.35 \times 10^{11}$ p/b was accelerated to the SPS top energy (450 GeV/c) [3]. Nevertheless, according to the HL-LHC project [4], beams with an intensity of up to $2.5 \times 10^{11}$ p/b

will be requested from the SPS. This means that one needs to almost double $N_b$, while maintaining the same bunch length at SPS extraction ($\tau_{4\sigma} \leq 1.7$ ns), restricted by the LHC 400 MHz RF system. The maximum bunch length allowed by the Beam Quality Monitor (BQM) for injection into the LHC is $\tau = 1.9$ ns.

Recent measurements for single high-intensity bunches ($N_b > 2.0 \times 10^{11}$ p/b) showed that longitudinal emittance increases during the cycle, pointing out that a $\mu w$ instability could be responsible for this effect.

## UNCONTROLLED EMITTANCE BLOW-UP

Longitudinal emittance blow-up is observed in the SPS for both single and multi-bunch beams. An example of bunch lengths measured in 2012 for single high-intensity bunches at the SPS flat top is presented in Fig. 1. The measurements were performed in a double RF system in BSM with RF voltages $V_{200} = 2$ MV and $V_{800} = 200$ kV in the 200 MHz and 800 MHz RF systems, respectively [5]. Note that $V_{200} = 2$ MV is much lower than the $V_{200} = 7$ MV that is used in normal operation in order to compress the bunch before extraction to the LHC.
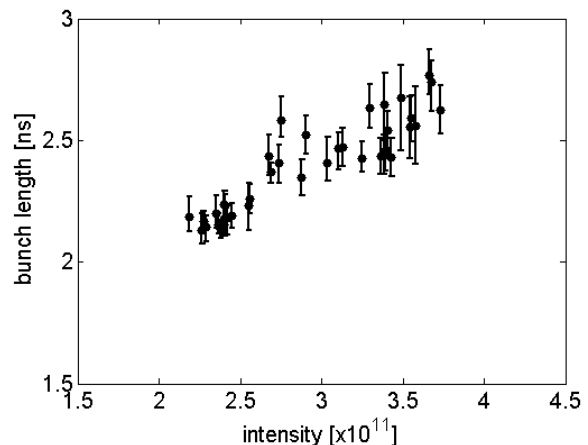


Figure 1: Measured bunch length as a function of intensity for a single bunch at the SPS flat top in a double RF system (BSM). The voltages $V_{200} = 2$ MV and $V_{800} = 200$ kV [5].

A strong increase of the bunch length with intensity is shown in Fig. 1 which can not be attributed to the potential well distortion with the SPS longitudinal impedance model [6]. In particular, in the current model, which includes the RF cavities, resistive wall, injection and extraction kickers, the low frequency reactive part of the SPS impedance is ${\rm Im}Z/n \approx 3.5 \ \Omega$, while much higher

impedance is needed to explain the observed emittance growth ($\mathrm{Im}Z/n \approx 15\ \Omega$) [7]. Therefore, a blow-up of the bunch must have occurred during the cycle.

Indeed, measurements performed in 2014 under similar conditions showed that instability occurs during the acceleration ramp. Examples are presented in Fig. 2, where the bunch length evolution during the cycle is depicted. As can be seen in the figure, for intensities above $2.5 \times 10^{11}$ p a blow-up in emittance takes place during the ramp, leading to larger bunch lengths at the SPS flat top. Note that the voltage program for the 200 MHz RF system was adjusted to have a constant bucket area of 0.5 eVs along the cycle. Usually, 0.6 eVs is used for the LHC type of beams. This was done in order to increase the filling factor and thus to increase Landau damping due to the non-linearity inside the bunch.





Figure 3: Example of measurements performed on the SPS flat bottom with long bunches ($\tau \approx 25$ ns) and RF off [8]. Top: bunch profile modulated at 200 MHz and at a higher frequency ($\sim 1.4$ GHz). Bottom: projection of the Fourier spectra of all the bunch profiles acquired during $\sim 100$ ms. Measurements in the Q26 optics with $N_b \sim 1 \times 10^{11}$.
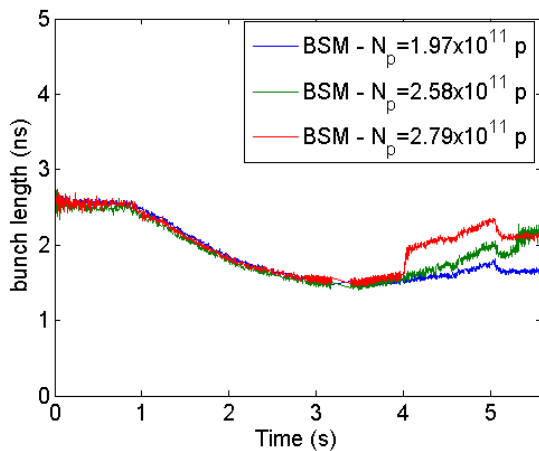


Figure 2: Measured bunch length along the SPS cycle for a single bunch with different intensities in double RF (BSM).

Similar behavior was also measured in the single RF system. However, in that case, the instability during the cycle was observed at lower intensity ($\sim 1.7 \times 10^{11}$ p) compared to the double RF (BSM).

Great effort was made during the last 2 years to identify the impedance sources, responsible for this instability, by beam measurements and simulations [8]. In addition, electromagnetic simulations and measurements in the lab were carried out to determine the impedance of different devices in the SPS ring [9]. An example of beam measurements performed at the SPS flat bottom with very long bunches ($\tau \approx 25$ ns) and RF off, similar to those done in the past [1], is presented in Fig. 3. A strong peak at a frequency around 1.4 GHz was observed [8].

A thorough, element-by-element impedance assessment was then started to find the source of the 1.4 GHz resonance. It has been found that this resonant peak originates from the impedance of certain SPS vacuum flanges [10]. Several types of these flanges are used for the connection of various machine elements and their total number in the ring is around 550. Electromagnetic simulations and RF mea-

surements [9] were carried out to determine the impedance of these elements, and for a subset of $\sim 120$ of them, a resonance at 1.4 GHz has been found with an $R_{\mathrm{sh}}/Q \sim 9$ k$\Omega$ and $Q \sim 200$. Significant resonances were also found from other types of vacuum flanges at around 1.2 GHz, 1.8 GHz and 2.5 GHz.

## MICROWAVE INSTABILITY DUE TO RESONANT IMPEDANCE

The effect that a resonant impedance at the high frequency of 1.4 GHz has on the bunch stability was studied in more detail both in single and double RF systems.

The fast $\mu w$ instability threshold can be estimated for a broad-band impedance using the Keil-Schnell-Boussard criterion [11]. However, when applied for the SPS case in the past, a much lower threshold in intensity was obtained [12]. Analytical solutions for the instability thresh-

olds can be calculated for a fast instability growth for a bunch with Gaussian distribution in the limiting cases of a broad-band ($f_r\tau \gg Q$) or narrow-band ($f_r\tau \ll Q$) resonant impedance [12, 13]. For the instability threshold of a single bunch in a single RF system defined by the interaction with a narrow-band resonator it is the value of $R_{sh}/Q$ which is important, while $R_{sh}/n_r$ is relevant for a broadband impedance.

Macroparticle simulations were carried out to verify this prediction, using the code BLonD [14]. The simulation was set up to match the experimental conditions at SPS flat top. The particle distribution closest to the measured one was found to be $F(H) = (1 - H/H_0)^2$, where $H$ is the single particle Hamiltonian and $H_0$ is the Hamiltonian that corresponds to the limiting phase space trajectory. The initial matched distribution was created iteratively and the particles were then tracked for 1.15 s (around twice the time of the SPS flat top). The criterion used to estimate the threshold was based on the bunch length growth and on its oscillation amplitude at the end of the simulation. In particular, the bunch was considered unstable when $\tau_f/\tau_i \geq 5\%$ or $\Delta\tau \geq 100$ ps, where $\tau_f$, $\tau_i$ are the final and initial bunch lengths and $\Delta\tau$ is the maximum bunch length oscillation amplitude.

Initially, the case with a single RF system was studied. In order to compare with the above-mentioned expectations, the same $R_{sh}/Q = 10$ kΩ was used while the value of $Q$ (and $R_{sh}$) was varied. The simulation results are summarized in Fig. 4 where the instability threshold as a function of bunch emittance is plotted.
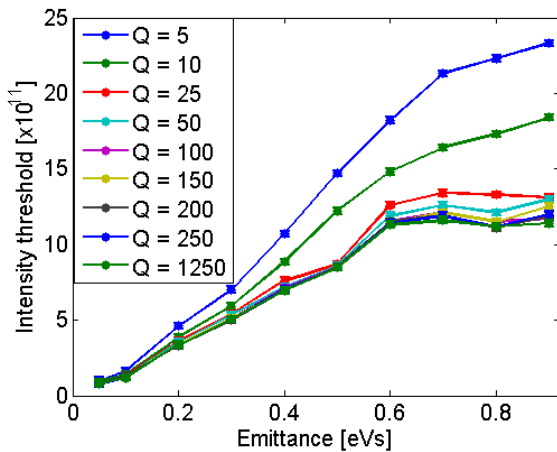


Figure 4: Instability threshold as a function of intensity for different $Q$ values, found in simulations for a single bunch at SPS flat top (450 GeV/c) in single RF and for a resonator with $R_{sh}/Q = 10$ kΩ. The voltage $V_{200} = 2$ MV.

For $Q \geq 50$ the instability threshold is practically unchanged, confirming the fact that only $R_{sh}/Q$ is important for the bunch stability when the resonator is in the narrowband regime. Note that for all the simulated bunches $f_r\tau < 4 \ll 50$. Instead, when $Q < 50$, $R_{sh}$ becomes important

for stability since the resonator approaches the broad-band regime. As a consequence, for instability in narrow-band impedance regime, damping the resonator does not help much since $R_{sh}/Q$ stays constant. In particular, a damping of more than a factor 50 should be achieved in order to increase the instability threshold.

Similar dependence on $R_{sh}/Q$ and $Q$ was also found for a double RF system when the harmonic and the voltage ratios are $h_2/h_1 = V_1/V_2 = 2$. The two operating modes of the double RF system were studied, namely the bunch-shortening mode (BSM) and the bunch-lengthening mode (BLM) in which, above transition, the phase between the two RF systems is $\pi$ and 0, respectively. The results for $Q = 250$ are presented in Fig. 5, together with the single RF case for comparison.
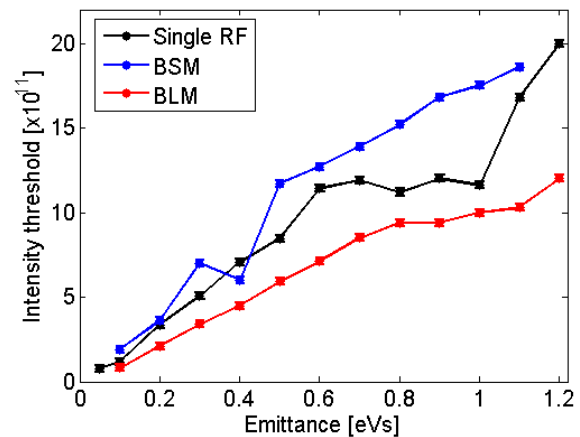


Figure 5: Instability threshold as a function of intensity found in simulations for a single bunch at the SPS flat top (450 GeV/c) in single and double RF systems (BSM and BLM) with $h_2/h_1 = V_1/V_2 = 2$. A resonator with $Q = 250$ and $R_{sh}/Q = 10$ kΩ was used as an impedance source. The voltages $V_{200} = 2$ MV and $V_{800} = 1$ MV.

From $\mu w$ theory, it is expected that the instability threshold increases with relative momentum spread ($\Delta p/p$) inside the bunch [11, 12, 13]. The fact that BSM, which has the maximum value of $\Delta p/p$, has the highest threshold is in line with this. Similarly, BLM has the lowest threshold amongst the three cases.

However, the previous result is not valid anymore when the harmonic ratio between the two RF systems is $h_2/h_1 = 4$, as presently in the SPS. Particle simulations performed for this harmonic ratio and for two different voltage ratios showed that above a certain emittance the instability threshold is higher in a single RF system (see Fig. 6).

A possible explanation of this fact can be obtained by inspecting the synchrotron frequency distribution inside the bunch $f_s(J)$, where $J$ is the action (similar to the $\varepsilon_l$). Examples of distributions calculated for a bunch of $\varepsilon_l = 0.6$ eVs are presented in Fig. 7. As one can see, in BSM, there are regions with zero derivative, $f'_s(J) = 0$ in the tails of the bunch which can reduce significantly
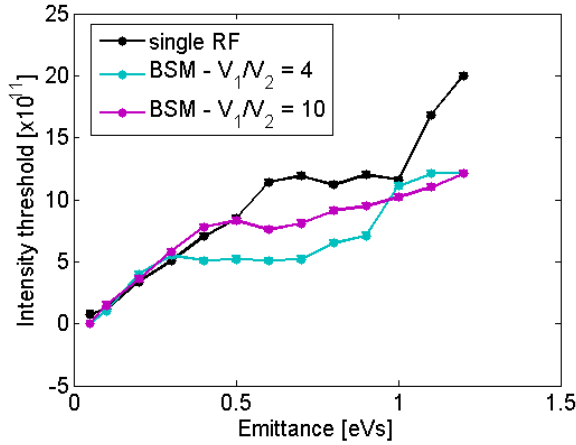
Figure 6: Instability threshold as a function of intensity found in simulations for a single bunch at SPS flat top (450 GeV/c) in single and double RF systems (BSM) with $h_2/h_1 = 4$. A resonator with $Q = 250$ and $R_{sh}/Q = 10$ kΩ was used. The voltage $V_{200} = 2$ MV.



Figure 8: Measured and simulated bunch length as a function of intensity for a single bunch at SPS flat top in double RF system (BSM). The voltages $V_{200} = 2$ MV and $V_{800} = 200$ kV.

the loss of Landau damping threshold, as has been shown in [15, 16]. Note that $\varepsilon_l \sim 0.6$ eVs corresponds to the typical emittance of LHC-type proton beams at SPS flat top.



Figure 7: Synchrotron frequency distribution inside the bunch, corresponding to the points with $\varepsilon_l = 0.6$ eVs in Fig. 6, with the same color convention.

## SPS LONGITUDINAL INSTABILITY

Macroparticle simulations were performed for comparison with measurements for single- and multi-bunch beams. The SPS impedance model [6], including in addition the impedance of the vacuum flanges, was used. The results for single high-intensity bunches in a double RF system (BSM) are shown in Fig. 8, where bunch lengths found from simulations and measurements at the SPS flat top are plotted together. For both of them, a strong increase of the bunch length with intensity is observed.

As aforementioned, this increase cannot be attributed to potential well distortion, but to a $\mu w$ type of instability instead. Indeed, clear instability thresholds can be observed in simulations. In particular, for the emittances of $\varepsilon_l = 0.35$ eVs and $\varepsilon_l = 0.45$ eVs the thresholds were found at $N_{th} = 2.5 \times 10^{11}$ and $N_{th} = 2 \times 10^{11}$, respectively. The final bunch lengths obtained in simulations are in very good agreement with the measurements. In fact, for the measurements done in 2014, the instability threshold has been found at around $N_{th} = 2.5 \times 10^{11}$, as in the simulations with $\varepsilon_l = 0.35$ eVs. Unfortunately, for the measurements performed in 2012, the threshold is not visible, since points at low intensities are missing. Note that in all these measurements the 200 MHz voltage was very low (2 MV), which is good for Landau damping, but unfavorable for $\mu w$ instability due to the low momentum spread. Furthermore, it was found from simulations that the threshold was increased by increasing the RF voltage, confirming the $\mu w$ nature of the instability.

Simulations were also carried out with a multi-bunch beam at the SPS flat top. At the moment, only six bunches (spaced by 25 ns) could be simulated and thus only qualitative conclusions can be drawn. For the same longitudinal emittance, the instability threshold for 6 bunches has been found to be almost twice lower than that for a single bunch. This result, presented in Fig. 9, is in agreement with measurements in the double RF system, where the single bunch instability threshold is approximately twice higher than the multi-bunch one.

In addition, in simulations only a coupling between a few bunches (3 or 4) was observed, and no coupled-bunch mode could be identified, similar to all beam observations. Indeed, in measurements bunches spaced by 25 ns or 50 ns are coupled, but the distance of 225 ns between the PS batches is enough to practically fully decouple them; in-
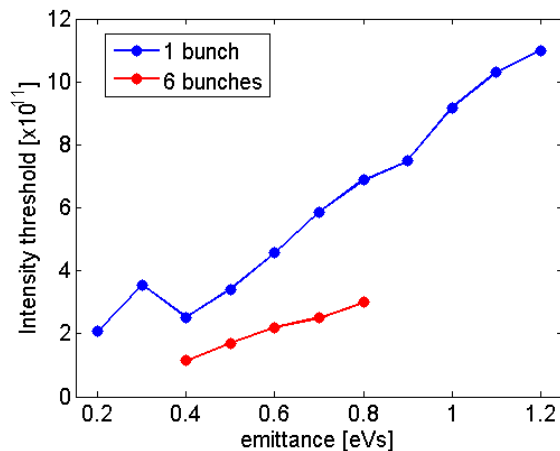
Figure 9: Instability threshold found in simulations for a single- and a 6-bunch beam at SPS flat top and double RF (BSM). The voltages $V_{200} = 7$ MV and $V_{800} = 640$ kV.

stability thresholds in the SPS with 1 to 4 batches are very similar [17].

Finally, simulations performed under similar conditions, both for single- and multi-bunch beams, but without the impedance of the vacuum flanges, showed that the instability threshold is twice higher. Therefore, measures for reducing this impedance should be considered in order to reach the intensity required by the HL-LHC project.

## CONCLUSIONS

Uncontrolled longitudinal emittance blow-up has been observed in the CERN SPS both for single- and multi-bunch beams. This is presently one of the main limitations for reaching the intensity required by the HL-LHC. Beam measurements revealed a strong signal at 1.4 GHz coming from the SPS vacuum flanges. The effect of this resonant impedance on beam stability was studied using macroparticle simulations. It was shown that for narrow-band resonators the instability thresholds scales with $R_{sh}/Q$, while for broad-band, $R_{sh}$ is important, as expected from theory. The cases of single and double RF systems were inspected. In particular, for the double RF system with harmonic ratio $h_2/h_1 = 2$, the intensity threshold scales with the relative momentum spread, i.e. it is higher in BSM and lower in BLM compared to the single RF. On the contrary, above a certain longitudinal emittance, beam stability becomes worse in BSM than in single RF when $h_2/h_1 = 4$. The microwave nature of the instability observed in the SPS was also confirmed by simulations using the current SPS impedance model. SPS vacuum flanges were identified as the responsible impedance source; measures for reducing this impedance are currently being considered.

## ACKNOWLEDGMENT

## REFERENCES

[1] T. Bohl, T.P.R. Linnecar, E. Shaposhnikova, "Measuring the resonance structure of accelerator impedance with single bunches," Phys. Rev. Let.,78, 3109 (1997).

[2] T. Bohl, T.P.R. Linnecar, E. Shaposhnikova, "Impedance reduction in the CERN SPS as seen from longitudinal beam measurements," EPAC 2002, Paris, France, June 2002.

[3] T. Argyropoulos et al., talks at LIU-SPS Beam Dynamics WG, CERN, Oct., Nov., Dec. 2012. http://cern.ch/spsu/

[4] L. Rossi, "LHC Upgrade Plans: Options and Strategy," IPAC'11, San Sebastian, Spain, Sep. 2011.

[5] H. Timkó et al., "Short High-Intensity Bunches for Plasma Wakefield Experiment AWAKE in the CERN SPS," IPAC'13, Shanghai, China, May 2013.

[6] C. Zannini et al., talk at LIU-SPS Beam Dynamics WG, CERN, March 2013. http://cern.ch/spsu/

[7] H. Timkó et al., talk at LIU-SPS Beam Dynamics WG, CERN, May 2013. http://cern.ch/spsu/

[8] T. Argyropoulos et al., "Identification of the SPS Impedance at 1.4 GHz," IPAC'13, Shanghai, China, May 2013.

[9] J. E. Varela et al., talks at LIU-SPS Beam Dynamics WG, CERN, May, July, Aug., Sep., Oct. 2013. http://cern.ch/spsu/

[10] E. Shaposhnikova et al., "Identification of High-frequency Resonant Impedance in the CERN SPS," IPAC'14, Dresden, Germany, June 2014.

[11] E. Keil and W. Schnell, "Concerning longitudinal stability in the ISR," CERN/ISR/TH/RF/69-48, 1969; D. Boussard, "Observation of microwave longitudinal instabilities in the CPS," CERN/LAB/II/RF/75-2, 1975.

[12] T. P. R. Linnecar, E. Shaposhnikova, "Microwave instability and impedance measurements in the CERN SPS," Part. Accel. 58, p.241-255, 1997.

[13] J. M. Wang and C. Pellegrini, "On the condition for a single bunch high frequency fast blow-Up," Proc.XI Int. Conf. on H.E.Ac, p.554, 1980.

[14] BLonD - Beam Longitudinal Dynamics code, http://blond.web.cern.ch/

[15] A. Burov, "Van Kampen modes for bunch longitudinal motion," Proc. HB2010, Morschach, Switzerland, 2010 and "Dancing bunches as van Kampen modes," Proc. PAC'11, New York, NY, USA, 2011.

[16] T. Argyropoulos, A. Burov. E. Shaposhnikova, "Loss of Landau damping for inductive impedance in a double RF system," IPAC'13, Shanghai, China, May 2013.

[17] T. Argyropoulos, E. Shaposhnikova, J. E. Varela, "Other means to increase the SPS 25 ns performance - longitudinal plane," LHC Performance Workshop (Chamonix 2014), France, Chamonix, Sep. 2014

# SYNCHROTRON FREQUENCY SHIFT AS A PROBE OF THE CERN SPS REACTIVE IMPEDANCE

A. Lasheen*, T. Argyropoulos, J. F. Esteban Müller, D. Quartullo, E. Shaposhnikova,
H. Timko, J. Varela Campelo, CERN, Geneva, Switzerland

*Abstract*

Longitudinal instability in the CERN SPS is a serious limitation for the future increase of bunch intensity required by the HiLumi LHC project. The impedance driving this instability is not known precisely and a lot of effort goes into creating an accurate impedance model. The reactive impedance of the machine can be probed by measuring the bunch length oscillations of a mismatched bunch at injection. The frequency of these oscillations as a function of intensity has a slope that depends on the reactive impedance and the emittance. Measurements were done for three values of longitudinal emittance and then compared with particle simulations based on the impedance model using particle distribution close to the measured one. Comparison of measured and calculated frequency shifts gives an estimation of the missing impedance in the model. In addition, scanning of initial emittance for diverse particle distributions in simulations shows that the frequency shift greatly depends on emittance and initial distribution. Small variations of these parameters can lead to very different results and explain partially the discrepancy between measured and calculated values of frequency shifts.

## INTRODUCTION

Reference measurements were done in the past in the SPS to monitor the evolution of the impedance from 1999 and successively after the 2001 impedance reduction program. Main changes were due to the installation of extraction kickers MKE in 2003 - 2006, and their shielding later [1]. New measurements were done in 2013 [2] and 2014, not only in order to continue the reference measurements, but mainly to test the SPS impedance model needed to simulate different intensity effects observed in the SPS. Below, simulations using this model are compared to measurements in order to test the model accuracy. This will allow to have a better understanding of SPS instabilities, as well as the synchrotron frequency distribution dependence on bunch intensity and bunch length.

Voltage induced due to the reactive impedance leads to the synchrotron frequency shift. This voltage can be found as the convolution of the reactive impedance with the beam spectrum (effective impedance), and is proportional to the bunch intensity $N_b$. The shift consists of two parts: the incoherent shift $\Delta f_{inc}$, corresponding to the convolution of the stationary bunch spectrum, and the coherent shift $\Delta f_{coh}$, corresponding to the convolution of the perturbation spectrum with the impedance. This perturbation can be due to a shift in the bunch position ($m = 1$, dipole) or a mismatch

of the bunch length ($m = 2$, quadrupole). The frequency of these oscillations can be written in the form [3]:

$$f_{s,m}(N_b) \approx m\, f_s^{(0)} + m\, \Delta f_{inc}(N_b) + \Delta f_{coh}(m, N_b), \quad (1)$$

with $f_s^{(0)}$ being the synchrotron frequency without intensity effects (first term of Eq. 3). One can then measure the oscillations of a mismatched bunch for several intensities in order to probe the effective reactive impedance. For a bunch with a parabolic line density, the dipolar incoherent and coherent frequency shifts are exactly canceling [3], making it difficult to measure intensity effects with dipole oscillations. Thus it is more practical to measure the quadrupole frequency shift.

Above transition, inductive effective impedance will produce $\Delta f_{inc} < 0$ and $\Delta f_{coh} > 0$, and vice-versa for capacitive impedance.

Below, measurements are compared to simulations and analytical calculations in order to study the effect of the different SPS impedance sources on the synchrotron frequency shift, as a function of the bunch distribution.

## MEASUREMENTS

The measurements of bunch length oscillations are done in the SPS just after injection (P = 25.92 GeV/c, above transition). The RF voltage is set to a value for which the injected bunch is mismatched, allowing the bunch length to oscillate for several periods (the emittance being small enough so that the oscillations are not damped too fast because of filamentation). These measurements were done for several emittances ($\epsilon_l \in [0.1, 0.20]$ eVs), and several intensities (N $\in [1, 10] \times 10^{10}$ ppb). Dipole oscillations were damped using a phase loop in order to measure only the quadrupole oscillations (referred to as oscillations for the rest of the paper). Two optics are available in the SPS (named Q26 and Q20) with transition gamma factors $\gamma_t = 22.8$ for Q26 and $\gamma_t = 18$ for Q20, which affect the synchrotron frequency. A single RF system (200 MHz) was used in measurements, with respective voltages of $V_{Q26} = 0.9$ MV for Q26 and $V_{Q20} = 2.5$ MV or $V_{Q20} = 4.5$ MV for Q20.

For each measurement set, bunch profiles were acquired every revolution turn for 1000 turns after injection and analyzed. From the oscillations of the bunch length (defined as $\tau = 4\sigma_{RMS}$), we extract the average bunch length, the peak-to-peak amplitude and the frequency of the oscillations (via FFT). Like this we get a scatter plot of the quadrupole frequencies as a function of intensity and average bunch length $f_2(\tau, N_b)$. For a narrow frame of bunch length $\tau = \tau_0 + \Delta\tau$, we plot the quadrupole frequency as a function of intensity as in Fig. 1(bottom). The top plot corresponds to a single point of the bottom one with

$\epsilon_1 = 0.1$ eVs and $N_b \approx 1 \times 10^{10}$ ppb. We can see the frequency shift with intensity effects, and fit them with linear function $f_2(\tau = \tau_0 + \Delta\tau, N_b) = a + b \times 10^{10} N_b$.
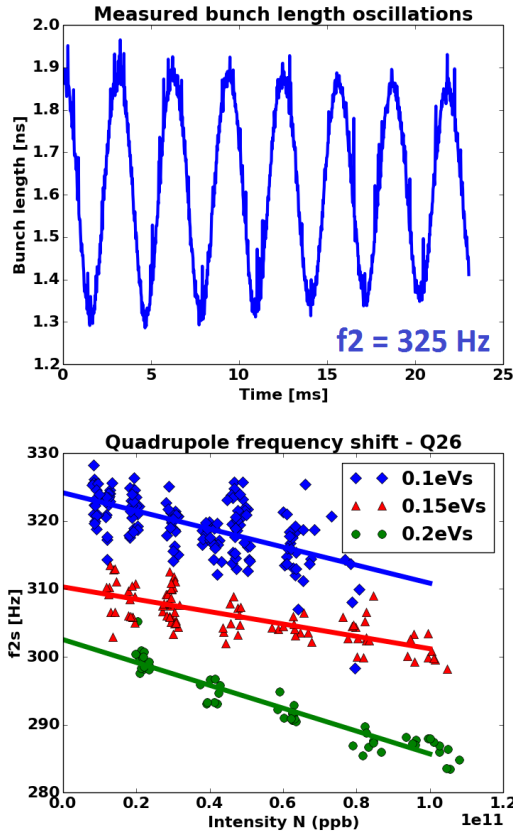


Figure 1: Bunch length oscillations for one measurement (top) and quadrupole oscillation frequencies as a function of intensity for different emittances (bottom).

The complete set of results for the 2013 and 2014 measurements are shown in the Table 1. In order to compare the Q26 and Q20 measurements, the slopes were rescaled by the factor $\sqrt{\eta_{Q26} V_{Q20}/(\eta_{Q20} V_{Q26})}$ (derived from Eq. 3), where $\eta = 1/\gamma_t^2 - 1/\gamma^2$ is the slippage factor. The averaged peak-to-peak amplitude of the oscillations is also included in the table in order to estimate the mismatch at injection. One can see that this amplitude is increasing with the average bunch length, showing that the mismatch is larger for longer bunches (Fig. 2). The standard deviation of the peak-to-peak amplitude is bigger than the one for the average bunch length, because of some scatter in the injected bunch length.

In comparison with previous reference measurements [2], the slope range for bunch lengths above 2 ns decreased from [-4.0, -3.4] Hz/$N_b \times 10^{-10}$ to [-1.68, -0.91] Hz/$N_b \times 10^{-10}$, showing a decrease of the inductive impedance due to the shielding of MKE kickers between 2009 and 2013.

## PARTICLE SIMULATIONS

Simulations were done with the BLonD tracking code [4], created at CERN for multi-particle simulations with intensity

Table 1: Measurement Results (Scaled to Q26(0.9))

| Optics (voltage [MV]) | Average bunch length [ns] | Av. peak-peak amplitude [ns] | Slope [Hz/Nb] $\times 10^{-10}$ |
|---|---|---|---|
| Q26(0.9) | $1.60 \pm 0.02$ | $0.53 \pm 0.06$ | $-1.33 \pm 0.07$ |
| Q26(0.9) | $2.09 \pm 0.02$ | $0.70 \pm 0.08$ | $-0.91 \pm 0.05$ |
| Q26(0.9) | $2.07 \pm 0.01$ | $0.76 \pm 0.05$ | $-1.40 \pm 0.06$ |
| Q26(0.9) | $2.44 \pm 0.01$ | $0.79 \pm 0.07$ | $-1.68 \pm 0.04$ |
| Q20(2.5) | $1.48 \pm 0.02$ | $0.42 \pm 0.05$ | $-1.3 \pm 0.2$ |
| Q20(2.5) | $1.70 \pm 0.03$ | $0.51 \pm 0.05$ | $-0.0 \pm 0.2$ |
| Q20(4.5) | $1.32 \pm 0.03$ | $0.68 \pm 0.07$ | $-2.1 \pm 0.2$ |
| Q20(4.5) | $1.52 \pm 0.03$ | $0.86 \pm 0.07$ | $-0.5 \pm 0.3$ |

effects. The parameters for the RF system, particle distributions, impedance and method of data analysis were set in order to reproduce the measurement conditions and be comparable. The SPS impedance model used in simulations is the result of a thorough and still ongoing survey of the different devices in the machine [5]. The plot of the total reactive impedance is shown in Fig. 3. Main contributors to the reactive impedance are listed here (approximate values of the low frequency reactive impedance are given as $\Im[Z/p]$ with $p = f/f_0$, with the impedance having an approximately constant value in this range):

- RF systems (travelling wave cavities, capacitive)
- Kickers (inductive, $\Im[Z/p] \approx 5.3\,\Omega$)
- Vacuum flanges (inductive, $\Im[Z/p] \approx 0.55\,\Omega$)
- Unshielded pumping ports (inductive, $\Im[Z/p] \approx 0.2\,\Omega$)
- Space charge (capacitive, $\Im[Z/p] = -0.9\,\Omega$ in Q26 and $\Im[Z/p] = -1.0\,\Omega$ in Q20)
- Resistive wall (inductive)
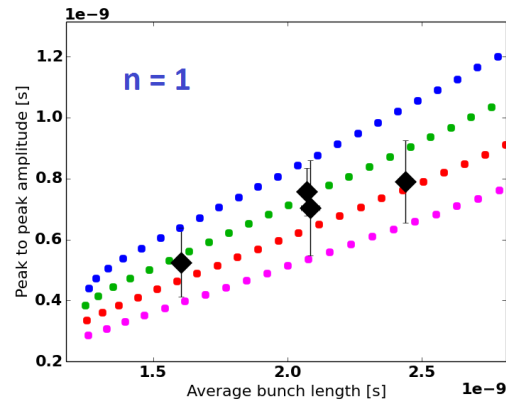


Figure 2: Peak-to-peak amplitude as a function of the average bunch length for the measurements (black) and simulations (colored) in Q26 optics.

Space charge was computed using the longitudinal space charge code LSC [6], for the averaged beam pipe geometry in the SPS and transverse bunch size (different momentum

spreads used in operation were taken into account for the dispersion). For the simulations presented here, average values of space charge impedance for the two different optics were taken.
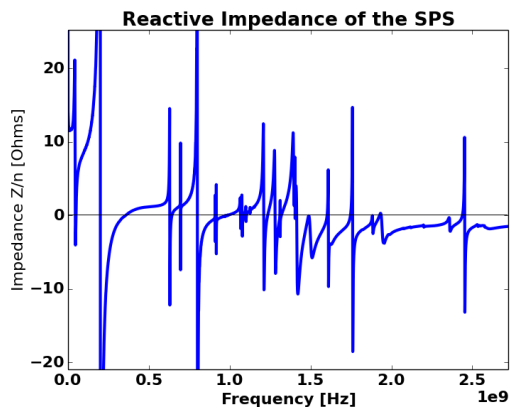


Figure 3: Reactive part of the SPS impedance model.

The exact injected distribution cannot be measured directly due to the bunch rotation used in the injector (PS), so a large range of distributions were covered in simulation to overcome these uncertainties. The injected profile was analyzed, and the closest distribution used in simulations was the binomial line density with $n$ varying between 1 (parabolic line density without tails) and 1.5 (an increasing $n$ gives more tails to the distribution).

$$\lambda(t) = \lambda_0 \left[ 1 - \left( \frac{t}{\tau_L} \right)^2 \right]^n \qquad (2)$$

The momentum spread was estimated from the peak-to-peak amplitude of the bunch length oscillations. The bunch was generated in simulations in order to cover the full range of peak-to-peak amplitudes observed in measurements. This is shown in Fig. 2, where each colored point corresponds to a simulation with a different initial distributions ($n = 1$ for the profile).

In simulations, the bunch size (momentum spread and bunch length), the distribution type (different $n$) and the intensity were scanned. The results are shown in Fig. 4 for Q26 and Fig. 5 for Q20 (2.5 MV only; 4.5 MV giving similar results), in comparison with simulations.

The simulations show an unexpected maximum around $\tau = 1.7$ ns for which the slope is almost 0, implying that the synchrotron frequency shift is acting like there is no impedance at all! This was not seen with the Q26 measurement in 2013, as no measurements were done in this region. This was, however, observed in simulations with $\tau \approx 1.6$ ns, for which very small changes in bunch length would give very different results in the slopes. This is now understood, as this point is in a region where the slope as a function of bunch length is varying a lot. Moreover, the two measurements sets around $\tau \approx 2.1$ ns give very different results, as the slopes are also sharply changing around this bunch
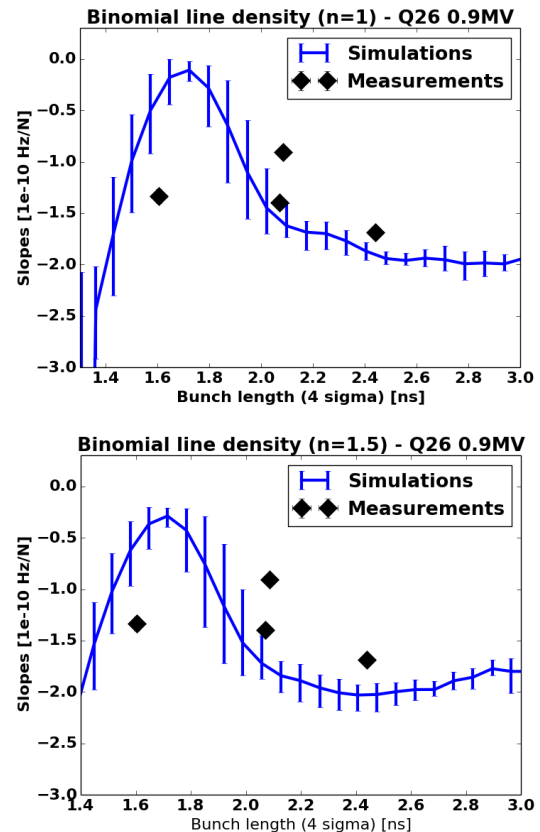


Figure 4: Slopes $b$ of synchrotron frequency shift with intensity as a function of bunch length, comparison of simulations and measurements in Q26 for V=0.9 MV with $n = 1$ for the injected distribution.

length. Another point is that small changes in the binomial function also lead to different results for the slopes.

The errorbars correspond to the deviation in the slopes due to the different momentum spreads chosen in simulations in Fig. 2. By comparing measurements with simulations, we can see that the measurements seem to be shifted by $\approx$ 100 ps to a larger bunch length. The source of this shift could be the measurement method, with the bunch length in measurements being larger due to e.g. pick-up cable length, or that some impedance depending on bunch length is missing in the present model.

Since the previous measurements in Q26 did not cover the region where the slope is at its maximum, measurements were repeated with the operational Q20 optics. Corresponding simulations are presented in Fig. 5.

Unfortunately, these measurements were done right after the end of the long shutdown at CERN, so that it was not yet possible to achieve all the desired bunch lengths. However, we managed to have a few measurements around $\tau = 1.7$ ns. Like in the measurements section, the slopes were scaled to the Q26 (0.9MV) settings to be comparable, but simulations were done under the same conditions as in measurements in the Q20 optics. They show the same pattern, with the slope being even positive at the maximum. Due to the small
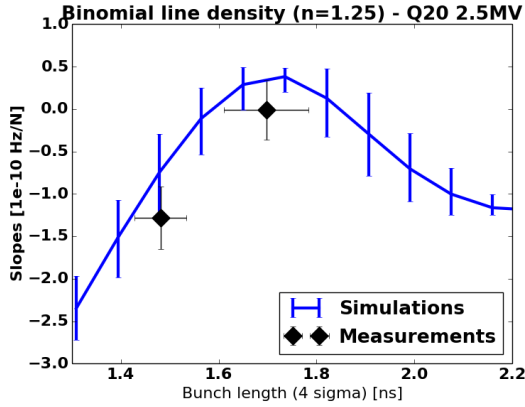
Figure 5: Slopes $b$ of synchrotron frequency shift with intensity as a function of bunch length, comparison of simulations and measurements in Q20 for V=2.5 MV with $n = 1.25$ for the injected distribution.

number of measurements, the uncertainties are bigger and more measurements would be needed.

One additional motivation for these measurements was the fact that controlled emittance blow-up in the SPS is done by applying RF noise with a fixed band-width relative to the synchrotron frequency. These simulations show that this synchrotron frequency shift is varying a lot as a function of the bunch length and should be taken into account in operation.

## QUADRUPOLE FREQUENCY SHIFT

In order to understand the source of this bunch length dependence, an analytical calculation of the quadrupolar frequency shift was done. First, the incoherent frequency was computed from potential well distortion [7]. The shift depends on the amplitude of the oscillations in longitudinal phase space $\hat{\tau}$. The effective impedance $Z_1$ for the incoherent shift is computed for a parabolic stationary spectrum using the following formulas:

$$f_s^2(N_b, \hat{\tau}) \approx f_{s0}^2 \left(1 - \frac{(2\pi h f_0 \hat{\tau})^2}{16}\right)^2 \left(1 + \frac{eN_b f_0 Z_1}{hV_0 \cos\phi_s}\right), \quad (3)$$

$$Z_1 = \int_{-\infty}^{+\infty} \frac{df}{f_0} \sigma_0 \Im(Z(f)) \frac{J_1(f\hat{\tau})}{f_0 \hat{\tau}/2}, \quad (4)$$

where $f_0$ is the revolution frequency, $f_{s0}$ the synchrotron frequency for the small amplitude of oscillations, $h$ the harmonic number, $V_0$ the RF voltage, $\phi_s$ the synchronous phase, $\sigma_0$ the stationary bunch spectrum, and $J_\nu(x)$ the Bessel function of order $\nu$.

Next, the coherent frequency shift is computed as in [8] (assuming again a parabolic bunch) and applied to the incoherent frequency $f_s$ in order to obtain the final quadrupolar frequency containing both contributions.

$$f_2(N_b) \approx 2f_s + \frac{3\Gamma(5/2)N_b e^2 \eta}{4\pi \sqrt{\pi} E f_s \tau_L^3} \left(\frac{Z}{p}\right)_{eff}, \quad (5)$$

$$\left(\frac{Z}{p}\right)_{eff} = \frac{\sum_{p=-\infty}^{p=+\infty} h_2 \frac{Z}{p}}{\sum_{p=-\infty}^{p=+\infty} h_2}; h_2(\omega_p) = \frac{\left[J_{5/2}(\omega_p \tau_L)\right]^2}{\omega_p \tau_L}, \quad (6)$$

where $\Gamma(5/2)$ is the gamma function, $e$ is the elemental charge, $E$ the beam energy, $\tau_L$ the binomial bunch length parameter as in Eq. 2, $h_2$ the perturbation spectrum for the quadrupole mode, and finally $\omega_p = p2\pi f_0$.

From Eq. 4 and Eq. 6, we can compute the effective impedances in order to obtain the incoherent and coherent shifts as a function of bunch length. The results are shown in Fig. 6, for the different sources of impedance. The analytical slope is finally computed by comparing the quadrupole frequency with ($f_2$) and without ($2f_s^{(0)}$) intensity, and results are given in Fig. 7 (top).
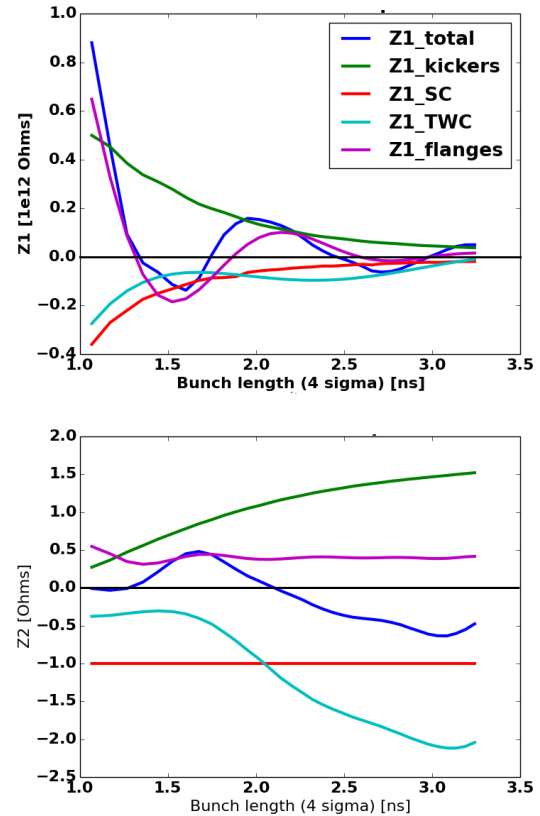


Figure 6: Effective impedance for the main impedance sources as a function of bunch length for the incoherent (top, $Z_1$) and coherent (bottom, $Z_2$) shifts (same color code, SC corresponds to space charge and TWC to the impedance of the RF systems). The slopes of incoherent and coherent shifts are directly proportional to these effective impedances.

For the effective impedance used in the incoherent shift, one can see a clear dependence on bunch length, varying from positive to negative, with a maximum capacitive impedance around $\tau \approx 1.6$ ns (implying a positive slope, for the same bunch length as the maximum in simulations and measurements!). The impedance of vacuum flanges, which is expected to be inductive, can also act as capacitive, depending on the bunch length. The other impedances vary with

bunch length but remain capacitive or inductive. This can be seen in Fig. 7 (bottom) from the fact that for $\tau \approx 1.6$ ns bunch length, the negative spectrum (parabolic bunch) is sampling a high value of inductive impedance, which is then converted into capacitive effective impedance.

Moreover, the maximum of the effective impedance causing coherent shift ($Z_2$) is around the same bunch length as the minimum of the effective impedance causing incoherent shift ($Z_1$). Since $Z_2 > 0$ at the maximum, the impedance is inductive, hence resulting in a positive slope of coherent shift. It seems though that the shape of $Z_2(\tau)$ is mainly due to the kickers and the RF systems' impedance, since effective impedances are varying a lot in this range.
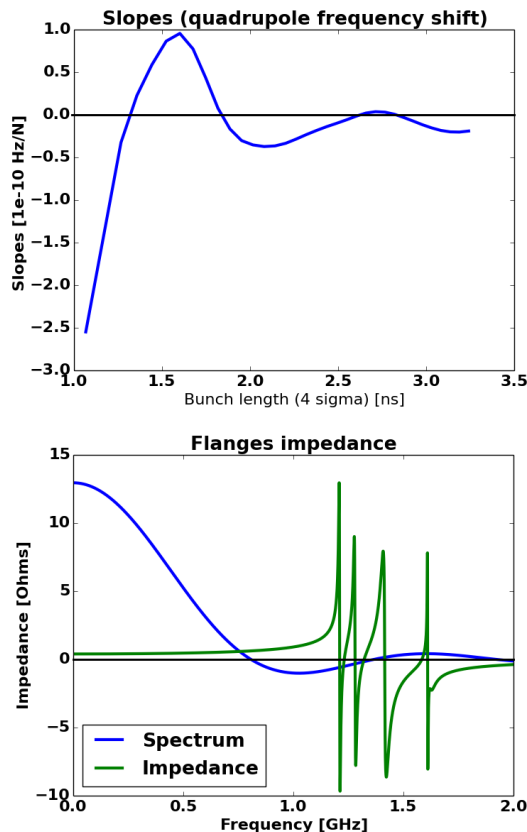


Figure 7: Top: Slopes of the synchrotron frequency shift as a function of bunch length for parabolic line density. Bottom: Spectrum and reactive impedance of flanges for the maximum slope value.

The shape of the curve resembles the one from simulations (Fig. 4). The maximum is also around the same bunch length $\tau \approx 1.6 - 1.7$ ns, and the relative values with respect to the maximum are very close to simulations. One can see though an important offset of the values of the slope (around $1 \times 10^{10}$ [Hz/N$_b$]) which is not understood yet. Note that analytical formulas are valid for small perturbations only, but large deviations exist in measurements. So it is more accurate to compare measurements to simulations rather than analytical formulas.

## CONCLUSIONS

A dependence of the synchrotron frequency shift on bunch length was measured in the SPS and reproduced in simulations. The results are in good agreement with the actual SPS impedance model. The reason for this dependence was studied and it has been shown that the interaction of a parabolic bunch spectrum with the impedance of the SPS vacuum flanges caused an incoherent frequency shift. This shift can be inductive or capacitive as a function of the bunch length, and may lead to the cancellation of the slope at certain bunch length. Further studies are planned in order to understand the discrepancy between theory and what is observed in measurements and simulations. New methods are also planned, like applying a fast voltage increase as a source of the mismatch to a matched bunch. Like this, one can have a better control of the perturbation and initial bunch distribution. Experiments at flat top energy, where the space charge impedance is negligible, can help to study the effect of space charge on the synchrotron frequency shift.

## ACKNOWLEDGMENTS

## REFERENCES

[1] E. Shaposhnikova et al., "Reference Measurements of the Longitudinal Impedance in the CERN SPS", PAC'09, Vancouver, BC, Canada, (2009).

[2] T. Argyropoulos et al., "Reference Measurements of the Longitudinal Impedance", *Meetings of the LIU-SPS BD WG*, CERN, http://cern.ch/spsu/

[3] J. L. Laclare, "Bunched Beam Coherent Instabilities", CERN 87-03, p.264, *CAS Proceedings*, (1987).

[4] BLonD, Beam Longitudinal Dynamics code: http://blond.web.cern.ch/

[5] B. Salvant, J. Varela Campelo, C. Zannini, "SPS Impedance Model Update", *Meetings of the LIU-SPS BD WG*, CERN, http://cern.ch/spsu/

[6] L. Wang, "The geometry effect of the space charge impedance LSC code", *ICFA mini-Workshop on "Electromagnetic wake fields and impedances in particle accelerators"*, Erice, Italy, (2013).

[7] K. Y. Ng, *Physics of Intensity Dependent Beam Instabilities*, Ed. World Scientific Publishing, (2006).

[8] A. Chao, *Physics of Collective Beam Instabilities in High Energy Accelerators*, Ed. John Wiley & Sons, (1993).

# STUDIES ON CONTROLLED RF NOISE FOR THE LHC

H. Timko*, P. Baudrenghien, E. Shaposhnikova, CERN, Geneva, Switzerland

T. Mastoridis, California Polytechnic State University, San Luis Obispo, USA

## Abstract

RF phase noise is purposely injected into the LHC 400 MHz RF system during the acceleration ramp for controlled longitudinal emittance blow-up, in order to maintain longitudinal beam stability. Although the operational blow-up works reliably, studies of the injected RF noise are desirable not only to allow for a better-controlled, more flexible blow-up, but also for other applications such as the mitigation of machine-component heating through appropriate bunch shaping. Concerning the noise injection, an alternative algorithm was developed and implemented in the hardware, but first tests revealed unexpected modulation of the achieved bunch length along the ring, and subsequently, theoretical studies have been launched. In this paper, we present a summary of ongoing measurement analysis and simulation studies that shall explain previous observations, predict what can be expected in different cases, and thus help to optimise the RF noise in general.

# INTRODUCTION

Controlled longitudinal emittance blow-up is necessary in the LHC to maintain longitudinal beam stability during the acceleration ramp. For a constant stability margin, the emittance $\varepsilon$ should be increased with energy as $\varepsilon \propto \sqrt{E}$ [1], resulting in a roughly constant bucket filling factor and relative synchrotron frequency spread. In practice, a good blow-up was achieved by a feedback that scales the RF phase noise $\varphi_N(t)$ to keep the bunch length constant [2, 3]. At flat top, also bunch shaping through noise injection can be desirable, for instance to mitigate machine-component heating.

The noise spectrum $S_\varphi(f)$ applied determines in what frequency range diffusion is triggered in the bunch, and hence, determines also the resulting bunch shape. Diffusion under external noise [4–6] and bunch shaping with band-limited white noise [7] has been studied in the past. Controlled emittance blow-up for the SPS and LHC was designed and implemented [2,8] subsequently. In the LHC, a band-limited white noise spectrum is applied, however, feedback loops complicate the analysis. A constant relative noise band is chosen with the range $(0.86–1.1) f_{s0}$ (Fig. 1a), where $f_{s0}$ is the synchrotron frequency of the synchronous particle. In a single-RF system this will affect the core of the bunch that has a maximum phase amplitude of synchrotron oscillations in the range of $\varphi_{max} = (0–1.52)$ rad (Fig. 1b).

Operationally, $\varphi_N(t)$ is applied through the phase loop (PL), as an additional phase shift to the phase correction between bunch and RF phase [2]. This works reliably, and even for a full machine the beam can be brought stably through the acceleration ramp, with a typical target bunch length of 1.2 ns

---

* helga.timko@cern.ch
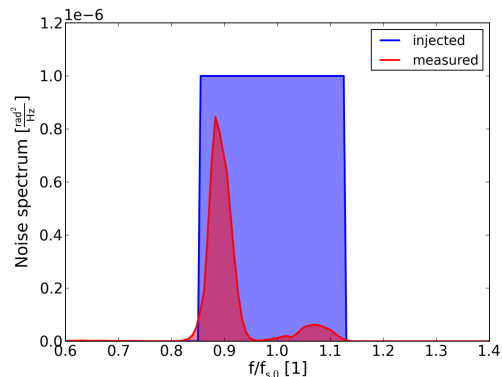
(a) Injected (blue) and measured (red) noise power spectral density. The measured noise is applied through the PL.
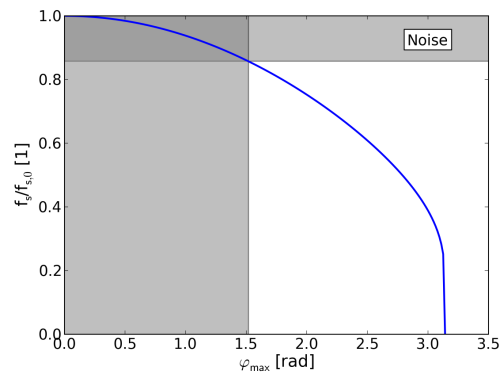


(b) Synchrotron frequency distribution in a single-RF system as a function of maximum phase coordinate. The dashed region marks the range affected by the injected noise.

Figure 1: LHC controlled longitudinal emittance blow-up.

achieved homogeneously ($\pm 30$ ps) for all bunches [2]. However, since the phase loop corrects the centre-of-mass motion, the effective noise spectrum is reduced greatly around $f_{s0}$, see Fig. 1a. This modification of the spectrum makes it difficult to shape bunches in a well-determined way.

Alternatively, $\varphi_N(t)$ can be applied through the cavity controller (CC). The PL is still required for the ramp, but an interaction between the noise and the PL can be avoided: using a symmetric filling pattern, and injecting the noise on a revolution frequency side-band, the noise is practically invisible to the PL. This scheme was tested in early 2012, and indeed, $S_\varphi(f)$ in the cavity field reproduced the desired spectrum exactly [9]. At the time, however, this noise injection scheme could not be made operational, because tests with few bunches led to a bifurcation of the final bunch length: although on average the target bunch length was obtained, the bunches were either too short or too long. Further studies are planned after the start-up of the LHC early 2015.
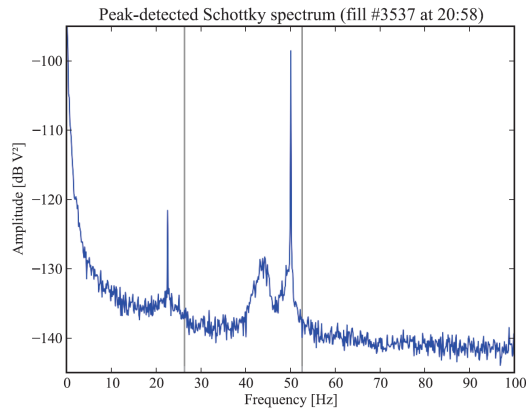
Figure 2: Schottky spectrum of LHC bunches at flat top energy (from [10], measured at 4 TeV, 12 MV). The vertical lines mark $f_{s0} = 26.3$ Hz and $2f_{s0} = 52.6$ Hz.

Another motivation for our studies is that the peak-detected Schottky signal of bunches at flat top revealed a 'hole' in the bunch distribution somewhat below $2f_{s0}$ (see Fig. 2, [10]). Note that, using this measurement technique, the dipole band is distorted and the quadrupole band gives the best reproduction of the particle distribution [11]. In principle, it is not excluded that the 50 Hz line could be related to creating this hole, as the core gets depopulated when the 50 Hz line is crossed [12]. However, this happens quite early during the acceleration ramp ($f_{s0} = 55.2$ Hz and 24.0 Hz at flat bottom and flat top, respectively), and during the ramp the emittance is blown up roughly by a factor 4, using a noise spectrum that follows $f_{s0}$ and thus mixes different frequencies. Both these facts make it unlikely that the observed depopulation is due to the 50 Hz line. Instead, it could be related to the operational emittance blow-up applied through the PL. Understanding the origin of this is important because bunches with such a distribution are intrinsically more unstable and result also in a different heating of machine components.

## SIMULATION MODEL

The CERN BLonD simulation code [13] has been extended to contain a complete model of the LHC controlled noise injection during the acceleration ramp. For the time being, the code is restricted to single-bunch simulations. The incoherent synchrotron frequency shift in the LHC ($\sim 0.01 f_{s0}$ [2]) is negligible compared to the noise bandwidth, and thus, intensity effects were neglected.

The phase noise $\varphi_N(t)$ was generated in a similar fashion as in the LHC [14]. The double-sided power spectral density $S_\varphi(f)$, $[S_\varphi(f)] = \frac{\text{rad}^2}{\text{Hz}}$, is transformed to $\varphi_N(t)$ via a real FFT, such that one data point per turn is obtained. Just like in measurements, a flat spectrum between $(0.86\text{–}1.1)f_{s0}$ is applied. Since $f_{s0}$ and the revolution period change during the ramp (Fig. 3), the spectrum is adjusted every 10,000 turns and $\varphi_N(t)$ is re-generated with a new seed for the random number generator. Furthermore, the amplitude $A_S$ of the spectrum $S_\varphi(f)$ is scaled such that the r.m.s. phase noise
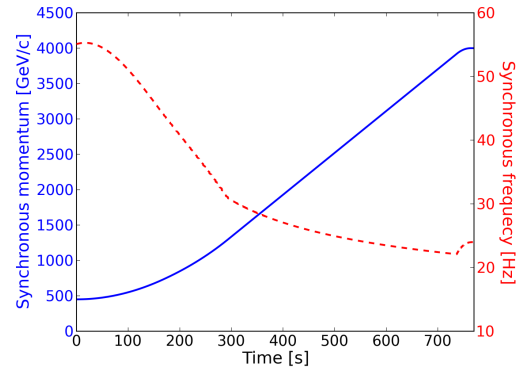


Figure 3: Beam momentum and synchrotron frequency during the LHC acceleration ramp, used both in the machine and in simulations. The voltage is increased linearly from 6 MV to 10 MV during this time.

$\varphi_N^{\text{rms}} = \sqrt{\int S_\varphi(f)df} = \sqrt{2 \times 0.24 f_{s0} A_S}$ remains constant. We compare two cases, $\varphi_N^{\text{rms}} = 2°$ and $0.2°$, with the latter being more realistic for the ramp. $\varphi_N^{\text{rms}} = 0.2°$ results in $A_S = 4.4 \times 10^{-7}$ rad$^2$/Hz and $A_S = 1.0 \times 10^{-6}$ rad$^2$/Hz at flat bottom and flat top energies, respectively.

Also the PL is modelled in simulations according to the real LHC implementation [15]. The PL calculates every turn the phase difference $\Delta\varphi_{\text{PL}} = \varphi_{\text{COM}} - \varphi_s$ between the bunch centre-of-mass $\varphi_{\text{COM}}$ and the RF phase, which in this case is substituted by the synchronous phase $\varphi_s$ calculated from the design beam momentum and RF voltage. In the equations of motion, the RF angular frequency is then corrected in the subsequent turn by the PL to $\omega_{\text{RF}}^{(n+1)} = h\omega_{s0}^{(n+1)} - g\Delta\varphi_{\text{PL}}^{(n)}$, where $h\omega_{s0}$ is the design RF angular frequency and $g = 1/(5 \text{ turns})$ is the PL gain. $\varphi_N(t)$ is then added either to the phase correction $\varphi_{\text{PL}}$ (PL case) or directly in the energy kick in the equations of motion (CC case).

During acceleration, an additional feedback on the bunch length is acting, which regulates the phase noise amplitude to maintain a constant bunch length. The feedback 'measures' the bunch length $\tau_{\text{meas}} = 4/2.355\tau_{\text{FWHM}}$ [1] every 3 s (33,740 turns) and compares it to the target 4-sigma bunch length $\tau_{\text{targ}} = 1.2$ ns. For the subsequent 3 s, $\varphi_N(t)$ is multiplied by the factor $x$ determined through the recursion [2] $x^{(n+1)} = ax^{(n)} + k(\tau_{\text{targ}} - \tau_{\text{meas}})$, with $x^{(0)} = 1$, limiting $x$ to the range $[0, 1]$, and using the same constant $a = 0.8$ and gain $1.5 \times 10^9$ s$^{-1}$ as in the LHC.

## SIMULATION RESULTS

### Flat Bottom Simulations

First, we describe simulation results of noise injected at flat bottom energy. These simulations were done without the bunch-length feedback. Noise was injected during 88.9 s ($10^6$ turns) and the bunch was relaxed during 8.89 s ($10^5$ turns) subsequently. Both injection through PL and CC, as well as $\varphi_N^{\text{rms}} = 0.2°$ and $2°$ were studied. In addition, to

---

[1] For a Gaussian bunch, FWHM $= 2\sqrt{2\ln 2}\sigma \approx 2.355\sigma$. Hence, we scale by $4/2.355$ to obtain the corresponding 4-sigma bunch length.

Table 1: Comparison of r.m.s., Gaussian fit, and FWHM Bunch Lengths for Different Blow-up Settings at Flat Bottom. All bunch length values are 4-sigma. The FWHM value is scaled such that all three methods give the same result for a Gaussian bunch. The time needed to reach steady-state is shown as well. The RF bucket length is 2.5 ns.

| Loop | $\varphi_N^{\text{rms}}$ | Seed | 4× r.m.s. | 4-sigma Gaussian fit | 4/2.355× FWHM | Time constant |
|------|------|------|-----------|----------------------|---------------|---------------|
| | | *Initial distribution* | 1.26 ns | 1.22 ns | 1.09 ns | – |
| PL | 0.2° | multi-seed | 1.27 ns | 1.26 ns | 1.18 ns | > 100 ns |
| | | single-seed | 1.27 ns | 1.25 ns | 1.18 ns | 85 s |
| | 2° | multi-seed | 1.46 ns | 1.68 ns | 1.97 ns | 3 s |
| | | single-seed | 1.41 ns | 1.62 ns | 1.85 ns | 4 s |
| CC | 0.2° | multi-seed | 1.50 ns | 1.72 ns | 1.97 ns | 25 s |
| | | single-seed | 1.41 ns | 1.60 ns | 1.76 ns | 15 s |
| | 2° | multi-seed | 1.75 ns | 2.03 ns | 2.27 ns | 6 s |
| | | single-seed | 1.53 ns | 1.78 ns | 2.01 ns | 1.2 s |
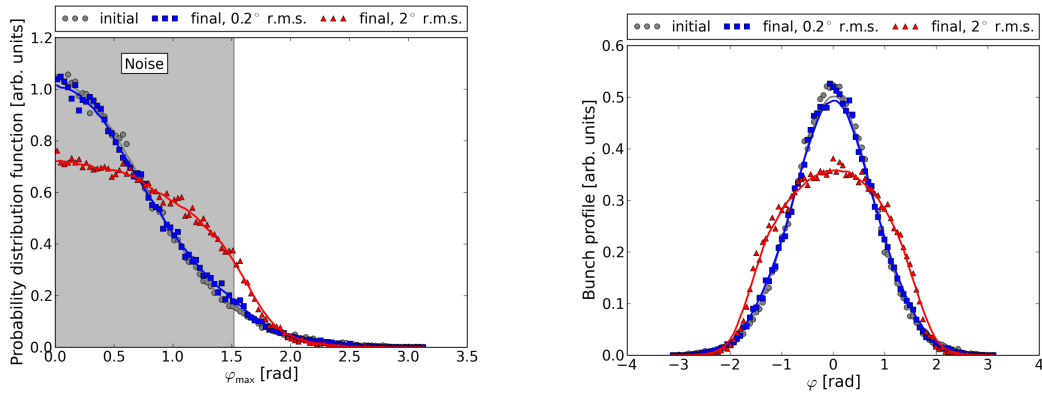


(a) Noise injection through the PL with 0.2° (blue) and 2° (red) r.m.s. phase noise. Initial distribution in grey.
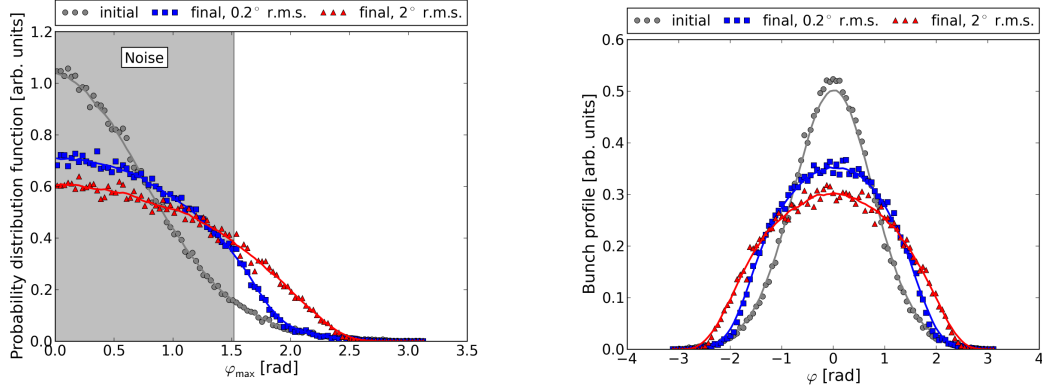


(b) Noise injection through the CC with 0.2° (blue) and 2° (red) r.m.s. phase noise. Initial distribution in grey.

Figure 4: Injection of multi-seed noise at flat bottom. Comparison of initial and final probability density functions (left) and bunch profiles (right).

study the effect of periodicity in the random number generator, the noise was generated from the same distribution in two different manners: once using a single seed, and once changing the seed every 10,000 turns (as done during the ramp). All simulations presented here were using the same initial matched distribution of 50,001 macro-particles.

The initial and final bunch profiles as well as the probability distribution functions as a function of the maximum phase coordinate are shown in Fig. 4. When the noise is injected through the PL, the core population is clearly higher than in the CC case. The difference is even more promi-

nent with $\varphi_N^{\text{rms}} = 0.2°$. This reflects well the fact that the PL reduces the noise spectrum around $f_{s0}$ significantly (cf. Fig. 1a). For the same injection method, the factor 10 difference in $\varphi_N^{\text{rms}}$ has a dramatic impact on the final bunch shape. Comparing the PL, $\varphi_N^{\text{rms}} = 2°$ case with the CC, $\varphi_N^{\text{rms}} = 0.2°$ case, it requires about this factor of 10 in phase (factor 100 in $A_S$) to compensate for the difference between PL and CC.

In Figure 4, we showed only the multi-seed cases. The final distributions of the single-seed cases are very similar, apart from being blown up less. The main difference between the single- and multi-seed cases is in the blow-up efficiency

reflected by the final bunch length, see Tab. 1. This can be explained by the single-seed case introducing numerically a periodicity in the phase noise, which creates 'islands' in the phase space of the bunch. With multiple seeds, on the other hand, one can ensure that the complete phase-space region targeted by the noise spectrum is indeed affected. Hence, the bunch is blown up more.

Given that the bunch distribution is changing during the blow-up, it is non-trivial to choose a good measure of the bunch length. In Tab. 1 we compare three different methods: r.m.s., Gaussian fit, and FWHM. While r.m.s. is the natural measure to track bunch lengthening due to diffusion, with the Gaussian fit or FWHM values additional information on the bunch shape can be obtained. Comparing r.m.s. and Gaussian fit values, for instance, one can see that the initial distribution is close to Gaussian, but the final distribution is far from it. The most sensitive measure is FWHM, whose value is the lowest for the initial and the highest for the final distribution. Indeed, also in the LHC it is chosen for the bunch-length feedback because it reflects well the average 'curvature' (shape) of the bunch.

When applying a noise of constant spectrum, the bunch will diffuse during a given time span, after which the bunch profile reaches a steady state, even though the bunch is still being shaken. The typical time evolution of the (r.m.s.) bunch length is shown in Fig. 5. The bunch length saturates with a $ae^{-t/\tau} + b$ trend; the time constants $\tau$ are summarised in Tab. 1 as well. A theoretical estimate of the time constants to expect in the different cases is not easy to obtain, because (i) the noise spectrum is band-limited, (ii) the PL distorts the spectrum, and (iii) the short-bunch approximation cannot be applied either. However, we can draw a few important conclusions from the data:

- the noise realisation (seeding) can affect the bunch length growth rate significantly,
- the multi-seed realisation blows up the bunch more and with a longer time constant,
- for $\varphi_N^{\text{rms}} = 2°$, the time constants are a few hundred synchrotron periods only and become comparable for the PL/CC cases,
- $\varphi_N^{\text{rms}} = 0.2°$, the difference between PL and CC both in final bunch length and time constant is significant.

### Simulations During the Acceleration Ramp

In the following, we present some first results of simulations with the acceleration ramp, applying $\varphi_N^{\text{rms}} = 0.2°$ either through the PL or the CC. In both cases, the bunch-length feedback was on; the evolution of the phase-noise scaling factor and the resulting bunch length during the ramp are shown in Fig. 6. When injecting the noise through the CC, $\tau_{\text{targ}} = 1.2$ ns can on average be met throughout the whole ramp, with about (20–40) % of $\varphi_N(t)$. Note that the 4-sigma r.m.s. bunch length deviates from $\tau_{\text{targ}}$ as the shape of the bunch is changing. However, $\varphi_N^{\text{rms}} = 0.2°$ is insufficient to blow up the beam through the PL; even with 100 % of $\varphi_N(t)$, the bunch length shrinks below 0.7 ns. Qualitatively,
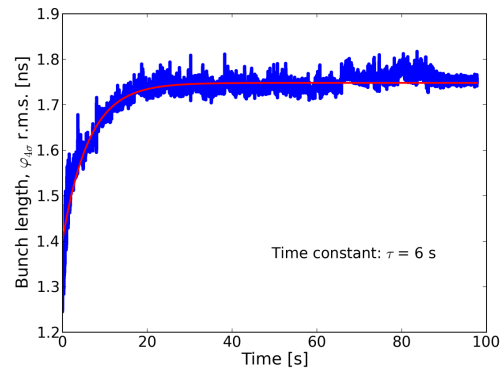


Figure 5: Typical evolution of 4-sigma r.m.s. bunch length over time (blue) and the fit of the form $ae^{-t/\tau} + b$ (red).

this is in line with the results from flat bottom simulations. Further simulations with increased $\varphi_N^{\text{rms}}$ are underway.

The 4-sigma bunch lengths at the end of the ramp are: 0.66 ns r.m.s., 0.65 ns Gaussian fit, and 0.63 ns full-width (4/2.355× FWHM) with the PL; 1.05 ns r.m.s., 1.15 ns Gaussian fit, and 1.18 ns full-width with the CC. As expected, the shrinking bunch with insufficient blow-up remains Gaussian. On the other hand, the bunch that is blown up through the CC is rounder, with a denser core up to ±1.2 rad, sharply decreasing till ±1.7 rad, with no tail population at all. The low tail population is consistent with earlier observations [9] and is due to the mixture of controlled emittance increase and decreasing bucket filling factor during the ramp, cf. Fig. 7. The initial and end-of-ramp ($8.5 \times 10^6$ turns, 756 s) bunch profiles are shown as well.

Looking closer at the right-hand-side plot in Fig. 6, one can see that the bunch length follows the same pattern as the scaling factor $x$ of the bunch-length feedback. Also, $\varphi_N(t)$ needs to be adjusted much more in the beginning of the ramp than later.

## CONCLUSIONS AND OUTLOOK

Noise generation, phase loop, and bunch-length feedback have been implemented in the CERN BLonD code, creating a valuable tool for the realistic simulation of controlled bunch shaping and emittance blow-up during the ramp in the LHC. First simulation results at flat bottom and during the acceleration ramp have been presented. Simulations reproduce the reduced efficiency of the phase-loop-injected noise in the core of the bunch.

The blow-up results in a round bunch profile that is far from Gaussian. Bunch lengths obtained with different methods – r.m.s., Gaussian fit, and FWHM – differ largely. Hence, also for on-line monitoring of the bunch length in the LHC, a suitable choice of bunch length definition is important. Out of the three studied, the FWHM measure is the most sensitive to the bunch shape.

First simulations of noise injection during the acceleration ramp confirm the experimental observations that after the blow-up the bunch has a rounder core and lower tail
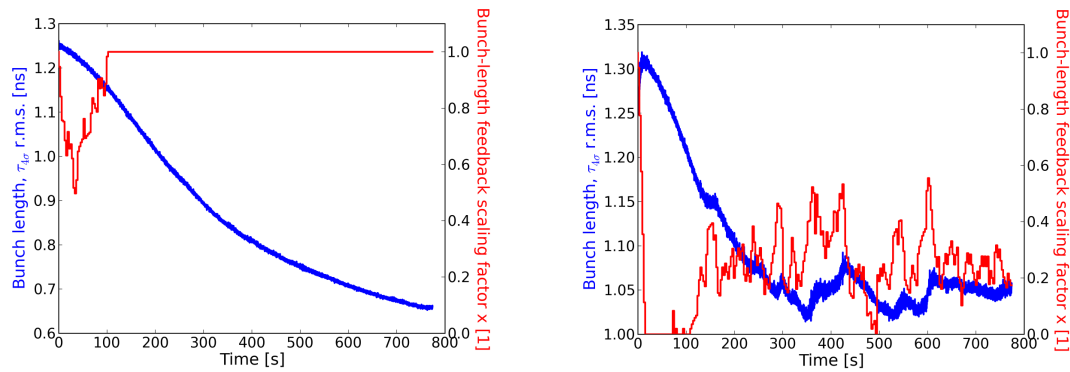
Figure 6: Bunch-length feedback scaling factor $x$ and resulting 4-sigma r.m.s. bunch length during the ramp, with PL (left) and CC (right).
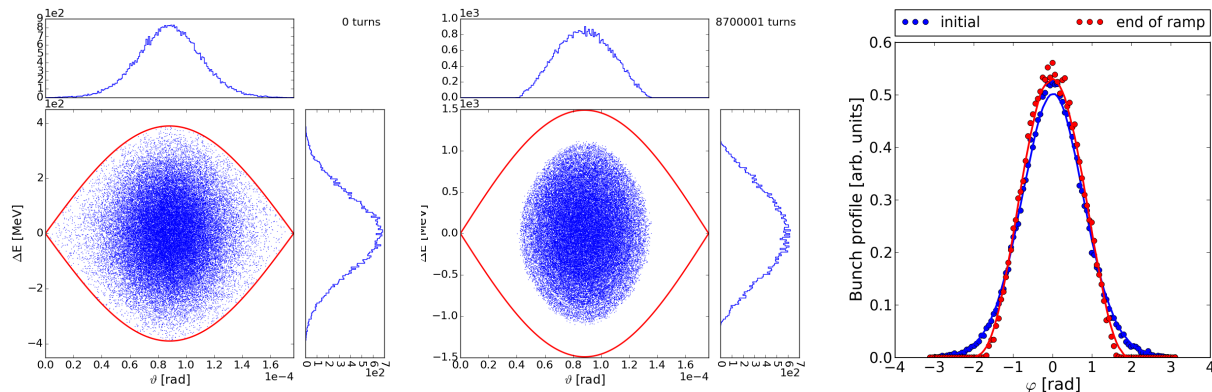


Figure 7: Initial (left) and final (middle) phase space and bunch profiles (right); $\vartheta = \varphi/35640$. Blow-up through the CC.

population. To obtain the same final bunch length, different noise amplitudes for injection through phase loop and cavity controller are required, since the phase loop reduces the effective noise spectrum.

Studies of controlled noise injection during the ramp will be continued to optimise the blow-up for the next LHC run. To better model the noise injection through the cavity controller, multi-bunch simulations are planned in the long term. This requires not only the implementation of multi-bunch capabilities in BLonD, but also an overall optimisation of the run-times for demanding simulations such as the LHC ramp. The LHC re-commissioning early next year will give a good opportunity to test new schemes and settings in real life.

## REFERENCES

[1] E. Shaposhnikova, "Longitudinal beam parameters during acceleration in the LHC", LHC Project Note 242, Geneva, (2000).

[2] P. Baudrenghien et al., "Longitudinal emittance blow-up in the LHC", IPAC'11, San Sebastian, Spain, TUPZ010 (2011).

[3] E. Shaposhnikova, et al., "Loss of Landau damping in the LHC", IPAC'11, San Sebastian, Spain, MOPC057 (2011).

[4] S. Krinsky, J.M. Wang, "Bunch diffusion due to RF noise", Part. Accel. 12, 107–117 (1982).

[5] G. Dôme, "Diffusion due to RF noise", CERN Accelerator School '85, Oxford, UK, 370–401 (1985).

[6] S.V. Ivanov, "Longitudinal diffusion of a proton bunch under external noise", IHEP Preprint 92-43, Protvino (1992).

[7] T. Toyama, "Uniform bunch formation by RF voltage modulation with a band-limited white signal", NIM A, 447, 317–327 (2000).

[8] J. Tückmantel et al., "Experimental studies of controlled longitudinal emittance blow-up in the SPS as LHC injector and LHC test-bed", LHC Project Report 761, Geneva, (2004).

[9] P. Baudrenghien, T. Mastoridis, "Longitudinal emittance blowup in the large hadron collider", NIM A, 726, 181–190 (2013).

[10] T.E. Levens et al., "A beam-synchronous gated peak-detector for the LHC beam observation system", IBIC'13, Oxford, UK, MOPC35 (2013).

[11] E. Shaposhnikova, et al., "Longitudinal peak detected Schottky spectrum", HB'10, Morschach, Switzerland, TUO1C04 (2010).

[12] J. Tückmantel, "Simulation of LHC bunches under influence of 50-Hz-multiple lines on the cavity field", LHC Project Note 404, Geneva, (2007).

[13] BLonD Beam Longitudinal Dynamics simulation code website: http://blond.web.cern.ch

[14] J. Tückmantel, "Digital generation of noise-signals with arbitrary constant or time-varying spectra", LHC Project Report 1055, Geneva (2008).

[15] P. Baudrenghien et al., 'The LHC low level RF', EPAC'06, Edinburgh, UK, TUPCH195 (2006).

# FAST TRANSVERSE INSTABILITY AND ELECTRON CLOUD MEASUREMENTS IN FERMILAB RECYCLER

J. Eldred, Department of Physics, Indiana University, Bloomington, IN 47405, USA

P. Adamson, D. Capista, N. Eddy, I. Kourbanis, D.K. Morris, J. Thangaraj, M.J. Yang,
R. Zwaska, FNAL, Batavia, IL 60510, USA

Y. Ji, Department of Physics, Illinois Institute of Technology, Chicago, IL 60616, USA

## Abstract

A new transverse instability is observed that may limit the proton intensity in the Fermilab Recycler. The instability is fast, leading to a beam-abort loss within two hundred turns. The instability primarily affects the first high-intensity batch from the Fermilab Booster in each Recycler cycle. This paper analyzes the dynamical features of the destabilized beam. The instability excites a horizontal betatron oscillation which couples into the vertical motion and also causes transverse emittance growth. This paper describes the feasibility of electron cloud as the mechanism for this instability and presents the first measurements of the electron cloud in the Fermilab Recycler. Direct measurements of the electron cloud are made using a retarding field analyzer (RFA) newly installed in the Fermilab Recycler. Indirect measurements of the electron cloud are made by propagating a microwave carrier signal through the beampipe and analyzing the phase modulation of the signal. The maximum betatron amplitude growth and the maximum electron cloud signal occur during minimums of the bunch length oscillation.

## INTRODUCTION

Beginning in July 2014, a fast intensity-induced transverse instability was observed in the proton beam of the Fermilab Recycler. This instability is currently a limiting factor on the stable proton intensity in the Recycler. The Recycler is currently being commissioned from slip-stacking [1, 2]. The instability has the unusual feature of selectively impacting the first high-intensity batch. Our studies focus on electron cloud because it is the most probable mechanism for the Reycler instability.

A qualitatively similar phenonenon, refered to as a "first pulse" electron cloud instability, has been observed at Los Alamos National Laboratory (LANL) [3, 4]. It should be noted, however, that the LANL macropulse timing structure is a very different timescale from the Fermilab batch timing structure [5].

The azimuthal space in the Fermilab Booster is divided into 84 buckets with typically 82 of those buckets are filled during operation. The Booster extracts to the Recycler (or the Main Injector) at a rate of 15 Hz and each Booster pulse is known as a batch. Six 84-bucket Booster batches and a 84-bucket kicker gap fill the 588-bucket azimuthal space of the Booster Recycler. During slip-stacking operation another six Booster batches can be injected.

When the first batch exceeds a certain intensity threshold (originally 3e12), the Recycler instability causes the horizon-tal betatron dipole oscillation to grow dramatically and can lead to ~ 25% loss within the first 150 turns. At this point, the beam is aborted to minimize loss activation as described in [1]. The rapid amplitude growth of the instability is only consistent with electron cloud [6, 7, 8]. Below the intensity threshold, the increased betatron oscillation amplitude is only apparent in the first batch.

If the first batch is just below threshold, the subsequent batches can have intensities above the single-batch intensity threshold without significant beam loss. When the Recycler beam is running in this configuration the most significant betatron excitation appears in the second batch, followed by the first batch. This configuration, with the first batch at ~ 80% intensity of subsequent batches, enables the greatest total beam intensity at normal loss rates. On July 24th the Recycler titanium sublimation pumps were fired [9] and on August 1st the Recycler switched to running with the first batch at lower intensity then subsequent batches. The maximum beam intensity was 22e12 protons on August 1st 2014 but gradually increased to 26e12 protons by August 10th 2014. The change in the instability threshold is consistent with beampipe conditioning effects which increase the threshold associated with electron cloud [10, 11].

The Recycler is outfitted with a digital damper system designed to mitigate transverse instabilities during antiproton accumulation (see [12]). The damper system is at least an order of magnitude too weak to prevent losses from this new instability in the Recycler. This Recycler instability also occurs when the damper system is turned off.

The shorter bunch lengths appear to lower the intensity threshold of the Recycler instability. In one illuminating study (July 16th 2014), six batches each with 3.3e12 protons were injected into the Recycler with a deliberate RF phase mismatch to induce a bunch length oscillation. Figure 1 shows that the instability immediately overpowers the damper when the bunch length is short but the betatron motion damps and decoheres when the bunch length is long. This figure also demonstrates that the instability begins in the horizontal plane but the betatron motion spreads to the vertical plane via the linear coupling of the lattice [13]. It appears in this case that the instability begins the middle of the batch and migrates to the tail of the batch. If the instability has increased the emittance in the center of the batch than this would delay the onset of the electron cloud and could account for the movement of the instability towards the tail of the batch.
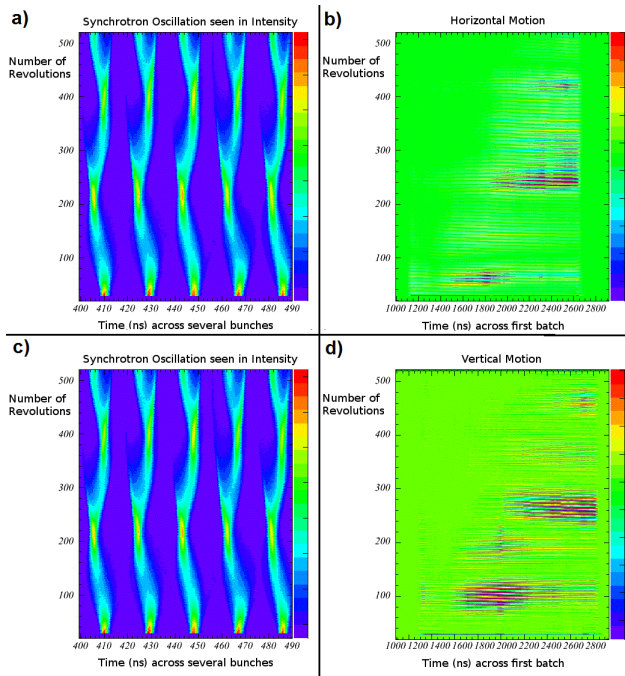
Figure 1: Plots produced from resistive wall current monitor and stripline BPM signals used in the digital damper system.**a,c)** Intensity plot as a function of revolution number and time within each revolution. **b)** Horizontal motion as a function of revolution number and time within each revolution. **d)** Vertical motion as a function of revolution number and time within each revolution.

The Recycler instability is encountered in the Recycler during normal tuning conditions. For the measurements described in this paper, the horizontal and vertical chromaticities are approximately -5. Further description of the Recycler lattice and tuning parameters can be found in [14]. The vacuum in the Recycler was measured to be good quality, typically 1e-10 torr at the ion pumps.

In the next section we describe the symptoms of the instability measured by beam position instrumentation. In particular we map out changes in the betatron oscillation amplitude, the particle losses, and the bunch length. In following two sections we present two methods measuring electron cloud in the Recycler. In the first method the electron cloud is detected directly by a retarding field analyzer (RFA) and in the second method the presence of the electron cloud is infered by the phase-modulation of a microwave signal traveling through the beampipe. Penultimately, we present simulation results describing a plausible mechanism by which electron cloud could exhibit the batch-selective feature observed in the Recycler instability. In the final section, we summarize and describe future actions.

## STRIPLINE MEASUREMENTS OF BEAM POSITION

An in-depth study of the Recycler instability was conducted on July 18th 2014 by studing the motion of the beam with a stripline beam position monitor. The specifications and calibration procedures of the stripline BPM are described in [15].

In this study, a single batch was injected with an intensity of 3.2e12 which is just above the theshold intensity (at the time). The digital damper system was turned off and beam loss abort occurs after 165 revolutions. The bunches undergo a bunch-length oscillation due to the mismatch between the Recycler and the Booster. In this study the vertical motion was small compared to the horizontal motion. The motion within the bunch was relatively uniform - the amplitude and tune of the oscillation was consistent head to tail.

Figure 2. shows the horizontal position averaged within each bunch and displayed across one batch. Oscillations are too fine to make out by eye. Figure 3 shows average Fourier transform of the horizontal position. The Fourier spectrum reveals the horizontal motion is dominated by low frequency components and oscillations at the betatron tune.
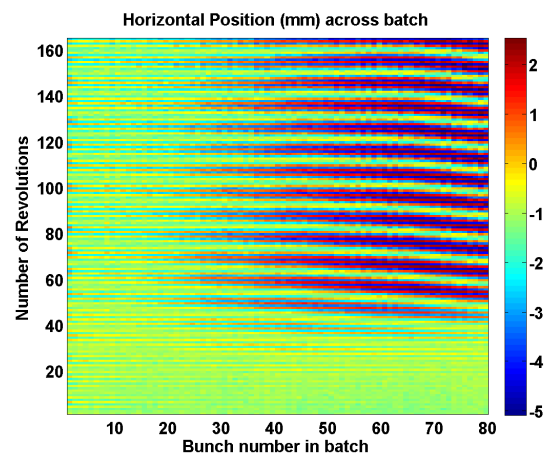


Figure 2: Stripline measurements of horizontal beam position visualized across the batch and across times.
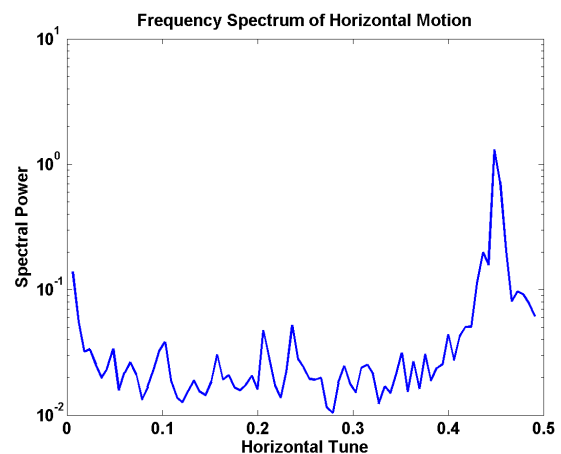


Figure 3: For several points of each bunch, the horizontal frequency spectrum is taken and summed. The peak shown in this plot is located at 0.4485 which corresponds to the horizontal betatron tune.

The instability manifests as a growing betatron oscillation and therefore the amplitude and tune of the betatron oscillation can be used as an effective metric of the instability. We divide the dataset into overlapping 12-revolution windows and for each window we calculate the best-fit betatron tune and its amplitude.

Figure 4 shows the horizontal betatron amplitude across the batch. The betatron amplitude grows rapidly ($\sim 20$ revolution doubling time) and appears to level off around the 70th revolution. The betatron amplitude growth is concentrated in the second half of the batch and obtains the maximum betatron oscillation amplitude between the 60th and 70th bunch in the batch. The moiré patten in Figure 4 is most likely an aliasing effect.
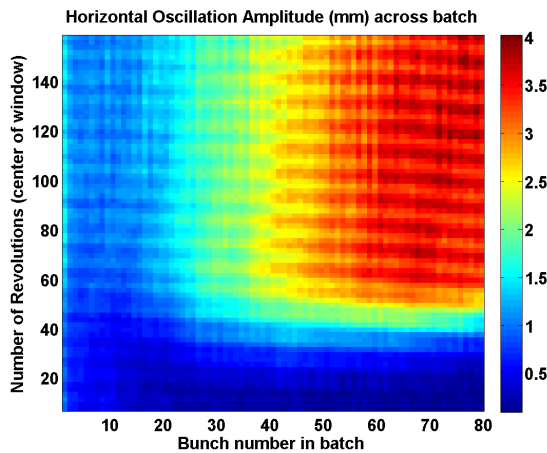


Figure 4: Horizontal betatron amplitude across batch and over time.

Figure 5 shows the particle losses across the batch. The particle losses are calculated by changes in the stripline sum signal. The losses occur in the second half of the batch and increase as the betatron amplitude growth rate decreases. Figure 6 shows the batch-average of the betatron amplitude growth rate juxtaposed with the batch-total of the particle loss. The decrease in the betatron amplitude growth rate is not consistent with a selection effect from the loss of particles with high betatron amplitudes.

Figure 7 shows the bunch length across the batch. The bunch length is calculated as the standard deviation of the (stripline) intensity distribution. The bunch lengths are consistent across the batch but vary from $\sim 1.4$ ns to $\sim 1.9$ ns over a half synchrotron period. Figure 8 show the batch-average of the betatron amplitude growth rate juxtaposed with the batch-average of the bunch length. The minimum of the bunch length oscillation coincides with the maximum betatron amplitude growth rate.

The Recycler instability can be compared to the electron cloud instability seen in the CERN SPS by Cornelis [7]. Our results seem consistent with the horizontal motion but not the vertical motion. Simulations of electron cloud instabilities also predict rapid transverse emittance growth [8, 16, 17].
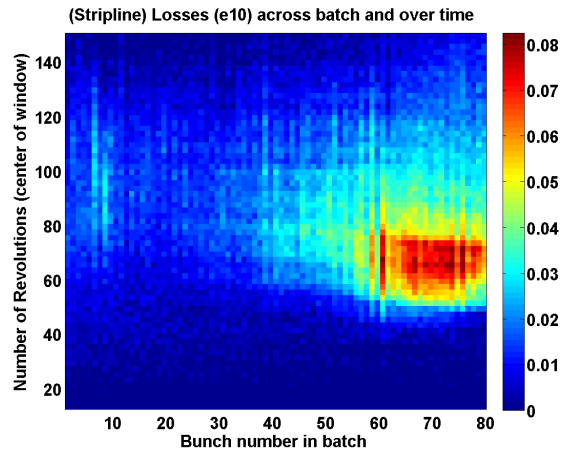


Figure 5: Particle losses across batch and over time.
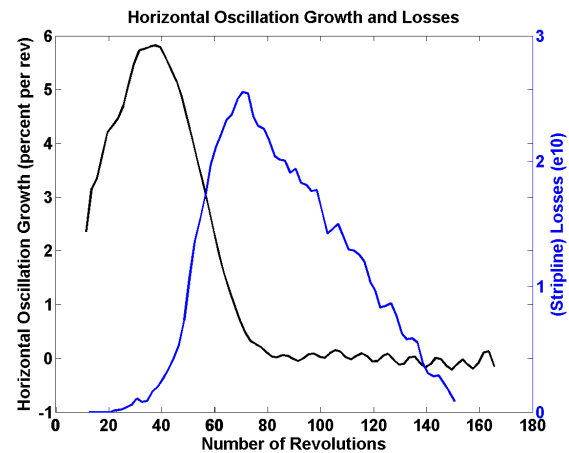


Figure 6: The left axis (black) indicates the betatron amplitude growth rate averaged across the batch and the right axis (blue) indicates the particle losses summed across the batch.
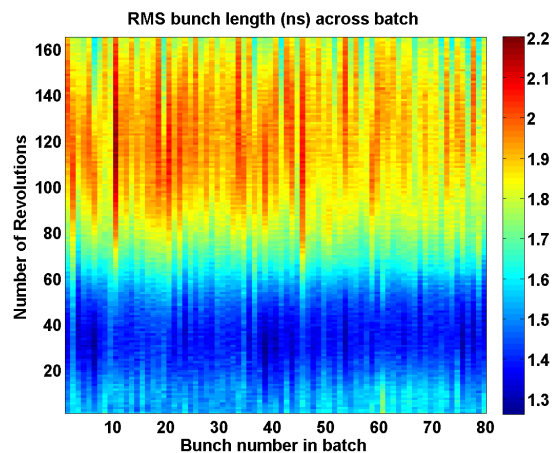


Figure 7: Bunch length across batch and over time.
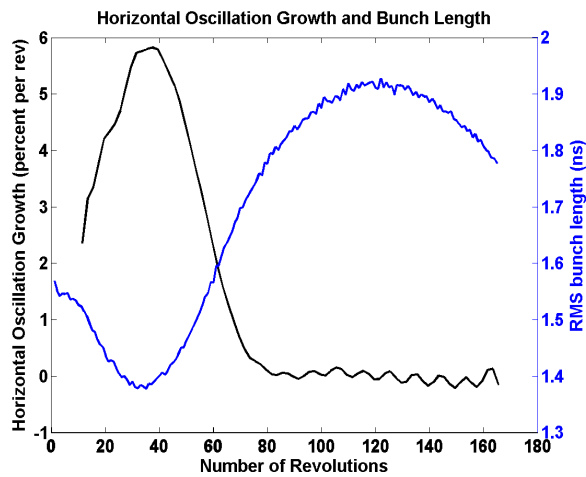
Figure 8: The left axis (black) indicates the betatron amplitude growth rate averaged across the batch and the right axis (blue) indicates the bunch length averaged across the batch.

## DIRECT MEASUREMENT OF ELECTRON CLOUD

From September 5th to October 23rd there was a pre-scheduled shutdown period in which an RFA electron cloud detector was installed in the Recycler at MI-52. Details about the design and characterization of the RFAs are given in [18] and [11]. Other accelerators have deployed similar collectors to study electron cloud [19, 20, 21]. An RFA signa of 1V is estimated to represent an electron flux of $\sim 1e7$ electrons per second per square centimeter. The RFA was installed on 100 ft of new stainless steel beampipe with no previous history of electron cloud conditioning. This RFA has been exposed to less than a week of scrubbing and we have not yet run high-intensity multiple-batch Recycler cycles since the shutdown. Consequently we expect the electron cloud measured by the newly installed RFA would be typical of a higher SEY than would generally be found in the rest of the Recycler.

Figure 9 and Figure 10 show the RFA response to a single 3.1e12 batch cycle and a six batch 2.6e12 cycle respectively. In Figure 9 we see that when the batch is injected the electron cloud RFA is composed of several sharp peaks spaced at half synchrotron period intervals and declining in height. In Figure 10 we see a similar signal at each batch injection but with the signals rising with each subsequent injection.

The sharp peaks in the electron cloud signal occur at minimums of the bunch length oscillation. An increase in electron cloud density is the expected response to a reduction in bunch length [22]. The greatest oscillation amplitude growth due to the Recycler instability also occurs at bunch length minimums (Figure 1 and Figure 8).

In Figure 10, the sharp peaks in electron cloud signal decline in height more gradually than in Figure 9. The gradual decline in the electron cloud peak height may be explained by filamentation of the synchrotron oscillation. The initial, very rapid decline in the electron cloud peak height appears
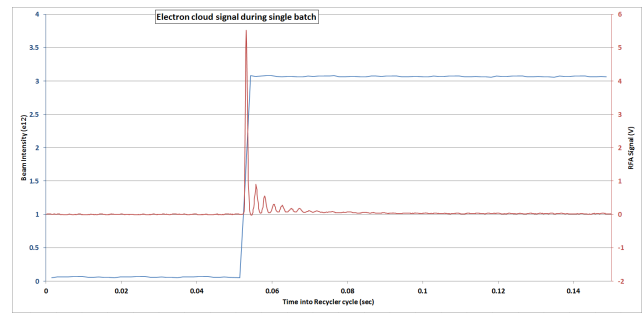
Figure 9: The left axis (blue) indicates the total beam intensity stored in the Recycler and the right axis (red) indicates the magnitude of the RFA ecloud signal. The traces correspond to a single 3.1e12 batch Recycler cycle.
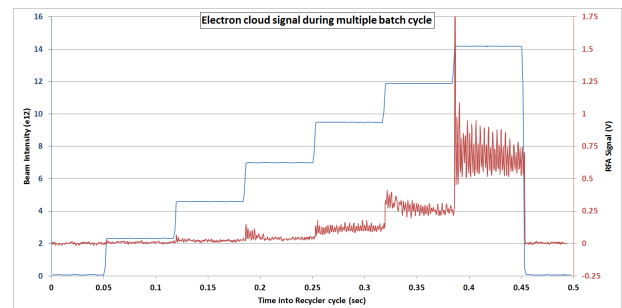


Figure 10: The left axis (blue) indicates the total beam intensity stored in the Recycler and the right axis (red) indicates the magnitude of the RFA ecloud signal. The traces correspond to a six batch 2.6e12 Recycler cycle.

to only occur at high beam intensities. One explanation is that the first electron cloud peak dramatically increases the transverse emittance of the beam. In the next electron cloud peak, the beam has a larger transverse emittance and therefore does not produce an electron cloud of the same density (see [8]). This model of close feedback between the transverse beam emittance and the electron cloud density is a novel regime of electron cloud dynamics.

## MICROWAVE MEASUREMENTS OF ELECTRON CLOUD

On August 20th 2014 a study of the Recycler electron cloud was conducted with microwave electronics. At the time of these measurements, the first batch is was operating at an intensity of $\sim 3.6e12$ and subsequent batches at an intensity of $\sim 4.5e12$ per batch. On each day, two "split-plate" BPMs in the Recycler (VP201 and VP203) [23] were disconnected and used to transmit a microwave signal through the beampipe in order to infer the presence of electron cloud in the Recycler. These studies follow the technique implemented in the Fermilab Main Injector by Crisp et. al. in [24] and also by others [25, 26, 27].

Unlike the RFA electron cloud measurement shown in this paper, the microwave technique can measure the electron cloud in dipole regions with typical beampipe conditioning.

In addition, we currently have only measured high-intensity multiple-batch cycles with the microwave technique.

A schematic of the electronic setup used for these studies is shown in Figure 11. The signal generator is used to drive a ~ 1.9GHz carrier signal which is then passed through an amplifier and a high-pass filter. This carrier signal is sent into a Recycler BPM used as a microwave transmitter, is propagated through the Recycler beampipe, and is received by the second Recycler BPM used as a microwave receiver. This carrier signal then passes through another high-pass filter and is recorded by the signal analyzer. Using the split-plate BPMs as improvised microwave antennas results in a ~ −80 dB transmission loss.
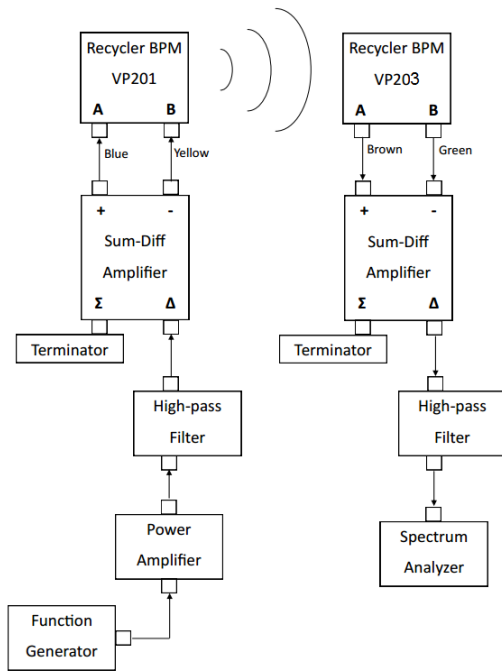


Figure 11: Flow-chart schematics of the microwave electronics used to measured the electron cloud. The signal generator creates a signal at a single carrier frequency, next this signal propagates through the electron cloud, and lastly this signal is examined for phase modulation in the signal analyzer.

In the presence of an electron cloud of uniform density, the carrier signal receieves a phase delay approximately [26] given by

$$\phi \approx \frac{L}{c} \frac{\omega_P^2}{2\sqrt{\omega^2 - \omega_c^2}} \qquad (1)$$

where $L$ is the path length and $\omega_c$ is the cut-off frequency of the beampipe. The plasma frequency $\omega_P$ can be approximated (in Hz) by

$$\omega_P \approx 2\pi 9 \sqrt{\rho_e} \qquad (2)$$

where $\rho_e$ is the density of the electron cloud in electrons per cubic meter.

The density of the electron cloud is modulated by the revolution harmonics of the proton beam (~90 KHz) and therefore the carrier frequency is phase-modulated (PM) in the presence of the electron cloud. Consequently, the electron cloud signal is seen as 90kHz sidebands on either side of the carrier frequency. The contribution that each batch makes to the sideband is $2\pi/7$ out of phase with the contribution made by the adjacent batch. This creates a possible ambiguity betweeen changes in the density of the electron cloud and change in the distribution of the electron cloud.

From Eq. 1 it can be seen that the optimal carrier signal is near the cut-off frequency of the beampipe because that greatly enhances the magnitude of the electron cloud phase-delay while keeping the amplitude of the carrier signal high. For the measurements presented in this paper we used 1.977 GHz as our carrier frequency, but our choice of carrier frequency may not be completely optimized.

For a 1.977000 GHz carrier frequency and a 90 kHz modulation frequency, the lower sideband frequency is 1.976910 GHz. Figure 12 shows the average spectral power of the lower sideband frequency as a function of time within the Recycler cycle. The beam background trace may be indicating the operation of the Recycler kickers because the sharp peaks coincide with the six batch injections into the Recycler as well as the batch extraction from the Recycler. The electron cloud measurement trace also shows sharp peaks at batch injection and these peaks are a statistically significant margin above the sharp peaks in the beam background trace.
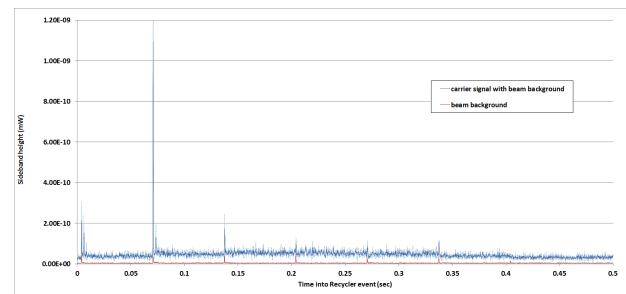


Figure 12: Spectral power of the lower sideband frequency averaged over 40 Recycler cycles and for each of two conditions. In the "beam background" condition (red), the spectal power is measuring cycle-dependent background from the beam harmonics and accelerator electronics. In the "carrier signal with beam background" a carrier signal is also propagated through the beampipe and the trace includes the sideband of this signal.

Figure 13 zooms in on the gradual features of the traces shown in Figure 12 to reveal "plateaus". The plateaus are the piecewise constant features that increase in magnitude up to third and fourth batch and then decrease in subsequent batches. Recall that the contribution of each batch to the sideband height is $2\pi/7$ out of phase with the previous batch. Consequently, these plateaus are actually consistent with the case in which each batch generates a comparable amount of

electron cloud while passing a given section of beampipe. In that case, the plateaus are indicating an electron cloud density relatively uniform across the second and subsequent batches (with electron cloud flux increasing proportionally with the number of batches) [28].
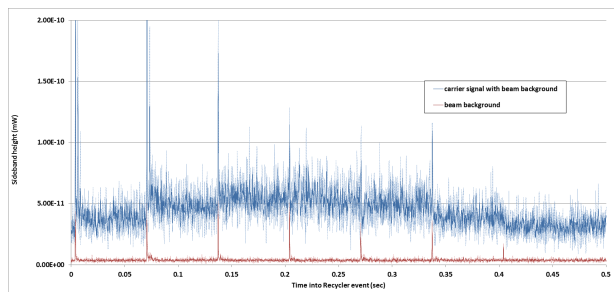


Figure 13: Spectral power of the lower sideband frequency averaged over 40 Recycler cycles with and without a carrier signal. This plot zooms in on the plateaus of the measurement trace.

Figure 14 zooms in the sharp peaks at the first two batch injections shown in Figure 12 and Figure 13. At each injection, there are actually two or three sharp peaks each declining in height with respect to the previous peak. The peaks are spaced at half-synchrotron period intervals because they coincide with the minimums of the bunch length oscillation.

The sharp peaks of the measurement trace (Figure 12) that occur at the second injection are always significantly higher than that of the first injection; the peaks at the first injection are higher still than those at the third and subsequent injections. The profile of injection peak heights matches the profile of the instability observed in the beam while these measurements were taken. These measurements are taken with the first batch at $\sim 80\%$ the intensity of subsequent batches, with the largest betatron oscillation amplitude observed in the second batch.

However, it is difficult to identify a mechanism which would account for this selective generation of electron cloud. Moreover, this profile of the electron cloud does not match the profile observed in the low-intensity multiple-batch RFA signal (Figure 10). If the electron cloud density after the first two batches is sufficiently great, its possible that the electron cloud instability could rapidly increase the emittance of the third batch in the $\sim 30$ revolutions before its first bunch length minimum. However, one would naively expect that this rapid emittance growth would co-occur with rapid betatron amplitude growth which is not observed in the third batch. Another hypothesis would be that the electron cloud temporarily modifies the SEY of the beampipe by desorbing large quantities of gas. However the maximum electron cloud density would be many orders of magnitudes too small to alter the SEY of the beampipe on this timescale.

During the shutdown, spare split-plate BPMs in the Recycler (VP130 and VP202) were connected to the microwave electronics (Figure 11). Consequently, future microwave
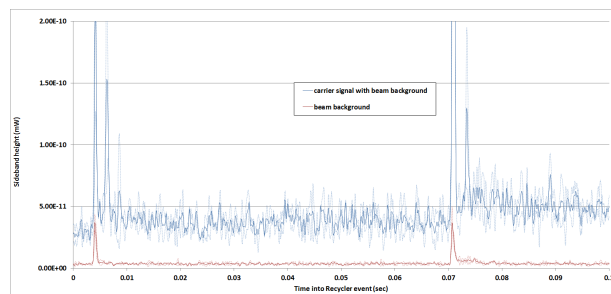
Figure 14: Spectral power of the lower sideband frequency averaged over 40 Recycler cycles with and without a carrier signal. This plot zooms in on the features of the sharp peaks at batch injection.

Table 1: Recycler and Parameters Used for POSINST Simulation of Electron Cloud Striping

| | |
|---|---|
| Beam Kinetic Energy ($E$) | 8 GeV |
| Beam Distribution Transverse sigma ($\sigma_x$) | 3 mm |
| Beam Distribution Longitudinal sigma ($\sigma_z$) | 0.75 m |
| Full Bunch Intensity | 5e10 |
| Buckets per batch | 84 |
| Filled buckets per batch | 82 |
| Number of batches | 6 |
| Beampipe SEY (maximum) | 2.2 |
| Beampipe geometry | elliptical |
| Beampipe horizontal major axis | 94 mm |
| Beampipe vertical major axis | 44 mm |
| Dipole field strength | 1.375 T |

measurements of electron cloud in the Recycler will not require disconnecting any instruments currently used to monitor beam position.

## SIMULATION DATA OF ELECTRON CLOUD STRIPING

In this section we present one mechanism for the electron cloud instability to be batch-selective. Electron cloud has been observed forming stripes in the presence of a strong dipole field [19]. Simulations indicate that in low electron cloud densities, the electron cloud is confined to a single vertical stripe centered on the beam. As the electron cloud density starts to near a maximum saturation point, the structure of the electron cloud changes to two vertical stripes with a bimodal horizontal distribution [29].

We conducted electron cloud simulations using POSINST [30], an electron cloud simulation program that relies on the Furman-Pivi model of secondary electron yield (SEY) [31]. The simulations presented in this paper use realistic parameters for the Recycler, shown in Table 1, with the possible exception of the SEY. The SEY for the simulation was 2.2, the SEY of completely unconditioned stainless steel [32]. We find that the electron cloud generated in each revolution is independent of the previous revolution.

The simulations indicate that the electron cloud density in the beampipe increases every revolution until the end of the last batch, at which point it falls off rapidly. The electron cloud density within in the one sigma ellipse of the beam, however, can obtain an early maximum. Figure 15 shows the electron density within one sigma of the beam for a cycle in which all batches have the same intensity (5e10 per bunch). Figure 16 shows the electron density within one sigma of the beam for a cycle in which the first batch has 75% the intensity of subsequent batches (3.5e10 per bunch). In Figure 15 the peak electron cloud density near the beam is obtained during the first batch and in Figure 16 the peak electron cloud density near the beam is obtained during the second batch. This matches the batch-selectivity observed in the Recycler instability - a modest decrease in the intensity of the first batch moves the instability from the first batch to the second batch and the instability becomes less severe.
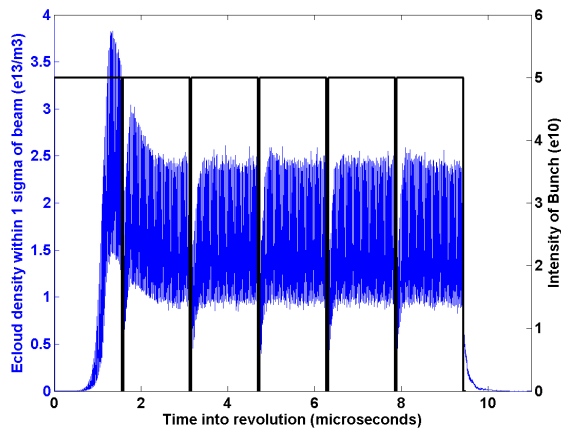


Figure 15: Simulated electron cloud density within 1 sigma of the beam (blue) for a beam structure with six batches of equal intensity (black). The maximum electron cloud density (within 1 sigma of the beam) is 3.83e13 per cubic meter and is obtained after the 71st bunch. The batches are 84 (18.8ns) buckets long with 82 buckets filled with 5e10 intensity bunches.

The electron cloud density within one sigma of the beam peaks because of the formation of stripes in the dipole field. Figure 17 shows simulated particles distributed in a single stripe at the 60th bucker and Figure 18 shows simulated particles distributed in two stripes at the 212th bucket. Both distributions are drawn from the same simulation run shown Figure 16. The discrete lines that compose the stripes in Figure 17 and Figure 18 are not numerically stable features of the simulation and should be regarded as a approximate description of the more continuous distributions shown in [29] and [17]. We have also conducted simulations without a strong dipole field and we do not find particles distributed in stripes or find an early peak in the electron cloud density near the beam.

This dipole-striping model presently represents our best explanation for the observed batch-selectivity of the electron

cloud instability [33]. It should be noted that this model predicts only the batch-selectivity of the electron cloud instability (seen in the microwave data).
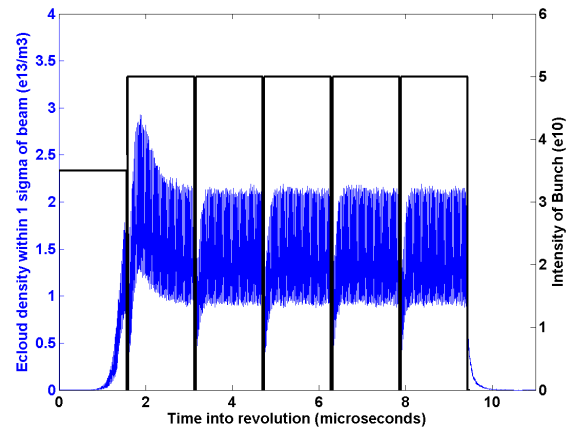


Figure 16: Simulated electron cloud density within 1 sigma of the beam (blue) for a beam structure with the first batch at 75% the intensity of subsequent five batches (black) The maximum electron cloud density (within 1 sigma of the beam) is 2.93e13 per cubic meter and is obtained after the 98th bunch. The batches are 84 (18.8ns) buckets long with 82 buckets filled with 3.5e10 and 5e10 intensity bunches.
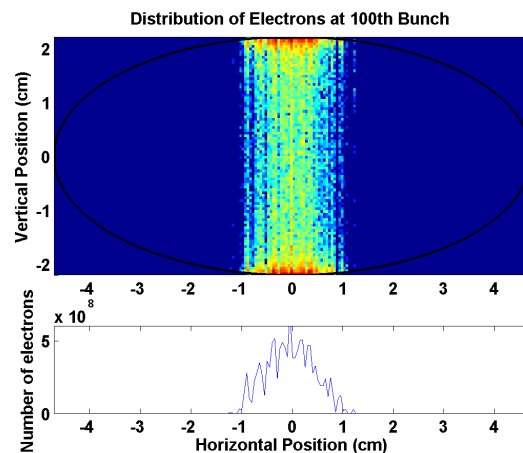


Figure 17: (top) 2D histogram showing the positions of particles in an electron cloud simulated by POSINST. The color indicates the number of particles on a log scale. (bottom) 1D histogram showing the horizontal distribution of particles. The particles are located within a single vertical stripe and have a unimodal horizontal distribution.

## CONCLUSIONS

We will continue to study this new instability and the electron cloud in the Recycler. The September-October shutdown provided an opportunity for dedicated RFA and microwave electron cloud instrumentation to be installed in the Recycler. Within a week or two we will be able to observed the RFA signal near the multiple batch intensity threshold.
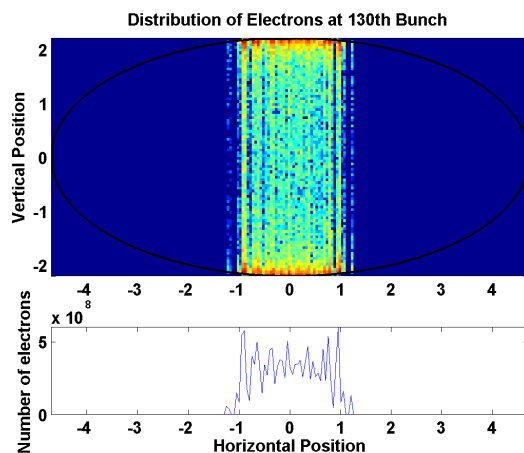
Figure 18: (top) 2D histogram showing the positions of particles in an electron cloud simulated by POSINST. The color indicates the number of particles on a log scale. (bottom) 1D histogram showing the horizontal distribution of particles. The particles are located within two overlapping vertical stripes and have a bimodal horizontal distribution.

If the instability is indeed caused by electron cloud, it is possible that commissioning of the Recycler for slip-stacking in the coming months will sufficiently condition the beampipe to effectively eliminate losses from the instability. If so, this paper has provided the first glimpse into the nature of electron cloud instabilities at Fermilab Recycler. If incidental beampipe conditioning is not sufficient to raise the instability threshold, we are considering dedicated scrubbing cycles with the purpose of advancing the rate of conditioning. We have also discussed the possibility of upgrading the digital damper system in the Recycler.

This paper has informed the greater accelerator community of a new instability both worth avoiding and worth studying. We describe the salient dynamical features of the instability in detail. The connection between the electron cloud in the Recycler is compelling. The electron cloud in the Recycler shows a dramatic dependence on bunch length and transverse emittance. This works underscores the need to understand the diversity of electron cloud phenomena.

## REFERENCES

[1] B. C. Brown, P. Adamson, D. Capista et al., Phys. Rev. ST Accel. Beams **16**, 071001 (2013) http://journals.aps.org/prstab/abstract/10.1103/PhysRevSTAB.16.071001

[2] J. Eldred, R. Zwaska, these proceedings, MOPAB12, Proc. HB14.

[3] R. J. Macek, A. A. Browman, M. J. Borden et al., Proc. ECLOUD04, http://mafurman.lbl.gov/ECLOUD04_proceedings/Macek_StatusReport-PSR-v3.pdf

[4] R. J. Macek, T. Spickermann, A. Browman et al. Proc. HB2006, www.jacow.org/abdwhb06/PAPERS/THAW04.PDF

[5] R. McCrady, B. Blind, J. D. Gilpatrick et al., Proc. BIW10, http://www.jacow.org/BIW2010/papers/weianb01.pdf

[6] R. McCrady, R. Macek, T. Zaugg et al., Proc. PAC07, http://www.jacow.org/p07/PAPERS/MOPAS050.PDF

[7] K. Cornelis, Proc. ECLOUD2, http://conf-ecloud02.web.cern.ch/conf-ecloud02/papers/allpdf/cornelis.pdf

[8] G. Rumolo, G. Arduini, E. Métral et al., Phys. Rev. Lett. **100**, 144801 (2008) http://journals.aps.org/prl/pdf/10.1103/PhysRevLett.100.144801

[9] G. Jackson, Fermilab Recycler Ring Technical Design Report, Fermi National Accelerator Facility, 1996 http://inspirehep.net/record/428434

[10] R. Zwaska, Proc. PAC11, http://www.jacow.org/PAC2011/papers/moobs4.pdf

[11] M. Backfish, Masters thesis, Indiana University, 2013 http://inspirehep.net/record/1294079/files/fermilab-masters-2013-03.pdf

[12] P. Adamson, W. J. Ashmanskas, G. W. Foster et al., Proc. PAC05, www.jacow.org/p05/PAPERS/MPPP015.PDF

[13] M. Xiao, M. Yang, D. E. Johnson et al., Proc. PAC05, www.jacow.org/p05/PAPERS/MPPE052.PDF

[14] M. Xiao, Proc. IPAC12, http://www.jacow.org/IPAC2012/papers/tuppr085.pdf

[15] J. Crisp, K. Gubrienko, V. Seleznev, Fermilab Report No. BEAMS-DOC-339-v2, 1998, https://beamdocs.fnal.gov/AD-private/DocDB/ShowDocument?docid=339

[16] K. Li, G. Rumolo, Proc. IPAC11, www.jacow.org/IPAC2011/papers/MOPS069.PDF

[17] E. Benedetteo, Ph.D. thesis, Turin Polytechnic, 2006 http://inspirehep.net/record/887199

[18] C. Y. Tan, K. L. Duel, R. Zwaska, Proc. PAC09, www.jacow.org/pac2009/papers/th5rfp041.pdf

[19] J. R. Calvey, W. Hartung, Y. Li et al., arXiv:1408.5741 (2014) https://inspirehep.net/record/1312222

[20] C. Yin Vallgren, G. Arduini, J. Bauche et al. Phys. Rev. ST Accel. Beams **14**, 071001 (2011) http://journals.aps.org/prstab/abstract/10.1103/PhysRevSTAB.14.071001

[21] A. Pertica, S. J. Payne, Proc. ECLOUD12, http://inspirehep.net/record/1254612

[22] F. Caspers, S. Gilardoni, E. Mahner et al., Proc. IPAC12, www.jacow.org/IPAC2012/papers/WEPPR010.PDF

[23] J. Fitzgerald, J. Crisp, E. McCrory et al., AIP Conf. Proc. **451**, 370 (1998) http://scitation.aip.org/content/aip/proceeding/aipcp/10.1063/1.57018

[24] J. Crisp, N. Eddy, I. Kourbanis et al., Proc. PAC09, www.jacow.org/d09/papers/tupb23.pdf

[25] S. De Santis, J. M. Byrd, F. Caspers et al., Phys. Rev. Lett. **100**, 094801 (2008) http://journals.aps.org/prl/pdf/10.1103/PhysRevLett.100.094801

[26] S. Federmann, F. Caspers, E. Mahner, Phys. Rev. ST Accel. Beams **14**, 012802 (2011) http://journals.aps.org/prstab/pdf/10.1103/PhysRevSTAB.14.012802

[27] S. De Santis, J. Sikora, D. Alesini et al., Proc. IPAC12, `www.jacow.org/IPAC2012/papers/MOPPR073.PDF`

[28] The plateaus are also consistent with amplitude modulation caused by electronic mixing between the higher beam harmonics and the carrier frequency. However, this interpretation does not seem likely because the RFA data indicates plateaus of genuine electron cloud signal.

[29] P. Lebrun, P. Spentzouris, J. Cary et al. Proc. ECLOUD10, `http://www.lepp.cornell.edu/Events/ECLOUD10/proceedings/papers/MOD03.pdf`

[30] M. T. F. Pivi, M. A. Furma,S. Federmann, F. Caspers, and E. Mahner `https://journals.aps.org/prstab/pdf/10.1103/PhysRevSTAB.6.034201`

[31] M. A. Furman, M. T. F. Pivi, Phys. Rev. ST Accel. Beams **5**, 124404 (2002) `https://journals.aps.org/prstab/pdf/10.1103/PhysRevSTAB.5.124404`

[32] D. J. Scott, D. Capista, K. L. Duel et al., Proc. IPAC12, `www.jacow.org/IPAC2012/papers/MOPPC019.PDF`

[33] For now we equate increasing electron cloud density near the beam with an increasing severity of the electron cloud instability. But as Burov argues in [34], electron cloud density may not always be a good proxy for the magnitude of the electron cloud instability and instead the presence of the electron cloud may even be stabilizing. Electron clouds introduce both impedance and nonlinearity and these need to be incorporated into a full model of transverse collective instabilities to make an absolute statement about the influence of electron cloud on transverse stability.

[34] A. Burov, Fermi National Accelerator Laboratory Report No. FERMILAB-PUB-13-005-ADD, 2013, `http://inspirehep.net/record/1210188/files/fermilab-pub-13-005-ad.pdf`

# TRANSVERSE EMITTANCE PRESERVATION STUDIES FOR THE CERN PS BOOSTER UPGRADE

E. Benedetto, C. Bracco, B. Mikulec, V. Raginel, G. Rumolo,  CERN, Geneva, Switzerland,
V. Forte, CERN, Geneva, Switzerland, and Université Blaise Pascal, Clermont-Ferrand, France

## Abstract

As part of the LHC Injectors Upgrade Project (LIU), the CERN PS Booster (PSB) will undergo an ambitious upgrade program, which includes the increase of injection energy from 50 MeV to 160 MeV and the implementation of an H⁻ charge-exchange injection from the new Linac 4. Compared to rings characterized by similar space-charge tune spreads (about 0.5 at low energy), the peculiarity of the PSB is the small transverse emittance that needs to be preserved in order to provide high brightness beams to the LHC. We here try to identify what is the minimum emittance that can be achieved for a given intensity, via measurements, scaling estimates and simulation studies. The latest are based on our best knowledge of the optics model and take into account known perturbations such as the one induced by the short and fast ramping chicane injection magnets.

## INTRODUCTION

CERN PS Booster is the first circular accelerator in the LHC proton injector chain and it is where the transverse emittance is defined.

It is made of four superposed rings and accelerates protons up to 1.4 GeV (it will be upgraded to 2 GeV) for the downstream machine, the Proton Synchrotron (PS).

Currently it has a conventional multi-turn injection of 50 MeV protons from Linac 2 and the plan is to replace it with a H⁻ charge-exchange injection from Linac 4 at 160 MeV [1]. These upgrades will allow increasing the beam brightness, i.e. the intensity in a given emittance, for the same space-charge tune spread, to reduce the injection losses, which in the present machine are dominated by the interaction with the injection septum, and to better control the filling of the transverse phase-space.

Particles are injected at a given working point $(Q_x, Q_y)$ around (4.3, 4.5), to optimize multi-turn injection and allocate the maximum possible space-charge tune spread, which in the PSB is around 0.5. The tunes are then reduced during acceleration, as soon as the necktie gets smaller, down to about (4.2, 4.2) at extraction. Figure 1 shows the working point variation during the ramp for the LHC-type beam discussed in the following section, which is injected at a slightly larger horizontal tune, as a result of beam optimization in operation.

With respect to the production of the high intensity beams, in which the goal is to minimize the injection losses [2], for the LHC beams the challenges are to assure a good quality beam in the three planes and to minimize the transverse emittance blow-up.
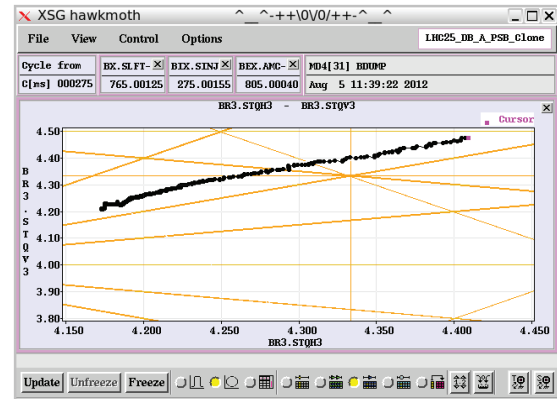


Figure 1: The working point during acceleration of the LHC-type beams goes from around (4.4,4.47) down to (4.18,4.20).

## MEASUREMENTS

In 2012 a measurement campaign has been done for the LHC operational beams, with the aim to quantify and define a budget for the emittance blow-up in the entire injection chain.

Figure 2 summarizes the major results for the PSB, i.e. the curve of the average normalized transverse emittance as a function of the beam intensity, at constant longitudinal emittance. The horizontal and vertical emittances have been measured at the extraction flat-top in Ring 3, which featured the best performances, as the result of a careful optimization [3].

Different beam intensities have been produced by increasing the number of injected turns from 1 to 4 and the only other parameter which was slightly changed and optimized for each measurement point was the tune at injection. Two sets of measurements appear in the plot, for different longitudinal emittances, that are 1.20 eVs and 0.86 eVs (matched area), corresponding to the two main LHC beams produced in 2012, i.e. respectively the standard LHC25ns and the BCMS [4].

The first consideration is that the points lie on a straight line on the emittance versus intensity plot; the second is that the slope increases for a smaller longitudinal emittance.

Additional measurements [3] show that, provided that the working point is optimized all along the cycle, the transverse normalized emittance is constant during acceleration (however measurements at injection are difficult to read due to scattering at the wires, which induces 10% blow-up during the measurement itself). This indicates that the final values of the transverse emittance

are dominated by space-charge effects at injection energy and by the multi-turn injection process itself.
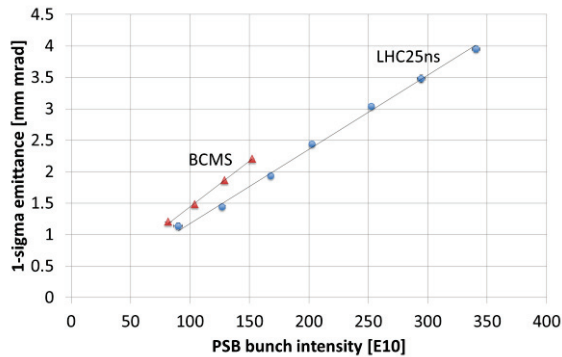


Figure 2: Emittance vs intensity curve for the LHC25ns beam (1.20 eVs) and the BCMS beam (0.86 eVs) [3].

## SCALING FOR LINAC4

The future change of injection energy with Linac4 gives a factor $(\beta\gamma^2)^{160MeV}/(\beta\gamma^2)^{50MeV} = 2.04$ reduction of the space-charge tune spread for the present beams.

The baseline of LIU is to keep the same tune spread as of today at the PSB injection [4], and to inject twice as many protons in a given emittance. The other possibility could be to reduce the emittances for a given intensity by the same amount.

With this assumption, the slopes of the lines in Fig. 1 should scale down as $1/(\beta\gamma^2)$, i.e. by a factor ~2. In addition to this consideration, any increase of the longitudinal emittance will help further to decrease the slope.

## SIMULATIONS EFFORT

A campaign is ongoing to confirm in simulations the predictions from the scaling estimates. The effort profits from work done in the past and/or for different and specific purposes and includes:

- Code consolidation and benchmarking of the simulation tools with ad-hoc measurements
- Benchmarking of the simulations of the present injection scheme with measurements of operational beams
- Study of the best injection scenario in the transverse and longitudinal plane
- Improvement of the machine optics model taking into account the new hardware

The codes chosen are Orbit [5] for the injection studies and PTC-Orbit [6], i.e. its version with the PTC tracking libraries included, for the longer-term simulations.

### Code consolidation and benchmarking with ad-hoc measurements

Measurements have been done in 2012-2013 to analyse space-charge effects in the PSB at 160 MeV, using the special magnetic cycle that was created in the past with an energy plateau at 160 MeV to allow for Machine Development Studies in view of the Upgrade. These are summarized in [7,8] while the results of benchmarking

with simulations are presented in [9]. A very good agreement was found in terms of beam losses and profile evolutions in the 3 planes, provided that our best knowledge of the machine is included in the simulations.

In parallel with these studies, a large effort is ongoing within the CERN Space-Charge Study Group to consolidate our simulation tools and to cross-benchmark the different codes. This is the subject of Ref. [10].

### Simulations of the present injection scheme

The first attempt to reproduce with simulations the present multi-turn injection is documented in [11]. The injection septum and the slow kickers displacing the closed orbit towards the injection septum have been modelled in Orbit. A good agreement was found for the production of an LHC-type beam with a 2-turn injection, but there were still discrepancies for the other variety of beams that the PSB can produce, especially the ones involving a larger number of injection turns. This can be due to missing ingredients in the optics model and/or to the large uncertainties in the definition of the injection settings, such as offsets in positions and angles and the parameters related to the kickers, i.e. calibration curves to get the strength, and the start timing with respect to injection. Simulations put in evidence how the evolution of beam losses and the build-up of emittance during the injection process are strongly dominated by the presence of the septum and by the injection settings. Moreover, space-charge plays a significant role in this process, therefore needs to be properly taken into account, as it helps in the homogenization of the profiles during injection.

### Studies of the best injection parameters

In order to preserve a small emittance during the H- charge-exchange injection process, the studies aim at optimizing [12]:

- The optics parameters and offsets of the incoming Linac4 beam within the geometrical constrains of the tight space and apertures available in the injection region
- The longitudinal distribution of the incoming beam, assuming no longitudinal painting in order to minimize the number of injected turns
- The painting bump
- The injection working point

### Improvement of the optics knowledge and modelling of the new injection hardware

Beam based measurements are ongoing to build up a detailed linear and non-linear optics model of the PS Booster [13]. The final goal is to implement, in a deterministic way, a resonance compensation scheme to accommodate a larger possible space-charge tune spread. Moreover, the outcome of these studies is used in the space charge simulations [9] to provide a detailed set of errors that represent the machine.

Concerning the lattice perturbations induced by the new injection chicane magnets, these are caused by two mechanisms.

First of all, in order to satisfy the stringent space constraints, short rectangular magnets with a maximum deflection of 66 mrad are required and introduce edge-focusing errors. Since the vertical tune of the machine is close to the half-integer resonance, this induces strong beta-beating in the vertical plane [14]. This effect vanishes as the chicane bump collapses.

Second effect, but of a comparable size, the ramp-down of the magnets within 5 ms induces Eddy currents in the vacuum chamber and generates multipolar components varying with time [15]. This translates again in vertical beta-beating due to the large horizontal orbit excursions inside the magnets, which cause quadrupolar feed-down effects. Perturbations due to Eddy currents depend linearly on the ramp rate and the effects on the beam are proportional to the offset from the magnet center.

To compensate for the beta-beating caused by the rectangular magnets edge effects and by Eddy current induced perturbations, additional trims on the two defocusing lattice quadrupoles QDE3 and QDE14 are envisaged [15].

These magnets and the correcting trims are now modelled in time-varying tables, acquired as input for PTC-Orbit.

## EMITTANCE BLOW-UP DUE TO SPACE-CHARGE AND INTERACTION WITH RESONANCES

The aim of these simulations is to identify the minimum emittance that can be achieved for a given intensity.

The errors included in the model are the perturbations at the chicane magnets due to edge effect and Eddy currents. This provides the excitation of the half-integer and 20% vertical beta-beating, which is corrected down to a few % by the special trims on the two lattice quadrupoles, as described above. In addition to that, it induces the excitation of the integer lines, which are not compensated. The model does not include any non-linear perturbations, except for the sextupolar components due to Eddy currents, which are negligible in strength.

We start with a transversely matched Gaussian distribution, while in the longitudinal plane the distribution is uniform in phase and parabolic in energy spread and evolves in an $h=1+h=2$ accelerating bucket. Then we follow the emittance evolution versus time for the first 7 ms. The working point is assumed constant and is set to (4.28, 4.55).

The injection process is not simulated, as the focus is on the blow-up during the fall of the chicane (injection is completed within the first 20 μs). Although final simulations should be end-to-end and include the injection painting as well, this approach is here justified by the results of Fig. 3, i.e. that the emittance reached at the end of the chicane bump is independent of the starting value (provided that the final value is larger than the initial one).
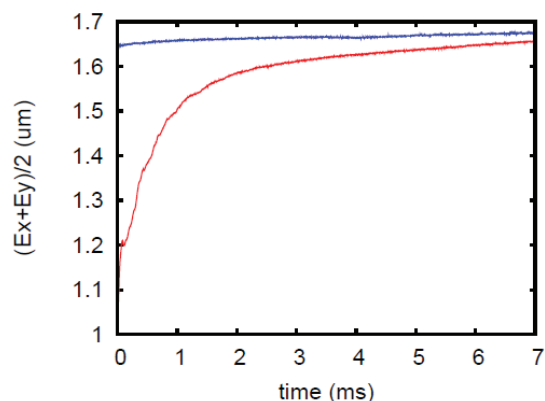


Figure 3: Normalized emittance evolution for 350e10 ppb intensity and a longitudinal emittance of 1.20e Vs, if starting from 1μm emittance or from 1.65 μm at injection.

The results obtained so far, still preliminary, are shown in Fig .4. In blue and in red are the lines of Fig. 1, scaled down by the factor 2 to account for the increase of the injection energy, as discussed in a previous section. The green triangles and the blue crosses show two different sets of data for different longitudinal emittances, respectively 1.17eVs and 1.48eVs. The simulated points lie as well on straight lines and it is confirmed that the increase in longitudinal emittance helps in improving the beam brightness. However, the curves have a slope which is a factor 25% smaller, while in our predictions they should have matched.

In order to include other perturbations in addition to the ones at the chicane magnets, the set of quadrupolar errors extracted from the beam-based measurements of 2012 [9] has been added to the model. A first attempt to identify the minimum emittance that can be reached was unsuccessful. The new errors were exciting the half-integer line, which was not compensated and, since the vertical tune was set to 4.55, it caused a large beam blow-up. For our second attempt, we lowered the working point to (4.28, 4.45) so that the space-charge tune footprint could be below the half integer, and the results are plotted as red squares in Fig. 4. Not much difference in terms of emittance blow-up was found with respect to the chicane-only case, apart for a small increase in the vertical plane due to the lower working point which makes the footprint touch the vertical integer.

Figure 5 shows the projections of the horizontal and vertical tune footprint. The initial tune spread for an intensity of 350e10 ppb and a starting emittance of 1μm in both planes is in red. Since it is largely below the integer, blow up occurs mostly in the horizontal plane, and bring the tune footprint to the situation in blue. For comparison, in green is the initial footprint if starting the simulations with emittances of 1.7 μm.
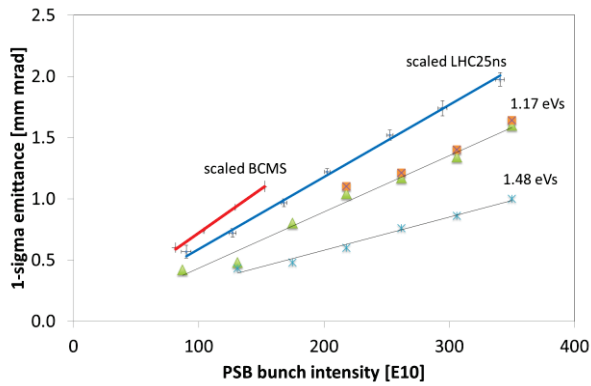
Figure 4: Emittance versus intensity, assuming injection at 160 MeV from Linac4. Blue and Red are the measurements results of Fig. 1 scaled by a factor 2. Green triangles: simulations assuming 1.17eVs longitudinal emittance. Blue crosses: simulations with 1.48 eVs. Red squares: simulations with 1.17 eVs, Qv=4.45 and a more complete linear errors model.
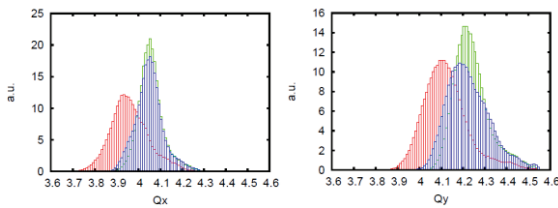


Figure 5: Tune footprint, horizontal and vertical projections: Red: initial tune spread for a beam of 350e10 ppb and 1μm emittances. Blue: final (after 7ms) for the same beam. Green: initial footprint for 350e10 ppb and 1.7 μm. Longitudinal emittance is 1.17 eVs.

## EMITTANCE BLOW-UP DURING THE INJECTION PROCESS

Other important sources of emittance blow-up are during the injection process itself, in particular Multiple Coulomb Scattering at the foil, mismatch at injection and jitters and/or ripples in the injection equipment.
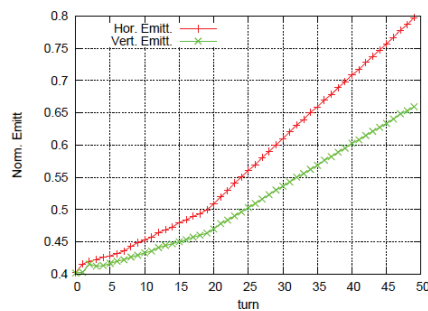


Figure 6: Simulated horizontal and vertical normalized emittance blow-up due to scattering at a 200 μg/cm² graphite foil. The multi-turn injection lasts 20 turns and the beam is not removed from the foil after injection has completed. Space-charge is not included.

Figure 6 shows the horizontal and vertical blow-up due to Multipole Coulomb Scattering at a Graphite foil of 200 μg/cm². For this exercise we have assumed an injection of 20 turns, without painting, after which the beam is kept on the foil. One can notice the change of slope in the emittance blow-up once injection is completed. Indeed, during the multi-turn injection process, the number of foil traversal per particle is half the number of turns (if no transverse painting is applied). This consideration should be taken into account when evaluating the emittance blow-up with analytical formula, however one should not forget to consider the time needed to remove the beam from the foil, which in our case is of the order of 7 extra foil traversals for the entire beam.

For the simulations shown in Fig. 7, a target intensity of 165e10 protons in a transverse emittance of ≤ 1μm has been considered (BCMS type beam). No longitudinal painting is used in order to minimize the number of injection turns. Also no transverse painting is applied, to generate a minimum possible emittance. In ideal conditions, the transfer line optics is matched with the PSB optics at injection (beta functions and dispersion) and no offset is applied between the injected and the circulating beam. A nominal normalized transverse emittance of 0.4 μm is assumed for the beam from Linac4. A uniform distribution in phase (±1.9 rad, corresponding to 616 ns bunch length) and parabolic in $\Delta p/p$ (±1.1e-3, corresponding to an energy offset of ±0.336 MeV) is considered for these studies.

Assuming 40 mA from Linac4, the injection process requires 7 turns injected plus about 7 turns to move away from the foil, implying an increase of transverse emittance of about $\Delta\varepsilon_x$=0.12 μm and $\Delta\varepsilon_y$=0.08 μm.

Figure 7 shows the effect of different injection scenarios, with respect to the ideal case, taking into account injection offsets, mismatch and a larger number of turns, e.g. in case the current from Linac4 would be lower. In particular:

a) Ideal optics and Linac4 current of 40 mA.
b) 25% mismatch of the optics parameters (beta functions and dispersion)
c) Mismatch as in (b) plus a constant offset of 2 mm between injected and circulating beam (steering and/or orbit errors)
d) Mismatch and offset as in (b) and (c) plus Linac4 current limited to 20 mA. This requires doubling the number of injection turns and, as a consequence, of stripping foil crossings.

The result of the simulations, for the different mentioned scenarios, shows a final transverse emittance of ~0.9 μm, still within the target.
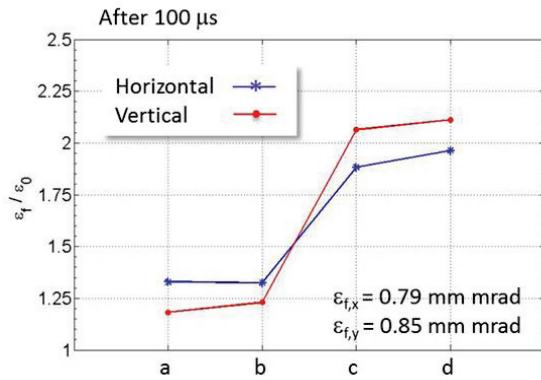
Figure 7: Ratio between final $\varepsilon_f$ (after 100 µs) and initial $\varepsilon_i$ emittance for different non-ideal scenarios (mismatched optics, orbit offset and reduced Linac4 current). A factor of two emittance blow-up is observed for the most conservative case (d).

## CONCLUSIONS

In the present PSB, the emittance is determined by space-charge effects at injection energy and by the conventional multi-turn injection process itself. The relation between transverse emittance and intensity is linear and depends on the longitudinal emittance.

Within the LIU project, the injection energy will be increased to 160 MeV, thus allowing for the injection of twice as much intensity in a given emittance. Moreover the new H- injection scheme will relax some of the constraints linked to the conventional multi-turn proton injection allowing for more flexibility in the shaping of the emittances. We expect two major contributions in the definition of the transverse emittance: the blow-up due to the injection process itself, e.g. foil scattering and injection errors or ripples, and the space-charge effects at low energy, knowing that the expected tune spread with the upgrade will still be of the order of 0.5.

The effects of blow-up at injection are evaluated for the production of a 1 µm emittance beam, and preliminary results are shown concerning the attempt to verify the scaling (proportional to $\beta\gamma^2$) of the measured emittance versus intensity for the Linac4 injection energy. Discrepancies by a factor 25% between simulations and scaled measurements may be due to missing ingredients in the model, i.e. higher order resonances, or simply due to differences in the injection process and/or in the contribution of the dispersion.

In parallel with improving the PSB optics model, efforts needs to be pursued in benchmarking the code with measurements data and in the basic understanding of effects related to space-charge in interplay with resonances.

## ACKNOWLEDGMENT

## REFERENCES

[1] W. Bartmann, "New PSB H- Injection and 2 GeV Transfer to the PS", HB2014 Proceedings.

[2] S. Gilardoni, "Long-term Beam Losses in the CERN Injector Chain", HB2014 Proceedings.

[3] B. Mikulec, "Performance reach of LHC beams", in LIU Beam Studies Review, 28 August 2012, CERN, Geneva, CH, http://indico.cern.ch/event/200692/

[4] G. Rumolo, et al., "Expected Performance in the Injectors at 25ns without and with Linac4", in Review of LHC and Injector Upgrade Plans Workshop, 29-31 October 2013, Archamps, FR.

[5] J.D. Galambos, J.A. Holmes, D.K. Olsen, ORBIT User Manual Version 1.10, 2011.

[6] E. Forest, A. Molodozhentsev, A. Shishlo, J. Holmes. "Synopsis of the PTC and ORBIT Integration", KEK. Internal Report (A), 4 November. 2007.

[7] B. Mikulec, et al., "Tune Spread Studies at Injection Energies for the CERN Proton Synchrotron Booster", in Proc. HB2012, MOP249, 17-21 September 2012, Beijing, China.

[8] V. Forte, et al., "Space charge studies in the PSB - MD report", CERN-ACC-NOTE-2014-0056, 2014.

[9] V. Forte, E. Benedetto, M. McAteer, "The CERN PS Booster Space Charge Simulations with a Realistic Model for Alignment and Field Errors", in Proc. IPAC'14, TUPRI029, Dresden, Germany (2014).

[10] F. Schmidt, "Code Requirements for Long Term Tracking with Space Charge", these proceedings HB2014.

[11] V. Raginel, et al., "Multi-turn injection of 50 MeV protons into the CERN Proton Synchrotron Booster", in Proc. NAPAC'13, Pasadena, CA, USA, pp.442-444, (2013).

[12] C. Bracco, et al, PSB injection beam dynamics, LIU Day 2014, 11 April 2014, CERN, Geneva. CH, https://indico.cern.ch/event/299470/

[13] M.J. McAteer, et al., "Preliminary Results of Linear Optics From Orbit Response in the CERN PSB", in Proc. IPAC'13, TUPWO047, Shanghai, China (2013).

[14] M. Aiba, et al., "Assessment of CERN PSB Performance with Linac4 by Simulations of Beams with Strong Direct Space Charge Effects", in Proc. IPAC'10, TUPD013, Kyoto, Japan (2010).

[15] E. Benedetto, et al., "Detailed Magnetic Model Simulations of the H- Injection Chicane Magnets for the CERN PS Booster Upgrade, Including Eddy Currents, and Influence on Beam Dynamics", in Proc. IPAC'14, TUPRI027, Dresden, Germany (2014).

# DPA AND GAS PRODUCTION IN INTERMEDIATE AND HIGH ENERGY PARTICLE INTERACTIONS WITH ACCELERATOR COMPONENTS

A.Yu. Konobeyev[#], U. Fischer, KIT, Karlsruhe, Germany

*Abstract*

A brief overview of methods for the calculation of the number of stable defects in irradiated materials is presented. Special attention is given to the evaluation of gas production cross-sections performed using nuclear models, experimental data, and systematics. The perspective of the use of evaluated data files for dpa and gas production calculations is discussed.

## INTRODUCTION

A calculation of radiation damage and gas production rates in materials is a challenging task combining the modelling of nuclear interactions, the simulation of the material behaviour, and taking into account, as far as possible, experimental data.

The calculation of atomic displacement cross-section consists of two independent parts: the calculation of recoil energy distributions for involved nuclear reactions and the evaluation of the number of stable displacements in materials. The report presents a brief overview of methods of calculation and main important results obtained for the number of defects produced in materials under irradiation. Special attention is given to the evaluation of gas production cross-sections using results of nuclear model calculations, experimental data, and systematics predictions.

## DPA PRODUCTION

The dpa production (radiation damage) rate is calculated by summing of integrals of particle- and energy-dependent displacement cross-section $\sigma_d$ and particle flux over all particle types. The displacement cross-section for incident particle with the kinetic energy $E_p$ is calculated as follows:

$$\sigma_d(E_p) = \sum_i \int_{E_d}^{T_i^{max}} (d\sigma_i(E_p, T_i)/dT_i) \, N_D(T_i) \, dT_i \qquad (1)$$

where $d\sigma_i/dT_i$ is the recoil atom energy distribution for i-th reaction; $N_D(T_i)$ is the number of Frenkel pairs produced by the primary knock-on atom (PKA) with the kinetic energy $T_i$, $T_i^{max}$ is the maximal kinetic energy of the PKA in *i*-th reaction; $E_d$ is the effective threshold displacement energy of material.

*Estimating the Number of Stable Defects*

The number of stable displacements $N_D$ can be calculated using different approaches with varying degrees of complexity of code implementation and accuracy of predictions.

_____
#alexander.konobeev@kit.edu

**The NRT displacement model** [1] remains popular in spite of well known shortcomings such as neglecting of an athermal recombination and the use of isotropic displacement energy [2]. The model in more general form [3] is implemented in NJOY [4], LAHET [5], MCNP [6] and other codes, which maintains its popularity for applications. According to the model the number of stable defects produced by the ion with the kinetic energy $T_{PKA}$ is equal to

$$N_{NRT}(T_{PKA}) = (0.8/2E_d) T_{dam}(T_{PKA}), \qquad (2)$$

where $T_{dam}$ is the energy transferred to lattice atoms reduced by the losses for electronic stopping of atoms in displacement cascade.

The measure of deviations of the $N_D$ number obtained experimentally or theoretically from one predicted by NRT is quantified as "defect production efficiency"

$$\xi = N_D(T_{PKA})/N_{NRT}(T_{PKA}), \qquad (3)$$

The NRT model has "internal" limitations like for the maximal kinetic energy of PKA [1,7]. Predicted $N_{NRT}$ numbers differs with some exceptions from the measured values for neutron irradiation in reactors [8,9] as for high energy protons [8], and results of molecular dynamics (MD) simulations. For example, the typical $\xi$ value obtained using MD for iron and nickel at $T_{dam}$ below 100 eV exceeds one, and is about 0.3 at 10 -100 keV [2].

**The binary collision approximation model (BCA)** is a popular method for the simulation of ion interactions with materials, which should be used with care for the estimation of realistic number of stable defects produced under irradiation.

An attempt to reproduce results of MD simulations by a proper choice of BCA parameters leads in many cases to an uncertainty of predictions at ion energies outside MD modelling [8,9]. The recent evaluation of popular BCA code SRIM [10] stated the problem of the calculation of correct number of stable displacements "in any absolute sense" [11].

One of advantages of BCA is the relative simplicity of the direct implementation in codes for the simulation of the particle transport using the Monte Carlo method.

**The molecular dynamics** simulation is the most adequate method to get realistic number of stable defects produced in irradiated materials.

The electronic losses and interatomic potential are still crucial points concerning the reliability of simulations. At least for iron and copper the total number of stable displacements calculated using MD with modern interatomic potentials are in agreement with experimental

data [2,8]. However, the fraction of defects in clusters calculated using different potentials varies significantly [2].

The number of works relating to MD simulations is definitely large and only a limited part concerns the information on stable displacements in materials relevant to the present report. The following works presenting calculated $N_D$ values for different materials are to be mentioned, for metals: Al [12-14], Ti [13], V [15-17], Fe [18-24], Ni [13,14,25-27], Cu [13,14,28-33], Zr [13,30,34,35], Mo [36], W [15,28,37,38], Pt [14], Au [14], alloys: Fe-Cr [22,39,40], Fe-Cr-C [41], Ni₃Al [13], Ni-Fe [25], Cu-Au [42], U-Mo [43], semiconductors: Si [14,44], Ge [14], GaN [45], carbides: SiC [46,47], Fe₃C [48], WC [49], oxides: MgO [50], $UO_2$ [51], spinels: $MgAl_2O_4$ [52], $MgGa_2O_4$ [52], $MgIn_2O_4$ [52], and zirconolite, $CaZrTi_2O_7$ [53]. Other important papers concerning materials discussed can be found in reference sections of corresponding publications.

Apparently, the range of MD application is limited by ion energies, where energetic losses are properly treated. Ref.[54] presents a brief discussion. With an exception of Ref.[19] where the maximal energy of simulation for iron, $E_{MD}$ is equal to 200 keV and the corresponding PKA energy about 425.5 keV, other works have focused on simulations with $E_{MD}$ energies up to several tens of keV.

The $N_D$ values obtained in MD simulations demonstrate rather weak temperature dependence [11]. In general, $N_D$ decreases with the increase of temperature [18,29]; whereas the comparison some results, for example, for copper in Ref.[28] at 10K Ref. and Ref.[29] at 300 K does not show any significant difference.

The modelling using MD is complicate enough and restricted by the ion-energies to be directly implemented in high energy particle codes.

The $N_D$ values obtained in Refs.[12-53] and experimental data [8,55-58] can be applied for evaluation of the radiation damage in materials after an extrapolation of MD results to the range of higher energies of PKA.

**Extrapolation of MD results to higher energies** outside the range of simulations is necessary to estimate radiation damage rate of materials irradiated with intermediate and high energy particles in different units.

The simple solution is to use a "constant efficiency" approximation, where the ξ value at the maximal energy of MD simulation $E_{MD}^{(max)}$ is used for all energies above $E_{MD}^{(max)}$. The approximation was applied in Ref.[28] for the analysis of the damage production in Cu and W irradiated with 1.1 and 1.94 GeV protons [57].

Recently proposed alternative to the NRT formula [2,59] also assumes the constant efficiency at high PKA energies. An athermal recombination corrected displacement damage (arc-dpa) [2,59] is calculated with the following efficiency value

$$\xi(E) = (1-c)\,(2E_d/0.8)^{-b}\,E^b + c, \qquad (3)$$

where "b" and "c" are parameters, "c" corresponds to the saturation at high energies [2], and it supposed that b < 0.

The approximation seems reasonable up to rather high energies of PKA, where deviations from measured data [58] are established [9].

The other way to get the number of stable defects at high PKA energies is the modelling using combined BCA-MD method [60,61].

**The BCA-MD simulation** seems to be an effective approach for the evaluation of the number of defects produced in materials under the irradiation with intermediate and high energy particles.

The idea is to perform BCA simulations for atomic collisions caused by all PKAs produced in the nuclear reaction up to a certain "critical" energy of ions. Below this energy, which is usually taken equal to 30-60 keV [9], the BCA modelling is stopped and the number of defects is estimated according to results of MD simulations.

Figure 1 shows the example of combined BCA-MD modelling. Other examples and details can be found in Refs.[9,60-64].

As well as the "pure" BCA" model, the combined BCA-MD method is rather easily implemented in Monte Carlo particle transport codes.
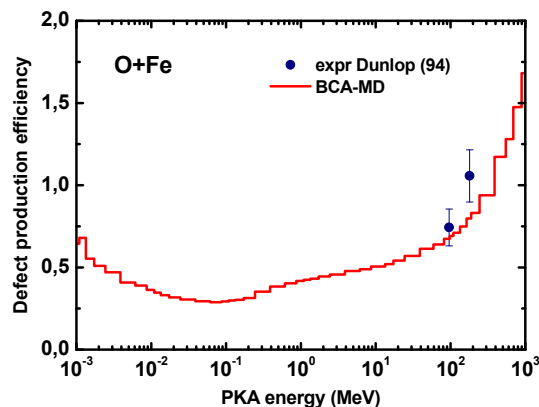


Figure 1: The ξ values the O+Fe irradiation.

**Kinetic Monte Carlo** (KMC) [65] is the method for the simulation of the long-term defect evolution. While the MD technique provides the information about atomistic processes up to nanoseconds, the KMC method is able to track the cascade damage up to seconds [28,66] and hours [67]. In the KMC method the primary defects such as individual point defects, clusters, and impurities are considered as "objects", which evolution is tracked over time [65]. Various approaches in KMC modelling like object KMC, event KMC, and atomic KMC differ in the details of simulation, description of object interaction and treatment of time scales [65,66].

It may seem reasonable to apply for the evaluation of radiation damage the $N_D$ values predicted by KMC, as it is done, for example, for iron in Ref.[67], and not ones estimated with MD or BCA-MD simulations. At the same time, the uncertainties concerning KMC simulations make the direct use of KMC results rather premature [68].

## Calculation of Recoil Energy Distributions

The calculation of recoil energy distributions in nuclear reactions is another integral part of displacement cross-section computations.

The $d\sigma/dT$ values can be obtained using an information from evaluated data files such as ENDF/B or calculated using theoretical models suitable for the description of elastic and non-elastic interaction of primary particles with material.

Figure 2 shows an example of $d\sigma/dT$ values calculated using various nuclear models [6,69] for non-elastic interactions of 1 GeV protons with $^{56}$Fe. The difference in corresponding $\sigma_d$ values calculated using the NRT model is illustrated in Fig. 3. Other examples of energy recoil distributions calculated using evaluated data libraries and nuclear model codes can be found in Ref.[70].
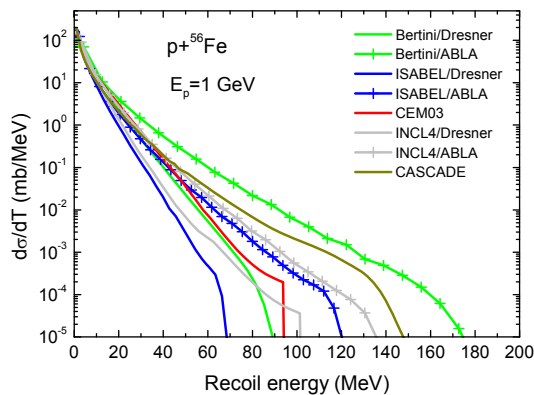


Figure 2: Example of calculated $d\sigma/dT$ values.

The difference in calculated recoil energy distributions using various models leads to statistically different results of $\sigma_d$ cross-section. In this case the evaluated value of displacement cross-section is calculated as a weighted sum of results obtained using different models [60,61]. Weights reflect the "quality" of corresponding nuclear models in describing experimental data relevant to the task and can be calculated as inverse values of deviation factors, discussed e.g. in Ref.[71].

## Modelling Using High Energy Particle Transport Codes

Three general approaches can be used for improved calculations of radiation damage rate using particle transport codes. In the first approach the simulation of nuclear and atomic interactions with primary particles are supplemented by direct BCA or BCA-MD modelling. An advantage of the method is complete sequential simulation of damage production during the irradiation. Problems concern the possible use of experimental information for defect production and the computational time. In most cases, the approach has no advantage over less time-consuming methods discussed below.

The next approach uses $N_D$ values calculated using BCA-MD(+KMC) and corrected applying available

experimental data. The $\xi(E)$ obtained in a parameterized form or pointwise is used for all PKAs generated after elastic and non-elastic interactions of particles with atoms. The approach is implemented in MARS15 [72], FLUKA [73], and PHITS [74] codes. For light targets, it seems reasonable to use individual $\xi(E)$ values for PKAs with different Z and A produced in nuclear reactions.
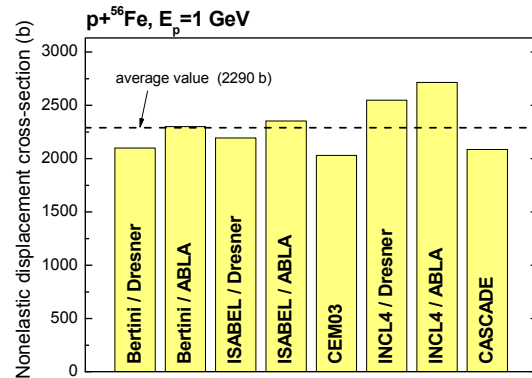


Figure 3: Example of calculated $\sigma_d$ values.

The third approach applies evaluated atomic displacement cross-sections. It is the most flexible way to use available experimental data for defect production and to apply advanced nuclear models for calculation of recoil energy distributions and systematics data.

Recently displacement cross-sections were evaluated for neutron and proton interactions with Al, Ti, V, Cr, Fe, Ni, Cu, Zr, and W at incident energies from $10^{-5}$ eV to 3 GeV [75]. The evaluated data can be supplemented by estimated covariance matrices relating to uncertainties of applied model parameters [76].

## GAS PRODUCTION

A reliable estimation of gas production rate in nuclear reactions is performed either by using well tested nuclear models describing the emission of light fragments in nuclear reactions, or by using evaluated data properly combining available measured and systematics data with results of model calculations with optimized parameters.

The progress in the accuracy of gas production cross-sections calculations at intermediate and high energies of primary particles is primarily associated with the constant development and improvement of computational methods implemented in MARS15 [72], CEM03 [77], Geant4 [78], FLUKA [73] , INCL4 [79], and CASCADE [69,80] codes. At incident nucleon energies below 100-200 MeV an important role plays the development of models implemented in TALYS [81,82] and EMPIRE [83] codes. Illustrations of the difference in gas production cross sections calculated using different models can be found in Ref.[70].

The use of evaluated H- and He-isotopes production cross-sections is the most flexible and reliable way to get gas production rates under irradiation. As a rule, the cross-section evaluation procedure comprises an analysis

of measurements, calculations using nuclear models relevant for specific energy ranges, and the proper statistical combination of theoretical and experimental data, taking into account calculated and experimental uncertainties.

Recently, proton-, deuteron-, triton-, $^3$He-, and $^4$He-production cross-sections for neutron and proton induced reactions were evaluated for Al, Cr, Fe, Ni, W [75], and Ti [84] at incident energies from $10^{-5}$ eV to 3 GeV.

Even if no experimental data are available for the investigated target, the calculated H and He-isotope production cross sections can be corrected using "reference data for gas production cross-sections" obtained in Ref.[85]. The data [85] concern information on proton, deuteron, triton, $^3$He, and $^4$He production cross-sections for 278 stable target nuclei from Li to B at fixed incident proton energies 62, 90, 150, 600, 800, and 1200 MeV. To obtain such data [85], the atomic mass dependence of corresponding cross sections was evaluated using available experimental data and results of calculations using different nuclear models, in contrast to the usual evaluation of the energy dependence of cross sections for investigated reactions.

## CONCLUSION

The methods for the calculation of the number of stable defects, $N_D$ in irradiated materials, the NRT model, the BCA model, the simulations using MD, and KMC are briefly discussed. In most cases, the calculation of radiation damage rate in materials requires the information on $N_D$ values at the energies outside MD simulations. The use of combined BCA-MD method for the estimation of $N_D$ at such energies is promising.

Various approaches including the use of evaluated data files for reliable assessment of radiation damage and gas production rates are discussed.

## REFERENCES

[1] M.J. Norgett, M.T. Robinson, I.M. Torrens, Nucl. Eng. Des. 33, 50 (1975).
[2] K. Nordlund, A. Meinander, F.Granberg et al. *Primary Radiation Damage in Materials*, OECD-NEA-WPMM PRD (2013).
[3] M.T. Robinson, J. Nucl. Mater. 216, 1 (1994).
[4] NJOY 99, Nuclear Data Processing System, http://t2.lanl.gov/codes/njoy99/index.html
[5] LAHET 2.8, RSICC CCC-810 (2000).
[6] MCNP6.1, RSICC CCC-810 (2013).
[7] A.Yu. Konobeyev, Yu.V. Konobeev, Yu.A. Korovin, J. Nucl. Sci. Technol. Suppl. 2, 1236 (2002).
[8] C.H.M. Broeders, A.Yu. Konobeyev, J. Nucl. Mater. 328, 197 (2004).
[9] A.Yu. Konobeyev, U. Fischer, "What We Can Improve in the Calculation of Displacement Cross-Sections", INDC(NDS)-0624, (Vienna, 2012) p.24.
[10] J.F. Ziegler, M.D. Ziegler, J.P. Biersack, Nucl. Instr. Meth. Phys. Res. B268, 1818 (2010); http://www.srim.org/
[11] R.E. Stoller, M.B. Toloczko, G.S. Was et al, Nucl. Instr. Meth. Phys. Res. B310, 75 (2013).
[12] A. Almazouzi, M.J. Caturla, M. Alurralde et al, Nucl. Instr. Meth. Phys. Res. B153, 105 (1999).
[13] D.J. Bacon, F. Gao, Yu.N. Osetsky, J. Nucl. Mater. 276, 1 (2000).
[14] K. Nordlund, M. Ghaly, R.S. Averback et al Phys. Rev. B57, 7556 (1998).
[15] C. Björkas, K. Nordlund, S. Dudarev, Nucl. Instr. Meth. Phys. Res. B267, 3204 (2009).
[16] E. Alonso, M.-J. Caturla, T. Diaz de la Rubia, J.M Perlado, J. Nucl. Mater. 276, 221 (2000).
[17] K. Morishita, T. Diaz de la Rubia, J. Nucl. Mater. 271&272, 35 (1999).
[18] R.E: Stoller, J. Nucl. Mater. 276, 22 (2000).
[19] R.E. Stoller, "Primary Radiation Damage Formation," In: Comprehensive Nuclear Materials, Ed: R.J.M. Konings, (Elsevier 2012), v.1, p.293.
[20] L.Malerba, J. Nucl. Mater. 351, 28 (2006).
[21] L. Malerba, M.C. Marinica, N. Anento et al, J. Nucl. Mater. 406, 19 (2010).
[22] K. Vörtler, C. Björkas, D. Terentyev, L. Malerba, K. Nordlund, J. Nucl. Mater. 382, 24 (2008).
[23] M.J. Aliaga, A. Prokhodtseva, R. Schaeublin, M.J. Caturla, J. Nucl. Mater. 452, 453 (2014).
[24] D. Terentyev, C. Lagerstedt, P. Olsson et al, Nucl. Mater. 351, 65 (2006).
[25] Ch. Wang, W. Zhang, C. Ren, P. Huai, Zh. Zhu, Nucl. Instr. Meth. Phys. Res. B321, 49 (2014).
[26] A. Almazouzi, M.J. Caturla, T. Diaz de la Rubia, M. Victoria, EPFL Supercomputing Rewiev, No. 10., Fed. Inst. Technol., 1998, p.10 (cited by Ref.[14]).
[27] Z. Yao, M.J. Caturla, R. Schäublin, J. Nucl. Mater. 367-370, 298 (2007).
[28] M.J. Caturla, T. D. de la Rubia, M. Victoria et al, J. Nucl. Mater. 296, 90 (2001).
[29] J R.E. Voskoboinikov, Yu.N. Osetsky, D.J. Bacon, J. Nucl. Mater. 377, 385 (2008).
[30] R.E. Voskoboinikov, Yu.N. Osetsky, D.J. Bacon, Nucl. Instr. Meth. Phys. Res. B242, 68 (2006).
[31] D.J. Bacon, Yu.N. Osetsky, Mater. Sci. Eng. A365, 46 (2004).
[32] D.J Bacon, Yu.N Osetsky, R Stoller, R.E Voskoboinikov, J. Nucl. Mater. 323, 152 (2003).
[33] Yu.N. Osetsky, D.J. Bacon, B.N. Singh, J. Nucl. Mater. 307-311, 866 (2002).
[34] S. Di, Zh. Yao, M.R. Daymond, F. Gao, Nucl. Instr. Meth. Phys. Res. B303, 95 (2013).
[35] F. Gao, D.J. Bacon, L.M. Howe, C.B. So, J. Nucl. Mater. 294, 288 (2001).
[36] A.P. Selby, D. Xu, N. Juslin et al, N.A. Capps, B.D. Wirth, J. Nucl. Mater. 437, 19 (2013).
[37] T. Troev, N. Nankov, T. Yoshiie, Nucl. Instr. Meth. Phys. Res. B269, 566 (2011).
[38] J. Fikar, R. Schaeublin, Nucl. Instr. Meth. Phys. Res. B255, 27 (2007).
[39] D.A. Terentyev, L. Malerba, R. Chakarova et al, J. Nucl. Mater. 349, 119 (2006).

[40] J.-H. Shim, H.-J. Lee, B.D. Wirth, J. Nucl. Mater. 351, 56 (2006).

[41] A. Meinander, K.O.E. Henriksson, C. Björkas et al, J. Nucl. Mater. 442 (2013) S782.

[42] H.F. Deng, D.J. Bacon, Phys. Rev. B53, 11376 (1996).

[43] X.-F. Tian, H.-X. Xiao, R. Tang, Ch.-H. Lu, Nucl. Instr. Meth. Phys. Res. B321, 24 (2014).

[44] V.A. Borodin, Nucl. Instr. Meth. Phys. Res. B282, 33 (2012).

[45] J. Nord, K. Nordlund, J. Keinonen, Phys. Rev. B68, 184104 (2003).

[46] F. Gao, W.J. Weber, Phys. Rev. 66, 024106 (2002).

[47] F. Gao, W.J. Weber, Phys. Rev. 63, 054101 (2000).

[48] K.O.E. Henriksson, K. Nordlund, Nucl. Instr. Meth. Phys. Res. B277, 136 (2012).

[49] P. Träskelin, C. Björkas, N. Juslin et al, Nucl. Instr. Meth. Phys. Res. B257, 614 (2007).

[50] B.P. Uberuaga, R. Smith, A.R. Cleave et al, Phys. Rev. B71, 104102 (2005).

[51] G. Martin, P. Garcia, L. Van Brutzel et al, Nucl. Instr. Meth. Phys. Res. B269, 1727 (2011).

[52] D. Bacorisen, R. Smith, B.P. Uberuaga et al, Phys. Rev. B74, 214105 (2006).

[53] L. Veiller, J.-P. Crocombette, D. Ghaleb, J. Nucl. Mater. 306, 61 (2002).

[54] C.P. Race, D.R. Mason, M.W. Finnis et al, Rep. Prog. Phys. 73, 116501 (2010).

[55] S.J. Zinkle, C. Kinoshita, J. Nucl. Mater. 251, 200 (1997).

[56] S.J. Zinkle, B.N. Singh, J. Nucl. Mater. 199, 173 (1993).

[57] G.A. Greene, C.L. Snead Jr., C.C. Finfrock, A.L. Hanson, M.R. James, W.F. Sommer, E.J. Pitcher, L.S. Waters, *Int. Meet. Nucl. Appl. Acce l. Techn. (AccApp'03)*, San Diego, June 1-5, 2003, American Nuclear Society, La Grande Park, p. 881, (2004).

[58] A. Dunlop, D. Lesueur, P. Legrand, H. Dammak, J. Dural, Nucl. Instr. Meth. Phys. Res. B90, 330 (1994).

[59] K. Nordlund, "Modified NRT Equations for Damage and Mixing Developed by the OECD NEA Primary Damage Group", INDC(NDS)-0624, (Vienna, 2012) p. 18.

[60] A.Yu. Konobeyev, C.H.M. Broeders, U. Fischer, *Int. Meet. Nucl. Appl. Accel. Technol. (AccApp' 07),* Pocatello, July 30 - August 2, 2007, p.241 (2007).

[61] A.Yu. Konobeyev, U. Fischer, L. Zanini, *Int. Meet. Nucl. Appl. Accel. Technol. (AccApp'11),* Knoxville, April 3-7, 2011 (2011).

[62] C.H.M. Broeders, A.Yu. Konobeyev, K. Voukelatou, "IOTA - a Code to Study Ion Transport and Radiation Damage in Composite Materials, FZKA 6984 (2004)"; http://bibliothek.fzk.de/zb/berichte/FZKA6984.pdf

[63] C.H.M. Broeders, A.Yu. Konobeyev, J. Nucl. Mater. 336, 201 (2005).

[64] C.H.M. Broeders, A.Yu. Konobeyev, C. Villagrasa, J. Nucl. Mater. 342, 68 (2005).

[65] C.S. Becquart, B:D. Wirth, "Kinetic Monte Carlo Simulations of Irradiation Effects", In: Comprehensive Nuclear Materials, Ed: R.J.M. Konings, (Elsevier 2012), v.1, p.393.

[66] H.Xu, R.E. Stoller, Y.N. Osetsky, J. Nucl. Mater. 443, 66 (2013).

[67] T. Suzudo, S.I. Golubov, R.E. Stoller et al, J. Nucl. Mater. 423, 40 (2012).

[68] V.A. Pechenkin, private communication (2013).

[69] V.S. Barashenkov, Comp. Phys. Comm. 126, 28 (2000).

[70] A.Yu. Konobeyev, U. Fischer, "Evaluation of displacement and gas production cross-sections for structure materials using advanced simulation methods and experimental data", INDC(NDS)-0648, (Vienna, 2013) p.22.

[71] A.Yu. Konobeyev, U. Fischer, A.J. Koning et al, J. Korean Phys. Soc. 59, 927 (2011).

[72] N.V. Mokhov, "Recent MARS15 Developments: Nuclide Inventory, DPA and Gas Production", *46th ICFA Adv. Be am Dyn. Wor ksh. High-Intensity and High-Brightness Hadron Beams (HB2010),* Sep 27 - Oct 1 2010. Morschach, Switzerland.

[73] A. Fasso, A. Ferrari, J. Ranft, P. Sala; http://www.fluka.org

[74] Y. Iwamoto, K. Niita, T. Sawai et al, Nucl. Instr. Meth. Phys. Res. B274, 57 (2012).

[75] A.Yu. Konobeyev, U. Fischer, DXS Files; https://www-nds.iaea.org/various1.htm

[76] A.Yu. Konobeyev, U. Fischer, A.J. Koning et al, J. Korean Phys. Soc. 59, 935 (2011).

[77] S.G. Mashnik, L.M. Kerby, Nucl. Instr. Meth. Phys. Res. A764, 59 (2014).

[78] J. Allison, K. Amako, J. Apostolakis et al, EEE Transactions on Nuclear Science, 53, 270 (2006); M. Kelsey, V. Ivantchenko, M. Verderi et al, "Geant4"; http://geant4.web.cern.ch

[79] S. Leray, A. Boudard, B. Braunn et al, Nucl. Data Sheets, 118, 312 (2014).

[80] A.Yu. Konobeyev, U. Fischer, P.E. Pereslavtsev, D. Ene, Nucl. Data Sheets, 118, 112 (2014).

[81] A.J. Koning, S. Hilaire, M.C. Duijvestijn, "TALYS", *Int. Conf. Nuclear Data for Science and Technology*, April 22-27, 2007, Nice, EDP Sciences, 2008, p. 211; http:// www.talys.eu

[82] A.Yu. Konobeyev, U. Fischer, A.J. Koning, et al, J. Korean Phys. Soc. 59, 935 (2011).

[83] M. Herman, R. Capote, M. Sin et al, "EMPIRE-3.2. (Malta). Nuclear Reaction Model Code http://www.nndc.bnl.gov/empire

[84] S. Akca, A.Yu. Konobeyev, U.Fischer, "Evaluated gas production cross-section data for natural titanium irradiated with protons at energies up to 3 GeV", 2014, to be published.

[85] A.Yu. Konobeyev, U. Fischer, "Reference Data for Evaluation of Gas Production Cross-Sections in Proton Induced Reactions at Intermediate Energies", KIT Report 7660, 2014; http://digbib.ubka.uni-karlsruhe.de/volltexte/1000038463

# NOVEL MATERIALS FOR COLLIMATORS AT LHC AND ITS UPGRADES*

A. Bertarelli[#], A. Dallocchio, M. Garlasché, L. Gentini, P. Gradassi, M. Guinchard, S. Redaelli, A. Rossi, O. Sacristan de Frutos, CERN, Geneva, Switzerland
F. Carra, CERN, Geneva, Switzerland; Politecnico di Torino, Turin, Italy
E. Quaranta, CERN, Geneva, Switzerland; Politecnico di Milano, Milan, Italy

## Abstract

Collimators for last-generation particle accelerators like the LHC, must be designed to withstand the close interaction with intense and energetic particle beams, safely operating over an extended range of temperatures in harsh environments, while minimizing the perturbing effects, such as instabilities induced by RF impedance, on the circulating beam. The choice of materials for collimator active components is of paramount importance to meet these requirements, which are to become even more demanding with the increase of machine performances expected in future upgrades, such as the High Luminosity LHC (HL-LHC). Consequently, a far-reaching R&D program has been launched to develop novel materials with excellent thermal shock resistance and high thermal and electrical conductivity, replacing or complementing materials used for present collimators. Molybdenum Carbide - Graphite and Copper-Diamond composites have been so far identified as the most promising materials. The manufacturing methods, properties and application potential of these composites will be reviewed along with the experimental program which is to test their viability when exposed to high intensity particle beams.

## INTRODUCTION

The introduction in recent years of new, extremely energetic particle accelerators such as the Large Hadron Collider (LHC) [1] brought about the need for advanced cleaning and protection systems, such as collimators, in order to safely increase the energy and intensity of particle beams to unprecedented levels. LHC collimators must adopt materials able to withstand the extreme conditions (temperatures, pressures and densities) induced by the accidental impact of particle beam pulses; on top of outstanding thermal shock resistance, these materials are typically required a number of additional relevant properties, such as high electrical conductivity, geometrical stability and resistance to radiation damage. These requirements are set to become even more compelling in consideration of the High-Luminosity upgrade of the LHC (HL-LHC) [2], expected to increase by a factor of two beam intensity and energy: Carbon-

Carbon (C-C) composites used for primary and secondary collimators may limit the accelerator performance as a result of the high impedance induced by C-C low electrical conductivity, while the Tungsten alloy (Inermet180) used in tertiary collimators has very low robustness in case of beam impacts.

To face these challenges, an intense R&D program has been launched at CERN in recent years to explore or develop a palette of novel materials which are to combine the excellent properties of graphite or diamond, specifically their low density, high thermal conductivity, low thermal expansion, with those of metals and transition metal-based ceramics possessing high mechanical strength and good electrical conductivity. This article presents the most promising materials identified so far, namely Molybdenum Carbide - Graphite (MoGr) and Copper-Diamond (CuCD).

## MOLYBDENUM CARBIDE - GRAPHITE

Pure molybdenum possesses very high melting point, low Coefficient of Thermal Expansion (CTE) and excellent mechanical strength and electrical conductivity, while graphitic materials feature low density, extremely high service temperature, large damping properties (particularly useful in attenuating shock waves) and, if graphite crystallite ordering is sufficiently extended (high graphitization degree), excellent thermal conductivity and very low CTE, at least in the direction aligned with graphite basal plane. At high temperatures, molybdenum rapidly reacts with carbon, forming stable carbides ($MoC_{1-x}$) which, in spite of their ceramic nataure, retain a good electrical conductivity; in this respect, MoGr is therefore a ceramic-matrix composite. Several MoGr grades, in the frame of a collaboration between CERN and italian SME BrevettiBizz, were investigated, with processing temperatures ranging from 1700º C to 2600º C [3].

A broad range of compositions, powder types and dimensions were tested: the best results so far were obtained for a sintering temperature of 2600º C. The C-phase can be composed of natural graphite flakes or by a mixture of natural graphite and mesophase pitch-based carbon fibres (Fig. 1).
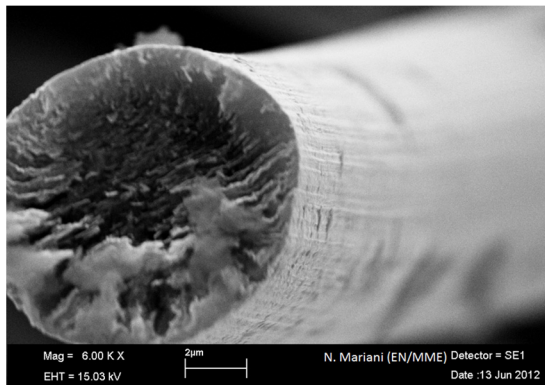
Figure 1: Micrograph of a pitch-derived carbon fiber.

The material is produced by Liquid-Phase Sintering (LPS) at a temperature above the melting point of molybdenum carbide (2589° C); the final result is a very homogeneous structure with a regular distribution of carbide particles and a high degree of graphitization of the carbonaceous phase.

To favour liquid carbide infiltration and material compaction rate, a significant quantity of molten carbides is allowed to flow out of the moulds during LPS, so that the final density of the material is reduced to ~2.5 g cm$^{-3}$; thanks to the extensive graphitization process occurring during high temperature sintering, very likely catalysed by the carbide liquid phase, MoGr possesses in the preferential direction, an electrical conductivity of ~1 MSm$^{-1}$, one order of magnitude higher than the Carbon-Carbon composite used in Phase I collimator. This property can be further increased up to 18 MSm$^{-1}$ by cladding or coating the external surface with pure molybdenum; excellent adhesion was obtained between Mo layer and bulk material thanks to the formation of a homogeneous carbide interface (Fig. 2).

Electromagnetic simulations were performed to evaluate the effects on beam impedance when, on a LHC secondary collimator jaw, C-C is replaced with Mo-coated MoGr. The results showed a reduction by a factor of 10 in the collimator impedance for frequencies over 10 MHz [4] (Fig. 3).
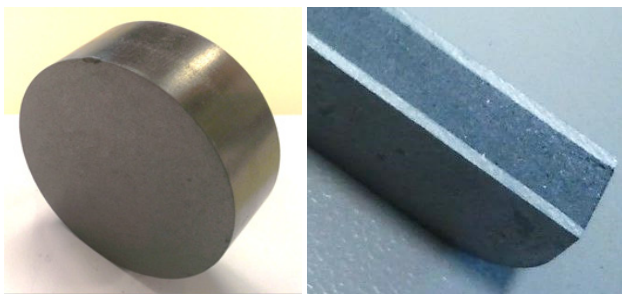


Figure 2: MoGr sintered plate, H=25mm and D=90mm (left); Mo-coated MoGr specimen (right).

On top of low density and good electrical conductivity, MoGr presents outstanding thermal properties: the thermal conductivity at room temperature (RT) is ~770 Wm$^{-1}$K$^{-1}$ (Fig. 4), almost twice that of pure copper while

CTE in the preferential plane is 1.8x10$^{-6}$ K$^{-1}$ for temperatures spanning from RT to 2000 °C.
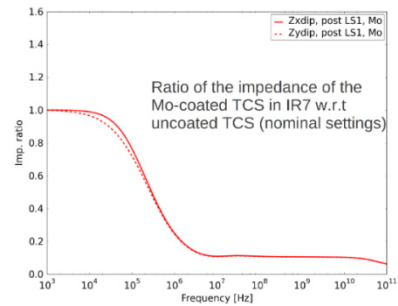


Figure 3: Collimator beam impedance: ratio of a Mo-coated MoGr to a C-C jaw.

Relevant reference properties of MoGr are provided in Table 1.
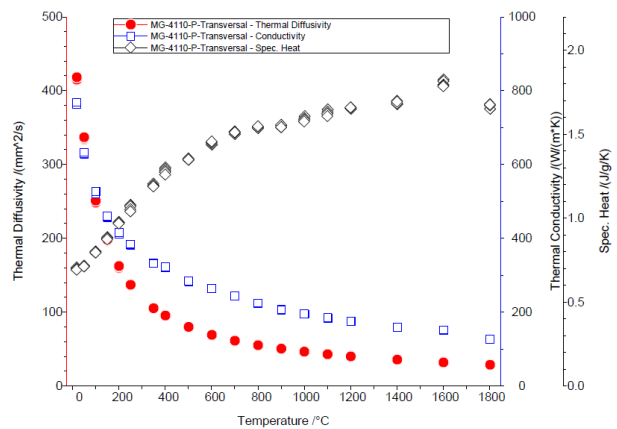


Figure 4: Thermal conductivity, diffusivity and specific heat of MoGr between RT and 1800º C.

Table 1: MoGr Properties

| | |
|---|---|
| Density $\rho$ | 2.5 g/cm$^3$ |
| CTE $\alpha_\perp$ (RT to 1000° C) | 1.8x10$^{-6}$ K$^{-1}$ |
| CTE $\alpha_{//}$ (RT to 1000° C) | 12x10$^{-6}$ K$^{-1}$ |
| Thermal conductivity $\lambda_\perp$ (RT) | 770 Wm$^{-1}$K$^{-1}$ |
| Thermal conductivity $\lambda_{//}$ (RT) | 85 Wm$^{-1}$K$^{-1}$ |
| Electrical conductivity $\sigma_\perp$ (RT) | 1÷18 MSm$^{-1}$ |
| Electrical conductivity $\sigma_{//}$ (RT) | 0.3 MSm$^{-1}$ |
| Young's Modulus $E$ (Flexural) | 53 GPa |
| Ultimate Strength $R_m$ (Flexural) | 85 MPa |

## COPPER-DIAMOND

Copper-Diamon is produced by RHP Technology (Austria) by Solid-State Sintering; the initial volumetric composition is 60% diamond, 39% copper and 1% boron. A higher content in diamond would not allow a good material compaction, which is also pursued by making

use of diamonds of various sizes, in order to optimize the filling of the interstitials. Unlike MoGr, the main issue for the material adhesion is the low chemical affinity between the two main elements, which leads to a lack of bonding between copper and diamond: this would jeopardize not only mechanical strength, but also thermal conductivity. Boron is added to offset such limitation, since this element promotes the formation of carbides at the diamond/copper interface, improving material internal bonding (Fig. 5).
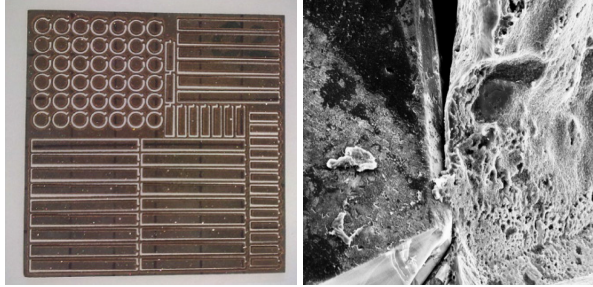


Figure 5: CuCD specimens (left); micrograph of CuCD fracture surface: note small B carbide platelet bridging diamond grain to Cu matrix (right).

CuCD possesses very good thermal and electrical conductivity (Table 2). However, density and CTE are higher than MoGr, and the industrialization of the material is difficult: while thin samples of constant section can be produced via water-jet cutting (Fig. 6), more complicated shapes with precise tolerances are extremely difficult and expensive to machine.



Figure 6: CuCD samples after water-jet cutting; marks in the water flow direction and porosity are clearly visible.

Table 2: CuCD Properties

| | |
|---|---|
| Density $\rho$ | 5.4 g/cm$^3$ |
| CTE $\alpha$ (RT to 900° C) | $6 \div 12 \times 10^{-6}$ K$^{-1}$ |
| Thermal Conductivity $\lambda$ (RT) | 490 Wm$^{-1}$K$^{-1}$ |
| Electrical Conductivity $\gamma$ (RT) | 12.6 MSm$^{-1}$ |
| Young's Modulus $E$ (Flexural) | 220 GPa |
| Ultimate Strength $R_m$ (Flexural) | 70 MPa |

## FIGURES OF MERIT

In order to classify and rank potential materials against the large number of requirements which are defined for beam interacting devices in general and collimators in particular, Figures of Merit (FoMs) were proposed in the past [5, 6]. In this paper, we partly redefine FoMs on the basis of the experience gathered in the last years, exploiting the data acquired during two characterization campaigns launched in 2012 at CERN HiRadMat facility [7, 8]. The new indexes rely on constant, uniform material properties at an arbitrary reference temperature; for anisotropic materials, relevant properties are averaged over the 3 directions. The most relevant figures of merit are:

- Thermomechanical Robustness
- Thermal Stability
- Electrical Conductivity
- Radiation Resistance

### Thermomechanical Robustness

An index, called Thermomechanical Robustness Index (TRI), is proposed to evaluate the material robustness against particle beam impacts. This index is based on the ratio between material admissible strain and actual strain: in fact, thermal shock problems are to a large extent governed by the thermal deformation induced by a sudden temperature change.

$$TRI = \frac{\varepsilon_{adm}}{\varepsilon_{ref}} \cdot \left(\frac{T_m}{\Delta T_q} - 1\right)^m \qquad (1)$$

$\varepsilon_{adm}$ and $\varepsilon_{ref}$ are respectively the admissible strain and the actual strain induced by a reference beam impact; $T_m$ is the melting (or degradation) temperature; $\Delta T_q$ is the temperature increase generated by the reference energy deposition; $m$ is a coefficient related to the material loss of strength with temperature increase. These quantities are expressed by Equations (2), (3) and (4).

$$\varepsilon_{Adm} = \frac{R_M}{\overline{E} \cdot (1 - \nu)} \qquad (2)$$

$$\varepsilon_{ref} = \overline{\alpha} \cdot \Delta T_q \qquad (3)$$

$$\Delta T_q = \frac{C_R \rho^n}{c_p X_g} \qquad (4)$$

$\overline{E}$ is the (averaged) Young's modulus, $\nu$ the Poisson's ratio, $\overline{\alpha}$ the (averaged) CTE, $c_p$ the specific heat, $X_g$ the geometric radiation length, $C_R$ an arbitrary scaling factor and $n$ a constant related to the energy distribution generated by the impact.

Equation (4) implies that the energy deposited by a given number of particles, and therefore the material temperature increase, is related to the material density and to the geometric radiation length; we have empirically observed that the coefficient $n$ for materials impacted by protons at several hundreds GeV is ~0.2.

Combining (1), (2), (3) and (4), the TRI can be written as:

$$TRI = \frac{R_M c_p X_g}{\overline{E}(1 - \nu)\overline{\alpha} C_R \rho^n} \cdot \left(\frac{T_m c_p X_g}{C_R \rho^n} - 1\right)^m \qquad (5)$$

### Thermal Stability

The Thermal Stability Index (TSI) provides an indication of the ability of the material to maintain the

geometrical stability of the component under steady-state particle losses. It is related to the inverse of the curvature of an elongated structure induced by a non-uniform temperature distribution, and is calculated with Equation (6). Here $\bar{\lambda}$ is the (averaged) thermal conductivity and $C_S$ a scaling factor.

$$TSI = \frac{\bar{\lambda} X_g}{\bar{\alpha} C_S \rho^n} \qquad (6)$$

### Electrical Conductivity

Since collimators are the accelerator devices sitting closest to the circulating beam, their contribution to the machine global impedance is by far the highest. The part of the beam coupling impedance related to the resistive losses in the material surrounding the beam, the so-called resistive wall impedance, is directly related to the material electrical resistivity. Therefore maximizing the electrical conductivity of the jaw materials can play a major role in minimizing the risk of impedance-induced beam instabilities.

### Radiation Resistance

Irradiation of materials by energetic particles causes microstructural defects which translate into a degradation of the thermo-physical properties. Radiation resistance is defined as the ability of the material to maintain its properties under and after irradiation. Several tests are being performed in various facilities (GSI, Kurchatov Institute, BNL) in order to evaluate the radiation resistance of the materials of interest at energies up to 1.14 GeV. First results for MoGr and CuCD should soon become available.

A summary of the first 3 FoMs for MoGr and CuCD compared to those of present collimator materials is provided in Table 3. As it can be seen, while C-C is penalized by its limited electrical conductivity in spite of its outstanding TRI, MoGr shows the best compromise as far as these 3 indexes are concerned.

Table 3: Relevant Figures of Merits for A Selection of Present and Future Collimator Materials

|          | C-C    | Inermet180 | MoGr    | CuCD   |
|----------|--------|------------|---------|--------|
| TRI [-]  | 1237   | 0.5        | 634     | 6.8    |
| TSI [-]  | 44.6   | 0.1        | 69.4    | 9.9    |
| γ [MS/m] | ~0.14  | 8.6        | ~1÷18   | ~12.6  |

## HIRADMAT EXPERIMENTS

After the first experiments performed at HiRadMat facility in 2012, CuCD and MoGr emerged as the materials which better survived the impact of $1.95 \times 10^{13}$ protons at 450 GeV. The design of a new secondary collimator for the HL-LHC upgrade (TCSPM) has therefore been based on these two novel materials [9].

The proposed modular design allows to house in the collimator jaw both CuCD and MoGr inserts; for manufacturing reasons, the 1 m-long active jaw is divided in 10 separate composite blocks (Fig. 7).

The jaw assembly is clamped, to guarantee the contact force required for an effective cooling while assuring the possibility of differential sliding between components with mismatching CTE (Fig. 8).
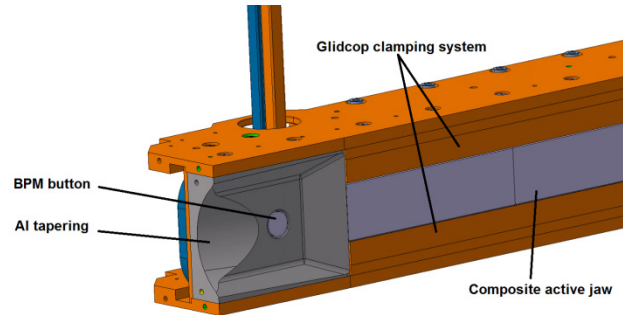


Figure 7: HL-LHC secondary collimator (TCSPM), 3D view of the jaw extremity.
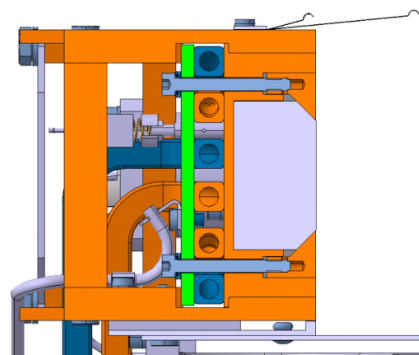


Figure 8: Jaw cross-section, view of the clamping system.

In order to test the collimator resistance against particle beam impacts at HL-LHC intensities and to select the best material for a prototype to be successively installed in the LHC, a new experiment in the HiRadMat facility is planned for late spring 2015. The experiment, named HRMT23, will consist of a stainless steel vacuum tank hosting three independent collimator jaws sharing the same supporting system (Fig. 9).
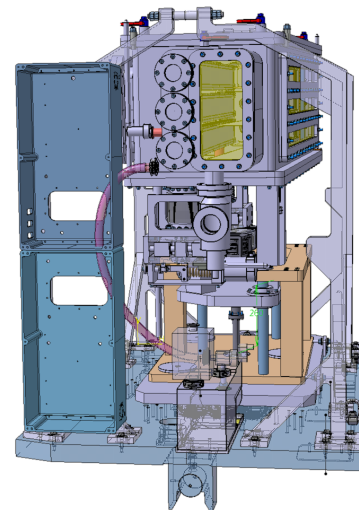


Figure 9: HRMT23 test bench.

The jaws to be tested are two TCSPM, with MoGr and CuCD inserts respectively, and a TCSP. Each jaw will be independently impacted by a number of particle pulses with increasing intensities up to the maximum available at the time of the experiment, the design case being that of HL-LHC beam injection error scenario ($6.4 \times 10^{13}$ protons). Simulations are being performed to evaluate the response of the different jaws to this impact scenario (Figs. 10-11).
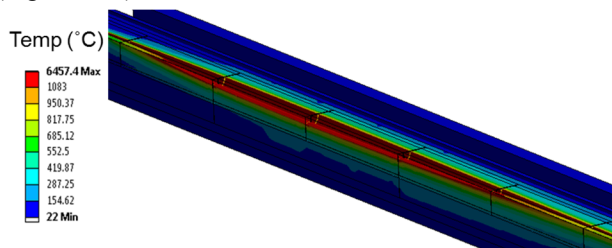


Figure 10: CuCD jaw impacted by $6.4 \times 10^{13}$ protons, temperature distribution. The red region is above melting point.
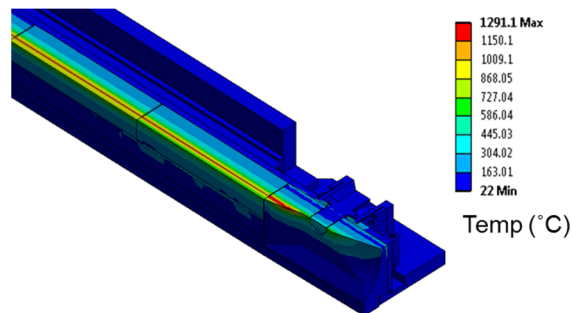


Figure 11: MoGr jaw impacted by $6.4 \times 10^{13}$ protons, temperature distribution. The temperature peak is on the Glidcop tapering. No melting of MoGr inserts is expected.

The experiment instrumentation will allow to characterize in real time the component response during the impact and will likely include resistive strain gauges, temperature, displacement and vacuum probes, microphones and water pressure sensors. The most delicate instruments, such as high-speed camera and laser-Doppler vibrometer, will be positioned in a radiation-protected bunker in the tunnel TT40, parallel to the HiRadMat beam line.

## CONCLUSIONS

In the frame of the future High Luminosity upgrade of the LHC, a novel class of materials combining carbon allotropes, graphite or diamond, with metals or transition metal-based ceramics has been investigated at CERN and collaborating institutes and industries in recent years. Amongst the several materials which were studied, the most interesting results have been reached with Molybdenum Carbide – Graphite (MoGr) and Copper-Diamond (CuCD). The former is obtained by rapid hot pressing up to temperature of 2600° C in the presence of a liquid phase. The high temperature reaction between

molybdenum and graphite promotes the complete transformation of molybdenum in refractory $MoC_{1-x}$ while liquid carbides catalyse and enhance carbon re-ordering and graphitization; mesophase pitch-derived carbon fibres can also be added to further increase graphitization and mechanical strength. This leads to outstanding thermo-physical properties, with thermal conductivity in the vicinity of 800 $Wm^{-1}K^{-1}$ and CTE in the range of $1 \div 2$ x $10^{-6}$ $K^{-1}$.

CuCD, obtained by solid-state hot pressing, is particularly attractive for its high electrical conductivity, although the limited melting point somehow limits its robustness against high energy beam impacts.

A new set of figures of merit has been proposed, on the basis of the experience gathered with recent HiRadMat experiments, to compare and rank materials for beam interacting devices in general and collimators in particular.

A new experiment allowing to test under direct beam impact three independent collimator jaws is planned at CERN HiRadMat facility for late spring 2015; two of these jaws, based on a new design for the future HL-LHC Collimators, make use of MoGr and CuCD. The experiment is also aimed at validating material and design for a full-scale HL-LHC prototype to be later installed in the LHC for machine development tests.

## REFERENCES

[1] The LHC Design Report, http://ab-div.web.cern.ch/ab-div/Publications/LHC-DesignReport.html, July 2004.

[2] HL-LHC: High Luminosity Large Hadron Collider, http://hilumilhc.web.cern.ch/HiLumiLHC/index.html

[3] A. Bertarelli, F. Carra, N. Mariani, S. Bizzaro, "Development and testing of novel advanced materials with very high thermal shock resistance", Tungsten, Refractory and Hardmetals Conference, Orlando, May 2014.

[4] N. Mounet, "Collimator impedance", presented at the LHC collimation review, CERN, Geneva, May 2013. https://indico.cern.ch/event/251588/

[5] A. Dallocchio, A. Bertarelli, G. Arnau, K. Artoos, "Advanced materials for future Phase II collimators", PAC09, Vancouver, 2009.

[6] A. Bertarelli et al., "Research and development of novel advanced materials for next-generation collimators", IPAC2011, San Sebastián, 2011.

[7] M. Cauchi et al., "High energy beam impact tests on a LHC tertiary collimator at the CERN high-radiation to materials facility", Phys. Rev. ST Accel. Beams 17, 021004.

[8] A. Bertarelli et al., "An experiment to test advanced materials impacted by intense proton pulses at CERN HiRadMat facility", Nuclear Instruments and Methods in Physics Research B 308 (2013) 88–99.

[9] F. Carra et al., "Mechanical engineering and design of novel collimators for HL-LHC", IPAC2014, Dresden, June 2014.

# WG-A SUMMARY

J. Holmes, SNS, U.S.A.
Y-H. Chin, KEK, Tsukuba, Japan
S. Machida, STFC RAL, Didcot, U.K.

*Abstract*

WG-A took three main themes this year, short term beam loss, instability and space charge and long term beam loss. In the following, three conveners will summarise each theme.

## BACKGROUND

At this workshop, working groups were asked to consider the following general questions:

- Is it possible to understand the beam losses in detail and to predict them?
- What really has to be provided by simulation and diagnostics to make this possible?
- What seems actually feasible/has been delivered?
- If a detailed understanding of losses would be possible, how would it affect operation/tuning/hardware improvements?
- How important is a detailed understanding for decreasing/limiting the beam losses?

Working Group A was tasked with the topics of Beam Dynamics in Rings. We broke the discussion for rings down into three specific areas:

- Short-tem beam loss – Beam loss in short cycling rings.
- Instability and space charge.
- Long-term beam loss – Beam loss in long cycling rings.

Our consideration of the general questions led us to pose specific questions for each of the three areas:

*Beam loss in fast cycling rings*

- Are single particle resonances important? If so, to what order do these need to be taken into account?
- Is the beam loss due to coherent (excluding instability) or incoherent phenomena?
- What techniques can be used to mitigate beam loss mechanisms that are independent of intensity? How will such losses be detected?

*Instability and space charge*

- Do we have a reasonable model of instability including space charge effects? What are the concerns – Emittance growth? Beam loss? Other?
- Can we separate pure space charge problems from impedance related instabilities (incl. electron clouds) in observation?
- How important is it to include space charge effects when we design mitigation methods?

*Beam loss in long cycling rings*

- Can we define dynamic aperture concept with space charge? Is it a right way to understand long-term beam loss?
- Is it possible to identify the source of beam loss; instability with slow growth rate or resonance coupled with space charge?
- To what energy range must we consider direct space charge effects?

## BEAM LOSS IN SHORT CYCLING RINGS BY J. HOLMES

Presentations included:
- R. Macek, LANL, "Understanding Beam Losses in High Intensity Proton Accumulator Rings".
- K. Seiya, FNAL, "The Status of the Proton Improvement Plan (PIP) at Fermilab Booster".
- C. Warsop, RAL, "High Intensity Loss Mechanisms on the ISI Rapid Cycling Synchrotron".

Presentations included from other sessions that had a direct bearing on this topic included:
- H. Hotchi, JAEA/J-PARC, "Lessons from 1 MW Proton RCS Beam Tuning", Plenary session.
- I. Hofmann, GSI, "Grid Noise and Entropy Growth in PIC Codes", WG-B with A/C.
- M. Blaskiewicz, BNL, "Instabilities and Space Charge", WG-A – instabilities.
- V. Kornilov, GSI, "Instability Thresholds of the Head-Tail Modes in Bumches with Space Charge", WG-A– instabilities.
- S. Cousineau, ORNL, "Status of Preparations for a 10 us H-Laser-Assisted Stripping Experiment", WG-D.

*Response to questions*

Question 1: Are single particle resonances important? If so, to what order do these need to be taken into account?

Even in fast cycling rings, low order single particle resonances must be avoided. In addition to integer and half-integer resonances, low (certainly second, third, and fourth) order coupling resonances, and especially sum resonances, should be avoided in choosing operating scenarios. It is important to include the effect of space charge on the tune distribution in choice of operating point. In addition to avoiding low order resonances, correction of the driving terms may be important in certain situations.

Question 2:

Is the beam loss due to coherent (excluding instability) or incoherent phenomena?

Beam loss in rapid cycling rings can be caused both by coherent and incoherent phenomena. Coherent phenomena, such as space charge forces, must be incorporated when considering beam loss due to resonances, a traditionally incoherent process. However, for a well-tuned rapid cycling ring in which instabilities are avoided or mitigated, effects such as stripper foil scattering or collimation provide the dominant losses. Such losses, due to the interaction of beam with materials, are statistical and incoherent in nature. Other losses in rapid cycling rings involve beam capture and extraction. Such losses can also be regarded as incoherent, although for high intensity beams it may be necessary to include space charge effects in a quantitative description.

Question 3:
What techniques can be used to mitigate beam loss mechanisms that are independent of intensity? How will such losses be detected?

We assume that, in the statement of question 3, mechanisms that are independent of intensity means losses that vary linearly with intensity. We expect such losses to be caused incoherent processes, such as foil scattering or collimation. In the case of foil scattering, beam loss monitors show clearly the sections of the accelerator in which the losses occur, and radiation surveys during maintenance confirm the BLM readings. The best strategy for the minimization of beam loss due to foil stripping is choice of a painting scheme that minimizes foil hits by the circulation beam. Laser stripping is now under study as a long range alternative to beam stripper foils, but the practical use of this techniques is still likely to be decades away.

## Other Thoughts and Observations Regarding Beam Loss in Short Cycling Rings

These are issues that arose during the discussion.
- Injection foil scattering/excited $H^0$: PSR, SNS, ISIS, J-PARC RCS, CERN PSB
    - Understood theoretically and supported by simulations
    - Mitigate by painting to reduce foil hits
- Injected beam capture: FNAL Booster, ISIS, CERN PSB
    - Understood theoretically and supported by simulations
    - Chop beam (inject into bucket), improve RF
- Extraction: FNAL Booster
    - Lose 3 of 84 bunches
    - Cogging to create notch
- Half integer resonance: ISIS, PSR high intensity
    - Understood theoretically and supported by simulations: beam broadening
    - Mitigate by sufficient aperture
- Machine resonances: CERN PSB

    - Understood theoretically including space charge?
    - Mitigate by choice of working point, compensate with multipoles
- Collective instabilities: SNS, J-PARC RCS, ISIS
- ~Equal tune operating point: SNS, J-PARC, CERN PSB option
    - Montague resonance understood theoretically, complicated in practice
    - In SNS, we live with it
- Extraction kicker: SNS, J-PARC
    - Long bunches, coasting bunch not bad model
    - Landau damping from chromaticity, bunching fixes it in SNS
- Head-Tail: ISIS
    - Resistive wall, lack theoretical understanding
    - Correct with feedback damping
- Electron Cloud: PSR, SNS, …
    - Simplified theoretical models and simulations
    - Mitigation: coat beam pipe for low SEY, solenoids, maintain beam gap, bunch shaping

## INSTABILITY AND SPACE CHARGE   BY Y-H. CHIN

We have been given three questions to discuss on and answer during this session:

Question 1:
Do we have a reasonable model of instability including space charge effects?
What are the concerns - emittance growth? beam loss? other?

Simulation-wise, we have reasonably good models, but still more effects such as magnet non-linearities need to be included. Theory-wise, good progresses have been made, but still more works need to be done for reasonable predictions of instabilities under strong space-charge effects. The beam loss may be more concern than the emittance growth in many cases. Often, instabilities result in sudden large losses of particles and thus may cause intolerable activation of a machine. Unless you stop them immediately, possible emittance growth, another side effect of the instability, may not matter too much.

Question 2:
Can we separate purely space charge problem and impedance related instability  (incl. electron clouds) in observation?

If the question is about the resonance creation by the space charge effect in phase space and resulting emittance growth, the impedance related instabilities are generally fast acting (short term) effects, since they may cause sudden losses of large amount of particles. On the other hand, the space-charge related resonance effects are more slowly acting (long term) effects, such as slow growth of

emittance. In this regard, it may be possible to separate the two effects experimentally.

Question 3:
How important to include space charge effects when we design mitigation methods?

We can somehow expect some benefits from the space charge effect on instability mitigation, in particularly, in low energy rings (anyway, it is already there for free). But, it is hard to predict exactly how much. Setting (or keeping) a large chromaticity is a common way to suppress (or control) head-tail instabilities (e.g., RCS and MR) to some extent. But, it is too risky to give a full rely on them, and it may be better to prepare a transverse feed-back system for case that you suddenly find it indispensable for stable operation of a machine. You can also have a more knob to control beam behavior. In fact, the developments of intra-bunch feedback systems are under way in many rings such as LHC, SPS, PS, MR and others.

## Comments by the WG-A convener

At last, but not least, I would like to point out that I was very impressed by a variety of enthusiastic works by young scientists from Europe, US and Asia (China, mostly), in particular, at the last WG-A session on Thursday. Their topics include:

- Microwave instabilities
- Reactive impedance and synchrotron frequency
- Controlled RF noise
- E-p instability
- Emittance preservation
- Intra-bunch feedback system

The time allocated for each talk was modest (15min for each), but it gave them great opportunities to present their beam-dynamics oriented works to experts around the world and to exchange expertise. In my opinion, these beam-dynamic oriented works do not get a fair share of opportunities of oral presentations in large conferences such as IPAC. We should keep this tradition in future HB workshops.

## BEAM LOSS IN LONG CYCLING RINGS BY S. MACHIDA

Presentations included:
- S. Gilardoni, CERN, "Long term beam losses in the CERN injector chain".
- Y. Sato, KEK, "Recent commissioning of high intensity proton beams in J-Parc MR".
- G. Franchetti, GSI, "Plan of mitigation on long term beam loss problems at FAIR accelerators".
- E. Benedetto, CERN, "Transverse emittance preservation studies for the CERN PSB upgrade".

Contrary to fast cycling accelerators where intensity is not an issue and power is limited by more fundamental mechanism like foil scattering, we can see that long cycling

accelerators still have "conventional problems" although advances for the last decade is enormous and we have much better understanding and cures. We will list some examples of this "conventional problems" below.

- Injection matching: CERN PS, J-Parc MR
  - Vertical injection error is inevitable in CERN PS. It couples with image charge and current.
  - Longitudinal mismatch in J-Parc MR enlarges tune spread after injection.
- Longitudinal bunch manipulation: CERN SPS, J-Parc MR
  - Need control of voltage for either better phase space matching or reduction of beam loss later.
  - Better diagnostics (PS tomography in phase space) in CERN helps a lot.
- Transverse feedback: CERN PSB, PS, J-Parc MR
  - Instability along the cycle in PSB.
  - Headtail instability, injection oscillations in PS.
  - Kicker impedance in J-Parc MR.
  - All can be cured by transverse feedback.
- Better understanding of halo generation: CERN PS, GSI SIS-18
  - Trapping/scattering mechanism coupled with tune modulation was proposed a decade ago.
  - Experimental verification in PS and SIS-18 in 1-D island.
  - Concept is extended to 2-D island around "fixed lines" which agrees experimental observation in PS in 2012.
- Better operating points: CERN PSB, PS, J-Parc MR
  - Better understanding of tune space with space charge theoretically and numerically.
  - Equal emittance removes restriction of Montague resonance.
  - Reconsidering the strength of resonance lines in PS from different view point.
- Resonance correction with space charge: GSI SIS-18
  - Compensation of resonance driving term ($Qx+2Qy=11$) without space charge.
  - Correction works with space charge.
  - Compensation is localised so that it does not affect tune area outside of the resonance.
- Recipe of emittance preservation: CERN PSB, PS
  - Choose bare tune such that beam core will not be suffered from integer resonance.

# WG B- Beam Dynamics In High Intensity Linacs

D. Raparia, BNL, Upton, USA

I. Hofmann, GSI Helmholtzzentrum für Schwerionenforschung GmbH, Germany

Y. He, Chinese Academy of Sciences Institute of Modern Physics, China

## Abstract

Grid noise and entropy growth, equi-partioning, equi tune depression, halo, and losses were a few topics, which were discussed thoroughly during parallel session for beam dynamics in high intensity linacs (group B). Linac designs for the future, under construction, upgrade and the existing linacs from around the world were presented in three working sessions.

A total of 17 talks were presented. Three presentations are general beam dynamics in nature and twelve talks were project specific. One talk was new experimental work on the Gabor lens to neutralize space charge. The detail of each contribution can be found in these proceedings. Here we report the summary of the discussions and some concluding remarks of general interest to all the projects presented in the working group.

## INTRODUCTION

Beam Dynamics of High Intensity Linacs (working group B) had 17 invited/contributed talks and two poster presentations. Unfortunately five participants could not attend due to visa problems. Two talks were upgraded from the poster session.

Three talks were presented on tele-conference. The first time it took unusually long time to set up, and one of the discussion sessions was cancelled. These presentations included two on linac beam dynamics, nine on design of linacs for specifics projects. Out of them two talks were designed to generate discussion and had one two hours long discussion session.

## GENERAL BEAM DYNAMICS FOR LINACS

Noll presented his new code BENDER, which allows fully self-consistent inclusion of space charge compensating electrons.

Hofmann discussed grid noise and entropy growth in PIC code, in particular with TraceWin examples. He found in his studies there exists an optimum number of grid cells below which grid heating dominates and above collision heating. Secondly, anisotropy effects are in good agreement with theory.

Nghiem proposed new concepts and methods for beam analysis, beam loss prediction, beam optimization, beam measurement and beam characterization in case of "very high intensity beams".

Eshraqi proposed a linac design based on equi-tune-depression instead of equi-partition lattice design for linacs. He showed that since linac beams are usually pretty spherical choosing an equi-partitioned point in the linac is very close to having an equi-tune-depressed lattice.

Other noteworthy results were reported by Yong Liu. For J-PARC linac simulations he showed that his non equi-partitioned lattice is an order of magnitude more sensitive to errors than an equi-partitioned lattice.

For the Gabor lens study partial agreement with modelling was achieved, but more work is needed to better understand the limitations.

Groenings work on emittance transfer between horizontal/vertical is of interest for linacs as injectors into rings with horizontal multi-turn injection. The transfer requires stripping and matches with low charge state ion linacs as for the FAIR synchrotron.

In HB2012, Lagniel raised the question about validity of equi-partition theory and lattices in his talk entitled, "Equipartition Reality or Swindle"[1], Discussions in HB2012 hinted there is more work (simulations) needed to reach consensus [2]. Since then further simulations were published by Hofmann in response to Lagniel's arguments [3].

## BEAM DYNAMICS DESIGN OF LINACS

Table 1 gives a brief description of the linacs discussed in the WG-B at HB2014. Two high power linacs, ESS and ADS, were optimized for different parameters. The ESS linac is optimized for cost by reducing the number of cavities and increasing the peak current by 25% and the cavity gradient by 11.25% keeping the beam power at 5 MW. The ADS lattice is optimized for losses by increasing the longitudinal acceptance and avoiding the longitudinal parametric and transverse structure resonances and longitudinal –transverse coupling.

The J-PARC linac was upgraded to 400 MeV from 181 MeV, ion source and RFQ were also changed with better performing units. They were expecting a signature of intra-beam-stripping but did not fine any indication of intra-beam stripping. The SNS linac production tune still does not match with modelling in spite of better calibration of the measurement devices and modified methods. The linac was able to achieve the design goal of 1.4 MW beam power.

## DISCUSSIONS SESSION

In the discussion session following topics were discussed:

- Equi-partition verse equi-tune-depressed lattice were discussed:

It was not clear, if the equi-tune-depression idea has a real physics basis other than intuition.

- Non-equipartitioned J-PARC linac lattice is more sensitive to error:
  In HB2012 it was reported that intra-beam stripping optimized lattices will have 50% more emittance growth [3], but no one suspected that the error sensitivity would be an order of magnitude worse. The suspicion is that due to the bigger beam size in intra-beam stripping lattices, they sample more nonlinearity of the RF field.

- Grid noise and entropy growth in PIC codes:
  In the interest of keeping simulation noise at low level it is not advisable to go beyond 8-10 grid cells in TraceWin or work with less than $10^5$ particles (error studies).

- Relations between emittance and halo:
  Several examples were discussed, where these two quantities do not depend on each other.

- Automatic correction for closed orbit and micro-loss:
  While automated closed orbit correction is successfully working in several accelerators, the same algorithm should work to reduce losses. It could lead to local minimization, since one cannot go very far from the working point with full power, which might damage the accelerator before finding the minimum. This technique may reduce losses but cannot predict a path to upgrade.

- Figure of merit: emittance or losses:
  High power linacs with fixed target are usually CW and have their figure of merit as beam loss, whereas high intensity linacs as pulsed injectors need as figure of merit the emittance.

## REFERENCES

[1] Jean-Michel Lagniel, "Equipartition, Reality or Swindle?", HB2012

[2] D. Raparia, P. A. P. Nghiem and Z. Li, "Summary of Working group B", HB2012

[3] I. Hofmann, "A New Approach to linac resonances and equipartition?" http://arxiv.org/abs/1210.7991

**Table 1: LINAC Presented in HB2014**

| | Ions | RR (Hz), PL(ms) /CW | Freq. MHz | C mA | E GeV | P MW | $Trans_{SC}$ MeV | Structures | Chop. Loc. | $E_{RFQ}$(MeV) $L_{MEBT}$(m) |
|---|---|---|---|---|---|---|---|---|---|---|
| ESS | P | RR :14 PL:2.86 | 352.2/704 | 62.5 | 2.0 | 5 | 90 | DTL,SSR,EC1,EC2 | MEBT | E: 2.5 L: 4 |
| FRIB | P-U | CW | 40.25/80.5/322 | 8.4p | 0.2 (/u) | 0.400 | 0.3 (/u) | QWR,HFR | - | E: 0.3/u L: 4.8 |
| C-ADS | P | CW | 162.5,325/650 | 10 | 1.5 | 15 | 2.1/3.2 | HW09,SSR12,SSR21, SSR40,EC63,EC82 | - | E: 2.1,(3.2) L: 2.7 ,4 |
| C-SNS | H⁻ | RR: 25 PL=0.5 | 324 | 20 | 80 | | - | DTL | LEBT | E: 3 L: 0 |
| T-Singhua | P | RR: 50 PL: 0.5 | 325 | 50 | 13 | 0.16 | - | DTL | - | E: 3 L: 0 |
| J-PARC | H⁻ | RR: 25 Pl: 0.5 | 324/972 | 50 | 400 | | - | DTL,ACL | MEBT | E: 3 L: 3 |
| SNS | H⁻ | RR: 60 PL: 1 | 402/804 | 38 | 1 | | 185 | DTL,CCL,EC62,EC82 | LEBT & MEBT | E: 2.5 L: 3.64 |
| IFMIF | D+ | CW | 175 | 2x125 | 0.04 | 2x5 | 5 | HW | LEBT | E: 5 L: 9.8 |

# WORKING GROUP C SUMMARY: COMPUTATIONAL CHALLENGES, NEW CONCEPTS, AND NEW PROJECTS

Steven M Lund*, Facility for Rare Isotope Beams, Michigan State University, USA
Giuliano Franchetti, GSI, Germany
Hiromi Okamoto, Hiroshima University, Japan

*Abstract*

We summarize workshop discussions held in Working Group C at the 54th ICFA Advanced Beam Dynamics Workshop on High-Intensity, High-Brightness, and High Power Hadron Beams (HB2014; East Lansing, Michigan) taking place 10–14, November, 2014. The charge of Working Group C was to formulate a workshop-oriented agenda on *Computational Challenges, New Concepts, and New Projects*. In this summary, we list topics selected and linked presentations that were delivered, and summarize discussions held. Only limited attempts are given to summarize details of individual presentations. Focus is primarily on recommendations based on material presented both in the topically grouped talks and in linked workshop discussion sections immediately following each group of talks.

## INTRODUCTION

The charge of Working Group C (WGC) to address *Computational Challenges, New Concepts, and New Projects* is very broad to cover adequately in 14 invited presentations of 25 minutes duration (20 minutes + 5 minutes discussion) each and approximately 100 minutes of workshop discussion time. Moreover, the potential for the WGC charge to overlap and conflict with Working Groups A (*Beam Dynamics in Rings*; WGA) and B (*Beam Dynamics in LINACS*; WGB) was significant. In an attempt to focus to a reasonably limited agenda to be productive, the conveners tried to pick workshop-oriented topics to group into four sessions with 25 minute joint discussion periods held after the topically grouped talks. Care was taken to minimally overlap with topics taken up in WGA and WGB. Topics likely of interest in WGA and WGB were organized in the overall workshop agenda (two parallel sessions) to allow joint sessions. Topical groupings in WGC were as follows:

- First Session, Tuesday morning, Nov. 11th.
  **Computational: Simulation Infrastructure**
  **New Concepts: Scaled Experiments**

- Second Session, Tuesday afternoon, Nov. 11th.
  (Combined with WGA,WGB)
  **New Concepts: Nonlinear Integrable Optics**

- Third Session, Wednesday morning, Nov. 12th.
  **Computational Challenges: Long Path Length Simulations / Benchmarking**

---

* lund@frib.msu.edu

- Fourth Session, Thursday afternoon, Nov. 13th.
  (Combined with WGA,WGB)
  **New Projects: New Projects: ISIS Upgrade, FFAG, Beam-Beam, Electron Lenses**

In the four WGC topical summary sections that follow, we give titles and speakers of invited presentations delivered and primarily summarize highlights of 25 minute discussions held (following each session listed). Discussions were largely, but not exclusively, stimulated by the talks within the immediately preceding sessions. Individual talks can be obtained (provided speakers did not opt out) on the HB2014 web site [1]. Recommendations given reflect perceptions of the conveners based on discussions held. Efforts were made to be balanced in summary, but limitations on the conveners backgrounds may result in some of these being of limited value.

## SIMULATION INFRASTRUCTURE AND SCALED EXPERIMENTS

Framing invited presentations delivered under simulation infrastructure were [1]:

- Jean-Luc Vay (LBNL), *Needs and considerations for a consortium of accelerator modeling*;

- Ji Qiang (LBNL), *Development of integrated workflow for end-to-end modeling of accelerators*;

and a single presentation for scaled experiments was [1]:

- Hiromi Okamoto (Hiroshima University), *Recent results from the S-POD trap systems on the stability of intense Hadron beams*.

The talks by J.-L. Vay and J. Qiang were invited to cover code collaborations and infrastructure issues which could benefit from community discussion in the workshop. The talk by H. Okamoto was grouped since it overviews an experimental alternative to simulation to efficiently model aspects of beam physics with a trap experiment.

Consensus appeared strong that the code consortium initiative (Consortium for Advanced Modeling for Particle Accelerators; CAMPA) reported by J.-L. Vay is a good cause for community support. If successful, many will benefit in the long term and duplicative efforts will be minimized, allowing resources to be more productively employed to extend and improve the simulation tools. The goal is to provide reliable tools for accelerator modeling

from components to full systems. A well motivated strategy of integrating new models without disturbing existing users/developers is being employed. Increased reliability, leveraged effort/funding, and benefits for more unified input/output should result from broad acceptance of the model of integration offered by CAMPA. Preliminary DOE funding is limited. Initial (through 2015) members include LBNL, FNAL, and SLAC. Recommendations suggested by discussion points include:

- Efforts should be expanded beyond the three initial CAMPA partners as soon as funding allows.

- National laboratories may be the natural host for CAMPA since it will need consistent long-term support, but a framework should be adopted to allow participation by universities, companies, and international partners to further leverage effort.

- Previous impressive successes with the Los Alamos Code Group (LACG) in distributing legacy codes (POISSON, TRACE, PARMELA, PARMTEQ etc) should not be neglected. Support of such legacy codes as well as possibly more advanced tool kit components could bring many more users and justify more DOE support. LANL reports that updates of widely used LACG codes such as PARMELA (rewritten in C++) are being carried out and will be made available. Incorporating and leveraging these efforts seems logical.

- Codes for design of optical elements (magnetic and electric) and RF cavities should also be included in the effort since they are also central to design activities.

- Issues of ownership, credit, and distribution of funding will need to be addressed for broad participation.

End-to-end modeling efforts such as those outlined by J. Qiang with the IMPACT code can help support performance claims made for proposed facilities to help justify funding and put concepts on a firmer foundation. Efforts like this fit in well with the CAMPA consortium reported on by J.-L. Vay which also includes the IMPACT code and LBNL. Benefits can be obtained by self-consistently simulating systems fully within an integrated suite of simulation tools since many issues can be more efficiently and reliably evaluated. Questions/comments brought up in discussion include:

- Rings may prove especially difficult for self-consistent (including space-charge effects) modeling and injection of beams into rings via multi-turn stacking and painting. Such processes open questions as to whether it is possible, or even necessary, to carry out detailed upstream modeling in an end-to-end context.

- Even in linear accelerators beam sources and the initial transport near the source can be extremely challenging to simulate self-consistently and seamlessly integrating results may be difficult.

- Initiatives like CAMPA proposed above may provide long-range hope for achieving this vision.

Some of these issues are also brought up in the section on Long Path Length Simulations / Benchmarking.

It appears well established with results reported by H. Okamoto that small Paul-trap based experiments can be applied to effectively model various scalable processes in Hadron beams using an analogy between ions confined in the trap and beam-frame processes in an accelerator. Experiments can be small in scale and inexpensive. Low particle energies and apparatus field strengths have no potential for machine damage. These features make such systems ideal for dedicated physics experiments and student training. Processes amenable to scaling such as lattice focusing properties, halo, and space-charge transport limits induced by resonances appear possible to address with these systems. Unfortunately, the US program at the Princeton Plasma Physics Laboratory exploiting this beam frame analogy with a trap to investigate space-charge physics recently lost funding — apparently due to ongoing DOE budget stress in plasma physics. The remaining US program at the University of Maryland [2] using low energy electrons in a ring to investigate scalable physics is considerably larger with different technical issues. Consensus appeared strong that these experiments are beneficial to our community. It is noted that even idealized theory and simulations provide useful guidance for machine tuning. Paul trap experiments augment what is learned from these directions with an experimental and student training component and can be much faster (one machine cycle per ms at Hiroshima U. trap) than even idealized numerical simulations. Rutherford-Appleton Lab reported (D. Kelliher, short discussion presentation) ongoing plans in a collaboration with Hiroshima U. to construct a trap experiment similar to the systems reported by H. Okamoto. This is welcome news given the demise of the US program due to funding issues. Recommendations include:

- The broader Hadron accelerator community should be more active in conveying specific ideas of scalable processes that can be probed with trap facilities.

- Diagnostics presently employed (confined charge and density profile as function of time via dumping) are very limited. This restricts possibilities to exploit the traps more fully. If constraints needed for generation (electron impact ionization and potentially others) can be addressed, the experiments should become more useful with more detailed phase-space diagnostics. We recommend that attention be given to this.

- Paul traps might provide a natural step for laboratory tests of Nonlinear Integrable Optics (see also the summary on Nonlinear Integrable Optics) and this should be examined.

## NONLINEAR INTEGRABLE OPTICS

Invited presentations delivered in this section to cover ongoing efforts in Nonlinear Integrable Optics (NIO) were [1]:

- Sergei Nagaitsev (FNAL), *The IOTA ring: present status and plans*;

- Stephen Webb (Radia-Soft), *Chromatic and space charge effects in nonlinear integrable optics*;

- Rami Kishek (U. Maryland/UMER), *UMER 2.0: Adapting the University of Maryland Electron Ring to explore intermediate space-charge and nonlinear optics for Hadron beam facilities*.

The final presentation by R. Kishek on the University of Maryland Electron Ring (UMER) was also technically a scaled experiment topic, but covered plans to adapt the UMER ring to experimentally explore nonlinear integrable optics by modifying their low energy electron beam ring. The NIO topic is a natural fit to the workshop given the high community interest in improved transport promised by this concept. The session was well attended from other workshop working groups.

The workshop discussion/debate following the presentations on NIO was lively and productive. There appears to be both enthusiasm and healthy skepticism on aspects of and promises afforded by NIO. Much work remains to be done before the concept can be considered as a replacement to conventional (quadrupole) linear focusing in practical applications. However, the promise of having significantly diminished beam halo generation (from mismatch and other sources) and better stability properties (from large intrinsic tune spread) relative to linear focusing, and thereby potentially more compact and cheaper machines is highly significant. Support appeared high on seeing efforts to develop NIO progress. Even in the event of a practical failure, exploring NIO to a definitive conclusion should increase understanding of beam transport and provide excellent student training to support our field. It is worthwhile noting that various laser/plasma acceleration and focusing concepts have received much better funding in the face of significantly larger and more difficult confounding technical issues faced. Even with the significant advances made in those fields, practical applications such as colliders or even compact front-ends based on laser/plasma technology are likely much further from fruition and more expensive to address than for the corresponding case with NIO. We should be doing a better job as a community to support efforts to bring NIO to a logical conclusion — while remaining mindful of not over-selling consistent with a field building significant scale facilities that must deliver. Recommendations include:

- The IOTA ring appears well motivated and the FNAL team is appropriate to investigate/leverage the concept. It is unfortunate that this effort appears stalled due to a lack of funding given that needs are relatively modest. We endorse efforts to secure funding to complete the ring so relevant tests can be expeditiously carried out.

- Efforts to adapt the UMER ring to explore aspects of NIO appear well motivated. This also fits the funda-

mental physics and student training role of the group. We endorse U. Maryland efforts in this reorientation of their program.

- Paul traps (see H. Okamoto presentation in section on Simulation Infrastructure and Scaled Experiments) with adaptable electric focusing might prove amenable to economically explore long path length transport aspects of NIO. We advocate exploring this more fully. Given funding issues with IOTA, trap experiments might provide a more rapid and economical partial step to explore concept viability.

Constructive criticisms of the ongoing efforts on NIO that may be addressable within the context of ongoing efforts include:

- Single particle analysis of the dynamic aperture with applied magnetic fields as likely manufactured and realistic lattice errors should be clearly presented to better contrast the idealized situation with linear focusing. This may be easier to analyze than issues being presented (chromaticity, halo generation, ..) and help clarify system properties.

- A moment (envelope) level of beam description would be useful, even if idealized, to better understand beam matching properties to the nonlinear lattice at finite intensity.

- Halo contrasts of NIO to linear focusing may be hard to make without matching characterizations to the nonlinear lattice (see above) clarify a consistent basis contrast. Halo production results shown may be misleading given the extreme initialization assumptions made in the linear focusing case. However, useful results on halo *extents* (and apertures needed to contain) in phase-space are probably obtainable at present and could be contrasted between NIO and linear focusing in an "equivalent" focusing and intensity sense to help draw useful conclusions.

- An engineering survey should be carried out to explore potential issues with making magnets needed for NIO lattices including limitations on pole-tip field strengths. Scaling relative to "equivalent" linear optics incorporating aperture clearances to confine halo together with magnet technology limits could better characterize what savings might result if the promises of NIO on improved transport are realized. This could better motivate efforts/funding if potential savings are significant.

## LONG PATH LENGTH SIMULATIONS / BENCHMARKING

Invited presentations delivered to cover long path length simulations and code benchmarking were [1]:

- Frank Schmidt (CERN), *Code requirements for long term tracking with space charge*;

- Jeffery Holmes (SNS), *Status of PY-ORBIT and noise control in PIC codes*;

- Kazuhito Ohmi (KEK), *Artificial noise in PIC codes and consequences on long term tracking*;

- Ingo Hofmann (GSI), *Grid Noise and Entropy Growth in PIC Codes*.

Here, at the request of WGB, we have included the presentation by I. Hofmann in WGB within the scope of our summary discussions since the topic relates to computational issues taken up in WGC. These individual topics were selected to continue previous productive workshop discussions on this long-running and difficult topic [3]. The emphasis was primarily on rings and the issue of self-consistent space-charge modeling. However, aspects are also relevant to linacs and near-source transport.

Presentations on this topic made clear it will likely be a long struggle to self-consistently incorporate space-charge effects within realistic models and gain confidence in results. Much careful work will be required and new or improved simulation methods may prove necessary. Long path lengths and highly nonlinear models combined with difficult to resolve numerical convergence issues in statistics and gridding in many models open considerable challenges. Even with relatively simple idealized particle-in-cell (PIC) models, for example, may be difficult to achieve due to "expensive" scaling in numerical requirements for clear convergence. As F. Schmidt pointed out, benchmarking both in a code-code (also algorithm-algorithm) and code-experiment sense will be needed to gain confidence in results. Needs include analytic results to check simulations against, other "verified" codes, and reliable experimental data. Recommendations and comments brought out be the presentations include:

- Benchmarking libraries should be accumulated to aid sorting out difficult issues. For example, extensions of efforts like the GSI benchmarking efforts on space-charge induced trapping [4] would be useful.

- Needs may change with questions asked and space-charge intensity: particle orbits become nonlinear when space-charge is included and most reasoning is based on idealized KV (linear space-charge) beam models. What is adequate/optimal may change with the specifics of the problem and understanding extreme limits (even if idealized or not accessible) may help guide efforts.

- Even though plasmas are an extreme limit (essentially full space-charge depression), it is possible that our field can derive benefits from the large body of work on self-consistent modeling in plasma physics (see also comments on orbits above).

- It would be useful to see more tests of methods/algorithms by neutral parties who might compare strengths and weaknesses of various methods on a consistent basis. Results may change with system parameters, model dimension, and questions asked.

- Tests might have better guiding value if kept as simple as possible till effects and simulation needs are better understood. Some test cases appear to have multiple effects with significant impact occurring simultaneously making it difficult to draw clear conclusions on needs and limits.

- Can theory (see I. Hoffman presentation) provide guidance on numerical noise properties and the limits imposed if test cases are simple enough?

- Are "frozen" models with high detail (see K. Ohmi presentation) provide a way to bypass present practical difficulties in numerical convergence to address a variety of questions in real systems?

One sub-topic debate opened in the workshop is illustrative on challenges involved. Brief discussions session presentations by H. Zhang (JLAB) and B. Erdelyi (North Illinois U.) suggested intriguing possibilities with employing a Fast Multipole Method (FMM) to efficiently solve Poisson's equation (including structures and boundary conditions in some manifestations). Such methods open prospects for removing grid effects and simulation noise if fields are applied directly to the particles. Insofar as physical particle numbers are used, it was emphasized that collisional effects would be physical though examples cited appeared to have relatively low particle numbers. Results presented suggest advantages of the FMM relative to PIC methods. But the presentation by J. Holmes appeared contradictory with a FMM applied to a ring problem appearing unfavorable relative to a PIC method due, presumably, to numerical capacity limiting particle number resulting in enhanced collisional effects. Continued exploration of such issues to a clear conclusion might provide long-term benefits even if it must first be done within idealized contexts. Guidance on where various methods might prove optimal by a neutral party might provide significant long-term benefit.

## NEW PROJECTS

Invited presentations delivered to cover selected new projects which did not all within the scope of the other working groups were:

- Dean Adams (STFC/RAL), *Ring Simulation and Beam Dynamics Studies for ISIS Upgrades 0.5 to 10 MW*;

- Suzie Sheehy (RAL), *Characterization of a 150 MeV FFAG*;

- Christoph Montag (BNL), *Recent results on beam-beam effects in space charge dominated colliding ion beams at RHIC*;

- Xiaofeng Gu (BNL), *The physics and use of electron lenses at BNL.*

The S. Sheehy presentation was kindly delivered on short notice to fill in an unexpected opening in the schedule and may not be archived on the workshop web site [1]. Because the New Projects component of WGC involves less focused topics, here we carry out a more conventional summary followed by more limited recommendations.

The ISIS upgrade (see D. Adams presentation) is a major project in RAL. One option is to increase the injection energy from 70 MeV to 180 MeV at $8 \times 10^{13}$ ppp for 0.5 MW operation. A number of studies supporting the upgrade were carried out using the ORBIT code including transverse injection painting and foils, resonances, and longitudinal dynamics. Resonance issues were studied by analyzing working points and driving terms. Detailed simulation studies suggested that losses can be manageable. Another upgrade scenario to a 2-10 MW RCS ring for a short pulse facility was reported initiated with both 1D injection/acceleration and 3D injection studies carried out.

FFAG accelerators will need to accelerate intense beams to realize their full promise. RAL is evaluating their use as part of an alternative upgrade path for ISIS. In the presentation by S. Sheehy, initial activities using a scaling FFAG associated with measuring and correcting the closed orbit (which has properties different from conventional synchrotrons) were reported. To investigate space-charge effects in the complex magnetic geometry and related enhancement by a machine tune migration with energy gain, plans include use of simulation tools in support of the program.

Beam-beam issues are reported on in two presentations from BNL. Potential detrimental space-charge issues have been a concern in beam-beam and research on the issue is covered by C. Montag. At BNL, Au collision at 2.5–10 GeV/nucleon are of concern in RHIC. Results reported suggest that observed beam decay is not related to space-charge and an associated change of tune. Diffusion studies agreed with experimental results from 2010, and helped set a new working point improving performance in 2014. The computer model used was relatively simple, yet adequate to identify physics, match previous experimental results, and guide improvements. Complex hardware needed to evaluate beam-beam mitigation via electron lenses are being developed and the status of these efforts were reported on by X. Gu. Resonances induced by Coulomb forces are not only induced internally within a beam. In colliders, the Coulomb force of one beam influences the other beam with associated resonance effects. Compensation/mitigation of the beam-beam effect is foreseen via electron lenses to produce a "counter" space-charge effect. Hardware needs are considerable. Solenoids with fields up to 6 Tesla are used. In BNL these lenses are constructed and evaluated for use in head-on beam-beam compensation. The effect of the lenses on orbit and tune were measured and found to be as expected. Future steps will require the use of separate, dedicated hardware.

In this topical of WGC, the common theme is that upgrades of existing facilities are reached through detailed space-charge simulation studies. This requires reliable, benchmarked codes. Comments/recommendations include:

- ISIS upgrade activities illustrate well the need for effective benchmarked code tools to explore loss issues guiding significant facility upgrades.

- Support of FFAG development opens needs for code extensions to deal with the complex applied fields, bunch-bunch interactions, and long path length.

- Frozen simulation models (see Sec. Long Path Length Simulations) may address some facility support issues.

- Beam-Beam space-charge appears not to be playing a significant role at RHIC. Nevertheless, results suggest that the facility may be employable in an R&D sense to develop complex plasma lens technology to address the issue for parameters where the effect may be more severe.

- Beyond substantial technical hardware challenges, the effective use of electron lenses to mitigate space-charge tune shift needs a careful study to verify that the lenses will not produce new detrimental resonances (forces compensated on average) to offset benefits suggested.

## ACKNOWLEDGMENTS

## REFERENCES

[1] Presentations are archived on the HB2014 web site: `http://frib.msu.edu/misc/hb2014/index.html`

[2] See information presented on: `http://www.umer.umd.edu`

[3] The topic was discussed at HB2012 (see: `http://hb2012.ihep.ac.cn` and associated material archived on jacow at http://jacow.elettra.eu) and the 2013 CERN space-charge workshop (see `http://indico.cern.ch/event/221441/`).

[4] See: `http://web-docs.gsi.de/~giuliano/research_activity/trapping_benchmarking/main.html`

# SUMMARY FROM WORKING GROUP F:

# INSTRUMENTATION AND BEAM MATERIAL INTERACTIONS

R. Dölling, Paul Scherrer Institute, Villigen, Switzerland

M. Minty[#1], Brookhaven National Laboratory, Upton, NY 11973, U.S.A.

N.V. Mokhov[#2], Fermilab, Batavia, IL 60510, U.S.A.

T. Toyama, High Energy Research Organization (KEK), Tsukuba, Japan

## Abstract

This workshop on High-Intensity, High Brightness and High Power Hadron Beams, held in East Lansing, MI and hosted by Facility for Rare Isotope Beams (FRIB), included a Working Group which combined the topics of Instrumentation and Beam Material Interactions. Continuing with the HB Workshop series tradition, progress, status and future developments of hadron accelerators in these subfields were presented and discussed. Leveraging off of experiences from existing accelerators including FNAL, IFMIF, JPARC, the LHC, RHIC and the SNS, this workshop provided occasion to discuss new technical challenges for beam instrumentation and beam material interactions as relevant for future high power hadron beam facilities both approved (e.g. FRIB, ESS) and in planning (e.g. CADS). Discussions between this and the other working groups during this workshop were quite lively as necessitated by the need to seriously address strong interdependencies (between beam dynamics, technologies, instrumentation and interaction of the beams with materials such as targets, beam dumps and collimators) in the regime of megawatt beam powers as anticipated in approved and future accelerators.

## WG-F ORGANIZATION

At this HB workshop, the topics of Instrumentation and Beam Material Interactions (BMI) were combined into a single working group. Working group F consisted of (1) two sessions with nine talks on Instrumentation, (2) one joint discussion session with working group A (beam dynamics in circular accelerators), (3) one joint discussion session with working groups B (beam dynamics in linear accelerators), (4) one session including discussion with three talks on Beam Material interactions and (5) seven posters contributed to the general poster session.

Since the HB workshop series places strong focus on beam dynamics, the selection of talks for WG-F aimed to reflect this. The instrumentation sessions therefore included topics such as beam profile and halo measurements and

their relevance to beam dynamics analyses and simulations as well as comparisons of beam measurements with predictions.

The Beam Material Interactions session included presentations on activation and radiation damage / material response to high-power beams, thermo-mechanical simulations including design tools for targets, collimators and beam dumps, irradiation facilities capable of supporting future desired measurements, and novel materials for interception of high power beams. The orientation of this working group was therefore quite distinct from the IBIC, Linac, Cyclotron or IPAC conferences. Selected highlights from the presentations in WG-F are summarized below.

## INSTRUMENTATION

Challenges in existing and future accelerators [1-3]: Experiences at the LHC were presented [1] providing vital input for the design of instrumentation for future high power accelerators (either high in beam current or in beam energy, or both). This includes all aspects related to avoiding uncontrolled beam losses such as measurements of beam loss and halo, sophisticated collimation schemes and machine protection systems. An outstanding challenge at the LHC pertains to precise measurement of the transverse beam emittances of the high brightness beams. Wire scanners are used for profile measurements at low beam intensities and for cross-calibration of other beam size measurements. These include necessarily non-invasive measurement devices including ionization profile monitors, synchrotron light monitors and transverse Schottky measurements. Under development are synchrotron light-based interferometric measurement and, as shown in Fig. 1, a novel non-invasive beam-gas vertex monitor. Based on concepts used by the LHCb vertex detector, this detector will allow measurement of the absolute transverse profiles using reconstruction of the location of inelastic beam-gas interactions based on particle tracking with coincidence detectors [1].

Multi megawatt accelerators of the future require fast beam loss detection (for damage protection) and high dynamic range (to avoid activation) which demands the use

---
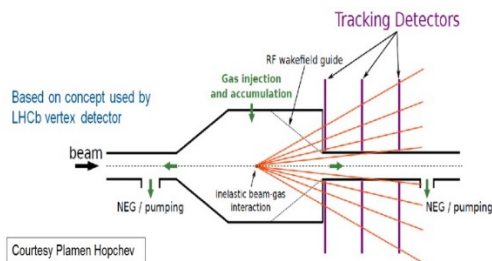
Figure 1. Novel beam gas vertex monitor being prototyped in the LHC for commissioning in 2015 [1].

of complementary devices to detect errant beams and slow losses [2, 3]. In addition, non-invasive beam profile measurements, both transverse and longitudinal, are needed. Under consideration for transverse profiling at ESS [2] are wire scanners, ionization profile monitors, beam-induced fluorescence monitors, electron beam scanners and possibly gas jets. A challenge unique to FRIB, shown in simulation in Fig. 2, involves the need to monitor and control multi-charge state composite beams in regions of high dispersion [3].
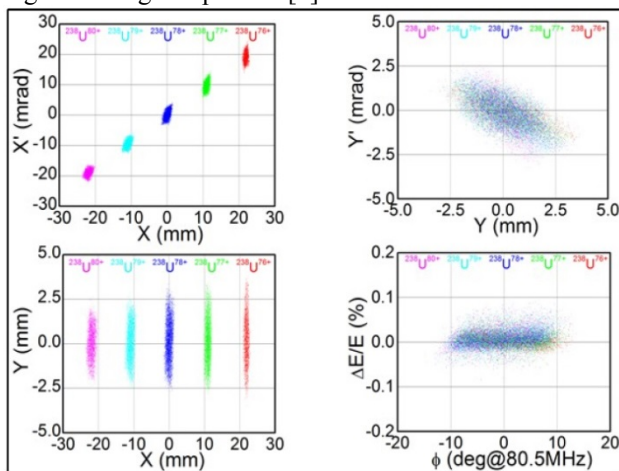


Figure 2. Phase space and physical space for a five-charge-state beam in the first folding segment with high dispersion at FRIB [3].

<u>Developments in simulations of beam loss</u> [4, 5]: New simulation results were presented on the topic of beam losses in high intensity linacs. As applied to IFMIF, a "Particle Swarm Optimization" (stochastic optimization technique), was utilized to optimize simulated transport of high intensity beams through a linac in the presence of multiple, operationally-realistic machine errors.

A "catalogue of detailed losses" was developed using simulations for all phases of accelerator operation [6, 7] at IFMIF and CADS [8]. Low loss tuning strategies aim to use densely placed "micro-loss monitors", such as crystalline CVD diamond detectors, capable of detecting fractional beam losses of <1E-6. While acknowledged that the simulations are not precise at this level, such simulations will be invaluable during commissioning and operation of future high power accelerators.

<u>Developments in simulations of beam loss with comparisons between simulation and experiment</u> [9, 10]: In preparation for LHC operation with 6.5 TeV beams and as partially motivated by recent observations of "unidentified falling objects", very challenging studies were presented involving comparison of extensive simulations to detailed beam experiments performed to determine thresholds for quench-preventing BLM-based beam-aborts and for determining BLM thresholds for real beam-induced quenches [9]. In the steady-state, quench levels were understood within a factor of two while on the short time scales of UFO-induced beam losses (0.1-10 ms), the comparisons between experiment and simula-tions of particle loss are not yet consistent with those from detailed electro-thermal analyses [9].

On the topic of ion-induced beam losses at the LHC [10], detailed studies of ion beam losses from collimation cleaning were presented. Standard code (ICOSIM) for heavy ion loss map simulation was shown to not explain certain features of the measured beam losses. The agree-ment between measurement and simulation was signify-cantly improved, as shown in Fig. 3, using SixTrack with ion-equivalent proton rigidities and a very detailed simulation of fragmentation [10].

<u>Beam halo considerations including definition</u> [4, 11]: With accelerator designs aiming for increased total intensity and/or beam energy, unintentional beam losses become even more important as even a very small fraction of the total beam can lead to component damage and/or practical difficulties related to serviceability of accelerator components. Particles not following the design trajectory and/or not having design beam focussing properties may eventually contribute to the "beam halo" and cause unintended beam loss.

The sources of beam halo fall into two categories [11]: those with unavoidable physical origins (such as space charge, beam-gas scattering in an imperfect vacuum) and those of practical origin as resulting for example from small deviations from design parameters (e.g. errors in magnet alignment, parameter mismatches both transverse and longitudinal between linear and circular accelerators) and consequences of external perturbations including noise in power supply currents, rf cavity voltages, environmental factors leading to vibrations in component position, etc. Many diagnostics have been implemented world-wide to enable detection of the beam profile over a wide dynamic range to include measurement of the beam halo. A broad overview was given in Ref. [11].

A topic of ongoing discussion concerns how to quantify beam halo. Methods used in the past for characterization include definition in terms of the kurtosis of the density profile, ratio of halo to core, ratio of beam core to offset and the Gaussian area ratio method [11]. Recent work with focus on high power beam transport in linear accelerators offered a new measure of beam halo: definition of the core-halo limit as the location of biggest
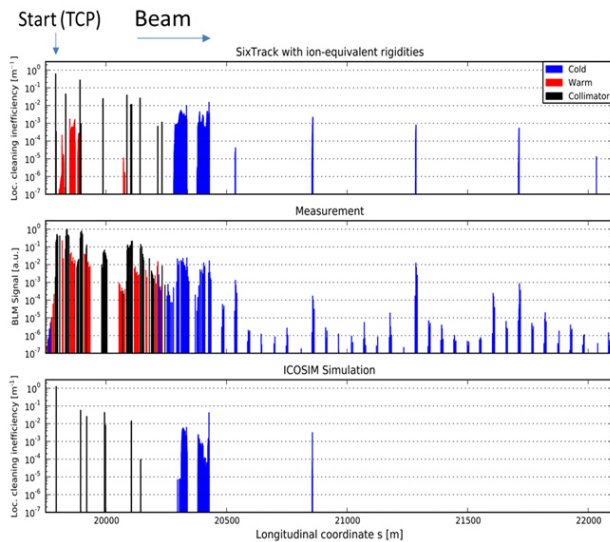
Figure 3. Simulations of ion beam losses in the LHC before (bottom) and after (top) code refinements compared with measurements (middle) from Ref. [9].

slope variation in the beam density profile, e.g. where the second derivative of the density is a maximum [4]. Concerning future designs, the need for clear specifications for the required measurements was emphasized and these should be agreed upon by accelerator physicists, collimation experts and beam diagnostics specialists [11].

Beam halo dynamics in linear transport lines [4-8]: As shown in Fig. 4, results from the Particle Swarm Optimization (see developments in simulations of beam loss above), revealed that off-axis particle transport (beam "halo") could be minimized at the expense of non-preservation of the rms beam emittance, an observable often used as a measure in quantifying the efficiency of beam transmission. This simulation results are not inconsistent with beam tuning experiences at the SNS [4].

Beam halo dynamics in circular accelerators [12]: Simulations and experimental results of beam halo diffusion and population density in the Tevatron and the LHC were presented. As a function of normalized action, measured diffusion coefficients were measured for both colliding and non-colliding beams at the Tevatron and the LHC, as shown in Fig. 5. At the LHC with collisions, the diffusivity was reported to be consistent with emittance growth. At the Tevatron, by comparing data with antiprotons only and colliding beams, the measured diffusion coefficient revealed a 1-2 order of magnitude increase attributed to the beam-beam interaction. In a separate set of measurements utilizing a hollow electron beam in the electron lens at the Tevatron, the measurements of diffusion coefficient versus vertical collimator position revealed what is believed to be a first time direct observation of controlled diffusion enhancement in a specific amplitude range.
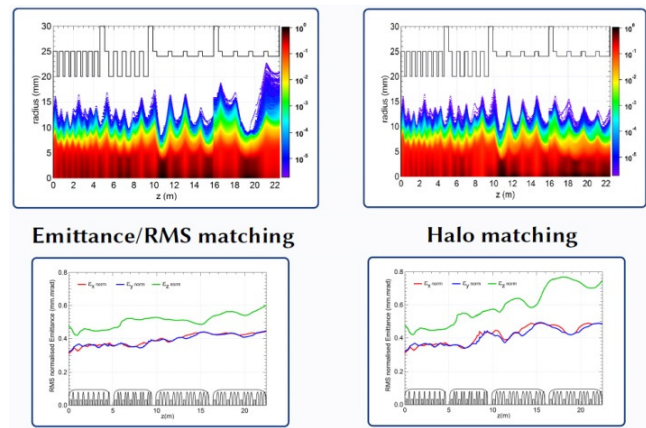


Figure 4. Simulation results (Particle Swarm Optimization) for the IFMIF linac [4, 5].
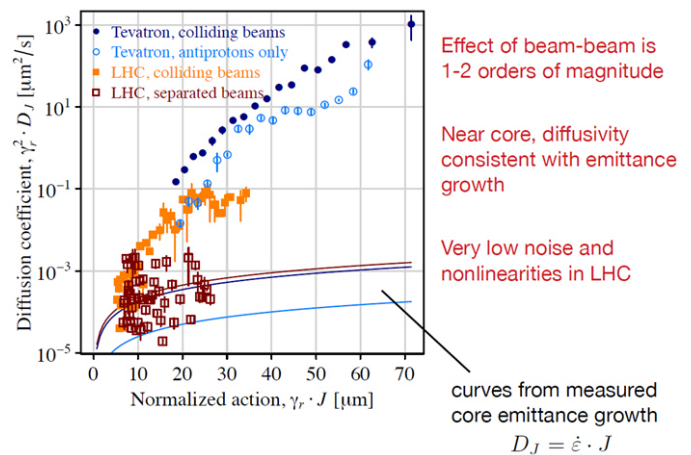


Figure 5. Measurements of beam halo diffusion rates in the TeVatron and in the LHC [12].

Developments in combined beam core and beam halo diagnostics [11, 13-15]: Qualitative measures of the portions of the beam contained within the undesired beam "halo" require absolute calibration most easily determined by additional measurement of the beam core (defined here as those particles contained within the area of interest).

From J-PARC two diagnostics each combining different measurement techniques provide large dynamic range [13-15]. From the J-PARC rapid cycling synchrotron (RCS), with results shown in Fig. 6, scintillator-based measurements of the beam core were combined with data from wires applied as scrapers to sample the beam halo and a portion of the beam core. With this topology, a dynamic range of 1E4 was demonstrated [13].

Also from J-PARC, state-of-the-art high dynamic range beam profile measurements were presented using beams extracted from the RCS prior to injection into the J-PARC main ring [15]. The beam core was measured using optical transition radiation from a thin (10 µm) Titanium
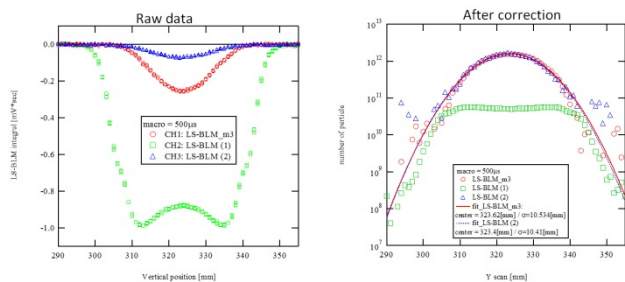
Figure 6. Measurements of beam core and halo from the J-PARC RCS [13].

foil while the beam halo was measured using fluorescence from a chromium doped Aluminum screen. Measurements (see Fig. 7) demonstrated >1E6 dynamic range achieved by this composite diagnostic. This device is unique in that it measures the two dimensional distribution of the beams as shown in Fig. 8. The measurements revealed different properties of the beam core and halo depending on the details of the beam injection scheme (target admittance of phase space painting). From Figs. 7 and 8, more than six orders of dynamic range for the projected profile have been reached and four to five orders for the two-dimensional profile.

Another beam halo diagnostic: the electron back–scattering detector [1, 11]: Numerous presentations included mention of a relatively new development, presented first at IBIC14 [16] with adaptation aspects presented at the Beam Halo Workshop [17]. This novel detection concept utilizes Compton backscattered electrons generated by grazing collisions between a hadron (proton or ion) beam and an electron beam provided in this application by an electron lens. Recent data from RHIC confirmed more than sufficient measurement sensitivities with counting rates consistent with expectation. The design features an elegantly simple detection technique (scintillators and photomultipliers) and has provided already meaningful data derived from beam-gas scattering. The concept is being considered for use as an option for the HL-LHC together with the hollow electron lens design from the Tevatron [1].

Other non-intercepting beam diagnostics [18, 19]: Recent developments in ionization profile monitors were presented as relevant in the context non-invasive beam size monitoring at the LHC. Simulations showed that the electric field of the proton beams perturbs the to-be-collected electrons (those released in the ionization process) at high particle beam brightness. To combat this, an electron "sieve" will be used to filter out electrons of different gyration radii. This should allow for a correction of the disturbance. In addition, the Timepix3 ultrahigh bandwidth, radiation hard, hybrid pixel detector developed at CERN (CERNs Medipix chip) will be used to enable bunch-by-bunch beam profile measurements.

A concept and simulations for an improved version of an existing beam current monitor at PSI were presented [20, 21]. The device, presently under construction, will be
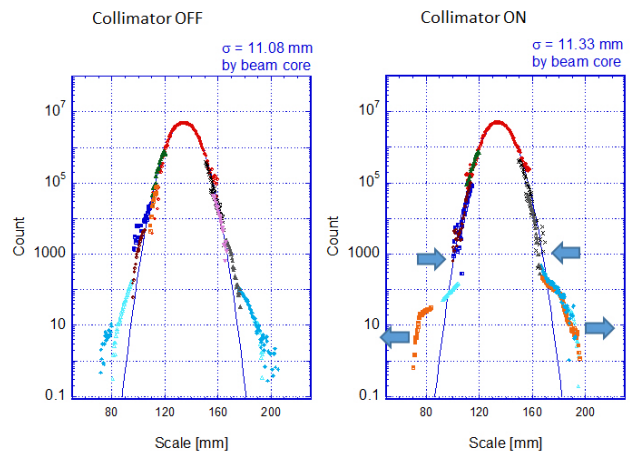
Figure 7. Horizontal projections from a high dynamic range beam profile monitor from J-PARC [14].
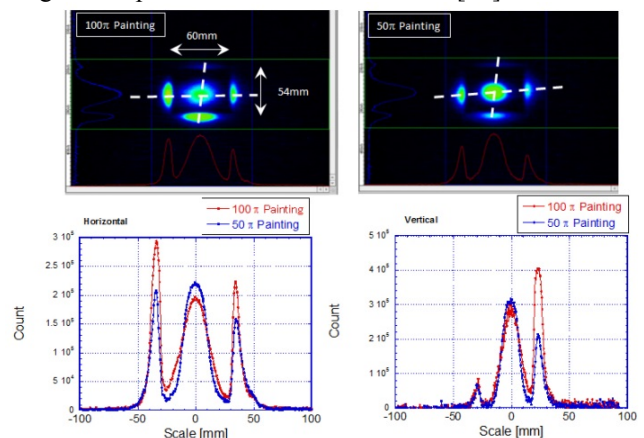


Figure 8. Measurements of the two-dimensional beam profile including the beam core and beam halo in a wide dynamic range diagnostic developed at J-PARC [14].

used in a location with high heat load from secondary particle showers. It is based on a low-Q resonator made from graphite. The new design with increased and fixed gap width should be less sensitive to drifts caused by unequal thermal expansion [20, 21].

## BEAM MATERIAL INTERACTIONS

The consequences of impact of high-intensity or/and high-power hadron and heavy-ion beams − or just their fraction − on components of accelerators, beam-lines, target stations, collimators, absorbers, detectors, shielding, and environment can be quite severe or even catastrophic. Depending on material, level of energy deposition density and its time structure, one can face a variety of effects in materials under irradiation affecting their lifetime (melting, thermal shocks and quasi-instantaneous damage; critical property deterioration; and radiation damage to inorganic materials due to atomic displacements and helium production) and component performance (superconducting magnet quench; single-event effects in electronics; detector performance deterioration as well as radioactivation, prompt dose and impact on environment).

Therefore, these effects along with the progress towards the ways to mitigate and model these are traditionally considered at the HB workshops. Three original talks were presented at this one followed by discussions.

Material response to high power beams [22]: The techniques to measure and characterize changes of material properties under intense beam impact were described for the three states of targets. For solid materials, the key phenomenon is material stress. The studies include its minimization via target segmentation, avoiding the stress concentration, compressive preloading, optimization of beam size/shape, and appropriate material choice. The characterization of the materials is done via a stress quality factor. Direct measurements of material strength are done at the Stress Test Lab at RAL. These include dynamic measurements as well as studies of material fatigue. The example that illustrates the latter phenomenon is the proton beam window for the ESS beams. The fatigue is related the peak power deposition of 0.5 kW/cm$^3$ under a pulsed operation at 14 Hz. Al6061-T6 was found to be the preferred material for the window cooled by Helium at 10 bar.

A second state of the target is liquids. A typical representative of this type is flowing mercury used at the Spallation Neutron Sources. A quite interesting technique was developed at J-PARC for the in-situ measurements of vibration induced by a proton beam. The bubbling mitigation effect on pressure waves was confirmed in these studies. A third type of targets – between solid and liquid – is studied at RAL for the fluidized tungsten powder recirculated in helium pneumatically. The advantages of this technique are that material is already fragmented, there is no cavitation, thermal stress is contained within grains, and the target can be continuously reformed, pumped away and externally cooled.

DPA and gas production in intermediate and high energy particle interactions with accelerator components [23]: A brief overview of recent developments in modelling primary radiation damage relevant to Displacement-per-Atom (DPA) calculations was presented. Problems and perspectives of advanced radiation damage and gas production calculations at intermediate beam energies were also discussed. The author has described the key features of the existing approaches to estimate the number of stable defects. The methods include:

- Norgett, Robinson, Torrens (NRT) model, widely used as is or with various corrections.

- Binary collision approximation (BCA) model.

- Molecular dynamics (MD).

- MD extrapolation to high energies using various assumptions.

- BCA-MD combination with BCA used above a critical energy (~30-60 keV) and MD below this energy. Similar to NRT, this method is easily implemented in Monte-Carlo particle transport codes.

- Kinetic Monte Carlo (KMC), a promising method to simulate the long-term defect evolution.

Although quite different with respect to capabilities, complexity of code implementation and accuracy of predictions, the methods find their ways in numerous applications related to material damage by high-intensity beams.

At accelerators, radiation damage to structural materials is amplified by increased hydrogen and helium gas production for high-energy beams. In SNS-type beam windows, the ratio of He/atom to DPA is about 500 of that in fission reactors. These gases can lead to grain boundary embrittlement and accelerated swelling. Nuclear models implemented in popular computer codes predict gas production cross-section with varying degrees of success depending on the energy of projectiles. The use of cross-sections evaluated using nuclear model calculations and measured data is one of the most reliable and flexible approaches for advanced calculation of gas production rate, certainly at intermediate energies. The database created at KIT includes 278 targets from $^7$Li to $^{209}$Bi, and incident proton energies: 62, 90, 150, 600, 800, 1200 MeV.

Novel materials for collimators at LHC and its upgrades [24]: This presentation was focused on materials for one of the most critical and – at the same time – very challenging components of the Large Hadron Collider (LHC), its beam collimation system. The following key properties of the materials are to be optimized to meet the LHC operation, performance and lifetime requirements:

- **Electrical Conductivity** Maximize to limit Resistive-wall Impedance.

- **Thermal Conductivity** Maximize to maintain geometrical stability understeady-state losses.

- **Coefficient of Thermal Expansion** Minimize to increase resistance to thermal shock induced by accidental beam impact.

- **Melting/Degradation Temperature** Maximize to withstand high temperatures reached in case of accidents.

- **Specific Heat** Maximize to improve thermal shock resistance (lowers temperature increase).

- **Ultimate Strength** Maximize to improve thermal shock resistance (strain to rupture).

- **Density** Balance to limit peak energy deposition while maintaining adequate cleaning efficiency.

- **Radiation-induced Damage** Minimize to improve component lifetime under long term particle irradiation.

It is realized that no existing material can simultaneously meet all the requirements. Therefore, the extensive R&D program on novel materials has been launched at CERN in collaboration with EU institutes and industries (EuCARD,

EuCARD2 and HiLumi). Its aim is to explore composites combining the best properties of graphite and diamond with those of metals and transition metal-based ceramics (high ultimate strength and good electrical conductivity). Materials investigated include Copper-Diamond (CuCD), Silver-Diamond (AgCD), Molybdenum-Copper-Diamond (MoCuCD), and Molybdenum Carbide-Graphite (MoGr). Production techniques include rapid hot pressing, liquid phase sintering, and liquid infiltration. It has already been found that the most promising ones are CuCD and (especially) MoGr.

To compare and rank materials against the most relevant requirements, several Figures-of-Merit (FOM) have been derived. These are: (a) Thermomechanical Robustness Index (TRI) related to the ability of a material to withstand the impact of a short beam pulse; (b) Thermal Stability Index (TSI) related to the ability of the material to maintain the geometrical stability of the component under irradiation; and (c) Electrical Conductivity, with resistive-wall impedance being inversely proportional to electrical conductivity and therefore the highest electrical conductivity is sought for materials sitting closest to circulating beams.

The highlights on the comprehensive beam test program have been given which include HiRadMat at CERN with 450-GeV protons, GSI with 10 MeV to 1.2 GeV ion beams ranging from carbon to uranium, and BLIP at BNL with 100 to 200 MeV proton beams.

The Beam-Materials Interactions session was wrapped-up by discussions. It was stressed that material response to the beam impact depends on variety of factors: material, level of energy deposition density (EDD), its time structure, environment and many others. The issues and questions were outlined such as quantities responsible for radiation damage (DPA, gas production, fluence and dose), as well as model/code capabilities and uncertainties in prediction of these values. It was stressed that the link of calculated values to observable changes in the critical properties of the materials remains on the top of the wish-list. The group has agreed that the well-thought experiments – covering various regions of the parameter space - are extremely desirable, including measurements with charged particle beams, their relation to neutron data and degradation measurements at cryogenic temperatures.

## BEAM INSTRUMENTATION DISCUSSION SESSIONS

During the first shared Instrumentation and Beam Dynamics discussion session P. Nghiem presented more on the topic of beam halo definition, which resulted in lively discussion. Next, the slide shown in Fig. 9 was used to introduce the topic of what types and quality of measurements, including correlations, would be most desired for furthering and validating simulations. Topics discussed included the types and numbers of measurements needed to predict subsequent beam loss and the

degree of coordination between simulations and experiments as desirable to motivate specifications for instrumentation requirements and new instrumentation designs.
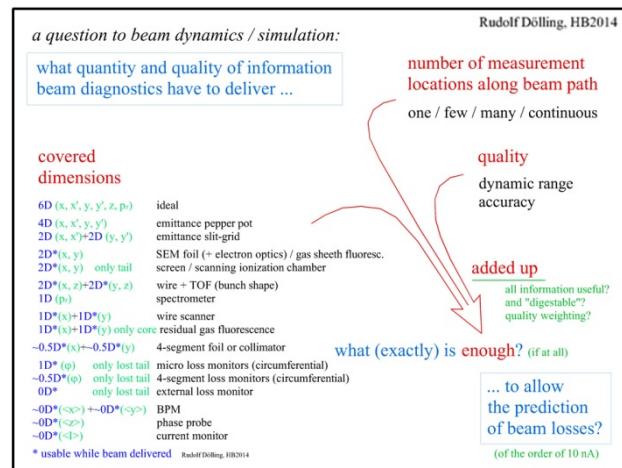


Figure 9: A very general and simple question. Answers, seemingly elusive, could help focus further developments in beam diagnostics (and simulations).

During the second discussion session, a by-request presentation by P. Hermes on the topic of comparisons between measurements and simulations as well as developments in simulation strategies for heavy ion beams in the LHC was presented (see developments in simulations of beam loss with comparisons between simulation and experiments, above). In the short amount of time remaining, two questions were posed. The first, raised by Working Group A, Beam Dynamics in Circular Accelerators, concerned the ability of beam diagnostics to discern space-charge related effects from beam instabilities. Responses pertained to beam loss minimization (difficult with instabilities that saturate) and impedance detection (coherent oscillations). The second provocative question concerned whether or not simulations of beam loss for future accelerators are sufficiently mature so as to guarantee successful commissioning and operation of future multi-Megawatt accelerators. The often cited specification of beam loss at the level 1E-6 and energy loss levels of 1 W/m were stated, by the conveners with audience corroboration, as too general.

For these discussion sessions topical questions (http://frib.msu.edu/misc/hb2014/QuestionABCF.html) were distributed in advance of the conference soliciting input. This strategy was marginally (at best) successful, maybe because of the many different backgrounds (machines, reasons for halo formation, interests and ways to consider these topics) which makes it more difficult to find a common starting point. (However, this is at the same time a potential source for collaboration and finding fresh views.) It remains the feeling that the organisation of these sessions must be improved in order to use the precious time similar effectively as it is done in the many bilateral

discussions during coffee or other "unplanned" times, and that we have not yet found the optimal Ansatz.

## OTHER

As topics in beam instrumentation and dynamics were presented in many other talks – both plenary and in the parallel working group sessions - this report, regrettably, does not include all great contributions to this conference. Pertaining to a subset of that, select additional important findings from the conference includes:

- The success of the LHC collimator design (with 100+ collimators) is truly noteworthy with no unintentional quenches to date. The design methodologies should be kept alive and, if not already done, applied to collimation system designs for future accelerators.

- Experience from existing high power accelerators shows that reliability may be compromised by not anticipating or realizing the impact of certain physical phenomena with examples including SNS (space charge, intrabeam stripping), LHC (unidentified falling objects, electron clouds)

- Safety margin criteria for future accelerators are often cited in terms of figures of merit (maximum permissible beam loss = 1E-6 of total current, maximum power deposition of 1W/m). These are too general and should not be interpreted as specifications by engineers.

- A fractional beam loss is not a good measure for a safety margin, rather the total absolute beam loss and/or total power deposition.

- The available computing power was considered a limiting factor for understanding beam halo transport in the past. With today's technologies, is this still the case? Has our understanding of beam halo improved commensurately? Do we think to still need such simulations?

- Will simulations guarantee that we can achieve the requirements on maximum allowable beam loss in future accelerator designs (FRIB, ESS, ADSs)? Should we expect them to?

- On the topic of "what is halo": perhaps need to expand to multiple definitions which depend on context, definition of dynamic aperture also in question.

## REFERENCES

[1] E.B. Holzer, "Beam diagnostic challenges for high energy hadron colliders", WEO2AB04, HB2014 proceedings.

[2] A Jansson, "Beam instrumentation and limitations for multi-MW pulsed proton linacs", TUO2AB01, HB2014 proceedings.

[3] S. Lidia, "Instrumentation design and challenges at FRIB", WEO2AB01, HB2014 proceedings.

[4] N. Chauvin, "Halo matching for high intensity linacs and dedicated diagnostics", TUO2AB02, HB2014 proceedings.

[5] P.A.P. Nghiem, N. Chauvin, et al (2014), "Dynamics of the IFMIF very high-intensity beam", Laser and Particle Beams, 32, pp 109-118. doi:10.1017/S0263034613001055.

[6] N. Chauvin, "Catalogue of losses for the linear IFMIF prototype accelerator", THO2LR04, HB2014 proceedings.

[7] N.A.P. Nghiem, N. Chauvin et al, "A catalogue of losses for a high power, high intensity accelerator", Laser and Particle Beams, 32, pp 461-469. doi:10.1017/S0263034614000391

[8] Z. Wang, "Nonlinear optimization in high intensity superconducting linac lattice of CADS", WEO3LR03, HB2014 proceedings.

[9] M. Sapinski, "Beam loss mechanism, measurements and simulations at the LHC (quench tests)", WEO2AB02, HB2014 proceedings.

[10] P.D. Hermes, "Studies on heavy ion losses from collimation cleaning at the LHC", MOPAB43, HB2014 proceedings.

[11] K. Wittenburg, "Beam diagnostics for the detection and understanding of beam halo" TUO2AB03, HB2014 proceedings.

[12] G. Stancari, "Measurements of beam halo diffusion and population density in the Tevatron and in the Large Hadron Collider" WEO3AB01, HB2014 proceedings.

[13] K. Yamamoto, "Beam instrumentation at the 1 MW proton beam of J-PARC RCS" WEO2AB03, HB2014 proceedings.

[14] M. Yoshimoto, "Beam halo measurement using a combination of a wire scanner type beam scraper and some beam loss monitors in J-PARC 3 GeV RCS", MOPAB44, HB2014 proceedings.

[15] Y. Hashimoto, "Two-dimensional and wide dynamic range profile monitors using OTR/fluorescence screens for diagnosing beam halo of intense proton beams", TUO2AB04, HB2014 proceedings.

[16] P. Thieberger et al, "The electron backscattering detector (eBSD), a new tool for the precise mutual alignment of the electron and ion beams in electron lenses", International Beam Instrumentation Conference, Monterey, CA (2014).

[17] P. Thieberger et al, "Scattered electrons as possible probes for beam halo diagnostics", Workshop on Beam Halo Monitoring, Menlo Park, CA (2014).

[18] M. Sapinski, "Feasibility study of a novel, fast read-out system for an ionization profile monitor based on a hybrid pixel detector", MOPAB41, HB2014 proceedings.

[19] M. Sapinski, "Investigation of the effect of beam space-charge on electron trajectories in ionization profile monitors", MOPAB42, HB2014 proceedings.

[20] J. Sun, "Simulation of a new beam current monitor under heavy heat load", MOPAB47, HB2014 proceedings.

[21] J. Sun, "Design of a new beam current monitor under heavy heat load", MOPAB48, HB2014 proceedings.

[22] G. Skoro, "Material response to high power beams", THO4AB01, HB2014 proceedings.

[23] A. Konobeev, "DPA and gas production in intermediate and high energy particle interactions with accelerator components", THO4AB02, HB2014 proceedings.

[24] A. Bertarelli, "Novel materials for collimators at LHC and its upgrades", THO4AB03, HB2014 proceedings.

## List of Authors

**Bold** papercodes indicate primary authors

### — A —

| | |
|---|---|
| Abbon, P. | TU02AB02 |
| Abelleira, J.L. | **M0PAB02**, WE04AB02 |
| Abeyratne, S. | **M0PAB21** |
| Adams, D.J. | M0PAB38, M0PAB40, TU03LR03, WE01LR02, **TH03LR02** |
| Adamson, P. | TH04LR04 |
| Adonin, A. | WE01AB01 |
| Akino, A. | TU02AB04 |
| Aleksandrov, A.V. | WE03AB02, TH02LR01 |
| Alessi, J.G. | TH01AB03 |
| Altinbas, Z. | TH03LR03 |
| Amundson, J.F. | TU02LR01 |
| Angoletta, M.E. | TU01AB02 |
| Arduini, G. | M0XLR01, TH01LR01 |
| Argyropoulos, T. | TU01AB02, **TH04LR01**, TH04LR02 |
| Aumon, S. | TH01LR03 |

### — B —

| | |
|---|---|
| Baartman, R.A. | **M0ZLR10** |
| Baily, S.A. | M0PAB30 |
| Balhan, B. | WE04AB02 |
| Banfi, D. | M0XLR01 |
| Barranco, J. | M0XLR01 |
| Bartmann, W. | M0PAB02, **WE04AB02** |
| Bartosik, H. | M0XLR01, TH01LR01 |
| Baudrenghien, P. | TU01AB02, TH04LR03 |
| Beaudoin, B. | TU04LR03 |
| Beebe, E.N. | TH01AB03 |
| Bellan, L. | TU04AB01 |
| Benedetto, E. | M0XLR01, WE04AB02, TH01LR01, **TH04LR05** |
| Bernal, S. | TU04LR03 |
| Bertarelli, A. | **TH04AB03** |
| Bertrand, P. | **TU03AB03** |
| Bin, D.T. | TU03AB01 |
| Blas, A. | M0PAB10, TU01AB02 |
| Blaskiewicz, M. | M0PAB08, **WE01LR01** |
| Bohl, T. | TU01AB02 |
| Boine-Frankenheim, O. | M0PAB11, WE01LR02, WE04LR03 |
| Borburgh, J. | M0PAB02, WE04AB02 |
| Bracco, C. | WE04AB02, TH04LR05 |
| Bravin, E. | M0PAB02 |
| Brennan, J.M. | M0PAB08 |
| Bruce, R. | M0XLR01, M0PAB43 |
| Brüning, O.S. | M0XLR01 |
| Bruhwiler, D.L. | TU04LR02 |
| Bruno, D. | TH03LR03 |
| Bultman, N.K. | M0ZLR07 |
| Bustinduy, I. | **TU01AB04** |
| Butterworth, A.C. | TU01AB02 |

### — C —

| | |
|---|---|
| Calabretta, L. | TU04AB01 |
| Calaga, R. | M0XLR01 |
| Campelo, J.V. | TH04LR02 |
| Capista, D. | TH04LR04 |
| Carli, C. | WE04AB02 |
| Carra, F. | TH04AB03 |
| Casagrande, F. | M0ZLR07 |
| Cerutti, F. | M0XLR01 |
| Chalykh, B.B. | TU04AB01 |
| Chauvin, N. | **TU02AB02**, WE04LR01, **TH02LR04** |
| Cheng, C. | TU03AB01 |
| Chin, Y.H. | M0PAB23, TH02AB02, **TH03AB01**, FR01AU01 |
| Compton, C. | M0ZLR07 |
| Comunian, M. | TU04AB01, WE04LR01, TH02LR04, FR02AU01 |
| Costanzo, M.R. | TH03LR03 |
| Cousineau, S.M. | WE02LR02, **WE03AB02**, TH02LR01 |

### — D —

| | |
|---|---|
| Dallocchio, A. | TH04AB03 |
| Damerau, H. | M0XLR01, **TU01AB02**, TH01LR01 |
| Danilov, V.V. | TU04LR02, WE03AB02, TH02LR01 |
| Davidson, K.D. | M0ZLR07 |
| De Maria, R. | **M0XLR01** |
| Dehning, B. | M0PAB41, M0PAB42 |
| Di Giovanni, G.P. | WE04AB02 |
| Dickerson, C. | **TU03AB02** |
| Dixon, K. | M0ZLR07 |
| Dölling, R. | FR02AU02 |
| Drees, K.A. | M0PAB05 |
| Drewyor, B. | M0ZLR07 |
| Droba, M. | M0PAB19, WE04LR02 |
| Du, C.T. | TU03AB01, TH02LR02 |
| Du, L. | TU03AB01, **TH02LR02** |
| Du, X. | WE01AB01 |
| Duperrex, P.-A. | M0PAB47, M0PAB48 |

### — E —

| | |
|---|---|
| Eddy, N. | TH04LR04 |
| Eldred, J.S. | **M0PAB12**, **TH04LR04** |
| Erdelyi, B. | M0PAB21, M0PAB31 |
| Eshraqi, M. | M0PAB18, **TU01LR03** |
| Esposito, L.S. | M0XLR01 |
| Esteban Müller, J.F. | TH04LR02 |

### — F —

| | |
|---|---|
| Facco, A. | M0ZLR07 |
| Fang, X. | TH02AB01 |
| Fartoukh, S.D. | M0XLR01 |

| | |
|---|---|
| Feng, Y.C. | TH02AB01 |
| Feyzi, F. | M0ZLR07 |
| Findlay, A. | TU01AB02 |
| Fischer, U. | TH04AB02 |
| Fischer, W. | **TH03LR03** |
| Fitterer, M. | M0XLR01 |
| Forte, V. | WE04AB02, TH01LR01, TH04LR05 |
| Fox, J.D. | M0PAB24, TH03AB04 |
| Franchetti, G. | **TH01LR03**, FR01AU03 |
| Fraser, M.A. | TH01AB01 |
| Fu, S. | TU01LR02 |
| Fukunishi, N. | **M0ZLR09** |
| Fukushima, K. | TU02LR03 |

**— G —**

| | |
|---|---|
| Ganni, V. | M0ZLR07 |
| Garcia, F.G. | WE03AB02 |
| Garlaschè, M. | TH04AB03 |
| Garoby, R. | M0XLR01, TU01AB02 |
| Gee, A.J. | **M0PAB31** |
| Geng, H. | TH02LR03 |
| Gentini, L. | TH04AB03 |
| Gibson, P.E. | M0ZLR07 |
| Gilardoni, S.S. | M0XLR01, M0PAB10, TU01AB02, WE04AB02, **TH01LR01**, TH01LR03, **FR01AU04** |
| Giovannozzi, M. | M0XLR01, TH01LR01 |
| Glasmacher, T . | **M0O1LR01**, M0ZLR07 |
| Goddard, B. | M0XLR01, WE04AB02, TH01LR01 |
| Gorini, B. | M0XLR01 |
| Gorlov, T.V. | WE03AB02, **TH02LR01** |
| Gradassi, P. | TH04AB03 |
| Gräwer, G. | WE04AB02 |
| Groening, L. | **WE01AB01**, **WE03LR04** |
| Grudiev, A. | **WE04AB01** |
| Gu, X. | TH03LR03 |
| Guan, W.Q. | TU03AB01 |
| Guan, X. | TU03AB01, TH02LR02 |
| Guinchard, M. | TH04AB03 |
| Guo, J.W. | TH02AB01 |

**— H —**

| | |
|---|---|
| Haber, I. | TU04LR03 |
| Hähnel, H. | WE01AB01 |
| Hancock, S. | TU01AB02, TH01LR01 |
| Hanke, K. | M0XLR01, WE04AB02, TH01LR01 |
| Hara, K. | TU01AB01 |
| Harada, H. | M0PAB44, WE02AB03, TH01LR02, **TH03AB02**, TH03AB03 |
| Hasegawa, K. | TU01AB01 |
| Hashimoto, Y. | **TU02AB04**, WE02AB03 |
| Hatakeyama, S. | WE02AB03 |
| Hayashi, N. | WE02AB03 |
| He, Y. | M0YLR05, WE03LR03, FR01AU02 |
| He, Y. | TU03AB01 |
| He, Z.Q. | **M0PAB35**, TU04AB03 |

| | |
|---|---|
| Henderson, S. | **M0XLR03** |
| Hermes, P.D. | **M0PAB43** |
| Hock, J. | TH03LR03 |
| Höfle, W. | M0PAB24, TU01AB02, TH03AB04 |
| Hoff, L.T. | M0ZLR07 |
| Hofmann, I. | **WE04LR03**, FR01AU02 |
| Holland, K. | M0ZLR07 |
| Hollinger, R. | WE01AB01 |
| Holmes, J.A. | **WE02LR02**, FR01AU01 |
| Holzer, E.B. | **WE02AB04** |
| Hotchi, H. | **M0XLR02**, WE02AB03, TH03AB02, TH03AB03 |
| Hourican, M. | WE04AB02 |
| Huang, L. | **TH02AB03** |
| Huang, M.Y. | **WE04AB03** |
| Huang, N. | WE04AB03 |
| Hui, G. | TU03AB01 |
| Huschauer, A. | WE04AB02, TH01LR01, TH01LR03 |
| Hwang, J.G. | TU04AB02 |

**— I —**

| | |
|---|---|
| Iadarola, G. | M0XLR01 |
| Igarashi, S. | M0PAB51, TH01LR02 |
| Ikegami, M. | M0ZLR07, **TU04AB03** |
| Irie, Y. | TH02AB02 |
| Ito, K. | TU02LR03 |

**— J —**

| | |
|---|---|
| Jain, A.K. | TH03LR03 |
| Jang, H. | TU04AB02 |
| Jang, J.-H. | TU04AB02 |
| Jansson, A. | **TU02AB01** |
| Jeon, D. | **TU04AB02** |
| Ji, Y. | TH04LR04 |
| Jiang, C. | TU03AB01 |
| Johnson, M.J. | M0ZLR07 |
| Jones, B. | M0PAB04, M0PAB38, M0PAB40, TU03LR03, WE01LR02, TH03LR02 |
| Jones, S. | M0ZLR07 |
| Jowett, J.M. | M0PAB43 |

**— K —**

| | |
|---|---|
| Kamigaito, O. | FR02AU01 |
| Karpov, I. | **M0PAB11** |
| Keller, O. | **M0PAB41** |
| Kelliher, D.J. | **M0PAB26**, M0PAB27 |
| Kelly, M.P. | M0ZLR07 |
| Kester, O.K. | M0PAB19, WE03LR04 |
| Kesting, F. | TH01LR03 |
| Kim, E.-S. | TU04AB02 |
| Kim, H.J. | TU04AB02 |
| Kinsho, M. | M0PAB44 |
| Kishek, R.A. | TU04LR02, **TU04LR03** |
| Klaproth, S. | M0PAB19 |
| Koeth, T.W. | TU04LR03 |

**List of Authors**

| | |
|---|---|
| Kolski, J.S. | **MOPAB46**, TU03LR01 |
| Konobeev, A. | **TH04AB02** |
| Kornilov, V. | MOPAB11, MOPAB38, TU03LR03, **WE01LR02** |
| Koseki, T. | TH01LR02 |
| Kotrle, G. | MOPAB48 |
| Kourbanis, I. | TH04LR04 |
| Kowalska, M. | TH01LR01 |

### — L —

| | |
|---|---|
| Lamont, M. | MOXLR01 |
| Lasheen, A. | **TH04LR02** |
| Laxdal, R.E. | MOZLR07 |
| Li, J. | TU03AB01 |
| Li, K.S.B. | WE04AB01, TH03AB04 |
| Li, Z. | TU02LR01 |
| Li, Z. | TH02LR03 |
| Lidia, S.M. | MOZLR07, TU04AB03, **WE02AB01** |
| Liebermann, H. | TH01LR03 |
| Lindroos, M. | **MOYLR06** |
| Liu, C. | **MOPAB05**, **MOPAB08** |
| Liu, H.C. | **TU01LR02** |
| Liu, S.H. | WE03LR03 |
| Liu, Y. | WE03AB02 |
| Liu, Y.D. | TH02AB03 |
| Liu, Z. | MOPAB35, TU04AB03 |
| Lu, W. | TH02AB01 |
| Lund, S.M. | **MOPAB17**, TU04AB03, **FR01AU03** |
| Luo, Y. | TH03LR03 |
| Luttrell, N.F. | WE03AB02 |

### — M —

| | |
|---|---|
| Macek, R.J. | **TU03LR01** |
| Machicoane, G. | MOZLR07 |
| Machida, S. | MOPAB26, MOPAB27, **FR01AU01** |
| Magan, M. | TU01AB04 |
| Maier, M.T. | WE03LR04 |
| Marroncle, J. | TU02AB02 |
| Marti, F. | MOZLR07, TU04AB03, **FR02AU01** |
| Marusic, A. | MOPAB05 |
| Mastoridis, T. | TH04LR03 |
| McAteer, M. | TH01LR01 |
| Meddahi, M. | MOXLR01, WE04AB02, TH01LR01 |
| Meigo, S.I. | TH03AB02 |
| Meng, C. | TH02LR03 |
| Menshov, A.A. | WE03AB02 |
| Mernick, K. | MOPAB08, WE01LR01 |
| Métral, E. | MOXLR01, TH01LR01 |
| Meusel, O. | MOPAB19, WE04LR02 |
| Mi, C. | TH03LR03 |
| Michnoff, R.J. | TH03LR03 |
| Mickat, S. | WE01AB01 |
| Mikulec, B. | MOXLR01, WE04AB02, TH01LR01, TH04LR05 |
| Miller, S.J. | MOZLR07 |
| Miller, T.A. | TH03LR03 |

| | |
|---|---|
| Minty, M.G. | MOPAB05, MOPAB08, **FR02AU02** |
| Mitsuhashi, T.M. | TU02AB04 |
| Miyamoto, R. | **MOPAB18**, TU01AB04 |
| Mokhov, N.V. | FR02AU02 |
| Molendijk, J.C. | TU01AB02 |
| Molodozhentsev, A.Y. | **MOPAB51** |
| Montag, C. | MOPAB05, MOPAB08, **TH03LR04** |
| Montesinos, E. | TU01AB02 |
| Montgomery, E.J. | TU04LR03 |
| Morris, D. | MOZLR07 |
| Morris, D.K. | TH04LR04 |
| Mounet, N. | MOXLR01 |
| Mustapha, B. | TU03AB02, **TH01AB01** |

### — N —

| | |
|---|---|
| Nagaitsev, S. | **TU04LR01**, TU04LR02 |
| Nakamura, K.G. | TH03AB01 |
| Ng, C.-K. | TU02LR01 |
| Nghiem, P.A.P. | TU02AB02, **WE04LR01**, TH02LR04 |
| Nolen, J.A. | MOZLR07 |
| Noll, D. | MOPAB19, **WE04LR02** |
| Nomura, M. | TU01AB01 |

### — O —

| | |
|---|---|
| Obina, T. | TH03AB01 |
| Ohmi, K. | **WE02LR03** |
| Ohmori, C. | **TU01AB01** |
| Okabe, K. | MOPAB44, WE02AB03 |
| Okada, M. | TH03AB01 |
| Okamoto, H. | **TU02LR03**, FR01AU03 |
| Okano, T. | TU02LR03 |
| Okuno, H. | **TH01AB02** |
| Oliver, C. | WE04LR01, TH02LR04 |
| Omet, C. | TH01LR03 |
| Omori, Y. | TU02AB04 |
| Ondreka, D. | TH01LR03 |
| Orzhekhovskaya, A. | WE01AB01 |
| Ostroumov, P.N. | MOZLR07, TU03AB02, TH01AB01 |
| Otsu, S. | TU02AB04 |

### — P —

| | |
|---|---|
| Palmieri, A. | **TH01AB04** |
| Pang, X. | **MOPAB30** |
| Paoluzzi, M.M. | TU01AB02 |
| Papaphilippou, Y. | MOXLR01, TH01LR01 |
| Pardo, R.C. | TU03AB02 |
| Payne, S.J. | TU03LR03 |
| Pei, S. | TH02LR03 |
| Peng, J. | TU01LR02 |
| Peng, S. | MOZLR07 |
| Perrelet, D. | TU01AB02 |
| Perry, A. | TH01AB01 |
| Pieloni, T. | MOXLR01 |
| Pikin, A.I. | **TH01AB03**, TH03LR03 |
| Pine, B.G. | **MOPAB39**, MOPAB40, TU03LR03, |

**List of Authors**

| | |
|---|---|
| | WE01LR02, TH03LR02 |
| Pisent, A. | **TU04AB01** |
| Plum, M.A. | **WE03LR01**, WE03AB02, TH02LR01, |
| | FR01AU04 |
| Popielarski, J. | M0ZLR07 |
| Popielarski, L. | M0ZLR07 |
| Pozdeyev, G. | M0ZLR07, M0PAB17, TU04AB03, |
| | **WE01AB03** |
| Prior, C.R. | M0PAB26, M0PAB27, TH03LR02 |

### — Q —

| | |
|---|---|
| Qian, C. | TH02AB01 |
| Qiang, J. | **M0PAB29**, TU02LR01, **TU02LR02** |
| Qiu, J. | WE04AB03 |
| Quaranta, E. | TH04AB03 |
| Quartullo, D. | TH04LR02 |

### — R —

| | |
|---|---|
| Raginel, V. | TH04LR05 |
| Raich, U. | M0PAB02 |
| Rakhman, A. | WE03AB02 |
| Raparia, D. | **FR01AU02** |
| Ratzinger, U. | M0PAB19, WE01AB01, WE04LR02 |
| Redaelli, S. | M0XLR01, M0PAB43, TH04AB03 |
| Rees, G.H. | TH03LR02 |
| Ren, H.T. | M0PAB17 |
| Rivetta, C.H. | M0PAB24, **TH03AB04** |
| Rock, S.M. | M0PAB24 |
| Rogers, C.T. | M0PAB27 |
| Roser, T. | **M0YLR04** |
| Rossi, A. | TH04AB03 |
| Rossi, C. | TU01AB02 |
| Rossi, L. | M0XLR01 |
| Ruisard, K.J. | TU04LR03 |
| Rumolo, G. | M0XLR01, WE04AB02, TH01LR01, |
| | TH04LR05 |
| Russo, A.D. | TU04AB01 |
| Russo, T. | M0ZLR07 |
| Rybarcyk, L. | M0PAB30 |

### — S —

| | |
|---|---|
| Sacristan De Frutos, O. | TH04AB03 |
| Saha, P.K. | WE02AB03, TH02AB02, TH03AB02, |
| | **TH03AB03** |
| Saito, K. | M0ZLR07 |
| Sakai, H. | TU02AB04 |
| Salvachua, B. | M0PAB43 |
| Samms, T. | TH03LR03 |
| Sapinski, M. | M0PAB41, M0PAB42, **WE02AB02** |
| Sato, Y. | **TH01LR02**, M0PAB51 |
| Schaumburg, H.D. | M0PAB21 |
| Schenk, M. | WE04AB01 |
| Schlitt, B. | WE01AB01 |
| Schmidt, F. | **WE02LR01**, TH01LR03 |
| Schnase, A. | TU01AB01 |

| | |
|---|---|
| Schreiber, G. | WE01AB01 |
| Schulte, K. | **M0PAB19**, WE04LR02 |
| Scrivens, R. | TH01AB03 |
| Seiya, K. | **TU03LR02** |
| Sermeus, L. | WE04AB02 |
| Shaposhnikova, E.N. | M0XLR01, TU01AB02, TH01LR01, |
| | TH04LR02, TH04LR03 |
| Sheehy, S.L. | M0PAB26, **M0PAB27** |
| Shimada, T. | TU01AB01 |
| Shin, I. | TU04AB02 |
| Shirakata, M.J. | TH01LR02 |
| Shishlo, A.P. | WE02LR02, WE03LR01, WE03AB02 |
| Shobuda, Y. | **M0PAB23**, **TH02AB02**, TH03AB01 |
| Shornikov, A. | TH01AB03 |
| Simeoni, W. | WE04LR01 |
| Singh, R. | TH01LR03 |
| Škoro, G. | **TH04AB01** |
| Smith, H. V. | **M0PAB04**, M0PAB40, TU03LR03, |
| | TH03LR02 |
| Smith, K.S. | M0PAB08 |
| Sordo, F. | TU01AB04 |
| Spiller, P.J. | **M0ZLR08** |
| Stancari, G. | **WE03AB01** |
| Steerenberg, R. | WE04AB02 |
| Stem, W.D. | TU04LR03 |
| Sterbini, G. | M0XLR01, **M0PAB10**, WE04AB02, |
| | TH01LR01 |
| Stern, E.G. | TU02LR01 |
| Sun, J.L. | **M0PAB47**, **M0PAB48** |
| Sun, L.T. | **TH02AB01** |
| Sutter, D.F. | TU04LR03 |
| Swann, L.S. | M0PAB41 |
| Szoke, Z. | WE04AB02 |

### — T —

| | |
|---|---|
| Takano, J. | TH01LR02, M0PAB51 |
| Takata, K. | M0PAB23 |
| Takayanagi, T. | TH03AB03 |
| Takeda, Y. | WE03AB02 |
| Tamura, F. | TU01AB01, TH01LR02, TH03AB02 |
| Tan, Y. | TH03LR03 |
| Tang, C.-X. | TU03AB01, TH02LR02 |
| Tang, J.Y. | TH02LR03 |
| Tang, R. | TU03AB01, TH02LR02 |
| Tejima, M. | TU02AB04 |
| Than, R. | TH03LR03 |
| Thangaraj, J.C.T. | TH04LR04 |
| Thieberger, P. | TH03LR03 |
| Thomsen, H.D. | M0PAB18 |
| Tiede, R. | WE01AB01 |
| Timko, H. | TH04LR02, **TH04LR03** |
| Tobiyama, M. | TH03AB01 |
| Toda, M. | TU01AB01 |
| Todesco, E. | M0XLR01 |
| Tomás, R. | M0XLR01 |
| Toyama, T. | M0PAB23, TU02AB04, WE02AB03, |

**List of Authors**

| | |
|---|---|
| | TH02AB02, FR02AU02, TH03AB01 |
| Turgut, O. | **MOPAB24**, TH03AB04 |

**— U —**

| | |
|---|---|
| Uriot, D. | TU02AB02, WE04LR01, TH02LR04 |

**— V —**

| | |
|---|---|
| Valentino, G. | MOPAB43 |
| Valette, M. | WE04LR01 |
| Valishev, A. | MOXLR01, TU04LR02 |
| Vay, J.-L. | **TU02LR01** |
| Vilsmeier, D.M. | **MOPAB42** |
| Vormann, H. | WE01AB01 |

**— W —**

| | |
|---|---|
| Wang, B.C. | TU03AB01 |
| Wang, M.W. | TH02LR02 |
| Wang, S. | TU01LR02, **WE03AB03**, WE04AB03, TH02AB03, FR01AU04 |
| Wang, S.L. | TU03AB01 |
| Wang, X.W. | TU03AB01, TH02LR02 |
| Wang, Z.J. | **WE03LR03** |
| Warsop, C.M. | MOPAB38, MOPAB39, **MOPAB40**, **TU03LR03**, WE01LR02, TH03LR02 |
| Wasef, R. | WE04AB02, TH01LR01, TH01LR03 |
| Webb, S.D. | **TU04LR02** |
| Wei, J. | **MOZLR07**, MOPAB35, TU04AB03 |
| Wei, Y. | WE04AB02 |
| Wenander, F.J.C. | TH01AB03 |
| Weterings, W.J.M. | WE04AB02 |
| White, S.M. | TH03LR03 |
| Wiesner, C. | WE04LR02 |
| Wilcox, C.C. | MOPAB40 |
| Williamson, R.E. | **MOPAB38**, MOPAB40, TU03LR03, WE01LR02, TH03LR02 |
| Wittenburg, K. | **TU02AB03** |

| | |
|---|---|
| Wollmann, D. | MOPAB43 |

**— X —**

| | |
|---|---|
| Xiao, C. | WE01AB01 |
| Xiao, C. | WE03LR04 |
| Xiao, Y.S. | TU03AB01 |
| Xing, Q.Z. | **TU03AB01**, TH02LR02 |
| Xu, T. | MOZLR07 |

**— Y —**

| | |
|---|---|
| Yamada, S. | TH01LR02 |
| Yamamoto, K. | **WE02AB03** |
| Yamamoto, M. | TU01AB01, TH02AB02 |
| Yamamoto, N. | TH01LR02 |
| Yamazaki, Y. | MOZLR07, TU04AB03 |
| Yan, F. | **TH02LR03** |
| Yang, M.-J. | TH04LR04 |
| Yang, Y. | TH02AB01 |
| Yang, Y.G. | TU03AB01 |
| Yoshii, M. | TU01AB01 |
| Yoshimoto, M. | **MOPAB44**, WE02AB03 |

**— Z —**

| | |
|---|---|
| Zerbe, K. | MOPAB19 |
| Zhang, H.Y. | TU03AB01 |
| Zhang, T.J. | **WE01AB02** |
| Zhang, W.H. | TH02AB01 |
| Zhang, X.Z. | TH02AB01 |
| Zhang, Y. | MOPAB35, TU04AB03 |
| Zhao, H.W. | **MOYLR05**, TH02AB01 |
| Zhao, Q. | MOPAB17, **TU01LR01**, TU04AB03 |
| Zheng, S.X. | TU03AB01, TH02LR02 |
| Zheng, Z. | MOPAB35 |
| Zimmermann, F. | MOXLR01 |
| Zinkann, G.P. | TU03AB02 |
| Zwaska, R.M. | MOPAB12, **TU01AB03**, TH04LR04 |

# Institutes List

**ANL**
Argonne, Illinois, USA
- Dickerson, C.
- Erdelyi, B.
- Henderson, S.
- Kelly, M.P.
- Mustapha, B.
- Nolen, J.A.
- Ostroumov, P.N.
- Pardo, R.C.
- Zinkann, G.P.

**BNL**
Upton, Long Island, New York, USA
- Alessi, J.G.
- Altinbas, Z.
- Beebe, E.N.
- Blaskiewicz, M.
- Brennan, J.M.
- Bruno, D.
- Costanzo, M.R.
- Drees, K.A.
- Fischer, W.
- Gu, X.
- Hock, J.
- Jain, A.K.
- Liu, C.
- Luo, Y.
- Marusic, A.
- Mernick, K.
- Mi, C.
- Michnoff, R.J.
- Miller, T.A.
- Minty, M.G.
- Montag, C.
- Pikin, A.I.
- Raparia, D.
- Roser, T.
- Samms, T.
- Smith, K.S.
- Tan, Y.
- Than, R.
- Thieberger, P.
- White, S.M.

**CalPoly**
San Luis Obispo, California, USA
- Mastoridis, T.

**CEA/DSM/IRFU**
France
- Chauvin, N.
- Marroncle, J.
- Nghiem, P.A.P.

**CEA/IRFU**
Gif-sur-Yvette, France

- Abbon, P.
- Uriot, D.
- Valette, M.

**CERN**
Geneva, Switzerland
- Abelleira, J.L.
- Angoletta, M.E.
- Arduini, G.
- Argyropoulos, T.
- Balhan, B.
- Banfi, D.
- Barranco, J.
- Bartmann, W.
- Bartosik, H.
- Baudrenghien, P.
- Benedetto, E.
- Bertarelli, A.
- Blas, A.
- Bohl, T.
- Borburgh, J.
- Bracco, C.
- Bravin, E.
- Bruce, R.
- Brüning, O.S.
- Butterworth, A.C.
- Calaga, R.
- Campelo, J.V.
- Carli, C.
- Carra, F.
- Cerutti, F.
- Dallocchio, A.
- Damerau, H.
- De Maria, R.
- Dehning, B.
- Di Giovanni, G.P.
- Esposito, L.S.
- Esteban Müller, J.F.
- Fartoukh, S.D.
- Findlay, A.
- Fitterer, M.
- Forte, V.
- Fraser, M.A.
- Garlaschè, M.
- Garoby, R.
- Gentini, L.
- Gilardoni, S.S.
- Giovannozzi, M.
- Goddard, B.
- Gorini, B.
- Gradassi, P.
- Grudiev, A.
- Gräwer, G.
- Guinchard, M.
- Hancock, S.
- Hanke, K.
- Hermes, P.D.
- Holzer, E.B.

- Hourican, M.
- Huschauer, A.
- Höfle, W.
- Iadarola, G.
- Jowett, J.M.
- Keller, O.
- Kowalska, M.
- Lamont, M.
- Lasheen, A.
- Li, K.S.B.
- McAteer, M.
- Meddahi, M.
- Mikulec, B.
- Molendijk, J.C.
- Montesinos, E.
- Mounet, N.
- Métral, E.
- Paoluzzi, M.M.
- Papaphilippou, Y.
- Perrelet, D.
- Pieloni, T.
- Quaranta, E.
- Quartullo, D.
- Raginel, V.
- Raich, U.
- Redaelli, S.
- Rossi, A.
- Rossi, C.
- Rossi, L.
- Rumolo, G.
- Sacristan De Frutos, O.
- Salvachua, B.
- Sapinski, M.
- Schmidt, F.
- Scrivens, R.
- Sermeus, L.
- Shaposhnikova, E.N.
- Shornikov, A.
- Steerenberg, R.
- Sterbini, G.
- Swann, L.S.
- Szoke, Z.
- Timko, H.
- Todesco, E.
- Tomás, R.
- Valentino, G.
- Vilsmeier, D.M.
- Wasef, R.
- Wei, Y.
- Wenander, F.J.C.
- Weterings, W.J.M.
- Wollmann, D.
- Zimmermann, F.

**CIAE**
Beijing, People's Republic of China
- Zhang, T.J.

**CIEMAT**
Madrid, Spain

- Oliver, C.

**DESY**
Hamburg, Germany
- Wittenburg, K.

**ESS Bilbao**
Bilbao, Spain
- Bustinduy, I.
- Magan, M.
- Sordo, F.

**ESS**
Lund, Sweden
- Eshraqi, M.
- Jansson, A.
- Lindroos, M.
- Miyamoto, R.

**Fermilab**
Batavia, Illinois, USA
- Adamson, P.
- Amundson, J.F.
- Capista, D.
- Eddy, N.
- Eldred, J.S.
- Kourbanis, I.
- Mokhov, N.V.
- Morris, D.K.
- Nagaitsev, S.
- Seiya, K.
- Stancari, G.
- Stern, E.G.
- Thangaraj, J.C.T.
- Valishev, A.
- Yang, M.-J.
- Zwaska, R.M.

**FRIB**
East Lansing, Michigan, USA
- Bultman, N.K.
- Casagrande, F.
- Compton, C.
- Davidson, K.D.
- Drewyor, B.
- Facco, A.
- Feyzi, F.
- Gibson, P.E.
- Glasmacher, T .
- He, Z.Q.
- Hoff, L.T.
- Holland, K.
- Ikegami, M.
- Johnson, M.J.
- Jones, S.
- Lidia, S.M.
- Liu, Z.

**Institutes List**

- Lund, S.M.
- Machicoane, G.
- Marti, F.
- Miller, S.J.
- Morris, D.
- Nolen, J.A.
- Peng, S.
- Popielarski, J.
- Popielarski, L.
- Pozdeyev, G.
- Ren, H.T.
- Russo, T.
- Saito, K.
- Wei, J.
- Xu, T.
- Yamazaki, Y.
- Zhang, Y.
- Zhao, Q.
- Zheng, Z.

**GANIL**
Caen, France
- Bertrand, P.

**GSI**
Darmstadt, Germany
- Adonin, A.
- Aumon, S.
- Boine-Frankenheim, O.
- Du, X.
- Franchetti, G.
- Groening, L.
- Hofmann, I.
- Hollinger, R.
- Kester, O.K.
- Kesting, F.
- Kornilov, V.
- Liebermann, H.
- Maier, M.T.
- Mickat, S.
- Omet, C.
- Ondreka, D.
- Orzhekhovskaya, A.
- Schlitt, B.
- Schnase, A.
- Schreiber, G.
- Singh, R.
- Spiller, P.J.
- Vormann, H.
- Xiao, C.

**HU/AdSM**
Higashi-Hiroshima, Japan
- Fukushima, K.
- Ito, K.
- Okamoto, H.
- Okano, T.

**IAP**
Frankfurt am Main, Germany
- Droba, M.
- Hähnel, H.
- Kester, O.K.
- Klaproth, S.
- Meusel, O.
- Noll, D.
- Ratzinger, U.
- Schulte, K.
- Tiede, R.
- Wiesner, C.
- Zerbe, K.

**IBS**
Daejeon, Republic of Korea
- Jang, H.
- Jang, J.-H.
- Jeon, D.
- Kim, H.J.
- Shin, I.

**IF-UFRGS**
Porto Alegre, Brazil
- Simeoni, W.

**IHEP**
Beijing, People's Republic of China
- Fu, S.
- Geng, H.
- Huang, L.
- Huang, M.Y.
- Huang, N.
- Liu, H.C.
- Liu, Y.D.
- Meng, C.
- Pei, S.
- Peng, J.
- Qiu, J.
- Tang, J.Y.
- Wang, S.
- Yan, F.

**IIT**
Chicago, Illinois, USA
- Ji, Y.

**Illinois Institute of Technology**
Chicago, Illlinois, USA
- Perry, A.

**IMP**
Lanzhou, People's Republic of China
- Fang, X.
- Feng, Y.C.
- Guo, J.W.
- He, Y.
- Liu, S.H.
- Lu, W.

**Institutes List**

- Qian, C.
- Sun, L.T.
- Wang, Z.J.
- Yang, Y.
- Zhang, W.H.
- Zhang, X.Z.
- Zhao, H.W.

**Indiana University**
Bloomington, Indiana, USA
- Eldred, J.S.

**INFN/LNL**
Legnaro (PD), Italy
- Bellan, L.
- Comunian, M.
- Facco, A.
- Palmieri, A.
- Pisent, A.

**INFN/LNS**
Catania, Italy
- Calabretta, L.
- Russo, A.D.

**Institute of High Energy Physics (IHEP)**
People's Republic of China
- Wang, S.L.

**ISA**
Aarhus, Denmark
- Thomsen, H.D.

**ITEP**
Moscow, Russia
- Chalykh, B.B.

**J-PARC, KEK & JAEA**
Ibaraki-ken, Japan
- Hashimoto, Y.
- Koseki, T.
- Sato, Y.
- Takano, J.
- Tejima, M.
- Toyama, T.
- Yamada, S.
- Yamamoto, N.

**JAEA/J-PARC**
Tokai-Mura, Naka-Gun, Ibaraki-Ken, Japan
- Harada, H.
- Hatakeyama, S.
- Hayashi, N.
- Hotchi, H.
- Kinsho, M.

- Meigo, S.I.
- Nomura, M.
- Okabe, K.
- Saha, P.K.
- Shimada, T.
- Shirakata, M.J.
- Shobuda, Y.
- Takayanagi, T.
- Tamura, F.
- Yamamoto, K.
- Yamamoto, M.
- Yoshimoto, M.

**JLab**
Newport News, Virginia, USA
- Dixon, K.
- Ganni, V.

**KEK**
Ibaraki, Japan
- Chin, Y.H.
- Hara, K.
- Hasegawa, K.
- Igarashi, S.
- Irie, Y.
- Mitsuhashi, T.M.
- Molodozhentsev, A.Y.
- Obina, T.
- Ohmi, K.
- Ohmori, C.
- Okada, M.
- Sato, Y.
- Takano, J.
- Takata, K.
- Takeda, Y.
- Tobiyama, M.
- Toda, M.
- Toyama, T.
- Yoshii, M.

**KIT**
Eggenstein-Leopoldshafen, Germany
- Fischer, U.
- Konobeev, A.

**KNU**
Deagu, Republic of Korea
- Hwang, J.G.
- Kim, E.-S.

**Kyoto University**
Kyoto, Japan
- Nakamura, K.G.

**LANL**
Los Alamos, New Mexico, USA
- Baily, S.A.

**Institutes List**

- Kolski, J.S.
- Macek, R.J.
- Pang, X.
- Rybarcyk, L.

**LBNL**
Berkeley, California, USA
- Qiang, J.
- Vay, J.-L.

**LHEP**
Bern, Switzerland
- Schenk, M.

**Mitsubishi Electric System & Service Co., Ltd**
Tsukuba, Japan
- Akino, A.
- Omori, Y.
- Otsu, S.
- Sakai, H.

**NINT**
Xi'an, People's Republic of China
- Wang, B.C.

**Northern Illinois University**
DeKalb, Illinois, USA
- Abeyratne, S.
- Erdelyi, B.
- Gee, A.J.
- Schaumburg, H.D.

**NUCTECH**
Beijing, People's Republic of China
- Guan, W.Q.
- He, Y.
- Li, J.

**ORNL**
Oak Ridge, Tennessee, USA
- Aleksandrov, A.V.
- Cousineau, S.M.
- Danilov, V.V.
- Gorlov, T.V.
- Holmes, J.A.
- Liu, Y.
- Menshov, A.A.
- Plum, M.A.
- Rakhman, A.
- Shishlo, A.P.

**Politecnico/Milano**
Milano, Italy
- Quaranta, E.

**PSI**
Villigen PSI, Switzerland
- Duperrex, P.-A.
- Dölling, R.
- Kotrle, G.
- Sun, J.L.

**RadiaSoft LLC**
Boulder, Colorado, USA
- Bruhwiler, D.L.
- Webb, S.D.

**RIKEN Nishina Center**
Wako, Japan
- Fukunishi, N.
- Kamigaito, O.
- Okuno, H.

**SCU**
Chengdu, People's Republic of China
- Li, Z.

**SLAC**
Menlo Park, California, USA
- Fox, J.D.
- Li, Z.
- Ng, C.-K.
- Rivetta, C.H.
- Turgut, O.

**Stanford University**
Stanford, California, USA
- Rock, S.M.

**STFC/RAL/ASTeC**
Chilton, Didcot, Oxon, United Kingdom
- Kelliher, D.J.
- Machida, S.
- Prior, C.R.
- Rees, G.H.
- Rogers, C.T.
- Sheehy, S.L.

**STFC/RAL/ISIS**
Chilton, Didcot, Oxon, United Kingdom
- Adams, D.J.
- Jones, B.
- Payne, S.J.
- Pine, B.G.
- Škoro, G.
- Smith, H. V.
- Warsop, C.M.
- Wilcox, C.C.
- Williamson, R.E.

**TEMF, TU Darmstadt**
Darmstadt, Germany
- Boine-Frankenheim, O.
- Karpov, I.

**TRIUMF, Canada's National Laboratory for Particle and Nuclear Physics**
Vancouver, Canada
- Baartman, R.A.
- Laxdal, R.E.

**Tsinghua University**
Beijing, People's Republic of China
- Wang, M.W.

**TUB**
Beijing, People's Republic of China
- Bin, D.T.
- Cheng, C.
- Du, C.T.
- Du, L.
- Guan, X.
- Hui, G.
- Jiang, C.
- Tang, C.-X.
- Tang, R.
- Wang, X.W.
- Xiao, Y.S.
- Xing, Q.Z.
- Yang, Y.G.
- Zhang, H.Y.
- Zheng, S.X.

**UMD**
College Park, Maryland, USA
- Beaudoin, B.
- Bernal, S.
- Haber, I.
- Kishek, R.A.
- Koeth, T.W.
- Montgomery, E.J.
- Ruisard, K.J.
- Stem, W.D.
- Sutter, D.F.

**Université Blaise Pascal**
Clermont-Ferrand, France
- Forte, V.

**UTK**
Knoxville, Tennessee, USA
- Garcia, F.G.
- Luttrell, N.F.